SCHOLARLY PUBLICATIONS

A CURRENT AWARENESS BULLETIN
OF RESEARCH OUTPUT

@DTU

(86th Edition)

FEBRUARY 2019

BY: CENTRAL LIBRARY

DELHI TECHNOLOGICAL UNIVERSITY
(FORMERLY *DELHI COLLEGE OF ENGINEERING)*
GOVT. OF N.C.T. OF DELHI
SHAHBAD DAULATPUR, MAIN BAWANA ROAD
DELHI 110042

PREFACE

This is the **Eighty Sixth** Issue of Current Awareness Bulletin started by Delhi Technological University, Central Library. The aim of the bulletin is to compile, preserve and disseminate information published by the faculty, students and alumni for mutual benefits. The bulletin also aims to propagate the intellectual contribution of Delhi Technological University (DTU) as a whole to the academia.

The bulletin contains information resources available in the internet in the form of articles, reports, presentations published in international journals, websites, etc. by the faculty and students of DTU. The publications of faculty and student which are not covered in this bulletin may be because of the reason that the full text either was not accessible or could not be searched by the search engine used by the library for this purpose.

The learned faculty and students are requested to provide their uncovered publications to the library either through email or in CD, etc. to make the bulletin more comprehensive.

This issue contains the information published during **February, 2020**. The arrangement of the contents is alphabetical. The full text of the article which is either subscribed by the university or available in the web is provided in this bulletin.

Central Library

CONTENTS

1. A Binary PSO Approach for Improving the Performance of Wireless Sensor Networks, ***6.Ajay Kaushik***[1], ***6.Mononito Goswami***[1], ***6.Minkush Manuja***[1], ***3.S. Indu*** and ***3.Daya Gupta***[1], [1]Computer Science and [2]Electronics, DTU

2. A Blockchain Based Approach For An Efficient Secure KYC Process With Data Sovereignty, ***3.Dr. Manoj Kumar***[1], ***8.Nikhil***[1] and ***8.Parina Anand***[2], [1]Computer & [2]IT, DTU

3. A comparative study on bio-inspired algorithms for sentiment analysis, ***6.Ashima Yadav*** and ***3.Dinesh Kumar Vishwakarma***, IT, DTU

4. A dictionary matrix generation based compression and bitwise embedding mechanisms for ECG signal classification, ***6.Dinesh Kumar Atal*** and ***3.Mukhtiar Singh***, Electrical, DTU

5. A Novel Hot Spot Mitigation Circuit for Improved Reliability of PV Module, Santosh Ghosh, ***3.Vinod K. Yadav*** and Vivekananda Mukherjee, Electrical, DTU

6. Adaption of Power Gating in Positive Feedback Adiabatic Logic Circuits, ***6.Aarushi Mann***, ***8.1.Naman Malhotra*** and ***3.Neeta Pandey***, Electronics, DTU

7. Aluminum–air batteries: A viability review, ***6.P. Goel***, ***6.D. Dobhal*** and ***3.R.C. Sharma***, Chemistry, DTU

8. ANFIS-Based Control of Multi-objective Grid Connected Inverter and Energy Management, ***6.Shikha Gupta***, ***3.Rachana Garg*** and ***3.Alka Singh***, Electrical, DTU

9. Application of Fuzzy Logic for the Cost Overrun Analysis in Construction Projects, Savita Sharma, ***3.Pradeep K.Goyal*** and R.C.Chhipa, Civil, DTU

10. COMPUTATIONAL AEROACOUSTIC ANALYSIS OF FLAP DEFLECTION AND CAMBER OF AN AIRFOIL, ***8.Vishesh Kashyap***, Mechanical, DTU

11. COUNTERMEASURES AGAINST LOCAL SCOURING AT CIRCULAR BRIDGE PIERS USING COLLAR AND COMBINATION OF SLOT AND COLLAR, ***6.Geeta Devi*** and ***3.DR. Munendra Kumar***, Civil, DTU

12. Edge Detection using Ant Colony Optimization under Novel Intensity Mapping Function and Weighted Adaptive Threshold ***3.Akshi Kumar***[1] and ***6.Sahil Raheja***[2], [1]Computer and [2]IT, DTU

13. EFFECT OF DIFFERENT PORT ANGLE IN AN IC ENGINE ON THE SWIRL AND MASS FLOW RATE, ***7.1.ADHIRATH MANDAL*** and HAENGMUK CHO, Production, DTU

14. Electrochemical Study of Hydrothermally Synthesised Reduced MoS2 Layered Nanosheets, ***6.Ritika Khatri*** and ***3.Nitin K. Puri***, Physics, DTU

15. Electronically controllable third-order quadrature sinusoidal oscillator employing CMOS-OTAs, Komal, ***7.1.K. L. Pushkar*** and Ramnish Kumar, Electronics, DTU

16. Elucidating the Mechanism of Action of Crocin, a Therapeutic Agent for Cancer and Inflammation, ***7.1.Vani Venugopal*** and ***3.Dr. Asmita Das***, Biotechnology, DTU

17. Emerging Trends in Microfluidics Based Devices, ***8.Shipra Solanki***[1,2], ***3.Chandra M Pandey***[2], ***3.Rajinder K Gupta***[2] and ***3.Bansi D Malhotra***[1], [1]BioTech & [2]Chemistry, DTU

18. Importance of Energy Audit in Diesel Engine Fuelled with Biodiesel Blends: Review and Analysis, Sanjay Mohite and ***3.Sagar Maji***, Mechanical, DTU

19. Inadequate Earthing (Grounding) in Distribution Sector – Root Cause for Many Maladies, ***7.1.Dr. Rajesh Kumar Arora***, Electrical, DTU

20. Influence of processing parameters of friction stir welding on microstructure and mechanical properties of dissimilar aluminum alloys- A review, ***6.Husain Mehdi*** and ***3.R.S. Mishra***, Mechanical, DTU

21. Innovative Way of Understanding Test Results Obtained by Dga Test of Power Transformers Based on Ieee & Iec Standards, ***7.1.Dr. Rajesh Kumar Arora***, Electrical, DTU

22. Investigation of mechanical properties and heat transfer of welded joint of AA6061 and AA7075 using TIG+FSP welding approach, ***6.Husain Mehdi*** and ***3.R.S. Mishra***, Mech, DTU

23. Modeling of Mutually Coupled Switched Reluctance Motors Based on Net Flux Method, Siddharth Mehta, Md Ashfanoor Kabir, Iqbal Husain and ***8.1.Prerit Pramod***, Electical, DTU

24. Multimodal KDK Classifier For Automatic Classification of Movie Trailers, ***3.Prashant Giridhar Shambharkar[1]***, ***6.M N Doja[1]***, ***Dhruv Chande[2]***, ***6.Kartik Bansal[2]*** and ***6.Kunal Taneja[2]***, [1]Computer and [2]IT, DTU

25. Parametric Analysis of Smartphone Camera for a Low Cost Particle Image Velocimetry System, ***8.1.Vishesh Kashyap[1]***, ***8.1.Sushrut Kumar[1]***, Nehal Amit Jajal, Mrudang Mathur and ***3.Raj Kumar Singh[1]***, Mechanical, DTU

26. Performance evaluation of single effect Li/Br-H2O vapour absorption systems using multi cascading of vapour compression cycles for ultra-low temperature applications, ***3.Radhey Shyam Mishra***, Mechanical, DTU

27. Predicting the Remaining Useful Life of Ball Bearing Under Dynamic Loading Using Supervised Learning, ***6.S. Singh***, ***6.T. Agarwal***, ***3.G. Kumar***, O.M. Yadav, Mech, DTU

28. Quintessence behavior via matter creation cosmology, ***3.C. P. Singh*** and ***6.Ajay Kumar***, Mathematics, DTU

29. Response surface methodological evaluation of drilling for the optimization of residual compressive strength of bio-based RPUF composite, ***6.Anuja Agrawal[1]***, ***3.Raminder Kaur[1]*** and ***3.R S Walia[2]***, Applied Chemistry[1] and Mechanical[2], DTU

30. Reviewer Credibility and Sentiment Analysis Based User Profile Modelling for Online Product Recommendation, SHIGANG HU, ***3.AKSHI KUMAR***, FADI AL-TURJMAN, ***8.SHIVAM GUPTA***, ***8.SIMRAN SETH*** AND ***8.SHUBHAM***, CSE, DTU

31. Single OTRA based low power grounded capacitance multiplier, ***8.1.Shashwat Singh***, ***8.1.Jatin***, ***3.Neeta Pandey*** and ***3.Rajeshwari Pandey***, ECE, DTU

32. Strategic issues in supply chain management of Indian SMEs due to globalization: an empirical study, Rajesh Kumar Singh and ***6.1.Ravinder Kumar***, Mechanical, DTU

33. Stress–strain characteristics of landfill clay cover barriers under geogrid reinforcements, ***8.1.Akshit Mittal[1]*** and ***3.Amit Kumar Shrivastava[2]***, ENVT & Civil, DTU

34. Study on groundwater quality and status of Amas Block in Gaya District of Bihar with special reference to fluoride contamination, ***6.A. Krishan*** and ***3.R.K. Mishra***, Environmental, DTU

35. Suitable selection of napkins in Hotel industry for sustainable development, ***7.1.Sachin Jaisar*** and ***3.Saurabh Agrawal***, Mechanical, DTU

36. Temperature-assisted Broadly Tunable Supercontinuum Generation in Chalcogenide Glass-based Capillary Optical Fiber, SATYA PRATAP SINGH, JASLEEN KAUR, KESHAV SAMRAT MODI, UMESH TIWARI AND ***3.RAVINDRA KUMAR SINHA***, Physics, DTU

37. Therapeutic Targets Prediction of Tumor Specific Antigen for Vaccine Design, ***6.Sunil Kumar*** and ***3.Dr. Asmita Das***, Biotechnology, DTU

38. Thermodynamic performance evaluation of double effect H2O-Li/Br vapour absorption systems using multi cascading of vapour compression cycles for ultra-low temperature applications, ***3.R.S. Mishra***, Mechanical, DTU

39. Understanding of Grounding & Eff ective Grounding System for Substations, ***7.1.Rajesh Kumar Arora*** and IPS Paul, Electrical, DTU

1. *Chancellor*

2. *Pro Vice Chancellor*	***2.1.*** *Ex Pro Vice Chancellor*
3. *Faculty*	***3.1.*** *Ex Faculty*
4. *Teaching-cum-Research Fellow*	***4.1.*** *Asst. Librarian*
5. *Alumni*	
6. *Research Scholar*	***6.1.*** *Ex Research Scholar*
7. *PG Scholar*	***7.1.*** *Ex PG Scholar*
8. *Undergraduate Student*	***8.1.*** *Ex Undergraduate Student*

Wireless Personal Communications
https://doi.org/10.1007/s11277-020-07188-3

A Binary PSO Approach for Improving the Performance of Wireless Sensor Networks

Ajay Kaushik[1] · Mononito Goswami[1] · Minkush Manuja[1] · S. Indu[2] · Daya Gupta[1]

© Springer Science+Business Media, LLC, part of Springer Nature 2020

Abstract
Wireless sensor networks are used for low-cost unsupervised observation in a wide-range of environments and their application is largely constrained by the limited power sources of their constituent sensor nodes. Techniques such as routing and clustering are promising and can extend network lifetime significantly, however finding an optimal routing and clustering configuration is a NP-hard problem. In this paper, we present an energy efficient binary particle swarm optimization based routing and clustering algorithm using an intuitive matrix-like particle representation. We propose a novel particle update strategy and an efficient linear transfer function which outperform previously employed particle update strategies and some traditional transfer functions. Detailed experiments confirmed that our routing and clustering algorithm yields significantly higher network lifetime in comparison to existing algorithms. Furthermore, our results suggest that Binary PSO is better equipped to solve discrete problems of routing and clustering than its continuous counterpart, PSO.

Keywords Wireless sensor networks · Binary PSO · Routing · Clustering · Network lifetime

1 Introduction

A WSN consists of spatially dispersed tiny sensor devices, networked together over a wireless medium, and one or more conveniently located powerful sinks collecting information from these sensor nodes (SNs). Characterized by their scalability, mobility, fault tolerance and simplicity of use, WSNs have emerged as effective low-cost alternatives for unsupervised observation of a wide range of environments, and have been used in diverse areas

Ajay Kaushik, Mononito Goswami and Minkush Manuja have contributed equally to this work.

✉ S. Indu
s.indu@dce.ac.in

[1] Department of Computer Science and Engineering, Delhi Technological University, Delhi, India

[2] Department of Electronics and Communication Engineering, Delhi Technological University, Delhi, India

Published online: 04 February 2020

of application such as agriculture, military, inventory, environment monitoring etc. However, WSNs and their widespread application is primarily constrained by the limited energy sources of SNs. Many novel areas of research such as low-powered energy communication hardware [5], energy-aware medium access control [32] etc. have emerged to tackle these issues. Energy efficient routing and clustering protocols present a promising solution to various energy limitation issues faced by WSNs.

Liu [22] presented an extensive survey on clustering and routing protocols and expounded various advantages of clustering such as localization of route setup within a cluster and increased scalability of response to events in the environment. Routing in WSNs can be classified as flat and hierarchical [22]. While in a flat routing framework all nodes have the same functionality, in hierarchical routing different nodes perform different tasks. Hierarchical routing WSNs are organized into many clusters, and each cluster comprises of a leader referred as the cluster head (CH), and multiple SNs. CHs might transmit data to the sink either directly, or indirectly via other CHs through a multi-hop routing path. The latter scenario is referred to as a two-tier WSN.

In hierarchical networks, CHs bear the transmission load of multiple SNs and also expend energy for aggregating and eliminating redundant data from SNs. This can result in their overloading and early death [14]. In this regard, multiple researchers [3, 20, 21] suggested using special nodes with extra energy, called gateways. In the remainder of the paper, we use the term gateways and CHs interchangeably. Moreover like SNs, CHs are also battery-powered and therefore have a limited power supply. In WSNs with static sinks, CHs close to the sink can die prematurely since they lie at the intersection of several multi-hop routes and consequently expend a significant amount of power to transmit huge quantities of information from other nodes to the sink [16]. The death of a CH can potentially destabilize the network, disrupt its topology and lead to packet loss. Therefore, it is important to balance loads on CHs and SNs in order to prolong the lifetime of a network (Fig. 1).

Both routing and clustering are NP-hard problems. Furthermore, the computational complexity of finding an optimal routing and clustering configuration rises as the size of the WSN increases. For a WSN having $|\mathcal{G}|$ gateways and $|\mathcal{S}|$ SNs, if each gateway and SN on an average has $\overline{\mathcal{G}}$ and $\overline{\mathcal{S}}$ gateways within communication range, there are $|\mathcal{G}|^{\overline{\mathcal{G}}}$ and $|\mathcal{S}|^{\overline{\mathcal{G}}}$ possible routing and clustering configurations, respectively. Therefore, brute force approaches are extremely inefficient in solving these problems. In order to obtain good routing and clustering configurations efficiently and quickly, meta-heuristic approaches such as BPSO, Genetic Algorithms (GA), Ant Colony Optimization (ACO) etc. are highly suitable. In the past, meta-heuristic algorithms have shown promising results in finding optimal routing and clustering configurations [20, 21, 27].

In this paper, we develop routing and clustering algorithms based on *Binary Particle Swarm Optimization* (BPSO). We chose BPSO partly since its continuous counterpart, Particle Swarm Optimization had performed extremely well in solving the routing and clustering problem [20], and more so because we expect BPSO to be better suited for the optimization problems at hand by virtue of its discrete nature. Experimental results comparing both the algorithms confirm the superior optimization performance of BPSO over continuous PSO (Sect. 7.6). However, using BPSO is not straightforward owing to the multi-dimensional nature of routing and clustering. In particular, routing and clustering require a unique two-dimensional particle representation different from the uni-dimensional representation that traditional applications of BPSO use (Sect. 6.1.2). The new particle representation also necessitates new velocity and position update strategies that take into account the

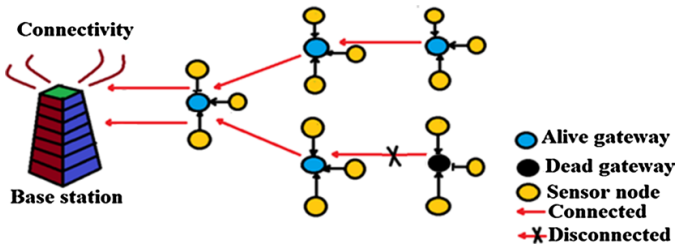


Fig. 1 A two-tier WSN

two-dimensional nature of the particles (Sect. 6.1.4). In this paper, we propose a novel *stochastic position update* strategy and note significant improvements in the optimization process over its alternative, the max update strategy proposed by Izakian et al. [15] (Sect. 7.4). Still, the velocity matrices lie in a continuous space, while the routing and clustering configurations are discrete in nature, and therefore BPSO uses a *transfer function* to map a continuous search space into a discrete binary space (Sect. 6.1.8). To this end we propose a novel *linear* transfer function ξ_L which is not only computationally simple but also outperforms traditional alternatives such as *sigmoid* ξ_S and *hyperbolic tan* ξ_T transfer functions in terms of network lifetime (Sect. 7.3).

In order to evaluate routing and clustering configuration, prior work Kuila and Jana [20] usually deploy CHs and SNs uniformly randomly across the deployment region. However, rigorous experiments on the uniform deployment revealed that the CHs closer to the base station expend a huge amount of energy to forward incoming packets from other CHs, and thus die quickly. To this end, we also examined a random *Gaussian deployment* of gateways to increase their number around the base station, and found the that it increases the network lifetime significantly.

Thus, our major contributions can be summarized as follows:

- BPSO based routing and clustering algorithms along with carefully designed fitness functions and a novel particle representation. In particular, we model the lifetime of a WSN in terms of its constituent CHs, and devise fitness functions which can effectively prolong network lifetime.
- A novel stochastic particle position update strategy to drive the optimization process in a efficient manner.
- A novel computationally-simple linear transfer function ξ_L that outperforms traditional non-linear transfer functions (sigmoid ξ_S and hyperbolic tan ξ_T) in terms of metrics such as network lifetime.
- A detailed performance comparison of discrete BPSO and its widely-used continuous counterpart PSO, highlighting the former's superior performance in solving the considered optimization problems.
- An analysis of a gaussian strategy for randomly deploying CHs in the sensing area. The gaussian strategy effectively balances the load of CHs near the base station.

The paper is organized as follows. Relation to prior work is presented in Sect. 2. Section 3 provides a brief overview of binary particle swarm optimization. Section 4 discusses the energy model and terminologies, while Sect. 5 formulates the problem statement. Section 6 discusses the proposed algorithms. The experimental setup and detailed experimental results are given in Sect. 7 and we conclude the paper with avenues of future work in Sect. 8.

2 Literature Review

A lot of research has been done in last few decades to achieve an energy efficient WSN. Heinzelman et al. [14] proposed a low energy adaptive clustering hierarchy (LEACH). A drawback of LEACH is that the CHs are selected without considering the crucial parameters like residual energy which makes the algorithm inefficient in some cases [23]. Heinzelman et al. [14] presented LEACH-C where the base station takes the responsibility of cluster formation. In Younis and Fahmy [33] another extension to LEACH protocol, hybrid energy efficient distributed clustering (HEED) is proposed. HEED mainly focus on the residual energy of each SN. Souissi and Meddeb [26] proposed a weight based clustering algorithm which minimizes intra cluster distance. Later, Tang et al. [28] proposed the concept of a high energy relay node to be placed between CHs for long distance communication. Cardinality of CHs was proposed by Gupta and Younis [10] where cardinality was defined in terms of number of SNs associated with a CH. Many approaches have been used in which nature inspired algorithms are used to improve the WSN lifetime. Kuila et al. [21] proposed a genetic algorithm based load balancing, clustering algorithm. Heinzelman et al. [13] presented a single hop routing model in which direct transmission of energy takes place during the routing process. A minimum hop model was proposed by Gupta and Younis [11]. They emphasized on finding a multi hop route which minimizes the number of hops required to send data from a SN to the sink. Heinzelman et al. [14] presented a random routing model where a SN i randomly selects the next hop j, given that j is in transmission range of i and is located close to the sink. Bari et al. [3] used GA for WSN routing. Later, Gupta et al. [12] proposed another routing algorithm that uses GA for minimizing network energy dissipation. Kuila and Jana [20] try to find a tradeoff between number of hops and transmission distance in such a way to find equilibrium between delay and transmission distance. Srinivasa Rao and Banka [27] proposed an energy efficient clustering approach using a chemical reaction optimization approach. The gravitational search algorithm was used by Ebrahimi Mood and Javidi [8] to achieve an energy efficient network. Later, Kaur and Mahajan [17] presented a tree based data aggregation protocol to achieve energy efficient WSN.

3 Binary Particle Swarm Optimization: An Overview

Particle swarm optimization (PSO) is a popular optimization technique for non-linear continuous functions, originally introduced by Kennedy and Eberhart [18, 25]. PSO is inspired by flocks of birds and their search for food and shelter, and has been successfully used to solve a number of problems [6, 9, 18, 29]. The PSO algorithm comprises of a swarm (flock) of dynamic and interactive particles (birds) that intelligently search through a high-dimensional search space using collaborative trial and error. Each particle represents a potential solution to the problem having a randomly-initialized position and velocity. Each particle's velocity governs the next position that it flies to. PSO iteratively improves each potential solution based on a measure of quality (called the *fitness function*), guided by the direction of its fittest position (*pbest*), and the fittest position of any particle in the swarm (*gbest*). The fittest position that a particle has visited thus far (*pbest*), and the fittest position that the swarm has achieved (*gbest*) represent the cognitive and social components that guide the swarm's search for the solution (food).

A few years later, Kennedy and Eberhart [19] presented the binary version of their algorithm for discrete optimization problems. While BPSO inherits all the basic ideas

of its continuous counterpart, it defines a particle's position and velocity in terms of changes in probabilities that a bit will be in one state or another. In the binary setting, each particle can be viewed as a vertex of a D-dimensional hypercube. Furthermore, the velocity of a particle in each dimension denotes the probability that the corresponding position bit will be ON (1) or OFF (0). Unlike other optimization paradigms, the position of a particle in BPSO is transitory i.e. a particle may have different positions in different instances given the same velocity. For example, consider Eq. 6 which maps the velocity $v_{i,d}^t$ of a particle to its position at the next time step $\rho_{i,d}^{t+1}$. Notice that the final position of a particle does not depend solely on its velocity, but also on the random number $r_{i,d}$.

Formally, we denote a particle ρ_i in a D-dimensional space as:

$$\rho_i = [x_{i,1}, x_{i,2}, \ldots, x_{i,D}] \tag{1}$$

where each $x_{i,d} \in \{0, 1\}$, $d \in \{1, 2, \ldots, D\}$. Each particle ρ_i possesses velocity represented as:

$$V_i = [v_{i,1},\ v_{i,2},\ \ldots\ , v_{i,d}]^T \tag{2}$$

where each $v_{i,d} \in [v_{min}, v_{max}]$, v_{min} and v_{max} denote the maximum and minimum velocity. Let us denote the personal best position of a particle, and the global best position of swarm as:

$$pbest_i = [\rho x_{i,1},\ \rho x_{i,2}, \ldots,\ \rho x_{i,D}]^T \tag{3}$$

$$gbest_i = [gx_{i,1},\ gx_{i,2},\ \ldots,\ gx_{i,D}]^T \tag{4}$$

Then, Eqs. 5 and 6 can be used to update the position and velocity of the ith particle's dth dimension at the tth iteration:

$$V_{i,d}^{t+1} = V_{i,d}^t + c_1 r_1 (pbest_{i,d}^t - \rho_{i,d}^t) + c_2 r_2 (gbest_{i,d}^t - \rho_{i,d}^t) \tag{5}$$

$$\rho_{i,d}^{t+1} = \begin{cases} 1 \text{ if } \xi_S(v_{i,d}^t) > r_{i,d} \\ 0 \text{ otherwise} \end{cases} \tag{6}$$

where $\xi_S(v_{i,d}^t) = \frac{1}{1+e^{-v_{i,d}^t}}$. ξ denotes a transfer function (Sect. 6.1.8). Traditionally, BPSO uses the sigmoid ξ_S transfer function.

c_1 and c_2 are positive acceleration constants that govern the influence of the cognitive and social components on the search process. Also, r_1, r_2 and $r_{i,d}$ are uniform random numbers in the range [0, 1]. Algorithm 3 presents the BPSO optimization algorithm for minimization problems.

4 Energy Model and Terminologies

4.1 Energy Model

We used the simplified first-order radio model Heinzelman et al. [14] to dissipate energy of SNs and CHs. In this model, the transmitter expends energy to run the power amplifier and transmitter electronics, while the receiver expends energy to run the receiver electronics.

The energy expended to transmit a l-bit message over the distance d, using free-space and multi-path fading channels is given by Eq. 7:

$$E_T(l,d) = \begin{cases} lE_{elec} + lE_{fs}d^2, & \text{when } d < d_o \\ lE_{elec} + lE_{mp}d^4, & \text{when } d \geq d_o \end{cases} \tag{7}$$

where E_{Elec}, E_{fs} and E_{mp} is the energy required by the electronics circuit, and the amplifier in the free-space and multipath models respectively and $d_o = \sqrt{\frac{E_{fs}}{E_{mp}}}$. To receive a l-bit message, the receiver expends energy as given by Eq. 8:

$$E_R(l) = lE_{elec} \tag{8}$$

The electronics energy E_{elec} depends on a number of factors such as digital coding, modulation, filtering and spreading of the signal. On the other hand, the amplifier energy E_{fs} and E_{mp} depend on the distance to the receiver and the acceptable bit error-rate.

4.2 Network Model

Our WSN model comprises of a number of immobile SNs and gateways which are deployed uniform randomly at the start of the simulation.[1] Each SN communicates with a single gateway in its communication range, and is said to be assigned to that gateway. These assignments result in clusters of SNs, which allow data from nodes within a cluster to be processed locally (in their assigned gateway) and reduce the data that needs to be transmitted to the base station. Similar to LEACH [14], the operation of our model is divided into rounds. In each round, SNs collect data and send it to their corresponding CH. A CH is a gateway to which all SNs of a cluster are assigned. In the remaining sections of the paper, we refer to CHs and gateways interchangeably. A CH aggregates data to eliminate redundant information and transmits it to the remote base station via the next hop CH. In order to save energy, all nodes turn off their radios between adjacent rounds. In the presented model, MAC transmissions are accomplished using Time-Division Multiple Access (TDMA) protocol [4].

5 Problem Formulation

Table 1 summarizes the notations used in our algorithms. The lifetime of a WSN is an important measure for evaluating different application-specific network configurations. Several metrics have been proposed in the literature to measure the lifetime of a sensor network [7] based on the number of alive nodes, sensor coverage, connectivity and quality of service requirements. Among these, the n-of-n lifetime (L_n^n) is one the most widely used definitions of network lifetime:

$$L_n^n = \min_{i \in N} L_i$$

In this definition, the lifetime of a network is the time until the first node dies. This is a convenient definition since it is easy to compute, and does not have to consider changes in topology after the death of the first node. L_n^n is used when all the nodes are of equal

[1] Gateways can also be deployed using a gaussian distribution centred at the coordinates of the base station. We will discuss deployment strategies in greater detail in Sect. 7.

Table 1 A summary of notation

Abbreviation	Full form
WSN	Wireless sensor network
SN	Sensor node
CH	Cluster head
BPSO	Binary particle swarm optimization
Notation	**Definition**
$\mathbb{S}$	Set of SNs such that $\mathbb{S} = \{s_1, s_2, ...s_{\lvert\mathbb{S}\rvert}\}$, where $\lvert\mathbb{S}\rvert$ is the number of SNs in the network
$\mathbb{C}$	Set of CHs such that $\mathbb{c} = \{c_1, c_2, ...c_{\lvert\mathbb{C}\rvert}\}$, where $\lvert\mathbb{C}\rvert$ is the number of CHs in the network
$\mathbb{b}$	Base station
$d(e_i, e_j)$	A function which returns the Euclidean distance between $(e_i, e_j) \in \mathbb{S} \cup \mathbb{C} \cup \mathbb{b}$
$\mathcal{D}$	*Communication range* of SNs and CHs.
pCH_{s_i}	The set of probable CHs of a SN $s_i \in \mathbb{S}$ such that $pCH_{s_i} = \{c_i \mid d(s_i, c_i) \leq \mathcal{D}\ \&\ c_i \in \mathbb{C}\}$
CH_{s_i}	The CH assigned to s_i
pNH_{c_i}	The set of probable next hop CHs of a CH $c_i \in \mathbb{C}$ which are closer to $\mathbb{b}$, such that $pNH_{c_i} = \{c_j \mid c_j \in (\mathbb{C} - c_i)\ \&\ d(c_j, \mathbb{b}) \leq d(c_i, \mathbb{b})\ \&\ d(c_i, c_j) \leq \mathcal{D}\}$
NH_{c_i}	The next hop relay of CH c_i

importance and favours algorithms that uniformly deplete the energy of each node in the network [7]. Since it may be either inconvenient or impossible to recharge and replace node batteries [14], in this paper, our main objective is to maximize n-of-n network lifetime of a sensor network.

The n-of-n network lifetime can be expressed in terms of residual energy of cluster heads at the start of network operation and the highest energy expended per round by any CH as shown in Eq. 9:

$$L_n^n = \min_{i \in N} L_i \ = \ \min_{c_i \in \mathbb{C}} \left\lfloor \frac{E_{res}(c_i)}{E(c_i)} \right\rfloor \tag{9}$$

where $E_{res}(c_i)$ is the residual energy of the CH c_i, and $E(c_i)$ is the energy it expends per round. It must be noted that in the real life $E(c_i)$ may vary for every round of operation due to extraneous factors, however for the sake of simplicity we assume that $E(c_i)$ is constant throughout the operation of a CH. If the residual energy (E_{res}) for all CHs is equal at the start of operation, then the lifetime of a network has an inverse relationship with the highest energy expended per round by any CH, as shown in Eq. 10:

$$L_n^n = \min_{i \in N} L_i \ = \ \min_{c_i \in \mathbb{C}} \left\lfloor \frac{E_{res}(c_i)}{E(c_i)} \right\rfloor \approx \min_{c_i \in \mathbb{C}} \left(\frac{\epsilon}{E(c_i)} \right) \tag{10}$$

where $\forall c_i \in \mathbb{C},\ E_{res}(c_i) = \epsilon$. Alternatively, ϵ is called the initial energy of CHs.

Each CH expends energy for receiving data sensed by its member SNs, aggregating the data, and eventually sending it to the base station. Furthermore, every CH c_i also consumes energy to forward data received from any CH c_j whose routing path to the base station passes through c_i. Therefore, the energy expended by each CH has two components: an *intra-cluster* component due to receiving, aggregating and transmitting data sensed by its member SNs, and a *forwarding* component due to relaying data sensed in other parts of the network. The intra-cluster component shown in Eq. 11 is formulated using Eqs. 7 and 8 as follows:

$$E_{\mathcal{C}}(c_i) = \eta\, E_R(l) + \eta\, E_D(l) + E_T(m, d(c_i, NH_{c_i})) \tag{11}$$

where η is the number of member SNs of c_i, $\eta E_R(l)$ is the total energy expended by c_i to receive l-bit messages from each of its η member SNs, and $\eta E_D(l)$ is the total amount of energy consumed in aggregating a total of $\eta \times l$ bits of messages from member SNs (each member SN sends a l-bit message to the CH) into a fixed m-bit packet which is transmitted from the CH c_i to the base station. This aggregation mechanism, where SNs transmit l-bit messages to their assigned CH, which thereby aggregates all the messages into a single m-bit message, follows from prior work [8, 20, 27]. The energy spent on transmitting the aggregated m-bits of packet is given by $E_T(m,\ d(c_i, NH_{c_i}))$.

Similarly, the forwarding component is formulated in Eq. 12:

$$E_{\mathcal{F}}(c_i) = \mathcal{N}(c_i)E_R(m) + \mathcal{N}(c_i)E_T(m, d(c_i, NH_{c_i})) \tag{12}$$

where $\mathcal{N}(c_i)$ is the number of inbound data packets from all CHs c_j whose next hop relay is c_i. We can recursively compute $\mathcal{N}(c_i)$ as shown in Eq. 13:

$$\mathcal{N}(c_i) = \begin{cases} 0, & \text{if } NH_{c_j} \neq c_i \forall\ c_j\ \in\ \mathbb{C} \\ \sum(\mathcal{N}(c_j) + 1) & \text{otherwise} \end{cases} \tag{13}$$

The total energy expended by a CH c_i is given in Eq. 14:

$$\begin{aligned} E(c_i) &= E_{\mathcal{C}(c_i)} + E_{\mathcal{F}(c_i)} \\ &= \eta\, E_R(l) + \eta\, E_D(l) + \mathcal{N}(c_i)E_R(m) + (\mathcal{N}(c_i) + 1)E_T(m, d(c_i, NH_{c_i})) \end{aligned} \tag{14}$$

Therefore, the energy consumed by a CH depends on the number of SNs assigned to it (η), the number of inbound data packets ($N(c_i)$) and the distance between the CH and its next hop ($d(c_i, NH_{c_i})$). While $N(c_i)$ and ($d(c_i, NH_{c_i})$) depends on the routing setup, η depends on the clustering configuration of the network. By carefully formulating fitness functions for routing and clustering, we can effectively minimize the energy consumption for each CH and prolong their lifetime. Mathematically,

$$max(L_n^n) \propto max\left(\min_{c_i\ \in\ \mathbb{C}}\left(\frac{1}{E(c_i)}\right)\right) \tag{15}$$

Essentially, maximizing network lifetime is equivalent to maximizing the lifetime of the CH which has minimum lifetime.

6 BPSO-Based Routing and Clustering

The network is setup in three different phases: bootstrapping, routing, and clustering. First each entity (CH and SN) in the network is assigned a unique ID. Next, each entity broadcasts it's ID using the Carrier Sense Multiple Access with Collision Avoidance (CSMA/CA) MAC layer protocol, which allows all the gateways and SNs to collect IDs of entities which are within their communication range. This information is then sent to the base station which executes the proposed routing and clustering algorithm. The base station utilizes the best route returned by the routing algorithm to find the best clustering configuration.

Later, each gateway is informed of its next hop relay, while each SN is informed about the ID of the gateway that it is assigned to.

6.1 Routing Algorithm

6.1.1 Formulating the Routing Problem

Our main objective for routing is to minimize the forwarding energy $E_F(c_i)$ of CHs in order to effectively minimize their total energy consumption $E(c_i)$ and thereby increase their lifetime. We must remember that the routing setup influences the essential components of $E_F(c_i)$, namely the number of inbound packets ($\mathcal{N}(c_i)$) and the distance between a CH and its next hop ($d(c_i, NH_{c_i})$).

6.1.2 Particle Representation in BPSO

Representing particles is fundamental to designing effective BPSO algorithms since it maps a BPSO particle to the solution of a problem. Our particle representations, namely the *indirect* and *direct* representation, are inspired from Izakian et al. [15]. In the direct representation or alternatively the *position vector* of a particle, a solution is encoded as a $1 \times m$ vector where each dimension contains an integer in the closed interval $[1, n]$. Figure 2 illustrates the direct representation of a particle representing a routing solution. We note the following characteristics of the direct representation:

1. The length of the vector m is equal to the number of CHs in the network $|\mathbb{C}|$.
2. The ith dimension of the vector is j, if the CH c_i routs to c_j i.e. $NH_{c_i} = c_j$.
3. Since a CH can route to another CH or the base station, each dimension must contain an integer in the closed interval $[1, m + 1]$. The ith dimension of the vector is $m + 1$ if the CH c_i routs directly to the base station $\mathbb{b}$ i.e. $NH_{C_i} = \mathbb{b}$. Alternatively, we can justify the choice of interval $[1, m + 1]$ by arguing that n must be equal to the number of potential next hop relays for any CH, and since a CH can route to any entity in $\mathbb{C} \cup \mathbb{b}$, we have: $n = |\mathbb{C} \cup \mathbb{b}| = |\mathbb{C}| + 1 = m + 1$.
4. In Fig. 2, $m = 5$ and the CH c_1 routs to c_2; c_2, c_3 and c_4 route to c_5 and c_5 routs to the $\mathbb{b}$.

In the indirect representation or alternatively the *position matrix* of a particle, a solution is encoded as a $n \times m$ matrix, where each cell contains either 0 or 1 representing the absence or presence of a communication link. As an example, consider Fig. 3 which illustrates the indirect representation of the same routing configuration as Fig. 2. The indirect representation of a routing particle has the following properties:

1. All elements of the matrix have either the value 0 or 1.
2. m is equal to the number of CHs in the network $|\mathbb{C}|$ and $n = m + 1$.
3. $M[c_i, c_j] = 1$ if c_j routs to c_i and 0 otherwise.

c_1	c_2	c_3	c_4	c_5
2	5	5	5	6

Fig. 2 A *direct* representation of a routing particle (*position vector*)

Fig. 3 An *indirect* representation of a routing particle (*position matrix*)

	c_1	c_2	c_3	c_4	c_5
c_1	0	0	0	0	0
c_2	1	0	0	0	0
c_3	0	0	0	0	0
c_4	0	0	0	0	0
c_5	0	1	1	1	0
b	0	0	0	0	0

4. In each column of the matrix M only one element is 1 and all other elements are 0. This is because a CH c_j only routs to a single CH c_i.

As apparent from Figs. 2 and 3 , the direct and indirect representations of a particle are easily convertible to each other. While the indirect representation results in sparse matrices consisting of binary numbers, the direct representation is concise and requires less memory. While we use the direct representation to encode our particles for both routing and clustering, the indirect representation is useful in interpreting velocity matrices.

6.1.3 Particle Velocity, pbest and gbest

Each particle's velocity can be represented as a $n \times m$ matrix where each element lies between v_{min} and v_{max}. If V_k represents the velocity of the kth particle, then its velocity matrix is given by:

$$V_k(i,j) = v \in [v_{min}, v_{max}] \; \forall i,j, \; i \in \{1,2,\ldots n\}, j \in \{1,2,\ldots m\} \tag{16}$$

The velocity matrix has the same shape as the position matrix, since the velocity $V_k(i,j)$ essentially indicates the probability that c_j routs to c_i.[2]

Since a particle's *pbest* and the swarm's *gbest* also represent routing configurations, they can be also be represented by direct and indirect representations discussed in the previous section.

6.1.4 Updating a Particle's Velocity and Position

Most researchers [1, 24, 30], using BPSO in the past have used uni-dimensional position and velocity matrices to represent solutions. However, in this paper we use two-dimensional position[3] and velocity matrices to intuitively represent routing and clustering configurations. Figures 3 and 4 concretely illustrate the difference between two-dimensional and uni-dimensional position matrices, respectively.

Two-dimensional position matrices require different position and velocity update strategies than their uni-dimensional counterparts, which give rise to the need of new velocity and *position update strategies*.

[2] This is true for routing particles. For clustering particles, the $V_k(i,j)$ instead, indicates the probability that the SN s_j is assigned to the CH c_i.

[3] A minor implementation detail for the sake of completeness: we use position vectors (direct representation of particles) instead of matrices to save space. However, a uni-dimensional *decimal* position vector (Fig. 2) is essentially a two-dimensional binary position matrix (Fig. 3) and Sect. 6.1.2.

a_1	a_2	a_3	a_4	a_5
1	1	0	1	0

Fig. 4 An example of a uni-dimensional position matrix. This position matrix may represent a solution to the 0/1 knapsack problem by considering a_i to be the ith object, where 1 indicating that the ith object is included in the knapsack

6.1.5 A Two-Dimensional Velocity Update Strategy

The velocity of particles having two-dimensional position matrices can be updated by augmenting the velocity update equation used in traditional BPSO (refer Eq. 5) with two positional indices to refer any element present in the ith row and jth column of its velocity matrix. Accordingly, the two-dimensional velocity update strategy is given by Eq. 17:

$$\begin{aligned} V_k^{t+1}(i,j) = V_k^t(i,j) + c_1 r_1 (pbest_k^t(i,j) - X_k^t(i,j)) \\ + c_2 r_2 (gbest_k^t(i,j) - X_k^t(i,j)) \end{aligned} \tag{17}$$

where $X_k^{t+1}(i,j)$ represents the element of the ith row and the jth column of the kth particle's position matrix at the $t+1$th time step while $V_k^{t+1}(i,j)$ represents the ith row and the jth column of the kth particle's velocity matrix. c_1 and c_2 are positive acceleration constants that govern the influence of the cognitive and social components on the search process. Also, r_1, r_2 are uniform random numbers in the range [0, 1].

6.1.6 Max and Stochastic Position Update Strategies

In addition to velocity update, the position update strategy is principal to the optimization process since it facilitates a particle's exploration and exploitation of the search space. A *correct* position update strategy for the routing problem must ensure that the updated position of a particle represents a valid routing configuration. Therefore, it must ensure that in the updated routing configuration:

1. Each column in a particle's routing position matrix M must contain a single 1 only.
2. Each gateway must only route to another gateway in its communication range.

Condition 2 can be easily handled by initializing the velocities in each dimension i of a column j to negative infinity if c_i is not in the communication range of c_j, as shown in Eq. 18.

$$V_k^{t+1}(i,j) = -\infty \ \forall i,j \ s.t. \ d(c_i, c_j) > \mathcal{D} \tag{18}$$

Initializing the velocity to negative infinity ensures that any updates to the velocity $V_k^{t+1}(i,j)$ always results in negative infinity. Furthermore, we constrain our normalizing function ξ, such that it always returns 0 on an input of $-\infty$ i.e. $\xi(-\infty) = 0$. This ensures that the

probability that c_j routs to c_i always remains 0 i.e. $P_k^{t+1}(i,j) = 0$ and therefore, $\mathbb{N}_{c_j}$ can never take the value i.

A *naive position update strategy* can be formulated by making the same additions to Eq. 6 as the two-dimensional velocity update strategy:

$$M_k(i,j)^{t+1} = \begin{cases} 1 \text{ if } \xi(\ V_k^{t+1}(i,j)\ ) > r \\ 0 \text{ otherwise} \end{cases} \tag{19}$$

where $\xi : [v_{min}, v_{max}] \cup \{-\infty\} \rightarrow [0,1]$ is a normalizing function (detailed explanation in Sect. 6.1.8). However, it can be clearly seen that the naive strategy may lead to an invalid routing configuration since it has no way of guaranteeing that conditions 1 and 2 hold for the updated position of a particle.

To this end, Izakian et al. [15] had proposed what we call the *Max position update strategy*. The Max update strategy however limits the exploration, and therefore results in premature convergence to local optima. To overcome its limitations, we propose the *Stochastic update strategy* which encourages more exploration owing to its probabilistic nature (Sect. 7.4). We now explain the max and stochastic update strategies in detail.

For each gateway c_j, let the random variable $\mathbb{N}_{c_j}$ map its next hop NH_{c_j} to integers in the closed interval $[1, m+1]$, such that if $NH_{c_j} = c_i$ then $\mathbb{N}_{c_j}, i \in [1, m+1]$. Therefore, each column of the position matrix and each element of the position vector can be summarized using random variables $\mathbb{N}$ as $[\ \mathbb{N}_{c_1}\ \mathbb{N}_{c_2} \ldots \mathbb{N}_{c_{|C|}}\ ]$.

Let us consider that we carry out the following transformations in each particle's velocity matrix:

1. *Normalization* Pass each velocity element $V_k^t(i,j)$ through a normalizing function ξ such that it lies in the range [0, 1].
2. *Re-scaling* Re-scale each column such that the sum of the velocity elements in a column is 1.

These transformations result in the Probability Matrix P in which each element $P[i,j]$ represents the probability that c_j routs to c_i i.e. $P(NH_{c_j} = c_i) = P[i,j]$. The second transformation ensures that sum of the probabilities of all mutually exclusive events such as $NH_{c_j} = c_i$ and $NH_{c_j} = c_k$ is 1. Both the transformations can be summarized in Eq. 20:

$$P_k^t(i,j) = \frac{\xi(V_k^t(i,j))}{\sum_{i=1}^{m} \xi(V_k^t(i,j))},\ \forall i \in\ [1,n], j,\ \in\ [1,m] \tag{20}$$

Each column in the probability matrix P can be seen as representing a discrete probability distribution, which provides the probabilities that a particular gateway routs to another gateway in the network or base station. Alternatively, for each gateway c_j, the random variable $\mathbb{N}_{c_j}$ has a probability distribution given by the jth column of the probability matrix P.

Algorithm1: Max Position Update Strategy

Input: Probability matrix (P)
Output: Arouting solution: $S_r = \{c_i \ \forall j \in \{\ 1,\ 2,\ 3... \ \mathbb{C}|\}$ such that $c_i = NH_{c_j}$

```
1  begin
2      Initialize S_r ← φ
3      for j ← 1 to |ℂ| do
4          NextHop_j ←0
5          MaximumProb_j ←0
6          for i ← 1 to |ℂ|+1 do
7                                          // |ℂ|+1 denotes the base station
8              if P[i][j] >MaximumProb_j then
9                  MaximumProb_j ← P[i][j]
10                 NextHop_j ← i
11             end
12         end
13         S_r ← S_r ∪ NextHop_j
14     end
15     return S_r
16 end
```

Given the Probability Matrix P of a particle, the Max [15] and Stochastic strategies update the positions of particles as follows:

- *Max Position Update strategy* Izakian et al. [15] proposed the following equation for updating a particle's position:

$$X_k^{t+1}(i,j) = \begin{cases} 1 \text{ if } P_k^t(i,j) = max\{\xi(V_k^t(i,j))\} \ \forall i \in \{1,2,\dots n\} \\ 0 \text{ otherwise} \end{cases} \tag{21}$$

  where $X_k^{t+1}(i,j)$ represents the element of the ith row and the jth column of the kth particle's position matrix at the $t+1$th time step while $P_k^t(i,j)$ represents the ith row and the jth column of the kth particle's probability matrix at the same time.

  Therefore, Eq. 21 assigns c_i as next hop to c_j ($X_k^{t+1}(i,j) = 1$) when the probability $P(NH_{c_j} = c_i) = P[i,j]$ is the highest. If $P[i,j] = P[k,j]$ *i.e.* the probability that c_j routs to either c_i or c_k is equal,[4] then the next hop CH is chosen at random between them. We must note that Eq. 21 ensures that condition 1 always holds.
- *Stochastic position update strategy* Our proposed update strategy is consistent with the stochastic nature of the position update equation of classical BPSO. In this strategy, for each gateway c_j we sample the probability distribution corresponding to $\mathbb{N}_{c_j}$ once, using *inverse transform sampling*. The sampled value $\phi \in [1, m+1]$ indicates the updated next hop relay c_ϕ of c_j.

[4] The probability of routing to c_i or c_k must be larger than any other CH.

Algorithm 2: Stochastic Position Update Strategy

Input: Probability matrix (P)
Output: A routing solution: $S_r = \{c_i \; \forall j \in \{1,\ 2,\ 3...\ |\mathbb{C}|\}\}$ such that $c_i = NH_{c_j}$

```
1  begin
2      Initialize S_r ← φ
3      for j ← 1 to |ℂ| do
4          CDF ← φ
5          CDF ← (CDF ∪ P[1][j]);
6          for i ← 2 to |ℂ| + 1 do
7              CDF ← CDF ∪ CDF[i − 1] + 𝒫[i][j];
8          end
9          Generate a uniform random number r ∼ Unif(0, 1)
10         for i ← 1 to |ℂ| + 1 do
11                                   // |ℂ| + 1 denotes the base station
12             if CDF[i] ≥ r then
13                 S_r ← S_r ∪ i
14                 break;
15             end
16         end
17     end
18     return S_r
19 end
```

Algorithms 1 and 2 can be used to carry out max and stochastic position updates, respectively. Both the algorithms take the Probability matrix P as input, and return the routing solution S_r. Both the algorithms can be easily modified to support clustering.

Algorithm 1 assumes that CHs are enumerated from 1 to $|\mathbb{C}|$, and $|\mathbb{C}| + 1$ represents the base station such that a CH c_j is denoted by j. For each j it then finds the row i corresponding to the maximum probability value ($P[i][j]$) in the column j of the probability matrix P. Subsequently, it assigns i (corresponding to c_i) as the next hop relay of j (corresponding to c_j).

Time and Space Complexity Analysis The time complexity of Algorithm 1 is $\mathcal{O}(|\mathbb{C}|^2)$ in the worst case owing to the two nested *for* loops in lines 3 and 6 which are executed for every combination of a gateway and its probable next hops. The algorithm however, has constant space complexity ($\mathcal{O}(1)$).[5]

Like Algorithm 1, Algorithm 2 also assumes that CHs are enumerated from 1 to $|\mathbb{C}|$, and $|\mathbb{C}| + 1$ represents the base station. Then, for each CH j, the algorithm iteratively builds a array *CDF* which represents its discrete Cumulative Distribution Function. This array (CDF_j) is subsequently utilised to perform *inverse transform sampling* to find the next hop relay i (corresponding to CH c_i) for the cluster head j.

The worst case time complexity of Algorithm 2 is also $\mathcal{O}(|\mathbb{C}|^2)$ due to the nested *for* loops on lines 3 and 6 which are executed for every combination of a gateway and its probable next hops. Unlike Algorithm 1, this algorithm has a linear ($\mathcal{O}|\mathbb{C}|$) space complexity owing to the generation of the *CDF* array.

While both the update strategies have comparable time complexities, the stochastic strategy has slightly higher (linear) space complexity in comparison to the max strategy (constant). While space complexity is undoubtedly an important factor in practical applications, we must also consider the significantly superior optimization performance (Sect. 7.4) of the stochastic strategy as against the max strategy.

[5] Since the S_r array which stores the routing solution is an output, it is not counted into space complexity.

6.1.7 Stochastic Update Strategy Parallels the Particle Update Equation in Classical BPSO

The position update equation of classical BPSO is given by Eq. 22:

$$\rho_{i,d}^{t} = \begin{cases} 1 \text{ if } \xi_S(\, v_{i,d}^{t+1}\,) > r_{i,d} \\ 0 \text{ otherwise} \end{cases} \tag{22}$$

where $\xi_S(v_{i,d}^{t+1}) = \frac{1}{1+e^{-v_{i,d}^{t+1}}}$ and $r_{i,d}$ is a uniformly distributed random number in the range [0, 1]. It can be seen that the velocity $v_{i,d}^{t+1}$ serves as a probability threshold that partitions the interval $[\xi_S(v_{min}),\ \xi_S(v_{max})]$ into two sub-intervals $I_1 = [\xi_S(v_{min}),\ \xi_S(v_{i,d}^{t+1})]$ and $I_2 = [\xi_S(v_{i,d}^{t+1}),\ \xi_S(v_{max})]$. If the uniformly distributed random number $r_{i,d} \in [0, 1]$ lies in interval I_1 then the corresponding bit is set to 1, whereas if it lies in I_2 then the bit is set to 0. Therefore, if the optimal solution contains 1 at some position, then BPSO learns to gradually increase the corresponding velocity in order to increase the length of interval I_1 and accordingly increase the chance that the random number $r_{i,d}$ lies inside it.

In order to understand the essence of the BPSO optimization process in case of the stochastic update strategy, let us assume that gateway c_j routs to gateway c_i in the optimal solution. BPSO gradually increases the velocity $V_k^{t+1}(i, j)$ thereby increasing the probability mass on the outcome i of the random variable $\mathbb{N}_{c_j}$. Increasing the probability mass on the outcome i increases the chance of i being sampled from the probability distribution of $\mathbb{N}_{c_j}$ such that $NH_{c_j} = c_i$. Like the position update equation in classical BPSO, the stochastic update strategy ensures that the position of a particle is ephemeral, i.e. the same velocity matrix can be interpreted as an altogether different position matrix and routing configuration. On the other hand, the max update strategy would always return the same position matrix for the same velocity matrix (Sect. 6.1.11).

6.1.8 The Choice of the Transfer Function ξ

A transfer function $\xi : [v_{min}, v_{max}] \cup \{-\infty\} \rightarrow [0, 1]$ is a mapping that takes an input in the closed interval $[v_{min}, v_{max}]$ or $-\infty$ and outputs a number in the closed interval [0, 1]. The transfer function is also called the *normalizing* function, and helps in the process of mapping a continuous search space to a discrete binary space. While routing and clustering configurations are discrete in nature, the velocity matrices lie in a continuous space. BPSO essentially *searches* for a velocity matrix in a continuous search space which maps to the optimal routing or clustering configuration in the discrete space.

Transfer functions must be effective as well as computationally simple since they are evaluated in numerous occasions, for every dimension of each particle every time its position is updated. To get an idea as to how many times a transfer function is called while executing BPSO for routing, let us consider a WSN with 60 gateways. Let us also assume that we run BPSO for 300 iterations with a swarm size of 50. Therefore, the transfer function is applied $60 \times 61 \times 50 \times 300$ or 54,900,000 times in total.

In this paper, we propose a *linear transfer function* ξ_L which not only reduces the *computational complexity* of BPSO, but also outperforms traditional alternatives such as sigmoid ξ_S and hyperbolic tan ξ_T transfer functions in terms of network lifetime and average increase in network lifetime (Sect. 7.3).

$$\xi_L(V_k^{t+1}(i,j)) = \frac{V_k^{t+1}(i,j) - v_{min}}{v_{max} - v_{min}} = \frac{V_k^{t+1}(i,j)}{v_{max} - v_{min}} + \frac{-v_{min}}{v_{max} - v_{min}} \tag{23}$$

Traditional transfer functions, ξ_S and ξ_T are given by Eqs. 24 and 25, respectively:

$$\xi_S(V_k^{t+1}(i,j)) = \frac{1}{1 + e^{(V_k^{t+1}(i,j))}} \tag{24}$$

$$\xi_T(V_k^{t+1}(i,j)) = \frac{tanh(V_k^{t+1}(i,j)) + 1}{2} \tag{25}$$

It must be noted that the slope of the linear transfer function ξ_L depends on the difference between v_{min} and v_{max}, in contrast to ξ_S and ξ_T which have fixed slopes.

6.1.9 Fitness Function

Now we design a fitness function in order to evaluate each particle of the population. The fitness function is a measure of *goodness* of a routing solution offered by a particle. Since our main objective for routing is to minimize the forwarding energy $E_{\mathcal{F}_{c_i}}$ of CHs, the fitness function for routing is given by:

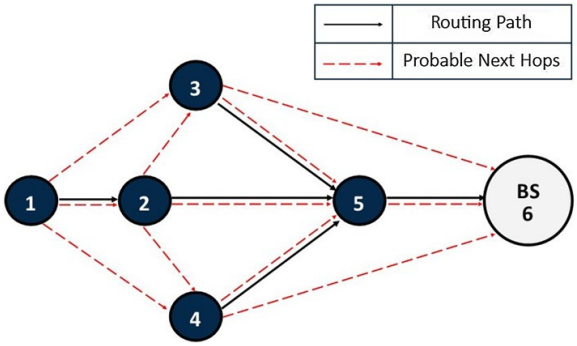
$$fitness = \arg\max_{i \in \mathbb{C}} E_{\mathcal{F}}(c_i) \tag{26}$$

The lower is the fitness value, the better is the particle position and corresponding routing configuration.

6.1.10 A Summary of BPSO-Based Routing

Algorithm 3 presents the proposed BPSO based routing algorithm which *minimizes* the routing fitness given by Eq. 26. It takes the coordinates of all the CHs ($\mathbb{S}$) and the number of particles in the swarm (N_p) as input. The algorithm begins by *randomly* initializing each particle's velocity matrix in the range $[v_{min}, v_{max}]$ (Sect. 6.1.3). In order to ensure that Condition 2 (Sect. 6.1.6) holds, every cell $V(i,j)$ for which c_j is *not* in the communication range of c_i, is initialized to $-\infty$. Next, the global best (*gbest*) position and personal best (*pbest*) positions of all particles in the swarm are updated by comparing their fitness values in lines [3-5]. In order to compute the fitness of a particle its position, which corresponds to a routing configuration, must be found. To this end, its velocity matrix (V) is transformed into a probability matrix (P) using Eq. 20, and then a routing configuration (position) is generated either using the Max (Algorithm 1) or Stochastic (Algorithm 2) position update strategy. Subsequently, a particle's fitness is calculated using Eq. 26. The algorithm then proceeds to optimize the routing configuration in an iterative fashion (lines [7–17]) by first updating each particle's velocity matrix using Eq. 17, finding their new fitness values and updating the global and their personal best positions in the same way as discussed above. Thus, the velocity updates for each particle is encapsulated in the *Update*(P_i) procedure.

Fig. 5 A possible routing path



Algorithm 3: BPSO Algorithm (Minimizer)

Input: Set of CHs $\mathbb{C} = \{c_1,\ c_2, \ldots\ c_{|\mathbb{C}|}\}$, Swarm size $= N_p$
Output: A routing solution: $S_r = \{c_j\ \forall i \in \{1,\ 2,\ 3 \ldots\ |\mathbb{C}|\}\}$ such that $c_j = NH_{c_i}$

begin
  Initialize each particle $P_i\ \forall i \in \{1,\ 2,\ 3, \ldots |N_p|\}$
  for $i \leftarrow 1$ **to** $|N_p|$ **do**
    Evaluate $fitness(P_i)$
    Assign
    $gbest = pbest_j \mid fitness(pbest_j) = min(fitness(pbest_j))\ \forall\ j \in \{1, 2, \ldots |N_p|\}$
  end
  while ! $Terminate$ **do**
    for $i \leftarrow 1$ **to** $|N_p|$ **do**
      $Update(P_i)$
      if $fitness(P_i) < fitness(pbest_i)$ **then**
        $pbest_i = P_i$
      end
      if $fitness(pbest_i) < fitness(gbest)$ **then**
        $gbest = pbest_i$
      end
    end
  end
  $S_r = Generate_Solution(Gbest)$
end

6.1.11 Illustration

Let us consider a WSN with 5 gateways $\mathbb{C} = \{c_1, c_2, c_3, c_4, c_5\}$ and 15 SNs $\mathbb{S} = \{s_1, s_2, \ldots, s_{15}\}$. Therefore, the dimensions of the routing position vector and matrix are 1×5 and 6×5 respectively. The velocity matrix has the same shape as the position matrix. The directed acyclic graph $G(V, E)$ shown in Fig. 5 illustrates the WSN. The vertices (V) of the graph G represents the set of gateways ($\mathbb{C}$) and the base station ($\mathbb{b}$). The set of edges (E) consists of dotted red lines which denote probable next hops and black lines which denote the chosen routing path. Table 2 comprises of the probable next hops for each gateway $c_j \in \mathbb{C}$. Algorithm 3 can be used to perform BPSO-based routing.

We initialize the velocity matrix V_k of a particle k by setting each of its elements $V_k(i,j)$ to a random number between $v_{max} = 10$ and $v_{min} = -10$ if c_i is a probable next hop of c_j i.e. $c_i \in pNH_{c_j}$, and $-\infty$ otherwise.

Table 2 Probable next hops for each gateway

Gateway (c_i)	c_1	c_2	c_3	c_4	c_5
Probable next hops (pNH_{c_i})	$\{c_2, c_3, c_4\}$	$\{c_3, c_4, c_5\}$	$\{c_5, \mathbb{b}\}$	$\{c_5, \mathbb{b}\}$	$\{\mathbb{b}\}$

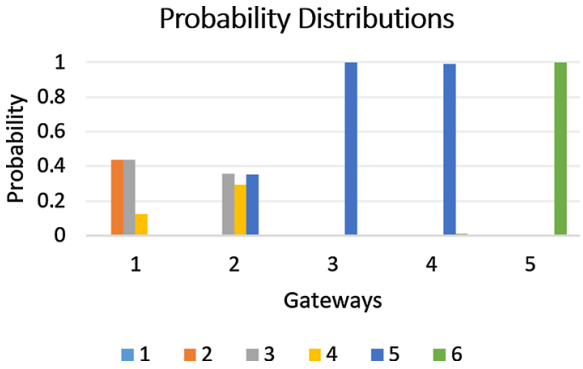


Fig. 6 Probability distributions of random variables $\mathbb{N}_{c_1}, \mathbb{N}_{c_2}$ etc

$$V_k = \begin{pmatrix} -\infty & -\infty & -\infty & -\infty & -\infty \\ 6.49 & -\infty & -\infty & -\infty & -\infty \\ 6.19 & 3.00 & -\infty & -\infty & -\infty \\ -4.22 & 1.46 & -\infty & -\infty & -\infty \\ -\infty & 4.21 & 7.71 & -4.54 & -\infty \\ -\infty & -\infty & -8.33 & -8.90 & -9.39 \end{pmatrix}$$

$$P_k = \begin{pmatrix} 0 & 0 & 0 & 0 & 0 \\ 0.4368 & 0 & 0 & 0 & 0 \\ 0.4366 & 0.3544 & 0 & 0 & 0 \\ 0.1264 & 0.2929 & 0 & 0 & 0 \\ 0 & 0.3577 & 0.9997 & 0.9906 & 0 \\ 0 & 0 & 0.0002 & 0.0093 & 1 \end{pmatrix} \tag{27}$$

After using the sigmoid transfer function to normalize the elements of V_k and re-scaling the probability values using Eq. 20, the probability matrix P_k is given by P_k. Each column j of the probability matrix P_k represents a probability distribution of the random variable $\mathbb{N}_{c_j}$. The probability distributions of all the random variables $\mathbb{N}_{c_1}$, $\mathbb{N}_{c_2}$, $\mathbb{N}_{c_3}$, $\mathbb{N}_{c_4}$ and $\mathbb{N}_{c_5}$ are illustrated in Fig. 6. Using the probability matrix P and the max update strategy, the indirect and direct encoding of the particle is given by: $X_k = \begin{pmatrix} 2 & 5 & 5 & 5 & 6 \end{pmatrix}$. On the other hand, the stochastic update strategy could also yield the following particles[6]: $X_k = \begin{pmatrix} 2 & 5 & 5 & 5 & 6 \end{pmatrix}$ or $\begin{pmatrix} 3 & 3 & 5 & 5 & 6 \end{pmatrix}$

[6] It must be noted that the following solutions are not exhaustive.

6.2 Clustering Algorithm

6.2.1 Formulating the Clustering Problem

Our main objective for clustering is to maximize the lifetime of the network and minimize the energy dissipation of SNs. As discussed in Sect. 5, maximizing the lifetime of a network is equivalent to maximizing the lifetime of the gateway with the minimum lifetime. After the routing configuration is finalised, clustering adjusts the number of SNs assigned (η) to each gateway, such that gateways having high forwarding energy are assigned fewer SNs and dissipate less intra-cluster energy.

At the same time, it is important to maximise the lifetime of SNs since they perform the basic function of sensing and collecting data. SNs also dissipate a significant amount of energy in transmitting data to their assigned CHs. In order to transmit a l-bit message to a CH at a distance d, the SN dissipates energy as follows: $E_T(s_i) = E_T(l, d)$. While maximising the lifetime of CHs by reducing the number of SNs that are assigned to each CH, some SNs may be assigned to CHs far away from them. These SNs may die quickly due to long distance communication with their respective CHs. Therefore, SNs must be assigned to their nearest CH whenever possible.

6.2.2 Particle Representation and Velocity Matrices

Clustering particles and their *pbest* and *gbest* can also be represented using direct and indirect representation. The direct representation or the position vector of a clustering particle exhibits the following characteristics:

1. The length of the vector m is equal to the number of SN in the network $|\mathbb{S}|$.
2. The ith dimension of the vector is j if the SN s_j is assigned to the CH c_i.
3. SNs can only be assigned to a single CH in the network, and therefore each dimension of the position vector must contain an integer in the closed interval $[1, |\mathbb{C}|]$.

Similarly, some characteristics of the indirect representation of a clustering particle are as follows:

1. All elements of the matrix M have either the value 0 or 1. Same as the direct representation, m is equal to the number of SNs in the network $|\mathbb{S}|$ and $n = |\mathbb{C}|$.
2. $M[c_i, s_j] = 1$ if s_j is assigned to c_i and 0 otherwise.
3. In each column of the matrix M only one element is 1 and all other elements are 0 since each SN can be assigned to a single CH only.

Figures 7 and 8 illustrate direct and indirect representations of a clustering particle, respectively.

The velocity vector of each clustering particle has the same shape as its position matrix i.e. $|\mathbb{C}| \times |\mathbb{S}|$. Equation 17 and either the stochastic or the max update strategy can be used to update the velocity and position of the particles, respectively.

Time and Space Complexity Analysis. of Max & Stochastic strategies Following an analysis similar to Sect. 6.1.6, both the Max and Stochastic update strategies have a time complexity of $\mathcal{O}(|\mathbb{S}| \times |\mathbb{C}|)$ owing to the nested *for* loops which must now iterate over every

s_1	s_2	s_3	s_4	s_5	s_6	s_7	s_8	s_9
c_2	c_5	c_2	c_5	c_3	c_4	c_1	c_1	c_3

Fig. 7 A direct representation of a clustering particle (*position vector*)

Fig. 8 An indirect representation of a clustering particle (*position matrix*)

	s_1	s_2	s_3	s_4	s_5	s_6	s_7	s_8	s_9
c_1	0	0	0	0	0	0	1	1	0
c_2	1	0	1	0	0	0	0	0	0
c_3	0	0	0	0	1	0	0	0	1
c_4	0	0	0	0	0	1	0	0	0
c_5	0	1	0	1	0	0	0	0	0

combination of a CH and every SN. Moreover, the Max update strategy has constant space complexity ($\mathcal{O}(1)$) while the Stochastic strategy has a space complexity of $\mathcal{O}(|\mathbb{S}|)$ owing to the generation of a *CDF* array with as many dimensions as the number of SNs in the WSN.

6.2.3 Fitness Function

The fitness function is derived in keeping with the main objective of clustering i.e. to prolong the lifetime of gateways and SNs. Therefore, our first objective is to maximize the lifetime of the WSN, or alternatively maximise the lifetime of the gateway with the minimum lifetime. We must note that maximizing the lifetime of a gateway takes into account the residual energy $E_{res}(c_i)$ of gateways at the start of WSN operation. Consequently, the clustering algorithm can assign fewer member SNs to gateways having less residual energy. In addition, the lifetime of SNs can be prolonged if they are assigned to the CHs nearest to them. Therefore, we must also minimize the average distance between SNs and their corresponding CHs in order to minimise their energy consumption. We can therefore construct the following fitness function:

$$fitness = \kappa \times \frac{L_n^n}{\frac{1}{|\mathbb{S}|}\sum_{i=1}^{|\mathbb{S}|} d(s_i, CH_{s_i})} \tag{28}$$

The higher is the fitness of a solution, the better is the position of a particle.

6.2.4 A Summary of BPSO-Based Clustering

Algorithm 3 (Sect. 6.1.10) can be slightly modified to serve as the BPSO-based clustering algorithm, with the only difference being that:

- it would take the coordinates of all SNs ($\mathbb{S}$) as input instead of the set of CHs ($\mathbb{C}$), and return a clustering solution S_c as output,
- the fitness of each particle is evaluated using Eq. 28,
- and the clustering fitness given by Eq. 28 is *maximised* unlike the routing fitness which is minimised. In particular, after initialization, positions corresponding to the maximum fitness are assigned as the *pbest* and *gbest*, respectively (line 5). Again in lines 10 and 13, positions corresponding to *greater* fitness is assigned as the *pbest* and *gbest* positions, respectively (Table 3).

Table 3 Energy and distance parameters

Energy and distance parameters	Values
Area	$500 \times 500\,\mathrm{m}^2$
SNs	200–500
Gateways	60, 90
Initial energy of SNs	2.0 J
Initial energy of CHs	10.0 J
E_{elec}	50 nJ/bit
E_{fs}	10 pJ/bit/m^2
E_{mp}	0.0013 pJ/bit/m^2
E_{DA}	5 nJ/bit
Communication range	150 m
d_o	87.0 m
Packet Size (l)	4000 bits
Message Size (m)	200 bits

Table 4 Parameters of the BPSO optimizer

BPSO parameters	Values
N_p	60
c_1	2
c_2	2
v_{max}/v_{max} (ξ_L)	$+2.5/-2.5$
v_{max}/v_{max} (ξ_S & ξ_T)	$+40/-40$

7 Experimental Evaluation

7.1 Experimental Setup

In this section, we evaluate the effectiveness of our proposed algorithm and compare them against state-of-the-art models. We carried out several experiments with different numbers of SNs ranging from 200 to 500 in two different gateway configurations, with 60 and 90 gateways, respectively. For a true comparison with previous literature, our simulation parameters were the same as Kuila and Jana [20]. Each SN had 2J of initial energy while each gateway had 10 J ($\epsilon = 10$). We assume that the communication energy dissipation is based on the first-order radio model (Sect. 4.1). Furthermore, we use the same energy and distance constants as Heinzelman et al. [14] in our simulations (Table 4). We implemented and simulated our algorithms using Python, and all experiments were carried out in a computer system with an Intel i7-8550U chipset, 2GHz CPU and 16 GB RAM running Microsoft Windows 10.

Our proposed algorithms are simulated for WSNs which have a sensing field of $500 \times 500\ m^2$ area and for each of the networks, the base station is situated at the centre of the region i.e. (250, 250). In order to optimize the performance of our algorithms, we fine tuned various parameters of BPSO and selected the parameters for which our algorithms performed the best. We tested the following ranges of parameter values: c_1 and c_2

Table 5 Comparison of Gaussian and uniform deployment: the Gaussian deployment results in lower maximum forwarding energy of gateways and higher network lifetime

Parameters	Gaussian deployment			Uniform deployment		
	Average	Max	Min	Average	Max	Min
Starting $max(E_{\mathcal{F}}(c_i))$ (J)	0.0077	0.0088	0.0063	0.0102	0.0095	0.0082
Final $max(E_{\mathcal{F}}(c_i))$ (J)	**0.0023**	0.0024	0.0020	0.0040	0.0049	0.0029
Starting $max(E_{\mathcal{C}}(c_i))$ (J)	0.0028	0.0041	0.0023	0.0031	0.0041	0.0027
Final $max(E_{\mathcal{C}}(c_i))$ (J)	0.0020	0.0022	0.0017	0.0020	0.0026	0.0014
Lifetime (rounds)	**2483**	3071	2149	1754	2111	1538

The best values are highlighted with bold

in $[1, 3]$, $\mathbb{N}_p = [10, 100]$ and $v_{max} = [1, 100]$. Based on experimental results, our algorithms performed the best for parameter values shown in Table 4.

7.2 Gaussian Gateway Deployment is Better than Uniform Deployment

In our experiments, SNs and gateways are deployed uniformly randomly across the sensing area for a true comparison with previous literature. Our experiments revealed that CHs closer to the base station expend a huge amount of forwarding energy to route in-bound data packets towards the base station, and therefore die quickly. To this end, we examine a random-gaussian deployment of gateways, which can effectively reduce their forwarding energy by randomly placing more gateways nearer to the base station. Increasing the number of gateways around the base station distributes the routing load among multiple gateways, reduces their forwarding energy and effectively increases their lifetime (refer Table 5). The gaussian-random coordinates of gateways can be generated as shown in Eq. 29:

$$(x_i, y_i) = (r_{i,1} \sim \mathcal{N}(\mathbb{c}, \mathbb{s}), r_{i,2} \sim \mathcal{N}(\mathbb{c}, \mathbb{s})) \tag{29}$$

Here, (x_i, y_i) denotes the x and y-coordinate pair of the ith gateway, and $r_{i,1}$ and $r_{i,2}$ are sampled from a gaussian distribution having $\mathbb{c}$ mean and $\mathbb{s}$ standard deviation. The parameter $\mathbb{c}$ corresponds to the coordinates of the base station which is situated at (250, 250), and therefore we set $\mathbb{c} = 250$. On the other hand, the parameter $\mathbb{s}$ corresponds to the spread of gateways from the base station and determines the concentration of gateways around the base station and the extent of gateway coverage in the WSN. For our experiments, we found that $\mathbb{s} = 100$ provided sufficient coverage and good network performance.

For our experiments, we consider a WSN with the same parameters as shown in Table 4 and having 60 gateways and 200 SNs. Table 5 summarizes experimental results derived by running the proposed algorithms on 40 independent distributions of SNs and CHs for both the deployment strategies. It must be noted that SNs are uniform randomly distributed across the sensing field in both the deployment strategies. Both the routing and clustering algorithms used the stochastic position update strategy and the proposed linear transfer function with $v_{max}/v_{min} = +2.5/-2.5$. The gaussian deployment of

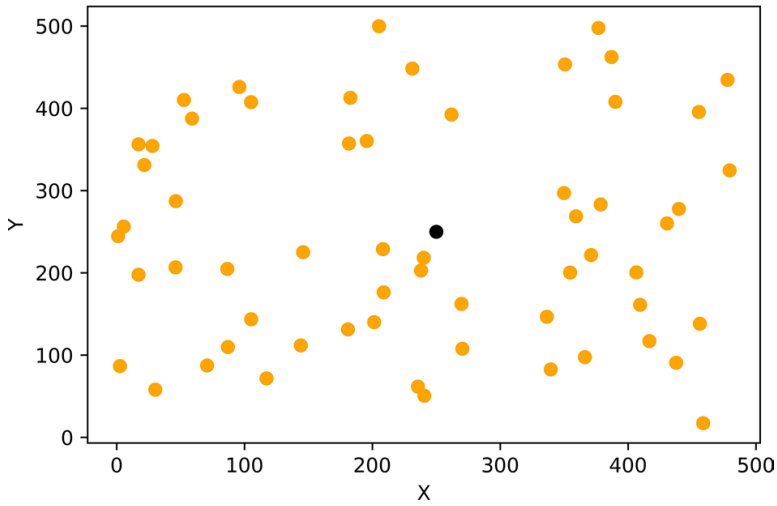


Fig. 9 Gateways deployed using Uniform random deployment are spread uniformly across the WSN

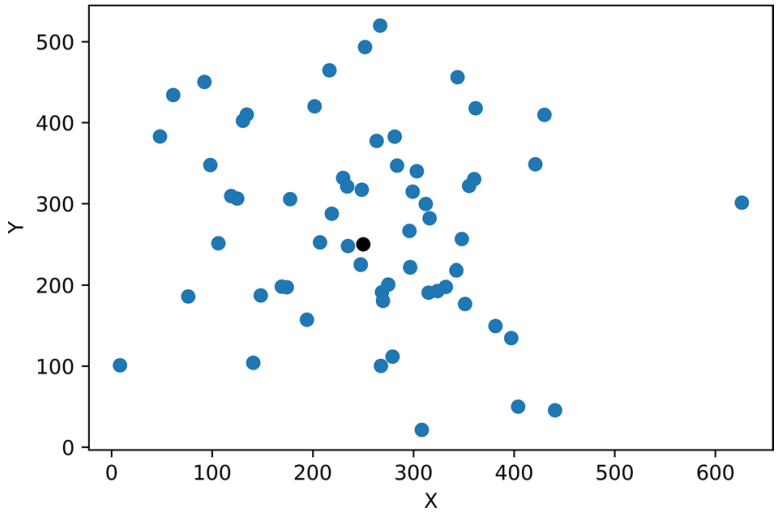


Fig. 10 Gateways deployed using Gaussian deployment are concentrated around the base station

gateways results in a 42.5% reduction in the maximum forwarding energy[7] on an average, and a significantly longer network lifetime. Furthermore, we observe that while the forwarding energy reduces sharply in case of the gaussian deployment, the inter-cluster component is comparable in both the deployment strategies. Figs. 9 and 10 illustrate 60 gateways deployed using the uniform-random and gaussian distributions, respectively. The base station is represented by a black dot and is situated at (250, 250). From the figures, it can be seen that a large number of gateways are concentrated around the base station for the gaussian deployment.

Despite the impressive performance of the gaussian deployment, gateways are distributed uniform-randomly in all the following experiments to present a true comparison with previous work.

7.3 The Linear Transfer Function ξ_L Outperforms Traditional ξ_S and ξ_T

For comparing the performance of our proposed *linear* transfer function against *sigmoid* and *hyperbolic tan*, we consider the same network parameters as given in Table 4. We

[7] Maximum forwarding energy of any gateway in the network.

Table 6 Comparison between transfer functions: the linear transfer function outperforms other traditional transfer functions

Parameters	Linear ξ_L			Sigmoid ξ_S			tanh ξ_T		
	Average	Max	Min	Average	Max	Min	Average	Max	Min
Routing time (s)	**125.6**	139.75	53.42	149.7	167.8	143.32	158.6	178.50	150.73
Clustering time (s)	**470.12**	516.94	413.90	531.17	587.66	492.30	566.41	632.33	524.54
Average Lifetime (rounds)	**1739**	2135	1497	1592	1787	1168	1695	1897	1276

The best values are highlighted with bold

chose to compare against sigmoid and hyperbolic tan transfer functions only, since they have been widely used in the past for a number of applications [1, 24, 30, 31]. We tuned the maximum and minimum velocity parameters for each of the transfer functions in the range [1, 100], and chose the values of v_{max} and v_{min} (refer Table 4) for which they performed the best. We found that the linear transfer function performed well for $v_{max} = 2.5$ and $v_{min} = -2.5$ for which it linearly approximates the sigmoid function over a large range. Table 6 summarizes the experimental results on 40 randomly and independently generated sets of coordinates of gateways and SNs for each network configuration having 200, 300, 400 or 500 SNs. We chose to test the three transfer functions on the same sets of coordinates to do away with any variation due to input coordinates. We found that the linear transfer function performed well for $v_{max} = 2.5$ and $v_{min} = -2.5$ for which it linearly approximates the sigmoid function over a large range (refer Fig. 11).

Firstly, we evaluated the transfer functions based on the average network lifetime achieved by our routing and clustering algorithms using each transfer function. Our results revealed that the linear transfer function resulted in a longer network lifetime on an average for each network configuration (refer Fig. 12). Next, we evaluated the average increase in lifetime for 40 runs of our algorithm using each transfer function. The average increase in lifetime (First Gateway Died) can be computed as follows:

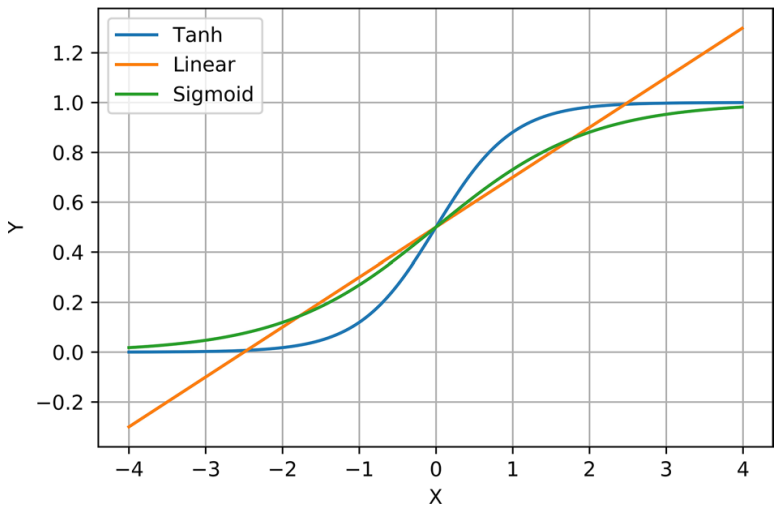


Fig. 11 Various transfer functions

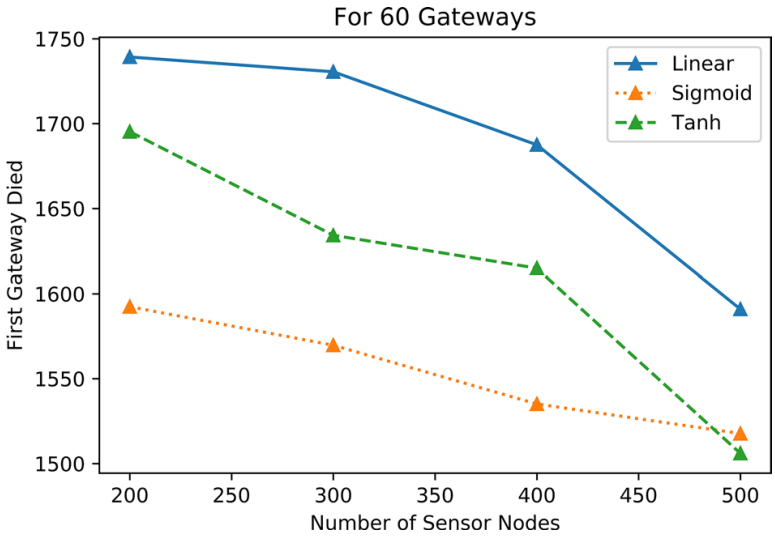


Fig. 12 First gateway died: the linear transfer function achieves a high network lifetime consistently

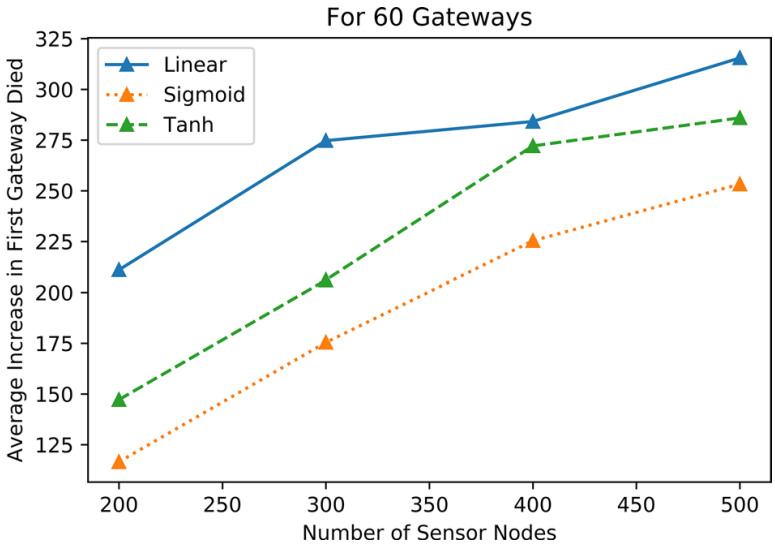


Fig. 13 Average increase in first gateway died: the linear transfer function mostly results in a higher average increase in lifetime

$$Average\ increase\ in\ lifetime = \frac{gbest_k.lifetime - gbest_1.lifetime}{Number\ of\ runs} \tag{30}$$

where k is the number of iterations and $gbest_i.lifetime$ is the lifetime of the *gbest* particle at the ith iteration. We found that the *linear* transfer function increased the network lifetime more on an average in comparison to *sigmoid* and *hyperbolic tan* transfer functions for all the network configurations (Fig. 13).

The increasing trend in the average increase in lifetime can be attributed to the fact that network configurations with greater numbers of SNs have a larger clustering search space, and therefore at the start of the optimization process, randomly-generated yet good clustering solutions occur with a smaller probability. From Figs. 14 and 15 we can see that the *linear* transfer function updates the global best solution more often than *tanh* and *sigmoid* transfer functions. This is due to the fact that our linear function does not have a *vanishing gradient*, and therefore is equally sensitive to a change in a particle's position at all velocities i.e. the proportion of rise in the probability that a bit is ON to an equal rise in velocity remains constant across the interval $[v_{min}, v_{max}]$.

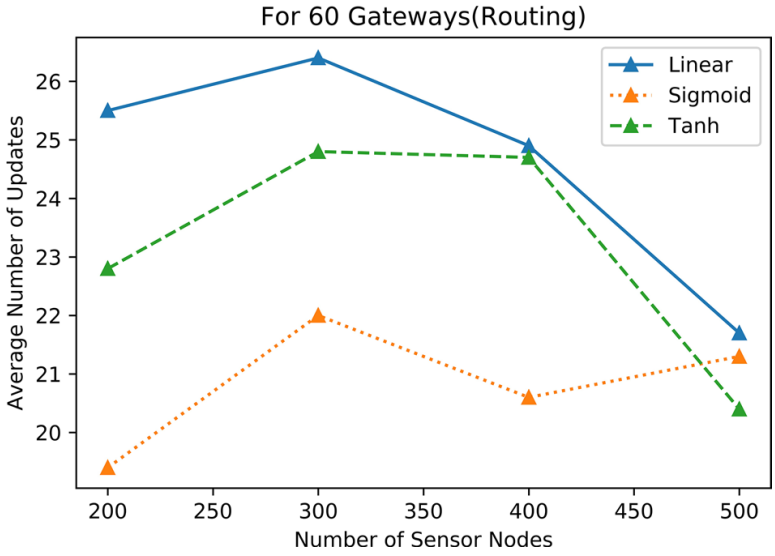


Fig. 14 Average updates in routing: the linear transfer function has greater updates than other transfer functions

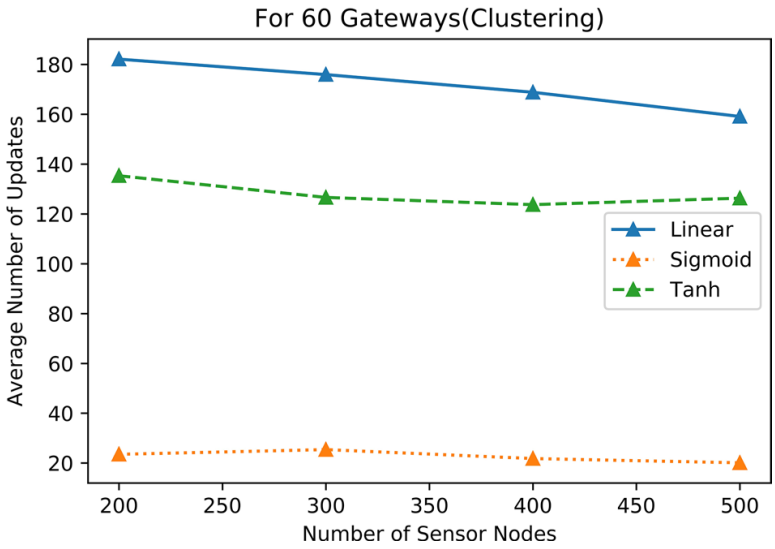


Fig. 15 Average updates in clustering: the linear transfer function has greater updates other transfer functions

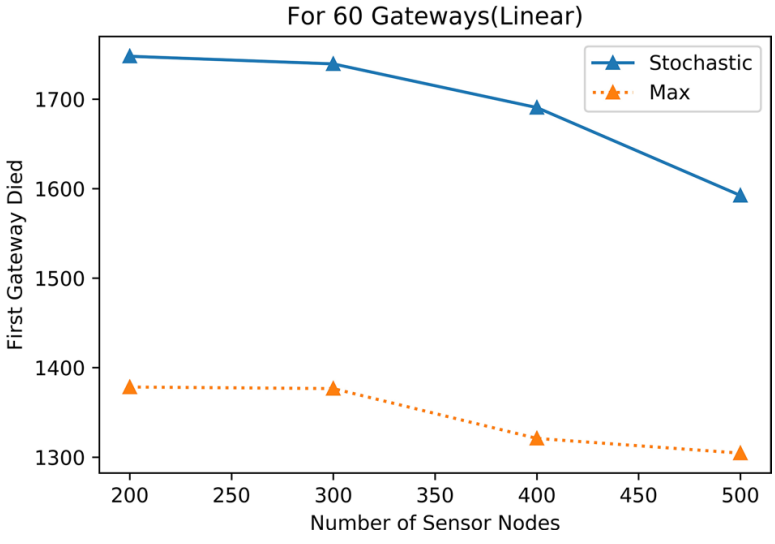


Fig. 16 Lifetime versus number of SNs: stochastic update strategy outperforms the max update strategy in increasing the lifetime of the network

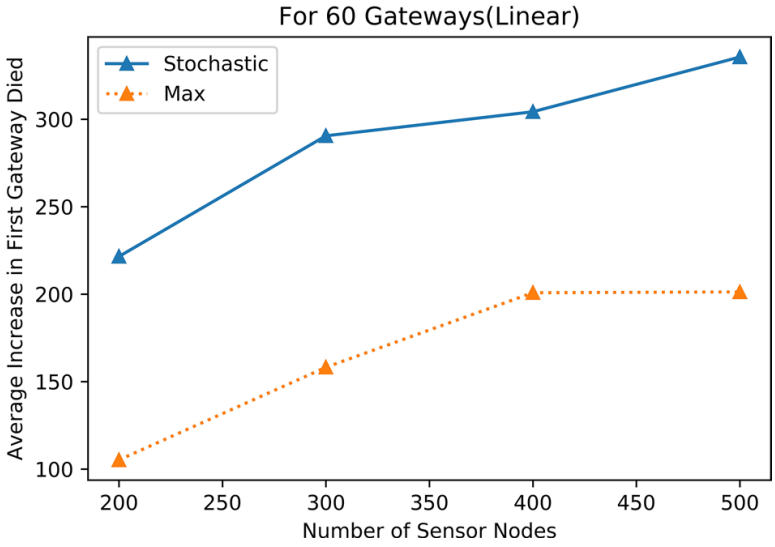


Fig. 17 Average increase in lifetime (first gateway died) versus number of SNs: the stochastic update strategy increases network lifetime more than the max update strategy

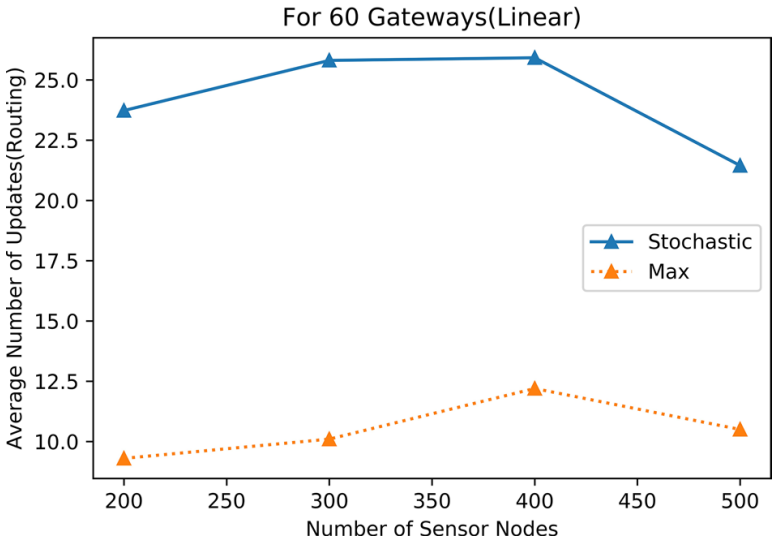


Fig. 18 Average updates in routing: the stochastic update strategy achieves a higher number of updates than the max update strategy

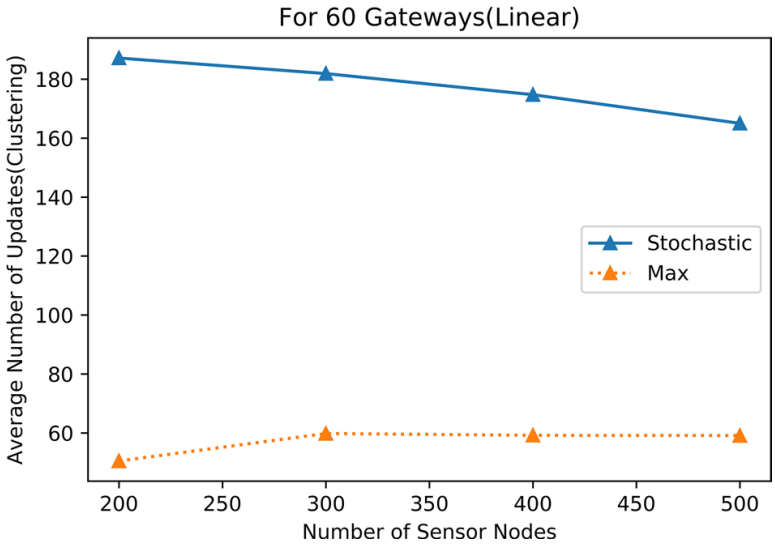


Fig. 19 Average updates in clustering: the stochastic update strategy achieves a significantly higher number of updates than the max update strategy

For the WSN configuration with 200 SNs, we also evaluated the running time (refer Table 6) of our algorithms using the three transfer functions. Our results revealed that using the *linear* transfer function as against *sigmoid* and *tanh*, led to a 7–12% reduction

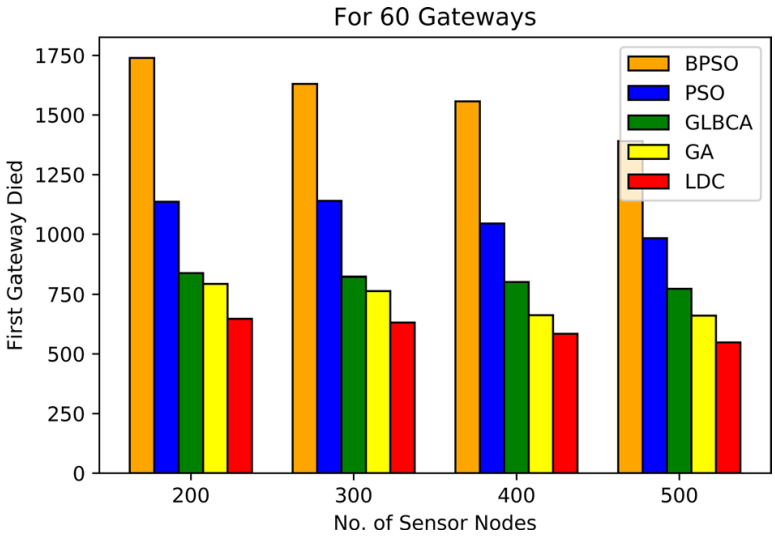


Fig. 20 Network lifetime (60 gateways): BPSO achieves significantly high network lifetime

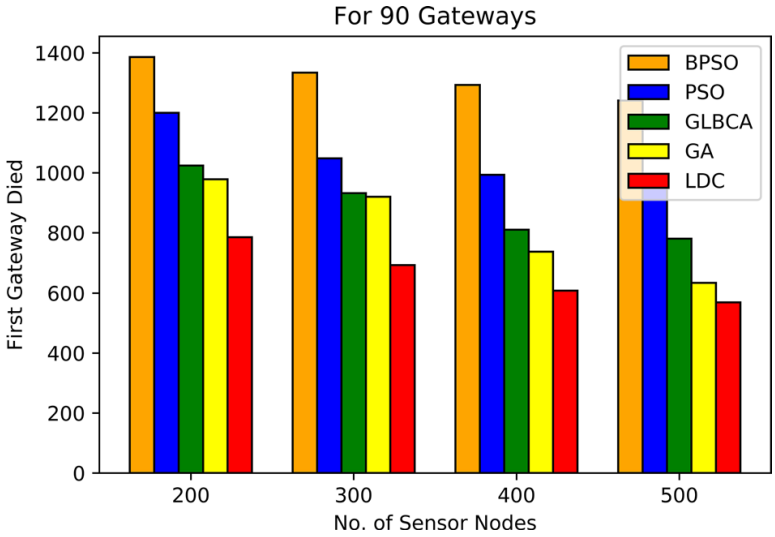


Fig. 21 Network lifetime (90 gateways): BPSO outperforms other state-of-the-art algorithms in terms of lifetime (first gateway died)

in average routing time and 11.5–17% reduction in average clustering time. This reduction can be attributed to the computational simplicity of the linear transfer function.

7.4 The Stochastic Update Strategy Outperforms Max Update Strategy

In order to evaluate the performance of the stochastic and max position update strategies, we compared the average lifetime and average increase in lifetime produced by our routing and clustering algorithms for both the position update strategies. We evaluated both the strategies on 40 sets of randomly and independently generated coordinates for each network configuration. Our results (refer Figs. 16, 17) confirmed that the stochastic update strategy outperforms the max update strategy, by achieving considerably longer network lifetimes and a significant increase in the lifetime on an average for all the network configurations.

Figures 18 and 19 illustrate the average number of updates for the global best solution during routing and clustering. Clearly, the stochastic update strategy updates the global best solution more often than the max update strategy. This is due to the fact that the stochastic update strategy encourages more exploration owing to its probabilistic nature.

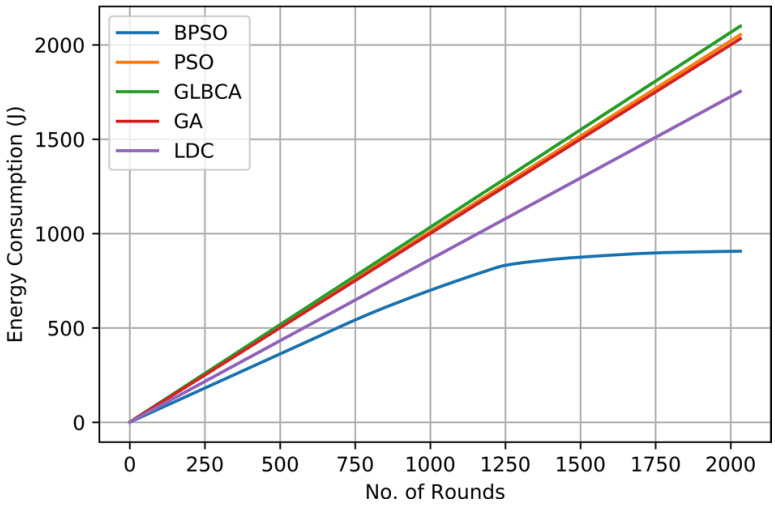


Fig. 22 Energy consumption: our algorithm consumes appreciably lower energy than state-of-the-art of algorithms

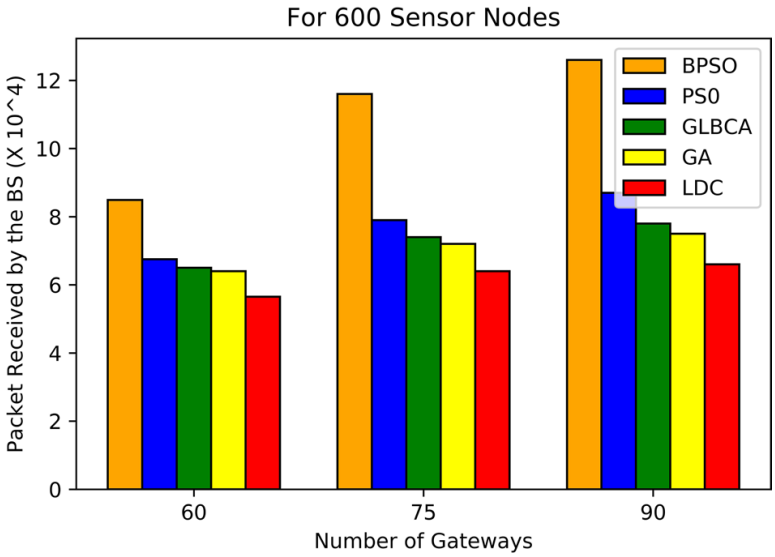


Fig. 23 Packets received by base station (BS): our algorithm delivers significantly higher packets to BS than state-of-the-art of algorithms

7.5 Lifetime Comparison with State-of-the-Art Algorithms

In order to compare the performance of our routing and clustering algorithms with other state-of-the-art algorithms, we executed the PSO-based routing and clustering algorithm proposed by Kuila and Jana [20] and three other clustering algorithms: *GA-based clustering* [21], *Greedy Load-Balanced Clustering Algorithm* (GLBCA)[23] and *Least Distance Clustering* (LDC) [2]. All these clustering algorithms assumed that the base station is within the direct communication range of all the gateways and therefore did not consider multi-hop routing. For a true comparison with our proposed algorithms, we executed the popular GA-based multi-hop routing algorithm proposed by Bari et al. [3] for each of the three-clustering algorithm (GA-based clustering, GLBCA and LDC). We ran our experiments for 40 sets of independently and uniform-randomly generated coordinates of gateways and SNs for each unique network configuration. Moreover, we compared the lifetime of the network for several network configurations by varying the number of SNs between 200 and 500, and for 60 and 90 gateways. Figures 20 and 21 illustrate the results we obtained. It can be seen that our proposed algorithm leads to a better network lifetime than other state-of-the-art algorithms. This is due to the fact that our proposed routing

Table 7 Comparison of PSO and BPSO: BPSO is better equipped to find an efficient routing & clustering solution than PSO

Parameters	BPSO			PSO		
	Average	Max	Min	Average	Max	Min
Routing fitness	**0.0043**	0.0050	0.0026	0.0049	0.0052	0.0035
Clustering fitness	**38.0543**	51.3592	30.5490	17.678	27.7224	13.628
Average Distance (m)	**45.0937**	47.7760	41.8986	76.2279	80.3659	70.9511
Lifetime (rounds)	**1739**	2135	1497	1428	1921	1029
Increase in routing fitness	**0.006419**	0.0140	0.0032	0.00492	0.0084	0.0018
Increase in clustering fitness	**20.0213**	28.2360	15.2126	3.1582	4.8947	1.0198
Extent of Optimization (rounds)	**1294**	1373	1079	768	844	550

The best values are highlighted with bold

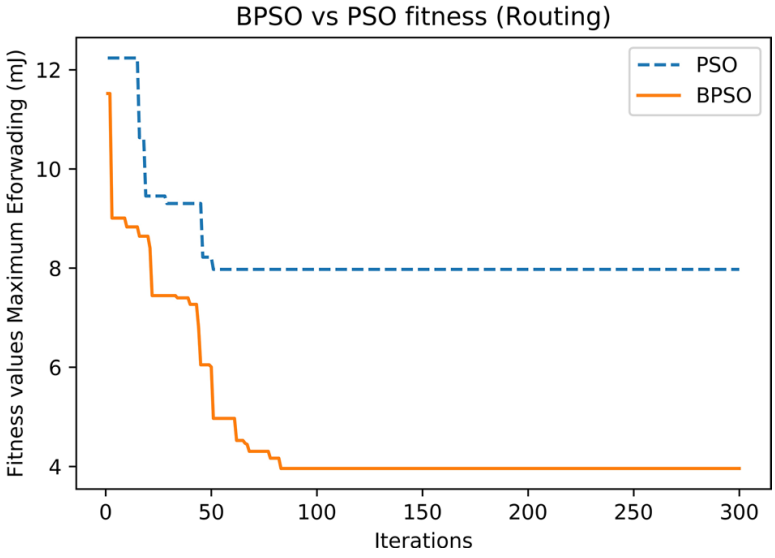


Fig. 24 BPSO versus PSO routing fitness: BPSO is less prone to local minima as compared to its counterpart

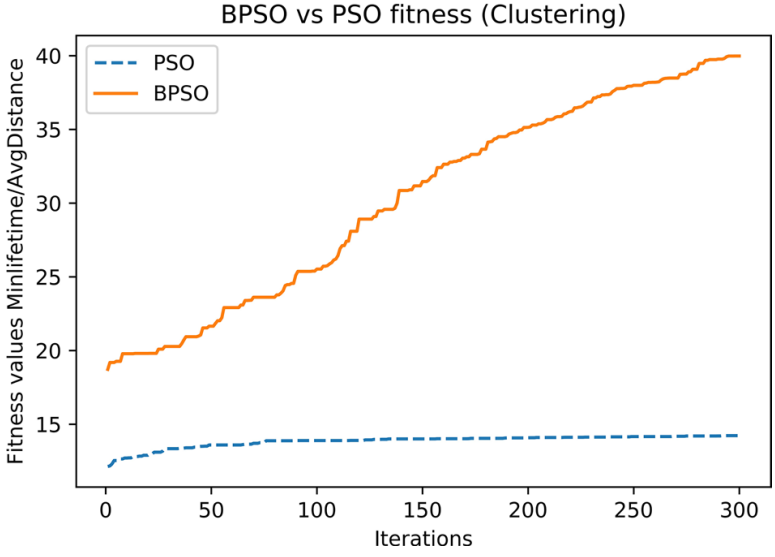


Fig. 25 BPSO versus PSO clustering fitness: BPSO is less prone to local maxima as compared to its counterpart

algorithm recognizes that gateways dissipate a significant amount of forwarding energy (refer Table 5), and minimizes it to effectively prolong network lifetime (Figs. 22, 23).

From Fig. 23, it can be observed that the total packets received by the base station in our approach is appreciably higher than other algorithms. This is a direct consequence of the fact that our approach has a better network lifetime than other state-of-the-art algorithms. Figure 22, compares the energy consumption of our algorithm with other state-of-the-art algorithms for 60 gateways and 600 SNs. Our WSN has significantly lower energy consumption as compared to other algorithms. This demonstrates the efficacy of our proposed fitness functions which are directly aimed at minimizing forwarding and intra-cluster energy consumption of CHs, thereby minimizing the total energy consumption of the network.

7.6 BPSO Outperforms PSO at Routing and Clustering

In this sub-section, we compare the performance of continuous PSO and its discrete counterpart BPSO. For this comparison, we ran PSO and BPSO-based routing and clustering on a WSN having the same network parameters as Table 4 having 200 SNs and 60 gateways. Both the algorithms were run on 40 sets of input coordinates using our fitness functions. We represented particles in PSO in the same manner as Kuila and Jana [20][8] and used their indexing function to map particle positions in a continuous space to a discrete space. As discussed previously, BPSO searches for a velocity matrix in a continuous search space which maps to a *good* particle position in a discrete space. In contrast, PSO searches for a velocity vector which maps to *good* particle position, both of which are in a continuous search space. In PSO, the indexing function is used to map the continuous position of a particle to a discrete routing or clustering configuration.

Our results summarized in Table 7 suggest that BPSO achieves a significantly longer average network lifetime than PSO. Furthermore, BPSO is better able to minimize the routing fitness and average distance of SNs from their clusters. Figures 24 and 25 illustrate the routing and clustering fitness per iteration for both BPSO and PSO for the same set of input coordinates. It can be clearly seen that BPSO quickly minimizes the routing fitness and reaches a fitter routing solution in comparison to PSO. During clustering, BPSO starts at a higher fitness than PSO owing to its better routing solution, and improves the fitness over iterations. Furthermore, in order to evaluate the overall increase in lifetime due to optimization over random routing and clustering configurations, we ran BPSO and PSO based routing and clustering for a single iteration over the same sets of 40 input coordinates. The routing and clustering solutions after a single iteration are as good as random. The results summarized in Table 7 show that BPSO increases the lifetime of a WSN by 1294 rounds over a random routing and clustering configuration on an average, as against PSO which is only able to increase the lifetime by 768 rounds. During both routing and clustering, BPSO was able to effectively optimize the fitness functions, while PSO repeatedly got trapped in local maxima. This is due to the fact that BPSO is better suited to handle discrete problems such as finding optimal routing and clustering solutions.

[8] Refer Kuila and Jana [20] for more details.

8 Conclusion and Future Work

In this paper, we proposed an energy efficient BPSO based routing and clustering algorithm, which uses an intuitive two-dimensional particle representation along with a novel particle update strategy and transfer function. Results from detailed experimental evaluation show that our transfer function and particle update strategy outperform traditional transfer functions and particle update strategies proposed in the past. Our experiments also reveal that our algorithm effectively maximizes network lifetime, and achieves a significantly higher lifetime in comparison to state-of-the-art algorithms. Furthermore, our results confirm that BPSO is better equipped to solve discrete optimization problems like efficient routing and clustering than continuous PSO. Future work may include experimenting with fitness functions which take into account the reliability of wireless links.

References

1. Bansal, J. C., & Deep, K. (2012). A modified binary particle swarm optimization for knapsack problems. *Applied Mathematics and Computation*, *218*(22), 11042–11061.
2. Bari, A., Jaekel, A., & Bandyopadhyay, S. (2008). Clustering strategies for improving the lifetime of two-tiered sensor networks. *Computer and Communications*, *31*(14), 3451–3459. https://doi.org/10.1016/j.comcom.2008.05.038.
3. Bari, A., Wazed, S., Jaekel, A., & Bandyopadhyay, S. (2009). A genetic algorithm based approach for energy efficient routing in two-tiered sensor networks. *Ad Hoc Networks*, *7*(4), 665–676. https://doi.org/10.1016/j.adhoc.2008.04.003.
4. Baronti, P., Pillai, P., Chook, V. W., Chessa, S., Gotta, A., & Hu, Y. F. (2007). Wireless sensor networks: A survey on the state of the art and the 802.15. 4 and zigbee standards. *Computer Communications*, *30*(7), 1655–1695.
5. Calhoun, B. H., Daly, D. C., Verma, N., Finchelstein, D. F., Wentzloff, D. D., Wang, A., et al. (2005). Design considerations for ultra-low energy wireless microsensor nodes. *IEEE Transactions on Computers*, *54*(6), 727–740. https://doi.org/10.1109/TC.2005.98.
6. Chatterjee, S., Sarkar, S., Hore, S., Dey, N., Ashour, A. S., & Balas, V. E. (2017). Particle swarm optimization trained neural network for structural failure prediction of multistoried RC buildings. *Neural Computing and Applications*, *28*(8), 2005–2016.
7. Dietrich, I., & Dressler, F. (2009). On the lifetime of wireless sensor networks. *ACM Transactions on Sensor Networks (TOSN)*, *5*(1), 5.
8. Ebrahimi Mood, S., & Javidi, M. (2019). Energy-efficient clustering method for wireless sensor networks using modified gravitational search algorithm. *Evolving Systems*. https://doi.org/10.1007/s12530-019-09264-x.
9. Ghamisi, P., & Benediktsson, J. A. (2015). Feature selection based on hybridization of genetic algorithm and particle swarm optimization. *IEEE Geoscience and Remote Sensing Letters*, *12*(2), 309–313.
10. Gupta, G., & Younis, M. (2003). Load-balanced clustering of wireless sensor networks. In *IEEE international conference on communications, 2003. ICC '03* (Vol. 3, pp. 1848–1852). https://doi.org/10.1109/ICC.2003.1203919
11. Gupta, G., & Younis, M. (2003). Performance evaluation of load-balanced clustering of wireless sensor networks. In *10th international conference on telecommunications, 2003. ICT 2003* (Vol. 2, pp. 1577–1583). IEEE.
12. Gupta, S. K., Kuila, P., & Jana, P. K. (2013). GAR: An energy efficient GA-based routing for wireless sensor networks. In *International conference on distributed computing and internet technology* (pp. 267–277). Springer.
13. Heinzelman, W. R., Chandrakasan, A., & Balakrishnan, H. (2000). Energy-efficient communication protocol for wireless microsensor networks. In *Proceedings of the 33rd annual Hawaii international conference on system sciences* (p. 10). IEEE.
14. Heinzelman, W. B., Chandrakasan, A. P., & Balakrishnan, H. (2002). An application-specific protocol architecture for wireless microsensor networks. *IEEE Transactions on Wireless Communications*, *1*(4), 660–670. https://doi.org/10.1109/TWC.2002.804190.

15. Izakian, H., Ladani, B. T., Abraham, A., & Snásel, V. (2010). A discrete particle swarm optimization approach for grid job scheduling. *International Journal of Innovative Computing, Information and Control*, *6*, 1–15.
16. Jaichandran, R., Anthony, I. A., & Emerson, R. J. (2010). Effective strategies and optimal solutions for hot spot problem in wireless sensor networks (WSN) (pp. 389–392). https://doi.org/10.1109/ISSPA.2010.5605518.
17. Kaur, S., & Mahajan, R. (2018). Hybrid meta-heuristic optimization based energy efficient protocol for wireless sensor networks. *Egyptian Informatics Journal*, *19*(3), 145–150.
18. Kennedy, J., & Eberhart, R. (1995). Particle swarm optimization (PSO). In *Proceedings of IEEE international conference on neural networks, Perth, Australia* (pp. 1942–1948).
19. Kennedy, J., & Eberhart, R. C. (1997). A discrete binary version of the particle swarm algorithm. In *1997 IEEE international conference on systems, man, and cybernetics. Computational cybernetics and simulation* (Vol. 5, pp. 4104–4108). IEEE.
20. Kuila, P., & Jana, P. K. (2014). Energy efficient clustering and routing algorithms for wireless sensor networks: Particle swarm optimization approach. *Engineering Applications of Artificial Intelligence*, *33*, 127–140. https://doi.org/10.1016/j.engappai.2014.04.009.
21. Kuila, P., Gupta, S., & Jana, P. (2013). A novel evolutionary approach for load balanced clustering problem for wireless sensor networks. *Swarm and Evolutionary Computation*, *12*, 48–56. https://doi.org/10.1016/j.swevo.2013.04.002.
22. Liu, X. (2012). A survey on clustering routing protocols in wireless sensor networks. *Sensors*, *12*(8), 11113–11153. https://doi.org/10.3390/s120811113.
23. Low, C. P., Fang, C., Ng, J. M., & Ang, Y. H. (2008). Efficient load-balanced clustering algorithms for wireless sensor networks. *Computer and Communications*, *31*(4), 750–759. https://doi.org/10.1016/j.comcom.2007.10.020.
24. Pedrasa, M. A. A., Spooner, T. D., & MacGill, I. F. (2009). Scheduling of demand side resources using binary particle swarm optimization. *IEEE Transactions on Power Systems*, *24*(3), 1173–1181.
25. Shi, Y., & Eberhart, R. C. (1999). Empirical study of particle swarm optimization. In *Proceedings of the 1999 congress on evolutionary computation-CEC99 (Cat. No. 99TH8406)* (Vol. 3, pp. 1945–1950). IEEE.
26. Souissi, M., & Meddeb, A. (2016). Minimum energy multi-objective clustering model for wireless sensor networks (pp. 769–773). https://doi.org/10.1109/IWCMC.2016.7577154.
27. Srinivasa Rao, P. C., & Banka, H. (2017). Energy efficient clustering algorithms for wireless sensor networks: Novel chemical reaction optimization approach. *Wireless Networks*, *23*(2), 433–452. https://doi.org/10.1007/s11276-015-1156-0.
28. Tang, J., Hao, B., & Sen, A. (2006). Relay node placement in large scale wireless sensor networks. *Computer and Communications*, *29*(4), 490–501. https://doi.org/10.1016/j.comcom.2004.12.032.
29. Taormina, R., & Chau, K. W. (2015). Data-driven input variable selection for rainfall-runoff modeling using binary-coded particle swarm optimization and extreme learning machines. *Journal of Hydrology*, *529*, 1617–1632.
30. Taşgetiren, M. F., & Liang, Y. C. (2003). A binary particle swarm optimization algorithm for lot sizing problem. *Journal of Economic and Social Research*, *5*(2), 1–20.
31. Thilagavathi, S., & Geetha, B. G. (2015). Energy aware swarm optimization with intercluster search for wireless sensor network. *The Scientific World Journal*. https://doi.org/10.1155/2015/395256.
32. Yigitel, M. A., Incel, O. D., & Ersoy, C. (2011). QoS-aware mac protocols for wireless sensor networks: A survey. *Computer Networks*, *55*(8), 1982–2004. https://doi.org/10.1016/j.comnet.2011.02.007.
33. Younis, O., & Fahmy, S. (2004). Heed: A hybrid, energy-efficient, distributed clustering approach for ad hoc sensor networks. *IEEE Transactions on Mobile Computing*, *03*(4), 366–379. https://doi.org/10.1109/TMC.2004.41.

Publisher's Note Springer Nature remains neutral with regard to jurisdictional claims in published maps and institutional affiliations.



Ajay Kaushik has done Ph.D. from Department of Computer Engineering at Delhi Technological University (DTU), Delhi, India. He is presently working as an assistant professor in Galgotias University. His areas of interest are Wireless sensor networks, Internet of Things and Nature Inspired Intelligence. He has published many research papers in reputed journals and international conferences. He did his M.Tech. (Master of Technology), Post B.Tech. in Computer Science and Engineering from Kurukshetra University, Kurukshetra. He qualified UGC NET-JRF with a percentage of 70.8% in year 2013. He has always been among the top rank-holders of the university in these courses.



Mononito Goswami is a pre-final year student pursuing Computer Engineering from Delhi Technological University, India. His research interests include Machine Learning, Swarm Intelligence, Deep learning and Artificial Intelligence in Education. He was a Summer Scholar in Carnegie Mellon University, USA, and has published a student paper on Intelligent Tutoring Systems in AAAI 2019. In the summer of 2019, he interned as a research scholar in the Robotics Institute in Carnegie Mellon University.



Minkush Manuja is a pre-final year student pursuing Computer Engineering from Delhi Technological University, India. His research interests include Machine learning for computer security, nature-inspired optimization and Deep Learning. He is currently working on optimization of multi-objective cost functions using meta-heuristic optimization. He interned at Tower Research Capital, India in the summer of 2019.



Prof. S. Indu is a Professor in the Department of Electronics and communication Engineering, Delhi Technological University, Delhi, and is currently the dean of the student welfare department there. She has done Ph.D. in Computer Engineering from University of Delhi and M.Tech., Post B.Tech. from University of Kerala, Kerala. She was awarded the Best Branch Counselor award 2013 IEEE USA. Her research interests are in the field of Computer Vision, Image Processing, and wireless sensor network. She has 3 completed sponsored research projects. She has published around 120 papers in reputed journals, national and international conferences.



Prof. Daya Gupta is a Professor in the Department of Computer Engineering, Delhi Technological University, Delhi. She has done Ph.D. in Computer Engineering from University of Delhi and M.Sc. (Mathematics), Post M.Sc. Diploma (Computer Science) from IIT, Delhi. She is a senior member of IEEE and a life member of CSI. Her research interests are in the field of requirement engineering, network security, ad hoc networks and image classification in remote sensing. She has published several research papers in international journals and conferences and has chaired sessions and delivered invited talks at many national and international conferences.

ResearchGate

See discussions, stats, and author profiles for this publication at: https://www.researchgate.net/publication/338992286

A Blockchain Based Approach For An Efficient Secure KYC Process With Data Sovereignty

Research · January 2020

CITATIONS
0

READS
21

2 authors:



Manoj Kumar
Delhi Technological University
24 PUBLICATIONS **29** CITATIONS
SEE PROFILE



Nikhil Yadav
Delhi Technological University
1 PUBLICATION **0** CITATIONS
SEE PROFILE

Some of the authors of this publication are also working on these related projects:

SMS-based FAQ Retrieval View project

All content following this page was uploaded by Manoj Kumar on 03 February 2020.

The user has requested enhancement of the downloaded file.

A Blockchain Based Approach For An Efficient Secure KYC Process With Data Sovereignty

Dr. Manoj Kumar, Nikhil, Parina Anand

Abstract|: - The Know Your Customer process followed by the banking institutions today is highly inefficient and inconvenient for both banks and the customers. The process is redundant and increases operational costs. Moreover, it has little to no safeguards for user's privacy. This paper proposes a blockchain based approach to decentralise the storage of personal data and remove the need to trust a third party. Additionally, our proposed solution focuses on the problem of data ownership which we solve by storing it in an encrypted format which can only be decrypted by the user. In our implementation, the user has his PII (Personally Identifiable Information) on a QR code in an encrypted format, ensuring two-layer security of data. The banks only have access to the data when the customer explicitly gives it to them. Consequently, implementing the proposed system along with the coordination between the banks, the regulator and other stakeholders will ensure an enhanced user experience and save costs for the service providers.

Index Terms: Blockchain, Digital Identity, Fintech, Know your customer, Smart Contracts

1. INTRODUCTION

Know Your Customer (henceforth KYC) refers to the verification process performed by banks and other financial institutions to ascertain the identity of customers or businesses they intend to do business with. The objective of KYC guidelines is to prevent banks from being used, intentionally or unintentionally, by criminal elements for money laundering activities. ([1]) In India, all Scheduled Commercial Banks (excluding Regional Rural Banks), all financial institutions and local area banks are required to follow the Reserve Bank of India Know Your Customer (KYC) Directions, 2016[2] and update the KYC data ranging from at least once in every ten years for low risk customers to once in every two years for high risk customers . Besides being a legal and regulatory requirement, KYC is considered as a priority exercise by banks to prevent financial frauds. With the increasing menace of organised crime, terrorist financing, and money laundering, KYC policies are now an indispensable tool to combat illegal transactions in the field of international finance. According to a recent Thomas Reuters Survey[3], the average global annual spending on KYC by financial institutions with $10 billion or more in revenue have increased to $150 million this year from $142 million in 2016. Besides the annual expenditure, banks have to pay hefty fines for non-compliance which usually occurs due to volatility, uncertainty, complexity, and ambiguity in the process. The same survey also reports the average onboarding time increased to 32 days from 28 days in 2016, indicating a poor user experience. This highlights the urgent need to revamp the KYC-compliance process and record keeping system. It is a pain point for both the financial institutions and the customers, thus affecting transactional experience.

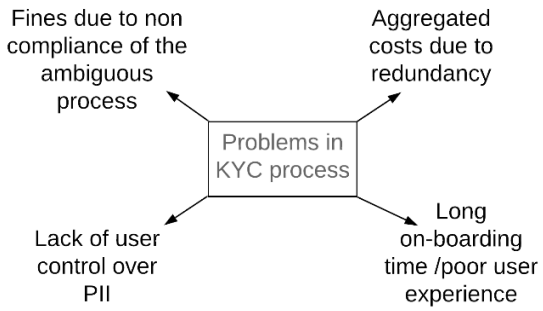


Figure 1: *Problems in KYC system*

locks. This makes it almost impossible to tamper with any transactions in the blockchain. Thus, a blockchain offers highly desirable characteristics of immutability, unhackability, decentralization, and trustlessness to a system. Blockchain technology has gained prominence due to the widespread use of bitcoin. Bitcoin, introduced in 2009 by Satoshi, is a digital currency in which encryption techniques are used to regulate the generation of units of currency and verify the transfer of funds[7]. It is a purely peer-to-peer version of electronic cash that does not require any third party and is not governed by any central body[8]. While blockchain was initially only used as a ledger for transactions of cryptocurrencies, newer platforms like ethereum emerged which are capable of running complete decentralized applications by means of a smart contract. Smart contracts are self-executing programs deployed on a blockchain that can perform certain tasks like transfer of assets whenever a predefined set of conditions are met. Thus blockchain is now finding applications in a wide range of fields ranging from supply chain management and fintech to healthcare and philanthropy. The main problems with the current KYC system are aggregated costs and poor customer experience due to redundancy in the process. A blockchain based solution solves this by ensuring that all nodes access the same data which acts as the single source of truth. With our solution, the KYC verification needs to be done only once by a bank. All other banks can access this verified KYC information whenever the customer requires. Figure 2 and 3 show the traditional KYC

- *Author: Dr. Manoj Kumar is an associate professor at Department of Computer Science and Engineering, Delhi Technological University.*
- *Author: Nikhil is pursuing Bachelors of Technology from Department of Computer and Science and Engineering from Delhi Technological University*
- *Author: Parina Anand is pursuing their Bachelors of Technology from Department of Information Technology from Delhi Technological University*

process followed by the changes which will transpire after our solution is implemented.

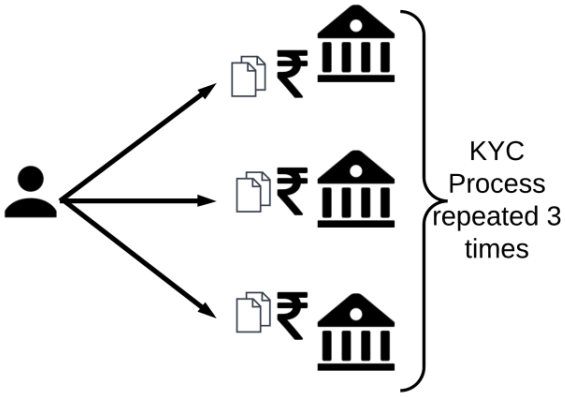


Figure 2: *Current KYC system*

Another important problem this solution intends to solve is of data ownership. Data ownership means having the rights to control access to particular data. All personally identifiable information about an individual should be owned by her. No other entity should be able to use it without due permissions. The General Data Protection Regulation 2018 that came into force on 25th May 2018 emphasises on the same. The provisions from this act that could affect any decentralized KYC system are consent and data subject right. Clear consent of user in plain language, distinguishable from other matters should be taken with the purpose for data processing attached to that consent. It must be as easy to withdraw the consent as it is to give it. Right to be forgotten under Data Subject rights, also known as Data Erasure, entitles data subject to have his/her personal data erased and ceased from further dissemination and potentially have third parties stop further use of data.[9] Our solution, in alignment with the principles of GDPR, does not store the user data on the blockchain which makes the right to erasure and right to forget easy and practical as the control on data always remains with the user. Apart from that, user data is only stored in the centralised databases of financial institutes approved by the user, these institutes can delete the user data as per the guidelines of regulatory authorities. It can be argued that a centralised distributed system would achieve similar results in security and efficiency without the need of a blockchain. Such a solution would create an additional cost for the regulator and in essence frees banks from the responsibility of knowing their customers. Thus it is unlikely that any government would undertake such a task. Our solution is in accordance with the current guidelines of regulatory bodies where banks are responsible for the KYC of their customers as well as the costs incurred. In section 2 we have discussed some of the already proposed methods of KYC using DLT. In section 3 after discussing two important concepts used in our proposed solution, we have explained our proposed solution in a 2 phase step-wise manner. Finally, section 4 concludes the proposal with suggested changes for specific applications along with some future use cases.

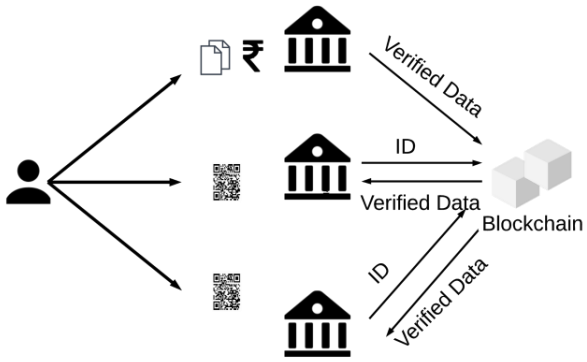


Figure 3*: Proposed KYC implementation*

2. RELATED PAST WORK

Bhaskaran et al (2018)[10] suggest an approach to address the problems of redundancy by sharing KYC data using blockchain. Their solution uses Hyperledger Fabric which provides membership services providers required for certification and identity management. In the given solution the customer gives his private data to a provider who then submits it to the blockchain for validation and recording in an encrypted format. Now, other services can access this data only if consent is provided by the user. The problem with this kind of approach is that sensitive data like this should not be stored on an immutable ledger even after encryption because of regulations and if in case the encryption algorithm used breaks sometime in the future all personal data will get compromised. Vimalkumar et al. (2018)[11] suggest that user data which is required for exercising due diligence can be stored on a blockchain and an ID to which his data will be mapped can be given to the user. This ID can be later used for subsequent KYC processes. However, this practice is not only costly but inefficient as the amount of data stored on blockchain is either limited by protocol or involves paying a huge transaction fee. Storing a single 256-bit word requires 20000 gas. A kilobyte is thus 640k gas or 0.032 ETH which at the current rate of $147.26 USD is $4.72 USD. Thus, storing just 1MB data would cost $4760 USD approximately which is extremely expensive. The blockchain based KYC system proposed by Moyano et al. (2017)[12] aims to proportionally distribute the cost incurred in the core KYC verification process amongst all participating institutions. It also gives a series of conditions which must be fulfilled to ensure the correct incentive model for the participating institutions. The data, according to their design, will be stored in smart contracts owned by the customer and not the institution.

3. PROPOSED SOLUTION

In this section, we enumerate the steps required to implement the above proposed, blockchain based KYC process. Having explored the major problems plaguing the traditional KYC process, we propose an implementation trying to mitigate them. We will discuss the architecture and design decisions that need to be taken to implement the KYC process. Before this, we look at a few concepts required to understand the process

3.1 Digital Signature

A digital signature is a mathematical technique used to verify the contents of a document as well as the identity of its sender. It combines the mechanism of hashing and asymmetric encryption to produce a form of the document that can ensure authentication, non-repudiation, and integrity of its contents. A hash is a one-way function that transforms a given message to a fixed length string such that a small change in the message would drastically change the hash. This ensures the integrity of the message. To encrypt it, a key pair is generated using any standard asymmetric encryption algorithm. The private key from this key-pair is used to encrypt the hash. This encrypted hash along with information, like the algorithm used, is the digital signature. The technique encrypts the hash value instead of the message itself because the hash function dramatically shortens the message. This reduces the computational complexity of the signing algorithm.

To complete the verification process, the signature is decrypted with the public key of the key-pair. The data provided is hashed and both hash values are compared. Tampering of even a single bit will be detected by this process. The verification is successful if both the hashes match. Quick Response Code (QR Code) is machine readable optical label that can store data in four modes namely numeric, alphanumeric, byte/binary, and kanji. It uses the Reed–Solomon error correction algorithm which provides four correction levels. The correction level is inversely proportional to the storage of the QR code.

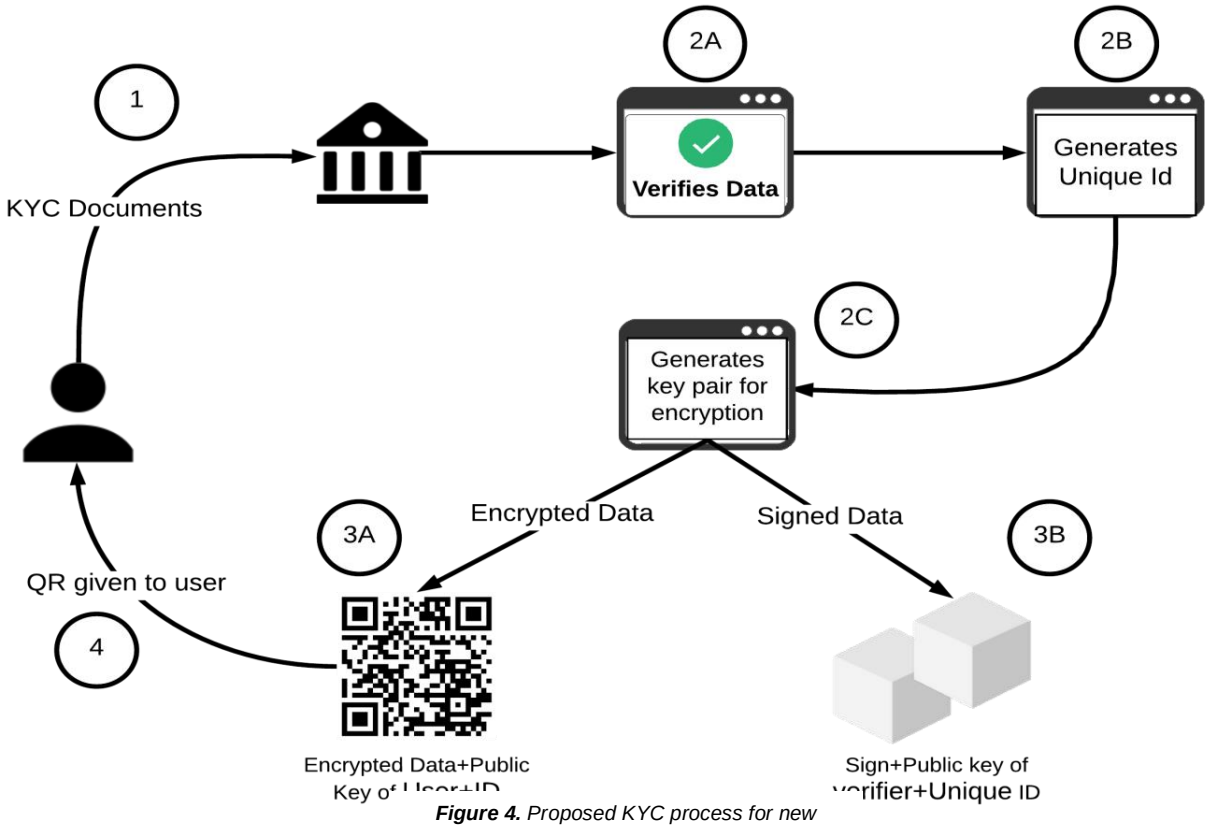


Figure 4. *Proposed KYC process for new users*

Besides these characteristics, they are easy to handle for the user and can be scanned quickly with simple scanning devices. In our implementation, we store the customer's data in an encrypted form in a QR code. This ensures that the ownership of the data lies with the user.

Using a blockchain to store data has its disadvantages. It is very expensive to store a large volume of data on-chain as it is required to be downloaded by every node. There are huge transaction fees and protocol limitations for storing data on a blockchain. The allowed size is usually in the range of kilobytes. Also, storing personally identifiable information (PII) on a blockchain directly would violate the GDPR. To solve this problem, our implementation uses the concept of digital signatures and QR codes. The QR codes are used to locally store the data with the customers themselves. The digital signatures ensure the data cannot be tampered with.

3.2 New Customer (Figure 4)

According to our solution, the following procedure would be followed whenever a customer will first avail the services of any financial institution that needs to do KYC for its customers. In addition to the traditional due diligence process, the financial institution would take below-described steps to remove the redundancy of the system in a trustless manner.

1) A new customer (user) submits the required KYC documents to the bank.
2) The bank employee(verifier) performs the following steps:
    a) Verifies the documents and performs due diligence (according to regulations as done currently)
    b) Once the documents are verified, the verifier creates a unique ID for the user on the blockchain. This id is created by creating a hash of personal details along with the time stamp when the request was initiated to ensure uniqueness of id.
    c) Next, the verifier generates a key pair for the user to encrypt their personal information.
3) The verifier then:
    a) Encrypts the user data with the public key of the key pair generated for the user in the previous step and generates a QR code containing:
        i. Encrypted data (KYC data of the user)
        ii. User's public key
        iii. Unique id of the user
    b) Signs the data and pushes the signature to the blockchain.
4) The blockchain now contains:
    a) Digital signature on user data (signed by the verifier)
    b) Public key of the verifier
    c) Unique Id to which the data is mapped on the blockchain.

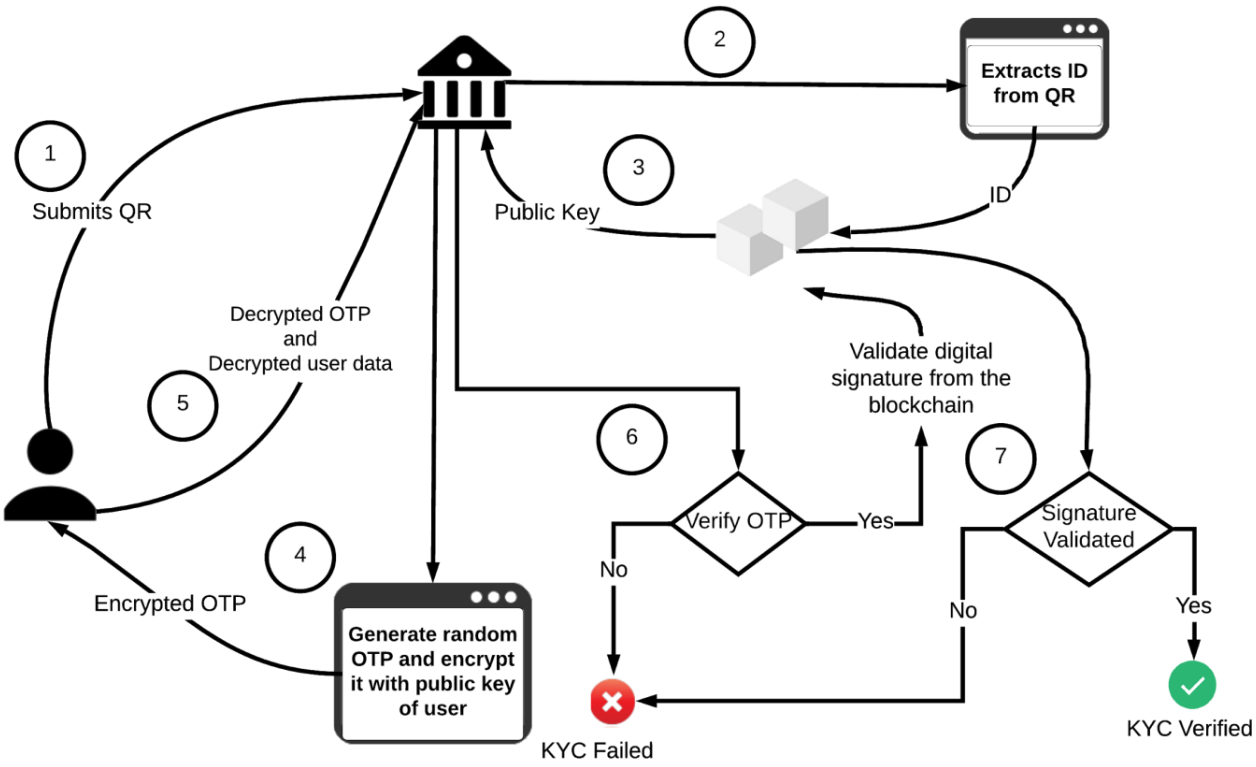


Figure 5: *Proposed KYC process for subsequent KYC verifications*

3.3 Verification (Figure 5)

1) The user will present his QR code to the concerned authority (Bank) to scan.
2) Bank will extract user id from the QR code
3) They will now request the user's public key from the blockchain which was created at the time user's data was added to the ledger.
4) Bank will now generate an OTP for this user and encrypt it using user's public key. This OTP will now be sent to the user as an email or SMS.
5) The user can now decrypt this OTP using his private key which will prove that the user has access to his private key as well as access to his mobile number or email account.
6) Verification of the OTP proves that the user is who he claims to be (this introduces two factor authentication in the system).
7) Now the user will decrypt his personal data stored in the encrypted format in his QR code and send it to the Bank where the data can be validated by checking it with the signed copy of this data (digital signature) stored on blockchain by the bank

officials. Successful validation of the signature implies KYC verification is successful.

The process starts with the user providing his documents to the financial institution which allows them to carry out the due diligence process in the traditional way and hence there is no need to change any regulations or restructure the financial institutions. After verification, the verifier signs the user's KYC data digitally, enabling the validation of KYC when required and also making the verifier accountable for the verification process. These digital signatures are stored on the blockchain creating a trustless environment between multiple financial institutions by making these signatures immutable. User data is stored in an encrypted format in the QR code thus preventing data theft on loss or unauthorized scan of the QR code. At the time of verification, an OTP is sent to the user for 2-factor authentication to prevent the misuse of lost private keys. The user can later show this QR code of verified data to any other bank and get his KYC done, not requiring the verification process to be repeated. Only the user has access to his private key that decrypts the data of the QR code. Hence, access to data is user controlled, ensuring user's privacy.

4. CONCLUSION AND FUTURE SCOPE

The future of any industry is in complete digital transformation which can only ensue from infrastructure level changes. There is a need to change the core processes to drive operating efficiency. This can be only achieved by being open to adopting disruptive and innovative technologies. Our proposed solution has aimed to reinvent the traditional KYC process. This paper has offered an approach which solves the problem of redundancy and inefficiency in the current KYC process, bringing down the operational costs for the system drastically. By using a blockchain based approach and distributing the data storage systems, we also remove the presence of a single point of failure. Additionally, our proposed solution solves on the problem of data ownership by storing the data in an encrypted format with the user being in control of keys required to decrypt the data. In a blockchain-based solution, the kind of blockchain used is an important decision determined by various factors. The proposed solution is independent of the choice of blockchain since we never store the actual customer data on the blockchain. Public blockchain as the name suggests can be accessed by anyone with an internet connection. A permissioned blockchain is considered to be semi-decentralized and unlike public blockchain, one cannot just join the network unless invited by the network administrator. The network is controlled by a number of companies where each might operate a node. This type of blockchain can be used in cases where sensitive data cannot be risked to the public internet. However, the nodes of a permissioned blockchain are hosted by only the members of the consortium, which makes it less secure than a public network with a large number of nodes. Another important factor is that in a public blockchain, smaller organizations can join the network easily, without needing lobbying powers to become part of a consortium, making it more democratic. The proposed solution can also be used as an identity system in sectors where identity document forgery is rampant but it is not feasible to carry out verification. In such a case, an already existing system with a single source of truth can be a more feasible alternative. We can also customize the process to implement it as an identity system in sectors which require selected information from customers by modifying the smart contract. For instance, in movie theatres and clubs, the staff requires only the age of the customer to grant entry, all other PII should not be their concern. The modified KYC would be applied here and age will be verified efficiently. The proposed solution can be improved to ensure proportional sharing of the cost of conducting the core KYC verification process among all the participating members. This can be achieved by introducing an incentivized token-based system. In such a system, it would become important to ensure that no institution can claim compensation without conducting the core process. It would also ensure they do not become a free rider by avoiding payment for using the information generated by other member institutions. [11]

5. REFERENCES

[1] "'Know Your Customer' (KYC) Guidelines - Anti-Money Laundering Standards". Archived from the original on 2012-08-01.

[2] Master Direction - Know Your Customer (KYC) Direction, 2016 of RBI Circular dated, February 25, 2016 https://rbidocs.rbi.org.in

[3] Press release by Thomas Reuters dated October 26, 2017 https://www.thomsonreuters.com

[4] Buckley, Ross & Arner, Douglas & Barberis, Janos. (2016). The Emergence of Regtech 2.0: From Know Your Customer to Know Your Data. Journal of Financial Transformation. 44. 79-86. DOI=https://dx.doi.org/10.2139/ssrn.3044280.

[5] Blockchain Revolution 2016 by Don & Alex Tapscott

[6] Bitcoin and Cryptocurrency Technologies. 2016. Arvind Narayanan, Joseph Bonneau, Edward W. Felten, Andrew Miller, Steven Goldfeder, Jeremy Clark. https://bitcoinbook.cs.princeton.edu/

[7] Oxford dictionary https://en.oxforddictionaries.com

[8] Bitcoin white paper. 2008. Satoshi Nakamoto. https://bitcoin.org/bitcoin.pdf

[9] Trunomi, E. G. P. P. Gdpr key changes https://www.eugdpr.org/

[10] Bhaskaran, Kumar & Ilfrich, Peter & Liffman, Dain & Vecchiola, Christian & Jayachandran, Praveen & Kumar, Apurva & Lim, Fabian & Nandakumar, Karthik & Qin, Zhengquan & Ramakrishna, V. & Teo, Ernie & Suen, Chun. (2018). Double-Blind Consent-Driven Data Sharing on Blockchain. 385-391. DOI=https://doi.org/10.1109/IC2E.2018.00073

[11] Vimalkumar Pachaiyappan and R. Kasturi. 2018. Block Chain Technology (DLT Technique) for KYC in FinTech Domain: A Survey. International Journal of Pure and Applied Mathematics Volume 119 No. 10 2108, 259-265.https://acadpubl.eu/jsi/2018-119-10/articles/10c/36.pdf

[12] Parra-Moyano, Jose & Ross, Omri. (2017). KYC Optimization Using Distributed Ledger Technology. SSRN Electronic Journal. DOI=https://dx.doi.org/10.2139/ssrn.2897788.

View publication stats

Cluster Computing
https://doi.org/10.1007/s10586-020-03062-w

A comparative study on bio-inspired algorithms for sentiment analysis

Ashima Yadav[1] · Dinesh Kumar Vishwakarma[1]

Received: 9 October 2019 / Revised: 9 December 2019 / Accepted: 27 January 2020
© Springer Science+Business Media, LLC, part of Springer Nature 2020

Abstract
Data mining is one of the most explored and ongoing areas of research. Sentiment analysis is a popular application of data mining, where the information regarding the customer's emotions or attitude is extracted by applying various methods or techniques. The earlier work in sentiment analysis deals with supervised, unsupervised machine learning-based approaches and lexicon-based approaches. Nature-inspired algorithms are recently becoming an emerging topic of research for developing new algorithms and for optimizing the results as nature serves as an excellent source of inspiration. These techniques are divided into bio-inspired algorithms, physics–chemistry based algorithms, and others. This survey mainly deals with bio-inspired algorithms, which consist of swarm intelligence based and non-swarm intelligence-based algorithms. We present a comprehensive review of the significant bio-inspired algorithms that are popularly applied in sentiment analysis. We discuss state-of-the-art on these significant algorithms along with a comparative study on these algorithms by reviewing eighty articles from various journals, conferences, book chapters, etc. Finally, this review draws some essential conclusions and identifies some research gaps to motivate researchers in this area.

Keywords Data mining · Evolutionary computing · Optimization · Review · Sentiment analysis

1 Introduction

Social media has become an authoritative source of communication among people to share their opinion and views about any entity. Many business organization needs to study these opinions of the users. Moreover, people rely on the feedback provided by various users on the web. This can significantly affect the buying behavior of the product. Hence, analyzing the opinions or sentiments of the user emerges as an essential field to study. Sentiment analysis (SA) is the study which deals with identifying and categorizing people's opinion, sentiment, emotion, attitude towards any topic, people, product or event. The opinion is further categorized as positive, negative, or neutral [1].

As the number of electronic devices like smartphones, tablets, cameras are increasing, the amount of data generated from them is growing tremendously [2]. Hence, the field of SA is getting a lot of attention from the researchers. People can express their opinions in the form of text, speech, videos, emoticons, etc. [3, 4]. The widespread applications of SA justify the importance of this field. It is popularly applied for business review analysis where product reviews on e-commerce websites like Amazon are evaluated to understand the popularity of the product and accordingly change the business strategies [5]. Similarly, reviews related to hotels [6], social media [7], booking sites [8], etc. are classified for determining their polarity. SA is popularly used in financial market for predicting the stock market price by analyzing the user's sentiments or opinions [9]. Nowadays, social media have become a crucial medium for politicians to connect with the public. People are expressing their opinion on political campaigns through social media sites. This generates a huge amount of opinionated data, which helps to predict the election results by categorizing the data into respective sentiments [10].

SA is also used for crime prediction as the people can easily create, circulate and consume information from any location with the help of Internet [11]. Finally, the impact

✉ Dinesh Kumar Vishwakarma
dvishwakarma@gmail.com

Ashima Yadav
ashimayadavdtu@gmail.com

[1] Biometric Research Laboratory, Department of Information Technology, Delhi Technological University, New Delhi 110042, India

Published online: 03 February 2020

of emergency responders during any disaster can be examined by mining the sentiments of the affected people during and after the disaster [12]. Hence, motivated by these applications, this review aims to study bio-inspired algorithms as they are widely being used among researchers for SA. Bio-inspired algorithms are nature-inspired metaheuristic algorithms which are popularly used for optimization, thus increasing the classification accuracy and reducing the processing time. The bio-inspired algorithms focused for this survey includes eight swarm intelligence based algorithms: Particle Swarm Optimization (PSO) that is inspired by flocking behaviour of birds, Ant Colony Optimization (ACO) which mimics the behaviour of ants by spreading and transmitting pheromone, Firefly Algorithm (FFA) based on the behaviour of fireflies by producing bioluminescence for attracting the prey, Cuckoo Search (CS) inspired by the behaviour of obligate brood parasitism or holoparasite species, Bat Algorithm (BA) that mimics the echolocation power of the bats, Artificial bee colony (ABC) based on the foraging behavior of bees, Glowworm swarm optimization (GSO) established on the behavior of glow worms, Shuffled Frog Leaping (SFL) based on the memetic activity of frogs and one non-swarm intelligence based algorithms: Flower pollination algorithm (FPA) inspired by the pollination process of the flowers, as these are the signature algorithms that are popularly used for sentiment classification. Hence, the significant contributions of this study are as follows:

- Analyzing the year-wise trend of bio-inspired algorithms from 2010 to 2019 and identifying the dominant techniques based on bio-inspired algorithms for SA.
- Presenting a comparative study on these algorithms by discussing their applications, advantages, and disadvantages.
- Providing a detailed review of the notable work done in this area by discussing the popular SA, algorithm applied, datasets used, and results obtained on them. To the best of our knowledge, no previous study has focused on the bio-inspired algorithm for SA.
- Identifying the research gaps and future prospects by reviewing the most noteworthy work in this field.

The organization of the paper is shown in Fig. 1. In Sect. 2, we discuss the major bio-inspired algorithms in SA along with a comparative study on them. In Sect. 3, we present the review methodology and data analysis. In Sect. 4, we discuss the literature review summary and potential research directions. Finally, in Sect. 5, we present the conclusion of the paper.

2 Bio-inspired algorithms in sentiment analysis

Nature has been the biggest inspiration for designing many algorithms as it provides some of the efficient processes to solve problems. These categories of algorithms are known as nature-inspired algorithms. These algorithms help in solving the optimization problems, which gives the best possible solution among the set of feasible solutions. Optimization plays a significant role in today's world. For example, people continuously focus to optimize their learning styles. Similarly, businessmen always try to optimize their market decisions and strategies. Hence, optimization is related to every discipline of life and has universal applicability.

Optimization algorithms are categorized in many ways [13, 14]. Yang [15] classifies the algorithms based on their nature into three categories: Deterministic algorithm, Stochastic algorithm, and Hybrid algorithm. In the deterministic algorithm, the algorithm follows the same path and produces the same output for a given set of input. The stochastic algorithm has some randomness as they generate a random number by some method to execute the trail. They are further divided into two types [15]: Heuristic algorithm and Metaheuristic algorithm. Heuristic algorithms are based on the 'trial and error' concept. They generate "good enough solutions" for difficult optimization problems in a reasonable amount of time; however, they do not guarantee an optimal solution [16]. These algorithms are based on experience and an expert's knowledge to explore the search space. On the other hand, metaheuristic algorithms are the set of high-level strategies that enhance the efficiency of heuristic algorithms by guiding and modifying their operations efficiently for producing high-quality results [17]. The major advantage of these algorithms is that they require no special knowledge about the optimization problem to be solved [18].

Figure 2 presents the taxonomy of nature-inspired algorithms, as discussed in [19]. These algorithms are divided into bio-inspired algorithms, physics–chemistry based algorithms, and others. The focus of our review is the bio-inspired algorithm (highlighted in Fig. 2), which are discussed in the subsequent sections.

2.1 Particle swarm optimization (PSO)

Particle swarm optimization is an optimization algorithm that is inspired by bird flocking behaviour of the birds [20]. In real life, the flocks of birds fly together in the sky following specific rules and patterns to look for food. They achieve an optimum state by continuously adjusting their position and speed. The bird closest to the food will chirp

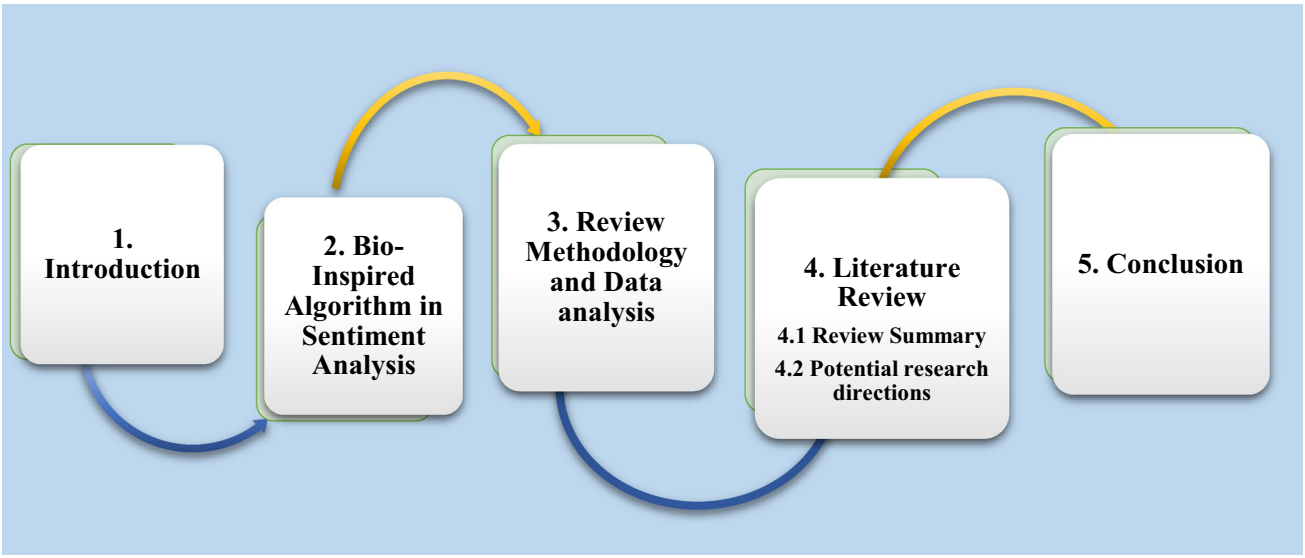


Fig. 1 Organization of the paper

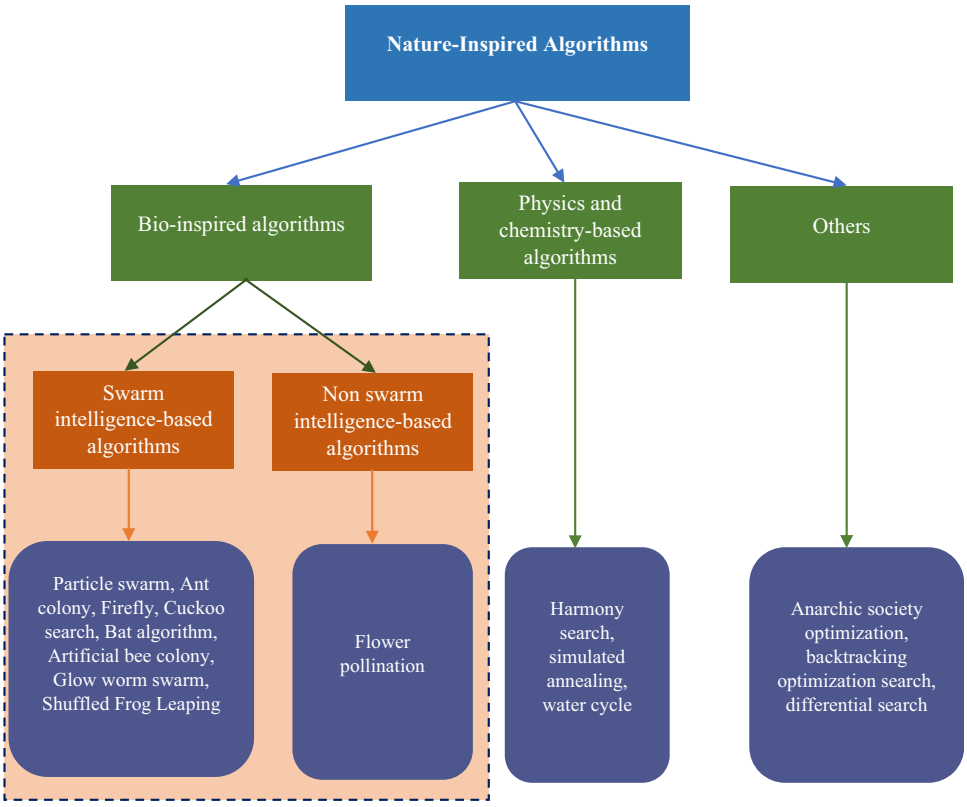


Fig. 2 Taxonomy of nature-inspired algorithms [19]

so that the other birds can follow it. This procedure continues until all the birds have found the food. Similarly, in PSO, particles are equivalent to the birds. So, the particle's fitness value is calculated by a fitness function and the velocity helps in the flying of particle. PSO uses specific topologies that contain nodes and edges. Each node depicts a particle in the swarm and the edges represent the neighbor relationship between the nodes (pairs of particles).

Rana et al. [21] discussed aspect level SA. Initially, correlation between the aspect terms and opinion words were extracted using sequential patterns. Then, implicit aspects were identified and finally, a hybrid approach was proposed, based on Google similarity distance along with

PSO for grouping synonyms. Opinion summarization is the task of creating a crisp summary from a huge collection of reviews. Suganya et al. [8] proposed a fitness proportionate binary PSO (*FBPSO*) algorithm to improve the accuracy of customer review summarization. The features were summarized for identifying the opinions and generating a text-based summary. Experimental results on the hotel review dataset of TripAdvisor have shown that the proposed algorithm gave better results when compared with the probability ranking algorithm. Li et al. [22] developed a global optimization-based approach called *PSOGO-Senti* to improve SA by optimizing the feature selection process. Moreover, Support Vector Machine (SVM) was also applied for classification. The proposed algorithm was compared with Genetic Algorithm (GA) and grid search algorithm. The final outcome indicated the efficacy of the algorithm for multi-polarity SA. Moreover, five-polarity sentiment classification gave largest improvements.

The PSO algorithm maintains two variables: *pBest* and *gBest*. The *pBest* variable is called the personal best, which indicates the amount of fitness attained by the particle. The *gBest* variable is a global variable that indicates the particle closest to the food. The particle velocity is calculated as in Eq. (1) below:

$$v_{t+1} = v_t + w_1 * rand * (pBest - p) + w_2 * rand * (gBest - p) \quad (1)$$

here v_{t+1} is the particle's velocity at time $t + 1$, v_t is particle's velocity at time t, w_1 is weight of local information, *rand* is some random value, p is particle's position, *pBest*. Is personal best, w_2 is weight of global information, *gBest* is global best.

The position of the particle is calculated as in Eq. (2):

$$x_{t+1} = x_t + v_{t+1} \quad (2)$$

here x_{t+1} is particle's position at time $t + 1$ and x_t is particle position at time t.

Slowik et al. [23] discussed two versions of PSO. The first version was called as local PSO (LPSO) and the second version was called as global PSO (GPSO). LPSO was used in problems when more than one global solution was obtained. In GPSO, the best global solution was searched by the algorithm. Earlier, PSO was used majorly for optimization purposes, though it is coming up with various new versions now. In some variants, the convergence of the PSO algorithm was improved. Researchers have highlighted some problems in PSO, which includes increasing the efficiency of the algorithm, self-adaptation of the parameters, dealing with convergence in multi-objective PSO [24–26]. Kristiyanti et al. [27] discussed a comparison for feature selection task in SVM by comparing three algorithms called GA, PSO, and Principle Component Analysis (PCA). SVM is a popular technique for data classification. By using these three algorithms combined with SVM, the classification accuracy of SVM was improved. They used cosmetic products review from Amazon. The accuracy achieved by using GA was 94.00%, PSO showed an accuracy of 97.00% and PCA showed an accuracy of 83.00%. Hence, SVM based PSO shows more accurate results for classification problems. Akhtar et al. [28] presented a framework for aspect-based SA using two steps: feature selection and ensemble construction. They used Conditional Random Field (CRF), SVM, and maximum entropy (ME) as base classifiers and PSO based feature selection gave the solution for each classifier. They also discussed a domain-independent model to achieve aspect-based SA. Hence, the performance of the classifiers were improved by properly training the relevant feature set.

Liu et al. [29] applied multi-swarm particle swarm optimization (MSPSO) for extracting emotional features in online course reviews. These reviews gave an idea about the opinion or feelings of the learners and helped in improving the teaching strategies. The training step was initially divided into subspaces. Then in each subspace, group of particles were made for finding the best feature selection strategy. These strategies were used to extract features which were highest in the rank. The dataset consists of the course reviews from the Massive Open Online Course (MOOC) platform. Experimental results indicated that around 72.19% of subjects approved with the results which demonstrate the efficiency of the proposed algorithm for recognizing sentiments in course review dataset.

Basari et al. [30] compared SVM and SVM-PSO for sentiment classification. They used movie reviews from Twitter to classify a movie as good or bad. PSO was used along with SVM to improve the classification results of SVM. The SVM classifier was run for every set of the parameter in the initial population of PSO. The experimental results show that the classification accuracy increased from 71.87 to 77.00% by using SVM-PSO without data cleaning and from 72.20 to 76.20% with data cleaning. The precision also gets increased to 81.87%. However, the paper was restricted to binary sentiment classification only. The author did not consider multiple sentiments for classification.

2.2 Ant colony optimization (ACO)

Ant Colony Optimization is a metaheuristic optimization algorithm based on the behavior of ants [31, 32]. In real life, ants look for food by spreading and transmitting a pheromone, which is a chemical substance. The path where the concentration of pheromone is more signifies that it is the shortest path, and this path will be taken by the rest of the ants to look for food. Hence, ants keep on looking for an optimal path by continuously searching for a track

linking their colony and source of food. The characteristics of this algorithm is that it is decentralized, which further makes the algorithm more flexible and robust. This algorithm does not need any prior knowledge as a random path is selected in the beginning.

2.2.1 Initialization

Initially, at the beginning of the process, a constant amount of pheromone is assigned to each ant. The probability for choosing the next node j from the node i by an ant is determined by the Eq. (3) below:

$$P_{i,j} = \frac{(\tau_{ij})^{\alpha}(\eta_{ij})^{\beta}}{\sum_{k=1}^{n}(\tau_{ij})^{\alpha}(\eta_{ij})^{\beta}} \quad (3)$$

here τ_{ij} is the pheromone value, η_{ij} is inverse the distance between two nodes, α is the history coefficient, β is the heuristic coefficient.

2.2.2 Pheromone update

The ants perform the modification of the environment in two ways:

2.2.2.1 Local pheromone update The ants update the pheromone on the edges while moving between the nodes using the Eq. (4) given below:

$$\tau_{i,j} = (1-\rho) * \tau_{i,j} + \rho * \tau_{i,j}^{0} \quad (4)$$

here $\tau_{i,j}$ represents the pheromone value for the edge (i, j) where ρ is the pheromone factor, $\tau_{i,j}^{0}$ is the initial value of the pheromone.

2.2.2.2 Global pheromone update Finally, global pheromone is updated after every iteration. It is updated with the best solution obtained so far using the Eq. (5) given below:

$$\tau_{i,j} = (1-\rho) * \tau_{i,j} + \rho * \Delta\tau_{i,j} \quad (5)$$

$\Delta\tau_{i,j}$ denote the maximized solution cost of the best solution obtained so far. The rest of the symbols have the same meaning, as discussed.

Chakraborty et al. [33] used Facebook for fetching the data related to the terror attacks on India and Mumbai to show the rise of social awareness after any natural or manmade disaster. They used ACO to study the relationship of the ants along with the opinions and sentiments of the crowd in case of any crisis or disaster. They presented different types of case studies and introduced a tool called pheromone tracing. The rate of sentiment flow with respect to different datasets were presented. Ahmad et al. [34] proposed a hybrid algorithm of ACO and K- Nearest Neighbor (KNN) for selecting relevant features from a review dataset. When comparing the algorithm with other baselined algorithms like Information Gain GA (IG-GA) and Information Gain Rough Set Attribute Reduction (IG-RSAR), better results were obtained. Goel et al. [35] performed SA using ACO as it helped in representing the people who were involved in online communications as the members of swam. The accuracy achieved on Twitter data is 90.04% and on Reddit data is 72.66%. They also concluded that ACO performed better than other traditional algorithms as they mimic human behavior.

Forsati et al. [36] presented an algorithm called enRiched Ant Colony Optimization (RACO), which is a new variant of ACO for feature selection. The proposed RACO algorithm was different from ACO as it considered previously traversed edges along with the pheromone values to generate diverse solutions. They also proposed Capability RACOFS (C-RACOFS) and Improver RACOFS (I-RACOFS), which were variants of RACOFS. The dataset was downloaded from UCI. The RACOFS algorithm showed superiority in kappa statistics and classification accuracy on small and medium datasets. This proved that traversing the previous iterations have shown improved results whereas hybrid algorithms gave better results in large datasets. Slowik et al. [23] discussed many real-life applications of ACO. Similar to PSO, ACO was also used extensively for feature selection. Mavrovouniotis et al. [37] presented a memetic ACO algorithm in which they integrated the local search operators to apply in a dynamic traveling salesman problem (DTSP). As a result, the quality of solutions improved significantly and proved to be useful for solving the DTSP, due to excellent adaptation qualities of ACO. Shirzad et al. [38] presented a multi objective ACO engine for optimal pressure dependent dynamic design of water distribution networks (WDN). In multi objective ACO, a colony with a fixed number of ants travel in their relevant graph. As a result, ACO was used for minimizing the costs of pipe laying and rehabilitation and for increasing the reliability of WDN. Banerjee et al. [39] introduced an ACO model that was tested on real-world blogs. The results obtained were promising enough for trend prediction.

ACO was also used in the wireless sensor network (WSN). Deif et al. [40] discussed the problem related to the failure of WSN when they were deployed. These failures may be due to different factors like a failure of hardware, battery depletion, and so on. ACO was applied for obtaining the optimized solution of the problem involved in deploying the WSN that meets a basic level of reliability at minimum deployment cost. The ACO algorithm showed better results as compared with the greedy heuristic algorithm, as accuracy was increased by 20%. Wang et al. [41]

discussed the application of ACO in computer vision. They proposed a visual tracker that used iterated ant particle filter for visual tracking. The results indicated that the suggested algorithms gave superior performance than traditional algorithms.

2.3 Firefly algorithm (FFA)

FFA is yet another metaheuristic optimization algorithm that mimics the behavior of fireflies, also known as lightning bugs [14, 42]. An essential feature of fireflies is that they produce bioluminescence for attracting the prey, sending warning messages, and communicating with other fireflies using various flashing patterns. FFA makes certain assumptions [43]:

1. Fireflies are the insects that are unisexual. So, they get lured to every other firefly despite their sex.
2. The attractiveness and the bright light of the firefly are directly related to each other but show inverse behavior with the farness between the fireflies. Thus, the dazzling of the firefly will decrease with the increase in distance.
3. The bright light of the firefly is associated with the shape or landscape of the objective function, which means that in case of a maximization problem, attractiveness varies with the cost function.

The intensity of light L is inversely proportional to the distance r, as shown in Eq. (6) below:

$$L = \frac{1}{r^2} \tag{6}$$

The intensity of light along with the attractiveness decreases when the distance increases, the combined effect on intensity of light and absorption is approximated using the Gaussian function of Eq. (7):

$$L_r = L_0 e^{-\gamma r^2} \tag{7}$$

Let β_0 be the firefly's attractiveness at $r = 0$ and as the attractiveness of fireflies is solely linked to the intensity of light. So, the attractiveness β is defined by the function [43] in Eq. (8):

$$\beta = \beta_0 e^{-\gamma r^2} \tag{8}$$

Yang et al. [43] presented a study regarding the application and recent advancement in the firefly algorithm. They discussed the efficiency of the firefly algorithm. One of the reasons for its efficiency is the automatic subdivision in which the whole population is subdivided into various groups that swarm around to get the best solution. Also, fireflies can find all the optima simultaneously. Hence, this subdivision makes FFA fit for multimodal optimization problems. They discussed that the firefly algorithm could be used to provide an equilibrium between the component's exploration and exploitation, which was necessary for the efficiency of the metaheuristic algorithm. They also discussed various applications of the firefly algorithm, which includes digital image compression, solving engineering design problems, NP-hard scheduling problems, performing classification and clustering, and optimization.

Rajput et al. [44] presented a hybrid algorithm in which the firefly algorithm was applied on the stock reviews to optimize the results. The stock market analysis is an application of SA. They consider six companies for the analysis: BHEL, Idea, PNB, ICICI Bank, Vedanta, and TATA Steel. They applied SVM for classification, and the firefly algorithm to improve or optimize the results. The results produced are beneficial in terms of precision, recall, and accuracy. Emary et al. [45] discussed a modified version of FFA for choosing a minimum set of features and obtaining better classification accuracy. They explained the behavior of fireflies and artificial fireflies. They used eighteen sets of data from the UCI repository. Better results were obtained by using FFA, which proved that FFA can be used as an efficient algorithm for searching in feature selection problems. It was able to explore the feature space quickly for obtaining an optimal subset by minimizing the fitness function. FFA have given the least classification error as compared to the other two algorithms on fifteen datasets. Banati et al. [46] presented an e-marketing strategy using FFA on the reviews of a digital camera. The proposed strategy was split into three stages, where the first stage deals with the market analysis in which the user's review were collected. Then feature selection was performed using FFA and finally, the interest of the users was estimated. In the second stage, market segmentation was performed by generating user segments that were focused on similar product features. In the final stage, the product was promoted where the best segments were selected, and the best seeds were identified for the promotion of the product. Hence, the accuracy of the various modules was improved by using the FFA.

2.4 Cuckoo search (CS)

CS is a member of the family of the bio-inspired algorithm, which is based on the behavior of obligate brood parasitism or holoparasite species [47]. These species cannot construct nests on their own, and they use the nest of other species to lay eggs. Cuckoos are an example of such species. Hence, CS is based on the behavior of cuckoos. If the host birds find that the eggs present in their nests are of the different bird, then either the eggs are discarded by them, or they discard their nests to build new ones. The eggs, which are not thrown away by the host birds, grow and become mature cuckoos. CS algorithm is implemented for

calculating the global optimum of a function. The main rules used by CS are discussed below:

1. Every cuckoo bird has a natural feature of laying the eggs and then chooses a nest arbitrarily to dump the eggs.
2. The high-quality eggs are the only eggs that are further forwarded to the upcoming generation.
3. In CS, the count of host nests is not changed, and the bird locates the egg with a probability p (of either 0 or 1).

Devi et al. [48] proposed a hybrid algorithm of CS and SVM for predicting the stock market. They compared the CS-SVM with artificial neural networks (ANN) and SVM methods. The accuracy obtained on the BSE-Sensex dataset was 82.21% and on the CNX-Nifty dataset was 83.22%. The model could be further improved by incorporating various other factors like dollar price, gold price, etc. as they have an impact on the stock market index. Redmond et al. [49] proposed a framework which preprocesses the information from any emoji to enhance the tweet. They used tweets from the micro-blogging site Twitter. The framework involved the following steps: In the first step, emoji and emoticons were converted into their word representatives. Then pre-processing was performed on the data, which includes tokenization, removal of stop words etc. The dimensions were reduced by using singular value decomposition and dimensionality reduction. The extended binary cuckoo search (EBCS) was used for obtaining a reduced set of dimensions. Finally, SVM was applied for classifying a tweet either as positive or negative. Experimental results indicated that the accuracy was increased from 75 to 82%.

Rajamohana et al. [50] discussed an algorithm for selecting the features using CS with Harmony search (HS) and Naïve Bayes for classifying the reviews either as *spam* or *ham* review. The pitch adjustment rate of the HS was used in CS as a mutation operator, and every element was fine-tuned using the PAR operator. The results showed that the proposed algorithm gave an accuracy of around 91.12% as compared to 82.34% accuracy achieved by binary CS. Pandey et al. [7] applied CS and K-means clustering on Twitter. The work involved three steps: In the first step, pre-processing was applied to tweets for eliminating the noisy words. In the next phase, feature extraction was performed to calculate eleven features on the Twitter dataset. Finally, K-means clustering and cuckoo search were applied. The obtained results were compared with different algorithms, such as: PSO, differential evolution (DE), CS, improved CS, gauss-based CS, and two n-grams approach.

2.5 Bat algorithm (BA)

Bats use a high-frequency system in which they make calls to their surroundings so that they can get an idea about the distance between them and the nearby objects with the help of echoes that are reflected from the objects and returned to them [51]. This frequency system is known as echolocation. The BA is based on this behavior. Bats use this behavior to locate their food or prey. The frequency used by the bats is so high that human beings are not able to hear them. The BA is built on the following rules [51]:

1. Bats use echolocation to locate their food or prey by sensing the distance. They further know about all the barriers in the background in some way.
2. Bats fly in a random direction with the following parameters to locate their prey:
   (a) v_i = Bat's velocity
   (b) y_i = Bat's current position
   (c) f_{min} = Fixed frequency of bats
   (d) λ = Varying wavelength
   (e) A_o = Loudness
   (f) r = Pulse emission rate

   Bats can adjust the values of λ, f_{min}, and r based on the target's distance.
3. It is presumed that the value of loudness is changed from the largest positive value called A_o to the minimum value called A_{min}.

The position x_i of the bat and its velocity v_i [51] is shown in Eq. (9):

$$f_i = f_{min} + (f_{max} - f_{min})\beta \tag{9}$$

here β is a random vector, taken from the uniform distribution, values of f_{min}, f_{max} depends on the size of the problem. The following Eq. (10) uses a random walk for generating a new solution on every bat:

$$y_{new} = y_{old} + <A^{t+1}> \tag{10}$$

here $\varepsilon \in [-1, 1]$, $<A^{t+1}>$ denotes the average loudness value of all the bats at time t.

Khurana et al. [52] applied BA in analyzing the sentiments expressed in tweets. This was the first application of BA in SA for classifying the tweets as positive, negative, or neutral. Initially, the data preprocessing was performed by discarding the special symbols, replacing the acronyms with their full forms, correcting the spellings, etc. Finally, Bat inspired classifier was used to compute the polarity of a sentence. The unigram and unigram + POS were used to assess the performance of the classifier. The major drawback of the proposed algorithm was that they had not considered the semantic features in the experiment. Finally, the results signify that the proposed algorithm performed

better than SVM as it achieved an accuracy of 57.89%. BA was also used for feature selection. Nakamura et al. [53] discussed a binary bat algorithm (BBA) for finding the optimal set of features which can increase the accuracy of the dataset. BBA was the binary version of BA in which the bat's position uses only binary values. The algorithm was compared with the Binary version of PSO, Binary version of FFA, HS, and Binary Gravitational Search Algorithm (GSA). The output showed that the BBA performed better than other algorithms in three datasets: Australian (accuracy of 77.25%), Breast Cancer (accuracy of 96.31%), and Mushrooms (accuracy of 100%). The significant advantage of the proposed algorithm was that it was able to give better results by getting trained on a smaller number of extracted features. This showed that the algorithm obtained an optimal feature set as compared to other optimization techniques. However, for DNA dataset and German Number dataset, the proposed algorithm was not able to outperform the results obtained by HS and GSA algorithms.

Fister et al. [54] discussed a review on the recent developments in BA. They also presented variants of BA, which includes binary BA, discrete binary BA, chaotic BA, cloud model based BA, Gaussian walk BA, compact BA, and modified BA. They further discussed the applications of BA and the critical challenges in BA. One of the key issues faced by the author was to improve the rate of convergence of BA. The BA can be used in combination with other algorithms. However, the best values of the parameters that are dependent on the algorithm were not clear, and setting their values was a difficult task. Chakri et al. [55] presented a modified version of bat algorithm called a directional BA (dBA), which improved the performance of BA by enhancing the exploration and exploitation ability in BA. They carried three experiments to show the success of the dBA algorithm and it was compared with standard BA, CS, HS, GA, DE, PSO. The results indicated that the dBA algorithm had shown better performance. They enhanced the exploration and exploitation capabilities making new search more beneficial. Moreover, the dBA algorithm can also be applied to tackle many real-world problems in the future.

2.6 Other algorithms

Apart from the above-mentioned algorithms, various other bio-inspired algorithms have also gained attention for SA. The artificial bee colony (ABC) algorithm is actively used for optimization and is based on the foraging behavior of bees [56]. Dhurve et al. [57] used ABC for optimizing the feature subset selection. They used KNN, Naïve Bayes (NB), SVM methods for classification and parts of speech, Bag of Words (BOW), Bag of Nouns (BON), stop word removal, and ABC for feature selection. Sumathi et al. [58] also used ABC for optimizing the feature subset. The results were compared with Inverse Document Frequency (IDF), and the classification accuracy was increased by 1.63%. Ecology Inspired Artificial Bee Colony algorithm (EI-ABC) was the algorithm used by Ramaswamy et al. [59] with a fuzzy classifier to increase the classification accuracy. Saravanan et al. [60] proposed an approach in which initially the data was pre-processed, and then an Improved High Adjective Count (IHAC) algorithm was applied for extracting the features. The results indicated that the proposed approach gave a precision of 94.45%, with an average accuracy of 93.05%.

Flower pollination algorithm (FPA) [61] was a non-swarm intelligence-based algorithm inspired by the pollination process of the flower where the transfer of pollens takes place with the help of pollinators like birds, insects, etc. which helps in fertilization. A hybrid algorithm for selecting the features was proposed by [62] for spam detection. They used the hybrid algorithm of Improved Binary particle swarm optimization (iBPSO) and Binary Flower Pollination Algorithm (BFPA) along with NB and KNN to improve the process of classification. The results were compared with CS and Shuffled Frog Leaping Algorithm (SFLA) algorithms, and the proposed algorithm outperformed the existing algorithms by giving an accuracy of 94.43%. A pollination based optimization (PBO) algorithm was proposed by Kaur et al. [63] for text clustering along with K-mean clustering to obtain accurate clusters. The experimental results on four different datasets proved that the PBO + K-means showed good results when compared with PBO, K-means, and other hybrid clustering algorithms.

Another bio-inspired algorithm used in SA is Glowworm swarm optimization (GSO), which was established on the behavior of glow worms [64]. The glow worms use a pigment called luciferin for attracting other glow worms as the pigment brightens the glow-worm, which makes them more attractive. Alboaneen et al. [65] proposed an approach for analyzing the tweets in which the feature set was reduced by using mutual information (MI), and then the weights and biases of the network were optimized by using GSO based multi-layer perceptron (MLP). The results were compared with GA and biogeography-based optimization (BBO) algorithms. Experimental outcomes showed that GSO algorithms gave the best classification accuracy of 54%.

Shuffled Frog Leaping (SFL) is a population based swarm intelligence algorithm inspired by the memetic activity of frogs [66]. As the frogs move towards the goal in search of food, they continuously change their position as soon as they are infected by better ideas. Yuvaraja et al. [67] applied Binary Shuffled Frog Algorithm (BSFA) on

the Twitter dataset. For classification, the Radial Basis Function (RBF) performed better than KNN, NB, and Logistic Model Tree (LMT). RBF was applied with various feature selection techniques like IG, GA, and BSFA. Experimental results showed that BSFA-RBF improved the accuracy by 1.57% when compared with other algorithms. A framework proposed by Rajamohana et al. [68] used SFLA for feature selection. Initially, the data was collected, and pre-processing was done to remove the irrelevant features. Then the values of TF-IDF were calculated, followed by the feature selection process using SFLA. Finally, a comparison was done on the classification results of the NB classifier with the results of the BPSO algorithm, and the proposed framework gave an accuracy of 93% as compared to the classification accuracy of BPSO which was 90%.

2.7 Comparative analysis of bio-inspired algorithms

Based on the previous study, we have provided a comparative analysis of the bio-inspired algorithms by summarizing their applications, advantages, and disadvantages in the field of SA. This comparative analysis will give the readers a broader view to analyze which algorithm will be beneficial for their research. Hence, Table 1 highlights the comparative analysis for each of the nine popular bio-inspired algorithms.

As seen in Table 1, for some algorithms we have not mentioned the advantages/disadvantages due to the unavailability of enough literature in SA for them. The above table gives a clear picture to the readers about the strengths and weaknesses of these bio-inspired algorithms. Moreover, we have also compared the results of all the nine algorithms by implementing them on the smartphone product review dataset [86]. For pre-processing the sentences, we have used tokenization, stop words removal, and stemming. Since SVM is the most popular classifier for sentiment classification, hence we have used SVM for the final sentiment classification. The experimental settings are the same as discussed in [86]. As the size of the dataset is small, hence all the experiments were performed using tenfold cross-validation settings, where the final accuracy was computed by averaging the values across each of the tenfolds. The results are shown in Fig. 3.

From Fig. 3 we can conclude that PSO + SVM has shown the highest accuracy of 93.84%, followed by ACO + SVM with an accuracy of 91.03%. These results justify the popularity of PSO among researchers. Hence, the optimization algorithms were able to reduce the number of features to produce an optimal feature set. This increased the accuracy of the sentiment classification as opposed to using a full set of features.

3 Review methodology and data analysis

A systematic literature review critically examines all the established works from the reputed e-databases. Hence, we have extracted all the relevant articles from the prominent digital libraries which include: IEEE Xplore, Elsevier, Springer, ACM, Wiley, and Google Scholar.

Figure 4 gives an overview of the number of articles reviewed for this study. As seen in the Fig, the work done in this area is published in some of the top and most reputed journals/conferences.

We have studied over 200 research papers from the above-mentioned digital libraries and have shortlisted 80 articles that we found relevant for this survey. The search terms which were applied to these databases include *sentiment analysis, opinion mining, bio-inspired algorithm sentiment analysis, nature-inspired techniques, optimization*. The synonyms of these terms were also involved in carrying an exhaustive search on the databases.

To further examine the research in this area, we present Fig. 5, which looks into the detailed analysis of number of articles published in the list of the bio-inspired algorithms (PSO, ACO, FFA, CS, BA, ABC, FPA, GSO, and SFL). It is evident from the figure that the most popular algorithm among researchers for SA is PSO, followed by ACO. The least used algorithms are GSO, FPA, and BA.

Figure 6 shows the year-wise trend of published work in this area. We have reviewed the articles from the year 2010 onwards. As seen in the figure, the number of published articles increased from the year 2015, and since then, the trend of published work is growing. This signifies that research in this field is rising vastly, which further motivates us to study this area by reviewing the major work published in this field.

4 Literature review

This section discusses the previous work done in this field to draw essential conclusions and identify the future gaps which will motivate researchers to work in this area.

4.1 Review summary

We present an overview of some of the crucial studies done in this area by highlighting the SA task, language, algorithm applied, the dataset used, and the highest results obtained on them for each of the reviewed articles. Table 2 presents a summary of some of the important works done in the field of SA using bio-inspired algorithms.

Kalarani et al. [94] extracted the POS features along with sentiment topic features and calculated the maximum

Table 1 Comparative analysis of algorithms

Method	Applications	Advantages	Disadvantages
PSO	Optimizing parameters of classifier [69, 70]	Reduces the feature set with strong search capability [71, 74]	Fine-tuning on parameter's value required for multi-objective optimization [72]
	Aspect term extraction [71]	Optimize more than one function simultaneously [72]	Performs poorly for multi-domain datasets [75]
	Affective design to improve customer satisfaction [72]	Discover reliable and interesting rules for sentiment mining [72]	
	Review spam detection [73]	Easily provide solutions for discrete problems [74]	
		Converge quickly [74]	
		Robust for multi-polarity sentiment classification [22]	
ACO	Feature selection process [76]	Shown good results with smaller number of feature set [76]	Can get stuck in local optima. Hence, hybrid approach with local search procedure is necessary [36]
	Optimizing parameters of classifier like SVM [77]	Fast and efficient to generate quality and optimal feature set [78] [76]	
FFA	Aspect based SA [79]	Easily detect the influential word in a sentence [79]	
	Temporal SA [79]	Effectively identify and capture the sentiment variation [79]	
	Stock market prediction [44]	More robust and stable than PSO [45]	
	Promoting products online [46]		
CS	Opinion spam detection [50]	Able to identify the emoji and emoticons for effective sentiment classification [49]	Can get stuck into local optimum [7]
	Stock market prediction [48]	Works well in classifying the online review sentiments and tweets [80] [47]	
	Fine-tuning parameters of classifiers [48]		
BA	Ranking features and opinion scores [81]	Increases processing time [81]	Can trap in local minimum for multimodal test functions [81]
	Unsupervised feature selection [82]	Reduces processing cost [81]	
		Have good generalization capacity [53]	
ABC	Solving combinatorial optimization problems [83]	Low computational complexity [83]	Time-consuming in finding the optimal clusters [84]
	Finding an initial set of optimal cluster centroids [84]	Robust with few control parameters [84]	
		Deal with noisy and short messages [84]	
FPA	Review spam detection [85]	Efficient and simple [61]	
	Global optimization [85]		
GSO	Feature selection optimization [65]		
SFL	Analyze reviews on social networks [68]	Hybrid approach of SFL with PSO gives better results [62]	
		Faster convergence rate [62]	

relevance and minimum redundancy mutual information for the combined feature set. Finally, the firefly algorithm was applied for feature selection, and the feature subset was passed to the SVM and ANN classifier, which classified the sentiments of the movie reviews. The experimental results show that the proposed method reduces the training time and improves accuracy. Souza et al. [80] presented an unsupervised clustering based algorithm on discrete PSO for binary sentiment classification. Text processing was done by tokenization and word bi-grams models. In the feature transformation phase, opinions were represented using a Vector space model and Term frequency-inverse document frequency (TF-IDF). The PSO based algorithm considered clustering as the objective function which has to be optimized. Experimental results indicate that the PSO was able to outperform the conventional clustering techniques: K-means and Agglomerative on IMDb (Internet Movies Database), Sentiment 140, and OBCC corpora for binary sentiment classification.

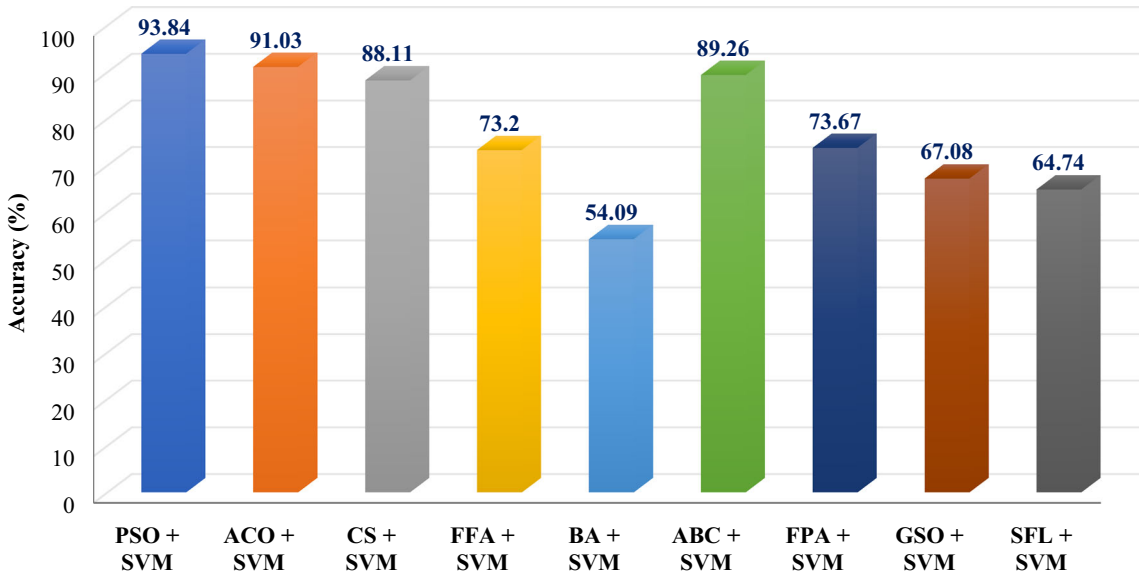


Fig. 3 Comparative results of bio-inspired algorithms on Smart phone review dataset for sentiment classification

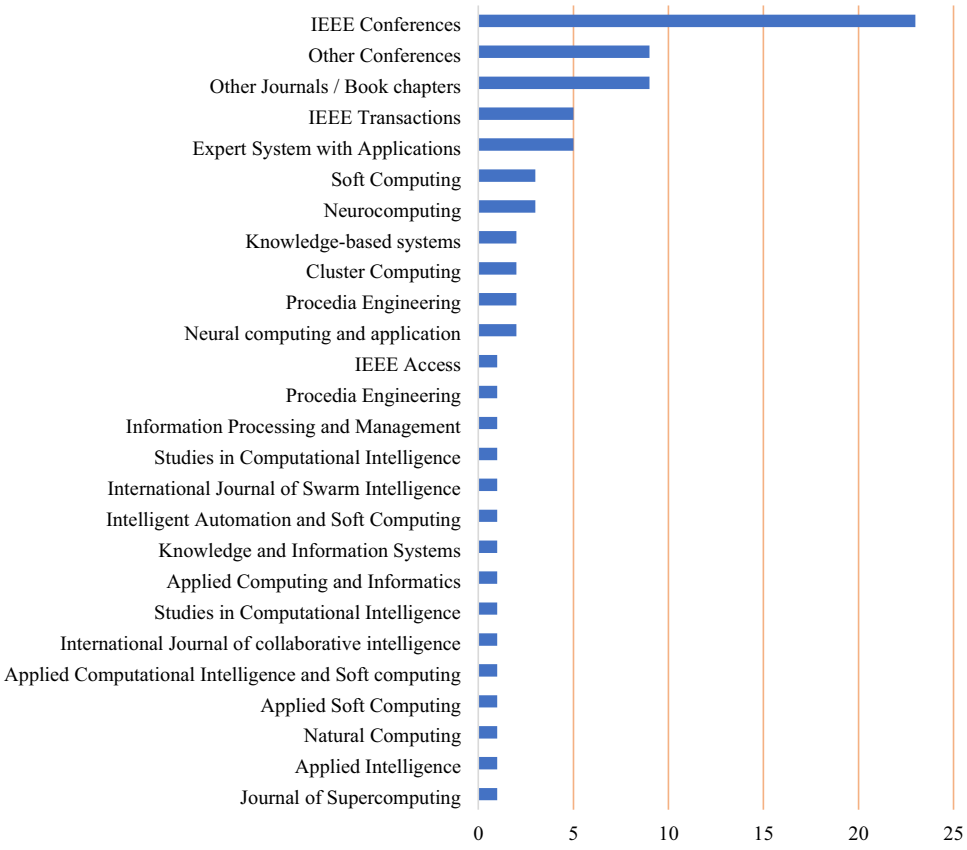


Fig. 4 Count of number of reviewed articles from journals/conferences/books

Budhi et al. [70] proposed a system to find the best machine learning classifier for sentiment polarity prediction. The system was composed of two layers: a multi PSO based layer and a knockout layer. The multi-PSO based layer was formed by *n* PSO clusters where each cluster was allocated to a classifier. The knockout layer finally compared the accuracy of all the classifiers and selects the best classifier with the optimal parameters. Souza et al. [75] applied PSO and GA optimization algorithm followed by a decision tree classifier. The dataset was composed of real-time Twitter tweets that were tokenized and pre-processed before feeding them for classification. The proposed

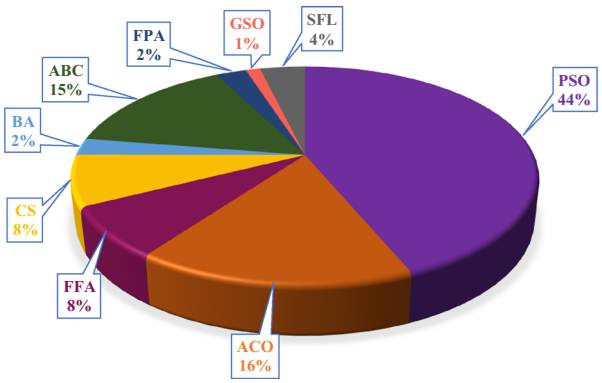


Fig. 5 Distribution of reviewed articles published in each algorithm

algorithm was experimented for ternary sentiment classification and multi-class emotion classification. The overall accuracy obtained for ternary sentiment classification is 90%. Alfarraj et al. [91] proposed a novel method that was based on PSO for aspect-based SA. The method focused on the most important aspects of the product, and the efficiency of the PSO was improved using the probabilistic rank estimation process. Gupta et al. [71] utilized PSO with CRF to get the most appropriate features for aspect-based sentiment classification. The stop words, PoS, context words, dependency relation, WordNet, named-entity recognition, and semantic orientation were considered as the features for aspect term extraction. The experimental results were performed on the SemEval-2014 Task 4 dataset, and the proposed algorithm was able to fetch the most relevant features for this task. Jain et al. [90] proposed the *Senti-NSetPSO* method which was a hybrid combination of PSO and Neutrosophic set for document-based sentiment classification. The Neutrosophic set was the extension of fuzzy sets. Hence, the *Senti-NSetPSO* method can be used for finer-grained classification into the most positive and most negative classes. The advantage of the *Senti-NSetPSO* was that it reduced the need for pre-processing the text and feature extraction phase for large-sized documents.

Rajamohana et al. [73] developed a framework for review spam detection. PSO was used for selecting the best features and it removed the redundant and noisy features to obtain an optimized feature set. This optimal feature set was passed to the NB classifier, which helps to classify the review as real or fake. The experimental results on the hotel review dataset show that the proposed framework was able to outperform the previous machine learning techniques in terms of execution time and accuracy. Hence, optimization algorithms can also be used for detecting fake reviews on social media platforms. Similarly, Rajamohana et al. [97] applied improved binary PSO and cuckoo search for review spam detection. Shang et al. [95] proposed sentiment classification oriented based fitness proportionate selection binary particle swarm optimization (SCO-FS-BPSO) for selecting the optimal features in sentiment classification. The traditional binary PSO doesn't give attention to the single-particle and focused more on the particle's overall performance. Moreover, it made the search space more discrete, so the particles cannot be explained easily and all these problems made them unsuitable for feature selection. Hence, the SCO-FS-BPSO algorithm overcame these problems. Experimental results on UCI datasets show that the proposed algorithm was computationally efficient and enhanced the performance of feature selection for sentiment classification. Alarifi et al. [92] presented a greedy approach that was based on cat swarm optimization (CSO) and LSTM. The sentiment features were analyzed using the greedy approach, and optimized features were selected using the objective feature. The final features were fed to the rule-based classifier for classification. The experimental results show that the

Fig. 6 Year-wise trend of the published work

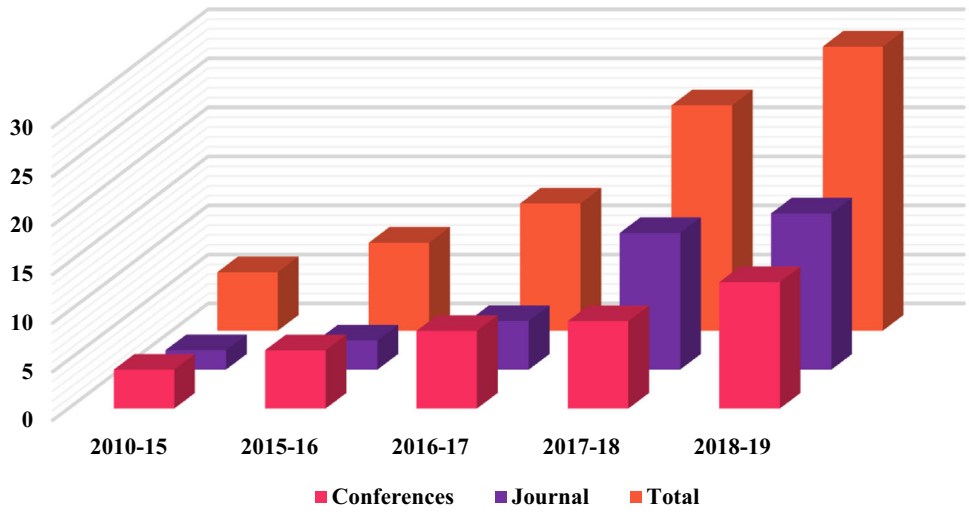


Table 2 Summary of the crucial work

Refs	Task	Algorithm	Data set/data source	Language	Accuracy/ F1 score (%)
[70]	Binary sentiment classification	PSO + MLP	Amazon review + Yelp + Movie review	English	88.0
[80]	Binary sentiment classification	Self-adaptive PSO + CS	IMDb + Sentiment 140 + OBCC	English + Brazilian Portuguese	87
[87]	Binary sentiment classification	PSO + NB	News articles	English	76.0
[84]	Binary sentiment classification	Tf-idf + SVD + ABC + K-means	Twitter	English	71 (F1 score)
[30]	Binary sentiment classification	PSO + SVM	Twitter movie review	English	77
[86]	Binary sentiment classification	PSO + SVM	Smartphone product review	English	94.50
[88]	Binary sentiment classification	PSO + SVM	Movie review	English	81.60
[35]	Binary sentiment classification	ACO	Twitter, Reddit	English	90.04
[77]	Binary sentiment classification	SVM + ACO	Twitter	English	86.74
[44]	Binary sentiment classification	SVM + Firefly	Company dataset	English	90
[67]	Binary sentiment classification	BSFA + RBF	Twitter	English	93
[48]	Binary sentiment classification	SVM + CS	BSE-Sensex and CNX-Nifty	English	83.22
[49]	Binary sentiment classification	SVD (Singular Value Decomposition) + Binary CS + SVM	Tweets containing emoticons and emoji from Twitter	English	82
[89]	Ternary sentiment classification and emotion detection	PSO + GA + Decision tree	Twitter	English	90.4
[75]	Binary and ternary sentiment classification	Discrete PSO + IDPSO (Discrete Improved Self-Adaptive PSO)	Movie Review + Sentiment140 + OBCC	English + Brazilian Portuguese	79
[7]	Ternary sentiment classification	CS + K-means	Twitter	English	84.16
[52]	Ternary sentiment classification	BA	Twitter	English	57.89
[90]	Document-level sentiment classification	Neutrosophic Fuzzy Set and PSO	Blitzer, aclIMDb, Polarity	English	62
[69]	Document-level sentiment Classification	PSO + SVM	Movie review	English	85
[79]	Aspect based SA	CRF + Firefly	Laptop and restaurant review	English	75.5
[91]	Aspect-based SA	PSO + probabilistic ranking	Twitter, movie review, customer reviews	English	96.5
[28]	Aspect based SA	PSO	Restaurant reviews and laptop reviews	English	80.07
[71]	Aspect based classification	PSO + CRF	Restaurant and laptop reviews	English	78.48
[92]	Feature selection optimization	CSO + LSTM	Amazon	English	96.89
[93]	Feature selection optimization	WOA + IG + PSO	Opinion corpus for Arabic, Arabic twitter, Political, Software	Arabic	95.93
[76]	Feature selection optimization	ACO + KNN	Customer reviews	English	82.7 (F1 score)

Table 2 (continued)

Refs	Task	Algorithm	Data set/data source	Language	Accuracy/ F1 score (%)
[94]	Feature selection optimization	Firefly + SVM + ANN	Movie reviews	English	87.5
[74]	Feature selection optimization	PSO + GA	Movie review	English	80.87
[27]	Feature selection optimization	PSO + SVM, SVM + GA, SVM + GA + PCA	Cosmetic product review from Amazon	English	97
[95]	Feature selection optimization	SCO-FS-BPSO	UCI datasets: Madelon, Semeion Handwritten Digit	English	93.8
[29]	Feature selection optimization	Multi-swarm PSO	MOOC	English	90.6
[36]	Feature selection optimization	Variants of ACO—RACO, C-RACOFS, I-RACOFS	UCI Machine Learning Repository	English	95.04
[50]	Feature selection optimization and review spam detection	CS + Harmony Search + NB	Reviews of Chicago hotels	English	91.12
[96]	Feature selection optimization	IG + PSO + SVM	Election Tweets	English	94.80
[97]	Feature selection optimization and review spam detection	PSO + CS + NB + KNN	Reviews of Chicago hotels	English	96.97
[98]	Feature selection optimization	ABC + CART	IMDb dataset	English	95.20
[58]	Feature selection optimization	ABC + Fuzzy rule induction	IMDb dataset	English	93.75
[60]	Feature selection optimization	ABC	Customer review dataset and additional review datasets	English	93.05
[59]	Feature selection optimization	ABC + Fuzzy rule selection	IMDb	English	97.25
[65]	Feature selection optimization	GSO based MLP	Twitter	English	54
[62]	Feature selection optimization + review spam detection	Hybrid iBPSO + BFPA	Chicago hotel dataset	English	94.43
[73]	Review spam detection using sentiments	PSO + NB	Hotel review dataset	English	94.21
[99]	Verb Expression's Sentiment classification	PSO + Linear regression	Amazon reviews	English	78 (F1 score)
[100]	Financial market prediction	PSO + SVM	News data	German and English	59.15

proposed approach has outperformed the results obtained by PSO on the Amazon review dataset.

Many researchers have employed PSO + NB for classifying news articles [87], online product reviews [86], and movie reviews [88] into positive and negative class (binary sentiment classification). However, for classifying Twitter tweets, Orkphol et al. [84] used TF-IDF for feature extraction and SVD for feature selection. The initial centroids were obtained by ABC. Then K-means along with SentiWordnet was employed to calculate the sentiment polarity. Similarly, Kaur et al. [77] also applied TF-IDF for feature extraction followed by SVM + ACO for investigating the polarity of tweets. On the other hand, Nagarajan et al. [89] utilized PSO + GA followed by decision tree for training the twitter tweets. The experimental results show that the proposed method has correctly

classified over 90% of tweets and has outperformed other machine learning classifiers. Nirmala et al. [69] showed that PSO could be used for determining the optimal values for the parameters of the SVM classifier. This increased the accuracy of the SVM classifier for document-level sentiment classification. Joseph et al. [79] proposed an algorithm to extract and categorize the aspects of a sentence using CRF and Firefly algorithm. The algorithm was able to identify the most important word for generating the aspect terms which further boosts the aspect categorization task for aspect-based sentiment classification.

The feature selection task is one of the most popular jobs where optimization algorithms are being applied. Tubishat et al. [93] improved the traditional whale optimization algorithm (WOA) which was based on hunting mechanism of whales. Hence, to reduce the search space for WOA, information gain technique was used for feature selection. Experimental results show that the proposed algorithm overcomes the problem of local optima and improves the classification accuracy in four Arabic datasets. Similarly, Ahmad et al. [76] applied ACO for feature selection and KNN for classification of customer reviews, whereas Kurniawati et al. [96] used hybrid method of IG + PSO for selecting the feature set and classifying the dataset of election results using SVM classifier. Sonagi et al. [74] proposed a hybrid combination of PSO + GA algorithm for optimizing the feature selection process. The proposed algorithm was able to converge quickly with strong search capability for finding the optimal feature set. Sharmila et al. [98] proposed ecologically inspired ABC which evolved the population of individuals using specific ecological concepts. The sentiments were classified with KNN and CART classifiers to get the optimized results. Bio-inspired algorithms were also applied for several tasks like financial market prediction and verb expression based sentiment classification. Chiong et al. [100] applied SVM and PSO based approach for predicting the price of stock market by extracting the sentiment specific features from the financial news dataset. They further compared the obtained accuracy with deep learning-based approaches. Experimental results indicate that the proposed approach outperformed the results of deep learning-based methods and state-of-the-art results. Jiang et al. [99] utilized verb expressions in a sentence for sentiment classification as the verb expressions contain opinionated words, which indicate the business companies to improve their products. The author used linear regression optimized by PSO to classify the amazon reviews, and the computation speed of the algorithm was increased drastically. Hence, from this exhaustive review, we can draw the following conclusions:

- The prevalent SA tasks which use bio-inspired algorithms are binary and ternary sentiment classification (positive, negative, and neutral), document-level sentiment classification, aspect-based sentiment classification, feature-selection optimization, review spam detection, and financial market prediction. Amongst these tasks, feature-selection optimization and binary sentiment classification are the most common tasks.
- The most popular choice among researchers is the combination of PSO, followed by SVM on the online review and news datasets. The accuracy achieved by PSO + SVM have outperformed much state-of-the-art on these datasets.
- Similarly, PSO is the most widely used algorithm in SA, followed by ACO, and English remains the leading language for SA.
- The dominant classification techniques for the bio-inspired algorithm in SA are Support Vector Machine, Naïve Bayes, decision trees, K-means, K-nearest neighbor, Logistic regression, and neural network.
- The evaluation metrics used are Accuracy, Precision, Recall (Sensitivity), F1 score, Area under the curve (AUC), Receiver Operating Characteristic (ROC), Mean Square Error (MSE), and Root Mean Square Error (RMSE).
- In SA, most of the datasets are prepared by fetching data from various social media sites using the respective API's or by collecting the reviews from multiple online platforms. The most common social media sites/ online platforms are: Twitter, Amazon, IMDb, Yelp, TripAdvisor, Facebook, Flickr, Getty Images, YouTube, and Google play/restaurant/ customer reviews.

4.2 Potential research directions

Finally, we found many research gaps in the previous literature. This could serve as potential research directions for SA. These are summarized as follows:

- The bio-inspired techniques can be explored on other SA tasks which are as explained as follows:
  - Implicit sentiment detection [101]: Most of the existing work on SA has focused on explicit sentiment detection [102, 103] in which the aspect term appears as a noun phase in the sentence. However, very less work has been done for extracting the implicit aspects. Implicit aspects are not specified explicitly in the text, which makes implicit sentiment detection a challenging task. The combination of explicit and implicit sentiments will increase the overall sentiment classification process [104] as implicit aspects convey opinions for understanding the customer reviews. Hence,

applying the optimization algorithms for extracting implicit features might boost the overall SA process.
  - Context-based SA [105]: Sometimes the meaning of a word becomes clear when the context is taken into consideration. The context of a word can be the set of previous words or the set of words following it [106]. This context can effect the polarity of the sentence as a word can have multiple meanings in different contexts. Hence, developing context-dependent SA models becomes a crucial task. The major challenge here is that the present literature lacks a proper definition for different types of context.
  - Emotion detection [107]: Emotion is defined as a 'feeling' or 'reaction' that people expresses on specific events and can be classified into happy, sad, angry, disgust, fear, etc. Sometimes emotion detection and sentiment detection are used interchangeably, but these two terms are quite different from each other as sentiment denotes a more general idea of determining the polarity of emotion. People are frequently expressing their emotions on multiple topics through social media, speech or videos [108]. Hence, these emotions need to be detected for analyzing the behavior of the people.
  - Irony and sarcasm detection [109, 110]: Sometimes a sentence may contain some irony or sarcastic words, which can affect the polarity of a sentence. For example: Consider the sentence, "I would recommend this book to someone who has insomnia" contains a positive word 'recommend', which conveys a positive sentiment. However, the statement is sarcastic and hence the polarity of the sentence is reversed. Detecting such sarcastic statements becomes a challenging task for sentiment classification. Moreover, the unstructured or informal language adds as a potential challenge for the researchers as people are commonly using slang or offensive words in their statements, which are computationally difficult to detect.

- Several new popular bio-inspired techniques [111] are being developed such as whale-optimization algorithm [112] which is based on the behavior of humpback whales, cat swarm optimization [113] which is inspired by the alert nature of the cats, lion optimization algorithm [114] which is based on the social behavior of lions, and forest optimization algorithms [115] inspired by lifetime of trees in a forest which can be used to optimize the feature selection process for sentiment classification, as these techniques are recently getting more attention from the researchers. These algorithms are very competitive as compared to state-of-the-art optimization methods.
- Nowadays, apart from text based SA, multiple modalities are considered in the form of text + images + speech for multimodal sentiment classification [116, 117]. For example: On various social media platforms like Facebook, users are expressing their opinion on some topics by posting their reactions (in the form of emoticons). Hence, multimodal data in the form of pictures, emoticons, GIF's, videos, and speech are extensively used to extract and analyze the sentiments expressed by people. However, bio-inspired algorithms are not explored for multimodal classification. This can be one of the prime areas for new researchers in this field.
- Apart from English, several studies in SA have focused on other languages like Chinese [118], Arabic [119], Vietnamese [120], etc. Considering the different languages around the world and the expressive power of each of them, languages like Hindi, French, Spanish, Arabic, Chinese, Japanese can be explored for SA using bio-inspired algorithms. Moreover, mashup languages like Hinglish (Hindi + English) can also be used in this area. However, no such research is observed for bio-inspired algorithms. It will be interesting to see how these algorithms will perform in analyzing the sentiments of different languages.
- Nowadays deep learning-based approaches [121] are also growing in demand as they are capable of handling the multimodal data. However, these techniques require considerable amount of data to learn the optimal features from the dataset and perform classification. Hence, a hybrid approach can be developed where bio-inspired algorithms can extract the optimized feature set from the data and deep learning models like Convolutional neural networks (CNNs) or Recurrent neural networks (RNNs) can be trained according to the extracted feature set for classifying the sentiments.

5 Conclusion

With the tremendous amount of data that is being generated on the web, achieving an optimal solution related to data-driven problems is getting extremely challenging. The intelligent bio-inspired algorithms are becoming the need of the hour for addressing complex real-world issues more efficiently and rapidly. These algorithms are increasingly being applied to solve difficult optimization problems as they have shown remarkable results and robustness for numerous optimization problems in different fields. However, many researchers are still unaware of the progress of

these algorithms due to the absence of significant literature in this field. Most of the existing literature has focused on few algorithms like genetic algorithms, neural networks, PSO, and ACO. However, in this survey, we identify some of the popular algorithms that have a broader set of applications so that we can outline their scope and objective through this detailed review. This survey reviews some of the significant work on bio-inspired based SA. We present a taxonomy for nature-inspired algorithms. Then we discuss the nine prominent bio-inspired algorithms: PSO, ACO, CS, FFA, BA, ABC, FPA, GSO, and SFL to give an overview of the unique characteristics and features of these algorithms. We also provide a comparative analysis of these algorithms by discussing their applications, advantages, disadvantages, and finally comparing their performance on the smartphone product review to get in-depth knowledge about each of the algorithms. We also present detailed statistics about the year-wise trend of bio-inspired algorithms for SA and an algorithm-wise distribution of the reviewed articles. Finally, by discussing some of the notable work in this area, we identify the potential research directions.

From this survey, we conclude that these bio-inspired algorithms have tremendous capability in solving the different optimization problems. In sentiment analysis, the most crucial task is the feature engineering process, which directly impacts the performance of the algorithm. By using these algorithms for getting an optimized feature set, we can enhance the accuracy of the sentiment classification process. Moreover, it is being used for document-level sentiment classification, aspect-based sentiment classification, and multi-class sentiment classification. We found that the most popular approach among researchers is applying PSO with SVM classifier for classifying the text into various classes. This makes PSO as one of the most popular algorithms for sentiment classification, followed by ACO. The least used algorithms are GSO, FPA, and BA. Although there can't be a single best algorithm applicable for every set of problems, still this review aims to give a general idea about what algorithm can be useful for their application.

The future work in this area can include designing a new nature-inspired algorithm which could have much more significant results than the established algorithms. Moreover, as mentioned in the review, some of the recent algorithms like whale-optimization algorithm, cat swarm optimization, lion optimization, and forest optimization algorithms are not explored in sentiment analysis. Hence, it will be exciting to see the applications and performance of these new algorithms as compared to the already established ones. Finally, we have identified some key areas like implicit sentiment detection, context-based SA, emotion detection, and irony detection that can serve as potential research opportunities for researchers. Most of the previous work in this field has focused on textual data. However, multiple modalities in the form of image, video, or speech can be combined for extracting the visual sentiments from visual data. Finally, an interesting area can be developing a hybrid approach of deep learning-based techniques with bio-inspired algorithms and analyzing their impact on SA. Hence, we hope this review will arouse the interest of readers and will be beneficial for researchers who are keen to work in this area.

References

1. Liu, B.: Sentiment analysis and subjectivity. In: Handbook of Natural Language Processing, no. 1, pp. 1–38 (2010)
2. "What happens in an Internet minute?" [Online]. https://www.visualcapitalist.com/what-happens-in-an-internet-minute-in-2019/
3. Agarwal, A., Yadav, A., Vishwakarma, D.K.: Multimodal sentiment analysis via RNN variants. In: Proceedings—2019 IEEE/ACIS 4th International Conference on Big Data, Cloud Computing, and Data Science, BCD 2019, pp. 19–23 (2019)
4. Yadav, A., Agarwal, A., Vishwakarma, D.K.: XRA-net framework for visual sentiments analysis. In: IEEE Fifth International Conference on Multimedia Big Data (BigMM), pp. 219–224 (2019)
5. Haque, T.U., Saber, N.N., Shah, F.M.: Sentiment analysis on large scale amazon product reviews. In: 2018 IEEE International Conference on Innovative Research and Development (ICIRD), pp. 1–6 (2018)
6. Zvarevashe, K., Olugbara, O.O.: A framework for sentiment analysis with opinion mining of hotel reviews. In: Conference on Information Communications Technology and Society (ICTAS), pp. 1–4 (2018)
7. Chandra Pandey, A., Singh Rajpoot, D., Saraswat, M.: Twitter sentiment analysis using hybrid cuckoo search method. Inf. Process. Manag. **53**(4), 764–779 (2017)
8. Suganya, B.: Particle swarm optimization based feature selection and summarization of customer reviews. Int. Conf. Emerg. Trends Eng. Sci. Sustain. Technol., pp. 131–135 (2017)
9. Bhardwaj, A., Narayan, Y., Vanraj, P., Dutta, M.: Sentiment analysis for Indian stock market prediction using Sensex and nifty. Procedia Comput. Sci. **70**, 85–91 (2015)
10. Kušen, E., Strembeck, M.: Politics, sentiments, and misinformation: an analysis of the Twitter discussion on the 2016 Austrian Presidential Elections. Online Soc. Netw. Media **5**, 37–50 (2017)
11. Wang, X., Gerber, M.S., Brown, D.E.: Automatic crime prediction using events extracted from twitter posts. 2012.
12. Ragini, J.R., Anand, P.M.R., Bhaskar, V.: Big data analytics for disaster response and recovery through sentiment analysis. Int. J. Inf. Manage. **42**(May), 13–24 (2018)
13. Christensen, J., Bastien, C.: Introduction to general optimization principles and methods. Nonlinear Optim. Veh. Saf. Struct., pp. 107–168 (2016).
14. Yang, X.: Nature-Inspired Metaheuristic Algorithms. Luniver Press, Bristol (2010)
15. Yang, X.S.: Nature-Inspired Optimization Algorithms, pp. 1–263. Elsevier, Amsterdam (2014)

16. Beheshti, Z., Shamsuddin, S.M.: A review of population-based meta-Heuristic algorithm. Int. J. Adv. Soft Comput. Appl. **5**, 1 (2013)
17. Voss, S., Martello, S., Osman, I. H., Roucairol, C.: Meta-heuristics: Advances and trends in local search paradigms for optimization. Springer, New York (2012)
18. M. Gavrilas, Heuristic and metaheuristic optimization techniques with application to power systems. Proc. 12th WSEAS Int. Conf. Math. Methods Comput. Tech. Electr. Eng., pp. 95–103 (2010)
19. Fister, I., Yang, X.S., Brest, J., Fister, D.: A brief review of nature-inspired algorithms for optimization. Elektroteh. Vestnik/ Electrotechnical Rev. **80**(3), 116–122 (2013)
20. Kennedy, J., Eberhart, R.: Particle swarm optimization. In: Proceedings of IEEE E International Conference on Neural Networks, pp. 1942–1948 (1995)
21. Rana, T.A., Cheah, Y.N.: Hybrid rule-based approach for aspect extraction and categorization from customer reviews. Proceedings 2015 9th International Conference IT Asia Transform. Big Data into Knowledge, CITA 2015 (2015)
22. Li, X., Li, J., Wu, Y.: A global optimization approach to multi-polarity sentiment analysis. PLoS ONE **10**(4), 1–18 (2015)
23. Slowik, A., Kwasnicka, H.: Nature inspired methods and their industry applications—Swarm Intelligence Algorithms. IEEE Trans. Ind. Informatics **1**(11), 1–1 (2017)
24. Yang, B., Chen, Y., Zhao, Z.: Survey on applications of particle swarm optimization in electric power systems. Control Autom. 2007. ICCA 2007. IEEE Int. Conf., vol. 00(3), pp. 481–486 (2007)
25. Chen, C.-Y., Ye, F.: Particle swarm optimization algorithm and its application to clustering analysis. 2004 IEEE Conf. Netw. Sens. Control **1**, pp 789–794 (2004)
26. Tsai, M.-C. T., Chen, K.-H., Lin, H.-C.: An application of PSO algorithm and decision tree for Medical Problem. 2015 IEEE 15th Int. Conf. Bioinforma. Bioeng. BIBE 2015, pp. 124–126 (2015)
27. Kristiyanti, D.A., Wahyudi, M.: Feature selection based on genetic algorithm, particle swarm optimization and principal component analysis for opinion mining cosmetic product review. 2017 5th Int. Conf. Cyber IT Serv. Manag. (2017)
28. Akhtar, M.S., Gupta, D., Ekbal, A., Bhattacharyya, P.: Feature selection and ensemble construction: a two-step method for aspect based sentiment analysis. Knowl. Based Syst. **125**, 116–135 (2017)
29. Liu, Z., Liu, S., Liu, L., Sun, J., Peng, X., Wang, T.: Sentiment recognition of online course reviews using multi-swarm optimization-based selected features. Neurocomputing **185**, 11–20 (2016)
30. Basari, A.S.H., Hussin, B., Ananta, I.G.P., Zeniarja, J.: Opinion mining of movie review using hybrid method of support vector machine and particle swarm optimization. Procedia Eng. **53**, 453–462 (2013)
31. Dorigo, M.: Optimization, Learning and Natural Algorithms. Ph.D. Thesis (1992)
32. Dorigo, M., Thomas, S.: Ant Colony Optimization. Cambridge, MA, USA MIT Press (2004)
33. Chakraborty, B., Banerjee, S.: Modeling the evolution of post disaster social awareness from social web sites. In: 2013 IEEE International Conference on Cybernetics, pp. 51–56 (2013)
34. Ahmad, S. R., Yusop, N.M.M., Bakar, A.A., Yaakub, M.R.: Statistical analysis for validating ACO-KNN algorithm as feature selection in sentiment analysis. AIP Conf. Proc., vol. 1891 (2017)
35. Goel, L., Prakash, A.: Sentiment analysis of online communities using swarm intelligence algorithms. 2016 8th Int. Conf. Comput. Intell. Commun. Networks, pp. 330–335 (2016)
36. Forsati, R., Moayedikia, A., Jensen, R., Shamsfard, M., Meybodi, M.R.: Enriched ant colony optimization and its application in feature selection. Neurocomputing **142**, 354–371 (2014)
37. Mavrovouniotis, M., Muller, F.M., Yang, S.: Ant colony optimization with local search for dynamic traveling salesman problems. IEEE Trans. Cybern. **47**(7), 1743–1756 (2017)
38. Shirzad, A., Tabesh, M.: Multiobjective optimization of pressure dependent dynamic design for water distribution networks. Water Resour. Manag. **31**(9), 2561–2578 (2017)
39. Banerjee, S., Agarwal, N.: Analyzing collective behavior from blogs using swarm intelligence. Knowl. Inf. Syst. **33**(3), 523–547 (2012)
40. Deif, D.S., Member, S., Gadallah, Y., Member, S.: An ant colony optimization approach for the deployment of reliable wireless sensor networks. IEEE Access **5**, 10744–10756 (2017)
41. Wang, F., Lin, B., Li, X.: An ant particle filter for visual tracking. In: 2017 IEEE/ACIS 16th International Conference on Computer and Information Science (ICIS), pp. 417–422 (2017)
42. Yang, X.S.: Firefly algorithms for multimodal optimization. Proc. fifth Symp. Stoch. Algorithms, Found. Appl. Lect. Notes Comput. Sci., vol. 5792, pp. 169–178 (2009)
43. Yang, X.S., He, X.: Firefly algorithm: recent advances and applications. Int. J. Swarm Intell. **1**, 1–36 (2013)
44. Rajput, V.S., Dubey, S.M.: A new approach of firefly algorithm for optimizing reviews of opinion mining. In: 2016 International Conference on Global Trends in Signal Processing, Information Computing and Communication, pp. 18–23 (2016)
45. Emary, E., Zawbaa, H.M., Ghany, K.K.A., Hassanien, A.E., Parv, B.: Firefly optimization algorithm for feature selection. In: Proc. 7th Balk. Conf. Informatics Conf. - BCI '15, pp. 1–7 (2015)
46. Banati, H., Bajaj, M.: Promoting products online using firefly algorithm. In: 2012 12th International Conference on Intelligent Systems Design and Applications (ISDA), vol. 2, pp. 11–21 (2005)
47. Yang, X.S., Deb, S.: Cuckoo search via Lévy flights. World Congr. Nat. Biol. Inspired Comput., pp. 210–214 (2009)
48. Devi, K.N., Bhaskaran, V.M., Kumar, G.P.: Cuckoo optimized SVM for stock market prediction. ICIIECS 2015 - 2015 IEEE International Conference on Innovations in Information, Embedded and Communication Systems (2015)
49. Redmond, M., Salesi, S., Cosma, G.: A novel approach based on an extended cuckoo search algorithm for the classification of tweets which contain emoticon and Emoji. In 2017 2nd International Conference on Knowledge Engineering and Applications (2017)
50. Rajamohana, S.P., Umamaheswari, K., Keerthana, S.V.: An effective hybrid Cuckoo Search with Harmony search for review spam detection. in *3rd International Conference on Advances in Electrical, Electronics, Information, Communication and Bio-Informatics (AEEICB17)*, pp. 524–527 (2017)
51. Yang, X.S.: A new metaheuristic Bat-inspired Algorithm. Nat. Inspired Coop. Strateg. Optim. (NICSO 2010), vol. 284, pp. 65–74 (2010)
52. Khurana, H., Sahu, S.K.: Bat inspired sentiment analysis of Twitter data. Prog. Adv. Comput. Intell. Eng. **2**, 639–650 (2018)
53. Nakamura, R.Y.M., Pereira, L.A.M., Costa, K.A., Rodrigues, D., Papa, J.P., Yang, X.S.: BBA: A binary bat algorithm for feature selection. In: Brazilian Symposium of Computer Graphic and Image Processing, pp. 291–297 (2012)
54. Fister, I.J., Fister, I., Yang, S.-S., Fong, S., Zhuang, Y.: Bat algorithm: recent advances. Int. Symp. Comput. Intell. Inform. **15**(1), 163–167 (2014)
55. Chakri, A., Khelif, R., Benouaret, M., Yang, X.S.: New directional bat algorithm for continuous optimization problems. Expert Syst. Appl. **69**, 159–175 (2017)

56. Karaboga, D., Basturk, B.: A powerful and efficient algorithm for numerical function optimization: artificial bee colony (ABC) algorithm. J. Glob. Optim. **39**(3), 459–471 (2007)
57. Dhurve, M.R., Prof, A., Seth, M.: A survey on weighted sentiment analysis using artificial bee colony algorithm. Int. J. Adv. Res. Comput. Eng. Technol. **4**(4), 1173–1178 (2015)
58. Sumathi, M., Karthik, T., Marikkannan, S.: Artificial bee colony optimization for feature selection in opinion mining. J. Theor. Appl. Inf. Technol. **66**(1), 368–379 (2014)
59. Ramaswamy, S.: An improved fuzzy classifier using EI ABC. World Appl. Sci. J. **35**(1), 33–42 (2017)
60. Saravanan, T.M., Tamilarasi, A.: Effective sentiment analysis for opinion mining using artificial bee colony optimization. Res. J. Appl. Sci. Eng. Technol. **12**(8), 828–840 (2016)
61. Yang, X.S.: Flower pollination algorithm for global optimization. Int. Conf. Unconv. Comput. Nat. Comput. Lect. Notes Comput. Sci., 240–249 (2012)
62. Rajamohana, S.P., Umamaheswari, K.: A hybrid approach to optimize feature selection process using iBPSO-BFPA for review spam detection. Appl. Math. Inf. Sci. **11**(5), 1443–1449 (2017)
63. Kaur, M., Kaur, N.: Text clustering using PBO algorithm for analysis and optimization. Int. J. Curr. Eng. Technol. **4**(6), 3876–3878 (2014)
64. Krishnanand, K.N., Ghose, D.: Glowworm swarm optimisation: a new method for optimising multi-modal functions. Int. J. Comput. Intell. Stud. **1**(1), 93–119 (2009)
65. Alboaneen, D.A., Tianfield, H., Zhang, Y.: Sentiment analysis via Multi-layer perceptron trained by meta-heuristic optimisation. In: 2017 IEEE International Conference on Big Data (BIGDATA), pp. 4548–4553 (2017)
66. Eusuff, M.M., Lansey, K.E.: Optimization of water distribution network design using the shuffled frog leaping algorithm. J. Water Resour. Plan. Manag. **129**(3), 210–225 (2003)
67. Yuvaraj, N., Sabari, A.: Twitter sentiment classification using binary shuffled frog algorithm. Intell. Autom. Soft Comput. **23**(2), 373–381 (2017)
68. Rajamohana, S.P., Umamaheshwari, K., Karthiga, R.: Sentiment analysis using shuffled frog leaping algorithm. Int. J. Adv. Res. Comput. Sci. Softw. Eng. **6**(12), 138–142 (2017)
69. Nirmala, D.K., Jayanthi, P.: Sentiment classification using SVM and PSO. Int. J. Adv. Eng. Technol. **7**(2), 411–413 (2016)
70. Budhi, G.S., Chiong, R., Hu, Z., Pranata, I., Dhakal, S.: Multi-PSO based classifier selection and parameter optimisation for sentiment polarity prediction. In: 2018 IEEE Conference on Big Data and Analytics, ICBDA, pp. 68–73 (2018)
71. Gupta, D.K., Reddy, K.S.: PSO-ASent: feature selection using particle swarm optimization for aspect based sentiment analysis. In: Natural Language Processing and Information Systems. NLDB 2015. Lecture Notes in Computer Science, vol. 9103, pp. 220–233 (2015)
72. Jiang, H., Kwong, C.K., Park, W.Y., Yu, K.M.: A multi-objective PSO approach of mining association rules for affective design based on online customer reviews. J. Eng. Des. **29**(7), 381–403 (2018)
73. Rajamohana, S.P., Umamaheswari, K.: An integrated evolutionary algorithm for review spam detection on online reviews. Adv. Nat. Appl. Sci. **10**(17), 228–236 (2016)
74. Sonagi, A., Gore, D.: Efficient sentiment analysis using hybrid PSO-GA approach. Int. J. Innov. Res. Comput. Commun. Eng. **5**(2), 1302–1309 (2017)
75. Souza, E., Oliveira, A.L.I., Oliveira, G., Silva, A., Santos, D.: An unsupervised particle swarm optimization approach for opinion clustering. In: Proceedings-2016 5th Brazilian Conference Intelligence Systems BRACIS 2016, pp. 307–312 (2016)
76. Ahmad, S.R., Bakar, A.A., Yaakub, M.R.: Ant colony optimization for text feature selection in sentiment analysis. Intell. Data Anal. **23**(1), 133–158 (2019)
77. Kaur, J., Sehra, S.S., Sehra, S.K.: Sentiment analysis of Twitter data using hybrid method of support vector machine and ant colony optimization. Int. J. Comput. Sci. Inf. Secur. **14**(7), 222–226 (2016)
78. Ahmad, S.R., Bakar, A.A., Yaakub, M.R., Moziyana, N., Yusop, M.: Statistical validation of ACO-KNN algorithm for sentiment analysis. J. Telecommun. Electron. Comput. Eng. **9**(2), 165–170 (2017)
79. Joseph, A.: Sentiment analysis using CRF and optimal temporal boundary. Indian J. Educ. Inf. Manag. **5**(April), 1–8 (2016)
80. Souza, E., Santos, D., Oliveira, G., Silva, A., Oliveira, A.L.I.: Swarm optimization clustering methods for opinion mining. Nat. Comput. (2018). https://doi.org/10.1007/s11047-018-9681-2
81. Saravanan, T.M., Tamilarasi, A.: An efficient hierarchical improved relevance vector machine for effective sentiment analysis. Int. J. Comput. Technol. Appl. **10**(20), 139–152 (2017)
82. Rani, A.S.S., Scholar, P.G.: Unsupervised feature selection using binary bat algorithm. In: IEEE Sponsored 2nd International Conference on Electronics and Communication Systems (ICECS 2015), pp. 451–456 (2015)
83. Palanisamy, S., Kanmani, S.: Artificial bee colony approach for optimizing feature selection. Int. J. Comput. Sci. Issues **9**(3), 432–438 (2012)
84. Orkphol, K., Yang, W.: Sentiment analysis on microblogging with K-means clustering and artificial bee colony. Int. J. Comput. Intell. Appl. **18**(2), 1–22 (2019)
85. Rajamohana, S., Umamaheswari, K., Abirami, B.: Adaptive binary flower pollination algorithm for feature selection in review spam detection, pp. 1–4 (2017)
86. Wahyudi, M., Kristiyanti, D.A.: Sentiment analysis of smartphone product review using support vector machine algorithm-based particle swarm optimization. J. Theor. Appl. Inf. Technol. **91**(1), 189 (2016)
87. Idrus, A., Brawijaya, H.: Sentiment analysis of state officials news on online media based on public opinion using naive bayes classifier algorithm and particle swarm optimization. In: 6th International Conference on Cyber and IT Service Management, CITSM 2018, pp. 1–7 (2018)
88. Umamaheswari, K., Rajamohana, S.P., Aishwaryalakshmi, G.: Opinion mining using hybrid methods. In: International Conference on Innovations in Computing Techniques (ICICT 2015), pp. 18–21 (2015)
89. Nagarajan, S.M., Gandhi, U.D.: Classifying streaming of Twitter data based on sentiment analysis using hybridization. Neural Comput. Appl. **31**(5), 1425–1433 (2019)
90. Jain, A., Pal Nandi, B., Gupta, C., Tayal, D.K.: Senti-NSetPSO: large-sized document-level sentiment analysis using Neutrosophic Set and particle swarm optimization. Soft Comput. **24**, 1–13 (2019)
91. Alfarraj, O., AlZubi, A.A.: A novel approach for ranking customer reviews using a modified PSO-based aspect ranking algorithm. Cluster Comput. **22**, 1–7 (2018)
92. Alarifi, A., Tolba, A., Al-Makhadmeh, Z., Said, W.: A big data approach to sentiment analysis using greedy feature selection with cat swarm optimization-based long short-term memory neural networks. J. Supercomput. (2018). https://doi.org/10.1007/s11227-018-2398-2
93. Tubishat, M., Abushariah, M.A.M., Idris, N., Aljarah, I.: Improved whale optimization algorithm for feature selection in Arabic sentiment analysis. Appl. Intell. **49**(5), 1688–1707 (2019)

94. Kalarani, P., Selva Brunda, S.: Sentiment analysis by POS and joint sentiment topic features using SVM and ANN. Soft Comput. **23**(16), 7067–7079 (2019)
95. Shang, L., Zhou, Z., Liu, X.: Particle swarm optimization-based feature selection in sentiment classification. Soft Comput. **20**(10), 3821–3834 (2016)
96. Kurniawati, I., Pardede, H.F.: Hybrid method of information gain and particle swarm optimization for selection of features of SVM-based sentiment analysis. In: 2018 International Conference on Information Technology Systems and Innovation, pp. 1–5 (2019)
97. Rajamohana, S.P., Umamaheswari, K.: Hybrid optimization algorithm of improved binary particle swarm optimization (iBPSO) and cuckoo search for review spam detection. In: Proceedings on 9th International Conference Machine Learning and Computing - ICMLC 2017, pp. 238–242 (2017)
98. Sharmila, R., Sivajothi, M.: Eco inspired bees: a novel feature selection mechanism for sentiment analysis. Int. J. Pure Appl. Math. **114**(2), 307–327 (2017)
99. Jiang, D., Tao, Q., Wang, Z., Dong, L.: An intelligent logistic regression approach for verb expression's sentiment analysis. In: Proceedings of Recent Developments in Intelligent Computing, Communication and Devices, vol. 752, pp. 173–181 (2019)
100. Chiong, R., Adam, M.T.P., Fan, Z., Lutz, B., Hu, Z., Neumann, D.: A sentiment analysis-based machine learning approach for financial market prediction via news disclosures. In Proceedings of the 2018 Genetic and Evolutionary Computation Conference Companion, pp. 278–279 (2018)
101. Tubishat, M., Idris, N., Abushariah, M.A.M.: Implicit aspect extraction in sentiment analysis: review, taxonomy, oppportunities, and open challenges. Inf. Process. Manag. **54**(4), 545–563 (2018)
102. Poria, S., Cambria, E., Gelbukh, A.: Aspect extraction for opinion mining with a deep convolutional neural network. Knowl. Based Syst. **108**, 42–49 (2016)
103. Ding, X., Liu, B., Yu, P.S.: A holistic lexicon-based approach to opinion mining. In: Proceedings of the 2008 International Conference on Web Search and Data Mining, pp. 231–239 (2008)
104. Van De Kauter, M., Breesch, D., Hoste, V.: Fine-grained analysis of explicit and implicit sentiment in financial news articles. Expert Syst. Appl. **42**(11), 4999–5010 (2015)
105. Ansari, O., Zahir, J., Mousannif, H.: Context-based sentiment analysis: a survey. In: International Conference on Model and Data Engineering, Part of the Communications in Computer and Information Science book series, pp. 91–97 (2018)
106. Katz, G., Ofek, N., Shapira, B.: ConSent: Context-based sentiment analysis. Knowl. Based Syst. **84**, 162–178 (2015)
107. Sailunaz, K., Alhajj, R.: Emotion and sentiment analysis from Twitter text. J. Comput. Sci. **36**, 101003 (2019)
108. Sailunaz, K., Dhaliwal, M., Rokne, J., Alhajj, R.: Emotion detection from text and speech: a survey. Soc. Netw. Anal. Min. **8**(28), 1–26 (2018)
109. van Hee, C., Lefever, E., Hoste, V.: Exploring the fine-grained analysis and automatic detection of irony on Twitter. Lang. Resour. Eval. **52**, 1–25 (2018)
110. Bharti, S.K., Vachha, B., Pradhan, R.K., Babu, K.S., Jena, S.K.: Sarcastic sentiment detection in tweets streamed in real time: a big data approach. Digit. Commun. Netw. **2**, 108–121 (2016)
111. Darwish, A.: Bio-inspired computing: Algorithms review, deep analysis, and the scope of applications. Futur. Comput. Informatics J. **3**(2), 231–246 (2018)
112. Mirjalili, S., Lewis, A.: The whale optimization algorithm. Adv. Eng. Softw. **95**, 51–67 (2016)
113. Chu, S.-C., Tsai, P., Pan, J.-S.: Cat Swarm Optimization. In: Pacific Rim International Conference Artificial Intelligence Part Lecture Notes in Computer Science B, pp. 854–858 (2006)
114. Yazdani, M., Jolai, F.: Lion optimization algorithm (LOA): a nature-inspired metaheuristic algorithm. J. Comput. Des. Eng. **3**(1), 24–36 (2016)
115. Ghaemi, M., Feizi-Derakhshi, M.R.: Forest optimization algorithm. Expert Syst. Appl. **41**(15), 6676–6687 (2014)
116. Soleymani, M., Garcia, D., Jou, B., Schuller, B., Chang, S.F., Pantic, M.: A survey of multimodal sentiment analysis. Image Vis. Comput. **65**, 3–14 (2017)
117. Poria, S., Cambria, E., Howard, N., Bin Huang, G., Hussain, A.: Fusing audio, visual and textual clues for sentiment analysis from multimodal content. Neurocomputing **174**, 50–59 (2016)
118. Sun, X., Li, C., Ren, F.: Sentiment analysis for Chinese microblog based on deep neural networks with convolutional extension features. Neurocomputing **210**, 227–236 (2016)
119. Baly, R., Hajj, H., Habash, N., Shaban, K.B., El-Hajj, W.: A sentiment treebank and morphologically enriched recursive deep models for effective sentiment analysis in Arabic. ACM Trans. Asian Low-Resour. Lang. Inf. Process. **16**, 4–21 (2017)
120. Trinh, S., Nguyen, L., Vo, M., Do, P.: Lexicon-based sentiment analysis of facebook comments in Vietnamese language. Recent Dev. Intell. Inf. Database Syst. Part Stud. Comput. Intell. B **642**, 263–276 (2016)
121. Yadav, A., Vishwakarma, D.K.: Sentiment analysis using deep learning architectures: a review. Artif. Intell. Rev. (2019). https://doi.org/10.1007/s10462-019-09794-5

Publisher's Note Springer Nature remains neutral with regard to jurisdictional claims in published maps and institutional affiliations.



Ashima Yadav received B.sc (Hons) in Computer Science from University of Delhi, New Delhi, India in 2013, and M.C.A. from Guru Gobind Singh Indraprastha University, New Delhi, India in the year 2016. She is currently working towards the Ph.D. degree from the Department of Information Technology, Delhi Technological University, New Delhi, India. Her current research interest includes deep learning, natural language processing, machine learning, Emotion Recognition, and sentiment analysis.



Dinesh Kumar Vishwakarma (M'16, SM'19) received the B.Tech. degree from Dr. Ram Manohar Lohia Avadh University, Faizabad, India, in 2002, the M.Tech. degree from the Motilal Nehru National Institute of Technology, Allahabad, India, in 2005, and the Ph.D. degree from Delhi Technological University, New Delhi, India, in 2016. He is currently an Associate Professor with the Department of Information Technology, Delhi Technological University, New Delhi. His current research interests include Computer Vision, Machine Learning, Deep Learning, Sentiment Analysis, Fake News and Rumour Analysis, Crowd Behaviour Analysis, Person Re-Identification, Human Action and Activity Recognition. He is a reviewer of various Journals/Transactions of IEEE, Elsevier, and Springer. He has been awarded with "Premium Research Award" by Delhi Technological University, Delhi, India in 2018.

Multimedia Tools and Applications
https://doi.org/10.1007/s11042-020-08671-6

A dictionary matrix generation based compression and bitwise embedding mechanisms for ECG signal classification

Dinesh Kumar Atal [1] · Mukhtiar Singh [1]

Received: 10 April 2019 / Revised: 6 December 2019 / Accepted: 9 January 2020
Published online: 27 January 2020
© Springer Science+Business Media, LLC, part of Springer Nature 2020

Abstract

The Electrocardiogram (ECG) signal processing is one of the exciting research areas in recent days. Ensuring security to the patient's confidential information is a demanding critical task in many healthcare systems. So, the traditional works developed the security mechanisms for embedding the original ECG signal with the image, audio, or video. But, it does not focus on reducing the size of the original message before transmitting it to others. Also, it has significant limitations of inefficient security, increased complexity, and reduced classification accuracy. To rectify this issue, our research proposed the new embedding mechanism to improve the security of patient's health information. In this system, the original ECG signals compressed at the initial stage by using the proposed Dictionary Matrix Generation (DMG) algorithm. Then, the compressed signals embedded within the cover image by using the Bitwise Embedding (BE) mechanism. At the receiver side, the bedded goal is de-embedded and decompressed by using the DMG and BE algorithms. The features such as spectral and peak values of the signal are extracted for increasing the efficiency of classification. Classification and detection of abnormality present in ECG signal of patient is the most essential part. To achieve this, we proposed the Modified Dynamic Classification (MDC) algorithm based on the features. In this work, the novelty is implemented in the compression, embedding, and classification stages. The proposed system reduces the data loss during transmission, memory storage and time complexity. The overall process evaluated by using PTB diagnostic ECG database**.** In experiments, the proposed classification technique provides the accuracy of 98.39% and it proved that the proposed method had highest performances than existing methods such as PNN, SVM and RF classification.

Keywords Electrocardiogram (ECG) signal · Dictionary matrix generation · Bitwise embedding · Modified dynamic classification (MDC)

✉ Mukhtiar Singh
smukhtiar_79@yahoo.co.in

[1] Department of Electrical Engineering, Delhi Technological University, Bawana Road, Delhi 110042, India

1 Introduction

An electrocardiogram is an essential diagnosing graphic trace to analyze the electrical activities of the heart muscles that is recorded by the placement of 12 different electrodes arranged on designated areas of the body [22]. The ECG signal is widely used by medical experts to monitor the rhythm and functioning of the heart [29]. Based on the conditions of the heartbeat, the ECG can vary from one person to another person, which traces the P, Q, R, S, and T waves for analysis [4, 14]. It offers a large amount of information for providing appropriate treatment to cardiac patients. The majority of the clinically useful information in terms of recognizing the abnormality [10, 20] in the ECG is originated in the amplitudes and intervals defined by characteristics features. The fiducial ECG [35] features are illustrated in Table 1, in which the P wave indicates the atrial depolarization. Q wave is the first negative diversion after P. R wave is the first positive diversion, S wave is the first negative diversion after R, and T wave denotes the ventricular repolarization [33].

Table 1 describes the amplitude and intervals of standard ECG waves. It contains the features of P wave, R wave, Q wave, T wave and P-R interval. And the parameters of Q-T interval, S-T segment, QRS interval, P-R interval and heart rate.

1.1 Background and related work

As far as the multimedia and cloud dependent applications are concerned, it is very important to discuss some base and useful ideals paving the way for the improvisations as the age goes on. In this way, usefulness of encoding the medias was pioneered by [32]; [37] understood the importance of smart transferring of the medias and concentrated more on developing the improvised data transmitting medium; Using IoT-Internet of Things, [26, 31] implemented better media handling intelligent city schema. [31, 36] tried to redress some concerns arising because of security level breaches in Cloud computational and IoT applications. On considering the importance of transmitting maps and detailing the image, dehazing of individualistic image was done by [50] for removing the unwanted hindrances while processing the images. Secret image size reduction (SISR) algorithm was used by [2] to enhance the quality of the Stego with the help of text size reduction and Mapping of the Fibonacci bit-plane.

Then, if we take the healthcare applications [17, 23, 33, 38], protecting the privacy of the patient's ECG data is one of the critical processes in recent studies. The Steganography [27] technique that hides the secret data behind the image, audio, or video. This technique aims to transmit the data from the sender to the receiver securely. Also, maintaining the secrecy of private data is one of the critical issues in many application areas [23]., the steganographic approach [38] is widely used, which provides a reliable solution to security-related problems [25]. In the traditional works, the most straightforward methods are used to hide the secret in

Table 1 Amplitude and Intervals of Standard ECG waves

ECG Parameter	Amplitude (mV) &wave/interval duration (s)	ECG Parameter	Interval/Wave duration (s)
P wave	0.25 mV	Q-T interval	0.35 to 0.44 s
R wave	1.60 mV	S-T segment	0.05 to 0.15 s
Q wave	0.025 mV	QRS interval	0.08 to 0.12 s
T wave	0.1 to 0.5 mV	R-R interval	0.6 to 1.20 s
P-R interval	0.12 to 0.20 s	Heart rate	60–100 bpm

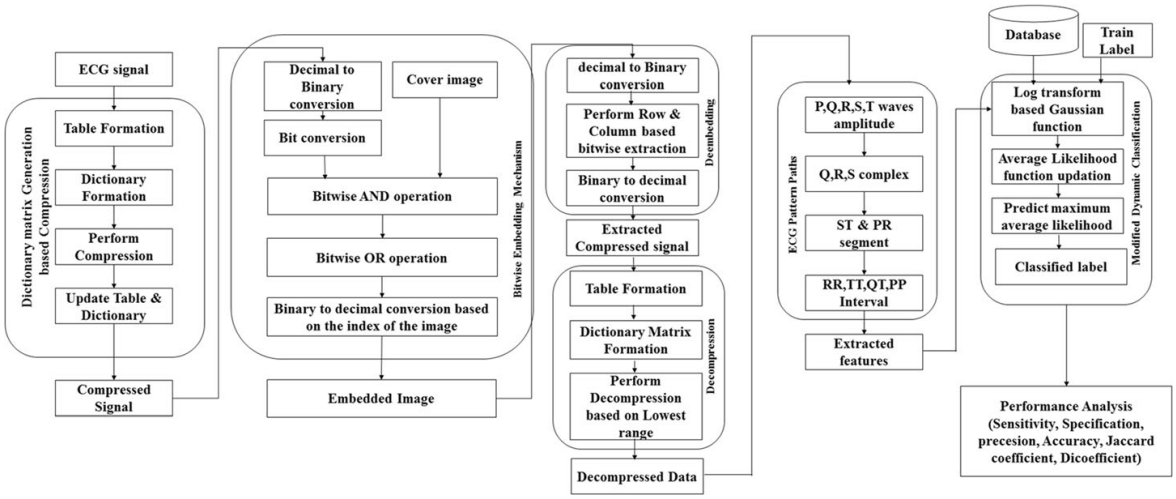


Fig. 1 Flowchart of the proposed system

image, and it embeds the secret image into the host image by applying the transformation techniques [8]. But, these mechanisms have the limitations of reduced visual quality, increased complexity, and inefficient security [39].

Sulam, et al. [38] introduced a different learning-based classification framework for identifying the person with the use of their ECG signals. Here, the embedded points have been separated based on the similarity by using the diffusion algorithm. The major limitation observed from this paper was its inability to determining the states of the same system. *Marakarkandy and Tiwari* [24] implemented a wavelet-based steganography method for ensuring the patient's confidentiality. This approach integrated the benefits of both encryption and scrambling, which provided an integrated ECG signal for protecting the private data. Here, the watermarked ECG signal has been utilized to perform the diagnosis by removing all the hidden information. The stages involved in the watermark embedding operation were as follows:

- Key sharing
- ASCII code generation
- Embedding based on LSB
- Wavelet coefficients

However, the suggested technique is not found to be highly efficient in terms of security. *Hu* et al. [16] integrated the watermarking and compression approaches for ECG signal processing by quantizing the vectors. The confidentiality and reliability of the user's data have been ensured by mitigating the data dimensionality. Here, the original ECG signal has been segmented and embedded by using the watermarking technique. After inserting, the inverse DWT has been applied for de-embedding the signal. *Chowdhury* et al. [9] analyzed various compression techniques used for ECG signal processing with Phono-cardiography dependent information. However, this paper required to increase the compression ratio of the suggested method. *Li,* et al [28] developed a Quantization Codeword Correlation Network (QCCN) for analyzing the low bit rate speech signals during steganalysis. Here, three different types of speech signals, such as noisy, periodic, and impulsive, were analyzed concerning various sound channels and descriptions of the phoneme. *Holub and Fridrich* [15] implemented a new steganalysis approach for

reducing the complexity of features with the use of the un-decimated Discrete Cosine Transformation (DCT) technique. Here, the effect of both quantization and normalization was investigated for increasing efficiency. *Denmark and Fridrich* [11] suggested a new scheme for embedding the JPEG images by using the steganography mechanism. This paper intended to determine the steganographic changes with reduced embedding cost.

Reddy et al [34] investigated the characteristics of ECG signals based on the processes of filtering, feature extraction, peak value estimation, and abnormality detection. It classifies the heart abnormalities such as Tachycardia and Bradycardia based on the signal features. *Al Rahhal* et al. [3] recommended an in-depth learning approach for classifying the abnormal ECG signals. This paper aimed to extract the essential functions of ECG for a better classification. *Ghasemzadeh* et al. [13] implemented a audio steganalysis system for the Human Auditory System (HAS). This paper intended to reduce the dimension of Reversed Mel-Frequency Cepstral Coefficients (R-MFCC) features. *Patil*et al. [30] recommended a Discrete Wavelet Transformation (DWT) and Singular Value Decomposition (SVD) techniques for securely transmitting the patient's informationwith the help of curvelet. *Awasthi and Madhe* [5] used the Percentage Residual Difference (PRD) for evaluating the wavelet-based ECG steganography system. The steps involved in this system were scaling, shifting, encryption, packet decomposition, embedding, de-embedding, and decryption. *Jovanovic et al* [21] developed a QRS detection algorithm for eliminating the artifacts from the ECG signal. This paper aimed to detect the QRS waves by detecting the peaks and reducing the noise from the given message. *Wu* et al. [46] developed a reversible data hiding scheme for ensuring the privacy of the patient's data. In this mechanism, the benefits of both histogram shifting and thresholding were incorporate for providing increased security.

Jero et al. [18] suggested the curvelet transformation method for improving the security of data by hiding the patient's information. Here, the watermark embedding technique was utilized to convert the 1D ECG signal to the 2D ECG signal. *Awasthi and Madhe* [6] used the wavelet transformation technique for analyzing the encrypted ECG signals. In this paper, different wavelets such as conflict, biorthogonal, and eyelets were used to analyze the energy of both original and encrypted ECG signals.

Wu et al. [43] implemented a multi-view of low-rank dictionary learning algorithm for efficient classification. Here, the low-rank regularization term was utilized to noise reduction. Also, it intended to reduce the redundancy in dictionaries based on the structural incoherence constraint. *Wu* et al. [45] designed a discriminant tensor dictionary learning algorithm to develop an image set based classification. *Wu* et al. [44] stated a multi-view discriminant dictionary learning algorithm for efficiently analyses the diversity in different views.

[49] suggested an improvised for segmenting the clinical images by making use of ACM-Active Contour Model).*XiaoChen* [7] contributed to the matting of the images by devising a whole feature covering sampling kind of methodology. Another instant of image specific contribution towards the segmentation was given by [48]. This work made use of ACM in combination with the local patch alikeness. Then, the complex classification issues were tackled by [12] with the help of Modified PNNs- Probabilistic Neural Networks. They had taken 10 categories of ailments in the human heart for proceeding with their work. [42] had taken up the work of identifying the myocardial infarction ailments by making use of RF-Random Forest Classifiers.

In various literature surveys, they found that computer assisted automatic analysis and classification of ECG signal with higher accuracy. And there were more different

statistical techniques to classify the normal and abnormal signals. The traditional the security mechanisms do not focuses on reducing the size for embedding the original ECG signal. However, it reduces the computational complexity, security and standardization of ECG features. It had nonexistence of optimal classification rules for efficient ECG classification. So, the classification requires to get trained in such a way.

1.2 Motivation

The motivation behind this work is to increase the security level during the transmission of ECG signals. On analyzing the existing techniques, it is detected that the majority of them have inherent problems associated with reduced security, computational complexity, and data handling during e-health applications at healthcare centers. For compression, the majority of the previous research work deals with lossy as well as lossless compression of the signals. The lossless techniques are preferable because of their enhanced performance and preserving the original quality. Some of the lossless and lossy techniques [46], particularly for ECG Compression, are compared. The Bit compression ratio (BCR) level achieved falls in the range of 1.92 to 2.43, which needs to be improved. Thus, efficient signal processing techniques have been implemented in this work, in which the security is focused on the following stages: compression, embedding, and classification.

1.3 Contribution

The significant contributions of this work are presented in three stages, such as compression, embedding, and classification. During compression, the original signal is compressed without any information loss. Then, the embedding process is performed to ensure the security of the message, so the unauthenticated users could be prevented from accessing the patient's health information. Moreover, in classification, the corresponding class of the signal is also predicted to assist the diagnosis.

- Compression is used here to boost up the signal transmission from laboratory to hospitals also it reduces the energy consumption which is achieved using the proposed method Dictionary Matrix Generation based Compression Technique.
- Embedded is used to secure the signal access from the unauthenticated users to protect the patient's health data which is performed by Bitwise Embedding mechanism [1]. The bitwise mechanism also used to calculate the embedding efficiency, capacity and quality.
- Feature extraction of ECG signal is made to fetch parameters of ECG signal to define the characteristic of the signal. With the retrieved information, detection of anomalies can be done earlier
- The significant benefits of classification is data accuracy, efficiency and reduced complexity to identify the healthy signals and various types of unhealthy signals using Modified Dynamic Classification Algorithm

The remaining sections in the paper are organized as follows: The description of the proposed embedding based ECG signal classification system with its clear flow chart and results of feature extraction are presented in Section 2. The results of the existing and proposed signal classification techniques are evaluated and compared by using various performance measures in Section 3. Finally, the paper is concluded in Section 4.

2 Proposed method

This section presents a brief description of the proposed compression and embedding based ECG signal classification system. The proposed system comprises the following steps:

1. Compression
2. Embedding
3. De-embedding and De-compression
4. Feature extraction
5. Classification

Figure 1 describes the overall flow of proposed system. At first, the given ECG signal is compressed, in which the table formation, dictionary formation, table update, dictionary update, and compression processes are performed. After compression, it is embedded with the cover image by using the BE mechanism. Then, the embedded image at the receiver side de-embedded and decompressed. Consequently, the ECG features such as spectral and peak values of the de-embedded signal are extracted for classification using the MDC algorithm.

2.1 Compression

Compression is one of the essential stages in many images processing applications, which efficiently reduced the size or dimensionality of the data for efficient analysis. The traditional works do not focus on a compression-based embedding for ECG signal classification. Instead of that, it utilized some encryption algorithms for converting the original signal into an encrypted signal. But, it leads to increased data dimensionality and inefficient security. Thus, this paper aims to develop a new compression mechanism for reducing the size of the signal. In this stage, the input ECG signal as shown in Fig. 2is compressed by using the proposed DMG technique, which forms the table initially with the attributes of the lowest range, final code, and length of code. Then, the most economical range is updated based on the input data, in which if the signal data is lesser than the threshold, the value is updated as 1; otherwise, it is updated as 0. After that, the dictionary is formed by estimating the length of signal data. In which, final bit, prefix bit, code length, and signal data are calculated before compression. Finally, the compression is performed by checking whether the final code value is empty or not; based on this, the dictionary value is updated, and the signal is compressed as shown in Fig.3.

Figure 2 describes the input of ECG signal, it contains low amplitude voltages in high offsets presents and noise. ECG signal consist the components of Heart rate, PR interval, QRS interval, QT interval, and ST segment. Figure 3 describes the output of compressed ECG signal using proposed DMG technique.

2.2 Embedding

After compressing the signal, it is embedded with any cover image by using the proposed BE algorithm to hide the patient confidential ECG information. Bitwise or bit-level operations form the basis of embedded algorithms. In this algorithm, the compressed signal and the cover image are taken as the input. Then the compressed data is converted into the binary format by applying the decimal to binary conversion. Then, each binary bit embedded concerning the row and column of the image matrix. For this embedding, the bitwise AND and OR operations

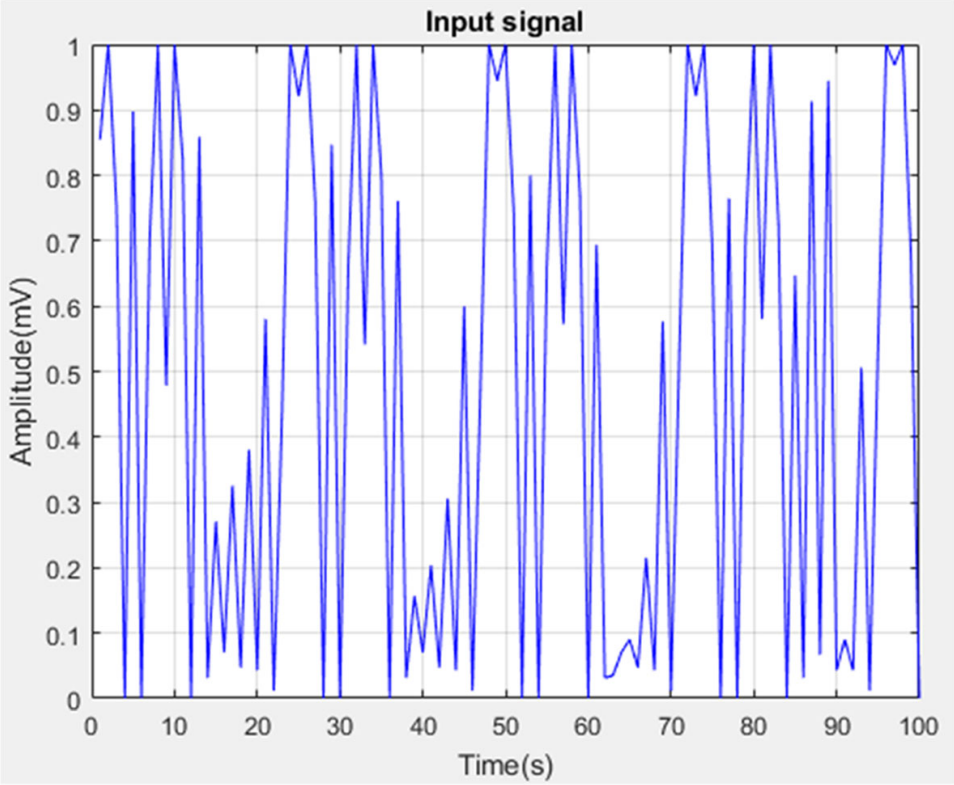


FIG. 2 Input ECG signal

are performed for all the bits; then, the value is updated with the index of the image. Then, this process is repeated for the 8-bit binary data; based on this process, the compressed signal is embedded with the image. Here, the signal embedding is mainly performed for increasing the

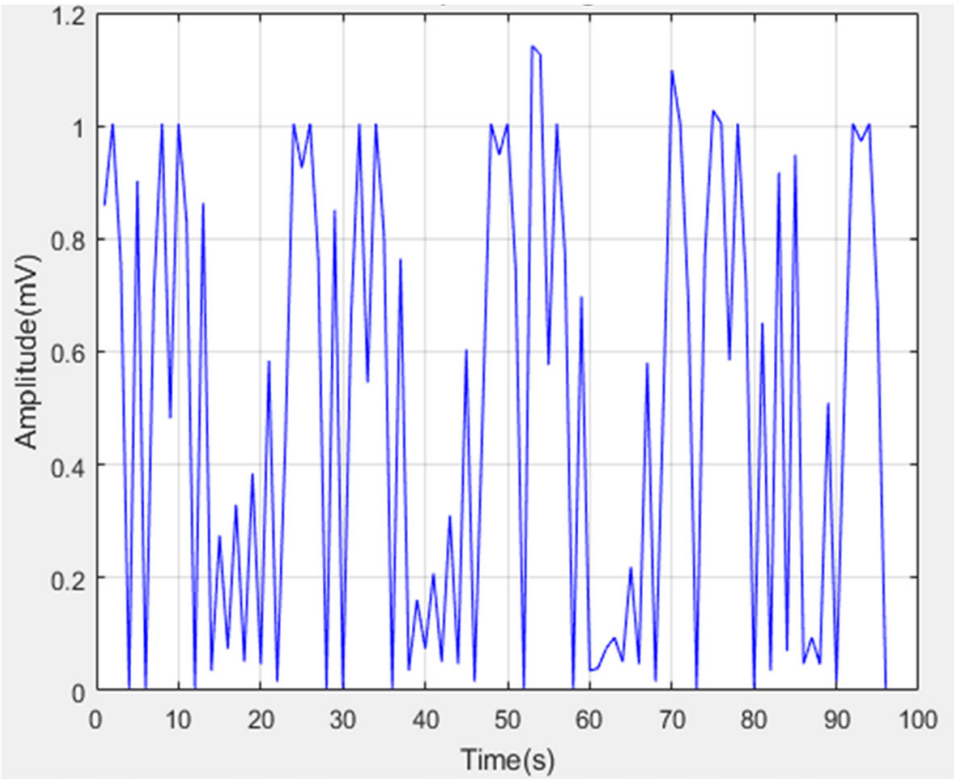


FIG. 3 Compressed signal

security level of signal information. Once the signal is embedded with the image, it can be transferred to the corresponding receiver. This embedded image can be used for e-health applications at distance places or from one hospital to another for specific caring of patients without data loss and maintaining privacy too.

2.3 De-embedding and de-compression

When the receiver gets this data, the signal can be de-embedded by using the BE De-embedding algorithm. In this stage, the size of the embedded image and the compressed data size are estimated at first. Then, the de-embedding steps are performed for the entire image by initializing the zero matrices with the dimension of the 8-bit binary value. For the 1st bit of the image, the row value is incremented with 1. If the row value reaches the row size of the embedded image, the column value and starting row value are incremented from the initial. If the column value reaches the column size of the embedded image, the loop can be a break. Similarly, the row values are updated and de-embedded for all the 8-bits of the picture. After that, the binary to decimal conversion is performed to update the compressed signal.

After de-embedding the signal, it can be decompressed for detecting the abnormality of the signal. Here also, the same processes, such as table formation, dictionary formation, update, and decompression, are performed. Based on the input data, the lowest range is updated, in which if the compressed data is greater than the threshold, the decoded value is computed for the decompressed image; otherwise, the compressed data can be decompressed. Consequently, the code length is reduced to 1; based on this, the final code is updated with the original code value. Then, the decompressed data is assigned along with the original data. If the length of output data is less than the compressed data, the dictionary is updated with the output zeros of unique code. Finally, the data is decompressed, and the original signal is obtained.

Figure 4 describes the obtained original signal or decompressed signal using BE De-embedding algorithm. Applying the proposed compression method and embedding mechanism on ECG signals, then it could be sent to a central monitoring station or healthcare system through the internet or other communication techniques for the analysis and classification purpose. The same procedure is followed here to validate the classification accuracy using the decompressed signals at the receiver site.

2.4 Feature extraction results and ECG patterns

The main reason for retrieving the features of the ECG signal is to derive the set of parameters that used to characterize the signal. Here, the features of the decompressed signal are extracted, which includes spectral and peak values by the supervised neural modified dynamic classification algorithm. Usually, the peak values can vary from patient to patient, so it is essential to extract the necessary features from the signal. The spectral function is utilized to analyze the energy content of various frequency bands, which is varied from the range of 0.5 to 9 Hz.

Moreover, the peak values of P, Q, R, S, and T waves are estimated for efficient classification. The benefits of amplitudes and intervals are extracted for the proposed work that varies for each ECG input signal of the PTB diagnostic ECG database. A total of 126 records from the database are tested for the present study, and simplification out of all, one document from each diagnostic class is selected here to show different ECG features in Table 2 and corresponding ECG patterns in fig. 3. In Table 3, the most distinguishable morphological ECG changes are shown for various cardiac diseases that usually recognized in the present work.

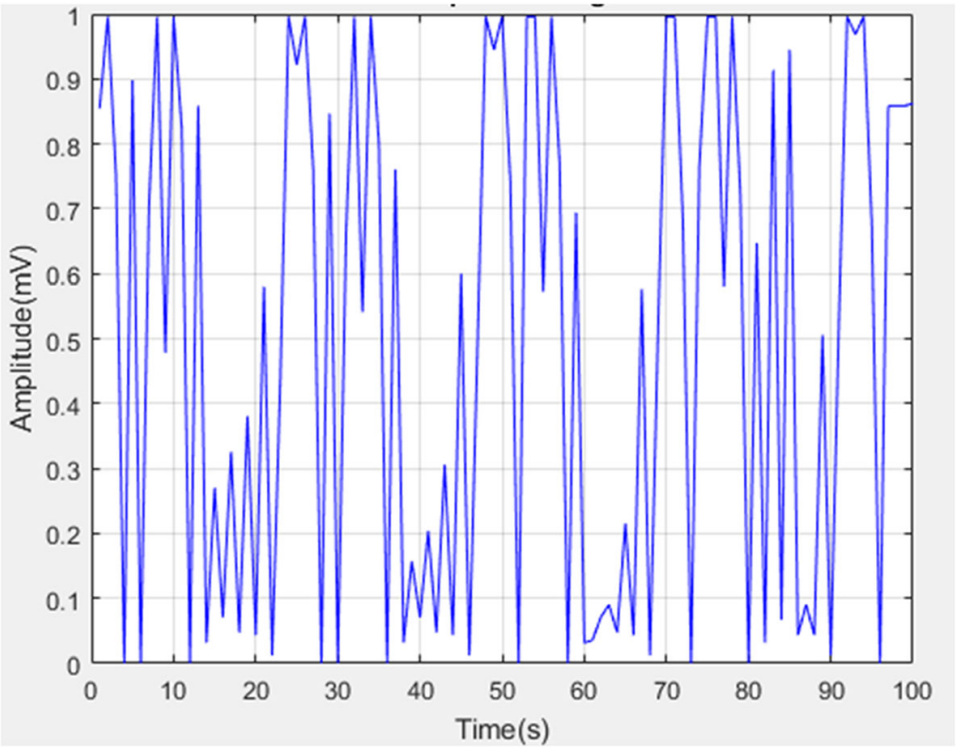


FIG. 4 Decompressed signal

Some specific abnormal/irregular values of ECG morphological features are shown in bold fonts in Table 2.

Figure 5 describes the various (a-h) ECG patterns of extracted features using MDC technique for the healthy controls and various heart diseases such as Bundle Branch Block, Cardiomyopathy, Dysrhythmia, Myocardial Infarction etc.

Table 2 Extracted ECG features for different Heart Diseases

ECG ⇒ Databases / **ECG Parameters ⇩** (Amplitude –mV & Interval - second)	**B_s0451_re.dat** (B: Bundle Branch Block)	**C_s0456_re.dat** (C: Cardiomyopathy/Heart Failure)	**D_s0018cre.dat** (D:Dysrhythmia)	**Hes0302lre.dat** (He: Healthy Controls)	**Hys0390lre.dat** (Hy: Myocardial HyperTrophy)	**Ins0021bre.dat**(In:Myocardial Infarction)	**Ms0509_re.dat** (M: Myoca-rditis)	**Vs0030_re.dat** (V:Valvular Heart Disease)
P-Wave Amplitude	0.2941	**0.8980**	0.3020	0.2235	0.3059	0.3098	**0.9608**	**0.9804**
Q-wave Amplitude	0.0353	**0**	0.0157	0.0627	**0**	**0.0078**	**0.0667**	0.0118
R-wave Amplitude	0.9529	0.9961	0.9882	0.9686	0.9961	0.9882	0.9961	0.8353
S-wave amplitude	0.0118	0.4784	0.3451	0.0353	0.9020	**0**	0.5961	0.0078
T-wave Amplitude	0.1098	**0.9961**	**0.9961**	**0.9725**	**0.9961**	0.6039	**0.9373**	**0.9804**
QRS complex	**0.4000**	0.3000	0.3000	0.3000	0.3000	**0.4000**	0.3000	0.2000
ST segment	0.1000	0.1000	0.1000	0.1000	0.1000	0.1000	0.1000	**0.2000**
PR segment	0.3000	0.3000	0.3000	0.3000	0.3000	0.3000	0.4000	0.3000
RR interval	0.8000	0.7000	0.7000	0.6000	0.8000	0.8000	0.7000	0.9000
TT interval	0.7000	0.7000	0.7000	0.8000	0.8000	0.8000	0.8000	0.8000
QT interval	0.5000	0.4000	0.4000	0.4000	0.4000	**0.5000**	0.4000	0.4000
PP interval	0.8000	0.8000	0.8000	0.7000	0.9000	0.9000	0.8000	0.8000

Table 3 General Changes in ECG Morphology for Heart Diseases [22]–[24]

Sr. No.	Heart Diseases/ Conditions	Most Distinct Morphological ECG changes seen
1.	Bundle Branch Block	Prolonged Ventricular depolarization (QRS)
2.	Cardiomyopathy/Heart Failure	QS inferiorly and Tall/ flat/Inverted T waves throughout, Abnormal Q waves
3.	Dysrhythmia	Irregular Heart Rhythms like Tachycardia, Bradycardia, Atrial flutter, Atrial fibrillation, Premature ventricular contractions, Long QT syndrome, Ventricular fibrillation, etc.
4.	Healthy Controls	Negligible, ± 5–10% changes may be seen due to artifacts
5.	Myocardial Infarction	Deep Q wave, ST elevation or depression, Inverted T wave (Ischemia)

2.5 Modified dynamic ECG pattern classification

After Feature extraction, the signals are classified as bundle branch block, cardiomyopathy/ heart failure, healthy control, dysrhythmia, myocardial hypertrophy, myocarditis, myocardial infarction and valvular heart disease by using Modified Dynamic Classification (MDC) algorithm. It is shown in different patterns (a-h) of fig. 3.This technique extracted the transformation function for generating the feature space. Then, it is discovered with the larger margins for optimizing the transformation function. In this mechanism, the set of transformation parameters are initialized randomly for each class, then the fitness function is estimated by using the initial transformation parameter and training feature vector. Subsequently, the objective function is minimized for each category, and the optimized transformation function is utilized to transform all the training feature vectors. By Bayesian theory, the I-dimensional feature matrix X of conditional probability belonging to the class of another I-dimensional feature row vector which is obtained with log transform based Gaussian function. The average

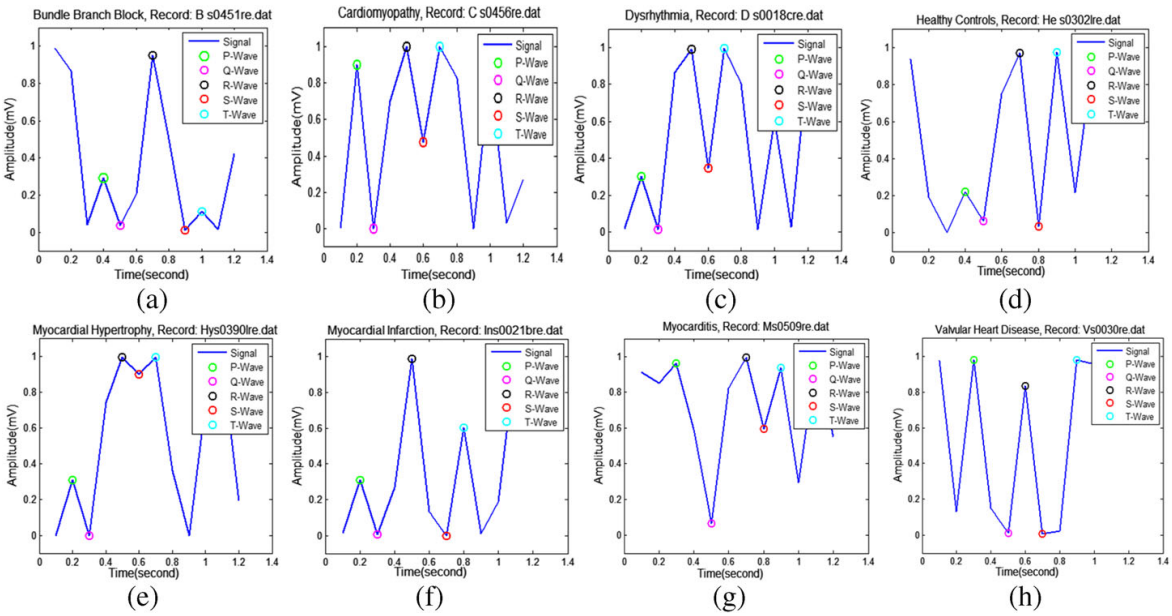


FIG. 5 ECG patterns (a-h) of extracted features using MDC Technique for different heart diseases

likelihood belongs to the same class and predicts the maximum likelihood value among the class. Assign the corresponding class as the resultant label.

The significant benefits of using the technique are increased classification accuracy, efficiency, and reduced complexity. Here, the label, training, and testing features are given as input, then the row and column size of these features are computed. After that, the vector is estimated for each test sample concerning the number of classes. The lowest value and its corresponding index are calculated from the vector; based on this value. The classified label is determined as bundle branch block, cardiomyopathy/heart failure, healthy control, dysrhythmia, myocardial hypertrophy, myocardial infarction, myocarditis, and valvular heart disease.

3 Performance analysis of experimental results

In this section, the results of proposed method and existing classification techniques are validated by using various performance measures. It includes sensitivity, accuracy, specificity, Jaccard, dice, precision, and recall. In this evaluation, the existing Probabilistic Neural Network (PNN) classification technique [12] is compared with the proposed MDC technique. The database used to evaluate this system is the PTB diagnostic ECG database [40]. The database comprises with 549 records from 290 subjects (aged 17 to 87, mean age 55.5,81 women, mean 57.2; 209 men, mean period 61.6; ages were not recorded for one female and 14 male subjects). In dataset, each topic is defined by one to five records. The diagnostic classes of cardiac diseases presented in this database are mentioned in Table 4. Moreover, the MATLAB simulation tool is used to evaluate the results of these techniques.

Table 4 defines the diagnostic classes of healthy controls and cardiac diseases such as Bundle Branch Block, Cardiomyopathy, Dysrhythmia, Myocardial Infarction. It represents with number of subjects and nuber of records used for present work.

3.1 Compression ratio (CR), signal to noise ratio (SNR), bit error rate (BER), and root mean square error (RMSE), percentage RMS difference (PRD), wavelet based diagnostic distortion (WEDD)

Table 5 describes the proposed method comparison with various compression techniques such as Huffman coding [47], Golomb-Rice coding [41], and zero run-length encoding [19]. This comparison takes along with the measures of compression ratio, Signal to noise ration, Bit error rate and Root mean square error.

Table 4 Diagnostic classes of cardiac diseases

Diagnostic Classes	*Number of subjects* [15]*	*Number of Records used for present work*
Bundle branch block	15	17
Cardiomyopathy/Heart failure	18	19
Dysrhythmia	14	16
Healthy controls	52	29
Myocardial infarction	148	30

Table 5 Comparison of compression techniques

Compression techniques	CR	SNR	BER	RMSE
Proposed- Dictionary matrix compression	4.5511	37.524	0.1514	0.493
Huffman coding	2.932	27.952	0.6621	0.52
Golomb-Rice coding	1.657	16.628	0.92	0.93
zero run-length encoding	1.8798	22.461	0.5664	0.69

The CR defined as the total swept volume of the cylinder and bottom dead center (BDC) of piston, that is divided by the top dead center (TDC) compressed volume of piston.

$$\mathrm{CR} = \frac{\left(\frac{\pi}{4}\mathrm{B}^2\mathrm{S}\right) + \mathrm{V_c}}{\mathrm{V_c}} \tag{1}$$

The SNR is described as the ratio of signal power to the noise power, it described as decibels.

$$\mathrm{SNR} = 10.\log_{10}\left(\frac{P_{signal}}{P_{noise}}\right) \tag{2}$$

The RMSE is used to measure the difference between predicted values by a model and the values observed from the environment that is being modeled.

$$\mathrm{RMSE} = \sqrt{\frac{\sum_{i=1}^{n}\left(\mathrm{X_{exp,i}} - \mathrm{X_{est,i}}\right)^2}{\mathrm{n}}} \tag{3}$$

The BER defined as a rate of bits that have errors associated to the received total number of bits in a transmission.

$$\mathrm{BER} = \frac{\text{Bits received correctly}}{\text{Total bits embedded}} \times 100 \tag{4}$$

Table 6 defines the comparison of proposed method of embedding technique with existing embedding methods such as Chaotic Map, and LSB steganography.

The percentage rms difference (PRD) defined as the normalized value that express the inaccuracy between original signal and reconstructed signal.

$$\mathrm{PRD} = \left(\frac{\mathrm{rms_e}}{\mathrm{rms_v}}\right) \mathrm{x}\ 100 \tag{5}$$

The Wavelet based diagnostic distortion (WEDD) is calculated from the energy of Wavelet coefficients for each band.

Table 6 Comparison of embedding techniques

Embedding techniques	PRD	SNR	WEDD
Chaotic Map	0.135	33.75	31.4
LSB Steganography	0.114	38.19	35.42
Proposed	0.0996	42.36	41.68

$$\mathrm{WEDD} = \sum_{j=0}^{j=L} W_j * PRD_j \tag{6}$$

3.2 Sensitivity, specificity, and accuracy

The signal classification system analyses the performance measures of sensitivity, accuracy and specificity. Sensitivity is defined as the true positive (TP) ratio and the summation of true positive values and false negative (FN) values.

Sensitivity is measured by the ratio of positives and the sum of true positives and false negatives. Specificity estimates when the actual condition is not present, the negative classification of cardiac disease.

$$Sensitivity = \frac{TP}{TP + FN} \tag{7}$$

$$Specificity = \frac{TN}{TN + FP} \tag{8}$$

The efficiency truth of the signal classification is calculated with the use of accuracy. Accuracy is estimated with the values of both specificity and sensitivity that is calculated by:

$$Accuracy = \frac{TN + TP}{(TN + TP + FN + FP)} \tag{9}$$

Where TP represents the True Positive, TN represents the True Negative, FP denotes the False Positive, and FN indicates the False Negative. In these results, it is evident that the proposed MDC provides improved results compared to the other methods PNN, SVN and Random Forest as shown in Fig.7.

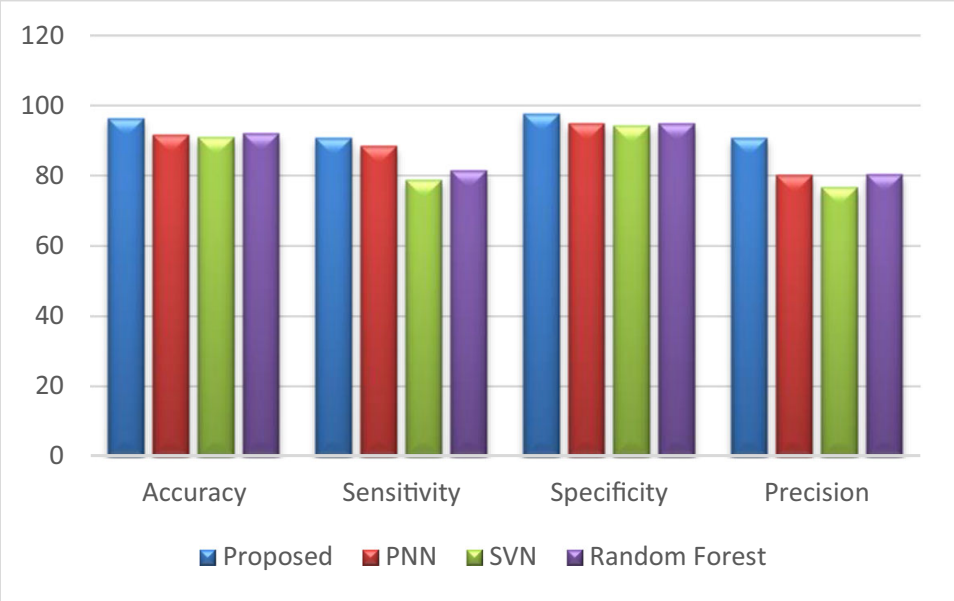


Fig. 6 Performance Analysis by Proposed method, PNN, SVN and Random Forest

Precision used to evaluate the effectiveness of embedding based ECG signal classification techniques. Precision is defined as the positive predictive value that provides the results relevant to an accurate classification. Then, it is estimated based on the ratio of true positives and true positives plus false positives.

Based on the values of TP, TN, FP, and FN, the precision is estimated as shown in the following equations:

$$Precision = \frac{TP}{(TP + FP)} \tag{10}$$

Figure 6 evaluates the sensitivity, specificity, and accuracy of existing and proposed classification techniques. Proposed method had the accuracy of 96.3964%, sensitivity contains 90.8026%, specificity of 97.7109% and precision contains 90.816%. In these results, it is evident that the proposed MDC provides improved results compared to the other methods.

3.3 Similarity coefficients

The similarity level of the classification estimated with Jaccard co-efficient, Dice co-efficient, and kappa co-efficient. Jaccard coefficient measures the similarity between the group of sets, and it can be estimated by divide the intersection size and union sets size. Precision is defined as the ratio of true positive to all determined positives (tp + fp). Recall defined as the ratio of true positive to all actual positives (tp + fn). Dice is calculated by using recall and precsion. The kappa coefficient measures the difference between the detected compliance of two images.

These measures are calculated as follows:

$$Jaccard = \frac{|Y_{x1} \cap Y_{x2}|}{|Y_{x1} \cup Y_{x2}|} \tag{11}$$

Dice is utilized to segregate the similarity between two various images named Y_1 and Y_2, and it is evaluated by,

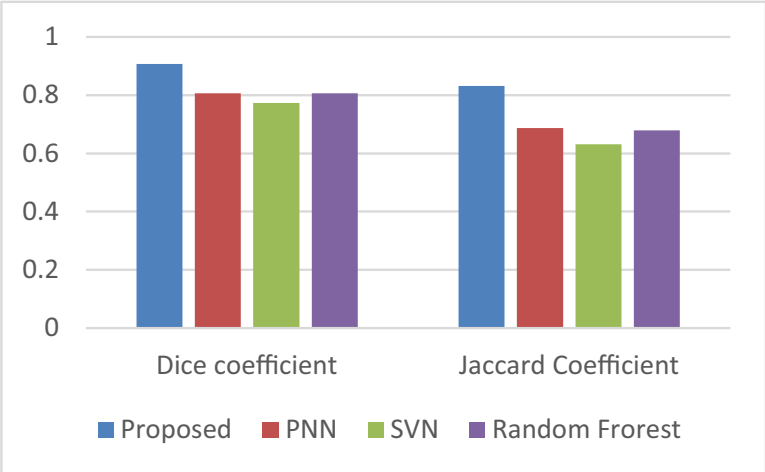


Fig. 7 Jaccard and dice

$$D_s = \frac{2.|Y_{x1} \cap Y_{x2}|}{|Y_{x1}| + |Y_{x2}|} \tag{12}$$

$$\text{Kappa Coefficient} = \frac{(\text{n*sum } A_{i+}) - \text{sum } (A_{i+} * A_{+i})}{n^2 - \text{sum } (A_{i+} * A_{+i})} \tag{13}$$

Figure 7 depicts the Jaccard and Dice performance measures of proposed method (MDC) and existing method (PNN). Proposed method contains the jaccard co-efficient value of 0.83% and the dice co-efficient is 0.9%.

3.4 Peak signal to noise ratio

PSNR defined as the ratio between the power of noise and maximum power of the signal. It is used to analyze the image quality between the input image and a compressed image. It is calculated as follows:

$$PSNR = 10log_{10}\left(\frac{R^2}{MSE}\right) \tag{14}$$

Where R is the signal pixel value (max).

Figure 8 shows the PSNR metric of the existing LSB (Least Significant Bit) and proposed techniques.

Due to the increased PSNR, the execution time of the proposed technique is reduced to 1.90 s. From the evaluation, it is observed that the proposed method gives better compression results compared than other methods.

3.5 Overall performance

The efficiency of the proposed and existing classification techniques are validated concerning various abnormalities/diagnostic classes of the ECG signal. The results of the existing PNN (Probabilistic Neural Network) [12], SVM (Support Vector Machine) [10], RF(Random Forest) [42], and proposed MDC classification techniques are illustrated in Table 5 to Table 8 concerning PTB diagnostic ECG datasets. From the results and analyzing all the parameters, it is evident that the

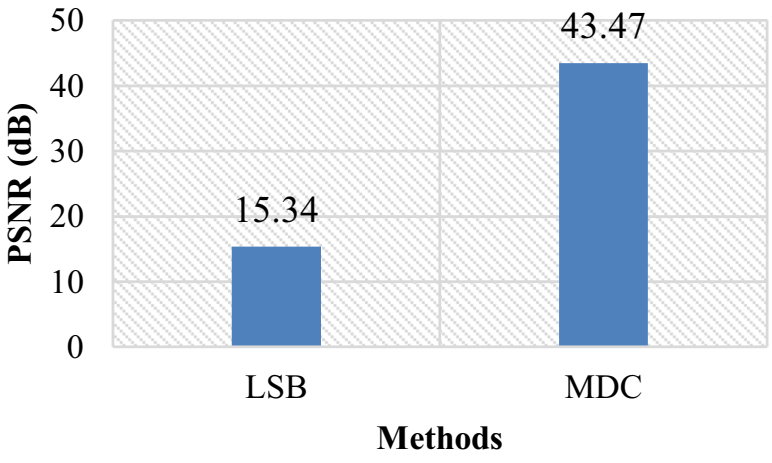


Fig. 8 PSNR analysis

Table 7 Overall Performance of Proposed MDC method along with comparison of PNN, SVM and Random Forest

	Bundle branch block				Cardiomyopathy/Heart failure			
	Proposed	PNN	SVM	Random Forest	Proposed	PNN	SVM	Random Forest
Accuracy	97.2973	79.2793	94.5946	91.8919	97.2973	95.4955	90.991	94.5946
Sensitivity	88.8889	42.5	86.6667	70	94.4444	100	71.4286	88.2353
Specificity	98.9247	100	95.8333	96.7033	97.8495	94.8454	95.5556	95.7447
Precision	94.1176	100	76.4706	82.3529	89.4737	73.6842	78.9474	78.9474
Dice Coefficient	0.9143	0.5965	0.8125	0.7568	0.9189	0.8485	0.75	0.8333
Jaccard Coefficient	0.8421	0.425	0.6842	0.6087	0.85	0.7368	0.6	0.7143
	Dysrhythmia				Healthy controls			
	Proposed	PNN	SVM	Random Forest	Proposed	PNN	SVM	Random Forest
Accuracy	96.3964	96.3964	92.7928	96.3964	95.4955	93.6937	90.991	89.1892
Sensitivity	87.5	100	78.5714	92.8571	92.8571	100	88	79.3103
Specificity	97.8947	95.9596	94.8454	96.9072	96.3855	92.1348	91.8605	92.6829
Precision	87.5	75	68.75	81.25	89.6552	75.8621	75.8621	79.3103
Dice Coefficient	0.875	0.8571	0.7333	0.8667	0.9123	0.8627	0.8148	0.7931
Jaccard Coefficient	0.7778	0.75	0.5789	0.7647	0.8387	0.7586	0.6875	0.6571
	Myocardial infarction							
	Proposed	PNN	SVM	Random Forest				
Accuracy	95.4955	93.6937	85.5856	88.2883				
Sensitivity	90.3226	100	69.4444	77.4194				
Specificity	97.5	92.0455	93.3333	92.5				
Precision	93.3333	76.6667	83.3333	80				
Dice Coefficient	0.918	0.8679	0.7576	0.7869				
Jaccard Coefficient	0.8485	0.7667	0.6098	0.6486				

Table 8 Confusion matrix for Proposed method

	Bundle branch block	Dysrhythmia	Cardiomyopathy/ Heart failure	Healthy controls	Myocardial infarction
Bundle branch block	16	0	0	2	0
Cardiomyopathy/Heart failure	0	0	17	1	0
Dysrhythmia	0	14	1	0	1
Healthy controls	0	0	1	26	1
Myocardial infarction	1	2	0	0	28

proposed MDC technique provides better performance measure results compared than existing classification technique by efficiently compressing the signal.

Table 7 describes the overall Performance of Proposed MDC method along with comparison of existing methods such as PNN, SVM and Random Forest. This comparison makes with the performance measures of accuracy, sensitivity, specificity, precision, Dice-coefficient, and Jaccard coefficient. This performance measures provides for the healthy controls and various cardiac diseases such as Bundle Branch Block, Cardiomyopathy, Dysrhythmia, Myocardial Infarction. For detecting bundle branch block disease, the proposed method had the accuracy of 97.30%. For detecting Cardiomyopathy disease, proposed method contains 97.30% of accuracy. For detecting Dysrhythmia disease, the proposed method had the accuracy of 96.40%. For detecting Myocardial infarction disease, proposed method contains 95.50% of accuracy. For detecting healthy control, the proposed method contains 95.50% of accuracy. This analysis proved the proposed method had highest classification accuracy and other measures.

The overall proposed system takes 1.8632 s of computational time for the process of compression, embedding, decompression and classification.

Table 8 describes the proposed method confusion matrix for the healthy controls and various heart diseases such as Bundle Branch Block, Cardiomyopathy, Dysrhythmia, Myocardial Infarction.

Table 9 provides the confusion matrix of existing PNN method for the healthy controls and various heart diseases such as Bundle Branch Block, Cardiomyopathy, Dysrhythmia, Myocardial Infarction.

Table 10 describes the confusion matrix of existing SVM method for the healthy controls and various heart diseases such as Bundle Branch Block, Cardiomyopathy, Dysrhythmia, Myocardial Infarction.

Table 11 describes the confusion matrix of existing Random Forest method for the healthy controls and various heart diseases such as Bundle Branch Block, Cardiomyopathy, Dysrhythmia, Myocardial Infarction.

Table 9 Confusion matrix for PNN method

	Bundle branch block	Dysrhythmia	Cardiomyopathy/ Heart failure	Healthy controls	Myocardial infarction
Bundle branch block	17	4	5	7	7
Cardiomyopathy/Heart failure	0	0	14	0	0
Dysrhythmia	0	12	0	0	0
Healthy controls	0	0	0	22	0
Myocardial infarction	0	0	0	0	23

Table 10 Confusion matrix for SVM method

	Bundle branch block	Dysrhythmia	Cardiomyopathy/ Heart failure	Healthy controls	Myocardial infarction
Bundle branch block	13	0	0	1	0
Cardiomyopathy/Heart failure	1	0	15	2	1
Dysrhythmia	0	11	1	0	2
Healthy controls	2	2	0	21	1
Myocardial infarction	1	3	3	5	26

4 Conclusion

The analysis of ECG signal is the most significant for the diagnosis of heart disease. Classification of ECG signal is one of the issues in existing classification approaches. And maintain the security of patient health information is essential. This study proposed a novel compression based embedding mechanism for providing increased security to the patient's ECG signal during e-health applications. A Dictionary Matrix generation technique is presented to compress the original ECG signal and Bit Embedding (BE) mechanism to embed the compressed sign with the cover image, which efficiently increases the security of the patient's health information. At the receiver side, the signal is further de-embedded and decompressed. To achieve the highest accuracy of classification, the Modified Dynamic Classification (MDC) algorithm was used. This efficient method classifies the abnormality of the signal using the extracted features. The chief aspect of this paper is to achieve the high level of security during the transmission of ECG signals and highest classification level for diagnosis. This work is highly suitable for e-health applications because, during the transmission of signal information, it is essential to secure the signal. So, the proposed technique is highly ideal for ensuring the secure transmission of signals by implementing the security mechanisms such as compression, embedding, and further classification at the receiver end. It reduces the transmission delay, saves storage memory, and speeds up the real time diagnosis with feedback. The experimental results estimate the efficiency of the proposed technique by using the measures of sensitivity, specificity, accuracy, precision, recall, Jaccard, and dice. Then, the PTB diagnostic ECG database is utilized to compare the results of existing PNN, SVM, and RF classification methods with the proposed method for proving the efficacy. In this research, we have used heart disease database and future work will be extended other such related bio-medical signals database. Deep learning approaches will be also engaged for efficient classification. The present work utilized the PTB diagnostic ECG databases, other ECG databases could be utilized with different classification techniques as a future work.

Table 11 Confusion matrix for Random Forest method

	Bundle branch block	Dysrhythmia	Cardiomyopathy/ Heart failure	Healthy controls	Myocardial infarction
Bundle branch block	14	0	1	0	1
Cardiomyopathy/Heart failure	1	0	15	0	1
Dysrhythmia	0	14	0	1	1
Healthy controls	2	1	2	26	3
Myocardial infarction	0	1	1	2	24

References

1. Abdulla AA (2015) Exploiting similarities between secret and cover images for improved embedding efficiency and security in digital steganography. University of Buckingham, Buckingham
2. Abdulla AA, Sellahewa H, Jassim SA (2014) Stego quality enhancement by message size reduction and fibonacci bit-plane mapping. International Conference on Research in Security Standardisation:151–166
3. Al Rahhal MM, Bazi Y, AlHichri H, Alajlan N, Melgani F, Yager RR (2016) Deep learning approach for active classification of electrocardiogram signals. Inf Sci 345:340–354
4. Ardan A, Ma'arif M, Aisyah Z, Olivia M, Titin S (2019) Myocardial infarction detection system from PTB diagnostic ECG database using Fuzzy inference system for ST waves. J Phys Conf Ser:012071
5. Awasthi D, Madhe S (2015) Evaluation of wavelet based ECG steganography system by using Percentage Residual Difference (PRD) measurements. in Communications and Signal Processing (ICCSP), 2015 International Conference on, pp. 0559–0563.
6. Awasthi D, Madhe S (2015) Analysis of encrypted ECG signal in steganography using wavelet transforms. in Electronics and Communication Systems (ICECS), 2015 2nd International Conference on, pp. 718–723.
7. Chen X, He F, Yu H (2019) A matting method based on full feature coverage. Multimed Tools Appl 78: 11173–11201
8. Cheng L-T, Yang C-Y (2018) High performance electrocardiogram steganography based on fast discrete cosine transform. International Journal of Computer and Information Engineering 12:509–514
9. Chowdhury M, Poudel K, Hu Y (2018) Phonocardiography Data Compression Using Discrete Wavelet Transform," 2018 IEEE Signal Processing in Medicine and Biology Symposium (SPMB), pp. 01–03.
10. Cuadros J, Dugarte N, Wong S, Vanegas P, Morocho V, Medina R (2019) ECG multilead QT interval estimation using support vector machines. Journal of healthcare engineering, vol 2019
11. Denemark T, Fridrich J (2017) Steganography with multiple JPEG images of the same scene. IEEE Transactions on Information Forensics and Security
12. Feng N, Xu S, Liang Y, Liu K (2019) A probabilistic process neural network and its application in ECG classification. IEEE Access 7:50431–50439
13. Ghasemzadeh H, Khass MT, Arjmandi MK (2016) Audio steganalysis based on reversed psychoacoustic model of human hearing. Digital signal processing 51:133–141
14. Haddadi R, Abdelmounim E, El Hanine M, Belaguid A (2019) A wavelet-based ECG delineation and automated diagnosis of myocardial infarction in PTB database. in Third International Conference on Computing and Wireless Communication Systems, ICCWCS 2019
15. Holub V, Fridrich J (2015) Low-complexity features for JPEG steganalysis using undecimated DCT. IEEE Transactions on Information Forensics and Security 10:219–228
16. Hu Y-H, Li Y-H, Zhao M (2019) Integration of information hiding and compression for biomedical signals. Journal of Internet Technology 20:975–982
17. Ibaida A, Khalil I (2013) Wavelet-based ECG steganography for protecting patient confidential information in point-of-care systems. IEEE Trans Biomed Eng 60:3322–3330
18. Jero SE, Ramu P (2016) Curvelets-based ECG steganography for data security. Electron Lett 52(4), 283–285. Available: http://digital-library.theiet.org/content/journals/10.1049/el.2015.3218
19. Jha CK, Kolekar MH (2017) ECG data compression algorithm for tele-monitoring of cardiac patients. International Journal of Telemedicine and Clinical Practices 2:31–41
20. Jha CK, Kolekar MH (2019) Diagnostic quality assured ECG signal compression with selection of appropriate mother wavelet for minimal distortion. IET Sci Meas Technol 13:500–508
21. Jovanovic BD, Litovski VB, Pavlović M (2015) "QRS complex detection based ECG signal artefact discrimination," Facta Universitatis. Series: Electronics and Energetics 28:571–584
22. Li H, Liang H, Miao C, Cao L, Feng X, Tang C et al (2016) Novel ECG signal classification based on KICA nonlinear feature extraction. Circuits, Systems, and Signal Processing 35:1187–1197
23. Liji C, Indiradevi K, Babu KA (2016) Integer-to-integer wavelet transform based ECG steganography for securing patient confidential information. Procedia Technology 24:1039–1047
24. Marakarkandy B, Tiwari MR (2015) Secure Steganography, Compression and Transmission of ECG signal for Protecting Patient Confidential Information in Point-of-Care Systems. International Journal of Application or Innovation in Engineering & Management (IJAIEM) 4:94–99
25. Mathivanan P, Jero SE, Ramu P, Ganesh AB (2018) QR code based patient data protection in ECG steganography. Australasian physical & engineering sciences in medicine 41:1057–1068
26. Memos VA, Psannis KE, Ishibashi Y, Kim B-G, Gupta BB (2018) An efficient algorithm for media-based surveillance system (EAMSuS) in IoT smart city framework. Futur Gener Comput Syst 83:619–628
27. Meng R, Zhou Z, Cui Q, Sun X, Yuan C (2019) A novel steganography scheme combining coverless information hiding and steganography. Joural of Information Hiding and Privarcy Protection 1:43–48

28. Mohagheghi E, Gabash A, Li P (2017) A framework for real-time optimal power flow under wind energy penetration. Energies 10:535
29. Pasolli E, Melgani F (2015) Genetic algorithm-based method for mitigating label noise issue in ECG signal classification. Biomedical Signal Processing and Control 19:130–136
30. Patil V, Patil M (2018) Curvelet Based ECG Steganography for Protection of Data. in Computational Vision and Bio Inspired Computing, ed: Springer, pp. 238–248
31. Plageras AP, Psannis KE, Stergiou C, Wang H, Gupta BB (2018) Efficient IoT-based sensor BIG data collection–processing and analysis in smart buildings. Futur Gener Comput Syst 82:349–357
32. Psannis KE, Ishibashi Y (2006) Impact of video coding on delay and jitter in 3G wireless video multicast services. EURASIP J Wirel Commun Netw 2006:024616
33. Rani R, Chouhan V, Sinha H (2015) Automated detection of qrs complex in ECG signal using wavelet transform. International Journal of Computer Science and Network Security (IJCSNS) 15:1
34. Reddy KG, Vijaya P, Suhasini S (2017) ECG Signal Characterization and Correlation To Heart Abnormalities. International Research Journal of Engineering and Technology (IRJET) 4:1212–1216
35. Sankari V, Nandhini K (2014) Steganography technique to secure patient confidential information using ECG signal. in Information Communication and Embedded Systems (ICICES), 2014 International Conference on, pp. 1–7
36. Stergiou C, Psannis KE, Kim B-G, Gupta B (2018) Secure integration of IoT and cloud computing. Futur Gener Comput Syst 78:964–975
37. Stergiou C, Psannis KE, Plageras AP, Ishibashi Y, Kim B-G (2018) Algorithms for efficient digital media transmission over IoT and cloud networking. Journal of Multimedia Information System 5:27–34
38. Sulam J, Romano Y, Talmon R (2017) Dynamical system classification with diffusion embedding for ECG-based person identification. Signal Process 130:403–411
39. Świerkosz A, Augustyniak P (2018) Optimizing wavelet ECG watermarking to maintain measurement performance according to industrial standard. Sensors 18:3401
40. (2017). The PTB Diagnostic ECG Database. Available: https://www.physionet.org/physiobank/database/ptbdb/
41. Tsai T-H, Kuo W-T (2018) An efficient ECG lossless compression system for embedded platforms with telemedicine applications. IEEE Access 6:42207–42215
42. Wang Z, Qian L, Han C, Shi L (2020) Application of multi-feature fusion and random forests to the automated detection of myocardial infarction. Cogn Syst Res 59:15–26
43. Wu F, Jing X-Y, You X, Yue D, Hu R, Yang J-Y (2016) Multi-view low-rank dictionary learning for image classification. Pattern Recogn 50:143–154
44. Wu F, Jing X-Y, Yue D (2017) Multi-view discriminant dictionary learning via learning view-specific and shared structured dictionaries for image classification. Neural Process Lett 45:649–666
45. Wu F, Jing X-Y, Zuo W, Wang R, Zhu X (2017) Discriminant tensor dictionary learning with neighbor uncorrelation for image set based classification. in Proceedings of the 26th International Joint Conference on Artificial Intelligence, pp. 3069–3075.
46. Wu W, Liu B, Zhang W, Chen C (2015) Reversible data hiding in ECG signals based on histogram shifting and thresholding," in Future Information and Communication Technologies for Ubiquitous HealthCare (Ubi-HealthTech), 2015 2nd International Symposium on, pp. 1–5.
47. Yildirim O, San Tan R, Acharya UR (2018) An efficient compression of ECG signals using deep convolutional autoencoders. Cogn Syst Res 52:198–211
48. Yu H, He F, Pan Y (2018) A novel region-based active contour model via local patch similarity measure for image segmentation. Multimed Tools Appl 77:24097–24119
49. Yu H, He F, Pan Y (2019) A novel segmentation model for medical images with intensity inhomogeneity based on adaptive perturbation. Multimed Tools Appl 78:11779–11798
50. Zhang S, He F, Ren W, Yao J (2018) Joint learning of image detail and transmission map for single image dehazing. Vis Comput:1–12

Publisher's note Springer Nature remains neutral with regard to jurisdictional claims in published maps and institutional affiliations.



Dinesh Kumar Atal (M'17) received B.Tech. Degree in Biomedical Engineering in 2005 from Guru Jambheshwar University of Science and Technology, Hisar (Haryana) India and M.Tech. Degree in Electrical Engineering with specialization in Instrumentation and Control from Deenbandhu Chhotu Ram University of Science and Technology, Sonipat (Haryana) India in 2011. Dinesh's research interests include machine learning, data compression, filtering, classification algorithms, signals and image processing of human physiological signals. He has published several journal and conference papers on ECG and EEG signals analysis and processing. He has Biomedical Industrial experience where he has learnt the hardware and software designing of ECG, EEG, EMG machines with their quality control procedures. Dinesh is a graduate student member of IEEE (membership no. 93344398) and has also the membership of IEEE Engineering in Medicine and Biology society.



Mukhtiar Singh (M'11) is presently working as Professor, in the Deptt. of electrical engineering, Delhi Technological University, Delhi, Since July-2015. Prior to Joining DTU, he was with deptt. of electrical engineering, DCRUST, Murthal, Since july 2002. Dr. Singh has completed his B. Tech and M. Tech. Degrees in electrical engineering from NIT, Kurukshetra (Erstwhile REC Kurukshetra), in 1999 and 2001, respectively. During March 2007 to Sept.-2010, he has been on study leave to pursue Ph.D from Ecole de Technologie Superieure, University of Quebec, Montreal, Canada with the financial support from Govt. of India under national overseas scholarship. He is also recipient of IEEE student scholarship for one of the best paper in 34th IEEE conference on Industrial electronics, IECON-2008, held at Orlando, Florida, USA. Dr. Singh is also the winner of Researchers Merit Scholarship of University of Quebec for the three years consecutively, 2008, 2009, and 2010. Dr. Singh research interests include Power Electronics, Artificial Intelligence, Signal Processing and analysis of human physiological signals.

This article has been accepted for publication in a future issue of this journal, but has not been fully edited. Content may change prior to final publication. Citation information: DOI 10.1109/TDMR.2020.2970163, IEEE Transactions on Device and Materials Reliability

A Novel Hot Spot Mitigation Circuit for Improved Reliability of PV Module

Santosh Ghosh, Vinod K. Yadav, *Member, IEEE* and Vivekananda Mukherjee

***Abstract*—Generation of hot spot in photovoltaic (PV) cells, under mismatch condition, is a reliability and safety issue associated with PV systems since its very early applications in satellites. Some of the solutions to this long-standing problem, proposed by the researchers in the past, were though effective in reducing the hot spot temperature, but were not accepted widely in commercial scale, because of design complexity and significant cost implications. The main aim if this paper is to presents a novel hot spot mitigation circuit (HSMC), which effectively reduces temperature of the cells under mismatch conditions through a modified bypass arrangement, and thereby increase the reliability of the complete PV system. Special attention is paid to ensure, that the proposed solution does not increase complexity of the bypass circuit, to restrict its impact on the project cost and system reliability. Experimental investigation is carried out to quantify the comparative performance of the proposed HSMC vis-à-vis standard bypass circuit (SBC). Thermographic images revealed that temperature of the cells, under mismatch condition, reduced by up to 10.3 °C when protected by the proposed HSMC, while the temperature increased by 6 °C under protection of the SBC under same ambient and operating conditions.**

***Index Terms*—Bypass circuit, hot spot, mismatch, partial shading, PV system reliability.**

I. Introduction

PV technology started emerging in human lives with its incipient application in satellites in 1958 [1]. It took another three decades for PV to be techno-commercially attractive enough for only few terrestrial applications, after scientists and researchers around the world started exploring PV technology possibilities, post oil crisis in 1973. But the scenario changed completely since the beginning of 21st century. Currently, it has become techno-commercially more attractive than any other means of energy conversion, ever known to mankind. As a result, new PV systems of over 100 MW are being added to global capacity every day, since 2013 [2].

However, generation of hot spot under mismatch conditions is a long-standing problem associated with PV systems since its very early applications in satellites and still persistent even today. It does not only impact the PV performance but also causes serious safety and reliability concerns. PV systems are, basically, interconnected matrix (in series and parallel, depending upon desired voltage and current level of the system, respectively) of numerous, nearly identical, PV cells. The large number of series connected cells makes the PV systems extremely sensitive to the mismatch of PV cells, unless high level of redundancy is built in the PV array design [3].

In the real-world scenario, cell characteristics may vary widely from each other due to presence of micro crack, surface defects, lack of homogeneity, and parametric drifts due to light induced degradation (LID), potential induced degradation (PID) during its operational life and non-uniform aging of PV cells [4]. The mismatch between the modules may occur to a greater degree in the event of replacement of damaged ones in the array with modules from different manufacturer under practical difficulties, which may happen quite often, inadvertently, in practical scenarios. Mismatch condition may appear due to partial shading condition (PSC) as well, caused by nearby building, tree, cloud movement and non-uniform deposition of aerosols. Under these conditions, the nonproductive or underproductive cells get reverse biased and act as a load to the illuminated strings. As a result, temperature of these affected cells increases, and causes localized over heating or hot spotting. Quite often, the hot spot temperature increases far beyond the safe operating temperature limit (around 85 °C) and reaches up to 150 °C [5]. At elevated temperature, efficiency and peak power output reduce drastically (illustrated in Section II, in detail).

Apart from reduction of PV performance, the elevated temperature impacts the module reliability as well, in two ways. Firstly, due to localized overheating, thermal runaway or secondary break down occurs and the reverse current conducts through a narrow channel. The local temperature may reach as high as 400 °C under such conditions, which eventually leads to irreversible damage of PV cells [6]. Experimental investigation under control environment shows that the irreversible damage of cells occurs at a reverse current of merely 4.6 A [7].

Secondly, the electrical joints become weak over time and, eventually, disconnect in some cases under prolonged operation at elevated temperature and repeated thermal cycle. This phenomenon causes electrical arc and the protective glass

S. Ghosh is with the Corporate R&D Department, Kirloskar Brothers Limited, Baner-98/3-7, Pune, India-411045 (e-mail: Santosh.ghosh@kbl.co.in).

V. K. Yadav is with the Department of Electrical Engineering, Delhi Technological University, New Delhi, India-110042 (e-mail: vinodkumar@dtu.ac.in).

V. Mukherjee is with the Electrical Engineering Department, Indian Institute of Technology (Indian School of Mines), Dhanbad, Jharkhand, India-826004 (e-mail: vivek_agamani@yahoo.com).

Copyright © 2020 IEEE. Personal use of this material is permitted. However, permission to use this material for any other purposes must be obtained by sending a request to pubs-permissions@ieee.org.

1530-4388 (c) 2019 IEEE. Personal use is permitted, but republication/redistribution requires IEEE permission. See http://www.ieee.org/publications_standards/publications/rights/index.html for more information.

This article has been accepted for publication in a future issue of this journal, but has not been fully edited. Content may change prior to final publication. Citation information: DOI 10.1109/TDMR.2020.2970163, IEEE Transactions on Device and Materials Reliability

cover shatters in some cases due to generation of extremely high temperature. The encapsulating material used in solar modules (i.e. ethyl vinyl acetate) is highly inflammable and quite often catches fire at elevated temperatures, when comes in contact with atmospheric oxygen [8]. The severity of high thermal stress on power loss and intensity of induced thermal fatigue vary widely in modules produced by different manufacturers [9]. Hence, unfavorable environmental factors and mismatch conditions not only impact the PV module efficiency and reduce performance ratio of the project, but also cause serious safety and reliability issues pertaining to PV systems [10]-[14].

Traditionally, to provide redundancy in the matrix of PV cells and, thereby, eliminate hot spot generation in the event of mismatch conditions, a bypass diode (BPD) is connected across a group of series connected PV cells (generally, one third of cells of a module). Though application of BPD is most commonly used technique across PV industries to mitigate the impact of hot spot under mismatch conditions, it does not eliminate the reverse bias voltage across the shaded cell completely, and only restricts it to certain extent (illustrated in Section II, in detail). To overcome the limitations of the conventional technique and, thereby, increase PV reliability, a modified bypass circuit is proposed in this paper.

Ensuing this introductory section, rest of the paper is organized as follows. The theoretical background of crystalline PV cell behavior, under high temperature, is presented in Section II. Different reverse breakdown mechanisms of PV cells are discussed in this section, as well. Section III delineates different solutions proposed in the recent past and discusses their short comings. Theoretical considerations behind proposed hot spot mitigation circuit (HSMC) is presented in Section IV. Section V focusses on the result of the experimental study on efficacy of proposed HSMC in mitigating hot spot temperature followed by conclusions in Section VI.

II. Theoretical Background

The current and the voltage between the bus bars over *n*-layer and back contacts over *p*-layer of a PV cell has a nonlinear relationship and are functions of irradiance and temperature. The output characteristics of PV cells can be represented by an equivalent circuit model illustrated in Fig. 1 [15]. Applying Kirchhoff's current law on the equivalent circuit model, the interrelation between output current and voltage can be expressed, mathematically, as in (1).

$$I = I_{PH} - I_S\left(e^{\frac{qV+qIR_S}{AkT}} - 1\right) - \frac{V+IR_S}{R_{SH}} \quad (1)$$

where I_S is the saturation current (non-illuminated) of diode D, A is the ideality factor of diode D, q is the elementary charge, T is the temperature of the cell and k is Boltzmann constant (1.38×10^{-23} J/K).

At elevated temperature, the band-gap energy of crystalline silicon decreases, and hence, photons of longer wavelengths get absorbed. Secondly, life of the minority carrier gets enhanced as well. These two factors increase the short circuit current (I_{SC}) of the PV cells marginally. However, with

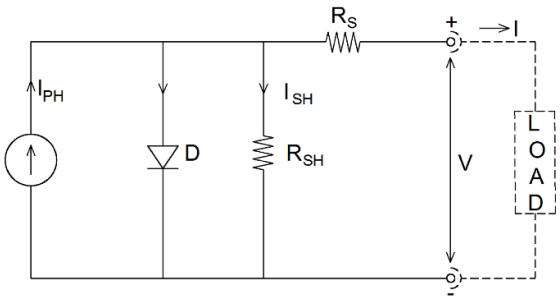


Fig. 1. Single diode equivalent circuit model of PV cell.

increase in temperature, the saturation current decreases exponentially and as a result, open circuit voltage (V_{OC}) gets reduced. Due to which, the PV cell efficiency and peak power output reduce drastically at elevated temperature [16]. The interdependency of the voltage at cell terminal (V) and the photo current (I_{PH}) on the irradiance and the cell temperature can be mathematically expressed as follows:

Photo current at ambient condition, $I_{PH\text{-}A} = C_{TI}\, C_{SI}\, I_{PH\text{-}R}$ (2)

Voltage at ambient condition, $V_A = C_{TV}\, C_{SV}\, V_R$ (3)

where radiation coefficient of current (C_{SI}), temperature coefficient of current (C_{TI}), radiation coefficient of voltage (C_{SV}) and temperature coefficient of voltage (C_{TV}) are defined in (4) – (7), in order.

$$C_{SI} = S_A / S_R \quad (4)$$

$$C_{TI} = 1 + \beta_T (T_R - T_A)/S_R \quad (5)$$

$$C_{SV} = 1 + \lambda_T \xi_S (S_A - S_R) \quad (6)$$

$$C_{TV} = 1 + \lambda_T (T_A - T_R) \quad (7)$$

Here, S is the irradiance, λ_T is the open circuit voltage coefficient, ξ_S is the rate of change in the cell operating temperature and β_T is the short circuit current coefficient. Subscripts A and R indicate ambient and standard test condition (STC), respectively. The impact of temperature on PV cell characteristics is graphically illustrated in Fig. 2.

Elevated temperature has bigger impact on the PV system reliability, than on PV performance, especially, when hot spot is generated in the PV cells under mismatch conditions. The prevalent method of protecting PV cells from mismatch conditions is to connect a BPD across each sub-panel in the module (refer Fig. 3). The reverse voltage across the non-productive or underproductive cell can be quantified by

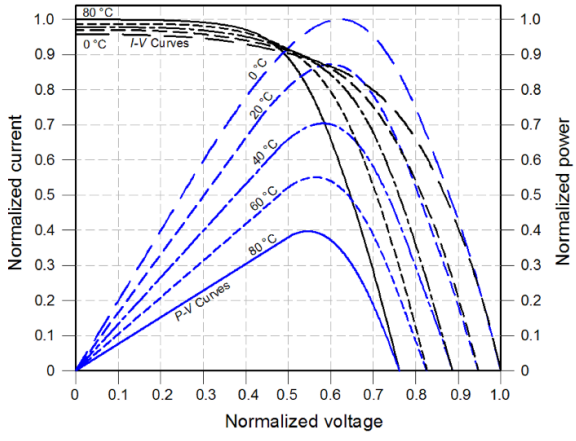


Fig. 2. Temperature dependent characteristics of PV cell.

1530-4388 (c) 2019 IEEE. Personal use is permitted, but republication/redistribution requires IEEE permission. See http://www.ieee.org/publications_standards/publications/rights/index.html for more information.

This article has been accepted for publication in a future issue of this journal, but has not been fully edited. Content may change prior to final publication. Citation information: DOI 10.1109/TDMR.2020.2970163, IEEE Transactions on Device and Materials Reliability

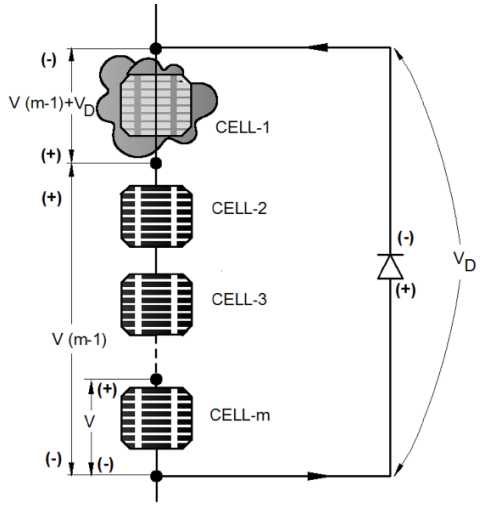


Fig. 3. Reverse bias voltage across the shaded cell, under standard BPD.

applying Kirchhoff's voltage law on the close loop formed by the BPD as in (8).

$$-V_{R\,(max)} = \sum_{n=1}^{(m-1)} V_{OC,n} + V_D \tag{8}$$

Substituting open circuit voltage of the PV cells (V_{OC}=0.6 V) and forward voltage drop of the BPD (V_D=0.5 V) in (8), maximum value of V_R may be obtained as 11.9 V, 14.3 V and 19.1 V for 60, 72 and 96 cell-module, respectively. Apparently, at these voltage levels, PV cells should be safe, as theoretically reverse break down of flat defect free *p-n* junction, with base doping concentration of 1×10^{16} cm^{-3}, should occur at reverse bias of over 60 V [17]. Hence, the BPD has been adopted an industrial standard for protecting the PV cells under mismatch conditions. However, the reverse breakdown characteristics of PV cells change from that of simple *p-n* junctions due to various additional manufacturing processes it undergoes to get converted to a PV cell. During various thermo-chemical processes, micro defects are generated, and the *p-n* junctions get contaminated, due to which, the PV cells exhibit different reverse break down characteristics than that of the simple flat *p-n* junction. For alkaline texturized PV cells, the avalanche break down occurs from -15 to -20 V [18], and it occurs merely at -13 V [19] for the acidic texturized ones.

Breitenstein *et al.* [20] extensively investigated reverse break down characteristics of silicon PV cells (multi-crystalline) experimentally and categorized the phenomenon in to three types, as shown in Fig. 4 [20]. The break down which starts occurring below -5 V is designated as Type-1. This occurs due to contamination of emitter surface by aluminum particles in the back-contact printing process. In Type-1 break down, the current increases linearly and occurs at low voltage region (see Fig. 4), hence, it is not fatal for PV cells. The breakdown occurring at voltages higher than that of Type-1 (i.e. between -7 to -11 V) is designated as Type-2 breakdown. This phenomenon was observed to be occurring due to the presence of iron precipitates in crystallographic grain boundaries. In Type-2, the current increases exponentially (weakly) with increase in the reverse voltage and does not impact the cells fatally, akin to Type-1. However, the reverse current in the voltage range of Type-1 and Type-2 break down has positive temperature coefficient [20]. Hence, the impact of reverse current in Type-1 and Type-2 will worsen at higher temperatures. The breakdown mechanism, which causes most severe and irreversible damage to the PV cells is avalanche breakdown, and this is designated here as Type-3breakdown. In case of Type-3, the current increases strongly exponentially with the increase in reverse voltage (see Fig. 4). The avalanche breakdown (i.e., Type-3) is observed to be occurring at -13 to -18 V for PV cells. Global breakdown voltage of PV cells reduces even further for higher doping concentration [21].

This implies that the prevalent industrial practice of connecting one BPD across each sub-panel is not effective in preventing the avalanche breakdown of the cells under mismatch conditions, as the reverse voltage which acts across the PV cells under mismatch condition matches exactly at which avalanche breakdown (i.e., Type-3) occurs. Some of the alternative solutions, proposed by the researchers in the recent past, and their shortcomings are discussed in Section III of the current work.

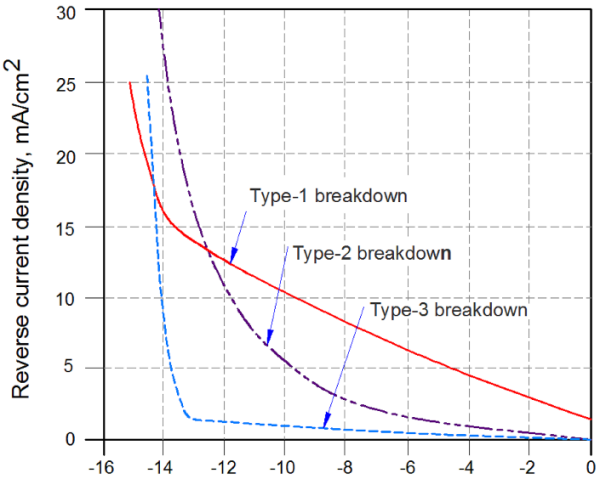


Fig. 4. Different reverse breakdown characteristics.

III. Review of State-of-the-Art Hotspot Mitigation Techniques

As illustrated in Section II, redundancy provided by the BPD to the matrix of PV cells as per standard industrial practice is not effective enough. The researchers have proposed various alternative solutions in the recent past. The state-of-the-art hot spot mitigation techniques (developed in research scale) are briefly discussed in the subsequent paragraphs.

It is evident from (8) that the reverse voltage acting across the nonproductive cells can be reduced by reducing the number of PV cells (*m*) connected across each BPD. Hence, reducing "*m*" or increasing the number of BPD in a module apparently seems to be the most obvious solution. Meyer and Dyk [16] proposed to connect BPD across each PV cell (i.e., *m*=1) to provide maximum possible redundancy to the PV cell matrix and, thereby, reduce the reverse voltage across

1530-4388 (c) 2019 IEEE. Personal use is permitted, but republication/redistribution requires IEEE permission. See http://www.ieee.org/publications_standards/publications/rights/index.html for more information.

This article has been accepted for publication in a future issue of this journal, but has not been fully edited. Content may change prior to final publication. Citation information: DOI 10.1109/TDMR.2020.2970163, IEEE Transactions on Device and Materials Reliability

nonproductive cells to minimum (refer (8)). However, this would double the number of components and the soldered joints in the modules. It is found that the temperature of a single defective diode may rise up to as high as 219 °C [22]. Hence, the reliability of PV modules would be reduced on account of higher number of components, though reverse break down of cells would be eliminated. To avoid increase in number of additional components and joints, Yoshioka *et al.* [23] proposed integrated manufacturing of BPDs along with each PV cells. However, whether the BPDs are integrated during cell manufacturing or during module manufacturing stage, higher number of BPDs will result into higher conduction loss when those are active [24], and secondly, cost of PV module and PV project, eventually, will increase. Hence, the above solutions did not get wide acceptability for field implementation.

In the recent past, implementation of distributed maximum peak power point tracking algorithm in module level DC-DC converters [25-27] and inverters [28], have gain popularity as an industry response to the problems of mismatch conditions. These module level converters and inverters optimize the output of individual modules locally and thereby reduce the mismatch losses. In addition, the module level inverters increase the system reliability as well, as those operate on low voltage and, thereby, eliminate the chances of high voltage failures, which is a common reliability issue associated with string inverters. Sharma and Agarwal [29] proposed improved algorithm for reduction of mismatch loss by using shunt-series compensating converters (current compensator in parallel with each module and voltage compensator in series with each strings). However, these module level converters and inverters have to process the full power capacities of the modules and are required in large numbers, hence, have high cost implications, especially for large scale projects. To optimize the project cost, Shenoy *et al.* [30] proposed converters for processing the differential power only, which are required to be partially rated. Several researchers have also advocated solutions based on static or dynamic reconfiguration of PV arrays to enhance power output in mismatch conditions [31], [32]. The authors of [4] proposed a nonlinear integer programming problem to maximize the power output by rearranging the nonuniformly aged PV modules. These solutions involved large number of switches and complicated switching circuits, and hence will also impact the reliability of the PV system in long term.

The solutions discussed above are focused on reducing the mismatch losses and thereby improving the power output under mismatch conditions, however, these solutions do not address the issue of local hot spot generation in the modules due to mismatch conditions that arises within, due to defective cells, non-uniform deposition of aerosols and PSC etc. To address this issue, Kim and Krein [33] developed a MOSFET based dual-switch device comprising of an active open circuiting switch (in series with the string) and a bypass switch (in parallel with the string), working in tandem, as illustrated in Fig. 5. Dhimish *et al.* [34] experimentally studied the

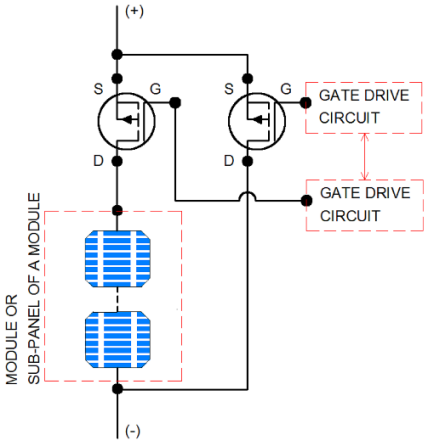


Fig. 5. MOSFET based dual switch concept.

concept proposed by Kim and Krein [33] while implementing the same both at sub-panel level and at module level. In both the studies ([33], [34]), it was demonstrated that the temperature of the nonproductive cell reduced when the series MOSFET was turned OFF and the bypass MOSFET was turned ON simultaneously (refer Fig. 5). However, in both the studies (refer [33, 34]), the method of activating the MOSFETs in tandem was not discussed. For field implementation, a gate activating circuit will be needed to generate the gate pulse for the MOSFETs automatically, by sensing the hot spot condition by interrupting the maximum power point tracking and measuring the sub-panel or module impedance periodically, which involves complex circuitry in itself. The performance of the switch activation circuit in tandem, its reliability under different site conditions and non-significant cost implications are the barrier for field implementation of some of the similar active bypass switches proposed by the researchers in the past (see [35], [36]) in large scale.

In the present work a novel HSMC is proposed, maintaining a balance between its efficacy in reducing hot spot temperature, impact on reliability of PV system due to additional components, complexity of circuit and increase in cost thereof. The proposed HSMC requires only one additional IGBT (per sub-panel) in the prevalent bypass circuit of commercial PV modules, and most importantly, it does not require a separate gate activation circuit or complex algorithm for its operation, as discussed in Section IV in detail.

IV. Proposed HSMC and Experimental Setup

The proposed HSMC is illustrated in Fig. 6, in which an additional IGBT is connected in series with the sub-panels along with the prevalent BPDs. IGBT is a superior solid-state switch than the MOSFET, which is proposed by the researchers in the past, for the intended application on several counts as briefly discussed in ensuing paragraph.

Firstly, the ON state resistance and power loss of IGBT are substantially lower than that of a MOSFET, due conduction through minority carriers (holes) as well, in addition to electrons. Secondly, though both the IGBT and the MOSFET

1530-4388 (c) 2019 IEEE. Personal use is permitted, but republication/redistribution requires IEEE permission. See http://www.ieee.org/publications_standards/publications/rights/index.html for more information.

This article has been accepted for publication in a future issue of this journal, but has not been fully edited. Content may change prior to final publication. Citation information: DOI 10.1109/TDMR.2020.2970163, IEEE Transactions on Device and Materials Reliability

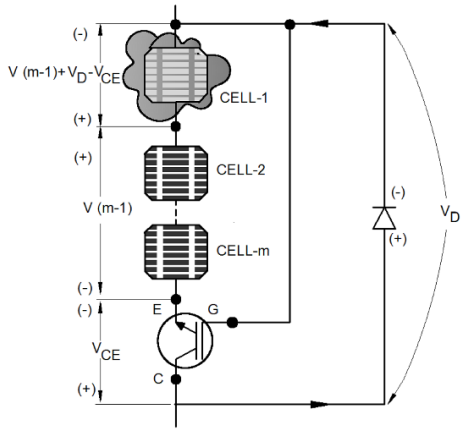


Fig. 6. Reduced reverse bias voltage across shaded cell, under the proposed HSMC.

are voltage-controlled switches, their responses differ for variable gate voltages. Under normal operating conditions, the sub-panel will apply gate-emitter (V_{GE}) (see Fig. 6) of 10 to 16 V depending upon the size of the module. And, at higher V_{GE}, the saturation characteristics of IGBT improves, and hence, the ON state resistance further drops. The gate voltage dependent saturation characteristics of IGBT has been experimentally verified before connecting to the PV module (see Fig. 7). In case of MOSFET, there is negligible gain in ON state conductance at gate voltage over 10 V. Next, large scale PV arrays are designed for 1000 V or 1500 V. Hence, the solid-state switches being used in series with the PV strings need to be compatible with these voltages for field application. While IGBTs are suitable for application at these voltage levels, MOSFETs are not. Finally, the ON state resistance of MOSFET shows continuous dependence on temperature, while it remains almost constant for IGBT. The advantages discussed above makes IGBT as obvious choice for the intended application. The above theoretical considerations were verified experimentally in [37], though under a single cell shading scenario only. The simulated result of its application in a large array found to be in good agreement as well, in [37].

As illustrated in Fig. 6, in normal operating condition, the IGBT is provided with the emitter-gate voltage from the sub-panel generated voltage itself ($V_{GE} = m \times V$), which keeps the IGBT in ON state. As the proposed circuit does not require a separate gate drive circuit, increase in cost due to the HSMC is negligible (<USD 1, per sub-panel) and the system reliability is not impacted due to additional complex circuits. In the event of partial shading or other mismatch conditions, the gate voltage drops and the IGBT is moved to nonlinear area of operation. As a result, the reverse voltage across the nonproductive cell gets reduced by voltage drop in the IGBT (i.e., V_{CE}). The reduced reverse voltage may be quantified by (9). The additional voltage drop in (9) (compare with (8)) reduces the reverse voltage below Type-3, (i.e. avalanche break down voltage) and, hence, the hot spot in the affected cell is no longer created.

$$-V_{R\,(max)} = \sum_{n=1}^{(m-1)} V_{OC,n} - V_{CE} + V_D \quad (9)$$

The efficacy of the proposed HSMC is experimentally studied on two identical 250 W_P poly crystalline modules under same ambient and operating conditions. One of the modules was used with standard BPDs, as supplied by the manufacturer, whereas the other one was integrated with the proposed HSMC. The standard bypass circuit of the first sub-

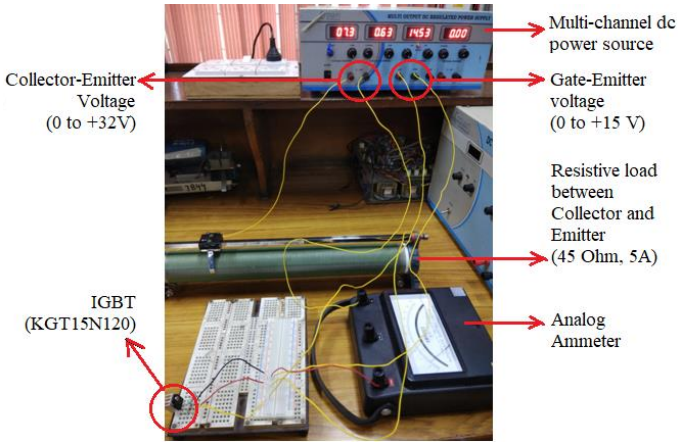


Fig. 7. Setup for testing gate voltage dependent characteristics of IGBT.

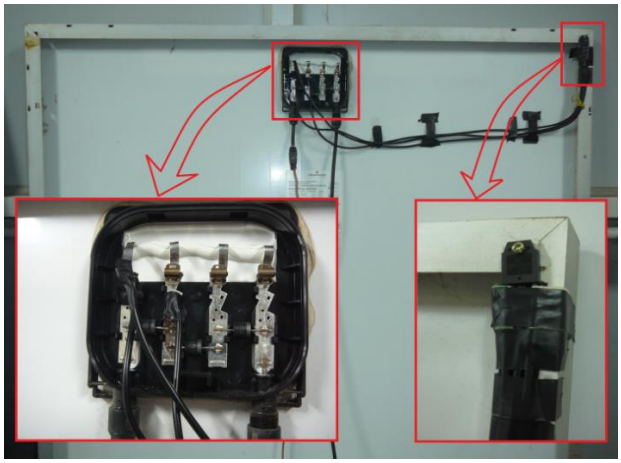


Fig. 8. PV module with HSMC connected to the first sub-panel.

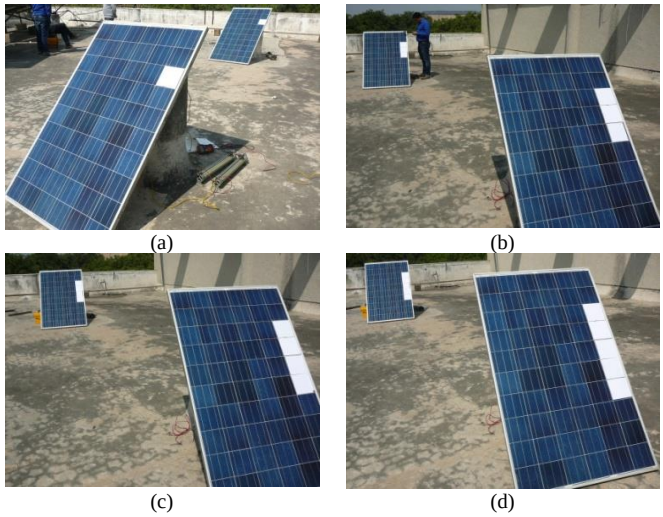


Fig. 9. PV modules with different number of cells shaded (a) one cell, (b) three cells, (c) four cells, and (d) five cells.

1530-4388 (c) 2019 IEEE. Personal use is permitted, but republication/redistribution requires IEEE permission. See http://www.ieee.org/publications_standards/publications/rights/index.html for more information.

This article has been accepted for publication in a future issue of this journal, but has not been fully edited. Content may change prior to final publication. Citation information: DOI 10.1109/TDMR.2020.2970163, IEEE Transactions on Device and Materials Reliability

panel was modified in one of the modules, by connecting the proposed HSMC in parallel to it, as shown in Fig. 8. The IGBT was physically installed on the aluminum frame in order to shift the location of heat loss to an external and accessible part under mismatch conditions. Different number of cells was shaded in both the modules simultaneously (see Fig. 9), under same ambient and operating conditions. Thermographic measurements of the shaded PV cells, BPDs and HSMC were carried out at all the simulated shading scenarios, as this technique is effective in identifying the hot spot location and estimation of intensity of impact of mismatch conditions in PV systems [39]. The result of the experimental investigation is presented in Section V.

V. Result and Discussion

Thermographic images of both the modules were captured after shading different number of cells under same ambient and operating conditions. The natural irradiance varied between 850 W/m^2 and 995 W/m^2 during the period of study. However, both the modules were placed close enough to be naturally irradiated at same intensity at any point of time. A fixed resistive load of 4.5 Ω was connected to both the modules, to set output current of about 7 A (at 950 W/m^2) from both the modules, under fully exposed (unshaded) condition. The number of shaded cells was varied starting from one up to five. The thermal profile of the cells, BPDs and IGBT were compared for different number of shaded cells.

Temperature of the shaded cells, in the module with standard bypass circuit (SBC), was observed to be increasing compared to the average temperature of the module, e.g. with only one cell shaded, the temperature increased by 6 ℃ within 15 minutes (refer Fig. 10). The positive difference between the shaded cell and rest of the module was observed when the shading area increased as well, though the rate of rise of temperature decreased. However, the temperature of the covered cell in the module connected to HSMC decreased for all the shading scenario (see Figs. 11–13). The temperature of single shaded cell decreased to 39.7 ℃ within same duration (about 15 minutes), whereas the average temperature of the rest of the module was about 50 ℃ (refer Fig. 11).

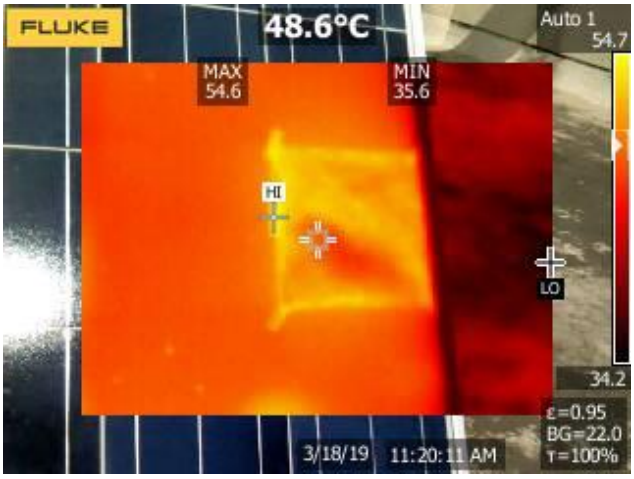


Fig. 10. Thermographic image of module connected to standard BPD, when one cell was shaded.

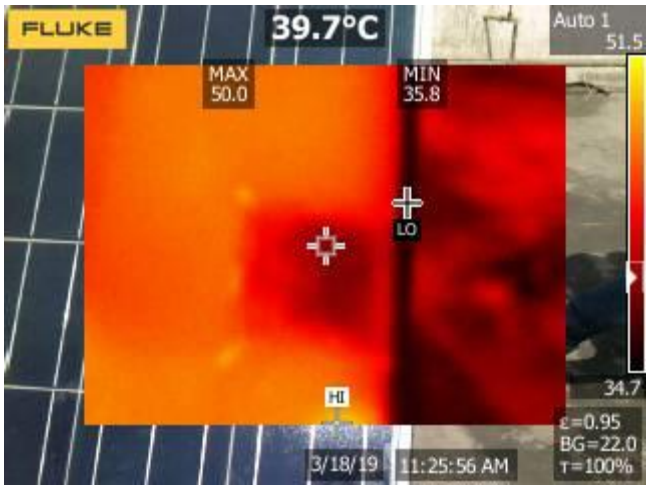


Fig. 11. Thermographic image of module connected to proposed HSMC, when one cell was shaded.

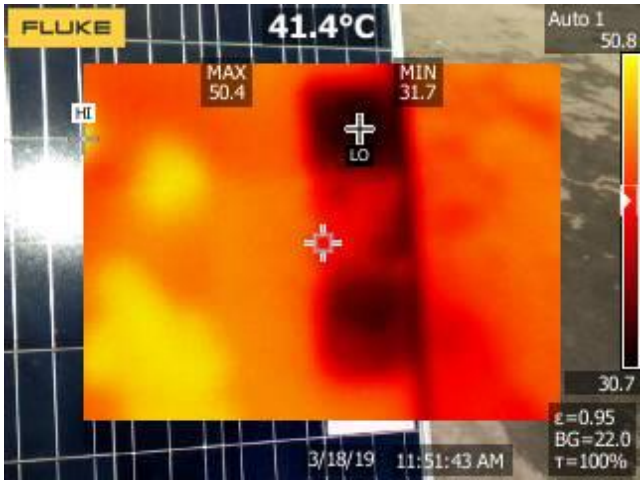


Fig. 12. Thermographic image of module connected to proposed HSMC, when three cells were shaded.

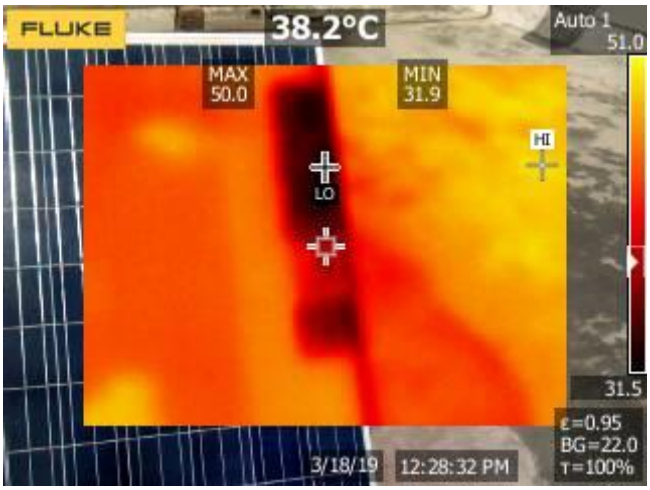
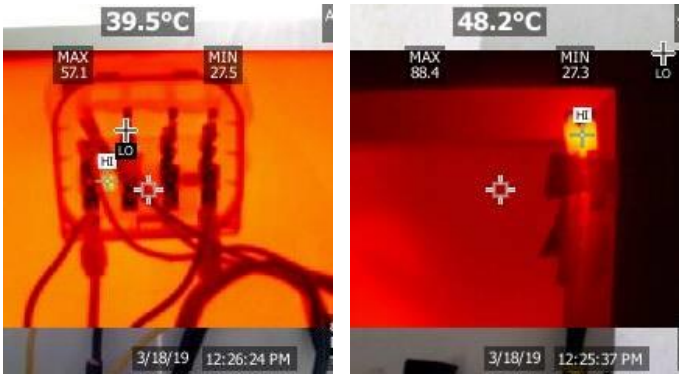


Fig. 13. Thermographic image of module connected to proposed HSMC, when five cells were shaded.

1530-4388 (c) 2019 IEEE. Personal use is permitted, but republication/redistribution requires IEEE permission. See http://www.ieee.org/publications_standards/publications/rights/index.html for more information.

This article has been accepted for publication in a future issue of this journal, but has not been fully edited. Content may change prior to final publication. Citation information: DOI 10.1109/TDMR.2020.2970163, IEEE Transactions on Device and Materials Reliability



(a) **(b)**

Fig. 14. Thermographic image of components of bypass circuits under 5 cell shading scenario (a) BPD of SBC, and (b) IGBT of proposed HSMC.

The difference in the temperature further increased as the shading area was increased (compare with Figs. 12 and 13).

The fundamental reason behind this phenomenon is that the cells connected to standard BPD undergoes avalanche break-down under PSC (illustrated in Section II, with the help of supporting theories and equations, in detail). As a result, the reverse current flowed through the nonproductive cells and, hence, the temperature of the shaded cells increased. The result of the experimental study (see Fig. 10) corroborates the above. Whereas, the reverse breakdown was prevented by the proposed HSMC by reducing the reverse voltage acting across the nonproductive cells (refer (9)). Under the PSC, gate-emitter voltage of the IGBT (used in the proposed HSMC) reduced and, hence, its ON state voltage drop increased. As a result, the reverse voltage across the shaded cells reduced below the avalanche break down voltage. Secondly, as the cells were shaded, heat flux from the sun did not reach the cell surface. This implies that under HSMC, neither there were internal heat generation in the cells nor were those heated by external sources and, hence, the temperatures of the cells reduced compared to the exposed and productive cells in the surroundings.

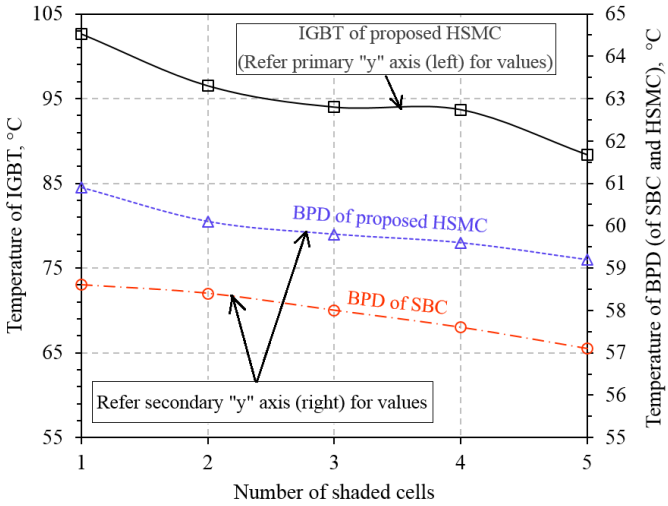


Fig. 15. Temperature of IGBT and BPDs of proposed HSMC and SBC under different shading scenarios.

Thermographic image of the BPDs and IGBTs were simultaneously captured as well (refer Fig. 14) to understand behavior of the components of two different bypass circuits under different shading scenarios. The temperature of the BPD in the proposed HSMC was found to be about 2 ℃ hotter than the BPD of SBC (refer Fig. 15). This indicates that the bypass path worked more effectively in HSMC due to the additional voltage drop in the IGBT. Akin to the temperature of the shaded cells, the temperature of the BPDs in both the circuits reduced with increase in the shading area within the respective sub-panels.

It may be observed from Fig. 15 that the maximum temperature of the IGBT was 102.6 ℃ under single cell shading scenario, which reduced to 88.4 ℃ when five cells were shaded. Further, the temperature of the BPDs reduced with increase in the shading area as well. The reason behind the observed reduction in temperature with the increase in shading area is the reduction in current through the IGBT and BPD. The current through the semiconductor devices reduced due to the following phenomena. Firstly, as mentioned in Section V, a fixed resistive load of 4.5 Ω was connected to both types of modules at fully exposed condition, as well as under all the shading patterns. When the number of shaded cells was increased, the voltage and power output of the module reduced and so did the current through the cells and the IGBT connected in series with those, as the connected resistive load was constant. And secondly, as discussed in Section IV, the saturation characteristics of IGBT is sensitive to V_{GE}. And in this case, the V_{GE} reduced with the increase in the number of shaded cells (refer Fig. 6). A lower V_{GE} pushed the IGBT to nonlinear region of operation and the ON state resistance of IBGT increased. As a result, the current through the BPD increased and current through the IGBT, which is in series with the shaded cells decreased with the increase in the shading area. The temperature trend of BPD plotted in Fig. 15 corroborates the above phenomenon. It can be observed that the temperature of the BPD of HSMC was higher than that of BPD of SBC for all the shading patterns. This indicates that the current through the shaded cells got restricted by the IGBT and, hence, current through the BPD increased which, in turn, increased temperature of the BPD of the proposed HSMC more than that of the BPD of SMC.

VI. Conclusion

In the present work, a novel hot spot mitigation circuit (referred as HSMC) is proposed, which successfully balances its efficacy in reducing the cell temperature under mismatch conditions and increase in complexity of the bypass circuit. In the proposed circuit, only one self-activated IGBT is used in addition to the prevalent BPDs. This result of the experimental study revealed that the prevalent BPD became marginally hotter when coupled with proposed HSMC, but the shaded cells became substantially cooler than the average temperature of the unshaded area of the modules. When a single cell gets damaged due to hot spot or otherwise, the complete module becomes unserviceable and, hence, affects the reliability of the

1530-4388 (c) 2019 IEEE. Personal use is permitted, but republication/redistribution requires IEEE permission. See http://www.ieee.org/publications_standards/publications/rights/index.html for more information.

This article has been accepted for publication in a future issue of this journal, but has not been fully edited. Content may change prior to final publication. Citation information: DOI 10.1109/TDMR.2020.2970163, IEEE Transactions on Device and Materials Reliability

whole PV system. With the use of proposed HSMC, the location of heat generation is moved from the intricately located PV cells to the externally located, accessible, easily replaceable and inexpensive semiconductor device i.e. IGBT. Hence, the proposed solution will potentially increase the reliability of PV modules manifold.

REFERENCES

[1] V. Smil, "March 1958: The first PVS in orbit [Numbers Don't Lie]," *IEEE Spectrum*, vol. 55, no. 3, pp. 26-26, Mar. 2018.

[2] Frankfurt School-UNEP Centre/BNEF, "Global trends in renewable energy investment," 2017. [Online], Available: http://www.fs-unep-centre.org

[3] R. G. Ross, "Photovoltaic Array Reliability Optimization," *IEEE Trans. Rel.*, vol. R-31, no. 3, pp. 246-251, Aug. 1982.

[4] Y. Hu, J. Zhang, P. Li, D. Yu and L. Jiang, "Non-uniform aged modules reconfiguration for large-scale PV array," *IEEE Trans. Device Mater. Rel.*, vol. 17, no. 3, pp. 560-569, Sept. 2017.

[5] S. Pennisi, F. Pulvirenti and A. La-Scala, "Low-power cool bypass switch for hot spot prevention in photovoltaic panels," *ETRI J.*, vol. 33, no. 6, pp. 880-886, Dec. 2011.

[6] A. Amerasekera, M.-C. Chang, J. Saatchi, A. Chatterjee, K. Mayaram and J. –H. Chern, "Self-heating effects in basic semiconductor structures," *IEEE Trans. Electron. Devices*, vol. 40, no. 10, pp.1836-1844, Oct. 1993.

[7] M. Barbato, M. Meneghini, A. Cester, G. Mura, E. Zanoni and G. Meneghesso, "Influence of shunt resistance on the performance of an illuminated string of solar cells: theory, simulation, and experimental analysis," *IEEE Trans. Device Mater. Rel.*, vol. 14, no. 4, pp. 942-950, Dec. 2014.

[8] F. Fertig, S. Rein, M. Schubert and W. Warta, "Impact of junction breakdown in multi-crystalline silicon solar cells on hot-spot formation and module performance," in *Proc. Eur. Photovolt. Sol. Energy Conf. Exhib.*, Sep. 2011, pp. 1168-1178.

[9] S. Kawai, T. Tanahashi, Y. Fukumoto, F. Tamai, A. Masuda and M. Kondo, "Causes of degradation identified by the extended thermal cycling test on commercially available crystalline silicon photovoltaic modules," *IEEE J. Photovolt.*, vol. 7, no. 6, pp. 1511-1518, Nov. 2017.

[10] S. Oprea, A. Bâra, D. Preoţescu and L. Eleſterescu, "Photovoltaic power plants (PV-pp) reliability indicators for improving operation and maintenance activities. a case study of PV-pp Agigea located in Romania," *IEEE Access*, vol. 7, pp. 39142-39157, Mar. 2019.

[11] S. E. De León-Aldaco, H. Calleja and J. A. Alquicira, "Reliability and mission profiles of photovoltaic systems: A FIDES approach," *IEEE Trans. Power Electron.*, vol. 30, no. 5, pp. 2578-2586, May 2015.

[12] M. Theristis and I. A. Papazoglou, "Markovian reliability analysis of standalone photovoltaic systems incorporating repairs," *IEEE J. Photovolt.*, vol. 4, no. 1, pp. 414-422, Jan. 2014.

[13] J. Oh *et al.*, "Reduction of PV module temperature using thermally conductive backsheets," *IEEE J. Photovolt.*, vol. 8, no. 5, pp. 1160-1167, Sept. 2018.

[14] C. G. Zimmermann, "The impact of mechanical defects on the reliability of solar cells in aerospace applications," *IEEE Trans. Device Mater. Rel.*, vol. 6, no. 3, pp. 486-494, Sept. 2006.

[15] M. G. Villalva, J. R. Gazoli and E. R. Filho, "Comprehensive approach to modeling and simulation of photovoltaic arrays," *IEEE Trans. Power Electron.*, vol. 24, no. 5, pp. 1198-1208. May 2009.

[16] E. Meyer and E. E. V. Dyk, "Assessing the reliability and degradation of photovoltaic module performance parameters," *IEEE Trans. Rel.*, vol. 53, no. 1, pp. 83-92, Apr. 2004.

[17] S. M. Sze and G. Gibbons, "Effect of junction curvature on breakdown voltage in semiconductor," *Solid-State Electron.*, vol. 9, no. 9, pp. 831-845, Sep. 1966.

[18] D. Lausch, K. Petter, H.V. Wenckstern and M. Grundmann, "Correlation of pre-breakdown sites and bulk defects in multicrystalline silicon solar cells," *Physica Status Solidi RRL*, vol. 3, no.2-3, pp. 70-72, Mar. 2009.

[19] J. Bauer *et al.*, "Hot spots in multicrystalline silicon solar cells: avalanche breakdown due to etch pits," *Physica Status Solidi RRL*, vol. 3, no. 2-3, pp. 40-42, 2009.

[20] O. Breitenstein *et al.*, "Understanding junction breakdown in multi crystalline solar cells," *J. Appl. Phys.*, vol. 109, no. 7, Apr. 2011.

[21] M.Wagner, B. Gründig-Wendrock, P. Palinginis and C. Knopf, "Shunts, diode breakdown and high reverse currents in multicrystalline silicon solar cells," in *Proc. 24th EUPVSEC*, 2009, pp. 2028-2031.

[22] S. W. Ko *et al*., "Electric and thermal characteristics of photovoltaic modules under partial shading and with a damaged bypass diode," *Energy*, vol. 128, no. 1, pp. 232-243, Jun. 2017.

[23] H. Yoshioka *et al*., "Non-hot-spot PV module using solar cells with bypass diode function," in *Proc. IEEE Photovolt. Spec. Conf.*, 1996, pp. 1271-1274.

[24] S. Daliento, L. Mele, P. Spirito, R. Carta and L. Merlin, "Experimental study on power consumption in lifetime engineered power diodes," *IEEE Trans. Electron. Devices*, vol. 56, no. 11, pp. 2819–2824, Nov. 2009.

[25] H. J. Bergveld *et al*., "Module-level DC/DC conversion for photovoltaic systems: the delta-conversion concept," *IEEE Trans. Power Electron.*, vol. 28, no. 4, pp. 2005-2013, Apr. 2013.

[26] C. Olalla, D. Clement, M. Rodriguez and D. Maksimovic, "Architectures and control of submodule integrated dc-dc converters for photovoltaic applications," *IEEE Trans. Power Electron.*, vol. 28, no. 6, pp. 2980-2997, Jun. 2013.

[27] G. Adinolfi, G. Graditi, P. Siano and A. Piccolo, "Multiobjective optimal design of photovoltaic synchronous boost converters assessing efficiency, reliability, and cost savings," *IEEE Trans. Ind. Informat.*, vol. 11, no. 5, pp. 1038-1048, Oct. 2015.

[28] S. Harb and R. S. Balog, "Reliability of candidate photovoltaic module-integrated-inverter (pv-mii) topologies—a usage model approach," *IEEE Trans. Power Electron.*, vol. 28, no. 6, pp. 3019-3027, Jun. 2013.

[29] P. Sharma and V. Agarwal, "Maximum power extraction from a partially shaded PV array using shunt-series compensation," *IEEE J. Photovolt.*, vol. 4, no. 4, pp. 1128-1137, Jul. 2014.

[30] P. S. Shenoy, K. A. Kim, B. B. Johnson and P. T. Krein, "Differential power processing for increased energy production and reliability of photovoltaic systems," *IEEE Trans. Power Electron.*, vol. 28, no. 6, pp. 2968-2979, Jun. 2013.

[31] B. I. Rani, G. S. Ilango and C. Nagamani, "Enhanced power generation from PV array under partial shading conditions by shade dispersion using Su Do Ku configuration," *IEEE Trans. Sustain. Energy*, vol. 4, no. 3, pp. 594-601, Jul. 2013.

[32] G. Petrone, G. Spagnuolo, Y. Zhao, B. Lehman, C. A. R. Paja and M. L. O. Gutierrez, "Control of photovoltaic arrays: dynamical reconfiguration for fighting mismatched conditions and meeting load requests," *IEEE Ind. Electron. Mag.*, vol. 9, no. 1, pp. 62-76, Mar. 2015.

[33] K. A. Kim and P. T. Krein, "Reexamination of photovoltaic hot spotting to show inadequacy of the bypass diode," *IEEE J. Photovolt.*, vol. 5, no. 5, pp. 1435-1441, Sep. 2015.

[34] M. Dhimish, V. Holmes, B. Mehrdadi, M. Dales and P. Mather, "Output-power enhancement for hot spotted polycrystalline photovoltaic solar cells," *IEEE Trans. Device Mater. Rel.*, vol. 18, no. 1, pp. 37-45, Mar. 2018.

[35] V. d'Alessandro, P. Guerriero, and S. Daliento, "A simple bipolar transistor-based bypass approach for photovoltaic modules," *IEEE J. Photovolt.*, vol. 4, no. 1, pp. 405-413, Jan. 2014.

[36] G. Acciari, D. Graci, and A. L. Scala, "Higher PV module efficiency by a novel CBS bypass," *IEEE Trans. Power Electron.*, vol. 26, no. 5, pp. 1333-1336, May 2011.

[37] S. Ghosh, V. K. Yadav and V. Mukherjee, "Improvement of partial shading resilience of PV array though modified bypass arrangement," *Renew. Energy*, vol. 143, pp. 1079-1093, Dec. 2019.

[38] Y. Hu, W. Cao, J. Ma, S. J. Finney and D. Li, "Identifying PV module mismatch faults by a thermography-based temperature distribution analysis," *IEEE Trans. Device Mater. Rel.*, vol. 14, no. 4, pp. 951-960, Dec. 2014.

1530-4388 (c) 2019 IEEE. Personal use is permitted, but republication/redistribution requires IEEE permission. See http://www.ieee.org/publications_standards/publications/rights/index.html for more information.

Volume 7 Issue 3 (2019) 281-284 ISSN 2347 - 3258
International Journal of Advance Research and Innovation

Adaption of Power Gating in Positive Feedback Adiabatic Logic Circuits

Aarushi Mann, Naman Malhotra, Neeta Pandey*
Department of Electronics and Communication Engineering, Delhi Technological University, Delhi, India

Article Info
Article history:
Received 16 January 2019
Received in revised form
25 July 2019
Accepted 28 July 2019
Available online 15 September 2019

Keywords:
Adiabatic Logic, Low power, VLSI, Power Gating

Abstract
Positive Feedback Adiabatic Logic (PFAL), a quasi static and differential logic adiabatic family, is one of the most robust, with significant reduction in power consumption has been chosen in this work. Power Gating has been adapted in order to further reduce power dissipation. It is accomplished by sleep state control units that switch circuits between awake and idle. Two power gating methodologies, footer and header, have been evaluated and compared. The functional verification and power evaluations have been performed using TSPICE simulations with 180nm TSMC CMOS parameters. Power consumption has also been examined by varying supply voltage, frequency of the power clock signal and load capacitance. The observed overhead in awake state power dissipations is compensated for with the significant decrease in idle state power dissipation.

1. Introduction

Excessive and continual use of portable electronics like smartphones, tablets and laptops is the norm of today's world. With electronic devices penetrating every part of our life right from the early morning news on a tablet to late night chat on our smart phones, longer battery lifetime is the need of the hour [1]. Power dissipation of the circuit, being the most important factor dictating its battery lifetime, is desired to be as low as possible. Low power VLSI design is thus, a very crucial step in design of modern electronics [2].

Many techniques like voltage scaling and shrinking feature size have been employed in static CMOS, the most popular logic family in IC design, which help in reducing power dissipation [1]. CMOS logic suffers from primarily three factors of power dissipation, dynamic (switching), static and short circuit power dissipation. The dynamic power dissipation is directly proportional to the input frequency, thus the former increases with an increase in the latter [2]. Recent devices perform extremely fast computations and processes, as they are designed to work at higher frequencies, hence dissipate large amounts of power. Adiabatic logic is yet another logic style wherein charge is recovered back to power supply from the load capacitance. Therefore, thislogic style has great potential to reduce power dissipation beyond the limit imposed by static CMOS logic style [3].

Adiabatic logic design reduces power dissipation drastically. This logic provides a method to utilize the energy stored in load capacitors unlike the traditional way of wasting the energy stored in load capacitor by discharging it to the ground. Different topologies of adiabatic circuit designing has been developed, they use sinusoidal or four phase trapezoidal power supply [4].

With the advent of modular designing and different circuits combining to together function as a whole unit, there is a lot of power wasted on the sub-circuits that are not computing at each instant of time [5].

Therefore these sub-circuits can be turned off while they are not contributing anything to the whole unit,this is achieved by introducing Power Gating in the circuit. Two methodologies for power gating have been employed in this paper, namely, header and footer, specifically on adiabatic full adder circuits because of their wide range of applications [1]. Adders are used in a variety of application ranging from basic arithmetic blocks to advanced systems like DSP, filtering and image processing [6].

This paper is organized in seven sections including the introductory one. The second section discusses about Positive Feedback Adiabatic Logic Family which has been studied in detail for power evaluations. Section 3 sheds light on methods to further minimize power in adiabatic circuits. This section discusses about the two gating methods used to design circuits. The fourth section briefly discusses about full adders. Section 5 comprises of the functional verifications andpower evaluations. Conclusions have been drawn in the next section followed by references in the last section.

2. Positive Feedback Adiabatic Logic (PFAL)

The PFAL family consists of a latch made by two cross coupled inverters (M1, M2, M3 and M4), which provides the positive feedback [7]. The generic cell of PFAL is show in Fig. 1.

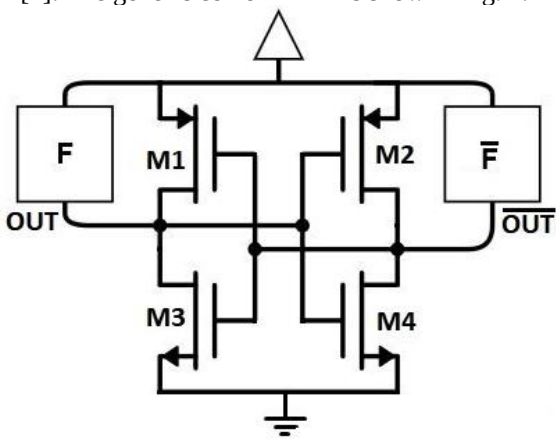


Fig. 1: Generic cell of PFAL

It generates both the output and its complement when both input and complement of input is applied. The NMOSs M3, M4 and PMOSs M1, M2 form the cross coupled inverters that drive the two complementary outputs. The two NMOS networks F and its complement $\overline{F}$ act as the pull up networks in the PFAL family. When the function block F is active the output OUT is charged and its complement $\overline{OUT}$ is discharged and vice versa for when function block $\overline{F}$ is active. PFAL is one of the adiabatic logic families that use a four phase trapezoidal power clock as shown in Fig.2. The adiabatic families make use of sinusoidal or trapezoidal power supply [8].

The four phases are evaluate phase, where the actual computation of output takes place, hold phase for holding the output stable for the next cascaded block, third phase is the when the charge is recovered from load capacitance back to

***Corresponding Author,**
E-mail address:n66pandey@rediffmail.com;
Phone No--+91-98687 80900
All rights reserved: http://www.ijari.org

source hence it is called recovery phase, finally the last wait phase has been introduced to maintain symmetry, in this phase both output nodes remain discharged [1,8].

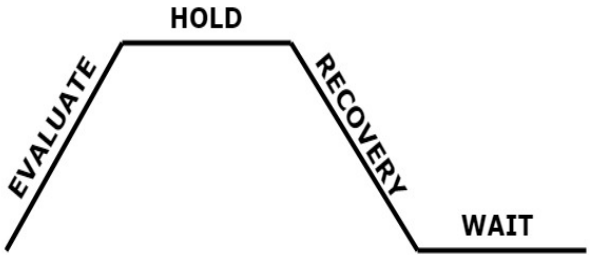


Fig. 2: Four Phase Trapezoidal Clock

3. Further Power Reduction

Techniques like voltage scaling, transistor sizing, power gating and shrinking feature size have been employed to reduce power dissipation [9]. Power gating being a coherent and robust has been adapted to PFAL, here state control transistors are used to switch circuit between active and ideal states. Two different gating methods, header and footer, have been mentioned in this work employed using a full adder [10]. Power gating is an approach to occasionally turn off the circuits, by isolating one of the power rails Vclk or ground which are not operational [1,10]. The generic cell of a power gated PFAL family is shown in Fig.2.

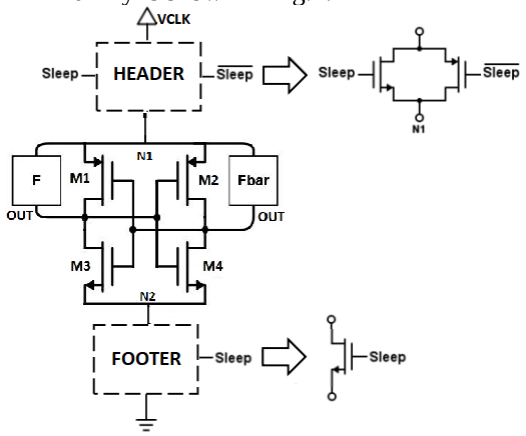


Fig. 3: Generic cell of a power gated PFAL family

Figure 2, shows footer sleep state control unit which has a NMOS connected to the main circuit and the ground, as it required for passing a strong low (0V) [3]. This NMOS creates a virtual ground on Node N2 in awake state whereas in the idle state, this node N2 becomes a floating state [3, 11].

Similarly, the header sleep state control unit is a transmission gate (TG) for passing the trapezoidal clock, which consists of both high and low voltage signals, so as to create a Virtual Vclk at node N1 in awake state and no charging path in idle state [3, 11].

4. Low Power Full Adder

Full adders are rudimentary yet extremely salient building blocks of any digital system. Thus we initiate the efforts for more efficient full adders in terms of performance, accuracy, power requirements, speed and flexibility. The modern day devices are moving towards digitization and fast data computation [12].

An adder is a potent circuit that performs addition of numbers. Addition is a basic operation used to realize complex mathematical operators like integration, differentiation and equations utilizing subtraction, multiplication and division which can be implemented by monitored use of adders in a particular way, hence an adder plays a vital role in all computations [12].

With the demand for high speed processing and low power design being accelerated by expanding computer and signal processing applications, it makes adders even more important. Adders are used as basic building blocks in DSP systems, filtering, digital image processing and machine learning applications [12].

A full adder is a three input-two output adder, where the two outputs are denoted as Sum and C_{out} (CARRY), with inputs A, B and the input carry C [13]. The governing equations for functionality of a full adder are given in (1) and (2)

$$SUM = A \oplus B \oplus C \quad (1)$$

$$CARRY = A.B + B.C + C.A \quad (2)$$

Sum is implemented as exclusive-OR of the three inputs of the full adder and the output Cout is implemented as mentioned in Eqn. 2. PFAL based Full adder implementation is depicted in Fig.4.

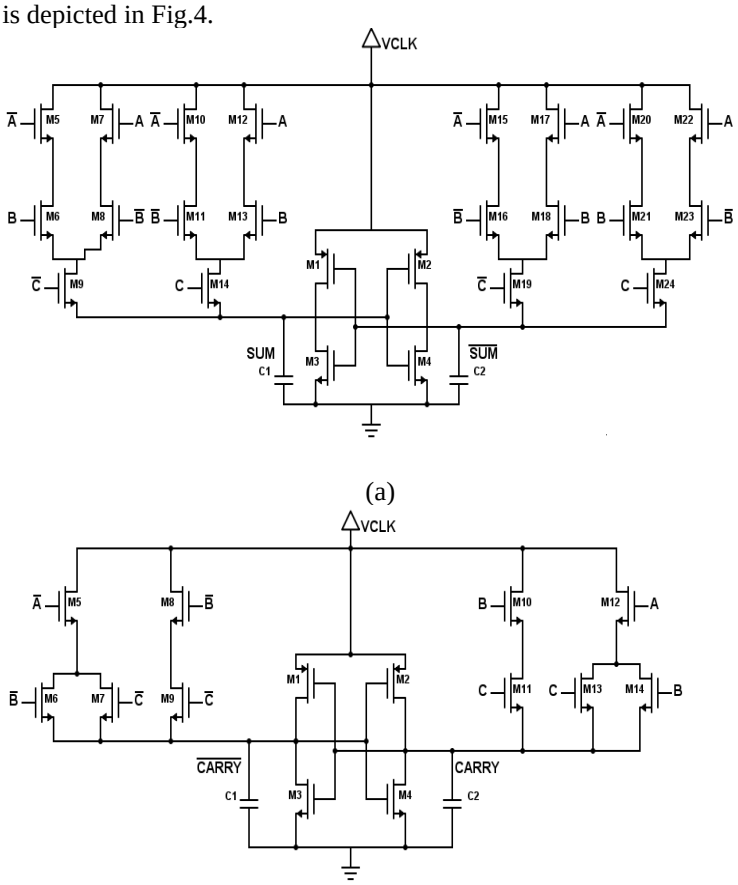


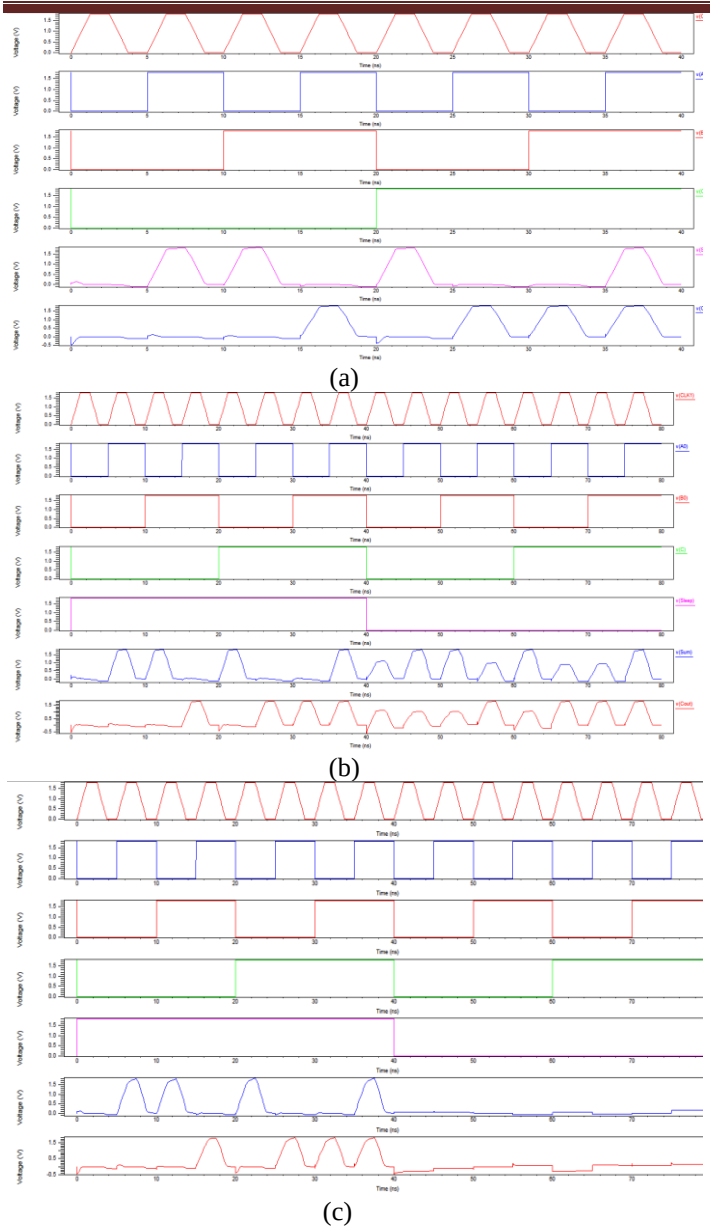
Fig. 4: Schematic of PFAL based Full adder (a) Sum (b) Cout

5. Simulation Results

This section entails the functional verification of PFAL based Full Adder of Fig. 4 and its gated version obtained by applying the concept given in Fig. 3. The technology node of 180 nm TSMC CMOS is considered and a trapezoidal power clock of frequency 200MHz is applied.

5.1 Functional Verification

The time domain simulation of PFAL based un-gated Full adder, footer gated and header gated full adder functions are placed in Fig. 5. In awake state i.e. Sleep signal is high and the output follows the full adder functionality whereas for a low on sleep makes output in floating state/ grounded for footer/ header gated scheme.



(a)

(b)

(c)

Fig. 5: Time domain simulation waveforms for (a)un-gated, (b)footer gated and (c) header gated PFAL based Full adder

5.2 Variation of Power Dissipation with Load Capacitance

The evaluations have been performed at a power supply of 1.8V and a constant input frequency of 200 MHz for full adder. The results have been in compiled in graph in Fig.6

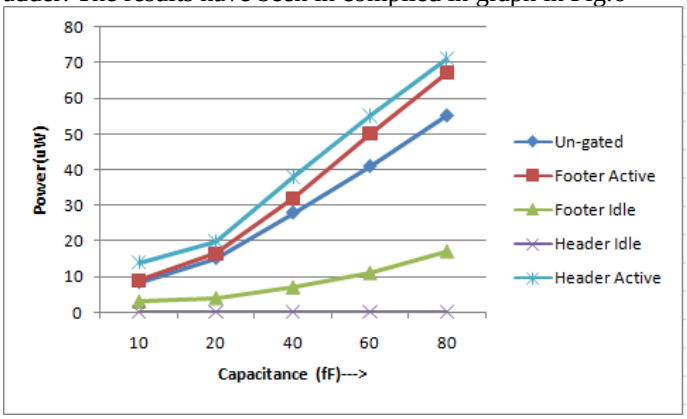


Fig. 6: PFAL based Full Adder Power Dissipation w.r.t Load Capacitance

The power dissipation of the gated PFAL full adder is measured for various load capacitances ranging from 10fF to 80fF. Power dissipated increases with increase in load capacitance. Gated circuit in active state consume more power than its ungated counterpart throughout the range of capacitances.

5.3 Variation of Power Dissipation with Supply Voltage

The evaluations have been performed at a load capacitance of 10fF and a constant input frequency of 200 MHz for full adder. The results have been in compiled in graph in Fig.7

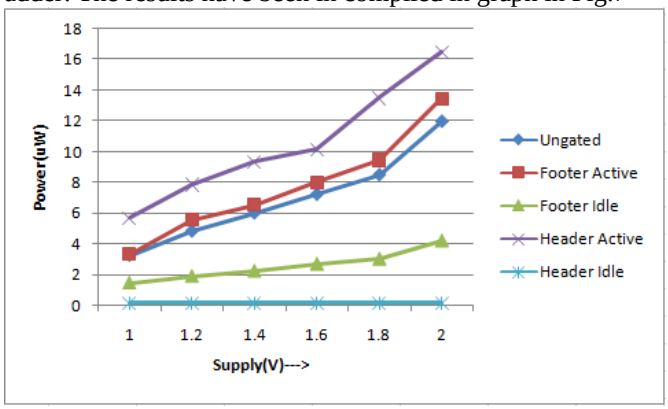


Fig. 7: PFAL Based Full Adder Power Dissipation w.r.t Supply Voltage

The graph shows the increasing trend of the power dissipation with supply voltage, with gated active circuits dissipating more power than ungated counterpart, with header active circuits consuming notably more power. On the other hand, header idle circuits dissipate negligible power as compared to footer idle.

5.4 Variation of Power Dissipation with Input Frequency

The evaluations have been performed at a power supply of 1.8V and a constant input frequency of 200 MHz for full adder. The results have been in compiled in graph in Fig.8

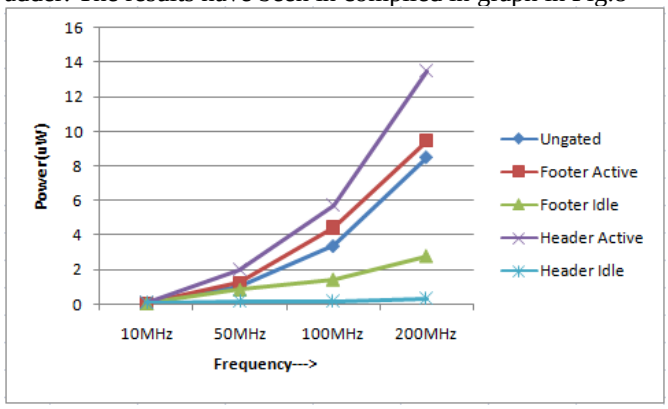


Fig. 8: PFAL based Full Adder Power Dissipation w.r.t Input Frequency

As seen in the graph the power dissipation increases with frequency and a sharp rise is observed after 100MHz. Similar trend is observed here with with header idle circuits having negligible dissipation while its active state has largest power dissipation. The footer gated circuits have less active power than header but there is significant dissipation in idle state.

6. Conclusions

In the present paper, full adder has been implemented using ungated and gated topologies of PFAL. The performance of the full adder has been evaluated using 180nm TSMC parameters on TSPICE. The variation of power consumption with load capacitance, input frequency and supply voltages

depict that the gating in adiabatic circuits further reduces power up to a large extent.

The observed overhead in awake state power dissipations is compensated for with the significant decrease in idle state power dissipation, with footer gated structures having approximately one fourth power dissipation in idle state as compared to its ungated counterpart. Whereas header gated structures have almost negligible idle state power consumption. . Power saving has been achieved remarkably in the proposed power efficient 1-bit full adder using gated PFAL.

References

[1] P Teichmann. Adiabatic Logic, In Future Trend And System Level Perspective,Springer Series In Advance Microelectronics, 2012

[2] JM Rabaey, A Chandrakasan, B Nikolic. Digital Integrated Circuits, A Design Perspective, Second Edition, 2003

[3] SM Kang, Y Leblebici. CMOS Digital Integrated Circuits Analysis & Design, Third Edition, 2002

[4] S Machanooru, N Bandi. A novel low power high speed positive feedback adiabatic logic, International Conference on Innovations in Information, Embedded and Communication Systems, 10.1109/ICIIECS.2017.8275936, 2017, 1-5

[5] P Teichmann, J Fischer, S Henzler. Power clock Gating in Adiabatic Logic Circuits, Proc. PATMOS, 2005, 638–646.

[6] M Deenadhayalan, R Poomurugan. Low Power Efficient D-Latch Based Carry-Select Adder, International Conference on Electrical, Information and Communication Technology, 2015, 15-16.

[7] S Machanooru, N Bandi. A Novel Low Power High Speed Positive Feedback Adiabatic Logic, International Conference On Innovations In Information, Embedded And Communication Systems, 10.1109/ICIIECS.2017.8275936, 2017, 1-5.

[8] AK Bakshi, M Sharma. Design of basic gates using ECRL and PFAL, International Conference on Advances in Computing, Communications and Informatics, 2013, 580-585.

[9] KK Sahu. Adiabatic Logic Design for Low Power VLSI Applications, 111EI0259, 2014-2015

[10] W Morell, A Srivastava. Evaluation of Four Power Gating Schemes Applied To ECRL Adiabatic Logic, 2018

[11] S Syedhusain, L Papayee. A Robust and Reconfigurable Multi-Mode Power Gating Architecture, International Conference on Electrical, Information and Communication Technology, 2015, 213-216.

[12] M Deenadhayalan, R Poomurugan. Low Power Efficient D-Latch Based Carry-Select Adder, International Conference on Electrical, Information and Communication Technology, 2015, 15-16.

[13] AK Yadav, BP Shrivatava, AK Dadoriya. Low power high speed 1-bit full adder circuit design at 45nm CMOS technology, International Conference on Recent Innovations in Signal Processing and Embedded Systems, 2017, 427-432.

Journal of Energy Storage 28 (2020) 101287

Contents lists available at ScienceDirect

Journal of Energy Storage

journal homepage: www.elsevier.com/locate/est

Aluminum–air batteries: A viability review

P. Goel, D. Dobhal, R.C. Sharma*

Department of Applied Chemistry, Delhi Technological University, Delhi 110042, India

ARTICLE INFO

Keywords:
Aluminum–air batteries
Aluminum anode
Oxygen reduction reaction
Air cathode
Electrolyte
Battery design

ABSTRACT

Aluminum–air (Al–air) batteries, both primary and secondary, are promising candidates for their use as electric batteries to power electric and electronic devices, utility and commercial vehicles and other usages at a relatively lower cost. This paper provides an analysis of the performance of these batteries with a component by component comparison with other technologies. It also aims to identify the major impediments that must be overcome for the battery. Al alloys are inexpensive and provide better electrochemical performances as compared to pure Al. The oxygen reduction reaction (ORR) at the cathode is traditionally controlled by platinum and other noble catalysts, but several carbonaceous materials, transitional metal oxides, and polymer-based systems may be satisfactory alternatives. The aqueous alkali electrolytes, though widely used at present, may be suitably replaced by non-aqueous electrolytes, aprotic and ionic liquids for both primary and secondary batteries. The different types of design and assembly for greater performance and economic viability are also described. This review may serve as a scientific tool for the progression of research on Al–air battery system.

1. Introduction

To meet the global focus on clean energy sources, efforts are being made to find more reliable and efficient energy technologies that can sustain human life. Li-ion batteries currently occupy the majority share in the electric vehicle (EV) market [1]. However, with the safety concerns [2], low driving range, instability of Li in humid climates [3] and low electrochemical efficiency, there is a need to research other battery technologies. Among the potential candidates, metal-air batteries stand out with their high energy density and the use of ambient air which reduces their weight and frees up space.

For the metal-air batteries, Li, Zn, Mg, Al, Fe and Ca are the most commonly used metals. In brief, these metal-air batteries are described here before an in-depth analysis of Al–air batteries is done. Theoretical specific energy densities and open-circuit voltages (OCV) of different types of battery systems have been listed in Table 1. Li–air batteries have energy densities of around 5–10 times that of the Li-ion batteries and show the highest theoretical energy density of 12 kWh/kg [4]. Zinc-air batteries have a theoretical energy density of 1.35 kWh/kg and are rechargeable but with a limited life cycle [5]. However, the problems associated with this battery are (i) dendrite formation which causes short-circuiting and shedding of zinc, and (ii) high charge overpotential for oxygen reduction reaction (ORR) and oxygen evolution reaction (OER) that lead to sluggish rates. Mg–air batteries have an energy density of around 6.5 kWh/kg and a theoretical voltage of 3.1 V [6]. The main challenges are of the corrosion of the metal anode and a sluggish ORR leading to low coulombic efficiency. Most Mg batteries are primary in nature, and there are major challenges to make them rechargeable. Few reports [7,8] have described secondary Mg–air batteries with non-aqueous electrolytes.

The Al–air battery is a promising technology that can fulfill the projected future energy demands. Al–air battery has a practical energy density of 4.30 kWh/kg. This is lower than only Li–air battery which has a practical energy density of 5.20 kWh/kg and is much higher than Zn–air which has a practical energy density of 1.08 kWh/kg [4,9]. A thermodynamic study by Luntz et al. [10] has shown that the maximum open-circuit potential of Al anode can be −1.87 V vs. standard hydrogen electrode at pH 14.6 instead of the widely cited −2.34 V. This value cannot be changed by removing parasitic reactions.

Al-based batteries may offer significant cost savings and safety improvements over Li-ion batteries as these possess lower reactivity, easy handling, and greater safety. Al–air batteries have been designed using aqueous, organic, ionic-liquid (IL), and polymer gel-based electrolytes. Al–air batteries with IL electrolytes exhibit rechargeable properties. Polymer gel electrolytes eliminate the problems associated with leakage of the battery systems using liquid electrolytes but yield lower energy densities.

From the above discourse, it is clear that Al–air battery is uniquely positioned amongst metal–air battery systems. The key advantages of the Al–air battery are: (i) energy density (watt-hours per kilogram) is as

* Corresponding author.
E-mail address: rcsharma@dce.ac.in (R.C. Sharma).

https://doi.org/10.1016/j.est.2020.101287
Received 25 October 2019; Received in revised form 12 February 2020; Accepted 12 February 2020
2352-152X/ © 2020 Elsevier Ltd. All rights reserved.

Table 1
Open circuit voltage (OCV) of metal air batteries [2,3,10].

Type	Open circuit voltage at 25 °C (V)	Theoretical energy densities (Wh/kg)
Pb acid	2.10	40
Ni-Cd	1.20–1.25	70
Ni–MH	1.50	100
Li-ion	3.60–3.85	400
Li—air	2.96	11,840
Al–air	2.73	8130
Na–air	1.94	2260
Mg–air	3.10	6462
Ca–air	3.12	4180
Zn–air	1.65	1353
Si–air	0.8–1.1	8470

much as five to ten times to that of Li-ion batteries, (ii) Al-anode is extremely light (cathode is effectively reduced to a wire mesh and membrane layer), inexpensive, non-toxic and safe, (iii) Al-based redox couple provides much higher storage capacity as Al possesses high theoretical ampere-hour capacity and overall specific energy, (iv) the electrochemical equivalence of Al is much lower (2.98/Ahg) than that of Li (3.86/Ahg) and other metals (v) Al can be easily recycled. However, the development of viable Al–air batteries, which are acceptable to consumers, need solutions to the problems being faced today by Al-air battery technologists. These problems are - (1) high rate of aluminum self-corrosion in alkaline solutions under both open- circuit and discharge conditions, (2) byproducts such as Al_2O_3 and $Al(OH)_3$ accumulate at both the anode and cathode, which also suppress electrochemical reactions, (3) complicated nature of trivalent Al^{3+} intercalation into the cathode, (4) irreversible nature of formation of hydrated alumina, (5) quick loss of charge on storage leading to meager shelf life. Douglas P. Hart and many experts are of the opinion that future Al-air batteries shall have high specific energy which will be significantly higher than the 400 Wh/kg of a Li-ion battery, which shall enable smaller and lighter Al–air batteries facilitating miniaturization of electronic products and high capacity electric vehicles for public transportation.

There have been many reviews on Al–air batteries [9,11–16], which have focused on the components of the batteries, mainly anode, cathode, and electrolytes. This present review attempts to focus on the design and assembly (Fig. 1.) of Al–air battery and their comparison with other battery technologies, apart from updating on the battery components. This review aims to be a toolbox for assembling an Al–air battery. Economic and market viability is the main concern where one has to take into account the status of technology available, the cost of raw materials and ease of construction, apart from scientific research.

Let us have a look at the economics of the EV battery. The present fuel cost is 4.2 cents/km and projected is 3.2 cents/km [17]. This is comparable to internal combustion engines (ICEs) which have a current

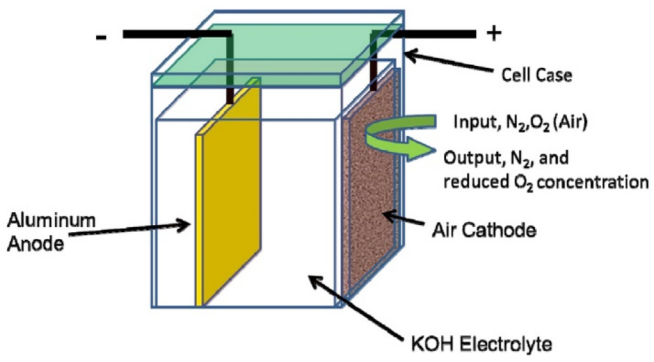


Fig. 1. Al-air battery construction [16].

Table 2
Comparison of Al-air battery costs to internal combustion engines (ICEs) [17].

Cost component	Al-air		ICEs
	Current	Projected	
Fuel cost (cents/km)	4.2	3.2	3.1
Purchase price (US$)	20,150	20,150	15,500
Life cycle cost (cents/km)	26.8	25.0	22.0

fuel cost of 3.1 cents/km as given in Table 2. The purchase price of Al/air EVs is around 25% more than the ICEs as of now, this puts the life cycle cost of ICEs and Al–air EVs at 22.0 cents/km and 26.8 cents/km (current) and 25.0 cents/km (projected). Further, ICEs have reached maturity from a research point of view while Al–air batteries still have the potential for optimization. Taking into account a similar mass of 1088 kg for both the Al–air and ICEs in a vehicle capable of driving 400 km, the Al–air EV, with further research, can be a potential replacement for the ICE.

The electrochemical reactions for the Al-air batteries are as follows:

- At anode: $Al(s) + 3OH^-(aq) \rightarrow Al(OH)_3(s) + 3e^- - 2.35V$
- At Cathode: $O_2(g) + 2H_2O(l) + 4e^- \rightarrow 4OH^-(aq) + 0.40V$
- Overall: $4Al(s) + 3O_2(g) + 6H_2O(l) \rightarrow 4Al(OH)_3(s) - 2.75$ V

2. Anode

Aluminum has been used as an anode in metal-air and metal-ion batteries for many years because of its high energy density, negative charge potential, recyclability, and abundance. It has been manufactured for over 60 years and is also readily available. The commercially available grades of Al, 2N5 (99.5% purity) and 4N (99.99% purity) have both been used as an anode. The impurities present in Al anode and the products formed during anode reactions constitute layers that impede the battery performance [18]. However, the 2N5 grade Al is a suitable anode for high power discharge conditions. It has been observed [17] that these commercially available 2N5 and 4N grade Al suffer, in different degrees, with the problems of (i) corrosion yielding the products $Al(OH)_4^-$ and $Al(OH)_3$, (ii) hydrogen evolution due to these parasitic reactions as given by the equation, $Al + 3H_2O \rightarrow Al(OH)_3 + 3/2H_2$ and, (iii) passivation by the formation of an oxide film almost instantaneously when introduced to air or water.

The fabrication process itself can also affect the conductivity of the Al anode, for example, binders such as Terpineol can have a negative effect on the conductivity of the Al anode. Therefore, laser sintering is a preferred method that can fabricate Al anodes in a non-invasive and accurate way. A study [19] reported significant improvements from 2 mAh/g for non-sintered samples to 121 mAh/g for samples sintered using a 10 W laser.

It is also imperative that the effect of grain size and crystal orientation be taken into account while developing Al anode. A finer grain structure of Al anode has better battery performance than a coarse grain structure. It has been concluded that with a decrease in grain size, the anti-corrosion property and electrochemical activity of Al anode increases. Fan and Lu [20] analyzed the microstructure of different extruded Al samples using Electron Back Scatter Diffraction (EBSD) (Fig. 2) and proposed that increasing the number of passes decreased the grain size until 7 passes, which was directly proportional to lower hydrogen evolution. Anisotropic Al performs better than polycrystalline Al (Fig. 3) due to crystal defects. Crystal plane (001) showed the lowest corrosion rates and gives the highest capacity density of 2541.4 mAh/g due to lowest surface energy [21].

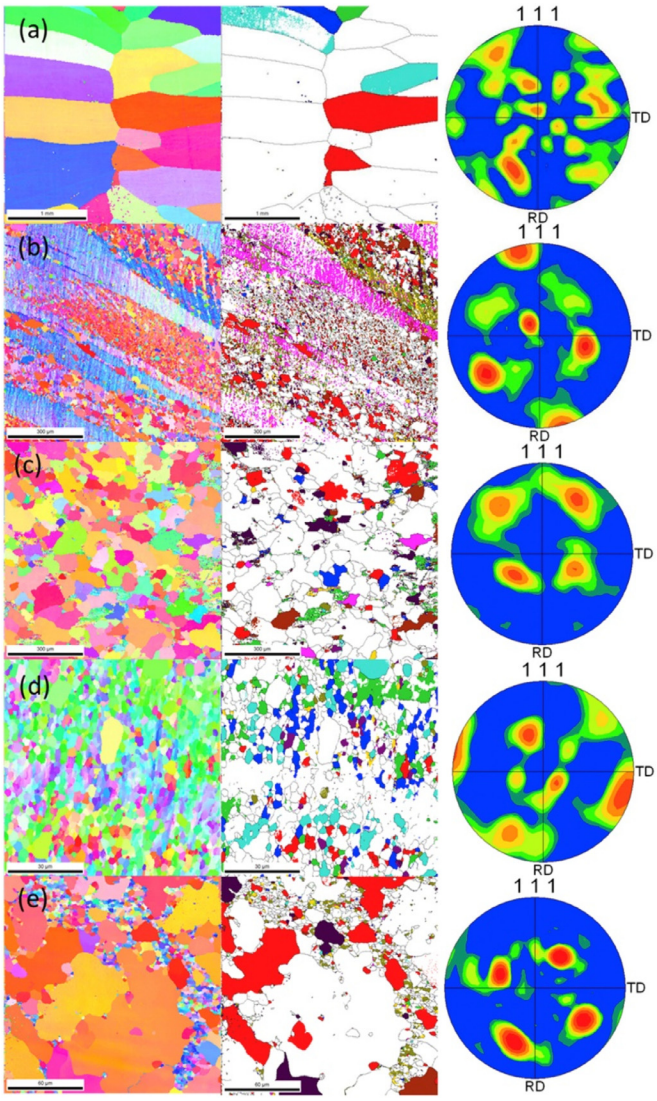


Fig. 2. Electron Back Scatter Diffraction (EBSD) analysis of grain boundary map, orientation maps and {111} pole figures after different Equal Channel Angular Pressing (ECAP) passes: (a) cast (b) 3 passes (c) 5 passes (d) 7 passes (e) 9 passes [20].

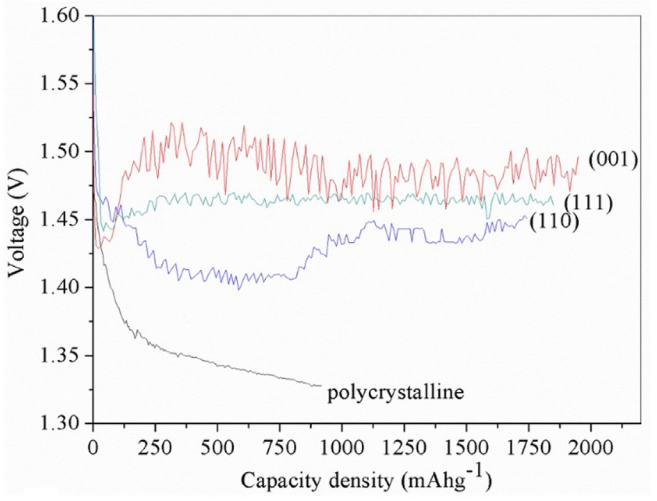


Fig. 3. Discharge behavior of Al–air battery based on monocrystalline and polycrystalline Al Anodes at 10 mA/cm current densities in 4 M KOH [21].

2.1. Aluminum alloys

Pure aluminum, when used as an anode in the presence of an aqueous electrolyte, corrodes rapidly and undergoes a vigorous reaction to yield hydrogen [22]. Alloys of Al have been studied to overcome the limitations of pure Al and also to improve the electrochemical efficiency of the anode. Different elements such as Ga, Ti, In, and Sn have been considered as alloying elements in the composition of Al alloys. Zinc is commonly used to reduce the corrosion of the anode by increasing the hydrogen evolution potential. Park et al. [23] tested Al–Zn alloys as anode and noted that this alloy gave a shorter voltage stabilization time than pure 4N Al. Also, it showed a higher corrosion rate which is attributed to the presence of Fe and Si (Al used for the alloy was 99.75% as opposed to 99.99%). Thus, the increase in the corrosion by Fe and Si overshadowed the advantageous effects of Zn. Further, Al–Zn alloys showed the formation of two oxidation layers, type 1 (consisting of porous $Zn(OH)_2$ and defective ZnO) and type 2 (consisting of protective ZnO). Type 2 layer reduces the discharge performance of the battery. This effect of the passive layer can be lessened by taking an Al–Zn–In alloy, which is not only cheaper but also improves the battery performance by inhibiting type 2 film formation.

The performance of Al − 1Mg − 0.1Ga − 0.1Sn (wt%) and Al − 1Mg − 1Zn − 0.1Ga − 0.1Sn (wt%) anodes was also studied [24]. The importance of Zn as an alloying element was established as Zn-containing alloys showed better electrochemical performance as well as a lower corrosion rate. The element Pb lessens the hydrogen evolution by increasing the hydrogen evolution overpotential. In addition [25], Ga inhibits the oxide film thereby activating the Al, especially in NaCl solution, where it can activate the Al sites by adsorbing Cl^- ions [26].

The Al–Bi–Pb–Ga (composition by weight 0.15Bi–0.15Pb–0.035Ga–Al (wt%)) anodes [27] have also shown promising results with the peak power density more than double that of pure Al (253.4 ± 2.5 mW/cm^{2}vs. 108.5 ± 2.5 mW/cm^2 in 4 M KOH), higher anodic efficiency (85.40 ± 5 svs. 73.6 ± 1.0% in 4 M KOH), and a smaller charge transfer resistance (for 2 M NaCl solution). In KOH solution, the alloy also gives lower self-corrosion rate comparable to pure Al due to Bi, Pb, and Ga which increase the hydrogen evolution overpotential. Similarly, a quaternary alloy of Al (purity 99.8%) containing Pb, Ga, and In gave comparable corrosion rates and open circuit potentials to super pure Al (99.99%) in the same testing conditions, indicating alloying to show tenable results [28,29].

The most promising alloy is the Cu-deposited 7075-T7351 Al alloy (5.6–6.1 Zn, 2.1–2.5 Mg, 1.2–1.6 Cu, <0.5 Si, Fe, Mn, Ti, Cr (wt%)) [30]. The electrochemically deposited Cu results in a homogenous adsorbed layer that reduces the rate of hydrogen evolution by forming a barrier with the solution. This does not interfere with the efficiency of Al as an anode. Copper, in fact, improves the discharge activity and increases the battery potential (Table 3) by decreasing the anodic resistance.

It is evident that Al-alloys not only provide a higher power to cost ratio as compared to pure Al but also decrease the hydrogen evolution and corrosion rate. The presence of Zn along with the absence of Fe and Si is expected to increase the efficiency of the battery. Improving the technology related to the process of fabrication, such as sintering, can drastically improve anode performance. More efforts are needed to reduce the fabrication cost and enhance the production of these alloys so that these alloys can replace pure 4N Al as the anode.

3. Cathode

The air cathode comprises of an oxygen reducing catalyst, a current collector and a composite electrode (Fig. 4.). This electrode is composed of a gas diffusion layer (GDL) and a hydrophobic polymer film such as polytetrafluoroethylene (PTFE) or polyvinylidene difluoride (PVdF). The film binds the material and also prevents the seepage of electrolyte into the electrode [31]. The current collector is typically a plate or a

Table 3
Anode cell potentials of different Al Alloys in 4 M NaOH and at 20 mA/cm^2.

Al/Al alloy anode	Cell potential (V)	Reference
Al	1.22–1.46	[21,23]
Al–0.4Si–1.6Cu–0.3Mn–5.5Zn–0.5Fe–0.2Ti–2.5Mg–0.3Cr/Cu ED	1.37	[24]
Al–0.9Mg–0.1Mn–0.02In	1.49	[23]
Al–0.9Mg–1Zn–0.1Mn–0.05Bi-0.02In	1.55	[23]
Al-1Mg-0.1Ga-0.1Sn	1.56	[19]
Al–1Mg–1Zn–0.1Ga–0.1Sn	1.60	[19]

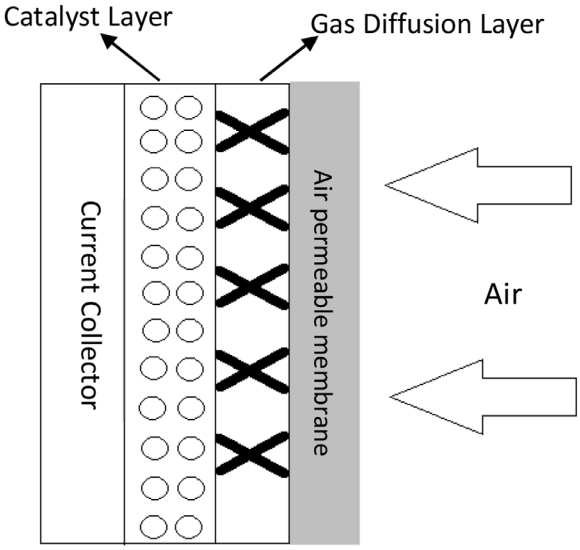


Fig. 4. Air cathode |structure.

mesh made of nickel that imparts mechanical strength to the cell and supports the transfer of electrons [32].

The commercial applicability of Al–air batteries is majorly hindered by the sluggish oxygen reduction reaction (ORR) that takes place at the cathode. The proper design and assembly of cathode along with the incorporation of suitable electrocatalyst to alter the activity for ORR is a must to make Al–air batteries viable. As the chemistry behind the reaction remains the same, research on oxygen reduction reactions for Zn–air, Li–air and polymer electrolyte membrane fuel cells (PEMFC) can be applied to the air cathode of the Al–air battery. The main goal of the choice of material still remains to suppress the formation of by-products and increase the rate of electrode kinetics. The best candidate for air cathode will be amongst the following discussed below.

3.1. Noble metals and alloys

Platinum (Pt) and silver (Ag) have been used as catalysts in batteries and fuel cells for many decades because of their high electrocatalytic activity and stability. Pt is commonly utilized in either its nanoparticle form with a form of carbon as support (these are the current state of the art Pt/C catalysts) to enhance the surface area or as a Pt-metal alloy. The activity of Pt nanoparticles (NPs) is strongly dependent on its shape; a 7 nm cubic Pt NP gives four times the current density of 3 nm polyhedral Pt NP or 5 nm truncated cubic Pt NP indicating the dominance of the shape effect for the particles [33]. Wang et al. [34] have also reported that the core shell structured Pt-alloy nanoparticles enhances not only the catalytic activity but also the durability of the catalyst to electronic and straining effects (Fig. 5). Further, the size of the Pt NPs is also an important factor that can significantly increase the ORR properties of air cathodes [35].

Pt-metal alloys have shown better performance than Pt element at the cost of a more complicated synthesis and elaborate preparation.

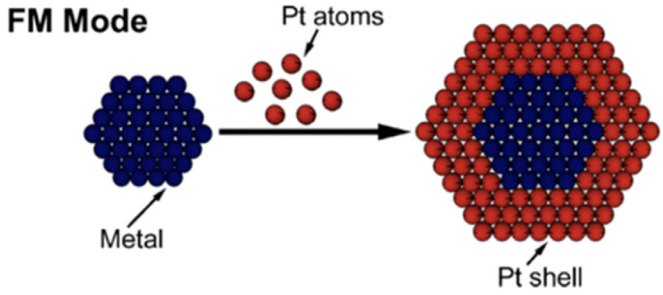


Fig. 5. PtM core–shell structure [34].

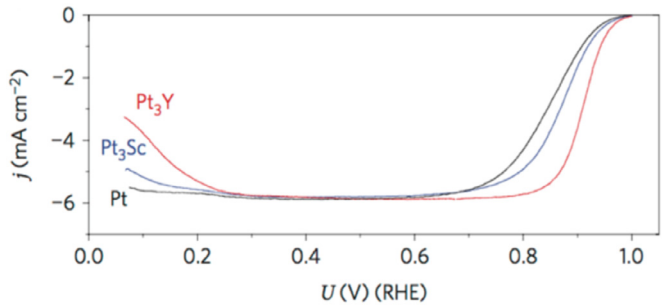


Fig. 6. Voltammogram of Pt, Pt3Sc and Pt3Y [36].

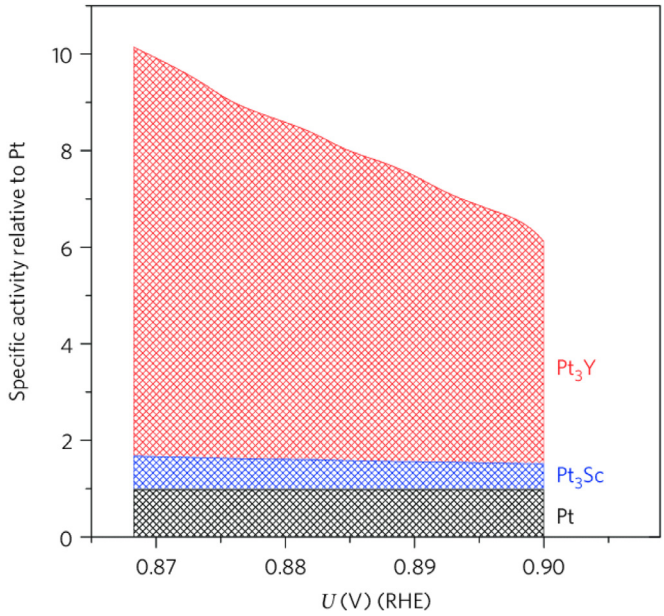


Fig. 7. Activity increase relative to Pt of Pt3Sc and Pt3Y [36].

Pt_3X alloys of Y and Sc showed better activities than the element Pt. From Fig. 6 and Fig. 7, at 0.87 V, Pt_3Sc had an 80% higher activity than Pt and Pt_3Y had an increase in activity by one order [36]. The high cost

and scarcity of Pt will continue to be an obstacle especially for Al–air batteries that have a distinct benefit of using a cheap and commonly available metal anode. An expensive air-cathode will nullify the advantage of a cheaper anode and will be counterproductive for the viability of Al–air battery.

Ag, on the other hand, is around 54 times cheaper than Platinum (April 2019) and its concentration is around 5–15% in air cathodes [37]. Lei et al. [38] showed that Ag–Cu nanoalloyed films have overpotential characteristics similar to the commercially available Pt/C and Ir/C based Zn–air batteries at 20 mA/cm^2. The cycle performance of the rechargeable battery was also good with a round trip efficiency of 52.3% for a Zn-air cell.

3.2. Carbonaceous materials

Carbon-based catalysts have become a favored choice due to their relatively lower cost as compared to Pt and Ag, and their ability to exist in a wide number of structural forms. As these materials have been extensively documented [39,40], we shall focus on the notable advancements in this area.

Carbon catalysts can be fundamentally understood in two parts, (i) a carbon base such as carbon nanotubes and nanofibers (1D), graphene and graphite nanosheets (2D), or 3D nanospheres, and (ii) a dopant such as other forms of carbon, metals, metal oxides (perovskite, spinel, etc.), metal nitrides and non-metals.

Shen et al. [41] studied and analyzed a bifunctional Co-N/CN catalyst (at 800 °C) which shows an onset potential of 0.987 V and favors a 4-electron reduction process (Figs. 8 and 9.). Its OER activities are also notable, showing an onset potential of 0.98 V as compared to 1.06 V of commercial Pt/C and similar current densities. This indicates the viability of cheaper catalysts as reliable alternatives and also points towards the possibility of secondary Al–air batteries.

It has been reported [42–44] that Fe encapsulated in CNTs leads to decreased local work functions on the surface of carbon that increases ORR activity which can be further enhanced by doping with nitrogen. Such doping is done alongside the growth of carbon nanostructures [45,46]. Further, in a comparative study by Zou et al. [47], it was found that ultra-thin CNTs with a high N concentration are catalytically the most effective for ORR. As an example, nitrogen-doped CNTs with encapsulated ferric carbide nanoparticles pyrolyzed at 800 °C (Fe_3C@NCNTs-800) showed significantly better onset potentials (Fig. 10) (measured against Ag/AgCl) of 0.098 V as opposed to N—CNTs and even slightly better than the commercially used Pt/C [48].

These methods are energy intensive; one may focus on environmentally benign methods [49] of catalyst synthesis such as nitrogen-doped carbon nano onion (N-CNO) that were produced from the biomass collagen. These were reported to have a notable onset potential, high current density and considerably more durability than Pt/C as

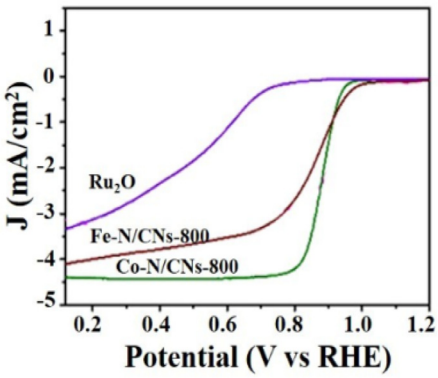


Fig. 8. LSV curves of CO—N/CNs 800 compared to other synthesized electrodes (adapted from [41]).

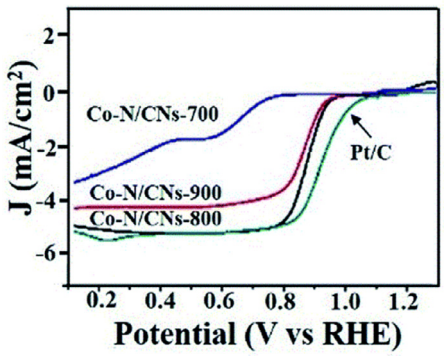


Fig. 9. LSV curves of Co–N/CNs 800 compared to other catalysts (adapted from [41]).

well as the advantage of using an environmentally conscious method of synthesis. Other studies have also studied low-cost precursors for high performance ORR catalyst carbon catalysts [50,51].

3.3. Transition metal oxides

Transition metal oxides, nitrides, and sulfides are other alternatives to the conventional noble catalysts. The oxides are inexpensive, naturally abundant, and environmentally benign, and have the ability to mix for synergistic effects. The major drawback of transition metal oxides is their lower conductivity which slows down electron transfer. There is the possibility of the oxygen reduction reaction following a $2e^- + 2e^-$ pathway as opposed to the preferred $4e^-$ one. Transition metal catalysts doped with more conductive materials (carbon based nanostructures and graphene) have been found better catalysts for ORR [52,53]. Rotating ring disk electrode (RRDE) studies [54] on Me-doped carbon supported MnO_x nanoparticles (Me = Ni, Mg) showed that the $2e^-$ pathway is certainly present, although it can be significantly reduced with Ni and Mg doping (Ni > Mg). These pathways have still not been completely established as Mn_xO_y (3, 4 and 2, 3) nanofibers and xerogels showed electron transfer values (n) of 3.5–3.7 that are only slightly lesser than the standard Pt/C catalysts [55]. In 2003, a study [56] suggested that the mechanism of manganese dioxide (MnO_2) catalysts follow through the chemical oxidation of the Mn^{3+} ions (that is the $4e^-$ reduction process) rather than the $2e^-$ pathway. We believe, a focused and definite study is still needed in order to completely characterize the mechanism of reduction of transition metal oxides.

Transition metals such as Co, Mn, Fe, and Ni have been studied for their catalytic activity. Studies on cobalt since the 1970s [57] have focused on more efficient methods of synthesis for better homogeneity, morphology, and purity. Recently, research has focused on Mn substituted CoO_x [58,59]. The study by Liang et al. [59] on the spinel $MnCo_2O_4$/graphene hybrid shows better ORR characteristics of the hybrid than Pt/C in alkaline conditions. Such hybrids are a necessity with the Co_3O_4 showing little activity on its own. Cobalt oxide nanoparticles are also supported with carbon bases and the synthesized compounds have shown good chemical activity and superior stability to Pt/C catalysts [60,61].

Manganese is a versatile material that can exist in many oxidation states and is the 10th most abundant material on earth. Low cost, ability to exist in many valence states and structural diversity of Mn has made it a key candidate for a bifunctional catalyst. The effect of structure on the catalytic activity of Mn_xO_y was recorded by Mao et al. [62] in decreasing order of activity as γ-MnOOH ~ α-Mn_2O_3 > Mn_3O_4 > Mn_5O_8 as well as Cao et al. [56] as δ-MnO_2 ~ α-MnO_2 > γ-MnO_2 > λ-MnO_2 > β-MnO_2 in an air atmosphere. Generally, manganese oxides exhibit low conductivity and thus carbon is used as support [53,54]. Monophasic nanofibres produced from Mn_3O_4 and xerogels consisting of a mix of Mn_3O_4 and Mn_2O_3 (with residual carbon as an impurity) have

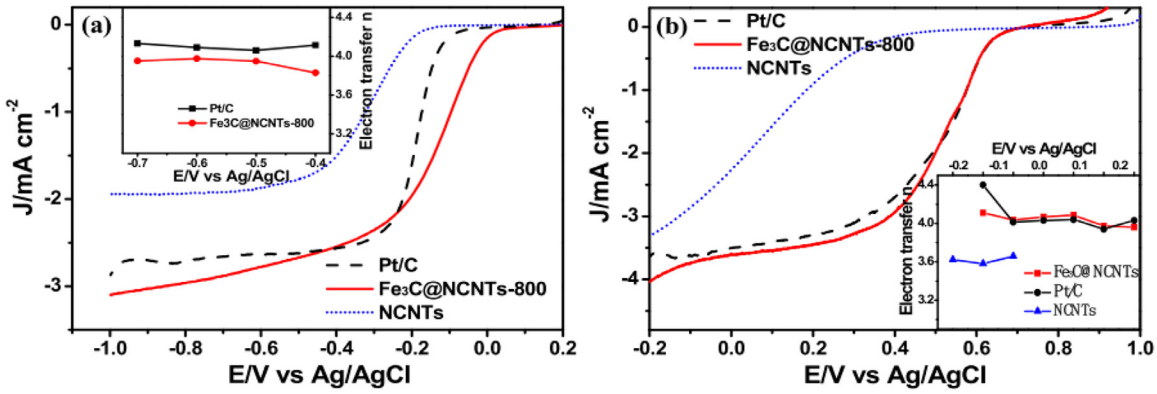


Fig. 10. Linear sweep |voltammograms (LSV) of Fe3C@N-CNTs-800, N-CNTs, and Pt/C in (a) Alkaline and (b) Acid media. Also mentioned are the electron transfer values (*n*) [48].

exhibited excellent catalytic activities [55]. We believe that α-MnO_2 nanorods are a promising and viable alternative to Pt/C given that the doped (Ag, Co, Ru) α-MnO_2 nanorods are reported to have an average electron transfer number of almost 4 and excellent ORR characteristics [63,64]. However, practical studies [65] of MnO_2 nanorods in Al-air batteries still found room for improvement with the MnO_2 microspheres taking 2 h to achieve stable discharge as opposed to less than an hour for Pt/C.

In the perovskite family, a novel $La_{0.9}Y_{0.1}MnO_3$ (LYM-10) developed has an onset potential of 0.909 V that is higher than Sr doped Mn-based perovskites [66,67]. These perovskites, along with spinels, are an attractive choice for researchers as they allow partial cation substitution enabling the tuning of their properties to form many oxides [68,69].

Although nickel is more conductive than manganese and has the capability for OER, it has not found use in ORR due to many drawbacks and problems explained [52]. These problems can be somewhat mitigated with the use of carbon as a base, but even then, the results remain unsatisfactory. One such study by Liu et al. [70] showed the poor activity of Ni/NiO multifunctional catalysts for ORR. Nickel has, however, performed well as a dopant and has been incorporated in many transition oxides of manganese [71,72], cobalt [73–80] and iron [81–83].

Pure iron oxides show poor ORR activity [84] and still, are in need of further research to increase their catalytic activities to be comparable with Pt/C catalysts. A review [85] of the Fe–N/C catalysts identified that the ORR catalytic activity was strongly dependent upon the carbon support, source of metal and nitrogen, and thermal treatment conditions. The review also established that a correct combination of the above parameters could produce viable Pt-free cathodes. The mechanism by which catalytic activities could be enhanced is not completely defined at this point in time but there is a general consensus that using carbon support with nitrogen doping increases catalytic activities. Wang et al. [86] embedded Fe_3O_4 nanoparticles in N, P-doped carbon nanofibers (FeCNFs-N), and both the N-doped carbon and Fe_3O_4 nanoparticles were reported to be active centers (bifunctionality) for ORR and OER with a better electrochemical performance of the FeCNFs–N than Pt/C (Fig. 11.). FeO_x can also be incorporated with iron phthalocyanine to achieve a better onset potentials than Pt/C catalysts as well as excellent ORR activity [87]. Apart from oxides, transition metal nitrides, sulfides, and carbides have also been considered as potential candidates for cathode catalyst [88–91] .

3.4. Polymers and polymer-based complexes

Electronically conducting polymers (ECPs) are a class of compounds that have the potential to be a low cost and stable alternative to the noble metal catalysts. ECPs are highly versatile and can be used in a range of different applications, from electrode materials to matrices in which certain elements can be embedded. ECPs such as polyaniline

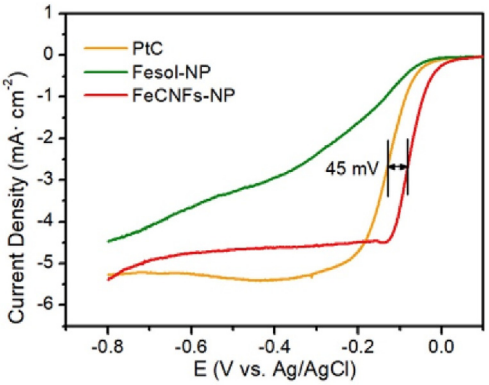


Fig. 11. LSV curves of different samples in O2 saturated 0.1 M KOH at 1600 rpm [86].

(PANI) have been used as dopants for decades and a systematic review of their catalytic activities was first done in 2005 [92] in which reduction capability of the conducting polymers was analyzed. It was reported that ORR of the chemisorbed oxygen molecules was possible. However, it was also reported that these polymers lack bifunctionality, which is not a drawback for a primary Al–air battery but may hinder further development of secondary batteries. Yuan et al. [93] reported that doping PANI with C, N, Fe, and Co [92–96] further improved its catalytic activity.

There are many studies done on other conducting polymers for ORR, such as polypyrrole (PPy) [97–101], polythiophene (PTh) [102–106], and poly(3,4-ethylenedioxythiophene) (PEDOT) [107–110]. Among these, PPy is considered to be most promising due to its high catalytic activity and a high magnitude of current, second only to PANI (Fig. 12.). As of date, there is a lack of analysis in literature for both the doping of PPy and the activity of PPy as a catalyst. The few studies that have been done on its morphology, empirically point to annealing and the tubular structure (as opposed to granular) as factors that provide good ORR properties [111–113]. The addition of PPy has shown significant improvements in perovskite catalysts (despite its lower conductivity) due to its ability to adsorb oxygen better than the perovskite structure [114].

We believe that for Al–air batteries, transition metal oxides and carbon electrodes are an attractive choice for air cathodes as these follow a $4e^-$ pathway and are naturally abundant which makes them inexpensive. The electrochemical performances of these cathodes are close to that of Pt/C, therefore, making it commercially viable for use in an Al–air battery.

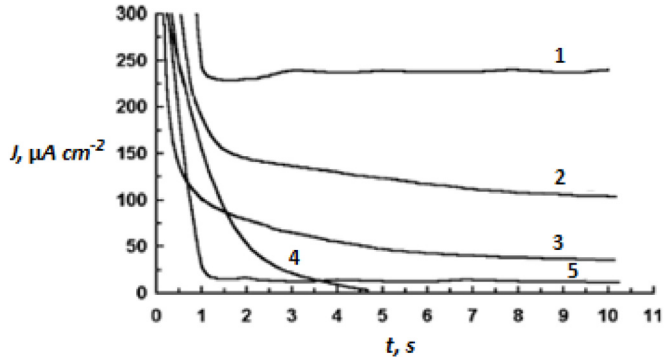


Fig. 12. Amperometric *J–t* response obtained with conducting polymer (1) PANI, (2) PPy, (3) PTh, (4) PEDOT, and (5) carbon-based electrodes (5-mm diameter) in oxygen-saturated 1 M HCl solution. The electrodes were polarized at 0.0 V vs. SHE [93].

4. Electrolytes

An electrolyte is a conductive medium that allows the movement of ions from the cathode to the anode.The electrolyte controls the hydrogen evolution and the precipitation reactions at the Al anode, as well as determines the overall potential of the cell. Research on Al–air battery has focused on using aqueous, non-aqueous, mixed and aprotic electrolytes. In this section, our focus is on currently employed electrolytes as well as new classes that are being researched for Al–air batteries. The additives added to electrolytes to improve their anodic utilization and decrease hydrogen evolution are also discussed. A summary of the energy densities of Al–air batteries with different electrolytes is compiled in Table 4.

4.1. Aqueous electrolytes

Alkaline aqueous electrolytes have been widely used as electrolytes for Al–air batteries and have been studied for more than half a century [115,116]. Aqueous KOH and NaOH are most widely used. These electrolytes give high ionic conductivity, low overpotential, non-toxicity and fast ORR [14].

Kapali et al. [26] have systematically analyzed the alkaline electrolytes specifically for Al–air batteries. Alkaline electrolytes containing a complex of citrate, stannate, and calcium (alkaline citrate cum stannate) showed the highest solubility of Al, lowest corrosion rate, a wide range of temperance for tolerance of Al and the highest OCV. Different concentrations of single components - stannates, indates, gallates, manganates, were tested. Potassium manganate (concentration 10^{-3} M) was reported to be the most effective with a coulombic efficiency of Al-anode to be greater than 90% [117,118] while the corrosion rate remained similar. Amongst binary systems, namely, gallate + indate, manganate + indate, bismuthate + stannate and stannate + indate, stannate + indium hydroxide (Na_2SnO_3 + $In(OH)_3$) were the best among the class, coulombic efficiencies being as high as 96% with a significant decrease in the corrosion rate. However, major problems associated with alkaline aqueous electrolytes are the evaporation of water, low energy density, and carbonation of the electrolyte that impedes air access to the cathodes [13].

Table 4
Al-air batteries energy densities using different electrolytes.

Battery system	Practical energy density (Wh/kg)	References
Al–air (aqueous electrolyte)	300–500	[4,17]
Al–air (ionic liquid electrolyte)	2300	[111]
Al–air (xanthan gel electrolyte)	1430	[122]
Al–air (polymer gel electrolyte)	1230	[115]

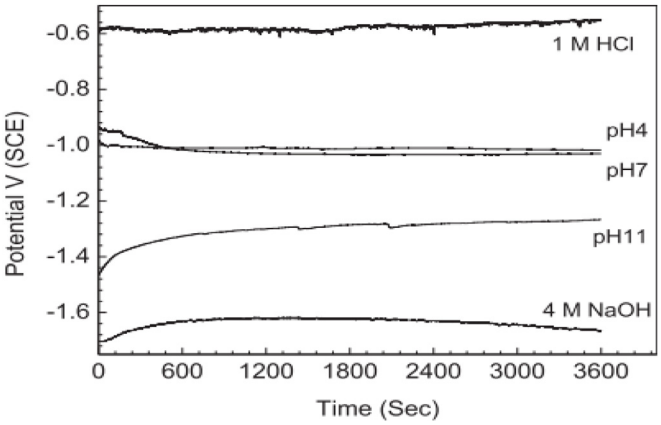


Fig. 13. Evolution of the open circuit potential vs. time in different solutions for samples of the alloy [128].

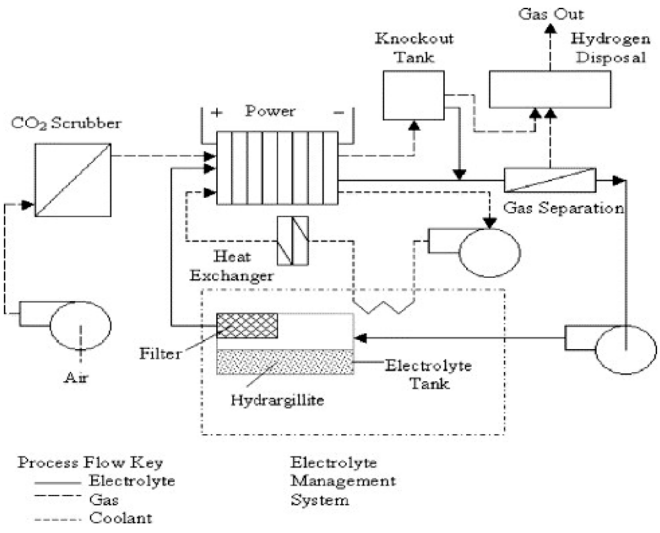


Fig. 14. Basic flow diagram of an Al–air battery system [154].

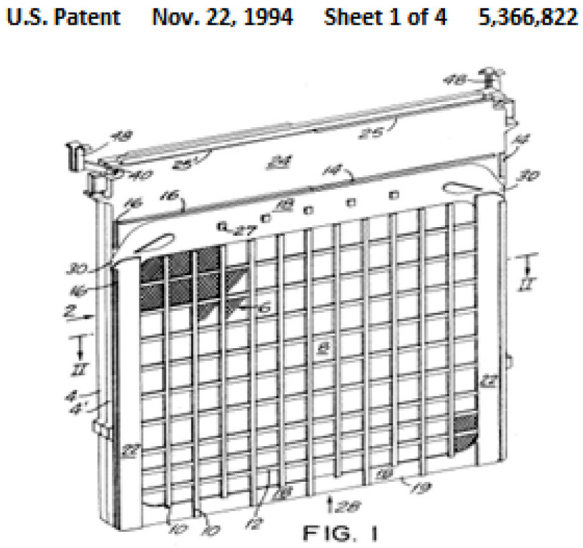


Fig. 15. US4925744A.

Neutral salt electrolytes were first documented, to the best of our knowledge, in a patent in 1975 (US3887399A). Numerous studies have recorded the use of the saline electrolyte with a potential in the range of

0.65–1.1 V [119–124]. When compared, neutral electrolyte has shown lower performance (energy density in the neutral electrolyte was one-third of that in the alkaline electrolyte) due to higher passivation on the anode [125]. Neutral electrolytes (specifically sodium salt) remain significant mainly due to their potential application in metal-air batteries in marine vehicles that can use the seawater directly, and studies have shown that these can serve as large capacity, medium power sources for marine applications [126].

Acidic aqueous electrolytes have their own advantages and disadvantages, most notably the elimination of carbonation. When 3 M H_2SO_4 was used with 0.04 M HCl as an electrolyte, then the OCV was found to be less in magnitude (more positive) as compared to KOH and NaOH electrolytes [127]. These results are further confirmed by studies by Ma et al. [128,129] where the OCV decreases with a decrease in pH of the electrolyte (Fig. 13). The paper also provides an understanding of the mechanism of corrosion in both alkaline and acidic solutions. While the acidic solutions cause Al corrosion due to pitting which exposes only cubic planes, the alkaline solutions cause crystallographic corrosion[1] [130]. The acidic electrolytes yield a lower corrosion rate than alkaline electrolytes.

4.1.1. Additives for aqueous electrolytes

The addition of additives to aqueous electrolytes generally (1) suppresses parasitic corrosion of aluminum, (2) lowers hydrogen evolution and (3) increases anodic utilization. While all the three functions are interrelated, in our opinion, their most essential function is the reduction of Al-anode corrosion.

Different organic and inorganic additives have been developed that can be added to aqueous electrolytes. Such additives systems are, 8-hydroxyquinoline and ZnO complex [131], 1-allyl-3-methylimidazolium bis(trifluoromethylsulfonyl)imide (IL) [132], carboxymethyl cellulose and ZnO [133], dicarboxylic acids [134] and L-cysteine and cerium nitrate [135]. Strictly on the basis of the rate of hydrogen evolution rate, a direct comparison reveals that the ionic liquid additive imide provided the lowest hydrogen gas evolution rate with rates lesser than 0.1 ml/min cm^2 for concentration greater than 1 mM. The mechanism by which the additives work has been well described in [132,136]. In brief, there is an adsorption of one of the compounds of the additive system with a protective layer generation (in many cases by the ZnO) around the anode.

4.2. Non-aqueous electrolytes

Non-aqueous electrolytes are capable of overcoming the limitations of aqueous systems. Advantages include higher energy density, suppressing anodic corrosion and higher battery voltage [12], apart from the reversibility of electrode reactions necessary for the development of a secondary Al–air battery. Specifically, the problem of the loss of ionic conductivity that results from the precipitation reactions can be easily addressed. Non-aqueous electrolytes can be classified into (1) aprotic electrolytes, and (2) polymer electrolytes.

Aprotic electrolytes are commonly employed for Li–air batteries [137–139] and have the potential to be suitable for use in Al–air battery systems. First published in 2013 [140], room temperature ionic liquids (RTIL) such as $EMIm(HF)_{2.3}F$ have been reported to be an excellent corrosion inhibitor and provides high energy density (2.3 kWh/kg). The ionic liquids possess high conductivity, chemical stability and low viscosity. Several studies reported [141–144] low corrosion rates and durability of Al–air ionic liquid systems.

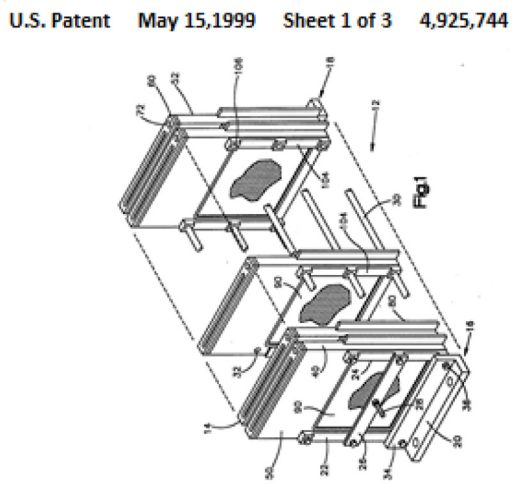


Fig. 16. US5366822.

Polymer electrolytes are essentially cathode-anode separators that absorb an electrolyte (such as KOH) and maintain the potential difference in a battery. Typically, they are thin films that are prepared using polymer casting, solvent evaporation, and spray deposition methods. PVA/PAA solid polymer electrolyte (SPEs) used with Al–air gave a power density of 1.2 mW/cm^2 which was lower than that compared for Zn–air likely due to a deactivated Al surface [145]. A PVA (4 wt%)/ZnO film in 2 M KOH has also been recorded showing stability up to 2.15 V [146]. Other polymer electrolytes have also been used for metal-air batteries such as PEO-PVA-glass fiber electrolytes for Zn–air [147], LiTFSI-PMMITFSI–silica–PVdF-HFP polymer composites for Li–air [148].

Polymer gel electrolytes (PGEs) developed for metal-air batteries absorb aqueous solutions such as KOH to yield a polymer-based gel that has good ionic conductivity. The advantages of PGEs are mainly the ability to avoid leakage and thermal and electrochemical stability. Recent studies on poly(acrylamide) [149,150], poly(acrylic acid) [150], polysaccharides [151–153] have been performed out of which xanthan, and κ-carrageenan showed excellent discharge characteristics for solid-state Al–air batteries. We believe that aprotic electrolyte and polymer electrolyte will help in overcoming problems of corrosion and provide a high energy density and OCV.

5. Design and assembly of Al–air batteries

Appropriate design and assembly of Al–air battery can provide enhanced performance, battery life and higher shelf life. The Al–air battery feeds directly to the electric power control system that runs the motor that drives the wheels of a car. A fully functioning Al–air battery has the following components: the Al–air battery, a crystallizer to control the composition of the electrolyte, CO_2 absorber, gas separator to separate out hydrogen from the electrolyte, and a cooling system for thermal control. An example of such an arrangement is given in Fig. 14. [154]. A major problem in Al–air battery design is the short life of the cell and its rapid loss of charge. To prolong the life of the cell, the electrolyte can be displaced with an oleophobic oil which stops the corrosion of anode during standby [155].

Al–air battery with sliding mechanism design [150] would remove the Al-anode from the gel electrolyte when not in use. Commercially patents on general metal-air batteries have given different structures. A 1994 patent (Fig. 15) (US5366822) describes a modular cell for a multi-cell battery system that has on both of its ends the air cathodes, and the other components sandwiched in the middle. In 1999, another battery

[1] Crystallographic corrosion is the corrosion of single crystals of high-purity aluminum in which the rate of attack being dependent on the orientation of the corroding surface. For a 15-percent NaOH solution, corrosion apparently progressed by revealing facet surfaces of the [335] type, while corrosion in aqua regia-hydrofluoric acid mixture revealed etch pits with surfaces of the [100] type.

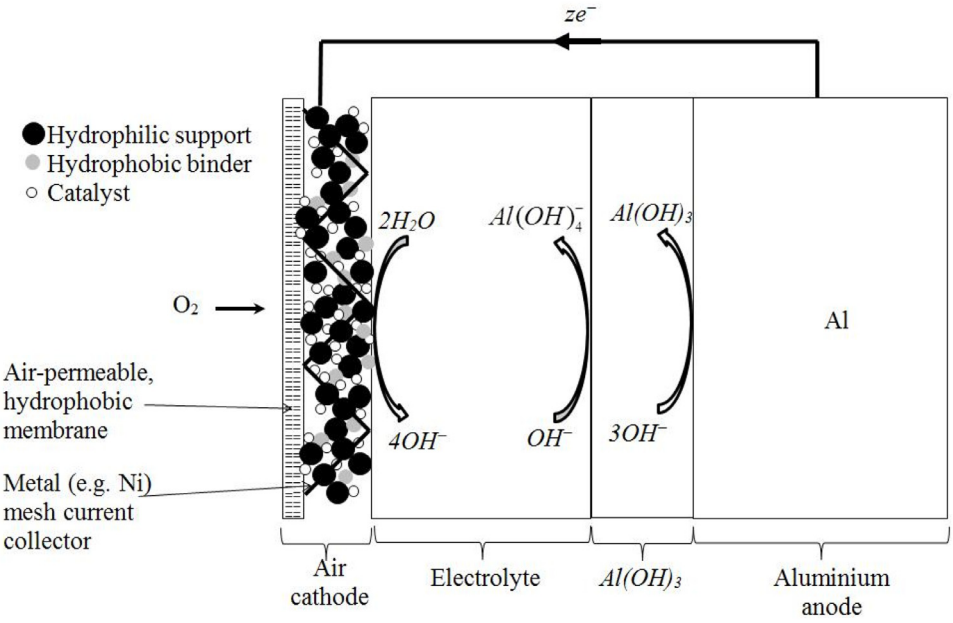


Fig. 17. Illustration of the structure of an Al–air battery using a 3-layer gas diffusion electrode and pure Al-anode with its passive hydroxide layer [118].

pack was patented (US6517967B1) with its intended use in cellular phones. This design aimed at maximizing bulk airflow as well as molecular diffusion while maintaining a compact design. The battery components are being housed with different techniques to increase efficiency, minimize corrosion and enhance battery efficacy (CN103872349A, US4942100A, US4925744A, [118]). Recently, a management system for the electrolyte in a battery has been patented (Fig. 16) (CN109638317A) that included filtration, valves, protective fluid and electrolyte that circulate through the battery.

6. Conclusion and outlook

Al–air batteries have the potential to satisfy consumer needs. The wide range of applications (from vehicles to marine systems), environmentally benign reactions, use of ambient air and the abundance of aluminum make Al–air system a promising source of energy for the future. However, the present Al–air battery technology, in our opinion, still requires establishing the industrial scalability of the electrodes and the electrolyte.

Certain problems exist that are intrinsic to the battery, including anode corrosion, pore blockage, sluggish ORR for non-noble cathodes, carbonation in aqueous electrolytes, the lack of compelling reports for viable secondary Al–air batteries and the absence of a defined method for replacing the anode in a primary battery. Further research on Al–air battery needs to focus on optimizing the combination of cathode, anode, electrolyte and other battery components that will allow ease of scalability, good performance, and economic production.

As of now, for anodes, there are plenty of Al alloys that offer distinctive benefits and would be more suitable as anodes for Al–air batteries in comparison to pure Al that is too expensive for practical commercial purposes. For cathodes, carbonaceous materials are, in our opinion, the most attractive choice, especially given their versatility and relative lower cost. Electrolytes have conventionally been aqueous KOH, and the Al-batteries with KOH have not faced many disadvantages. The polymeric solid-state electrolytes and ionic liquids show great potential. The design and assembly of battery components need further innovation although the widely accepted design utilizes a tri-slotted form (Fig. 17.). New designs may incorporate thin membranes for anode, electrolyte and cathode separation (when the battery is not in use) facilitating both the technological and financial viabilityof the Al–air battery system.

Declaration of Competing Interest

The authors declare no conflict of interest.

Acknowledgments

The authors are thankful to Prof. Yogesh Singh, Vice Chancellor, Delhi Technological University. This research did not receive any specific grant from funding agencies in the public, commercial, or not-for-profit sectors.

Supplementary materials

Supplementary material associated with this article can be found, in the online version, at doi:10.1016/j.est.2020.101287.

References

[1] J. Song, W. Yan, H. Cao, Q. Song, H. Ding, Z. Lv, Y. Zhang, Z. Sun, Material flow analysis on critical raw materials of lithium-ion batteries in China, J. Clean. Prod. 215 (2019) 570–581, https://doi.org/10.1016/j.jclepro.2019.01.081.
[2] R. Spotnitz, J. Franklin, Abuse behavior of high-power, lithium-ion cells, J. Power Sources 113 (2003) 81–100, https://doi.org/10.1016/S0378-7753(02)00488-3.
[3] A. Kraytsberg, Y. Ein-Eli, Review on Li-air batteries - Opportunities, limitations and perspective, J. Power Sources 196 (2011) 886–893, https://doi.org/10.1016/j.jpowsour.2010.09.031.
[4] J.S. Lee, S.T. Kim, R. Cao, N.S. Choi, M. Liu, K.T. Lee, J. Cho, Metal-air batteries with high energy density: Li-air versus Zn-air, Adv. Energy Mater. 1 (2011) 34–50, https://doi.org/10.1002/aenm.201000010.
[5] J. Goldstein, I. Brown, B. Koretz, New developments in the Electric Fuel Ltd. zinc/air system, J. Power Sources 80 (1999) 171–179, https://doi.org/10.1016/S0378-7753(98)00260-2.
[6] T. Zhang, Z. Tao, J. Chen, Magnesium-air batteries: from principle to application, Mater. Horizons 1 (2014) 196–206, https://doi.org/10.1039/c3mh00059a.
[7] R. Mori, Rechargeable aluminum-air battery using various air-cathode materials and suppression of byproducts formation on both anode and air cathode, ECS Trans. 80 (2017) 377–393, https://doi.org/10.1149/08010.0377ecst.
[8] N. Jayaprakash, S.K. Das, L.A. Archer, The rechargeable aluminum-ion battery, Chem. Commun. 47 (2011) 12610–12612, https://doi.org/10.1039/c1cc15779e.
[9] M.A. Rahman, X. Wang, C. Wen, High energy density metal-air batteries: a review, J. Electrochem. Soc. 160 (2013) A1759–A1771, https://doi.org/10.1149/2.062310jes.
[10] L.D. Chen, J.K. Nørskov, A.C. Luntz, Al-air batteries: fundamental thermodynamic limitations from first-principles theory, J. Phys. Chem. Lett. 6 (2015) 175–179, https://doi.org/10.1021/jz502422v.
[11] K.T. Chau, Y.S. Wong, C.C. Chan, Overview of energy sources for electric vehicles, Energy Convers. Manag. 40 (1999) 1021–1039, https://doi.org/10.1016/S0196-

8904(99)00021-7.
[12] Z.L. Wang, D. Xu, J.J. Xu, X.B. Zhang, Oxygen electrocatalysts in metal-air batteries: from aqueous to nonaqueous electrolytes, Chem. Soc. Rev. 43 (2014) 7746–7786, https://doi.org/10.1039/c3cs60248f.
[13] Q. Li, N.J. Bjerrum, Aluminum as anode for energy storage and conversion: a review, J. Power Sources 110 (2002) 1–10, https://doi.org/10.1016/S0378-7753(01)01014-X.
[14] M. Mokhtar, M.Z.M. Talib, E.H. Majlan, S.M. Tasirin, W.M.F.W. Ramli, W.R.W. Daud, J. Sahari, Recent developments in materials for aluminum-air batteries: a review, J. Ind. Eng. Chem. 32 (2015) 1–20, https://doi.org/10.1016/j.jiec.2015.08.004.
[15] D.R. Egan, C. Ponce De León, R.J.K. Wood, R.L. Jones, K.R. Stokes, F.C. Walsh, Developments in electrode materials and electrolytes for aluminiumeair batteries, J. Power Sources 236 (2013) 293–310, https://doi.org/10.1016/j.jpowsour.2013.01.141.
[16] A. Kindler, L. Matthies, High specific energy and specific power aluminum/air battery for micro air vehicles, Micro-Nanotechnol. Sensors, Syst. Appl. VI. 9083 (2014), https://doi.org/10.1117/12.2051820.
[17] S. Yang, H. Knickle, Design and analysis of aluminum/air battery system for electric vehicles, J. Power Sources 112 (2002) 162–173, https://doi.org/10.1016/S0378-7753(02)00370-1.
[18] Y.J. Cho, I.J. Park, H.J. Lee, J.G. Kim, Aluminum anode for aluminum-air battery - Part I: influence of aluminum purity, J. Power Sources 277 (2015) 370–378, https://doi.org/10.1016/j.jpowsour.2014.12.026.
[19] Y. Yu, M. Chen, S. Wang, C. Hill, P. Joshi, A. Hu, Laser sintering of Al nanoparticles for Al-air batteries, J. Laser Appl. 30 (2018) 032605, , https://doi.org/10.2351/1.5040651.
[20] L. Fan, H. Lu, The effect of grain size on aluminum anodes for Al-air batteries in alkaline electrolytes, J. Power Sources 284 (2015) 409–415, https://doi.org/10.1016/j.jpowsour.2015.03.063.
[21] L. Fan, H. Lu, J. Leng, Z. Sun, C. Chen, The effect of crystal orientation on the aluminum anodes of the aluminum-air batteries in alkaline electrolytes, J. Power Sources 299 (2015) 66–69, https://doi.org/10.1016/j.jpowsour.2015.08.095.
[22] S. Lameche-Djeghaba, A. Benchettara, F. Kellou, V. Ji, Electrochemical behaviour of pure aluminium and Al-5%Zn alloy in 3% NaCl solution, Arab. J. Sci. Eng. 39 (2014) 113–122, https://doi.org/10.1007/s13369-013-0876-7.
[23] I.J. Park, S.R. Choi, J.G. Kim, Aluminum anode for aluminum-air battery – Part II: influence of in addition on the electrochemical characteristics of Al-Zn alloy in alkaline solution, J. Power Sources 357 (2017) 47–55, https://doi.org/10.1016/j.jpowsour.2017.04.097.
[24] J. Ma, J. Wen, J. Gao, Q. Li, Performance of Al-1Mg-1Zn-0.1ga-0.1Sn as anode for Al-air battery, Electrochim. Acta 129 (2014) 69–75, https://doi.org/10.1016/j.electacta.2014.02.080.
[25] N.G. Wang, R.C. Wang, C.Q. Peng, Y. Feng, X.Y. Zhang, Influence of aluminium and lead on activation of magnesium as anode, Trans. Nonferrous Met. Soc. China 20 (2010) 1403–1411, https://doi.org/10.1016/S1003-6326(09)60312-5.
[26] M. Srinivas, S.K. Adapaka, L. Neelakantan, Solubility effects of Sn and Ga on the microstructure and corrosion behavior of Al-Mg-Sn-Ga alloy anodes, J. Alloys Compd. 683 (2016) 647–653, https://doi.org/10.1016/j.jallcom.2016.05.090.
[27] Q. Wang, H. Miao, Y. Xue, S. Sun, S. Li, Z. Liu, Performances of an Al-0.15 Bi-0.15Pb-0.035 Ga alloy as an anode for Al-air batteries in neutral and alkaline electrolytes, RSC Adv. 7 (2017) 25838–25847, https://doi.org/10.1039/c7ra02918g.
[28] V. Kapali, S. Venkatakrishna Iyer, V. Balaramachandran, K.B. Sarangapani, M. Ganesan, M. Anbu Kulandainathan, A. Sheik Mideen, Studies on the best alkaline electrolyte for aluminium/air batteries, J. Power Sources 39 (1992) 263–269, https://doi.org/10.1016/0378-7753(92)80147-4.
[29] H. Moghanni-Bavil-Olyaei, J. Arjomandi, Enhanced electrochemical performance of Al-0.9Mg-1Zn-0.1Mn-0.05Bi-0.02In fabricated from commercially pure aluminum for use as the anode of alkaline batteries, RSC Adv. 6 (2016) 28055–28062, https://doi.org/10.1039/c6ra02113a.
[30] R.N. Mutlu, B. Yazıcı, Copper-deposited aluminum anode for aluminum-air battery, J. Solid State Electrochem. 23 (2019) 529–541, https://doi.org/10.1007/s10008-018-4146-1.
[31] Y. Li, K. Huang, J.D. MacGregor, Y. Xing, The role of ptfe in cathode transition layer in aqueous electrolyte Li-air battery, Electrochim. Acta 191 (2016) 996–1000, https://doi.org/10.1016/j.electacta.2016.01.143.
[32] X.Z. Yuan, H. Wang, PEM fuel cell fundamentals, 2008. 10.1007/978-1-84800-936-3_1.
[33] C. Wang, H. Daimon, T. Onodera, T. Koda, S. Sun, A general approach to the size- and shape-controlled synthesis of platinum nanoparticles and their catalytic reduction of oxygen, Angew. Chem. - Int. Ed. 47 (2008) 3588–3591, https://doi.org/10.1002/anie.200800073.
[34] Y.-J. Wang, N. Zhao, B. Fang, H. Li, X.T. Bi, H. Wang, Carbon-supported Pt-based alloy electrocatalysts for the oxygen reduction reaction in polymer electrolyte membrane fuel cells: particle size, shape, and composition manipulation and their impact to activity, Chem. Rev. 115 (2015) 3433–3467, https://doi.org/10.1021/cr500519c.
[35] K. Ichihashi, S. Muratsugu, S. Miyamoto, K. Sakamoto, N. Ishiguro, M. Tada, Enhanced oxygen reduction reaction performance of size-controlled Pt nanoparticles on polypyrrole-functionalized carbon nanotubes, Dalton Trans. 4 (2019), https://doi.org/10.1039/c9dt00158a.
[36] J. Greeley, I.E.L. Stephens, A.S. Bondarenko, T.P. Johansson, H.A. Hansen, T.F. Jaramillo, J. Rossmeisl, I. Chorkendorff, J.K. Nørskov, Alloys of platinum and early transition metals as oxygen reduction electrocatalysts, Nat. Chem. 1 (2009) 552–556, https://doi.org/10.1038/nchem.367.
[37] J.J. Martin, V. Neburchilov, H. Wang, W. Qu, Air cathodes for metal-air batteries and fuel cells, 2009 IEEE Electr. Power Energy Conf. (2009), 2009.
[38] Y. Lei, F. Chen, Y. Jin, Z. Liu, Ag-Cu nanoalloyed film as a high-performance cathode electrocatalytic material for zinc-air battery, Nanoscale Res. Lett. 10 (2015) 0–7, https://doi.org/10.1186/s11671-015-0900-9.
[39] Y.J. Wang, H. Fan, A. Ignaszak, L. Zhang, S. Shao, D.P. Wilkinson, J. Zhang, Compositing doped-carbon with metals, non-metals, metal oxides, metal nitrides and other materials to form bifunctional electrocatalysts to enhance metal-air battery oxygen reduction and evolution reactions, Chem. Eng. J. 348 (2018) 416–437, https://doi.org/10.1016/j.cej.2018.04.208.
[40] G. Wu, A. Santandreu, W. Kellogg, S. Gupta, O. Ogoke, H. Zhang, H.L. Wang, L. Dai, Carbon nanocomposite catalysts for oxygen reduction and evolution reactions: from nitrogen doping to transition-metal addition, Nano Energy 29 (2016) 83–110, https://doi.org/10.1016/j.nanoen.2015.12.032.
[41] J. Shen, L. Meng, Y. Liu, C. Chen, Y. Zhu, C. Li, Preparation of Co-N carbon nanosheet oxygen electrode catalyst by controlled crystallization of cobalt salt precursors for all-solid-state Al-air battery, RSC Adv. 8 (2018) 22193–22198, https://doi.org/10.1039/c8ra03245a.
[42] D. Deng, L. Yu, X. Chen, G. Wang, L. Jin, X. Pan, J. Deng, G. Sun, X. Bao, Iron encapsulated within pod-like carbon nanotubes for oxygen reduction reaction, Angew. Chem. - Int. Ed. 52 (2013) 371–375, https://doi.org/10.1002/anie.201204958.
[43] K. Mamtani, D. Jain, D. Dogu, V. Gustin, S. Gunduz, A.C. Co, U.S. Ozkan, Insights into oxygen reduction reaction (ORR) and oxygen evolution reaction (OER) active sites for nitrogen-doped carbon nanostructures (CNx) in acidic media, Appl. Catal. B Environ. 220 (2018) 88–97, https://doi.org/10.1016/j.apcatb.2017.07.086.
[44] Y. Liu, J. Li, W. Li, Y. Li, F. Zhan, H. Tang, Q. Chen, Exploring the nitrogen species of nitrogen doped graphene as electrocatalysts for oxygen reduction reaction in Al-air batteries, Int. J. Hydrog. Energy 41 (2016) 10354–10365, https://doi.org/10.1016/j.ijhydene.2015.10.109.
[45] D. Yu, Q. Zhang, L. Dai, Highly efficient metal-free growth of nitrogen-doped single-walled carbon nanotubes on plasma-etched substrates for oxygen reduction, J. Am. Chem. Soc. 132 (2010) 15127–15129, https://doi.org/10.1021/ja105617z.
[46] M.S. Saha, R. Li, X. Sun, S. Ye, 3-D composite electrodes for high performance PEM fuel cells composed of Pt supported on nitrogen-doped carbon nanotubes grown on carbon paper, Electrochem. Commun. 11 (2009) 438–441, https://doi.org/10.1016/j.elecom.2008.12.013.
[47] X. Zou, L. Wang, B.I. Yakobson, Mechanisms of the oxygen reduction reaction on B- and/or N-doped carbon nanomaterials with curvature and edge effects, Nanoscale 10 (2018) 1129–1134, https://doi.org/10.1039/c7nr08061a.
[48] G. Zhong, H. Wang, H. Yu, F. Peng, Nitrogen doped carbon nanotubes with encapsulated ferric carbide as excellent electrocatalyst for oxygen reduction reaction in acid and alkaline media, J. Power Sources 286 (2015) 495–503, https://doi.org/10.1016/j.jpowsour.2015.04.021.
[49] K. Chatterjee, M. Ashokkumar, H. Gullapalli, Y. Gong, R. Vajtai, P. Thanikaivelan, P.M. Ajayan, Nitrogen-rich carbon nano-onions for oxygen reduction reaction, Carbon N. Y. 130 (2018) 645–651, https://doi.org/10.1016/j.carbon.2018.01.052.
[50] Q. Ren, H. Wang, X.F. Lu, Y.X. Tong, G.R. Li, Recent progress on MOF-derived heteroatom-doped carbon-based electrocatalysts for oxygen reduction reaction, Adv. Sci. (2018) 5, https://doi.org/10.1002/advs.201700515.
[51] B.C. Hu, Z.Y. Wu, S.Q. Chu, H.W. Zhu, H.W. Liang, J. Zhang, S.H. Yu, SiO 2 -protected shell mediated templating synthesis of Fe-N-doped carbon nanofibers and their enhanced oxygen reduction reaction performance, Energy Environ. Sci. 11 (2018) 2208–2215, https://doi.org/10.1039/c8ee00673c.
[52] H. Osgood, S.V. Devaguptapu, H. Xu, J. Cho, G. Wu, Transition metal (Fe, Co, Ni, and Mn) oxides for oxygen reduction and evolution bifunctional catalysts in alkaline media, Nano Today 11 (2016) 601–625, https://doi.org/10.1016/j.nantod.2016.09.001.
[53] J. Masa, W. Xia, I. Sinev, A. Zhao, Z. Sun, S. Grützke, P. Weide, M. Muhler, W. Schuhmann, Mn_xO_y/NC and Co_xO_y/NC nanoparticles embedded in a nitrogen-doped carbon matrix for high-performance bifunctional oxygen electrodes, Angew. Chem. - Int. Ed. 53 (2014) 8508–8512, https://doi.org/10.1002/anie.201402710.
[54] I. Roche, E. Chaînet, M. Chatenet, J. Vondrák, Carbon-supported manganese oxide nanoparticles as electrocatalysts for the oxygen reduction reaction (ORR) in alkaline medium: physical characterizations and ORR mechanism, J. Phys. Chem. C. 111 (2007) 1434–1443, https://doi.org/10.1021/jp0647986.
[55] L. Delmondo, G.P. Salvador, J.A. Muñoz-Tabares, A. Sacco, N. Garino, M. Castellino, M. Gerosa, G. Massaglia, A. Chiodoni, M. Quaglio, Nanostructured Mn_xO_y for oxygen reduction reaction (ORR) catalysts, Appl. Surf. Sci. 388 (2016) 631–639, https://doi.org/10.1016/j.apsusc.2016.03.224.
[56] Y.L. Cao, H.X. Yang, X.P. Ai, L.F. Xiao, The mechanism of oxygen reduction on MnO_2-catalyzed air cathode in alkaline solution, J. Electroanal. Chem. 557 (2003) 127–134, https://doi.org/10.1016/S0022-0728(03)00355-3.
[57] D.B. Meadowcroft, Low-cost carbon monoxide electrode material, Nature 226 (1970) 847–848, https://doi.org/10.1038/226847a0.
[58] M. Sugawara, M. Ohno, K. Matsuki, Oxygen reduction catalysis of Mn-Co spinel oxides on a graphite electrode in alkaline solution, J. Mater. Chem. 7 (1997) 833–836, https://doi.org/10.1039/a607324g.
[59] Y. Liang, H. Wang, J. Zhou, Y. Li, J. Wang, T. Regier, H. Dai, Covalent hybrid of spinel manganese-cobalt oxide and graphene as advanced oxygen reduction electrocatalysts, J. Am. Chem. Soc. 134 (2012) 3517–3523, https://doi.org/10.1021/ja210924t.
[60] S. Guo, S. Zhang, L. Wu, S. Sun, Co/CoO nanoparticles assembled on graphene for electrochemical reduction of oxygen, Angew. Chem. - Int. Ed. 51 (2012)

11770–11773, https://doi.org/10.1002/anie.201206152.
[61] M. Li, L. Bai, S. Wu, X. Wen, J. Guan, Co/CoO_x nanoparticles embedded on carbon for efficient catalysis of oxygen evolution and oxygen reduction reactions, ChemSusChem 11 (2018) 1722–1727, https://doi.org/10.1002/cssc.201800489.
[62] L. Mao, T. Sotomura, K. Nakatsu, N. Koshiba, D. Zhang, T. Ohsaka, Electrochemical characterization of catalytic activities of manganese oxides to oxygen reduction in alkaline aqueous solution, J. Electrochem. Soc. 149 (2002) A504, https://doi.org/10.1149/1.1461378.
[63] Z. Awan, Z.K. Ghouri, S. Hashmi, Influence of Ag nanoparticles on state of the art MnO_2 nanorods performance as an electrocatalyst for lithium air batteries, Int. J. Hydrog. Energy 43 (2018) 2930–2942, https://doi.org/10.1016/j.ijhydene.2017.12.083.
[64] M. Lübke, A. Sumboja, L. McCafferty, C.F. Armer, A.D. Handoko, Y. Du, K. McColl, F. Cora, D. Brett, Z. Liu, J.A. Darr, Transition-metal-doped α-MnO2 nanorods as bifunctional catalysts for efficient oxygen reduction and evolution reactions, ChemistrySelect 3 (2018) 2613–2622, https://doi.org/10.1002/slct.201702514.
[65] K. Chen, M. Wang, G. Li, Q. He, J. Liu, F. Li, Spherical α-MnO 2 supported on N-KB as efficient electrocatalyst for oxygen reduction in Al-air battery, Materials (Basel) (2018) 11, https://doi.org/10.3390/ma11040601.
[66] Y. Xue, H. Miao, B. Li, S. Sun, Q. Wang, S. Li, L. Chen, Z. Liu, Promoting effects of Ce0.75Zr0.25O2 on the La0.7Sr0.3MnO3 electrocatalyst for the oxygen reduction reaction in metal-air batteries, J. Mater. Chem. A. 5 (2017) 6411–6415, https://doi.org/10.1039/c6ta09795b.
[67] Z. Wang, Y. You, J. Yuan, Y.X. Yin, Y.T. Li, S. Xin, D. Zhang, Nickel-doped La0.8Sr0.2Mn1-x NixO3 nanoparticles containing abundant oxygen vacancies as an optimized bifunctional catalyst for oxygen cathode in rechargeable lithium-air batteries, ACS Appl. Mater. Interfaces 8 (2016) 6520–6528, https://doi.org/10.1021/acsami.6b00296.
[68] W. Zhou, J. Sunarso, Z.-.G. Chen, L. Ge, J. Motuzas, J. Zou, G. Wang, A. Julbe, Z. Zhu, Novel B-site ordered double perovskite Ba $_2$ Bi $_{0.1}$ Sc $_{0.2}$ Co $_{1.7}$ O $_{6-x}$ for highly efficient oxygen reduction reaction, Energy Environ. Sci. 4 (2011) 872–875, https://doi.org/10.1039/C0EE00451K.
[69] L. Malavasi, C.A.J. Fisher, M.S. Islam, Oxide-ion and proton conducting electrolyte materials for clean energy applications: structural and mechanistic features, Chem. Soc. Rev. 39 (2010) 4370–4387, https://doi.org/10.1039/b915141a.
[70] X. Liu, W. Liu, M. Ko, M. Park, M.G. Kim, P. Oh, S. Chae, S. Park, A. Casimir, G. Wu, J. Cho, Metal (Ni, Co)-metal oxides/graphene nanocomposites as multifunctional electrocatalysts, Adv. Funct. Mater. 25 (2015) 5799–5808, https://doi.org/10.1002/adfm.201502217.
[71] E.M. Benbow, S.P. Kelly, L. Zhao, J.W. Reutenauer, S.L. Suib, Oxygen reduction properties of bifunctional α-manganese oxide electrocatalysts in aqueous and organic electrolytes, J. Phys. Chem. C. 115 (2011) 22009–22017, https://doi.org/10.1021/jp2055443.
[72] J. Ponce, J.L. Rehspringer, G. Poillerat, J.L. Gautier, Electrochemical study of nickel-aluminium-manganese spinel NixAl1-xMn2O4 electrocatalytical properties for the oxygen evolution reaction and oxygen reduction reaction in alkaline media, Electrochim. Acta 46 (2001) 3373–3380, https://doi.org/10.1016/S0013-4686(01)00530-8.
[73] L. Wang, C. Lin, D. Huang, F. Zhang, M. Wang, J. Jin, A comparative study of composition and morphology effect of Ni x Co 1-x (OH) 2 on oxygen evolution/reduction reaction, ACS Appl. Mater. Interfaces 6 (2014) 10172–10180, https://doi.org/10.1021/am5014369.
[74] Y. GUO, T. LIU, K. SUN, Co 3 O 4 NPs embedded in N-doped carbon fibers as a bifunctional electrocatalyst for oxygen reduction and evolution reactions, (2016) 13–18. 10.1142/9789813141612_0003.
[75] X. Liu, M. Park, M.G. Kim, S. Gupta, G. Wu, J. Cho, Integrating NiCo alloys with their oxides as efficient bifunctional cathode catalysts for rechargeable zinc-air batteries, Angew. Chem. - Int. Ed. 54 (2015) 9654–9658, https://doi.org/10.1002/anie.201503612.
[76] X.Z. Yuan, W. Qu, X. Zhang, P. Yao, J. Fahlman, Spinel NixCO2-xO4 as a bifunctional air electrode for zinc air batteries, ECS Trans 45 (2013) 105–112, https://doi.org/10.1149/04529.0105ecst.
[77] C. Jin, F. Lu, X. Cao, Z. Yang, R. Yang, Facile synthesis and excellent electrochemical properties of NiCo 2O4 spinel nanowire arrays as a bifunctional catalyst for the oxygen reduction and evolution reaction, J. Mater. Chem. A. 1 (2013) 12170–12177, https://doi.org/10.1039/c3ta12118f.
[78] Z. Zhang, X. Wang, G. Cui, A. Zhang, X. Zhou, H. Xu, L. Gu, NiCo2S4 sub-micron spheres: an efficient non-precious metal bifunctional electrocatalyst, Nanoscale 6 (2014) 3540–3544, https://doi.org/10.1039/c3nr05885a.
[79] S. Amira, M. Ferkhi, M. Belghobsi, A. Khaled, F. Mauvy, J.C. Grenier, Synthesis, characterization, and electrochemical behavior of a new Nd 1.9 Sr 0.1 Ni 0.9 Co 0.1 O 4 ± δ material as electrocatalyst for the oxygen reduction reaction, Ionics (Kiel) (2019), https://doi.org/10.1007/s11581-019-02922-9.
[80] D.U. Lee, B.J. Kim, Z. Chen, One-pot synthesis of a mesoporous NiCo2O4 nanoplatelet and graphene hybrid and its oxygen reduction and evolution activities as an efficient bi-functional electrocatalyst, J. Mater. Chem. A. 1 (2013) 4754–4762, https://doi.org/10.1039/c3ta01402a.
[81] L. Cao, Y. Ma, A. Song, L. Bai, P. Zhang, X. Li, G. Shao, Stable composite of flower-like NiFe-layered double hydroxide nucleated on graphene oxide as an effective catalyst for oxygen reduction reaction, Int. J. Hydrogen Energy 44 (2019) 5912–5920, https://doi.org/10.1016/j.ijhydene.2019.01.075.
[82] D.M. Nguyen, M.H. Nguyen, Q.B. Bui, A novel electrocatalyst based on Fe 2 Ni 1 nanoparticles anchored nitrogen doped graphene nanosheets towards efficient oxygen reduction reaction, J. Alloys Compd. (2019) 734–742, https://doi.org/10.1016/j.jallcom.2018.12.041.
[83] K. Gong, D. Su, R.R. Adzic, Platinum-monolayer shell on AuNi0.5Fe nanoparticle core electrocatalyst with high activity and stability for the oxygen reduction reaction, J. Am. Chem. Soc. (2010) 14364–14366.
[84] M. Wang, Y. Yang, X. Liu, Z. Pu, Z. Kou, P. Zhu, S. Mu, The role of iron nitrides in the Fe-N-C catalysis system towards the oxygen reduction reaction, Nanoscale 9 (2017) 7641–7649, https://doi.org/10.1039/c7nr01925d.
[85] C.W.B. Bezerra, L. Zhang, K. Lee, H. Liu, A.L.B. Marques, E.P. Marques, H. Wang, J. Zhang, A review of Fe-N/C and Co-N/C catalysts for the oxygen reduction reaction, Electrochim. Acta 53 (2008) 4937–4951, https://doi.org/10.1016/j.electacta.2008.02.012.
[86] M. Wang, C. Zhang, T. Meng, Z. Pu, H. Jin, D. He, J. Zhang, S. Mu, Iron oxide and phosphide encapsulated within N,P-doped microporous carbon nanofibers as advanced tri-functional electrocatalyst toward oxygen reduction/evolution and hydrogen evolution reactions and zinc-air batteries, J. Power Sources 413 (2019) 367–375, https://doi.org/10.1016/j.jpowsour.2018.12.056.
[87] Y. Cheng, J. Liang, J.P. Veder, M. Li, S. Chen, J. Pan, L. Song, H.M. Cheng, C. Liu, S.P. Jiang, Iron oxide nanoclusters incorporated into iron phthalocyanine as highly active electrocatalysts for the oxygen reduction reaction, ChemCatChem 10 (2018) 475–483, https://doi.org/10.1002/cctc.201701183.
[88] D.J. Ham, J.S. Lee, Transition metal carbides and nitrides as electrode materials for low temperature fuel cells, Energies 2 (2009) 873–899, https://doi.org/10.3390/en20400873.
[89] X. Tian, J. Luo, H. Nan, H. Zou, R. Chen, T. Shu, X. Li, Y. Li, H. Song, S. Liao, R.R. Adzic, Transition metal nitride coated with atomic layers of Pt as a low-cost, highly stable electrocatalyst for the oxygen reduction reaction, J. Am. Chem. Soc. 138 (2016) 1575–1583, https://doi.org/10.1021/jacs.5b11364.
[90] J. Xie, Y. Xie, Transition metal nitrides for electrocatalytic energy conversion: opportunities and challenges, Chem. - A Eur. J. 22 (2016) 3588–3598, https://doi.org/10.1002/chem.201501120.
[91] V. Trapp, P. Christensen, A. Hamnett, New catalysts for oxygen reduction based on transition-metal sulfides, J. Chem. Soc. - Faraday Trans. 92 (1996) 4311–4319, https://doi.org/10.1039/ft9969204311.
[92] V.G. Khomenko, V.Z. Barsukov, A.S. Katashinskii, The catalytic activity of conducting polymers toward oxygen reduction, Electrochim. Acta 50 (2005) 1675–1683, https://doi.org/10.1016/j.electacta.2004.10.024.
[93] Y. Yuan, J. Ahmed, S. Kim, Polyaniline/carbon black composite-supported iron phthalocyanine as an oxygen reduction catalyst for microbial fuel cells, J. Power Sources 196 (2011) 1103–1106, https://doi.org/10.1016/j.jpowsour.2010.08.112.
[94] N. Gavrilov, I.A. Pašti, M. Mitrić, J. Travas-Sejdić, G. Ćirić-Marjanović, S.V. Mentus, Electrocatalysis of oxygen reduction reaction on polyaniline-derived nitrogen-doped carbon nanoparticle surfaces in alkaline media, J. Power Sources 220 (2012) 306–316, https://doi.org/10.1016/j.jpowsour.2012.07.119.
[95] Y. Zhang, X. Zhuang, Y. Su, F. Zhang, X. Feng, Polyaniline nanosheet derived nitrogen-doped carbon nanosheets as efficient metal-free catalysts for oxygen reduction reaction, J. Mater. Chem. A. 2 (2014) 7742–7746, https://doi.org/10.1039/c4ta00814f.
[96] M. Ferrandon, A.J. Kropf, D.J. Myers, K. Artyushkova, U. Kramm, P. Bogdanoff, G. Wu, C.M. Johnston, P. Zelenay, Multitechnique characterization of a polyaniline-iron-carbon oxygen reduction catalyst, J. Phys. Chem. C. 116 (2012) 16001–16013, https://doi.org/10.1021/jp302396g.
[97] Z. Lin, G.H. Waller, Y. Liu, M. Liu, C. ping Wong, 3D Nitrogen-doped graphene prepared by pyrolysis of graphene oxide with polypyrrole for electrocatalysis of oxygen reduction reaction, Nano Energy 2 (2013) 241–248, https://doi.org/10.1016/j.nanoen.2012.09.002.
[98] Q. Liu, Z. Pu, C. Tang, A.M. Asiri, A.H. Qusti, A.O. Al-Youbi, X. Sun, N-doped carbon nanotubes from functional tubular polypyrrole: a highly efficient electrocatalyst for oxygen reduction reaction, Electrochem. Commun 36 (2013) 57–61, https://doi.org/10.1016/j.elecom.2013.09.013.
[99] L. Osmieri, C. Zafferoni, L. Wang, A.H.A. Monteverde Videla, A. Lavacchi, S. Specchia, Polypyrrole-derived Fe − Co − N − C catalyst for the oxygen reduction reaction: performance in alkaline hydrogen and ethanol fuel cells, ChemElectroChem 5 (2018) 1954–1965, https://doi.org/10.1002/celc.201800420.
[100] I.M. Minisy, N. Gavrilov, U. Acharya, Z. Morávková, C. Unterweger, M. Mičušík, S.K. Filippov, J. Kredatusová, I.A. Pašti, S. Breitenbach, G. Ćirić-Marjanović, J. Stejskal, P. Bober, Tailoring of carbonized polypyrrole nanotubes core by different polypyrrole shells for oxygen reduction reaction selectivity modification, J. Colloid Interface Sci. 551 (2019) 184–194, https://doi.org/10.1016/j.jcis.2019.04.064.
[101] R.N. Singh, B. Lai, M. Malviya, Electrocatalytic activity of electrodeposited composite films of polypyrrole and CoFe2O4 nanoparticles towards oxygen reduction reaction, Electrochim. Acta 49 (2004) 4605–4612, https://doi.org/10.1016/j.electacta.2004.05.015.
[102] M.T. Giacomini, M. Balasubramanian, S. Khalid, J. McBreen, E.A. Ticianellia, Characterization of the activity of palladium-modified polythiophene electrodes for the hydrogen oxidation and oxygen reduction reactions, J. Electrochem. Soc. 150 (2003) A588, https://doi.org/10.1149/1.1562932.
[103] M.T. Giacomini, E.A. Ticianelli, J. McBreen, M. Balasubramanian, Oxygen reduction on supported platinum/polythiophene electrocatalysts, J. Electrochem. Soc. 148 (2002) A323, https://doi.org/10.1149/1.1354610.
[104] S.R. Sulub, W. Martínez-Millán, M.A. Smit, Study of the catalytic activity for oxygen reduction of polythiophene modified with cobalt or nickel, Int. J. Electrochem. Sci. 4 (2009) 1015–1027.
[105] S.J. Han, H.J. Jung, J.H. Shim, H.C. Kim, S.J. Sung, B. Yoo, D.H. Lee, C. Lee, Y. Lee, Non-platinum oxygen reduction electrocatalysts based on carbon-supported metal-polythiophene composites, J. Electroanal. Chem. 655 (2011) 39–44,

https://doi.org/10.1016/j.jelechem.2011.02.012.
[106] R.P. Kingsborough, T.M. Swager, Electrocatalytic conducting polymers: oxygen reduction by a polythiophene-cobalt salen hybrid, Chem. Mater. 12 (2000) 872–874, https://doi.org/10.1021/cm9907099.
[107] A.D. Chowdhury, N. Agnihotri, P. Sen, A. De, Conducting CoMn2O4 - PEDOT nanocomposites as catalyst in oxygen reduction reaction, Electrochim. Acta 118 (2014) 81–87, https://doi.org/10.1016/j.electacta.2013.11.165.
[108] S.K. Singh, X. Crispin, I.V. Zozoulenko, Oxygen reduction reaction in conducting polymer PEDOT: density functional theory study, J. Phys. Chem. C. 121 (2017) 12270–12277, https://doi.org/10.1021/acs.jpcc.7b03210.
[109] R. Kerr, C. Pozo-Gonzalo, M. Forsyth, B. Winther-Jensen, Influence of the polymerization method on the oxygen reduction reaction pathway on pedot, ECS Electrochem. Lett. 2 (2013) F29–F31, https://doi.org/10.1149/2.010303eel.
[110] J.A. Vigil, T.N. Lambert, K. Eldred, Electrodeposited MnOx/pedot composite thin films for the oxygen reduction reaction, ACS Appl. Mater. Interfaces 7 (2015) 22745–22750, https://doi.org/10.1021/acsami.5b07684.
[111] A. Morozan, P. Jégou, S. Campidelli, S. Palacin, B. Jousselme, Relationship between polypyrrole morphology and electrochemical activity towards oxygen reduction reaction, Chem. Commun. 48 (2012) 4627–4629, https://doi.org/10.1039/c2cc30871a.
[112] K. Lee, L. Zhang, H. Lui, R. Hui, Z. Shi, J. Zhang, Oxygen reduction reaction (ORR) catalyzed by carbon-supported cobalt polypyrrole (Co-PPy/C) electrocatalysts, Electrochim. Acta 54 (2009) 4704–4711, https://doi.org/10.1016/j.electacta.2009.03.081.
[113] H.N. Cong, K. El Abbassi, J.L. Gautier, P. Chartier, Oxygen reduction on oxide/polypyrrole composite electrodes: effect of doping anions, Electrochim. Acta 50 (2005) 1369–1376, https://doi.org/10.1016/j.electacta.2004.08.025.
[114] D.G. Lee, S.H. Kim, S.H. Joo, H. Il Ji, H. Tavassol, Y. Jeon, S. Choi, M.H. Lee, C. Kim, S.K. Kwak, G. Kim, H.K. Song, Polypyrrole-assisted oxygen electrocatalysis on perovskite oxides, Energy Environ. Sci. 10 (2017) 523–527, https://doi.org/10.1039/c6ee03501a.
[115] S. Zaromb, The use and behavior of aluminum anodes in alkaline primary batteries, J. Electrochem. Soc. 109 (2007) 1125, https://doi.org/10.1149/1.2425257.
[116] L. Bockstie, D. Trevethan, S. Zaromb, Control of Al corrosion in caustic solutions, J. Electrochem. Soc. 110 (2007) 267, https://doi.org/10.1149/1.2425727.
[117] M. Park, Development of anodes for aluminium/air batteries – solution phase inhibition of corrosion, 20 (1990) 405–417.
[118] D.R. Egan, C. Ponce De León, R.J.K. Wood, R.L. Jones, K.R. Stokes, F.C. Walsh, Developments in electrode materials and electrolytes for aluminiumeair batteries, J. Power Sources 236 (2013) 293–310, https://doi.org/10.1016/j.jpowsour.2013.01.141.
[119] M. Akmal, R. Othman, M.H. Ani, Comparative electrochemical performance characteristics of aluminium-air cell employing seawater and nacl electrolytes, Adv. Mater. Res 701 (2013) 314–318, https://doi.org/10.4028/www.scientific.net/amr.701.314.
[120] S. Gudić, J. Radošević, I. Smoljko, M. Kliškić, Cathodic breakdown of anodic oxide film on Al and Al-Sn alloys in NaCl solution, Electrochim. Acta 50 (2005) 5624–5632, https://doi.org/10.1016/j.electacta.2005.03.041.
[121] H.A. El Shayeb, F.M.A. El Wahab, S.Z. El Abedin, Electrochemical behaviour of Al, Al ± Sn, Al ± Zn and Al ± Zn ± Sn alloys in chloride solutions containing stannous ions, Corros. Sci. 43 (2001) 1071–1080.
[122] S. Gudić, I. Smoljko, M. Kliškić, Electrochemical behaviour of aluminium alloys containing indium and tin in nacl solution, Mater. Chem. Phys. 121 (2010) 561–566, https://doi.org/10.1016/j.matchemphys.2010.02.040.
[123] H.A.N.G. Guangchuan, Neutral electrolyte aluminum air battery with open configuration, 2 (2006) 360–363.
[124] N. Kuzmanic, Electrochemical properties of aluminium anodes for Al / air batteries with aqueous sodium chloride electrolyte, (2012) 969–977. 10.1007/s10800-012-0465-6.
[125] L. Fan, H. Lu, J. Leng, Performance of fine structured aluminum anodes in neutral and alkaline electrolytes for Al-air batteries, Electrochim. Acta 165 (2015) 22–28, https://doi.org/10.1016/j.electacta.2015.03.002.
[126] E. Budevski, I. Iliev, A. Kaisheva, A. Despić, K. Krsmanović, Investigations of a large-capacity medium-power saline aluminium-air battery, J. Appl. Electrochem. 19 (1989) 323–330, https://doi.org/10.1007/BF01015230.
[127] M. Rota, C. Comninellis, S. Moller, F. Holzer, O. Haas, Bipolar Al/O2 battery with planar electrodes in alkaline and acidic electrolytes, J. Appl. Electrochem. 25 (1995) 114–121, https://doi.org/10.1007/BF00248167.
[128] J. Ma, J. Wen, Q. Li, Q. Zhang, Electrochemical polarization and corrosion behavior of Al e Zn e In based alloy in acidity and alkalinity solutions, Int. J. Hydrog. Energy 38 (2013) 14896–14902, https://doi.org/10.1016/j.ijhydene.2013.09.046.
[129] J. Ma, J. Wen, Q. Li, Q. Zhang, Effects of acidity and alkalinity on corrosion behaviour of Al e Zn e Mg based anode alloy, J. Power Sources 226 (2013) 156–161, https://doi.org/10.1016/j.jpowsour.2012.10.075.
[130] T.H. Orem, Influence of crystallographic orientation on the corrosion rate of aluminum in acids and alkalies, J. Res. Natl. Bur. Stand. 58 (1934) 157, https://doi.org/10.6028/jres.058.022 (1957).
[131] C. Zhu, H. Yang, A. Wu, D. Zhang, L. Gao, T. Lin, Modified alkaline electrolyte with 8-hydroxyquinoline and zno complex additives to improve Al-air battery, J. Power Sources 432 (2019) 55–64, https://doi.org/10.1016/j.jpowsour.2019.05.077.
[132] M.A. Deyab, 1-Allyl-3-methylimidazolium bis(trifluoromethylsulfonyl)imide as an effective organic additive in aluminum-air battery, Electrochim. Acta. 244 (2017) 178–183, https://doi.org/10.1016/j.electacta.2017.05.116.
[133] J. Liu, D. Wang, D. Zhang, L. Gao, T. Lin, Synergistic effects of carboxymethyl cellulose and ZnO as alkaline electrolyte additives for aluminium anodes with a view towards Al-air batteries, J. Power Sources 335 (2016) 1–11, https://doi.org/10.1016/j.jpowsour.2016.09.060.
[134] D.P. Wang, D.Q. Zhang, K.Y. Lee, L.X. Gao, Performance of AA5052 alloy anode in alkaline ethylene glycol electrolyte with dicarboxylic acids additives for aluminium-air batteries, J. Power Sources 297 (2015) 464–471, https://doi.org/10.1016/j.jpowsour.2015.08.033.
[135] D. Wang, H. Li, J. Liu, D. Zhang, L. Gao, L. Tong, Evaluation of AA5052 alloy anode in alkaline electrolyte with organic rare-earth complex additives for aluminium-air batteries, J. Power Sources 293 (2015) 484–491, https://doi.org/10.1016/j.jpowsour.2015.05.104.
[136] D. Gelman, I. Lasman, S. Elfimchev, D. Starosvetsky, Y. Ein-Eli, Aluminum corrosion mitigation in alkaline electrolytes containing hybrid inorganic/organic inhibitor system for power sources applications, J. Power Sources 285 (2015) 100–108, https://doi.org/10.1016/j.jpowsour.2015.03.048.
[137] J. Lu, L. Li, J. Park, Y. Sun, F. Wu, K. Amine, Aprotic and aqueous Li − O 2 batteries, (n.d.).
[138] L. Hu, S.S. Zhang, Z. Zhang, Electrolytes for lithium and lithium-ion batteries, Green Energy Technol. 172 (2015) 231–261, https://doi.org/10.1007/978-3-319-15458-9_8.
[139] V.S. Bryantsev, V. Giordani, W. Walker, M. Blanco, S. Zecevic, K. Sasaki, J. Uddin, D. Addison, G.V. Chase, 2011 Predicting solvent stability in aprotic electrolyte Li–air batteries: nucleophilic substitution by the superoxide anion radical (O2•–), J. Phys. Chem. A (2011) 12399–12409.
[140] D. Gelman, B. Shvartsev, Y. Ein-Eli, Aluminum-air battery based on an ionic liquid electrolyte, J. Mater. Chem. A. 2 (2014) 20237–20242, https://doi.org/10.1039/c4ta04721d.
[141] M. Kar, T.J. Simons, M. Forsyth, D.R. MacFarlane, Ionic liquid electrolytes as a platform for rechargeable metal-air batteries: a perspective, Phys. Chem. Chem. Phys. 16 (2014) 18658–18674, https://doi.org/10.1039/c4cp02533d.
[142] H. Wang, S. Gu, Y. Bai, S. Chen, F. Wu, C. Wu, High-Voltage and noncorrosive ionic liquid electrolyte used in rechargeable aluminum battery, ACS Appl. Mater. Interfaces 8 (2016) 27444–27448, https://doi.org/10.1021/acsami.6b10579.
[143] C. Ferrara, V. Dall'Asta, V. Berbenni, E. Quartarone, P. Mustarelli, Physicochemical characterization of AlCl3-1-ethyl-3-methylimidazolium chloride ionic liquid electrolytes for aluminum rechargeable batteries, J. Phys. Chem. C. 121 (2017) 26607–26614, https://doi.org/10.1021/acs.jpcc.7b07562.
[144] D. Gelman, B. Shvartsev, I. Wallwater, S. Kozokaro, V. Fidelsky, A. Sagy, A. Oz, S. Baltianski, Y. Tsur, Y. Ein-Eli, An aluminum – ionic liquid interface sustaining a durable Al-air battery, J. Power Sources 364 (2017) 110–120, https://doi.org/10.1016/j.jpowsour.2017.08.014.
[145] G.M. Wu, S.J. Lin, C.C. Yang, Alkaline Zn-air and Al-air cells based on novel solid PVA/PAA polymer electrolyte membranes, J. Memb. Sci. 280 (2006) 802–808, https://doi.org/10.1016/j.memsci.2006.02.037.
[146] M. Mokhtar, E.H. Majlan, A. Ahmad, S.M. Tasirin, W.R.W. Daud, Effect of ZnO filler on PVA-Alkaline solid polymer electrolyte for aluminum-air battery applications, J. Electrochem. Soc. 165 (2018) A2483–A2492, https://doi.org/10.1149/2.0381811jes.
[147] C.C. Yang, S.J. Lin, Alkaline composite PEO-PVA-glass-fibre-mat polymer electrolyte for Zn-air battery, J. Power Sources 112 (2002) 497–503, https://doi.org/10.1016/S0378-7753(02)00438-X.
[148] D. Zhang, R. Li, T. Huang, A. Yu, Novel composite polymer electrolyte for lithium air batteries, J. Power Sources 195 (2010) 1202–1206, https://doi.org/10.1016/j.jpowsour.2009.08.063.
[149] M.J. Tan, B. Li, P. Chee, X. Ge, Z. Liu, Y. Zong, X.J. Loh, Acrylamide-derived freestanding polymer gel electrolyte for flexible metal-air batteries, J. Power Sources 400 (2018) 566–571, https://doi.org/10.1016/j.jpowsour.2018.08.066.
[150] Z. Zhang, C. Zuo, Z. Liu, Y. Yu, Y. Zuo, Y. Song, All-solid-state Al e air batteries with polymer alkaline gel electrolyte, J. Power Sources 251 (2014) 470–475, https://doi.org/10.1016/j.jpowsour.2013.11.020.
[151] F. Migliardini, T.M. Di Palma, M.F. Gaele, P. Corbo, Solid and acid electrolytes for Al-air batteries based on xanthan-HCl hydrogels, J. Solid State Electrochem 22 (2018) 2901–2916, https://doi.org/10.1007/s10008-018-4003-2.
[152] T.M. Di Palma, F. Migliardini, M.F. Gaele, P. Corbo, Physically cross-linked xanthan hydrogels as solid electrolytes for Al/air batteries, Ionics (Kiel) (2019), https://doi.org/10.1007/s11581-019-02965-y.
[153] T.M. Di Palma, F. Migliardini, D. Caputo, P. Corbo, Xanthan and κ-carrageenan based alkaline hydrogels as electrolytes for Al/air batteries, Carbohydr. Polym 157 (2017) 122–127, https://doi.org/10.1016/j.carbpol.2016.09.076.
[154] X. Zhang, S.H. Yang, H. Knickle, Novel operation and control of an electric vehicle aluminum/air battery system, J. Power Sources 128 (2004) 331–342, https://doi.org/10.1016/j.jpowsour.2003.09.058.
[155] B.J. Hopkins, Y. Shao-Horn, D.P. Hart, Suppressing corrosion in primary aluminum-air batteries via oil displacement, Science 362 (2018) 658–661, https://doi.org/10.1126/science.aat9149.

J. Inst. Eng. India Ser. B
https://doi.org/10.1007/s40031-020-00425-0

ORIGINAL CONTRIBUTION

ANFIS-Based Control of Multi-objective Grid Connected Inverter and Energy Management

Shikha Gupta[1] · **Rachana Garg**[1] · **Alka Singh**[1]

Received: 22 November 2018 / Accepted: 5 February 2020
© The Institution of Engineers (India) 2020

Abstract As a consequence of fast socio-economic progress, the requirement of auxiliary energy sources is creating new opportunities in the field of renewable energy sources (RES). This paper presents a hybrid photovoltaic (PV)–fuel cell (FC) energy structure for grid-connected applications. The key challenges associated with the integration of RES are managing harmonic distortions, voltage fluctuations and power sharing. To mitigate these problems and to enhance the overall performance of the system, multi-objective inverter based on hybrid intelligent controller, adaptive neuro-fuzzy inference system has been designed. In the proposed system, PV acts as a primary energy source, while FC serves as a secondary energy source. An overall power management strategy has been designed to manage power flows among the RES, load and grid. The effectiveness of the proposed multi-objective inverter control and energy management of the system is validated under MATLAB/Simulink platform.

Keywords Voltage source converter (VSC) · Fuel cell (FC) · Photovoltaic (PV) · Adaptive neuro-fuzzy inference system (ANFIS) · Power flow management

✉ Shikha Gupta
shikhaguptadtu@gmail.com

Rachana Garg
rachana16100@yahoo.co.in

Alka Singh
alkasingh.dr@gmail.com

[1] Department of Electrical Engineering, Delhi Technological University, Shahbad, Daulatpur, Delhi 110049, India

List of Symbols

$q^c_{H_2}$	Consumed hydrogen flow (kmol/s)
$q^i_{H_2}$	Flow of hydrogen intake (kmol/s)
I^c_{fc}	Feedback current of fuel cell stake (A)
N	Series cell numbers in stack
F	Faraday constant (C/kmol)
R	Universal gas constant (J/(kmol K))
T	Absolute temperature of (K)
P_{H_2}	Hydrogen gas partial pressure (atm)
n_{H_2}	Number of hydrogen moles in the anode channel
$q^o_{H_2}$	Output hydrogen flow (kmol/s)
K_{H_2}	Hydrogen flow valve molar constant (kmol/(s atm))
K_r	Valve constant of anode [$\sqrt{}$kmol kg(atm s)$^{-1}$]
r	Ohmic losses of solid oxide fuel cell stack (ohm)
E_o	Thermodynamics potential (V)
p_{H_2O}	Water partial pressure (atm)
p_{O_2}	Oxygen partial pressure (atm)
I_{ph}	Solar cell's photodiode current (A)
I_o	Diode saturation current (A)
I_{rr}	Insolation of Sun (W/m^2)
I_{sc}	Short-circuit current (A)
R_{sh}	Shunt resistance (Ω)
R_{se}	Series resistance (Ω)
K	Boltzmann constant (1.38*10–38 J/K)
Q	Electron charge (1.6*10–19 C)
T_{cell}	Cell's working temperature (K)
T_{ref}	Reference temperature (K)
I_{PV}	PV output current (DC)(kW)
V_{PV}	PV output voltage (DC) (V)
I_{FC}	FC stack output current in DC (A)
V_{FC}	FC output voltage in DC (V)
V	Solar cell terminal voltage (V)

Published online: 18 February 2020

V_g	Utility grid voltage (V)
I_g	Utility grid current (A)
I_{la}, I_{lb}, I_{lc}	Load current of phase 'a', 'b', 'c', respectively (A)
V_{dc}	DC bus voltage (V)
I_{VSC}	Current delivered by VSC (A)
P_L	Power demanded by the load (kW)
P_{dcb}	Power generated at DC bus (kW)
P_g	Power delivered or fed to the grid (kW)
P_{PV}	DC power generation of PV (kW)
P_{fc}	DC power generation of fuel cell (kW)

Introduction

Policy reforms and environmental concerns in tandem with continuous technological upgrades in power electronics are creating new opportunities in the growth of distributed renewable energy system. One attractive and sustainable alternative to meet continuous rising energy demand is renewable energy sources (RES) which can help in improving the fuel savings, energy efficiency and reliability [1]. The power system may contain several RES as alternative power sources, viz. solar cells, wind turbines, micro-turbines (natural gas), fuel cells (FC) and storage batteries. Rapid advancements in FC technology and global acceptability of photovoltaic (PV) cells have made these sources favourable options among available RES [2]. Hybrid architecture containing PV and FC has been reported in different research papers [3–8]. PV cells and FC cells are low voltage DC source but can generate enough DC voltage with the appropriate combination of cells, and this DC voltage can be converted into AC voltage through voltage source converters (VSC).

Energy generation and consumption need to be matched and coordinated well which requires the need for proper energy management approach. There are various approaches reported in the literature for energy management in RES-integrated systems such as constant monitoring of currents and voltages (power monitoring)-based energy management [9, 10], droop control technique-based energy management [11, 12], DC-link voltage measurement-based energy management [13, 14], bio-inspired-based energy management algorithms [15] and cloud computing energy management approach [16]. In this paper, an energy management algorithm based on continuous monitoring of current is proposed. This approach has the advantage of the lower number of sensors required in comparison with proposed approaches discussed in [9, 10], simple in computation in comparison with approaches [11–14] and easier to implement in contrast to approaches [11, 12, 15, 16].

High penetration of RES in the distribution system brings new challenges in terms of reliability, stability, power flow and efficiency of the system [17]. These challenges can be substantially addressed through inverter control [18]. Several benefits have been reported [19–23] for the integration of RES to a common DC bus which includes greater efficiency, removal of frequency cost-effectiveness and ability to operate for long distances. Integration of common DC bus with utility power delivery network involves major concerns such as active power control, the unregulated voltage drop at utility side and power quality (PQ) distortions at the customer side. In such type of systems, two working modes of inverters are defined as grid-forming and the grid-feeding mode [24]. Grid-feeding VSC can also be coded as grid following mode or PQ control mode [25]. In the grid-feeding mode, VSC is operated as a power generator source which delivers a predefined amount of active and reactive power to the source or grid [26]. Nowadays, mostly inverter-based RES like PV, wind and FC generation systems function as current or power sources in grid-following mode [27]. VSC inverters can be controlled to achieve multi-objectives, viz. extract generated power, manage power sharing, voltage regulation at DC side, and act as power quality conditioners. Due to multi-objective features, these inverters are cost-effective and occupy less space as compared to multiple inverter systems [28].

PQ standards have to be followed for interfacing the RES to the grid and to supply good quality power at the consumer end. The grid interfaced common DC bus system is reported in the literature; however, power quality along with the coordinated control has received less attention. The focus of this paper is also to design an ANFIS controller and observed its performance for steady-state and transient conditions in the presence of RES.

A conventional PI controller cannot regulate the voltage of DC bus successfully under a wide variety of dynamic operating conditions [29]. Under such conditions, an intelligent controller like a fuzzy controller is required. There are two major types of fuzzy control reported in various studies, i.e. the Mamdani type [30] and the Takagi–Sugeno (TS) [31, 32] type. Both can be segregated on the basis of the formulation of fuzzy rules. However, there are no standard methods available to design the rule base, but TS system significantly lessens the number of regulating parameters requisite by the rule-based Mamdani-type system. Moreover, to minimize the error, improvement in the tuning of membership functions (MFs) is required. A unique class of hybrid intelligent controller based on adaptive neuro-fuzzy inference system (ANFIS) is proposed to eliminate the limitations of conventional and intelligent controllers. Since ANFIS is established on the basis of neural networks and fuzzy logic control principles,

it offers dual advantages in a single model. In [27], developed system integrated with multiple inverters, and the proposed system uses one inverter which reduced the total cost of the system. In [29], ANFIS-based UPQC is developed, and this uses a grouping of series and shunt active power filter which is costlier than the shunt power filters; moreover, no active power source has been integrated to the system. In [33], Takagi–Sugeno has been implemented to DC bus control, and ANFIS gives better results for DC bus regulation and less complex in implementation. In [34], no active energy source has been integrated, so the system is acting only as shunt power compensator which added the cost of the system, whereas the proposed system is capable to deliver active power along with the reactive power compensation.

The prime objective of the developed system is to design a system having multifunctional VSC control along with energy management algorithm. The key objective features of the proposed system are:

1. To regulate the voltage at DC bus of the inverter using a superior ANFIS controller designed to handle variation in loads and generated powers.
2. To mitigate power quality problems in case of unbalance and nonlinear loads.
3. To maintain a balanced three-phase voltage at the point of common coupling (PCC) in case of unbalanced loads.
4. To supply active and reactive power requisite by the load and maintain unity power factor (UPF). The controller is designed such that the utility grid will only inject or absorb active power when both the primary and secondary RES have exhausted. Moreover, the reactive power demanded from the supply is negligible and met wholly from the inverter.
5. To achieve smooth and coordinated power sharing among the load, RES and grid using current-based energy management approach. The approach can be further extended to include more sources also.

Multi-objective VSC based on synchronous reference frame control technique is developed to achieve the objectives. The control idea is built on d-q transformation and then generating reference current signal which are further followed by an IGBT-based inverter. In the proposed system, FC is integrated with PV as a complementary energy source and together integrated to a common DC bus as shown in Fig. 1 which allows optimal utilization of RES and manages power allocation between energy sources and grid as per load requirement. The suggested multi-objective control scheme can be expanded to include additional RES systems without the major change in control topology and complexity.

System description

Figure 2 represents the architecture of the proposed system wherein 8 kW PV and 2 kW FC have been integrated to 800 V DC bus through separate unidirectional DC–DC boost converter control logic. The DC bus is interfaced to the utility via three-phase VSC. LCL filter is connected at the PCC. Simplified but effective perturbation and observations (PO) scheme is utilized to evacuate maximum power from PV. PV is considered as a primary energy source, while FC stack is used to act as a secondary energy source. This secondary energy source delivers power only when the load demand exceeds the power generation of primary source. In case of low load power demand, the surplus power is injected into the utility grid. This active power management is designed to be handled by the VSC control algorithm. Reactive power requirement of the load is catered through capacitor fed VSC. The complete control algorithm of VSC maintains source current harmonics within the prescribed limit. Discussion on detail modelling of the RES and DC–DC boost converter has not been covered in this paper due to well-established technology and reported in various studies, viz. [32–35].

PV Solar Cell Modelling

A mathematical model based on solar cell's singular diode (WS-50) is designed and can be represented by Eq. (1–2). The developed model can be implemented for any type of array structure through mathematical product between series (N_{ser}) and parallel cells (N_{par}) count as per Eq. (3) [33].

$$I = I_{ph} - I_0\left[e^{\frac{q(V+IR_{se})}{aKT}} - 1\right] - \frac{(V + IR_{se})}{R_{sh}} \tag{1}$$

$$I_{ph} = I_{sc*}\frac{I_{rr}}{1000^*}[1 + (T_{cell} - T_{ref}) * K \tag{2}$$

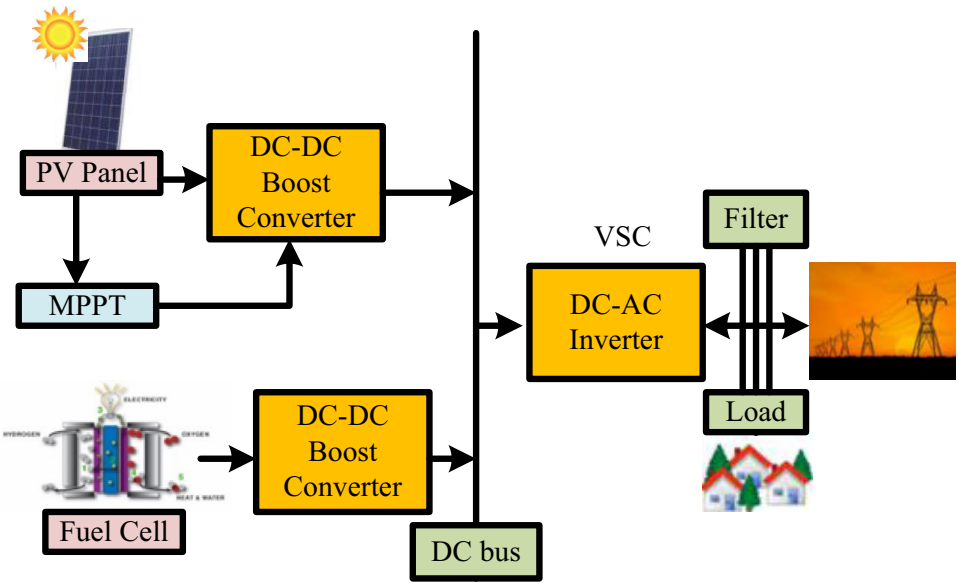
$$I = I_{ph}N_{par} - I_0N_{par}\left[e^{\left(\frac{q\left(V+IR_{se}\left(N_{ser}/N_{par}\right)\right)}{aKTN_{ser}}\right)} - 1\right] - \frac{V + R_{se}\left(\frac{N_{ser}}{N_{par}}\right)I}{R_{sh}\left(\frac{N_{ser}}{N_{par}}\right)} \tag{3}$$

where I_{ph} denotes photodiode current (A); I_0 represents diode's saturation current (A); I_{rr} indicates Sun insolation (W/m^2); V represents solar cell terminal voltage (V) at the output.

Fuel Cell Modelling

The solid oxide fuel cell (SOFC) model has been developed [34], assuming that hydrogen and oxygen are fed to stacks, the constant temperature is considered and with the

Fig. 1 System configuration



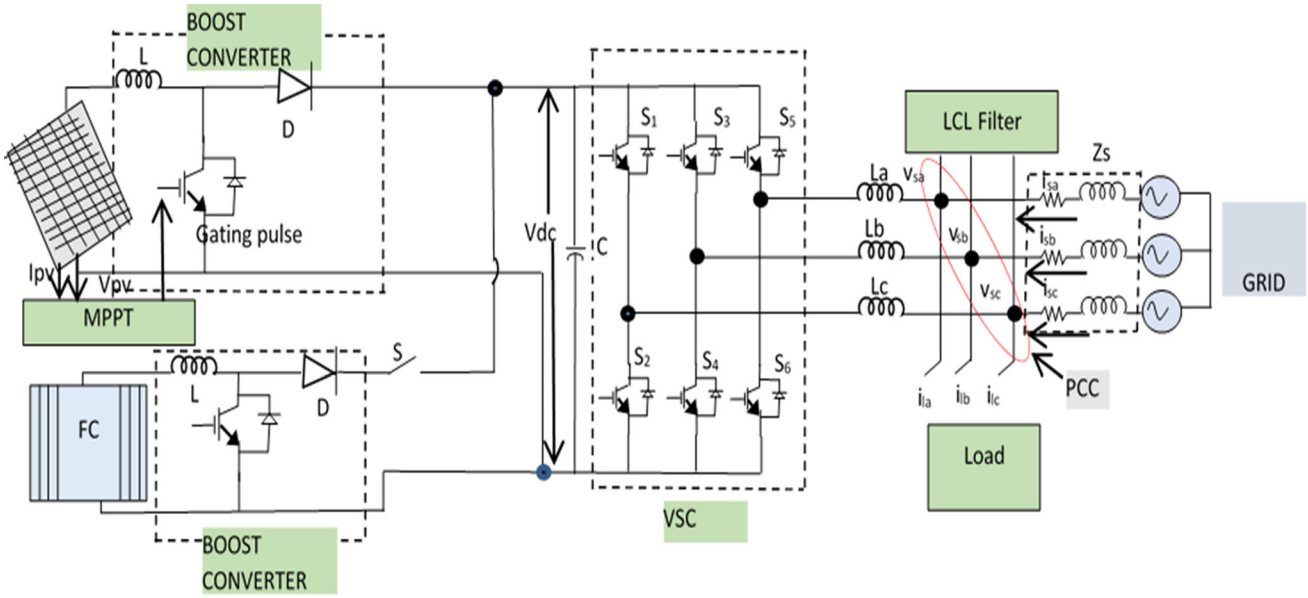


Fig. 2 Developed system architecture

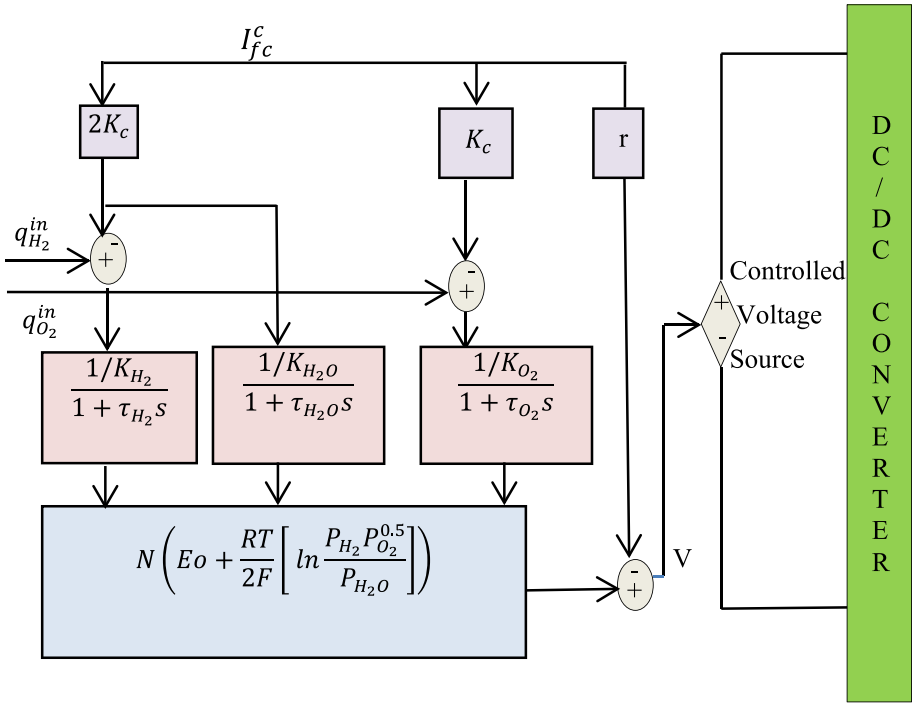
assumption that only ohmic losses are present. The SOFC model is developed on the bases of applied Nernst's equation and Ohm's law. Formulation of stack voltage is given as follows [34]:

$$V = N\left(E_o + \frac{RT}{2F}\left[\ln\frac{P_{H_2}P_{O_2}^{0.5}}{P_{H_2O}}\right]\right) - rI_{fc}^{c} \quad (4)$$

Figure 3 shows the SOFC stack dynamic model developed using the MATLAB/Simulink. Detail formulation of the presented model in Fig. 3 has been covered in the literature [34]. The output of stack voltage is linked to controlled voltage source, and further the DC–DC boost converter is integrated to boost up the voltage to 800 V.

VSC Control Design

VSC control algorithm is developed to achieve mitigation of harmonics in grid current, load balancing and operation under unity power factor voltage. This control arrangement ensures that the grid injects only the real power required by the load. In the proposed work, the synchronous reference frame (SRF) theory [35] is used to control the VSC. System controller function diagram is depicted in Fig. 4. The sensed load currents have been converted into two-phase



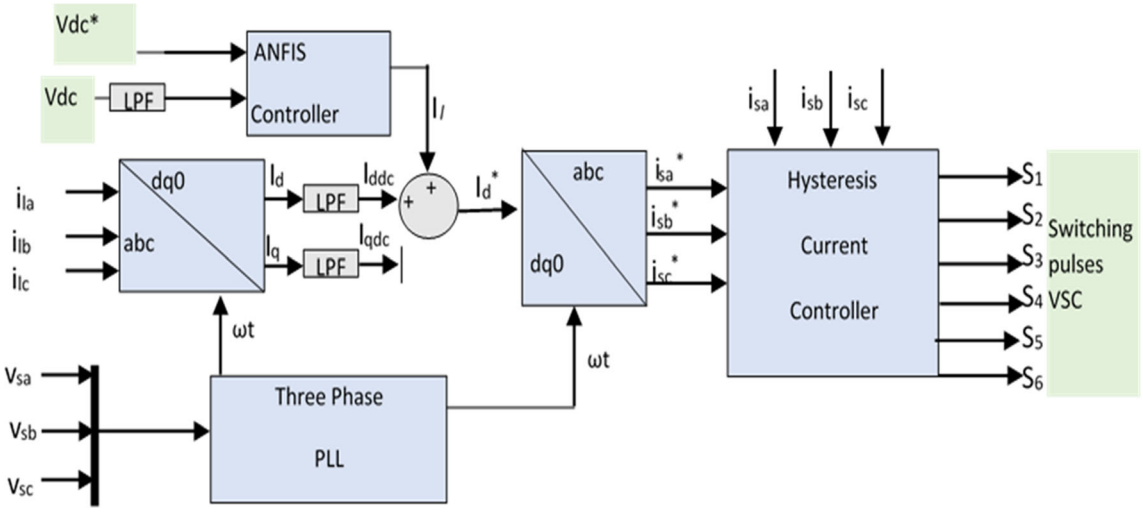


Fig. 3 SOFC stack dynamic model

Fig. 4 Control algorithm for VSC based on ANFIS controller

static coordinate through a–b–c to d–q–o transforming blocks with the usage of 'sine and cosine' signals which are generated through phase-locked loop (PLL). PLL evaluates the angle and maintains synchronization with supply voltage.

ANFIS controller is developed for maintaining DC bus voltage fix at a predefined value during dynamics of load and RES. Reference currents for the grid are generated by sensing the three-phase load currents and voltages at PCC. The controller is designed with the aim to the generation of d-axis component of load current along with losses of the inverter which will be provided by the VSC. The output of the ANFIS controller represents the switching losses. The generated reference grid currents must remain in the same phase as the voltage at PCC, and it can be acquired by reverse Park's transformation.

$$I_{\mathrm{d}}^{*} = I_{\mathrm{ddc}} + I_{\mathrm{l}} \tag{5}$$

Now, to generate the switching pulses, obtained reference grid currents and estimated source current pass through hysteresis current controller (HCC).

Energy Management System

This paper also proposes a simplified technique of energy management and power allocation. Power decisions have been taken on the basis of current calculations. The three-phase load currents have been converted to a single quantity (I_{l}) through the equation:

$$I_{\mathrm{l}} = \sqrt{\frac{2}{3}\left(i_{\mathrm{la}}^2 + i_{\mathrm{lb}}^2 + i_{\mathrm{lc}}^2\right)} \tag{6}$$

The complete load management scheme for the proposed system is shown in Fig. 5. System operation modes are described as:

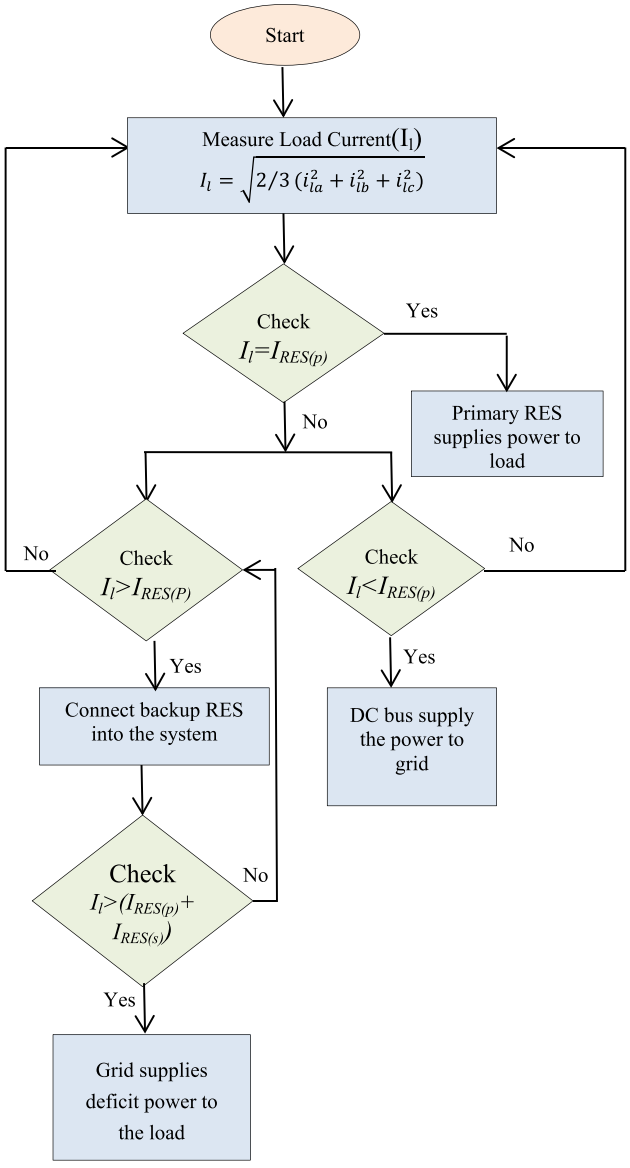


Fig. 5 Energy management algorithm

1. If load demand (I_{l}) is more than generated current by PV (I_{PV}), the FC (I_{FC}) will play an active role and will be connected at DC bus. The load equation under this node can be written as:

$$I_{\mathrm{l}} = I_{\mathrm{PV}} + I_{\mathrm{FC}} \tag{7}$$

2. If the current generated by PV is greater than load demand, the surplus current is delivered to the utility grid (I_{g}) and the current balances equation can be expressed as:

$$-I_{\mathrm{g}} = I_{\mathrm{PV}} - I_{\mathrm{l}} \tag{8}$$

3. If the generated PV and FC current together are not able to fulfil the requirement of the load (I_{l}), then utility grid will provide deficit requirement of the load. Therefore, the current equation under this node can be expressed as:

$$I_{\mathrm{g}} = I_{\mathrm{l}} - I_{\mathrm{PV}} - I_{\mathrm{FC}} \tag{9}$$

4. If the RES generation matches load demand, then the whole requirement of the load is supplied by RES only. The current balance equation is thus marked as:

$$I_{\mathrm{l}} = I_{\mathrm{PV}} + I_{\mathrm{FC}} \tag{10}$$

Considering the uncertainties arising due to PV generation, profiles program is formulated in order to maintain the supply–demand balance and more secondary energy sources are integrated into the system. The approach is generalized to integrate multiple RESs. The integration of multiple energy sources to the system changes the energy management system, which is generalized for the integration of more RES as:

$$\sum_{m=1}^{M} I_{\mathrm{l}} = \sum_{n=1}^{N} I_{\mathrm{RES}(p)} + \sum_{r=1}^{R} I_{\mathrm{RES}(S)} + \sum I_{\mathrm{grid}} \tag{11}$$

where the integration of $I_{RES(s)}$ is subjected to the availability of the primary RES-generated power and the requirement of the connected load. Here, m, n and r denote the number of connected loads, number of connected primary generation RESs and number of connected secondary RESs, respectively.

Design of ANFIS Controller to Control the DC Bus

A recently established soft computing hybrid intelligent controller, adaptive neuro-fuzzy inference system (ANFIS), has been implemented for the regulation of DC bus voltage. The ANFIS is an artificial neural network that uses a first-order Sugeno-type fuzzy inference system [29]. Since ANFIS integrates neural networks (learning and parallel data processing abilities) and fuzzy logic

(reasoning abilities), it offers the advantage of both in a single model. Typical architecture of five-layer feedforward network ANFIS is shown in Fig. 6 in which circular nodes symbolize to identify the fixed node and square symbolizes different adaptive abilities. It represents a multilayered feedforward network where each layer performs a particular function on the input signal. Designed ANFIS has dual inputs (x, y), dual membership functions (MFs) and a single output (z). The difference between actual and reference DC bus voltage considered an error (e) is one input x, and change in error (de) is second input y. Organization of the ANFIS in five layers and the function of each layer are specified.

In the first layer, each node (A_1, A_2, B_3, B_4) comprises the membership function allotted to each input (x and y). This layer is an adaptive node. The values of parameters of this layer change according to the error signal and generate the proper value of each membership function. Every node in this layer is characterized by its corresponding output function and stores the parameters to express a bell-shaped membership function that represents the profile of the linguistic variables (x and y). Layer 2 is also known as rule nodes; in this layer, the system recognizes the rules, and this is rule storage level. Each rule is represented by one node. In this layer, the outputs of the first layer have been multiplied with each other to determine the degree of fulfilment 'w_k' of the rule and forwarded to the next layer. Layer 3 is the average node layer; the third level calculates the regularized firing power of each rule, and a unit computes the relative degree of fulfilment for every rule. Layer 4 computes the consequent of the rule, and the junction point of this level is linked to all feed in junction points and with precisely single junction point in the third layer. Each junction in this layer computes the output for the rule. Finally, layer 5 computation of overall output is obtained by summing all incoming signals. The de-fuzzification process converts each fuzzy result into crisp output in layer 5 commonly known as output nodes. The feed out junction point estimates the ultimate output from the addition of all feed in signals coming from level 4.

Design of ANFIS for Voltage Regulation

In this work, ANFIS is used to maintain a constant DC bus of the grid-connected inverter. Neural network optimization has been used to generate a rule base for fuzzy logic control (FLC system). The MATLAB neuro-fuzzy toolbox has been used to control the FLC. To train the neural network, first, input–output data pairs have been collected and fed as an array to the toolbox, and this datum has been

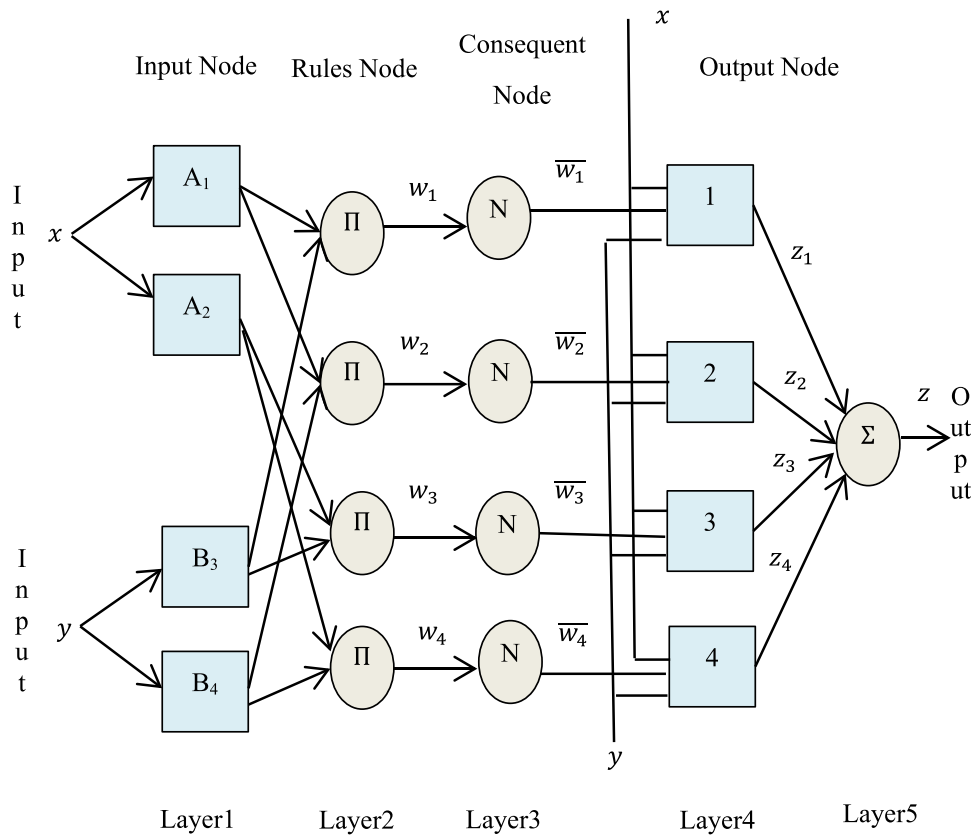


Fig. 6 Five-layer ANFIS feedforward network

used to generate FIS file using grid-partitioning method. The generated FIS file has two inputs and one output and has been fed to FLC. The rule base is Sugeno-based, and five Gaussian bell-shaped MFs have been used for both input and output as shown in Fig. 7. Both input and output MFs have same G_BELL shape MFs to conduct system training, and this type of function gives higher accuracy. The trained ANFIS holds five input MFs and 25 rule bases. The linguistic variable of error (e) signal from input variables of ANFIS is represented by In1mf1, In1mf2, In1mf3, In1mf4 and In1mf5. The linguistic variable of change in error (de) signal from output variables of ANFIS is represented by In2mf1, In2mf2, In2mf3, In2mf4 and In2mf5. Figure 7 shows the membership functions of input variables of ANFIS, linguistic variables and value ranges. The bell-shaped MFs were used in this work, while both input MFs have same G_BELL shape and distribution.

The output of Sugeno-type ANFIS contains real number; hence, the output cannot be represented like the input MFs, and the ANFIS output signal is made up of 25 real number ranging from − 3.515 to 0.9328. The rule base is tabulated in Table 1. MF parameters must be tuned by the training data. To update the weights of epoch, adaptive error back-propagation has been used. Training set (70%) and validation set (30%) are two sets, and this includes the testing dataset (15%) used to avoid overfitting problem. Now, the final error is obtained by the root-mean-square (RMS) comparison between the current and desired outputs. In this application, 3000 evenly sampled data points are chosen as the training dataset, and 500 data points are used as the validation data. Both datasets (testing and validation) differ from the training dataset. Simplified block diagram of ANFIS controller-based generation of reference current signal with SRF theory is shown in Fig. 4.

Performance Analysis of the Developed System

The performance of the system is investigated for achieving power flow management along with THD under prescribed limits and also provides load levelling. The model is analysed under varying load conditions. To analyse the performanceof the system, RESs are considered to be operated at their rated capacity. PV generation capacity is 8 kW, 2 kW FC system rating, DC bus voltage has been regulated at 800 V.

Figure 8 shows the transient process of the system comparing conventional PI control with ANFIS control. Figure 8 exhibits the superior performance of the ANFIS controller over the conventionally used PI controller during transient conditions as well as for starting condition. It is observed from Fig. 8 that the initial settling time is only 0.2 s for ANFIS controller, whereas in PI controller, it requires 0.35 s for regulating DC bus voltage. The overshoot observed in DC bus voltage using ANFIS controller is only 0.63%, and in case of PI controller, it is 5%. Similarly, almost no undershoot is observed with ANFIS controller, while it is 0.25% for the case of PI controller.

The behaviour of the system under dynamic load changes has been studied. The changes are introduced at 0.4 s in the form of additional load having rating of 4 kW, 0.5 kVAR. The DC bus voltage is stabilized faster than the traditional PI controller. The increase in the voltage is about 1%; in both the cases, ANFIS response undergoes only one-time overshoot, whereas PI witnessed overshoot twice, and there is almost no undershoot for ANFIS controller. It is evident from the comparison that ANFIS controller shows a faster response speed for regulating DC bus voltage. At 0.8 s, 4 kW, 0.5 kVAR load has been removed, the settling time during this dynamic change is .01 s for ANFIS controller and 0.022 s for the conventional PI controller, and almost no overshoot has been observed in case of ANFIS controller, whereas PI witnesses the 1.13% overshoot.

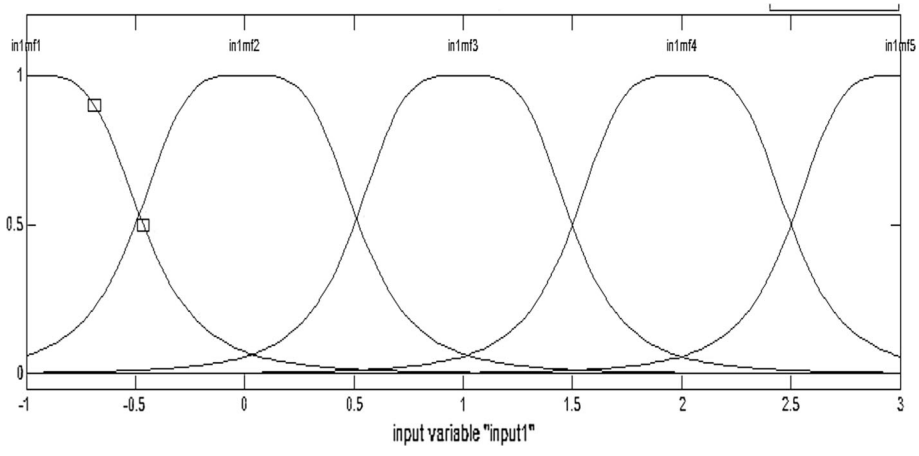


Fig. 7 Membership functions plot for input of ANFIS controller

Table 1 Rule base using ANFIS toolbox

de	*e* in1mf1	in1mf2	in1mf3	in1mf4	in1mf5
in2mf1	− 1.221	− 1.022	− 1.028	− 0.8012	− 0.1528
in2mf2	1.189	0.0297	1.319	− 0.02458	0.01552
in2mf3	− 3.515	0.641	0.9328	0.03428	0.006819
in2mf4	− 0.4305	0.4893	0.06705	0.004406	0.02793
in2mf5	− 0.07154	0.4702	0.03378	0.02392	0.4676

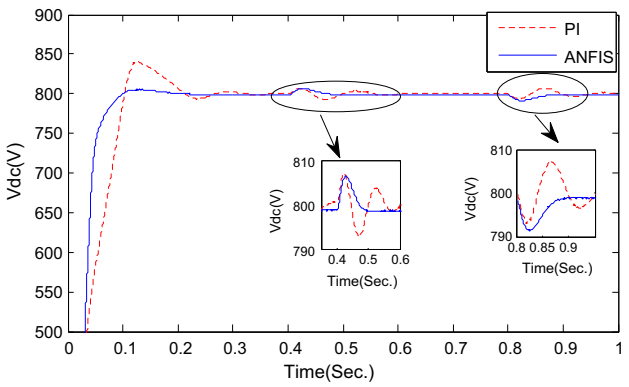


Fig. 8 DC bus voltage under the transient response of the system for PI and ANFIS

Figure 9 describes the graphical performance evaluation of the PI versus ANFIS. It can be clearly concluded that ANFIS controller shows better voltage regulation. The tracking of voltage is faster with reduced settling time to achieve steady state as compared to PI under different loading conditions.

Case-1 System Performance under Dynamic Load Change

To study the behaviour of the system under dynamic load change, the system is initially connected to the nonlinear load (diode bridge with 100 Ω, 0.9 mH). At 0.4 s, unbalanced three-phase linear load (Phase A = 35 Ω, Phase B = 44 Ω, Phase C = 50 Ω) has been connected to the system. Figure 10a shows that the supply currents under different loads are balanced and sinusoidal irrespective of the type of loads. The DC bus voltage has been maintained at 800 V under all dynamic changes by the ANFIS controller action. It can be also seen from Fig. 10a that the grid currents are balanced and sinusoidal and DC bus has been maintained at 800 V by ANFIS controller under dynamic load changes. Figure 10b shows the power allocation of the system as per the load requirement. Initially, load demand is 3 kW and is supplied through PV only and surplus power has been fed to the grid. At 0.4 s, the system shows sudden load change and linear unbalanced load is interconnected into the system. Now, the load power demand is 4 kW; this

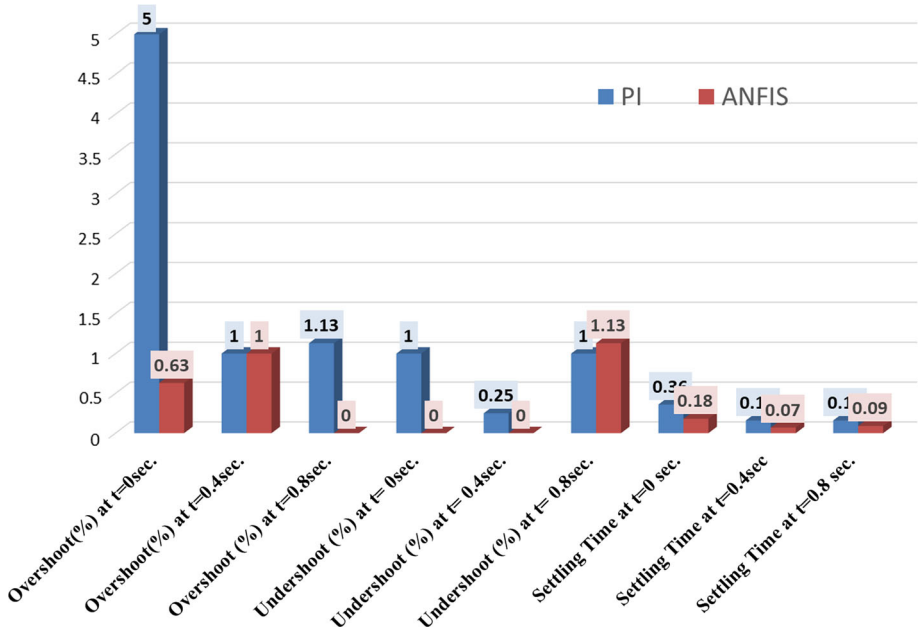
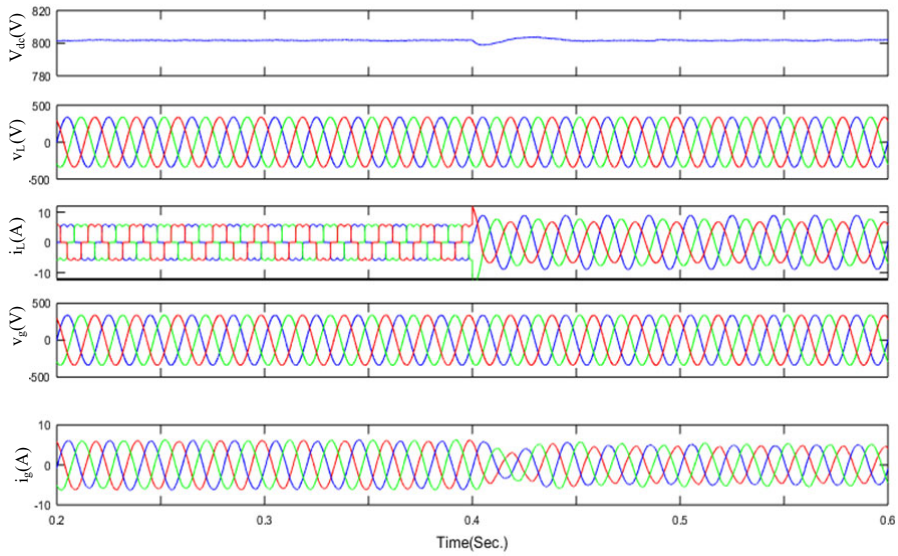
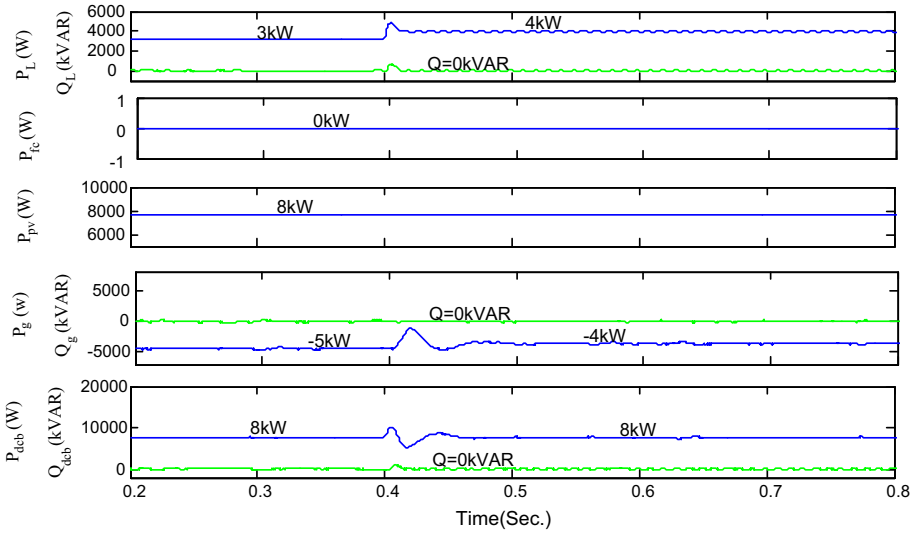


Fig. 9 Performance evaluation of PI and ANFIS controller



(a) System response under dynamic load change



(b) System power response under dynamic load change

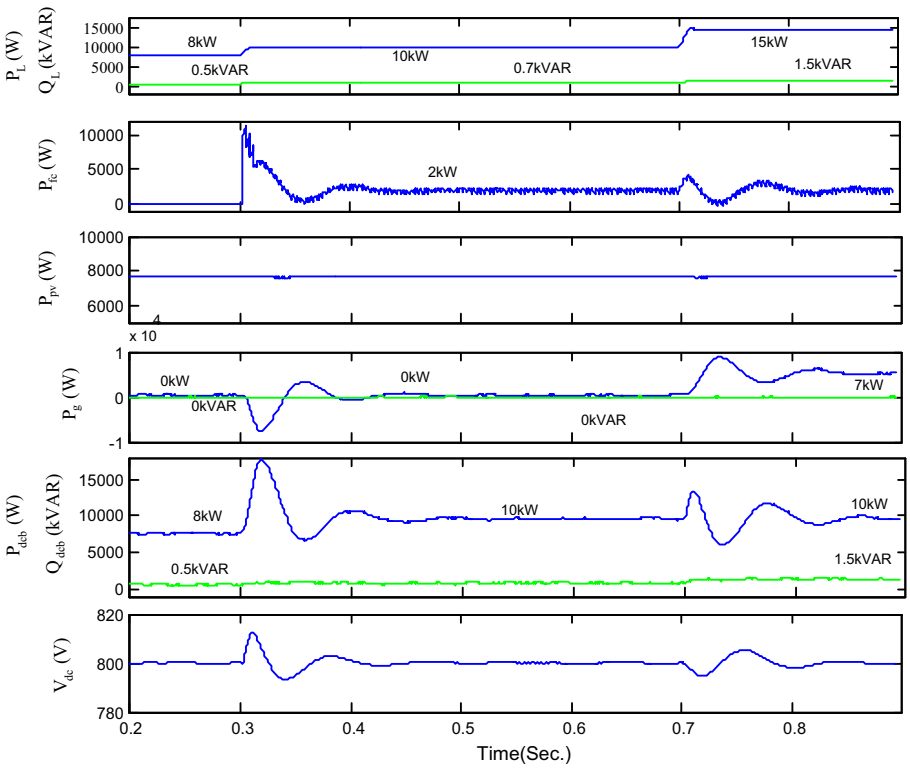
Fig. 10 **a** System response under dynamic load change. **b** System power response under dynamic load change

demand is also fully supplied by PV generation (less than 8 kW), and FC remains idle and generates no active power during this period.

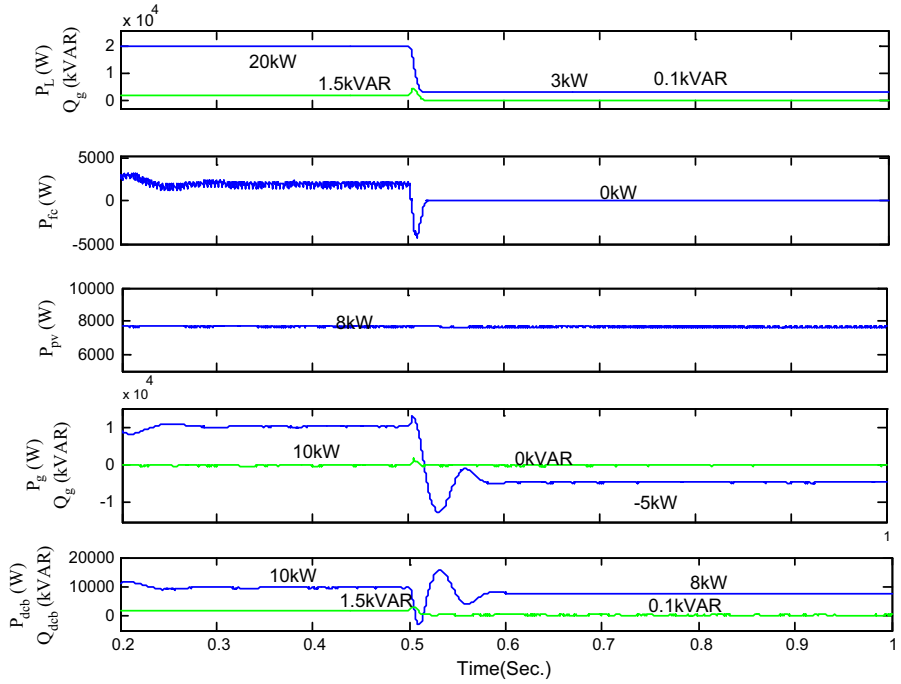
Case-2 System Performance with Variable Linear Load Demand

Integration of FC Generation Source in the System

In this case, behaviour of the system is analysed for the variable linear load. Figure 11a illustrates power allocation with variable linear load; initially, load demand is 8 kW, 0.5 kVAR. This active load power demand is supplied through PV only, and reactive power requirement of the load is catered through VSC; at 0.3 s, the load demand has been increased to 10 kW, 0.7 kVAR, and this increment has been sensed and FC integrated to the system to fulfil increased active load demand. At 0.7 s, an additional load of 5 kW, 1 kVAR has been added to the system. At this point of time, PV and FC together are unable to meet the active power requirement of the system; hence, additional power requirement has been met from the grid. Reactive power requirement of the load is still fulfilled through the VSC. It can be seen from Fig. 11a that DC bus has been regulated to 800 V by ANFIS controller under dynamic load changes also.



(a) System performance under variable linear load demand



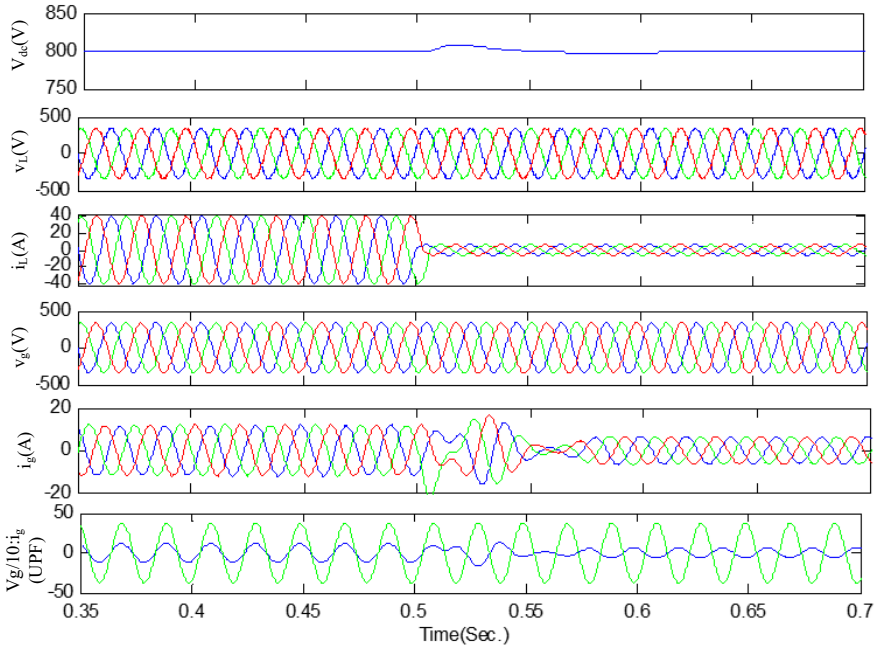
(b) System response under variable load

Fig. 11 **a** System performance under variable linear load demand. **b** System response under variable load. **c** System power response under variable linear load and power factor correction. **d** System response under power factor correction mode

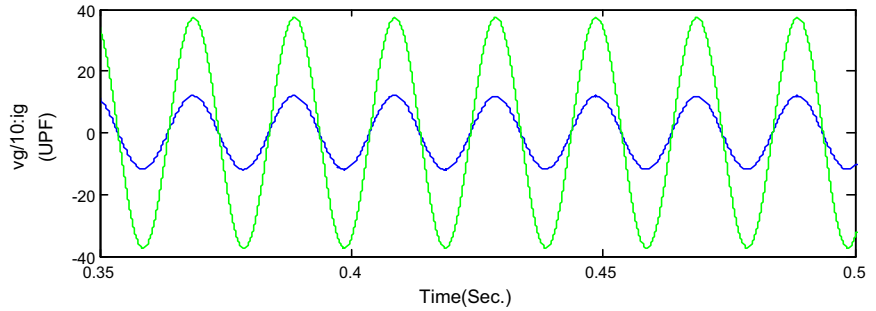
Disconnection of the FC Generation from the System

Figures 11b, c depict the system performance under reduced load demand. Initially, 20 kW, 1.5 kVAR load has been connected to the system. Figure 11b shows that the PV, FC and grid altogether fulfil the active power demand. Reactive power requirement of the load is fulfilled through capacitor fed VSC; hence, grid is free from supplying

Fig. 11 continued



(c) System power response under variable linear load and power factor correction



(d) System response under power factor correction mode

reactive power, and system is working under power factor correction mode. At 0.5 s load, demand has been decreased to 3 kW, 0.1 kVAR. At the instant of load reduction, load currents have been sensed through the controller and FC disconnected from the system and it can be observed in Fig. 11b. Since PV generation is 8 kW so that available power is surplus, hence, this 5 kW surplus power has been supplied to the utility. In Fig. 11b, positive value of grid power shows the power is absorbed by the load, whereas the negative sign of grid power implies that surplus power is injected to the grid. Utility supply voltage and current are shown in Fig. 11c. From Fig. 11d, it is noticed that the source current is perfectly sinusoidal and in phase with the source voltage which shows the system is working under unity power factor, and only active power has been delivered to load from the grid. At the instant, when power is injected to the grid, the current waveform has been inverted. DC bus has been regulated at the predefined constant reference. The results indicate that the system is appropriately responding to all load changes and the RES are also suitably activated if required. Additionally, improved power quality performance has been achieved. The source current THD of 02.27% is shown in Fig. 12.

Conclusions

This paper has been focused on design and analysis of ANFIS-based control of a multi-objective grid-connected inverter and energy management for a hybrid energy system comprising an FC and PV coupled to the utility grid. The developed control along with the energy management is capable to mitigate several power quality problems, UPF system and reactive power compensation. Energy management has been implemented successfully as PV behaves

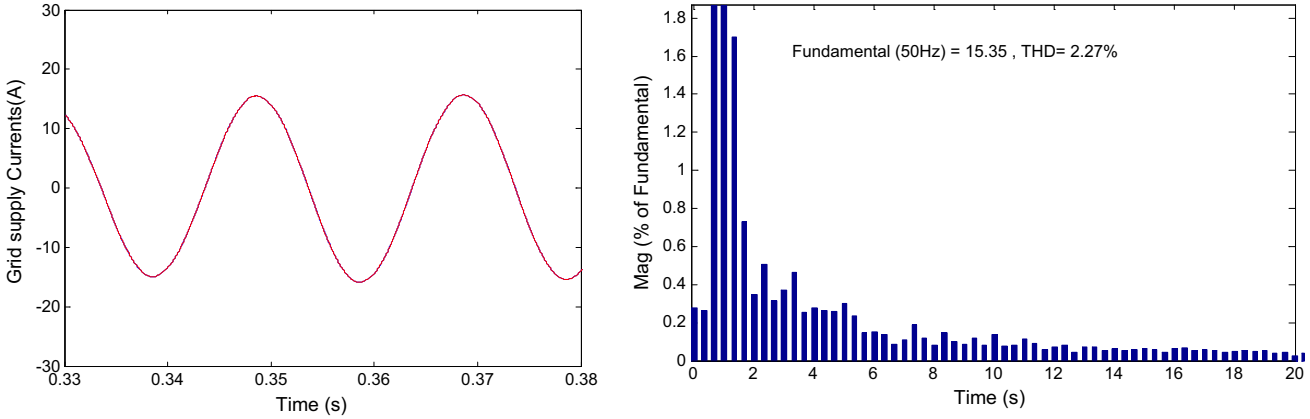


Fig. 12 Waveform and harmonic spectrum of supply current

as the primary source and FC plays the role of secondary energy source, and the result shows that the power allocation between PV, FC, load and grid is as per the availability of the generated power and load requirement. The performance of the several test cases, viz. variable linear load, unbalanced and nonlinear loads, has been depicted, and the simulation results give the satisfactory performance of the system under all the cases. Following outcomes can be concluded from the paper:

- The proposed ANFIS controller has been successfully applied to the FC and PV integrated system. Simulation results depict the improved system performance in terms of well-regulated DC bus voltage and faster dynamic response.
- The suggested multi-objective control scheme can be generalized to include additional RES systems without a major change in control topology and complexity, whereas minor modifications are required in the energy management system.
- Performance of the ANFIS controller versus conventionally used PI controller has been demonstrated. The ANFIS controller has achieved superior results in regulating constant DC bus voltage as compared to the PI controller. When the inverter can control the error quickly, the regulator performs outstandingly fast and robust dynamic response even under transient conditions.
- The control scheme for inverter has been developed to improve power quality features and also feed active power into the system. The inverter is controlled to act as reactive power compensator, and it improves the THD of source current to less than 5% stipulated limit.

Acknowledgment The authors are thankful to the Department of Science and Technology, Government of India for the Sponsored Project (EMR/2016/001874).

Appendix

Parameters for PV cell: $I_{mp} = 2.94$ A, $V_{mp} = 17.0$ V, $P_{max} = 50$ W, $I_{sc} = 3.17$ A, $V_{oc} = 21.0$ V, $K_v = 0.123$ V/K, $K_i = 4.4$ mA/K, no. of series module of WS-50 = 18, no. of parallel module of WS-50 = 10, L (boost converter) = 1.5 mH, C (boost converter) = 250 μF, AC line voltage = 415 V, 50 Hz, modulation index = 0.9, line impedance = Rs = .05 Ω, Ls = 1 mH, L_1, L_2(filter) = 1.2 mH, C (filter) = 1000 μF, DC bus capacitor = 1500 μF.

Fuel cell parameters: $r = 32813 \times 10^{-8}$ Ω, response time for oxygen flow and hydrogen flow is 78.3 s 26.1 s, respectively, $Ko_2 = 2.52 \times 10^{-3}$(kmol/atm), $K_{H2O-} = 2.81 \times 10^{-4}$(kmol/atm), $K_{H2} = 8.43 \times 10^{-4}$(kmol/atm), $T = 1273$ K, $F = 96487$ C/kmol, $R = 8314$ J/kmol K, standard potential = 1.18 V, No = 450, $K_{r-} = .842 \times 10^{-6}$ kmol/s (A).

References

1. Akash Talwariya, Pushpendra Singh, Mohan Kolhe, A stepwise power tariff model with game theory based on Monte-Carlo simulation and its applications for household, agricultural, commercial and industrial consumers. Int. J. Electr. Power Energy Syst. **111**, 14–24 (2019)
2. N.A. Ahmed et al., Development of an efficient utility interactive combined wind/photovoltaic/fuel cell power system with MPPT and DC bus voltage regulation. Electr. Power Syst. Res. **81**, 1096–1106 (2011)
3. J.J. Hwang, L.K. Lai, W. Wu, W.R. Chang, Dynamic modeling of a photovoltaic hydrogen fuel cell hybrid system. Int. J. Hydrog. Energy **34**(23), 9531–9542 (2009)
4. S.H. Hosseini, F. Nejabatkhah, S. Danyali, S. A. K. Mozaffari Niapour, Grid-connected three-input PV/FC/Battery power system with active power filter capability, in *Proceedings of 2nd IEEE Interenational Conference and Exhibition on innovative Smart Grid Technol (PES)* (2011), pp. 1–7
5. J. Paska, P. Biczel, Hybrid photovoltaic-fuel cell power plant, in *Proceedings of IEEE Russia Power Technology*, (2005), pp. 1–5

6. Y. Hidaka, K. Kawahara, Modeling of a hybrid system of photovoltaic and fuel cell for operational strategy in residential use, in *Proceedings of 47th IEEE International Universities Power Engineering Conference (UPEC)* (2012), pp. 1–6
7. G. Y. Choe et al., Comparative study of power sharing algorithm for fuel cell and photovoltaic hybrid generation system, in *Proceedings of International Power Electronics Conference (ECCE ASIA)* (2010), pp. 2615–2620
8. K. Seita, I. Takano, H. Nishikawa, Y. Sawada, A study of operation characteristics of UPFC type dispersed power supply system with FC, PV and EDLC by improved EMAP model, *in Proceedings of Power Systems Conference and Exposition (IEEE PES)*, (2004) pp. 289–294
9. A. Naik, R. Y. Udaykumar and V. Kole, Power management of a hybrid PEMFC-PV and ultracapacitor for stand-alone and grid connected applications, in *Proceedings of IEEE International Conference on Power Electronics, Drives and Energy Systems (PEDES)* (2012), pp. 1–5
10. B. Dong, Y. Li, Z. Zheng, L. Xu, Control strategies of microgrid with hybrid DC and AC buses, in *Proceedings of 14th European Conference on Power Electronics and Applications* (2011) pp. 1–8
11. D. Bo, Y. Li, Z. Zheng, Energy management of hybrid DC and AC bus linked microgrid, in *2nd International Symposium on Power Electronics for Distributed Generation Systems* (2010), pp. 713-716
12. F. Shahnia, R. Majumder, A. Ghosh, G. Ledwich, F. Zare, Operation and control of a hybrid microgrid containing unbalanced and nonlinear load. Elect. Power Syst. Res. **80**(8), 954–965 (2010)
13. L. Zhang, T. Wu, Y. Xing, K. Sun, J.M. Gurrero, Power control of DC microgrid using DC bus signaling, in *Proceedings of 26th Applied Power Electronics Conference and Exposition (APEC)* (2011), pp. 1926–1932
14. F. Ding, K.A. Loparo, C. Wang, Modeling and simulation of grid-connected hybrid AC/DC microgrid, in *IEEE Power and Energy Society General Meeting*, San Diego, CA (2012), pp. 1–8
15. C. M. Colson, M. H. Nehrir, Algorithms for distributed decision-making for multi-agent microgrid power management, in *IEEE Power and Energy Society General Meeting* (2011), pp. 1–8
16. G.T. Machinda, S. Chowdhury, S.P. Chowdhury, W.N. Mbav, Power management of inverter interfaced solar PV microgrid: a review of the current technological trend, in *Proceedings of 47th International Universities Power Engineering Conference (UPEC)* (2012), pp. 1–6
17. P. Singh, D.P. Kothari, M. Singh, V.S. Pareek, Voltage control in distribution networks having DGs by using UPFC. Int. J. Electron. Electr. Eng. Syst. (IJEEES) **2**(1), 31–38 (2010)
18. A.A. Moghaddam et al., Multi-objective operation management of a renewable MG (micro-grid) with back-up micro-turbine/fuel cell/battery hybrid power source. Energy **36**(11), 6490–6507 (2011)
19. A. Eid, Utility integration of PV-wind-fuel cell hybrid distributed generation systems under variable load demands. Int. J. Electr. Power Energy Syst. **62**, 689–699 (2014)
20. P. Singh, D.P. Kothari, M. Singh, Interconnected distribution network for the integration of distributed energy resources. Res. J. Appl. Sci. Eng. Technol. **7**(2), 240–250 (2014)
21. M. Guerrero, P.C. Loh, M. Chandorkar, T.-L. Lee, Advanced control architectures for intelligent micro grids—part I: decentralized and hierarchical control. IEEE Trans. Ind. Electron. **60**(4), 1254–1262 (2013)
22. T. Zhou, B. Francois, Energy management and power control of a hybrid active wind generator for distributed power generation and grid integration. IEEE Trans. Ind. Electron. **58**(1), 95–104 (2011)
23. J. He, Y.W. Li, M.S. Munir, A flexible harmonic control approach through voltage-controlled DG–grid interfacing converters. IEEE Trans. Ind. Electron. **59**(1), 444–455 (2012)
24. J. Schiffer et al., A survey on modeling of micro grid—from fundamental physics to phasors and voltage sources. Automatica **74**, 135–150 (2016)
25. F. Katiraei et al., Micro grids management. IEEE Power Energy Mag. **6**, 54–65 (2008)
26. R.N. Tripathi, A. Singh, T. Hanamoto, Design and control of LCL filter interfaced grid connected solar photovoltaic (SPV) system using power balance theory. Int. J. Electr. Power Energy Syst. **69**, 264–272 (2015)
27. J. Rocabert, A. Luna, F. Blaabjerg, P. Rodriguez, Control of power converters in AC microgrids. IEEE Trans. Power Electron. **27**, 4734–4749 (2012)
28. Z. Zeng et al., Topologies and control strategies of multi-functional grid-connected inverters for power quality enhancement: a comprehensive review. Renew. Sustain. Energy Rev. **24**, 223–270 (2013)
29. Kumar et al., Power quality profile enhancement of utility connected microgrid system using ANFIS-UPQC. Proc. Technol. **21**, 112–119 (2015)
30. S. Mikkili, A.K. Panda, Real-time implementation of PI and fuzzy logic controllers based shunt active filter control strategies for power quality improvement. Int. J. Electr. Power Energy Syst. **43**(1), 1114–1126 (2012)
31. T. Takagi, M. Sugeno, Fuzzy identification of systems and its applications to modeling and control. IEEE Trans. Syst. Man Cybern. **SMC-15**(1), 116–132 (1985)
32. S. Gupta, R. Garg, A. Singh, Grid integrated PMSG based wind energy system: modelling, control and simulation, in *Proceedings of IEEE 1st India International Conference Power Electronics Intelligent Control and Energy Systems (ICPEICES'16)* (2016), pp. 1–6
33. S. Gupta, R. Garg, A. Singh, TSFLC based DC link voltage regulation of grid connected DC micro grid. Int. J. Power Electron. **9**(3), 229–249 (2018)
34. B. Singh, P. Jayaprakash, D.P. Kothari, New control approach for capacitor supported DSTATCOM in three-phase four wire distribution system under non-ideal supply voltage conditions based on synchronous reference frame theory. Int. J. Electr. Power Energy Syst. **33**(5), 1109–1117 (2011)
35. Shikha Gupta, Rachana Garg, Alka Singh, Modeling, simulation and control of fuel cell based micro grid. J. Green Eng. **7**, 129–158 (2017)

Publisher's Note Springer Nature remains neutral with regard to jurisdictional claims in published maps and institutional affiliations.

Our Heritage

ISSN: 0474-9030
Vol-68-Issue-30-February-2020

Application of Fuzzy Logic for the Cost Overrun Analysis in Construction Projects

[1]**Savita Sharma, [2] Pradeep K.Goyal, [3] R.C.Chhipa**

[1] *Research Scholar, Suresh GyanVihar University, civil dept., Jaipur*

[2] *Associate Professor, Delhi Technological University, India*

[3] *Professor, Suresh Gyan Vihar University, Jaipur*

[1]savitasugotra@gmail.com, [2] pk_goyal2003@yahoo.co.in, [3]rc.chhipa@mygyanvihar.com

Abstract— **Construction industry plays an important role in economic growth and development of any country. It is found that construction projects are facing the problem of risk and uncertainties due to the involvement of various factors because of dynamic and complex behaviour of construction activities. The desired goal of construction projects are not achieved due to these risks and uncertainties and project failure may take place in terms of delay and cost overrun. Cost overrun has become a major problem in construction projects. There are several causes which are responsible for cost overrun such as poor planning, fluctuation in cost of material, delay in procurement of material, poor decision making, changes in design, adverse climatic condition etc. To handle the problem of cost overrun, there are found various risk assessment techniques in literature. Among these techniques fuzzy logic is considered appropriate techniques to tackle the complexity of the construction projects. An example problem is solved using the Fuzzy logic tool box of MATLAB for illustration. Applicability of the model for Indian conditions is discussed. The theory is applied to quantify the probability of cost overrun in construction project**.

Index Terms— cost overrun, construction industry, fuzzy logic.

I. INTRODUCTION

Construction industry plays a significant role in the development and economic growth of any country. Every day the number of projects is rapidly increasing, especially in developing countries and the main objectives are to complete the project within time period, stipulated budget with specified quality norms [1]. It has been observed that construction projects, worldwide are facing the problem of schedule and cost overruns due to the inherent risks and uncertainties. The cost is considered as a very important key parameter as available in the literature [2]-[4]. There are various causes which are responsible for cost overrun such as poor planning, fluctuation in cost of material, delay in procurement of material, poor decision making, changes in design, adverse climatic condition [5]-[9]. Therefore, construction industry demands systematic risk management approach to control the problem of cost overrun. Based on the extensive literature review, it has been observed that qualitative analysis based on fuzzy theory is considered suitable for handling the risk and uncertainty in construction project.

II. METHODOLOGY

Interview and questionnaire survey is conducted with the experts in Indian construction industry for prevailing cost overrun causes and judging their relative importance index. The questionnaire is prepared on the basis of the knowledge gained from relevant literature reviews, interviews and discussions. These various causes are categorized according to the source. To get a large number of filled questionnaires quickly, convenience and snowball sampling method was used to identify the sample element for questionnaire survey. The causes of cost overrun are ranked and assessed for their relative importance index.

The fuzzy logic model is designed to estimate the probability of cost overrun of the project in Mamdani-type inference using the fuzzy toolbox of MATLAB. There are five primary graphical user interface tools for building, editing, and observing Fuzzy inference systems in the fuzzy toolbox of MATLAB[10].

III. NUMERICAL STUDY

The survey is carried out in the Indian construction industry and analyzed. Model is developed in two stages:

Copyright © 2019Authors

ISSN: 0474-9030
Vol-68-Issue-30-February-2020

A. Stage 1: relative importance index of the causes of cost overrun

The cost escalation causes and their classification are given by Sharma and Goyal (2014) [11] for the construction industry. Based on the opinion of the expert, relative importance index for cost escalation causes are estimated for the Indian construction industry. The relative importance index for the related category of causes is calculated and rank of the category is determined with the help of relative importance index for the individual causes of the concerning category. The relative importance index of the various causes are calculated using the relation given below

$$\text{RII} = \frac{\sum W}{A*N}$$

Where W is the weighting given to each cause of cost overrun by the respondents (ranging from 1 to 5), A is the highest weight (i.e. 5 in this case) and N is the total number of respondents. Relative Importance Index of various categories of causes is given in Table1.

Table 1. Relative Importance Index of various categories of causes

1	Onwer related	0.72
2	Contractor related	0.89
3	Consultant related	0.75
4	Designrelated	0.66
5	Project related	0.54
6	Material related	0.66
7	Labour related	0.58
8	Equipment related	0.52
9	Contract related	0.69
10	Coordination/communication related	0.70
11	External	0.92

B. Stage 2: Model development in fuzzy environment

To develop the fuzzy model for estimating the probability of cost overrun of the project, the probability of cost overrun of the various categories are predicted first with the probability of cost overrun of basic causes of concerning categories. From the cost overrun probability of the categories the probability of cost overrun of the project is forecasted. The following steps are processed for the model development in fuzzy inferences:

(i)Defining input and output variables: Causes which are responsible for cost overrun recognized at stage one is considered as basic input variables. Output variable is taken as the probability of cost overrun of the category at level one. At next level the eleven categories of causes are considered as the input variables and the output is taken as the 'probability of cost overrun' of the project.

(ii)Define membership function: Membership functions associated with all the input and output for the entire fuzzy inference system for level one and two are defined in membership function editor. The t r i n g u l a r fuzzy numbers are being used in this paper as they are widely used in the literature.

(iii) Defining rules and assigning weights to the fuzzy rule: Rules are constructed based on the input and output. The inference rules in the fuzzy logic system are defined through "IF-THEN" clause.

Rule1: if the probability of owner category is critical the cost overrun is critical

Rule2: if the probability of owner category is high the cost overrun is high

The relative importance index of causes calculated at stage one is assigned as the fuzzy rules weights to construct the fuzzy assessment model for estimating the probability of cost overrun of the project.

(iv) Defuzzification: Defuzzification is the process in which outcomes of control models in the form of fuzzy numbers is converted into an exact output numbers. After defuzzification process the probability of the cost overrun of the project is estimated in precise value in the interval of zero to one. The process of defuzzification is shown in Fig.1.

Copyright © 2019Authors

ISSN: 0474-9030
Vol-68-Issue-30-February-2020

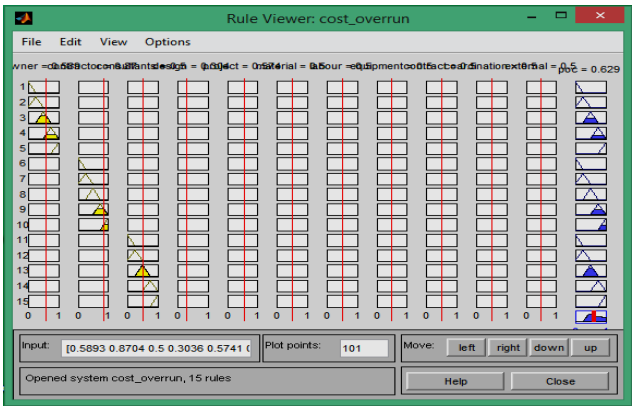


Fig.1: Defuzzification

(v) Surface view: The variation of the cost overrun of the project with respect to 'owner' and 'contractor' related category is displayed by surface viewer in Fig.2.

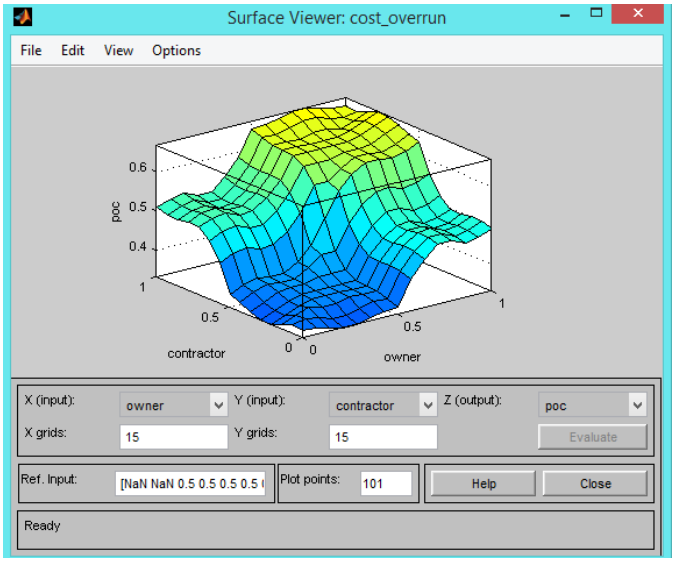


Fig.2: Variation of contractor and owner category with respect to cost overrun

CONCLUSION

The cost overrun problem has become very acute in construction industry. The problem is associated with every type of projects and locations. Indian construction industries are not the exception. There are several causes which are responsible for cost overrun in Indian construction industry such as poor planning, fluctuation in cost of material, delay in procurement of material, poor decision making, changes in design, adverse climatic condition etc. Application of fuzzy logic for the cost overrun analysis in construction projects is discussed in this paper using Fuzzy toolbox of MATLAB. The relative importance index for the causes of cost overrun prevailing in the Indian construction industry is calculated and rank of the related category is determined. Using the relative importance index, model has been developed in fuzzy inference system (FIS) to estimate the probability of cost overrun of the project. The model will be useful for contractor and owner for decision making.

REFERENCES

[1] Y. Frimpong, J. Oluwoye, L. Crawford, " Causes of delays and cost overruns in construction of groundwater projects in developing countries, Ghana as a case study," International Journal of Project Management, vol. 21, pp. 321-326, 2003.
[2] A. Franke, "Risk analysis in project management," International Journal of Project Management, vol. 5, no.1, pp. 129-34, 1987.
[3] J. H. Paek, Y.W. Lee and J.H. Ock, "Pricing Construction Risks: Fuzzy Set Theory,"Journal of Construction Engineering and Management, vol.119, no.4, pp. 743-756, 1993.
[4] T .Williams, "A classified bibliography of recent research relating to project risk management," European Journal of Operational Research, vol. 85, pp. 18-38, 1995.

Copyright © 2019Authors

ISSN: 0474-9030
Vol-68-Issue-30-February-2020

[5] D.C. Okpala, A.N. Aniekwu, "Causes of high costs of construction in Nigeria, " Journal of Construction Engineering and Management, ASCE, vol. 114 , no. 2, pp. 233-234, 1988.
[6] N. R. Mansfield, O.O. Ugwu, T. Doran, "Causes of delay and cost overruns in Nigerian construction projects," International Journal of Project Management, vol. 12, no. 4, pp. 254–260. 1994.
[7] P.F. Kaming, P.O. Olomolaiye, G.D. Holt , F.C. Harris, "Factors influencing construction time and cost overruns on high-rise projects in Indonesia, " Journal of Construction Management and Economics, vol. 15, no.1, pp. 83-94, 1997.
[8] P. A. Koushki, K. Al-Rashid and N. Kartam, "Delays and cost increases in the construction of private residential projects in Kuwait,"Construction Management and Economics, vol. 23, no. 3, pp. 285-294, 2005.
[9] M. Sambasivan and Y. W. Soon, "Causes and effects of delays in Malaysian construction industry," International Journal of Project Management, vol. 25, pp. 517–526, 2007.
[10]Fuzzy Logic Toolbox™ 2 User's Guide, MATLAB, the Math Works, Inc. (2008)
[11] S. Sharma and P.K. Goyal, "Cost overrun factors and project cost risk assessment in construction industry- a state of the art review, "International journal of civil engineering, vol. 3,no. 3, pp. 139-154, 2014.
[12]L. Zadeh, "Fuzzy sets", Information Control, 8: pp.338-353. 1965.

Copyright © 2019Authors

Paper No. 242/2019

COMPUTATIONAL AEROACOUSTIC ANALYSIS OF FLAP DEFLECTION AND CAMBER OF AN AIRFOIL

Vishesh Kashyap

Delhi Technological University, Shahbad Daulatpur, Main Bawana Road, Delhi, India, vishesh_bt2k16@dtu.ac.in

***Abstract**: A number of fields involve the study of noise generated by airfoils. As restrictions on the noise generated by machines such as jet engines and turbines become more stringent, there is a need to understand the phenomenon of aeroacoustics. In order to increase the lift of a wing, external flaps and highly cambered main elements are often deployed. These elements can also affect the noise created by the wing. A computational aeroacoustic analysis was carried out using ANSYS Fluent in order to assess the impact of these on the turbulence and noise generated by an airfoil. Airfoils with NACA 0012, NACA 4412 and Eppler 423 as the main element were studied at flap deflections of 0°, 15° and 30°. The SST k-ω turbulence model was used along with a broadband noise-based acoustic model solver. Values of turbulence intensity, surface acoustic power level and X and Y-direction self and shear noise were plotted along the surface of the airfoil, and a direct correlation between turbulence and surface acoustic power was observed. It was also observed that the acoustic power generated by the airfoil showed an increasing trend on the suction side, with increase in both camber and flap deflection. However, this was compensated for by a corresponding decrease on the pressure side. The self and shear noise were also shown to exhibit an increasing trend with camber and flap deflection, with the Y-directional sources dominating at higher flap deflections.*

***Keywords:** Aeroastics, CFD, CAA, self-noise, shear noise, turbulent boundary layer*

Notation

c	chord length
o	flap overhang
y	main element-flap gap
α	flap deflection
x	horizontal position
C_D	total drag coefficient
C_L	total lift coefficient
C_{Lf}	flap lift coefficient
C_{Lm}	main element lift coefficient

Subscript

D	drag
L	lift
Lf	flap lift
Lm	main element lift

1. INTRODUCTION

The generation of noise by airfoils is of interest over a vast number of disciplines. Wind turbine blades generate noise which influences people residing in the neighbourhood. Aircraft airframes as well as turbomachinery generate significant amounts of noise. Over the years there has been an effort to reduce the noise generated through these by changes in design as well as working conditions. With an increase in the stringency of norms regulating the generation of noise, it has become ever more important to understand and control the process.

Among the foremost industries where aeroacoustics finds relevance is the aerospace industry. Airframe noise emanating from high-lift devices of an aircraft when landing forms a major portion of the total noise generated [1]. In a comprehensive study on the self-noise created by airfoils, Brooks et al. [2] presented 3 main generation mechanisms based on the Reynolds number and angle of attack:

- Turbulent Boundary Layer – Trailing Edge (TBLTE) noise
- Laminar Boundary Layer – Vortex Shedding (LBL-VS) noise
- Separation – Stall (S-S) noise

TBL-TE takes place at high Reynolds numbers, due to the development of turbulent boundary layers over large regions of the airfoil. LBL-VS occurs at lower Reynolds numbers, due to vortex shedding caused by instabilities. SS occurs due to large scale separation created at large angles of attack. Attached or separated boundary layers generate broadband noise, whereas laminar boundary layers generate whistles, due to the development of vertical disturbances [3].

Over the years, Computational Fluid Dynamics (CFD) has proved an efficient tool to simulate fluid dynamics phenomena, including boundary layer and vortex shedding. This makes possible the simulation of aeroacoustic processes, which has been increasingly done using CFD and Computational Aeroacoustics (CAA). De Gennaro et al. [4] validated the use of CFD with the transitional k-ω [5] model for an isolated NACA 0012 airfoil, while Stepanov et al. [6] did the same for application in the aeroacoustic analysis of rotor blades with NACA 0012 airfoil section. Caicedo and Virk [7] conducted a multiphase numerical study of the aeroacoustic response of NACA 0012 airfoil, testing RANS, LES and DES approaches. Hosder et al. [8] created a CFD-based noise metric for the modelling of aerodynamic noise and conducted dimensional studies to validate the same.

Appendages such as flaps and slats are often included in airfoils in order to supplement the lift experienced by it. These appendages may also supplement the noise created by the airfoil. While flaps provide a large amount of lift, slats pre-

vent the separation of airflow over the main part of the airfoil. Dobrzynski et al. [9] showed that while slat noise dominated at lower frequencies, flap side-edge noise tended to at higher frequencies.

The deflection of flaps in airfoils is used to modulate the lift and drag generated by the airfoil across a range of applications, and lead to major changes in the same. Similarly, an increase in airfoil camber has also been shown to impact the lift and drag experienced by it. However, these changes in design are also bound to generate noise. Going through literature available, it is evident that computational research on the impact of flap deflection on the noise created by cambered airfoils is minimal. There is hence a need for a parametric investigation into the impact of flap deflect and camber on the noise created by airfoils. This study is an effort in the direction. The effect of flap deflection has been studied on non-cambered, moderately-cambered and highly-cambered airfoils in order to assess various parameters such as turbulence intensity, surface acoustic power level, self-noise and shear noise over the surface of the airfoil.

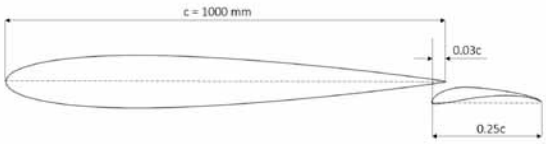
2. METHODOLOGY

A 2-dimensional (2D) CFD simulation was performed with the NACA 0012 (0% maximum camber), NACA 4412 (4% maximum camber) and Eppler 423 (9.5% maximum camber) airfoils as the main element of the airfoil and the high-lift Selig 1223 as the flap airfoil for all three configurations. Flap deflection was varied from 0° to 30°.

2.1. CAD Geometry

A 2D geometry for the analysis was created using SolidWorks 2018. It consisted of the main airfoil of chord length c and the flap of length 0.25c. The flap overhang o was of length 0.03c and the gap between the flap and the main airfoil at the trailing edge y was 0.02c. The deflection of the flap α was varied in each analysis. The geometry is shown in Fig. 1.

Fig. 1: Geometry of the double-element airfoil



2.2. Computational Domain

In order that efficient visualisation of the wake region and pressure contours of the airfoil is possible, a large computational domain is opted for. The length from the inlet and vertical walls to the airfoil is 10c, and the length from the airfoil to the outlet is 15c [10]. The inlet is modelled as a semicircle in order that changes in angle of attack may be achieved without altering the geometry. The computational domain is shown in Fig. 2.

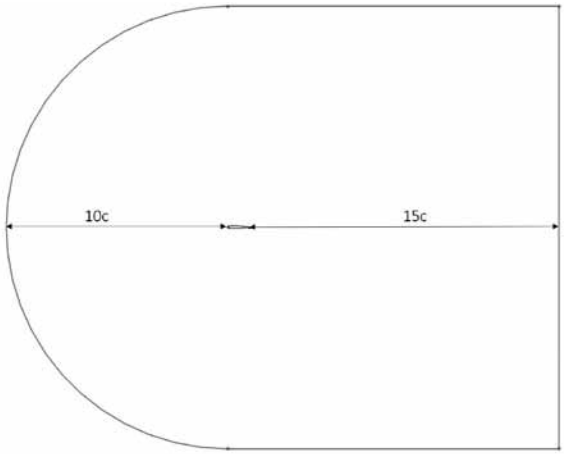


Fig. 2: Computational domain for the analysis

2.3. Meshing

The mesh was generated using ANSYS ICEM Mechanical. A high quality mesh was created with a base element size of 50 mm. A grid independence test was carried out in order to ascertain this length. Prismatic cells were used in order to model the boundary layer at the airfoil, allowing for cells of high aspect ratio, while reducing excessive stream-wise resolution. In order that flow close to the airfoil was predicted accurately, the first grid point y^+ was maintained close to 1.

Tab. 1 summarizes the number of elements and skewness characteristics for the 3 main airfoils studied. Fig. 3 shows the generated mesh.

Main Airfoil	No. of Elements	Minimum Skewness	Maximum Skewness	Average Skewness
NACA 0012	1,78,432	$1.3x^{10-}10$	0.119	$7.6x^{10}$-3
NACA 4412	1,79,943	$1.3x10^{-10}$	0.125	$7.7x10^{-3}$
Eppler 423	1,79, 990	$1.3x10^{-10}$	0.128	$7.7x10^{-3}$

Tab. 1: Elements and skewness characteristics for the airfoils

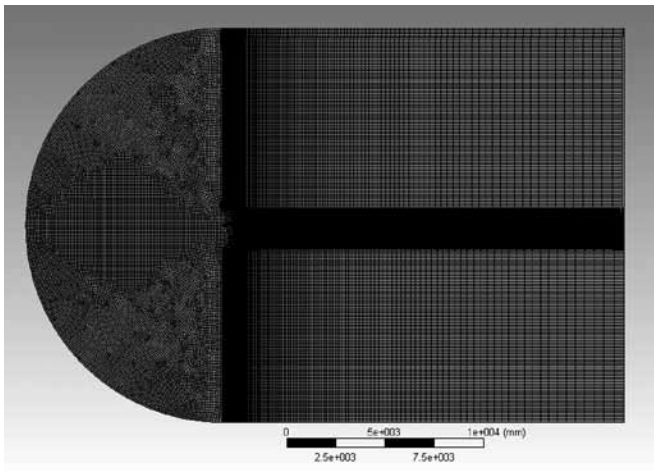


Fig. 3: Mesh generated for analysis

2.4. CFD Model

A 2D CFD analysis of the airfoils was conducted on ANSYS Fluent 18.2 [11]. The numerical model used for the analysis was the two-equation shear stress transport (SST) k-ω turbulence model, where k is the turbulent kinetic energy while ω is the specific turbulence dissipation rate [12]. The SST model considers values of shear stress, thus increasing the near-wall accuracy of the calculation. The transport equations of k and ω are given as follows.

$$\frac{\partial(\rho k)}{\partial t}+\frac{\partial(\rho k u_i)}{\partial x_i}=\frac{\partial}{\partial x_j}\left[\Gamma_k\frac{\partial k}{\partial x_j}\right]+\widetilde{G}_k-Y_k+S_k \quad (1)$$

$$\frac{\partial(\rho \omega)}{\partial t}+\frac{\partial(\rho\omega u_i)}{\partial x_i}=\frac{\partial}{\partial x_j}\left[\Gamma_\omega\frac{\partial \omega}{\partial x_j}\right]+G_\omega-Y_\omega+D_\omega+S_\omega \quad (2)$$

Where

$\widetilde{G}_k$ represents the generation of due to mean velocity gradients,
G_ω represents the generation of ω,
Γ_K and Γ_ω represent the effective diffusivity of k and ω respectively, which are calculated as described below.
Y_k and Y_ω represent the dissipation of k and ω respectively,
D_ω represents the cross-diffusion term,
S_k and S_ω are user-defined source terms.

The broadband noise-based acoustic model solver was used in conjugation, with a far field sound speed of 340 m/s and a far-field density of 1.225 kg/m^3, while the reference acoustic power was 10^{-12} W. Linearized Euler Equations (LEE) extend Lighthill's Analogy [13], dealing with only small perturbations. Linearized around a stationary mean flow, they may be written as follows [14].

$$\frac{\partial U}{\partial T}+\frac{\partial E}{\partial x}+\frac{\partial F}{\partial y}+H=S \quad (3)$$

Here,

$$U=\begin{pmatrix}\rho'\\ \rho_o u'\\ \rho_o v'\\ p'\end{pmatrix}$$

$$E=\begin{pmatrix}\rho' u_o+\rho_o u'\\ u_o\rho_o u'+p'\\ u_o\rho_o v'\\ u_o p'+\gamma p_o u'\end{pmatrix}$$

$$F=\begin{pmatrix}\rho' v_o+\rho_o v'\\ v_o\rho_o u'\\ v_o\rho_o v'+p'\\ v_o p'+\gamma p_o v'\end{pmatrix}$$

$$H=\begin{pmatrix}0\\ (\rho' u_o+\rho_o u')\frac{\partial u_o}{\partial x}+(\rho' v_o+\rho_o v')\frac{\partial u_o}{\partial y}\\ (\rho' u_o+\rho_o u')\frac{\partial v_o}{\partial x}+(\rho' v_o+\rho_o v')\frac{\partial v_o}{\partial y}\\ (\gamma-1)(p'\nabla.u_o-u'\frac{\partial p_o}{\partial x}-v'\frac{\partial p_o}{\partial y}\end{pmatrix}$$

Where

ρ_o, p_o and u_o are the density, pressure and velocity respectively of the mean flow and
ρ', p' and u' are small perturbations superimposed on it
γ is the ratio of specific heats, taken as 1.4 for air.

An air velocity of 30 m/s was imposed at the inlet, while ambient pressure was imposed at the outlet. Coupled pressure--velocity coupling scheme was used for calculating solutions with a least squares cell based gradient and second order spatial discretization for pressure, momentum, turbulent kinetic energy and specific dissipation rate.

The total drag and lift of the airfoil, as well as the individual lifts of the main element and the flap element were taken as output parameters. Analyses were carried out between flap deflection angles of 0° to 30°, at a gap of 15° between consecutive analyses. After all deflections had been analyses for one main airfoil, it was replaced by the next in the geometry. Each analysis was terminated when residuals of continuity, x-velocity, y-velocity, k and ω all reached 10^{-7}, ensuring high precision of results reported.

2.5. Grid Independence Test

In order to determine a base size for the mesh elements, a grid independence test was performed. The SST k-ω turbulence model was utilized for the analysis of an isolated NACA 0012 airfoil with an inlet velocity of 30 m/s. Grids with base element sizes 150 mm, 100 mm, 50 mm and 25 mm were studied. The values of pressure coefficient (C_p) over the surface of the airfoil were plotted against the relative horizontal chord position (x/c). The results of the analysis are presented in Fig. 4.

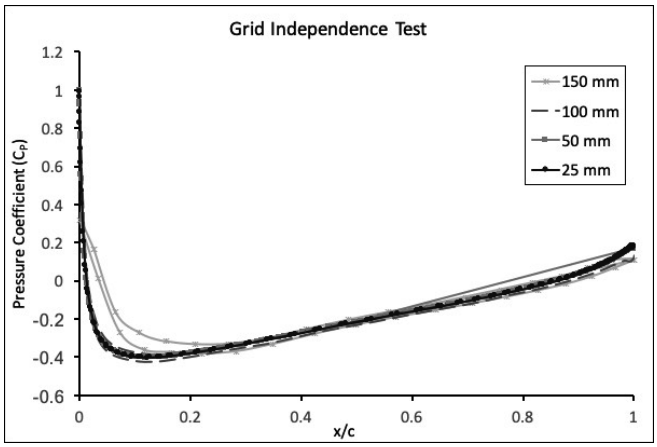


Fig. 4: Results of grid independence test

As is evident from the figure, the values of pressure coefficient for element sizes 150 mm and 100 mm deviate highly from others, while the values for sizes 500 mm and 25 mm are nearly concordant. Giving due consideration to the time of computation, which is higher for small elements, the element size 50 mm was chosen for further analysis.

2.6. Validation

The numerical model used in the study was validated by comparing values of pressure coefficient over the surface of an isolated NACA 0012 airfoil with those obtained by Marsden et al. [15] using CFD code and Lee and Kang [16] through

an experimental study. The values of pressure coefficient are plotted against x/c. The results are shown in Fig. 5. The values obtained through the current numerical methods are seen to be in close agreement with the reported values.

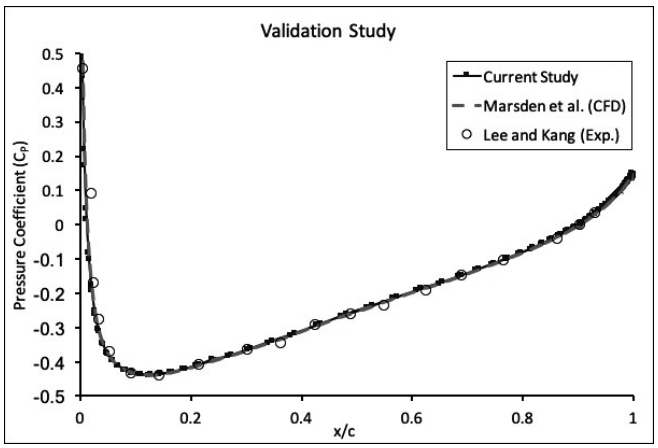


Fig. 5: Results of present study validated against CFD results of Marsden et al. and measurements of Lee and Kang

3. RESULTS AND DISCUSSION

Analysis was carried out in order to predict characteristics such as lift coefficient and drag coefficient as well as graphs of turbulence intensity, surface acoustic power level and self and shear noise from x-directional sources and y-directional sources at flap deflections 0°, 15° and 30°. Three different airfoils with main elements NACA 0012, NACA 4412 and Eppler 423 were studied. The results are discussed in subsequent sections.

3.1. Analysis with Main Element NACA 0012

The total drag coefficient C_D and total lift coefficient C_L as well as the components contributed by the main element C_{Lm} and flap C_{Lf} at various flap deflections are summarised in Tab. 2.

α	C_L	C_{Lm}	C_{Lf}	C_D
0°	0.682	0.569	0.113	0.015
15°	1.617	1.286	0.331	0.021
30°	1.821	1.446	0.375	0.0506

Tab. 2: Aerodynamic characteristics of airfoil with main element NACA 0012

Both lift coefficient and drag coefficient are seen to exhibit a considerable increase between flap deflections 0° and 30°. The increase in drag coefficient may be attributed to the increase in frontal area with increase in flap deflection. The presence of a flap increases the curvature of the airfoil, which causes the air to flow with a slower velocity under the airfoil. This in turn increases the pressure under the airfoil, producing lift. With increasing flap deflection, the curvature also increases, increasing lift. It is also observed that the lift coefficient of the flap is a substantial part of the total lift coefficient of the airfoil.

Fig. 6 presents the contours of turbulence intensity over the airfoil, while Fig. 7 contains graphs of turbulence intensity over the surface of the airfoil. An increase in flap deflection is found to produce an increasingly large region of flow separation, leading to an increasingly turbulent wake. The surface turbulence intensity on the suction side of both the main element and flap of the airfoil is found to increase with an increase in flap deflection, with a substantial increase being observed on the flap surface. This is due to adverse pressure gradients steepening with increase in angle of attack.

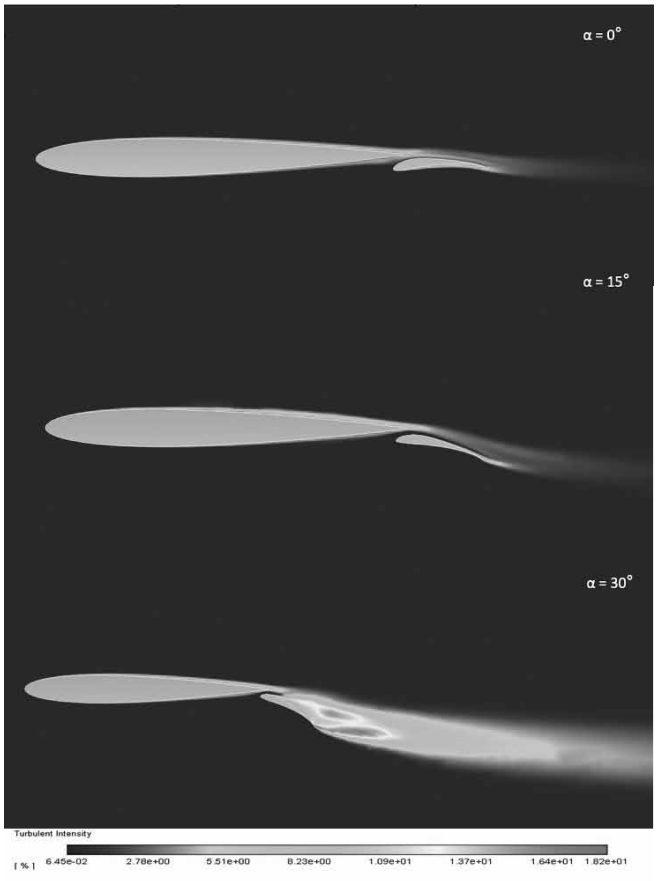


Fig. 6: Contours of turbulence intensity for α = 0°, 15° and 30° with main element NACA 0012

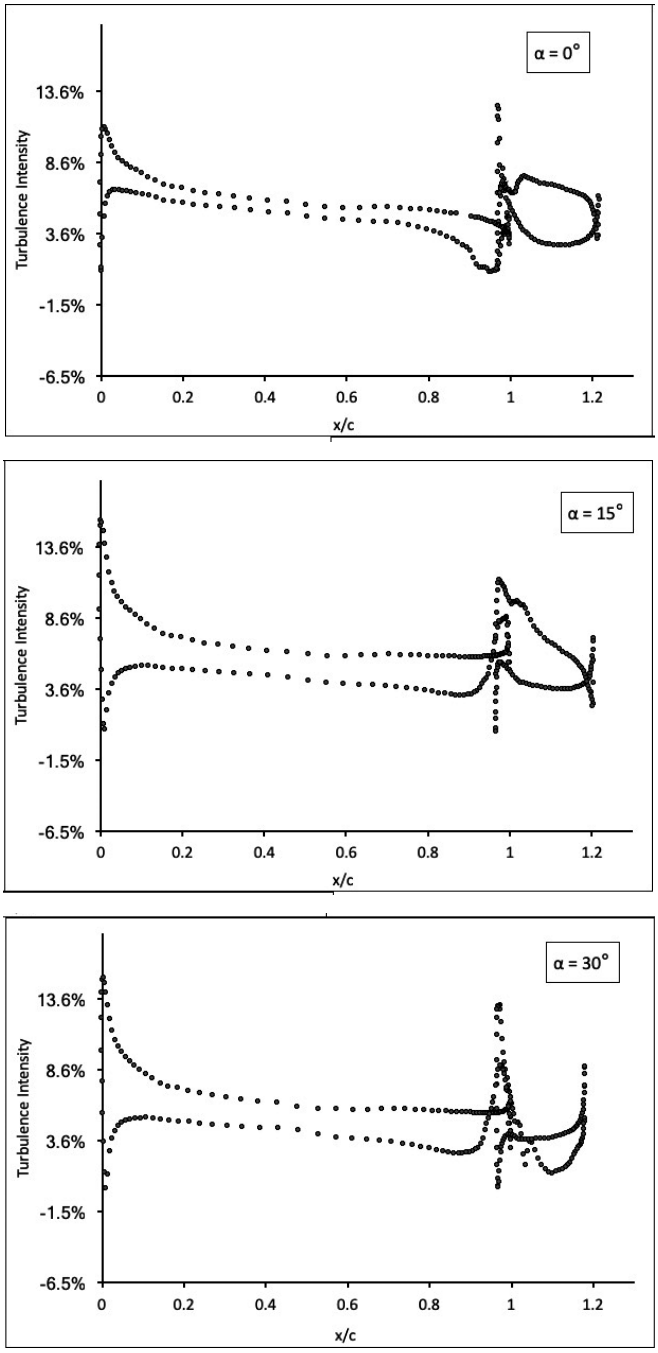


Fig. 7: Graph of turbulence intensity across airfoil profile for α = 0°, 15° and 30° with main element NACA 0012

Fig. 8 presents graphs of surface acoustic power level over the surface of the airfoil. It is evident from the figure that the noise produced by the airfoil at a point has a direct correlation with the turbulence intensity observed at the point. The surface acoustic power level is observed to increase particularly on the flap, with increase in flap deflection. A sudden increase in this quantity is observed around x/c=0.97, where the flap is located. The presence of the flap introduces a constrain in the flow, producing an acceleration that increases velocity and produces a region of increasingly low pressure. The turbulence caused by this phenomenon produces the peak in noise observed. A similar peak in surface acoustic power level is observed at the trailing edge of the flap. Due to the turbulent boundary layer passing the sharp trailing edge of the flap, the hydrodynamic turbulent energy is scattered, producing the noise. This trailing edge noise is observed to increase with angle of attack. This is in concordance with similar experimental results reported by Hutcheson and Brooks [17].

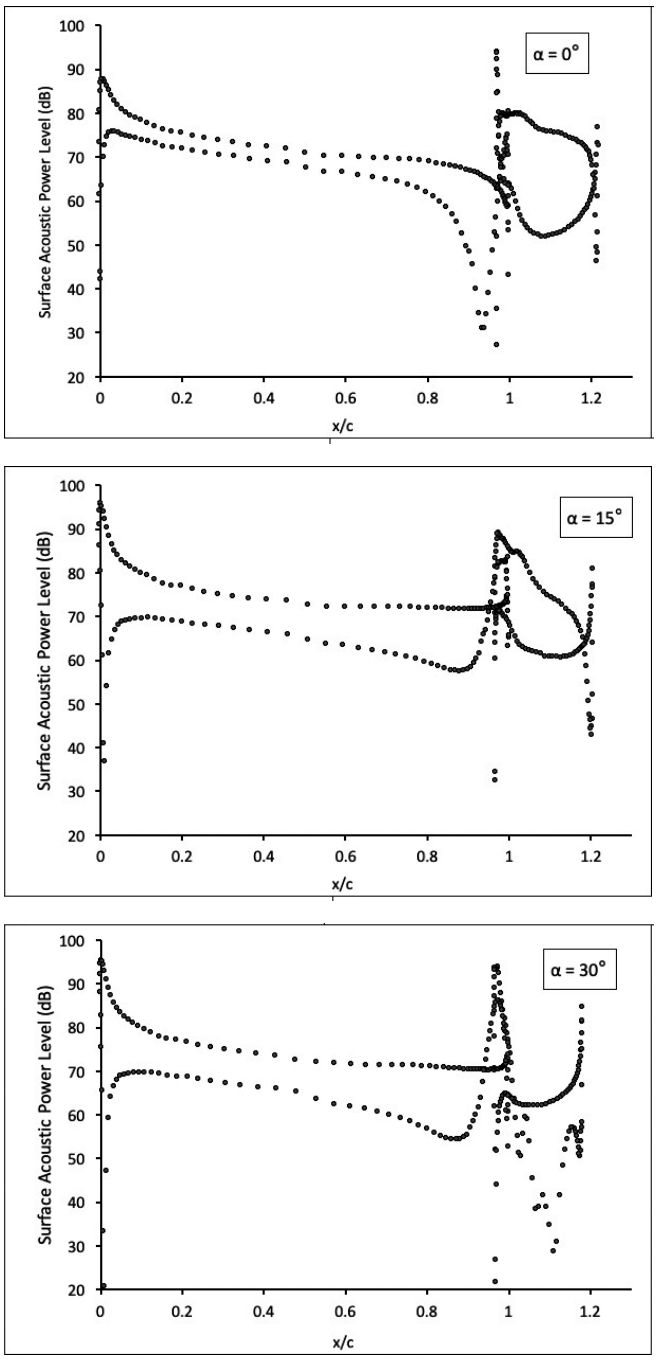


Fig. 8: Graph of surface acoustic power level across airfoil profile for α = 0°, 15° and 30° with main element NACA 0012

Figs. 9 and 10 contain the graphs of self and shear noise respectively due to X and Y-directional sources. It is observed that both self and shear noise follow trends similar to those of turbulence intensity and surface acoustic power level. The leading edge of the main airfoil, and the leading edge of the flap are observed to be regions of particularly high noise generation. When the leading edge of an airfoil interacts with turbulence structures in the free stream, large-scale pressure fluctuations are produced. This leads to turbulence, and the amplified unsteady lift generates broadband noise [18].

Significant peaks in noise are also observed at the trailing edges of the main element and the flap. This is the trailing edge noise caused due to interaction of the sharp trailing edge with the turbulent boundary layer, as mentioned previously. It is also noted that Y-directional sources (perpendicular to the direction of flow) are dominant at greater flap deflections. Tollmien-Schlichting waves are initiated due to the interaction of sound with the leading edge of the airfoil, and grow in amplitude (a y-directional source) along the airfoil.

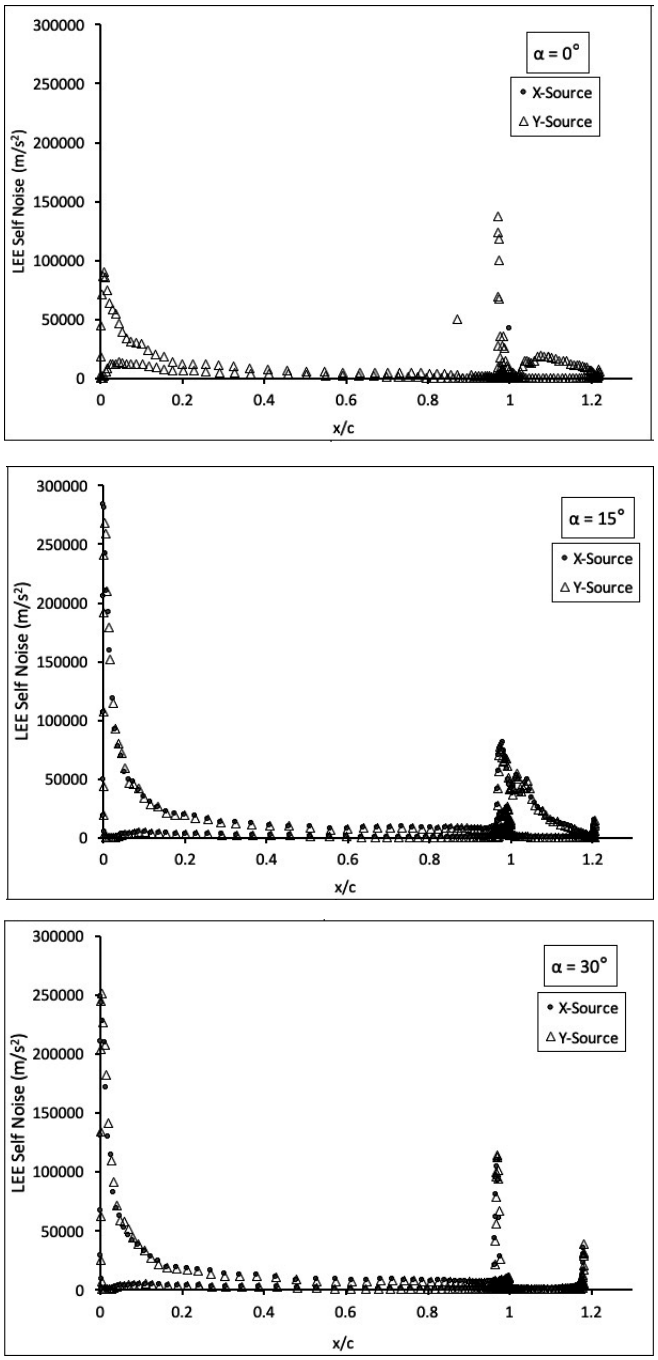


Fig. 9: Graph of LEE self-noise across airfoil profile for α = 0°, 15° and 30° with main element NACA 0012

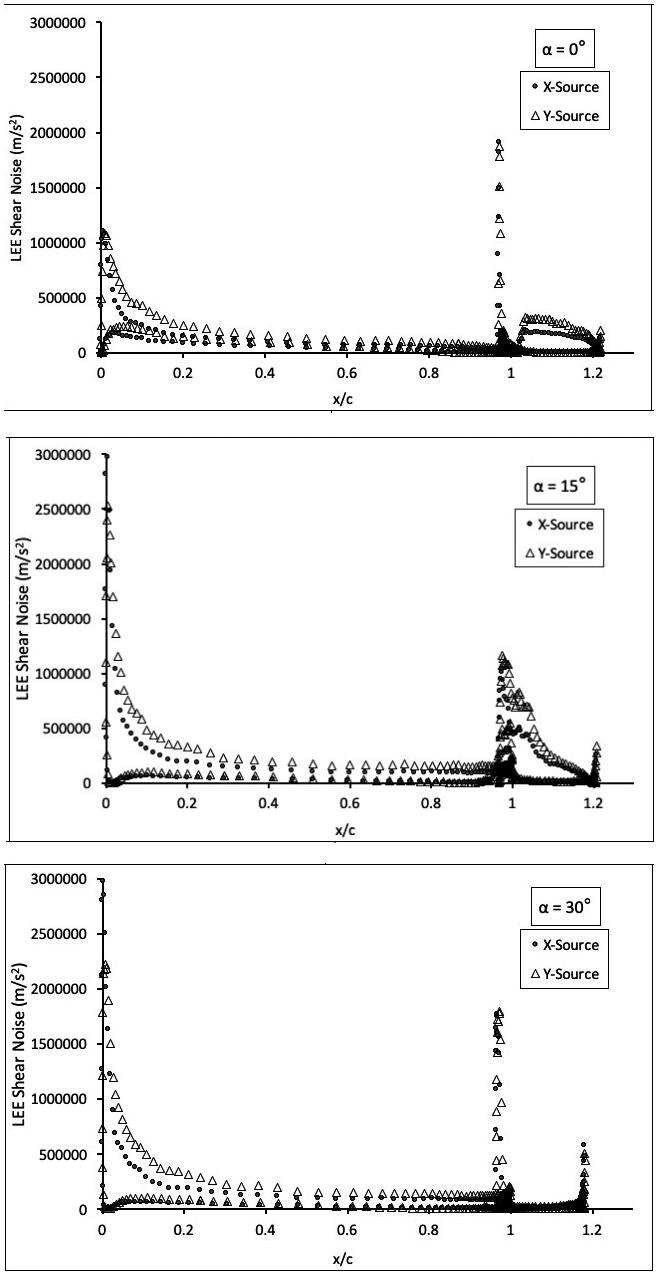


Fig. 10: Graph of LEE shear noise across airfoil profile for α = 0°, 15° and 30° with main element NACA 0012

3.2. Analysis with Main Element NACA 4412

Tab. 3 summarises the total drag coefficient C_D and total lift coefficient C_L as well as the components contributed by the main element C_{Lm} and flap C_{Lf} at various flap deflections on an airfoil with main element NACA 4412.

α	C_L	C_{Lm}	C_{Lf}	C_D
0°	0.726	0.712	0.014	0.024
15°	1.829	1.538	0.291	0.0220
30°	2.471	2.063	0.407	0.0354

Tab. 3: Aerodynamic characteristics of airfoil with main element NACA 4412

Both lift coefficient and drag coefficient show increasing trends with increase in angle of attack. The values for both

quantities are considerably greater than those observed for the airfoil with main element NACA 4412 for all cases. This effect can be attributed to the increased camber. The increase in curvature causes air to flow at a greater velocity above the airfoil, producing a low pressure region which in turn contributes to greater lift.

Fig. 11 contains the contours of turbulence intensity over the airfoil, while Fig. 12 contains graphs of turbulence intensity over the surface of the airfoil. It is observed that the intensity of turbulence increases gradually with increase in flap deflection angle, as does the difference among the turbulence intensities of the upper and lower surfaces of the airfoil. The turbulence at the suction side is observed to increase over the airfoil with main element NACA 0012.

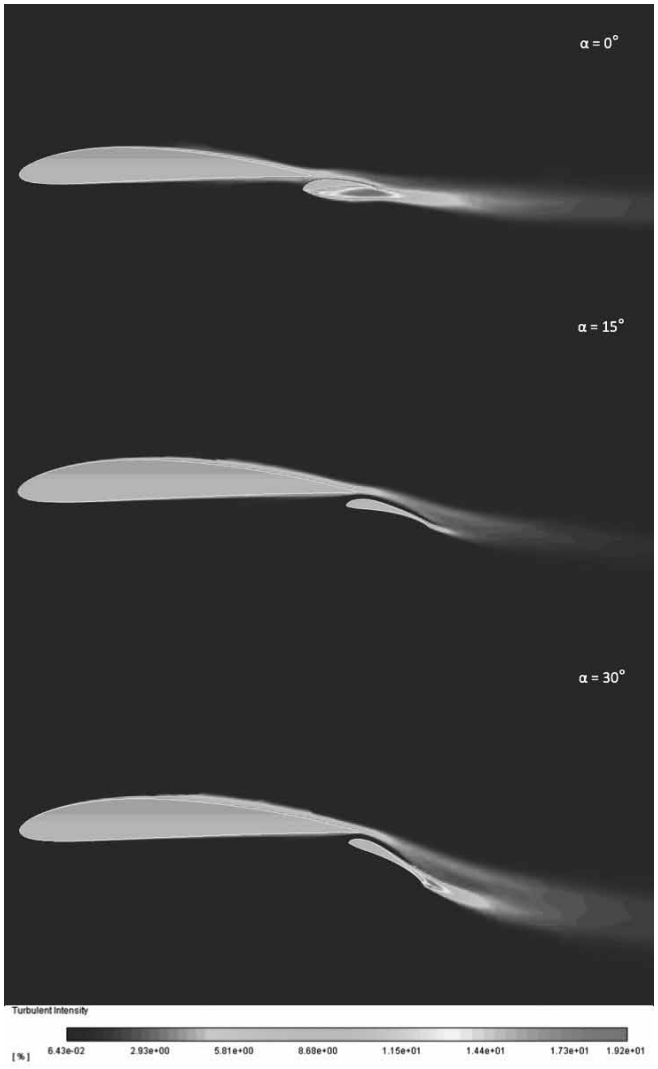


Fig. 11: Contours of turbulence intensity for α = 0°, 15° and 30° with main element NACA 4412

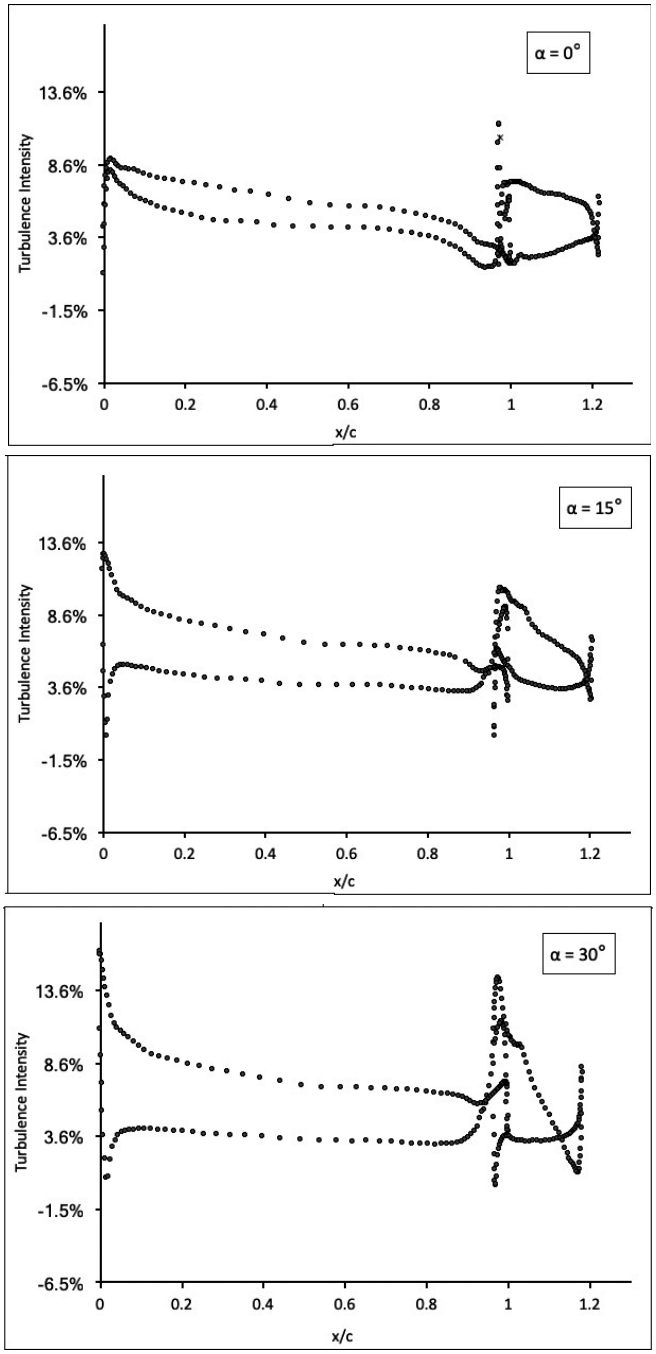


Fig. 12: Graph of turbulence intensity across airfoil profile for α = 0°, 15° and 30° with main element NACA 4412

The graph of surface acoustic power level over the airfoil is shown in Figure 13. A similar trend to that observed for turbulence intensity is observed. The surface acoustic power is seen to increase over the airfoil with main element NACA 0012 on the suction side, and decrease on the pressure side. Similar results were obtained computationally by Lee [19], who observed that an increase in camber also produces low frequency noise of the suction side.

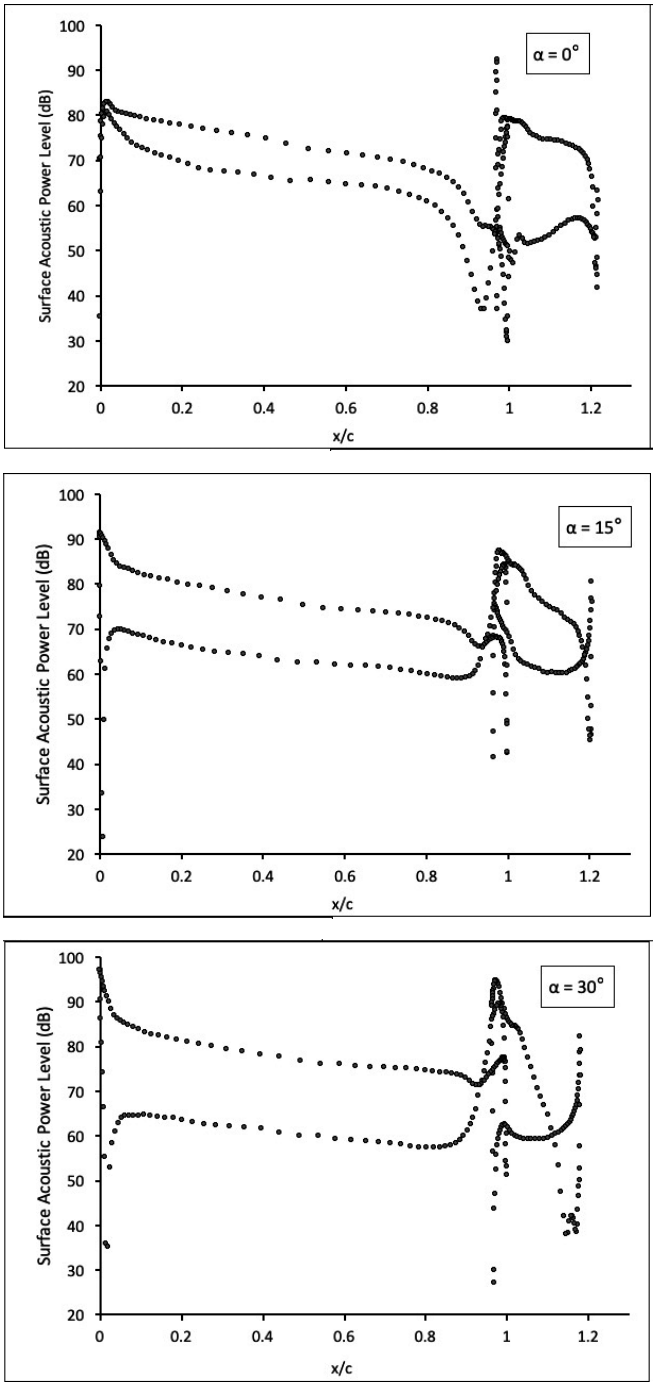


Fig. 13: Graph of surface acoustic power level across airfoil profile for α = 0°, 15° and 30° with main element NACA 4412

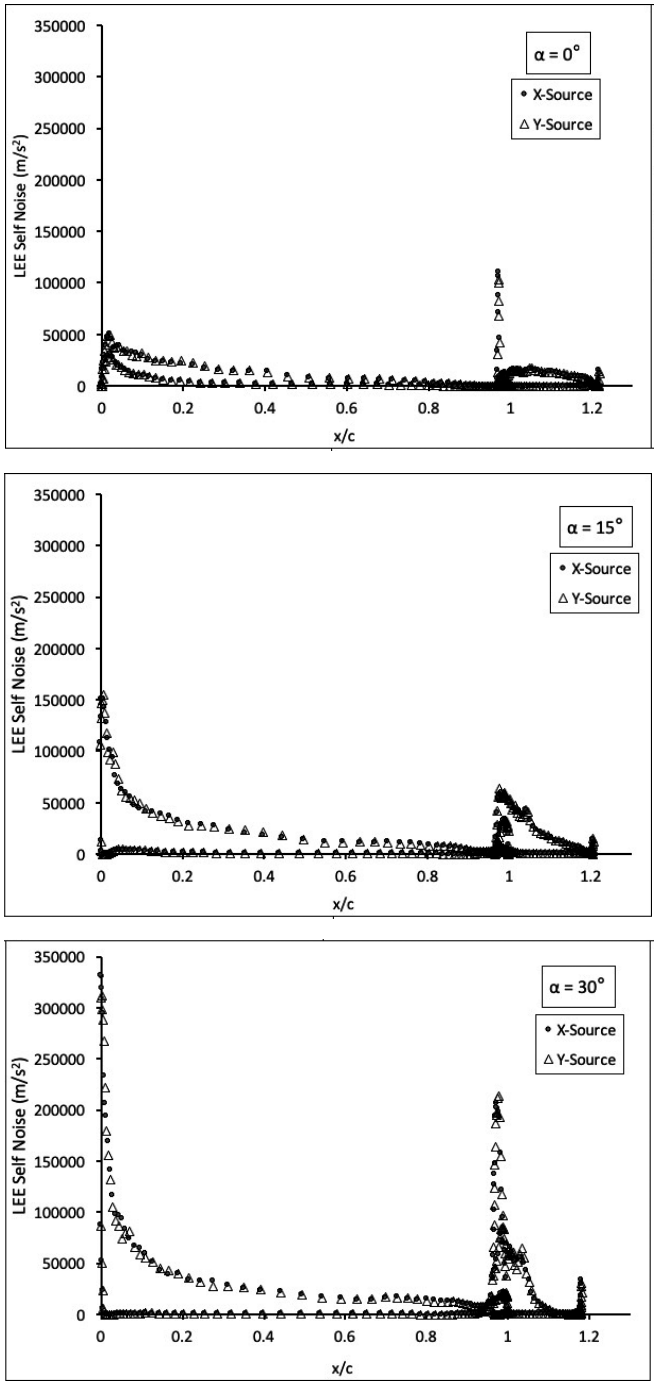


Fig. 14: Graph of LEE self-noise across airfoil profile for α = 0°, 15° and 30° with main element NACA 4412

Fig. 14 and 15 contain graphs of the X and Y-directional LEE Self Noise and Shear Noise respectively. While the trend of the graph is similar to the graph for the quantities observed for the airfoil with main element NACA 0012, the noise levels are observed to be higher on the suction side. The increase in camber leads to increased adverse pressure gradient and boundary layer thickness on the suction side, which leads to an increase in the level of noise produced. When the leading edge of an airfoil interacts with turbulence structures in the free stream, large-scale pressure fluctuations are produced. This leads to turbulence, and the amplified unsteady lift generated broadband noise [18].

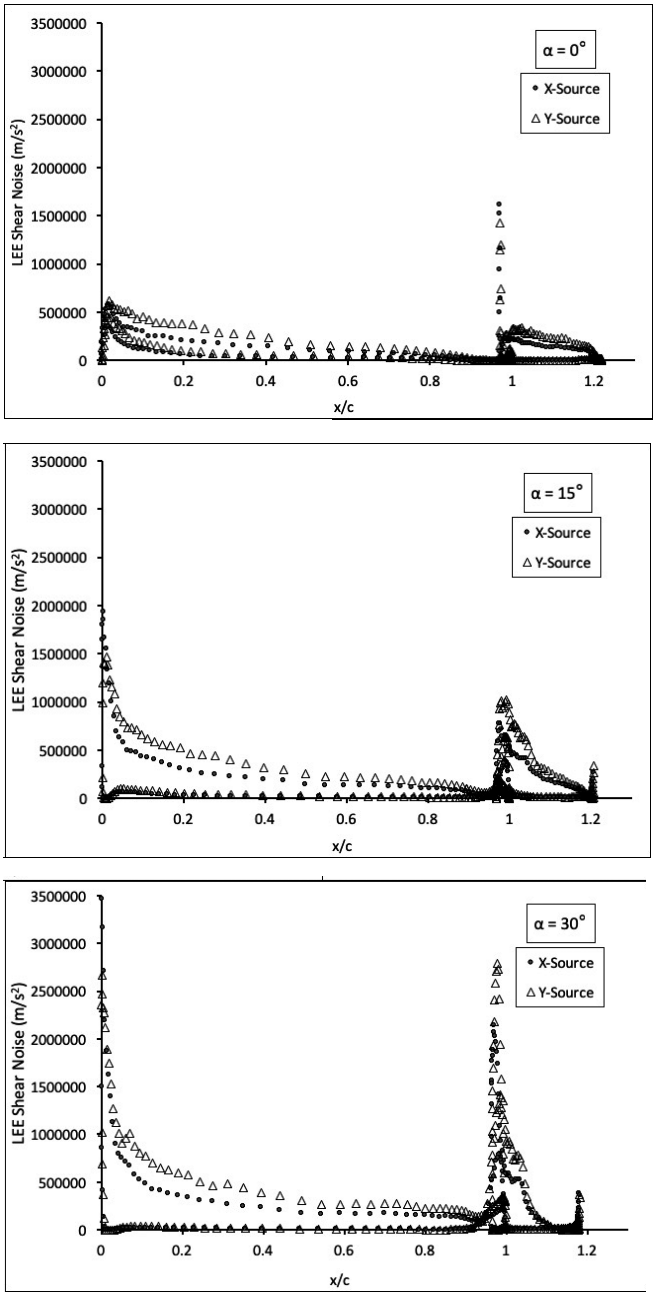


Fig. 15: Graph of LEE shear noise across airfoil profile for α = 0°, 15° and 30° with main element NACA 4412

3.3. Analysis with Main Element Eppler 423

Tab. 4 summarises the total drag coefficient C_D and total lift coefficient C_L as well as the components contributed by the main element C_{Lm} and flap C_{Lf} at various flap deflections on an airfoil with main element Eppler 423.

α	C_L	C_{Lm}	C_{Lf}	C_D
0°	1.420	1.410	0.010	0.034
15°	1.617	1.286	0.331	0.021
30°	2.961	2.654	0.307	0.039

Tab. 4: Aerodynamic characteristics of airfoil with main element Eppler 423

The values of lift and drag coefficients are observed to be the greatest among the three airfoils studied. This may be attributed to the high camber of the Eppler 423 airfoil. However, the value of flap lift coefficient at 0° flap deflection is observed to be lower than for the other two airfoils. This is due to the region of low pressure and high turbulence generated below the airfoil due to its highly cambered shape, which causes flow separation very close to the leading edge. This also increases the drag on the airfoil.

Fig. 6 presents the contours of turbulence intensity over the airfoil, while Fig. 7 contains graphs of turbulence intensity over the surface of the airfoil. It is observed that at 0° flap deflection, a region of high turbulence is created close to the leading edge of the airfoil on the pressure side. Also, the trend of the graphs is seen to be similar to the graphs of turbulence intensity in the other airfoils. However, an increase in turbulence is observed on the suction side of the airfoil while a decrease is observed on the pressure side. A relatively lower turbulence intensity is observed at the leading edge of the flap. Due to the highly cambered shape of the main airfoil, the highly constricted region between the main element and the flap is relatively shorter, which ensures a reduction in turbulence.

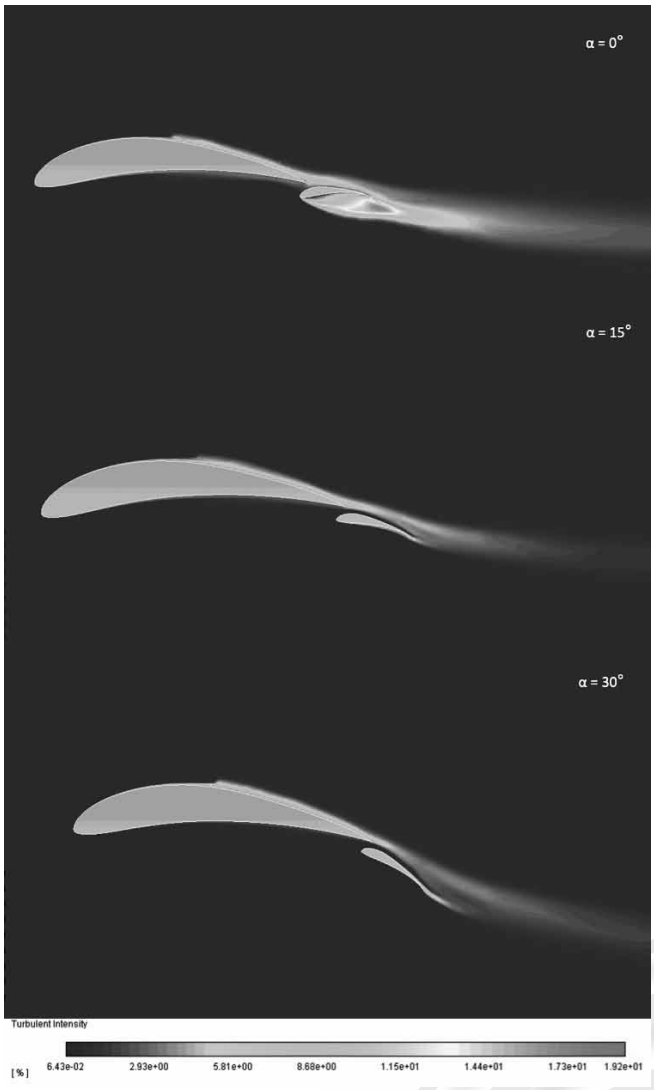


Fig. 16: Contours of turbulence intensity for α = 0°, 15° and 30° with main element Eppler 423

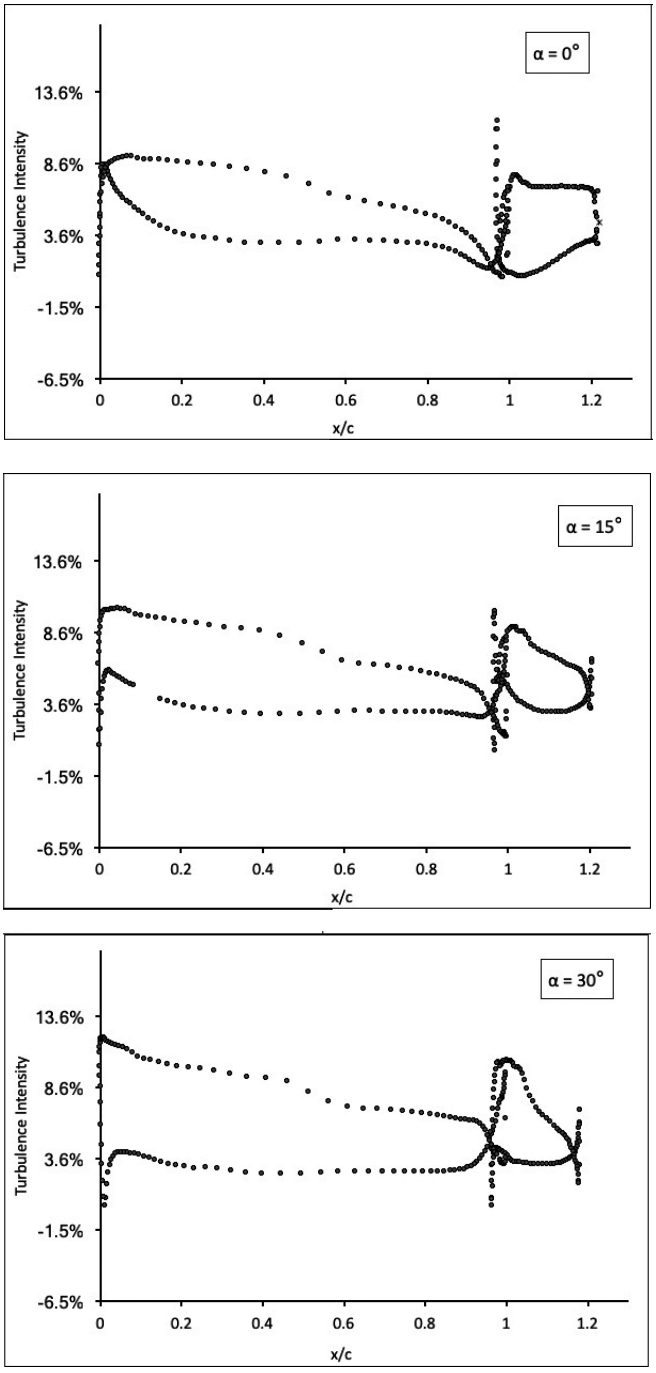


Fig. 17: Graph of turbulence intensity across airfoil profile for α = 0°, 15° and 30° with main element Eppler 423

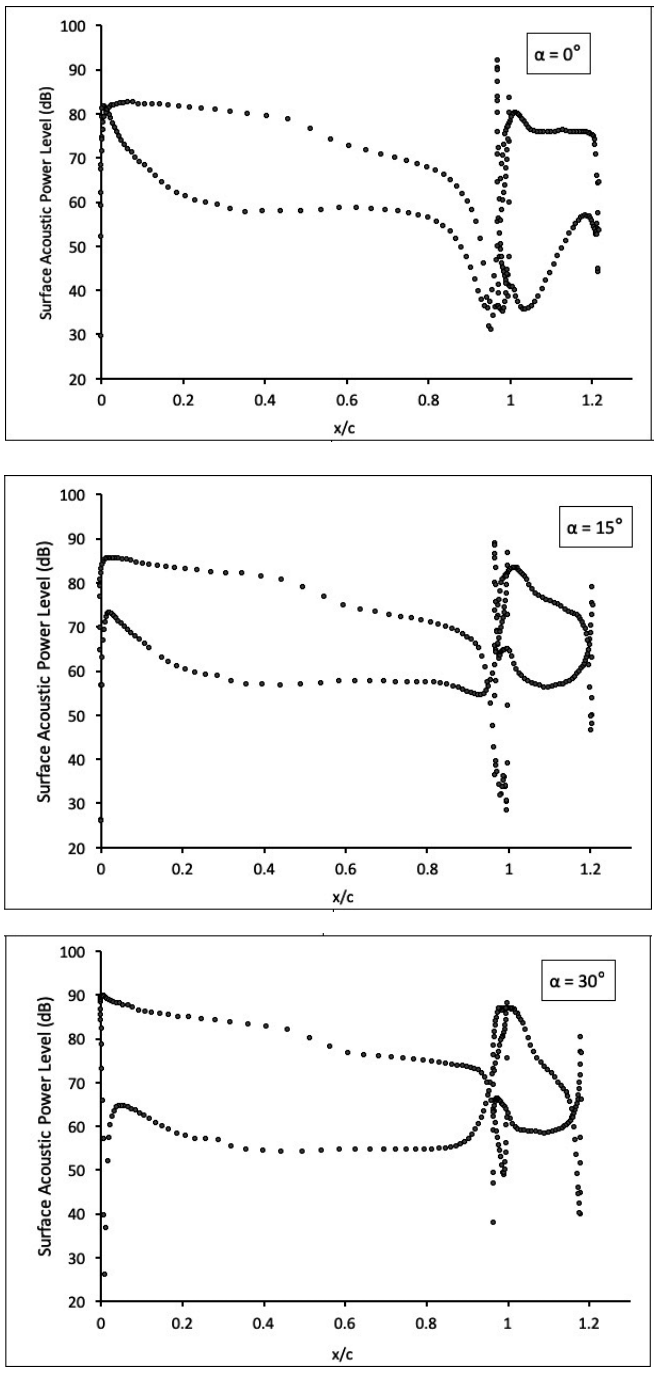


Fig. 18: Graph of surface acoustic power level across airfoil profile for α = 0°, 15° and 30° with main element Eppler 423

Fig. 18 shows the graphs for surface acoustic power level along the surface of the airfoil. This is observed to follow a similar trend to turbulence intensity, with the acoustic power increasing on the suction side and decreasing on the pressure side. The difference between the power observed on the suction and pressure side increases with flap deflection. A marginally lower surface acoustic power level is observed on the surface of the flap, and a trough close to x/c = 1 indicates a region of considerably low turbulence on the pressure side of the flap at the location. This can also be observed in Fig. 16.

Fig. 19 and 20 show the graphs for the X and Y-direction self--noise and shear noise respectively. A considerable increase in the high-noise region is observed over the previous two airfoils. This region is seen to increase with increase in the deflection of the flap. Similarly, a region of high noise is also observed on the suction surface of the flap, which increases with increase in flap deflection. The high camber of the main airfoil creates a considerably larger amount of disruption in the free stream, causing pressure fluctuations when turbulence structures interact with it. This in turn leads to broadband noise being created. The flap creates increasingly higher noise with increase in flap deflection, due to increase in the flow separation region.

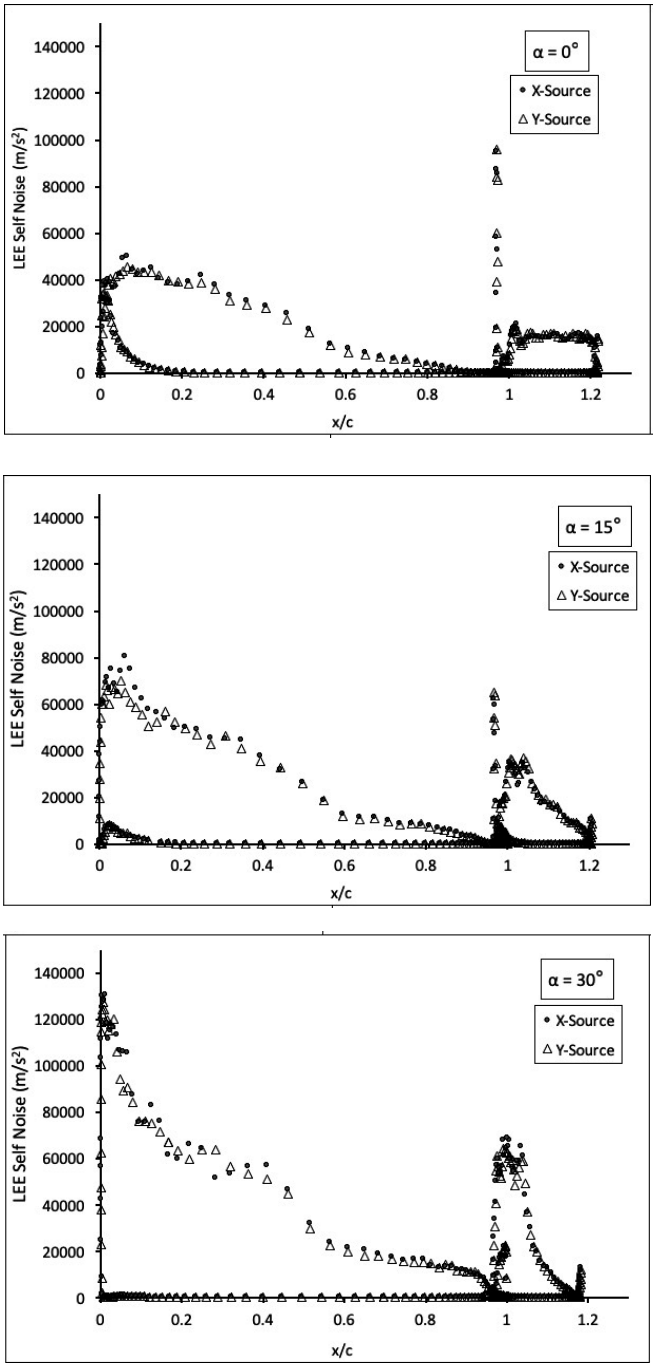


Fig. 19: Graph of LEE self-noise across airfoil profile for α = 0°, 15° and 30° with main element Eppler 423

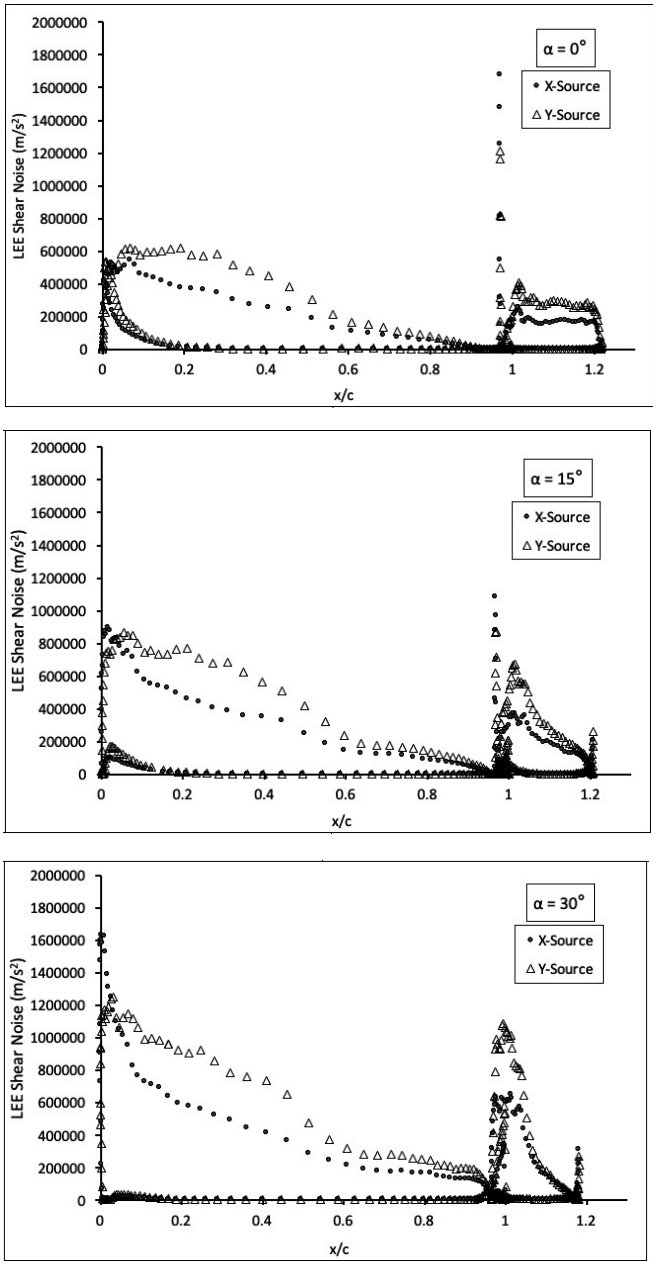


Fig. 20: Graph of LEE shear noise across airfoil profile for α = 0°, 15° and 30° with main element Eppler 423

4. CONCLUSION

2D CFD simulations were conducted using ANSYS Fluent in order to assess the impact of flap deflection and camber on the aerodynamic and aeroacoustic characteristics of airfoils. Analyses were conducted on airfoils with main elements NACA 0012 (maximum camber 0%), NACA 4412 (maximum camber 4%) and Eppler 423 (maximum camber 9.5%), with flap deflections 0°, 15° and 30°. The following inferences can be drawn from the results:

1. The lift coefficient of an airfoil increases with increase in main element camber. It also increases with increase in flap deflection. The drag coefficient also increases with increase in these quantities.
2. The flap lift coefficient decreases with an increase in main element camber.

3. The turbulence intensity observed on the suction side of the airfoil marginally increases with increase in main element camber, and that on the pressure side marginally decreases.A similar trend is observed in surface acoustic power level.
4. The difference between the turbulence intensities observed at the suction and pressure side of the airfoil increases with flap deflection, as does the surface acoustic power level.
5. A direct correlation can hence be drawn between the turbulence intensity and surface acoustic power level.
6. The X and Y-directional self and shear stresses increase on the suction side with increase in main element camber. They also increase with an increase in flap deflection. Y--directional sources dominate at higher flap deflections.

CONFLICT OF INTEREST
The author declares that he has no conflict of interest.

FUNDING
This research received no specific grant from any funding agency in the public, commercial, or not-for-profit sectors.

REFERENCES

[1] Wild, J., Pott-Pollenske, M., Nagel, B.: "An integrated design approach for low noise exposing high-lift devices," in 3rd AIAA Flow Control Conference, San Francisco, USA, 2006
[2] Brooks, T., Pope, D., A. Marcolini, A.: "Aerofoil self-noise and prediction," NASA Reference Publication 1218, 1989
[3] Roger, M., Moreau, S.: "Broadband Self-Noise from Loaded Fan Blades," AIAA Journal, vol. 42, no. 3, pp. 536-544, 2004
[4] de Gennaro, M., Hueppe, A., Kuehnelt, H., Kaltenbacher, M.: "Numerical Prediction of Laminar Instability Noise for NACA 0012 Aerofoil," in Numerical Analysis and Applied Mathematics ICNAAM 2011, AIP Conf. Proc. 1389, 2011
[5] Menter, F.: "Improved Two-Equation k-omega Turbulence Models for Aerodynamic Flows," NASA TM 103975, 1992
[6] Stepanov, R., Pakhov, V., Bozhenko, A., Batrakov, A., Kusyumov, A., Mikhailov, S., Barakos, G.: "Experimental and Numerical Investigation of Near-Field Rotor Aeroacoustics," in 44th European Rotorcraft Forum, Delft, The Netherlands, 2018
[7] Caicedo, E., Virk, M.: "Numerical Study of NACA 0012 Aeroacoustics Response for Normal and Icing Conditions," Applied Mechanics and Materials, vol. 875, pp. 89-93, 2018
[8] Hosder, S., Schetz, J., Mason, W., Grossman, B., Haftka, R.: "Computational-Fluid-Dynamics-Based Clean-Wing Aerodynamic Noise Model for Design," Journal of Aircraft, vol. 47, no. 3, pp. 754-762, 2010
[9] Dobrzynski, W., Nagakura, K., Gehlhar, B., Buschbaum, A.: "Airframe Noise Studies on Wings with Deployed High-Lift Devices," in 4th AIAA/CEAS Aeroacoustics Conference, Toulouse, France, 1998
[10] Matyushenko, A., Kotov, E., Garbaruk, A.: "Calculations of flow around airfoils using two-dimensional RANS: an analysis of the reduction in accuracy," St. Petersburg Polytechnical University Journal: Physics and Mathematics, vol. 3, no. 1, pp. 15-21, 2017
[11] ANSYS® Fluent Release 18.2
[12] Bardina, J., Huang, P., Coakley, T.: "Turbulence Modeling Validation, Testing, and Development," NASA Technical Memorandum 110446
[13] Lighthill, J.M.: "Sound Generated Aerodynamically I General Theory," Proceedings of The Royal Society, vol. A 221, pp. 564-587, 1952
[14] Bailly, C., Juve, D.: "Numerical Solution of Acoustic Propagation Problems Using linearized Euler's Equations," AIAA Paper A98-30841, 1998
[15] Marsden, O., Bogey, C., Bailley, C.: "Direct Noise Computation around a 3-D NACA 0012 airfoil," in 12th AIAA/CEAS Aeroacoustics Conference (27th AIAA Aeroacoustics Conference), Cambridge, Massachusetts, 2006
[16] Lee, H., Kang, S.: "Flow characteristics of transitional boundary layer on the NACA0012 airfoil in wakes,," in Proceedings of FEDSM'98, Washington, D.C., U.S.A., 1998.
[17] Hutcheson, F., Brooks, T.: "Effects of angle of attack and velocity on trailing edge noise determined using microphone array measurements," Aeroacoustics, vol. 1, no. 2006, pp. 39-66, 5.
[18] Staubs, J.: "Real Airfoil Effects on Leading Edge Noise," PhD Thesis, Virginia Polytechnic Institute and State University, 2008
[19] Lee, S.: "The Effect of Airfoil Shape on Trailing Edge Noise," Journal of Theoretical and Computational Acoustics, vol. 26, 2018



Vishesh Kashyap *is an undergraduate student in Mechanical Engineering at Delhi Technological University (formerly Delhi College of Engineering). His interests lie in computational fluid dynamics, experimental fluid mechanics and aerodynamics. Originally from Chandigarh, he currently lives in New Delhi.*

ResearchGate

See discussions, stats, and author profiles for this publication at: https://www.researchgate.net/publication/338866941

COUNTERMEASURES AGAINST LOCAL SCOURING AT CIRCULAR BRIDGE PIERS USING COLLAR AND COMBINATION OF SLOT AND COLLAR

Conference Paper · December 2018

CITATIONS
0

READS
3

2 authors, including:



Geeta Devi
Delhi Technological University
4 PUBLICATIONS **1** CITATION

SEE PROFILE

All content following this page was uploaded by Geeta Devi on 28 January 2020.

The user has requested enhancement of the downloaded file.

COUNTERMEASURES AGAINST LOCAL SCOURING AT CIRCULAR BRIDGE PIERS USING COLLAR AND COMBINATION OF SLOT AND COLLAR

Geeta Devi[1], DR. Munendra Kumar[2]
[1]*Research Scholar, Department of Civil engineering, DTU, Delhi,110042 India*
[2]*Associate Professor, Department of Civil Engineering, DTU, Delhi,110042 India*
Email: geetsharmacivilengg@gmail.com

ABSTRACT

Excessive scouring around the bridge pier is a threat to the stability of the bridge. It is utmost important for the human life and bridge safety that some countermeasures against scouring needs to be developed. This paper encompasses an experimental investigation on collar and combination of the slot with circular and square collar for a reduction in scour depth around the circular bridge piers. An experimental study was carried out in six different arrangements of collar and slot by varying values of Froude number under laminar flow.

Results from the present study reveal that scour depth increases with the increase in the Froude number and it decreases with the increase in the size of the collar. Combination of the circular collar and slot gives the minimum scour depth amongst all the arrangements.

Keywords: River hydraulics, Scouring, Circular Bridge Pier, Scour protection Device, Slot and Collar.

1. INTRODUCTION

Local Scour is the main causes of failure of many bridges inside the river, and it is the very unavoidable situation. Therefore, safe designing of the bridges is necessary, it is only possible by the accurate recognition, estimation, and change of bed level around the bridge pier.

The interaction between bridge piers and flowing water gives a three-dimensional flow field. on the upstream side of the flow field a strong pressure gradient generated and on the downstream side, negative stagnation pressure occurs. The approaching flow field from upstream results in the formation of horseshoe vortex and from downstream results in the formation of the Wake vortex. The combination of horseshoe and wake vortex cause the development of local scour. (Grimaldi, et al. 2009)

From the various researches, it is well documented that the main cause of failure of bridge pier is the occurrence of scouring around the piers Melville and Coleman 2000_. Posey _1974_, Odgaard and Wang_1987_, Graziano et al. _1990_, Chiew _1992_, Bertoldi and Kilgore _1993_, McCorquodale et al. _1993_, Parola _1993_, Jones et al. _1995_, Melville and Hadfield _1999 and other researchers have introduced different countermeasure devices. these devices are classified into two categories namely Armoring devices and flow-altering devices. Armoring devices includes Cable-tied blocks, tetrapods, dolos, placed riprap rocks, flexible mattresses, grout mats, and bags anchors and high-density particles etc. around pier foundation. Flow altering devices include sacrificial piles placed upstream of the pier, Iowa Vanes, and flow deflectors attached to the pier, such as collars and slots. (Zarrat, Mashahir and Nazariha FEBRUARY 2006)

Various countermeasures were used by the researchers and out of them, collars were considered by more researchers. collars prevent the reduces the scour by preventing the direct impact of

flow on the pier and also reduces the horseshoe vortex below the collar. (Mashahir, Zarrati and Mokallaf March 1, 2010)

Effect of Local scour is reduced by the use of collar with time aspect of the scour development. Collars are adopted mostly because of its existence and scour reduction efficiency. (Elsebaie February 2013)

The total scours around the bridge pier includes general scour, contraction scour and local scour. All over the world number of investigators are researching in the field of scouring and only limited success has been reported by using different model analysis physically and computationally. (M., et al. 2007)

2. MECHANISM OF LOCAL SCOUR AT BRIDGE PIERS

2.1 Traditional types of scour protection and principles of working

In alluvial channel bed, the formation of Scour hole is a matter of discussion in various researches. Engineers must take the precautions in designing so that this type of failures cannot occur because they lead to heavy loss of construction and human life. there are basically two approaches to the protection of the foundation of bridge pier

1. Placement of protection layer of coarser granular materials or placing of riprap
2. Protection using Collar or Caissons around the bridge pier. (Chiew September, 1992)

3. EXPERIMENTAL PROGRAM

Experimental work was conducted in hydraulics laboratory of Delhi Technological University, Delhi, India, in a 6 m long, 0.3m wide,0.45m deep Flume by using a cylindrical pier of diameter 5 cm and 60 cm length. The working section, in which the sample was situated was at a distance of 50 cm upstream from the entrance of the flume.

Experiments were conducted using the bed of cohesionless sand with three different uniform sizes of diameter 0.78mm, 1.18mm and 1.54 mm were laid laterally and 15 cm above the flume bed level. Value of the specific gravity of all the sands was 2.65. For performing the scouring process flume was cleaned by allowing free discharge through it. The uniform flow was attained by adjusting the bed slope. Bed of the sediments was leveled before the commencement of the experiments. For taking the observations of the scour depth a scale on the upstream side of the flow field was enabled.

In the present study, experiments include tests to study the effect of the collar, a slot, and a combination of both. Circular and square wooden collar of thickness 4 mm and a slot of dimension 1 cm width and 5 cm height was considered for experimental work. Collars of varying diameter 1.5D, 2.0D, 2.5D,3.0D and square collar of varying dimension 1.5D× 1.5D, 2D×2D, 2.5D× 2.5D, 3D× 3D was used in experiments.

An experimental program was conducted in six different arrangements of samples by increasing the value of Froude number. Three sets of same experiment series were conducted for observing the effects of collar and slot on Scour depth. The experimental summary is tabulated below in Table 1.

Table 1: Experimental summary

Sr. No	Experiments
1	For Cylindrical Pier of Diameter 5cm
2	For Cylindrical pier with a collar of diameter (1.5D to 3D)

3	For Cylindrical pier with a Square collar of dimension (1.5D×1.5D to 3D×3D)
4	For Cylindrical pier with Slot of Dim (5 cm ×1 cm)
5	For Cylindrical pier with slot and Circular collars
6	For cylindrical pier wit Square collars

4. ANALYSIS OF DATA

4.1 Scour reduction due to collar

From various researches, it is concluded that the use of collar can reduce the scour depth effectively because collar has a shielding effect against the erosion of sediment particles. (Thomas 1967)

if ds_c = Depth of Scour at a pier with a collar
ds_p= Depth of scour at a pier without a collar
Under uniform flow condition we can write:

$$\frac{ds_c}{ds_p} = f_1\left(\frac{B}{b}, \frac{H}{Y_o}\right) \quad (1)$$

or

$$\frac{ds_p - ds_c}{ds_p} = f_2\left(\frac{B}{b}, \frac{H}{Y_o}\right) \quad (2)$$

Eq. (2) forms the basis for studying the effect of collar size and elevation on scour depth. An additional parameter of collar thickness should also appear in eq.(2), but it is not taken consideration because in present study thickness of collar is negligible. (Kumar, Raju and Vitta December,1999)
In the present study, it was observed that deepest scour occurs at the upstream face for the small sized collar (1.5D) and the minimum was observed for the largest size (3D). As the diameter of the collar increases the scour depth decreases. it establishes an inverse relationship between collar diameter and scours depth. The pattern of scour depth by increasing diameter and Froude No. is shown in fig.1. for the circular collar.

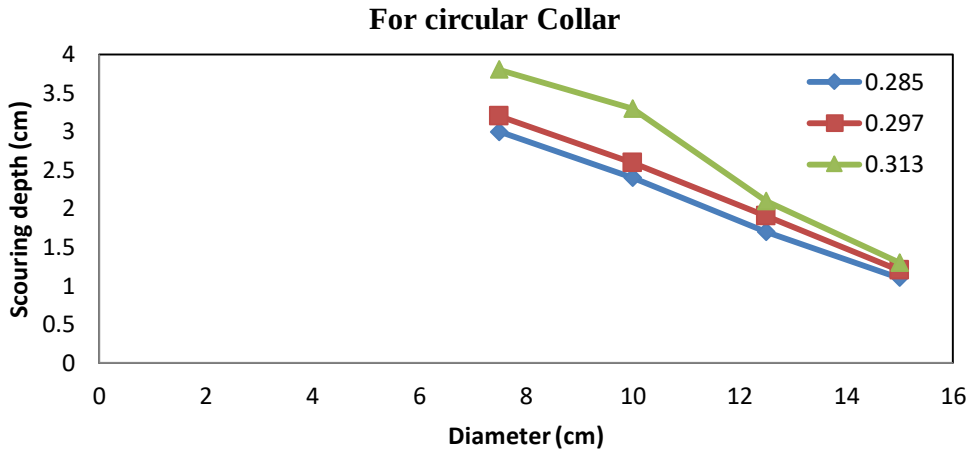


Figure 1: Variation of Scour depth by increasing diameter with Different Froude No.

In the present study, Square collars were also used to observe the effect of shape and size of the collar on scour depth. Figure 2. represents the pattern of scour depth by varying Froude no for square collars.

For Square Collar

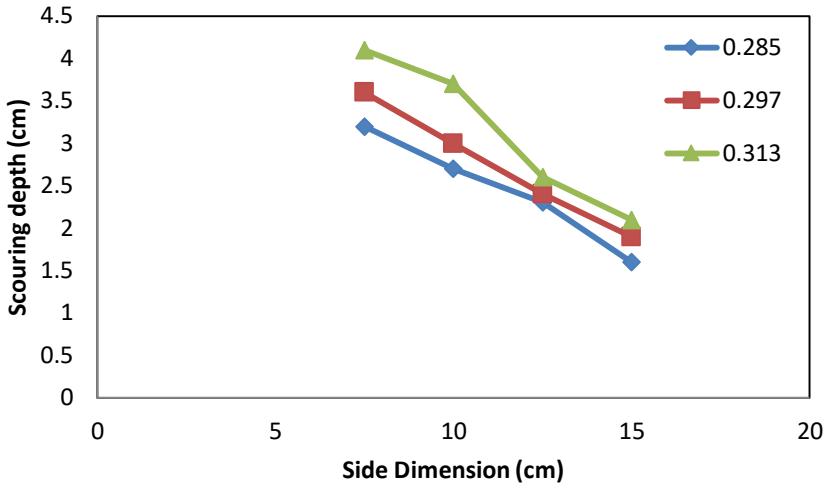


Figure 2: Variation of Scour depth by increasing size with Different Froude No.

4.2 Scour reduction due to slot

The principle of using slots are as follows:

1. To divert the Downflow away from the bed
2. To reduce the influence of Downflow on the bed

In the present study, the slot was located near the bed because the oncoming flow on the lowermost layer will get accelerated through a slot in the form of a horizontal jet which results in a reduction in scouring potential.

under uniform flow condition, we can write as:

if ds_s= Depth of scour at a pier with slot

$$\frac{ds_s}{ds_p} = f_1\left(\frac{w}{b}, \frac{Y_L}{Y_o}, \theta\right) \quad (3)$$

where θ = Angle of approach flow with slot axis

w = Width of slot

Equation (3) represents dimensionless geometric parameters which are related to slot only. This equation is based on assumption that effect of the flow and sediment parameters have been accounted for using ds_p. (Kumar, Raju and Vitta December,1999)

Figure 3 Represents the difference in the scour depth by using the slot in comparison of using the only pier. It shows a significant decrease in the scour depth.

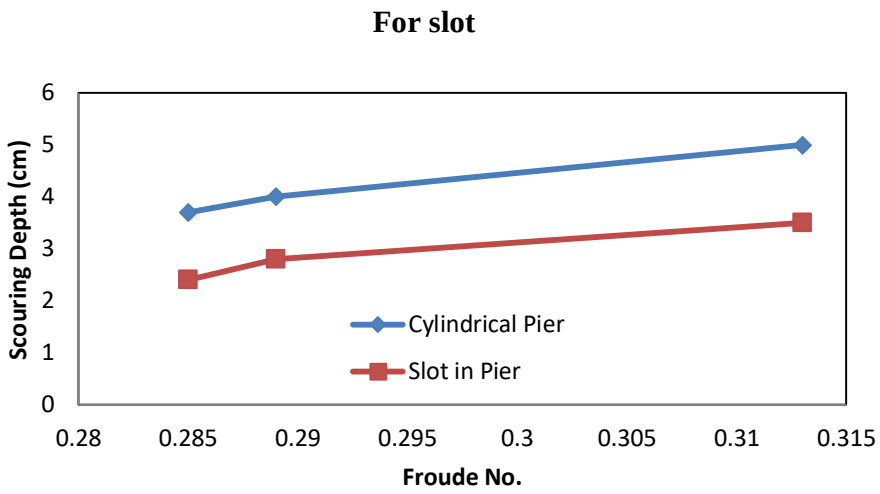


Figure 3: Representation of scour depth reduction by using slot

4.3 Scour reduction due to a combination of slot and collar

For more reduction the scour depth combinations of the slot and collars are adapted for circular as well as the square collar. when the slot is used together with collar, the results show an improved scour depth reduction. The use of a slot in combination with the circular collar reduces the scour depth by nearly 80%. Reduction in scours depth is shown in figure 4. Combination of the slot and square collar reduces the scour depth nearly by 75% and its representation is shown in figure 5.

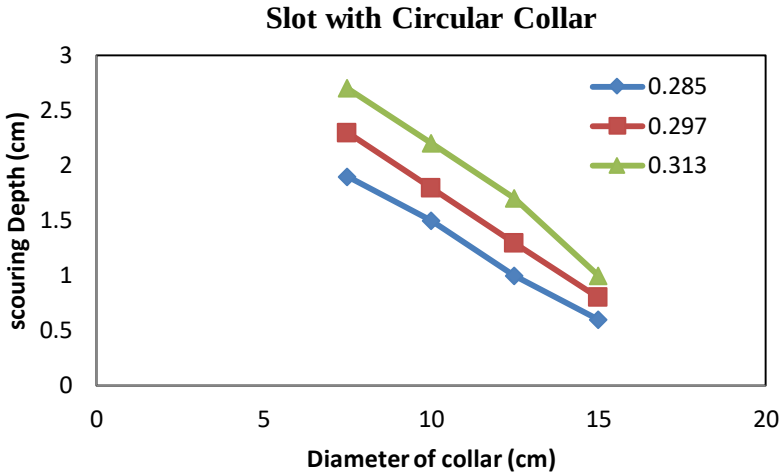


Figure 4: Variation of scour depth by using a combination of slot and circular collar for different Froude No.

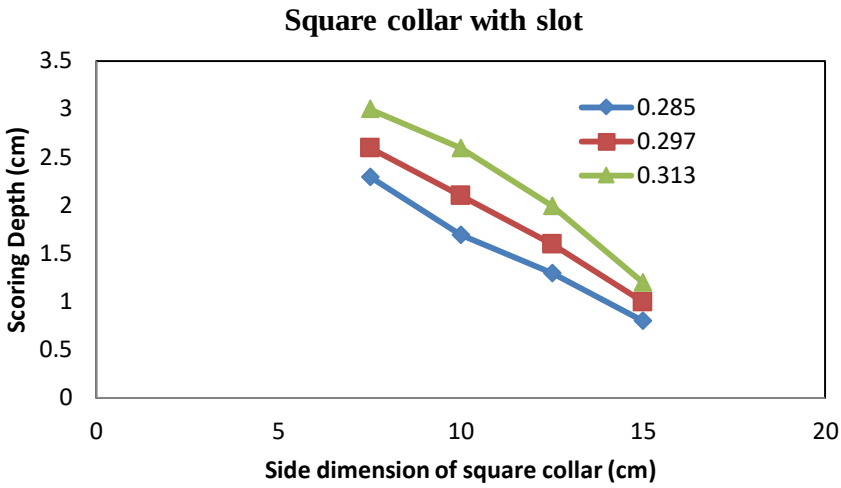


Figure 5: Variation of scour depth by using a combination of slot and square collar for different Froude No.

6. CONCLUSION

The present study investigated the effect of the collar, slot and combination of the two on the bridge pier scour. Experimental results of these protection devices show their efficiency in reducing scouring depth. Following observations were made by Experimental work:

- Scour depth Increases with the increase in the Froude No. by nearly 3%
- Scour depth decreases with the increase in the size of the collar. For the circular collar, the reduction in the scour depth was observed nearly 63% in comparison to the pier only. For the square collar, the reduction in scour depth was observed less in comparison of the circular collar it was 50%.
- By using the slot in the pier value of scouring reduction was observed at 75%. For further reduction in the scour depth combination of slot and collar were adopted. The combination of the slot with circular collar reduces the scour depth by 83% in comparison to the single pier scour and the combination of the slot with square collar gives the scour reduction value 78%.
- Maximum scour reduction was observed in the case of a combination of slot and the circular collar was nearly 83% for the Froude no 0.285 results are shown in figure no 4.

ACKNOWLEDGEMENT

The comments and suggestions of the reviewers, which improved the original manuscript are gratefully acknowledged. Experimental work was conducted in hydraulics laboratory at Delhi Technological university, Delhi and author is highly grateful.

REFERENCES

Chiew, Yee-Meng. "SCOUR PROTECTION AT BRIDGE PIERS." (Journal of Hydraulic Engineering,©ASCE) Vol. 118, no. No.9 (September, 1992).

Elsebaie, Ibrahim H. "An Experimental Study of Local Scour Around Circular Bridge Pier in Sand Soil." (International Journal of Civil & Environmental Engineering) 13, no. 03 (February 2013).

Grimaldi, Carmelo, Roberto Gaudio, Francesco Calomino, and António H. Cardoso. "Countermeasures against Local Scouring at Bridge Piers:Slot and Combined System of Slot and Bed Sill." (JOURNAL OF HYDRAULIC ENGINEERING © ASCE) 135, no. No. 5 (2009).

Kumar, Virender, Kittur G. Ranga Raju, and Nandanal Vitta. "REDUCTION OF LOCAL SCOUR AROUND BRIDGE PIERS USING SLOTS AND COLLARS." (Journal of Hydraulic Engineering ASCE) Vol. 125, no. No. 12 (December,1999).

M., Thamer A., et al. "Physical Modeling of Local Scouring around Bridge Piers in Erodable Bed." (J. King Saud Univ.@Engineering science) vol. 19, no. 2 (2007).

Mashahir, Mohammad B., Amir Reza Zarrati, and Ebrahim Mokallaf. "Application of Riprap and Collar to Prevent Scouring around Rectangular Bridge Piers." (JOURNAL OF HYDRAULIC ENGINEERING © ASCE) 136, no. No. 3 (March 1, 2010).

Thomas, Z. "An interesting hydraulic effect occurring at local scour." Netherlands: Proc.12th IAHR Congress,, 1967.

Zarrat, A.R, M. B. Mashahir, and M. Nazariha. "Reduction of Local Scour in the Vicinity of Bridge Pier Groups Using Collars and Riprap." *JOURNAL OF HYDRAULIC ENGINEERING © ASCE*, FEBRUARY 2006: 154-162.

View publication stats

© Universiti Tun Hussein Onn Malaysia Publisher's Office

IJIE

Journal homepage: http://penerbit.uthm.edu.my/ojs/index.php/ijie

The International Journal of Integrated Engineering

Edge Detection using Ant Colony Optimization under Novel Intensity Mapping Function and Weighted Adaptive Threshold

Akshi Kumar[1], Sahil Raheja[2*]

[1] Dept. of Computer Science and Engineering,
Delhi Technological University, Delhi, INDIA,

[2] Research Scholar, Department of Information Technology,
Delhi Technological University, Delhi, INDIA,

*Corresponding Author

DOI: https://doi.org/10.30880/ijie.00.00.0000.00.0000
Received 6 September 2018; Accepted 18 November 2018; Available online 31 January 2020

Abstract: Edge detection is a crucial phenomenon in image segmentation. In general, kernel based methods like Sobel, Canny, Roberts etc. are used which are based on first and second derivatives pixels intensity. However, these methods fail to find all the true edges. Moreover, number of falsely detected edges is much more than true edges. This happens due to a fixed threshold used in these methods. To reduce falsely detected edges, a method which can dynamically adjust its threshold is desirable. Artificial and swarm intelligence based methods are capable to handle minute details. In this work, Ant Colony Optimization (ACO) based method is detailed for edge detection. In this method, a novel function is used to capture intensity variation in a particular image. In learning based method adjustment of threshold is also necessary to obtain good results. In this work, we have considered weighted average for threshold update in contrast to earlier method where simple average is taken. The performance evaluation and comparison is made in terms of Peak-Signal-to Noise Ratio (PSNR), accuracy and F-Score and usefulness of proposed method is shown. Finally, results are compared in terms of F-score with recent methods. In the earlier compared method Sketch Token provide best F-score of 0.73 and with proposed method the obtained best F-score is 0. 97, therefore percentage improvement is of 32.80% is observed with proposed method.

Keywords: ACO, Sobel, Canny, F-Score

1. Introduction

Image edge detection is a prime problem in image segmentation. Edge detection is comprehensively used in various fields of engineering science and technology. An edge can be defined as a group of connected pixels lying between boundaries of two regions. An Edge is a local concept but the boundary is a global concept. The edge pixels are the pixels whose grey levels have big difference with the gray levels of their neighbourhood pixels [1-4]. Edge detection process could be defined as the technique of extracting the edges in a digital image. It is a set of arrangements of actions with the main purpose of identifying points in an image where variations or discontinuities in intensity take place. This set of action is vital to comprehend the substance of an image and with the help of these extracted edge points, we can have the important information in the field of machine vision and image analysis [1]. It goes about as a pre-processing stage for extraction of feature and object recognition [1]. It is generally used in starting phase of computer vision applications. In biometrics, edges are important to capture important features of biometric identifies. Similar in fog and rain streak detection, edge detection is used to enhance background edges, so that fog and rain

*Corresponding sahilraheja78 @gmail.com
2020 UTHM Publisher. All right reserved.

streaks can be removed from the images. The traditional methods are based on design of a kernel and depending on type of kernel, various edges are detected either using single or double thresholds [1]. Edge detection is heavily relying on intensity change, and a sharp change in intensity refers to an edge point. In gradient based method we count amplitude changes as

$$c(f) = N\{p \mid |f_p - f_{p-1}| \neq 0\} \quad (1)$$

where p and p - 1 index neighboring samples (or pixels). $|f_p - f_{p-1}|$ is a gradient w.r.t. p in the form of forward difference. $N\{\}$ is the counting operator, outputting the number of p that satisfies $|f_p - f_{p-1}| \neq 0$, that is, the L_0 norm of gradient. In gradient based method both magnitude and directions are important in classifying edge and non-edge pixels.

2. Background

In past various kernels based methods like Canny, Sobel, Robert, Laplacian and Prewitt etc. emerged [1]. These methods successfully find edges in different images. However, in these methods, edge detection is not prefect and in addition to the true edges, they also detect false edges. In fact, false edges are more in number than true edges. Therefore, novel techniques based on swarm intelligent have been proposed. One such technique is Ant Colony Optimization (ACO). This methodology is fundamentally based on the perception of real ant colonies. In early 1990s, this algorithm was presented by M. Dorigo and his colleagues [2]. A comparison of numerous methods of image edge detection of Gradient and Laplacian based edge detection was proposed by R. Maini and H. Aggarwal [3].

Problem: Algorithms that are gradient-based like Sobel, Canny and Prewitt filter etc. have a noteworthy disadvantage of being quite delicate to noise. The size and coefficients of kernel matrix can take fixed set of values and can't be adjusted to a given image. Thus, there is a need of adaptive edge detection algorithms which can provide robust solutions that can make the adjustments as per the changing levels of noise levels of these images to assist in recognizing contents of valid image from visual artifacts presented by noise. Therefore, techniques are needed which are adaptive in nature and which can automatically adjust threshold to produce more correct edges.

Literature Review:

In past, various ACO-based approaches for the edge detection in images and video frames have been proposed [4], [5] and [6]. First attempt for ACO based edge detection technique was proposed in [4], where it is shown that ACO can be successfully used in edge detection. In [5], ACO based technique is used to connect broken edges. In [6] ACO is used to detect edges and contour of an image. In edge detection methods, some kinds of mechanism are used to further enhance the detected edges (refer [7], [8] and [9]). In [7], image pre-processing of image is suggested before applying ACO and other techniques to enhance and then detect edges. In [8] histogram equalization based technique is proposed to further correctly detect edges. In [9] fuzzy based techqiues are used for the localization and detection of edges.

Proposed Solution:

However, in ACO based past method, four intensity mapping functions are considered and different images are tested on these functions, and the one which provides descent solution is chosen [4]. Ideally there are uncountable functions to represent various images. Moreover, none of above mentioned papers in past uses any statistical measure to observe the quality of edge detection.

In this paper, we have considered six image from Berkeley Segmentation Dataset which is a notable dataset used in edge detection [4]. For all six images, intensity variations are captured and on the basis of arising variations, a novel intensity mapping function which works well on most of the images is presented. The results are obtained in terms of PSNR (Peak Signal to Noise Ratio), Accuracy and F-measure. PSNR is a measure of quality of images while other two are related with correctly detected edges. The results are shown and compared with old famous Canny and Sobel edge detection methods. Finally, results are also compared with recently proposed other methods in terms of statistical measures.

3. Ant Colony Method and Edge Detection

In this ACO technique, a fixed number of ants which is decided by the size of an image proceed onward a 2-D picture, venturing starting with one pixel then onto the next to build a pheromone matrix, which is used for the identification of edge pixels. The development of the ants is coordinated by the nearby variety of the force values of image [4]. The procedure of image edge detection [4] contains the accompanying steps:

3.1 Initialization Phase

In this procedure for a picture (I : intensity of pixel) I_{MN} (where M and N represents in size) is input information on which ants travel to find solutions. The considered K ants are moved haphazardly over the entire picture with the end goal that the each pixel of the picture is seen as a node. The constant is τ allotted to every, which is the underlying estimation of each part of the pheromone matrix. Initially, each entry of the pheromone matrix $\tau^{(0)}$ is considered as a constant.

3.2. Construction Phase

One ant is irregularly chosen at the n-th construction-step from the K ants, and this ant moves continuously on the image for S steps. The ant movements to its neighboring node (x, y) depends on transition probability and is defined as

$$p^{n}_{(l,m)(x,y)} = \frac{\left(\tau^{(n-1)}_{x,y}\right)^{\alpha}(\eta_{x,y})^{\beta}}{\sum_{x,y\in\Omega_{(l,m)}}\left(\tau^{(n-1)}_{x,y}\right)^{\alpha}(\eta_{x,y})^{\beta}}, \quad y \in \Omega_{x} \qquad (2)$$

In the above equation, for node (x, y), $\tau^{(n-1)}_{x,y}$ is defined as the pheromone value. Parameter $\Omega_{(i,j)}$ represents the neighborhood nodes of the node (imp), the parameter $\eta_{x,y}$ defines the heuristic value at a particular node (x, y). The effect of the pheromone and the heuristic matrix is represented by the constants α and β respectively.

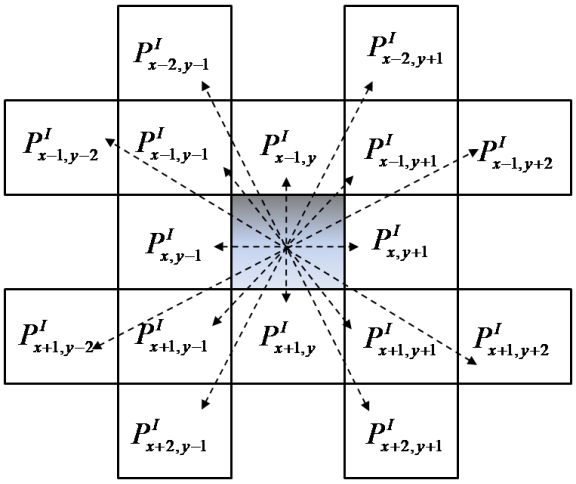


Fig. 1-Pictorial representation of clique

The procedure comprises two vital issues as:

1. Using the inner clique determine the heuristic data $\eta_{x,y}$ $\eta_{x,y} = \frac{1}{Z}G_c(x,y)$ (3)

   and

2. $Z = \sum_{x=1:M}\sum_{y=1:N} G_c(x,y)$ (4)

The parameter Z is used for normalization, while $P^I_{x,y}$ represents the intensity of the pixel at the (x, y) position of the image I_{MN}, the function $G_c(x, y)$ is a function of a local group of pixels (known as the *clique*), and its estimation relies on the changes in intensity values of image of the clique (as illustrated in Fig .1). For the pixel $P^I_{x,y}$ the function $G_c(x,y)$ is

$$G_c(P^I_{x,y}) = F\begin{bmatrix} \left|P^I_{x-2,y-1} - P^I_{x+2,y+1}\right| + \left|P^I_{x-2,y+1} - P^I_{x+2,y-1}\right| \\ + \left|P^I_{x-1,y-2} - P^I_{x+1,y+2}\right| + \left|P^I_{x-1,y-1} - P^I_{x+1,y+1}\right| \\ + \left|P^I_{x-1,y} - P^I_{x+1,y}\right| + \left|P^I_{x-1,y+1} - P^I_{x-1,y-1}\right| \\ + \left|P^I_{x-1,y+2} - P^I_{x-1,y-2}\right| + \left|P^I_{x,y-1} - P^I_{x,y+1}\right| \end{bmatrix} \quad (5)$$

The proposed intensity mapping function $F(\cdot)$ in above equation is

$$F(x) = \mu x + \sin\left(\frac{\pi x}{2\mu}\right) \quad \text{for } 0 \le x \le \mu \quad (6)$$

In general, to complete map pixel values of a particular image, $F(x)$ is unique for each image. The proposed function considers two types of variations, one is linear and other is sinusoidal which fit on large number of images as shown in result section. The parameter μ defined in the functions (8) modifies the functions' respective shapes. The acceptable range of the ants movement (i.e., $\Omega_{(i,j)}$ as in equation (4)) is considered to be the 8-connectivity neighborhood, as demonstrated in Fig . 2. The proposed function is further explored in result section.

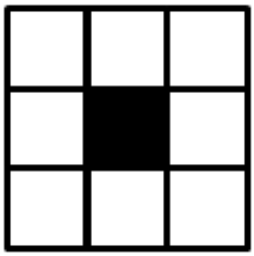


Fig. 2- Schematic of 8-connectivity neighborhood

3.3. Update Phase

In the update process, we update the pheromone matrix after the two operations of updation. The initial update is performed after the mobility of every ant in every development step. Every block of building of pheromone matrix is altered as

$$\tau^{(n-1)}_{x,y} = \begin{cases} (1-\rho)\tau^{(n-1)}_{x,y} + \rho\Delta^k_{i,j} & \text{if } (x, y) \in \text{vca} \\ \tau^{(n-1)}_{x,y} & \text{otherwise} \end{cases} \quad (7)$$

Where, 'vca' means 'visited current ant'. At this point, the parameter ρ, represents the rate of evaporation of pheromone, is estimated using the heuristic matrix. Second update is performed after the completion of the movement of the total ants in each step as

$$\tau^{(n)} = (1-\psi)\tau^{(n-1)} + \psi\tau^{(0)} \quad (8)$$

Now, the parameter ψ represents the pheromone decay coefficient expands the look for the consequent ants by diminishing the pheromone level on the visited edges. Along these lines, it gives a chance to the consequent ants to create fundamental arrangements. Consequently, the probability of reiteration turns out to be more improbable in a similar iteration [10].

3.4 Decision Phase

Finally, at each pixel position, decision has to be made to find out whether it is edge or not, by making application a threshold *Th* on the basis of last updated pheromone matrix $\tau^{(N)}$. The *Th* in this research article to be adaptively estimated on the basis of the technique created in [11]. We chose the initial threshold $Th^{(0)}$ as the pheromone matrix mean value. After this following steps are performed:

Step 1: Initialize $Th^{(0)}$ as

$$Th^{(0)} = \frac{\sum_{x=1:M} \sum_{y=1:N} \tau_{x,y}^{(n)}}{MN} \quad (9)$$

and fix the iteration index as q= 0.

Step 2: Now pheromone matrix $\tau^{(n)}$ is divided into two classes making use of $Th^{(q)}$, here the first class comprises entries of τ which is lesser than threshold $Th^{(q)}$, and the left over entries of τ in other half. After this, make the calculation of the mean of two classes as

$$m_L^{(q)} = \frac{\sum_{x=1:M} \sum_{y=1:N} c\tau_{x,y}^{(n)}}{\sum_{x=1:M} \sum_{y=1:N} \tau_{x,y}^{(n)}} \quad \text{for } c \le Th^{(q)} \quad (10)$$

$$m_U^{(q)} = \frac{\sum_{x=1:M} \sum_{y=1:N} c\tau_{x,y}^{(n)}}{\sum_{x=1:M} \sum_{y=1:N} \tau_{x,y}^{(n)}} \quad \text{for c} \ge Th^{(q)} \quad (11)$$

Step 3: Fix the index of iteration $q = q+ 1$, and we update the threshold as given below

$$Th^{(q)} = \frac{m_L^{(q)} + m_U^{(q)}}{2} \quad (12)$$

Step 4: In the case of $\left|Th^q - Th^{(q-1)}\right| > \varepsilon$, after this move on to *Step 2*; else, the iteration method is discontinued and a decision is made on all pixel's location (x, y) in order to find out edge using:

$$E_{x,y}^d = \begin{cases} 1 & \tau_{x,y}^{(n)} \ge Th^{(q)} \\ 0 & \text{elsewhere} \end{cases} \quad (13)$$

3.5. Proposed Modifications

In the first suggested modification step -3 is modified as

Step 3: Fix the index of iteration $q = q+ 1$, and we update the threshold as given below

$$Th^{(q)} = \frac{w_1 m_L^{(q)} + w_2 m_U^{(q)}}{2} \quad (14)$$

Where, w_1 and w_2 are the weights given to both thresholds satisfying $w_1 + w_2 = 1$.

In the second modifications step -4 is defined as:

Step 4: In continuation of step 4, following condition is also included. For each value of w_1 and w_2 threshold is evaluated and F-score is calculated, and finally select the value of w_1 and w_2 for which F-score is maximum.

4. Simulation and Results

The performance of ACO based edge detection method with novel intensity method is done by using computer simulation in MATLAB(R). In the simulation, BSD (Berkeley Segmentation Dataset) is considered. In total, we have considered six images defined as 1-6 (Fig. 3), along-with the ground truth images (g) which contain ideal edges.

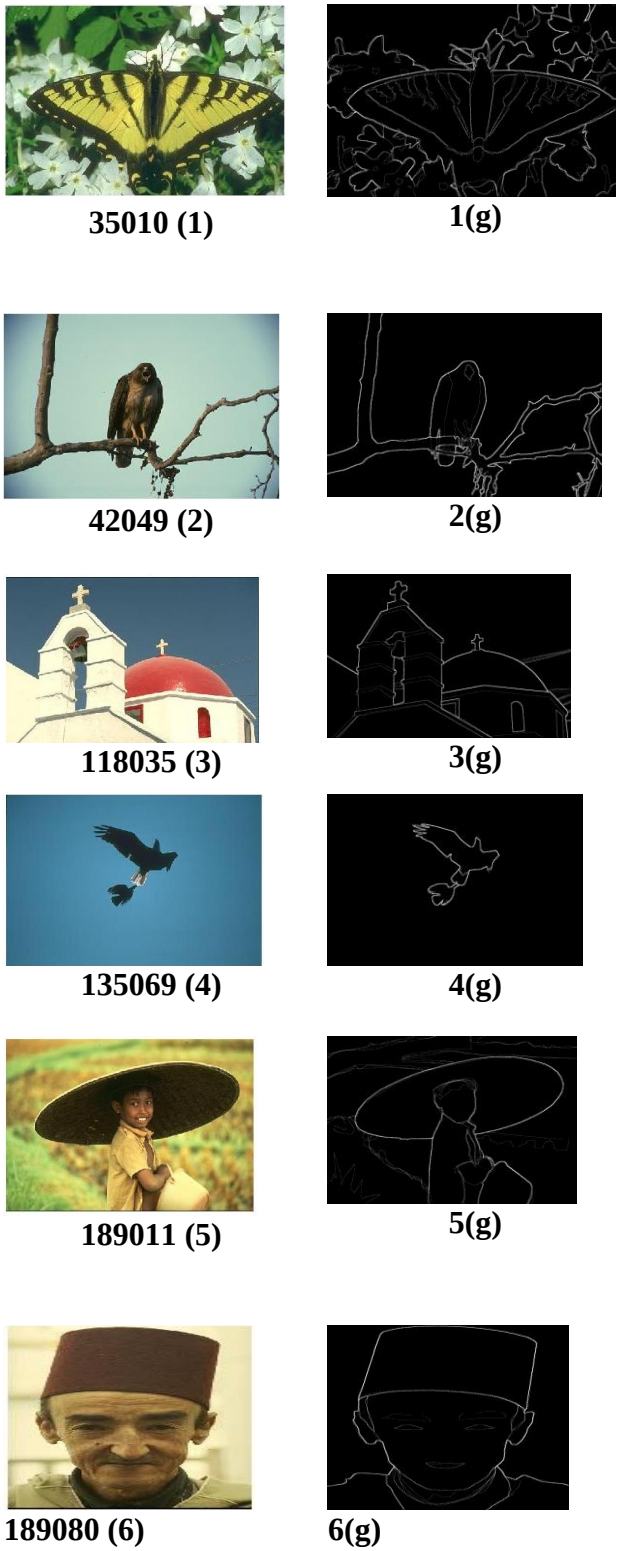


Fig. 3- BSD image database

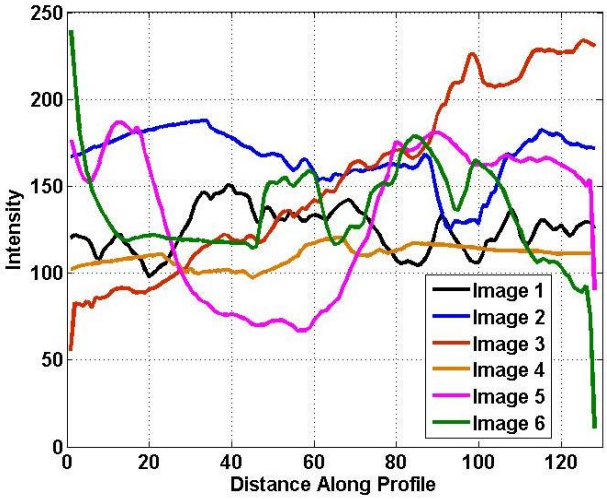


Fig. 4-Intensity profiles for all six images

In Fig. 4, intensity profiles for all six images are shown. In all six profiles, linear and sinusoidal variations can be seen, except in image 6 where a narrow spike can be seen. Thus, images where abrupt profiles changes are seen sinc function will be a better option, but still chosen function fit most of the images with fair accuracy. In particular, image 3 and 4 can be approximated by a linear function; similarly image 1 and 5 can be approximated with sinusoidal function, while image 2 and 6 is well approximated by addition of both linear and sinusoidal function. The difference between exact mapping and approximated function leads to difference of nearly 1.5 to 2.0 dB in PSNR while accuracy affected by 0.5 to 2.5%. We make the calculation of performance on the grounds of PSNR, Accuracy and F-measure. The (PSNR) is given by

$$PSNR = \frac{[255]^2}{MSE} \tag{15}$$

where:

$$MSE = \frac{[I_g(i,j) - I_o(i,j)]^2}{mn} \tag{16}$$

In above $I_g(i,j)$ is ground truth image and $I_o(i,j)$ is image obtained through Sobel, Canny and ACO methods. The accuracy is defined as

$$Accuracy = \frac{TE}{TE + FE} \tag{17}$$

where, TE=True Edges
FE=False Edges

This is an important factor and its ideal value is 1, but due to the false detection accuracy goes down, and in fact in many traditional methods more numbers of false edges are detected than true edges.

F- Measure is a test of accuracy, and it is a weight function of precision and recall. In case of equal weightage, it is the harmonic mean of precession and recall.

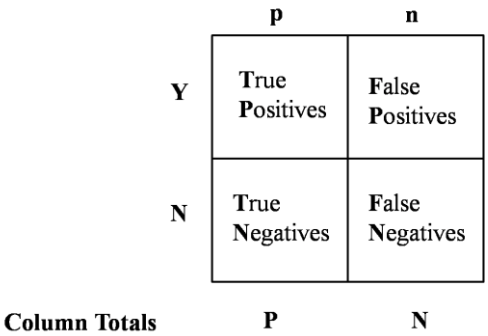


Fig. 5-Characteristic matrix

The important parameters are defined as:

$$P = \frac{TP}{TP + FP}, \quad R = \frac{TP}{TP + FN} \tag{18}$$

Where,
P=Precision
R=Recall
TP=True Positive
FP=False Positive
FN=False Negative
Finally the F-Score is given by

$$F = \frac{2PR}{P + R} \tag{19}$$

Where P is total positive, N is total negative and so on (Fig. 5). F-measure is a test of accuracy, in binary classification. It depends on both precession and recall to get test score. The maximum value of F is 1 with minimum as 0.

TABLE 1- Simulations Parameters [4]

Parameters	Value
Total number of construction steps	8
pheromone matrix, τ_{init} (Initial values)	0.0001
Pheromone information, α (Weighting factor)	1
Heuristic information, β (Weighting factor)	0.1
Connectivity neighbourhood, Ω	8
Functions adjusting parameter, μ	10
Total number of ants	vary
evaporation rate, ρ	0.1
Total number of ant's movement-steps, S	40
Pheromone decay coefficient, ψ	0.05
Tolerance value, ε	0.1
Threshold, Th	adaptive

The simulation parameters are detailed in Table 1. The total numbers of ants which is needed to be taken depends on image size. If image under consideration of size ($m \times n$) than the number of ants are $\lfloor \sqrt{mn} \rfloor$.

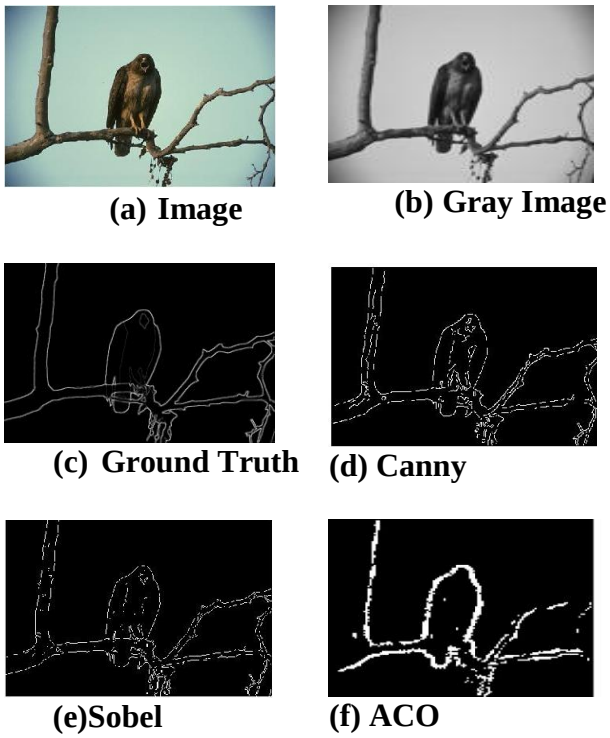


Fig. 6-Results comparison of different algorithms

In Fig. 6, six images (a-f) are shown. Images description is also given. If we carefully examine image (d) we observe that it detects most of the true edges but it also detects a large number of false edges. Sobel method tries to discard false edges, but in doing so it also discards true edges (e). However, ACO detects large numbers of true edges with few false edges (f). It is very difficult to judge the quality of image by using human visual system, Therefore, performance measures as discussed above, are used for comparisons of methods. In our work we have shown comparison with Sobel and Canny methods which are still used in edge detection methods, the main aim of choosing these two method is that we want to show that the effectiveness of ACO methods over currently used edge detection methods.

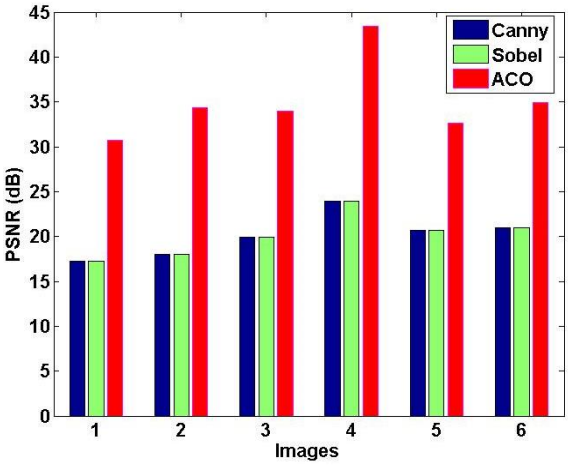


Fig. 7- PSNR comparison for different algorithms

In Fig. 7, PSNR (dB) is plotted for all six images under considerations. In terms of PSNR the performance of Canny and Sobel is nearly same, however in most of cases PSNR is below 20 dB except for image 4 where it is nearly 23.5 dB, which is of poor quality as in image processing a good quality image has PSNR> 30 dB. Thus, the edge detected images are not re-usable when we consider Sobel or Canny detection. While in case of ACO, the PSNR is above 30 dB, in all the cases and for image 4, it is nearly 44 dB which is of excellent quality.

In edge detection accuracy is an important phenomenon, as most of the kernel based method successfully identifies the edges, but in addition to this these methods also detects false edges. Infect, number of false edges is more in comparison to true edges. In Fig. 8, accuracy of different methods are shown, the performance of Canny method is better in comparison to Sobel method, still the accuracy is below 20%. In case of ACO the minimum accuracy is 87%. This happens because with ACO, the numbers of falsely accepted edges are very less sometime in state of confusion ACO reject true edges. Therefore, in ACO the numbers of detected true edges is much more than falsely accepted edges. Thus, accuracy is high.

In Fig. 9, F-score is shown for all six images. For each ground truth image score is 1. In our experiment, Sobel and Canny methods are considered without using any morphological operations. Thus, basic methods are full of errors and F-measure is less than one. However, further improvements are done to improve F-score as detailed in Table. The obtained F-score with ACO is of excellent quality and lies between 0.67 to 0.97.

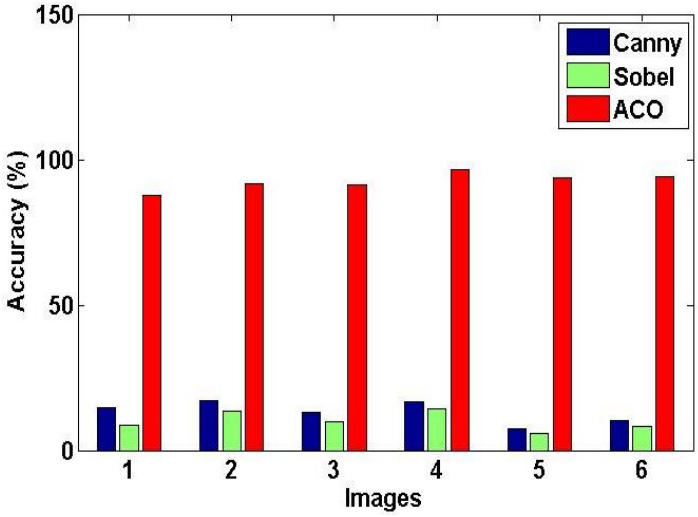


Fig. 8-Accuracy comparison for different algorithms

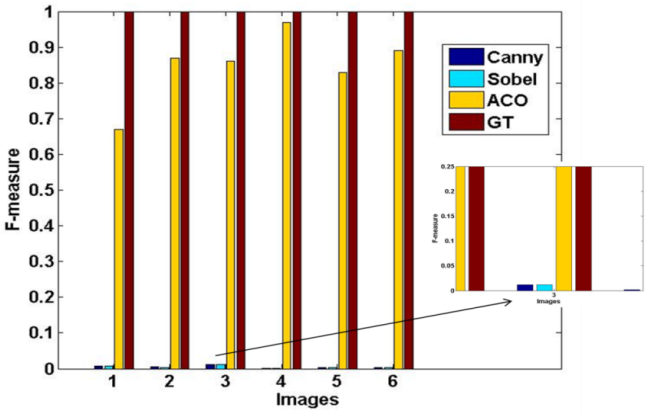


Fig. 9- F-measure comparison for different algorithms

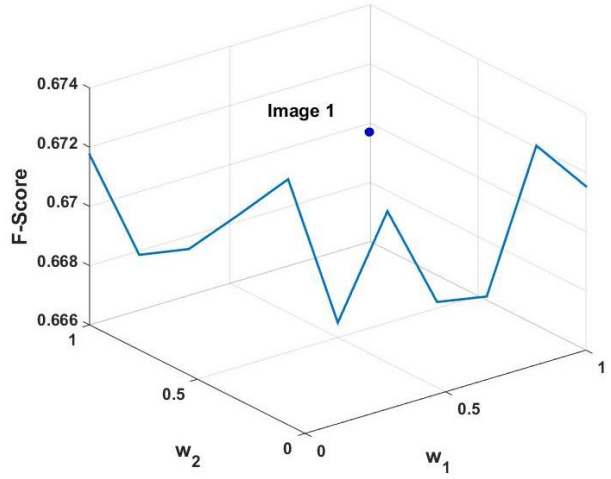


Fig. 10-F-measure variation for image 1

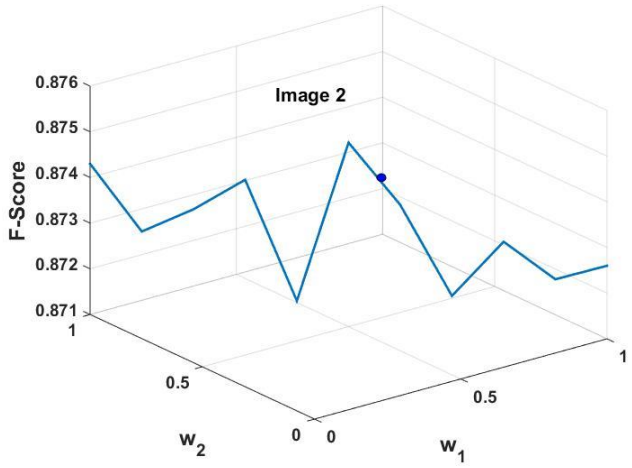


Fig. 11-F-measure variation for image 2

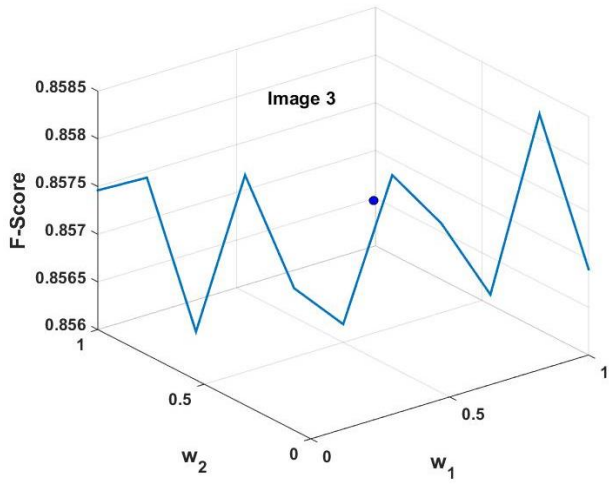


Fig. 12- F-measure variation for image 3

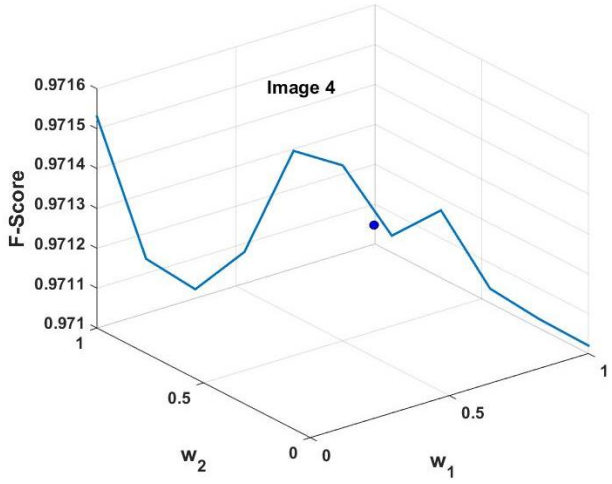


Fig. 13-F-measure variation for image 4

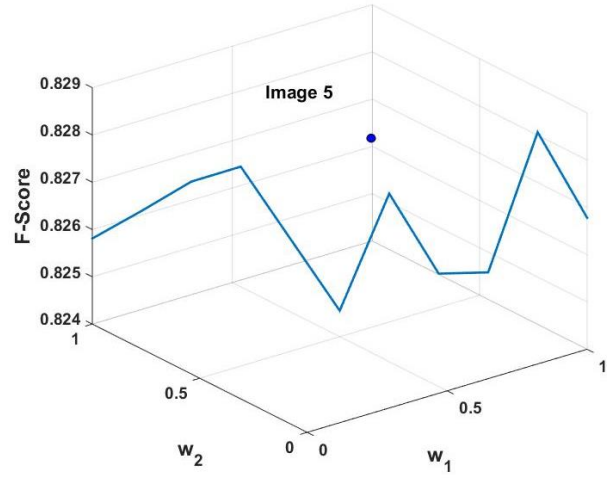


Fig. 14- F-measure variation for image 5

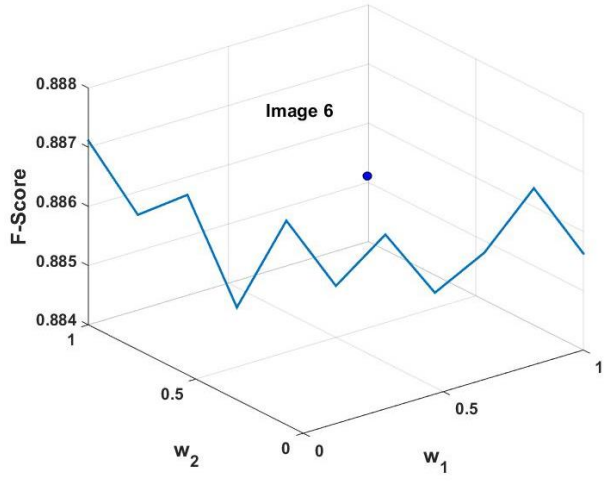


Fig. 15-F-measure variation for image 6

In Figs. 10-15, F-score variations are shown for all six images. The dot marked on each figure, is the value obtained from previous methods. It is clear from the figures that ups and downs are seen in results but better is

comparison to old methods. It is also noticeable that the number of edges in an image are very large in number, therefore a small increment in F-score bring significant improvement in edge detection. In Table 2, for all six images maximum value of F-score along with corresponding values of w_1 and w_2 are shown.

Table 2- F-Score and Weights

Image	Weight pair (w_1 ,w_2)	F-Score (old, new)
1	[(0,1)	(0.67153, 0.67282)
2	(0.5,0.5)	(0.87325 ,0.87503)
3	[(0.9, 0.1)	(0.85650, 0.85850)
4	(0,1)	(0.97108, 0.97153)
5	(0.9, 0.1)	(0.82623, 0.82854)
6	(0,1)	(0.88510, 0.88711)

5. Analysis

Thus, ACO- based edge detection scheme is a good choice for edge detection. The obtained F-score using other methods proposed recently are shown in Table 3. In the table F-score is presented after applying morphological operations. The F-measure for Canny and Sobel methods are 0.49 and 0.40 respectively. For the BEL method it is 0.63, while for gpb and structure forest is 0.71. For sketch token F-score is 0.73. However, in our case F-score varies from 0.67 to 0.97. It is also noticeable that in our method, we have not used any morphological operations for contour generation and edge joining etc.

TABLE 3- Comparison with Notable Works

Methods	Year	F-measure
Canny [12]	[1996]	0.49
Sobel [13]	[2009]	0.40
BEL [14]	[2006]	0.63
gPb [15]	[2011]	0.71
Sketch Token [16]	[2013]	0.73
Structured Forest [17]	[2013]	0.71
ACO	[2018]	0.67-0.97

6. Conclusions

In this paper, an ACO based edge detection method is detailed and obtained results are compared with recently proposed methods. In nut-shell we found the followings:

- In this work we have come up with novel pixel mapping function.
- It has been found that, ACO method is very efficient with average detection accuracy of nearly 87%.
- The F-score is very good and it out-performs the recently proposed methods.
- The PSNR value is of very good quality.

- The weighted method is effective in maximizing F-scores.
- Sketch Token provides best F-score of 0.73 and with proposed method the obtained best F-score is 0. 97, therefore percentage improvement is of 32.80% is observed with proposed method.

Future Work

The obtained results can be improved using further image processing operation as used in Canny edge detection method. Moreover, method could be searched to make edge detection mechanism free from mapping function by taking into account the gradient magnitude and directions even in ACO based detection. ACO method can be further improved by using fuzzy logic based false edge removals.

Acknowledgement

I would like to thank the reviewers for their valuable comments in improving the quality of this work.

References

[1] Singh RK, Shekhar S, Singh RB, Chauhan V (2014). A Comparative Study of Edge Detection Techniques. International Journal of Computer Applications, 1; 100(19).

[2] Dorigo M, Birattari M, Stutzle T (2006). Ant colony optimization. IEEE computational intelligence magazine, 1, 28-39.

[3] Maini R, Aggarwal H (2009). Study and comparison of various image edge detection techniques. International journal of image processing (IJIP), 1, 1-1.

[4] Tian J, Yu W, Xie S (2008). An ant colony optimization algorithm for image edge detection. In Evolutionary Computation, CEC, 751-756.

[5] Lu DS, Chen CC (2008). Edge detection improvement by ant colony optimization. Pattern Recognition Letters, 29, 416-425.

[6] Gupta C, Gupta S (2013). Edge detection of an image based on ant colony optimization technique. Int. J. Sci. Res.(IJSR). 2, 1256-1260.

[7] Reddy RV, Raju KP, Kumar MJ, Kumar LR, Prakash PR, Kumar SS (2017). Comparative Analysis of common Edge Detection Algorithms using Pre-processing Technique. International Journal of Electrical and Computer Engineering (IJECE)., 7, 2574-2580.

[8] Asharudeen M, Menon HP (2018). Edge detection Using Histogram Localization. Indonesian Journal of Electrical Engineering and Computer Science, 1, 11

[9] Alawad AM, Rahman FD, Khalifa OO, Malek NA (2018). Fuzzy Logic Based Edge Detection Method for Image Processing. International Journal of Electrical and Computer Engineering (IJECE). 8, 1863-1869.

[10] Xiao P, Li J, Li JP (2010). An improved ant colony optimization algorithm for image extracting. In Apperceiving Computing and Intelligence Analysis (ICACIA), International Conference , 17, 248-252.

[11] Otsu N (1979). A threshold selection method from gray-level histograms IEEE transactions on systems, man, and cybernetics. 9, 62-66.

[12] Canny J (1987). A computational approach to edge detection . In Readings in Computer Vision, 184-203.

[13] Vincent OR, Folorunso O. (2009). A descriptive algorithm for sobel image edge detection. In Proceedings of Informing Science & IT Education Conference (InSITE) 40, 97-107.

[14] Dollar P, Tu Z, Belongie S. Supervised learning of edges and object boundaries (2006). In Computer Vision and Pattern Recognition, 2006 IEEE Computer Society Conference, 1964-1971.

[15] Arbelaez P, Maire M, Fowlkes C, Malik J (2011). Contour detection and hierarchical image segmentation. IEEE transactions on pattern analysis and machine intelligence. 33, 898-916.

[16] Lim JJ, Zitnick CL, Dollár P. Sketch tokens (2013): A learned mid-level representation for contour and object detection. In Computer Vision and Pattern Recognition (CVPR), 3, 158-165.

[17] Dollár P, Zitnick CL (2013). Structured forests for fast edge detection. In Computer Vision (ICCV), 2013 IEEE International Conference, 1841-1848.

International Journal of Mechanical and Production Engineering Research and Development (IJMPERD)
ISSN(P): 2249–6890; ISSN(E): 2249–8001
Vol. 10, Issue 1, Feb 2020, 59–72
© TJPRC Pvt. Ltd.

TRANS STELLAR
•Journal Publications •Research Consultancy

EFFECT OF DIFFERENT PORT ANGLE IN AN IC ENGINE ON THE SWIRL AND MASS FLOW RATE

ADHIRATH MANDAL[1] & HAENGMUK CHO[2]

[1]*Doctorate Student, Department of Mechanical Engineering, Kongju National University, Republic of Korea*

[2]*Professor, Department of Mechanical Engineering, Kongju National University, Republic of Korea*

ABSTRACT

Diesel Engine is very popular and is being used in many industries. It is used in automobile for transmitting power to the wheels, used in generator sets for producing electricity and also used in the constructing machinery to mix the construction materials. Diesel engine is also used in telecommunication infrastructure and mining facilities. Internal combustion engine has four strokes. Intake, compression, expansion and exhaust strokes are the common four strokes in an internal combustion engine. Intake and compression stroke are the important strokes out of the four strokes in an IC engine. These two strokes define the air flow pattern in the combustion chamber, which then, render the fuel injection condition during compression stroke. However there are some problems such as decreased efficiency and enhanced emission are due to improper diffusion. Emission characteristics and combustion performance are directly affected by the air fuel mixing. Research communities are very interested in the internal combustion engine, air flow characteristics. To improve the efficiency of the engine and to reduce the emissions, research of basic flow dynamics in the cylinder is essential. This paper shows simulation analysis of different angles of the valve. The valve had different angles of 30^0, 45^0 and 60^0. Swirl and mass flow rates are compared in this paper.

KEYWORDS: IC Engine, Port Flow Simulation, Swirl, Mass Flow Rate & Valve

Received: Oct 01, 2019; **Accepted**: Oct 21, 2019; **Published**: Nov 30, 2019; **Paper Id.**: IJMPERDFEB20206

Original Article

1. INTRODUCTION

Diesel Engine is very popular and is being used in many industries. They are used in automobile for transmitting power to the wheels, used in generator sets from producing electricity and also used in the constructing machinery to mix the construction materials. Diesel engine is also used in telecommunication infrastructure and mining facilities. In many situations, the generator sets are used in remote locations where electricity is not available. To run the diesel generator sets, we need diesel or a hybrid fuel with renewable energy. Diesel engine is very commonly used because of its good fuel efficiency, cheap price of fuel and good reliability. Internal combustion engine has four strokes. Intake, compression, expansion and exhaust strokes are the common four strokes in an internal combustion engine. Intake and compression stroke are the important strokes out of the four strokes in an IC engine. These two strokes define the air flow pattern in the combustion chamber which then, render the fuel injection condition during compression stroke. However, there are some problems such as decreased efficiency and enhanced emission are because of improper diffusion. Emission characteristics and combustion performance are directly affected by the air fuel mixing. The emission performance could be improved by circulating air uniformly and widely in the combustion chamber 13.

But in recent years, we have seen that the price of diesel fuel is rising, as the fossil fuels are depleting and global warming issue is also rising. In many researches, biodiesel and biodiesel blends have been considered as a

good alternative to diesel. But with the use of biodiesel, NO_x emission increases. The increase in the NO_x emission is because of the high percentage of oxygen during combustion 4.

Because of the above reasons, the research community is very much interested in the internal combustion engine, air flow characteristics. To improve the efficiency of the engine and to reduce the emissions, research of basic flow dynamics in the cylinder is essential. The inlet ports in an IC engine should be designed in such a way that the swirl and tumble in the cylinder could be enhanced. Swirl and tumble are illustrated in figure 1. The yellow arrow refers to the swirl in the cylinder and the blue arrow refers to the tumble in the cylinder. As the air, which enters from the inlet port, the energy of the inlet jet will retain in the cylinder through the combustion cycle, which would increase the efficiency by mixing the fuel and air better. The inlet port in a compression ignition engine are so designed in such a way that the swirl is more present in the cylinder, but in the case of gasoline engine, the tumble is more present in the cylinder.

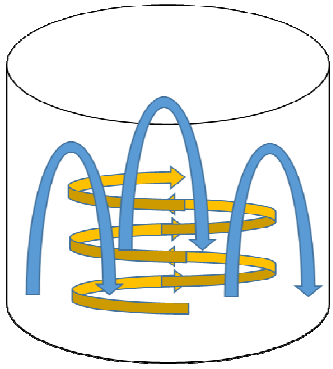


Figure 1: Description of Swirl and Tumble.

Swirl and tumble are directly linked with combustion efficiency. But too much swirl would increase the soot emission and consumption of fuel which is due to the fuel spray collision 4. In many researches, it was found that the inlet manifold was modified to increase the swirl and was validated with experimental data. It was found that the experimental data and simulation data were similar.

The main objective of this paper is to compare swirl and mass flow rate inside the combustion chamber for varying angle of the port with the help of CFD port flow simulation.

2. LITERATURE REVIEW

Mohammad Abdullah Mohamad Johar et al. researched the relationship between the geometry of the intake port and the mass flow rate in the cylinder head. The amount of air-fuel mixture moving through the intake port per second is referred as the mass flow rate. Ansys workbench simulation was utilised to study the mass flow through the intake port. As the cylinder and the intake port are symmetrical, the simulation was conducted only on the half part. The air-fuel mixture pressure was kept constant throughout the intake port during simulation. The valve opening was between 4mm to 10mm, same in the case of super flow. With these boundary conditions, the mass flow rate was recorded which corresponds with the valve lift. Intake port geometry was modified for this study. All the intake ports were used for the simulation and the mass flow rate varied with different intake port. It was noticed that the mass flow rate could be improved by 7.1% at 8mm lift of the valve. It was concluded that the highest mass flow rate could be achieved when the air is attached to the surface. But perfect intake port is only possible theoretically, which has straight intake port. Mass flow rate could be improved by reducing the sharp turns of the intake port 6. David Rathnaraj Jebamani et al. researched about the effectiveness of helical

port and the tangential port. It was a known fact that, helical port was better to obtain maximum swirl when compared to the tangential port. In this condition, volumetric efficiency was least sacrificed. Design of the swirl was so designed in such a way that the swirl ration was reduced, as at higher speed, it would reduce the emission. But it was observed that the helical port increased the particulate smoke emission at lower speed and also the mixing time of the air and fuel. It is very necessary to have an ideal swirl ratio for reduction of emission and the proper combustion. Therefore, to enhance the combustion in the engine cylinder, it is important to have changing swirl. The charging quantity and the swirl can easily be controlled by opening of the valve. Steady flow rig experiment was used to study the swirl when a helical intake port was used at different operating conditions. W06DTIE2 engine was used with different valve openings to experiment and the variation in the swirl. The area of the inlet port is varied by sliding the swirl plate.

This study was based on the swirl optimized combustion system, by varying the swirl plate mechanism which was studied experimentally and was compared with the results of the CFD. CFD was studied on a direct injection diesel engine on the port-cylinder system. The study was conducted under steady flow rig. Results showed that the variable swirl increased for 70% opening of the intake port and the swirl was decreased for 50% opening. It was concluded that the high swirl could reduce the NO_x and particulates. These are the two main pollutants, and can be reduced by increasing the swirl. It was also highlighted that the CFD tool could be used for optimisation of the intake system and this tool will reduce the experiments to be carried out 8. Soonseong Hong et al. studied the engine intake manifold and implemented design for six sigma in the intake manifold to optimize it. The main aim of this study is to increase strength of swirl and also to maximize the mass flow rate in the cylinder chamber. Factors which affect the mass flow rate and the swirl strength are prime pipe section shape, plenum shape, port diameter, primary and secondary length etc. All these factors were adopted. To calculate the mass flow rate and the swirl strength, L18 orthogonal table was used for CFD simulation calculation. From the results, it was clear that with S/N ratio was increasing for both swirl and mass flow rate. Which stated that the with increasing speed the combustion performance improved. By increasing the beta value using DFSS process, optimum mass flow rate was obtained, under the PDA system 9. S. Bari et al. researched the usage of biodiesel as an alternative fuel, as it is renewable and behaves similar to diesel fuel in an engine. It was also noticed that the amount of carbon dioxide emission is cancelled by the plant creating biodiesel raw material. Though biodiesel have disadvantage of having heavier molecules and higher viscosity which makes the atomisation and mixing with air slow and therefore the efficiency of the combustion is low. To solve these problems, guide vane swirl and tumble device was set up to increase the turbulence in the combustion chamber to increase the efficiency of the combustion. With the use of curved vanes temperature and pressure inside the cylinder were higher as compare to without vanes. Curved vanes showed higher tumble and cross tumble. Curved vanes had lower TKE (Turbulence Kinetic Energy). Fuel penetration was reduced with the GVSTD initially, but before TDC, the injection length increased. Increased injection length resulted in more carbon deposit on the piston. With the GVSTD, the cone angle was narrow 11. Haiqin Zhou et al. proposed a separate swirl combustion system through which air efficiency would be improved. Analysis of combustion and combustion performance was carried out using 3D simulation. Sensitivity analysis, Soot emission and indicated power were carried out by chamber geometry. Chamber geometry was optimised by the results of the sensitivity analysis. Emission and combustion performance with the best chamber geometry of single swirl combustion chamber was compared with the double swirl combustion chamber with different speed in a single cylinder diesel engine. The simulation results showed that the fuel distribution in inner and outer chamber was affected because of angle of inner chamber, SSCS combustion performance was influenced greatly. Second important parameter for optimization was the depth of the separated chamber, then the outer chamber, and then the

separated chamber diameter. Lastly, the volume ratio of inner to outer chamber and also the angle of the outer chamber. Best geometry was determined after examining the different velocity distribution, fuel/air mixture, soot emission and combustion performance with different SSCS chamber geometries,. Combustion and emission performance of DSCS was compared with SSCS. It was found that the indicated thermal efficiency was higher and had lower break-specific fuel consumption, compared to DSCS at different engine speeds 12. Himanth Kumar H Y et al. studied the 3D model and conducted numerical analysis. Numerical analysis was conducted on a 46mm diameter of inlet port, 43mm diameter of valve and the cylinder having 562mm length and 93.65mm of diameter. The focus of the study was to check the effect of valve lift on the fluid flow in the cylinder. It was known that the velocity of the flow will change for different valve lifts. It was concluded that, for achieving good efficiency, and to achieve low emission, it is very important to study the flow inside the intake port. With the help of CFD tool, the flow characteristics were studied. It was clear that the valve lift affected the flow, but there were some exception near the port blend upstream. It was also stated that the flow separation turns vital with valve lift. This was because of the losses increased with the increase in the valve lift 3. Xiangrong Li et al. researched about the lateral swirl combustion system (LSCS), which improved the soot emission, combustion and fuel efficiency in a direct injection diesel engine. Numerical simulation was implemented to further improve the LSCS performance and to analyse the effect of LSCS chamber geometries on combustion and emission characteristics under the condition of 2500 r/min and full load, exposing the relevant influence mechanisms. Accomplishment of chamber geometry optimization was completed which were based on the sensitivity analysis based on indicated power. The wall surface and the fuel spray jet has interplay in between, various fuels have different results. LSCS combustion performance had an effect on Split-flow geometry, where a dominant role was played by θ. Favourable flow guidance was created in the combustion chamber when θ was in 15–27^{o}range. After the geometrical optimization of the LSCS, fuel consumption decreased by 2.8 to 4.1 g/(kW.h) and soot emission decreased with the range between 69-75% under various engine speeds, as compared with the double swirl combustion system 13.

Federico Perini et al. studied the in-cylinder flow structure, in a swirl supported engine equipped with different piston geometries. The piston was having a conventional re-entrant bowl, first one had a cut-out valve and the second one had a cut-out valve and the third one had stepped-lip bowl. In an optical engine, particle image velocimetry was carried out to measure structure during intake and compression stroke and the swirl intensity. FRESCO code was used to build the optical diesel engine for computational model. Validation of the model was carried out in swirl-plane velocity field and multiple cycles were assessed for simulation overlapping. Study of flow topology was carried out which addressed the turbulence quantities and the bulk flow, swirl structure, operating parameters, squish flux and geometrics. It was observed that the conventional re-entrant bowls at intake had strong flow separation. Enclosed shape had better and strong squish flow, because of which neat TDC was stronger and 10% larger than SL bowl; Though it had more prominent global swirl than stepped-lip bowls, which was mainly because of lesser tilted swirl and stronger and more axisymmetric squish mechanism. Stepped-lip bowls had higher turbulence level and more in homogeneities. At the same time, it had faster turbulence at the TDC. With the valve cut-outs, velocity is large and the hit the piston surface which reduced the swirl ratio by 1.3% and turbulence increased by 4.6% 15. Guixin Wang et al. investigated a controllable intake swirl, its intake flow field in a diesel engine by using CFD. Two level characteristics were observed with the opening of the intake baffle with the variation of the intake swirl; though cut-off point of the baffle opening was 48^{0}. In the analysis of the baffle opening and valve lift, the flow coefficient was influenced and it was found that flow coefficient was more sensitive to valve lift. To calculate the controllable intake swirl and its characteristics in a diesel engine, mathematical model was used. A

combustion characteristic, which was influenced by swirl ratio was investigated. It was concluded that, in a diesel engine, the power performance had too much influence with swirl ratio. 5.79% increase in power performance was observed when the swirl ratio changed from 0.4 to 1.2, following which improvement in fuel consumption was observed 16. Alper Tolga Calik et al. studied MR-Process combustion chamber, which is different from the conventional combustion chamber in a diesel engine. Conventional CC has single swirl where as in case of MR-process it has twin swirl, helps in boosting better air fuel mixture. It is done by fuel spray vaporisation which is tangential to the piston wall. In the beginning of the study, a combustion chamber geometry of 2-valve was modified, to create twin swirl, known as Quasi MR-Process. The study summarised that, for twin swirl formation, a 4-valve engine was required. Designing an engine head with 4 valves (with two intake manifold), which would satisfy the ideal swirl condition in the combustion chamber, was a challenging task. Optimum values for swirl condition, air flow field and injection characteristics, experimental data were not available for MR-Process combustion chamber. Twin swirl initiation feasibility was investigated by numerical analysis of MR-Process combustion chamber. Twin swirls potential application was revealed in this study, utilizing closed cycle simulation. Existing swirl model (KIVA3V-R2) was altered to generate twin swirl, during the start of compression stroke. Initial swirl with different angular velocities and fuel spray injection directions was employed get the favourable air fuel mixture and to increase efficiency and lower the harmful gases. Results showed that MR-Process had potentiality to give better air fuel mixture and fuel efficiency, which would reduce the emission of harmful gases 18. Dan Moldovanu et al. optimise the combustion process in a compression ignited engine so that it could reduce the emission. Optimization was only possible by assuring a better air fuel mixture. Analysis of velocity and vertices formation inside the combustion chamber, in thirteen cases was carried out for numerical analysis using AVL FIRE Software. Software was used to create pure swirl motion, pure tumble motion, no air motion in in-cylinder and different combinations of swirl and tumble motion. Tumble and swirl motion cases were chosen combine 0%, 50%, 70% and 100%. At 100% tumble and 50% swirl motion, highest air motion (77.2 m/s at 736 degrees CA) was noted. While lowest velocity was noted when 100% swirl and 0% tumble, i.e., 71.07 m/s at 736 degrees, CA Various induced motion create vertices, which had influence on the air fuel mixture 19.

3. CAD MODEL

A 3D model of the cylinder, inlet port and valve was created with the help of Solidworks 2017. The model is shown in Figure 2. The dimension of the model is listed in Table 1. Figure 3 shows the imported CAD geometry in the Ansys software. During the geometry creation, 3 different post planes were created. The distance of the post planes from the reference planes were 30mm, 45mm and 60mm. The inlet plenum size was 100mm and the type of plenum was hemisphere, as shown in Figure 3. Three different types of valves were generated in Solid works, with different angles, 30^0,45^0 and 60^0.



Figure 2: CAD File for Port Flow Simulation.

Table 1: 3D Model Parts Dimension

Sl. No.	Part Name	Value
1	Diameter of inlet port	25.4 mm
2	Diameter of outlet port	25.4 mm
3	Diameter of the cylinder	89.90 mm
4	Length of the cylinder	110 mm
5	Valve lift	6 mm
6	Valve angle	30^0;45^0;60^0

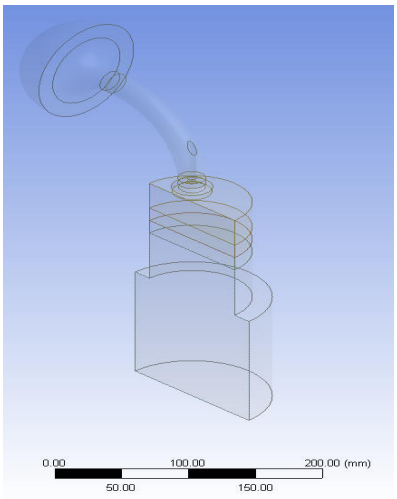


Figure 3: Imported CAD Geometry in Ansys.

4. MESHING

The 3D model was generated in Solidworks version 2018. To solve the problem, the geometry has to be decomposed in three stages. In the first stage, the geometry is decomposed in three stages and then, they are meshed. In the second step, with the use of the setup journal, the engine case is setup and in the final step, simulation is performed.

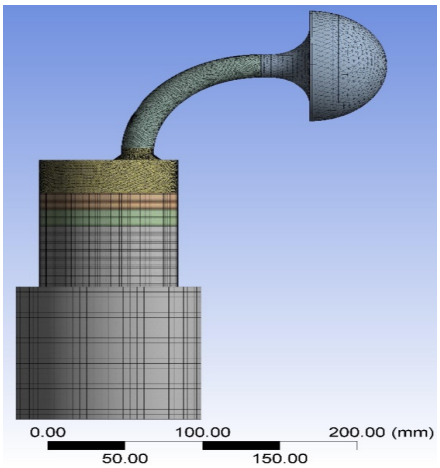


Figure 4: Meshed Geometry.

Most of the surface of the geometry was meshed with triangular element; the element size was 1.415 mm and the local min size was considered to be 0.315mm. In case of cylinder wall and the output plenum, the mapped mesh type was Hexa/Prism with 15mm minimum edge length. Number of elements used for generation of mesh was 1088684.

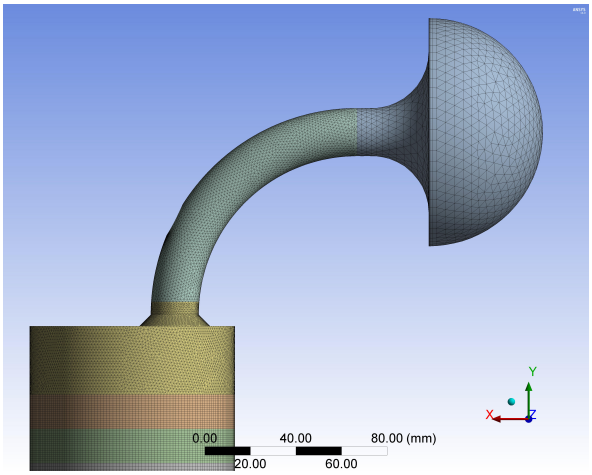


Figure 5: Meshing with Triangular Element.

5. MATHEMATICAL EQUATIONS

To solve a computational fluid dynamics problem, three equations are mainly used such as Energy Equation, Continuity Equation and Navier stroke Equation (momentum eq).

5.1 Energy Equation

This equation demonstrates that, per unit volume, the change in energy of the fluid moving through a control volume is equal to the summation of rate of heat transferred into the control volume, rate of work done by surface forces and work done because of gravity 3.

$$\frac{\partial}{\partial t}\left(\rho e+\frac{1}{2}\rho v^2\right)+\frac{\partial}{\partial x}\left(\rho ue+\frac{1}{2}\rho uv^2\right)+\frac{\partial}{\partial y}\left(\rho ve+\frac{1}{2}\rho vv^2\right)+\frac{\partial}{\partial x}\left(\rho we+\frac{1}{2}\rho wv^2\right)=k\left(\frac{\partial^2 T}{\partial x^2}+\frac{\partial^2 T}{\partial y^2}+\frac{\partial^2 T}{\partial xz^2}\right)-\left(u\frac{\partial p}{\partial x}+v\frac{\partial p}{\partial y}+w\frac{\partial p}{\partial z}\right)+\mu\left[u\frac{\partial^2 u}{\partial x^2}+\frac{\partial}{\partial x}\left(v\frac{\partial v}{\partial x}+w\frac{\partial w}{\partial x}\right)+v\frac{\partial^2 u}{\partial y^2}+\frac{\partial}{\partial y}\left(u\frac{\partial u}{\partial x}+w\frac{\partial w}{\partial y}\right)+w\frac{\partial^2 u}{\partial z^2}+\frac{\partial}{\partial z}\left(u\frac{\partial u}{\partial z}+v\frac{\partial v}{\partial z}\right)\right]+2\mu\left[\frac{\partial^2 u}{\partial x^2}+\frac{\partial u}{\partial y}\frac{\partial v}{\partial x}+\frac{\partial^2 v}{\partial y^2}+\frac{\partial v}{\partial z}\frac{\partial w}{\partial y}+\frac{\partial^2 w}{\partial z^2}+\frac{\partial w}{\partial x}\frac{\partial u}{\partial z}\right]+\rho u g_x+\rho v g_y+\rho w g_z$$

5.2 Continuity Equation

A continuity equation expresses a conservation law by "Equating a net flux over a surface with a loss or gain of material within the surface". Continuity equations is shown below 3.

$$\int_{cs}^{\square}\rho V dA+\frac{\partial}{\partial t}\int_{cv}^{\square}\rho dA=0$$

This equation is for principle of mass conversation for a one dimensional, steady, with one inlet and outlet.

$$\nabla(\rho V)+\frac{\partial \rho}{\partial t}=0$$

Where, $\nabla=\frac{\partial}{\partial x}\hat{\imath}+\frac{\partial}{\partial x}\hat{\jmath}+\frac{\partial}{\partial x}\hat{k}$

$$\frac{\partial \rho}{\partial x}+\frac{\partial(\rho.u)}{\partial x}+\frac{\partial(\rho.v)}{\partial y}+\frac{\partial(\rho.w)}{\partial z}=0$$

5.3 Navier Stroke Equation (Momentum Eq)

The momentum equation states that sum of forces acting on a fluid element to its acceleration or rate of change of momentum. The Newton's second law of motion F = ma is the basis of the momentum equation **3**.

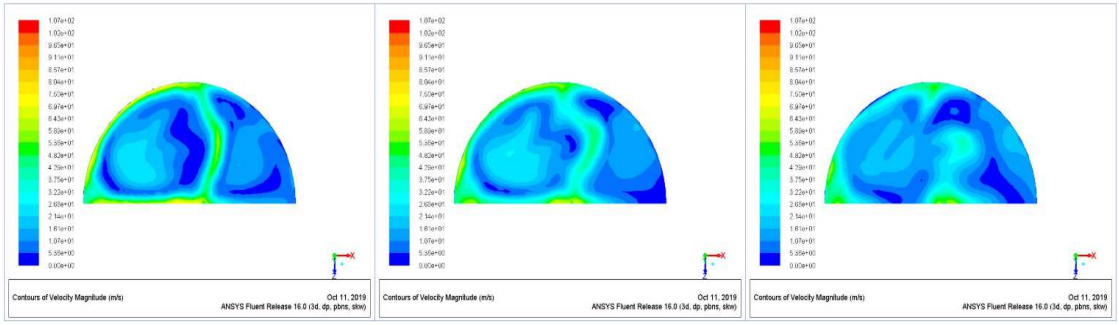
$$\rho\frac{\partial u}{\partial t}+\rho u\frac{\partial u}{\partial x}+\rho v\frac{\partial u}{\partial y}+\rho w\frac{\partial u}{\partial z}=\rho g_x-\frac{\partial p}{\partial x}+\mu\frac{\partial^2 u}{\partial x^2}+\mu\frac{\partial^2 u}{\partial y^2}+\mu\frac{\partial^2 u}{\partial z^2}$$

$$\rho\frac{\partial v}{\partial t}+\rho u\frac{\partial v}{\partial x}+\rho v\frac{\partial v}{\partial y}+\rho w\frac{\partial v}{\partial z}=\rho g_y-\frac{\partial p}{\partial y}+\mu\frac{\partial^2 v}{\partial x^2}+\mu\frac{\partial^2 v}{\partial y^2}+\mu\frac{\partial^2 v}{\partial z^2}$$

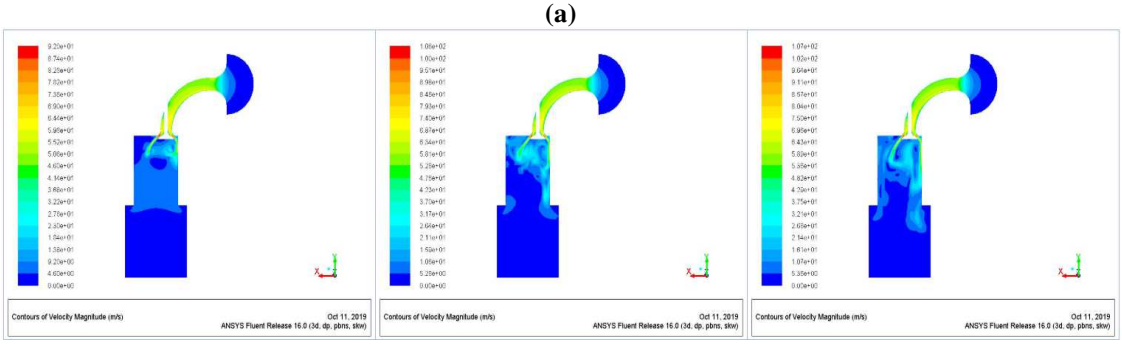
$$\rho\frac{\partial w}{\partial t}+\rho u\frac{\partial w}{\partial x}+\rho v\frac{\partial w}{\partial y}+\rho w\frac{\partial w}{\partial z}=\rho g_z-\frac{\partial p}{\partial z}+\mu\frac{\partial^2 w}{\partial x^2}+\mu\frac{\partial^2 w}{\partial y^2}+\mu\frac{\partial^2 w}{\partial z^2}$$

6. RESULTS AND DISCUSSIONS

The problem was solved with the help of using Ansys Fluent. The different valve angles (30^0; 45^0 & 60^0) were compared with each other. Below are the pictures of the air velocity inside the chamber. Figure 6Figure **8** show the velocity profile at different reference planes and timings. Figure 9–11 show the mass flow rate at different reference planes of different valves. Figure 12 shows the average mass flow rate.

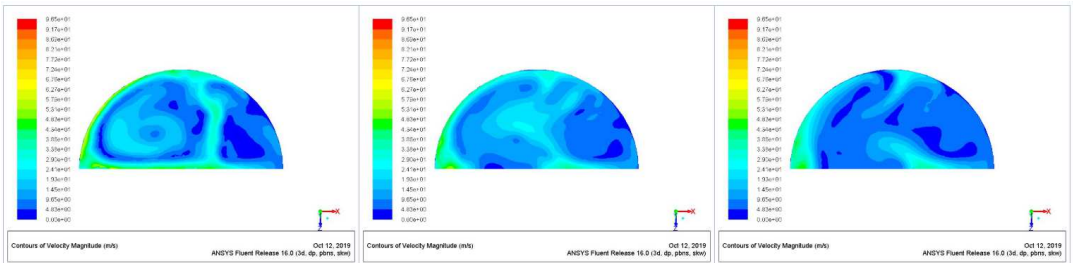


(a)

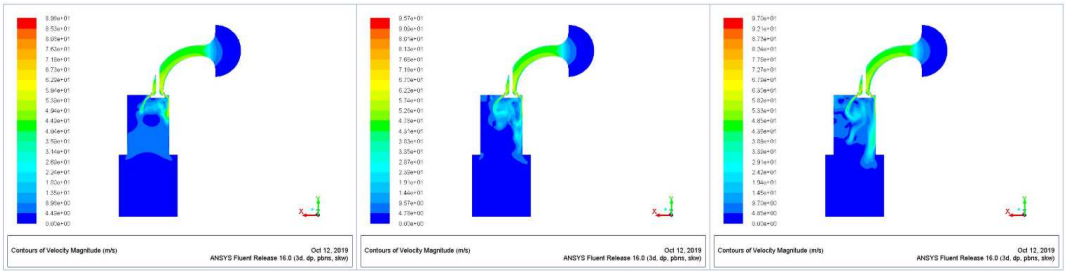


(b)

Figure 6: Velocity Profile at 45^0 Valve Geometry, (a) Velocity Profile at Different Reference Planes, (b) Velocity Profile at Different Time.

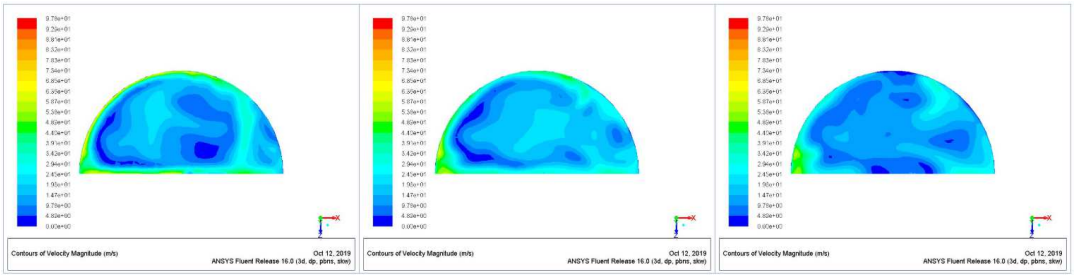


(a)

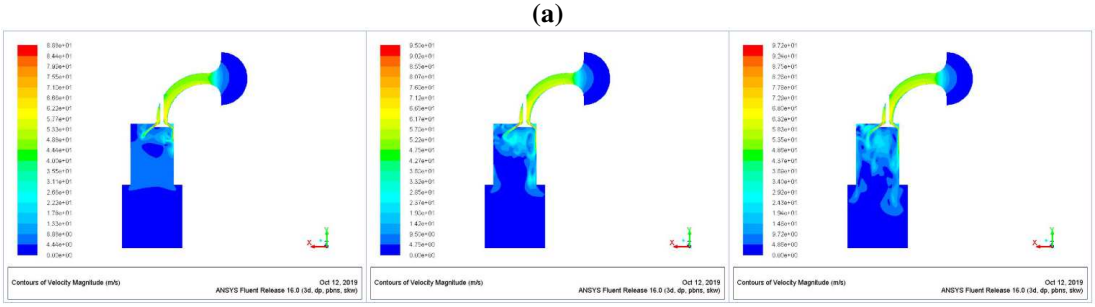


(b)

Figure 7: Velocity Profile at 60^0 Valve Geometry, (a) Velocity Profile at Different Reference Planes, (b) Velocity Profile at Different Time.

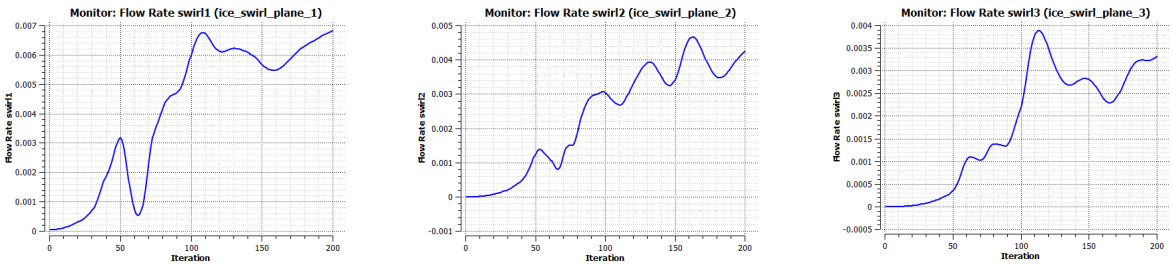


(a)



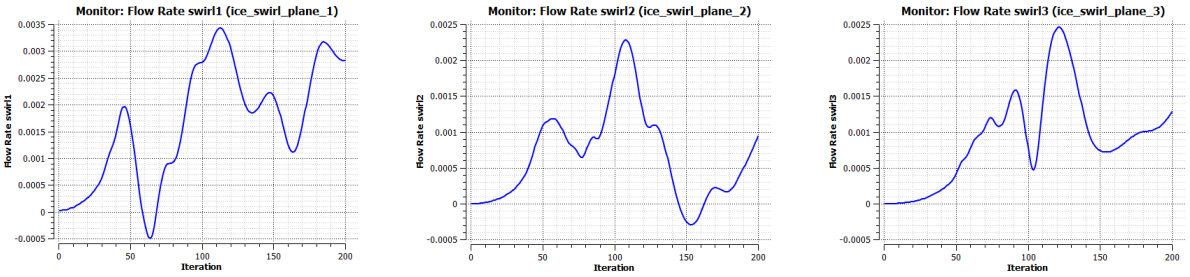
(b)

Figure 8: Velocity Profile at 30^0 Valve Geometry, (A) Velocity Profile at Different Reference Planes, (B) Velocity Profile at Different Time.



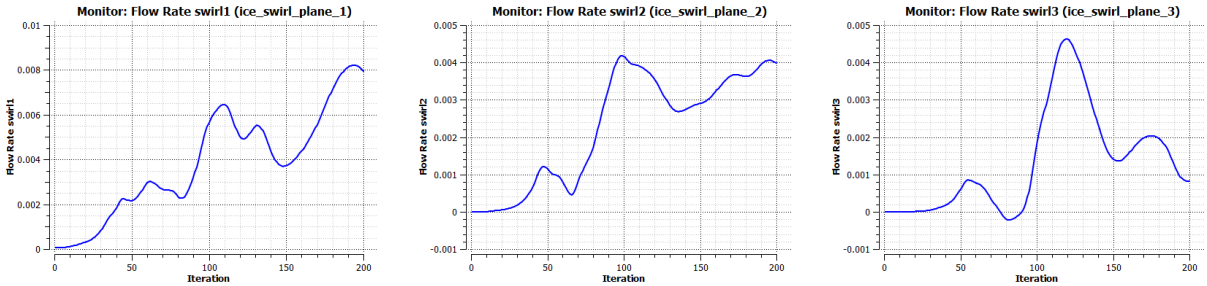
(a) **(b)** **(c)**

Figure 9: Velocity Profile at 45^0 Valve Geometry at 30mm, 45mm & 60mm Reference Plane Respectively.



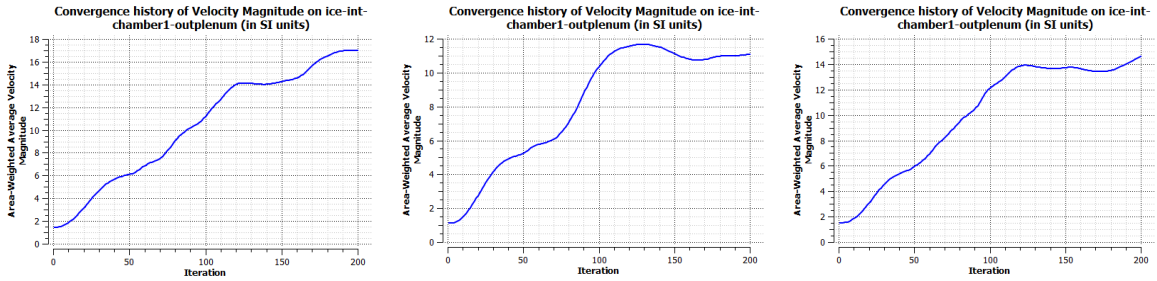
(a) **(b)** **(c)**

Figure 10: Velocity Profile at 60^0 Valve Geometry at 30mm, 45mm & 60mm Reference Plane Respectively.



(a) **(b)** **(c)**

Figure 11: Velocity Profile at 30^0 Valve Geometry at 30mm, 45mm & 60mm Reference Plane Respectively.



45^0 Valve Geometry **60^0 Valve Geometry** **30^0 Valve Geometry**

Figure 12: Area-weighted Average Velocity of Different Angle of Valve Geometry.

7. CONCLUSIONS

Air Fuel Mixture is very important for combustion to take place. Intake port plays a very critical function in the air flow inside the combustion chamber. The flow of air inside the combustion chamber helps in reaching better fuel efficiency and lower emission. This paper studied the valve design which could help in increasing the swirl and the mass flow rate in the combustion chamber. The study was concluded with the help of CFD IC engine module, Ansys. The valve angle was changed to 30^0, 45^0 & 60^0. Different CAD files were generated with the help of Solid works, the CAD files were imported into Ansys V16 in the IC Engine module. Port flow simulation was conducted on the generated files. Following conclusion was concluded from the analysis.

- When the port angle was set to 45^0, the swirl was limited to the upper region of the combustion chamber and the mass flow rate was higher
- In the second case, when the post angle was set to 60^0, the swirl in the chamber was better that 45^0 port angle, and the mass flow rate was less than the first condition

- In the third case, the post angle was set to 30^0. The swirl was less but the mass flow rate was higher.

Because of different angle of flow, the swirl and the mass flow rate changed. But from the above results, we could conclude that 45^0 port angle was a better option for swirl. Mass flow rate though 60^0 port angle should also be considered and experimental validation should be carried out in the future research.

8. ACKNOWLEDGEMENT

This work was supported by the National Research Foundation of Korea (NRF) grant funded by the Korea government (MSIT) (NRF-2019R1A2C1010557).

REFERENCES

1. *Haiqin Zhou, Xiangrong Li, Weihua Zhao, Fushui Liu. (2019). Effects of separated swirl combustion chamber geometries on the combustion and emission characteristics of DI diesel engines. Fuel 253. 488–500.*
2. *Mohamad Issa, Hussein Ibrahim, Richard Lepage, Adrian Ilinca. (2019). A Review and Comparison on Recent Optimization Methodologies for Diesel Engines and Diesel Power Generators. Journal of Power and Energy Engineering. 7. 31–56.*
3. *Himanth Kumar H Y, Jayashankar N. 2015. Port Flow Simulation of an Ic Engine. International Journal of Innovations in Engineering Research and Technology. 2. 9.*
4. *Arulprakasajothi Mahalingam, Yuvarajan Devarajan, Santhanakrishnan Radhakrishnan, Suresh Vellaiyan, Beemkumar Nagappan. 2018. Emissions analysis on mahua oil biodiesel and higher alcohol blends in diesel engine. Alexandria Engineering Journal. 57. 2627–2631.*
5. *A. Kalpakli Vester, Y. Nishio, P. H. Alfredsson. 2019. Investigating swirl and tumble using two prototype inlet port designs by means of multi-planar PIV. International Journal of Heat and Fluid Flow 75. 61–76.*
6. *Mohammad Abdullah Mohamad Johar, Mohd Farid Muhamad Said, Mohd Azman Abas, Zulkarnain Abdul Latiff, Mas Fawzi Ali, Nik Mohd Izual Nik Ibrahim. 2019. Flow Analysis of Intake Port Geometry of Spark Ignition Engine Using Simulation. Proceedings of the 3rd International Conference on Automotive Innovation Green Energy Vehicle. AIP Conf. Proc. 2059.*
7. *Thomas, J. O. S. E. P. H. (2014). Case study of error analysis of the usage of tense in English by year 1 engineering students from Tamil Medium Schools. IMPACT: International Journal of Research in Humanities, Arts and Literature, 2(3), 47–52.*
8. *David Rathnaraj Jebaman, Thathapudi Michael Narendra Kumar. 2008. Studies on Variable Swirl Intake System for Di Diesel Engine using Computational Fluid Dynamics. Thermal Science. 12. 25–32.*
9. *Soonseong Hong, Byungkeun Oh, Yongtae Kim, Wondae Jeon, Bongyong Jin. 2007. Optimization of Intake Manifold Design using DFSS (Design for Six Sigma). 14th Asia Pacific Automotive Engineering Conference Hollywood.*
10. *Rajasekaran, P., Vanangamudi, S., & Naveenchandran, P. Automation of hydraulic tyre wear testing machine using proportional control valve by interfacing programming logic circuit.*
11. *S. Bari, P. J. G. Johansen, A. J. T. Alherz. 2015. Simulation of improvements to in-cylinder mixing of biodiesel with air by incorporating guide vanes into the air intake system. Procedia Engineering 105. 480–487.*
12. *Haiqin Zhou, Xiangrong Li, Weihua Zhao, Fushui Liu. 2019. Effects of separated swirl combustion chamber geometries on the combustion and emission characteristics of DI diesel engines. Fuel 253. 488–500.*
13. *Xiangrong Li, Yanlin Chen, Liwang Su, Fushui Liu. 2018. Effects of lateral swirl combustion chamber geometries on the combustion and emission characteristics of DI diesel engines and a matching method for the combustion chamber geometry. Fuel 224. 644–660.*

14. *Arunachala, U. C., Rajat, A. C., Shah, D., & Sureka, U. (2019). Stability improvement in natural circulation loop using tesla valve–an experimental investigation. International Journal of Mechanical and Production Engineering Research and Development, 9(6), 13–24.*

15. *Federico Perini, Kan Zha, Stephen Busch, Eric Kurtz, Richard C Peterson, AlokWarey, Rolf D Reitz. 2018. Piston geometry effects in a light-duty, swirl-supported diesel engine: Flow structure characterization. International J of Engine Research .19(10). 1079–1098.*

16. *Guixin Wang, Wenbin Yu, Xiaobo Li, Yanpan Su, Rui Yang, Wentao Wu. 2019. Study on dynamic characteristics of intake system and combustion of controllable intake swirl diesel engine. Energy 180. 1008–1018.*

17. *Sakharkar, R. P., & Tasgaonkar, P. P. MPLS-traffic engineering load balance algorithm using uncommon path.*

18. *Alper Tolga Calik, Ozgur Oguz Taskiran, Rafig Mehdiyev. 2018. Numerical investigation of twin swirl application in diesel engine combustion. Fuel 224. 101–110.*

19. *Dan Moldovanu, Florin Mariaşiu, Norbert Bagameri. Influence of swirl and tumble motion inside the combustion chamber of a compression ignited engine on vertices formation. MATEC Web of Conferences 184, 01022.*

AUTHOR PROFILES



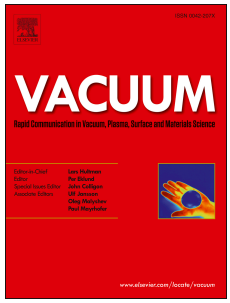
Adhirath Mandal has completed his bachelors in Mechanical & Automation Engineering from Guru Gobind Singh Indraprastha University, Delhi, India. After his graduation he has worked in a water RO Company for 1 year. He completed his M.Tech (masters) in production engineering from Delhi Technological University, Delhi, India. He has worked as Assistant Professor in engineering colleges in Delhi NCR. He has teaching experience of 3.5 year. He is pursuing his doctoral degree from Kongju National University, Cheonan, Korea in mechanical engineering. His area of interest is Biodiesel and electric vehicles. He has published papers in national and international journals. The papers are indexed in Scopus.



Professor HaengMuk Cho (Corresponding Author) is a renowned professor in South Korea. He is working as professor at Kongju National University in South Korea. He did Post Doctorate Fellowship from Department of Automotive Engineering of Loughborough University in UK and North Texas University in USA. He earned his PhD from Hanyang University, South Korea in 1997 and completed his M.D. in Environment Engineering from Yonsei University in S Korea. He is working on national and international projects in the field of Bio-fuels for IC engines and

renewable energy. Professor HaengMuk Cho is working in the field of Renewable Energy and Biofuels. He is also a member of many societies, like Korea Society of Automotive Engineers, Korean Society of Energy (Korea), Korea Society of Marine Engineering (Korea) & Korea Society of Environment Engineer (Korea). He has published many national and internal research papers. Most of his papers are indexed in Scopus and SCI.

Journal Pre-proof



Electrochemical Study of Hydrothermally Synthesised Reduced MoS_2 Layered Nanosheets

Ritika Khatri, Nitin K. Puri

PII: S0042-207X(20)30087-7

DOI: https://doi.org/10.1016/j.vacuum.2020.109250

Reference: VAC 109250

To appear in: *Vacuum*

Received Date: 12 October 2019

Revised Date: 4 February 2020

Accepted Date: 6 February 2020

Please cite this article as: Khatri R, Puri NK, Electrochemical Study of Hydrothermally Synthesised Reduced MoS_2 Layered Nanosheets, *Vacuum*, https://doi.org/10.1016/j.vacuum.2020.109250.

This is a PDF file of an article that has undergone enhancements after acceptance, such as the addition of a cover page and metadata, and formatting for readability, but it is not yet the definitive version of record. This version will undergo additional copyediting, typesetting and review before it is published in its final form, but we are providing this version to give early visibility of the article. Please note that, during the production process, errors may be discovered which could affect the content, and all legal disclaimers that apply to the journal pertain.

© 2020 Published by Elsevier Ltd.

Electrochemical Study of Hydrothermally Synthesised Reduced MoS_2 Layered Nanosheets

Journal Pre-proof

Ritika Khatri [1], Nitin K. Puri[1*]

[1]Nanomaterials Research Laboratory, Department of Applied Physics, Delhi Technological University, Delhi, 110042, Delhi

*Corresponding author, email: nitinkumarpuri@dtu.ac.in, nitinpuri2002@yahoo.co.in

Abstract

In this work, we report one-step, facile and cost-effective synthesis of 2-dimensional (2D) reduced MoS_2 (r-MoS_2) nanostructures via hydrothermal method using two reducing agents. The detection of hexagonal phase, estimation of lattice parameters and crystallite size is done using X-ray diffraction and Williamson-Hall plots are drawn to estimate strain produced in the sample. Scanning electron microscopy and Transmission electron microscopy confirms the formation of nanosheet like structures**.** MoS_2 reduced using hydrazine hydrate is found to have better electrochemical properties with heterogenous rate transfer constant equal to 5.03 X 10^{-4} cm/s and electroactive surface area calculated as 7.05 X10^{-4} cm^{-2}. Raman spectra, TEM images and W-H plots explains the better electrochemical performance of rMoS_2 synthesised using hydrazine hydrate. Also, it is observed that out of electrochemical impedance spectroscopy (EIS), cyclic voltammetry and differential pulse voltammetry, EIS turns out to be best technique for studying electrochemical properties of layered materials. This work provides theoretical guidance to use chemically synthesised rMoS_2 as a matrix for electrochemical sensing applications where an increase or decrease in current/resistance value gives confirmation of attachment of bio/gas molecules and determination of parameters like heterogenous rate transfer constant can indicate sensitivity towards a particular analyte.

Keywords: rMoS_2, Reducing Agents, Electrophoretic deposition, Electrochemical studies

1. Introduction

2D materials like graphene, transition metal chalcogenides, hexagonal boron nitride, Mxenes etc are gaining huge popularity in the inter-disciplinary fields of nanoscience and material science which includes physics, chemistry as well as biology. 2D nanomaterials

include benefits like low cost and high chemical stability. Amongst, these 2D nanomaterials
Journal Pre-proof
MoS_2 has gained wide popularity pertaining to its layered structure, abundance in nature as molybdenite, good rate of electron transfer, dependency of band gap on no. of layers, possibility of extraction in considerable amount [1] and its plentiful applications like supercapacitors [2] , Na/Li- ion batteries [3-5] , Hydrogen Evolution Reaction (HER) [6] , sensing [7] , electronic devices [8, 9] etc. It also possesses fine mechanical strength, even better than steel [10]. MoS_2 in its bulk form is a semiconductor with bandgap 1.2 eV, which widens up to 1.8 eV for monolayer MoS_2. Bulk MoS_2 however has low transfer of ions/electrons because it is stacking of large number of layers, which limits its conductivity [11]. Thus, an effective pathway to this is going to nanoscale, thus increasing the surface area and decreasing the total number of layers to decrease the pathway for diffusion. MoS_2 has characteristics similar to graphene like covalently bonded S-Mo-S sheets which have weak Vander Waal forces amongst them and therefore have the tendency to be extracted in form of nanosheets like structures [12] . MoS_2 can be synthesised using various methods, among which hydrothermal method is one of the methods which gives large yield, is simple to perform, has low cost and gives an option of controlling morphology of synthesised structures. Also, water is used as reaction solvent making this method environmentally friendly as well [13, 14].

Electrochemical activity of MoS_2 determines its use in various applications, but different properties of MoS_2 and different types of parameters are seen for different applications, for instance more no. of active sites will give a better HER and a low overpotential and Tafel plot will determine if a material is good for HER or not [6], while pseudocapacitive behaviour, charge-discharge rates, cycle stability will be seen for supercapacitor [2]. Charge-discharge capacity, cycling stability and specific capacity is seen for Na/Li ion batteries and potential for Na/Li ions intercalation among layers of MoS_2 will determine performance of batteries [3-5]. But for sensing, more surface area should be exposed with minimised interlayer spacing so that electron transfer is favoured with good value of heterogenous rate transfer constant [15].

Journal Pre-proof

MoS_2 nanostructures are heterogenous on their surface containing mono-/bi-/multi-layered structures of different shapes and sizes. These shapes and sizes depend upon different preparation methods and conditions. For instance, flower like MoS_2 nanostructures (mean diameter 500 nm) are shown to exhibit a better performance as an anode material for Li-ion batteries in comparison to sphere like MoS_2 nanostructures (5-10 µm) because, flower like MoS_2 nanostructures can have better structure change during the conversion process. In the electrochemical impedance spectroscopy (EIS) measurements flower like MoS_2 has a smaller value of charge transfer resistance R_{ct} than MoS_2 spheres, owing to the dense structures of spheres. Ultrathin nanosheets in flower like MoS_2 shortens the diffusion pathway for electrons and Li^+ ions, which enhances its electrochemical performance [16]. In another work, Ramadoss et al [17] have synthesised mesoporous structures of MoS_2 for supercapacitor applications where capacity is found to increase due to porous morphology and large surface area of nanostructures which reduces the pathway for ion diffusion which in turn enables fast electron transfer between working electrode and electrolyte. Chen et al [18] have synthesised MoS_2 nanosheets and nanosheets based hollow porous flat boxes and nanotubes (outside diameter 200-500 nm and thickness 50-70 nm) for electrochemical hydrogen evolution. MoS_2 flat boxes and nanotubes are found to exhibit better electrochemical performance than MoS_2 nanosheets because of a greater number of S^{2-} units, stable arrangement of nanosheets which exposes a greater number of active sites rendering them low overpotentials to reach 10 $mA.cm^{-2}$. Kumar et al [19] have reported synthesis of MoS_2 nanoclusters for electrochemical detection of 4 aminophenol (AP). Large surface area of MoS_2 nanoclusters exhibits high electrocatalytic activity towards 4-AP. MoS_2 nanoflakes (size $\geq$ 1 µm) for fabrication of screen-printed electrochemical sensor for detection of bovine serum has been developed by Kukkar et al [20]. A simple sensor with detection limit of 6 $pg.mL^{-1}$ is made by utilising cyclic voltammetry technique. Wang et al [21] synthesised three different morphologies of MoS_2 namely nanospheres (diameter 600-900 nm), nanoribbons (width 200-300 nm and length up to several micrometres) and nanoparticles (600 nm) and studied their electrochemical performance for Li-ion Batteries. MoS_2 nanospheres are found to exhibit best electrochemical performance

amongst all morphologies owing to large surface area which provides large number of reaction sites, reduced diffusion length for electrons and ions and can accommodate structural changes.

Journal Pre-proof

In our work, Hydrazine hydrate and citric acid are used as reducing agents to mediate the growth of MoS_2 nanostructure by aiding the reduction of oxidation state of Mo (VI) to Mo (IV). Due to excess of ammonia released during the hydrothermal synthesis of MoS_2, NH_3 intercalated MoS_2 nanosheets are formed leading to an increase in inter-layer spacing constituting the nanosheets [22, 23]. When we don't use reducing agents, samples obtained are not having pure crystalline phase of MoS_2. It has also been reported that intercalated MoS_2 is not of pure crystalline phase [13, 23] which renders it a low stability. Also, intercalated MoS_2 nanosheets increases overall distance between layers which will decrease the sensing response. We have also shown in our study that MoS_2 sample synthesised using citric acid as a reducing agent shows low electrochemical performance because of increase in stacking height of layers. Therefore, reduction of ammonia intercalated MoS_2 becomes very important such that the original nanosheet like structure is also retained. Min Li et al [13] and Mohsin Ali Raza Anjum et al [23] have given an additional treatment in H_2 reducing atmosphere to hydrothermally synthesised intercalated MoS_2 nano structures, whereas we have reduced ammonia intercalated MoS_2 nanostructures chemically during hydrothermal process only. However, hydrazine hydrate and citric acid leads to growth of these nanosheets in different ways which directly affects electrochemical properties of these nanostructures and their performance for various applications. Even though there are numerous reports of hydrothermal synthesis of MoS_2 and its electrochemical activity [2-7], but very less emphasis has been given on synthesis of chemically reduced MoS_2 and electrochemical study of electro-phoretically grown films. Therefore, this work discusses electrochemical properties of reduced MoS_2 for its prospective application in the field of electrochemical sensing.

2. Experimental Details

2.1 Materials and Solutions

Journal Pre-proof

Ammonium Molybdate Tetrahydrate $(NH_4)_6Mo_7O_{24}.4H_2O$ with 99.98% purity is purchased from Sigma Aldrich. Thiourea is purchased from SRL Pvt Ltd. Hydrazine hydrate, potassium bromide, sodium chloride and potassium chloride are purchased from Thermo Fisher Scientific. Concentrated hydro chloric acid is purchased from RFCL limited. All other chemicals including acetonitrile, potassium hexacyanoferrate (III)/ potassium ferricyanide ($K_3Fe(CN)_6$), potassium hexacyano ferrate(II) trihydrate/ potassium ferrocyanide ($K_4Fe(CN)_6.3H_2O$), sodium di hydrogen phosphate dihydrate ($NaH_2PO_4.2H_2O$, MW – 156.01 g/mol), di sodium hydrogen diphosphate dihydrate ($Na_2HPO_4.2H_2O$) and ethanol are purchased from Merck. All the above-mentioned chemicals are used without further purification. All solutions in the experiments are prepared with ultrapure water (Milli-Q water, 18.2 MΩ cm) from a Millipore Milli-Q system (Bedford, MA, USA). All the materials are of analytical grade and are used directly without further purification.

2.2 Preparation of MoS_2 Nanostructures

2.2.1 Preparation of MoS_2 without using reducing agents

0.08 M of ammonium molybdate tetrahydrate and 1.13 M of thiourea are dissolved in de-ionised water under continuous stirring for 30 minutes. The resulting solution is then put in a 50 mL Teflon-lined stainless-steel autoclave at a temperature of 230 ˚C for 24 hours. Then it is allowed to cool down to room temperature. The finally obtained product is collected by centrifugation and washed several times using water and ethanol. The precipitates are then vacuum dried at 140 ˚C for 8 hours. The reactions which occur during above procedure are written as follows:

$$CH_4\,N_2S + 2H_2O \rightarrow CO_2 \uparrow + 2NH_3 \uparrow + H_2S \uparrow \quad (1)$$

$$(NH_4)_6Mo_7O_{24}.4H_2O + 28H_2S + 8NH_3 \rightarrow 7(NH_4)_2MoS_4 + 28H_2O \quad (2)$$

This Sample is labelled as-prepared sample.

2.2.2 Preparation using Hydrazine Hydrate as a reducing agent (MoS_2HH)

0.08 M of ammonium molybdate tetrahydrate and 1.13 M of thiourea are dissolved in de-ionised water under continuous stirring for 30 minutes. 2 mL hydrazine hydrate is added into above prepared solution while stirring only. An acidic pH of 5 is maintained using dilute

HCL. The resulting solution is then put in a 50 mL Teflon-lined stainless-steel autoclave at a temperature of 230 ˚C for 24 hours. Then it is allowed to cool down to room temperature. The finally obtained product is collected by centrifugation and washed several times using water and ethanol. The precipitates are then vacuum dried at 140 ˚C for 8 hours. The reactions which occur during above procedure are written as follows:

Journal Pre-proof

$$CH_4N_2S + 2H_2O \rightarrow CO_2 \uparrow + 2NH_3 \uparrow + H_2S \uparrow \quad (3)$$

$$(NH_4)_6Mo_7O_{24}.4H_2O + 28H_2S + 8NH_3 \rightarrow 7(NH_4)_2MoS_4 + 28H_2O \quad (4)$$

$$(NH_4)_2MoS_4 + 2N_2H_4 \rightarrow MoS_2 + N_2 \uparrow + 2(NH_4)_2S \quad (5)$$

The sample is labelled as MoS_2HH.

2.2.3 Preparation using Citric Acid as a reducing agent (MoS_2CA)

0.08 M of ammonium molybdate tetrahydrate and 1.13 M of thiourea are dissolved in de-ionised water under continuous stirring for 30 minutes. 0.44 M of citric acid is added into above solution while stirring only. The resulting solution is then put in a 50 mL Teflon-lined stainless-steel autoclave at a temperature of 230 ˚C for 24 hours. Then it is allowed to cool down to room temperature. The finally obtained product is collected by centrifugation and washed several times using water and ethanol. The precipitates are then vacuum dried at 140 ˚C for 8 hours. The reactions which occur during above procedure are written as follows:

$$CH_4N_2S + 2H_2O \rightarrow CO_2 \uparrow + 2NH_3 \uparrow + H_2S \uparrow \quad (6)$$

$$(NH_4)_6Mo_7O_{24}.4H_2O + 28H_2S + 8NH_3 \rightarrow 7(NH_4)_2MoS_4 + 28H_2O \quad (7)$$

$$5O_2 + 2N_2 + 2C_6H_8O_7 + 2(NH_4)_2MoS_4 \rightarrow 2MoS_2 + 12CO_2 + 4(NH_4)_2S \quad (8)$$

This sample is labelled as MoS_2CA.

Equation (1), (3) and (6) shows the sulfureted reaction, equation (2), (4) and (7) shows the formation of an intermediate product $(NH_4)_2MoS_4$ while equation (5) and (8) shows the final reduction step of $(NH_4)_2MoS_4$ which leads to formation of MoS_2. Both these steps that is sulfurization and reduction are important for formation of single phase MoS_2 nanostructures without any presence of MoO_2 or MoO_3 intermediate phases [24] and to remove intercalated NH_3 ions between MoS_2 layers due to production of excess ammonia in equations (1) and (4),

respectively [23]. Final reduction step does not take place in case of as-prepared sample as no reducing agent is present to reduce $(NH_4)_2MoS_4$ due to which pure MoS_2 phase cannot be obtained as shown in **Fig. 2**. G Nagaraju et al [24] have reported the formation of MoS_2 Nano bundles citric acid as a reducing agent using a different sulphur source. However, temperature and time play a huge role in controlling the morphology in hydrothermal synthesis of MoS_2 nanostructures.

Journal Pre-proof

2.3 Preparation of MoS_2 based electrode for electrochemical Studies

MoS_2 is known to have an excess of surface negative charge [25, 26], therefore stable films of it can be made by applying an electric field to its stable colloidal suspension in between two electrodes. Electrophoretic method of film deposition offers many advantages like smoothness, homogeneity, uniformity and economic viability, therefore has been chosen for film formation [27, 28].

MoS_2HH and MoS_2CA are separately dispersed in de-ionised (DI) water, acetone, ethanol and acetonitrile with a concentration of 1 mg/mL and sonicated in an ultrasonic bath for 30 minutes at room temperature. The dispersion solutions for both the samples are shown in **Fig. 1** It is observed that in DI water and ethanol particles of samples are not uniformly and homogenously spread throughout the solution rather got settled at bottom. Films using electrophoretic deposition (EPD) are made using dispersions in acetone and acetonitrile. However, films for samples dispersed in acetone couldn't be uniformly formed, whereas films could be easily formed for samples dispersed in acetonitrile, hence conditions are optimised for dispersion of samples in acetonitrile.

Hence, MoS_2HH and MoS_2CA are separately dispersed in Acetonitrile with a concentration of 1 mg/mL and sonicated in an ultrasonic bath for 30 minutes at room temperature. This solution is then poured in a 2-electrode cell comprising of a Copper (Cu) working electrode (WE) and Platinum (Pt) as counter electrode (CE). Indium tin oxide (ITO) coated glass slide of dimension 2.5 cm * 1 cm is used as a conducting substrate for depositing film of MoS_2. ITO is attached to WE and put in the solution. Positive polarity is applied to WE and negative polarity is applied to CE. Under a potential of 40 V, negatively charged MoS_2

particles move towards ITO and films are formed by deposition of MoS_2 particles at the electrode-suspension interface. Films are deposited in an area of 1 cm X 1 cm by electrophoretic deposition.

Journal Pre-proof

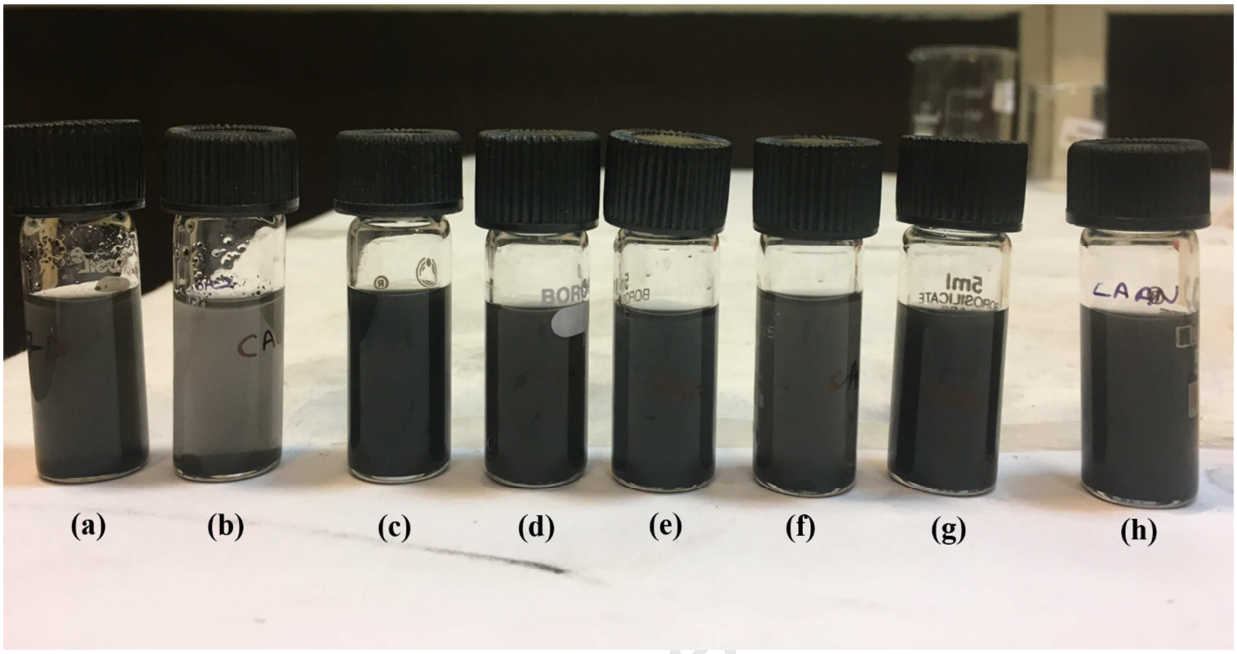


Fig. 1: Dispersion solution of (a) MoS_2HH in DI water (b) MoS_2CA in DI water (c) MoS_2HH in acetone (d) MoS_2CA in acetone (e) MoS_2HH in ethanol (f) MoS_2CA in ethanol (g) MoS_2HH in acetonitrile (h) MoS_2CA in acetonitrile.

3. Results and Discussion

3.1 Characterization

Various different techniques have been utilised to characterise as synthesised samples. X – Ray diffraction spectra has been recorded using a Bruker D8 Advance facility with Cu K_α radiation of wavelength 1.514 Å. Field emission scanning electron microscopy (FESEM) is done using TESCAN model LYRA 3 XMU and is used to examine the morphology of samples. Raman spectra is measured using WITec Raman spectrometer with an excitation wavelength of 532 nm. Fourier transform infrared spectroscopy (FT-IR) is performed using Perkin Elmer FT-IR spectrometer. JEOL transmission electron microscope is used to record TEM images. Elemental analysis of synthesised samples is carried out using energy dispersive X-ray fluorescence (EDXRF) technique, using Epsilon 5, PANalytical and CHNS elemental analysis using Vario Micro Cube Elemental Analysensysteme Germany. The electrochemical measurements are done at room temperature by a Metrohm Autolab Potentiostat/Galvanostat

using Nova software. The conventional three electrode electrochemical cell is used for electrochemical measurements using MoS_2/ITO as the working electrode, platinum (Pt) wire as the counter electrode, and silver/silver chloride (Ag/AgCl) electrode (in 3 M KCL) as the reference electrode. PBS solution (pH 7.0) containing 5 mM of $[Fe(CN)_6]^{3-/4-}$ and 0.9% NaCl is used as a supporting electrolyte.

Journal Pre-proof

3.1.1 XRD

Fig. 2 shows XRD patterns of samples prepared without using reducing agents (as- prepared sample) and with reducing agents which are (MoS_2HH) and (MoS_2CA). Identified peaks for MoS_2HH and MoS_2CA can be indexed to hexagonal MoS_2 (2H MoS_2) with JCPDS card no. 37-1492. A low intensity broadened (002) peak around 11˚ corresponds to low crystallinity of as-prepared sample and the Peaks (100) and (103) are also not distinguishably visible. Also, the (110) peak is shifted slightly left in comparison to MoS_2 samples prepared using reducing agents. From here it can be concluded that this sample prepared without using any reducing agents is not having pure crystalline phase of MoS_2 and hence further studies are not carried out on this sample. For the other two samples which are prepared using reducing agents, the peaks are found to be broadened and have weak intensity which is due to decrease in size as compared to bulk MoS_2. 002 peak which corresponds to periodicity along c direction is observed to be of less intensity and is broadened which shows that sample is in nano range, however its presence in both the samples (MoS_2HH and MoS_2CA) indicates that MoS_2 formed is not monolayer, rather stacking of large no. of layers [24, 29]. Also, the (002) peak which appears at 14.4˚ in case of bulk MoS_2 is shifted slightly towards low angle side (13.57˚) indicates an expansion towards (001) direction [30]. (002) peak arises because of interlayer Mo–Mo scattering and it can be seen that sample MoS_2HH has a relatively strong and sharp (002) peak in comparison to MoS_2CA, indicating a formation of well crystalline MoS_2HH with ordered stacking along the c-axis [31]. XRD data was analysed using XPowder software for structure determination. Best matching of peaks for both the samples was observed for hexagonal structure. Lattice parameters a, b and c are found using XPowder software and their

values are given as shown in **Table 1**, with reference to JCPDS value. Crystallite size is calculated for both the samples using Debye-Scherrer formula [32]

Journal Pre-proof

$$t = 0.9\lambda/(\beta cos\theta)$$

where t is the crystallite size (average crystallite diameter), λ is the X-ray wavelength i.e. 1.54064 Å, K is the shape factor (0.9), β is the line broadening at half the maximum intensity (FWHM), Θ=2Θ/2, i.e. the Bragg Angle (in radian). The average crystallite size and micro strain ε is also calculated using Williamson- Hall (W-H) plots using the relation [33]

$$\beta cos\theta = 4\varepsilon sin\theta + \frac{k\lambda}{D}$$

Where, β is full width at the half maxima (in radian), k is the shape factor, λ is wavelength of the incident X-rays (CuK_α, λ = 1.54064 Å). **Fig. 3** shows linearly fitted W-H Plots and their values are given in **Table 2**. All the peaks (002), (100), (103) and (110) are considered for both the samples. Inverse of y-intercept gives the crystallite size and the slope is a measure of micro strain in the sample, whose values are given in **Table 2**. Average crystallite size using Debye Scherrer equation is calculated with an experimental error of ±0.218 nm, while from W-H plots the crystallite size is calculated with an experimental error of ±5.664 nm. Also, it can be seen that strain in sample MoS_2CA is greater than MoS_2HH which could be possibly due to more stacking of layers in MoS_2CA which is further confirmed from Raman spectra **(Fig. 6)** and TEM images **(Fig. 7)** as well.

Journal Pre-proof

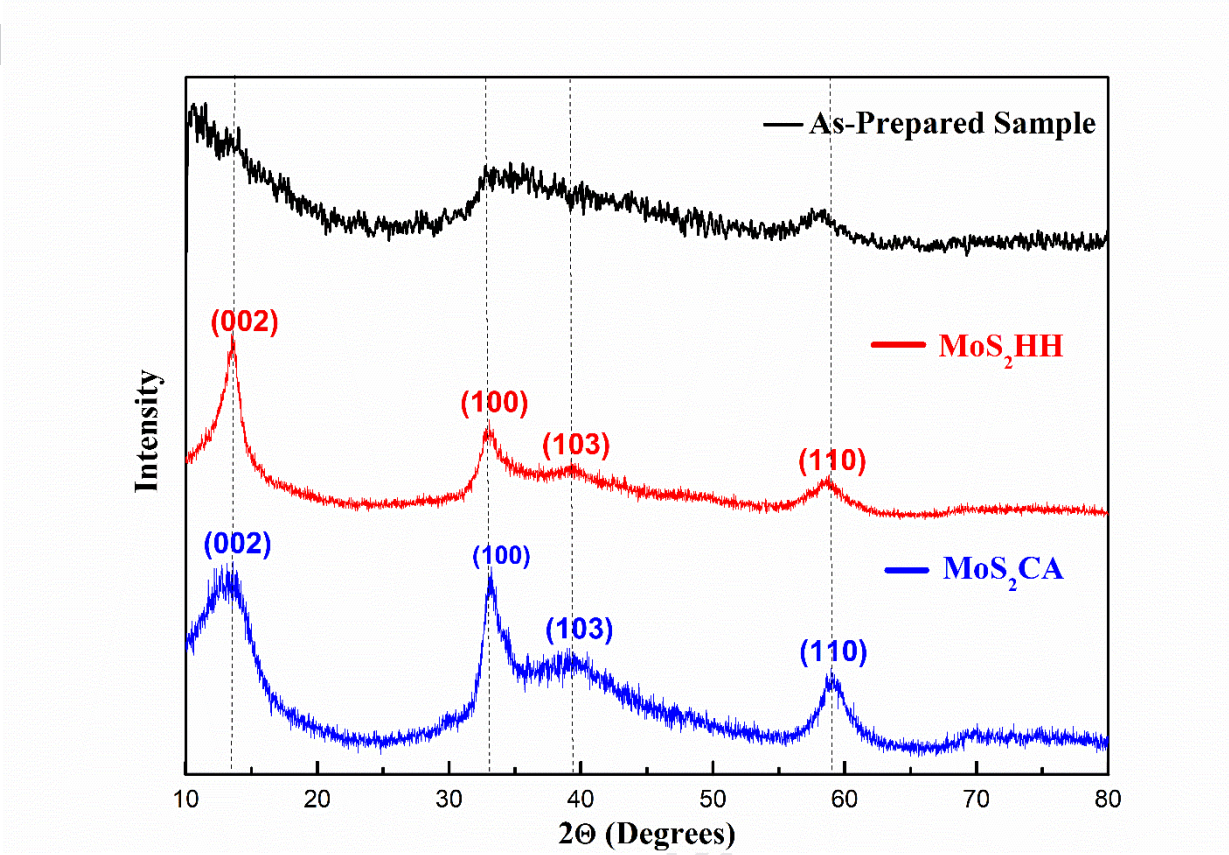


Fig. 2: XRD of as-prepared MoS_2, MoS_2HH and MoS_2CA

Lattice Parameters	**JCPDS (37-1492)**	**MoS_2HH**	**MoS_2CA**
a	3.1612Å	3.135 Å	3.111 Å
b	3.1612 Å	3.135 Å	3.111 Å
c	12.2985 Å	12.998 Å	13.654 Å
Volume of unit cell	106.43 $Å^3$	110.63 $Å^3$	114.44 $Å^3$

Table 1: Lattice parameters of two samples calculated using X-Powder software

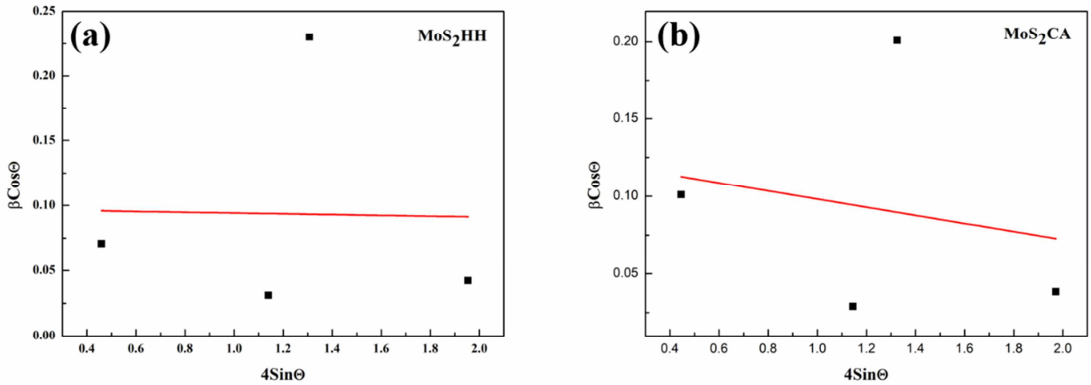


Fig. 3: W-H plots of (a) MoS_2HH and (b) MoS_2CA

Journal Pre-proof

Sample	Average Crystallite size from Scherrer Formula	Crystallite size from W-H Plots	Strain from W-H Plots
MoS_2HH	2.69 nm	1.42 nm	-0.00301
MoS_2CA	2.73 nm	1.15 nm	-0.02618

Table 2 : Crystallite size calculated using Scherer formula and W-H plots and strain estimation for two samples

3.1.2 FESEM

Fig. 4 shows the morphological structures of MoS_2 nanostructures formed using 2 different reducing agents. **Fig. 4 a**, **b and c** shows morphology obtained for MoS_2HH while **Fig. 4 d, e** and **f** shows the nanostructures obtained for MoS_2CA. At higher scales (**Fig. 4a and 4d**) flowers constituting a huge no. of nanopetals/nanosheets which are curled and stacked up together can be seen for both the samples. At small scales **(Fig. 4b, 4c, 4e and 4f),** these nanosheets are seen to be growing in all directions rendering an uneven surface morphology.

Journal Pre-proof

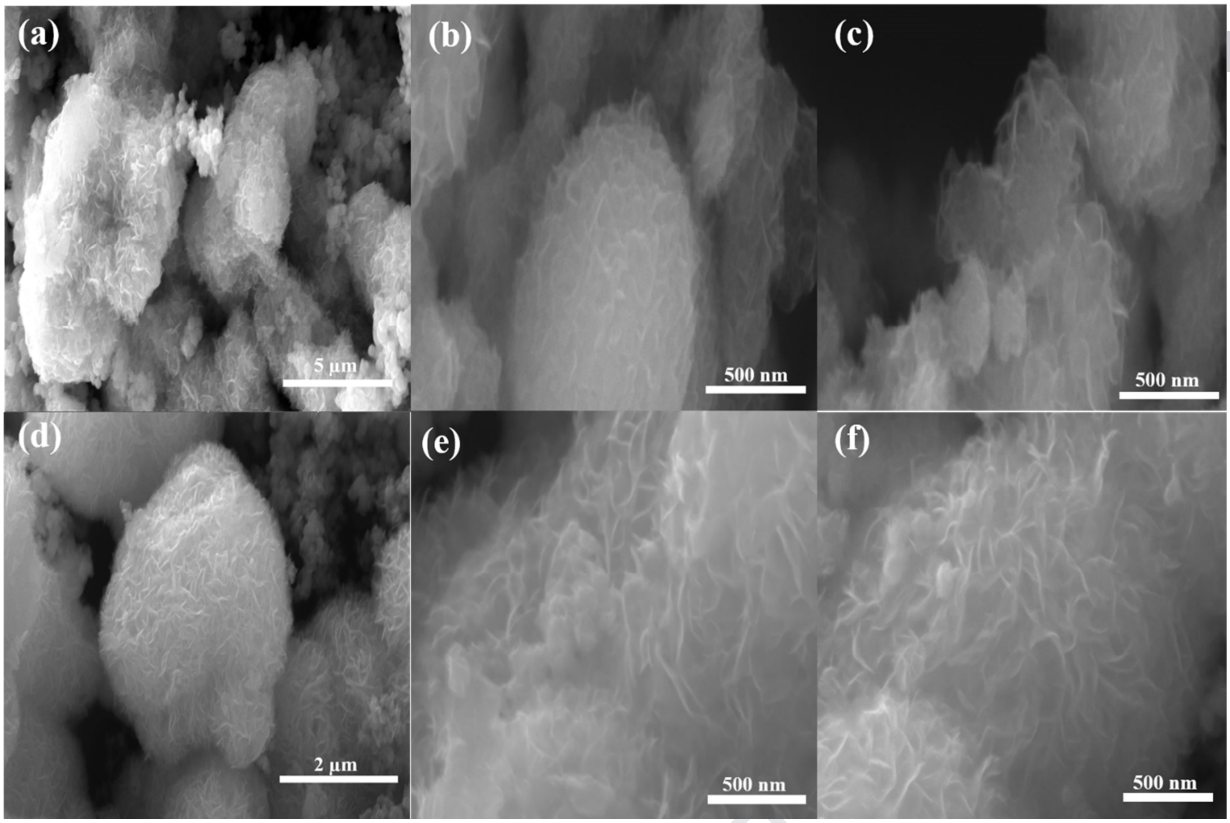


Fig. 4: FESEM Image of MoS_2 nanostructures (a, b, c) MoS_2HH (d, e, f) MoS_2CA

3.1.3 FTIR

The weak peak around 470 cm^{-1} can be attributed to Mo-S vibrations [34]. The absorption band at 1633 cm^{-1} and 1637 cm^{-1} in case of MoS_2HH and MoS_2CA respectively corresponds to Mo-O vibrations. Strong absorption peak which is observed at 3450 cm^{-1} can be attributed to stretching vibrations of O-H bonds [35]**.** Peak at 950 cm^{-1} correponds to the S-S bond. More intensity of transmittance peak in FTIR results for MoS_2CA clearly indicates more that more no. of O-H bonds is present than in MoS_2HH. These O-H bonds correspond to water molecules adsorbed on to the samples during synthesis process. Hydrazine hydrate is comparatively a stronger reducing agent than citric acid which removes more water molecules in comparison and decreases the total number of hydroxyl functional group (O-H) from the synthesised sample as evident from FTIR spectra. Another possible reason for more intensity of O-H peak could be O-H bonds itself present in citric acid (Chemical formula – $C_6H_8O_7$). In order to determine the hydroxide (OH) content present in both the samples, FT-IR spectral study has been used. The Beer-Lambert law relates the attenuation of light to the properties of the

Journal Pre-

material through which it is travelling. The Beer-Lambert law in terms of transmission intensities is given as follows [36]:

Journal Pre-proof

$$\epsilon cd = lg\frac{T_o}{T_D} \quad (1)$$

Where, ε is molar absorption coefficient in $M^{-1}cm^{-1}$, c is molar concentration in M, d is optical path length in cm, T_O is the highest transmission intensity, while T_D is the transmission intensity of OH bond. To determine the OH content present in the samples, absorption coefficient α_{OH} is calculated [37] which is given by following expression

$$\propto_{OH} = \frac{lg\frac{T_O}{T_D}}{d} \quad (2)$$

d is taken to be thickness of KBr pellet prepared of sample for FTIR, which is 1 mm for both MoS_2HH and MoS_2CA. Using equation (2), the calculated value of OH content in MoS_2HH is 2.73 cm^{-1} and for MoS_2CA it is 3.55 cm^{-1}. From the spectra also it is observed that MoS_2CA has more OH content which is shown by its value of absorption coefficient also.

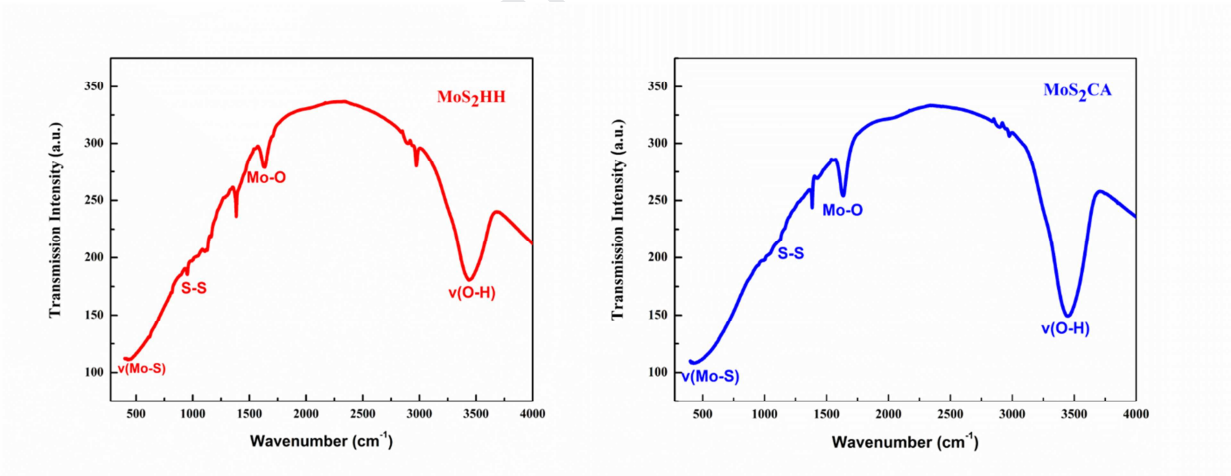


Fig. 5: FTIR of MoS_2HH and MoS_2CA

3.1.4 Raman Spectra

Fig. 6 shows Raman spectra of MoS_2HH and MoS_2CA excited by a laser source having wavelength of 532 nm. The Raman Spectrum of MoS_2 has two main peaks: an in plane (E^1_{2g}) mode located around 383 cm^{-1} and an out of plane mode (A_{1g}) located around 407 cm^{-1} corresponding to 2H-phase. The in-plane mode corresponds to the sulphur atoms vibrating in

Journal Pre-proof

one direction and the molybdenum atoms in other, while out of plane mode corresponds to the sulphur atoms vibrating out of plane. The difference (Δ) between (E^1_{2g}) and (A_{1g}) modes can be used to estimate the layer number of MoS_2 nanosheet [38, 39]. This value Δ is around 18 cm^{-1} for monolayer and approximately equal to 25 cm^{-1} for multilayer MoS_2 [40, 41]. For MoS_2HH, (E^1_{2g}) mode lies at 382.68 cm^{-1} and (A_{1g}) mode lies at 405.82 cm^{-1} leading to wavenumber Separation (Δ) of 23.14 cm^{-1}, while for MoS_2CA (E^1_{2g}) mode lies at 385.25 cm^{-1} and (A_{1g}) mode lies at 410.96 cm^{-1} leading to wavenumber Separation (Δ) of 25.71 cm^{-1}. Also, the Raman frequencies (E^1_{2g}) and (A_{1g}) peaks vary repeatedly with the number of layers of MoS_2 nanosheets, whereas intensities and widths of the peaks vary arbitrarily. Although the calculated Δ value shows the non-existence of one layer (1L), two layers (2L), three layers (3L) or four layers (4L) but the presence of stacked structures constituting more than four layers [42] [43]. With the increase in number of layers, atomic vibrations are supressed by Vander Waals forces leading to a higher force constant and blue shift of (A_{1g}) mode [22]. Here, a blue shift in (A_{1g}) mode of MoS_2CA confirms higher stacking height in comparison to MoS_2HH which is evident from XRD pattern and TEM **(Fig. 7)** images as well.

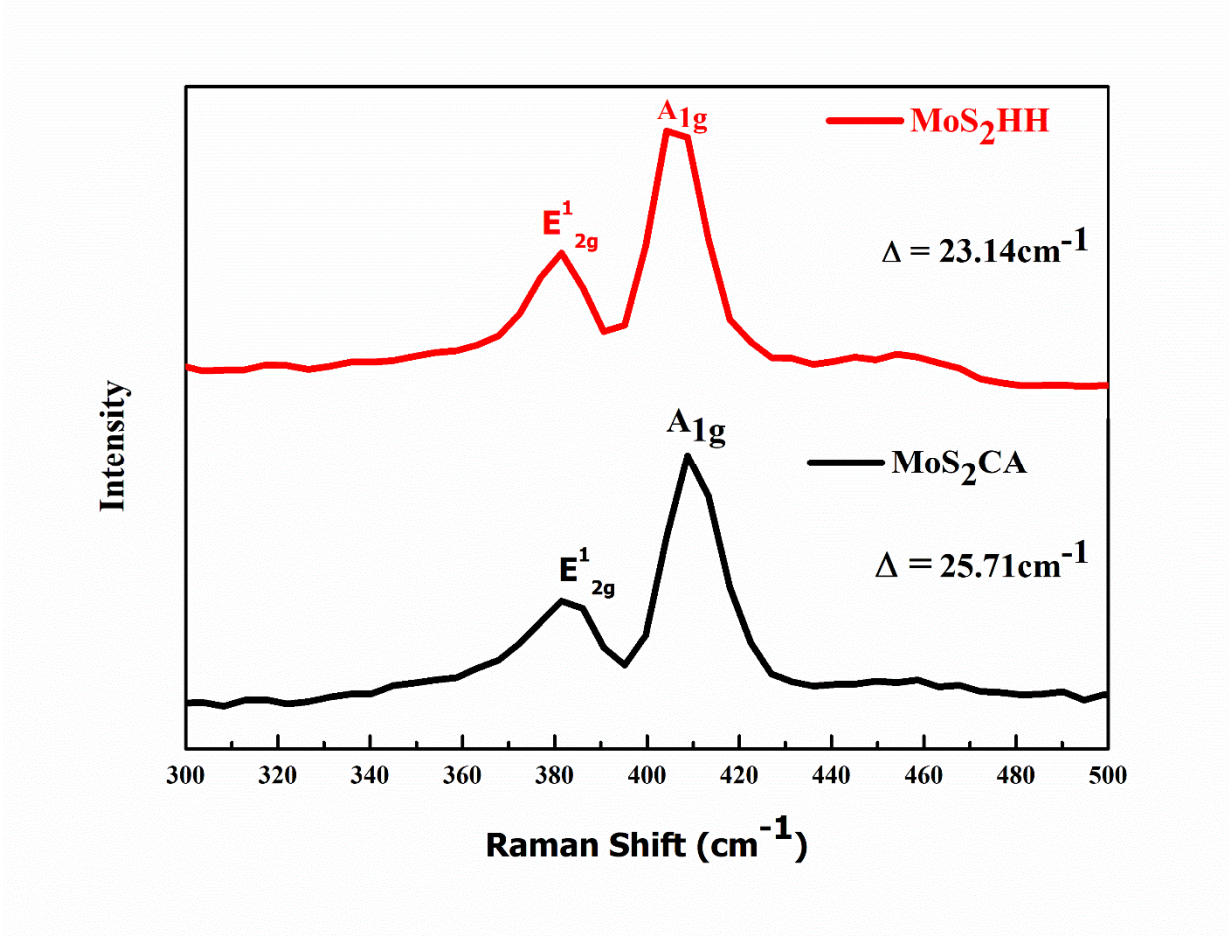


Fig. 6: Raman Spectra of MoS_2HH and MoS_2CA

Journal Pre-proof

3.1.5 TEM

TEM analysis is carried out by sonicating dispersions of both samples in ethanol and loading a single drop on TEM copper grid. From the TEM images **(Fig. 7)** it can be observed that layered nanosheets can be observed for both the samples. However, for MoS_2HH these sheets are in tight contact with each other making the nanosheet film more stable, while for MoS_2CA the nanosheets are not tightly packed together. Increase in stacking height of MoS_2CA is also evident from blue shift of A_{1g} mode in Raman spectra. Both hydrazine hydrate and citric acid acts as reducing agent to reduce the oxidation state of Mo (VI) to Mo (IV), but besides this citric acid also acts as a surfactant to grow nanosheets in a particular way. Such kind of morphological direction to nanostructures by citric acid has also been reported for MoO_2 nano discs [44]. In another work, the effect of citric acid on the growth of ferric oxide was studied, where the size of nanoparticles decreases with increase in concentration of citric acid [45]. This happens, because adsorption of surfactant molecules hinders the growth of Fe_2O_3 nanoparticles. Same thing is perhaps happening in our case where, citric acid molecules are attached on to the layers of MoS_2 nanostructures not allowing them to form tightly packed structures, as seen in TEM images. Therefore, sheets obtained here for MoS_2CA are of small lateral length, growing randomly and increasing the overall stacking length of layers.

Journal Pre-proof

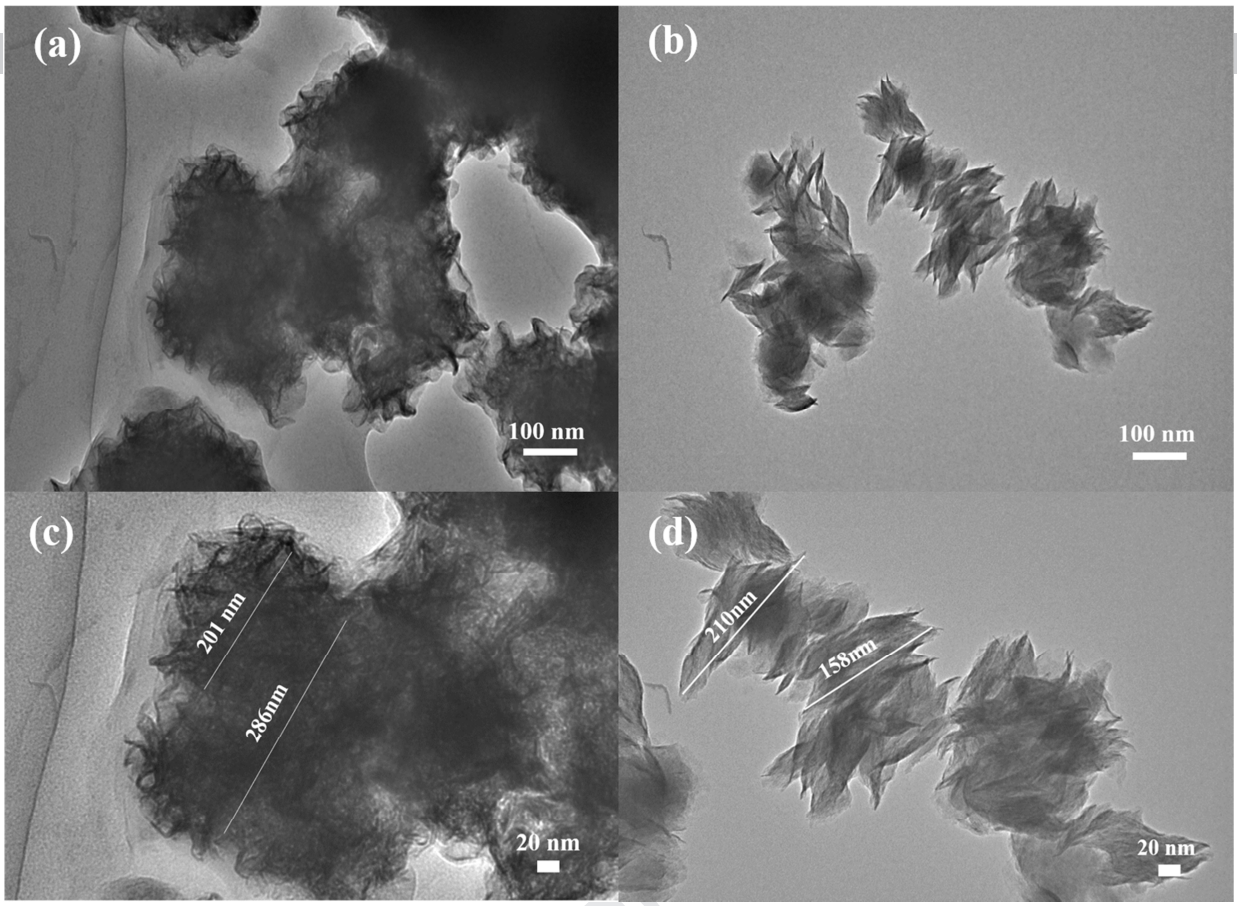


Fig. 7: TEM image (a) MoS_2HH at 100 nm (b) MoS_2CA at 100 nm (c) MoS_2HH at 20 nm (d) MoS_2CA at 20 nm

3.1.6 EDXRF

The purpose of this technique is to determine the Molybdenum (Mo) elemental composition of samples. MoS_2HH and MoS_2CA samples are mixed with boric acid to form a pellet by applying a pressure of 5 tons for 10 seconds. The elemental composition of Mo is listed in **Table 3** for MoS_2HH and MoS_2CA.

3.1.7 CHNS

To identify the sulphur (S) content present in synthesised MoS_2 samples and presence of other impurity elements like carbon (C), hydrogen (H) and nitrogen (N), CHNS analysis is done. The elemental percentage for above stated elements is given in **Table 3**. It can be seen that elemental N impurity in MoS_2HH is more in comparison to MoS_2CA, while elemental C impurity in MoS_2CA is more than in MoS_2HH, which clearly indicates that hydrazine hydrate is a source of more N impurity in MoS_2HH, while citric acid is source of C impurity in

MoS_2CA. Total C, H, N contamination is 7.59% and 5.06% in MoS_2HH and MoS_2CA respectively.

Journal Pre-proof

Elemental Percentage	Mo	S	C	H	N
MoS_2HH	64.41%	28.01%	1.35%	1.86%	4.38%
MoS_2CA	61.30%	33.64%	3.14%	0.95%	0.97%

Table 3: Elemental composition of MoS_2HH and MoS_2CA determined using EDXRF and CHNS elemental analysis

3.2 Electrochemical Studies

In order to see electrochemical properties of MoS_2 samples prepared using 2 different reducing agents, electrochemical impedance spectroscopy, cyclic voltammetry and differential pulse voltammetry are conducted. Electrodes are made by deposition of prepared samples on ITO and are labelled as MoS_2HH_ITO and MoS_2CA_ITO. For these studies mentioned above 3-electrode cell is taken in which prepared electrodes are employed as working electrode and their electrochemical studies are recorded. The electroactive surface area and the heterogenous rate transfer constant are the main factors which determine the electrochemical performance and hence are found using these analytical techniques.

3.2.1 Electrochemical Impedance Spectroscopy (EIS)

Electrochemical impedance spectroscopy is done in a frequency range of 10^5 Hz to 0.1 Hz at a set potential of 0.01 V. Semi-circular diameter in case of MoS_2HH is smaller in comparison to that of MoS_2CA giving a R_{ct} value of 150 Ω and 456 Ω respectively. Larger resistance is offered to electrons in case of MoS_2CA which may be due to the larger height and irregular orientation of nanosheet arrays as observed in TEM images **(Fig. 7)** and confirmed from Raman spectra and XRD pattern as well. Whereas, MoS_2HH has stacked nanosheets therefore decreasing the overall distance that electron has to travel to reach conducting ITO substrate. Software simulated fitting of obtained impedance spectra is done using Randles

Journal Pre-proof

circuit given by R_s (C_{dl}[$R_{ct}W_z$]) having Warburg impedance in series with charge transfer resistance with this total series component parallel to double layer capacitance ($C_{dl.}$) which is in series with solution resistance R_s. It is observed that good fit for impedance spectra of both the samples can be obtained with χ^2 value given by 0.99908 and 0.99692 for MoS_2HH and MoS_2CA respectively. Heterogenous electron transfer constant (K_o) can be calculated using the following equation [15]

$$Ko = \frac{RT}{n^2F^2 2AR_{ct}C}$$

Where, R is universal gas constant, T is room temperature (25 ˚C), n is the no. of electrons transferred in redox event, F is Faraday's constant, A is electroactive surface area (in cm^2), C is bulk concentration of analyte. From here we can calculate value of K_o for MoS_2HH as 5.03 X 10^{-4} cm/s for electroactive area (7.05 X 10^{-4} cm^{-2}, as calculated using cyclic voltammetry) and K_o for MoS_2CA as 1.79 X 10^{-4} cm/s for electroactive area (6.51 X 10^{-4} cm^{-2}, as calculated using cyclic voltammetry).

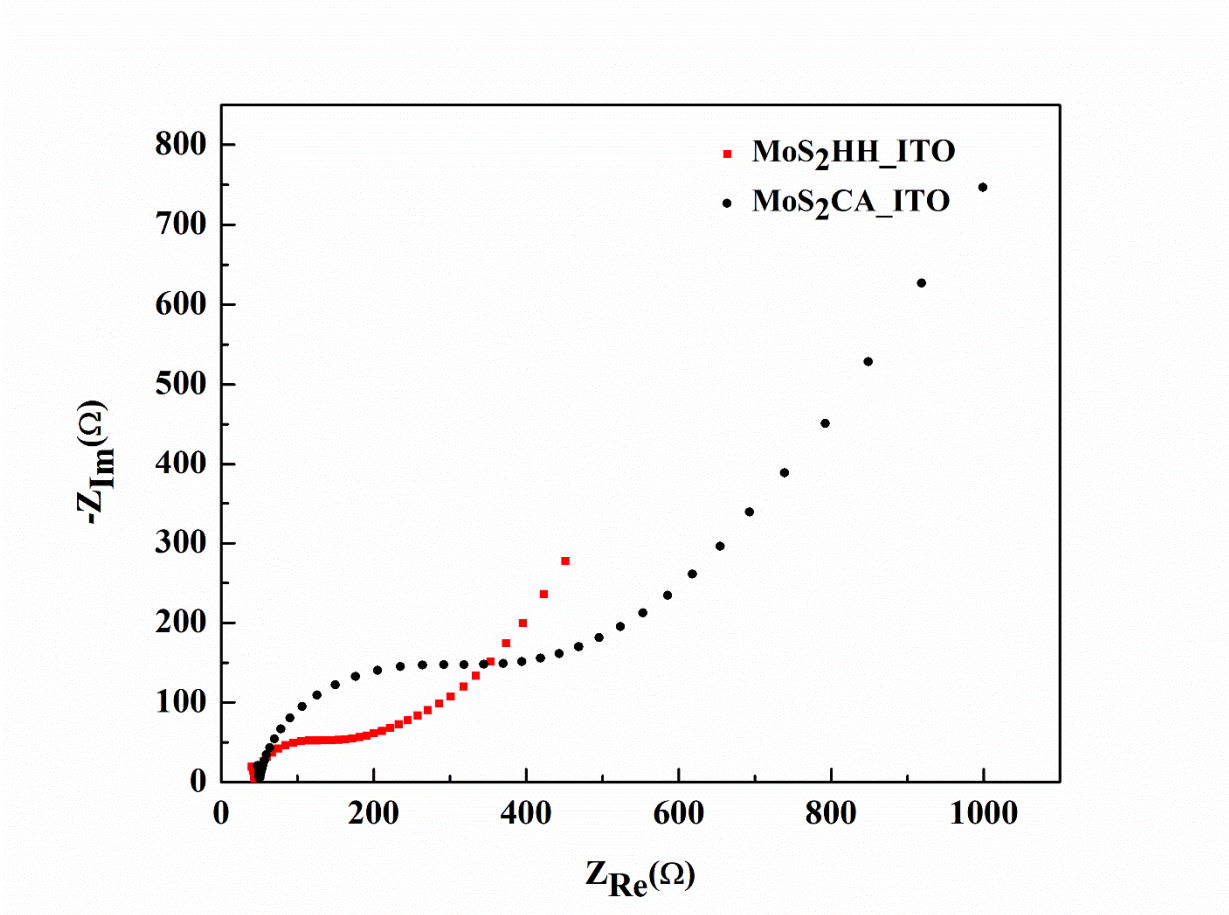


Fig. 8: Electron Impedance Spectroscopy of MoS_2HH_ITO and MoS_2CA_ITO

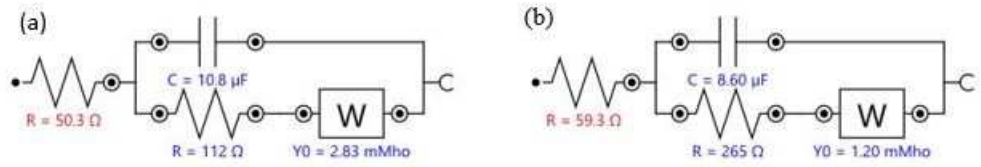


Fig. 9: Randle's Circuit (a) MoS_2HH_ITO (b) MoS_2CA_ITO

3.2.2 Cyclic Voltammetry (CV)

Cyclic voltammetry studies are done in a potential window of -0.6 V to 1.5 V at a scan rate of 50 mV/s **(Fig. 10)**. For MoS_2HH value of peak current in positive direction of voltage scan is found to be 546.17 µA at a potential of 0.693 V while the peak current in negative direction of voltage scan is -545.53 µA at a potential of -0.176 V. While for MoS_2CA same peak currents in two directions of potential scan were found to be a little lesser with a value of 504.15 µA at a potential value 0.544 V and -523.5 µA at a potential of -0.119 V. Scan rate study for both the samples is done using cyclic voltammetry in the potential window of -0.5 V to 1.2 V at a scan rate of 10 mV/s to 150 mV/s. **Fig. 12** shows the variation of peak anodic current (i_{pa}) and peak cathodic current (i_{pc}) with square root of scan rate which is a straight line showing that the process is diffusion-controlled [46] [47]. By diffusion controlled we mean that the electron transfer takes place between electrode and electrolyte solution and not by adsorption of analyte on electrode surface. For both the samples, electron transfer process is found to be diffusion controlled and can be fitted by the equations given as

$$I_{pa}(MoS_2HH) = 0.14137mA + \left[\left(0.05639mA\ X\sqrt{\frac{s}{mV}}\right)\ X\left(\sqrt{Scan\ Rate\frac{mV}{s}}\right)\right] \quad (11)$$

$R^2 = 0.99$

$$I_{pc}(MoS_2HH) = -0.08271mA + [\left(-0.07165mA\ X\sqrt{\frac{s}{mV}}\right)\ X\left(\sqrt{Scan\ Rate\frac{mV}{s}}\right)] \quad (12)$$

$R^2 = 0.99$

$$I_{pa}(MoS_2CA) = 0.14366mA + [\left(0.03369mA\ X\sqrt{\frac{s}{mV}}\right)\ X\left(\sqrt{Scan\ Rate\frac{mV}{s}}\right)] \quad (13)$$

$R^2 = 0.99$

Journal Pre-proof

$$I_{pc}(MoS_2CA) = -0.07235mA + [\left(-0.07525mA\, X\sqrt{\frac{s}{mV}}\right)\, X\left(\sqrt{Scan\, Rate\, \frac{mV}{s}}\right)] \quad (14)$$

Journal Pre-proof

$R^2 = 0.99$

Here, R is correlation coefficient

The peak current for a reversible couple is given by Randles-Sevcik equation [48]

$$ip = 0.446nFAC\sqrt{\left(\frac{nFvDo}{RT}\right)} \quad (15)$$

Where,

n is the no. of electrons transferred in redox event is Faraday's constant, A is electrode surface area (in cm^2), v is scan rate (in V/s), Do is diffusion coefficient of oxidised analyte (in cm^2/s), C is bulk concentration of analyte, R is universal gas constant, T is room temperature (25 ˚C). By substituting the value of Faraday's constant as 96485 C/mol, value of T as 25˚C and R as 8.314 J/K/mol equation (15) is reduced to

$$i_p = 2.69\, X10^5 n^{3/2} AC\sqrt{D_o v} \quad (16)$$

Now, by substituting the values of i_p, number of electrons transferred (n =1 for ferro/ferri), D_o (0.667 X 10^{-5} cm^2/sec for ferrocyanide [49], which is oxidized analyte for our system), C (5 X 10^{-3} mol cm^{-2}) and v (50 mV/s), the electroactive surface area of MoS_2HH electrode can be calculated as 7.05 X10^{-4} cm^{-2}, while for MoS_2CA it is 6.51 X 10^{-4} cm^{-2}.

The value of i_{pa}/i_{pc}= 1.001, for MoS_2HH, which is very close to unity showing that the redox system is nearly reversible, however its value for MoS_2CA is 0.96 which shows that system is semi-reversible.

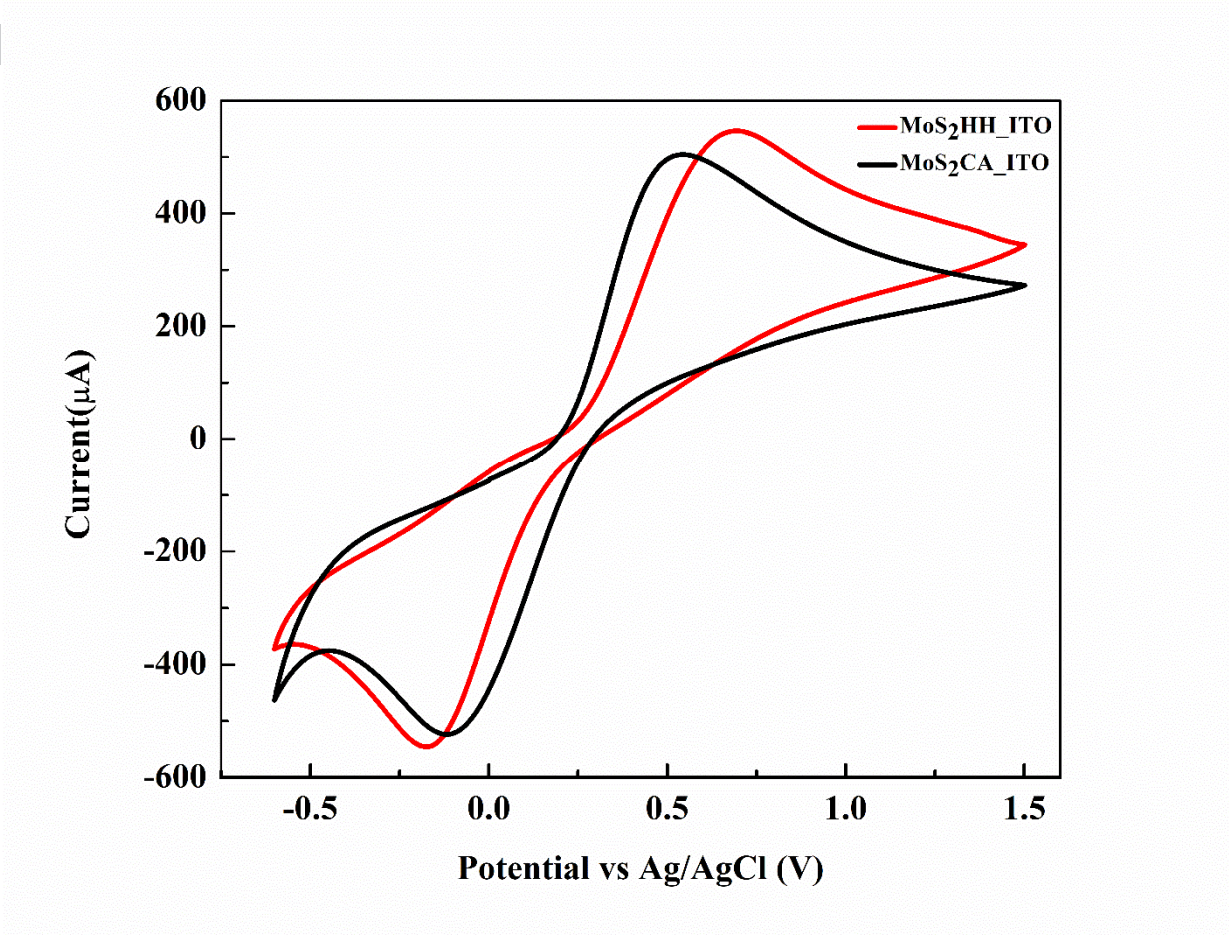


Fig. 10: Cyclic Voltammetry of MoS_2HH_ITO and MoS_2CA_ITO

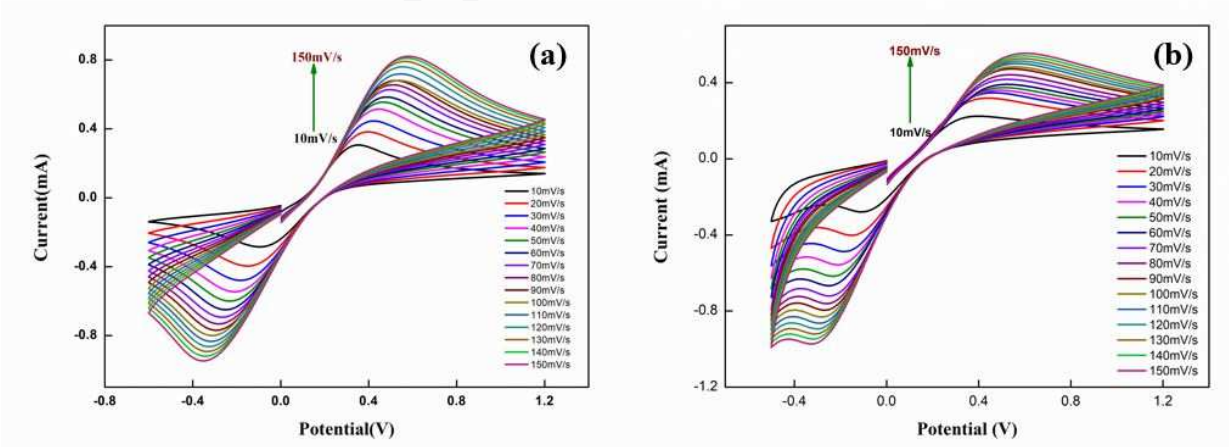


Fig. 11: Scan Rate study of (a) MoS_2HH_ITO and (b) MoS_2CA_ITO at scan rate varying from 10mV/s - 150mV/s

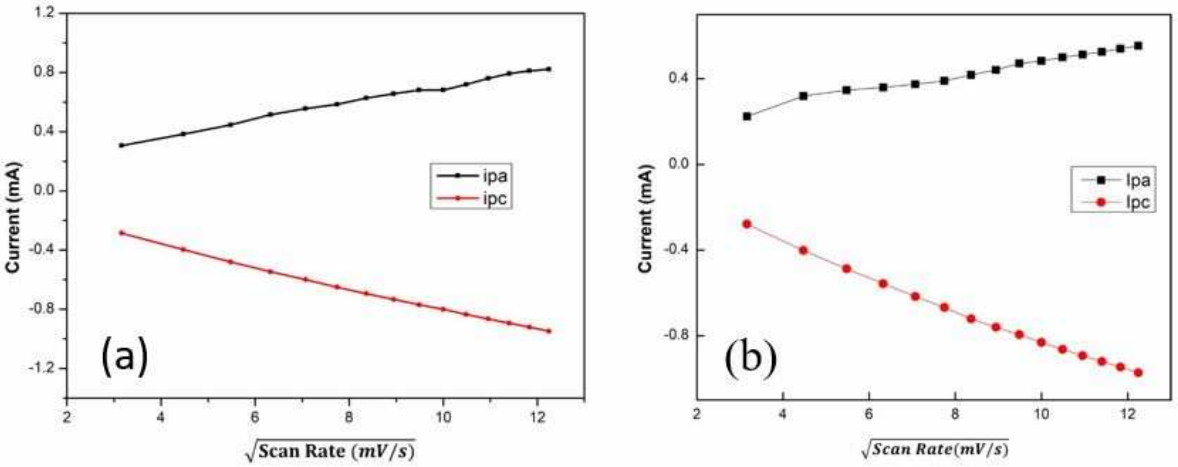


Fig. 12: Variation of i_{pa} and i_{pc} with under root of scan rate (a) MoS_2HH_ITO (b) MoS_2CA_ITO

3.2.3 Differential Pulse Voltammetry (DPV)

DPV studies were conducted in same electrochemical cell with same redox probes as used in CV with a step potential of 0.005 V in a potential window of 0 V to 0.6 V with a scan rate of 10 mV/s. For MoS_2HH peak current value is 72.02 µA which is reached at a potential of 0.33 V, while MoS_2CA shows peak current at 63.78 µA reaching at a potential of 0.28 V.

The results are similar to that of cyclic voltammetry, but in this case, it can be seen that the difference is more amplified, reason being in DPV we take a differential pulse which results in an enhanced response.

Journal Pre-proof

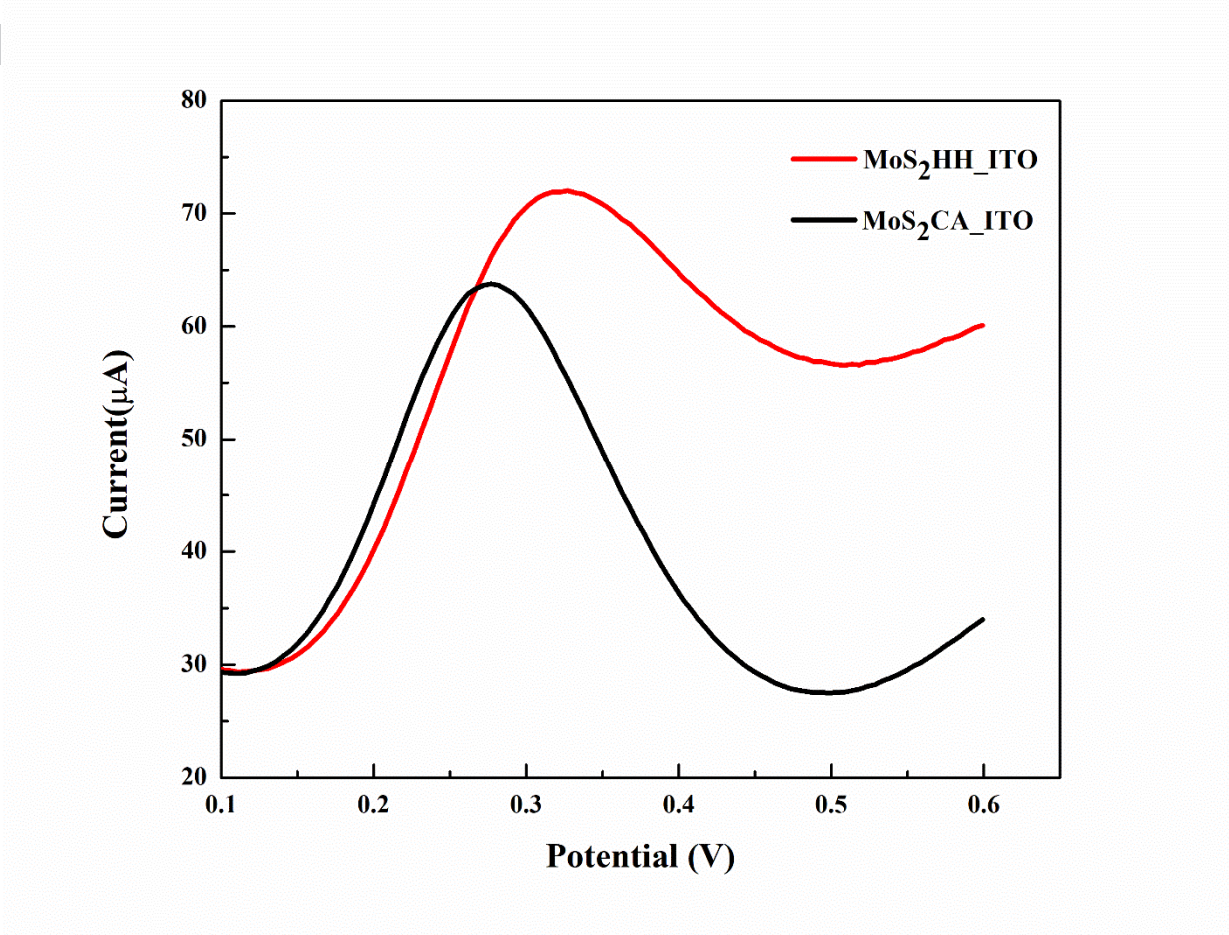


Fig. 13: Differential Pulse Voltammetry of MoS_2HH_ITO and MoS_2CA_ITO

Significant improvement in current value and resistance value for MoS_2HH is caused by increased effective surface area for heterogeneous electron transfer (HET), due to its high density, closely packed nanosheet surface. More, stacking height of layers is seen in case of MoS_2CA in TEM images **(Fig. 7)** whose confirmation is given by Raman spectra and XRD pattern as well. More stacking height of layers increases the diffusion distance of electrons which in turn increases the resistance value and decreases the current response as observed in EIS, DPV and CV respectively.

It can also be clearly observed that the difference between signals for two samples is maximum observable in EIS (67%) in comparison to DPV (13%) and CV (8.33%). This can be attributed to the layered structure of MoS_2 and excess negative charge on surface of MoS_2 which repels the negative redox probe which hinders the electron transport between redox couple and electrode surface [22] [31].

Journal Pre-proof

	R_{ct} (EIS)	i_p (CV)	i_p (DPV)
MoS_2HH_ITO	150 Ω	546.17 µA	72.02 µA
MoS_2CA_ITO	456 Ω	504.15 µA	63.78 µA
Percentage Change	67%	8.33%	13%

Table 4: Percentage change between results of different electrochemical techniques

	Heterogenous Rate Transfer Constant (K_o)	Electroactive Surface Area	Diffusion Controlled Process	Electrochemical Reversibility
MoS_2HH_ITO	5.03 X 10^{-4} cm/s	7.05 X 10^{-4} cm^{-2}	Yes	i_{pa}/i_{pc}= 1.001 ~Reversible
MoS_2CA_ITO	1.79 X 10^{-4} cm/s	6.51 X 10^{-4} cm^{-2}	Yes	i_{pa}/i_{pc}= 0.96 Semi reversible

Table 5: Comparison of parameters calculated using, used electrochemical techniques

Journal Pre-proof

4. Conclusion

rMoS_2 nanostructures were synthesised using a simple, one-step hydrothermal method by reducing MoS_2 using hydrazine hydrate and citric acid. Sample reduced using hydrazine hydrate is found to exhibit a higher electroactive surface area (7.05 X 10^{-4} cm^{-2}) and heterogeneous electron transfer constant (5.03 X 10^{-4} cm/s) thus imparting it better electrochemical properties which can be utilised for electrochemical sensing applications where an increase or decrease in current or resistance value can confirm the attachment of gas or biomolecules. Overall, diffusion distance is increased in case of MoS_2 sample reduced using citric acid which is due to stacking of layers confirmed by increase in crystallite strain estimated using W-H plots from XRD data, Blue shift in A_{1g} peak in Raman spectra and visible morphology from TEM images which renders it a low electroactive surface area (6.51 X 10^{-4}

cm^{-2}) and low heterogeneous electron transfer constant (1.79 X 10^{-4} cm/s). We believe that MoS_2 reduced using hydrazine hydrate can be further explored for its applications in sensing owing to its high surface area, good heterogeneous electron transfer constant and nanosheets like structure increasing the total surface area for loading of bio or gas molecules. It can also be concluded that EIS is a better technique for observing measurable difference for layered materials.

Journal Pre-proof

Acknowledgements

Authors are thankful to Prof. Yogesh Singh, Vice chancellor, Delhi Technological University, Delhi, India for arranging the research facilities. The financial support received from SERB, DST, India (EMR/2016/007479) is gratefully acknowledged. One of the authors, Ritika is also thankful to Kamal Arora, Kanika Sharma for their support and motivation in writing the manuscript and Sandeep Sarpal and Saroj Kumar Jha for their support in analysis of characterisation techniques results.

Highlights

- One step chemical reduction of MoS_2 nanostructures is achieved using hydrothermal method.
- Lattice parameters, Crystallite size and strain is determined for $rMoS_2$.
- Films of $rMoS_2$ are deposited using electrophoretic deposition.
- Electrochemical Studies are performed for $rMoS_2$.
- $rMoS_2$ synthesised using Hydrazine Hydrate has more electroactive surface area and heterogeneous rate transfer constant (K_o).
- Correlation between TEM, Raman and XRD explains better performance of sample reduced using hydrazine hydrate.

References:

[1] C. Anichini, W. Czepa, D. Pakulski, A. Aliprandi, A. Ciesielski, P. Samorì, Chemical sensing with 2D materials, Chemical Society Reviews 47(13) (2018) 4860-4908.

[2] L. Wang, Y. Ma, M. Yang, Y. Qi, Hierarchical hollow MoS2 nanospheres with enhanced electrochemical properties used as an electrode in supercapacitor, Electrochimica Acta 186 (2015) 391-396.

[3] J. Park, J.-S. Kim, J.-W. Park, T.-H. Nam, K.-W. Kim, J.-H. Ahn, G. Wang, H.-J. Ahn, Discharge mechanism of MoS2 for sodium ion battery: Electrochemical measurements and characterization, Electrochimica Acta 92 (2013) 427-432.

[4] W. Qin, T. Chen, L. Pan, L. Niu, B. Hu, D. Li, J. Li, Z. Sun, MoS2-reduced graphene oxide composites via microwave assisted synthesis for sodium ion battery anode with improved capacity and cycling performance, Electrochimica Acta 153 (2015) 55-61.
[5] V.H. Pham, K.-H. Kim, D.-w. Jung, K. Singh, E.-S. Oh, J.S. Chung, Liquid phase co-exfoliated MoS2–graphene composites as anode materials for lithium ion batteries, Journal of Power Sources 244 (2013) 280-286.
[6] Z. Li, J. Ma, Y. Zhou, Z. Yin, Y. Tang, Y. Ma, D. Wang, Synthesis of sulfur-rich MoS2 nanoflowers for enhanced hydrogen evolution reaction performance, Electrochimica Acta 283 (2018) 306-312.
[7] M. Pumera, A.H. Loo, Layered transition-metal dichalcogenides (MoS2 and WS2) for sensing and biosensing, TrAC Trends in Analytical Chemistry 61 (2014) 49-53.
[8] F. Urban, M. Passacantando, F. Giubileo, L. Iemmo, A. Di Bartolomeo, Transport and field emission properties of MoS2 bilayers, Nanomaterials 8(3) (2018) 151.
[9] A. Di Bartolomeo, A. Grillo, F. Urban, L. Iemmo, F. Giubileo, G. Luongo, G. Amato, L. Croin, L. Sun, S.J. Liang, Asymmetric schottky contacts in bilayer MoS2 field effect transistors, Advanced Functional Materials 28(28) (2018) 1800657.
[10] S. Bertolazzi, J. Brivio, A. Kis, Stretching and breaking of ultrathin MoS2, ACS nano 5(12) (2011) 9703-9709.
[11] L. Zhang, W. Fan, W.W. Tjiu, T. Liu, 3D porous hybrids of defect-rich MoS 2/graphene nanosheets with excellent electrochemical performance as anode materials for lithium ion batteries, RSC Advances 5(44) (2015) 34777-34787.
[12] A.B. Yousaf, M. Imran, M. Farooq, P. Kasak, Synergistic effect of Co–Ni co-bridging with MoS 2 nanosheets for enhanced electrocatalytic hydrogen evolution reactions, RSC advances 8(7) (2018) 3374-3380.
[13] M. Li, D. Wang, J. Li, Z. Pan, H. Ma, Y. Jiang, Z. Tian, Facile hydrothermal synthesis of MoS 2 nano-sheets with controllable structures and enhanced catalytic performance for anthracene hydrogenation, RSC Advances 6(75) (2016) 71534-71542.
[14] S. Vattikuti, C. Byon, Synthesis and characterization of molybdenum disulfide nanoflowers and nanosheets: nanotribology, Journal of Nanomaterials 2015 (2015) 9.
[15] D. Sandil, S. Srivastava, B. Malhotra, S. Sharma, N.K. Puri, Biofunctionalized tungsten trioxide-reduced graphene oxide nanocomposites for sensitive electrochemical immunosensing of cardiac biomarker, Journal of Alloys and Compounds 763 (2018) 102-110.
[16] P. Sun, W. Zhang, X. Hu, L. Yuan, Y. Huang, Synthesis of hierarchical MoS 2 and its electrochemical performance as an anode material for lithium-ion batteries, Journal of Materials Chemistry A 2(10) (2014) 3498-3504.
[17] A. Ramadoss, T. Kim, G.-S. Kim, S.J. Kim, Enhanced activity of a hydrothermally synthesized mesoporous MoS 2 nanostructure for high performance supercapacitor applications, New Journal of Chemistry 38(6) (2014) 2379-2385.
[18] L. Chen, H. Zhu, Molybdenum Sulfide Nanosheet-Based Hollow Porous Flat Boxes and Nanotubes for Efficient Electrochemical Hydrogen Evolution, ChemCatChem 10(2) (2018) 459-464.
[19] J.V. Kumar, R. Karthik, S.-M. Chen, K. Saravanakumar, M. Govindasamy, V. Muthuraj, Novel hydrothermal synthesis of MoS 2 nanocluster structure for sensitive electrochemical detection of human and environmental hazardous pollutant 4-aminophenol, RSC Advances 6(46) (2016) 40399-40407.
[20] M. Kukkar, A. Sharma, P. Kumar, K.-H. Kim, A. Deep, Application of MoS2 modified screen-printed electrodes for highly sensitive detection of bovine serum albumin, Analytica chimica acta 939 (2016) 101-107.
[21] X. Wang, Z. Zhang, Y. Chen, Y. Qu, Y. Lai, J. Li, Morphology-controlled synthesis of MoS2 nanostructures with different lithium storage properties, Journal of Alloys and Compounds 600 (2014) 84-90.
[22] F. Wang, M. Zheng, B. Zhang, C. Zhu, Q. Li, L. Ma, W. Shen, Ammonia intercalated flower-like MoS 2 nanosheet film as electrocatalyst for high efficient and stable hydrogen evolution, Scientific reports 6 (2016) 31092.
[23] M.A.R. Anjum, H.Y. Jeong, M.H. Lee, H.S. Shin, J.S. Lee, Efficient Hydrogen Evolution Reaction Catalysis in Alkaline Media by All-in-One MoS2 with Multifunctional Active Sites, Advanced Materials 30(20) (2018) 1707105.

[24] G. Nagaraju, C. Tharamani, G. Chandrappa, J. Livage, Hydrothermal synthesis of amorphous MoS 2 nanofiber bundles via acidification of ammonium heptamolybdate tetrahydrate, Nanoscale research letters 2(9) (2007) 461.
[25] T.N. Narayanan, C.S. Vusa, S. Alwarappan, Selective and efficient electrochemical biosensing of ultrathin molybdenum disulfide sheets, Nanotechnology 25(33) (2014) 335702.
[26] S. Su, W. Cao, W. Liu, Z. Lu, D. Zhu, J. Chao, L. Weng, L. Wang, C. Fan, L. Wang, Dual-mode electrochemical analysis of microRNA-21 using gold nanoparticle-decorated MoS2 nanosheet, Biosensors and Bioelectronics 94 (2017) 552-559.
[27] K. Arora, N.K. Puri, Electrophoretically deposited nanostructured PdO thin film for room temperature amperometric H2 sensing, Vacuum 154 (2018) 302-308.
[28] K. Zhang, H. Zhang, P. Liu, C. Zhang, W. Li, X. Chen, F. Ma, Electrophoretic deposition of graphene oxide on NiTi alloy for corrosion prevention, Vacuum 161 (2019) 276-282.
[29] K.-K. Liu, W. Zhang, Y.-H. Lee, Y.-C. Lin, M.-T. Chang, C.-Y. Su, C.-S. Chang, H. Li, Y. Shi, H. Zhang, Growth of large-area and highly crystalline MoS2 thin layers on insulating substrates, Nano letters 12(3) (2012) 1538-1544.
[30] S. Muralikrishna, K. Manjunath, D. Samrat, V. Reddy, T. Ramakrishnappa, D.H. Nagaraju, Hydrothermal synthesis of 2D MoS 2 nanosheets for electrocatalytic hydrogen evolution reaction, RSC Advances 5(109) (2015) 89389-89396.
[31] K.M. Kwok, S.W.D. Ong, L. Chen, H.C. Zeng, Constrained growth of MoS2 nanosheets within a mesoporous silica shell and its effects on defect sites and catalyst stability for H2S decomposition, ACS Catalysis 8(1) (2017) 714-724.
[32] L. Alexander, H.P. Klug, Determination of crystallite size with the X-Ray spectrometer, Journal of Applied Physics 21(2) (1950) 137-142.
[33] G. Williamson, W. Hall, X-ray line broadening from filed aluminium and wolfram, Acta metallurgica 1(1) (1953) 22-31.
[34] S. Liu, X. Zhang, H. Shao, J. Xu, F. Chen, Y. Feng, Preparation of MoS2 nanofibers by electrospinning, Materials Letters 73 (2012) 223-225.
[35] K.-J. Huang, L. Wang, Y.-J. Liu, H.-B. Wang, Y.-M. Liu, L.-L. Wang, Synthesis of polyaniline/2-dimensional graphene analog MoS2 composites for high-performance supercapacitor, Electrochimica Acta 109 (2013) 587-594.
[36] D. Swinehart, The beer-lambert law, Journal of chemical education 39(7) (1962) 333.
[37] H. Ebendorff-Heidepriem, W. Seeber, D. Ehrt, Dehydration of phosphate glasses, Journal of non-crystalline solids 163(1) (1993) 74-80.
[38] B. Sirota, N. Glavin, A.A. Voevodin, Room temperature magnetron sputtering and laser annealing of ultrathin MoS2 for flexible transistors, Vacuum 160 (2019) 133-138.
[39] M. Barzegar, A. Tiwari, On the performance of vertical MoS2 nanoflakes as a gas sensor, Vacuum 167 (2019) 90-97.
[40] H. Li, Q. Zhang, C.C.R. Yap, B.K. Tay, T.H.T. Edwin, A. Olivier, D. Baillargeat, From bulk to monolayer MoS2: evolution of Raman scattering, Advanced Functional Materials 22(7) (2012) 1385-1390.
[41] X. Li, H. Zhu, Two-dimensional MoS2: Properties, preparation, and applications, Journal of Materiomics 1(1) (2015) 33-44.
[42] Y. Wang, Y. Du, J. Deng, Z. Wang, Friction reduction of water based lubricant with highly dispersed functional MoS2 nanosheets, Colloids and Surfaces A: Physicochemical and Engineering Aspects 562 (2019) 321-328.
[43] A.P. Gaur, S. Sahoo, M. Ahmadi, S.P. Dash, M.J.-F. Guinel, R.S. Katiyar, Surface energy engineering for tunable wettability through controlled synthesis of MoS2, Nano letters 14(8) (2014) 4314-4321.
[44] V. Ramakrishnan, C. Alex, A.N. Nair, N.S. John, Designing Metallic MoO2 Nanostructures on Rigid Substrates for Electrochemical Water Activation, Chemistry–A European Journal 24(68) (2018) 18003-18011.
[45] A. Bee, R. Massart, S. Neveu, Synthesis of very fine maghemite particles, Journal of Magnetism and Magnetic Materials 149(1-2) (1995) 6-9.
[46] A. Vasudev, A. Kaushik, S. Bhansali, Electrochemical immunosensor for label free epidermal growth factor receptor (EGFR) detection, Biosensors and Bioelectronics 39(1) (2013) 300-305.
[47] B.R. Wiston, M. Ashok, Electrochemical performance of hydrothermally synthesized flower-like α-nickel hydroxide, Vacuum 160 (2019) 12-17.
[48] N. Elgrishi, K.J. Rountree, B.D. McCarthy, E.S. Rountree, T.T. Eisenhart, J.L. Dempsey, A practical beginner's guide to cyclic voltammetry, Journal of Chemical Education 95(2) (2017) 197-206.

Journal Pre-proof

[49] S. Konopka, B. McDuffie, Diffusion coefficients of ferri-and ferrocyanide ions in aqueous media, using twin-electrode thin-layer electrochemistry, Analytical Chemistry 42(14) (1970) 1741-1746.

Journal Pre-proof

Journal Pre-proof

List of Tables

Lattice Parameters	**JCPDS (37-1492)**	**MoS_2HH**	**MoS_2CA**
a	3.1612Å	3.135 Å	3.111 Å
b	3.1612 Å	3.135 Å	3.111 Å
c	12.2985 Å	12.998 Å	13.654 Å
Volume of unit cell	106.43 $Å^3$	110.63 $Å^3$	114.44 $Å^3$

Table 1: Lattice parameters of two samples calculated using X-Powder software

Sample	**Average Crystallite size from Scherrer Formula**	**Crystallite size from W-H Plots**	**Strain from W-H Plots**
MoS_2HH	2.69 nm	1.42 nm	-0.00301
MoS_2CA	2.73 nm	1.15 nm	-0.02618

Table 2 : Crystallite size calculated using Scherer formula and W-H plots and strain estimation for two samples

Elemental Percentage	Mo	S	C	H	N
MoS_2HH	64.41%	28.01%	1.35%	1.86%	4.38%
MoS_2CA	61.30%	33.64%	3.14%	0.95%	0.97%

Table 3: Elemental composition of MoS_2HH and MoS_2CA determined using EDXRF and CHNS elemental analysis

Journal Pre-proof

Journal Pre-proof

Sample	**R_{ct} (EIS)**	**i_p (CV)**	**i_p (DPV)**
MoS_2HH	150 Ω	546.17µA	72.02 µA
MoS_2CA	456Ω	504.15 µA	63.78 µA
Percentage Change	67%	8.33%	13%

Table 4: Percentage change between results of different electrochemical techniques

Sample	**Heterogenous Rate Transfer Constant (K_o)**	**Electroactive Surface Area**	**Diffusion Controlled Process**	**Electrochemical Reversibility**
MoS_2HH	5.03 X 10^{-4} cm/s	7.05 X 10^{-4} cm^{-2}	Yes	i_{pa}/i_{pc} = 1.001 ~Reversible
MoS_2CA	1.79 X 10^{-4} cm/s	6.51 X 10^{-4} cm^{-2}	Yes	i_{pa}/i_{pc} = 0.96 Semi reversible

Table 5: Comparison of parameters calculated using used electrochemical techniques

Journal Pre-proof

Fig. 1:

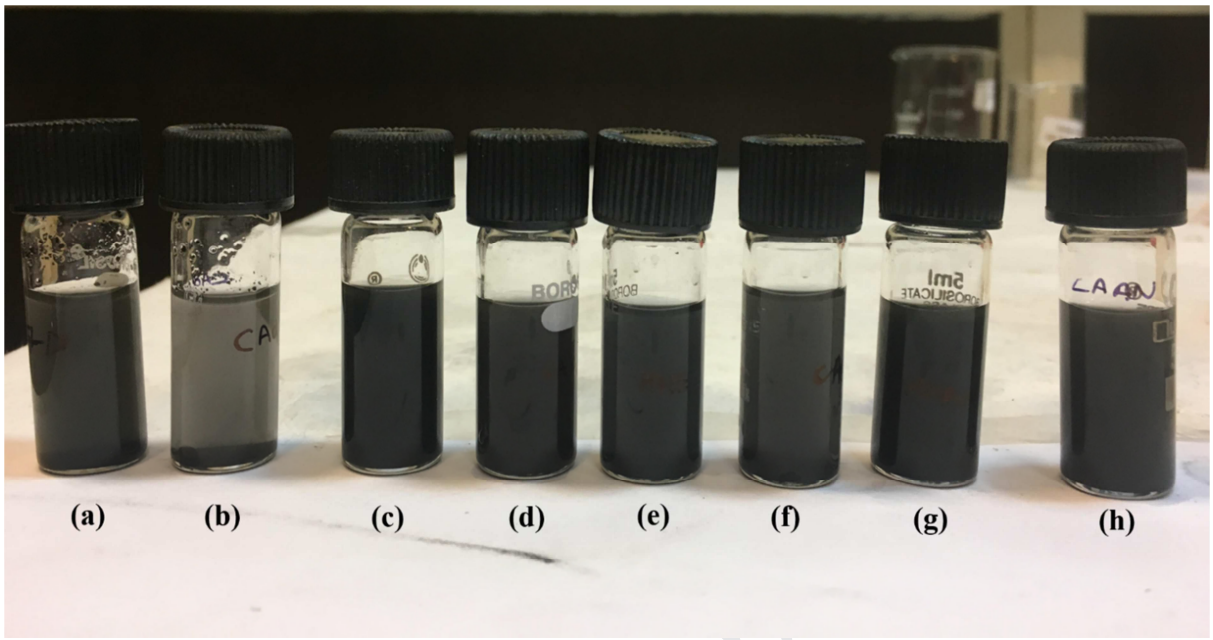


Fig. 2:

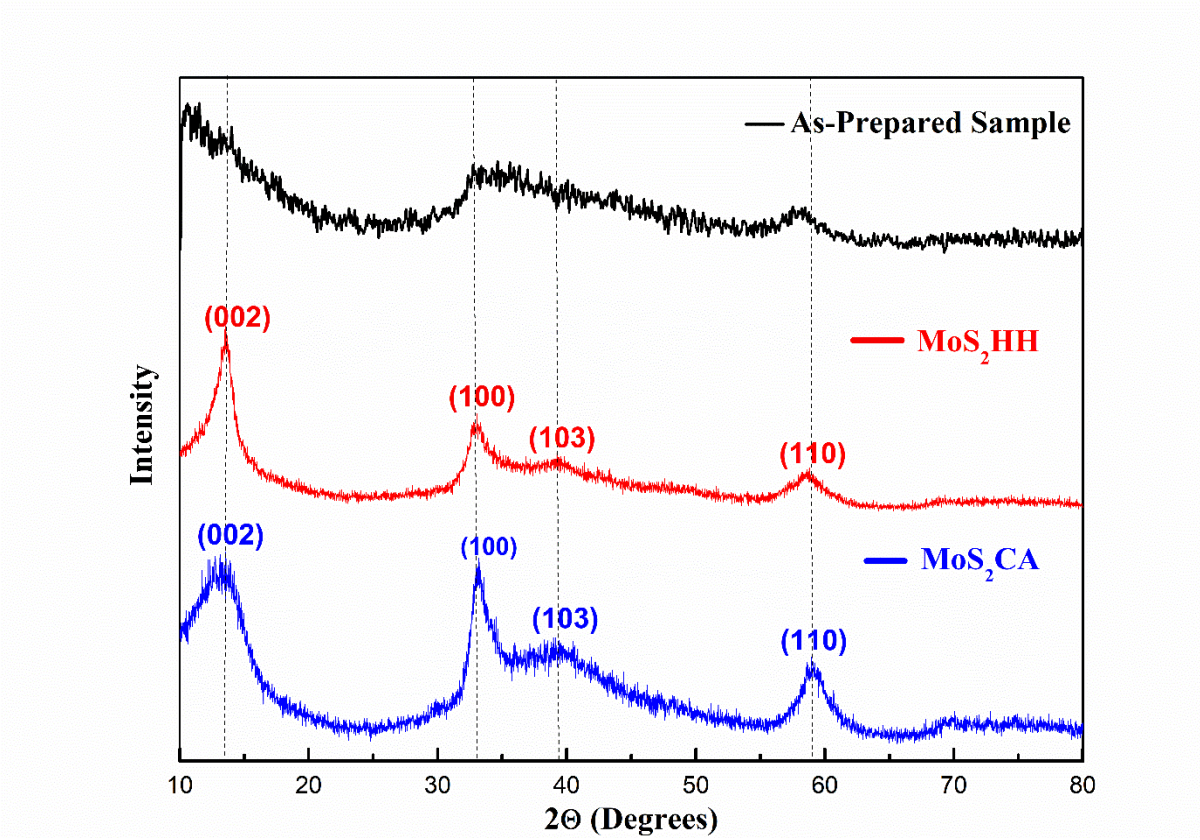


Fig. 3:

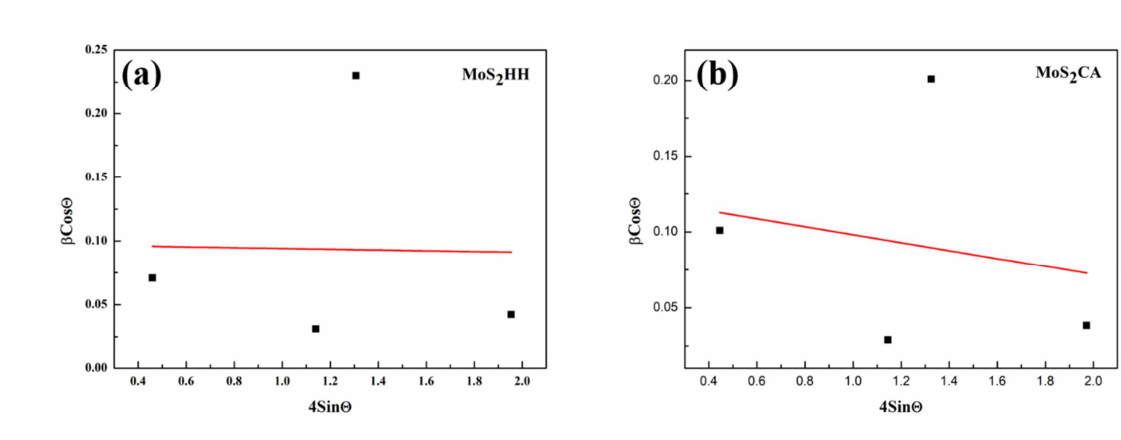

(a)
MoS2HH
βCosΘ
4SinΘ
(b)
MoS2CA
βCosΘ
4SinΘ

Fig. 4:

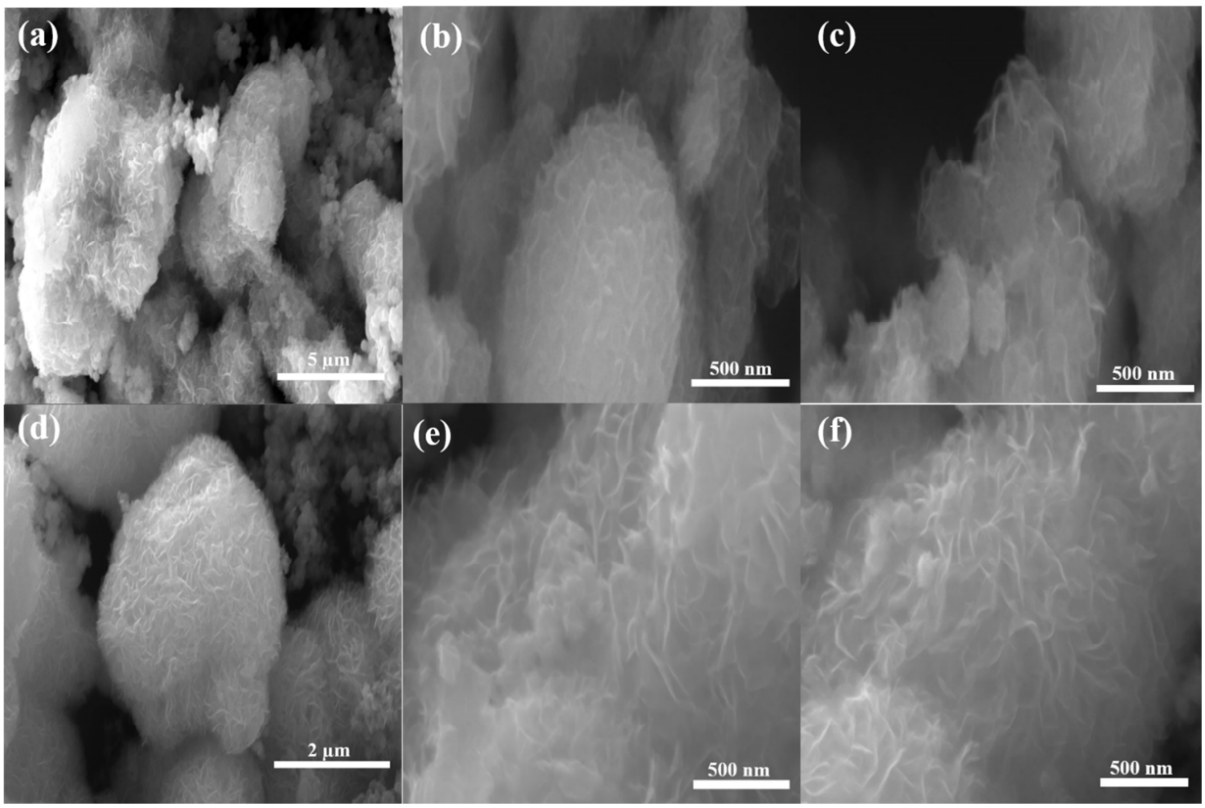

(a)
5 µm
(b)
500 nm
(c)
500 nm
(d)
2 µm
(e)
500 nm
(f)
500 nm

Fig. 5:

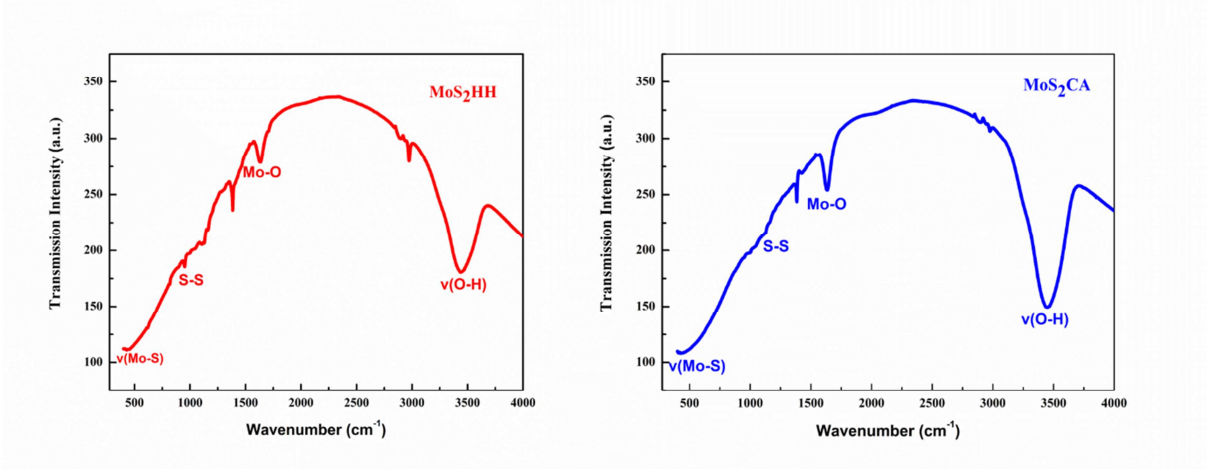


Fig. 6:

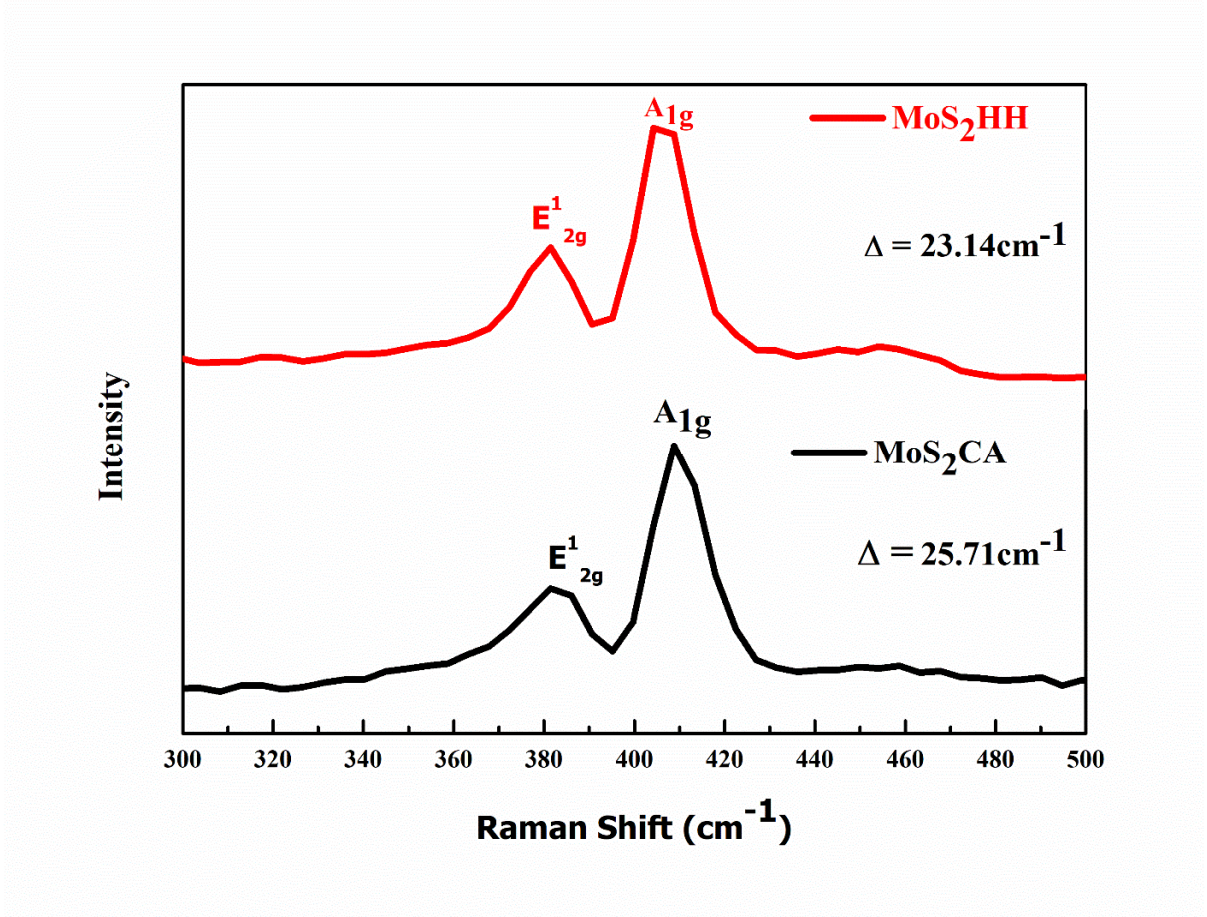


Fig. 7:

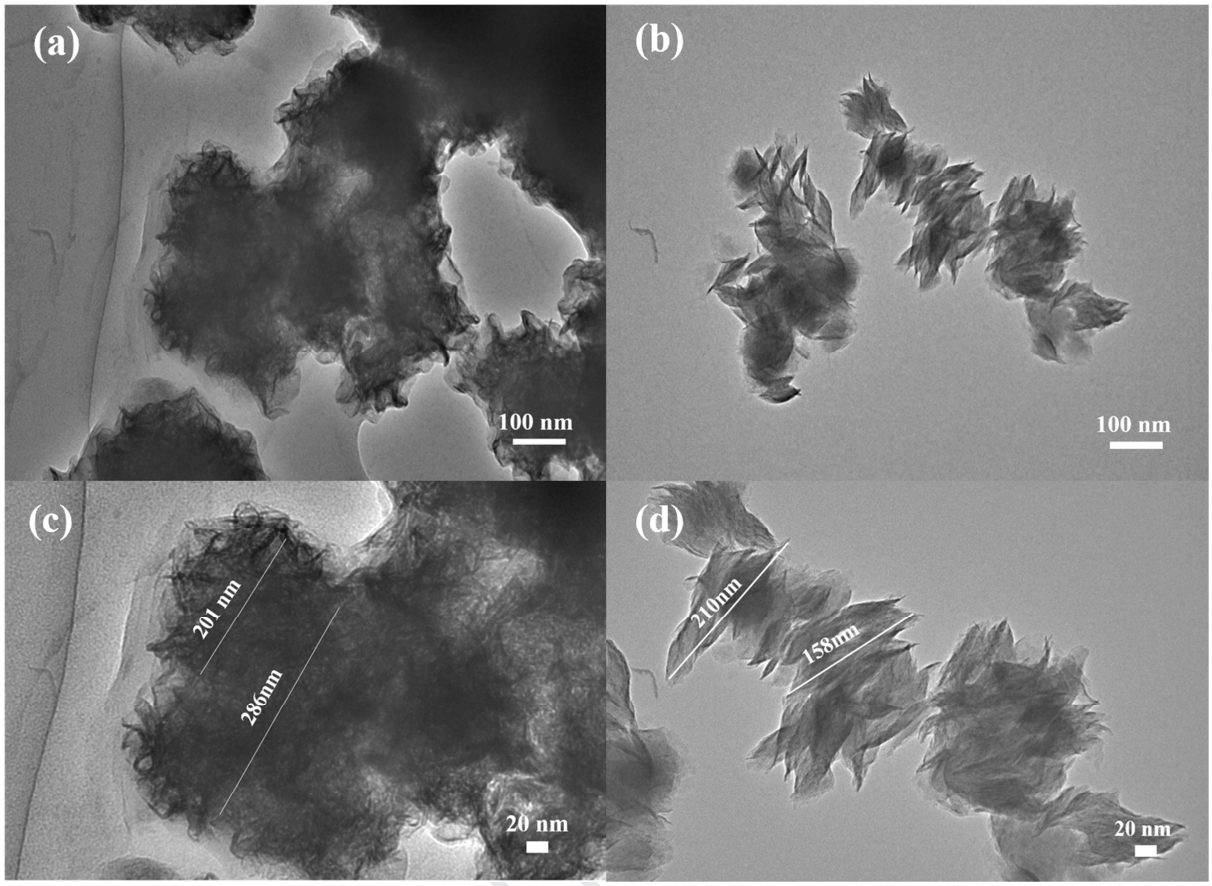


Fig. 8:

Journal Pre-proof

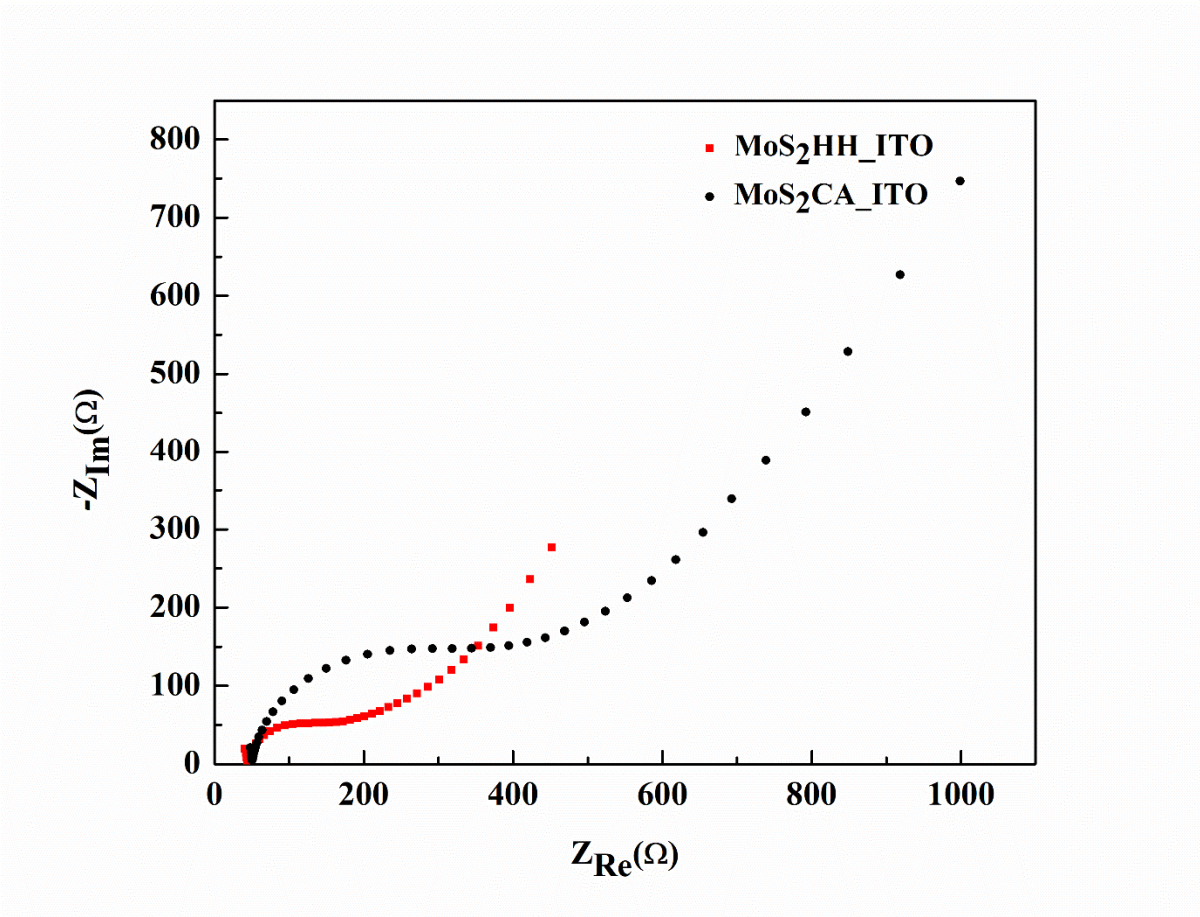

MoS2HH_ITO
MoS2CA_ITO
-ZIm(Ω)
ZRe(Ω)
0
100
200
300
400
500
600
700
800
0
200
400
600
800
1000

Fig. 9:

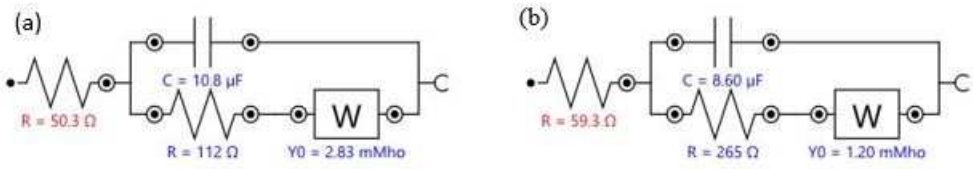

(a)
C = 10.8 µF
R = 50.3 Ω
R = 112 Ω
W
Y0 = 2.83 mMho
(b)
C = 8.60 µF
R = 59.3 Ω
R = 265 Ω
W
Y0 = 1.20 mMho

Fig. 10:

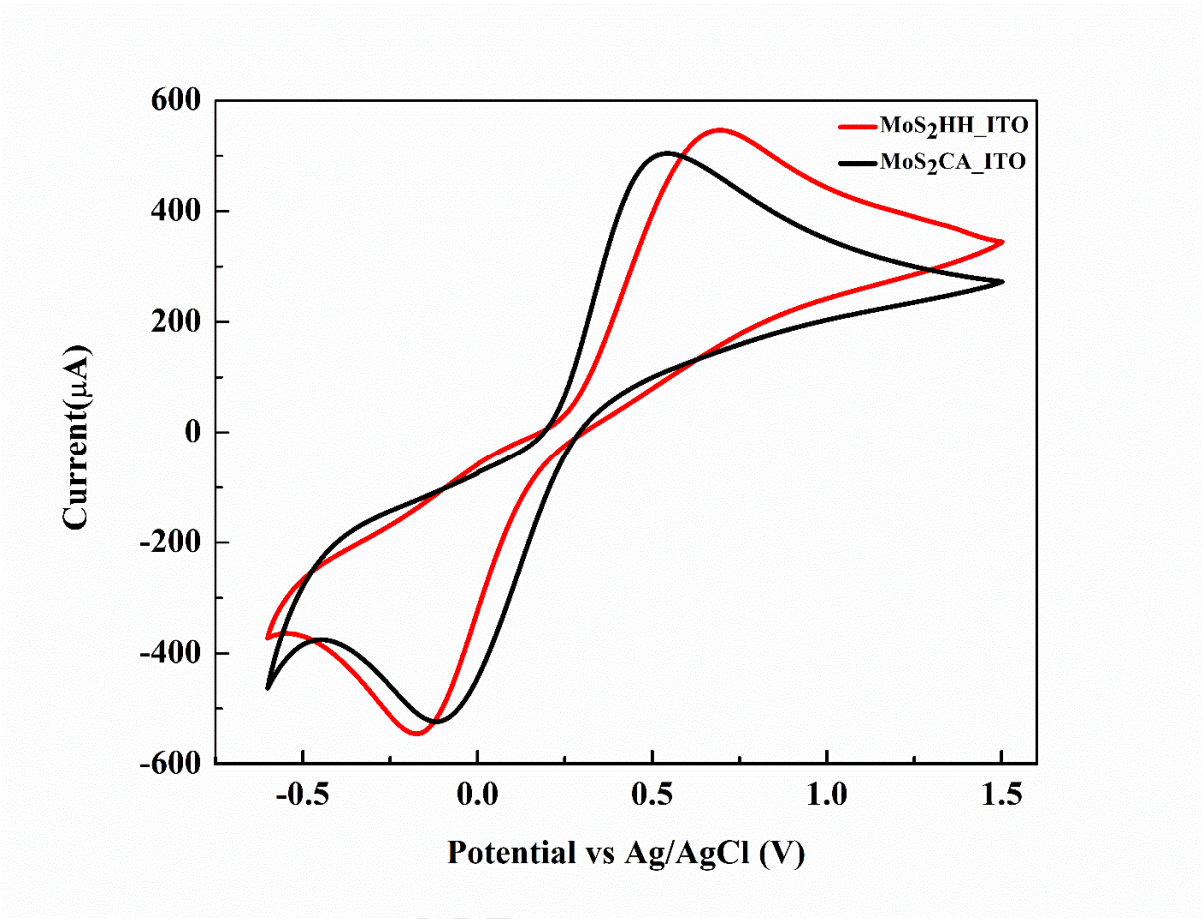


Fig. 11:

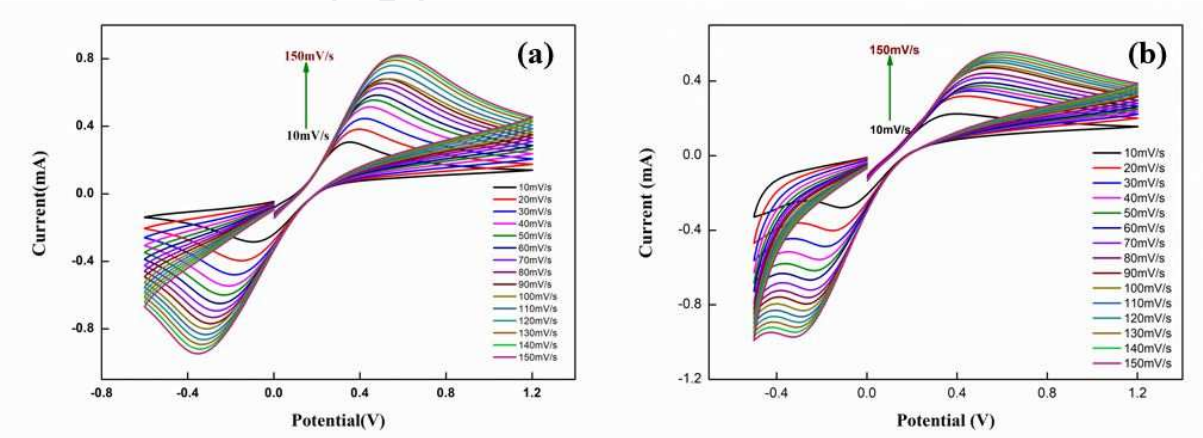


Fig. 12:

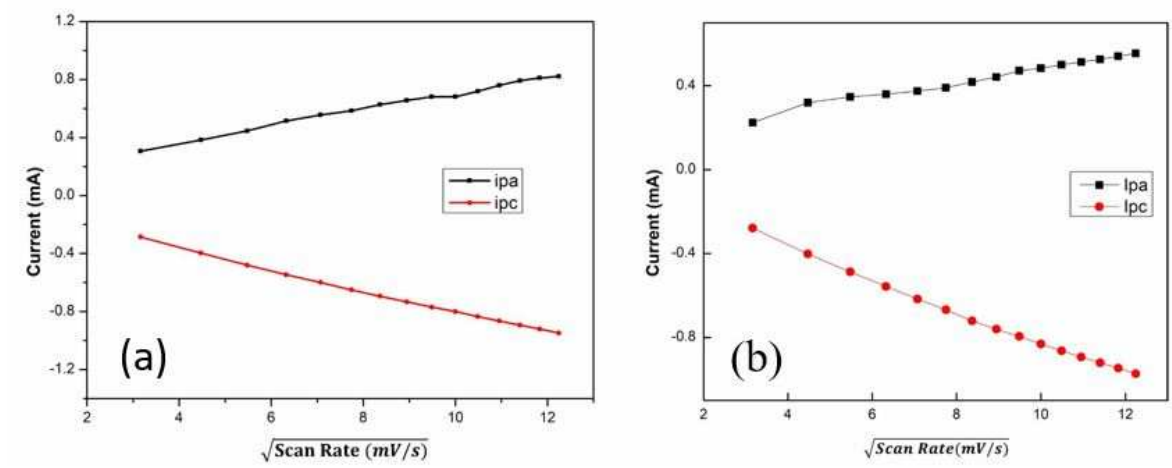


Fig. 13:

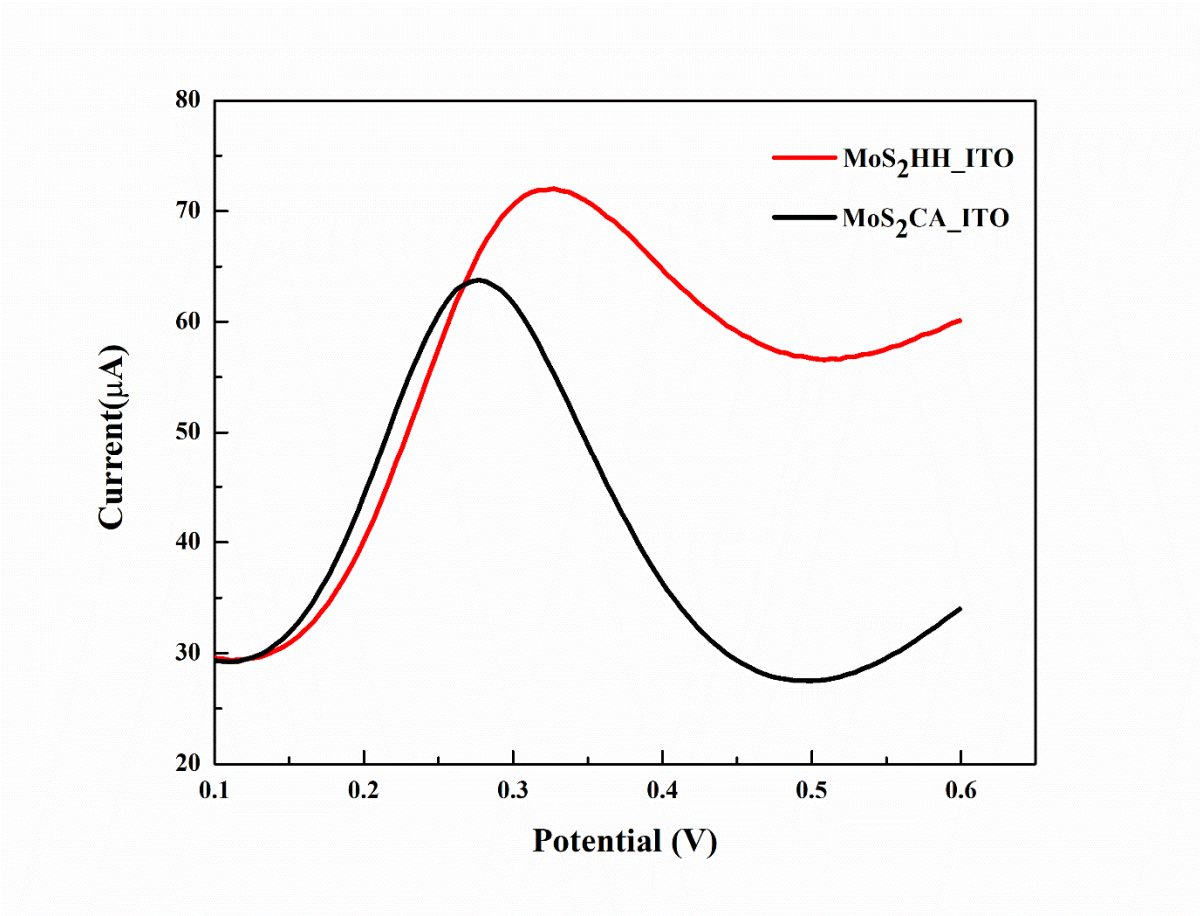


Figure Captions

1. **Fig. 1:** Dispersion solution of (a) MoS_2HH in DI water (b) MoS_2CA in DI water (c) MoS_2HH in acetone (d) MoS_2CA in acetone (e) MoS_2HH in ethanol (f) MoS_2CA in ethanol (g) MoS_2HH in Acetonitrile (h) MoS_2CA in acetonitrile.

Journal Pre-proof

2. **Fig. 2:** XRD of as-prepared MoS_2, MoS_2HH and MoS_2CA
3. **Fig. 3:** W-H plots of (a) MoS_2HH and (b) MoS_2CA
4. **Fig. 4:** FESEM Image of MoS_2 nanostructures (a, b, c) MoS_2HH (d, e, f) MoS_2CA
5. **Fig. 5:** FTIR of MoS_2HH and MoS_2CA
6. **Fig. 6:** Raman Spectra of MoS_2HH and MoS_2CA
7. **Fig. 7:** TEM image (a) MoS_2HH at 100 nm (b) MoS_2CA at 100 nm (c) MoS_2HH at 20 nm (d) MoS_2CA at 20 nm
8. **Fig. 8:** Electron Impedance Spectroscopy of MoS_2HH_ITO and MoS_2CA_ITO
9. **Fig. 9:** Randle's Circuit **(a)** MoS_2HH_ITO **(b)** MoS_2CA_ITO
10. **Fig. 10:** Cyclic Voltammetry of MoS_2HH_ITO and MoS_2CA_ITO
11. **Fig. 11:** Scan Rate study of **(a)** MoS_2HH_ITO and **(b)** MoS_2CA_ITO at scan rate varying from 10mV/s - 150mV/s
12. **Fig. 12:** Variation of i_{pa} and i_{pc} with under root of scan rate **(a)** MoS_2HH_ITO **(b)** MoS_2CA_ITO
13. **Fig. 13:** Differential Pulse Voltammetry of MoS_2HH_ITO and MoS_2CA_ITO

Journal Pre-proof

Journal Pre-proof

Highlights

- One step chemical reduction of MoS_2 nanostructures is achieved using hydrothermal method.
- Lattice parameters, Crystallite size and strain is determined for $rMoS_2$.
- Films of $rMoS_2$ are deposited using electrophoretic deposition.
- Electrochemical Studies are performed for $rMoS_2$.
- $rMoS_2$ synthesised using Hydrazine Hydrate has more electroactive surface area and heterogenous rate transfer constant (K_o).
- Correlation between TEM, Raman and XRD explains better performance of sample reduced using hydrazine hydrate.

Journal Pre-proof

Journal Pre-proof

Conflict of Interest and Authorship Conformation Form

Please check the following as appropriate:

✓ All authors have participated in (a) conception and design, or analysis and interpretation of the data; (b) drafting the article or revising it critically for important intellectual content; and (c) approval of the final version.

✓ This manuscript has not been submitted to, nor is under review at, another journal or other publishing venue.

✓ The authors have no affiliation with any organization with a direct or indirect financial interest in the subject matter discussed in the manuscript

✓ The following authors have affiliations with organizations with direct or indirect financial interest in the subject matter discussed in the manuscript:

Author's name	Affiliation
Ritika Khatri	**Delhi Technological University**
Nitin K. Puri	**Delhi Technological University**

Journal Pre-proof

Analog Integrated Circuits and Signal Processing
https://doi.org/10.1007/s10470-020-01593-1

MIXED SIGNAL LETTER

Electronically controllable third-order quadrature sinusoidal oscillator employing CMOS-OTAs

Komal[1] · K. L. Pushkar[2] · Ramnish Kumar[1]

Received: 5 June 2019 / Revised: 11 October 2019 / Accepted: 28 January 2020
© Springer Science+Business Media, LLC, part of Springer Nature 2020

Abstract
This paper describes a voltage mode third-order quadrature sinusoidal oscillator (TOQSO) based on operational transconductance amplifiers (OTAs). The proposed configuration uses three OTAs and three grounded capacitors. Outputs of two voltage mode sinusoids with 90° phase difference are found in the proposed oscillator circuit. The condition of oscillation and frequency of oscillation are independently electronically controllable by separate transconductances of the OTAs. The performance of TOQSO is tested by SPICE (version 16.5) simulation using TSMC 0.18 μm technology parameters and experimental results employing CA3080 type IC OTAs have been presented to confirm the workability of the proposed new configuration.

Keywords Operational transconductance amplifier · Third-order quadrature sinusoidal oscillator · Voltage-mode

1 Introduction

Oscillator is a very important research area in electronics engineering. Sinusoidal oscillators play a crucial role in different control systems, communication, signal processing and instrumentation and measurement systems [1–3]. Along with different kinds of sinusoidal oscillators, the quadrature sinusoidal oscillators (QSOs) are broadly employed because they provide quadrature outputs with 90° phase difference. These QSOs can be utilized in (1) telecommunications for quadrature mixers and single side band generators and (2) for the measurement purposes in vector generators and selective voltmeters [1]. Because of these applications various third-order QSOs have been realized with different active building blocks (ABBs) in the open literature [4–23]. As compared to second-order QSOs, the third-order QSOs provide (1) higher quality factor (2) higher accuracy and (3) lower harmonic distortion [9, 20, 23]. A brief account of the earlier work done on TOQSOs is as follows:

Horng et al. [1], presented three TOQSOs employing three second generation current conveyors (CCII±), 3/5 capacitors and 5/3 resistors [1]. Chen et al. [4], presented a TOQSO with controllable amplitude using two multi-output differential voltage current conveyor transcoductance amplifiers (MO-DVCCTAs), three GCs and two grounded resistors. This design provides independent control of CO and FO through grounded resistors [4]. Lawanwisuit and Sirripruchyanun [5], presented a high output-impedance current-mode TOQSO using two current controlled current conveyor transcoductance amplifiers (CCCCTAs) and three GCs. Pushkar, presented TOQSO using two voltage differencing buffered amplifiers (VDBAs) with independent electronic control of CO and FO [6]. Maheshwari presented a TOQSO using differential voltage current conveyors (DVCCs). Non-ideal aspect and parasitic effect are also studied [7]. Horng proposed a current-mode TOQSO using three current differencing transconductance amplifiers (CDTAs) and three GCs which give orthogonal

✉ K. L. Pushkar
klpushkar17@gmail.com

Komal
komalrohilla243@gmail.com

Ramnish Kumar
mail2ramnish@gmail.com

[1] Department of Electronics and Communication Engineering, Guru Jhambheshwar University of Science and Technology, Hisar, Haryana, India

[2] Department of Electronics and Communication Engineering, Greater Noida Institute of Technology, Greater Noida, U. P., India

Published online: 04 February 2020

control of CO and FO [8]. Horng et al. presented an electronically tunable TOQSO using three CDTAs and three GCs with independent electronic control of CO and FO [9]. A current-mode TOQSO was presented by Maheswari using three CCCIIs and three GCs, providing non-interactive control of CO and FO [10]. Horng presented another TOQSO employing two CCIIs, three resistors and three GCs. This circuit provides independent control of CO and FO through separate grounded resistors [11]. Maheshwari and Verma presented an electronically tunable TOQSO employing four CCCIIs, three GCs and a grounded resistor with independent control of CO and FO [12]. Chaturvedi and Maheshwari presented another TOQSO with current and voltage outputs using three DVCCs, three GCs and three grounded resistors. This circuit provides four quadrature current outputs at high impedance nodes and two quadrature voltage outputs [13]. Pandey et al. presented two TOQSOs based upon three operational transresistance amplifiers (OTRAs), five resistors and three capacitors with independent control of CO and FO [14]. Rai and Gupta, presented a capacitor controlled TOQSO based on three CMOS/FGCMOS inverters, three GCs and two resistors [15]. Pandey and Pandey presented two topologies of TOQSO employing two differential voltage current conveyor transconductance amplifiers (DVCCTAs) and three GCs and one resistor with independent control of CO and FO [16]. Malhotra et al. presented another TOQSO using three VDBAs and five grounded passive elements, the CO and FO can independently be adjusted [17]. Khaw-Ngam et al. presented mixed-mode TOQSO based on single modified current-controlled current follower transconductance amplifier (MCCFTA) employing three GCs with orthogonal control of CO and FO [18]. Another resistorless and electronically tunable TOQSO with current and voltage outputs was presented by Chen, Hwang and Ku using two VDTAs and three GCs, the circuit provides independent control of CO and FO [19]. Promee and Dejhan proposed two configurations of TOQSOs. The first structure employs three operational transconductance amplifiers (OTAs) and three GCs while second configuration uses four OTAs, three GCs and an electronic resistor [20]. Pushkar and Bhaskar presented a voltage-mode TOQSO based on two voltage differencing inverting buffered amplifiers (VDIBAs), three GCs and a resistor [21]. Bhaskar et al. presented TOQSO using three OTAs and three capacitors. In this paper one capacitor is floating. So this circuit is not compatible for IC fabrication due to this floating capacitor [22]. Maheshwari and Khan proposed a current controlled TOQSO using four CCCIIs. The circuit with GCs enjoys electronically tunable, non-interactive FO and CO, generates four quadrature current outputs at high impedance nodes and two quadrature voltage outputs [23].

Recently, OTA has been used in many signal processing and signal generation applications, for instance, see [24–29] and the references cited therein. OTA having several features such as (1) wide electronic tunability of parameter through an external current or voltage (2) high frequency application and suitable for IC implementation in bipolar and CMOS technology (3) less component count. Therefore, the purpose of this communication is to present a new TOQSO employing three OTAs and three GCs. The higher order oscillator circuits have high accuracy and good frequency response with low distortion. The proposed configuration is capable of providing independent electronic control of CO and FO. The SPICE simulation and experimental results are given to confirm the theoretical analysis of proposed configuration using 0.18 μm TSMC technology.

2 The proposed third-order quadrature oscillator configuration

The OTA is a voltage controlled current source device and having three terminals with electronic tuning, is characterized by the following equation.

$$I_o = g_m(V_+ - V_-) \tag{1}$$

The symbolic notation and equivalent model of OTA are shown in Fig. 1.

Figure 2 shows a new configuration of third-order quadrature sinusoidal oscillator with independent electronic control of FO and CO.

A straight forward analysis using ideal OTAs yields the expression for characteristic equation (CE) of Fig. 2 is given by Eq. (2).

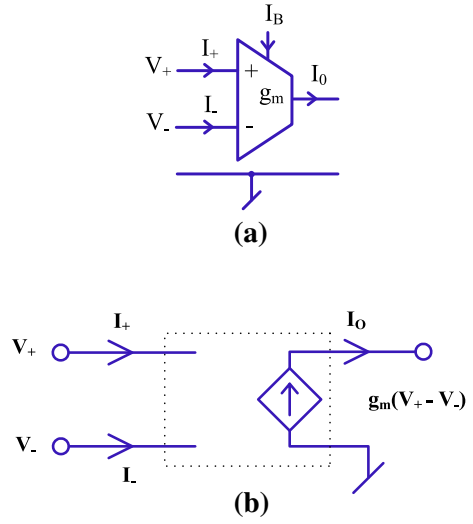


Fig. 1 **a** Symbolic notation **b** equivalent model of OTA

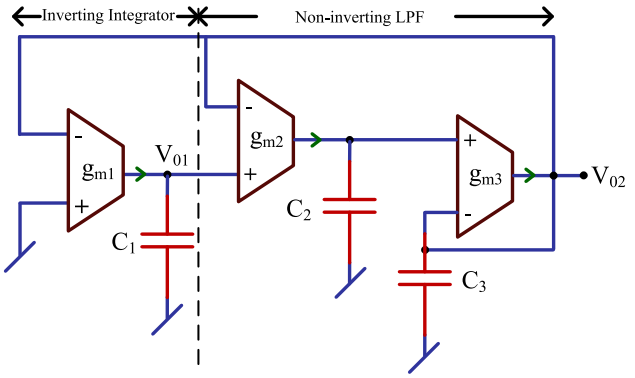


Fig. 2 New proposed TOQSO

$$s^3C_1C_2C_3 + s^2C_1C_2g_{m_3} + sC_1g_{m_2}g_{m_3} + g_{m_1}g_{m_2}g_{m_3} = 0 \tag{2}$$

The factorization of Eq. (2) can be found [given in Eq. (3)] by Routh's Hurwitz rule, array of this equation will have a pair of imaginary conjugate roots, if $C_3g_{m_1} = C_1g_{m_3}$.

$$\left(s+\frac{g_{m_3}}{C_3}\right)\left(s+j\sqrt{\frac{g_{m_1}g_{m_2}}{C_1C_2}}\right)\left(s-j\sqrt{\frac{g_{m_1}g_{m_2}}{C_1C_2}}\right) = 0 \tag{3}$$

$$CO: \quad C_3g_{m_1} = C_1g_{m_3} \tag{4}$$

$$FO: \quad \omega_0 = \sqrt{\frac{g_{m_1}g_{m_2}}{C_1C_2}} \tag{5}$$

Routine analysis yields relationship between V_{01} and V_{02} as:

$$\frac{V_{01}(s)}{V_{02}(s)} = -\frac{g_{m1}}{sC_1} \tag{6}$$

Under sinusoidal steady state, Eq. (6) becomes

$$\frac{V_{01}(j\omega)}{V_{02}(j\omega)} = -\frac{g_{m1}}{j\omega C_1}e^{-90^0} \tag{7}$$

From Eq. (7), it is clear that V_{01} and V_{02} are in quadrature.

3 Effects of non-idealities

The effect of OTA non-idealities includes finite input resistance (R_{zi}), finite output resistance (R_{z0}) and finite capacitance (C_z). The non-ideal expressions for CE and FO are given below.

$$\begin{aligned}
&s^3\left[\begin{array}{l} C_1C_2C_3 + C_{z_0}C_3\left(\begin{array}{l} C_1 + C_2 + \\ C_{z_0} + 2C_{z_+}\end{array}\right) + C_{z_0}C_2\left(\begin{array}{l} C_1 + C_{z_0} + \\ C_{z_+} + 3C_{z_-}\end{array}\right) \\ \quad + C_{z_0}C_1\left(3C_{z_-} + C_{z_0} + C_{z_+}\right) + C_{z_+}C_{z_-}\left(\begin{array}{l} 6C_{z_0} + 3C_1 + \\ 3C_{z_+} + 3C_2\end{array}\right) \\ \quad + C_{z_0}\left(\begin{array}{l} 3C_{z_0}C_{z_-} + C_{z_0}^2 + \\ 2C_{z_0}C_{z_+} + C_{z_+}^2\end{array}\right) + \left(\begin{array}{l} C_1C_3C_{z_+} + C_3C_{z_+}^2 + \\ 3C_1C_2C_{z_-} + C_2C_3C_{z_+}\end{array}\right)\end{array}\right] \\
&+ s^2\left[\begin{array}{l} \left(C_{z_0}C_1 + C_{z_0}C_2 + 2C_{z_+}C_{z_0}\right)\left(g_{m_3} + \frac{1}{R_{z_+}} + \frac{2}{R_{z_0}} + \frac{3}{R_{z_-}}\right) \\ \quad + C_{z_0}C_3\left(\frac{2}{R_{z_0}} + \frac{2}{R_{z_+}}\right) + C_{z_0}^2\left(g_{m_3} + \frac{2}{R_{z_+}} + \frac{3}{R_{z_0}} + \frac{3}{R_{z_-}}\right) \\ \quad + C_1C_2\left(g_{m_3} + \frac{1}{R_{z_0}} + \frac{3}{R_{z_-}}\right) + \left(C_1C_3 + C_3C_2\right)\left(\frac{1}{R_{z_+}} + \frac{1}{R_{z_0}}\right) \\ \quad + C_{z_-}\left(\begin{array}{l} \frac{3C_1}{R_{z_0}} + \frac{3C_1}{R_{z_+}} + \frac{3C_2}{R_{z_0}} + \frac{3C_2}{R_{z_+}} + \\ \frac{6C_{z_+}}{R_{z_+}} + \frac{6C_{z_0}}{R_{z_+}} + \frac{6C_{z_+}}{R_{z_0}} + \frac{6C_{z_0}}{R_{z_0}}\end{array}\right) \\ \quad + C_{z_+}\left(\begin{array}{l} \frac{3C_1}{R_{z_-}} + C_1g_{m_3} + C_{z_+}g_{m_3} + \frac{C_{z_+}}{R_{z_0}} + \frac{C_1}{R_{z_0}} + \frac{C_3}{R_{z_0}} + \\ \frac{3C_{z_+}}{R_{z_-}} + \frac{3C_2}{R_{z_-}} + \frac{C_2}{R_{z_0}} + \frac{2C_3}{R_{z_+}} + \frac{C_3}{R_{z_0}} + C_2g_{m_3}\end{array}\right)\end{array}\right] \\
&+ s\left[\begin{array}{l} C_1g_{m_2}g_{m_3} + C_{z_0}\left(\begin{array}{l} g_{m_2}g_{m_3} + \frac{6}{R_{z_-}R_{z_0}} + \frac{2}{R_{z_0}^2} + \frac{6}{R_{z_-}R_{z_+}} + \\ \frac{4}{R_{z_+}R_{z_0}} + \frac{1}{R_{z_+}^2} + \frac{3g_{m_3}}{R_{z_0}} + \frac{2g_{m_3}}{R_{z+}}\end{array}\right) \\ \quad + C_{z_+}\left(\begin{array}{l} \frac{2}{R_{z_0}^2} + \frac{3}{R_{z_-}R_{z_0}} + \frac{2}{R_{z_+}R_{z_0}} + \\ \frac{2g_{m_3}}{R_{z_+}} + \frac{2g_{m_3}}{R_{z_0}} + g_{m_2}g_{m_3} + \frac{3}{R_{z_-}R_{z_+}} + \frac{3}{R_{z_+}} + \frac{3}{R_{z_0}}\end{array}\right) \\ \quad + C_2\left(\frac{g_{m_3}}{R_{z_0}} + \frac{3}{R_{z_-}R_{z_0}} + \frac{1}{R_{z_0}^2} + \frac{3}{R_{z_-}R_{z_+}} + \frac{1}{R_{z_+}R_{z_0}} + \frac{g_{m_3}}{R_{z_+}}\right) \\ \quad + C_1\left(\frac{3}{R_{z_-}R_{z_+}} + \frac{3}{R_{z_-}R_{z_0}} + \frac{1}{R_{z_0}^2} + \frac{1}{R_{z_+}} + \frac{g_{m_3}}{R_{z_+}} + \frac{g_{m_3}}{R_{z_0}}\right) \\ \quad + C_{z_-}\left(\frac{3}{R_{z_0}^2} + \frac{6}{R_{z_+}R_{z_0}} + \frac{3}{R_{z_+}^2}\right) + C_3\left(\frac{1}{R_{z_0}^2} + \frac{2}{R_{z_+}R_{z_0}} + \frac{1}{R_{z_+}^2}\right)\end{array}\right] \\
&+ \left[\begin{array}{l} g_{m_1}g_{m_2}g_{m_3} + g_{m_2}g_{m_3}\left(\frac{1}{R_{z_+}} + \frac{1}{R_{z_0}}\right) + g_{m_3}\left(\frac{1}{R_{z_+}^2} + \frac{1}{R_{z_0}^2} + \frac{2}{R_{z_+}R_{z_0}}\right) \\ \quad + \frac{3}{R_{z_+}^2R_{z_-}} + \frac{3}{R_{z_0}^2R_{z_-}} + \frac{6}{R_{z_-}R_{z_0}R_{z_+}} + \frac{1}{R_{z_0}^3} + \frac{2}{R_{z_0}^2R_{z_+}} + \frac{1}{R_{z_+}^2R_{z_0}}\end{array}\right] = 0
\end{aligned} \tag{8}$$

By putting parasitic capacitance zero and parasitic resistance infinite in Eq. (8), we will get ideal CE Eq. (2).

$$\omega_0 = \sqrt{\frac{\begin{pmatrix} g_{m_1}g_{m_2}g_{m_3}R_{Z_0}^3R_{Z_+}^2R_{Z_-} \\ +\ g_{m_2}g_{m_3}\begin{pmatrix} R_{Z_0}^3R_{Z_+}R_{Z_-} \\ +R_{Z_0}^2R_{Z_+}^2R_{Z_-} \end{pmatrix} \\ +\ g_{m_3}\begin{pmatrix} R_{Z_0}^3R_{Z_=} + R_{Z_+}^2R_{Z_0}R_{Z_-} \\ +2R_{Z_0}^2R_{Z_+}R_{Z_-} \end{pmatrix} + 3R_{Z_0}^3 \\ +\ 3R_{Z_0}R_{Z_+}^2 + 6R_{Z_0}^2R_{Z_+} + R_{Z_+}^2R_{Z_-} \\ +\ 2R_{Z_0}R_{Z_+}R_{Z_-} + R_{Z_0}^2R_{Z_-} \end{pmatrix}}{\begin{pmatrix} (C_1C_{Z_0} + C_2C_{Z_0} + 2C_{Z_0}C_{Z_+}) \\ \begin{pmatrix} g_{m_3}R_{Z_0}^3R_{Z_+}^2R_{Z_-} + R_{Z_0}^3R_{Z_+}R_{Z_-} \\ +2R_{Z_0}^2R_{Z_+}^2R_{Z_-} + 3R_{Z_0}^3R_{Z_+}^2 \end{pmatrix} \\ +\ C_3C_{Z_0}\left(2R_{Z_0}^2R_{Z_+}^2R_{Z_-} + 2R_{Z_0}^3R_{Z_+}R_{Z_-}\right) \\ +\ C_{Z_0}^2\begin{pmatrix} g_{m_3}R_{Z_0}^3R_{Z_+}^2R_{Z_-} + \\ 2R_{Z_0}^3R_{Z_+}R_- + 3R_{Z_0}^2R_{Z_+}^2R_{Z_-} + 3R_{Z_0}^3R_{Z_+}^2 \end{pmatrix} \\ +\ C_3(C_1+C_2)\left(R_{Z_0}^3R_{Z_+}R_{Z_-} + R_{Z_0}^2R_{Z_+}^2R_{Z_-}\right) \\ +\ \left(R_{Z_0}^3R_{Z_+}R_{Z_-} + R_{Z_0}^2R_{Z_-}R_{Z_+}^2\right) \\ \begin{pmatrix} 3C_{Z_-}C_1 + 3C_{Z_-}C_2 + 6C_{Z_-}C_{Z_+} + \\ 6C_{Z_-}C_{Z_0} + 2C_3C_{Z_+} \end{pmatrix} \\ +\ \left(g_{m_3}R_{Z_0}^3R_{Z_+}^2R_{Z_-} + R_{Z_0}^2R_{Z_+}^2R_{Z_-} + 3R_{Z_0}^3R_{Z_+}^2\right) \\ \left(C_1C_2 + C_{Z_+}C_2 + C_{Z_-}C_1 + C_{Z_+}^2\right) \end{pmatrix}}}$$

4 Sensitivity analysis

The active and passive sensitivities of the proposed TOQSO are calculated but not mentioned due to very large expressions.

Since the parasitic capacitances are very small and parasitic resistances are very high [30].

It may be easily calculated from sensitivity expressions that all the active and passive sensitivities are less than unity in magnitude obtained as

$$S_{C_1}^{\omega_0} = S_{C_2}^{\omega_0} = -\frac{1}{2}$$

$$S_{g_{m_1}}^{\omega_0} = \frac{1}{2} = S_{g_{m_2}}^{\omega_0},$$

$$S_{C_3}^{\omega_0} = 0 = S_{g_{m_3}}^{\omega_0}$$

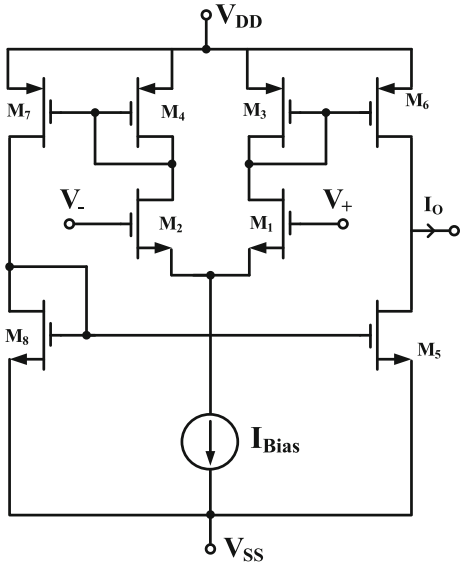


Fig. 3 An exemplary CMOS implementation of OTA [29] $V_{DD} = -V_{SS} = 0.9$ V

Table 1 The aspect ratios of MOSFETs

MOS transistor	Aspect ratio (W/L)
M1, M2	3.6/.36
M3, M4, M5, M8	1.44/.36
M6, M7,	2.88/.36

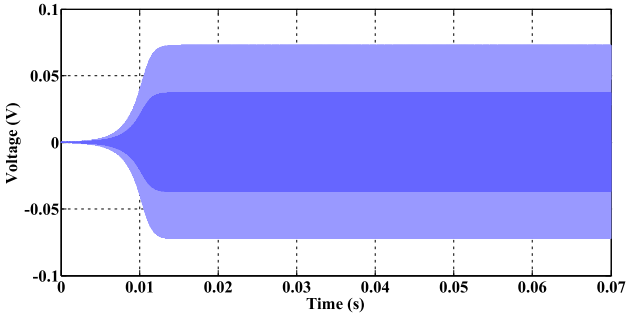


Fig. 4 Transient response of proposed TOQSO

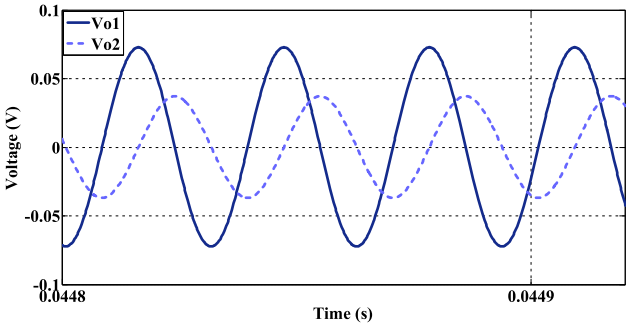


Fig. 5 Steady state response of proposed TOQSO

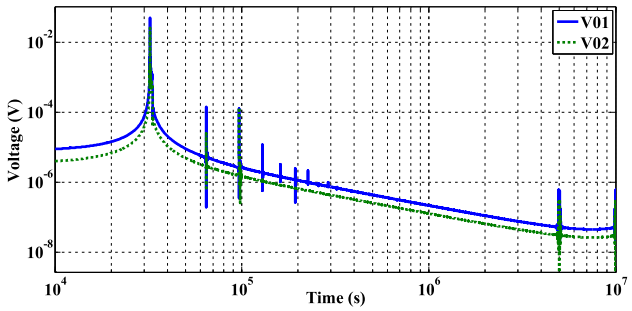


Fig. 6 Frequency spectrum of proposed TOQSO

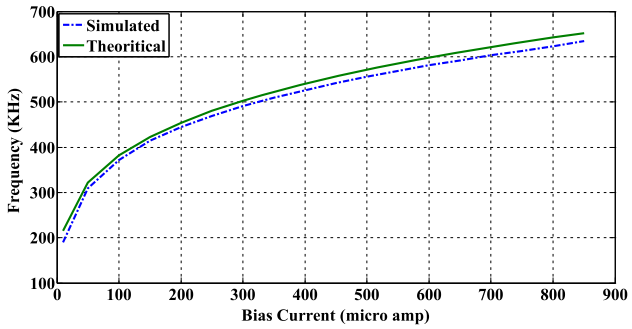


Fig. 7 Variation in frequency of proposed TOQSO with respect to biasing current of OTA

5 Results

5.1 Simulation results

The new proposed voltage-mode quadrature sinusoidal oscillator was tested through PSPICE simulations using the CMOS implementation of OTA as shown in Fig. 3. The CMOS OTA is implemented using 0.18 μm TSMC real transistor models. The aspect ratios of transistors used in Fig. 3 are given in Table 1. The passive elements for the simulation of proposed TOQSO were selected as $C_1 = C_2 = C_3 = 10$ nF. The transconductances of OTAs were controlled by the bias currents $I_{b1} = 774$ μA, $I_{b2} = 57.6$ μA, and $I_{b3} = 755$ μA. PSPICE generated output waveforms indicating transient and steady state responses of the proposed configuration of Fig. 2 are shown in Figs. 4 and 5 respectively. These results, thus, confirm the validity of the proposed TOQSO configuration. Figure 6 describes the frequency spectrum of the proposed TOQSO which yield THD of 0.37% and 0.49% for output waveforms V_{o1} and V_{o2} respectively. Figure 7 shows the variation in frequency of TOQSO with respect to biasing current of OTA (g_{m2}). Table 2 compares the main features of proposed TOQSO with other reported TOQSOs.

Table 2 Comprehensive Comparison of previously reported TOQSOs

References	No. of active devices used	No. of passive elements used			Output signals		Independent electronic control of CO and FO	
		R	GC	FC	CM	VM	CO	FO
[1]	3CCII	5	3	0	0	2	No	No
[4]	2MO-DVCCTA	2	3	0	2	3	No	No
[5]	2CCCCTA	0	3	0	0	2	Yes	Yes
[6]	2VDBA	1	2	1	0	2	Yes	Yes
[7]	3DVCC	3	3	0	5	2	Yes	Yes
[8]	3CDTA	0	3	0	2	0	Yes	No
[9]	3CDTA	0	3	0	0	2	Yes	Yes
[10]	3CCCII	0	3	0	4	2	Yes	Yes
[11]	2CCII	3	3	0	2	2	No	No
[12]	4CCCII	1	3	0	0	3	Yes	Yes
[13]	3DVCC	3	3	0	4	2	No	No
[14]	3OTRA	5	0	3	0	2/2	No	No
[15]	3CMOS/FGMOS INVERTER	2	3	0	0	2/2	Yes	No
[16]	2DVCCTA	1	3	0	3	3	No	Yes
[17]	3VDBA	2	3	0	0	2	Yes	No
[20]	3OTA	0	3	0	0	2	Yes	No
[21]	2VDIBA	1	3	0	0	2	Yes	Yes
[22]	3OTA	0	2	1		2	Yes	Yes
[23]	4CCCII	0	3	0	4	0	Yes	Yes
Proposed	3OTA	0	3	0	0	2	Yes	Yes

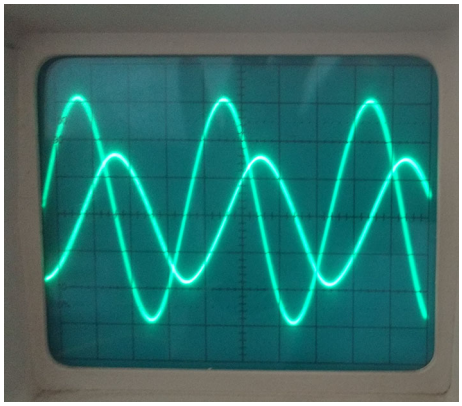


Fig. 8 Experimental results for steady state response of proposed TOQSO

5.2 Experimental results

The workability of the proposed TOQSO circuit has been checked experimentally using CA3080A type IC OTAs. Figure 8 represents the experimental results of proposed TOQSO (Fig. 2) with $C_1 = C_2 = C_3 = 10$ nF and DC power supply of 6 V for the frequency of 33.231 kHz. The experimentally measured frequency of the proposed oscillator was found 32.98 kHz that concurs with designed value. These experimental results, thus, confirm the validity of the proposed TOQSO.

6 Conclusion

A new voltage-mode third-order quadrature sinusoidal oscillator with independent electronic control of both FO and CO employing three OTAs and three GCs (suitable for IC implementation) is proposed. The proposed configuration provides non-interactive electronic control of FO and CO. The comparison of recently proposed TOQSO with other TOQSOs employing different active building blocks is also included. The active and passive sensitivities of the proposed TOQSO are less than unity. The proposed TOQSO generates accurate and low THD sine waves. Simulation results using TSMC 0.18 μm CMOS technology and experimental results employing CA3080 IC OTAs have been presented to confirm the workability of the proposed new configuration.

Acknowledgements The authors would like to acknowledge Professor D. R. Bhaskar, Delhi Technological University, Delhi for his help in the preparation of this manuscript. The authors also wish to thank the anonymous reviewers for their comments and suggestions which have been very useful in improving the presentation of the manuscript.

References

1. Horng, J. W., Hou, C. L., Chang, C. M., Chung, W. Y., Tang, H. W., & Wen, Y. H. (2005). Quadrature oscillators using CCIIs. *International Journal of Electronics, 92*(1), 21–31.
2. Gibson, J. D. (1997). *The communication handbook*. Boca Raton: CRC Press.
3. Senani, R., Bhaskar, D. R., Singh, V. K., & Sharma, R. K. (2016). *Sinusoidal oscillators and waveform generators using modern electronic circuit building blocks*. Switzerland: Springer. ISBN 978-3-319-23712-1.
4. Chen, H. P., Hwang, Y. S., & Ku, Y. T. (2017). A systematic realization of third-order quadrature oscillator with controllable amplitude. *International Journal of Electronics and Communications, 79,* 64–73.
5. Lawanwisut, S., & Siripruchyanun, M. (2009). High output-impedance current-mode third-order quadrature oscillator based on CCCCTAs. In *Proceedings of the IEEE region 10 conference (TENCON '09)*, pp. 1–4.
6. Pushkar, K. L. (2017). Voltage-mode third-order quadrature sinusoidal oscillator using VDBAs. *Circuits and Systems, 8*(12), 285–292.
7. Maheshwari, S. (2009). Quadrature oscillator using grounded components with current and voltage outputs. *IET Circuits Devices Systems, 3*(4), 153–160.
8. Horng, J. W. (2009). Current-mode third-order quadrature oscillator using CDTAs. *Active Passive Electronic Components,* Article ID 789171, 5.
9. Horng, J. W., Lee, H., & Wu, J. Y. (2010). Electronically tunable third-order quadrature oscillator using CDTAs. *Radioengineering, 19*(2), 326–330.
10. Maheshwari, S. (2010). Current-mode third-order quadrature oscillator. *IET Circuits Devices Systems, 4*(3), 188–195.
11. Horng, J. W. (2011). Current/voltage-mode third order quadrature oscillator employing two multiple outputs CCIIs and ground capacitor. *Indian Journal of Pure and Applied Physics, 49*(7), 494–498.
12. Maheshwari, S., & Verma, R. (2012). Electronically tunable sinusoidal oscillator circuit. *Active and Passive Electronic Components,* Article ID 719376, 6.
13. Chaturvedi, B., & Maheshwari, S. (2013). Third-order quadrature oscillator circuit with current and voltage outputs. *ISRN Electronics,* Article ID 385062, 8.
14. Pandey, R., Pandey, N., Komanapalli, G., & Anurag, R. (2014). OTRA based voltage mode third order quadrature oscillator. *ISRN Electronics,* Article ID 126471, 5.
15. Rai, S. K., & Gupta, M. (2015). A third order quadrature sinusoidal oscillator based on CMOS/FGCMOS Inverters. In *International conference on signal processing, computing and control (2015 ISPCC).*
16. Pandey, N., & Pandey, R. (2015). Approach for third order quadrature oscillator realization. *IET Circuits Devices Systems, 9*(3), 161–171.
17. Malhotra, C., Ahalawat, V., Kumar, V. V., Pandey, R., & Pandey, N. (2016). Voltage differencing buffered amplifier based quadrature oscillator. In *1st IEEE international conference on power electronics, intelligent control and energy systems (ICPEICES-2016).*
18. Khaw-ngam, K., Kumngern, M., & Khateb, F. (2017). Mixed-mode third-order quadrature oscillator based on single MCCFTA. *Radio Engineering, 26*(2), 522–535.
19. Hua-Pin, C., Yuh-Shyan, H., & Yi-Tsen, K. (2017). A new resistorless and electronic tunable third-order quadrature oscillator with current and voltage outputs. *IETE Technical Review, 35,* 426–438.

20. Prommee, P., & Dejhan, K. (2002). An integrable electronic-controlled quadrature sinusoidal oscillator using CMOS operational transconductance amplifier. *International Journal of Electronics, 89*(5), 365–379.
21. Pushkar, K. L., & Bhaskar, D. R. (2018). Voltage-mode third order quadrature oscillator using VDIBAs. *Analog Integrated Circuits and Signal Processing, 98*(1), 201–207.
22. Bhaskar, D. R., Pushkar, K. L., Raj, A., & Singh, G. (2019). OTA based third-order quadrature oscillator. In *1st international conference on signal processing, VLSI and communication engineering 2019, DTU, India*.
23. Maheswari, S., & Khan, I. A. (2005). Current controlled third-order quadrature oscillator. *IEE Proceedings Circuits Devices System, 152*(6), 605–607.
24. Bhaskar, D. R., Abdalla, K. K., & Senani, R. (2011). Electronically-controlled current-mode second order sinusoidal oscillators using MO-OTAs and grounded capacitors. *Circuits and Systems, 2*(2), 65–73.
25. Bhaskar, D. R., Tripathi, M. P., & Senani, R. (1993). Systematic derivation of all possible canonic OTA-C sinusoidal oscillators. *Journal of the Franklin Institute, 330*(5), 885–903.
26. Senani, R. (1989). New electronically tunable OTA-C sinusoidal oscillator. *Electronics Letters, 25*(4), 286–287.
27. Abuelma'atti, M. T. (1989). New minimum component electronically tunable OTA-C sinusoidal oscillators. *Electronics Letters, 25*(17), 1114–1115.
28. Abuelma'atti, M. T. (1990). A new minimum component active-C OTA based linear voltage (current) controlled sinusoidal oscillator. *IEEE Transactions on Instrumentation and Measurement, 39*(5), 795–797.
29. Bhaskar, D. R., Singh, A. K., Sharma, R. K., & Senani, R. (2005). New OTA-C universal current-mode/trans-admittance biquads. *IEICE Electronics Express, 2*(1), 8–13.
30. Kamat, D. V., Ananda Mohan, P. V., & Gopalakrishna Prabhu, K. (2010). Novel first-order and second-order current-mode filters using multiple-output operational transconductance amplifiers. *Circuit System Signal Process, 29,* 553–576.

Publisher's Note Springer Nature remains neutral with regard to jurisdictional claims in published maps and institutional affiliations.



Komal was born in village Ganauar, Sonipat, Haryana, India, on 10th October 1991. She received B.Tech. in Electronics and Communication Engineering from Maharshi Dayanand University, Rohtak, Haryana, India, in 2012 and M.Tech. in Electronics and Communication Engineering from Maharshi Dayanand University, Rohtak, Haryana, India, in 2015. Currently she is an Research Scholar in Guru Jambheshwar University of Science and Technology, Hisar, Haryana, India. Her research area of interest is Analog Signal Processing/Generation using modern analog active building blocks.



K. L. Pushkar was born in village Roshangpur, Auraiya, U. P., India, on 17th August 1969. He received B.Tech. in Electronics Engineering from I.E.T. Lucknow, in 1994, M.E. in Communication Systems from IIT Roorkee (erstwhile University of Roorkee), in 1999 and additional M.E. in ECE from Delhi Technological University (erstwhile Delhi College of Engineering) in 2008. He completed his Ph.D. from Jamia Millia Islamia (A Central University) University, Delhi in 2014. Currently he is working as Dean Academics in Greater Noida Institute of Technology [(GNIOT) affiliated to GGSIPU New Delhi], Uttar Pradesh, India. His current research interest is in Analog Signal Processing and Generation employing modern active building blocks.



Ramnish Kumar received his B.E. in Electronics and Communication Engineering from C.R.S.C.E. (now DCRUST), Murthal, Sonepat, Haryana, India. M.Tech from R.E.C., Kurukshetra, Haryana, India. He compeleted his Ph.D. from Guru Jambheshwar University of Science and Technology, Hisar, Haryana, India. Presently he is working as an Assistant Professor in Department of ECE., Guru Jambheshwar University of Science and Technology, Hisar, Haryana, India, since 2006. His current research interest is Device Modeling, Analog Signal Processing and Generation employing modern active building blocks.

European Journal of Sustainable Development Research
2020, 4(2), em0118
e-ISSN: 2542-4742
https://www.ejosdr.com/

Importance of Energy Audit in Diesel Engine Fuelled with Biodiesel Blends: Review and Analysis

Sanjay Mohite [1,2]*, Sagar Maji [3]

[1] Department of Mechanical Engineering, National Institute of Technology, Kurukshetra, Haryana, INDIA
[2] Department of Mechanical Engineering, Brahma Valley College of Engineering & Research Institute, Nashik, INDIA
[3] Department of Mechanical Engineering, Delhi Technological University, New Delhi, INDIA
***Corresponding Author:** smohite001@yahoo.com

Citation: Mohite, S., & Maji, S. (2020). Importance of Energy Audit in Diesel Engine Fuelled with Biodiesel Blends: Review and Analysis. *European Journal of Sustainable Development Research, 4*(2), em0118. https://doi.org/10.29333/ejosdr/7596

ARTICLE INFO

Received: 9 Jun. 2019
Revised: 30 Dec. 2019
Accepted: 30 Dec. 2019

ABSTRACT

Number of experiments have been performed on various performance and emission characteristics, effect of biodiesel blends on lubricity and input and output energy distribution in diesel engine fuelled with biodiesel blends. It is also reviewed that energy audit is used in buildings, plants, process and equipments and energy audit method was developed for fishing vessels based on similar systems for land based industries. In land based businesses, industries and households, energy audits are presently used to investigate the use of energy and to identify opportunities for the efficiency improvement and effectiveness in the energy use. Energy audits have been used in various sectors, industries and utilities. This paper is a review paper of energy audit and it is found that there is a vast scope for implementation of standardized energy audit in diese engines fuelled with biodiesel blends. Its objective is to find out a standard energy audit method for diesel engine fuelled with biodiesel blends which evaluate the feasibility of biodiesel blend as fuel and also harmonise the research of biodiesel as fuel.

Keywords: energy audit, biodiesel blends, diesel engine, performance and emission characteristics, heat flow analysis

ABBREVIATIONS

A/F Ratio	: Air Fuel Ratio
BSEC	: Brake Specific Energy Consumption
BSFC	: Brake Specific Fuel Consumption
BTE	: Brake Thermal Efficiency
EGT	: Exhaust Gas Temperature
JB	: Jatropha Biodiesel
KB	: Karanja Biodiesel
PB	: Polanga Biodiesel

INTRODUCTION

It is reported that an energy audit is used to find out energy use within a structure, plant, process or equipment system and also investigate the energy conservation. The first step of energy audit is the determination of the ways in which energy is consumed, which includes how, what, when, where, why and how much quantity of energy is consumed. If consumption of energy is found out, then, it is simpler to investigate methods to reduce energy consumption with improved management, efficiency and conservation (Parker, 2015).

The latest concept of the energy audit is to focus on the strategy of cost effectiveness towards energy conservation with the considerations of energy costs, government regulations, new technologies, environmental concerns and emerging services in business. Residential, commercial and industrial types of facility are auditable. The audit can be applied to a facility or it can be applied on a focus area of the structure, specified equipments, isolated processes and systems. Energy audit's scope may include electric, gas, oil, water and sewage etc. types of utility services. The audit of refrigerants, boilers emissions and chemical process

Copyright © 2020 by Author/s and Licensed by Modestum Ltd., UK. This is an open access article distributed under the Creative Commons Attribution License which permits unrestricted use, distribution, and reproduction in any medium, provided the original work is properly cited.

application may include impact parameters of environment. All types of energy audits comprise of data collection, data analysis and recommendations. Energy audits can be generally classified into three categories (Braquet, 1999):

1. Walk through audit which means simple audit, preliminary audit or screening audit.

2. Site Energy Audit which means mini-audit, general audit, complete site audit.

3. Comprehensive Audit which means detailed audit or technical analysis audit**.**

Energy audits are designed to get the information of energy conservation opportunities. Preliminary survey is the first step of energy audit. Energy consumption indices or performance characteristics for the consumer group under study can be computed with the help of design survey instrument. The objective is not to develop an analytical model which consider all the variable which influence energy consumption. The objective is to make a simple survey instrument to take appropriate measures (Turley & Bui, 1981). Researchers defined energy audit as a process of evaluation of use of energy in a building and identify scope for the energy consumption reduction (Thumann & Younger, 2010). Energy audit data is used to offer an optimum combination of hybrid renewable energy systems resulting in reduction of dependency on diesel fuel for the island (Khan et al., 2016).

At the initial stage, a standard energy audit method is required to evaluate the feasibility of biodiesel blend as fuel in diesel engine. If biodiesel blend is found suitable, detail energy audit can be done further. If biodiesel blend is not found suitable at primary stage of energy audit, further consideration of blend as fuel is not required which saves time and money. The objective of this study is to find out the importance of Energy Audit in Diesel engine fuelled with Biodiesel blends.This research is being done to identify the scope of energy audit in evaluation of diesel engine fuelled with biodiesel blends. In this research and analysis paper, it is found that a standardised energy audit is required to harmonise the research of biodiesel as fuel. In this paper, some important parameters have been selected to include it in standard energy audit.This is done on the basis of their influence on other parameters.

VARIOUS APPLICATIONS OF ENERGY AUDIT

Energy audits are effective tool which access energy use in building and also compute expenditure to save energy. In energy audits, ASHRAE determined guidelines for four levels of energy audits. Level 0: Preliminary analysis of energy use, Level 1: Walk through analysis. Level 2: Analysis and survey of energy. Level 3: Detailed analysis for capital investment decisions (Niu & Leicht, 2016).

The traditional energy audit is just not sufficient for today's projects of energy. Traditional energy audit follows a snap shot approach which considers all present conditions static for the projected time. In investment grade audit, a component of assessment in risk is used which assesses conditions in the particular building with the consideration of human aspects (Hansen, 1999). An energy audit, which is also known as feasibility study concerns about the thorough examination of two years of utility bills, mathematical modelling of energy use when the system is supposed to operate properly, routine plant operation's review and list of upgrades with their costs of installation and savings in a building (Audin, 2002). Researchers presented a critical overview of the Infrared thermography applications in the building energy audit (Lucchi, 2018). Reseachers reported design and application of a smart energy audit which is incorporated in building. Researchers also adopted methods to detect fault in plant (Belussi et al., 2017). A good energy audit is used to make valuable decisions on the investment for the best energy efficiency. Energy audit development involves identification and communication of the best energy conservation measures (Anina & Rottmayer, 2016). Reduction of energy consumption and impact on the environment are some of the objectives of the energy audit. Energy and environment are associated with a green energy audit. This green energy audit provides methods for the optimisation of energy performance of buildings and make them sustainable (Dall et al., 2012).

An energy audit is an important step for the improvement of energy efficiency at the facility level. An energy audit was conducted in a paper mill plant in Guangdong Province in China to identify energy conservation and opportunities for CO_2 emission reduction (Kong et al., 2013). It is mandatory to implement energy audit in large companies regularly according to Energy efficiency directive of the European Commission (Nabitz & Hirzel, 2019).Researchers conducted an energy audit which was relied on brick, refractory and insulation with its effect on efficiency and reliability of boiler and savings of fuel. Researchers concluded that if brick, refractory and insulation are not installed in a proper way, then more quantity of fuel is consumed by the boiler. Researchers has concluded that after correction and changes, a significant annual savings in energy (pulverize coal) cost is achieved (Bases, 2004).

Life cycle analysis's methodology was used to develop a model based on computer for the evaluation of energy use in the mechanised wood harvesting system. Program of visual basic was used in the computer model. Energy audit was based on consumption of fuel and oil and the energy consumption in the manufacture of the machines and replacement parts. In this energy audit, the most important parameter was fuel consumption (82%) followed by oils (7%) and machine repairs and replacements (11%). An energy reduction strategy to reduce overall energy consumption upto 13% was suggested (Klvac et al., 2003).

A methodology was used for identification of opportunities to conserve energy through on-site audits of the manufacturing plants. These opportunities to conserve energy are categorised according to potential areas for savings such as motors and air compressors and are represented in view of energy savings, cost savings, implementation cost and payback period (Romero et al., 1999). Many companies realize that utilities cost can be decreased in the range of 10% to 30%. Therefore, management companies and brokers of real estate, mechanical and electrical contractors and equipment dealers have tried for marketing of energy audit. An energy audit can be conducted on two different companies with a duration of 5 hours and 80 hours respectively. This type of variations implies different ideas of customers and auditors (Avina, 2013).

When the data has put for a utility, the analysis tool would create a baseline assessment which provides an organised use of energy. The analysis tool determines a baseline of energy costs and consumption for a utility (Eisenberg, 2012). The main objective of all the data entry and the concerned software is to balance energy consumption for a facility (Cardenas- Lailhacar et al., 2005).

Compressed air is called fourth utility in industries and these air compressors are driven by electric motors. One to two weeks of detailed monitoring for equipments should be performed to check real data on compressed air flow, power, pressure and quality levels. Audit reports comprises of study, documentation, evaluation and suggestion to improve compressed air system economically (Koski, 2002).

Energy audit of a fibreboard drying production line find out that low energy efficiency is due to excessive loss of heat and lack of heat recovery. Heat may also be recovered from the exhaust, but it requires more equipments (Gong et al., 2011). Industry's operational programs such as integrity, safety, environmental protection, damage prevention, emergency management and security may be checked for their adequacy by the monitoring tool such as audit. Evaluation of the complete program can be performed with the help of comprehensive audit as a valuable tool (Mora et al., 2012).

The performance of an asset is evaluated by energy benchmarking and rating. Standardised formats defined the best in many cases. Examples of standard benchmarking and rating are energy labelling of home appliances and cars and also energy rating of the building. Researchers investigated that there were no well defined and standardised energy performance benchmarking and rating scheme for ships. Researchers introduced basic methodology, key performance indicators (KPI), their reference values and an energy rating scheme to fill the above mentioned gaps. It was investigated that proposed benchmarking and rating scheme can be used in ships, which can be used to make a difference between ships according to energy performance (Bazari, 2007).

An energy audit of a vehicle is a systematic way to assess current energy use. The purpose of the audit program is to investigate different areas for savings of fuel. The audit is an initial step in a process comprises of setting priorities to develop an energy management program. In energy audit, maintenance parameters which reduce friction losses and the parameters which affect engine performance are computed (Erkut & Maclean, 1992).

An audit provides a base to calculate energy, CO_2 emissions and financial savings which can be achieved with current technology and project the expected targets to meet Kyoto agreement or HECA legislation. It was concluded that individual audits would assess individual cities in formulating a saving of effective energy, emission reduction policy and the audits collection in a country helps their government to formulate a national approach towards energy efficiency and sustainability (Bennett & Newborough, 2001). Energy audit helps to minimize demand and consumption of energy in industry (Bellarmine & Arokiaswamy, 1996). It is reported that energy audit woule be a useful tool to overcome the information barriers and facilitate investments in energy efficiency measures (Kalantzisn & Revoltella, 2019). It is reported that an energy audit would be a method to determine the most economical measures, which improves energy efficiency in an organisation (Knorring, 2019). Energy Audit is used in industries under the new law by the authorities of Morocco.The energy audit proposes a plan which has a potential for reduction of the consumption of lighting energy (Boharb et al., 2016). Problems in environment can be solved with the use of renewable energy technologies and efficient energy utilisation. Energy conservation is important for sustainable development (Dincer, 1999).

Thomas et al. (2010) investigated an energy audit method for fishing vessels based on similar systems for land based industries. They performed an energy audit for an Australian fishing vessel which recommends to improve efficiency. In land based businesses, industries and households, energy audits are presently used to evaluate the energy use and investigate opportunities for the improvement of efficiency and effectiveness in the use of energy. This energy audit investigate the field where savings can be made and recommend changes to make vessel more efficient. In this energy audit, individual vessel was analysed to investigate the use of energy in it. They proposed a sample energy audit for an Australian fishing vessel which made recommendation for efficiency improvement to reduce cost of fuel.

The efficiency, the losses of energy and the prospects for improvement in 12.8 litre heavy duty and 6.7 litre medium duty diesel engine have been analysed in the experimental work. In this experimental work, two baseline diesel engines were tested and analysed in the laboratory. Abilities of emerging technologies to reduce consumption of fuel with focus on each loss mechanism was found out with the application of energy audit and technology forecasting. Improvements in fuel consumption were investigated with improvement in the heavy duty diesel engine in this research work with the help of future technology (Thiruvengadam et al., 2014). Brief description of energy audit and items on which energy audits are implemented are listed in **Table 1**.

There are various investgations made by researchers in their respective studies. Some general observations which can be investigated from the literature are as follows:

Energy audit is used in various buildings, plants, process and machines. An energy audit method was developed and used for fishing vessels based on similar systems for land based industries. In land based businesses, industries and households, energy audits are presently used to find out the energy use and to identify opportunities for the improvement in efficiency and effectiveness in the energy use.

Efficiency, energy losses and the prospects for improvement in heavy duty and medium duty diesel engine have been investigated in the experimental work. In the experimental work, it is also concluded that the emerging technologies were used to improve efficiency including higher compression ratio, optimised controls, improvements in EGR, low friction lubricants, decrease in engine friction, decrease in parasitic load, improvements in turbocharging, fuel injection, design of optimized cylinder head and waste heat recovery system. These engine efficiency's emerging technologies have the ability to decrease fuel consumption significantly (Thiruvengadam et al., 2014). Various applications are energy audit are illustrated in **Figure 1**.

Table 1. Energy audit application

S. No	Brief description of energy audit	Items on which energy audit implemented	References
1	Energy audit	Island	Khan et al. (2016)
2	Energy audit	Building	Thumann & Younger (2010)
3	ASHRAE determined guidelines for four levels of energy audits	Building	Niu & Leicht (2016)
4	Investment grade audit	Building	Hansen (1999)
5	Feasibility study	Building	Audin (2002)
6	Energy audit	Valuable decisions on the investment for the best energy efficiency	Anina & Rottmayer (2016)
7	Green energy audit	Building	Dall et al. (2012)
8	Identify energy conservation and opportunities for CO_2 emission reduction	Paper mill plant	Kong et al. (2013)
9	Energy audit	Boiler	Bases (2004)
10	On-site audits	Manufacturing plants	Romero et al. (1999)
11	Energy audits	Companies	Avina (2013)
12	Energy audits	Utility	Eisenberg (2012)
13	Balance energy consumption	Facility	Cardenas- Lailhacar et al. (2005)
14	Energy audits	Compressed air	Koski (2002)
15	Energy audit	Fibreboard drying production line	Gong et al. (2011)
16	Comprehensive audit	Industry's operational program	Mora et al. (2012)
17	Proposed benchmarking and rating scheme	Ships	Bazari (2007)
18	Computerised transportation program of audit	Vehicle, transportation.	Erkut & Maclean (1992)
19	Individual audits	Individual cities	Bennett & Newborough (2001)
20	Energy audit	Industry	Bellarmine & Arokiaswamy (1996)
21	Energy audit	Industry	Boharb et al. (2016)
22	Energy audit method	Fishing vessels	Thomas et al. (2010)
23	Detailed energy audit analyses	Diesel engines	Thiruvengadam et al. (2014)

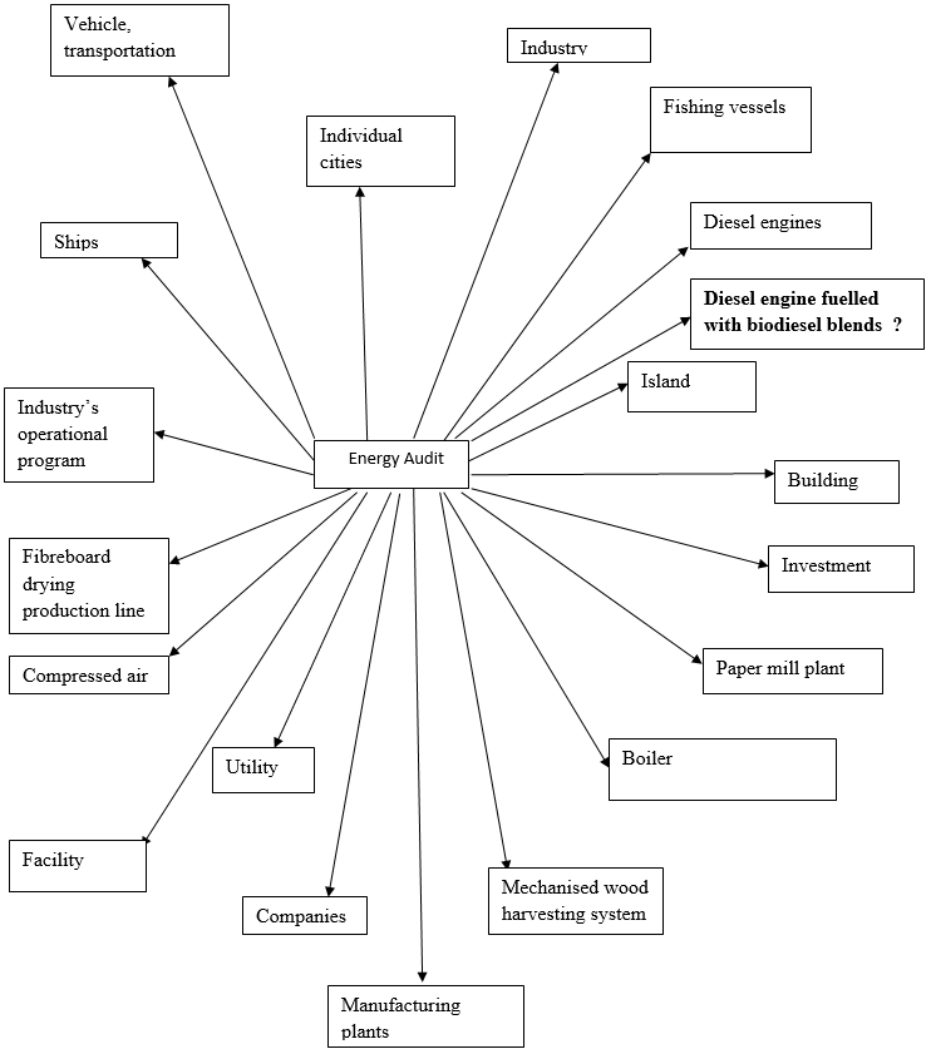


Figure 1. Various applications of energy audit

RESEARCH GAPS

Energy audits have been used in various sectors, industries and utilities. Hence a standard energy audit method is required for diesel engine fuelled with biodiesel blends which incorporates the effect of biodiesel blends on a diesel engine with important and effective parameters and also reveals the use of fuel energy distributions in diesel engines at initial stage. At present, there is no specific reference available regarding energy audit of diesel engine fuelled with biodiesel blends.If biodiesel blend is not found suitable in energy audit, further consideration of blend as fuel is not required which saves time and money.

METHODOLOGY

The present review of energy audit is based on comprehensive literature review of energy audit regarding its applications. Research gap is found out. Various performance and emission characteristics alongwith heat flow analysis parameters have been discussed. On the basis of discussion, the important parameters have been chosen based on their effective influence on other parameters and are listed in energy audit.

RESULT & DISCUSSION

The importance of the performance and emission characteristics of the diesel engine fuelled with biodiesel blends has been discussed in this section:

Brake Thermal Efficiency (BTE)

The ratio of work output to the quantity of fuel energy supplied is called brake thermal efficiency of an engine. It is also known as fuel conversion efficiency (Mohite et al., 2016). Higher BTE indicates better work output from the fuel energy. BTE is one of the performance parameters which indicates the quantity of transformation of chemical energy of fuel into useful work output in diesel engines. Researchers conducted tests on engine with Soybean oil biodiesel and investigated similar engine performance with methyl, ethyl and butyl esters as compared to diesel. They did not investigate much difference in thermal efficiency resulting from the use of various fuels. Slight loss of power was reported with biodiesel use which was attributed to lower heating values (Sahoo et al., 2009). Researcher reported decrease in torque with increase in Cottonseed oil biodiesel in the blends and it was attributed due to higher viscosity and lower calorific values of Cottonseed oil biodiesel (Aydin & Bayindir, 2010). BTE decreases with the addition of biodiesel in fuel blends which may be attributed due to higher BSFC due to lower heating value of biodiesel. Higher value of BTE was investigated to be 35% for the B10 to B20 fuel blend at CR of 17.9 whereas lower BTE was reported for the fuel blend for B30 to B40 at CR of 17.7 (Sivaramakrishnan & Ravikumar, 2014). Higher value of BTE was found to be 21.1% for B0. Higher value of BTE of 20.51%, 20.4%, 20.4% and 20.3% were found for B10, B20, B30 and B50 respectively. Lower BTE for fuel blends may be attributed due to lower calorific values and also increase in consumption of blend fuel as compared to that of diesel (EL- Kasaby & Nemit-allah, 2013).

Brake Specific Fuel Consumption (BSFC)

BSFC is the flow rate of fuel per unit brake power output. It indicates the engine's efficiency.BSFC is found to measure the fuel efficiency of an engine. Lower value of BSFC is required. This is found to be one of the important parameter to compare while using various test fuels. The relationship between the amount of fuel injected, its density, its viscosity and its calorific values is found to play an important role in the determination of BSFC. BSFC is found to be reduced with increase in load for all fuels which may be due to increase in fuel percentage required to operate the engine and is lower than the increase in brake power percent. This is because of reduction in heat losses at higher loads. Multi-cylinder turbocharged diesel engine was tested at full load at speed of 1400 rpm. BSFC of biodiesel was 13.8% higher in comparison to diesel which was attributed due to lower calorific value of biodiesel. If the viscosity and density of biodiesel blend are higher than that of diesel then it causes increase in BSFC also. Calorific value of biodiesel was 12% lower than that of diesel. Specific fuel consumption increased with the use of biodiesel which may be attributed due to lower calorific value of biodiesel. Biodiesel is found to have lower specific energy content as compared to diesel. Since biodiesels have lower heating value in comparison to diesel, therefore, BSFC increases with the biodiesel concentration in the blends (Canakci, 2007; Shahabuddin et al., 2013; Um & Park, 2010).

Exhaust Gas Temperature (EGT)

EGT indicates the exhaust gase temperature which comes out of the engine indicating the combustion effectiveness and conversion of thermal energy in an engine. The amount of energy released was found to indicate combustion temperature. EGT was found to be measured 30 mm distant from the combustion chamber which indicates combustion temperature. EGT of B20 was found to be nearly same as that of diesel fuel. Lowest EGT was investigated with the use of diesel as compared to biodiesel blends at low speeds. This is due to oxygenated nature of biodiesel causing proper combustion (El- Kasaby & Nemit-allah, 2013). The researchers also investigated that different types of biodiesel blends did not make any difference in EGT. The general trend is that EGT increases with load. Researchers investigated that operating parameters of the engine which causes lower BSFC and higher BTE also causes lower EGT. Researchers investigated that increase in biodiesel concentration in blends cause increase in EGT. EGT of B20, B40, B60, B80 and B100 were found to be higher by 2.3%, 6.3%, 8.7%, 11.3% and 14% respectively as compared to that of diesel fuel. It would also be reported that there is 5^0C increase in EGT with a 20% increase in biodiesel concentration in

blend fuels which may be due to increase in heat losses in fuel blends. EGT of diesel were investigated to be 131^{0}C, 160^{0}C, 186^{0}C, 212^{0}C and 240^{0}C whereas EGT of B100 biodiesel were investigated to be 152^{0}C, 182^{0}C, 211^{0}C, 243^{0}C and 272^{0}C at 0%, 25%, 50%, 75% and 100% load respectively. Similar findings were reported by other researchers also (Raheman & Ghadge, 2008). Increase in engine efficiency causes reduction in exhaust energy. It was also investigated that decrease in adiabatic flame temperature was one of the reason for the decrease in EGT (Jacobs, 2015).

Mechanical Efficiency

Mechanical efficiency is the ratio of brake work at the crankshaft to indicated work in the combustion chamber of an engine (Mohite et al., 2016). Mechanical efficiency is also known as the ratio of brake power to the sum of brake power and friction power. Some portion of the indicated work is found to be used to expel exhaust gases, induct fresh air and also to overcome friction of piston, bearings and other mechanical components of the engine. Thus mechanical efficiency is found to measure the ability of the diesel engine to overcome the loss due to friction power.

Volumetric Efficiency

The effectiveness of induction process in an engine is found to comprise of the intake manifold, air filter, intake valve and is measured by volumetric efficiency. Four stroke engines have separate induction systems and therefore, volumetric efficiency is applicable in four stroke engines.Volumetric efficiency of a diesel engine is the ratio of actual consumption to theoretical consumption of air. Volumetric efficiency is closely related to exhaust gas temperature. Higher exhaust gas temperature causes rise in retained gas temperature, which results in the increase in temperature of incoming fresh air. The actual consumption of air is found to be inversely proportional to the density of air. Density of air will be lower at higher temperature. Volumetric efficiency is also found to be reduced with increase in brake power. This is due to reduction in air fuel ratio with an increase in brake power. The maximum amount of air input into the cylinder during each cycle is found to determine the power and performance of an engine. The higher the quantity of air input, higher quantity of fuel could be burned with higher energy conversion into power output. Density of atmospheric air multiplied by swept volume is the mass of air which should be consumed for each cycle in an engine ideally. Volumetric efficiency is found to measure the effectiveness of the induction process of an engine. Rise of temperature of incoming fresh air is found in the cylinder due to higher EGT. Biodiesel concentration in blends causes reduction in the density of incoming fresh air due to rise in temperature. This increases the actual consumption of air causing an increase in volumetric efficiency (Mohite et al., 2016).

Air- Fuel Ratio

Air fuel ratio may be defined as the ratio of air flow rate to fuel mass flow rate in an engine. Air fuel ratio influences the quality of emission. This ratio should be in the combustible range for proper combustion.

Unburned Hydrocarbon Emission

HC emission act as irritants and odorants in the atmosphere. Some portions of HC emissions react with atmospheric gases to form photochemical smog. Photochemical smog is not desirable. Diesel engines have only 20% of HC emissions in comparison to petrol engine. The reason is that the diesel engine operate with lean fuel air mixture. HC emissions are directly proportional to fuel- air mixture. Large amount of HC emissions are emitted with rich fuel air mixture. This is due to lack of oxygen to react with all the carbon with the use of rich fuel air mixture (Pulkrabek, 2003).There is a significant reduction in HC emission with the use of biodiesel as compared to that of diesel. A minimum of 33ppm HC emission was reported with the use of B30 biodiesel blend indicating that HC emission reduces with the increase in biodiesel concentration in fuel blends at CR of 18. This may be due to higher temperature and pressure at higher compression ratio. This may also be due to addition of oxygenate fuels. Oxygen enrichment is found to favour HC oxidation in the expansion and exhaust process. The reduction in HC emission was investigated to be linear with the addition of biodiesel in blends. The higher and lower values of HC produced were reported to be 0.0299 g/kWh and 0.01554 g/kWh respectively which were found to be lower than that of Euro Norms-IV i.e. 0.5 g/kWh (Huang et al., 2005; Muralidharan & Vasudevan, 2011; Sivaramakrishnan & Ravikumar, 2014). HC emission was investigated to be decreased with the use of biodiesel blends as compared to that of diesel. This is due to effective oxidation which is caused by presence of excess oxygen in biodiesel (Ramalingam et al., 2018).

Carbon Monoxide Emission

Emission of carbon monoxide is not desirable and it also represent loss of chemical energy which are not fully used in engine (Pulkrabek, 2003).Diesel engine operates with overall lean mixture and therefore, it has very low CO emission as compared to petrol engine. Chemical energy which is not fully utilised to develop power output in engine, is lost and may be represented by the CO emission. A significant reduction in CO emission was found at all engine speed with the use of biodiesel blends. This is due to higher oxygen content in biodiesel as compared to that of diesel, which causes proper combustion thereby reducing the CO emission. Combustion process is found to be accelerated by fuel based oxygen (Hosseini et al., 2017). Researchers investigated the CO reduction with increase in brake power at all loads. CO emission is reported to be lower for biodiesel blends as compared to that of diesel which may be attributed due to presence of excess oxygen in biodiesel (Ramalingam et al., 2018). CO emission was reported to be decreased with the use of biodiesel blends as compared to that of diesel fuel. This is due to oxygen content in biodiesel. This is due to lower C/H ratio of biodiesel as compared to that of diesel. It is also found that decrease in CO is not dependent on biodiesel concentration in blends (Rajaraman et al., 2009).

Nitrogen Oxide Emission

Oxides of nitrogen are found to be present in exhaust gases of an engine. They contain major part of Nitric oxide (NO) with minor part of Nitrogen dioxide (NO_2) and small amount of other oxides of nitrogen. The NO_x emission also causes photochemical smog which is not desirable (Pulkrabek, 2003). During combustion process, NOx are produced in the combustion chamber due to the chemical reaction between atomic oxygen and nitrogen. Chemical reactions which produces NOx are dependent on temperature at the time of reaction and therefore, NOx emissions are minimum at lower loads. Higher amount of NOx was found to be emitted with the use of biodiesel blends at all engine speeds. Higher NOx emission was found with the use of biodiesel blends due to the following reasons (El- Kasaby & Nemit-allah, 2013):

1. Higher adiabatic flame temperature of biodiesel causes complete combustion which results in higher temperature and NOx emission. Quantity of double bonded molecules are higher in biodiesel as compared to diesel. Adiabatic flame temperatures of these double bonded molecules are higher resulting in increase in NOx emission for biodiesel.

2. Oxidation of nitrogen results in the formation of NOx in combustion chamber. The NOx formation rate was found to be a function of flame (combustion) temperature, stay time of nitrogen at the temperature and oxygen content in the combustion chamber. At high flame temperature, there would be dissociation of nitrogen N_2 and oxygen O_2 into atomic states in the combustion chamber which is found to be participated in a number of reactions. There are three principal reactions resulting in production of NOx according to Zeldovich mechanism:

$$N_2 + O \text{-----} \rightarrow NO + N$$

$$N + O_2 \text{----} \rightarrow NO + O$$

$$N + OH \text{--} \rightarrow NO + H$$

NO_x was reported to be increased with load for all test blend fuels. This is due to more quantity of fuel injection and their combustion in the cylinder with increase in engine load resulting in higher gas temperature and consequently more NO_x formation (Rajaraman et al., 2009).

Brake Specific Energy Consumption (BSEC)

It is the product of brake specific fuel consumption and calorific value. Therefore, BSEC is one of the important parameter to evaluate the performance characteristics because it takes into account the calorific value of fuels in blends. It includes the brake specific fuel consumption and calorific value of blend fuel. BSEC may also be defined as the energy input, which is needed to produce unit brake power. Therefore, BSEC has been chosen as a key parameter for an energy audit of diesel engine fuelled with a biodiesel blend fuel. It also facilitates the proper evaluation of blend fuels as its capability to run a diesel engine (Fattah et al., 2014; Imtenan et al., 2015). Reduction in BSEC is observed with increase in load due to reduction in brake specific fuel consumption at higher loads. Increase in BSEC is observed respectively with the increase in the biodiesel concentration in blend fuel. This may be caused due to dependence of BSEC on BSFC directly as it is a product of calorific value and brake specific fuel consumption (Mohite et al., 2016 d).Researchers investigated increase in BSEC with the use of biodiesel blends. An increase of 20.21% higher than that of diesel for BSEC was reported with the use of JB 100 at 1200 rpm. Increase of 2.68%, 5.84% and 13.31% in BSEC were observed for KB 20, KB50 and KB 100 respectively as compared to diesel at 2200 rpm. Similarly, an increase in BSEC of 2.86%, 6%, 12.37%, 2.59%, 5.84% and 13.31% as compared to diesel, were reported for JB 20, JB 50, JB100, PB20, PB 50 and PB 100 respectively at rated speed. PB20 fuel was found to be the best BSEC as it has a minimum increment of BSEC (2.59%) at rated speed in comparison to all test fuels. Higher biodiesel concentration in blend fuels causes an increase in BSEC which may be caused due to lower calorific value of biodiesel blends as compared to diesel (Sahoo et al., 2009). BSEC may indicates the engine's efficiency with which the input fuel energy is used during combustion. BSEC reduction indicates proper use of chemical energy of fuel into useful work output. Combustion quality may be represented as depleted by an increase in BSEC (Paul et al., 2017). Specific energy consumption is the energy amount which is required to develop unit power. Fuels with different calorific values can be compared with this parameter. BSEC is directly proportional to the calorific value of fuel and the fuel injected into the combustion chamber. Researchers investigated decrease in BSEC with the increase in load from 0% to 100%. BSEC of the engine was found to be higher at lower load and was found to be decreased with an increase in load (Babu & Anand, 2017; Senhur et al., 2017).

Heat Flow Analysis

Heat flow analysis is one of the key factor to find out the heat energy's utilisation and wastages. Major factors of heat energy consumption are brake power output, coolant medium, exhaust gas and radiation. Energy crisis and global warming endanger the peaceful existence of human being. This problem can be solved with the increase in dependency on alternative fuels and also minimize energy losses. In this view, thermal balance study in an engine with the use of different biodiesel is fruitful. All energy flows in and out of the engine have been shown with the help of thermal balance. Researchers reported an increase in heat loss to cooling water and heat loss to lubricating oil whereas heat to engine brake power, heat loss to exhaust and heat loss to radiation (unaccounted) were found to be reduced with the increase in the biodiesel concentration in blend as compared to diesel. Thermal balance sheet of the energy and mass inflows and outflows should be drawn to get the inside picture of the system in an easy way. This is called as energy balance or heat balance which is basic analysis of the first law of thermodynamics (Abedin et al., 2015). This study is also useful to test efficiencies due to change in engine design of injectors, pumps, valves, intercoolers and other advanced technologies. Researchers reported that energy balance measurement was required to be analysed on the basis of energy distribution in comparison to direct measurement of fuel energy input due to high uncertainty of fuel energy content i.e. 7%. Therefore, the amount of energy distributed in different parts of the engine was measured and compared on a percentage basis instead of the amount of energy input by fuel. Therefore, direct energy balance between diesel and biodiesel fuels can be compared. This permitted the uncertainties of the results which were required to be small and based primarily on the accuracy of

measurement equipment (Wallace & Kremer, 2008). About 35% of the total chemical energy of the fuel converts into useful work output and 30% of chemical energy of fuel is lost by the exhaust gases in the form of chemical energy and enthalpy in an engine. The remaining 1/3rd of fuel energy may be dissipated to the surrounding. At the time of combustion, temperature upto and above 2700K may reach in the combustion chamber of an engine and materials of the engine causes failure due to this much higher temperature, if proper heat transfer does not occur. But it is also necessary to operate an engine as hot as possible to get higher thermal energy (Pulkrabek, 2003). Diesel and biodiesel fuels have different physical properties which affect the characteristics of heat release (Shahabuddin et al., 2013).

With the use of Rice oil biodiesel, the total heat release was reported to be reduced as compared to diesel (Um & Park, 2010). An advanced knowledge of energetic potentiality and exhaust emission of biodiesel is required with the increase in the alternative fuel use. Energy and exergy analyses were performed to assess the distribution of energy and also for the characterisation of waste heat energy in diesel engine (Magno et al., 2015).

It was investigated that two third of energy of input fuel was lost to exhaust gas and cooling medium. Distribution of fuel energy supplied to the engine is given by the first law of thermodynamics and it also helps to identify the losses which are avoidable. The exergy concept is introduced with the improvement of energy analysis by the second law of thermodynamics. Suitable engine operating conditions identify to perform energy and exergy analysis of diesel engine under mapping characteristics. There are some studies which deal with energy and exergy analysis of diesel engine, but detailed research is not available for all ranges of engine operation. Development of diesel engine based on cogeneration systems at different engine speeds and loads can be increased with the knowledge of energy flow at different operating conditions (Abusoglu & Kanoglu, 2008; Fu et al., 2013; Magno et al., 2015; Ozkan et al., 2013). Combustion energy is converted into useful work with the release of some of its portions into exhaust gas and cooling medium. Lubricating oil also carries a small amount of heat energy which is found to be negligible. Heat radiation and friction losses in diesel engine are responsible for the loss of remaining part of the combustion energy. According to the second law of thermodynamics, some part of heat loss can be utilized for the enhancement in efficiency of diesel engines (Magno et al., 2015). Energy analysis is used to design engine properly to reduce energy losses. Researchers found out various losses such as heat loss to cooling water, exhaust gas and other miscellaneous losses to reduce losses for the higher power output (Madheshiya & Vedrtnam, 2018). Researchers investigated change of 37% of input energy into mechanical energy and loss of 63% of input energy in different ways (Khoobbakht et al., 2016). Researchers investigated similar energetic performance of biodiesel and diesel in diesel engine. Input heat energy was distributed as 37.4% to coolant, 31.1% to exhaust and 29.6% to useful power output with the use of biodiesel. Input heat energy was distributed as 37.5% to coolant, 31.4% to exhaust and 29.2% to useful power output with the use of diesel in diesel engine. Nominal disparities of -0.1%, -0.3% and 0.4% were investigated respectively between diesel and biodiesel with their use in diesel engine. Researchers investigated the energy balance study to monitor the quantity of energy used in a diesel engine with diesel and biodiesel fuel with the measurement of energy output and losses in diesel engine. The aim of the research is to authenticate the functionality of the diagnostic system, find the different ways of energy transfer for fuels in a diesel engine and to use heat transfer modes of conduction, convection and radiation to determine energy transfer and also to design a controlled and instrumented energy management system properly (Wallace & Kremer, 2008). Similar energetic performance in terms of fuel energy input, brake thermal efficiency, combustion efficiency, heat loss and exhaust loss were reported with the use of biodiesel and their blends as compared to diesel. The difference in heat loss, exhaust loss and brake power output were reported to be +2.3%, -2.9% and 0.6% with the use of pure biodiesel as compared to diesel in diesel engine respectively (Canakci & Hosoz, 2006). It is required to focus on the decrease of heat losses under different operating conditions to improve engine performance. Researchers investigated that heat losses in diesel engine was found to be more with the use of biodiesel as compared to diesel in the study of energy balance in diesel engine (Ramadhas et al., 2006). Researchers conducted experimental study of heat balance and reported that losses in diesel engine were found to be higher with the biodiesel use (Benjumea et al., 2009). Researchers investigated that heal loss to cooling water and lubricating oil were reported to be higher with biodiesel as compared to that of diesel. This is because of proper combustion of biodiesel fuel. Loss of heat to cooling medium was found to be higher in the range of 1% to 3% and heat loss to lubricating oil was found to be in the range of 1% to 2% with the addition of 5% to 10% biodiesel in diesel as blend fuel. It was also investigated that heat loss to exhaust gas was found to be higher with the use of diesel in comparison to biodiesel blends. This may be due to higher concentration of HC and CO emission with the use of diesel fuel as compared to that of biodiesel blends. Researchers investigated change of 22.56% of input energy into usefuel work, 24.47% of heat loss to cooling water, 21.04% of heat loss to lubricating oil and 18.9% of heat loss to exhaust with the use of B10 biodiesel blend fuel. If this was compared with B20 blend, change of heat into brake power was slightly reduced, heat loss to cooling water & lubrication oil were increased whereas heat loss to exhaust and unaccounted heat loss were reduced. It was also found that 23.72% of input fuel energy was change into useful brake power with the diesel use. This was due to higher heating value and lower viscosity of diesel as compared to that of biodiesel blends (Abedin et al., 2015). In this respect, heat energy consumption to useful power, its losses to cooling medium, exhaust gases and radiation would be taken into account while analyzing energy audit.

Friction Power

Lubricity reduces friction causing an increase in mechanical efficiency. Researchers investigated decrease in wear with the biodiesel use in blend fuel. Researchers also investigated decrease in the coefficient of friction with the increase in biodiesel concentration in blend (Fazal et al., 2014). Researchers conducted experiments on an engine with a B15 blend of Palm biodiesel in diesel fuel for 300 h and reported that B15 exhibited decreased in wear as compared to that of diesel (Kalam & Masjuki, 2002). Researchers also investigated decrease in wear and friction for short term use. Biodiesel was found to provide better lubricity resulting in reduced wear as compared to diesel during short term tests (Sundus et al., 2017). Sliding parts of diesel engine produces friction which causes reduction in the reliability of engine parts. Different techniques are being used to decrease friction

Table 2. Effect of energy audit parameters

Parameter	Importance of parameter	Effects on other parameters
BSEC	BSEC may also be defined as the energy input, which is found to produce unit brake power. BSEC facilitates correct evaluation of diesel engine with blended fuel having different densities and calorific values.	It is found to consider BSFC and calorific value of blend fuel.
HBP	HBP means brake thermal efficiency as it represents the change of the amount of fuel energy to useful work i.e. brake power from total fuel energy.	Brake thermal efficiency
HJW	HJW is found to represent the amount of fraction of heat energy which is lost in cooling medium.	This is found to represent the increase in temperature of combustion chamber, cylinder and the whole diesel engine. It is also found to effect brake thermal efficiency.
HEgas	HEgas is found to represent the amount of fraction of heat energy which is lost in exhaust gas.	EGT, Volumetric Efficiency, A/F Ratio, BTE
HRAD	HRAD is found to represent the quantity of fraction of heat energy which is lost in radiation and also in unaccounted losses.	Brake thermal efficiency
Friction Power	This power is found to be used in the friction between moving parts of the engine, draw fresh air into the intake system and to the engine accessories driving.	Mechanical Efficiency
Smoke opacity	Smoke opacity is found to be a measurement of smoke and soot.	HRAD

such as coatings, texturing, lightweight use of materials and lubricity improvement. The most important parameter is found to be lubricity to increase engine life. Lubrication is necessary to decrease friction in sliding parts of engine. Lubricity of fuel depends on quantity of viscosity. Presence of fatty acid in biodiesel causes a lubricating thin film which causes decrease in frictional coefficient (Mosarof et al., 2016). Researchers conducted four ball wear tests under 40 kg load for 1 h at the speed of 600 rpm to 1500 rpm to compare lubricity of diesel, biodiesel and its blends. Reduction in wear and friction was found with the increase of biodiesel concentration in blend fuel. Wear of steel ball was found to be decreased by 10% with the use of B20 blend fuel at 1500 rpm speed. Wear was found to be decreased further with increase in concentration of biodiesel in blend fuel and it was found that the wear was decreased by 20% with the use of B100 biodiesel fuel as compared to that of diesel (Fazal et al., 2013, 2014).

Smoke Emission

Radiation by soot was found to be a source of losses in efficiency of engines. The soot was found to be luminous during combustion and it was found to be an important source of radiation (Benajes et al., 2015). Smoke opacity increase with load due to increase in fuel consumption. Smoke opacity reduces due to the oxygen in biodiesel as compared to that of diesel. Biodiesel is found to have lower carbon to hydrogen ratio and lack of aromatic compounds as compared to diesel. The higher quantity of oxygen and lower quantity of carbon decreases the smoke formation resulting in reduction of smoke opacity. On the other hand, high sulphur content results in increase in smoke opacity of diesel. Soot concentration increased with load. Soot concentration was found to be reduced with the use of biodiesel blend fuels as compared to that of diesel fuel. This is due to absence of aromatic compounds, sulphur and presence of oxygen in biodiesel, which results in proper combustion of fuel (Rajaraman et al., 2009). With the use of biodiesel, smoke opacity was found to be approximately 22.5% decreased as compared to that of diesel (Ozsezen & Canakci, 2010). Similar trends were reported by various researchers. Reductions of 28.6%, 50%, 62% and 74% in PM emissions were reported with the use of B10, B20, B50 and B100 biodiesel blends respectively. This is because of higher oxygen content, lower or no sulphur and aromatic content and lower carbon content of biodiesel, which causes reduction in PM emission as compared to that of diesel (Hasan and Rahman, 2017). 87.7% arguments of researchers investigated that biodiesel causes decrease in PM emission as compared to that of diesel. Researchers also investigated significant decrease in smoke of the range of 50% to 72.73% with the use of 8 types of biodiesel fuels as compared to that of diesel. There was a remarkable reduction in PM emission with the increase in biodiesel concentration in blend (Xue et al., 2011). The high temperature burned gases and the soot particles are found to be sources of radiation in the diesel engine (Heywood, 2012). Thus, it is found that smoke is more harmful and it also helps to increase heat loss to radiation. Therefore, this characteristic must be chosen as a key parameter in the Energy Audit as compared to other emission parameter. Thus, increase in smoke emission causes increase in heat loss to radiation. Thus, emission of smoke is directly proportional to heat loss.

Out of all these above parameters, the important parameters have been chosen based on their effective influence on other parameters and are listed in energy audit at initial stage. These important parameters are shown in **Table 2**.

CONCLUSIONS

Energy audit can be chosen as one of the methodology to evaluate the feasibility of biodiesel blends as fuel. The selection of performance and emission characteristics for energy audit of diesel engine fuelled with biodiesel blends is one of the important aspect. In this review and analysis, brake specific energy consumption, heat flow analysis which consists of heat utilization in brake power, losses of heat to the cooling water, exhaust gas and radiation, friction power and smoke emission have been chosen as important performance and emission characteristics which should be included in energy audit of diesel engine fuelled with biodiesel blends. This selection is based on their effect on other parameters.This energy audit shall be standardized to harmonize biodiesel research as fuel.

REFERENCES

Abedin, M. J., Masjuki, H. H., Kalam, M. A., Sanjid, A., & Rahman, S. M. A. (2015). Thermal balancing of a multi-cylinder diesel engine operating on diesel, B5 and palm biodiesel blends. *Journal of Clean Energy Technologies*, *3*(2), 115-118. https://doi.org/10.7763/JOCET.2015.V3.178

Abusoglu, A., & Kanoglu, M. (2008). First and second law analysis of diesel engine powered cogeneration systems. *Energy Conversion and Management*, *49*, 2226-2031. https://doi.org/10.1016/j.enconman.2008.02.012

Avina, J. M., & Rottmayer, S. P. (2016). Virtual audits: the promise and the reality. *Energy Engineering*, *113*(6), 34-52. https://doi.org/10.1080/01998595.2016.11772067

Audin, L. (2002). How long since your last energy audit. *Strategic Planning for energy and Environment*, *22*(1), 72-75. https://doi.org/10.1080/10485230209509606

Avina, J. (2013). How to avoid energy audit disasters: a guide to picking a quality energy auditor. *Energy Engineering*, *110*(6), 7-12. https://doi.org/10.1080/01998595.2013.10753692

Aydin, H., & Bayindir, H. (2010). Performance and emission analysis of cottonseed oil methyl ester in a diesel engine. *Renewable Energy*, *35*, 588-592. https://doi.org/10.1016/j.renene.2009.08.009

Babu, D., & Anand, R. (2017). Effect of biodiesel-diesel-n-pentanol and biodiesel-diesel-n-hexanol blends on diesel engine emission and combustion characteristics. *Energy*, *133*, 761-776. https://doi.org/10.1016/j.energy.2017.05.103

Bases, G. J. (2004). An energy audit that saved real energy and money, *Proceedings of NAWTEC 12, 12th North American Waste to Energy Conference*, May 17-19, 2004, Savannah, Georgia, USA, NAWTEC 12-2221.

Bazari, Z. (2007). Ship energy performance benchmarking/ rating; methodology and application. *Journal of Marine Engineering and Technology*, *6*(1), 11-18. https://doi.org/10.1080/20464177.2007.11020197

Bellarmine, G. T., & Arokiaswamy, N. S. S. (1996). Energy management techniques to meet power shortage problems in India. *Energy Conversion and Management, 37*(3), 319-328. https://doi.org/10.1016/0196-8904(95)00181-6

Belussi, L., Danza, L., Salamone, F., Meroni, I., Galli, S., & Svaldi, S. D. (2017). Integrated smart system for energy audit: methodology and application. *Energy Procedia*, *140*, 231-239. https://doi.org/10.1016/j.egypro.2017.11.138

Benajes, J., Martin, J., Garcia, A., Villalta, D., & Warey, A. (2015). Incylinder soot radiation heat transfer in direct injection diesel engine. *Energy Conversion and Management*, *106*, 414-427. https://doi.org/10.1016/j.enconman.2015.09.059

Benjumea, P., Agudelo, J., & Agudelo, A. (2009). Effect of altitude and palm oil biodiesel fuelling on the performance and combustion characteristics of a HSDI diesel engine. *Fuel*, *88*, 725-731. https://doi.org/10.1016/j.fuel.2008.10.011

Bennett, M., & Newborough, M. (2001). Auditing energy use in cities. *Energy Policy*, *29*, 125-134. https://doi.org/10.1016/S0301-4215(00)00108-7

Boharb, A., Allouhi, A., Saidur, R., Kousksou, T., Jamil, A., Mourad, Y., & Benbassou, A. (2016). Auditing and analysis of energy consumption of an industrial site in Morocco. *Energy*, *101*, 332-342. https://doi.org/10.1016/j.energy.2016.02.035

Braquet, L. (1999). Three levels of energy audits (pre-contract considerartions). *Strategic Planning for Energy and the Environment*, *19*(1), 28-36. https://doi.org/10.1080/10485236.1999.10530576

Canakci, M. (2007). Combustion characteristics of a turbocharged DI compression ignition engine fueled with petroleum diesel fuels and biodiesel. *Bioresource Technology*, *98*, 1167-1175. https://doi.org/10.1016/j.biortech.2006.05.024

Canakci, M., & Hosoz, M. (2006). Energy and Exergy analyses of a diesel engine fuelled with various biodiesels. *Energy Sources Part B: Economics, Planning and Policy*, *1*(4), 379-394. https://doi.org/10.1080/15567240500400796

Cardenas- Lailhacar, C., Schaub, D., Venkat, S., Capehart, B. L., Capehart, L. C., & Pawlik, K. E. (2005). A case study for energy auditing using an interactive energy balance. *Strategic Planning for Energy and the Environment, 25*(1), 34-62. https://doi.org/10.1080/10485230509509679

Dall, G., Specher, A., & Bruni, E. (2012). The green energy audit, a new procedure for the sustainable auditing of existing buildings integrated with the LEED Protocols. *Sustainable Cities and Society*, *3*, 54-65. https://doi.org/10.1016/j.scs.2012.02.001

Dincer, I. (1999). Environmental impacts of energy. *Energy Policy, 27*, 845-854. https://doi.org/10.1016/S0301-4215(99)00068-3

Eisenberg, M. (2012). That's a bright idea! Using USEPA's energy use assessment tool to control costs. *Journal (American Water works Association)*, *104*(12), 20-84.

EL- Kasaby, M., & Nemit-allah, M.A. (2013). Experimental investigations of ignition delay period and performance of a diesel engine operated with Jatropha oil biodiesel. *Alexandria Engineering Journal*, *52*, 141-149. https://doi.org/10.1016/j.aej.2012.12.006

Erkut, E., & Maclean, D. (1992). Alberta's energy efficiency branch conducts transportation audits. *Interfaces*, *22*(3), 15-21. https://www.jstor.org/stable/25061618

Fattah, I. M. R., Masjuki, H. H., Kalam, M. A., Wakil, M. A., Ashraful, A. M., & Shahir, S. A. (2014). Experimental investigation of performance and regulated emissions of a diesel engine with Calophylum inophyllum biodiesel blends accompanied by oxidation inhibitors. *Energy Conversion and Management, 83*, 232-240. https://doi.org/10.1016/j.enconman.2014.03.069

Fazal, M. A., Haseeb, A. S. M. A., & Masjuki, H. H. (2014). A critical review on the tribological compatibility of automotive materials in Palm biodiesel. *Energy Conversion and Management*, *79*, 180-186. https://doi.org/10.1016/j.enconman.2013.12.002

Fazal, M. A., Haseeb, A. S. M. A., & Masjuki, H. H. (2013). Investigation of friction and wear characteristics of Palm biodiesel. *Energy Conversion and Management*, *67*, 251-256. https://doi.org/10.1016/j.enconman.2012.12.002

Fu, J., Liu, J., Feng, R., Yang, Y., Wang, L., & Wang, Y. (2013). Energy and exergy analysis on gasoline engine based on mapping characteristics experiment. *Applied Energy*, *102*, 622-630. https://doi.org/10.1016/j.apenergy.2012.08.013

Gong, Z. X., Stanovsky, J., & Mujumdar, A. S. (2011). Energy audit of a fibreboard drying production line using Simprosys software. *Drying Technology*, *29*(4), 408-418. https://doi.org/10.1080/07373937.2010.498069

Hasan, M. M., & Rahman, M. M. (2017). Performance and emission characteristics of biodiesel –diesel blend and environmental and economic impacts of biodiesel production: a review. *Renewable and Sustainable energy Reviews*, *74*, 938-948. https://doi.org/10.1016/j.rser.2017.03.045

Hansen, S. J. (1999). Investment Grade energy audits. *Cogeneration and Competitive Power Journal*, *13*(3), 63-70. https://doi.org/10.1080/10668683.1999.10530346

Heywood, J. B. (2012). Internal Combustion Engine Fundamentals. India: Tata McGraw Hill Edition.

Hosseini, S. H., Taghizadeh-Alisaraei, A., Ghobadian, B., & Abhaszadeh-Mayvan, A. (2017). Performance and emission characteristics of a CI engine fuelled with carbon nano-tubes and diesel –biodiesel blends. *Renewable Energy*, *111*, 201-213. https://doi.org/10.1016/j.renene.2017.04.013

Huang, Z., Lu, H., Jiang, D., Zeng, K., Liu, B., Zhang, J., & Wang, X. (2005). Performance and emission of a CI engine fueled with diesel/oxygenate blends for various fuel delivery advance angles. *Energy Fuels*, *19*, 403-410. https://doi.org/10.1021/ef049855d

Imtenan, S., Masjuki, H. H., Varman, M., Fattah, I. M. R., Sajjad, H., & Arbab, M. I. (2015). Effect of n-butanol and diethyl ether as oxygenated additives on combustion emission performance characteristics of a multiple cylinder diesel engine fuelled with diesel – jatropha biodiesel blend. *Energy Conversion and Management, 94*, 84-94. https://doi.org/10.1016/j.enconman.2015.01.047

Jacobs, T. J. (2015). Waste heat recovery potential of advanced internal combustion engine technologies. *Journal of Energy Resources Technology*, *137*, 1-14. https://doi.org/10.1115/1.4030108

Kalam, M. A., & Masjuki, H. H. (2002). Biodiesel from palm oil- an analysis of its properties and potential. *Biomass Bioenergy*, *23*, 471-479. https://doi.org/10.1016/S0961-9534(02)00085-5

Kalantzis, F., & Revoltella, D. (2019). Do energy audits help SMEs to realize energy-efficiency opportunities? *Energy Economics*, *83*, 229–239.https://doi.org/10.1016/j.eneco.2019.07.005

Khan, M. R. B., Jidin, R., & Pasupuleti, J. (2016). Energy audit data for a resort island in the South China Sea. *Data in Brief, 6*, 489-491. https://doi.org/10.1016/j.dib.2015.12.033

Khoobbakht, G., Akram, A., Karimi, M., & Najafi, G. (2016). Exergy and energy analysis of combustion of blended levels of biodiesel, ethanol and diesel fuel in a DI diesel engine. *Applied Thermal Engineering*, *99*, 720-729. https://doi.org/10.1016/j.applthermaleng.2016.01.022

Klvac, R., Ward, S., Owende, P. M. O., & Lyons, J. (2003). Energy audit of wood harvesting system. *Scandinavian Journal of Forest Research*, *18*(2), 176-183. https://doi.org/10.1080/02827580310003759

Knorring, H. V. (2019). Energy audits in shipping companies. *Transportation Research Part A, 125*, 35-55. https://doi.org/10.1016/j.tra.2019.04.017

Kong, L., Price, L., Hasanbeigi, A., Liu, H., & Li, J. (2013). Potential for reducing paper mill energy use and carbon dioxide emissions through plant –wide energy audits: a case study in China. *Applied Energy*, *102*, 1334-1342. https://doi.org/10.1016/j.apenergy.2012.07.013

Koski, M. A. (2002). Compressed air energy audit, the real story. *Energy Engineering*, *99*(3), 59-70. https://doi.org/10.1016/j.tra.2019.04.017

Lucchi, E. (2018). Applications of the infrared thermography in the energy audit of buildings: A review. *Renewable and Sustainable Energy Reviews, 82*, 3077–3090.https://doi.org/10.1016/j.rser.2017.10.031

Madheshiya, A. K., & Vedrtnam, A. (2018). Energy- exergy analysis of biodiesel fuels produced from waste cooking oil and mustard oil. *Fuel*, *214*, 386-408. https://doi.org/10.1016/j.fuel.2017.11.060

Magno, A., Mancaruso, E., & Vaglieco, B. M. (2015). Effects of both blended and pure biodiesel on waste heat recovery potentiality and exhaust emissions of a small CI engine. *Energy*, *86*, 1-11. https://doi.org/10.1016/j.energy.2015.04.092

Mohite, S., Kumar, S., & Maji, S. (2016). Performance Characteristics of mix oil biodiesel blends with smoke emissions, *International Journal of Renewable Energy Development*, *5*(2), 163-170. https://doi.org/10.14710/ijred.5.2.163-170

Mora, R. G., Paviglianiti, J., Slocomb, R., Mota, A. B., & Zaidi, M. (2012). Trends on integrity management programs (IMP) and management system (MS) audit and incident findings, *Proceedings of the 2012, 9th International Pipeline Conference IPC 2012*, Sept 24-28, 2012, Calgony, Alberta, Canada, IPC 2012-90046.

Mosarof, M. H., Kalam, M. A., Masjuki, H. H., Alabdulkarem, A., Ashraful, A. M., Arslan, A., Rashedul, H. K., & Monirul, I. M. (2016). Optimization of performance, emission, friction and wear characteristics of Palm and Calophyllum biodiesel blends. *Energy Conversion and Management*, *118*, 119-134. https://doi.org/10.1016/j.enconman.2016.03.081

Muralidharan, K., & Vasudevan, D. (2011). Performance, emission and combustion characteristics of a variable compression ratio engine using methyl esters of waste cooking oil and diesel blends. *Applied Energy*, *88*(11), 3959-3968. https://doi.org/10.1016/j.apenergy.2011.04.014

Nabitz, L., & Hirzel, S. (2019).Transposing The Requirements of the Energy Efficiency Directive on Mandatory Energy Audits for Large Companies: A Policy-Cycle-based review of the National Implementation in the EU-28 Member States. *Energy Policy*, *125*, 548-561. https://doi.org/10.1016/j.enpol.2017.12.016

Niu, M., & Leicht, R. M. (2016). Information exchange requirements for building walk through energy audits. *Science and Technology for the Built Environment*, *22*(3), 328-336. https://doi.org/10.1080/23744731.2016.1151713

Ozkan, M., Ozkan, D.B., Ozencer, O., & Yilmaz, H. (2013). Experimental study on energy and exergy analyses of a diesel engine performed with multiple injection strategies; effect of pre-ignition timing. *Applied Thermal Engineering*, *53*, 21-30. https://doi.org/10.1016/j.applthermaleng.2012.12.034

Ozsezen, A. N., & Canakci, M. (2010). The emission analysis of an IDI diesel engine fuelled with methyl ester of waste frying palm oil and its blends. *Biomass and Bioenergy*, *34*(12), 1870-1878. https://doi.org/10.1016/j.biombioe.2010.07.024

Parker, S. A. (2015). Ideas that works! The midnight audit. *Strategic Planning for Energy and the Environment*, *35*(1), 7-9. https://doi.org/10.1080/10485236.2015.11439120

Paul, A., Panua, R., & Debroy, D. (2017). An experimental study of combustion, performance, exergy and emission characteristics of a CI engine fueled by diesel-ethanol-biodiesel blends. *Energy*, *141*, 839-852. https://doi.org/10.1016/j.energy.2017.09.137

Pulkrabek, W. W. (2003). Engineering Fundemantals of the Internal Combustion Engine. University of Wisconsin-Patteville, Prentice Hall, Upper Saddle River, New Jersey, 07458.

Raheman, H., & Ghadge, S. V. (2008). Performance of diesel engine with biodiesel at varying compression ratio and ignition timing. *Fuel*, *87*, 2659-2666. https://doi.org/10.1016/j.fuel.2008.03.006

Rajaraman, S., Yashwanth, G. K., Rajan, T., Sivakumaran, R., & Raghu, P. (2009). Experimental investigation of performance and emission characteristics of Moringa oil methyl ester and its diesel blends in a single cylinder direct injection diesel engine, *Proc. of the ASME 2009 Inter. mechanical Eng. congress and expo.. IMECE 2009, Nov 13-19, Lake Buena Vista, FL, USA IMECE 2009-11265.*

Ramadhas, A. S., Jayraj, S., & Muraleedharan, C. (2006). Theoretical modelling and experimental studies on biodiesel fuelled engine. *Renewable Energy*, *31*, 1813-1826. https://doi.org/10.1016/j.renene.2005.09.011

Ramalingam, S., Rajendran, S., & Ganesan, P. (2018). Performance improvement and exhaust emission reduction in biodiesel operated diesel engine through the use of operating parameters and catalytic converter: a review. *Renewable and Sustainable Energy Reviews*, *81*, 3215-3222. https://doi.org/10.1016/j.rser.2017.08.069

Romero, H., Ambriz, J. J., Ortiz, J. N., & Sheffield, J. W. (1999). Joint Mexico / USA Energy audit- a case study. *Energy Engineering*, *96*(6), 17-28. https://doi.org/10.1080/01998595.1999.10530478

Sahoo, P. K., Das, L. M., Babu, M. K. G., Arora, P., Singh, V. P., Kumar, N. R., & Varyani, T. S. (2009). Comparative evaluation of performance & emission characteristics of jatropha, karanja & polanga based biodiesel as fuel in a tractor engine. *Fuel*, *88*(9), 1698-1707. https://doi.org/10.1016/j.fuel.2009.02.015

Senhur, S., Asokan, M. A., Rahul, R., Francis, S., & Sreelekh, M. K. (2017). Performance, emission and combustion characteristics of diesel engine fuelled with waste cooking oil biodiesel/diesel blends with additives. *Energy*, *122*, 638-648. https://doi.org/10.1016/j.energy.2017.01.119

Shahabuddin, M., Liaquat, A. M., Masjuki, H. H., Kalam, M. A., & Mofijur, M. (2013). Ignition delay, combustion and emission characteristics of diesel engine fueled with biodiesel. *Renewable and Sustainable Energy Reviews*, *21*, 623-632. https://doi.org/10.1016/j.rser.2013.01.019

Sivaramakrishnan, K., & Ravikumar, P. (2014). Optimization of operational parameters on performance and emissions of a diesel engine using biodiesel. *International Jounal of Environmental Science and Technology*, *11*, 949-958. https://doi.org/10.1007/s13762-013-0273-5

Sundus, F., Fazal, M. A., & Masjuki, H. H., (2017). Tribology on the biodiesel: a study on enhancing biodiesel stability and its fuel properties. *Renewable and Sustainable Energy Reviews*, *70*, 399-412. https://doi.org/10.1016/j.rser.2016.11.217

Thiruvengadam, A., Pradhan, S., Thiruvengadam, P., Besch, M., & Carder, D. (2014). Heavy duty vehicle diesel engine efficiency evaluation and energy audit, Center for Alternative Fuels, Engines, and Emissions, West Virgina University, Morgantown, WV, *Final report on Oct, 2014 published by Oscar Delgado, the International Council on Clean Transportation, Washington DC.*

Thomas, G., O'Doherty, D., Sterling, D., & Chin, C. (2010). Energy audit of fishing vessels, *Proceedings of the Institution of Mechanical Engineers, Part M: Journal of Engineering for the Maritime Environment*, *224*(2), 87-101. https://doi.org/10.1243%2F14750902JEME186

Thumann, A., & Younger, W. (2010). *Handbook of energy audit*, 7th Edition, Lilburn, GA: the Fairmont Press, Inc.

Turley, R. E., & Bui, M. (1981). A practicable method to identify the excessive consumer of energy. *Interfaces*, *11*(1), 62-67.

Um, S., & Park, S.W. (2010). Modeling effect of the biodiesel mixing ratio on combustion and emission characteristics using a reduced mechanism of methyl butanoate. *Fuel*, *89*(7), 1415-1421. https://doi.org/10.1016/j.fuel.2009.10.026

Wallace S. J., & Kremer G. G. (2008). Diesel engine energy balance study operating on diesel and biodiesel fuels. *Proceedings of IMECE 2008, 2008 ASME International Mechanical Engineering Congress an exposition, Oct 31-Nov 6, 2008, Boston, Massachusetts, USA, IMECE 2008-67712.*

Xue, J., Grift, T. E., & Hansen, A. C. (2011). Effect of biodiesel on engine performance and emission. *Renewable & Sustainable Energy Reviews*, *15*, 1098-1116. https://doi.org/10.1016/j.rser.2010.11.016

Inadequate Earthing (Grounding) in Distribution Sector – Root Cause for Many Maladies

Dr. Rajesh Kumar Arora
Delhi Transco Limited

ABSTRACT

Earthing facilitates the efficient and quick operation of protective relays in case of any earth fault and provides safety to costly equipments as well as working personnel. This paper presents the basics, types and purposes of earthing system. A low voltage (LV) distribution system may be identified according to its earthing system. These are defined using the five letters T (Direct connection to earth), N (Neutral), C (Combined), S (Separate) and I (Isolated from earth). Paper provides information about applications and importance of different system of earthing like TT, IT, TN-S, TN-C, TN-C-S. The paper also highlights the importance of grounding in the distribution system.

Keywords : *Earthing (Grounding), Low Voltage Distribution System, System Earthing, Protective Earth (PE), PEN Conductor, Step & Touch Potential, GPR.*

www.IndianJournals.com
Members Copy, Not for Commercial Sale
Downloaded From - 14.139.251.200 on Tue 13-Feb-2020

1. INTRODUCTION

The process of transferring the immediate discharge of the electrical energy directly to the earth by the help of the low resistance wire is known as the electrical earthing. The electrical earthing is done by connecting the non-current carrying part of the equipment or neutral of supply system to the ground.

Every building, equipments, power plants, substation facilities included in electricity require earthing (grounding), either directly or through grounding system, the main objective of doing earthing in electrical network is safety.

But when the neutral for any system is not connected with the earth then it will be known as electrical system without earthing as depicted in Fig. 1.

Mostly, the galvanised iron is used for the earthing. The earthing provides the simple path to the leakage current and fault current in the system. The short-circuit current of the equipment passes to the earth which is assumed to have zero potential. Thus, protects the system equipments and personnel working with these equipment from damage as well as shock current as shown in Fig. 2.

Earthing is not likely to reduce the total magnitude of over voltages produce by lightening or switching surges, it can however mitigate the possibilities of excessive voltage stress on the phase to ground insulation of particular phase.

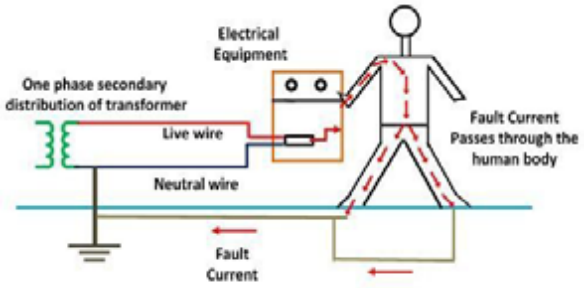


Fig. 1 : Electrical System without Earthing

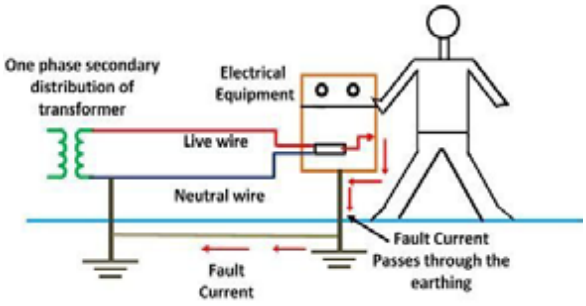


Fig. 2 : Electrical System with Earthing

The system earth resistance should be such that which any fault occurs against which earthing is designed to give protection, the protective gear will operate to make the faulty main or plant harmless. In most cases, such operation involves isolation of the faulty main or plant, for example by circuit breaker or fuses.

Distribution Transformer is the key element in the distribution system where the neutral point of the system is grounded. This transformer with the help of distribution lines distributes the electricity to the consumers. The actual picture of distribution transformer and role of

DT in distribution system are shown in Figure 3 and 4 respectively.



Fig. 3 : Distribution Transformer

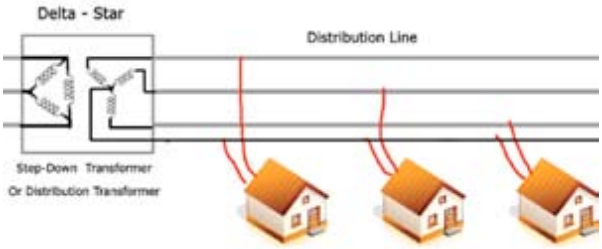


Fig. 4 : Role of Distribution Transformer in Distribution Network

www.IndianJournals.com
Members Copy, Not for Commercial Sale
Downloaded From - 14.139.251.100 on dated 13-Feb-2020

2. TYPES OF ELECTRICAL EARTHING (GROUNDING)

The electrical equipment mainly consists of two non-current carrying parts. These parts are neutral of the system or frame / support structure of the electrical equipment. From the earthing of these two non-current carrying parts of the electrical system, earthing can be classified into two types:

1. Neutral Earthing
2. Equipment Earthing

2.1 Neutral Earthing (System Grounding)

In neutral earthing, the neutral of the system is directly connected to earth with the help of some metallic conducting wire. The neutral earthing is also called the system earthing. Such type of earthing is mostly provided to the system which has star winding. For example, the neutral earthing is provided in the generator, transformer, motor etc as shown in Fig 5.

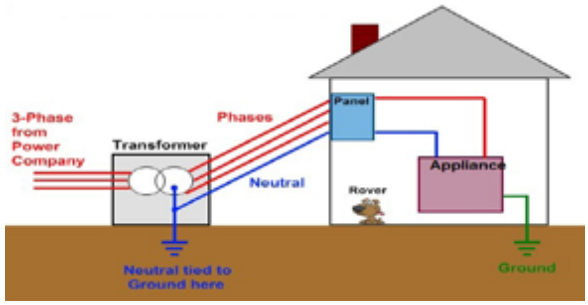


Fig. 5 : Neutral and Equipment Earthing

2.2 Equipment Earthing (Grounding)

Such type of earthing is provided to the electrical equipment. The non-current carrying part of the equipment like their metallic frame is connected to the earth by the help of the conducting wire as shown in Fig. 5. If any fault occurs in the apparatus, the short-circuit current to pass the earth by the help of wire. Thus, protect the system from damage.

3. IMPORTANCE / PURPOSE OF EARTHING

The main objective / purpose of earthing are:

- To Protect the workers who regularly come in contact with electrical devices that might give them a shock.
- To keep the voltage of the device constant in the healthy phase in case of single of single phase to ground fault.
- A good grounding path which has a low impedance value ensure that faults in the electrical path are cleared quickly. If the faults stay within the system for a long time, they can pose a serious threat to the stability of the system.
- Many modern electronic devices generate a form of 'electrical noise' that can cause damage to the device and reduce its efficiency, unless the device is property grounded.
- Surge protection device function better with the help of proper grounding.
- Malfunctioning electric devices often leak electricity, which has the potential to start a fire if not redirected safely.

The main objective of grounding electrical systems is to provide a suitably low resistance path for the discharge of fault current which ultimately provide safety to working personnel and costly installed equipments in the substation. The flow of heavy fault current results in rise of potential in the substation area and with respect to remote ground. There is need to ensure that the ground potential rise, and touch and step voltages are within permissible limits.

4. ROLE OF ADEQUATE EARTHING IN PREVENTION OF HAZARDS

In order to understand the role of adequate earthing design, abstract of IS 3043 are given below:

4.1 Basic Objective of System Earthing

- Earthing of system is designed primarily to preserve the security of the system by ensuring that the potential on each conductor is restricted to such a value that is consistent with the level of insulation applied.
- From the point of view of safety, it is equally important that earthing should ensure efficient and fast operation of protective gear in the case of earth faults.

- The system earth-resistance should be such that, when any fault occurs against which earthing is designed to give protection, the protective gear will operate to make the faulty main or plant harmless. In most cases, such operation involves isolation of the faulty main or plant, for example, by circuit-breakers or fuses.

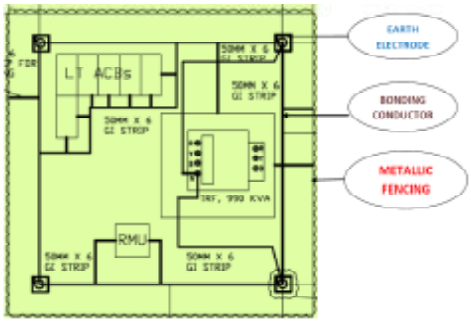


Fig. 6 : Earthing Layout of Distribution Transformer

4.2 Equipment Earthing

The basic objectives of equipment grounding are:

- to ensure freedom from dangerous electric shock voltages exposure to persons in the area;
- to provide current carrying capability, both in magnitude and duration, adequate to accept the ground fault current permitted by the over current protective system without creating a fire or explosive hazard to building or contents; and
- to contribute to better performance of the electrical system.

Neutral and equipment earthing of distribution transformer are shown in Figure 6.

Further, let us try to understand the above concepts as follow :

Voltage Exposure *:* When there is unintentional contact between an energized electric conductor and the metal frame or structure that encloses it or is adjacent, the frame or structure tends to become energized to the same voltage level as exists on the energized conductor. To avoid this appearance of this dangerous, exposed shock hazard voltage, the equipment grounding conductor must present a low impedance path from the stricken frame to the zero potential ground junction. The impedance should also be sufficiently low enough to accept the full magnitude of the line-to-ground fault current without creating an impedance voltage drop large enough to be dangerous.

Avoidance of Thermal Distress *:* The earthing conductor must also function to conduct the full ground fault current (both magnitude and duration) without excessively raising the temperature of the earthing conductor or causing the expulsion of arcs and sparks that could initiate a fire or explosion. The total impedance of the fault circuit including the grounding conductor should also permit the required current amplitude to cause operation of the protective system.

Preservation of System Performance *:* The earthing conductor must return the ground fault current on a circuit without introducing enough additional impedance to an extent that would impair the operating performance of the over current protective device, that is, a higher than necessary ground-circuit impedance would be acceptable if there is no impairment of the performance characteristics of the protective system.

Picture of fire of distribution transformer is shown in Figure 7.



Fig. 7 : Distribution Transformer on Fire

5. UNGROUNDED AND GROUNDED NEUTRAL SYSTEM

Generally earthing of neutral point of the transformer and the generator is called the system earthing. Now, if the neutral point for any system is connected to the earth then it will be called grounded system.

But when the neutral for any system is not connected with the earth then it will be called ungrounded system as shown in Figure 8. Connecting the neutral point to the earth through a resistance means resistance earthing and reactance earthing means connecting the neutral point to the earth through a resistance. When the neutral point connected to the earth directly it will call solidly grounded as shown in Figure 9.

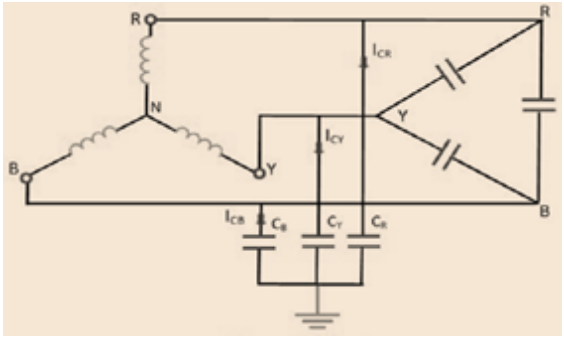


Fig. 8 : Ungrounded Neutral System

www.IndianJournals.com
Members Copy, Not for Commercial Sale
Downloaded From IP - 14.139.251.100 on dated 13-Feb-2020

5.1 Disadvantage of Ungrounded Neutral Earthing System

- **System Voltage Increase:** When the earth fault occurs in line then the potential of the faulty phase becomes equal to ground potential. However, the voltages of the two remaining healthy phases rise from their normal phase voltages to full line value. This may result in insulation breakdown.
- **Protection Complicacy:** In this system earth fault is not easy to sense and troubleshoot will become complicated.
- **Arcing Ground:** Sudden temporary fault can caused by failing of a branch creates an arc between the overload line and the ground. Arc extinguished and can re strike in a repeated regular manner. This is called arcing ground.
- **Static Induced Voltage:** Over voltage due to the static induced charges are not conducted to the earth.

www.IndianJournals.com Members Copy, Not for Commercial Sale Downloaded From IP - 20

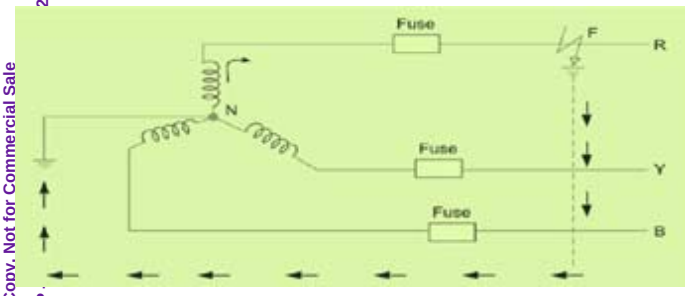


Fig. 9 : Grounded Neutral System

5.2 Advantage of Grounded Neutral Earthing System

- **The System Voltage Will not Increase in Case of Ground Fault:** When the healthy line of a grounded system i.e earthed the voltage of the healthy line will not increase w.r.t. earth as in the case of ungrounded earthing system.
- **Arcing Grounds are Eliminated:** If the neutral point of the system is earthed then the distribute capacitive current from the lines to earth will neutralized by the current from the neutral point to earth and the arcing grounds will eliminated.
- It will be a **stable neutral point**.
- Life of the **insulation** will increase.
- It will give general **safety** to personnel and the equipments due to operation of the **fuses**.
- Over voltage due to sudden lightning will discharged to the earth.
- Earth fault relaying will relatively simple.

6. EARTHING SYSTEM FOR LV NETWORK

A low voltage (LV) distribution system may be identified according to its earthing system. These are defined using the five letters T (direct connection to earth), N (neutral), C (combined), S (separate) and I (isolated from earth). The first letter denotes how the transformer neutral (supply source) is earthed while the second letter denotes how the metal work of an installation (frame) is earthed. The third and fourth letters indicate the functions of neutral and protective conductors respectively.

There are three possible configurations.

TN: transformer neutral earthed, frame connected to neutral.

- The TN system includes three sub-systems: TN-C, TN-S and TN-C-S
- TT: transformer neutral earthed and frame earthed.
- IT: unearthed transformer neutral, earthed frame.

6.1 TN Earthing System

In a TN earthing system, the supply source (transformer neutral) is directly connected to earth with one or more conductors and all exposed conductive parts of an installation are connected to the neutral or protective earth conductor. The three sub-systems in TN earthing system are described below with their key characteristics.

6.1.1 *TN-C Earthing System*

TN-C system has the following features:

- Neutral and protective functions are combined in a single conductor throughout the system. (PEN - Protective Earthed Neutral).
- The supply source is directly connected to earth and all exposed conductive parts of an installation are connected to the PEN conductor as shown in Fig. 10.

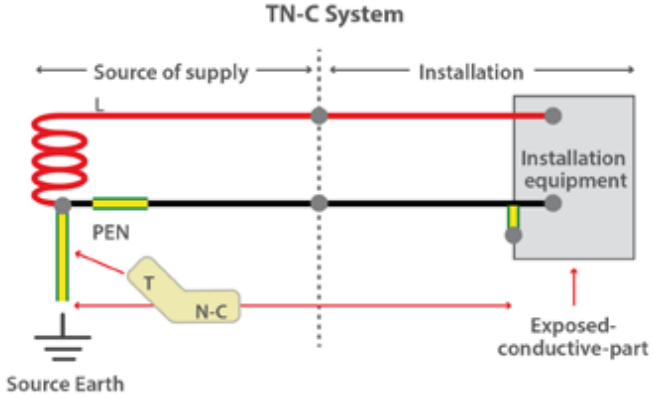


Fig. 10 : TN-C Earthing System

Advantages of TN-C Earthing System

- Earth fault loop impedance of TN-C earthing system is low.
- It does not requires earth electrode at site.
- It is economical.

Disadvantages of the TN-C Earthing System

- TN-C earthing system is least safest as compared to other earthing systems
- TN-C system is less effective for Electromagnetic Compatibility (EMC) problems.
- A fault in the LV network may cause touch voltages at other LV customers.

6.1.2 *TN-S Earthing System*

TN-S System has the following features:

- A TN-S System has separate neutral and protective conductors throughout the system.
- The supply source is directly connected to earth. All exposed conductive parts of an installation are connected to a protective conductor (PE) via the main earthing terminal of the installation as shown in Fig. 11.

www.IndianJournals.com
Members Copy, Not for Commercial Sale
dated 13-Feb-2020

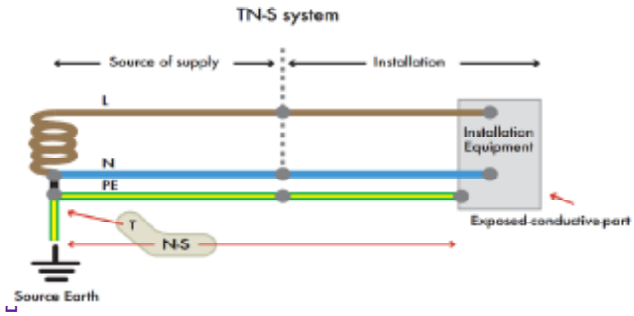


Fig 11 (a) : TN-S Earthing System

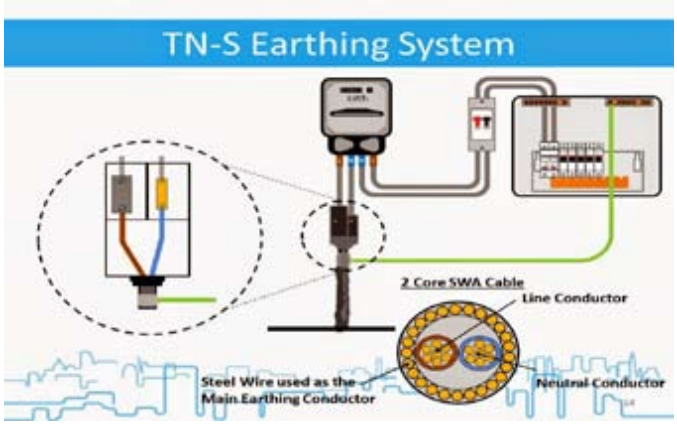


Fig. 11 (b) : TN-S Earthing System

Advantages of TN-S Earthing System

- Earth fault loop impedance is low
- TN-S is the safest system
- Electromagnetic interference is low
- It does not requires earth electrode at site
- TN-S earthing system could work with simple over current protection.

Disadvantages of the TN-S Earthing System

- Low power factor (high inductance of long cable)
- Requires extra equal potential bonding.
- On occurrence of an insulation fault, the short-circuit current is high and may cause damage to equipment or electromagnetic disturbance.

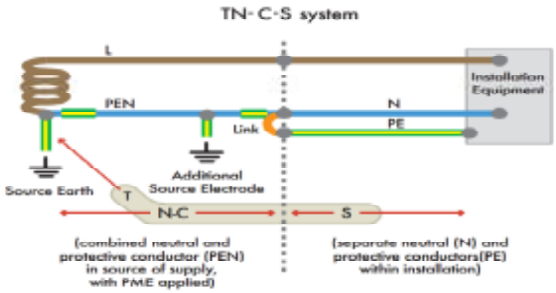


Fig. 12 : TN-C-S Earthing System

6.1.3 *TN-C-S Earthing System*

TN-C-S earthing system has the following features:

- Neutral and protective functions are combined in a single conductor in a part of the TN-C-S system. The supply is TN-C and the arrangement in the installation is TN-S as depicted in Fig. 12.
- Use of a TN-S downstream from a TN-C.
- All exposed conductive parts of an installation are connected to the PEN conductor via the main earthing terminal and the neutral terminal, these terminals being linked together.

This type of distribution is known also as protective multiple earthing and the PEN conductor is referred to as the combined neutral and earth (CNE) conductor. The supply system PEN conductor is earthed at several points and an earth electrode may be necessary at or near a consumer's installation.

Advantages of TN-C-S Earthing System

- This system is a safe system
- This system is less expensive

Disadvantages of the TN-C-S Earthing System

In the TN-C-S system, the TN-C (4 wires) system must never be used downstream of the TN-S (5 wires) system, since any accidental interruption in the neutral on the upstream part would lead to an interruption in the protective conductor in the downstream part and therefore a danger.

6.2 TT Earthing System

In this system, the supply source has a direct connection to earth. All exposed conductive parts of an installation also are connected to an earth electrode that is electrically independent of the source earth as shown in Fig. 13. The fault loop impedance is higher, and unless the electrode impedance is very low indeed.

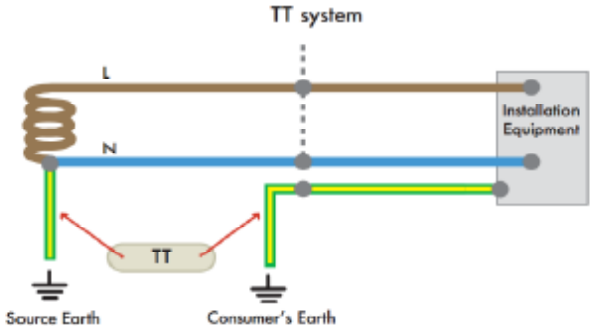


Fig. 13 : TT Earthing System

Advantages of TT System

- No risk of failure and suitable for premises where all AC power circuits are residual current device (RCD) protected.
- Faults in the LV and MV grid do not migrate to other customers in the LV grid.
- Simple earthing of the installation and the easiest to implement.

Disadvantages of the TT Earthing System

- Each customer needs to install and maintain its own ground electrode. Safety and protection depends on the customer, thus complete reliability is not assured.
- High over voltages may occur between all live parts and between live parts and PE conductor.
- Possible overvoltage stress on equipment insulation of the installation.

6.3 IT System Earthing

In this system, the supply source is either connected to earth through deliberately introduced high earthing impedance (Impedance earthed IT system) or is isolated from earth. All exposed conductive parts of an installation are connected to an earth electrode as shown in Fig. 14.

The conductive parts including metal body of the installations are connected to earthed through one or more local earth electrodes. These local electrodes do not have any direct connection to the source. It is pertinent to mention here that single phase IT system shown in Fig. 14 is not used in India.

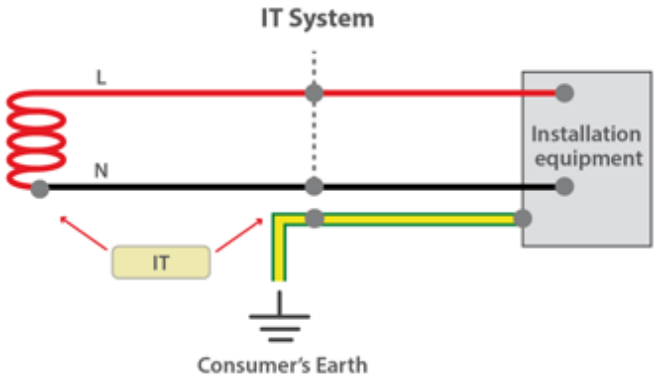


Fig. 14 (a) : IT Earthing System

Advantages of IT System

The main advantages of IT system are the followings;

- It improves the energy availability: this is interesting for applications where a loss of electricity supply can cause a risk to people (in hospitals for example), or a financial risk (for some process in industry).
- It can also eliminate the risks of fire or explosions in case of insulation fault, as the faulty current is very low.
- It will increase electrical device life time, as faulty current is low, it causes less stress on the equipment.
- Finally, it is possible to do preventive maintenance on the IT installation. Through the permanent insulation monitor device, we can detect insulation drops before they become insulation faults.

Disadvantage of IT System

- This system experience repeated arcing grounds.
- Insulation failure occurs during single phase to ground faults.
- Earth fault protection for unearthed system is difficult.
- Voltage due to lightning surges do not find path to earth.

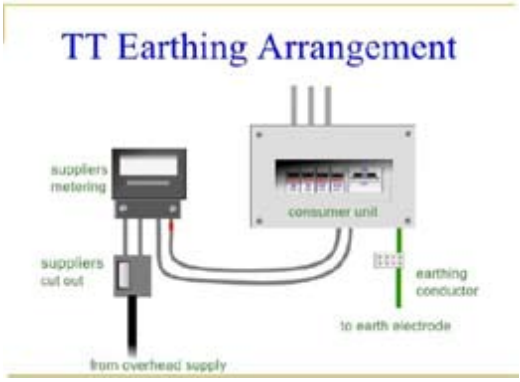


Fig. 14 (b) : IT Earthing System

www.IndianJournals.com
Members Copy, Not for Commercial Sale
Downloaded From IP - 14.139.251.100 on dated 13-Feb-20

7. COMPARISON OF ALL EARTHING SYSTEMS

Comparison of all earthing systems based on earth fault loop impedance, RCD preferred, need earth electrode at site, PE conductor cost, etc. has been carried out as follows (Table 1):

Table 1 : Comparison of all Earthing Systems

EARTHING SYSTEM CONDITIONS	TN-C	TN-S	TN-C-S	TT	IT
1. Earth Fault Loop Impedance (EFLI)	Low	Low	Low	High	Highest
2. RCD Preference	No	Optional	Optional	Yes	N.A.
3. Need of Earth Electrode at Site	No	No	Optional	Yes	Yes
4. PE Conductor Cost	Least	Highest	High	Low	Low
5. Risk of Broken Neutral	Highest	High	High	No	No
6. Safety	Least safe	Safest	Safe	Safe	Less safe
7. Electromagnetic Interference	High	Low	Low	Least	Least
8. Safety risks	Broken neutral	Broken Neutral	Broken neutral	High loop Impedance (step voltages)	Double fault, over voltage

We may also refer the Figure 15 to understand the protection system involved in three types of earthing system.

www.IndianJournals.com
Members Copy, Not for Commercial Sale
Downloaded From IP - 14.139.251.100 on dated 13-Feb-2020

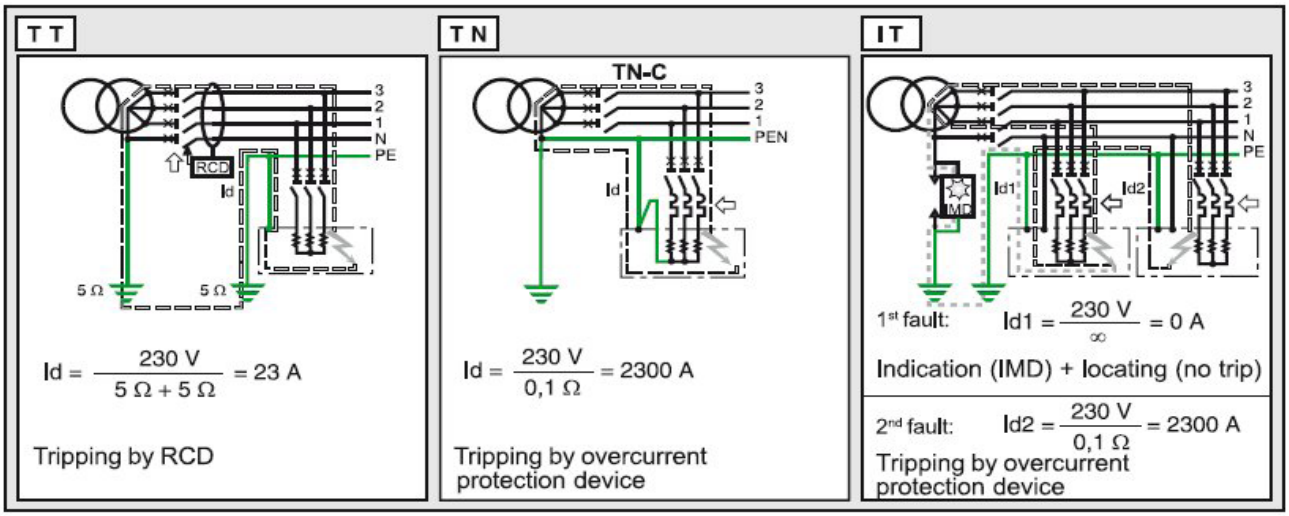


Fig. 15 : Protection Tripping in Different Earthing Systems

8. CONCEPT OF GPR STEP AND TOUCH POTENTIAL

In electrical engineering, earth potential rise (EPR) also called ground potential rise (GPR) occurs when a large current flows to earth through an earth grid impedance. The potential relative to a distant point on the Earth is highest at the point where current enters the ground, and declines with distance from the source. Ground potential rise is a concern in the design of electrical substations because the high potential may be a hazard to people or equipment.

The change of voltage over distance (potential gradient) may be so high that a person could be injured due to the voltage developed between two feet, or between the ground on which the person is standing and a metal object. Any conducting object connected to the substation earth ground, such as telephone wires, rails, fences, or metallic piping, may also be energized at the ground potential in the substation. This transferred potential is a hazard to people and equipment outside the substation. Various dangerous potential which may be encountered in any substation are depicted in Figure 16.

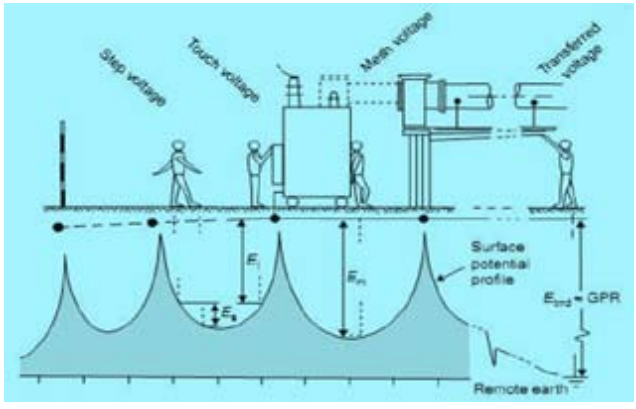


Fig. 16 : Various Dangerous Potentials during Fault

Many factors determine the level of hazard, including: available fault current, soil type, soil moisture, temperature, underlying rock layers, and clearing time to interrupt a fault.

An EPR event at a site such as an electrical distribution substation may expose personnel, users or structures to hazardous voltages. (Figure 17)

An engineering analysis of the power system under fault conditions can be used to determine whether or not hazardous step and touch voltages will develop. The result of this analysis can show the need for protective measures and can guide the selection of appropriate precautions.

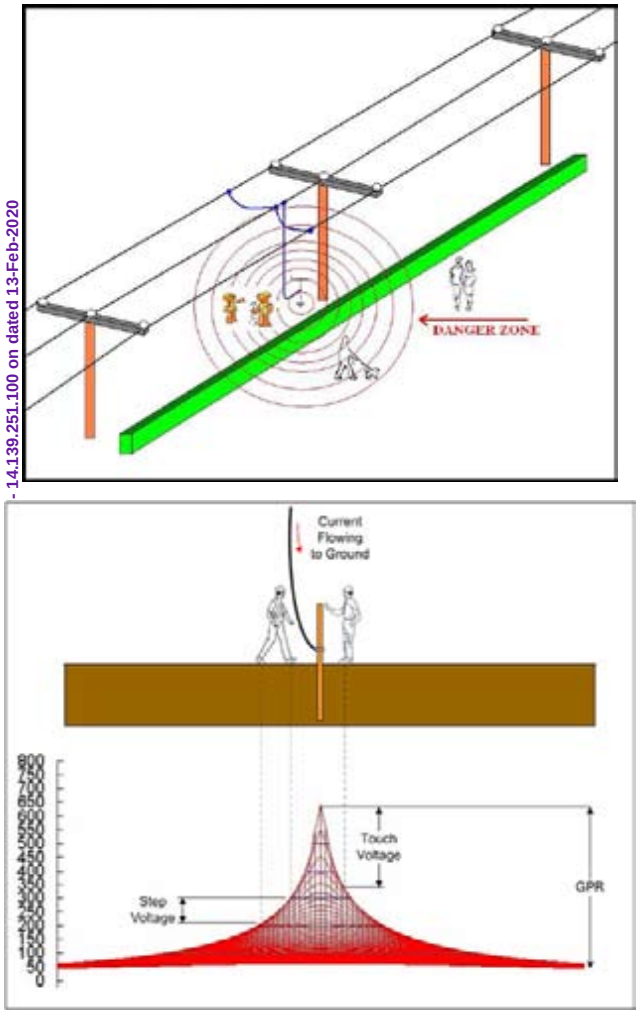


Fig. 17 : Concept of ESP and Danger of Touch & Step Potential

- **Step Potential :** Step potential is the step voltage between the feet of a person standing near an energized grounded object. It is equal to the difference in voltage, given by the voltage distribution curve, between two points at different distances from the electrode. A person could be at risk of injury during a fault simply by standing near the grounding point. (Figure 18)

- **Touch Potential :** Touch potential is the touch voltage between the energized object and the feet of a person in contact with the object. It is equal to the difference in voltage between the object and a point some distance away. The touch potential or touch voltage could be nearly the full voltage across the grounded object if that object is grounded at a point remote from the place where the person is in contact with it. (Figure 18)

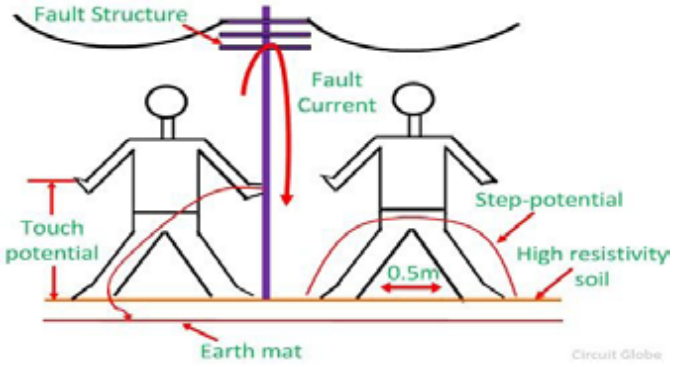


Fig. 18 : Illustrations of Step & Touch Potential

The more current that is pumped into the ground, the greater the hazard. Fault clearing time is an important factor to consider as well. The more time it takes the electric utility company to clear the fault, the more likely it is for a given level of current to cause the human heart to fibrillate.

A few engineers believe that Fibrillation Current for Step Potentials must be far greater than Touch Potentials, as current will not pass through any vital organs in the former case. This is not always true as personnel that receive a shock due to Step Potentials may fall to the ground, only to be hit again, before they can get up, when the automatic re-closers activate.

The impact of step and touch potential may become the cause of deaths of many living stock (animals) also as depicted by Figure 19 .



Fig. 19 : Electrocution of Elephants in the Field

How to Control Hazardous Potentials: Several methods may be used to protect employees from hazardous ground-potential gradients, including equipotential zones, insulating equipment, and restricted work areas.

www.IndianJournals.com
Members Copy, Not for Commercial Sale
- 14.139.251.100 on dated 13-Feb-2020

1. The creation of an equipotential zone will protect a worker standing within it from hazardous step and touch voltages. Such a zone can be produced through the use of a metal mat connected to the grounded object. Usually this metal mat (or ground mesh) is connected to buried ground rods to increase contact with the earth and effectively reduce grid impedance. In some cases, a grounding grid can be used to equalize the voltage within the grid. Equipotential zones will not, however, protect employees who are either wholly or partially outside the protected area. Bonding conductive objects in the immediate work area can also be used to minimize the voltage between the objects and between each object and ground. (Bonding an object outside the work area can increase the touch voltage to that object in some cases, however.)

2. The use of insulating personal protective equipment, such as rubber gloves, can protect employees handling grounded equipment and conductors from hazardous touch voltages. The insulating equipment must be rated for the highest voltage that can be impressed on the grounded objects under fault conditions (rather than for the full system voltage).

3. Workers may be protected from hazardous step or touch voltages by prohibiting access to areas where dangerous voltages may occur, such as within substation boundaries or areas near transmission towers. Workers required to handle conductors or equipment connected to a grounding system may require protective gloves or other measures to protect them from accidentally energized conductors.

In electrical substations, the surface may be covered with a high-resistivity layer of crushed stone or asphalt. The surface layer provides a high resistance between feet and the ground grid, and is an effective method to reduce the step and touch voltage hazard.

9. ELECTROCUTION TRIANGLE & SAFETY EFFECTIVENESS PYRAMID

In substation whenever fault occurs resulting in the flow of heavy current in the grounding system which may pose problems of GPR, step and touch potential in the vicinity. If the grounding system is not adequate may result in the electrocution of the working personal or passerby. The electrocution triangle and effectiveness of electrical safety in any system are depicted in Fig. 20 :

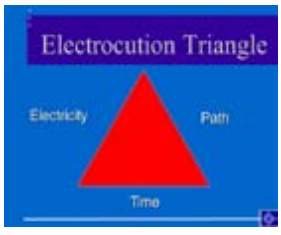




Fig. 20 : Accident Triangle & Pyramid of Prevention of Accidents

The accepted minimum value of body resistance is 500 ohms for electric shock hazard analysis. Although the resistance between hands with dry skin can range from 5,000 to 50,000 ohms, punctured skin reduces the body resistance to about that of salt water which is very low. Voltages above 240 volts readily penetrate dry skin, leaving a small, deep burn.

The maximum safe body current for short periods of time is given by Dalziel's equation of IEEE-80 and is an inverse function of time. Higher currents are permitted for shorter periods of time. Shock durations, or human exposure times for temporary personal protective grounding applications are determined from typical 50/60 Hz power system fault clearing time.

The fault clearing time is based on typical protective relaying and circuit breaker operating time. Plants and switchyards generally are protected by high-speed current differential relays with faster operating times compared to transmission lines employing zone distance relaying.

10. CONCLUSION

When a fault occurs in the distribution system, the current will enter the earth. This heavy fault current will develop hazard potential around earth electrode due to distribution of varying resistivity in the soil near earth electrode. The voltage drop in the soil surrounding the grounding system can present hazards i.e. Step and touch voltage for personnel standing in the vicinity of the grounding system.

Adequate designing of grounding system will help in mitigating or eliminating fire and accident hazard.

It is very important for an electrical engineer to understand the fundamental and importance of grounding system for the safety of staff and installed equipments in the network. Soil resistivity and proper measurement of resistivity & interpretation of results are prime factors for accurate designing of grounding system. Other important factors are fault current, grid current, surface material resistivity

www.IndianJournals.com
Members Copy, Not for Commercial Sale
Downloaded From IP - 103.225.210.10 on dated 3-Feb-2020

and type of protection system play crucial roles in the effective designing of grounding system of substation.

From the information provided in this paper it can be concluded that for LV system

- An improper grounding results in higher potential being created in the equipment that can damage equipment and pose safety threat to working personnel.
- It can delay in clearing of faults that will result in insufficient current flow.
- The dangers of a fire caused by leaking electricity are increased exponentially
- It can cause reduction in the operational efficiency of the machine.

Besides above, the choice of earthing system depends on the priority given to many aspects mentioned in Table 1 by the relevant distribution company and regulatory authority of county.

REFERENCES

1. IEEE Std. 80-2013, IEEE Guide for Safety in AC Substation Grounding, New York, NY: IEEE
2. IEEE: 81: 1983, IEEE Guide for Measuring Earth Resistivity, Ground Impedance, and Earth Surface Potentials of a Ground System
3. Manual on," Grounding of A C Power Systems," Publication No 302, C.B.I.P. New Delhi, Oct. 2007
4. I.S.3043 Indian Standard Code of Practice for Grounding.
5. CEA 'Measures relating to Safety and Electric Supply' and 'Technical Standards for Construction of Electrical Plants and Electrical Lines and Connection to Grid under Regulations 2010.
6. Notes of Zero Sequence Earthing
7. R Kumar, K Bansal, D K Saini, I P S Paul, "Importance and Need of Accurate Modelling of Soil of High Voltage Substation for Optimal Designing of Grounding System", IJEC, 7(1), pp. 29-44, 2015.
8. Books of Power System by V K Mehta and C L Wadhwa.

BIOGRAPHICAL DETAILS OF THE AUTHOR



Dr. Rajesh Kumar Arora obtained the B. Tech. & Master of Engineering (ME) degrees in Electrical Engineering from Delhi College of Engineering, University of Delhi, India in 1999 and 2003 respectively. He completed his Ph.D. in grounding system design from UPES, Dehradun. He is also certified Energy Manager and Auditor. He has worked in 400 kV and 220 kV Substation for more than 14 years in Delhi Transco Limited (DTL). He has also worked as Deputy Director (Transmission and Distribution) in Delhi Electricity Regulatory Commission (DERC) for 03 years and 06 months. He has also given his contribution in the OS department of DTL for more than 2 years and rendered his services in the SLDC of Delhi Transco Limited (DTL) also. Presently he is working in OS (Operation Services) department of DTL. His research interests include high voltage technology, grounding system, protection system, computer application and power distribution automation.

www.IndianJournals.com
Members Copy, Not for Commercial Sale
Downloaded From IP - 14.139.251.100 on dated 13-Feb-2024

Save one unit a day
Keep power cut away

International Journal of Research in Engineering and Innovation (IJREI)
journal home page: http://www.ijrei.com
ISSN (Online): 2456-6934

Influence of processing parameters of friction stir welding on microstructure and mechanical properties of dissimilar aluminum alloys- A review

Husain Mehdi, R.S. Mishra

Department of Mechanical Engineering, Delhi Technological University Delhi, India

Abstract

In this review paper, the effect of friction stir welding (FSW) on the metallurgical and mechanical properties of dissimilar aluminum alloy were studied. The joints were produced by using FSW with varying tool rotation and traverse speeds. The microstructural characterization by scanning electron microscopy equipped revealed a substantial grain refinement and a homogeneous distribution of reinforcement particles in the nugget zone. The grain size of the nugget zone was greatly influenced by weld pitch, as a key indicator to control the amount of heat input, exposure time and cooling rate. Vickers micro-hardness profile across the welding zone revealed a significant difference in micro-hardness among the base metal, heat affected zone, thermo-mechanically affected zone and nugget zone. This review concludes with recommendations for future research directions. ©2019 ijrei.com. All rights reserved.

Keywords: Mechanical Properties, Microstructure, Friction stir welding.

1. Introduction

Automobile and aircraft industries were focusing on weight reduction factor to improve the fuel economy and reduce the environmental pollution. Aluminum alloys attracted all these industries because of their excellent strength to weight ratio and damage tolerance. Joining of dissimilar aluminum alloys has lot of scope in automotive, aircraft and ship building industries. The first challenge within the fusion welding of aluminum alloy is cracking of weld due to solidification [1]. The FSW of AA6061 alloy for mechanical properties, microstructure development and its role on residual stress distribution in the weldment [2]. The Ultimate tensile strength (UTS) and Yield strength (YS) of the friction welded AA6061-T6 alloy joints. UTS and YS are increased with the increase of tool rotational speed, welding speed and tool axial force up to a maximum value and then decreased. Increase in rotational speed and axial force enhances % elongation, but decreased by increasing of welding speed, continuously [3]. The high heat input related to high thermal conductivity and a high coefficient of expansion (approximately twice as that of steel) may lead to severe distortion of elements throughout welding. For some dissimilar aluminum alloy welding, no filler metals exist which will manufacture crack free welds. Even though there is an affordable filler metal choice, one cannot come through satisfactory joint efficiencies. For these reasons, the fusion welding of dissimilar aluminum alloys are challenging one and mostly avoided in industries. Solid state welding processes favors the joining of dissimilar aluminum alloys [4].

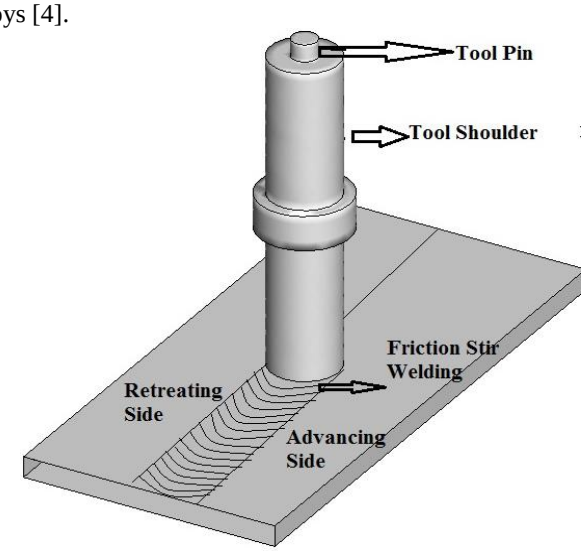


Figure 1: Friction stir welding

Corresponding author: Husain Mehdi
Email Address: husainmehdi4u@gmail.com
https://doi.org/10.36037/IJREI.2019.3612

Among the different solid state welding processes, Friction Stir Welding (FSW) is very attractive because of overcoming the variety of problems like porosity, solidification cracking, formation of brittle intermetallic and segregation. Different combinations of dissimilar aluminum alloys have been successfully welded with excellent joint strength as shown in fig.1. Moreover, FSW process has fascinated lot of researchers due to the potential engineering importance and problems related with conventional welding process.

Compared to many conventional fusion welding methods, the FSW process has the advantages such as good mechanical properties, low residual stress and distortion, and reduced occurrence of defects [5]. This welding technique, attracting an increasing amount of research interest, is applied to the aerospace, automotive, and shipbuilding industries. A thorough understanding of FSW process and the consequent evaluation of weld mechanical properties are needed for production of components and structures. For this reason, detailed researches are required [6]. It is well known that whatever the welding method is the main challenge for the manufacturer is selecting the optimum welding parameters which would produce an excellent welded joint. To predict the optimum welding parameters accurately without consuming time, materials, and labor effort, various methods are available and one such method is response surface methodology (RSM). In order to study the effect of FSW process parameters, most workers follow the traditional experimental techniques, i.e. varying one parameter at a time while keeping others constant. This conventional parametric design of experiment approach is time consuming and calls for enormous resources. Taguchi statistical design is a powerful tool to identify significant factor from many by conducting relatively less number of experiments. However, this design fundamentally does not account for the interaction among processing parameters. In view of cost and time saving, occasionally these interactions can be neglected. If mandatory, the missing interactions can be analyzed by further running the required experiments [7-9].

The mechanical properties of FSW joint are mainly dependent on chemical composition and processing parameters of alloying element. The microstructural analysis of FSW joints shows the formation of new grain size in the weld zone with different amount of heat input by controlling the processing parameter [10-14]. Friction stir welding conserves base material properties from the defects and renders the welds stable during the process of re-crystallization of grains [15]. The process also decreases the size of heat affected zone which is primarily responsible for impairment of the microstructure in conventional fusion welding. The friction stir welding is preferred over fusion welding due to a number of merits [16-19]. Investigations on mechanical failure of the welds have been carried out by several investigators [20−22] and they found that failure can take place in the WN, HAZ or TMAZ regions depending on the amount of heat input, which is usually governed by process parameters such as rotational speed and travel speed. The dependence of weld microstructure on processing parameters has also been revealed [23-24]. Most of these studies have been conducted on plates with thickness less than 10 mm, which are suitable to aerospace industry and currently FSW of aluminum alloys is widely employed in aerospace, shipping and automobile industries. Though it has been established that FSW of thick plates up to 25 mm is definitely possible with 80% joint efficiency [25], several details such as tool geometry and optimum parameters are not published. Variations in microstructures in the through thickness direction were not clearly investigated. As the thickness of the plate to be welded increases, variations in microstructures and properties can be expected which have not been widely investigated in the available literature.

However, there is little information related to FSW of dissimilar aluminum alloy. The present review paper firstly gives a brief description on the FSW process, and the weldability of aluminum alloys. This is followed by a detailed evaluation of a number of critical issues in FSW of dissimilar aluminum alloy focusing on the macrostructure and microstructure, mechanical properties as well as tool wear. Finally, conclusions are drawn with a particular view on future challenges and research directions.

2. Experimental procedure

The materials under investigation were different heat and non-heat treatable dissimilar aluminum alloys. Sheets with different thicknesses were friction stir welded by employing various welding advancing and rotating speeds of the tools, such tools were all threaded ones and they were characterized by different height and shoulder diameter. The welds were performed by employing different tools inclinations. All the sheets were machined before tests in order to eliminate surface in homogeneities. Tensile tests were performed in order to evaluate the mechanical properties obtained in the different welding conditions. The Residual Stresses (RS) were also calculated in longitudinal direction respect to the loading one, by employing the $\sin^2\psi$ method. The RS were measured in longitudinal direction, being the one affecting the crack tip stress field. The tensile tests were carried out at room temperature. Specimens were sectioned in the perpendicular direction to the weld line by employing an electrical discharge machine (EDM), The FSW, in fact, does not produce a symmetric deformation respect to the center line of the advancing tool. Due to such in homogeneities, when a clock wise direction rotation is employed, the less resistant zone results the one on the advancing side of the tool. Due to materials, thicknesses and tool differences they were taken some choices to build the database. The base materials indication come through the hardness. The effect of the tool dimension is indicated into the database through the shoulder diameter/pin height ratio. Revolutionary pitch effect is indicated into the database. A broader discussion is necessary for the indication of the residual stresses, they were measured in different points, for each sheet the distance between the measurement points were equal to the sheet thickness; after the calculation it was calculated the area of the plot residual stress-distance from the weld center, the value of such area, for each experimental condition was used as the indication of the residual stresses effect into the database. The effect of processing parameters on the mechanical properties was underlined through the ration between the FSW properties and base materials ones for yield stress, UTS and elongation (%).

3. Results and Discussions

3.1 Tensile strength

The tensile test results of 10-mm-weld and 16-mm-weld are summarized in Table 3. Compared with unwelded base material, samples transverse to the weld show reductions in strength and elongation. The joint efficiency (based on ultimate tensile strength) of 70% was measured in 10-mm-welds and they were found to fail in 45° shear mode in HAZ of the advancing side (Fig. 2). 16-mm-welds exhibited the joint efficiency of 53% and they were also found to fracture in HAZ of the advancing side in the same mode (Fig. 3) [26].

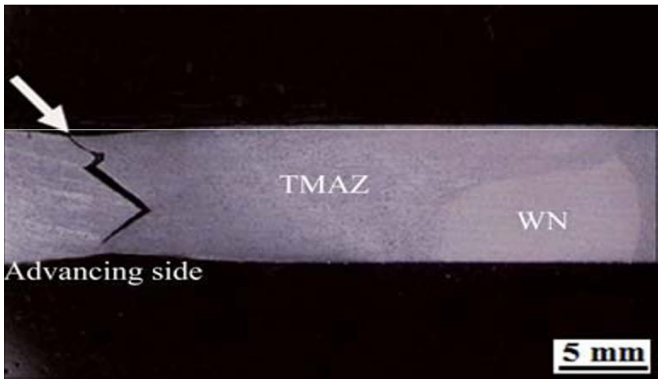


Figure 2: Cross section of fracture surface of tensile-tested 10-mm-welds (arrow shows failure location) [26]

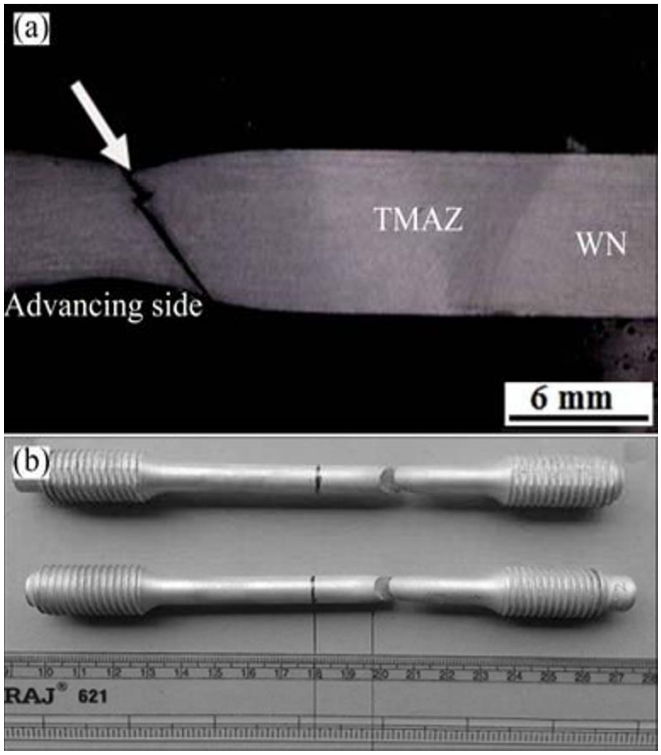


Figure 3: Tensile-tested 16-mm-welds: (a) Cross section of fracture surface; (b) failed specimens [26]

This may be attributed to two reasons: 1) the absence of finer grains, as the grain refinement plays a key role in material strengthening in HAZ; 2) presence of wide precipitate free zones along grain boundaries and partial dissolution of precipitates in the grain interiors in the HAZ, which are considered to be responsible for failure. Tensile failures near HAZ of the advancing side seem to be a common feature in aluminum alloy friction stir welds, as the same was reported in several different aluminum alloys by various researchers [27-29]. Welds made on 10 mm thick plates exhibited superior

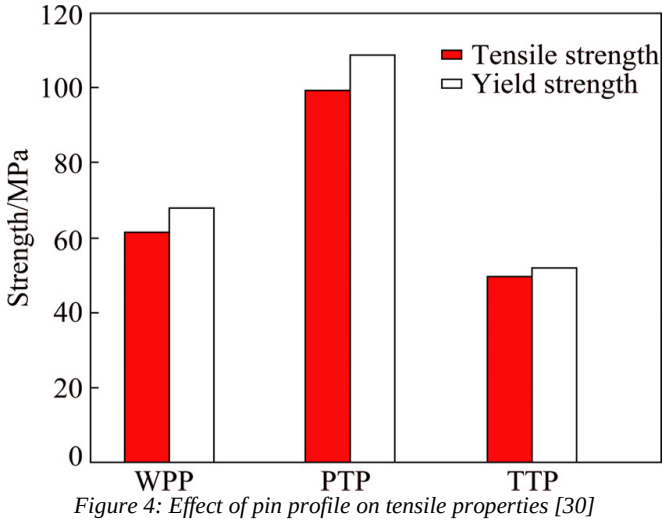


Figure 4: Effect of pin profile on tensile properties [30]

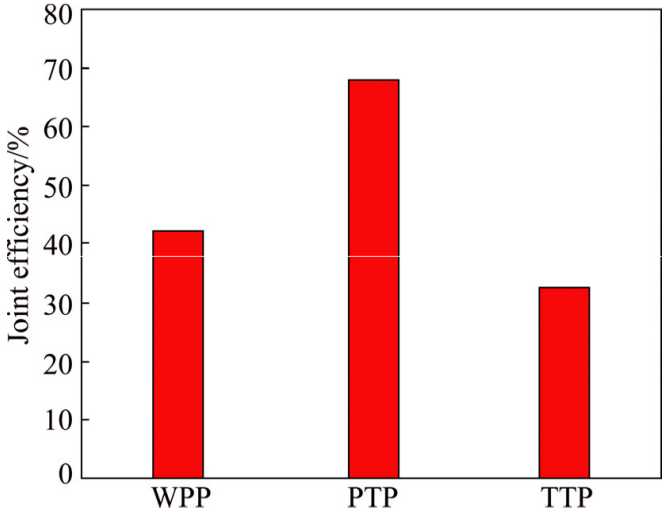


Figure 5: Effect of pin profile on joint efficiency [30]

Fig. 4 and 5 show the tensile properties of the joints fabricated with different pin profiles. Joints were fabricated with whorl pin profile (WPP) pin which resulted in the yield strength of 62 MPa, tensile strength of 69 MPa and joint efficiency of 43 %. Joints fabricated with plain taper pin profile (PTP) pin result in yield strength of 101 MPa, tensile strength of 116 MPa and joint efficiency of 68 %. Joints fabricated with WPP result in yield strength of 50 MPa, tensile strength of 51 MPa and joint efficiency of 32% [30]. Joints fabricated with PTP pin result in

high tensile properties. The degree of ductility can be measured by tensile fracture surface of the dissimilar joints. The WPP pin shows small cleavage-like facets in the fractographs (Fig. 6(a)). Few elongated dimples along with flat featureless surface are observed for the joints made with PTP pin (Fig. 6(b)). The fracture surface of taper treaded pin profile (TTP) pin has high degree of up and down so that it will not be seen clearly in the SEM image (Fig. 6(c)) [30]. Similar to PTP pin, the fractograph shows flat featureless surface. The effect on the mechanical properties of the weld with different tool pin profiles [31].

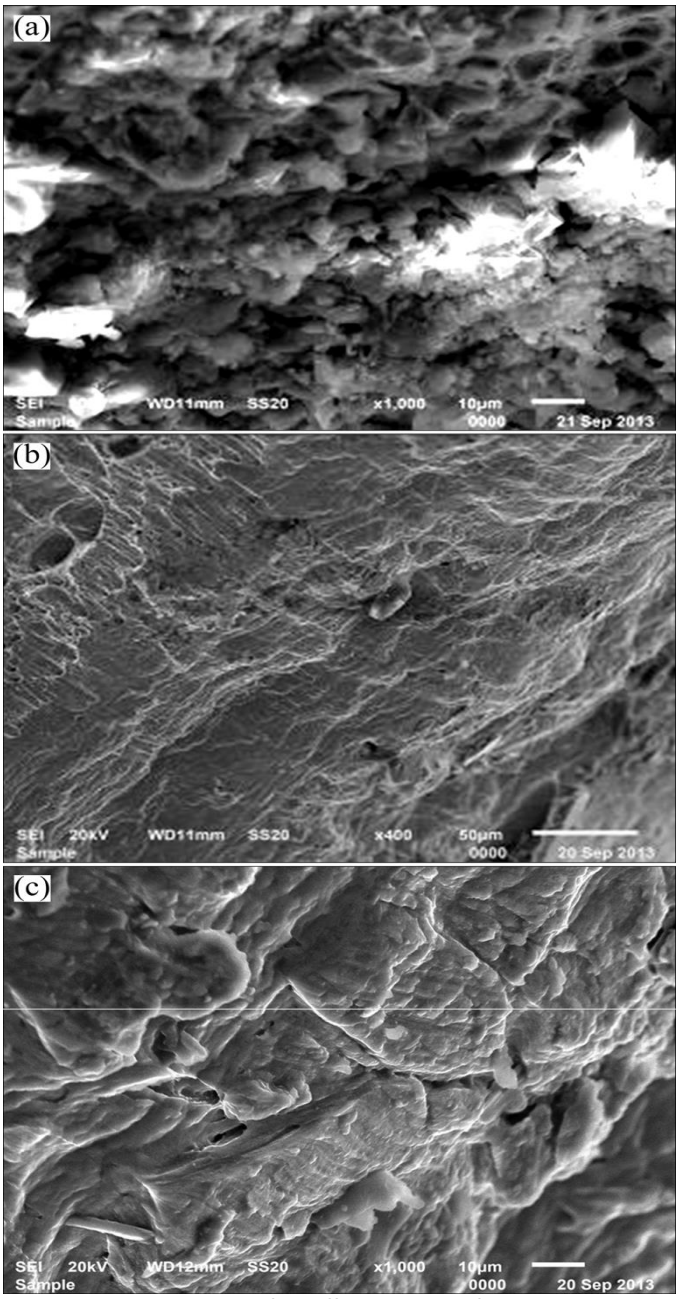


Figure 6: Fractographs for different pin profiles: (a) WPP, (b) PTP, (c) TTP [30]

The mechanical properties of the joints mainly rely upon the volume of deformed material created by the stirring action of the tool pin. The more material the tool stirs, the better the quality of the joints. However, for the joining of dissimilar materials like aluminum and copper, the dynamic to static volume ratio does not play role in deciding mechanical properties. If the amount of material stirring and mixing of material is improved, bulk amount of Cu particle contributes to form the stir zone. Thus, due to the diffusion of Cu and Al, a large amount of intermetallic phases like Al_2Cu and Al_4Cu_9 are formed at the interface and in the stir zone. The higher strength is attributed to the lower intermetallic phases. The reason for the higher bond strength of the lower intermetallic layer thickness is not certain but may be related to a defect content in a smaller volume of intermetallics. The reason behind the higher bond quality for the thin intermetallic layer is identified that there is lower defect content in a smaller volume of intermetallic. Thus, the tensile fracture happened at the interface. The same reason was reported by many researchers [32-34]. The tensile fracture follows the path which has soft or defective region along the weld joints. For the TTP joints, the fracture falls in the defective stir region

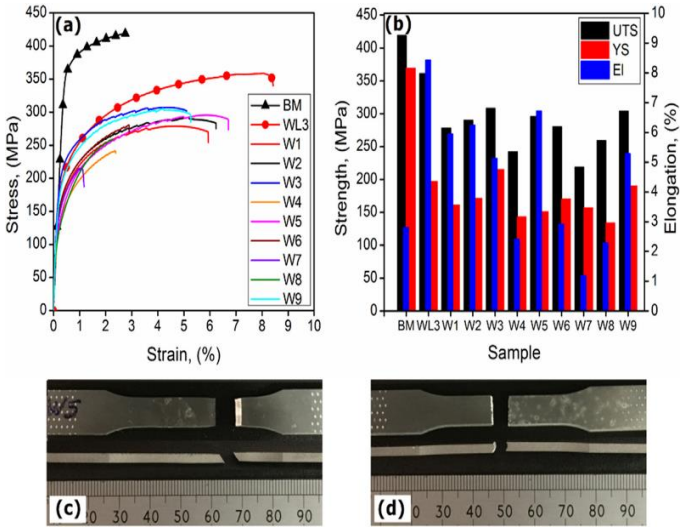


Figure 7: Tensile properties of BM, cross-weld (W1-W9), and longitudinal weld (WL3); (a) stress-strain curves, (b) bar graphs representing strength and % of elongation [35]

Fig. 7, shows the stress-strain curves of the BM, cross-weld (W_1-W_9), and longitudinal weld (WL_3). Their ultimate tensile strength (UTS), yielding stress (YS), and percentage of elongation (% El) are compared in the bar graph (Fig. 7(b)). Note that the cross-weld sample microstructure is heterogeneous as it is consist of four zones, i.e., BM, HAZ, TMAZ and NZ (Fig. 7(c)). Meanwhile, the longitudinal specimen contains only uniform fine equiaxed grains from the NZ. According to the stress-strain curves, the as-received AMC shows a tensile strength of about 419 MPa with a total elongation to failure of around 2.8% [35]. In contrast, the cross-weld samples exhibit a higher ductility with a drop in the tensile strength as compared with BM. The reduction in tensile strength of AMC (AA6061/Al_2O) FSW joints was also

reported by Cavaliere et al. [36]. Furthermore, the stress-strain curve related to BM shows continuous yielding, while most of the welded samples exhibit a distinct yielding serration phenomenon and similar findings have been reported by Mahmoudiniya et al. [37] and Pathak et al. [38]. Judging from Fig. 7(b), the mechanical properties of FSW joints are affected significantly by the welding parameters. It is shown that the joint fabricated at lowest heat input (W3) showing a higher strength (joint efficiency reaches about 75%) with the adequate elongation of around 5%. On the other hand, the joint welded at highest heat input and lower cooling rate (W7) shows a lowest joint strength (joint efficiency of about 52%) with a severe drop in the elongation. Surprisingly, the longitudinal welded samples (WL3) shows smooth curve characterized by a moderate combination between strength and elongation of about 361 MPa (86% joint efficiency), and 8.5% (67% increase in elongation) than the BM, respectively. This can be related to the homogeneous fine grain structure in the entire sample. The location of the fracture in the typically tested samples is shown in Fig. 7((c), and (d)). Under most welding conditions, the FSW joints exhibited shear fracture mode occurred in the HAZ (AS) (see Fig. 7(c)) oriented at an angle of about 45°, as also presented by Moreira et al. [39], because of the loss of strength in this area as observed in the microhardness measurements. However, in W8 FSW joints fracture occurred in the stirring zone (see Fig. 7(d)) [35],

3.2 Micro-hardness

A longitudinal micro-hardness profiling was carried out across all the zones; and it was measured to a depth of 4mm below the surface of the welds. An irregular shape profile was observed in the hardness distribution, as against the conventional W-shape trend due to the difference in the chemical composition of the alloys and the rate of precipitation. The Vickers micro-hardness profiles of welds are shown in Fig.8 for three samples (D_1, D_2 and D_3) after the welding process. The AA7075-T6 and AA6082-T6 parent metals had mean micro-hardness magnitudes of approximately 160HV0.2 and 91HV0.2, respectively [40].

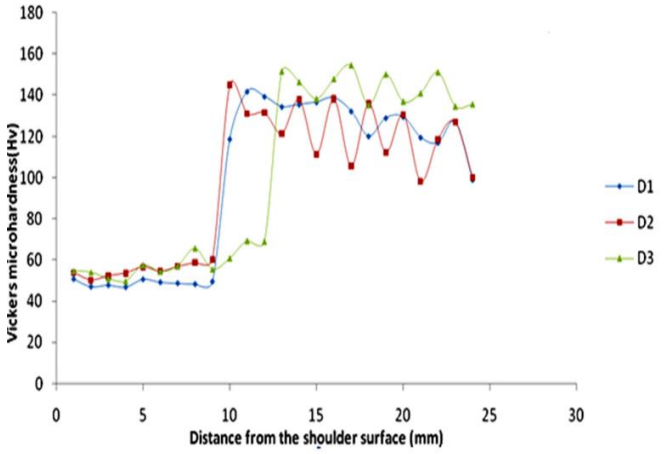


Figure 8: Micro-hardness profile of different samples [40]

As observed, all the welds displayed a unique pattern different from the usual profile. This is because a dissimilar FS weld behaves in a 'dissimilar manner' in response to the loading condition. During FSW of dissimilar welds, the Aluminum alloy 6xxx, the Al-Mg-Si (i.e. Supersaturated solid solution) decomposed through the sequence; GP--β"--β'--β (Mg precipitates through a sequence, as follows SS--GP--η'--($MgZn_2$) [41].

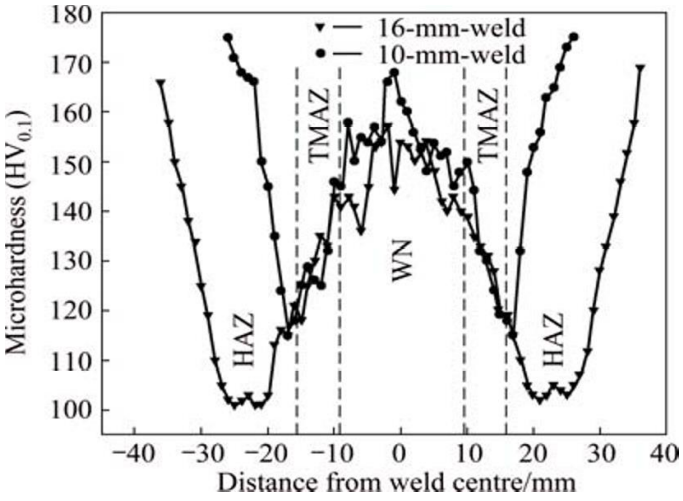


Figure 9: Microhardness profiles of friction stir welds made on 10 mm and 16 mm thick AA7075−T651 plates [26]

Vickers micro-hardness tests were conducted across the weld at middle thickness for both 10-mm-welds and 16-mm-welds, to ascertain the possible microstructure and property variation among various zones of the weldment. The representative hardness distributions are shown in Fig. 9. As it can be seen, both the distributions exhibit "W" shaped appearance, typical of 7xxx series alloys welded under conditions for which the nugget temperature is close to the solution heat treatment temperature. The weld nugget region of 10-mm-weld exhibits hardness which is close to T6 hardness, whereas in 16-mm-weld, the weld nugget hardness is found to be HV 155 (average) though the base plates recorded approximately the same hardness value. It is observed that in case of 10-mm-welds, the lowest hardness values are higher than those observed in 16-mm-welds. Both 10-mm-weld and 16-mm-weld record the lowest hardness values in HAZ on advancing side. Loss in hardness due to the welding process is significantly higher in the case of welds made on 16 mm thick plates, mainly due to the higher heat inputs employed to obtain sound welds [26].

The micro-hardness distributions of samples A and C measured along the mid-thickness of joints at different aging periods after FSW are shown in Fig. 10. The base material AA7075-T6 and AA5086-H32 demonstrated average Vickers micro-hardness values of about HV 165 and HV 86, respectively. The hardness of stir zone varied according to the ratio mix of AA5086 and AA7075 [42].

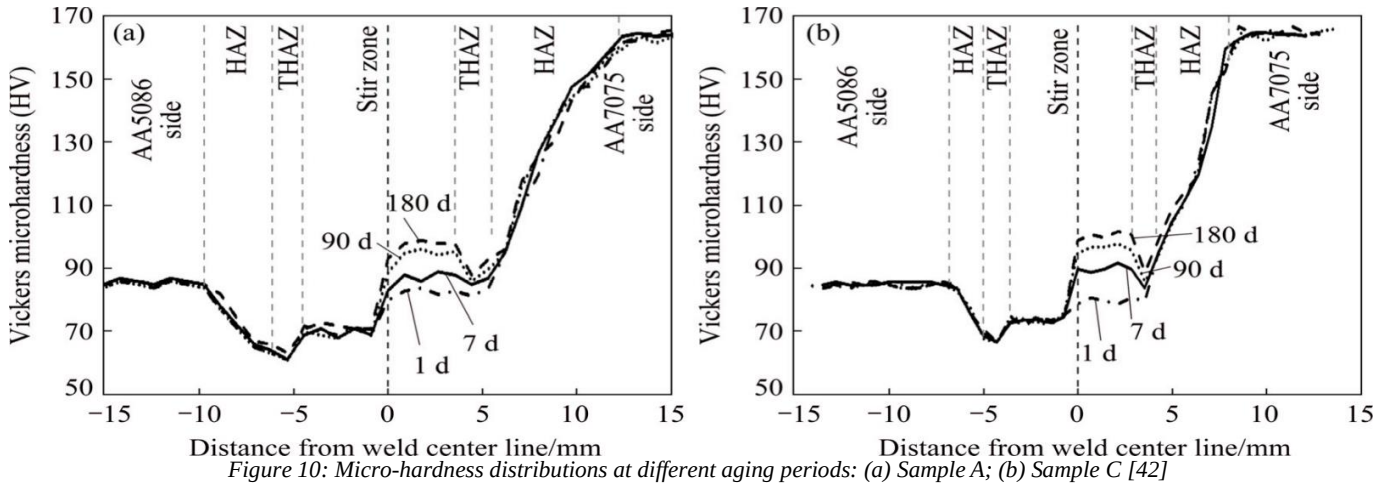


Figure 10: Micro-hardness distributions at different aging periods: (a) Sample A; (b) Sample C [42]

3.3 Microstructure Analysis

Optical microscopic examinations revealed that the processing parameters exhibit significant effects on formation of surface composite layer. When the target depth is too large (2.28 mm), the shoulder of tool pushed away all the preplaced SiC particles, and, basically no surface composite formed. Too small target depth (1.78 mm) was also ineffective to mix SiC particles into aluminum alloy. A target depth of 2.03 mm resulted in incorporation of SiC particles into aluminum matrix. However, the bonding of surface composite layer and substrate plate was influenced by the traverse speed. At higher traverse speed (101.6 mm/min), the surface composite layer was usually separated from the aluminum alloy substrate and the bonding was poor as shown in Fig. 11 [43].

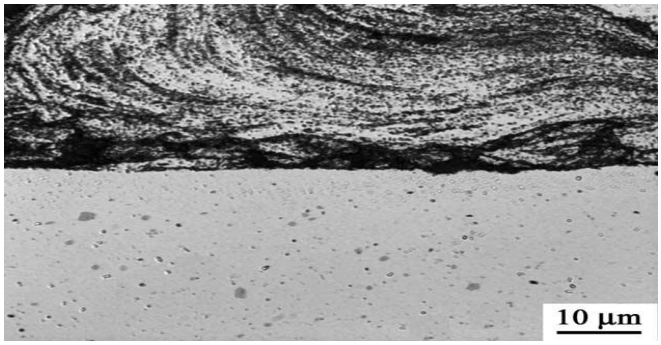


Figure 11: Optical micrograph showing poor bonding between surface composite and aluminum alloy substrate at higher traverse speed (101.6 mm/min)[43]

Fig. 12a shows an optical macrograph of a single pass run cross-section in which a typical basin shaped nugget can be clearly identified. Eutectic Si particles inside the nugget went through a complex material flow and, as a result, were highly refined. The extent of refinement is apparent in Fig. 12b, which shows the interface of the cast and FSPed regions. The size and shape of refined Si particles get clearer in the higher magnification image (Fig. 12c). The typical grain structure of the FSPed nugget is shown in Fig. 12d. The grains were mostly equiaxed; although in a few instances some grains aligned parallel to either the advancing or retreating side [44].

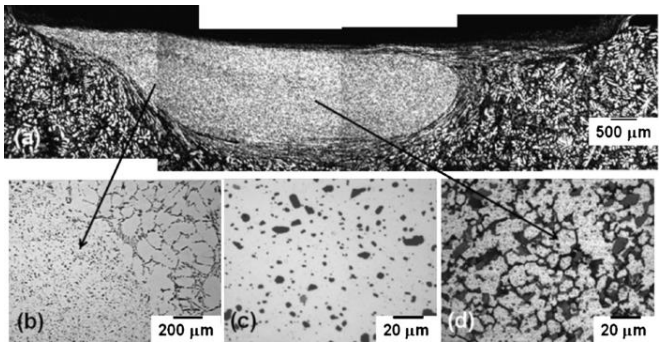


Figure 12: (a) Cross-section optical macrograph of a single pass run, (b) interface between cast and FSPed region showing extent of particle refinement, (c) higher magnification image shows size and shape of Si particles inside the FSPed nugget and (d) grain structure inside the nugget [44].

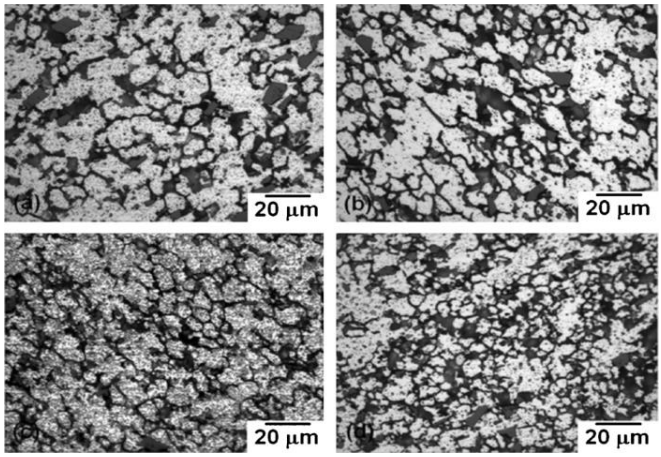


Figure 13: Optical micrographs showing grain structure of the single pass run FSPed nugget at various tool traverse speeds and a tool rotation rate of 2236 rpm: (a) 0.42 mm/s, (b) 0.98 mm/s, (c) 2.33 mm/s, and (d) 3.67 mm/s [44].

Fig. 13a–d shows the grain structure observed in the nugget of single pass runs, which were carried out at various tool travel speeds and a constant tool rotation rate. Higher tool travel speeds resulted in marginal increases in the volume fraction of finer grains [44].

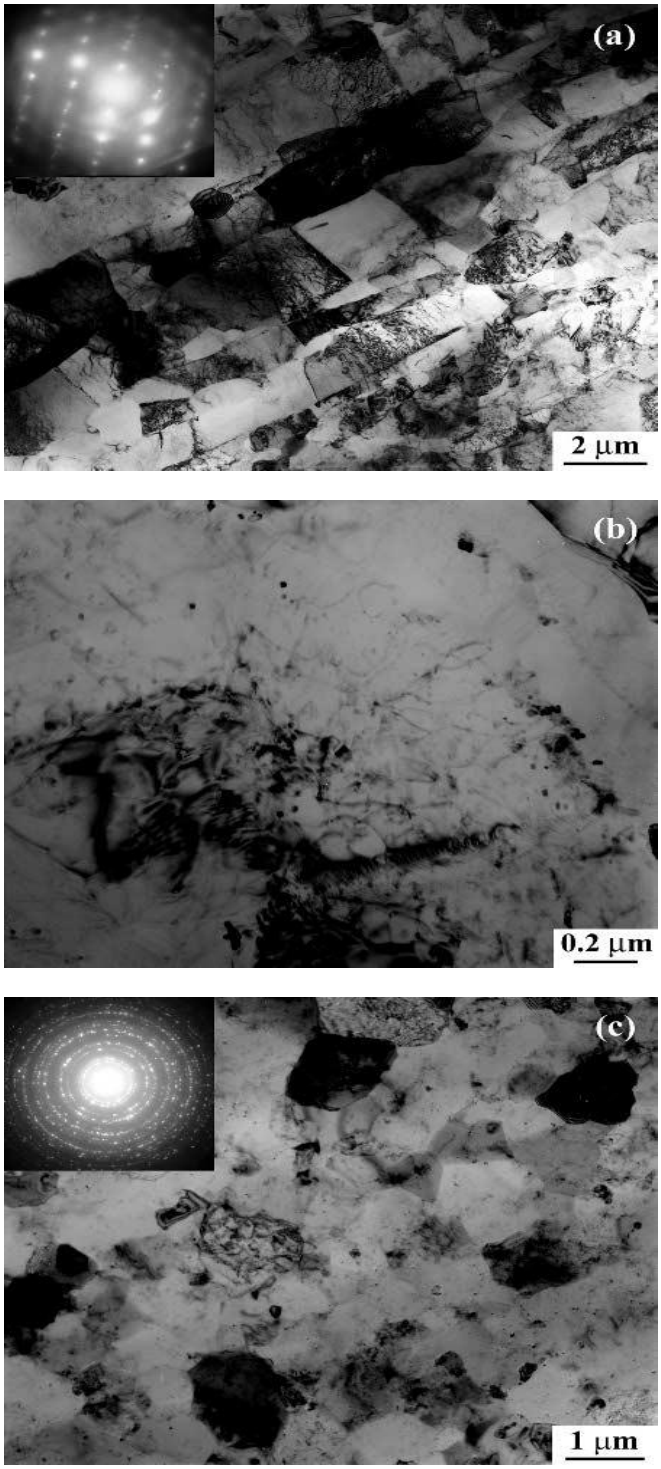




Figure 14: TEM micrographs showing (a) grains in as-extruded Al-4Mg-1Zr, and (b) Al Zr particles in as-extruded Al-4Mg-1Zr, (c) grains in FSP Al-4Mg1Zr and (d) Al_3 Zr particles in FSP Al-4Mg-1Zr

Figures 14(a) and (b) show the microstructure of the as extruded Al-4Mg-1Zr. Two observations can be made. First, the microstructure was characterized by predominantly low angle grain boundaries, with grains/sub grains aligned along the extrusion direction. Second, the grain size was non uniform.

The average sub grain sizes in the directions parallel (d_L) and normal (d_T) to the extrusion direction were determined by the mean linear-intercept technique (sub grain size = 1.78 x the mean linear intercept) to be 1.9 and 1.7 μm (averaging above 250 grains), respectively. Thus, the average sub grain size (d) was determined to be 1.8 μm ($d = (d_L\ d_T)^{1/2}$). The dispersoids in the alloy were determined to be Al Zr by energy-dispersive spectrometry. The average size of Al_3Zr dispersoids was estimated to be 21.7±11.8 nm (averaging 140 dispersoids).

Figures 14(c) and (d) show the microstructure of the FSP zone in the FSP Al-4Mg-1Zr. The bright-field TEM image shows well-defined grain boundaries (Fig.14c). Generally, the FSP microstructure was characterized by uniform and equiaxed recrystallized grains with predominant high-angle boundaries. The average grain size, determined by the mean linear-intercept technique, was 1.5 μm (averaging 123 grains). Compared to the as-extruded alloy (Figure 14d), the FSP Al-4Mg-1Zr exhibited a more uniform distribution of Al Zr dispersoids (Figure 14d). The average size of Al_3Zr dispersoids in the FSP alloy was determined to be 19.5±11.9 nm (averaging 140 dispersoids), which is similar to the as-extruded alloy.

3.4 Fractography

Fracture surfaces of the fatigue samples were evaluated to determine the difference in fracture behavior of as-cast and FSP samples. For as-cast samples, crack initiation was usually associated with casting defects. The crack path was generally rough and uneven indicating that the crack followed defects in the microstructure; see Fig. 15(a) and (b). Fatigue cracks propagated with significant amounts of crack branching and deflection. As seen in Fig. 15(c) and (d), for FSP samples, the fracture surfaces

were almost perpendicular to the longitudinal axis. The crack propagated primarily along the interface between the silicon particles and the aluminum matrix and is characterized by the formation of dimples on the fracture surface [45].

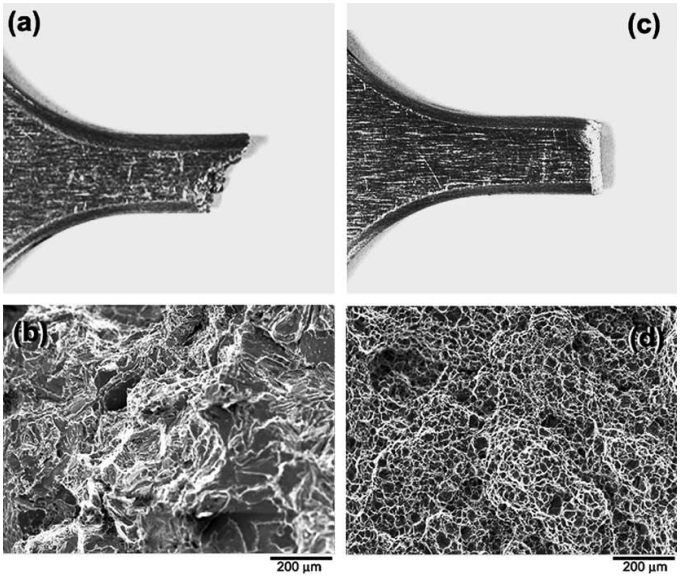


Figure 15: Fracture surfaces of (a) and (b) as-cast specimens, (c) and (d) friction stir processed specimen [45]

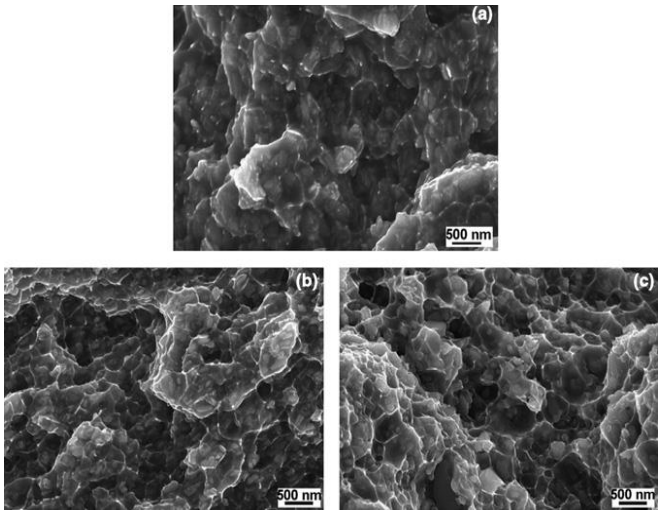


Figure 16: SEM images of fracture surfaces of (a) as-extruded material, (b) weld 1 and (c) weld 2 [46].

Fig. 16 shows the SEM fractographs taken from tensile specimens of the base and the welds tested at room temperature and an initial strain rate of $2x10^{-4}$ s^{-1}. There is a clear difference in the fracture morphology between the as-extruded material and the welds. The as-extruded material shows shallow dimples while the welds show deep dimples with second phase particles present within the dimples [46]. Matrix/particle interfacial debonding was observed in both the as-extruded material and its welds. The ductile fracture of alloys generally occurs by the formation and subsequent growth and coalescence of voids or cavities. If cavity nucleation could be delayed or suppressed, an improvement in ductility could be achieved [47]. For a void to nucleate at the matrix/particle interface, the maximum interfacial normal stress has to exceed the bonding strength of the interface [48-49]. Tszeng [49] investigated the interfacial stresses and void nucleation in discontinuously reinforced Al composite and found that the maximum interfacial normal stress is dependent on the particle shape and the volume fraction of the particles. High aspect ratio particles experience a high peak stress at the matrix/particle interface during the external uniaxial loading and thus void nucleation occurs at an earlier stage of the deformation.

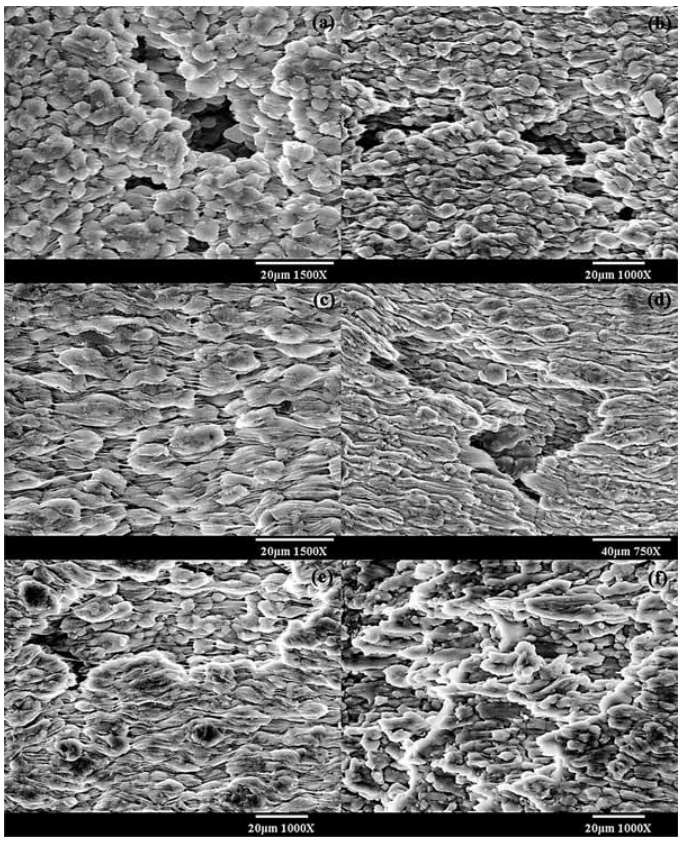


Figure 17: SEM micrographs showing surface morphologies of FSP 3.5 µm-7075Al superplastically deformed to failure at (a) 480^0 C and 1×10^{-1} s^{-1}, (b) 480^0 C and 3×10^{-2} s^{-1} , (c) 480^0 C and 1×10^{-2} s^{-1}, (d) 480^0 C and $3\times10^{-3}$$s^{-1}$, and (e) 470^0 C and 1×10^{-2} s^{-1} ; and fracture surface at (f) 470^0 C and 1×10^{-2} . (Tensile axis is horizontal) [50]

Fig. 17 shows the topography of the 3.8 µm7075Al deformed to failure at 480 and 470^0 C and various strain rates. At a high strain rate of $1\times10^{-1}$$s^{-1}$, grain boundary sliding and cavities induced by the grain boundary sliding were distinctly seen on the deformed specimen surface (Fig. 17a). When the strain rate was decreased to 3×10^{-2} s^{-1}, extensive grain boundary sliding along with somewhat elongated grains was observed (Fig. 17b). Further, some fibers developed between slid grains or on cavities. At a strain rate of 1×10^{-2} s^{-1}, extensive grain boundary sliding, considerable grain elongation, and the development of more fibers between slid grains became increasingly evident (Fig. 17c).

At a low strain rate of 3×10^{-3} s^{-1}, extensive grain boundary sliding and significant grain elongation resulted in the formation of strip or ribbon-like surface topography (Fig. 17d). The topography developed at 470^0C was similar to that at 480^0 C and was characterized by extensive grain boundary sliding and remarkable grain elongation (Fig. 9e). At 470^0 C, no fibers were detected (Fig. 9f) [50].

4. Conclusions

This review aims to outline the current joining of dissimilar aluminum alloy by Friction stir welding with a number of specific issues discussed including the FSW process, the application of weldability of dissimilar aluminum alloys, macro and microstructure, mechanical properties of FSW joint. A solid state welding process, is considered to be potentially a viable route for joining of aluminum alloys. Its potential benefits in cost reduction, joint efficiency improvement, and high production accuracy make it even more attractive for the non-weldable series AA2xxx, AA6xxx and AA7xxx. However, the maturity of using this joining process to weld dissimilar aluminum alloy are still at an early stage in research and has not yet been fully implemented in industry. The mechanical properties of Al-alloys joined by FSW are largely dependent on the combined effect of chemical composition and the FSW processing conditions. Therefore, the mechanical performance of FSW joints should be evaluated accordingly. Early researches showed that FSW is a potential welding process to achieve defect free joints of Al-alloys. There is a clear need for more efforts to understand the effect of FSW on these materials in adequate depth to meet design and production requirements. For instance, there is a need for systematic studies which take into account the effects of reinforcement percentage and types of reinforcement on joint efficiency. More work is needed to understand the performance of FSW joint of such as AA2124 and AA6092 as base matrices for different reinforcement percentages. Also there is a need for joining Al-alloys to other materials rather than monolithic aluminum alloys such as magnesium alloys, a new candidate material for aerospace application.

References

[1] Sevvel P and Jaiganesh V 2015 Effect of tool shoulder diameter to plate thickness ratio on mechanical properties and nugget zone characteristics during FSW of dissimilar Mg alloys Trans. Indian Inst. Met. 68 41–6.

[2] Madhusudhan Reddy, G., P. Mastanaiah, K. Sata Prasad, T. Mohandas. Transactions of the Indian Institute of Metals, 62 (1) (2009) 49-58.

[3] Elatharasan, G., Senthil Kumar, V.S. Procedia Engineering, 64 (2013) 1227 – 1234.

[4] Vishwakarma D K, Kumar N and Padap A K 2017 Modelling and optimization of aging parameters for thermal properties of al 6082 alloy using response surface methodology mater. res. express 4 1–12.

[5] Dawes C J. An introduction to friction stir welding and its development [J]. weld material fabrication, 1995, 63: 2-16.

[6] Thomas W M, Nicholas E D. friction stir welding for the transportation industries [J]. Materials design, 1997, 18: 269-273.

[7] Lee W B. Mechanical properties related to microstructural variation of 6061 Al alloy joints by friction stir welding [J]. Material Transactions, 2004, 45(5): 17001705.

[8] Elangovan K, Balasubramanian V. Influences of pin profile and rotational speed of the tool on the formation of friction stir processing zone in AA2219 aluminum alloy [J]. Journal of Materials Science Engineering A, 2007, 459: 718.

[9] Elangovan K, Balasubramanian V. Effect of tool pin profile and axial force on the formation of friction stir processing zone in AA6061 aluminum alloy [J]. International Journal of Advanced Manufacturing Technology. DOI: 10.1007/s00170-007- 1100-2.

[10] Husain Mehdi, Mishra RS (2016) Mechanical properties and microstructure studies in friction stir welding (FSW) joints of dissimilar alloy—a review. J Achiev Mater Manuf Eng 77(1):31–40 35.

[11] Husain Mehdi, Mishra RS (2017) Infuences of process parameter and microstructural studies in friction stir welding of diferent alloys: a review. Int J Adv Prod Ind Eng 509:55–62 36.

[12] Husain Mehdi, Mishra RS (2017) Mechanical and microstructure characterization of friction stir welding for dissimilar alloy—a review. Int J Res Eng Innov 1(5):57–67 37.

[13] Husain Mehdi, Mishra RS (2018) Analysis of material fow and heat transfer in reverse dual rotation friction stir welding: a review. Int J Steel Struct. https://doi.org/10.1007/s13296-018-0131-x.

[14] Husain Mehdi, Mishra, R.S. Study of the influence of friction stir processing on tungsten inert gas welding of different aluminum alloy. SN Appl. Sci. 1, 712 (2019) doi:10.1007/s42452-019-0712-0.

[15] Thomas WM, Nicholas ED, Needham JC, et al. Friction stir butt welding. International patent no 1991. PCT/GB92/02203.

[16] Chao YJ, Qi X. Thermal and thermo-mechanical modeling of friction stir welding of aluminium alloy 6061–T6. J Mater Process Manuf Sci. 1998;7(2):215–233

[17] Rao D, Heerens J, Alves Pinheiro G, et al. On characterisation of local stress-strain properties in friction stir welded aluminium AA 5083 sheets using micro-tensile specimen testing and instrumented indentation technique. Mater Sci Eng A. 2010;527(18–19):5018–5025.

[18] Amancio-Filho ST, Sheikhi S, Santos JF, et al. Preliminary study on the microstructure and mechanical properties of dissimilar friction stir welds in aircraft aluminium alloys 2024- T351 and 6056-T4. J Mater Process Technol. 2008;206(1–3):132–142.

[19] Threadgill PL, Leonard AJ, Shercliff HR, et al. Friction stir welding of aluminium alloys. Int Mater Rev. 2009;54(2):49–93.

[20] Peel M, Steuwer A, Preuss M, Withers P J. Microstructure, mechanical properties and residual stresses as a function of welding speed in aluminum AA5083 friction stir welds [J]. Acta Materialia, 2003, 51: 4791−4801.

[21] Reynolds A P, Lockwood W D, Seidel T U. Processing- property correlation in friction stir welds [J]. Materials Science Forum, 2000, 331−337: 1719−1724.

[22] Liu H J, Fujii H, Maeda M, Nogi K. Tensile properties and fracture locations of friction-stir-welded joints of 2017–T351 aluminum alloy [J]. Journal of Materials Processing Technology, 2003, 142: 692−696.

[23] Yang B, Yan J, Sutton M A, Reynolds A P. Banded microstructure in AA2024−T351 and AA2524−T351 aluminum friction stir welds: Part I. Metallurgical studies [J]. Materials Science and Engineering A, 2004, 364: 55−65.

[24] Hassan K A A, Norman A F, Prangnell P B. The stability of the nugget zone grain structure in AA7010 alloy friction stir welds during solution treatment [J]. Materials Science Forum, 2002, 396−402: 1549−1554.

[25] Prime M B, Gnäupel-Herold T, Baumann J A, Lederich R J, Bowden D M, Sebring R J. Residual stress measurements in a thick, dissimilar aluminum alloy friction stir weld [J]. Acta Materialia, 2006, 54: 4013−4021.

[26] T. Srinivasa Rao, G. Madhusudhan Reddy, S. R. Koteswara Rao, Microstructure and mechanical properties of friction stir welded AA7075−T651 aluminum alloy thick plates, Trans. Nonferrous Met. Soc. China 25(2015) 1770−1778.

[27] Mahoney M W, Rhodes C G, Flintoff J G, Spurling R A, Bingel W H. Properties of friction-stir-welded 7075 T651 aluminum [J]. Metallurgical and Materials Transactions A, 1998, 29: 1955−1964.

[28] Peel M, Steuwer A, Preuss M, Withers P J. Microstructure, mechanical properties and residual stresses as a function of welding speed in aluminum AA5083 friction stir welds [J]. Acta Materialia, 2003, 51: 4791−4801.

[29] Reynolds A P, Lockwood W D, Seidel T U. Processing- property correlation in friction stir welds [J]. Materials Science Forum, 2000, 331−337: 1719−1724.

[30] M. Felix Xavier Muthu, V. Jayabalan, Effect of pin profile and process parameters on microstructure and mechanical properties of friction stir welded Al-Cu joints, Trans. Nonferrous Met. Soc. China 26(2016) 984−993.
[31] Elangovan K, Balasubramanian V, Valliappan M. Influences of tool pin profile and axial force on the formation of friction stir processing zone in AA6061 aluminium alloy [J]. International Journal of Advanced Manufacturing Technology, 2008, 38: 285−295.
[32] Rattana, Borrisutthekul, Taisei, Yachi, Yukio, Miyashita, Yoshiharu, Mutoh. Suppression of intermetallic reaction layer formation by controlling heat flow in dissimilar joining of steel and aluminium alloy [J]. Material Science and Engineering A,2007, 467: 108−113
[33] Kim Y G, Fujii H, Tsumura T, Komazaki T, Nakata K. Three defect types in friction stir welding of aluminum die casting alloy [J]. Materials Science and Engineering A, 2006, 415: 250−254.
[34] Venkateswaran P, Reynolds A P. Factors affecting the properties of friction stir welds between aluminum and magnesium alloys [J]. Materials Science and Engineering A, 2012, 545: 26−37.
[35] Omar S. Saliha, Hengan Oua, Xingguo Weib, W. Suna, Microstructure and mechanical properties of friction stir welded AA6092/ SiC metal matrix composite, Materials Science & Engineering A 742 (2019) 78–88.
[36] P. Cavaliere, E. Cerri, L. Marzoli, J. Dos Santos, Friction stir welding of ceramic particle reinforced aluminium based metal matrix composites, Appl. Compos. Mater. 11 (2004) 247–258.
[37] M. Mahmoudiniya, A.H. Kokabi, S. Kheirandish, L.A. Kestens, Microstructure and mechanical properties of friction stir welded ferrite-martensite DP700 steel, Mater. Sci. Eng.: A (2018).
[38] N. Pathak, K. Bandyopadhyay, M. Sarangi, S.K. Panda, Microstructure and me- chanical performance of friction stir spot-welded aluminum-5754 sheets, J. Mater. Eng. Perform. 22 (1) (2013) 131–144.
[39] P.M.G.P. Moreira, A.M.P. de Jesus, A.S. Ribeiro, P.M.S.T. de Castro, Fatigue crack growth in friction stir welds of 6082-T6 and 6061-T6 aluminium alloys: a com- parison, Theor. Appl. Fract. Mech. 50 (2) (2008) 81–91.
[40] S.T. Azeez a, E.T. Akinlabi, Effect of processing parameters on microhardness and microstructure of a double-sided dissimilar friction stir welded aa6082-t6 and aa7075-t6 aluminum alloy, Materials Today: Proceedings 5 (2018) 18315–18324.
[41] Lorimer, G. W., and Nicholson, R. B., 1966. Further results on the nucleation of precipitates in the Al-Zn-Mg system. Acta Metallurgica, 14(8), 1009-1013.
[42] Jamshidi Aval Hamed, Effect of welding heat input and post-weld aging time on microstructure and mechanical properties in dissimilar friction stir welded AA7075−AA5086, Trans. Nonferrous Met. Soc. China 27(2017) 1707−1715.
[43] R.S. Mishra, Z.Y. Ma, I. Chari, Friction stir processing: a novel technique for fabrication of surface composite, Materials Science and Engineering A341 (2003) 307-310.
[44] S. Jana , R.S. Mishra, J.A. Baumann, G. Grant, Effect of process parameters on abnormal grain growth during friction stir processing of a cast Al alloy, Materials Science and Engineering A 528 (2010) 189–199.
[45] S.R. Sharma, Z.Y. Ma, R.S. Mishra, Effect of friction stir processing on fatigue behavior of A356 alloy, Scripta Materialia 51 (2004) 237–241.
[46] Y. Wang, X.L. Shi, R.S. Mishra, T.J. Watson, Friction stir welding of devitrified Al–4.0Y–4.0Ni–0.9Co alloy produced by amorphous powders, Scripta Materialia 56 (2007) 971–974.
[47] Good SH and Brown IM, the nucleation of cavities by plastic deformation, Acta Metallurgica 27 (1979)1-15.
[48] G. Le Roy, J.D. Embury, G. Edward, M.F. Ashby, Acta Metall. 29 (1981) 1509.
[49] Tszeng TC, Interfacial stresses and void nucleation in discontinuously reinforced composites, J Eng Mater Technol. 122 (2000) 86-92.
[50] Z.Y. Ma, R.S. Mishra, M.W. Mahoney, Superplastic deformation behaviour of friction stir processed 7075Al alloy, Acta Materialia 50 (2002) 4419–4430.

Cite this article as: Husain Mehdi, R.S. Mishra, Influence of processing parameters of friction stir welding on microstructure and mechanical properties of dissimilar aluminum alloys- A review, International Journal of Research in Engineering and Innovation Vol-3, Issue-6 (2019), 465-474. *https://doi.org/10.36037/IJREI.2019.3612*

Innovative Way of Understanding Test Results Obtained by DGA Test of Power Transformers Based on IEEE & IEC Standards

Dr. Rajesh Kumar Arora
Delhi Transco Limited

ABSTRACT

The transformer, being a key element in the transmission and distribution of electrical energy, improving its reliability is of utmost importance. System abnormalities, loading, switching and ambient condition normally contributes towards accelerated aging and sudden failure. Hence, it is, all the more essential, to employ continuous monitoring techniques and on-site diagnostics followed by quality maintenance for having trouble-free and reliable operation with minimum outages. This paper provides an overview of the latest condition monitoring, diagnosis technologies and detail of DGA testing & its interpretation using innovative method as per IEEE and IEC standards.

Keywords *: Dissolved Gases Analysis (DGA), Power Transformer, Transformer Oil Sampling, TDCG (Total Dissolved Combustible Gases)*

www.IndianJournals.com
Members Copy, Not for Commercial Sale
Downloaded From IP - 14.139.251.100 on dated 13-Feb-2020

Fig.1: Power Transformer in Substation

1. INTRODUCTION

Following are the major components, which have a direct bearing on reliability of the transformers:

1. Winding and electrical circuit,
2. Core and clamping structure,
3. Bushings and external connections,
4. Tap chargers,
5. Coolers and cooling medium,
6. Control and supervisory equipment

The transformers are in general classified into following categories from the condition point of view:-

1. **Normal**- When the transformer is *normal*, no action is required since there is no evidence of degradation.
2. **Aged and Normal**- ***Normal aged*** transformer cannot be totally defect free but it is usually taken as acceptable.
3. **Defective**- transformer gradually deteriorates more unless remedial action is carried out.
4. **Faulty-** may or may not be possible to improve condition by remedial action.
5. **Failed**- transformer cannot be kept in service. Remedial action is required before the transformer can be returned to service.

2. OVERVIEW OF CONDITION MONITORING & ONLINE/OFF-LINE DIAGNOSTICS TECHNIQUES

There is an increasing need for power utilities to use assets to their fullest while maintaining system reliability. Transformers, which have exceeded their design life or are approaching the end of their operating life, require all the more attention as compared to new transformers. The maintenance engineers are seriously reviewing their O & M procedure in order to:-

(a) Prevent forced outages,

(b) Incur less maintenance cost, and

(c) Have longer life of equipment.

To assess the extent of deterioration within the transformer, it is necessary to employ the appropriate diagnostic tool. Earlier techniques were:-

1. ***tan delta/Insulation*** resistance measurement of winding/bushing

2. monitoring of oil/winding temperature
3. fault gas analysis
4. Checking of BDV of oil.

Later on, ***Dissolved Gas Analysis*** and ***Furan analysis*** of oil were added and proved to be effective tools in the condition monitoring of transformers. However, presently, due to the marked improvement of technology, following additional diagnostic tests have been included for condition assessment of transformers, which have saved power transformers from undergoing major damages:

1. Partial Discharge Measurement (PDM),
2. Frequency Response Analysis (FRA),
3. Recovery Voltage Measurement (RVM),
4. Thermo vision Measurements.

Transformer operates under complex environmental conditions and variable thermal and electrical stresses during service. Therefore, premature failure of transformer may take place. Detection of faults in transformers at an early stage has advantages. It can prevent incipient faults from developing into major faults and avoid irreparable damage of the transformer. It has been observed that analysis of dissolved gases in oil is a reliable diagnostic tool by which fault at an early stage (***incipient fault***) can be detected. Dissolved gas analysis (DGA) is now a proved technique since last three decades.

DGA as one of the most powerful tools in this area being used by almost every utility in our country with many interpretation techniques like key gas method, Duval triangle method, Rogers ratio method etc.

www.IndianJournals.com
Members Copy, Not for Commercial Sale
Downloaded from IP - 24.19.22.130 on Wed Jul 17 2019 at 14:52:00 (UTC)

3. INCIPIENT FAULTS AND FAULTS GASES

Gases which are produced by the degradation of oil as a result of elevated temperatures may be caused by several factors as severe overloading, lighting, Switching transients, Mechanical flaws, Chemical decomposition of oil or insulation, overheated areas of the windings and Bad connections which have a high contact resistance. Gases that are produced in transformer oil can be divided into three groups as follows:

1. Hydrocarbon & Hydrogen	**2. Carbon Oxides**	**3. Non Fault Gases**
1. Methane (CH_4) **2.** Ethane (C_2H_6) **3.** Ethylene (C_2H_4) **4.** Acetylene (C_2H_2) **5.** Hydrogen (H_2)	**6.** Carbon monoxide (CO) **7.** Carbon dioxide (CO_2)	**8.** Nitrogen (N_2) **9.** Oxygen (O_2)

The generations of gases in oil by some typical fault in transformer active part modes are shown in Table 1. The temperature at which these gases are produced is given in Figure 2.

Table 1: Gas content in oil & Possible faults

Sl. No.	Types of Fault	Decomposable gases in transformer oil
1	Overheat of oil	CH_4, C_2H_4, H_2, (C_2H_6, C_2H_2)
2	Arcing in oil	H_2, C_2H_2, (CH_4, C_2H_4)
3	Overheat of solid insulating materials	CO, CO_2, (H_2, C_2H_4)
4	Overheat of oil and paper combination	CH_4, C_2H_4, CO, CO_2, H_2
5	Arcing of oil and paper combination	H_2, C_2H_2, CO, CO_2, (C_2H_4)

( ) shows gas contents which appear rarely

Fig. 2: Gas Generation Chart for Transformer Oil

4. DISSOLVED GAS ANALYSIS (DGA)

DGA has become a very popular technique for the monitoring the overall health of a transformer. By analyzing oil sample for dissolved gas content it is possible to assess the condition of the equipment and detecting faults at any early stage. Dissolved gas analysis like a blood test or a scanner examination of the human body it can warn about an impendent problem, give an early diagnosis, and increase the chances of finding the appropriate cure. So this technique is a very efficient fault diagnostic technique for transformer and lots of approaches have emerged to analyze the results.

Fig. 3: Oil Sampling of Power Transformer

The increasing in DGA not only indicates to the fault inside the transformer, but also to insufficient cooling system. The gases in oil tests commonly evaluate the concentration of hydrogen (H_2), methane (CH_4), acetylene (C_2H_2), ethylene (C_2H_4), ethane (C_2H_6), carbon monoxide (CO), carbon dioxide (CO_2), nitrogen (N_2) and oxygen (O_2). Oil sampling from power transformer is shown in Figure 3.

www.IndianJournals.com
Members Copy, Not for Commercial Sale
Downloaded From IP - 14.139.251.100 on dated 13-Feb-2020

Fig. 4: Collection of Oil from Sample Bottle for DGA Test

Method of collection of oil from sample bottle for DGA test and filling of oil in the testing kit for DGA are shown in Figure 4 & 5 respectively.

Data from DGA can:

1. Gives advance warning of developing faults
2. Assists in monitoring the rate of fault development
3. Assists in Confirming the presence of faults
4. Allows checks on new and repaired units
5. Assists the convenient scheduling of repairs.
6. Allows the monitoring of units under temporary overload.

The earliest possible detection of gases is required for the fault gas analysis technique to be successful. ***The following methods are used for detecting fault gases***:

1. Direct measurement of the amount of combustible gas in the ***gas space*** or relay (Total Combustible Gas -TCG).
2. Direct measurement of the amount of combustible gas dissolved in the oil (gas-in-oil monitors - TDCG).
3. Chromatographic separation and analysis for the individual components in a gas mixture extracted from a sample of the transformer oil or a sample of the transformer gas space.

Fig. 5: Filling of Oil in the Testing Kit for DGA

5. EVALUATION OF TRANSFORMER CONDITION USING INDIVIDUAL AND TDCG CONCENTRATIONS

It can be difficult to determine whether a transformer is behaving normally if it has no previous dissolved gas history. Also, considerable differences of opinion exist for what is considered a “normal transformer” with acceptable concentrations of gases.

A four-level criterion has been developed to classify risks to transformers, when there is no previous dissolved gas history, for continued operation at various combustible gas levels. The criterion uses both concentrations for separate gases and the total concentration of all combustible gases.

CONDITION 1: TDCG below this level indicates the transformer is operating satisfactorily (see Table 2). Any individual combustible gas exceeding specified levels should prompt additional investigation.

CONDITION 2: TDCG within this range indicates greater than normal combustible gas level. Any

individual combustible gas exceeding specified levels should prompt additional investigation.

CONDITION 3: TDCG within this range indicates a high level of decomposition. Any individual combustible gas exceeding specified levels should prompt additional investigation.

CONDITION 4: TDCG exceeding this value indicates excessive decomposition. Continued operation could result in failure of the transformer. Proceed immediately and with caution.

NOTE 1 – Table 2 assumes that no previous tests on the transformer for dissolved gas analysis have been made or that no recent history exists. If a previous analysis exists, it should be reviewd to determine if the situation is stable or unstable.

NOTE 2 – An ASTM round-robin indicated variability in gas analysis between labs. This should be considered when having gas analysis made by different labs.

Table 2 lists the dissolved gas concentrations for the individual gases and TDCG for Condition 1 through Condition 4. This table is used to make the original assessment of a gassing condition on a new or recently repaired transformer or is used if there are no previous tests on the transformer for dissolved gases or if there is no recent history. Users of this guide are advised that the dissolved gas concentrations contained in Table 2 are consensus values based on the experiences of many companies. The transformer operator may decide to use different dissolved gas concentrations for the individual gases (particularly acetylene) and TDCG based on engineering judgment and experience with other similar transformers.

Table 2 : Condition Assessment Based on TDCG

www.IndianJournals.com
Members Copy, Not for Commercial Sale
Downloaded From IP - 14.139.251.100 on dated 13-Feb-2020

6. OTHER METHODS OF INTERPRETATION OF DGA TEST

Insulating oils under abnormal electrical or thermal stress breakdown and liberate small quantity of gases. The composition of these gases is dependent upon type of fault. By means of DGA, it is possible to distinguish faults such as partial discharge (corona), overheating, and arcing in a great variety of oil filled equipment. DGA can give early diagnosis ad increase the chances of finding the appropriate cure. There are many methods of Interpretation of DGA test discussed below:-

The diagnostic theories based upon the thermal degradation principles employ an array of ratios of certain key combustible gases as the fault type indicators. These five ratios are:

Ratio 1 (R1) = CH_4/H_2

Ratio 2 (R2) = C_2H_2/C_2H_4

Ratio 3 (R3) = C_2H_2/CH_4

Ratio 4 (R4) = C_2H_6/C_2H_2

Ratio 5 (R5) = C_2H_4/C_2H_6

Evaluations of these ratio or gases are done through various methods for detecting possible faults which are detailed here after:

1.1 Evaluation by the Doernenburg Ratio Method

The method utilizes gas concentrations from which Ratios 1, 2, 3, and 4 are calculated.

The values for these gases are first compared to special concentrations—L1 in Table 3—to ascertain whether there really is a problem with the unit and then whether there is sufficient generation of each gas for the ratio analysis to be applicable. Then the ratios in the order Ratio 1, Ratio 2, Ratio 3, and Ratio 4 are compared to limiting values, providing a suggested fault diagnosis as given in Table 4. Table 4 gives the limiting values for ratios of gases dissolved in the oil and gases obtained from the transformer gas space or gas relay.

The step-by-step application of the Doernenburg ratio method for gases extracted from the transformer oil and gases obtained from the gas space or gas relays are as follows:

Step 1: Gas concentrations are obtained by extracting the gases and separating them by chromatograph.

Step 2: If at least one of the gas concentrations [in microliters/liter (ppm)] for H_2, CH_4, C_2H_2, and C_2H_4 exceeds twice the values for limit L1 (see Table 3) and

one of the other two gases exceeds the values for limit L1, the unit is considered faulty; proceed to Step 3 to determine validity of the ratio procedure.

Step 3: Determining validity of ratio procedure: If at least one of the gases in each ratio R1, R2, R3, or R4 exceeds limit L1, the ratio procedure is valid; otherwise, the ratios are not significant, and the unit should be resampled and investigated by alternate procedures.

Step 4: Assuming that the ratio analysis is valid, each successive ratio is compared to the values obtained from Table 4 in the order R1, R2, R3, and R4.

Step 5: If all succeeding ratios for a specific fault type fall within the values given in Table 4, the suggested diagnosis is valid.

Table 3: Limit Concentrations of dissolved gas for Doernenburg Method

Key Gas	Concentrations L1 [µL/L (ppm)]
Hydrogen (H_2)	100
Methane (CH_4)	120
Carbon monoxide (CO)	350
Acetylene (C_2H_2)	1
Ethylene (C_2H_4)	50
Ethane (C_2H_6)	65

6.2 Evaluation by the Rogers Ratio Method

The Rogers ratio method follows the same general procedure as the Doernenburg method, except only three ratios (R1, R2, and R5) are used. The validity of this method is based on correlation of the results of a much larger number of failure investigations with the gas analysis for each case.

Table 5 gives the values for the three key gas ratios corresponding to suggested diagnoses (cases). These ratios, according to Rogers, are applicable to both gases taken from the gas space (or relay) and gases extracted from the oil. The fault types (cases) given in Table 5 have been chosen by combining some cases from the number of fault types originally suggested by Rogers.

6.3 Evaluation by the Key Gas Method

The preceding discussion of the dependence on temperature of the types of oil and cellulose decomposition gases provides the basis for the qualitative determination of fault types from the gases that are typical, or predominant, at various temperatures. These significant gases and proportions are called “key gases.” Figure shown below indicates these “**key gases**” and relative proportions for the four general fault types.

1. **Thermal – Oil** : Decomposition products include ethylene and methane, together with smaller quantities of hydrogen and ethane. Traces of

www.IndianJournals.com Members Copy, Not for Commercial Sale Downloaded From IP - 14.139.251.120 on date 03-Feb-2020

Table 4: Ratios for key gases – Doernenburg

S. No	Suggested fault diagnosis	R1 CH_4/H_2	R2 C_2H_2/C_2H_4	R3 C_2H_2/CH_4	R4 CH_4/H_2
1	Thermal decomposition	>1.0	<0.75	<0.3	>0.4
2	Partial discharge (low-Intensity PD)	<0.1	NS	<0.3	>0.4
3	Arcing (high-intensity PD)	>0.1 to <1.0	>0.75	>0.3	>0.4

Table 5: Roger Ratios

S. No	Case	R2 C_2H_2/C_2H_4	R1 CH_4/H_2	R5 C_2H_2/CH_4	Suggested fault diagnosis
1	0	<0.1	>0.1 to <1.0	<0.1	Unit normal
2	1	<0.1	<0.1	<0.1	Low-energy density arcing-PD
3	2	0.1 to 3.0	0.1 to 1.0	>0.3	Arcing-High-energy discharge
4	3	<0.1	>0.1 to <1.0	0.1 to 3.0	Low temperature thermal
5	4	<0.1	<0.1	0.1 to 3.0	Thermal < 700^0C
6	5	<0.1	<0.1	>0.3	Thermal > 700^0C

acetylene may be formed if the fault is severe of involves electrical contacts.

Principle Gas : Ethylene

2. **Thermal – Cellulose:** Large quantities of carbon dioxide and carbon monoxide are evolved from overheated cellulose. Hydrocarbon gases, such as methane and ethylene, will be formed if the fault involves and oil-impregnated structure.

Principals Gas – Carbon Monoxide

3. **Electrical – Partial discharge**: **Low – Energy** electrical discharges produce hydrogen and methane, with small quantities of ethane and ethylene. Comparable amount of carbon monoxide and carbon dioxide may result from discharges in cellulose.

Principal Gas – Hydrogen

4. **Electrical – Arcing :** Large amount of hydrogen and acetylene are produced, with minor quantities of methane and ethylene. Carbon dioxide and carbon monoxide may also be formed if the fault involves cellulose. Oil may be carbonized.

Principal Gas – Acetylene

Figure 6 gives pictorial view of key gases method below.

6.4 Evaluation by Duval Triangle Method

The Duval Triangle diagnostic method for oil-insulated transformers was first developed in 1974 by Michel Duval of Hydro Quebec's Institute of Research (IREQ). This method has been proved to be accurate and dependable over many years and is now becoming popular for the fault diagnosis.

In this method uses three hydrocarbon gases only (C_2H_2, C_2H_4 and CH_4). These three gases correspond to the increasing levels of energy necessary to generate gases in transformers in service. The Triangle method is indicated in Figure 7.



Fig. 7: Duval Triangle Method of Interpretation of DGA Test Result

www.IndianJournals.com
Members Copy, Not for Commercial Sale
Downloaded From IP - 139.167.30.101 Downloaded on 03-Feb-2020

Fig. 6 : Key Gases Method of Interpretation of DGA Test Result

Triangle coordinates

% C2H2 = 100x / (x + y + z);
% C2H4 = 100y / (x + y + z);
% CH4 = 100z / (x + y + z);

With x = [C2H2]; y = [C2H4]; z = [CH4] in ppm

In addition to the 6 zones of individual faults mentioned (PD, D1, D2, T1, T2 or T3), an intermediate zone DT has been attributed to mixtures of electrical and thermal faults in the transformer.

6.5 Evaluation By IEC Gas Ratios Method

This method is based on the use of three basic gas ratios:

1. C_2H_2/C_2H_4 (R_2) 2. CH_4/H_2 (R_1) 3. C_2H_4/C_2H_6 (R_5)

Table 6: Abbreviations for IEC Gas Ratio Method

PD	Partial discharges
D1	Discharges of low energy
D2	Discharges of high energy
T1	Thermal fault, t < 300°C
T2	Thermal fault, 300°C < t < 700°C
T3	Thermal fault, t > 700°C

Table 7 applies to all types of equipment, with a few differences in gas ratio limits depending on the specific type of equipment.

Some overlap between faults D1 and D2 is apparent in table 6(B), meaning that a dual attribution of D1 or D2 must be given in some cases of DGA results. The distinction between D1 and D2 has been kept, however, as the amount of energy in the discharge may significantly increase the potential damage to the equipment and necessitate different preventive measures.

Note – Combinations of gas ratios which fall outside the range limits of Table 7 and do not correspond to a characteristic fault of this table may be considered a mixture of faults, or new faults which combine with a high background gas level.

7.0 INNOVATIVE WAY TO ANALYSE THE POSSIBLE FAULT

It is not less than a challenge for substation engineer to get proper interpretation of the DGA test result because this test decides the health of power transformer installed in the substation or system to certain extent. The same challenge was felt by author so an initiative was taken to develop some computer program which may help engineers to determine the health of the power transformer. After a lot of efforts a simple program RPDHT (Rajesh Arora Program for Determination of Heath of Transformer) has been developed which will give the possible fault in the transformer using all the available DGA interpretation method on the one sheet as shown in figure 8 below. This will definitely help the engineers to take decision for further action to save guard the power transformers, in case results are not satisfactory / beyond permissible limits.

Fig. 8: RPDHT Program for Interpretation of DGA Test Result

Table 7: DGA Interpretation Table for IEC Gas Ratio Method

S. No	Case	Suggested fault diagnosis	R2 C_2H_2/C_2H_4	R1 CH_4/H_2	R5 C_2H_2/CH_4
1	PD	Partoa; doscjarges	NS	>0.1	<0.2
2	D1	Discharges of low energy	>1	0.1-0.5	<1
3	D2	Discharges of high energy	0.5-2.5	0.1 -1	>2
4	T1	Thermal fault t<3000C	NS	>1but NS	<1
5	T2	Thermal fault 300^0 C< t<700^0C	<0.1	<1	1-4
6	T3	Thermal fault t > 700^0C	<0.2	<1	<4
		*NS=Non-significant whatever the value			

www.IndianJournals.com Members Copy, Not for Commercial Sale Downloaded From IP - 14.99.21.100 on dated 13-Feb-2020

10. CONCLUSION

The most important part of DGA test for power transformer is the accurate analysis and determination of possible fault in the transformer. Every method for interpretation of DGA has some limitations. To get the picture of all possible faults suggested by each method are available on the same table just a click away. This may simplify the work of transformer expert group / committee to arrive at a decision in respect to health of heart of any substation i.e. power transformer.

REFERENCES

1. IEEE C57.104 – 2008 Guide for the Interpretation of Gases Generated in Oil-Immersed Transformers.
2. IEC 60599 -Mineral oil-impregnated electrical equipment in service – Guide to the interpretation of dissolved and free gases analysis.
3. IS–10593-2008 Mineral Oil-Impregnated Electrical Equipment in Service – Guide to the Interpretation of Dissolved and Free Gases Analysis.

BIOGRAPHICAL DETAILS OF THE AUTHOR

Dr. RAJESH KUMAR ARORA obtained the B. Tech. & Master of Engineering (ME) degrees in Electrical Engineering from Delhi College of Engineering, Delhi, India. He completed his PhD in grounding system design from UPES, Dehradun, India. He is also certified Energy Manager and Auditor.

He has experience of more than 25 years in the different areas of power sector. His research interests include high voltage technology, grounding system, protection system, computer application in power system and power distribution automation. He has presented many papers in the national and international seminars or conferences. He has written articles for many leading magazines.

Presently he is working as Manager (Tech) in the operational services department of DTL.

www.IndianJournals.com
Members Copy, Not for Commercial Sale
Downloaded From IP - 14.139.251.100 on dated 13-Feb-2020

LIGHT UP YOUR OWN LIFE
BY
LIGHTING UP ANOTHER'S

This article has been accepted for publication in a future issue of this journal, but has not been fully edited. Content may change prior to final publication. Citation information: DOI 10.1109/TIA.2020.2968834, IEEE Transactions on Industry Applications

Modeling of Mutually Coupled Switched Reluctance Motors Based on Net Flux Method

Siddharth Mehta, *Student Member, IEEE,* Md Ashfanoor Kabir, *Member, IEEE,* Iqbal Husain, *Fellow, IEEE* and Prerit Pramod, *Senior Member, IEEE*

***Abstract*—Modeling and accurate estimation of mutual flux in switched reluctance motors are complex due to inter-phase flux interactions, magnetic saturation, and harmonics. The mutual flux contributes significantly towards torque production of mutually coupled switched reluctance motors (MCSRMs); therefore, their accurate modeling directly influences the control design. In this work, a net flux based machine model is proposed to model MCSRMs. The model utilizes dual-phase excitation and multi-phase excitation methods to generate the flux look-up tables (LUTs) from the finite element model of the MCSRM. The modeling process is simple as it does not require the segregation of the self and mutual flux components and machine performance can be predicted accurately using the net flux. The proposed modeling method is validated by implementing it for a fully-pitched and concentrated-wound MCSRM and evaluating accuracy against the finite element method. Details of the developed model are presented along with its comparison with existing methods. A prototype of a fully-pitched MCSRM has been built and the model is validated experimentally. Results show that the proposed model has excellent accuracy even under saturated operating conditions.**

***Index Terms*—Mutually coupled SRM, lookup table, torque prediction, torque ripple, machine modeling, mutual flux**

I. Introduction

SWITCHED reluctance motors (SRMs) are known for their simple structure, robust performance, and low construction cost. However, these motors have inherent shortcomings such as high torque ripple and structural vibrations, which makes them unsuitable for high-performance applications [1]. Even though the design and construction of SRM are simpler than permanent magnet (PM) topologies, but the complexity and difficulty faced in the control and modeling of SRM compensate the former. Their nonlinear flux characteristics, high sensitivity to rotor positions, unbalanced single-phase excitation and asymmetric half-bridge converter make the control and modeling process of SRM strenuous [2].

Mutually coupled switched reluctance motors (MCSRMs) can eliminate certain issues related to conventional SRMs while retaining their simplicity and robustness. MCSRMs utilize mutual inductance for the torque production [3], but self-inductance may or may not be utilized for torque production depending on the winding layout and the design of the stator and rotor teeth [4]–[6]. MCSRMs can be operated using unipolar [7] and bipolar excitations [8]. The focus in this work is on the MCSRMs with balanced trapezoidal bipolar excitation. Unlike conventional SRM, the three-phase windings of MCSRMs are connected in a Y configuration. This helps in driving the MCSRM using a conventional two step voltage source inverter (VSI) [8]. With at least two phases conducting at any time, MCSRMs allow improved utilization of magnetic material, and improved torque density and torque per unit copper loss as compared to SRMs. Hence, in the case of MCSRMs, both the electric and magnetic circuit utilization is improved [6].

The highly nonlinear nature of MCSRM requires a detailed machine model while developing the controller. To expedite the controller development process for MCSRMs, it is necessary to build a simple, fast, and accurate machine model that can reduce the dependency on the finite element (FE) model based coupled simulations. Similar to SRMs, MCSRMs also have a dependency on the rotor position, and the flux and torque characteristics are functions of multiple phase currents; this complicates the modeling process. Without a fast and accurate model, the only way to develop a high-performance controller is to depend on FE based machine model which is computationally time intensive [9]. To overcome these issues of MCSRMs, an accurate, simple, and fast model is developed in this work for MCSRMs that can utilize standard VSIs with balanced currents [10].

Prior works on MCSRM modeling include its analytical modeling based on magnetic circuit analysis predicting the flux linkage [11], [12]. However, the estimated flux for certain rotor positions deviates from the FE model and will result in inaccurate torque estimations. Hence, these models are not suitable for optimizing current profiles [13] for high-performance operations or for designing current controllers that require high fidelity machine models [2]. For the modeling of reluctance motors, look-up tables (LUTs) based models have been presented for both SRMs and MCSRMs [7], [14], [15]. For real-time controller implementation, LUTs are favorable as their execution in a digital signal processor (DSP) is less time consuming than analytical equations comprising of logarithmic, trigonometric or exponential functions [16]. LUT based models are preferred for SRMs and MCSRMs as the estimated motor parameters will be accurate and the implementation will be simple and fast. However, LUTs have

This work was supported by the ABB Distinguished Professorship and Nexteer Automotive Corporation funding for research on electric machines and drives at the FREEDM Center.

S. Mehta and I. Husain are with the Department of Electrical and Computer Engineering, North Carolina State University, Raleigh, NC 27606 USA (e-mail:smehta5@ncsu.edu; ihusain2@ncsu.edu).

M. A. Kabir is with the ABB Inc. US Corporate Research (e-mail: ashfanoor.kabir@us.abb.com).

P. Pramod is with the Research and Development department of Nexteer Automotive Corporation, Saginaw, Michigan, USA (email: prerit.pramod@nexteer.com).

0093-9994 (c) 2019 IEEE. Personal use is permitted, but republication/redistribution requires IEEE permission. See http://www.ieee.org/publications_standards/publications/rights/index.html for more information.

This article has been accepted for publication in a future issue of this journal, but has not been fully edited. Content may change prior to final publication. Citation information: DOI 10.1109/TIA.2020.2968834, IEEE Transactions on Industry Applications

the disadvantage of large memory requirements.

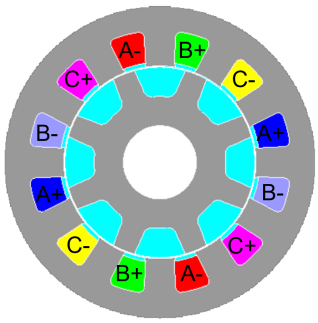
In [17], a model for the fully-pitched MCSRM is developed where the phase flux is estimated from the pole flux. However, this modeling method requires the transformation matrix to be non-singular and the model may not be valid for different winding configurations and different number of phases. Wasi et al. in [7] presented a modeling technique for unipolar excited MCSRMs based on [14]. Their model separates mutual and self-inductances to predict the performance, which is the conventional approach. This separation is difficult and the approximations become a major source of error. The inaccuracies occur since the mutual inductance calculations do not consider simultaneous current conduction in two phases. A LUT based dq model of MCSRM has been presented in [15] that requires 3D tables in addition to post processing of data by performing Fast Fourier Transform (FFT) which increases computational time and complexity. After performing FFT, there are two different 3D LUTs corresponding to the phase and magnitude which complicates the implementation of the model.

In this work, a new LUT based modeling technique is developed for MCSRMs that considers magnetic saturation as well as all the magnetic non-linearities. The model requires dual-phase and multi-phase excitation based flux extraction methods to improve accuracy, especially under saturated condition. This modeling technique considers the net flux linkage of a phase to predict the performance; hence, there is no requirement to separate the self and mutual flux linkage components [10].

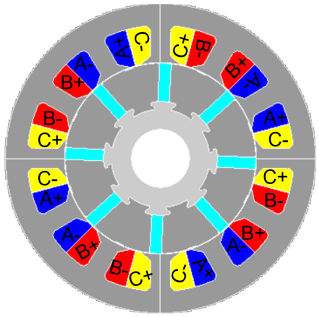
The proposed model eliminates the need for relying on FE models in optimizing model-based current controllers and can be utilized to obtain optimal current profiles to reduce torque ripple. The objective of this work is to develop a simple machine model that utilizes 2D LUTs with minimal use of 3D LUTs, and yet, still able to meet the same level of accuracy as that of an FE model at different operating conditions. The model developed in this work is primarily focused on MCSRMs that are operated using balanced bipolar currents excited. The topologies of MCSRMs considered in this research are shown in Section II. The process of extracting flux from the FE model and the description of the Net Flux Method (NFM) is discussed in Section III and IV, respectively. Set up of the machine model is illustrated in Section V with simulation and experimental results in Section VI and VII, respectively.

II. Mutually Coupled SRM Topologies

Two different topologies of 12 stator slots, 8 rotor poles (12/8) MCSRM are considered in this work as presented in Fig. 1; the motor parameters are given in Table I. The first one is a fully-pitched MCSRM (FP-MCSRM) and as the name suggests, the stator has windings extended over the full pole pitch [8]. The second topology considered is an MCSRM with fractional slot-concentrated windings, referred to as FrS-MCSRM, that has concentrated stator windings [18], similar to a conventional SRM. In FP-MCSRM, generally the width of the stator and rotor teeth are of the same size, or nearly the same to reduce the variation in self-inductance with respect to



(a)



(b)

Fig. 1. Finite element models of (a) FP-MCSRM and (b) FrS-MCSRM.

TABLE I
Parameters of MCSRMs

Parameter	FP-MCSRM	FrS-MCSRM
Rated Power (H.P.)	1	1
Rated Torque (Nm)	7.4	7.4
Base Speed (RPM)	1000	1000
DC Link Voltage (V)	60	60
Phase Resistance (Ω)	0.51	0.34
Rated Current (A)	10	8.5

the rotor position [8]. Hence, there would be minimal contribution of self-inductance to torque production. The maximum torque production is contributed from the variation of mutual flux. However, in the case of FrS-MCSRM [18], both self and mutual flux contribute significantly to torque production.

Unlike a conventional SRM that depends on self-inductance variation for torque production, an FP-MCSRM mostly depends on its mutual inductance variation to produce torque. In contrast, in the case of FrS-MCSRM, both self and mutual flux contribute significantly towards torque production and this topology can be considered as a hybrid of an SRM and an FP-MCSRM. Both the topologies are considered to validate the NFM model. The self and mutual inductance for both the topologies are shown in Fig. 2.

III. Flux Linkage Extraction Methods

The accuracy and simplicity of this model are dependent on how easily flux can be extracted from the FE model. Typical current shapes of a three phase MCSRM are shown in Fig. 3. It can be observed that the sum of the phase currents at any instant is always zero. Based on the balanced bipolar excitation pattern of an MCSRM, the operating regions can be divided

0093-9994 (c) 2019 IEEE. Personal use is permitted, but republication/redistribution requires IEEE permission. See http://www.ieee.org/publications_standards/publications/rights/index.html for more information.

This article has been accepted for publication in a future issue of this journal, but has not been fully edited. Content may change prior to final publication. Citation information: DOI 10.1109/TIA.2020.2968834, IEEE Transactions on Industry Applications

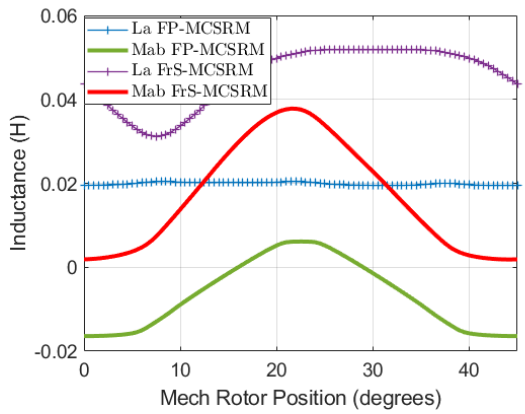


Fig. 2. Self (L_a) and mutual (M_{ab}) inductances for FP-MCSRM and FrS-MCSRM.

into a normal conduction period and a commutation period. Only two phases operate during the normal conduction period but all three phases conduct in the commutation period. For the development of this model, it is assumed that the current controller has a high enough bandwidth such that the current in the third phase can be regulated at 0 A during the normal conduction period at any operating condition. To model this machine, each conduction period is dealt with separately and is explained below.

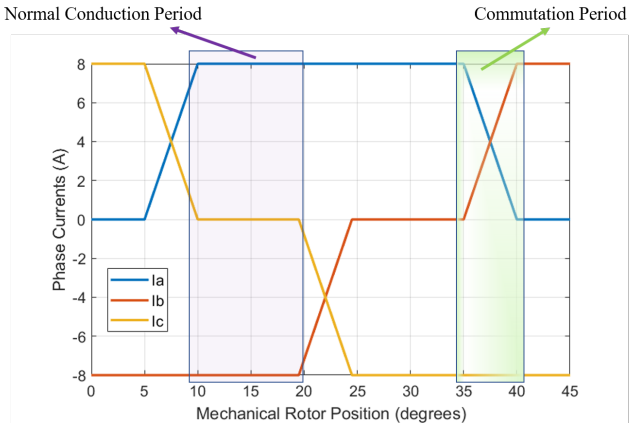


Fig. 3. Typical three phase bipolar currents of a MCSRM.

A. Normal Conduction Period

The two phases are operating in the normal conduction period have equal and opposite current magnitudes. To extract the flux characteristics from the FE model, the same magnitude of phase currents is passed through the phase coils simultaneously. The flux and torque profiles are recorded from the FE model for the two phase coils which are conducting. This is called dual-phase excitation (DPE).

To understand the importance of DPE, it is necessary to understand how the flux extraction process is done in the case of SRMs. In case of conventional SRMs, a single phase is excited and the flux is recorded from each phase. The phase conducting will have the self flux while the other two phases will have the mutual flux linked to the phase coils because of the current flowing through the first phase. This method is termed as the single phase excitation (SPE) process in this paper. The assumption in the SPE process is that the mutual flux is only dependent upon the current in the first phase. This assumption provides acceptable performance in case of SRMs since the effect of mutual flux is negligible. However, in the case of MCSRMs the effect of mutual flux is vital for torque production and the SPE approach will result in modeling inaccuracies. The SPE approach is also adopted for MCSRMs in [7] and it can be observed that the torque estimation is not accurate enough even after extracting data from the FE model.

In the DPE method, two phases are excited simultaneously with the same magnitude of DC current I, but with opposite polarity. The flux for each phase is obtained as a function of the rotor position and I. DPE ensures that saturation and excitation levels of the machine while capturing flux profiles, are close to that during the actual operation. The net phase flux is obtained as a function of the magnitude of phase currents in two phases and the rotor position as shown in (1). Here, λ_x is the net phase flux, i_x and i_y are the phase currents for two arbitrary phases, x and y which are in operation and θ is the rotor position and k is the absolute ratio of the phase currents. Since the phase currents are equal and opposite, $k = 1$ and net flux becomes a function of only two parameters I and θ.

$$\lambda_x = f(i_x, i_y, \theta) = f(I, k, \theta) = f(I, \theta) \tag{1}$$

Hence, if the flux and torque are extracted using the DPE, the flux characteristics can be organized in a 2D LUT. This is further verified using FE model based simulations of the FP-MCSRM. Flux density levels for SPE and DPE with 5 A excitation level of each phase are shown in Fig. 4 (a) and (b), respectively. In SPE, only one phase is excited with 5A and in DPE both the phases are excited with 5A but with opposite polarity. The difference in the magnetic saturation levels for both these approaches is significant even though the machine is operated with the same magnitude of currents. Having a realistic saturation and excitation level, as well as its implementation, in 2D LUT make DPE an effective way for extracting flux profiles for MCSRMs.

B. Commutation Period

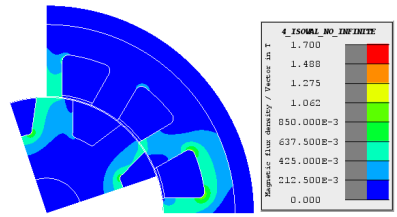
During the commutation period, all phases are operating and have different magnitudes of currents. The assumption made during the normal conduction period with DPE is no longer valid during phase commutation. To satisfy the modeling goal of achieving high accuracy, the excitation process of phase coils needs to be modified for the commutation period. In general, the commutation period has the major contribution towards torque ripple which makes it important to accurately predict the torque during the commutation period.

If all the currents are taken into consideration then the net phase flux, λ_x, will be a function of all the phase currents and rotor position as shown in (2).

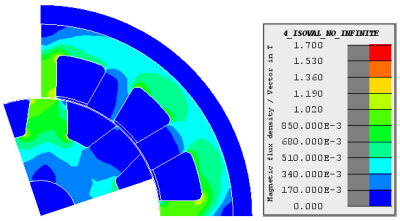
$$\lambda_x = f(i_x, i_y, i_z, \theta) \tag{2}$$

0093-9994 (c) 2019 IEEE. Personal use is permitted, but republication/redistribution requires IEEE permission. See http://www.ieee.org/publications_standards/publications/rights/index.html for more information.

This article has been accepted for publication in a future issue of this journal, but has not been fully edited. Content may change prior to final publication. Citation information: DOI 10.1109/TIA.2020.2968834, IEEE Transactions on Industry Applications



(a)



(b)

Fig. 4. Flux density plot for (a) SPE and (b) DPE method for 5A.

Since the currents are balanced, the sum of currents at the neutral point of the Y-connected phases will be zero. In reference to Fig. 3, when the rotor position is between 35° and 40°, phase A current i_a is turning off (trailing phase current, i_t), phase B current i_b is starting to build up (leading phase current, i_l) and phase C current i_c is unchanged (un-commutated phase current, i_u). To minimize the number of variables and provide simplicity, a ratio k is defined as shown in (3) which relates all the phase currents.

$$k = \mid \frac{i_l}{i_u} \mid \tag{3}$$

Now, all the phase currents are related in terms of the ratio k and the current in the un-commutated phase, I, as defined in (4)-(6).

$$i_u = I \tag{4}$$

$$i_l = -ki_u = -kI \tag{5}$$

$$i_t = (k-1)i_u = (k-1)I \tag{6}$$

The flux linkage is expressed as a function of three parameters as shown in (7) as compared to four variables shown earlier in (2).

$$\lambda_x = f(I, k, \theta) \tag{7}$$

This reduction of one variable helps in reducing the dimension of the LUTs from 4D to 3D. To extract the characteristics of the machine during the commutation period, three variables are varied, which are the I, k and θ in the FE model and the flux and torque characteristics are extracted. This is called multi-phase (MPE) excitation process. The commutation happens near the rotor position when the torque characteristics are going from positive region to the negative region. The particular rotor position when the torque characteristics become zero can be calculated using (8).

$$\theta_c = \frac{360}{2N_r}, \frac{360}{2N_r} \pm \frac{120}{N_r} \tag{8}$$

The MPE process is simulated in the FE model providing a range of 5° to 10° around θ_c. This is done to reduce the FE computation steps and for faster development of the model. For a 12/8 combination θ_c comes to be 22.5° and the MPE process can be simulated from 17.5° to 27.5° providing a range of 10°.

IV. Net Flux Method

Conventional modeling strategy specifically for reluctance motors follows a path to separate self and mutual inductance. Generally, mutual inductance is calculated assuming current to be flowing in only one phase and the current in other phases is zero [7], [14]. However, this is not the case when the machine is operating, since other phases are operating which will result in variation in permeability and thus affect the material's magnetic properties and influence the mutual as well as the self-inductance. Although the frozen permeability method can separate these components, it is very time-consuming, cumbersome and not accurate [19]. To avoid the process of this separation of self and mutual inductance, the net flux method is adopted.

In the normal conduction period, assuming phase A and B are in operation, phase fluxes can be represented as shown below

$$\lambda_{anet} = \lambda_{aa}(i_a, i_b, \theta) + \lambda_{ab}(i_a, i_b, \theta) \tag{9}$$

$$\lambda_{bnet} = \lambda_{bb}(i_a, i_b, \theta) + \lambda_{ab}(i_a, i_b, \theta) \tag{10}$$

Here, i_a and i_b are the phase currents, λ_{aa} and λ_{bb} are self flux linkages of phase A and phase B, respectively and λ_{ab} is the mutual flux linkage. In the NFM, λ_{anet} and λ_{bnet} are extracted from the FE model model and are used to estimate the net torque. In the conventional modeling strategy λ_{anet} is segregated to obtain λ_{aa} and λ_{ab} by running various multiple scenarios along with several assumptions which are not required in NFM; therefore, NFM reduces the time involved in characterizing MCSRMs. From further on in this paper, the subscript net will be dropped and the net flux linkage of any phase, say x will be represented by, λ_x.

The net flux linkage characteristics of the FP-MCSRM and the FrS-MCSRM obtained from the FE model using the DPE process are shown in Fig. 5. These characteristics are used to estimate the torque using equations (11)-(12). Other phases will have the same characteristics but phase shifted by $2\pi/N_R N_{ph}$, where N_{ph} is the number of phases.

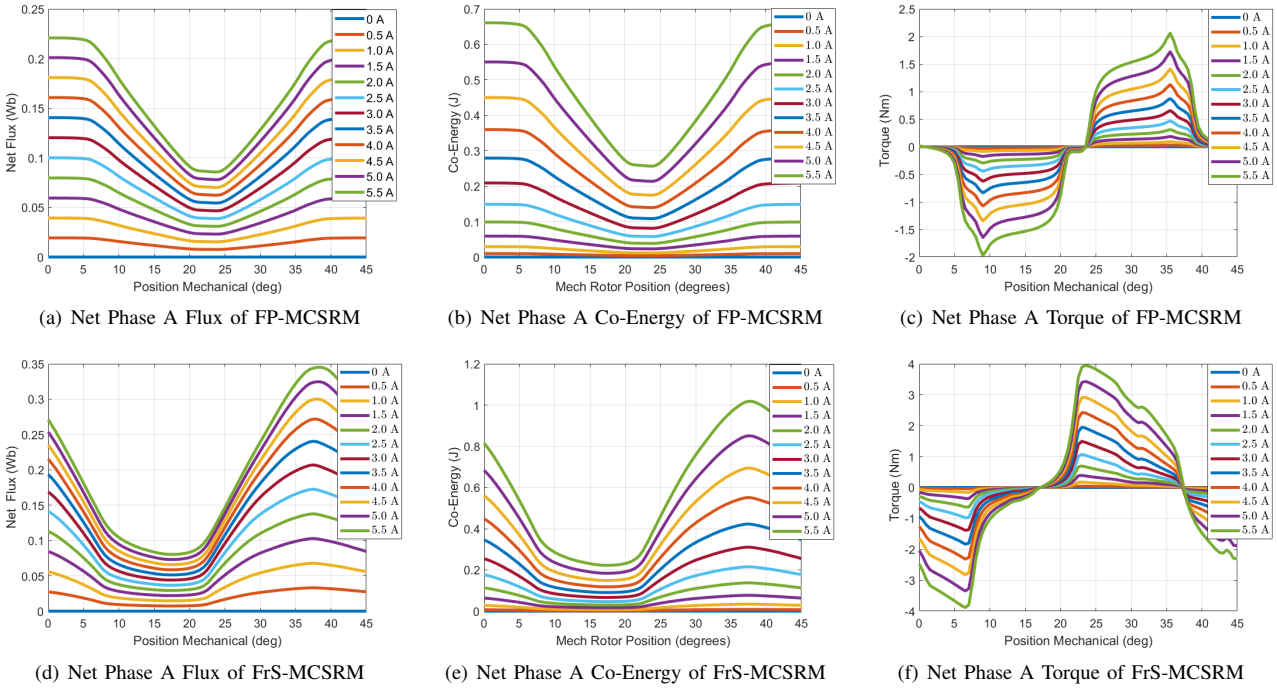
$$W'_x(i_x, i_y, \theta) = \int_0^I \lambda_x(i_x, i_y, \theta)\, di_x \tag{11}$$

$$T_x(i_x, i_y, \theta) = \frac{\partial W'_x(i_x, i_y, \theta), \theta)}{\partial \theta} \tag{12}$$

The co-energy and torque derived using (11) and (12) represents the net energy stored and the net torque produced for the same phase (phase x). Therefore, there is no need to estimate the mutual co-energy and mutual torque in this method. Similarly the co-energy and torque for the phase y can be estimated using λ_y in (11) and (12). The net co-energy and net torque characteristics for Phase A of FP-MCSRM and FrS-MCSRM are shown in Fig. 5. Once each phase's torque

0093-9994 (c) 2019 IEEE. Personal use is permitted, but republication/redistribution requires IEEE permission. See http://www.ieee.org/publications_standards/publications/rights/index.html for more information.

This article has been accepted for publication in a future issue of this journal, but has not been fully edited. Content may change prior to final publication. Citation information: DOI 10.1109/TIA.2020.2968834, IEEE Transactions on Industry Applications



(a) Net Phase A Flux of FP-MCSRM (b) Net Phase A Co-Energy of FP-MCSRM (c) Net Phase A Torque of FP-MCSRM

(d) Net Phase A Flux of FrS-MCSRM (e) Net Phase A Co-Energy of FrS-MCSRM (f) Net Phase A Torque of FrS-MCSRM

Fig. 5. Static motor characteristics of FP-MCSRM and FrS-MCSRM.

characteristics are obtained, the total torque produced by the motor when operating in normal conduction period will be a contribution from the two phases in conduction x and y, and is given by (13).

$$T_{net-DPE}(i_x, i_y, \theta) = T_{net-DPE}(I, \theta) = T_x + T_y \quad (13)$$

For the commutation region, all the phases are conducting, but it has been shown how the flux characteristics can be related to only three parameters in (7). To further simplify the model and to reduce the computation time involved in simulating FE models, the MPE process is limited to the vicinity of the commutation period. The commutation period can be identified by (8). The net flux and net torque characteristics for FrS-MCSRM during the commutation region are shown in Fig. 6 and similarly the commutation characteristics for the FP-MCSRM can also be extracted from the FE model. Like in (13), the net torque can be calculated in the commutation region as expressed in (14).

$$\begin{aligned} T_{net-MPE}(I,k,\theta)\Big|_k &= \frac{\partial}{\partial\theta}\Big(\int_0^{i_x} \lambda_x(I,k,\theta)\ di_x \\ &+ \int_0^{i_y} \lambda_y(I,k,\theta)\ di_y + \int_0^{i_z} \lambda_z(I,k,\theta)\ di_z\Big) \end{aligned} \quad (14)$$

The net torque for the MCSRM operated with trapezoidal currents is computed using (15).

$$T_{net} = T_{net-DPE} + T_{net-MPE} \quad (15)$$

A summary of the complete process is given below.

- Using the FE model of the MCSRM, run the DPE process by exciting two phases with the same magnitude of currents but with opposite polarities and record the net flux. Post process the next flux to obtain the torque characteristics.
- Next, in the FE model, run the MPE process in which all the phases are excited with currents as a function of k, I and θ. The net flux characteristics are extracted from the FE model and the torque characteristics can be estimated from the former. During the MPE process, I is varied from 0 to the rated value and k is varied between 0.1 to 0.9.

From the above method, it is observed that the NFM reduces computation and post processing time. The NFM method has two main advantages, first, net flux and net torque are the quantities available from the FE model as well as from real-time experiments. Second, self and mutual co-energy and torque components are not to be calculated separately. This reduces the computation time and improves the accuracy of the model. Mutual co-energy calculations can be severely complicated when more than two phases are in operation [2].

V. Machine Model

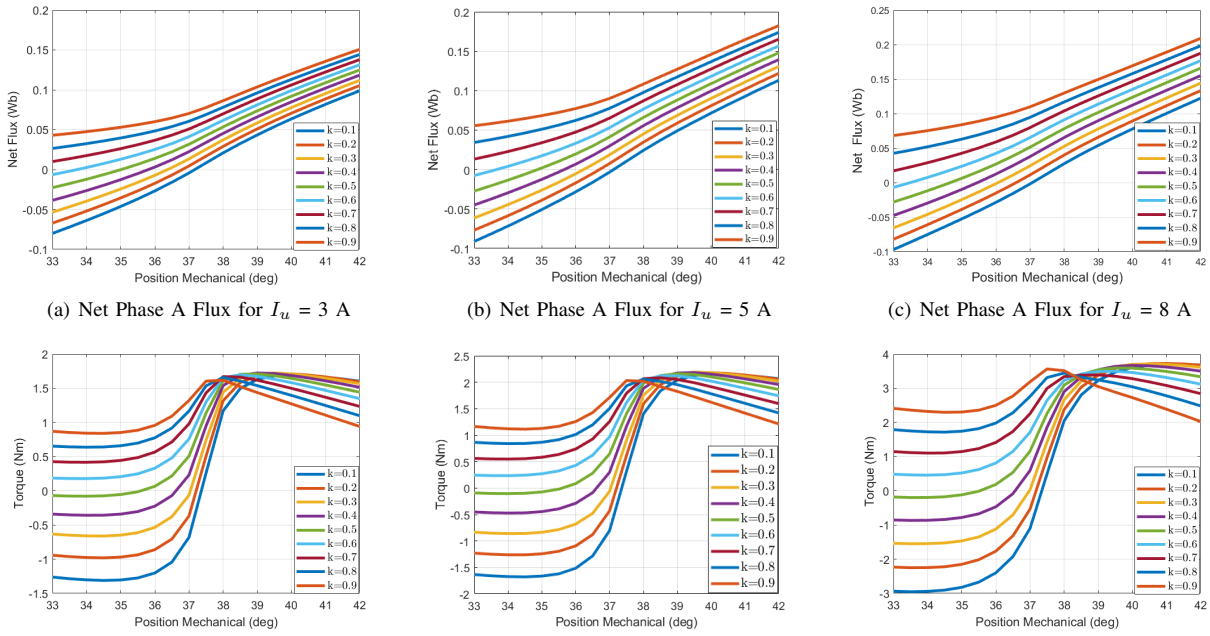
The machine model is constructed using the flux and torque characteristics obtained from the FE model. The phase voltages and the motor parameters are related to each other as shown in (16) for a normal conduction period considering that phase x and y are in operation.

$$\begin{bmatrix} v_x(t) \\ v_y(t) \end{bmatrix} = R \begin{bmatrix} i_x(t) \\ i_y(t) \end{bmatrix} + \frac{d}{dt} \begin{bmatrix} \lambda_x(t) \\ \lambda_y(t) \end{bmatrix} \quad (16)$$

During normal conduction period, λ_x is a function θ and $i_x = I$. The rate of change of flux can be expressed as in (17)

0093-9994 (c) 2019 IEEE. Personal use is permitted, but republication/redistribution requires IEEE permission. See http://www.ieee.org/publications_standards/publications/rights/index.html for more information.

This article has been accepted for publication in a future issue of this journal, but has not been fully edited. Content may change prior to final publication. Citation information: DOI 10.1109/TIA.2020.2968834, IEEE Transactions on Industry Applications



(a) Net Phase A Flux for I_u = 3 A (b) Net Phase A Flux for I_u = 5 A (c) Net Phase A Flux for I_u = 8 A

(d) Net Motor Torque for I_u = 3 A (e) Net Motor Torque for I_u= 5 A (f) Net Motor Torque for I_u= 8 A

Fig. 6. Commutation region characterises for FrS-MCSRM.

below:

$$\frac{d\lambda_x(t)}{dt} = \frac{\partial \lambda_x(I,\theta)}{\partial i_x}\frac{di_x(t)}{dt} + \frac{\partial \lambda_x(I,\theta)}{\partial \theta}\frac{d\theta(t)}{dt} \tag{17}$$

$$\frac{d\lambda_x(t)}{dt} = \psi_{incx}(I,\theta)\frac{di_x(t)}{dt} + \lambda_{incx}(I,\theta)\omega_e(t) \tag{18}$$

$$\psi_{inc}(i,\theta) = \frac{\partial \lambda(i,\theta)}{\partial i} \tag{19}$$

$$\lambda_{inc}(i,\theta) = \frac{\partial \lambda(i,\theta)}{\partial \theta} \tag{20}$$

$$\omega_e(t) = \frac{N_R}{2}\omega_m(t) \tag{21}$$

Here, i_x, i_y, v_x, and v_y represent the phase currents and phase voltages of phases x and y, respectively. ψ_{inc} and λ_{inc} are the incremental net inductance and incremental net flux linkage, respectively. ω_e and ω_m are the electrical and mechanical frequency of rotation. Using (16), (19), and (20), the phase voltage relation with the motors can be rewritten as shown in (22). This represents the relationship of the phase voltages with the phase currents in the normal conduction period.

$$\begin{aligned}\begin{bmatrix} v_x(t) \\ v_y(t) \end{bmatrix} &= R\begin{bmatrix} i_x(t) \\ i_y(t) \end{bmatrix} + \omega_e(t)\begin{bmatrix} \lambda_{incx}(I,\theta) \\ \lambda_{incy}(I,\theta) \end{bmatrix} \\ &+ \frac{d}{dt}\begin{bmatrix} i_x(t) \\ i_y(t) \end{bmatrix}\begin{bmatrix} \psi_{incx}(I,\theta) & 0 \\ 0 & \psi_{incy}(I,\theta) \end{bmatrix}\end{aligned} \tag{22}$$

Subsequently, in the commutation region, let us assume that phase x is leading, phase y is trailing, and phase z is the un-commutated phase. Now, the net flux linkage, λ_x is a function of I and θ and k. The rate of change of flux linkage is written in (23). Here, I is the current in the un-commutated phase, which is i_z.

$$\begin{aligned}\frac{d\lambda_x(t)}{dt} &= \frac{\partial \lambda_x(I,k_x,\theta)}{\partial i_x}\frac{di_x(t)}{dt} + \frac{\partial \lambda_x(I,k_x,\theta)}{\partial \theta}\frac{d\theta(t)}{dt} \\ &+ \frac{\partial \lambda_x(I,k_x,\theta)}{\partial k_x}\frac{dk_x(t)}{dt}\end{aligned} \tag{23}$$

This can be further simplified as shown in (24).

$$\begin{aligned}\frac{d\lambda_x(t)}{dt} &= \psi_{incx}(I,k_x,\theta)\frac{di_x(t)}{dt} + \lambda_{incx}(I,k_x,\theta)\omega_e(t) \\ &+ k_{incx}(I,k_x,\theta)\frac{dk_x(t)}{dt}\end{aligned} \tag{24}$$

Here,

$$k_{incx} = \frac{\partial \lambda_x}{\partial k_x} \tag{25}$$

Similarly, the rate of change of flux of phase y and z is expressed as

$$\begin{aligned}\frac{d\lambda_y(t)}{dt} &= \psi_{incy}(I,k_y,\theta)\frac{di_y(t)}{dt} + \lambda_{incy}(I,k_y,\theta)\omega_e(t) \\ &+ k_{incy}(I,k_y,\theta)\frac{dk_y(t)}{dt}\end{aligned} \tag{26}$$

In the above equations, $k_x = k$ and $k_y = (1-k)$. The un-commutated phase is dependent on the phase current I_z and θ only. Therefore,

$$\frac{d\lambda_z(t)}{dt} = \psi_{incz}(I,\theta)\frac{di_z(t)}{dt} + \lambda_{incz}(I,\theta)\omega_e(t) \tag{27}$$

0093-9994 (c) 2019 IEEE. Personal use is permitted, but republication/redistribution requires IEEE permission. See http://www.ieee.org/publications_standards/publications/rights/index.html for more information.

This article has been accepted for publication in a future issue of this journal, but has not been fully edited. Content may change prior to final publication. Citation information: DOI 10.1109/TIA.2020.2968834, IEEE Transactions on Industry Applications

Now, using, (16) and (24)-(27), the phase voltages for the commutation period can be represented as in (28).

$$\begin{aligned}\begin{bmatrix} v_x(t) \\ v_y(t) \\ v_z(t) \end{bmatrix} &= i_z(t)R \begin{bmatrix} -k_x(t) \\ -k_y(t) \\ 1 \end{bmatrix} + \frac{d}{dt}\begin{bmatrix} i_x(t) \\ i_y(t) \\ i_z(t) \end{bmatrix} \\ &\cdot \begin{bmatrix} \psi_{incx}(I,k_x,\theta) & 0 & 0 \\ 0 & \psi_{incy}(I,k_y,\theta) & 0 \\ 0 & 0 & \psi_{incz}(I,\theta) \end{bmatrix} \\ &+ \omega_e(t) \begin{bmatrix} \lambda_{incx}(I,k_x,\theta) \\ \lambda_{incy}(I,k_y,\theta) \\ \lambda_{incz}(I,\theta) \end{bmatrix} \\ &+ \begin{bmatrix} \frac{dk_x(t)}{dt} \\ \frac{dk_y(t)}{dt} \end{bmatrix} \begin{bmatrix} k_{incx}(I,k_x,\theta) & 0 \\ 0 & -k_{incy}(I,k_y,\theta) \end{bmatrix}\end{aligned} \tag{28}$$

VI. Simulation Results

For performance validation of the NFM, machine models for FP-MCSRM and FrS-MCSRM are simulated in Matlab/Simulink. The parameters of both the motors are provided in Table I. The flux linkages are extracted from the FE models of the motors using Altair Flux as per the DPE and MPE methods. In the DPE method, the net flux is recorded for I varying from 0 A to 12 A and the rotor position is varied from 0° to 45° for both the motors. For the MPE process, k is varied from 0.1 to 0.9 and the rotor position is limited to 33° to 42° for both the motors. Once the flux profiles are calculated from the FE model, they are post processed to estimate torque profiles shown in Figs. 5 (c) and (f) and Figs. 6 (c) and (d).

The NFM based machine model is tested with bipolar trapezoidal current waveforms as shown in Fig. 3. Although trapezoidal waveforms are used instead of square waveforms for MCSRMs, the model is also valid for square currents. A comparison between the torque waveforms from NFM and FE models for both the topologies are shown in Fig. 7 and Fig. 8. All the simulation results are presented at 500 RPM. The estimated torque profiles from the NFM and those form the FE models are within acceptable error, which validates the accuracy of the proposed model. Average torque, T_{avg}, and torque ripple, T_r, predicted in the NFM in comparison to FE model results are shown in Table II and III for FrS-MCSRM and FP-MCSRM, respectively. Furthermore, a comparison between the performance of the NFM and the SPE based models for FP-MCSRM is presented in Table IV. It is seen that the NFM based machine model has improved accuracy compared to SPE. Both the average torque prediction and torque ripple prediction by NFM are closer to that of FE model than the existing methods. The approach of utilizing net flux and net torque reduces several FE computation steps as well as minimizes the time and effort in the real-time scenario. This is achieved as the need to separate the flux and torque into self and mutual components is eliminated. This elimination helped in improving accuracy and simplifying the modeling process, which generally is a strenuous process for motors belonging to the class of SRMs.

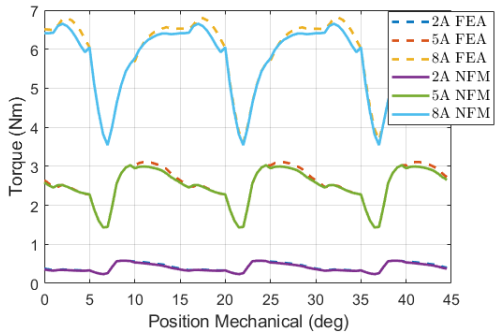


Fig. 7. Simulation results for torque profiles of FrS-MCSRM.

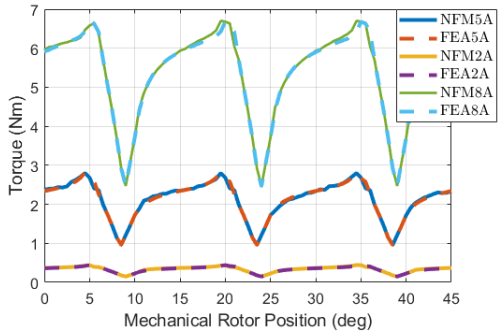


Fig. 8. Simulation results for torque profiles of FP-MCSRM.

TABLE II
Performance Comparison for FrS-MCSRM

Parameter	Model	2 A	5 A	8 A
T_{avg} (Nm)	NFM	0.405	2.513	5.802
T_{avg} (Nm)	FEA	0.416	2.55	5.90
T_r (%)	NFM	84.84	53.63	63.47
T_r (%)	FEA	82.5	55.33	65.66

TABLE III
Performance Comparison for FP-MCSRM

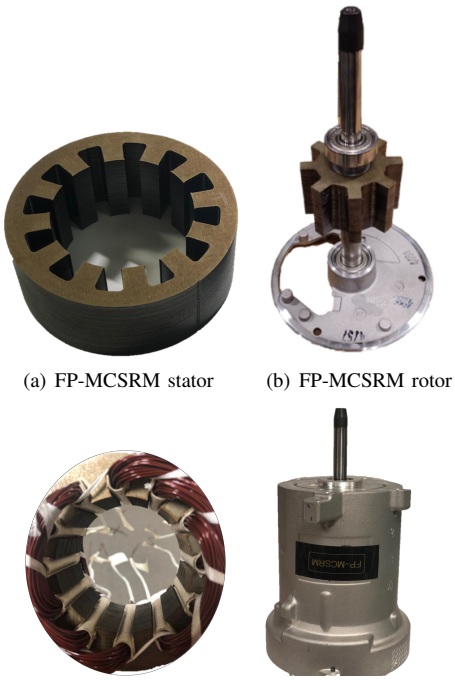
Parameter	Model	2 A	5 A	8 A	10 A
T_{avg} (Nm)	NFM	0.336	2.137	5.36	7.84
T_{avg} (Nm)	FEA	0.332	2.123	5.34	7.83
T_r (%)	NFM	88.14	86.45	78.47	71.50
T_r (%)	FEA	88.07	86.94	78.68	72.16

TABLE IV
Average Torque Comparison Between Single Phase Excitation (SPE) and Net Flux Method (NFM)

Model	2 A	5 A	8 A	10 A
SPE	0.30	1.96	5.07	7.97
NFM	0.336	2.137	5.36	7.84
FEA	0.332	2.123	5.34	7.83

0093-9994 (c) 2019 IEEE. Personal use is permitted, but republication/redistribution requires IEEE permission. See http://www.ieee.org/publications_standards/publications/rights/index.html for more information.

This article has been accepted for publication in a future issue of this journal, but has not been fully edited. Content may change prior to final publication. Citation information: DOI 10.1109/TIA.2020.2968834, IEEE Transactions on Industry Applications



(a) FP-MCSRM stator (b) FP-MCSRM rotor

(c) Fully-pitched winding (d) Assembled motor

Fig. 9. Prototyping stages of the 12/8 FP-MCSRM

VII. Experimental Verification

A 12/8, 150W, FP-MCSRM has been prototyped and the stages of prototyping are shown in Fig. 9. The parameters of the prototype FP-MCSRM are provided in Table V. The stator laminations have 12 slots which are wound with copper conductors of AWG 19 with each phase having two parallel paths. The number of turns per slot is 16 and the phase windings are connected in Y configuration. The shaft is inserted in the rotor using a hydraulic press and the stator is glued to the housing. To extract the flux and torque characteristics according to DPE, fixed currents are supplied simultaneously through 2 phases, ranging from 0 to 72 A in steps of 4 A. The motor is rotated at a fixed speed of 20 RPM. The current is regulated using a 12 V power supply with a current capability of 200 A and is operated in the constant current mode. During this test, torque, phase currents, and line-line voltages are recorded. An induction motor drive is used as the servo motor to rotate the test motors at constant speed. A torque sensor and a position encoder are used to obtain the data using a personal computer. The MCSRM drive under test is controlled from a separate computer and setup is shown in Fig. 10.

TABLE V
Parameters of Prototype FP-MCSRM

Parameter	Value
Rated Power (W)	150
Rated Torque (Nm)	1.5
DC Link Voltage (V)	12
Line-Line Resistance (mΩ)	65
Rated Current (A)	72

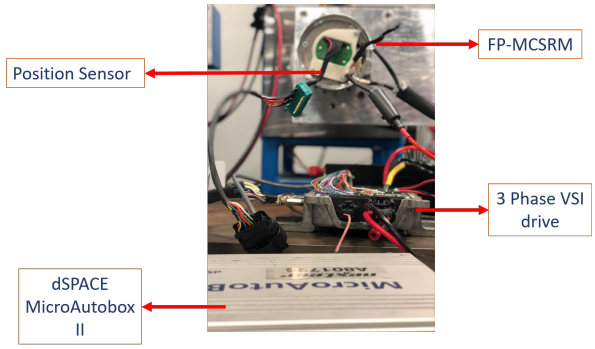


Fig. 10. Experimental test setup for FP-MCSRM drive.

TABLE VI
Performance Comparison for Prototype FP-MCSRM

Parameter	Model	20 A	40 A
T_{avg} (Nm)	NFM	0.1185	0.4889
T_{avg} (Nm)	Experiment	0.1094	0.4675
T_r (%)	NFM	58.38	49.5
T_r (%)	Experiment	62.48	44.06

A. Static Motor Characteristics

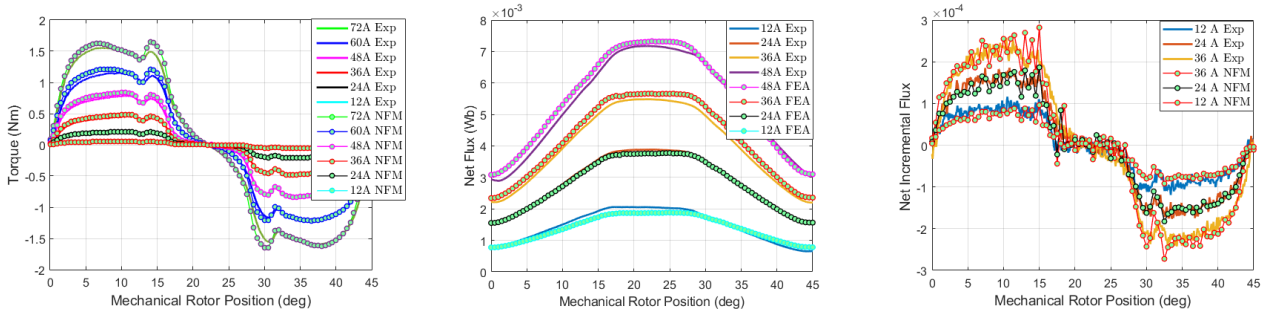
A comparison of the static torque characteristics between the experimentally measured torque of the 12/8 FP-MCSRM and the torque estimated from NFM using the flux profiles from the FE model is presented in Fig. 11 (a). The torque of the prototype FP-MCSRM is captured using a high precision torque sensor in an industrial facility and the precision of the sensor is ± 1 m-Nm. The close match between the estimated and the measured torque validates the applicability of the NFM model. The difference between the NFM torque and the experimental torque can be attributed to the material property uncertainties of the prototype FP-MCSRM as well as variation in speed and current regulations while extracting the experimental torque. Flux characteristics of the prototype FP-MCSRM are also extracted experimentally from the experimental torque characteristics by following the procedure as mentioned in [14]. A comparison of flux characteristics and incremental flux characteristics is presented in Fig. 11 (b) and (c), respectively.

B. Steady State Analysis

For a complete three phase continuous operation with bipolar-balanced trapezoidal currents, a hysteresis current controller has been implemented using dSPACE MicroAutobox-II. The motor is operated at 20 RPM and currents for phase A for peak currents of 20 A and 40 A. T_{avg} and T_r comparison analysis between the NFM and experimental results are shown in Fig. 12 and Table VI. A close match between the experimental and NFM predicted torques validate the applicability of the proposed model. The discrepancies between the experiment and the NFM can be caused by several reasons. However, the primary involves the rotor position sensor errors and the current sensor errors. Since the model and the motor itself depends upon these two parameters to predict the torque and the machine parameters, therefore any variation will result

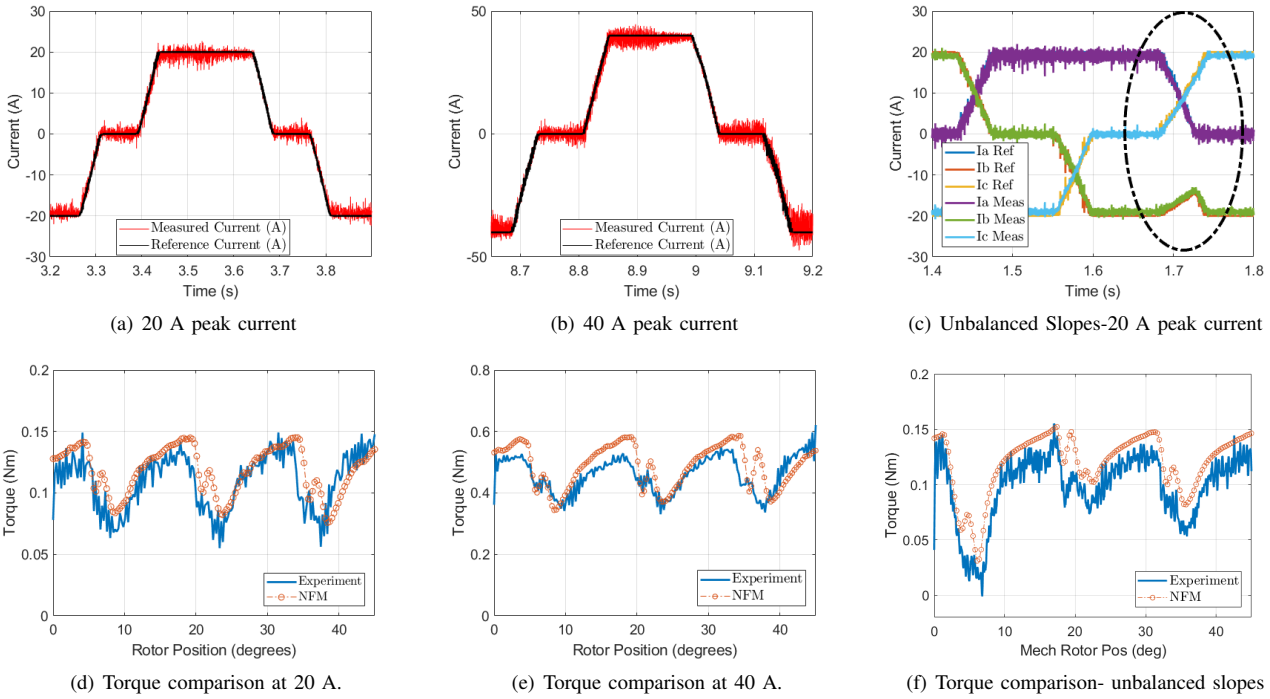
0093-9994 (c) 2019 IEEE. Personal use is permitted, but republication/redistribution requires IEEE permission. See http://www.ieee.org/publications_standards/publications/rights/index.html for more information.

This article has been accepted for publication in a future issue of this journal, but has not been fully edited. Content may change prior to final publication. Citation information: DOI 10.1109/TIA.2020.2968834, IEEE Transactions on Industry Applications



(a) Torque characteristics (b) Net flux linkage characteristics (c) Incremental flux linkage characteristics

Fig. 11. Experimental static motor characteristics of 12/8 FP-MCSRM.



(a) 20 A peak current (b) 40 A peak current (c) Unbalanced Slopes-20 A peak current

(d) Torque comparison at 20 A. (e) Torque comparison at 40 A. (f) Torque comparison- unbalanced slopes

Fig. 12. Reference currents and measured currents for 12/8 FP-MCSRM at 20 RPM.

in errors. The error in torque prediction is more for 40 A reference current as compared to that of 20 A because the NFM model uses the torque characteristics from the FE model rather than what is obtained from the experimental testing of the motor. The difference between the FE model and the experimental torque will increase as the saturation increases, which is evident from Fig. 11. The accuracy of prediction can be improved if the experimental torque characteristics are used instead of the characteristics obtained from the FE model. In addition, to show the applicability of the model, currents are profiled such that there is difference in the slopes of currents during the commutation region. This is shown in Fig. 12 (c) around the time frame of 1.7 to 1.8 seconds. Comparison between the torque predicted by the NFM and that obtained from the experiment is presented in Fig. 12 (f), which showed a good match between them.

C. Effect of Bandwidth on Torque Prediction

The NFM model is based on the assumption that the current regulator has a sufficiently high bandwidth such that it can regulate zero current in the third phase during the normal conduction period. The effect of bandwidth can be evaluated using the proportional-integral (PI) current controller and tuning it to obtain a first order closed loop characteristic of the system. The bandwidth, ω_b, referred in this work is the frequency at the -3 dB gain. The PI controller can be expressed in terms of the bandwidth and the machine parameters as shown in (29) [20].

$$G_{PI}(z) = \omega_b\left(\hat{\psi}_{inc} + \frac{\hat{R}T}{1 - z^{-1}}\right) \tag{29}$$

Here $\hat{\psi}_{inc}$ is the estimated value of the motor net incremental inductance, $\hat{R}$ is the estimated phase resistance and T is the switching time period which is 50 μs in this case. The test motor is operated at 200 RPM and 450 RPM. The bandwidth

0093-9994 (c) 2019 IEEE. Personal use is permitted, but republication/redistribution requires IEEE permission. See http://www.ieee.org/publications_standards/publications/rights/index.html for more information.

This article has been accepted for publication in a future issue of this journal, but has not been fully edited. Content may change prior to final publication. Citation information: DOI 10.1109/TIA.2020.2968834, IEEE Transactions on Industry Applications

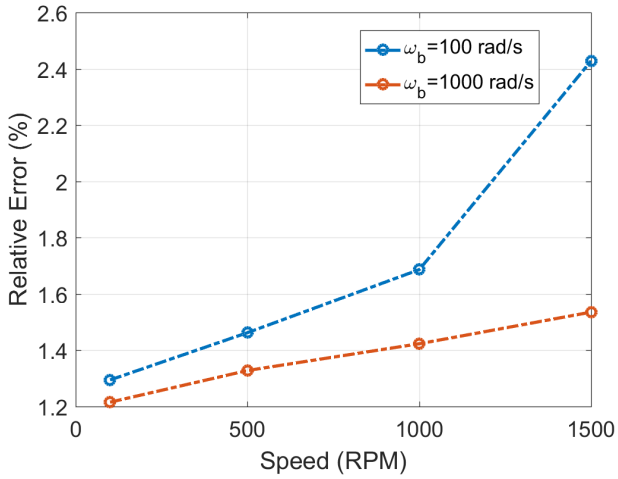


Fig. 13. Bandwidth sensitivity analysis

TABLE VII
PERFORMANCE COMPARISON AT DIFFERENT SPEEDS

Parameter	Model	200 RPM	450 RPM
T_{avg} (Nm)	NFM	0.1264	0.1261
T_{avg} (Nm)	Experiment	0.1275	0.1272

of the PI controller is set to 100 rad/s and a reference current profile with peak current of 20 A is set as the command. The comparative analysis between the NFM and the experimental results is presented in Table VII. Due to restrictions from the experimental setup, analysis at high-speeds is done through simulations. A comparative analysis, for different bandwidths, is presented between the NFM and the FE model in Fig. 13. It is observed from Fig. 13 that the error is reduced with increase in bandwidth. This is because the currents are regulated effectively by the current regulator, thus holding the assumptions true. However, it should be noted that even with low bandwidth, the torque prediction is not severely off because the current in the third phase during the normal conduction period is close to zero, and thus does not contribute significantly in torque production.

VIII. CONCLUSIONS

The machine model of MCSRM is developed based on the net flux method using LUTs. Utilizing net flux removes the process of segregating it into self and mutual flux components which simplifies the overall modeling process. Utilization of dual-phase excitation and multi-phase excitation methods to extract flux and torque characteristics have improved the modeling accuracy. The predicted average torque and torque ripple match well with that from the FE model even under magnetic saturation making the NFM model suitable for high-performance applications. Simplified calculations, fewer data storage requirements, reduced computation time, and improved accuracy are the key features of this developed NFM model. Applicability and accuracy of the developed model are evaluated against FE and existing models for two different MCSRMs. A prototype FP-MCSRM has been built and the simulation results are experimentally validated. Implementation of the developed model to characterize the motor requires less effort than existing methods. This developed model has eliminated the process of estimating mutual inductance and FE comparison against existing methods showed that this elimination has improved accuracy in torque prediction. Through the simulation results of both the MCSRMs and with the experimental evaluation of the FP-MCSRM, it can be concluded that the developed model is suitable for MCSRMs in general and this is the novel and unique feature of the NFM.

ACKNOWLEDGEMENT

The authors would like to acknowledge the support of Michael Bock, Robert Long, Jeff Klass, Jeff Zuraski and the management of Nexteer Automotive Corporation for helping in prototyping and experimental verification of results. The authors would also like to acknowledge the support of Altair for providing the finite element software.

REFERENCES

[1] A. Chiba, K. Kiyota, N. Hoshi, M. Takemoto, and S. Ogasawara, "Development of a Rare-Earth-Free SR motor with high torque density for hybrid vehicles," *IEEE Trans. Energy Convers.*, vol. 30, no. 1, pp. 175–182, Mar. 2015.

[2] R. Mikail, I. Husain, Y. Sozer, M. S. Islam, and T. Sebastian, "A fixed switching frequency predictive current control method for switched reluctance machines," *IEEE Trans. Ind. Appl.*, vol. 50, no. 6, pp. 3717–3726, Nov. 2014.

[3] G. J. Li, X. Ojeda, S. Hlioui, E. Hoang, M. Gabsi, and C. Balpe, "Comparative study of switched reluctance motors performances for two current distributions and excitation modes," in *2009 35th Annual Conference of IEEE Industrial Electronics*, Nov. 2009, pp. 4047–4052.

[4] M. A. Kabir and I. Husain, "Mutually coupled switched reluctance machine (MCSRM) for electric and hybrid vehicles," in *2014 IEEE PES General Meeting — Conference Exposition*, July 2014, pp. 1–5.

[5] Y. Tang, "Switched reluctance motor with fractionally pitched windings and bipolar currents," in *Conference Record of 1998 IEEE Industry Applications Conference. Thirty-Third IAS Annual Meeting (Cat. No.98CH36242)*, vol. 1, Oct. 1998, pp. 351–358 vol.1.

[6] B. C. Mecrow, "Fully pitched winding switched-reluctance and stepping-motor arrangements," *IEEE Proceedings*, vol. 140, no. 1.

[7] W. Uddin and Y. Sozer, "Modeling of mutually coupled switched reluctance motors for torque ripple minimization," in *2015 IEEE International Electric Machines Drives Conference (IEMDC)*, May 2015, pp. 1006–1010.

[8] M. Kabir and I. Husain, "Design of mutually coupled switched reluctance motors (MCSRMs) for extended speed applications using 3-phase standard inverters," *IEEE Trans. Energy Convers.*, vol. 31, no. 2, pp. 436–445, June 2016.

[9] Y. Xu and D. A. Torrey, "Study of the mutually coupled switched reluctance machine using the finite element-circuit coupled method," *IEE Proceedings - Electric Power Applications*, vol. 149, no. 2, pp. 81–86, Mar. 2002.

[10] S. Mehta, A. Kabir, and I. Husain, "Decoupled modeling of mutually coupled SRM using net flux method," in *2018 IEEE Transportation Electrification Conference and Expo (ITEC)*, June 2018, pp. 114–118.

[11] W. Uddin and Y. Sozer, "Analytical modeling of mutually coupled switched reluctance machines under saturation based on design geometry," *IEEE Trans. Ind. Appl.*, vol. 53, no. 5, pp. 4431–4440, Sept. 2017.

[12] J. M. Kokernak and D. A. Torrey, "Magnetic circuit model for the mutually coupled switched-reluctance machine," *IEEE Trans. Magn.*, vol. 36, no. 2, pp. 500–507, Mar. 2000.

[13] J. Ye and F. Hensley, "Torque ripple and copper loss minimization for a family of mutually coupled switched reluctance machines," in *2017 IEEE Applied Power Electronics Conference and Exposition (APEC)*, Mar. 2017, pp. 546–551.

[14] R. Mikail, I. Husain, and M. Islam, "Finite element based analytical model for controller development of switched reluctance machines," in *2013 IEEE Energy Conversion Congress and Exposition (ECCE)*, Denver, CO, 2013, pp. 920–925.

0093-9994 (c) 2019 IEEE. Personal use is permitted, but republication/redistribution requires IEEE permission. See http://www.ieee.org/publications_standards/publications/rights/index.html for more information.

This article has been accepted for publication in a future issue of this journal, but has not been fully edited. Content may change prior to final publication. Citation information: DOI 10.1109/TIA.2020.2968834, IEEE Transactions on Industry Applications

[15] J. Dong, B. Howey, B. Danen, J. Lin, J. W. Jiang, B. Bilgin, and A. Emadi, "Advanced dynamic modeling of Three-Phase mutually coupled switched reluctance machine," *IEEE Trans. Energy Convers.*, vol. 33, no. 1, pp. 146–154, Mar. 2018.
[16] D. A. Torrey and J. H. Lang, "Modelling a nonlinear variable-reluctance motor drive," *IEE Proceedings B - Electric Power Applications*, vol. 137, no. 5, pp. 314–326, Sept. 1990.
[17] B. C. Mecrow, C. Weiner, and A. C. Clothier, "The modeling of switched reluctance machines with magnetically coupled windings," *IEEE Trans. Ind. Appl.*, vol. 37, no. 6, pp. 1675–1683, Nov. 2001.
[18] M. A. Kabir and I. Husain, "Segmented rotor design of concentrated wound switched reluctance motor (SRM) for torque ripple minimization," in *2016 IEEE Energy Conversion Congress and Exposition (ECCE)*, Sept. 2016, pp. 1–6.
[19] G. J. Li, Z. Q. Zhu, X. Y. Ma, and G. W. Jewell, "Comparative study of torque production in conventional and mutually coupled SRMs using frozen permeability," *IEEE Trans. Magn.*, vol. 52, no. 6, pp. 1–9, June 2016.
[20] S. Mehta, P. Pramod, and I. Husain, "Analysis of dynamic current control techniques for switched reluctance motor drives for high performance applications," in *2019 IEEE Transportation Electrification Conference and Expo (ITEC)*, June 2019, pp. 1–7.



Siddharth Mehta (S'14) received his B.Tech. degree in electrical and electronics engineering from Vellore Institute of Technology (VIT)-Chennai, Tamil Nadu, India in 2015 and his M.S. degree in electrical engineering from North Carolina (NC) State University, Raleigh, NC, USA in 2017. He is currently working towards his Ph.D. degree in electrical engineering from NC State University.
He worked with GE Healthcare on medical devices in Bangalore, Karnataka, India; and designed and tested switched reluctance motor drives for steering applications at Nexteer Automotive Corporation, Saginaw, MI, USA. He is currently a Graduate Research Assistant with the Future Renewable Electric Energy Delivery and Management (FREEDM) Systems Center, Raleigh, NC. His research interests include modeling and control of electric motor drives and electric machine design.



Md Ashfanoor Kabir (S'10-M'18) received his Bachelors and Masters degrees in Electrical and Electronic Engineering (EEE) from Bangladesh University of Engineering and Technology (BUET), Bangladesh in 2009 and 2012, respectively. From 2009 to 2012, he served the Department of EEE, BUET as a lecturer. He received his Ph.D. degree from the department of Electrical and Computer Engineering at North Carolina State University, Raleigh, NC, USA. Currently he is working as a research scientist at ABB US Corporate Research Center, Raleigh, NC, USA.
His research interests include design, modelling and control of electric machines using variable speed drives with mechanical stress, vibration and noise analysis. He focuses on high performance, high reliability designs for industrial and traction, ultra-high speed machines with WBG drives, and integrated motor drives. He has received the NCSU graduate fellowship, ABB fellowship, NCSU research symposium award and grand prize in Appalachian state energy conference in 2017. He is a member of IEEE, IEEE-IAS, and reviewer of IEEE and IET journals on electric machines and drives.



Iqbal Husain (S'89-M'89-SM'99-F'09) received the Ph.D. degree in electrical engineering from Texas AM University, College Station, TX, USA, in 1993. He is the Director with the FREEDM NSF Engineering Center and the ABB Distinguished Professor with the Department of Electrical and Computer Engineering, North Carolina State University, Raleigh, NC, USA, where he also serves as the Director with the Advanced Transportation Energy Center. Prior to joining the North Carolina State University, he was with the University of Akron, where he built a successful power electronics and motor drives program. He was a Visiting Professor with Oregon State University, Corvallis, OR, USA, in 2001. His expertise is in the areas of power electronics, electric machines, motor drives, and system controls. In the FREEDM center, his research is focused on power electronics integration into power systems and transportation electrification. He has also developed innovative graduate and undergraduate courses on electric and hybrid vehicles and published a textbook on the subject.
Dr. Husain was the recipient of the 2006 SAE Vincent Bendix Automotive Electronics Engineering Award, the 2004 College of Engineering Outstanding Researcher Award, the 2000 IEEE Third Millennium Medal, and the 1998 IEEE-IAS Outstanding Young Member award. He was the Distinguished Lecturer of the IEEE Industry Applications Society for 2012-2013. He is the Editor-in-Chief for the IEEE ELECTRIFICATION MAGAZINE.



Prerit Pramod (M'14-SM'19) is the Senior Engineering Supervisor of the Electric Motor Drives team within the Research and Development department of Nexteer Automotive Corporation, Saginaw, MI, USA, and is responsible for developing and driving future motor and drives technologies for various automotive applications. He obtained his Master's degree in Electrical Engineering Systems, specializing in Control Systems and Signal Processing, from the University of Michigan, Ann Arbor, MI, USA in 2012 and his Bachelor's degree in Electrical Engineering from Delhi College of Engineering, University of Delhi, Delhi, India in 2010.
His research interests include design, modeling and sizing of electrical machines and power converters and the development and analysis of control, estimation and optimization algorithms for electric motor drive systems. He is the author of 18 granted US utility patents, 38 filed US utility patent applications, 4 defensive publications and 17 IEEE conference publications.

0093-9994 (c) 2019 IEEE. Personal use is permitted, but republication/redistribution requires IEEE permission. See http://www.ieee.org/publications_standards/publications/rights/index.html for more information.

Multimodal KDK Classifier For Automatic Classification of Movie Trailers

Prashant Giridhar Shambharkar, M N Doja, Dhruv Chandel, Kartik Bansal, Kunal Taneja

Abstract*: Movie trailer classification is a field of automation of analyzing the movie trailers and classify them into one of the various genres. In this paper, we proposed a classifier to identify the genre of a movie trailer by analyzing it's audio and visual features simultaneously. Our Approach decomposes a trailer video into frames and audio file and then analyze them based on certain specific features to categorize them into four genres. Our aim was to minimize the number of parameters involved in analyzing the trailer since other papers use many arguments which are impractical. The proposed classifier was trained on 4 audio, 2 broad visual features extracted from over 900 movie trailers distributed across 4 different genres, namely Drama, Horror, Romance, and Action. The Classifier Model has been trained using Neural Networks and Convolutional Neural Networks. Our Classifier Model can be used in Recommendation Systems and various websites like IMDB for automation of the genre classification process. As the common humanly approach is to generalize the results obtained from many inputs, the same way we use multiple models to obtain different outputs from multiple ANN models and then combine all the obtained results to get a final output. Also a Dataset containing 1000 movie trailers was introduced in this paper with trailers spanning to almost all Hollywood movies from 2010-2019 .After training and conducting Experiments on around 1000 movie trailers, the classifier model showed a maximum accuracy of 81 percent in determining top 1 genre and 91 percent in determining top 2 genres of a movie trailers in the test set.

Keywords*: movie trailer, movie genre classification, movie trailer genre classification, neural network, audio visual features, movie data-set.

I. INTRODUCTION

Video Classification is a well-researched topic; still, the results yet obtained are not satisfactory. Same is the issue with the topic we have researched upon, movie trailer genre classification. The difficulty in precisely approaching this field is that a single movie trailer is not always confined to a single genre. A single trailer may contain kiss scene stating it as a romantic trailer and few long talks stating it as a drama or a fight scene stating it as action trailer. So because of the absence of any such specific hard-and-fast rules of specifying a genre, it is not such an easy task to do.

Revised Manuscript Received on September 25, 2019.

Prashant Giridhar Shambharkar. Assistant Professor in Department of Computer Science & Engineering, Delhi Technological University, Delhi

Dr. M.N. Doja, Professor in the Department of Computer Engineering, Faculty of Engineering and Technology, Jamia Millia Islamia, New Delhi-

Dhruv Chandel Information Technology from Delhi Technological University.

Kunal Taneja Technology in the field of Information Technology Delhi Technological University, Information

Kartik Bansal, (B.Tech) in Information Technology from Delhi pursuing Bachelors in Technological University

A.Movie Trailers

Movie Trailers are a short representation of a movie, released before the whole movie is released. Movies are a vast money-making profession if approached correctly, and the way to reach out audiences is through previews or trailers. Trailers are a short and crisp representation of the whole movie plot at once. Trailers depict and give an idea to the audiences about what they can expect from the movie at whole. Genre is such an integral choice for targeting huge audiences so that producers and directors of the movie can release a trailer according to the type of audiences they want to target by analyzing their genre using our model.

B. The Curse Of Incorrect Correctness

Interpreting Genre of a movie trailer isn't an easy task as there is no particular set of rules describing different genres. Deciding genre of a movie is relatively is an easy task instead then interpreting the actual genre of trailers because trailers are like an ultra-compressed form of a plot of the movie.

Also, multiple genres can be interpreted by different persons for the precisely same trailers because of the individuality and everyone's different mood, setting, and way of thinking. So what sources are trustable to find correct genre?

One of the most reliable sources for determining the genre of movies is IMDB, but here comes the curse of incorrect correctness. IMDB describes the genre of the movie as a whole and not of the trailer. Many a time the genre depicted by the IMDB rating is not the genre depicted by the trailer. To state some :

- Drishyam: A movie with rated Genre by IMDB as Crime, Drama, and Thriller was interpreted as Horror by our model due to overall vibes of Horror from the movie trailer.
- IRON MAN 3:- A movie that we all know as an Action movie had minimal features of action in its trailer and thus our model classified it into Drama Genre.
- Buried(2010):-This movie is rated as Drama by IMDB while its trailer has a very dark background and audio like that of Horror and action and thus it was classified as Horror by our model.

So for overcoming these error, we have manually watched all the trailers of the test, and training set; compared them to IMDB rated genre to correctly classify them to correct classes.

C.*The Curse of Multiple Genre Correctness*

The Old times are gone where there were only 3-4 genres over which all the movies were based on. With time presently, there exist more than 30 movie genres like Action, Drama, Horror, Romance, Mystery, Sci-fi, Adaptation, Thriller, Melodrama, Psychic Thriller, and many more.

These genres aren't much different, but the thing is that different compositions of core genres give rise to these secondary genres. For instance:

- Thriller: This Genre can be considered as a crudely a combination both of Action and Horror.
- Melodrama: Melodrama genre can be considered as a combination of both Drama and Romance.
- Romance: Romance although considered a core genre but is more or less a type of Drama only with added sensuality and generous talks.
- Psychic Thriller: It is new rising core genre.

These are only a few to state many more different genres have their alternative interpretations like the above stated only.

Some examples for this are listed as :

- Khamoshiyan: It is classified in genres Drama, Horror and Romance by IMDB.
- Passengers: It's classified as Drama, Romance and Sci-fi by IMDB.
- KGF Chapter 1: It's classified as Action and Drama by IMDB.
- Crawl: It's classified as Action, Adventure and Drama by IMDB.

The contributions of this work are **(1)** Introducing a movie trailer video data-set named 'ALOO' (All Languages Organized Omnipotent) dataset publicly available for a research fraternity. **(2)** Introducing 3 new Audio and 1 new visual state of the art features useful in interpreting the genre of a movie trailer. **(3)** Source Code is made publicly available.

Further, in the paper In Section II, we discuss the related work done in this field, in section III we discuss The Public Dataset We Introduced for research community further in section IV we discuss the methodology that involves Data Pre-processing and Architecture Used in the classifier Models. Further, in section V, VI, and VII, we describe Implementation Details, Experimental Results, and Comparison with Other Models and Classifiers. In section VIII and IX, we discuss Future Scope and Conclusion in this Field of Research.

II. RELATED WORK

Video Classification field is already well researched by many people. Here we discuss about the work happening in the field of video classification using deep neural networks.

One of the foremost work was done in [8] , who basically used CNN as well as LSTM for video classification. They used the VGG convolution base and used techniques like Dense Optical Flow and Loose Labelling of frames to capture both spatial and temporal features of video along with CNN. Also, LSTM used by them worked on 9 frames at a time to give better accuracy than CNN. One of the drawbacks in their model is a large number of parameters involved along with VGG(about 13 crores), thereby leading to substantial computation time as compared to our model.

This paper [10] works on the concept of multiple label system, which enable the model to classify the trailer into more than 1 genre which is realistic in comparison to the single labeled which imparts single genre to all scenes. They used max-pooling and convolution to extract features. They made a deep neural network of 152 layers and trained on the ImageNet(1.2 million images and 21,000 classes) and Places365(1.8 million images and 365 classes). Residual net is pre-trained on ILSVRC 2012 subset of ImageNet.They also used audio features, but instead of extraction they transformed the spectrogram of the audio signal into 130x530 and passed it to CTT for the classification. Moreover, we got the result of 66% from audio. They used 3 different algorithms for calculating the results and thus got 64%, 74%, 72% accuracy. They claim that their all CTT models outperformed the LSTM models in MMC.

In [4] they Worked on audio and visual features for movie trailer genre classification. After using Bruteforce approach for extracting 277 Audio and Visual Features, they used SVM for classification of 7 movie genres and applied SAHS algorithm on it for feature selection and dimensionality reduction of their classifier model. However, the thing to think about is that their Dataset contains 223 movie trailer for 7 movie genres i.e., a tiny dataset and can easily overfit upon so many features to choose from. Also, similar Dataset not made publicly available for comparison make things even more thoughtful.

In [5] was a paper on which they worked specifically on movie clips and not a movie trailer, which is relatively less complicated field. They used 5 Audio and 4 Visual Features to differentiate between 5 genres, but the dataset again used was really small like only 200 movie clips for 5 moviegenres but the classifier model they presented was absurdly trained using neural network with 20000 epocs and 0.05 learning rate, which is very likely to show overfittingas suggested by some experts in the field of machine learning. Their classifier showed an accuracy of 87.5 percent, which is undoubtedly due to the high chances of over-fitting.

III. ALOO DATASET

D.*Training Set*

In this paper, we launch a state of the art data-set containing about 900 latest movie trailers, most of them ranging from movies released in the years 2010-2019.

Choosing the trailers for the movies during this period is a crucial step for any researcher because as times change the perspective of people, film directors and societies also change and so there is a surely a noteworthy change in the trailer of the movies over the period. Our movie trailer dataset mostly has HD trailers only so that, their quality can easily be moderated for any usage into lower resolutions also. Moreover, we have made the dataset available publicly for the research community so that no researcher has to devote their precious time in collecting and making an adequate dataset.

Moreover, due to the availability of the dataset in raw video form, the data can be pre-processed in any accessible format. The bifurcation of the dataset is stated in TABLE I.

Table 1: Dataset Bifurcation

GENRE OF TRAILER	TRAILER COUNT
ACTION	250
DRAMA	250
HORROR	200
ROMANCE	200

E. ***Test Set***

Testing a Model isn't an easy task as it seems to be. What most of the research papers do is that they train and test their models purely based on a common dataset on which they are working on. If we think mostly dataset on which researchers have worked, haven't been so vast, so in a way even if every time they reshuffle their data virtually their model's performance has been over-fitted to mostly every trailer of their dataset. So to counter this issue, in this paper, we have brutally tested the model and tried to make it work in all conditions. We have tested the model in 3 ways, as stated below.

1) First Approach was reshuffling the data every time and testing classifier's performance on the test set, which is 10 percent of the total dataset.
2) Second approach was using 10 percent of the training dataset to find validation accuracy of the model using k-fold cross-validation algorithm[9].
3) The third approach was that, we made a new dataset which consisting of new trailers which were not more than a month older from the date when the model was finalized and all these trailers in new test set were absent from the training set, therefore a total blind unseen test set for the classifier, and hence classifier was finally tested upon the latest movie trailers which were the need of the hour.

IV. PROPOSED METHODOLOGY

A. Data Preprocessing

Data Processing means converting a raw form of data into an analyzable and understandable form to perform various operations on it and extract various features from the raw data about the subject. Data Preprocessing was, again, an integral step to be performed.

Firstly we took the raw form of video and extracted frames from it at 1 FPS using OpenCV[3] and converted frames to the dimensions of 100*100*3. Then we extracted Audio from video using movies [1] into .mp3 format and Audio Features were extracted using Librosa[7].

This extracted data was stored and passed to respective models so to analyze them and study and extract various features from them. Later on, considering space efficiency, all the extracted data is deleted after performing adequate operations on them.

B. Features And Models Used

- Visual Features and Convolution Neural Network Model

This section shows us how Convolution Neural Network was able to extract features from the video and gave results.

Every video trailer is made up of many frames and frames are rendered at 30 fps (mostly). We extracted these frames but at a lower fps as at high fps frames are repeated, and that would not contribute any new information to the model. Frames are extracted from the video at 1 fps and then passed to the CNN model for the evaluation of scenes(8 classes). After obtaining these 8 features, we aimed to merge these 8 features to get the final results of 4 different classes. For this purpose, we implemented another Neural Network which classifies the trailer into 4 classes on the bases of these 8 features extracted from the Convolution Neural Network.

- Convolution Neural Network is one of the advanced forms of neural network. It was introduced by Yann LeCun in the year 1994, as stated in \cite{lecun1995convolutional}. Every layer tends to extract features from the image and pass it to the next layer. Each next layer created by convolution has degraded size by 2 in each dimension. A Convolving layer generates the next layer by convolving on the input layer. In our case, we used this algorithm to classify the images into different subcategories. Namely these category include :
  - Fight/Action
  - Drama/Comedy
  - Cars
  - Horror
  - Explosion
  - Party
  - Robot
  - Adult Content

We obtain percentages of each subclass through the Convolution Neural Network(CNN) model. This output layer of 8 values is used as the input layer for the next ANN model which uses a neural network to use these features and obtain the final result as *action, drama, horror, and romance.*

Convolution Neural Network(CNN) model was separately trained on the dataset of 5600+ images, which was self-made from the extracted images from the trailers. further ANN model was trained on the ALOO Dataset.

Unlike in [7] where only blue frames(middle frames) which were only from 5^{th} to 120^{th} second, which can be limited on the video dataset as most of the videos having length greater than 150 \textit{sec} could give wrong results, We extracted all images in the video at 1 fps, an to prevent the model on working not on trailer we set the limits to 500 *sec* since no trailer would be above 200 *sec*.

C. Audio Model And Audio Features

The Audio is extracted from the .mp4 format of the trailer in .mp3 format. The Audio is stored and passed to different classifier models to find the number of Significant Peaks, Average Time between peaks, MFCCs and RMS energy of the audio track.

Audio is then analyzed on the basis of features described using Neural Networks, and after passing any test audio, the classifier returns output in the form of 4 Genres.

- MFCC Features

  MFCC [11](Mel Frequency Cepstral Coefficients) is one of the most important single-frame audio features that describe the overall spectral shape of our spectrogram. MFCC is calculated by taking Discrete Cosine Transform of the logarithm of Mel frequencies obtained by mapping power of spectrum obtained by taking Fourier Transform of time series of an audio sample. MFCC helps in characterizing the spectral shape of sound on a non-linear mel scale(eg.0th coefficient tells us about overall loudness of audio,1st coefficient gives us an overview of the spectrum and other features dig into further detail of spectrum). We took first 13 MFCC of audio sample to classify trailers into 4 genres respectively by taking the average of 13 MFCC over all time frames since first 13 features give almost entire detail about the audio sample as used by other papers as well.

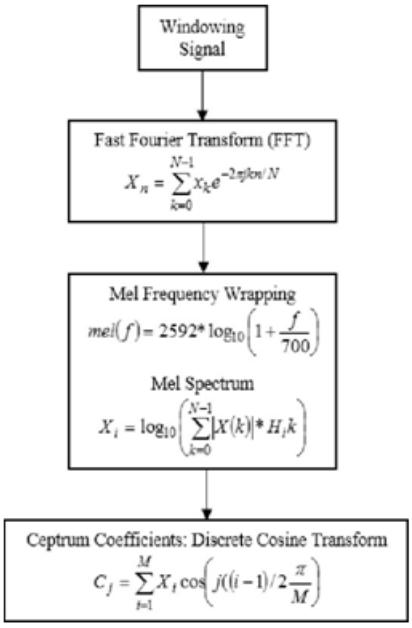


Figure 1: MFCC Evaluation [12]

- Number Of Significant Peaks

Number of Significant peaks is one of the new features we have introduced to this field of research. It was earlier used in onset detection of music signals [2]. Sound plays an important role in creating the mood of a person watching the video trailer. It modifies the subconscious of a human brain just to change the aura of one's mind. One of the factor human minds interpret about the sound while inspecting its genre is the sudden change in the sound effects.

These sudden changes are picked up by our model, and the total number of significant peaks per movie trailer are counted. Intuitively thinking more the movie trailer is active more will be the number of peaks and vice versa.

Therefore our model was trained on this feature to predict the genre of a movie trailer.

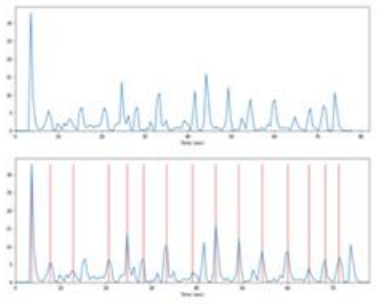


Figure 2:About Time(Romance)

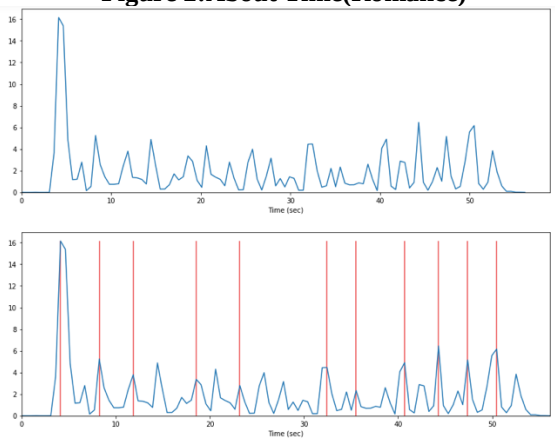


Figure 3: Blue Valentine(Drama)

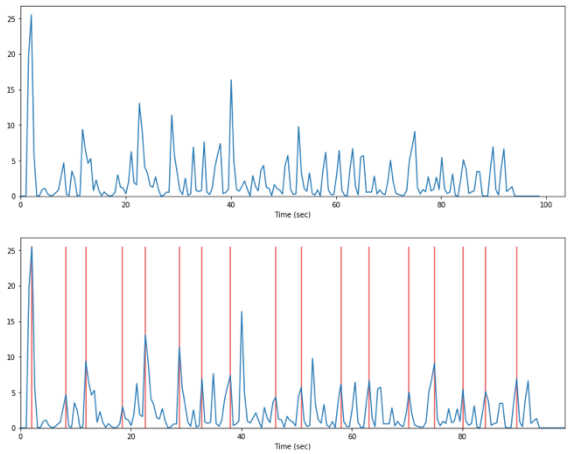


Figure 4: The Fate of Furious(Action)

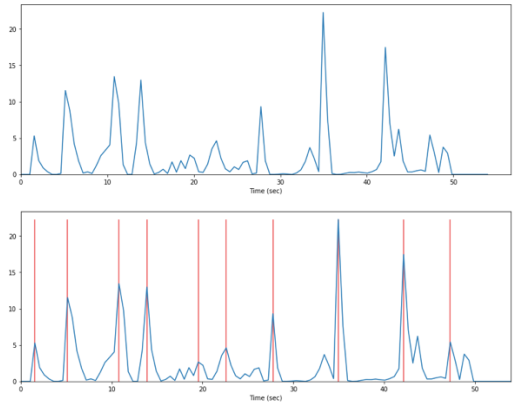


Figure 5: The Nun(Horror)

- Average Time Interval between Significant Peaks
  Average time interval between significant peaks is another new feature helpful in deciding the genre of a movie trailer. Either it is any genre, it has some significant peaks in it. Although the time span of movie trailers are almost the same still to eradicate any unwanted inaccuracy we take an average time interval in which the significant peaks occur throughout the movie trailer.
  As thought intuitively peaks occur at higher time intervals in horror trailers while in action trailer they occur more frequently. Drama and romance show similar kind of Average time intervals.
- RMS Energy
  The energy of an audio plot is approximately equal to the square of the amplitude of sound wave averaged over all time frames. RMS energy of audio is the root mean squared energy of an audio plot. Therefore average RMS energy of audio basically gives us an idea about average intensity of the sound of our movie trailer. This feature is useful since action trailers usually have quite high energy as compared to the drama and romance trailers in which intensity of sound remains quite low. Earlier energy plot has been used in order to detect significant peaks, but average RMS energy is used as a parameter value in our model itself.

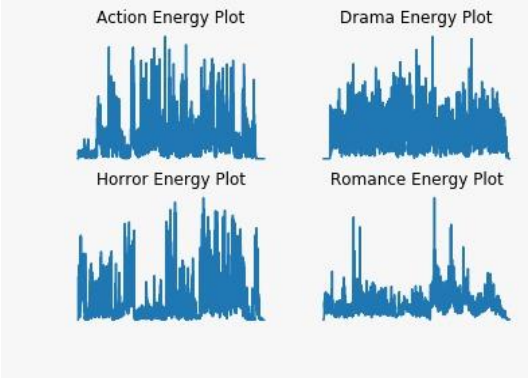


Figure 6: Energy Plots

D. Average RGB Factor And Net RGB Model

Net RGB model represents the whole movie trailer using a single color.

1. Firstly for all individual frames, an average RGB combination is found. For instance, if there are 200 frames, we will have a list of 200 RGB combinations for the whole trailer, with a single combination representing a single frame.
2. All the single combination are then summed up to find an average RGB combination representing the whole trailer.
3. This average RGB is passed through the Neural Network to analyze and give an output in the form of 4 genres.
   RGB factor is also a new factor what we introduced in this field of research. Earlier kind of similar approach which was used by many was using the lightning key, but it was a less accurate and more mathematical approach. We here took a simple approach to how humans interpret the visuals. Our subconscious mind acts to consider lightest and bright colors in romantic genre followed by drama, action, and horror movies. We used this approach to find a single mean color that could represent the whole trailer using one most dominant color throughout the movie trailer. This is a less mathematical and more accurate way to help classify movie trailers incorrect genres.

E. Result Combiner ANN

The Result Combiner is 4 layered neural network which takes in Outputs from all the classifier models in the form of percentages and after passing them through an ANN gives a final predicted genre of the movie trailer. This Final Result combiner acts like a feature selector for our classifier model, i.e., which feature to be considered for deciding one of the 4 genres accurately.

V. IMPLEMENTATION DETAILS

Implementation is to make sure what we planned works perfectly. Our implementation was based on the features extracted from 3 different models and ultimately achieving the genre from which most part of the genre belongs. Sometimes it's difficult to conclude the genre of the movie just on the basis of the trailer since the trailer constitutes the cut scenes to attract the mob. Our model aims not to give a positive result but what it sees from the trailer.

F. Convolution Neural Network Model

This sub-model works on the visual feature of the trailer and finds the 8 features, namely *fight, cars, drama/comedy, explosion, horror scenes, robots, romantic scenes, party* in the trailer and finally classify the video into one of the 4 classes.
When a video is passed to the model, firstly frames are extracted from the video at 1 fps. Then these frames having shape (SxSx3) are collected together to form a linear array using numpy and deducing the resolution of the image to 100 making shape (100x100x3), where S is the resolution of the image extracted, and 3 is for the RGB value layers thus formed is of the Red, Green, and Blue respectively. This whole array of shape (nx100x100x3) is passed as the input. The output is in the form of a linear array of shape (8,), which is interpreted as the percentage of frames belonging to each 8 sub-class. This array is further passed into another Artificial Neural Network(ANN) model, which ultimately classify into 4 class which we to make meaningful named to *action, drama, horror, romance*.

1. Architecture : We adopted very simple architecture to obtain good result instead of the huge and complex networks which take time to load. CNN model is has an architecture of 5 layers and further 4 more layers in the ANN model.

- First layer was the Convolution2D layer having activation as *relu* with input dimensions equal to 100x100x3 and output dimensions equal to 98x98x128, with convolving matrix of size 3x3.
- Second layer was of MaxPooling2D layer which picks the maximum from each set of 4 features. Output layer thus achieved is 49x49x128. Matrix used is of dimension 2x2.

- Third layer was again of the Convolution2D having activation *relu* with output dimension 47x47x64 and convolving matrix of dimension equal to 3x3.
- Fourth layer is the flatten layer which flatten all the values into a single array of size 141376.
- Fifth layer is the output layer and of the type dense with activation \textit{softmax} giving output as linear array of size 8.
- After that ANN model has 4 layers in which first layer is of dense type with input dimension as (8,) and output dimension equal to (128,) with activation *relu.*
- Second layer of ANN is again of dense type having output dimension equal to (64,) and activation *relu.*
- Third layer of the ANN model is dense layer with activation *relu* and output dimension as (32,).
- Fourth and the last layer of the ANN model is also dense layer with activation *softmax* and output dimension equal to (4,)

All these layers combine to form one of the 3 sub-models(CNN model).



Figure 7: CNN Model

2. Evaluation : We trained the CNN model on the dataset of 5600+ images classified into 8 classes, with 25 epochs. The optimizer used was Adam, and the learning rate was set to 10^{-4}. The evaluation was on the basis of accuracy. The loss function used was the Categorical Cross-entropy. We shuffled the dataset after every epoch. The batch size was set to 100, and validation split was 0.10. This experimental combination gave the accuracy equal to 73.2 percent and validation accuracy equal to 71.7 percent. The ANN model was trained on the dataset of 900 trailers whose features were first extracted from the CNN model in 8 classes. Then using these 8 features as the input ANN model was trained to have optimizer equal to Adam, learning rate as 10^{-4} loss function as categorical cross-entropy, and evaluation on the basis of accuracy. The batch size was set to 40, and data was shuffled after every epoch. From this, we got the validation accuracy of 73 percent.

3. Audio ModelAudio Model uses the ReLu activation function throughout the model, which outperforms all considerable activation functions like tanh, sigmoid, hard-sigmoid, relu.

The Audio model takes in input as all 16 audio features, namely the 13 MFCC, number of significant peaks, the average time difference in between the peaks and RMS energy.

Model is then applied to give out the percentages of each genre detected within a movie trailer using the Softmax activation function in the final prediction layer.

1. Architecture

   Audio ANN model basically consists of 4 Dense layers-3 hidden layers and 1 output layer.

- First Layer consists of 64 neurons taking in input of dimensions (16,) representing 16 audio features of a single movie trailer. ReLu activation is provided.
- Second Layer consists of 128 neurons and ReLu activation.
- Third Layer consists of 64 neurons and ReLu activation. Output from this layer is supplied to final output layer.
- Fourth Layer is final output layer that finally gives us outp't of dimension (4,) and it is Softmax activated.
- Total trainable parameters: 17,924 parameters.

2. Evaluation

We trained the ANN model on the dataset of about 672 movie trailers. For each trailer, audio features were extracted, and finally, a CSV file is stored containing 16 audio features of 672 movie trailers. The optimizer used was Adam(AMS grad variant), and the learning rate was set to10^{-4}. Model performance was evaluated on the basis of accuracy. Batch Size used was 64, and the number of epochs was set to 300. Validation set constitutes 10 percent of training data. The validation set was shuffled after each epoch. Loss Function used was Categorical Cross-Entropy. We achieved training accuracy close to 60 percent, whereas validation accuracy close to 55 percent.



Figure 8: Audio ANN Model

G. Net RGB Model

The RGB model is kind of straightforward model with only 3 dimensions in input as the average red, green, and blue color combination of the whole movie trailer. It serves similar architecture to that of the audio model but with a different combination of neurons to serve the best accuracy. In the RGB model, the mean value of RGB is found for each single movie trailer to get a (3,) vector, which serves as input to RGB ANN model.

1. Architecture : RGB ANN model comprises of total of 3 Dense Layers-2 Hidden Layers and 1 Output Layer.
   - First Layer consists of 128 neurons and ReLu activation and takes input of dimension (3,) for each movie trailer.
   - Second layer consists of 64 neurons and Relu activation and it's output is provided to output layer.
   - Third Layer is final output layer that finally gives us output of dimension (4,) and it is Softmax activated.
   - Total trainable parameters:9,028 parameters.

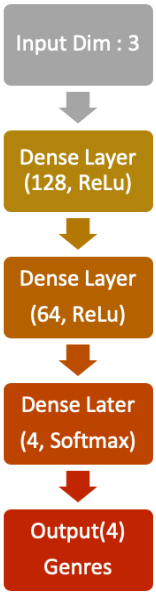


Figure 9: RGB ANN Model

2. Evaluation : We trained the RGB model on the dataset of about 520 movie trailers. For each trailer, mean RGB value is found, and finally, a CSV file is stored containing 3 RGB values of 520 movie trailers. The optimizer used was Adam(AMS grad variant was used), and the learning rate was set to 10^{-4}.Model performance was evaluated on the basis of accuracy. Batch Size used was 16, and the number of epochs was set to 300. Validation set constitutes 10 percent of training data. The validation set was shuffled after each epoch. Loss Function used was Categorical Cross-Entropy. We achieved both training and validation accuracy close to 50 percent.

H. Result Combiner ANN

Result Combiner ANN takes in input from all 3 models of dimension (12,) where each of the previous models was supplying (4,) output. Then Result Combiner ANN finally produces (4,) output representing percentages of all 4 genres. Its function is to combine the result of all 3 models.

1. Architecture : Result Combiner ANN consists of 4 Dense Layers- 3 Hidden Layers and 1 Output Layer.
   - First Layer consists of 32 neurons and ReLu activation and takes input of dimension (12,).
   - Second Layer consists of 64 neurons and ReLu activation.
   - Third Layer consists of 32 neurons and ReLu activation and supplies input to final output layer.
   - Fourth Layer is final output layer comprising of 4 neurons and Softmax activation thus giving final percentages of 4 genres predicted.
   - Total trainable parameters:4,740 parameters.

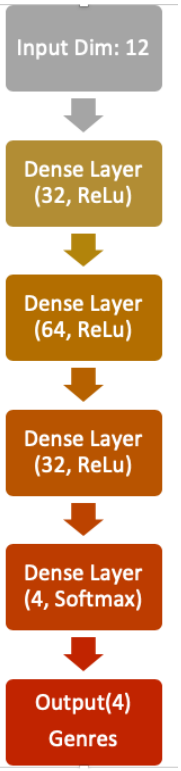


Figure 10: Result Combiner ANN Model

2. Evaluation : Result Combiner ANN model is trained on our training dataset "ALOO" comprising of 900 movie trailers, where 12 values are obtained for each trailer and stored in CSV file. The optimizer used was Adam(AMS grad variant was used), and the learning rate was set to 10^{-5}.Model performance was evaluated on the basis of accuracy. Batch Size used was 32, and the number of epochs was set to 500. Validation set constitutes 10 percent of training data. The validation set was shuffled after each epoch. Loss Function used was Categorical Cross-Entropy. The genre with the highest percentage obtained is our final predicted genre. We achieved both training and validation accuracy close to 80 percent.

VI. EXPERIMENTAL RESULTS

I. Test Dataset Description

We made a Test Dataset of 99 movie trailers on which finally our model performance can be seen.
Test Set comprises of :-

Genre	Number Of Trailer.
Action	24 Trailers
Drama	25 Trailers
Horror	25 Trailers
Romance	25 Trailers

Table 2: Test Set

J. Results

- TEST ACCURACY:- 81 percent
- CLASSIFICATION REPORT:-It is shown in Table III.

Table 3: Classification Report

GENRE	PRECISION	RECALL	F1-SCORE	SUPPORT
ACTION (0)	0.78	0.75	0.77	24
DRAMA (1)	0.79	0.92	0.85	25
HORROR (2)	0.78	0.84	0.81	25
ROMANCE (3)	0.9	0.72	0.8	25
MICRO AVG	0.81	0.81	0.81	99
MACRO AVG	0.81	0.81	0.81	99
WEIGHTED AVG	0.81	0.81	0.81	99

- CONFUSION MATRIX:- Refer to Fig. 11

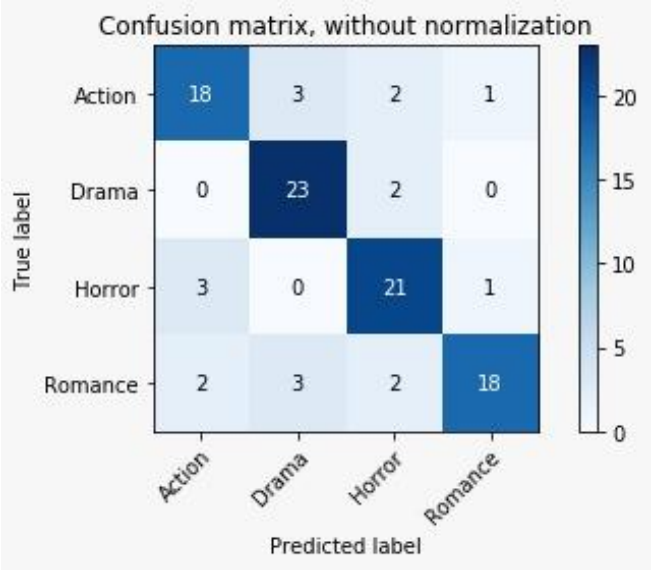


Figure 11: Confusion Matrix

- We tried different models to classify movie trailers into different genres before reaching to our final model. Results of all our models are shown in TABLE 4.

Table 4: Different Classifier Models

MODELS USED	FEATURES USED	ACCURACY
SVM (SUPPORT VECTOR MACHINES)	VISUAL	47%
CNN (CONVOLUTIONAL NEURAL NETWORKS)	VISUAL	62%
ANN (ARTIFICIAL NEURAL NETWORKS) AND CNN (CONVOLUTIONAL NEURAL NETWORKS)	VISUAL AND AUDIO	81%

VII. COMPARISON WITH OTHER MODELS/CLASSIFIERS

The metrics we here take in consideration while making the movie genre classifier are classifier are 'accuracy' and 'time-efficiency.'
While some classifiers work only over accuracy as a metric and do not consider the practicality of such applications, i.e., what will be the use of such movie trailer genre classifiers of they take up more than what a human will take to categorize the same by watching the trailer.
When a movie trailer of average duration (150 sec) is tested on machine with configurations of processor- intel i7 8th gen 8700Q , DDR4 8gb ram, it took about 45-60 sec to classify the trailer.
The 45-60 seconds included the time required to extract images, convert images, extract audio, analyze them, delete cache and give out results in .csv format, for a movie trailer of an average length of 2 minutes and 30 seconds which is a big thing in itself. Also, the parameters to consider, the introduced model uses overall very less number of trainable and non-trainable parameters if considered relative to the heftiness of the task of video processing.

VIII. FUTURE SCOPE

We thought about another feature which hasn't yet been introduced to this field of research. If we closely watch a movie trailer, we always notice that in Action and Horror Movies, the human voice content concerning the length of a video is less to what if Drama and Romantic movies are considered. This factor can be used to be incorporated in the audio model of the introduced classifier.
Further improvement in the time domain can be made by extracting frames in a lower resolution than the currently extracted HD resolution, so less disk read and write time is needed for the task.
Also Currently, we first extract the audio and convert it to .mp3 format for proper analysis, direct extraction of audio in .mp3 format from .mp4 format will help in improvement in time required for movie trailer analysis.

IX. CONCLUSION

Although the classifier we built is one of the best in class in terms of time and accuracy taken together giving an accuracy of nearly 81 percent.

Sometimes the classifier gets confused in between the Drama-Romance and Horror-Action genre of movie trailers due to similar cinematic attributes in the respective genres.
As a measure of accuracy, we tried to take the top 2 genres of movie trailers, which resulted in increased accuracy of 91 percent.
The parameters we considered while making the classifier model were of Time and accuracy hand-in-hand. The Time thus required to analyze a trailer of 150 at once was about 45-60 seconds.
Also, we considered, when we used the model to distinguish between Action and Non-Action movies, considering Action and Horror as Action and Drama and Horror as non-action movies the classifier gave us results with an overall accuracy of 80.795 percent.

ACKNOWLEDGEMENT

We want to express our sincere thanks towards Delhi Technological University, Jamia Millia Islamia, New Delhi for providing infrastructure and platform. Our heartfelt thanks to Siddhant Bhambri and Tenzin for their valuable and constructive suggestions during the planning and development of this research work. Their willingness to give their time so generously has been very much appreciated.

REFERENCES

1. Audio Extraction using moviepy Python library. https:// pypi.org/project/moviepy/.
2. Juan Pablo Bello et al. “A tutorial on onset detection in music signals”. In: IEEE Transactions on speech and audio processing 13.5 (2005), pp. 1035–1047.
3. Gary Bradski and Adrian Kaehler. Learning OpenCV: Computer vision with the OpenCV library. ” O’Reilly Media, Inc.”, 2008.
4. Yin-Fu Huang and Shih-Hao Wang. “Movie genre clas- sification using svm with audio and video features”. In: International Conference on Active Media Technology. Springer. 2012, pp. 1–10.
5. Sanjay K Jain and RS Jadon. “Movies genres classifier using neural network”. In: 2009 24th International Sympo- sium on Computer and Information Sciences. IEEE. 2009, pp. 575–580.
6. Yann LeCun, Yoshua Bengio, et al. “Convolutional net- works for images, speech, and time series”. In: The handbook of brain theory and neural networks 3361.10 (1995), p. 1995.
7. Brian McFee et al. “librosa: Audio and music signal analysis in python”. In: Proceedings of the 14th python in science conference. Vol. 8. 2015.
8. K Sivaraman and Gautam Somappa. “Moviescope: Movie trailer classification using deep neural networks”. In: Uni- versity of Virginia (2016).
9. Mervyn Stone. “Cross-validatory choice and assessment of statistical predictions”. In: Journal of the Royal Statistical Society: Series B (Methodological) 36.2 (1974), pp. 111– 133.
10. Joˆnatas Wehrmann and Rodrigo C Barros. “Movie genre classification: A multi-label approach based on convolutions through time”. In: Applied Soft Computing 61 (2017), pp. 973–982.
11. Wikipedia: Mel-frequency cepstrum. https://en.wikipedia. org/wiki/Mel-frequency cepstrum.
12. Figure 1 : https://www.semanticscholar.org/paper/Infant's-cry-sound-classification-using-Cepstrum-Rosita-Junaedi/76999fe56627320afc4ea1e5d626da48e4c36634/figure/6

AUTHORS PROFILE



Prashant Giridhar Shambharkar
B.E. From Amravati University, Done M.Tech From RGPV, Bhopal, Working as an Assistant Professor in Department of Computer Science & Engineering, Delhi Technological University, Delhi having 14+ years teaching experience of various Computer Engineering and IT related subjects, worked in various committee at responsible position, member of ISO 9001-2008 member at institution level, worked as exam coordinator, counsellor, mentor, time table in-charge, assistant centre superintendent in university exam, centre controller in UPSEE exam, Alumni Incharge, Organized Literary Activities, etc.
His area of interest includes Data mining, Real Time Systems. Guided many Graduate level projects and supervised M.Tech thesis. Member of ACM, Life member of CSI.



Dr. M.N. Doja is Professor in the Department of Computer Engineering, Faculty of Engineering and Technology, Jamia Millia Islamia, New Delhi-110025. He was the founder head of the Department of Computer Engineering for six years from its inception and has established the innovative and upcoming labs in the department. He started B.Tech. (Computer Engineering) and B.E. (Computer Engineering) as day and evening course respectively. He started Ph.D programme in the Department of Computer Engineering.
He has more than two decades of academic, research, training and administrative experiences in the field of Computer Engineering and Information Technology.
He received his B.Sc. (Engg), M.Tech. and Ph.D. degrees from B.I.T, I.I.T. Delhi and Jamia Millia Islamia, New Delhi respectively. His areas of research are Software Engineering, Networks, Security, Simulation, Operating System and Soft Computing. Prof. Doja is an active researcher. He has more than 100 publications in referred journals and conferences of international and national repute. He has been referee for a number of journals in the area of Computer Engineering and Information Technology. Several students have been awarded Ph.D under his able guidance and several students are working under his supervision. He is also author of a number of books in the area of Information Technology. He has successfully completed several projects including AICTE sponsored projects. He has chaired various sessions of various reputed conferences and delivered lectures on recent and burning topics in Computer Engineering and Information Technology as an invited speaker at a number of places across India and world. Prof. Doja is a member of Academic Council, Board of Research Studies and Board of Studies of a number of universities including Ambedkar University Lucknow, NSIT New Delhi, A.M.U. Aligarh, Guru Gobind Singh Indraprastha University Delhi, NIT Jalandhar, Hamdard University New Delhi etc. He has been a member of a number of committee for various universities in various capacities. He has been expert member/member of various committee constituted by UGC and AICTE. He has also been associated with the affiliation work of various universities like Guru Gobind Singh Indraprastha University Delhi, M.D. University Rohtak, U.P. Technical University Lucknow and Uttrakhand Technical University.



Dhruv Chandel Currently pursuing B.Tech in Information Technology from Delhi Technological University (formerly DCE). Proficient in languages like C, C++, Python. Skill Set consists of Web Developments using Django in backend and experience in fields of Data Mining, fine tuning Neural Networks and can handle various Machine Learning Techniques and algos. I am good at adapting and learning new skills when required and always interested in taking risks. Teamwork ,solving issue of compatibility with different OS's and confidence to present our work were the things are my speciality.
Have Good leadership and management skills and can adapt to new challenges and constraints.



Kunal Taneja 2nd year Student of Delhi Technological University, pursuing Bachelor of Technology in the field of Information Technology.
He has passed class X from Delhi public School ,Haridwar with 9.2 cgpa, completed class XII from Abhinav Public School with aggregate 94.2%.
He has always urge to constantly develop his skills and grow professionally. He is confident in his ability to come up with interesting ideas in the field of computer vision and artificial intelligence.
He have language proficiency in C, C++, Python, Dart. Also have dexterity in Data Structure and Algorithm, pursuing machine learning, artificial intelligence and have experience in openCV, keras, librosa. He have experience of learning app development using flutter.



Kartik Bansal Currently pursuing Bachelors in Technology(B.Tech) in Information Technology from Delhi Technological University (Previously known as DCE). Proficiency in languages like C, C++, Python, having good command over Data structures and Algorithms and currently learning and exploring the fields of Machine Learning, Deep Learning and Reinforcement Learning. Always ready to take up challenges and problems. Have curiosity in implementing different ideas and the approach for a particular task. Have excellent leadership qualities, persistent, focused, and confident about the work and always aspiring to learn new things. In this project he contributed in the model architecture design, Audio features extraction and optimization of neural networks. Wanted to grow both intellectually and professionally in coming years and explore the industry of Information Technology as far as possible.

Parametric Analysis of Smartphone Camera for a Low Cost Particle Image Velocimetry System

Vishesh Kashyap[1†], **Sushrut Kumar**[1], **Nehal Amit Jajal**[2], **Mrudang Mathur**[3] **& Raj Kumar Singh**[1‡]

[1]Department of Mechanical, Production & Industrial and Automobile Engineering, Delhi Technological University, Delhi, India

[2]Department of Mechanical and Aerospace Engineering, Ohio State University, U.S.A.

[3]Department of Mechanical Engineering, University of Texas at Austin, U.S.A.

arXiv:2002.01061v1 [eess.IV] 30 Jan 2020

Abstract. This study focuses on assessing smartphone camera characteristics for developing an economic smartphone-based Particle Image Velocimetry (PIV) system. In the investigation, flow around a cylinder was visualized using two commercially-available smartphones (OnePlus 5T and iPhone X) cameras and low-intensity laser diodes. Hydrogen bubbles generated from electrolysis (termed Bubble Image Velocimetry) of aluminum electrodes were used as seeding medium. OpenPIV, an open-source toolbox, was used for processing captured images and obtaining the flow fields. A parametric analysis of the two smartphones was conducted across varying camera characteristics such as ISO, exposure compensation and frame rate. The results obtained through experimentation were compared with the results of a validated computational fluid dynamics (CFD) study with the same flow conditions and were found to be in good agreement, with deviation ranging from 1% to 3.5% for iPhone X and 1% to 7% for OnePlus 5T. It was observed that a higher frame rate results in greater accuracy of the measurement. Further, an exposure compensation of -1 EV and an ISO of 400 was found to produce results with the least error as compared to CFD values.

Keywords Particle Image Velocimetry, Smartphones, Hydrogen Bubble Seeding

1 Introduction

Experimental fluid mechanics routinely requires the quantitative visualization and measurement of the overall flow properties of a fluid domain [1]. However, while flow measurement techniques such as Hot-Wire and Laser Doppler Anemometry are regularly used for measurements of such properties, they are restricted to measuring only at a few points of the domain simultaneously.

†Vishesh Kashyap and Sushrut Kumar have the Co-First/Equal authorship.

‡Corresponding Author E-mail : rajkumarsingh@dce.ac.in

Particle Image Velocimetry (PIV) is an experimental technique that involves the visualization of fluid flow under given experimental conditions. The main components of a PIV system are a laser, a camera, seeding particles and the channel, as shown in Figure 1. The fluid flowing through the channel is seeded with neutrally buoyant particles that remain suspended within it. These particles are illuminated by a plane of light originating from the laser and converted into a sheet by passing through an arrangement of cylindrical lenses. The flow of the seeding particles on the illuminated plane is analyzed using a correlation-based algorithm which determines the average motion of particles within small regions of the plane known as interrogation windows, between image pairs [2–4]. It then provides the flow profiles of the particles in form of vector lines. It may also provide parameters such as vorticity, given appropriate inputs such as time difference and reference distance [5].

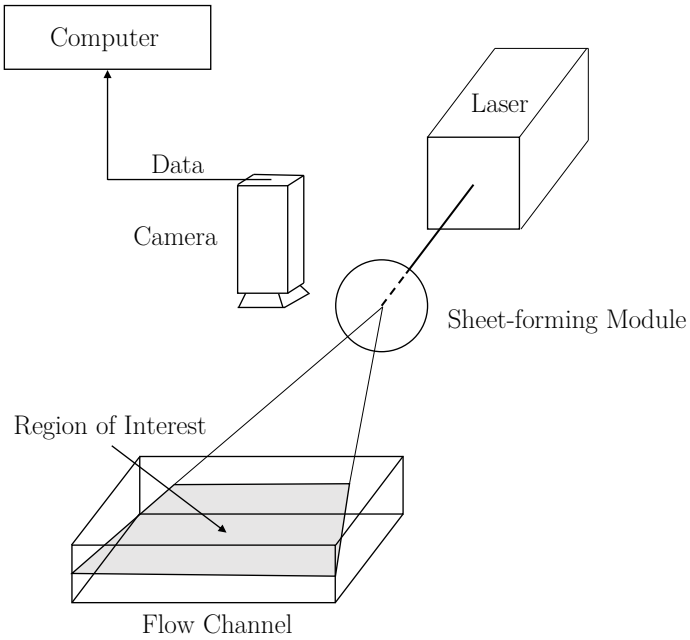


Figure 1: Basic components of a PIV system

Measurements using PIV must be of high accuracy and resolution for them to be usable for the calculation of quantities such as velocity, vorticity and other secondary variables [6–10]. However, one major hindrance to the application for PIV in research has been the cost of the system. Research grade systems often cost upwards of $100,000. This makes them inaccessible to a great number of researchers and students [11].

A number of considerations are integral to the reduction in cost of a PIV system. The seeding particles resist flow, and thus must be an appropriate size and density. These characteristics can be based on the resolution of the camera [12]. To ensure accurate measurement, a greater spatial concentration of seeding particles is required in the

region of measurement. Materials such as TiO_2 [13], Al_2O_3 [14], Polystyrene [15], resin [16] and microspheres [17] have in the past been used as seeding particles, primarily due to their non-corrosive, non-abrasive and chemically inert nature, with diameters of upto 0.5 mm [18, 19]. Dieter et al. [20] utilized hydrogen bubbles obtained by electrolysis of water in order to produce Eulerian flow vectors close to the air-water interface. Expensive seed particles have also attempted to be replaced by less costly alternatives such as fluorescent particles mixed with fluorescent dye [21] and white polystyrene beads [22]. In many of these solutions, the availability of the alternative is location-specific and sparse.

Commercial PIV applications typically utilize high-powered Nd:YAG (neodymium-doped yttrium aluminum garnet) [23, 24], ion [25] or argon [26, 27] lasers to illuminate the area of measurement. The pulse generation of these lasers is typically synchronized with the camera frame rate using separate equipment known as synchronizers. However, the price of these lasers is very high [28]. High-powered LEDs [29–32] with outputs over 10 W have been used to provide illumation as a cheaper option. Ring and Lemley [33] demonstrated the use of inexpensive laser diodes in PIV applications.

Typical modern PIV cameras contain a CCD or CMOS chip, which allows for the capturing of high-quality images and the reduction of image noise. Depending on the type of analysis, the frame rates of such cameras can be as high as 25600 frames-per-second (FPS). Modern PIV systems contain cameras with additional features such as multiple exposures, small pixel sizes (px) and short interframe time. However, these cameras are very expensive with costs upwards of $10000 common in the market. In recent years, similar features have become common in smartphone cameras, though at a much lower level. The OnePlus 5T (M1) and the iPhone X (M2) represented the highest end of camera features at the time experimentation was carried out. M2 has two 10 megapixel (MP) cameras, one each with a pixel size of 1.22 micron and 1.0 micron. M1 has pixel sizes of 1.12 micron and 1.0 micron. At a resolution of 1920 x 1080 px, M2 has a maximum frame rate of 240 FPS while M1 has a maximum of 60 FPS.

Adjusting the ISO or light sensitivity controls the amount of light the camera gets in order to form the image. A high ISO can introduce into the image noise in the form of extra grain. The PIV apparatus is operated in a darkened room, and hence the camera automatically sets ISO to high values. The automatic ISO value for the current study was observed to be in excess of 1000, which led to very bright images. The frame rate of the video defines the number of frames the camera captures per second. For the purpose of PIV measurements, a high frame rate is considered better since the relative movement of the seed particles among consecutive frames can be perceived better. Exposure compensation allows the user to override the common exposure settings chosen by the camera in favor of brighter or darker images. PIV typically requires two exposures in order that each may be isolated and cross-correlation analysis may be performed [34]. In smartphone cameras, adjustment of exposure is done by adjusting the exposure time, i.e. the time interval at which the two exposure shots are taken. While initial smartphone cameras did not allow for this, modern cameras can be used to adjust exposure compensation, which

may increase or decrease the exposure time.

Experimentation in an open channel allows for greater ease in the replacement of test bodies around which flow of liquid is to be visualized. A number of experimental studies of the velocity profile of developed open channel flow have been made [35, 36]. Various studies have been conducted over the decades to calculate the establishment length for an open channel under different conditions, yet there is limited information available to reach a parametric relation for the same [36].

While previous studies have attempted to develop economical alternatives to various elements of a PIV system [5,11,21,28] minimal research is available on the minimization of cost of the system along with an analysis of recording alternatives. This study involves the design and development of an inexpensive, yet accurate smartphone-based PIV system to be used for educational and research purposes. Hydrogen bubbles produced from the electrolysis of aluminum electrodes were used as seeding particles, commonly available laser diodes of power 1.5 Watt (W) for illumination and a smartphone camera for recording. The open-source PIV software OpenPIV [37] was used for analysis. The system has the advantage of convenient availability of components, ease of operation, repeatability and high adaptability. Measurements were carried out with a smartphone camera, at varying properties such as ISO, exposure compensation and frame rate.

2 Methodology

2.1 Design and Fabrication of Apparatus

The apparatus was designed and fabricated as well as experiments conducted at the Fluid Systems Laboratory, Delhi Technological University. The primary components of the apparatus were the channel for flow of water, electrodes for the production of hydrogen bubbles, pump for circulation and reservoirs for the provision of appropriate head and water collection.

An analytical study was carried out to determine the dimensions of the channel. Durst et al. [38] developed a parametric relation between the length of the channel (L) and the free surface level (D) in terms of the Reynolds Number (Re), as per equation (1).

$$\frac{L}{D} = [0.631^{1.6} + (0.0442Re)^{1.6}]^{\frac{1}{1.6}} \tag{1}$$

A region of interest was defined by studying velocities between 100 mm/s and 250 mm/s, constraining the length of the channel between 1900 and 2600 mm as per the space available. Figure 2 shows the development length of

the channel plotted against the free surface level at various velocities.

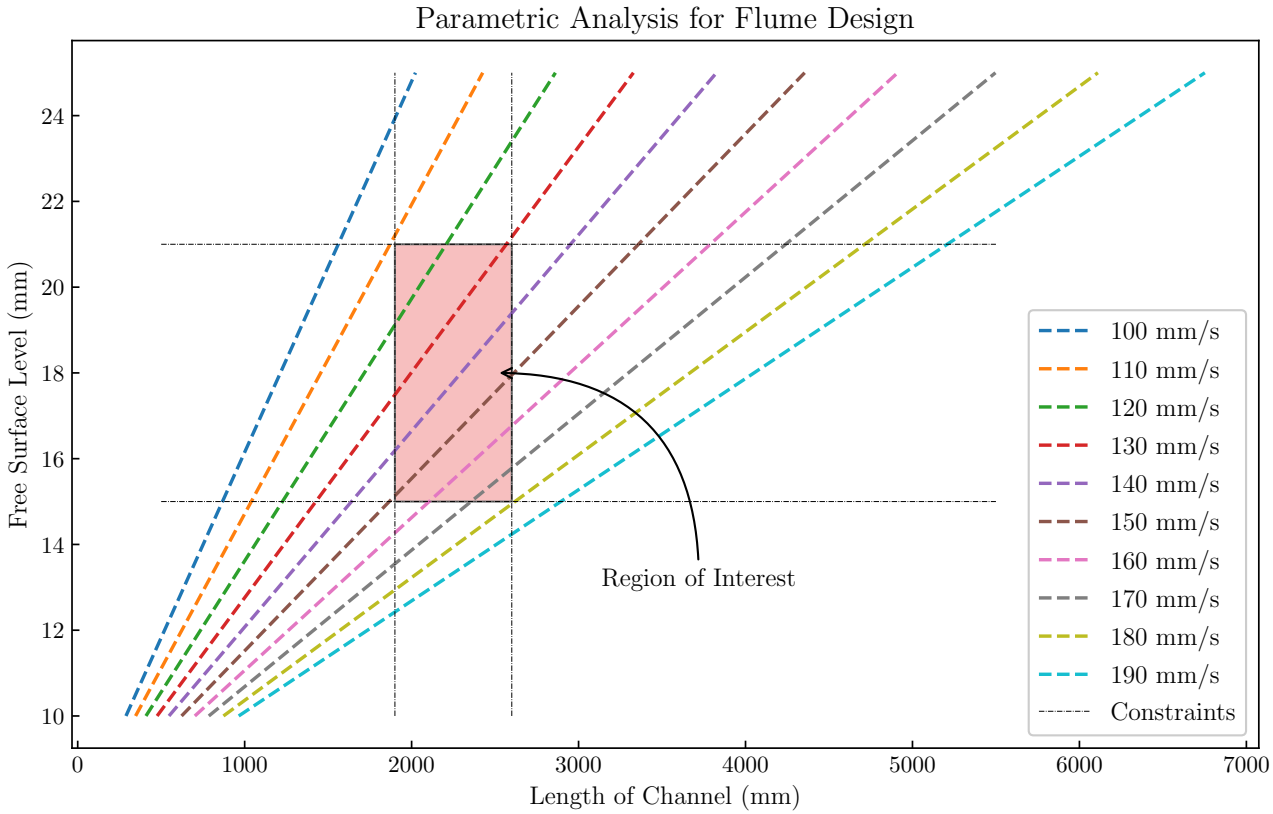


Figure 2: Analytical study for flume design

Based on the constraints, a velocity of 150 mm/s was chosen for further analysis, and a development length of 2137 mm was determined from the graph shown in Figure 2. The head of the upstream reservoir was fixed at 350 mm in order to obtain the required velocity of flow. Figure 3 represents the dimensions of the apparatus. The acrylic water channel was constructed through laser-cutting. The length of the water channel was 2.3 m, the width was 0.2 m and the height was 0.1 m. The recirculation was driven by a single-phase, 0.5 HP pump from the reservoir downstream to the one upstream, as shown in figure 3. Two aluminium electrodes of length 200 mm and radius 2.5 mm were placed on either side of the test body across the width of the channel and connected to a 5 W single phase variable transformer. The cathode was placed at 70 mm upstream and the anode 50 mm downstream from the test body. 50g salt was added to the upstream reservoir in order to increase the rate of electrolysis [39]. The electrodes were operated at a potential difference of 40 Volt (V). Hydrogen bubbles were generated by electrolysis. A 5 mW red (wavelength 650 nm) laser diode was used to illuminate the flow region. The laser module containing sheet-forming lenses was placed so as to create a laser sheet in a direction perpendicular to the flow of water and parallel to the ground. A mount was designed to ensure the parallelism of the plane of the laser sheet with respect to the free surface and the smartphone camera. The smartphone was placed at 100 mm above the base of the

channel and parallel to the ground at the position of the test body. The total cost of the experimental setup is INR 17300, and mentioned component-wise in Appendix I.

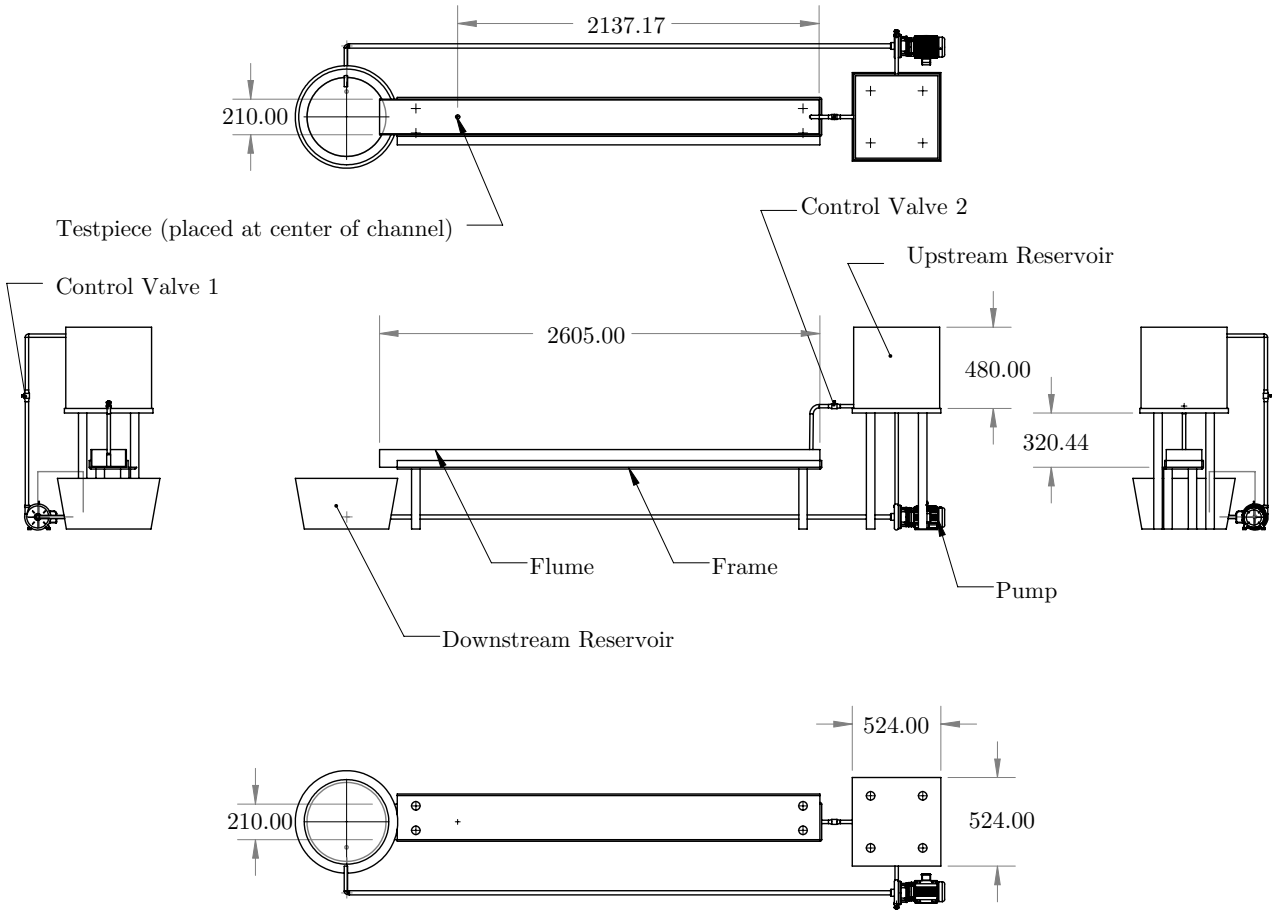


Figure 3: Schematic of Developed Apparatus

2.2 Experimentation

The cylindrical test body of radius 20 mm was placed at a distance of 2137 mm downstream. The mount containing the laser was placed to one side of the channel, perpendicular to the direction of flow. The laser sheet was parallel to the surface of water. The camera was placed directly above the specimen, as shown in figure 4. The upstream reservoir, downstream reservoir and flume were filled with water up to the required head, and the motor was started. The flow was allowed to stabilize by adjusting the speed of the motor to maintain a constant head in the upstream reservoir. When the flow was steady, a smartphone camera was used to record a video of length 10 seconds (s). The camera's field of view covered a length of 120 mm along the channel just above the free surface level at a height of 103 mm. At a video resolution of 1920×1080 px, this yielded an input of 0.0000625 m/px.

Videos for parametric analysis of frame rate, exposure compensation and ISO were recorded as per the available

settings in the phones, with the following conditions.

1. **Frame Rate:** Recordings were made at frame rates of 60 and 30 FPS for M1 and 240 FPS and 60 FPS for M2. The exposure compensation and ISO were kept constant at -1 EV and 400 respectively, at 1080p video mode.

2. **Exposure Compensation:** Recordings were made at exposure compensations of -2, -1, 0, 1 and 2 EV for M1 and M2. The ISO was kept constant at 400 for both smartphones, while the frame rate was 60 FPS at 1080p video mode.

3. **ISO:** Recordings were made at ISO modes of ISO 100, 200, 400 and 800 for M1. The frame rate was kept constant at 60 FPS and the exposure compensation at -1 EV, at 1080p video mode. M2 does not have a setting for variation of ISO.

The conditions are summarized in Table 1.

Table 1: Analysis settings for parametric study

Setting	**Phone**	**Value**	**Other Settings**	**No. of Readings**
Frame Rate	M1	30, 60 FPS	-1 EV, ISO 400	4
Frame Rate	M2	60, 240 FPS	-1 EV, ISO 400	4
Exposure Compensation	M1	-2, -1, 0, 1, 2 EV	60 FPS, ISO 400	3
Exposure Compensation	M2	-2, -1, 0, 1, 2 EV	60 FPS, ISO 400	4
ISO	M1	ISO 100, 200, 400, 800	60 FPS, -1 EV	5

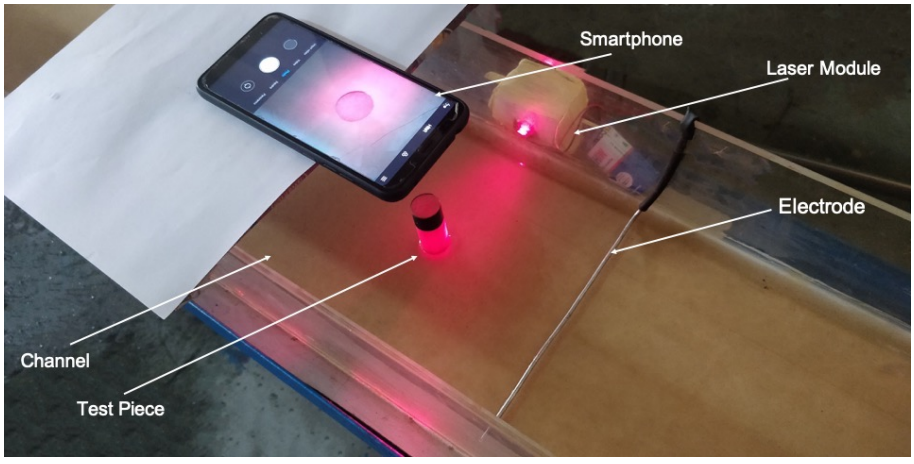


Figure 4: Region of experimentation and experimental setup.

2.3 Data Acquisition and Analysis

The software Free Video to JPG Converter [40] was used to split the recorded video into its constituent frames. The open-source MATLAB® toolbox OpenPIV was used for the analysis. An interrogation window of size 128 × 128

px was defined based on the number of particles in each window, and a pair of consecutive images was loaded into the toolbox. Metres per pixel (m/px) and time step dt (s) were taken as inputs. The value of velocity is calculated as per equation (2).

$$\text{Velocity}(\frac{m}{s}) = \frac{\text{meters per pixel } (\frac{m}{px}) \times \text{number of pixels } (px)}{\text{time step } (s)} \tag{2}$$

A vector field is constructed by OpenPIV by comparing the movement of particles between image pairs, and this process is repeated over every interrogation window of the region of interest. The result includes all the vectors normalized in comparison to the free stream velocity. OpenPIV then compiles a data file containing the calculated values of velocity in the X and Y direction of all the points studied. In this study, velocity values were obtained for a total of 75 points in 3 lines segments along the direction of flow as shown in Figure 5. The location of these segments was chosen in order to study the effectiveness of the smartphone cameras to appropriately capture the seeding particles in three distinct regions - at the centerline of the test piece (Line - 1), near the channel wall (Line - 2) and in a region between previous two (Line - 3).

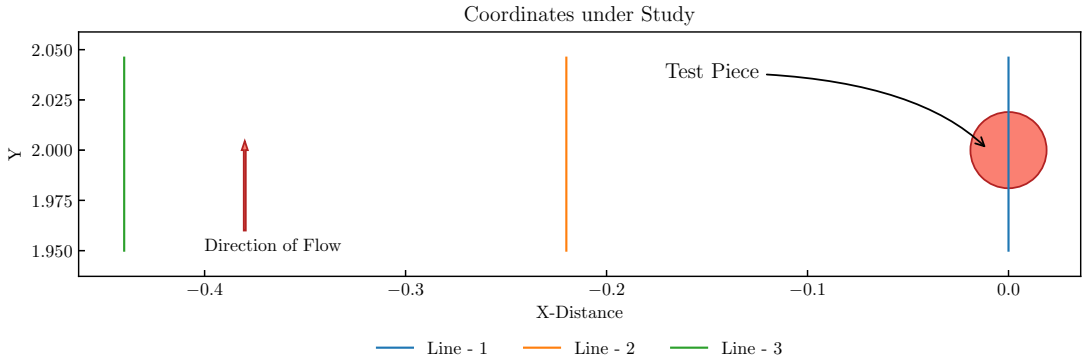


Figure 5: Lines studied for analysis.

2.4 Numerical Simulation

A Computational Fluid Dynamics (CFD) analysis was conducted in order to simulate the flow of water at the conditions of the present study. The analysis was performed by solving the RANS equations [41]. These are obtained by reynolds averaging the conservation form of transport equation. Equation 3 shows the continuity equation whereas Equation 4 is the momentum equation. In the equations, u_i is velocity of fluid, ρ is density, p is pressure, τ_{ij} represents the Reynolds stress terms and quantities with overbar are time average means.

$$\frac{\partial \bar{\rho}}{\partial t} + \frac{\partial \left(\bar{\rho}\hat{u}_i\right)}{\partial x_i} = 0 \tag{3}$$

$$\frac{\partial\left(\bar{\rho}\hat{u}_i\right)}{\partial t}+\frac{\partial\left(\bar{\rho}\hat{u}_i\hat{u}_j\right)}{\partial x_j}=-\frac{\partial\bar{p}}{\partial x_i}+\frac{\partial\bar{\sigma}_{ij}}{\partial x_j}+\frac{\partial\tau_{ij}}{\partial x_j} \tag{4}$$

The transport equations are discretised using the Finite Volume Method. The $k-\omega$ SST turbulence model was used to provide closure for the RANS equations. It is a two equation eddy viscosity model and is shown by Equation 5 and 6. The SST (Shear Stress Transport) formulation is helpful in working with high sensitivity of $k-\omega$ with inlet turbulence conditions [42].

$$\frac{\partial k}{\partial t}+U_j\frac{\partial k}{\partial x_j}=P_k-\beta^*k\omega+\frac{\partial}{\partial x_j}\left[\left(\nu+\sigma_k\nu_T\right)\frac{\partial k}{\partial x_j}\right] \tag{5}$$

$$\frac{\partial\omega}{\partial t}+U_j\frac{\partial\omega}{\partial x_j}=\alpha S^2-\beta\omega^2+\frac{\partial}{\partial x_j}\left[\left(\nu+\sigma_\omega\nu_T\right)\frac{\partial\omega}{\partial x_j}\right]+2\left(1-F_1\right)\sigma_{\omega2}\frac{1}{\omega}\frac{\partial k}{\partial x_i}\frac{\partial\omega}{\partial x_i} \tag{6}$$

SIMPLE algorithm (Semi-Implicit Method for Pressure Linked Equations) was used for pressure velocity coupling [43]. The simulations were conducted using ANSYS Fluent Academic Research 16.0. The computational domain follows the exact dimension of the actual apparatus. Grid independence tests were conducted and a cell size of 0.75 mm was determined for analysis. It was also ensured that the value of y+ always remained below 1 in the vicinity of cylinder and channel wall to be in accordance with law of wall function.

The inlet boundary condition was given as a velocity of 0.15 m/s and the outlet as pressure boundary condition with gauge pressure 0. Moreover, the boundary condition for cylinder and channel wall was set as no-slip. The drag coefficient obtained from the CFD study was observed to be 0.426. For purpose of validating the numerical simulation, this drag coefficient was correlated with previous literature data. As in published literature by Schlichting [44] and Pritchard [34], where Reynolds Number was plotted against drag coefficient, this value was experimentally found to be 0.420 in the conditions of the present study. These values are found to be within the margin of error ($< 1.5\%$). Thus the CFD simulation can be utilised for validating the PIV velocity data obtained from smartphones, M1 & M2. This is done by determining the velocity data from CFD simulation. The velocity field from the CFD analysis was determined for the three line segments chosen, as shown in Figure 6.

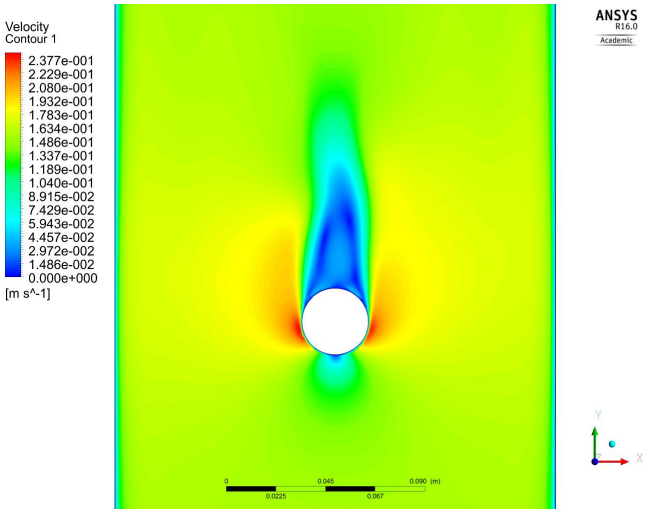


Figure 6: Velocity contours from top view of the CFD analysis

For the purpose of the study, the ordinates (Y) of the points under consideration were non dimensionalised as shown in Equation 7.

$$Y^* = \frac{Y}{Y_{\text{max}} - Y_{\text{center}}} \tag{7}$$

Where Y is the ordinate of the point under consideration, and Y_{max}, is the maximum variation of the line segment from its central value and Y_{center} is the value at the center of the line segment. The velocities were plotted in Figure 7 against values of Y^*.

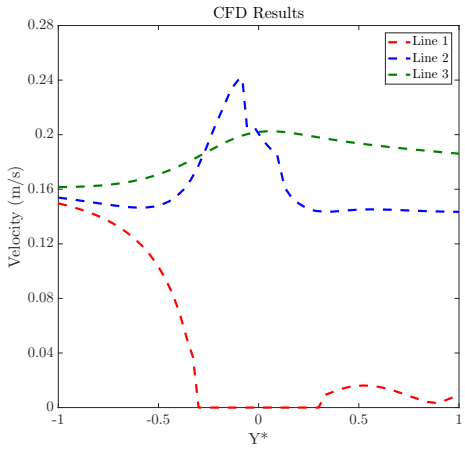


Figure 7: Velocity values plotted with Y^*

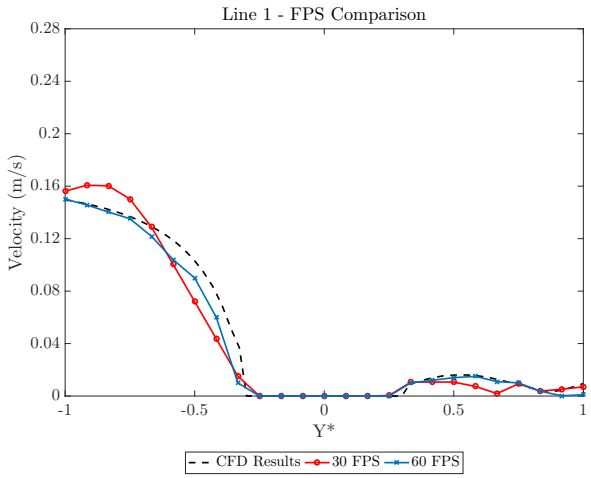
3 Results and Discussion

3.1 Analysis of Frame Rate

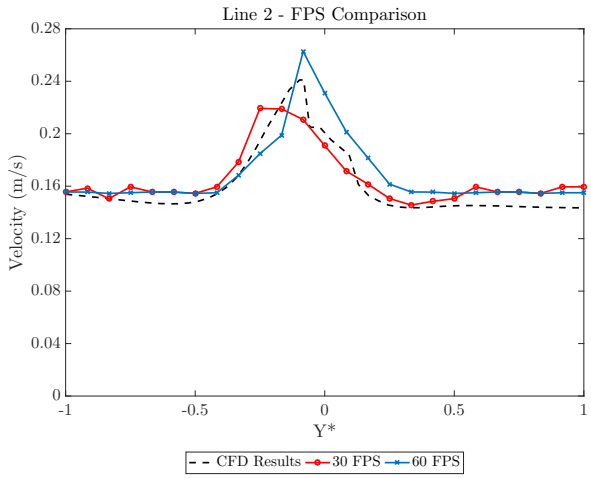
The velocities obtained through experimental analysis were compared with CFD values obtained for the same line segments. The velocities were plotted against values of Y^*. Figure 8 shows the observed velocities plotted against values of Y^* for various values of frame rate for M1, while Figure 9 shows these values for M2.

Table 2: Deviation at various values of FPS for M1 and M2

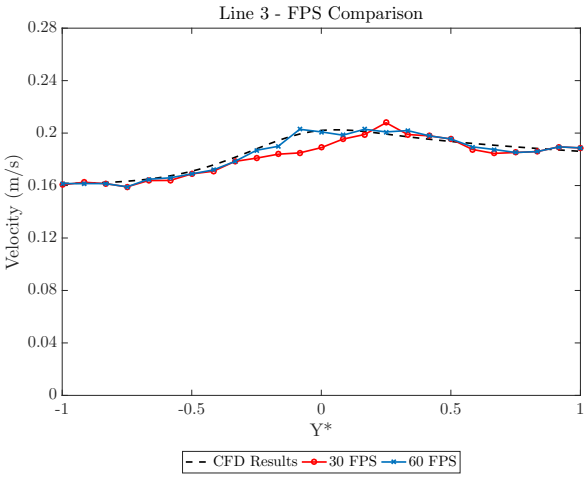
Phone	**Line**	**MAPE, 30 FPS**	**MAPE, 60 FPS**
M1	1	9.84%	7.18%
M1	2	10.03%	6.32%
M1	3	4.69%	1.09%
M2	1	8.56%	2.32%
M2	2	8.04%	3.54%
M2	3	2.34%	1.06%



(a)

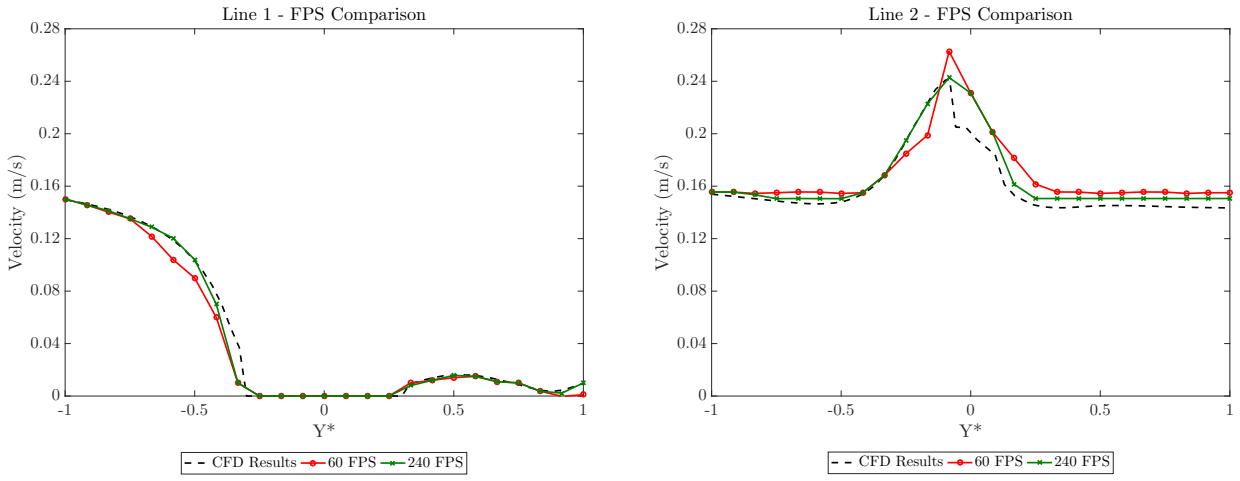


(b)



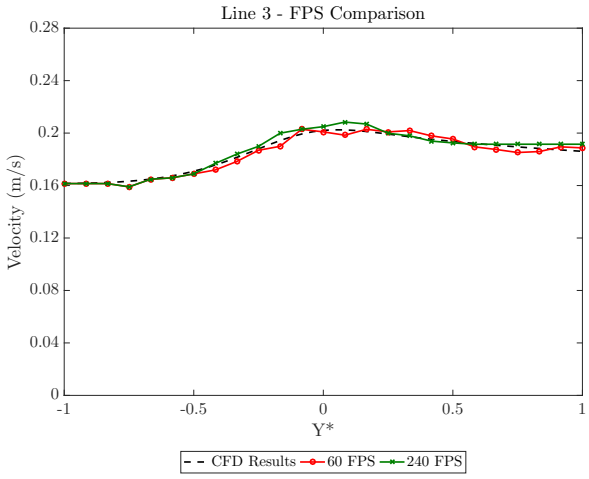
(c)

Figure 8: Values of velocities at various frame rates with change in Y-coordinate for M1



(a)

(b)



(c)

Figure 9: Values of velocities at various frame rates with change in Y-coordinate for M2

It can be observed from the graphs that an increase in the frame rate leads to greater concordance with the CFD values for the study. Table 2 elaborates on the mean absolute percentage error (MAPE) of the obtained values from the benchmark values for the two phones. It is evident from the data presented that the measurements done using M2 at 240 FPS are most reliable, with the lowest values of MAPE for all 3 lines. The data also reflects the inference from the graphs, that an increase in FPS increases the concordance with CFD values. In their study on the use of CCD pixel binning in PIV, Akselli et al. [45] asserted that increasing the frame rate of the camera had a significant positive impact on the results, even if it was at the cost of spatial resolution. An increase in frame rate means that pictures are captured at closer intervals in time, which allows for more reliable measurement of

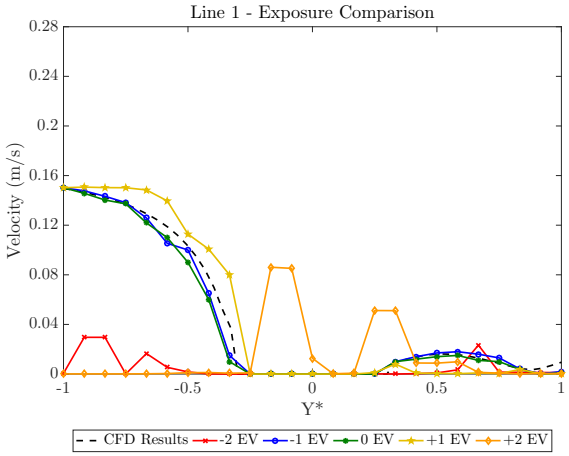
the exact trajectory of the flow by the PIV software. This is particularly important for complex flows, where the velocity or direction of flow may change rapidly with change in geometry or physical conditions.

3.2 Analysis of Exposure Compensation

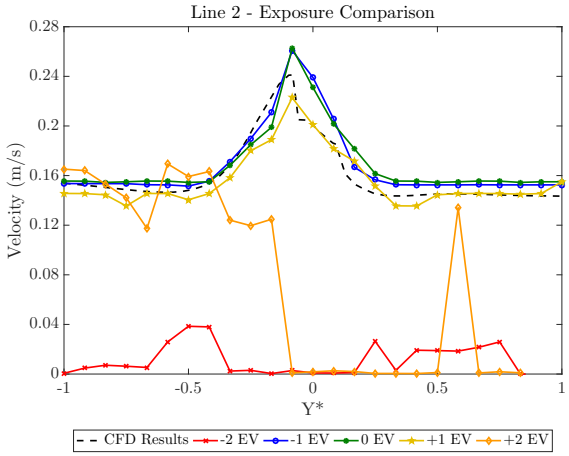
Figure 10 shows the observed velocities plotted against values of Y^* for various values of exposure compensation for M1, while Figure 11 contains these values for M2. The graphs indicate that the observations for exposure compensations of -2 and 2 are highly deviated, since they diverge considerably from the CFD values considered. The intermediate values of -1, 0 and 1 are observed to show comparatively greater agreement with these values. Table 3 depicts the MAPE of the obtained values from the benchmark values for the two phones.

Table 3: Deviation at various values of Exposure Compensation for M1 and M2

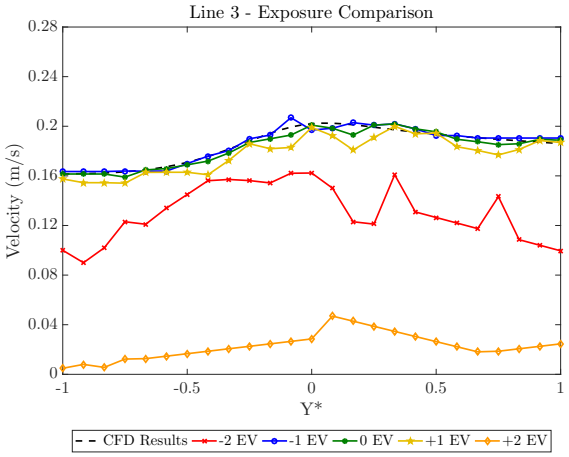
Phone	**Line**	**MAPE, -1 EV**	**MAPE, 0 EV**
M1	1	6.08%	7.56%
M1	2	5.68%	7.04%
M1	3	1.07%	2.34%
M2	1	2.47%	4.87%
M2	2	3.29%	4.94%
M2	3	0.99%	2.01%



(a)

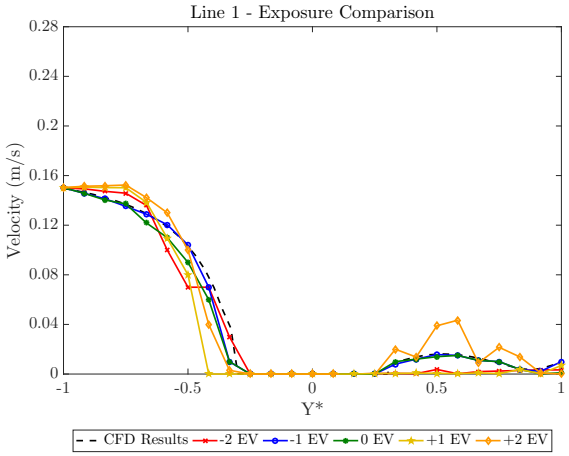


(b)

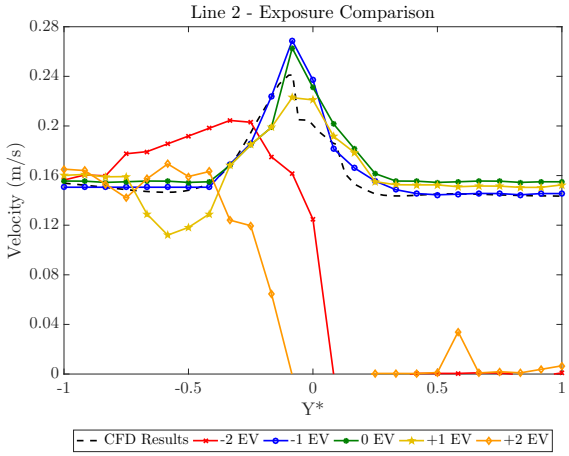


(c)

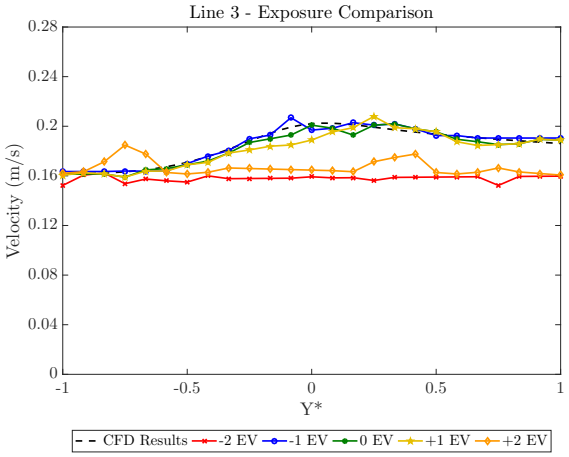
Figure 10: Values of velocities at various exposure compensations with change in Y-coordinate for M1



(a)



(b)



(c)

Figure 11: Values of velocities at various exposure compensations with change in Y-coordinate for M2

While it is evident from Figure 10 and Figure 11 that an exposure compensation of 1 EV gives significantly deviated results, the observations for -1 EV and 0 EV are observed to be relatively closer to CFD values. However, in each case studied, it was observed that an exposure compensation of -1 EV gave the greatest accuracy. Reducing the exposure time reduces the amount of light entering the camera. This also allows for greater autocorrelation, thus leading to more reliable results. However, reducing the exposure compensation beyond a point can lead to the amount of light not being enough to decipher even the seeding particles, which will lead to inaccurate results.

3.3 Analysis of ISO levels

Figure 12 shows the PIV-measured velocities plotted against values of Y^* for various values of ISO for M1. M2 does not have an option for adjustment of ISO levels. As in the case of exposure compensation, the extreme values of ISO are observed to be highly variant as compared to the CFD values for the analysis. Table 4 gives the MAPE of the obtained values from the benchmark values for the two phones. It is evident from the data obtained that an ISO of 400 gives the least deviated results, with a maximum deviation of about 6%. ISO governs the brightness of an image, and higher values of ISO can lead to grainy images, which reduce the quality of the image and render seeding particles less decipherable. At the same time, lower values can lead to exceedingly dark images. The ISO value was reduced, and 400 was observed to be the most suitable.

Table 4: Deviation at various values of ISO for M1

Phone	**Line**	**MAPE, 200 ISO**	**MAPE, 400 ISO**
M1	1	7.92%	5.23%
M1	2	6.45%	5.15%
M1	3	3.02%	0.99%

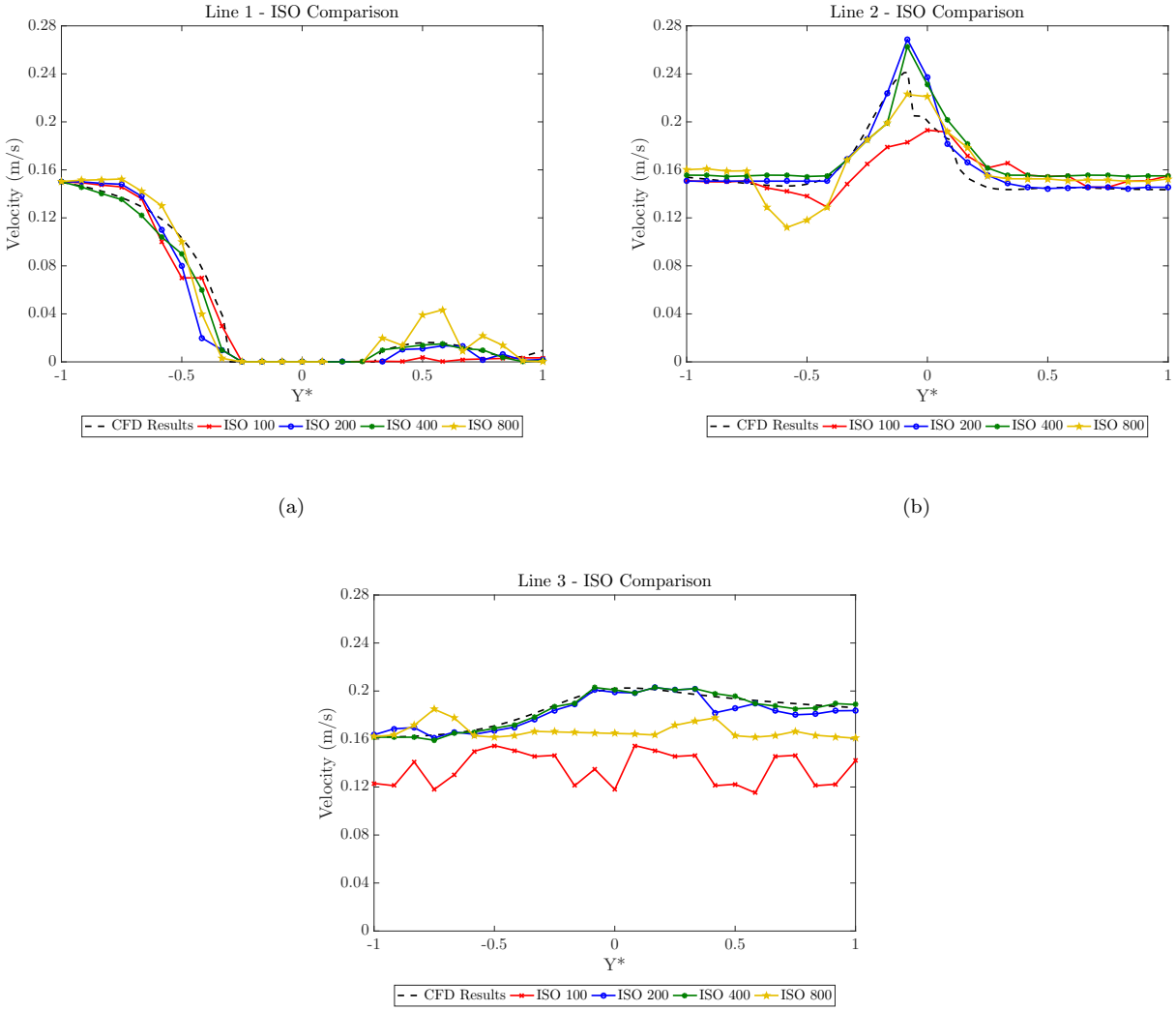


Figure 12: Values of velocities at various ISO levels with change in Y-coordinate for M1

3.4 Analysis of Deviation

The experimental observations were compared to the CFD results in each test conducted in the present study. The mean average deviation (MAD), standard deviation and mean absolute percentage errors(MAPE) were calculated, as shown in table 5.

Table 5: Deviation analysis of experimental observations.

S.No.	**Line**	**Phone**	**Characteristic**	**MAD (m/s)**	**Standard Deviation (m/s)**	**MAPE (%)**
1	Line 1	M1	Frame Rate (60 FPS)	0.0041	0.0047	7.18
2	Line 1	M1	Exposure Compensation (-1 EV)	0.0041	0.0047	7.08
3	Line 1	M1	ISO (400)	0.0031	0.0032	5.23
4	Line 1	M2	Frame Rate (240 FPS)	0.0013	0.0015	2.32
5	Line 1	M2	Exposure Compensation (-1 EV)	0.0013	0.0015	2.47
6	Line 2	M1	Frame Rate (60 FPS)	0.0108	0.0073	6.32
7	Line 2	M1	Exposure Compensation (-1 EV)	0.0108	0.0073	6.68
8	Line 2	M1	ISO (400)	0.0083	0.0074	5.15
9	Line 2	M2	Frame Rate (240 FPS)	0.0057	0.0053	3.54
10	Line 2	M2	Exposure Compensation (-1 EV)	0.0053	0.0080	3.29
11	Line 3	M1	Frame Rate (60 FPS)	0.0024	0.0019	1.09
12	Line 3	M1	Exposure Compensation (-1 EV)	0.0024	0.0019	1.07
13	Line 3	M1	ISO (400)	0.0022	0.0018	0.99
14	Line 3	M2	Frame Rate (240 FPS)	0.0022	0.0019	1.06
15	Line 3	M2	Exposure Compensation (-1 EV)	0.0022	0.0018	0.99

It was observed that the results obtained for the M2 were more accurate than those for the M1 in every case. The percentage deviation for the M2 was found to vary between 1% and 3.54%, while that for the M1 varied between 1% and 7.08%. The values obtained for Line 3 showed considerable agreement with the CFD results, while those for Line 1 showed a comparatively higher deviation. The average deviation for the M2 was calculated as 2.30% while that for the M1 was 4.51%. Figure 13 shows the resolved velocity vectors for the best setting from M2. Vectors at two regions are not present because of the lack of illumination predominantly on the right side of test piece.

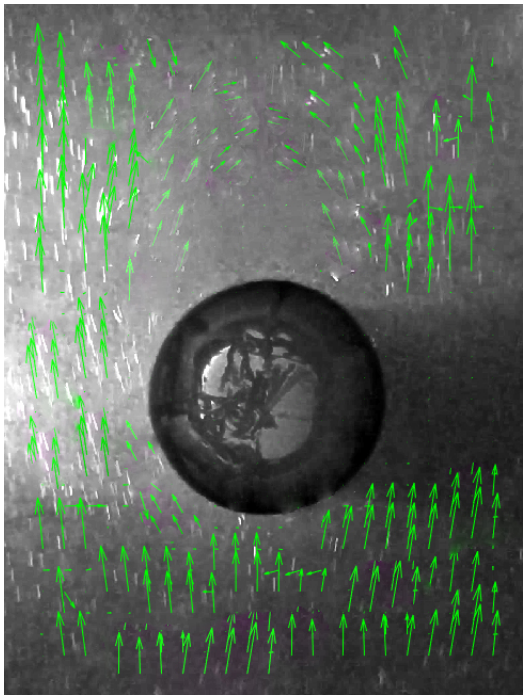


Figure 13: Velocity vectors for analysis with M2 at 240 FPS

4 Conclusion

A PIV system for flow visualization and measurement was constructed in INR 17300 (under USD 250). The designed system was able to observe the flow field in the region under study. It was observed that an increase in the value of frame rate increases the agreement of measurement. Further, an exposure compensation of -1 EV and an ISO of 400 were associated with the greatest agreement of measurement in the current study. The deviation for the optimum characteristics ranges from 1% to 3.5% for iPhone X and 1% to 7% for OnePlus 5T.

The given study also creates scope for further improvement in the area of smartphone-based PIV. As the frame rate capability of smartphones increases, so will the capacity of the system to give better results. An increase in camera quality (in terms of video resolution) can also be associated with an ability to resolve smaller seeding particles, improving output.

5 Acknowledgements

The authors would like to thank Third phase of Technical Education Quality Improvement Programme (referred to as TEQIP-III) at Delhi Technological University (DTU) for providing grant to carry out procurement of items and fabrication of apparatus necessary for carrying out the investigation. We would also like to thank the members of Fluid Mechanics Group and staff members of Fluid Systems Laboratory, DTU for providing technical support

during fabrication of the appratus and conduction of experiment.

6 Ethical statement

The authors declare that the contents of the paper are not published elsewhere or will not be submitted to any other place during the review process. We also have no conflict of interests.

Appendix I

The total cost of the apparatus in Indian Rupee is shown in Table 6.

Table 6: Total Cost of Apparatus

S. No.	**Component**	**Cost (INR)**
1	Open Channel(Acrylic)	6200
2	0.5 HP Pump	2700
3	Reservoirs (×2)	2100
4	Channel Frame	2000
5	Silicone and Epoxy	1600
6	1-Phase Variac	1600
7	PVC Fitting and Pipes	700
8	Laser Diode	200
9	Aluminium Electrodes	200
	Total	17300

References

[1] M. Raffel, C. E. Willert, F. Scarano, C. J. Kähler, S. T. Wereley, and J. Kompenhans, *Particle image velocimetry: a practical guide*. Springer, 2018.

[2] A. K. Prasad, "Particle image velocimetry," *Current Science-Bangalore-*, vol. 79, no. 1, pp. 51–60, 2000.

[3] F. Scarano, "Tomographic piv: principles and practice," *Measurement Science and Technology*, vol. 24, no. 1, p. 012001, 2012.

[4] K. Lasinger, C. Vogel, T. Pock, and K. Schindler, "Variational 3d-piv with sparse descriptors," *Measurement Science and Technology*, vol. 29, no. 6, p. 064010, 2018.

[5] W. G. Ryerson and K. Schwenk, "A simple, inexpensive system for digital particle image velocimetry (dpiv) in biomechanics," *Journal of Experimental Zoology Part A: Ecological Genetics and Physiology*, vol. 317, no. 2, pp. 127–140, 2012.

[6] C. Gray, "The development of particle image velocimetry for water wave studies.," 1989.

[7] R. J. Adrian, "Twenty years of particle image velocimetry," *Experiments in fluids*, vol. 39, no. 2, pp. 159–169, 2005.

[8] S. Discetti and R. J. Adrian, "High accuracy measurement of magnification for monocular piv," *Measurement Science and Technology*, vol. 23, no. 11, p. 117001, 2012.

[9] S. J. Beresh, J. F. Henfling, R. W. Spillers, and S. M. Spitzer, "'postage-stamp piv': small velocity fields at 400 khz for turbulence spectra measurements," *Measurement Science and Technology*, vol. 29, no. 3, p. 034011, 2018.

[10] S. Scharnowski, A. Sciacchitano, and C. Kaehler, "On the universality of keane & adrian's valid detection probability in piv," *Measurement Science and Technology*, 2019.

[11] B. P. Ring, D. K. Atkinson, A. W. Henderson, and E. C. Lemley, "Development of a low cost particle image velocimetry system for fluids engineering research and education," in *ASME 2013 Fluids Engineering Division Summer Meeting*, American Society of Mechanical Engineers Digital Collection, 2013.

[12] D. Mei, J. Ding, S. Shi, T. New, and J. Soria, "High resolution volumetric dual-camera light-field piv," *Experiments in Fluids*, vol. 60, no. 8, p. 132, 2019.

[13] E. Longmire and A. Alahyari, "Piv measurements in simulated microbursts," in *Proceedings 7th International Symposium on Applications of Laser Techniques to Fluid Mechanics, Lisbon*, 1994.

[14] Z.-C. Liu, C. Landreth, R. Adrian, and T. Hanratty, "High resolution measurement of turbulent structure in a channel with particle image velocimetry," *Experiments in fluids*, vol. 10, no. 6, pp. 301–312, 1991.

[15] B. Khoo, T. Chew, P. Heng, and H. Kong, "Turbulence characterisation of a confined jet using piv," *Experiments in fluids*, vol. 13, no. 5, pp. 350–356, 1992.

[16] M. Bown, J. MacInnes, R. Allen, and W. Zimmerman, "Three-dimensional, three-component velocity measurements using stereoscopic micro-piv and ptv," *Measurement Science and Technology*, vol. 17, no. 8, p. 2175, 2006.

[17] L. J. Graham and J. Soria, "A study of an inclined cylinder wake using digital particle image velocimetry," in *Proceedings 7th International Symposium on Applications of Laser Techniques to Fluid Mechanics, Lisbon*, 1994.

[18] A. Melling, "Tracer particles and seeding for particle image velocimetry," *Measurement Science and Technology*, vol. 8, no. 12, p. 1406, 1997.

[19] T. Van Overbrüggen, M. Klaas, J. Soria, and W. Schröder, "Experimental analysis of particle sizes for piv measurements," *Measurement Science and Technology*, vol. 27, no. 9, p. 094009, 2016.

[20] J. Dieter, R. Bremeyer, F. Hering, and B. Jähne, "Flow measurements close to the free air/sea interface," in *Proceedings 7th International Symposium on Applications of Laser Techniques to Fluid Mechanics, Lisbon*, 1994.

[21] F. Pedocchi, J. E. Martin, and M. H. García, "Inexpensive fluorescent particles for large-scale experiments using particle image velocimetry," *Experiments in Fluids*, vol. 45, no. 1, pp. 183–186, 2008.

[22] M. Walkden, G. Müller, T. Bruce, *et al.*, "Low-cost particle image velocimetry: system and application," in *The Eighth International Offshore and Polar Engineering Conference*, International Society of Offshore and Polar Engineers, 1998.

[23] D. P. Hart, "Sparse array image correlation," in *Developments in Laser Techniques and Fluid Mechanics*, pp. 53–74, Springer, 1997.

[24] Y. Hassan, R. Martinez, O. Philip, and W. Schmidl, "Flow measurement of a two-phase fluid around a cylinder in a channel using particle image velocimetry," *Transactions of the American Nuclear Society*, vol. 71, no. CONF-941102-, 1994.

[25] M. Oishi, H. Kinoshita, T. Fujii, and M. Oshima, "Phase-locked confocal micro-piv measurement for 3d flow structure of transient droplet formation mechanism in t-shaped microjunction," *Measurement Science and Technology*, vol. 29, no. 11, p. 115204, 2018.

[26] I. Grant, G. Smith, D. Infield, X. Wang, Y. Zhao, and S. Fu, "Measurements of the flow around wind turbine rotors by particle image velocimetry," in *Proc. 7th Int. Symp. on Applications of Laser Techniques to Fluid Mechanics, Lisbon*, 1994.

[27] I. Grant and X. Wang, "Directionally-unambiguous, digital particle image velocimetry studies using a image intensifier camera," *Experiments in fluids*, vol. 18, no. 5, pp. 358–362, 1995.

[28] C. Cierpka, R. Hain, and N. A. Buchmann, "Flow visualization by mobile phone cameras," *Experiments in Fluids*, vol. 57, no. 6, p. 108, 2016.

[29] C. Willert, B. Stasicki, J. Klinner, and S. Moessner, "Pulsed operation of high-power light emitting diodes for imaging flow velocimetry," *Measurement Science and Technology*, vol. 21, no. 7, p. 075402, 2010.

[30] N. A. Buchmann, C. E. Willert, and J. Soria, "Pulsed, high-power led illumination for tomographic particle image velocimetry," *Experiments in fluids*, vol. 53, no. 5, pp. 1545–1560, 2012.

[31] A. A. Aguirre-Pablo, M. K. Alarfaj, E. Q. Li, J. F. Hernández-Sánchez, and S. T. Thoroddsen, "Tomographic particle image velocimetry using smartphones and colored shadows," *Scientific reports*, vol. 7, no. 1, p. 3714, 2017.

[32] M. Mommert, D. Schiepel, D. Schmeling, and C. Wagner, "A flow-intrinsic trigger for capturing reconfigurations in buoyancy-driven flows in automated piv," *Measurement Science and Technology*, vol. 30, no. 4, p. 045301, 2019.

[33] M. B. P. Ring and E. C. Lemley, "Design and implementation of a low cost particle image velocimetry sys-tem for undergraduate research and education," *age*, vol. 24, p. 1, 2014.

[34] P. J. Pritchard and J. W. Mitchell, *Fox and McDonald's Introduction to Fluid Mechanics, Binder Ready Version*. John Wiley & Sons, 2016.

[35] M. S. Kirkgöz and M. Ardiçlioğlu, "Velocity profiles of developing and developed open channel flow," *Journal of Hydraulic Engineering*, vol. 123, no. 12, pp. 1099–1105, 1997.

[36] H. Bonakdari, F. Larrarte, L. Lassabatere, and C. Joannis, "Turbulent velocity profile in fully-developed open channel flows," *Environmental Fluid Mechanics*, vol. 8, no. 1, pp. 1–17, 2008.

[37] Z. J. Taylor, R. Gurka, G. A. Kopp, and A. Liberzon, "Long-duration time-resolved piv to study unsteady aerodynamics," *IEEE Transactions on Instrumentation and Measurement*, vol. 59, no. 12, pp. 3262–3269, 2010.

[38] F. Durst, S. Ray, B. Ünsal, and O. Bayoumi, "The development lengths of laminar pipe and channel flows," *Journal of fluids engineering*, vol. 127, no. 6, pp. 1154–1160, 2005.

[39] S.-Y. Hsu, "Effects of water flow rate, salt concentration and water temperature on efficiency of an electrolyzed oxidizing water generator," *Journal of Food Engineering*, vol. 60, no. 4, pp. 469–473, 2003.

[40] "Dvdvideosoft," 2018.

[41] S. Kumar, P. Gupta, and R. K. Singh, "Metaheuristic Optimization of Dual-Element Vertical Axis Wind Turbine Using Genetic Algorithm," vol. 2: Renewable Energy: Solar and Wind of *ASME Gas Turbine India Conference*, 12 2019.

[42] S. Kumar, P. Gupta, and R. K. Singh, "A Natural Evolution Based Numerical Optimisation Framework to Develop and Enhance Airfoil-Slat Arrangement," vol. 7: Fluids Engineering of *ASME International Mechanical Engineering Congress and Exposition*, 11 2019.

[43] A. Saxena, E. Ng, M. Mathur, C. Manchanda, and N. A. Jajal, "Effect of carotid artery stenosis on neck skin tissue heat transfer," *International Journal of Thermal Sciences*, vol. 145, p. 106010, 2019.

[44] H. Schlichting and K. Gersten, *Boundary-layer theory*. Springer, 2016.

[45] B. Akselli, A. Kholmatov, and H. Nasibov, "The use of ccd pixel binning in piv measurements," in *2009 International Symposium on Optomechatronic Technologies*, pp. 223–228, IEEE, 2009.

International Journal of Research in Engineering and Innovation (IJREI)
journal home page: http://www.ijrei.com
ISSN (Online): 2456-6934

Performance evaluation of single effect Li/Br-H_2O vapour absorption systems using multi cascading of vapour compression cycles for ultra-low temperature applications

Radhey Shyam Mishra

Department of Mechanical Engineering, Delhi Technological University Delhi, India

Abstract

Performance evaluation of LiBr-H2O vapour absorption systems using multi cascading of vapour compression systems using HFO-1234yf in medium temperature cycle for -50^{0}C and R-245fa in intermediate temperature cycle for -100^{0}C and R-236fa in low temperature cycle for -150^{0}C ultra-low temperature applications have been carried out It is found that overall first law efficiency (COP_Overall) for 123K evaporator temperature using R236fa is less than the overall first law efficiency (COP_Overall) for 273K evaporator temperature using 245fa. However when continuous improvement in second law (exergetic) performances which caused continuous reduction in system exergy destruction ratio. The percentage improvement in first law efficiency (COP_Overall) is found using single stage cascade vapour compression refrigeration system (VCRS) is 7.96% and using multi (two stages) cascade VCRS is 21.53% and using multi (three stages) cascade VCRS is 15.52% for all 10^{0}C of temperature overlapping however the percentage improvement in second law efficiency (exergetic efficiency) is found using single stage cascade vapour compression refrigeration system (VCRS) is 37.27% and using multi (two stages) cascade VCRS is 128% and using multi (three stages) cascade VCRS is 146.9% for all 10^{0}C of temperature overlapping. Similarly the percentage decrement in system exergy destruction ratio is found using single stage cascade vapour compression refrigeration system (VCRS) is 34.32% and using multi (two stages) cascade VCRS is 70.63% and using multi (three stages) cascade VCRS is 74.77% for all 10^{0}C of temperature overlapping. ©2020 ijrei.com. All rights reserved

Keywords: vapour absorption systems, vapour compression cycles, COP, Exergy.

1. Introduction

In the present-day, the situation, the energy, exergy, economy, environment and safety strategies are the key issues which are practicality restrained to evaluate refrigeration cycles both having higher as well as ultra-low evaporator temperatures. Although the ultra-low temperatures for cryogenics is approaching 0 K, and its applications such as freeze drying, pharmaceuticals, chemical and petroleum industry use cascade refrigeration cycles[1-2].

As reported by Chen et.al. [3], that the demand of refrigeration at the low evaporation temperature is increasing which ranges from high heat flux microchip technology to rapid freezing, freezing food and cold storage. The demand of refrigeration at the low evaporation temperature is increasing which ranges from high heat flux electronics to rapid freezing, frozen food and cold storage. Tassouet al. [4], suggested that the refrigeration is a necessary part of the food chain and to slow down the physical, chemical and microbiological activities that cause deterioration in food, the food is frozen between18 to35°C. Generally, technologies of mechanical refrigeration are invariably employed in these processes which either contribute electricity consumption and environmental impact or low performance.

These processes include vapor compression refrigeration, half, single, double and triple effect vapor absorption refrigeration systems. Although the performance of vapor compression refrigeration cycle succeeds the others yet its electricity consumption is higher. Rabah Gomri [5-6] carried out exergy analysis and thermo-economic optimization of the triple-effect Li/Br-water absorption refrigerating system and found maximum exergetic efficiency of triple effect refrigeration system is about 35.1 % for condenser 30°C , absorber cooling water temperature

Corresponding author: R.S. Mishra
Email Address: hod.mechanical.rsm@dtu.ac.in
http://doi.org/10.36037/IJREI.2020.4103

(25°C) and chilled water temperature (12°C/7°C) respectively. Colorado and Rivera [7] compared the thermal performance of a conventional vapor compression and compression-absorption single-stage and double-stage refrigeration systems. They recognized that in the current situation, the energy, exergy, economy, and environment and safety strategies are the main issues which are being considered to evaluate refrigeration cycles both having higher as well as lower evaporator temperatures. The low temperatures approaching 0 K, air conditioning and its applications such as freeze drying, pharmaceuticals, chemical and petroleum industry used cascade refrigeration cycles and also acknowledged that the electrical energy consumption in compression-absorption single-stage and double stage refrigeration system was 45% lower than that of vapour compression refrigeration cycle and the COP of double stage refrigeration system was 50% higher than that of single stage compression-absorption refrigeration system.

R.S. Mishra [8] compared three cascaded vapour compression systems cascaded with evaporator of LiBr-H_2O vapour absorption refrigeration system cascaded by condenser of single vapour compression refrigeration system using ecofriendly refrigerants (i.e. R1234yf, R134a, R-32, R507a, R227ea, R236fa, R245fa , R717) and energy and exergy analysis of all three systems were carried out because exergy (second law) analysis used to facilitates the identification of the system components with high exergy loss compared the performance parameters with three cascaded vapour absorption-single stage vapour compression refrigeration system and it was observed that 122% first law efficiency enhancement using triple effect VARS cascaded with VCRS and 79.45% enhancement in second law efficiency using triple effect VARS cascaded with VCRS. Similarly exergy reduction is 56.60% using triple effect VARS cascaded with single stage VCRS and 25.9% reduction using double effect VARS cascaded with single stage VCRS An Similarly performance parameters have been compared with three cascade vapour absorption-compression refrigeration system and it was observed that 22.87% first law efficiency enhancement using triple effect VARS cascaded with VCRS and 46.3% enhancement in second law efficiency using triple effect VARS cascaded with VCRS as compared with double effect vapour absorption refrigeration cascaded with single stage vapour compression refrigeration system. Similarly exergy reduction is 41.4% using triple effect VARS cascaded with single stage VCRS as compared to double effect VARS cascaded with single stage VCRS.

Tassouet al. [9] suggested that the refrigeration is a essential part of the food chain and to slow down the physical, chemical and microbiological activities that cause deterioration in food, the food is frozen between16°C. to35°C.

Generally, technologies of mechanical refrigeration are always employed in these processes which either contribute electricity consumption and environmental impact or lower performance. These processes include vapor compression refrigeration, half, single, double and triple effect vapor absorption refrigeration systems. Ayala et al. [10], analyzed Ammonia/Lithium Nitrate vapour absorption and Ammonia mechanical vapor compression combined refrigeration plant. They deduced that the over-all efficiency of the combined refrigeration plant was higher than that of individual compression or absorption refrigeration cycle and increased by 10%. A large number of studies are available in the literature on compression-absorption (combined) or cascade refrigeration cycles. The considered studies fall under two categories viz. single stage and double stage cycles. The first configuration is the combination of single effect VAR cycle coupled to a VCR cycle and the second configuration comprises of a double effect VAR cycle coupled to a VCR cycle. R.S. Mishra[11], develop an integrated solar refrigeration system where waste heat from different energy resources assists a combined vapour absorption compression system, and to analyze feasibility & practicality of that system of thermodynamically for improving its COP and exergetic efficiency by reduction of irreversibility in terms of exergy destruction /losses occurred in the system components. The combined thermodynamic first law efficiency in terms of coefficient of performance ($COP_{_Overall}$), second law efficiency in terms of exergetic efficiency and exergy destruction ratio based on exergy of product of a combined vapour absorption-compression system working with each of the following refrigerants in the cascaded vapour compression cycle R1234yf, R227ea, R236fa, R245fa, R143a,R134a, R32, R507 operating at -223 K evaporator temperature with temperature overlapping (Approach means the difference between cascaded condenser temperature of vapour compression cycle and evaporator temperature of vapour absorption refrigeration cycle working at 13.5 bar of highest generator pressure and 1.75 bar as lowest evaporator pressure have been presented and it is found thatR141b and R245fa gives better performances. Kairouani and Nehdi [12], analyzed aNH3-H2O vapor absorption cycle powered by geothermal energy-R717, R22 and R134a vapor compression cascade cycle and combined cycle. They concluded that the COP of cascade cycle was 5.5 and the COP value was 37–54% higher than that of vapor com-pression refrigeration cycle. Mishra [13] found that the thermodynamic performances in the case of cascaded half effect vapour absorption refrigeration system coupled with vapour compression cycle is improved by 44.65% increment of first law efficiency (i.e. over all COP), 172.87% increment of second law efficiency (i.e. exergetic efficiency) of the half effect vapour absorption refrigeration cascaded with vapour compression cycle using HFC-134a, 42.87% enhancement in first law efficiency (COP) of 142.73% increment of second law efficiency using HFO -1234yf for -50^{o}C of evaporator temperature of VCRS . Similarly 72.02% reduction in exergy destruction ratio based on exergy of output of the half effect vapour absorption refrigeration cascaded with vapour compression cycle using HFC-134a and 70.44% reduction in exergy destruction ratio using HFO-1234yf ecofriendly refrigerant for -50^{0}C of evaporator temperature of VCRS. The performances of single effect cascaded vapour absorption refrigeration system coupled with vapour compression cycle significantly higher than cascaded half effect vapour absorption refrigeration coupled with vapour compression cycle. Mishra[14] proposed four cascaded half effect, single effect, double effect and triple effect Lithium/Bromide vapour absorption–compression refrigeration systems using fifteen ecofriendly refrigerants such as hydrocarbons, HFC and HFO refrigerants and natural refrigerants to produce cooling capacity at -30^{0}C. The

comparison of four cascaded systems were also carried out at -55^{0}C using HFC refrigerants with R717 refrigerant. It is found that cascaded vapour compression absorption systems significantly improve first and second law performances as compared to simple vapour absorption refrigeration system.

R.S.Mishra [15], presented optimum thermodynamic performances of three cascade vapour compression refrigeration systems. The numerical thermal model have been developed for two stages cascade refrigeration systems and thermodynamic performances in terms of and first law efficiency, second law efficiency system exergy destruction ratio , first law efficiency of lower temperature and high temperature circuit have been computed. The effect of low temperature evaporator on the system first and second law performances and system exergy destruction ratio it was found that as low temperature evaporator temperature is decreasing , the first law and second law efficiencies are increasing and exergy destruction ratio is decreasing . from the developed thermal model, the optimum performance parameters in terms of the optimum temperature of high temperature evaporator for system-1(using HFO1234ze in HTC and HFO1234yf in LTC) was found between -6^{0}C to -7^{0}C, for sytem-2 (using HFO1234ze in HTC and HFC134a in LTC) : was found between -1^{o}C to -2^{0}C and for system-3using HFO-1234yf in HTC and HFC-134a in LTC was found between 1^{o}C to 2^{0}C of temperature and found that the volumetric refrigerating capacity of HFO R1234ze is below that of R134a and Its boiling point is also higher than that of R134a in the high temperature circuit of cascade refrigeration system in the range of HTC Circuit from 60^{o}C to -20^{o}C is suitable for replacing R134a and also concluded that the HFO R1234yf is suitable for replacing R134a in the low temperature circuit of cascade refrigeration system in the range of low temperature circuit (LTC) from -20^{o}C to -50^{o}C and found that by increasing evaporator temperature overall first law efficiency in terms of COP of the system is increases. Azhar and Siddiqui [16-17] analyzed gas operated H_2O-LiBr single to triple effect vapor absorption refrigeration cycles and a triple effect vapour absorption refrigeration cycle separately and used liquefied petroleum gas (LPG)and compressed natural gas (CNG) as sources of energy. They concluded that the COP of the triple effect cycle was 132% higher than the single effect. Thus the triple effect series flow VAR cycle is per-forming best among all. However, it requires input heat energy at the higher temperature range 175 to 200°C. They added that the maximum COP of triple effect vapor absorption refrigeration cycle was 2.16. V. Jain et al.[18]carried out thermodynamic analysis of vapor compression (R22, R410A, R407C andR134A)-single effect absorption (LiBr-H_2O) cascade refrigeration system and found that the COP of vapour compression section of CVCAS enhanced by 155% and electricity consumption reduced by 61% in comparison to a conventional VCRS. Moreover, evaporator and condenser changed irreversibility of the system significantly. R.S.Mishra [19] observed that two stage cascade refrigeration system using R1234ze in high temperature circuit and R1234yf in the low temperature evaporator (up to -50^{0}C) cascade system, can replace R134a. The numerical computations have been carried out for three stage proposed system (system-1: using R1234ze in high temperature circuit and R1234yf in intermediate temperature circuit and fifteen ecofriendly refrigerants in low temperature circuit). To validate the results obtained by developed model, proposed three stage cascade refrigeration system (system-1) and three stage conventional cascade refrigeration system (system-2) have been compared in terms of their thermal first and second law performances and power consumption by system and its compressors. The proposed three stage cascade refrigeration system (System-1) using HFO refrigerants up to -100^{o}C gives similar thermodynamic performances and 2% less power consumption than conventional three stage cascade refrigeration system (system-2). In case of three stage cascade refrigeration using HFO-1234ze in the high temperature circuit and HFO-1234yf in intermediate temperature circuit two stage refrigeration cascade system circuit andR245fa in low temperature circuit gives better thermal performances. The first and second law thermal performance parameters using HFO-245fa in low temperature circuit are around 0.75% higher than that of HFC-134a.Pratihar et al. [20] carried out simulation of a 400 kW NH_3-H_2O absorption-compression refrigeration system for summer air conditioning and concluded that the COP increased by 16% with increase in relative solution heat exchanger area from10 to 30% when compared to conventional R22 vapor compression chiller. Sun and Guo [21] carried out experiments on prototype of combined vapour compression-absorption refrigeration system driven by a gas engine and found that the primary energy utilization efficiency of combined system improved by the utilization of waste heat of gas engine in absorption refrigeration cycle. M. Dixit et al. [22] did thermodynamic and thermo-economic analyses of two stage hybrid absorption compression refrigeration system having LiBr-H_2O as working fluid and stated that hybrid system could be operated on low generator temperature and performed better than the two stage absorption refrigeration system .The COP and exergetic efficiency of optimized hybrid system were 0.43 and 11.68% respectively and the reduction in annual cost of operation was 5.2%. Similarly, Alvarez et al. [23] analyzed an alkali-nitrate triple-effect (single effect lithium, potassium, sodium nitrate cycle coupled to a double effect H_2O/LiBr cycle) absorption cycle for high temperature heat source. The alkali-titrate triple effect cycle was feasible efficient with slight higher COP than H_2O/LiBr triple effect cycle at generator temperature over 180°C.

The solar assisted half effect vapour absorption refrigeration system cascaded with vapour compression refrigeration system using ecofriendly refrigerants have not been studied in detail.

R.S.Mishra [24] investigated the performance of above system along with variation of performance parameters and its effect on system performances in terms of exergetic efficiency, coefficient of performance along with exergy destruction ratio based on exergy of product. Han et al [25] proposed a hybrid absorption-compression refrigerator powered by waste heat. They declared that the system COP was 41.9% higher than that of a simple NH_3absorption refrigerator and had confirmed performance improvement by exergy analysis and found that the COP of compression-absorption combined cycle was higher than VCR or vapor absorption refrigeration (VAR) cycle. Kaushik and Arora[26] had analyzed half; single and double effect series and

parallel flow vapor absorption cycles and defined that the generator temperature and COP for half, single and double effect series flow refrigeration cycles and found the COP of double effect system was about twice that of single effect. Cimsit and Ozturk [27] performed analysis of compression-absorption cascade refrigeration systems by using H_2O-LiBr and NH_3-H_2O pairs in vapour absorption refrigeration system and R134a, R410a and NH_3in vapor compression refrigeration system and predicted that the electrical energy consumption in cascade refrigeration cycle was 48–50% less than that of conventional vapour compression refrigeration cycle and the COP of the cascade refrigeration system enhanced by 33%. Garimellaet al.[28] proposed absorption/vapour compression cascade refrigeration system driven by waste heat used in naval ship and determined that the electricity consumption reduced by 30% than that of conventional vapour compression refrigeration system.

Wang et al.[29] studied solar assisted cascaded refrigeration system and found that the power consumption was reduced by 50% and the COP of the system reached up to 6.1.

Einiet al.[30] stated that the CO_2/NH_3cascade cycle was safer than the CO2/C3H8with no significance difference in economic and exergetic efficiency. Since the water is a natural refrigerant, it can be used safely with H_2OLi/Br in the high temperature circuit of cascade cycle. However, the safety group of R1234yf is A2L.Bhattacharyya et al.[31] evaluated a CO2-Propane cascade system for simultaneous refrigeration and heat pump system and concluded that the approach and overlap temperatures must be minimum possible for the optimization of system performance and found that the optimum value of intermediate temperature of cascade system decreases with decrease in approach temperature and with increase in overlap temperature. Mafi et al.[32] had carried out exergy analysis of multistage cascade low temperature cascade refrigeration system and found that the exergetic efficiency of the system was 30.88%. Chinnappa et al. [33] studied R22 vapour compression-NH_3-H_2O absorption cascade refrigeration by using solar energy and determined that the cascaded system saved electrical energy than that of vapour compression system. Additionally the use of HFO refrigerant having zero potential (ODP) and low global warming potential (GWP) i.e. R1234yf is strongly recommended by Regulation (EU) No 517/2014 [11] to reduce mitigating climate change risk, environmental impact and deterioration. Therefore, refrigerant R1234yf could be a choice for vapour compression refrigeration system. Cabello et al. [34] substituted R134a, which is a high GWP refrigerant to the low GWP refrigerant R152a in cascade refrigeration plants. The drop in replacement was technically and enthusiastically feasible. The GWP and ODP rating of R1234yf are 4 and 0.

Generally, the vapour compression refrigeration cycle and its configurations viz. double stage, triple stage or multistage cascade are employed for the production of low evaporation temperature at very high cooling power. Messineo [35] analyzed a two stage cascade refrigeration system using carbon dioxide (CO2) in low temperature circuit and ammonia (NH_3) in high temperature section. He reported that CO_2-NH_3cascade refrigeration system was a motivating alternative to R404A for low evaporation temperatures (30°C to50°C

Most of the research studies considered till date emphasize on VCR and VAR cycles (single and double effect) and compression-absorption (combined) or cascade cycles. Though, exhaustive research has been carried out on cascade cycles, very less consideration has been given to explore the thermodynamic performance of single effect VAR cycle coupled with multi cascaded VCRS. Additionally, none of the research work is available on thermodynamic performance analysis of compression-absorption single effect multi cascaded three stages refrigeration system. Accordingly, in the present communication, the thermodynamic and exergetic performance analysis of absorption compression (single effect H_2O-Li/Br) cascade refrigeration system has been carried out. The analysis is performed considering H_2O/LiBr in absorption system and R1234yf in medium temperature VCR system. R-245fa in intermediate temperature VCR system along with R-236fa in intermediate temperature VCR system. The effect of medium temperature evaporator temperature, intermediate temperature of evaporator using R1234yf, intermediate temperature evaporator temperature, intermediate temperature of evaporator using R245fa and low temperature evaporator temperature, intermediate temperature of evaporator using R236fa/ hydrocarbons (i.e. R290, R600a) and ethylene temperature overlapping in each cascade condenser, condenser , absorber temperatures generator and evaporator temperatures of single effect H_2O-Li/Br vapour absorption system , have been investigated on various performance parameters viz. COP, exergetic efficiency, total exergy destruction and exergy destruction ratio (EDR).Additionally, exergy destruction and EDR of system components have also been computed.

2. System Description

Integrated absorption-compression multi cascaded refrigeration system used for ultra-low temperature is considered in this investigation is comprises of single effect H_2O-Li/Br refrigeration system is in the high temperature section having Lithium Bromide (Li/Br) as an absorbent and water (H2O) as a refrigerant. The evaporator of vapour system (VARS) is coupled with the condenser of medium VCRS using HFO-1234yf as a refrigerant up to a Temperature of 223K*(i.e* -50ºC) and vapour compression refrigeration system (VCRS) is in the intermediate temperature section in which intermediate temperature is achieved using 245fa as a refrigerant up to a Temperature of 173K *(i.e.* -100ºC) and vapour compression refrigeration system (VCRS) is in the intermediate temperature section in which intermediate temperature is achieved using 236fa as a refrigerant up to a temperature of 123K *(i.e* -150ºC).

3. Results and Discussion

Following input variables have been chosen for validation of model

- Evaporator Temperature of single effect Li/Br vapour absorption refrigeration system= 8°C, Generator temperature=110°C.
- Evaporator Temperature of vapour compression

refrigeration system in the medium temperature circuit = -50°C

- Evaporator Temperature of vapour compression refrigeration system in the intermediate temperature circuit = -50°C
- Evaporator Temperature of vapour compression refrigeration system in the low temperature circuit = -150°C
- Temperature overlapping in the vapour absorption refrigeration evaporator temperature and vapour compression refrigeration condenser temperature using R1234yf is known as overlapping$_{_MTC}$ (approach$_{_MTC}$)= 10
- Temperature overlapping in the vapour compression refrigeration evaporator temperature using R-1234yf and vapour compression refrigeration condenser temperature using R2345f is known as over-lapping$_{_ITC}$ (approach$_{_ITC}$)=10
- Temperature overlapping in the vapour compression refrigeration evaporator temperature using R-123fa and vapour compression refrigeration condenser temperature using 245fa is known as overlapping$_{_MTC}$ (Approach$_{_LTC}$)=10
- Refrigerating Capacity=35.167 "kW"
- Condenser temperature =35°C,
- Absorber Temperature=35°C,
- MTC Compressor Efficiency=0.80,
- ITC Compressor Efficiency=0.80,
- LTC Compressor Efficiency=0.80,

Thermal performance of single effect vapour absorption refrigeration systemusing H_2O-Li/Br was computed by developed model is given below.

(i) First law efficiency of vapour absorption refrigeration system is (COP_VARS) =0.7496,
(ii) (ii) The second law efficiency of vapour absorption refrigeration system is the exergetic_efficiency= 0.2043.
(iii) (iii) The exergy destruction ratio based on out put(exergy of product) is EDR$_{_Output}$= 3.894
(iv) The exergy destruction ratio based on input (exergy of exergy of fuel) is EDR$_{_Input}$= 0.7957.

3.1 Effect of temperature overlapping in cascade condensers on total thermodynamic performances of three cascaded cycles in integrated system

Table-1(a) to Table-1(c) shows the variation of approach of combined single effect Li/Br vapour absorption refrigeration system cascaded with vapour compression refrigeration system using 1234yf ecofriendly refrigerant in medium temperature circuit and R245fa in intermediate temperature circuit and R236fa in the low temperature circuit. and it was observed that as temperature overlapping in increasing, the first law efficiency (COP) and second law efficiency (exergetic efficiency) of various combined cascade cycles of integrated multi cascaded system are decreasing as temperature overlapping in each stage is increasing. Similarly exergy destruction ratio based on exergy of product is also decreasing as temperature overlapping is increasing.

Table-1(a): First law performance in terms of COP$_{_Overall}$ with variations temperature over lapping (approach$_{_LTC}$) of single effect H_2O-Li/Br vapour absorption refrigeration system cascaded with vapour compression refrigeration system using 1234yf ecofriendly refrigerant in medium temperature circuit and R245fa in intermediate temperature circuit and R236fa in the low temperature circuit.

Temperature over lapping (approach$_{_LTC}$) in Low temperature condenser (^oC) using R236fa	Over all COP of system using to low evaporator temperature of 123K (i.e.-150^{o}C) using R236fa	Over all COP of system using to intermediate evaporator temperature of 173K (i.e.-100^{o}C) using R245fa	Over all COP of system using to intermediate evaporator temperature of 223K (i.e.-50^{o}C) using HFO-1234yf
0	0.8764	0.9109	0.8093
5	0.8711	0.9109	0.8093
10	0.8659	0.9109	0.8093
15	0.8609	0.9109	0.8093

Table-1(b): Second law performances in terms of total exergetic efficiencies with variations of temperature over lapping (approach$_{_LTC}$) of single effect Li/Br vapour absorption refrigeration system cascaded with Vapour compression refrigeration system using 1234yf ecofriendly refrigerant in medium temperature circuit and R245fa in intermediate temperature circuit and R236fa in the low temperature circuit.

Temperature over lapping (approach$_{_LTC}$) in Low temperature condenser (^oC) using R236fa	Over all exergetic efficiency of system using to low evaporator temperature of 123K (i.e.-150^{o}C) using R236fa	Over all exergetic efficiency of system using to intermediate evaporator temperature of 173K (i.e.-100^{o}C) using R245fa	Over all exergetic Efficiency of system using to intermediate evaporator temperature of 223K (i.e.-50^{o}C) using HFO-1234yf
0	0.5248	0.4665	0.2806
5	0.5145	0.4665	0.2806
10	0.5045	0.4665	0.2806
15	0.4948	0.4665	0.2806

Table-1(c): Exergy destruction ratio of system with variations in temperature over lapping (approach_$_{LTC}$) of single effect $H_2$0-Li/Br vapour absorption refrigeration system cascaded with vapour compression refrigeration system using 1234yf ecofriendly refrigerant in medium temperature circuit and R245fa in intermediate temperature circuit and R236fa in the low temperature circuit

Temperature over lapping (approach_$_{LTC}$) in Low temperature condenser (^{o}C) using R236fa	Over all Exergy Destruction Ratio of system using to low evaporator temperature of 123K (i.e.-150^{o}C) using R236fa	Over all Exergy Destruction Ratio of system using to intermediate evaporator temperature of 173K (i.e.100^{o}C) using R245fa	Over all Exergy Destruction Ratio of system using to intermediate evaporator temperature of 223K (i.e.-50^{o}C) using HFO-1234yf
0	0.9054	1.143	2.565
5	0.9438	1.143	2.565
10	0.9823	1.143	2.565
15	1.027	1.143	2.565

Table-1(d): First and second law performance with variations in temperature over lapping (approach_$_{ITC}$) of single effect LiBr vapour absorption refrigeration system cascaded with vapour compression refrigeration system using 1234yf ecofriendly refrigerant in medium temperature circuit and R245fa in intermediate temperature circuit and R236fa in the low temperature circuit.

Temperature over lapping (approach_$_{ITC}$) in intermediate condenser temperature (^{o}C) using R245fa	Over all COP of system using to low evaporator temperature of 123K using R236fa	Over all COP of system using to intermediate evaporator temperature of 173K using R245fa	Over all COP of system using to intermediate evaporator temperature of 223K using HFO-1234yf
0	0.8839	0.9351	0.8093
5	0.8748	0.9227	0.8093
10	0.8659	0.9109	0.8093
15	0.8574	0.8996	0.8093

Table-1(e):Second law performances (exergetic Efficiencies) with variations in temperature over lapping (approach_$_{ITC}$) of single effect Li/Br vapour absorption refrigeration system cascaded with Vapour compression refrigeration system using 1234yf ecofriendly refrigerant in medium temperature circuit and R245fa in intermediate temperature circuit and R236fa in the low temperature circuit.

Temperature over lapping (approach_$_{ITC}$) in intermediate temperature Condenser (^{o}C) using R245fa	Over all exergetic efficiency of system using to low evaporator temperature of 123K using R236fa	Over all exergetic efficiency of system using to intermediate evaporator temperature of 173K using R245fa	Over all exergetic Efficiency of system using to intermediate evaporator temperature of 223K using HFO-1234yf
0	0.5317	0.4969	0.2806
5	0.5178	0.4813	0.2806
10	0.5045	0.4665	0.2806
15	0.4915	0.4526	0.2806

Table-1(f): Exergy destruction ratio (EDR_$_{system}$) of system and % improvement in system first law performance with variations in temperature over lapping (approach_$_{ITC}$) of single effect Li/Br vapour absorption refrigeration system cascaded with Vapour compression refrigeration system using 1234yf ecofriendly refrigerant in medium temperature circuit and R245fa in intermediate temperature circuit and R236fa in the low temperature circuit.

Temperature over lapping (approach_$_{ITC}$) in intermediate temperature Condenser (^{o}C) using R245fa	Over all Exergy Destruction Ratio (EDR) of system using to low evaporator temperature of 123K using R236fa	Over all Exergy Destruction Ratio(EDR) of system using to intermediate evaporator temperature of 173K using R245fa	Over all Exergy Destruction Ratio(EDR) of system using to intermediate evaporator temperature of 223K using HFO-1234yf
0	0.8808	1.013	2.565
5	0.9311	1.078	2.565
10	0.9823	1.143	2.565
15	1.034	1.21	2.565

Table-1(g): First law Performances (COP_$_{Overall}$) with variations in temperature over lapping (approach_$_{LTC}$) of single effect H_2O- Li/Br vapour absorption refrigeration system cascaded with Vapour compression refrigeration system using 1234yf ecofriendly refrigerant in medium temperature circuit and R245fa in intermediate temperature circuit and R236fa in the low temperature circuit.

Temperature over lapping (approach_$_{MTC}$) in medium temperature Condenser (^{o}C) using R1234yf	Over all COP of system using to low evaporator temperature of 123K using R236fa	Over all COP of system using to intermediate evaporator temperature of 173K using R245fa	Over all COP of system using to intermediate evaporator temperature of 223K using HFO-1234yf
0	0.9278	0.9881	0.8764
5	0.8977	0.9502	0.8432
10	0.8659	0.9109	0.8093
15	0.8322	0.8698	0.7743

Table-1(h): second law Performances (exergetic efficiencies) variations with temperature over lapping (approach_LTC) of single effect H_2O-Li/Br vapour absorption refrigeration system cascaded with Vapour compression refrigeration system using 1234yf ecofriendly refrigerant in medium temperature circuit and R245fa in intermediate temperature circuit and R236fa in the low temperature circuit.

Temperature over lapping (approach_MTC) in medium temperature Condenser (°C) using R1234yf	Over all exergetic efficiency of system using to low evaporator temperature of 123K using R236fa	Over all exergetic efficiency of system using to intermediate evaporator temperature of 173K using R245fa	Over all exergetic Efficiency of system using to intermediate evaporator temperature of 223K using HFO-1234yf
0	0.5721	0.5459	0.3355
5	0.5391	0.5065	0.3076
10	0.5045	0.4665	0.2805
15	0.4679	0.4258	0.2639

Table-1(i): Exergy destruction ratio (EDR) of system with variations in temperature over lapping (approach_LTC) of single effect Li/Br vapour absorption refrigeration system cascaded with Vapour compression refrigeration system using 1234yf ecofriendly refrigerant in medium temperature circuit and R245fa in intermediate temperature circuit and R236fa in the low temperature circuit.

Temperature over lapping (approach_MTC) in medium temperature condenser (°C) using R1234yf	Over all Exergy Destruction Ratio of system using to low evaporator temperature of 123K using R236fa	Over all Exergy Destruction Ratio of system using to intermediate evaporator temperature of 173K using R245fa	Over all Exergy Destruction Ratio of system using to intermediate evaporator temperature of 223K using HFO-1234yf
0	0.7479	0.8317	1.981
5	0.8550	0.9744	2.261
10	0.9823	1.143	2.566
15	1.137	1.348	2.939

3.2 Effect of temperature overlapping on percentage improvements of thermodynamic performances

Table-2(a) to Table-2(i) show the variation of all three types of approaches of combined single effect Li/Br vapour absorption refrigeration system cascaded with vapour compression refrigeration system using 1234yf ecofriendly refrigerant in medium temperature circuit and R245fa in intermediate temperature circuit and R236fa in the low temperature circuit with percentage variation of thermodynamic first and second law performances and it was observed that as temperature overlapping in increasing, the first law efficiency (COP) and second law efficiency (exergetic efficiency) VCRS of cascaded system are decreasing as temperature overlapping is increasing. Similarly exergy destruction ratio based on exergy of product is also decreasing as temperature overlapping (approach) is increasing.

Table-2(a): % improvement in system first law Performance with variations in temperature over lapping (approach_LTC) of single effect H_2O-Li/Br vapour absorption refrigeration system cascaded with vapour compression refrigeration system using 1234yf ecofriendly refrigerant in medium temperature circuit and R245fa in intermediate temperature circuit and R236fa in the low temperature circuit

Temperature over lapping (Approach_LTC) in Low temperature Condenser (°C) using R236fa	(%) Overall improvement in First law efficiency (COP_Overall) of system using to low evaporator temperature of 123K using R236fa (%)	(%) Overall improvement in First law efficiency (COP_Overall) of system using to intermediate evaporator temperature of 173K using R245fa (%)	(%) Overall improvement in First law efficiency (COP_Overall) of system using to intermediate evaporator temperature of 223K Using HFO1234yf (%)
0	16.92	21.53	7.96
5	16.21	21.53	7.96
10	15.52	21.53	7.96
15	14.85	21.53	7.96

Table-2(b): % improvement in system first law Performance variations and % reduction in exergy destruction ratio (EDR_{System}) of system and with temperature over lapping (approach_LTC) of single effect H_2O-Li/Br vapour absorption refrigeration system cascaded with Vapour compression refrigeration system using 1234yf ecofriendly refrigerant in medium temperature circuit and R245fa in intermediate temperature circuit and R236fa in the low temperature circuit.

Temperature over laping (Approach_LTC) in Low temperature Condenser (°C) using R236fa	Over all (%) improvement in second law efficiency (exergetic Efficiency) of system using to low temperature evaporator temperature of 123K using R236fa (%)	Over all (%) improvement in second law law efficiency (exergetic Efficiency) of system using to intermediate temperature evaporator temperature of 173K using R245fa (%)	Over all (%) improvement in second law law efficiency (exergetic Efficiency) of system using to intermediate temp evaporator temp of 223K Using HFO-1234yf (%)
0	156.8	128.3	37.27
5	151.8	128.3	37.27
10	146.9	128.3	37.27
15	142.1	128.3	37.27

Table-2(c): % reduction in exergy destruction ratio of system and with varying temperature over lapping (approach_LTC) of single effect Li/Br vapour absorption refrigeration system cascaded with vapour compression refrigeration system using 1234yf ecofriendly refrigerant in medium temperature circuit and R245fa in intermediate temperature circuit and R236fa in the low temperature circuit.

Temperature over lapping (approach_LTC) in low temp condenser (°C) using R236fa	Over all (%) reduction in exergy destruction ratio (EDR) of system using to low evaporator temp of 123K using R236fa (%)	Over all (%) reduction in exergy destruction ratio (EDR) of system using to intermediate evaporator temperature of 173K using R245fa (%)	Over all (%) reduction in exergy destruction ratio (EDR) of system using to intermediate evaporator temperature of 223K using HFO-1234yf (%)
0	76.75	70.63	34.32
5	75.76	70.63	34.32
10	74.77	70.63	34.32
15	73.77	70.63	34.32

Table-2(d): % improvement in system first law performance variations with varying temperature over lapping (approach_ITC) of single effect H_2O-Li/Br vapour absorption refrigeration system cascaded with Vapour compression refrigeration system using 1234yf ecofriendly refrigerant in medium temperature circuit and R245fa in intermediate temperature circuit and R236fa in the low temperature circuit

Temperature over lapping (approach_ITC) in intermediate temp Condenser (°C) using R245fa	Over all (%) improvement in First law efficiency (COP_Overall) of system using to low evaporator temp of 123K using R236fa (%)	Over all (%) improvement in First law efficiency (COP_Overall) of system using to intermediate evaporator temp of 173K using R245fa (%)	Over all (%) improvement in First law efficiency (COP_Overall) of system using to intermediate evaporator temp of 223K using HFO-1234yf (%)
0	17.91	24.74	7.96
5	16.7	23.09	7.96
10	15.52	21.52	7.96
15	14.38	20.0	7.96

Table-2(e): % improvement in system second law Performance variations of system and with varying temperature over lapping (approach_ITC) of single effect H_2O-Li/Br vapour absorption refrigeration system cascaded with vapour compression refrigeration system using 1234yf ecofriendly refrigerant in medium temperature circuit and R245fa in intermediate temperature circuit and R236fa in the low temperature circuit.

Temperature over lapping (approach_ITC) in intermediate temperature Condenser (°C) using R245fa	Over all (%) improvement in second law efficiency (exergetic efficiency) of system using to low evaporator temperature of 123Kusing R236fa (%)	Over all (%) improvement in second law efficiency (exergetic efficiency) of system using to intermediate evaporator temperature of 173K using R245fa (%)	Over all (%) improvement in second law efficiency (exergetic efficiency) of system using to intermediate evaporator temperature of 223K using HFO-1234yf(%)
0	160.2	143.2	37.27
5	153.4	135.5	37.27
10	146.9	128.3	37.27
15	140.5	121.5	37.27

Table-2(f): % reduction Exergy destruction ratio (EDR) of system and with varying temperature over lapping (approach_LTC) of single effect H_2O-Li/Br vapour absorption refrigeration system cascaded with vapour compression refrigeration system using 1234yf ecofriendly refrigerant in medium temperature circuit and R245fa in intermediate temperature circuit and R236fa in the low temperature circuit.

Temperature over lapping (Approach_MTC) in medium temperature condenser (°C) using R1234yf	Over all (%) reduction in exergy destruction ratio (EDR) of system using to low evaporator temperature of 123K using R236fa (%)	Over all (%) reduction in exergy destruction ratio (EDR) of system using to intermediate evaporator temperature of 173K using R245fa (%)	Over all (%) reduction in exergy destruction ratio (EDR) of system using to intermediate evaporator temperature of 223K using HFO1234yf (%)
0	77.38	73.99	34.12
5	76.09	72.32	34.12
10	74.77	70.63	34.12
15	73.43	68.93	34.12

Table-2(g) % improvement in system first law performance (COP_Overall) variations with varying temperature over lapping (approach_MTC) of single effect H_2O-Li/Br vapour absorption refrigeration system cascaded with vapour compression refrigeration system using 1234yf ecofriendly refrigerant in medium temperature circuit and R245fa in intermediate temperature circuit and R236fa in the low temperature circuit.

Temperature over laping (approach_MTC) in medium temperature condenser (°C) using R1234yf	Over all COP of system using to low temperature evaporator temperature of 123K (i.e.-150°C) using R236fa	Over all COP of system using to intermediate temperature evaporator temperature of 173K (i.e.100°C) using R245fa	Over all COP of system using to intermediate temperature evaporator temperature of 223K (i.e.-50°C) using HFO-1234yf
0	0.9278	0.9881	0.8764
5	0.8977	0.9502	0.8432
10	0.8659	0.9109	0.8093
15	0.8322	0.8698	0.7743

Table-2(h): % improvement in system second law performance (exergetic efficiencies) variations and % reduction Exergy destruction ratio of system and with varying temperature over lapping (approach_MTC) of single effect H_2O-Li/Br vapour absorption refrigeration system cascaded with Vapour compression refrigeration system using 1234yf ecofriendly refrigerant in medium temperature circuit and R245fa in intermediate temperature circuit and R236fa in the low temperature circuit.

Temperature over laping (approach_MTC) in medium temperature condenser (°C) using R1234yf	Over all (%) improvement in second law efficiency (exergetic Efficiency) of system using to low evaporator temperature of 123K using R236fa (%)	Over all (%) improvement in second law efficiency (exergetic Efficiency) of system using to intermediate evaporator temperature of 173K using R245fa (%)	Over all (%) improvement in second law efficiency (exergetic Efficiency) of system using to intermediate evaporator temperature of 223K using HFO-1234yf (%)
0	180.0	167.2	64.16
5	163.8	147.9	50.56
10	146.9	128.3	37.27
15	129.0	108.4	24.23

Table-2(i): % reduction Exergy destruction ratio(EDR) of multi cascade system and with varying temperature over lapping (approach_LTC) of single effect H_2O-Li/Br vapour absorption refrigeration system cascaded with Vapour compression refrigeration system using 1234yf ecofriendly refrigerant in medium temperature circuit and R245fa in intermediate temperature circuit and R236fa in the low temperature circuit.

Temperature over laping (approach_MTC) in medium temp Condenser (°C) using R1234yf	Over all (%) reduction in exergy destruction ratio (EDR) of system using to low evaporator temp of 123K using R236fa (%)	Over all (%) reduction in exergy destruction ratio (EDR) of system using to intermediate evaporator temp of 173K using R245fa (%)	Over all (%) reduction in exergy destruction ratio (EDR) of system using to intermediate evaporator temp of 223K using HFO-1234yf (%)
0	80.79	78.64	49.13
5	78.04	74.97	47.25
10	74.77	70.63	34.12
15	70.75	65.37	24.5

3.3 Effect of generator temperature on total thermodynamic performances of three cascaded cycles in integrated system

Table-3(a) to Table-3(c) shows the variation of generator temperature of VARS on thermodynamic performances such as first law efficiency , second law efficiency and system exergy destruction of combined single effect Li/Br vapour absorption refrigeration system cascaded with Vapour compression refrigeration system using 1234yf ecofriendly refrigerant in medium temperature circuit and R245fa in intermediate temperature circuit and R236fa in the low temperature circuit and it was observed that as generator temperature increasing, the first law efficiency (COP_overall) of three cycles and second law efficiency (exergetic efficiency) of three cycles of combined vapour absorption cascaded refrigeration system is decreasing as generator temperature is increasing. Similarly exergy destruction ratio based on exergy of product is increasing

Table-3(a): Effect of generator *temperature of single effect H_2O- Li/Br VARS on thermodynamic performances (First law Performance (COP_Overall), vapour compression refrigeration system coupled with single effect vapour absorption refrigeration Li/Br system using 1234yf ecofriendly refrigerant in medium temperature circuit and R245fa in intermediate temperature circuit and R236fa in the low temperature circuit*

Generator Temperature of single effect H_2O-Li/Br vapour absorption refrigeration system (°C)	Over all COP of system using to low evaporator temperature of 123K using R23fa	Over all COP of system using to intermediate evaporator temperature of 173K using R245fa	Over all COP of system using to intermediate evaporator temperature of 223K using HFO-1234yf
90	0.880	0.9274	0.8252
95	0.8754	0.9221	0.820
100	0.9312	1.075	0.8156
105	0.8683	0.9137	0.8120
110	0.8659	0.9109	0.8093
115	0.8639	0.9085	0.8069

Table-3(b): Effect of generator *temperature of single effect H_2O Li/Br VARS on thermodynamic second law performance (exergetic efficiencies) with absorber temperature of vapour compression refrigeration system coupled with single effect vapour absorption refrigeration LiBr system using 1234yf ecofriendly refrigerant in medium temperature circuit and R245fa in intermediate temperature circuit and R236fa in the low temperature circuit*

Generator temp of single effect H_2O-Li/Br vapour absorption refrigeration system (°C)	Over all exergetic efficiency of system using to low evaporator temp of 123K using R236fa	Over all exergetic efficiency of system using to intermediate evaporator temp of 173K using R245fa	Over all exergetic eff of system using to intermediate evaporator temp of 223K using HFO-1234yf
90	0.5329	0.4995	0.3045
95	0.5252	0.4904	0.2975
100	0.5178	0.4819	0.2916
105	0.5109	0.4739	0.2858
110	0.5045	0.4665	0.2805
115	0.4983	0.4596	0.2765

Table-3(c): Effect of generator *temperature of single effect H_2O Li/Br VARS on thermodynamic system exergy destruction ratio with absorber temperature of vapour compression refrigeration system coupled with single effect vapour absorption refrigeration LiBr system using 1234yf ecofriendly refrigerant in medium temperature circuit and R245fa in intermediate temperature circuit and R236fa in the low temperature circuit*

Generator temperature of single effect H_2O-Li/Br vapour absorption refrigeration system (^oC)	Over all Exergy Destruction Ratio of system using to low temperature evaporator temperature of 123K using R23fa	Over all Exergy Destruction Ratio of system using to intermediate temperature evaporator temperature of 173K using R245fa	Over all Exergy Destruction Ratio of system using to intermediate temperature evaporator temperature of 223K using HFO-1234yf
90	0.8765	1.002	2.284
95	0.9042	1.039	2.357
100	0.9312	1.075	2.429
105	0.9573	1.11	2.499
110	0.9823	1.143	2.565
115	1.007	1.176	2.630

3.4 Effect of generator temperature on percentage improvements in total thermodynamic performances of three cascaded cycles in integrated system

Table-4(a) to Table-4(c) shows the variation of generator temperature with percentage improvement in thermodynamic performances such as first law efficiency , second law efficiency and system exergy destruction ratio of Combined single effect Li/Br vapour absorption refrigeration system cascaded with Vapour compression refrigeration system using 1234yf ecofriendly refrigerant in medium temperature circuit and R245fa in intermediate temperature circuit and R236fa in the low temperature circuit and it was observed that as generator temperature increasing, the percentages improvement in first law efficiency ($COP_{_Overall}$) of three cycles and second law efficiency (exergetic efficiency) of three cycles of multi cascaded single effect vapour absorption integrated refrigeration system are increasing as generator temperature is increasing. Similarly exergy destruction ratio based on exergy of product is also increasing as condenser temperature is decreasing.

Table-4(a): Effect of generator *temperature of single effect H_2O- Li/Br VARS on percentage improvement of thermodynamic performances (First law performance ($COP_{_Overall}$)of three cycles are , with generator temperature of vapour absorption refrigeration system coupled with three cascaded vapour compression refrigeration cycles using 1234yf ecofriendly refrigerant in medium temperature circuit and R245fa in intermediate temperature circuit and R236fa in the low temperature circuit*

Generator temperature of single effect H_2O-Li/Br vapour absorption refrigeration system (^oC)	Over all (%) improvement in First law efficiency (COP_Overall) of system using to low evaporator temperature of 123K using R236fa (%)	Over all (%) improvement in First law efficiency (COP_Overall) of system using to intermediate evaporator temperature of 173K using R245fa (%)	Over all (%) improvement in First law efficiency (COP_Overall) of system using to intermediate evaporator temperature of 223K using HFO-1234yf (%)
90	14.26	20.42	7.151
95	14.67	20.77	7.414
100	15.02	21.08	7.641
105	15.31	21.33	7.824
110	15.52	21.52	7.961
115	15.71	21.68	8.08

Table-4(b): Effect of generator *temperature of single effect H_2O- Li/Br VARS on percentage improvement of thermodynamic performances (second law performance (over all exergetic efficiencies)of three combined cycles are , with generator temperature of vapour absorption refrigeration system coupled with three cascaded vapour compression refrigeration cycles using 1234yf ecofriendly refrigerant in medium temperature circuit and R245fa in intermediate temperature circuit and R236fa in the low temperature circuit*

Generator temperature of single effect H_2O-Li/Br vapour absorption refrigeration system (^oC)	Over all (%) improvement in second law law efficiency (exergetic Efficiency) of system using to low evaporator temperature of 123K using R236fa (%)	Over all (%) improvement in second law law efficiency (exergetic Efficiency) of system using to intermediate evaporator temperature of 173K using R245fa (%)	Over all (%) improvement in second law law efficiency (exergetic Efficiency) of system using to intermediate evaporator temperature of 223K using HFO-1234yf(%)
90	104.8	91.96	17.04
95	116.3	102.0	22.67
100	137.3	102.1	32.78
105	137.3	120.2	32.78
110	146.9	128.3	37.27
115	155.9	136.0	41.48

Table-4(c): Table-4(b): Effect of generator *temperature of single effect H_2O- Li/Br VARS on percentage improvement of thermodynamic performances of three combined cycles are , with generator temperature in terms of exergy destruction ratios of vapour absorption refrigeration system coupled with three cascaded vapour compression refrigeration cycles using 1234yf ecofriendly refrigerant in medium temperature circuit and R245fa in intermediate temperature circuit and R236fa in the low temperature circuit*

Generator temperature of single effect H_2O-Li/Br vapour absorption refrigeration system (^oC)	Over all (%) reduction in exergy destruction ratio (EDR) of system using to low evaporator temperature of 123K using R236fa (%)	Over all (%) reduction in exergy destruction ratio (EDR) of system using to intermediate evaporator temperature of 173Kusing R245fa (%)	Over all (%) reduction in exergy destruction ratio (EDR) of system using to intermediate evaporator temp of 223K using HFO-1234yf (%)
90	69.17	64.76	19.68
95	71.01	66.68	24.41
100	72.5	68.25	28.27
105	73.74	69.55	31.46
110	74.77	70.63	34.12
115	75.66	71.56	36.41

3.5 Effect of absorber temperature on total thermodynamic performances of three cascaded cycles in integrated system

Table-5(a)to Table-5(c) show the variation of absorber temperature of combined single effect Li/Br vapour absorption refrigeration system cascaded with vapour compression refrigeration system using 1234yf ecofriendly refrigerant in medium temperature circuit and R245fa in intermediate temperature circuit and R236fa in the low temperature cycle and it was observed that as absorber temperature increasing, the first law efficiency (COP) and second law efficiency (exergetic efficiency) of cascaded system are decreasing as absorber temperature is increasing. Similarly exergy destruction ratio based on exergy of product is also increasing as absorber temperature is increased. Similarly solar collector area is also increasing as absorber temperature is increasing.

Table-5(a): Effect of absorber temperature of VARS Thermodynamic performances (first law Performance ($COP_{_overall}$), of vapour compression refrigeration system coupled with single effect vapour absorption refrigeration H_2O-Li/Br system using 1234yf ecofriendly refrigerant in medium temperature circuit and R245fa in intermediate temperature circuit and R236fa in the low temperature circuit

Absorber temperature of single effect H_2O-Li/Br vapour absorption refrigeration system (^oC)	Over all COP of system using to low temperature evaporator temperature of 123K using R23fa	Over all COP of system using to intermediate temperature evaporator temperature of 173K using R245fa	Over all COP of system using to intermediate temperature evaporator temperature of 223K using HFO-1234yf
30	0.8723	0.9183	0.8003
31	0.8709	0.9167	0.8149
32	0.8696	0.9151	0.8134
33	0.8683	0.9137	0.8119
34	0.8671	0.9123	0.8106
35	0.8659	0.9109	0.8093
36	0.8649	0.9097	0.8081
37	0.8638	0.9084	0.8069
38	0.8629	0.9073	0.8058
39	0.8619	0.9062	0.8048
40	0.8610	0.9052	0.8038
41	0.8602	0.9042	0.8028
42	0.8594	0.9033	0.8019
43	0.8587	0.9024	0.8011
44	0.8580	0.9016	0.8003
45	0.8573	0.9008	0.7996

Table-5(b): Effect of absorber temperature of VARS on Thermodynamic second law performances (exergetic efficiencies) of vapour compression refrigeration system coupled with single effect vapour absorption refrigeration H_2O-Li/Br system using 1234yf ecofriendly refrigerant in medium temperature circuit and R245fa in intermediate temperature circuit and R236fa in the low temperature circuit

Absorber temperature of single effect H_2O-Li/Br vapour absorption refrigeration system (^oC)	Over all exergetic efficiency of system using to low evaporator temperature of 123K using R236fa	Over all exergetic efficiency of system using to intermediate evaporator temperature of 173K using R245fa	Over all exergetic Efficiency of system using to intermediate evaporator temperature of 223K using HFO-1234yf
30	0.5060	0.4683	0.2818
31	0.5057	0.4679	0.2815
32	0.5053	0.4675	0.2812
33	0.5050	0.4672	0.2810
34	0.5047	0.4669	0.2807

35	0.5045	0.4665	0.2805
36	0.5042	0.4662	0.2803
37	0.5040	0.4660	0.2801
38	0.5037	0.4657	0.2799
39	0.5035	0.4654	0.2797
40	0.5033	0.4652	0.2795
41	0.5031	0.4650	0.2794
42	0.5029	0.4647	0.2792
43	0.5027	0.4645	0.2790
44	0.5025	0.4643	0.2789
45	0.5024	0.4641	0.2788

Table-5(c): Effect of absorber temperature of VARS on Thermodynamic system exergy destruction ratio with absorber temperature of vapour compression refrigeration system coupled with single effect vapour absorption refrigeration H_2O-Li/Br system using 1234yf ecofriendly refrigerant in medium temperature circuit and R245fa in intermediate temperature circuit and R236fa in the low temperature circuit with

Absorber temperature of single effect H_2O-Li/Br vapour absorption refrigeration system (^oC)	Over all Exergy Destruction Ratio of system using to low temperature evaporator temperature of 123K using R23fa	Over all Exergy Destruction Ratio of system using to intermediate temperature evaporator temperature of 173K using R245fa	Over all Exergy Destruction Ratio of system using to intermediate temperature evaporator temperature of 223K using HFO-1234yf
30	0.9763	1.135	2.549
31	0.9776	1.137	2.553
32	0.9789	1.139	2.566
33	0.9801	1.140	2.559
34	0.9812	1.142	2.562
35	0.9823	1.143	2.565
36	0.9833	1.145	2.568
37	0.9843	1.146	2.570
38	0.9853	1.147	2.573
39	0.9861	1.149	2.575
40	0.9870	1.150	2.578
41	0.9878	1.151	2.580
42	0.9886	1.152	2.582
43	0.9893	1.153	2.584
44	0.990	1.154	2.585
45	0.9906	1.154	2.587

3.6 Effect of absorber temperature on percentage improvements in total thermodynamic performances of three cascaded cycles in integrated system

Table-5(a)to Table-5(c) show the variation of absorber temperature of combined single effect Li/Br vapour absorption refrigeration system cascaded with vapour compression refrigeration system using 1234yf ecofriendly refrigerant in medium temperature circuit and R245fa in intermediate temperature circuit and R236fa in the low temperature cycle and it was observed that as absorber temperature increasing, the first law efficiency (COP) and second law efficiency (exergetic efficiency) of cascaded system are decreasing as absorber temperature is increasing. Similarly exergy destruction ratio based on exergy of product is also increasing as absorber temperature is increased. Similarly solar collector area is also increasing as absorber temperature is increasing.

Table-6(a): Effect of Thermodynamic performances (First law Performances (COP_overall), with absorber temperature of vapour compression refrigeration system coupled with single effect vapour absorption refrigeration LiBr system using 1234yf ecofriendly refrigerant in medium temperature circuit and R245fa in intermediate temperature circuit and R236fa in the low temperature circuit with absorber temperature

Absorber temperature of single effect H_2O-Li/Br vapour absorption refrigeration system (^oC)	Over all (%) improvement in First law efficiency (COP_Overall) of system using to low evaporator temperature of 123K using R236fa (%)	Over all (%) improvement in First law efficiency (COP_Overall) of system using to intermediate evaporator temperature of 173K using R245fa (%)	Over all (%) improvement in First law efficiency (COP_Overall) of system using to intermediate evaporator temperature of 223K using HFO-1234yf (%)
30	14.95	21.02	7.596
31	15.08	21.13	7.676
32	15.2	21.24	7.753
33	15.31	21.33	7.826
34	15.42	21.43	7.895
35	15.52	21.52	7.961

36	15.62	21.60	8.03
37	15.71	21.68	8.082
38	15.79	21.76	8.138
39	15.88	21.83	8.191
40	15.96	21.9	8.242
41	16.03	21.97	8.290
42	16.10	22.03	8.335
43	16.17	22.09	8.378
44	16.23	22.14	8.418
45	16.29	22.19	8.456

Table-6(b): Effect of thermodynamic performances Second law performances (exergetic efficiencies) with absorber temperature of vapour compression refrigeration system coupled with single effect H_2O-Li/Br vapour absorption refrigeration system using 1234yf ecofriendly refrigerant in medium temperature circuit and R245fa in intermediate temperature circuit and R236fa in the low temperature circuit with absorber temperature

Absorber temperature of single effect H_2O-Li/Br vapour absorption refrigeration system (^oC)	Over all (%) improvement in second law efficiency (exergetic Efficiency) of system using to low evaporator temperature of 123K using R236fa (%)	Over all (%) improvement in second law efficiency (exergetic Efficiency) of system using to intermediate evaporator temperature of 173K using R245fa (%)	Over all (%) improvement in second law efficiency (exergetic Efficiency) of system using to intermediate evaporator temperature of 223K using HFO-1234yf(%)
30	144.6	126.4	36.21
31	145.1	126.8	36.44
32	145.6	127.2	36.66
33	146.0	127.6	38.87
34	146.5	128.0	37.07
35	146.9	128.3	37.27
36	147.3	128.6	37.45
37	147.6	129.0	37.62
38	148.0	129.3	37.78
39	148.3	129.5	37.94
40	148.6	129.8	38.09
41	148.9	130.1	38.23
42	149.2	130.3	38.36
43	149.5	130.5	38.49
44	149.7	130.8	38.6
45	150.0	131.0	38.72

Table-6(c): Effect of Thermodynamic performances system exergy destruction ratio with absorber temperature of vapour compression refrigeration system coupled with single effect vapour absorption refrigeration LiBr system using 1234yf ecofriendly refrigerant in medium temperature circuit and R245fa in intermediate temperature circuit and R236fa in the low temperature circuit with absorber temperature

Absorber temperature of single effect H_2O-Li/Br vapour absorption refrigeration system (^oC)	Over all (%) reduction in exergy destruction ratio (EDR) of system using to low evaporator temperature of 123K using R236fa (%)	Over all (%) reduction in exergy destruction ratio (EDR) of system using to intermediate evaporator temperature of 173K using R245fa (%)	Over all (%) reduction in exergy destruction ratio (EDR) of system using to intermediate evaporator temperature of 223K using HFO-1234yf (%)
30	74.54	70.39	33.52
31	74.59	70.44	33.65
32	74.64	70.49	33.78
33	74.69	70.54	33.90
34	74.73	70.59	34.01
35	74.77	70.63	31.12
36	74.81	70.68	34.22
37	74.85	70.72	34.32
38	74.89	70.75	34.41
39	74.92	70.79	34.50
40	74.95	70.82	34.58
41	74.98	70.85	34.65
42	75.01	70.88	34.73
43	75.04	70.91	34.80
44	75.06	70.94	34.87
45	75.09	70.96	34.93

3.7 Effect of condenser temperature on total thermodynamic performances of three cascaded cycles in integrated system

Fig-7(a) to Table-7(c) show the variation of condenser temperature of combined single effect Li/Br Vapour absorption refrigeration system cascaded with Vapour compression refrigeration system 1234yf ecofriendly refrigerant in medium temperature circuit and R245fa in intermediate temperature circuit and R236fa in the low temperature circuit and it was observed that as condenser temperature increasing, the first law efficiencies ($COP_{_Overall}$) and second law efficiencies (exergetic efficiencies) of combined system is decreasing as absorber temperature is increasing. Similarly exergy destruction ratio based on exergy of product is also increasing as condenser temperature is increased.

Table-7(a): Effect of condenser *temperature of VARS on total Thermodynamic performances (First law Performance (COP_overall), with condenser temperature of vapour compression refrigeration system coupled with single effect vapour absorption refrigeration LiBr system using 1234yf ecofriendly refrigerant in medium temperature circuit and R245fa in intermediate temperature circuit and R236fa in the low temperature circuit with*

Condenser temperature of single effect H_2O-Li/Br vapour absorption refrigeration system (^oC)	Over all COP of system using to low evaporator temperature of 123K using R23fa	Over all COP of system using to intermediate evaporator temperature of 173K using R245fa	Over all COP of system using to intermediate evaporator temp of 223K using HFO-1234yf
30	0.8696	0.9152	0.8135
31	0.8690	0.9195	0.8127
32	0.8683	0.9137	0.8119
33	0.8675	0.9128	0.8110
34	0.8660	0.9118	0.8102
35	0.8659	0.9109	0.8093
36	0.8652	0.910	0.8084
37	0.8645	0.9092	0.8076
38	0.8638	0.9084	0.8068
39	0.8631	0.9076	0.8061
40	0.8626	0.9069	0.8054
41	0.8620	0.9063	0.8048
42	0.8615	0.9057	0.8042
43	0.860	0.9051	0.8037
44	0.8606	0.9047	0.8032

Table-7(b): Effect of condenser *temperature of VARS on total thermodynamic performance sin terms of Second law performances (exergetic efficiencies) with condenser temperature of vapour compression refrigeration system coupled with single effect vapour absorption refrigeration LiBr system using 1234yf ecofriendly refrigerant in medium temperature circuit and R245fa in intermediate temperature circuit and R236fa in the low temperature circuit with*

Condenser temperature of single effect H_2O-Li/Br vapour absorption refrigeration system (^oC)	Over all exergetic efficiency of system using to low evaporator temperature of 123K using R236fa	Over all exergetic efficiency of system using to intermediate evaporator temperature of 173K using R245fa	Over all exergetic Efficiency of system using to intermediate evaporator temperature of 223K using HFO-1234yf
30	0.5054	0.4676	0.2812
31	0.5052	0.4674	0.2811
32	0.5050	0.4672	0.2810
33	0.5048	0.4670	0.2808
34	0.5047	0.4668	0.2807
35	0.5045	0.4665	0.2805
36	0.5043	0.4663	0.2803
37	0.5041	0.4661	0.2802
38	0.5039	0.4659	0.2801
39	0.5038	0.4658	0.2799
40	0.5036	0.4656	0.2798
41	0.5035	0.4654	0.2797
42	0.5034	0.4653	0.2796
43	0.5033	0.4652	0.2795
44	0.5032	0.4651	0.2794
45	0.5031	0.4649	0.2793

Table-7(c): Effect of condenser *temperature of VARS on thermodynamic performances such as system exergy destruction ratios with condenser temperature of three vapour compression refrigeration systems coupled with single effect vapour absorption refrigeration H_2O-Li/Br system using 1234yf ecofriendly refrigerant in medium temperature circuit and R245fa in intermediate temperature circuit and R236fa in the low temperature circuit.*

Condenser temperature of single effect H_2O-Li/Br vapour absorption refrigeration system (°C)	Over all Exergy Destruction Ratio of system using to low evaporator temperature of 123K using R23fa	Over all Exergy Destruction Ratio of system using to intermediate evaporator temperature of 173K using R245fa	Over all Exergy Destruction Ratio of system using to intermediate evaporator temperature of 223K using HFO-1234yf
30	0.9888	1.139	2.586
31	0.9794	1.140	2.597
32	0.9801	1.140	2.599
33	0.9800	1.141	2.561
34	0.9816	1.142	2.563
35	0.9823	1.143	2.565
36	0.9830	1.144	2.567
37	0.9837	1.145	2.569
38	0.9844	1.146	2.571
39	0.9850	1.147	2.572
40	0.9856	1.148	2.574
41	0.9861	1.148	2.575
42	0.9866	1.149	2.577
43	0.9870	1.150	2.578
44	0.9875	1.150	2.579
45	0.9878	1.151	2.580

3.8 Effect of condenser temperature on percentage improvements in total thermodynamic performances of three cascaded cycles in integrated system

Table-8(a): Effect of condenser *temperature of VARS on thermodynamic performances (First law Performance (COP_overall) of vapour compression refrigeration system coupled with single effect vapour absorption refrigeration LiBr system using 1234yf ecofriendly refrigerant in medium temperature circuit and R245fa in intermediate temperature circuit and R236fa in the low temperature circuit*

Condenser Temperature of single effect H_2O-Li/Br vapour absorption refrigeration system (°C)	Over all (%) improvement in First law efficiency (COP_Overall) of system using to low evaporator temperature of 123K using R236fa (%)	Over all (%) improvement in First law efficiency (COP_Overall) of system using to intermediate evaporator temperature of 173K using R245fa (%)	Over all (%) improvement in First law efficiency (COP_Overall) of system using to intermediate evaporator temp of 223K using HFO-1234yf (%)
30	15.19	21.23	7.748
31	15.25	21.28	7.785
32	15.31	21.34	7.826
33	15.38	21.40	7.87
34	15.45	21.46	7.915
35	15.52	21.52	7.961
36	15.59	21.58	8.005
37	15.65	21.63	8.047
38	15.71	21.69	8.086
39	15.77	21.74	8.123
40	15.83	21.79	8.158
41	15.87	21.83	8.189
42	15.92	21.87	8.218
43	15.96	21.91	8.245
44	16.0	21.94	8.27
45	16.04	21.97	8.293

Table-8(b): Effect of condenser *temperature of VARS on thermodynamic Second law performances (Exergetic efficiencies) with condenser temperature of vapour compression refrigeration system coupled with single effect vapour absorption refrigeration LiBr system using 1234yf ecofriendly refrigerant in medium temperature circuit and R245fa in intermediate temperature circuit and R236fa in the low temperature circuit*

Condenser Temp of single effect H_2O-Li/Br vapour absorption refrigeration system (^oC)	Over all (%) improvement in second law efficiency (exergetic Efficiency) of system using to low evaporator temperature of 123K using R236fa (%)	Over all (%) improvement in second law efficiency (exergetic Efficiency) of system using to intermediate evaporator temperature of 173K using R245fa (%)	Over all (%) improvement in second law efficiency (exergetic Efficiency) of system using to intermediate evaporator temperature of 223K using HFO-1234yf (%)
30	145.6	127.2	36.65
31	145.8	127.4	36.76
32	146.0	127.6	36.88
33	146.3	127.8	37.0
34	146.6	128.1	37.13
35	146.9	128.3	37.27
36	147.1	128.5	37.39
37	147.4	129.8	37.52
38	147.7	129.0	37.63
39	147.9	129.2	37.74
40	148.1	129.4	37.84
41	148.3	129.5	37.93
42	148.5	129.7	38.02
43	148.6	129.8	38.10
44	148.8	130.0	38.17
45	148.9	130.1	38.24

Table-8(c): Effect of condenser *temperature of VARS on thermodynamic system exergy destruction ratio with condenser temperature of vapour compression refrigeration system coupled with single effect vapour absorption refrigeration LiBr system using 1234yf ecofriendly refrigerant in medium temperature circuit and R245fa in intermediate temperature circuit and R236fa in the low temperature circuit.*

Condenser Temperature of single effect H_2O-Li/Br vapour absorption refrigeration system (^oC)	Over all (%) reduction in exergy destruction ratio (EDR) of system using to low evaporator temperature of 123K using R236fa (%)	Over all (%) reduction in exergy destruction ratio (EDR) of system using to intermediate evaporator temperature of 173K using R245fa (%)	Over all (%) reduction in exergy destruction ratio (EDR) of system using to intermediate evaporator temperature of 223K using HFO-1234yf (%)
30	74.64	70.49	33.77
31	74.65	70.52	33.85
32	74.69	70.54	33.90
33	74.71	70.57	33.97
34	74.74	70.60	34.05
35	74.77	70.63	34.12
36	74.80	70.66	34.19
37	74.83	70.69	34.26
38	74.85	70.72	34.33
39	74.88	70.74	34.39
40	74.90	70.77	34.44
41	74.92	70.79	34.51
42	74.94	70.81	34.54
43	74.95	70.82	34.59
44	74.97	70.86	34.63
45	74.98	70.85	34.67

3.9 Effect of evaporator temperature of vapour absorption refrigeration system on percentage improvements in total thermodynamic performances of three cascaded cycles in integrated system

Table-9(a) to Table-9(c) shows the variation of VARS evaporator temperature with thermodynamic performances combined single effect Li/Br vapour absorption refrigeration system cascaded with vapour compression refrigeration system using R1234yf eco-friendly refrigerant and it was observed that as intermediate temperature circuit evaporator temperature is increasing from (-50^{o}C to -20^{o}C), the first law efficiency (COP_VCRS) of vapour compression system is increasing while and second law efficiency (exergetic efficiency) of cascaded vapour compression single effect vapour absorption refrigeration system is increasing as intermediate temperature circuit evaporator Temperature is increasing. Similarly exergy destruction ratio based on exergy of product is also increasing as intermediate temperature circuit evaporator temperature of combined single effect Li/Br vapour absorption refrigeration system cascaded with VCR.

Table-9(a): Effect of Thermodynamic performances (First law Performances (COP_Overall), with absorber temperature of vapour compression refrigeration system coupled with single effect vapour absorption refrigeration LiBr system using 1234yf ecofriendly refrigerant in medium temperature circuit and R245fa in intermediate temperature circuit and R236fa in the low temperature circuit with condenser *temperature of VARS*

Evaporator temperature of single effect H_2O-Li/Br vapour absorption refrigeration system (^oC)	Over all COP of system using to low evaporator temperature of 123K using R23fa	Over all COP of system using to intermediate evaporator temperature of 173K using R245fa	Over all COP of system using to intermediate evaporator temperature of 223K using HFO-1234yf
1	0.8532	0.8961	0.7950
2	0.8548	0.8979	0.7967
3	0.8564	0.8998	0.7986
4	0.8582	0.9018	0.8005
5	0.860	0.9040	0.8026
6	0.8619	0.9062	0.8047
7	0.8639	0.9085	0.8070
8	0.8659	0.9109	0.8093
9	0.8681	0.9134	0.8117
10	0.8704	0.9161	0.8143

Table-9(b): Effect of Thermodynamic Second law performance (Exergetic efficiency) with absorber temperature of vapour compression refrigeration system coupled with single effect vapour absorption refrigeration LiBr system using 1234yf ecofriendly refrigerant in medium temperature circuit and R245fa in intermediate temperature circuit and R236fa in the low temperature circuit with condenser temperature of VARS

Evaporator Temperature of single effect H_2O-Li/Br vapour absorption refrigeration system (^oC)	Over all exergetic efficiency of system using to low evaporator temperature of 123K using R236fa	Over all exergetic efficiency of system using to intermediate evaporator temperature of 173K using R245fa	Over all exergetic Efficiency of system using to intermediate evaporator temperature of 223K using HFO-1234yf
1	0.5240	0.4909	0.3113
2	0.5211	0.4873	0.3068
3	0.5182	0.4837	0.3023
4	0.5154	0.4802	0.2979
5	0.5126	0.4767	0.2935
6	0.5099	0.4733	0.2891
7	0.5071	0.4699	0.2848
8	0.5045	0.4665	0.2805
9	0.5018	0.4632	0.2762
10	0.4992	0.460	0.2720

Table-9(c): Effect of Thermodynamic system exergy destruction ratio with absorber temperature of vapour compression refrigeration system coupled with single effect vapour absorption refrigeration LiBr system using 1234yf ecofriendly refrigerant in medium temperature circuit and R245fa in intermediate temperature circuit and R236fa in the low temperature circuit with condenser *temperature of VARS*

Evaporator Temperature of single effect H_2O-Li/Br vapour absorption refrigeration system (^oC)	Over all Exergy Destruction Ratio of system using to low evaporator temperature of 123K usingR23fa	Over all Exergy Destruction Ratio of system using to intermediate evaporator temperature of 173K using R245fa	Over all Exergy Destruction Ratio of system using to intermediate evaporator temperature of 223K using HFO-1234yf
1	0.9084	1.037	2.212
2	0.9191	1.052	2.260
3	0.9297	1.067	2.308
4	0.9403	1.082	2.357
5	0.9508	1.098	2.408
6	0.9613	1.113	2.459
7	0.9718	1.126	2.511
8	0.9823	1.143	2.565
9	0.9927	1.159	2.62
10	1.003	1.174	2.676

3.10Effect of evaporator temperature of vapour absorption refrigeration system on percentage improvements in total thermodynamic performances of three cascaded cycles in integrated system

Table-10(a) to Table-10(c) shows the variation of VARS evaporator temperature with percentage improvement in thermodynamic performances combined single effect Li/Br vapour absorption refrigeration system cascaded with vapour compression refrigeration system using R1234yf eco-friendly refrigerant and it was observed that as intermediate temperature circuit evaporator temperature is increasing from (-50^{o}C to -20^{o}C), the first law efficiency (COP_VCRS) of vapour compression system is increasing while and second law

efficiency (exergetic efficiency) of cascaded vapour compression single effect vapour absorption refrigeration system is increasing as intermediate temperature circuit evaporator Temperature is increasing. Similarly exergy destruction ratio based on exergy of product is also increasing as intermediate temperature circuit evaporator temperature of combined single effect Li/Br vapour absorption refrigeration system cascaded with Vapour compression refrigeration.

Table-10(a): Effect of Thermodynamic performances (First law Performance (COP_VARS), Second law performance (Exergetic efficiency) and system exergy destruction ratio with absorber temperature of vapour compression refrigeration system coupled with single effect vapour absorption refrigeration LiBr system using 1234yf ecofriendly refrigerant in medium temperature circuit and R245fa in intermediate temperature circuit and R236fa in the low temperature circuit with condenser temperature of VARS

Evaporator Temp of single effect H_2O-Li/Br vapour absorption refrigeration system(°C)	Over all (%) improvement in First law efficiency (COP_Overall) of system using to low evaporator temp of 123K using R236fa (%)	Over all (%) improvement in First law efficiency (COP_Overall) of system using to intermediate evaporator temp of 173K using R245fa (%)	Over all (%) improvement in First law efficiency (COP_Overall) of system using to intermediate evaporator temp of 223K using HFO-1234yf (%)
1	16.65	22.51	8.689
2	16.52	22.39	8.60
3	16.37	22.26	8.505
4	16.21	22.12	8.406
5	16.05	21.98	8.302
6	15.88	21.83	8.193
7	15.71	21.68	8.08
8	15.52	21.52	7.961
9	15.3	21.35	7.836
10	15.2	21.17	7.707

Table-10(b): Effect of Thermodynamic performances (First law Performance (COP_VARS), Second law performance (Exergetic efficiency) and system exergy destruction ratio with absorber temperature of vapour compression refrigeration system coupled with single effect vapour absorption refrigeration LiBr system using 1234yf ecofriendly refrigerant in medium temperature circuit and R245fa in intermediate temperature circuit and R236fa in the low temperature circuit with condenser *temperature of VARS*

Evaporator Temperature of single effect H_2O-Li/Br vapour absorption refrigeration system (°C)	% improvement in Over allexergetic efficiency of system using to low evaporator temperature of 123K using R236fa	% improvement in Over allexergetic efficiency of system using to intermediate temperature evaporator temperature of 173K using R245fa	% improvement in Over allexergetic Efficiency of system using to intermediate evaporator temperature of 223K using HFO-1234yf
1	81.5	70.05	7.842
2	88.47	76.39	8.60
3	96.04	82.99	14.36
4	104.3	90.36	18.08
5	113.4	98.45	22.17
6	123.4	1.7.4	26.67
7	134.5	117.3	31.68
8	146.9	128.3	37.27
9	160.8	140.7	43.55
10	176.5	154.7	50.66

Table-10(c): Effect of Thermodynamic performances (First law Performance (COP_VARS), Second law performance (Exergetic efficiency) and system exergy destruction ratio with absorber temperature of vapour compression refrigeration system coupled with single effect vapour absorption refrigeration LiBr system using 1234yf ecofriendly refrigerant in medium temperature circuit and R245fa in intermediate temperature circuit and R236fa in the low temperature circuit with condenser *temperature of VARS*

evaporatorTemperature of single effect H_2O-Li/Br vapour absorption refrigeration system (°C)	% improvement in Overall Exergy Destruction Ratio of system using to low evaporator temperature of 123K using R23fa	% improvement in Overall Exergy Destruction Ratio of system using to intermediate evaporator temperature of 173K using R245fa	% improvement in Overall Exergy Destruction Ratio of system using to intermediate evaporator temperature of 223K using HFO-1234yf
1	63.13	57.91	10.22
2	64.88	59.79	13.66
3	66.59	61.65	17.07
4	68.28	63.48	20.48
5	69.94	65.3	23.88
6	71.57	67.09	27.28
7	73.18	68.87	30.7
8	74.77	70.63	34.12
9	76.34	72.39	37.57
10	77.9	74.13	41.04

3.11 Effect of temperature of MTC evaporator on overall system performances of cascade evaporators using ecofriendly refrigerants

In this section, the effect of various cascaded evaporator have been discussed in detail as given below.

Table-11(a) to Table-11(c) show the variation of medium temperature circuit evaporator temperature of combined single effect Li/Br vapour absorption refrigeration system cascaded with vapour compression refrigeration system using 1234yf ecofriendly refrigerant in medium temperature circuit and R245fa in intermediate temperature circuit and R236fa in the low temperature circuit and it was observed that as Low temperature circuit evaporator Temperature is increasing from (-50^{o}C to -20^{o}C), the first law efficiency ($COP_{_Cascade}$) of cascaded vapour compression single effect vapour absorption system is increasing while and second law efficiency (exergetic efficiency) of cascaded vapour compression half effect vapour absorption refrigeration system is decreasing as generator temperature is increasing. Similarly exergy destruction ratio based on exergy of product is also increasing as medium temperature circuit evaporator Temperature of combined single effect Li/Br Vapour absorption refrigeration system cascaded with vapour compression refrigeration system using 1234yf ecofriendly refrigerant in medium temperature circuit and R245fa in intermediate temperature circuit and R236fa in the low temperature circuit is increased.

Table11(a): Effect of evaporator Temperature of medium temperature circuit using HFO-1234yf refrigerants on the thermodynamic performance such as First law Performance (COP_overall), of vapour compression refrigeration system coupled with single effect vapour absorption refrigeration LiBr system using 1234yf ecofriendly refrigerant in medium temperaturet, R245fa in intermediate temperature circuit and R236fa in low temperature

evaporator Temperature of medium temperature circuit using HFO-1234yf refrigerants (^{o}C)	Over all first law efficiency ($COP_{_Overall}$) of system using to low evaporator temperature of 123K using R236fa (%)	Over all first law efficiency ($COP_{_Overall}$) of system using to intermediate evaporator temperature of 173K using R245fa (%)	Over all first law efficiency ($COP_{_Overall}$) of system using to intermediate evaporator temperature of 223K using HFO-1234yf (%)
-20	0.9389	1.036	1.012
-25	0.9296	1.015	0.9759
-30	0.9192	0.9997	0.9408
-35	0.9076	0.9794	0.9065
-40	0.8948	0.9577	0.8731
-45	0.8809	0.9348	0.8404
-50	0.8659	0.9109	0.8098

Table-11(b): Effect of evaporator Temperature of medium temperature circuit using HFO-1234yf refrigerants on the thermodynamic performance such as Second law performance (Exergetic efficiency) of vapour compression refrigeration system coupled with single effect vapour absorption refrigeration LiBr system using 1234yf ecofriendly refrigerant in medium temperature circuit and R245fa in intermediate temperature circuit and R236fa in the low temperature circuit

evaporator Temperature of medium temperature circuit using HFO-1234yf refrigerants (^{o}C)	Over all second law efficiency (exergetic efficiency) of system using to low evaporator temperature of 123K using R236fa (%)	Over all second law efficiency (exergetic efficiency) of system using to intermediate evaporator temperature of 173K using R245fa (%)	Over all second law efficiency (exergetic efficiency) of system using to intermediate evaporator temp of 223K using HFO-1234yf (%)
-20	0.4406	0.4572	0.2921
-25	0.4566	0.4656	0.2939
-30	0.4707	0.4712	0.2941
-35	0.4827	0.4741	0.2927
-40	0.4997	0.4743	0.2895
-45	0.4924	0.4717	0.2857
-50	0.5045	0.4665	0.2805

Table-11(c): Effect of evaporator temperature of medium temperature circuit using HFO-1234yf refrigerants on the thermodynamic performances: system exergy destruction ratio of vapour compression refrigeration system coupled with single effect vapour absorption refrigeration LiBr system using 1234yf ecofriendly refrigerant in medium temperature circuit and R245fa in intermediate temperature circuit and R236fa in low temperature

evaporator Temperature of medium temperature circuit using HFO-1234yf refrigerants (^{o}C)	Over all exergy destruction ratio (EDR) of system using to low evaporator temperature of 123K using R236fa (%)	Over all exergy destruction ratio (EDR) of system using to intermediate evaporator temperature of 173K using R245fa (%)	Over all exergy destruction ratio (EDR) of system using to intermediate evaporator temperature of 223K using HFO-1234yf (%)
-20	1.27	1.187	2.424
-25	1.19	1148	2.402
-30	1.124	1.122	2.40
-35	1.072	1.109	2.417
-40	1.031	1.108	2.45
-45	1.0	1.12	2.50
-50	0.9823	1.143	2.565

3.12 Effect of temperature of MTC evaporator on percentage improvement in overall system performances of cascade evaporators using ecofriendly refrigerants

Table-12(a) to Table-12(c) show the variation of medium temperature circuit evaporator temperature of combined single effect Li/Br vapour absorption refrigeration system cascaded with VCRS using 1234yf ecofriendly refrigerant in medium temperature circuit and R245fa in intermediate temperature circuit and R236fa in the low temperature circuit and it was observed that as Low temperature circuit evaporator Temperature is increasing from (-50^{o}C to -20^{o}C), the first law efficiency ($COP_{_Cascade}$) of cascaded vapour compression single effect vapour absorption system is increasing while and second law efficiency (exergetic efficiency) of cascaded vapour compression half effect vapour absorption refrigeration system is decreasing as generator temperature is increasing. Similarly exergy destruction ratio based on exergy of product is also increasing as medium temperature circuit evaporator Temperature of combined single effect Li/Br Vapour absorption refrigeration system cascaded with vapour compression refrigeration system using 1234yf ecofriendly refrigerant in medium temperature circuit and R245fa in intermediate temperature circuit and R236fa in the low temperature circuit is increased.

Table-12(a): Effect of evaporator temperature of medium temperature circuit using HFO-1234yf refrigerants on percentage improvement in thermodynamic performances such as first law performance ($COP_{_Overall}$) of vapour compression refrigeration system coupled with single effect vapour absorption refrigeration LiBr system using 1234yf ecofriendly refrigerant in medium temperature circuit and R245fa in intermediate temperature circuit and R236fa in the low temperature circuit

evaporator Temperature of medium temperature circuit using HFO-1234yf refrigerants (^{o}C)	Over all (%) improvement in first law efficiency ($COP_{_Overall}$) of system using to low evaporator temp of 123K using R236fa (%)	Over all (%) improvement in first law efficiency ($COP_{_Overall}$) of system using to intermediate evaporator temp of 173K using R245fa (%)	Over all (%) improvement in first law efficiency ($COP_{_Overall}$) of system using to intermediate evaporator temperature of 223K using HFO-1234yf (%)
-20	25.26	38.18	34.98
-25	24.01	35.88	30.09
-30	22.62	33.36	25.5
-35	21.08	30.65	20.93
-40	19.17	27.76	16.47
-45	17.52	24.71	12.15
-50	15.52	21.52	7.961

Table-12(b): Effect of evaporator Temperature of medium temperature circuit using HFO-1234yf refrigerants on percentage improvement in thermodynamic performances such as first law performance ($COP_{_Overall}$) of vapour compression refrigeration system coupled with single effect vapour absorption refrigeration LiBr system using 1234yf ecofriendly refrigerant in medium temperature circuit and R245fa in intermediate temperature circuit and R236fa in the low temperature circuit

evaporator Temp of medium temp circuit using HFO-1234yf refrigerants (^{o}C)	Over all (%) improvement in second law efficiency (exergetic Efficiency) of system using to low evaporator temp of 123K using R236fa (%)	Over all (%) improvement in second law efficiency (exergetic Efficiency) of system using to intermediate evaporator temp of 173K using R245fa (%)	Over all (%) improvement in second law efficiency (exergetic Efficiency) of system using to intermediate evaporator temp of 223K using HFO-1234yf (%)
-20	115.6	123.8	42.92
-25	123.5	127.8	43.35
-30	130.4	130.6	43.92
-35	136.2	132.0	43.22
-40	141.0	132.1	41.84
-45	144.5	130.9	39.84
-50	146.9	128.3	37.29

Table-12(c): Effect of evaporator temperature of medium temperature circuit using HFO-1234yf refrigerants on percentage improvement in the thermodynamic performances such as first law performance ($COP_{_Overall}$) of vapour compression refrigeration system coupled with single effect vapour absorption refrigeration LiBr system using 1234yf ecofriendly refrigerant in medium temperature circuit and R245fa in intermediate temperature circuit and R236fa in the low temperature circuit

evaporator Temperature of medium temperature circuit using HFO-1234yf refrigerants (^{o}C)	Over all (%) reduction in exergy destruction ratio (EDR) of system using to low evaporator temp of 123K using R236fa (%)	Over all (%) reduction in exergy destruction ratio (EDR) of system using to intermediate evaporator temp of 173K using R245fa (%)	Over all (%) reduction in exergy destruction ratio (EDR) of system using to intermediate evaporator temp of 223K using HFO-1234yf (%)
-20	67.39	69.51	37.76
-25	69.44	70.52	38.31
-30	71.12	71.18	38.35
-35	72.48	71.51	37.93
-40	73.53	71.53	37.08
-45	74.29	71.21	35.8
-50	74.77	70.63	34.12

3.13 Effect of temperature of ITC evaporator on overall system performances of cascade evaporators using ecofriendly refrigerants

Table-13(a) to Table-13 (c) shows the variation of Low temperature circuit evaporator Temperature of combined single effect Li/Br Vapour absorption refrigeration system cascaded with VCRS using 1234yf ecofriendly refrigerant in medium temperature circuit and R245fa in intermediate temperature circuit and R236fa in the low temperature circuit and it was observed that as Low temperature circuit evaporator Temperature is increasing from (-70^{o}C to -30^{o}C), the first law efficiency(COP_VCRS) of cascaded vapour compression system is increasing while and second law efficiency (exergetic efficiency) of Cascaded vapour compression single effect vapour absorption refrigeration system is increasing as Low temperature circuit evaporator Temperature is increasing. Similarly exergy destruction ratio based on exergy of product is also increasing as Low temperature circuit evaporator Temperature of combined single effect Li/BrVapour absorption refrigeration system cascaded with VCRS using R134a refrigerant is decreased.

Table-13(a): Effect of evaporator temperature of intermediate temperature circuit using R-245fa refrigerants (^{o}C) on Thermodynamic performances (First law Performance (COP_Overall), Second law performance and system exergy destruction ratio with absorber temperature of vapour compression refrigeration system coupled with single effect vapour absorption refrigeration LiBr system using 1234yf ecofriendly refrigerant in medium temperature, R245fa in intermediate temperature and R236fa in the low temperature with evaporator temperature of VARS

evaporator Temperature of intermediate temperature circuit using R-245fa refrigerants (^{o}C)	Over all first law efficiency ($COP_{Overall}$) of system using to low evaporator temperature of 123K using R236fa (%)	Over all first law efficiency ($COP_{Overall}$) of system using to intermediate evaporator temperature of 173K using R245fa (%)	Over all first law efficiency ($COP_{Overall}$) of system using to intermediate evaporator temperature of 223K using HFO-1234yf (%)
-70	0.9205	0.9857	0.8098
-75	0.90971	0.9706	0.8098
-80	0.8989	0.9556	0.8098
-85	0.888	0.9406	0.8098
-90	0.877	0.9257	0.8098
-95	0.8659	0.9109	0.8098
-100	0.8963	0.8549	0.8098

Table-13(b): Effect of evaporator Temperature of intermediate temperature circuit using R-245fa refrigerants (^{o}C) on Thermodynamic performances (First law Performance (COP_Overall), Second law performance (Exergetic efficiency) and system exergy destruction ratio with absorber temperature of vapour compression refrigeration system coupled with single effect vapour absorption refrigeration LiBr system using 1234yf ecofriendly refrigerant in medium temperature circuit and R245fa in intermediate temperature circuit and R236fa in the low temperature circuit with evaporator temperature of VARS

evaporator Temperature of intermediate temperature circuit using R-245fa refrigerants (^{o}C)	Over all second law efficiency (exergetic Efficiency) of system using to low evaporator temp of 123K using R236fa (%)	Over all second law efficiency (exergetic Efficiency) of system using to intermediate evaporator temp of 173K using R245fa (%)	Over all second law efficiency (exergetic Efficiency) system using to intermediate evaporator temp of 223K using HFO-1234yf (%)
-70	0.5157	0.4688	0.2805
-75	0.5145	0.4696	0.2805
-80	0.5127	0.4698	0.2805
-85	0.5105	0.4693	0.2805
-90	0.5077	0.4683	0.2805
-95	0.5045	0.4665	0.2805
-100	0.5007	0.4642	0.2805

Table-13(c): Effect of evaporator Temperature of intermediate temperature circuit using R-245fa refrigerants(^{o}C) on Thermodynamic performances (First law Performance (COP_Overall), Second law performance (Exergetic efficiency) and system exergy destruction ratio with absorber temperature of vapour compression refrigeration system coupled with single effect vapour absorption refrigeration LiBr system using 1234yf ecofriendly refrigerant in medium temperature circuit and R245fa in intermediate temperature circuit and R236fa in the low temperature cycle.

evaporator Temperature of intermediate temperature circuit using R-245fa refrigerants (^{o}C)	Over all exergy destruction ratio (EDR) of system using to low evaporator temperature of 123K using R236fa (%)	Over all exergy destruction ratio (EDR)) of system using to intermediate evaporator temperature of 173K using R245fa (%)	Over all exergy destruction ratio (EDR) of system using to intermediate evaporator temperature of 223K using HFO-1234yf (%)
-70	0.9390	1.133	2.565
-75	0.9437	1.131	2.565
-80	0.9503	1.129	2.565
-85	0.9588	1.131	2.565
-90	0.9695	1.136	2.565
-95	0.9823	1.143	2.565
-100	0.9974	1.154	2.565

3.14 Effect of ultra-low evaporator temperature on percentage improvements in total thermodynamic performances of three cascaded cycles in integrated system

Table-14(a) to Table-14(c) shows the variation of intermediate temperature circuit evaporator temperature with percentage improvement in thermodynamic performances combined single effect Li/Br vapour absorption refrigeration system cascaded with vapour compression refrigeration system using R1234yf eco-friendly refrigerant and it was observed that as intermediate temperature circuit evaporator temperature is increasing from (-50^{o}C to -20^{o}C), the first law efficiency (COP_VCRS) of vapour compression system is increasing while and second law efficiency (exergetic efficiency) of cascaded vapour compression single effect vapour absorption refrigeration system is increasing as intermediate temperature circuit evaporator Temperature is increasing. Similarly exergy destruction ratio based on exergy of product is also increasing as intermediate temperature circuit evaporator temperature of combined single effect Li/Br vapour absorption refrigeration system cascaded with Vapour compression refrigeration system using R236fa eco-friendly refrigerant is decreased.

Table-14(a): Effect of evaporator Temperature of intermediate temperature circuit using R-245fa refrigerants (^{o}C) on the percentage improvement of Thermodynamic performances (First law Performance (COP_Overall), Second law performance (Exergetic efficiency) and system exergy destruction ratio with absorber temperature of vapour compression refrigeration system coupled with single effect vapour absorption refrigeration LiBr system using 1234yf ecofriendly refrigerant in medium temperature circuit and R245fa in intermediate temperature circuit and R236fa in the low temperature

evaporator Temperature of intermediate temperature circuit using R-245fa refrigerants (^{o}C)	Over all (%) improvement in first law efficiency (COP$_{_Overall}$) of system using to low evaporator temp of 123K using R236fa (%)	Over all (%) improvement in first law efficiency (COP$_{_Overall}$) of system using to intermediate evaporator temp of 173K using R245fa (%)	Over all (%) improvement in first law efficiency (COP$_{_Overall}$) of system using to intermediate evaporator temp of 223K using HFO-1234yf (%)
-70	22.80	31.50	7.961
-75	21.36	29.48	7.961
-80	19.91	27.48	7.961
-85	18.45	25.48	7.961
-90	16.99	23.49	7.961
-95	15.52	21.52	7.961
-100	14.05	19.57	7.961

Table-14(b): Effect of evaporator temperature of intermediate temperature circuit using R-245fa refrigerants (^{o}C) on the percentage improvement of in terms of second law performances (exergetic efficiencies) of vapour compression refrigeration system coupled with single effect vapour absorption refrigeration H_2OLi/Br system using 1234yf ecofriendly refrigerant in medium temperature circuit and R245fa in intermediate temperature circuit and R236fa in the low temperature circuit.

evaporator Temperature of intermediate temperature circuit using R-245fa refrigerants (^{o}C)	Over all (%) improvement in second law efficiency (exergetic Efficiency) of system using to low evaporator temperature of 123K using R236fa (%)	Over all (%) improvement in second law efficiency (exergetic Efficiency) of system using to intermediate evaporator temperature of 173K using R245fa (%)	Over all (%) improvement in second law efficiency (exergetic Efficiency) of system using to intermediate temperature evaporator temperature of 223K using HFO-1234yf (%)
-70	152.4	129.4	37.27
-75	151.8	129.8	37.27
-80	150.9	129.9	37.27
-85	149.8	129.7	37.27
-90	148.5	129.2	37.27
-95	146.9	128.3	37.27
-100	145.0	123.7	37.27

Table-14(c): Effect of evaporator Temperature of intermediate temperature circuit using R-245fa refrigerants(^{o}C) on the percentage improvement of system exergy destruction ratio with absorber temperature of vapour compression refrigeration system coupled with single effect vapour absorption refrigeration LiBr system using 1234yf ecofriendly refrigerant in medium temperature circuit and R245fa in intermediate temperature circuit and R236fa in the low temperature circuit with evaporator temperature of VARS

evaporator Temperature of intermediate temperature circuit using R-245fa refrigerants (^{o}C)	Over all (%) reduction in exergy destruction ratio (EDR) of system using to low evaporator temp of 123K using R236fa (%)	Over all (%) reduction in exergy destruction ratio (EDR) of system using to intermediate evaporator temp of 173K using R245fa (%)	Over all (%) reduction in exergy destruction ratio (EDR) of system using to intermediate evaporator temp of 223K using HFO-1234yf (%)
-70	75.88	70.90	34.12
-75	75.76	70.99	34.12
-80	75.56	70.97	34.12
-85	75.37	70.96	34.12
-90	75.10	70.84	34.12
-95	74.77	70.63	34.12
-100	74.38	70.36	34.12

3.15 Effect of ultra-low evaporator temperature on total thermodynamic performances of three cascaded cycles in integrated system

Table-15(b): Effect of LTC evaporator *temperature on thermodynamic performances (first law performance ($COP_{Overall}$), of vapour compression refrigeration system coupled with single effect vapour absorption refrigeration H_2O-Li/Br system using 1234yf ecofriendly refrigerant in medium temperature circuit and R245fa in intermediate temperature circuit and R236fa in the low temperature circuit*

evaporator Temperature ofultra low temperature circuit using R-236fa refrigerants (°C)	Over all l first law efficiency ($COP_{Overall}$) of system using to low evaporator temperature of 123K using R236fa (%)	Over all law first law efficiency ($COP_{Overall}$) of system using to intermediate evaporator temperature of 173K using R245fa (%)	Over all law first law efficiency ($COP_{Overall}$) of system using to intermediate evaporator temperature of 223K using HFO-1234yf (%)
-120	0.9213	0.9109	0.8093
-125	0.9116	0.9109	0.8093
-130	0.9021	0.9109	0.8093
-135	0.8928	0.9109	0.8093
-140	0.8836	0.9109	0.8093
-145	0.8747	0.9109	0.8093
-150	0.8659	0.9109	0.8093
-155	0.8578	0.9109	0.8093

Table-15(b): Effect of LTC evaporator *temperature on thermodynamic performances (second law performances (exergetic efficiencies), of vapour compression refrigeration system coupled with single effect vapour absorption refrigeration H_2O-Li/Br system using 1234yf ecofriendly refrigerant in medium temperature circuit and R245fa in intermediate temperature circuit and R236fa in the low temperature circuit*

evaporator Temperature ofultra low temperature circuit using R-236fa refrigerants (°C)	Over all second law law efficiency (exergetic Efficiency) of system using to low evaporator temp of 123K using R236fa (%)	Over all second law law efficiency (exergetic Efficiency) of system using to intermediate evaporator temp of 173K using R245fa (%)	Over all second law law efficiency (exergetic Efficiency) of system using to intermediate evaporator temp of 223K using HFO-1234yf (%)
-120	0.5425	0.4665	0.2805
-125	0.5374	0.4665	0.2805
-130	0.5319	0.4665	0.2805
-135	0.528	0.4665	0.2805
-140	0.5191	0.4665	0.2805
-145	0.5120	0.4665	0.2805
-150	0.5045	0.4665	0.2805
-155	0.4964	0.4665	0.2805

Table-15(c): Effect of LTC evaporator *temperature Thermodynamic performances (First law Performance (COP_VARS), Second law performance (Exergetic efficiency) and system exergy destruction ratio with absorber temperature of vapour compression refrigeration system coupled with single effect vapour absorption refrigeration LiBr system using 1234yf ecofriendly refrigerant in medium temperature circuit and R245fa in intermediate temperature circuit and R236fa in the low temperature circuit*

evaporator Temperature of ultra-low temperature circuit using R-236fa refrigerants (°C)	Over all exergy destruction ratio (EDR) of system using to low temperature evaporator temperature of 123K (i.e.-150°C) using R236fa (%)	Over all (%) improvement in second law law efficiency (exergetic Efficiency) of system using to intermediate evaporator temperature of 173K using R245fa (%)	Over all (%) improvement in second law law efficiency (exergetic Efficiency) of system using to intermediate evaporator temperature of 223K using HFO-1234yf (%)
-120	0.8433	1.143	2.565
-125	0.8607	1.143	2.565
-130	0.8802	1.143	2.565
-135	0.9020	1.143	2.565
-140	0.9263	1.143	2.565
-145	0.9530	1.143	2.565
-150	0.9823	1.143	2.565
-155	1.014	1.143	2.565

3.16 Effect of ultra-low evaporator temperature on percentage total thermodynamic performances of three cascaded cycles in integrated system

Table-16(a): Effect of ultra-low evaporator temperature on percentage improvement of thermodynamic performances (First law Performance (COP_ Overall), of vapour compression refrigeration system coupled with single effect vapour absorption refrigeration LiBr system using 1234yf ecofriendly refrigerant in medium temperature circuit and R245fa in intermediate temperature circuit and R236fa in the low temperature circuit.

evaporator temperature of ultra-low temperature circuit using R-236fa refrigerants (ºC)	Over all (%) improvement in first law efficiency ($COP_{_overall}$) of system using to low evaporator temp of 123K using R236fa (%)	Over all (%) improvement in first law efficiency ($COP_{_overall}$) of system using to intermediate evaporator temp of 173K using R245fa (%)	Over all (%) improvement in first law efficiency ($COP_{_overall}$) of system using to intermediate evaporator temperature of 223K using HFO-1234yf (%)
-120	22.9	21.52	7.961
-125	21.61	21.52	7.961
-130	20.15	21.52	7.961
-135	19.1	21.52	7.961
-140	17.87	21.52	7.961
-145	16.68	21.52	7.961
-150	15.52	21.52	7.961
-155	14.4	21.52	7.961

Table-16(b): Effect of ultra low evaporator *temperatureon improvement of thermodynamic performances second law performances (Exergetic efficiencies) of vapour compression refrigeration system coupled with single effect vapour absorption refrigeration LiBr system using 1234yf ecofriendly refrigerant in medium temperature circuit and R245fa in intermediate temperature circuit and R236fa in the low temperature circuit*

evaporator temperature of ultra-low temperature circuit using R-236fa refrigerants (ºC)	Over all (%) improvement in second law efficiency (exergetic Efficiency) of system using to low evaporator temperature of 123K using R236fa (%)	Over all (%) improvement in second law efficiency (exergetic Efficiency) of system using to intermediate evaporator temperature of 173K using R245fa (%)	Over all (%) improvement in second law efficiency (exergetic Efficiency) of system using to intermediate temperature evaporator temperature of 223K using HFO-1234yf (%)
-120	165.5	128.3	37.27
-125	163.0	128.3	37.27
-130	160.3	128.3	37.27
-135	157.3	128.3	37.27
-140	154.1	128.3	37.27
-145	150.6	128.3	37.27
-150	146.9	128.3	37.27
-155	142.9	128.3	37.27

Table-16(c): Effect of ulta low evaporator *temperature on reduction in system exergy destruction ratio of vapour compression refrigeration system coupled with single effect vapour absorption refrigeration LiBr system using 1234yf ecofriendly refrigerant in medium temperature circuit and R245fa in intermediate temperature circuit and R236fa in the low temperature circuit*

evaporator Temperature ofultra low temperature circuit using R-236fa refrigerants (ºC)	Over all (%) reduction in exergy destruction ratio (EDR) of system using to low temperature evaporator temperature of 123K using R236fa (%)	Over all (%) reduction in exergy destruction ratio (EDR) of system using to intermediate temperature evaporator temperature of 173K using R245fa (%)	Over all (%) reduction in exergy destruction ratio (EDR) of system using to intermediate temperature evaporator temperature of 223K using HFO-1234yf (%)
-120	78.34	70.63	34.12
-125	77.9	70.63	34.12
-130	77.35	70.63	34.12
-135	76.83	70.63	34.12
-140	76.21	70.63	34.12
-145	75.33	70.63	34.12
-150	74.77	70.63	34.12
-155	73.5	70.63	34.12

3.17 Effect of ecofriendly refrigerants in Intermediate temperature cycle on total thermodynamic performances of three cascaded cycles in integrated system

Table-10(a) to Table-10(c) show the comparison between with ecofriendly refrigerants in terms of thermodynamic performances (First law performances ($COP_{_Overall}$), second law performance (Exergetic efficiencies) and system exergy destruction Ratios of three cascaded vapour compression refrigeration system coupled with single effect vapour absorption Refrigeration H_2O-Li/Br System using HFO-1234yf ecofriendly refrigerant in medium temperature cycle and following ecofriendly refrigerants in intermediate temperature cycle and R236fa refrigerant in the ultra-low temperature cycle and it is found that the first and second law performances of cascaded vapour compression - vapour single effect absorption system is higher by using HFO-1234yf ecofriendly refrigerant in medium temperature circuit and R236fa in ultra-low temperature circuit and found that by using R1234yf is slightly lower than R152a, R134a,R410a , R407c R245fa and higher than R227ea and R404a.

Table-17(a): Effect of ecofriendly refrigerants in medium temperature cycle on the *thermodynamic performances (First law Performance (COP_Overall), vapour compression refrigeration system coupled with single effect vapour absorption refrigeration LiBr system using 1234yf ecofriendly refrigerant in medium temperature circuit and R245fa in intermediate temperature circuit and R236fa in the low temperature circuit*

Ecofriendly refrigerants in MTC circuit	Over all first law efficiency (COP_Overall) of system using to low evaporator temperature of 123K using R236fa (%)	Over all first law efficiency (COP_Overall) of system using to intermediate evaporator temperature of 173K using R245fa (%)	Over all first law efficiency (COP_Overall) of system using to intermediate evaporator temperature of 223K using HFO-1234yf (%)
R-1234yf	0.8659	0.8659	0.8093
R407c	0.8690	0.9147	0.8125
R404a	0.8464	0.8859	0.7015
R-152a	0.9264	0.9863	0.8748
R410a	0.8936	0.9454	0.8390
R134a	0.9011	0.9545	0.8469
R227ea	0.8172	0.8519	0.7592

Table-17(b): Effect of ecofriendly refrigerants in medium temperature cycle on the *Second law performance (Exergetic efficiency) of vapour compression refrigeration system coupled with single effect vapour absorption refrigeration LiBr system using 1234yf ecofriendly refrigerant in medium temperature circuit and R245fa in intermediate temperature circuit and R236fa in the low temperature circuit*

Ecofriendly refrigerants in MTC circuit	Over all second law efficiency (exergetic efficiency) of system using to low evaporator temperature of 123K using R236fa (%)	Over all second law efficiency (exergetic efficiency) of system using to intermediate evaporator temperature of 173K using R245fa (%)	Over all second law efficiency (exergetic efficiency) of system using to intermediate evaporator temperature of 223K using HFO-1234yf (%)
R-1234yf	0.5045	0.4665	0.2805
R407c	0.5708	0.4703	0.8230
R404a	0.4822	0.4416	0.264
R-152a	0.5706	0.5441	0.3342
R410a	0.5349	0.5015	0.3042
R134a	0.5423	0.5109	0.3107
R227ea	0.4517	0.4084	0.2427

Table-17(c): Effect of ecofriendly refrigerants in medium temperature cycle on *system exergy destruction ratio with absorber temperature of vapour compression refrigeration system coupled with single effect vapour absorption refrigeration LiBr system using 1234yf ecofriendly refrigerant in medium temperature circuit and R245fa in intermediate temperature circuit and R236fa in the low temperature circuit*

Ecofriendly refrigerants in MTC circuit	Over all exergy destruction ratio (EDR) of system using to low evaporator temperature of 123K using R236fa (%)	Over all exergy destruction ratio (EDR) of system of system using to intermediate evaporator temperature of 173K using R245fa (%)	Over all exergy destruction ratio (EDR) of system of system using to intermediate evaporator temperature of 223K using HFO-1234yf(%)
R-1234yf	0.9823	1.143	2.565
R407c	0.9692	1.126	2.533
R404a	1.074	1.265	2.787
R-152a	0.8696	0.9939	2.287
R410a	0.7525	0.838	1.992
R134a	0.8422	0.9574	2.219
R227ea	1.2141	1.449	3.12

3.18 Effect of ecofriendly refrigerants in Intermediate temperature cycle on percentage improvements in total thermodynamic performances of three cascaded cycles in integrated system

Table-18(a) to Table-18(c) show the comparison between with ecofriendly refrigerants in terms of percentage improvements in thermodynamic performances (First law performances ($COP_{_Overall}$), second law performance (Exergetic efficiencies) and system exergy destruction Ratios of three cascaded vapour compression refrigeration system coupled with single effect vapour absorption Refrigeration H_2O-Li/Br System using HFO-1234yf ecofriendly refrigerant in medium temperature cycle and following ecofriendly refrigerants in intermediate temperature cycle and R236fa refrigerant in the ultra-low temperature cycle and it is found that the first and second law performances of cascaded vapour compression -vapour single effect absorption system is higher by using HFO-1234yf ecofriendly refrigerant in medium temperature circuit and R236fa in ultra-low temperature circuit and found that by using R32 is slightly lower than R245fa and higher than HFC-134a, R404a , R410a, R407c and R507a.

Table-18(a): Effect of ecofriendly refrigerants in medium temperature cycle(MTC) on the percentage improvement *thermodynamic performances (First law Performance (COP_VARS), of vapour compression refrigeration system coupled with single effect vapour absorption refrigeration LiBr system using 1234yf ecofriendly refrigerant in medium temperature circuit and R245fa in intermediate temperature circuit and R236fa in the low temperature circuit*

Ecofriendly refrigerants in MTC circuit	Over all (%) improvement in first law efficiency ($COP_{Overall}$) of system using to low evaporator temperature of 123K using R236fa (%)	Over all (%) improvement in first law efficiency ($COP_{Overall}$) of system using to intermediate evaporator temperature of 173K using R245fa (%)	Over all (%) improvement in first law efficiency ($COP_{Overall}$) of system using to intermediate evaporator temperature of 223K using HFO-1234yf (%)
R-1234yf	15.52	21.52	7.967
R407c	15.93	22.02	8.393
R404a	12.78	18.17	5.106
R-152a	19.24	26.12	11.3
R410a	23.59	31.58	16.7
R134a	20.21	27.33	12.98
R227ea	9.021	13.64	1.277

Table-18(b): Effect of ecofriendly refrigerants in medium temperature cycle on the *Second law performance (exergetic efficiencies) and of vapour compression refrigeration system coupled with single effect vapour absorption refrigeration LiBr system using 1234yf ecofriendly refrigerant in medium temperature circuit and R245fa in intermediate temperature circuit and R236fa in the low temperature circuit*

Ecofriendly refrigerants in MTC circuit	Over all (%) improvement in second law efficiency (exergetic Efficiency) of system using to low evaporator temperature of 123K using R236fa (%)	Over all (%) improvement in second law efficiency (exergetic Efficiency) of system using to intermediate evaporator temperature of 173K using R245fa (%)	Over all (%) improvement in second law efficiency (exergetic Efficiency) of system using to intermediate evaporator temperature of 223K using HFO-1234yf(%)
R-1234yf	146.9	128.3	37.27
R407c	148.5	130.2	38.51
R404a	136.0	116.1	29.22
R-152a	179.2	166.3	63.53
R410a	161.8	145.4	48.08
R134a	165.7	150.0	52.05
R227ea	121.1	99.85	18.75

Table-18(c): Effect of ecofriendly refrigerants in medium temperature cycle on *system exergy destruction ratio with absorber temperature of vapour compression refrigeration system coupled with single effect vapour absorption refrigeration LiBr system using 1234yf ecofriendly refrigerant in medium temperature circuit and R245fa in intermediate temperature circuit and R236fa in the low temperature circuit*

Ecofriendly refrigerants in MTC circuit	Over all (%) reduction in exergy destruction ratio (EDR) of system using to low evaporator temperature of 123K using R236fa (%)	Over all (%) reduction in exergy destruction ratio (EDR) of system using to intermediate evaporator temperature of 173K using R245fa (%)	Over all (%) reduction in exergy destruction ratio (EDR) of system using to intermediate evaporator temperature of 223K using HFO-1234yf (%)
R-1234yf	74.77	70.63	34.12
R407c	75.11	71.08	34.94
R404a	72.42	67.52	28.42
R-152a	80.67	78.48	48.83
R410a	77.67	74.47	41.25
R134a	78.37	75.41	43.02
R227ea	68.53	62.79	19.88

3.19 Effect of ecofriendly refrigerants in intermediate temperature cycle of cascaded vapour compression cycle on total thermodynamic performances of three cascaded cycles in integrated system

Table-19(a) to Table-19(c) show the comparison between with ecofriendly refrigerants in terms of thermodynamic performances (First law performances ($COP_{Overall}$), second law performance (Exergetic efficiencies) and system exergy destruction Ratios of three cascaded vapour compression refrigeration system coupled with single effect vapour absorption Refrigeration H_2O-Li/Br System using HFO-1234yf ecofriendly refrigerant in medium temperature cycle and following ecofriendly refrigerants in intermediate temperature cycle and R236fa refrigerant in the ultra-low temperature cycle and it is found that the first and second law performances of cascaded vapour compression - vapour single effect absorption system is higher by using HFO-1234yf ecofriendly refrigerant in medium temperature circuit and R236fa in ultra-low temperature circuit and found that by using R32 is slightly lower than R245fa and higher than HFC-134a, R404a , R410a, R407c and R507a.

Table-19(a): Effect of ecofriendly refrigerants in intermediate temperature cycle on *Thermodynamic performances (First law Performance (COP_overall), vapour compression refrigeration system coupled with single effect vapour absorption refrigeration LiBr system using 1234yf ecofriendly refrigerant in medium temperature circuit and R245fa in intermediate temperature circuit and R236fa in the low temperature circuit*

Ecofriendly refrigerants in Intermediate ITC circuit	Over all first law efficiency (COP_Overall) of system using to low evaporator temperature of 123K using R236fa	Over all first law efficiency (COP_Overall) of system using to low evaporator temperature of 123K using R245fa	Over all first law efficiency (COP_Overall) of system using to low evaporator temperature of 223K using R1234yf
R-245fa	0.8659	0.9109	0.8093
R134a	0.8652	09099	0.8093
R32	0.8590	0.9016	0.8093
R-507a	0.8643	0.9067	0.8093
R404a	0.8622	0.9059	0.8093
R 410a	0.8644	0.9088	0.8093
R407c	0.4444	0.8825	0.8093

Table-19(b): Effect of ecofriendly refrigerants in intermediate temperature cycle on over all second law efficiencies (exergetic efficiencies) *of vapour compression refrigeration system coupled with single effect vapour absorption refrigeration LiBr system using 1234yf ecofriendly refrigerant in medium temperature circuit and following ecofriendly refrigerants in intermediate temperature circuit and R236fa in the low temperature circuit*

Ecofriendly refrigerants in Intermediate ITC circuit	Over all second law efficiency (exergetic Efficiency) of system using to low evaporator temperature of 123K using R236fa	Over all second law efficiency (exergetic efficiency) of system using to intermediate evaporator temperature of 173K using R245fa	Over all second law efficiency (exergetic Efficiency) of system using to intermediate evaporator temperature of 223K using HFO-1234yf
R-245fa	0.5045	0.4665	0.2805
R134a	0.5033	0.4652	0.2805
R32	0.4939	0.4551	0.2805
R-507a	0.5020	0.4638	0.2805
R404a	0.4987	0.4603	0.2805
R 410a	0.5021	0.4639	0.2805
R407c	0.472	0.4319	0.2805

Table-19(c): Effect of ecofriendly refrigerants in intermediate temperature cycle on *system exergy destruction ratios of vapour compression refrigeration system coupled with single effect vapour absorption refrigeration LiBr system using 1234yf ecofriendly refrigerant in medium temperature circuit and following ecofriendly refrigerants in intermediate temperature circuit and R236fa in the low temperature circuit*

Ecofriendly refrigerants in Intermediate ITC circuit	Over all exergy destruction ratio (EDR) of system using to low evaporator temperature of 123K using R236fa	Over all exergy destruction ratio (EDR) of system using to intermediate evaporator temperature of 173K using R245fa	Over all exergy destruction ratio (EDR) of system using to intermediate evaporator temperature of 223K using HFO-1234yf
R-245fa	0.9823	1.143	2.565
R134a	0.987	1.149	2.565
R32	1.025	1.197	2.565
R-507a	0.9921	1.156	2.565
R404a	1.005	1.122	2.565
R 410a	0.9917	1.155	2.565
R407c	0.9917	1.315	2.565

3.20 Effect of ecofriendly refrigerants in Intermediate temperature cycle on percentage improvements in total thermodynamic performances of three cascaded cycles in integrated system

Table-20(a) to Table-20(c) show the comparison between with ecofriendly refrigerants in terms of thermodynamic performances (First law performances ($COP_{Overall}$), second law performance (Exergetic efficiencies) and system exergy destruction Ratios of three cascaded vapour compression refrigeration system coupled with single effect vapour absorption Refrigeration H_2O-Li/Br System using HFO-1234yf ecofriendly refrigerant in medium temperature cycle and following ecofriendly refrigerants in intermediate temperature cycle and R236fa refrigerant in the ultra-low temperature cycle and it is found that the first and second law performances of cascaded vapour compression - vapour single effect absorption system is higher by using HFO-1234yf ecofriendly refrigerant in medium temperature circuit and R236fa in ultra-low temperature circuit and found that by using R32 is slightly lower than R245fa and higher than HFC-134a, R404a , R410a, R407c and R507a

Table-20(a): Effect of ecofriendly refrigerants in intermediate temperature cycle on *Thermodynamic performances (First law Performance (COP_Overall), of vapour compression refrigeration system coupled with single effect vapour absorption refrigeration LiBr system using 1234yf ecofriendly refrigerant in medium temperature circuit and R245fa in intermediate temperature circuit and R236fa in the low temperature circuit*

Ecofriendly refrigerants in intermediate ITC circuit	Over all (%) improvement in first law efficiency (COP_Overall) of system using to low evaporator temperature of 123K using R236fa (%)	Over all (%) reduction in exergy destruction ratio (EDR) of system using to intermediate evaporator temperature of 173K using R245fa (%)	Over all (%) improvement in first law efficiency (COP_Overall) of system using to intermediate evaporator temperature of 223K using HFO-1234yf (%)
R-245fa	15.52	21.52	7.961
R134a	15.41	21.38	7.961
R32	15.49	20.26	7.961
R-507a	15.30	21.23	7.961
R404a	15.01	20.85	7.961
R 410a	15.31	21.24	7.961
R407c	12.65	17.73	7.961

Table-20(b): Effect of ecofriendly refrigerants in intermediate temperature cycle on *Second law performance (Exergetic efficiency) and of vapour compression refrigeration system coupled with single effect vapour absorption refrigeration LiBr system using 1234yf ecofriendly refrigerant in medium temperature circuit and R245fa in intermediate temperature circuit and R236fa in the low temperature circuit*

Ecofriendly refrigerants in Intermediate ITC circuit	Over all (%) improvement in second law efficiency (exergetic Efficiency) of system using to low evaporator temperature of 123K using R236fa (%)	Over all (%) improvement in second law efficiency (exergetic Efficiency) of system using to intermediate evaporator temperature of 173K using R245fa (%)	Over all (%) improvement in second law efficiency (exergetic Efficiency) of system using to intermediate evaporator temperature of 223K Using HFO-1234yf (%)
R-245fa	146.9	128.3	37.27
R134a	146.3	127.7	37.27
R32	141.7	122.7	37.27
R-507a	145.7	127.0	37.27
R404a	144.1	125.3	37.27
R 410a	145.7	127.0	37.27
R407c	131.0	111.3	37.27

Table-20(c): Effect of ecofriendly refrigerants in intermediate temperature cycle on *percentage reduction in system exergy destruction ratio of vapour compression refrigeration system coupled with single effect vapour absorption refrigeration LiBr system using 1234yf ecofriendly refrigerant in medium temperature circuit and R245fa in intermediate temperature circuit and R236fa in the low temperature circuit*

Ecofriendly refrigerants in Intermediate ITC circuit	Over all (%) reduction in exergy destruction ratio (EDR) of system using to low evaporator temperature of 123K using R236fa (%)	Over all (%) reduction in exergy destruction ratio (EDR) of system using to intermediate evaporator temperature of 173K using R245fa (%)	Over all (%) reduction in exergy destruction ratio (EDR) of system using to intermediate evaporator temperature of 223K using HFO-1234yf (%)
R-245fa	74.77	70.63	34.72
R134a	74.65	70.48	34.72
R32	73.68	69.25	34.72
R-507a	74.52	70.20	34.72
R404a	74.19	69.89	34.72
R 410a	74.53	70.33	34.72
R407c	71.27	66.21	34.72

3.21 Effect of ecofriendly refrigerants in ultra-low cascaded vapour compression cycle on total thermodynamic performances of three cascaded cycles in integrated system

Table-21(a) to Table-21(c) show the comparison between hydro carbons and ethylene with ecofriendly refrigerant R236fa in terms of thermodynamic performances (First law performances ($COP_{_Overall}$), second law performance (Exergetic efficiencies) and system exergy destruction Ratios of three cascaded vapour compression refrigeration system coupled with single effect vapour absorption Refrigeration H_2OLi/Br System using HFO-1234yf ecofriendly refrigerant in medium temperature cycle and R245fa in intermediate temperature cycle and following refrigerants in the ultra-low temperature cycle and it is found that the first and second law performances of cascaded vapour compression -vapour single effect absorption system is higher by using HFO-1234yf ecofriendly refrigerant in medium temperature circuit and R245fa in intermediate temperature circuit and following ecofriendly refrigerants in the low temperature circuit using R600a is maximum and lowest when using ethylene.

Table-21(a): Effect of ecofriendly refrigerants in ultra-low temperature cycle on *thermodynamic performances (First law Performance (COP_VARS), of vapour compression refrigeration system coupled with single effect vapour absorption refrigeration LiBr system using 1234yf ecofriendly refrigerant in medium temperature circuit and R245fa in intermediate temperature circuit and R236fa in the low temperature circuit*

Ecofriendly refrigerants in ultra-low temperature cycle	Over all (%) reduction in exergy destruction ratio (EDR) of system using to low evaporator temperature of 123K using R236fa (%)	Over all (%) reduction in exergy destruction ratio (EDR) of system using to intermediate evaporator temperature of 173K using R245fa (%)	Over all (%) reduction in exergy destruction ratio (EDR) of system using to intermediate evaporator temperature of 223K using HFO-1234yf (%)
R236fa	0.8659	0.9109	0.8093
R290	0.8664	0.9109	0.8093
R600a	0.8685	0.9109	0.8093
Ethylene	0.8566	0.9109	0.8093

Table-21(b): Effect of ecofriendly refrigerants in ultra-low temperature cycle on, *Second law performance (Exergetic efficiency) and system exergy destruction ratio of vapour compression refrigeration system coupled with single effect vapour absorption refrigeration LiBr system using 1234yf ecofriendly refrigerant in medium temperature circuit and R245fa in intermediate temperature circuit and R236fa in the low temperature circuit*

Ecofriendly refrigerants in ultra-low temperature cycle	Over all (%) improvement in second law efficiency (exergetic Efficiency) of system using to low evaporator temp of 123K using R236fa (%)	Over all (%) improvement in second law efficiency (exergetic Efficiency) of system using to intermediate evaporator temp of 173K using R245fa (%)	Over all (%) improvement in second law efficiency (exergetic Efficiency) of system using to intermediate evaporator temp of 223K using HFO-1234yf (%)
R236fa	0.5045	0.4665	0.2805
R290	0.5053	0.4665	0.2805
R600a	0.5094	0.4665	0.2805
Ethylene	0.4865	0.4665	0.2805

Table-21(c): Effect of ecofriendly refrigerants in ultra-low temperature cycle on *system exergy destruction ratio with absorber temperature of vapour compression refrigeration system coupled with single effect vapour absorption refrigeration H_2O- Li/Br system using 1234yf ecofriendly refrigerant in medium temperature circuit and R245fa in intermediate temperature circuit and R236fa in the low temperature circuit*

Ecofriendly refrigerants in ultra-low temperature cycle	Over all exergy destruction ratio (EDR) of system of system using to low evaporator temperature of 123K using R236fa (%)	Over all exergy destruction ratio (EDR) of system of system using to intermediate evaporator temperature of 173K using R245fa (%)	Over all exergy destruction ratio (EDR) of system of system using to intermediate evaporator temperature of 223K using HFO-1234yf(%)
R236fa	0.9823	1.143	2.565
R290	0.979	1.143	2.565
R600a	0.9630	1.143	2.565
Ethylene	1.056	1.143	2.565

3.22Effect of ecofriendly refrigerants on percentage improvements in total thermodynamic performances of three cascaded cycles in integrated system

Table-22(a) to Table-22(c) shows the comparison between hydro carbons and ethylene with ecofriendly refrigerant R236fa in terms of thermodynamic performances (First law performances ($COP_{_Overall}$), second law performance (Exergetic efficiencies) and system exergy destruction Ratios of three cascaded vapour compression refrigeration system coupled with single effect vapour absorption Refrigeration H_2OLi/Br System using HFO-1234yf ecofriendly refrigerant in medium temperature cycle and R245fa in intermediate temperature cycle and following refrigerants in the ultra-low temperature cycle and it is found that the percentage improvement in first and second law performances of cascaded vapour compression vapour single effect absorption system is higher by using HFO-1234yf ecofriendly refrigerant in medium temperature circuit and R245fa in intermediate temperature circuit and following ecofriendly refrigerants in the low temperature circuit using R600a is maximum and lowest when using ethylene.

Table-22(a): Effect of ecofriendly refrigerants in ultra-low temperature cycle on percentage improvement of *thermodynamic performances such as first law performance ($COP_{_overall}$), vapour compression refrigeration system coupled with single effect vapour absorption refrigeration LiBr system using 1234yf ecofriendly refrigerant in medium temperature circuit and R245fa in intermediate temperature circuit and R236fa in the low temperature circuit*

Ecofriendly refrigerants in ultra-low temperature cycle	% improvement in Overall First law efficiency ($COP_{_Overall}$) to low temperature evaporator of 123K using R236fa (%)	% improvement in Overall First law efficiency ($COP_{_Overall}$) of system using to intermediate evaporator temperature of 173K using R245fa (%)	% improvement in Overall First law efficiency ($COP_{_Overall}$) of system using to intermediate evaporator temperature of 223K using HFO-1234yf (%)
R236fa	15.52	21.52	7.964
R290	15.58	21.52	7.964
R600a	15.86	21.52	7.964
Ethylene	14.27	21.52	7.964

Table-22(b): Effect of ecofriendly refrigerants in ultra low temperature cycle on *percentage improvement in Second law performances (exergetic efficiencies) of vapour compression refrigeration system coupled with single effect vapour absorption refrigeration LiBr system using 1234yf ecofriendly refrigerant in medium temperature circuit and R245fa in intermediate temperature circuit and R236fa in the low temperature circuit*

Ecofriendly refrigerants in ultra-low temperature cycle	Over all (%) improvement in second law efficiency (exergetic Efficiency) of system using to low evaporator temperature of 123K using R236fa (%)	Over all (%) improvement in second law efficiency (exergetic Efficiency) of system using to intermediate evaporator temperature of 173K using R245fa (%)	Over all (%) improvement in second law efficiency (exergetic Efficiency) of system using to intermediate evaporator temperature of 223K using HFO-1234yf(%)
R236fa	146.9	128.3	37.27
R290	147.3	128.3	37.27
R600a	149.3	128.3	37.27
Ethylene	138.1	128.3	37.27

Table-22(c): Effect of ecofriendly refrigerants in ultra low temperature cycle on *percentage reduction of exergy destruction ratios of vapour compression refrigeration system coupled with single effect vapour absorption refrigeration LiBr system using 1234yf ecofriendly refrigerant in medium temperature circuit and R245fa in intermediate temperature circuit and R236fa in the low temperature circuit*

Ecofriendly refrigerants in ultra-low temperature cycle	Over all (%) reduction in exergy destruction ratio (EDR) of system using to low evaporator temperature of 123K using R236fa (%)	Over all (%) reduction in exergy destruction ratio (EDR) of system using to intermediate evaporator temperature of 173K using R245fa (%)	Over all (%) reduction in exergy destruction ratio (EDR) of system using to intermediate evaporator temperature of 223K using HFO-1234yf (%)
R236fa	74.77	70.63	34.12
R290	74.86	70.63	34.12
R600a	75.27	70.63	34.12
Ethylene	72.89	70.63	34.12

4. Conclusions and Recommendations

The following conclusions were drawn from present investigations.

- Thermodynamic performance in terms of first law efficiency($COP_{_Cascade_System}$) of combined cascaded vapour compression -single effect vapour absorption refrigeration system using using 1234yf ecofriendly refrigerant in medium temperature circuit and R245fa in intermediate tempe138.1rature circuit and R236fa in the low temperature circuit than R1234yf ecofriendly refrigerant in medium temperature circuit and R245fa in intermediate temperature circuit and R236fa in the low temperature circuit.
- Thermodynamic performance in terms of second law efficiency(Exergetic Efficiency) of combined cascaded vapour compression single effect vapour absorption refrigeration system using HFC-134a ecofriendly refrigerant in medium temperature circuit and R245fa in intermediate temperature circuit and R236fa in the low temperature circuit ishigher than the combined cascaded vapour compression single effect vapour absorption refrigeration system using 1234yf ecofriendly refrigerant in medium temperature circuit and R245fa in intermediate temperature circuit and R236fa in the low temperature circuit than R1234yf ecofriendly refrigerant in medium temperature circuit and R245fa in intermediate temperature circuit and R236fa in the low temperature circuit.
- As Low temperature circuit evaporator Temperature is decreasing , the first law performances (($COP_{_Cascade_System}$) and second law efficiency (Exergetic efficiency) of cascaded vapour compression -single effect vapour absorption refrigeration system is decreasing and exergy destruction ratio of combined vapour compression-single effect vapour absorption system is increasing.
- The best thermodynamic performances in terms of first and second law efficiencies have been found by using R152a in medium temperature circuit.
- Use of hydrocarbon is also feasible by considering safety measures because hydrocarbons are flammable and R600a gives best thermodynamic performances.
- Thermodynamic performances in terms of first and second law efficiencies also affected by variation of generator temperature and also decreasing as generator temperature is increasing.
- Thermodynamic performances in terms of first and second law efficiencies also affected by variation of absorber temperature and also decreasing as absorber temperature is increasing.
- Thermodynamic performances in terms of first and second law efficiencies also affected by variation of condenser temperature and also decreasing as condenser temperature is increasing.
- Thermodynamic performances in terms of first and second law efficiencies also affected by variation of approach (temperature over lapping) and also decreasing as temperature over lapping is increasing because larger value of temperature overlapping (approach) in each cascade heat exchanger circuit reduces the COP and exergetic efficiency of the system.

References

[1] R.S. Mishra [2014] Performance Optimization of Four Stage Cascade Refrigeration Systems using Energy-Exergy Analysis in the R1234ze & R1234yf in High Temperature Circuit and Eco friendly Refrigerants in Intermediate Circuits and Ethane in the Low Temperature Circuit for Food, Pharmaceutical, Chemical Industries" International Journal of Advance

Research and Innovation, ISSN 2347 - 3258 , Volume 2, Issue 4 , page- 701-709

[2] R.S. Mishra[2014] Use of Hydrocarbons in Low Temperature Circuit in Terms of First Law and Second Law Efficiency of Four Stage Cascade Refrigeration of Semen Preservation" International Journal of Advance Research and Innovation (IJARI), ISSN 2347 - 3258 , Volume 2, Issue 4, page725-731.

[3] Y. Chen, W. Han, H. Jin,[2017] Proposal and analysis of a novel heat-driven absorption–compression refrigeration system at low temperatures, Applied Energy Vol-185 , page-2106–2117.

[4] S.A. Tassou, J.S. Lewis, Y.T. Ge, A. Hadawey, I. Chaer, A review of emerging technologies for food refrigeration applications, applied Thermal Engineering. 30 (2010)263–276.

[5] Rabah Gomri R and Hakimi R [2009] second law analysis of double effect vapour absorption cooler system , International journal of energy conversion and management, Elsevier , Vol-49, page-3343-48.

[6] Rabah Gomri R [2008] second law comparison of single and double effect vapour absorption refrigeration system, International journal of energy conversion and management, Elsevier , Vol-50, page-1279-1287.

[7] D. Colorado, W. Rivera, (2015) Performance comparison between a conventional vapour compression and compression-absorption single-stage and double-stage systems used for refrigeration, Applied. Thermal. Engineering. 87 273–285.

[8] R.S. Mishra [2018] Comparison of thermal performances of single effect, double effect and triple effect LiBr-H2O absorption system cascaded with vapour compression refrigeration systems using ecofriendly refrigerants, International Journal of Research in Engineering and Innovation (IJREI), ISSN (Online): 2456-6934, Vol-2, Issue-6 (2018), 610-621, journal home page:

[9] S.A.Tassou, J.S. Lewis, Y.T. Ge, A. Hadawey, I. Chaer, A review of emerging technologies for food refrigeration applications, Appl. Thermal Engg. 30 (2010)263–276.

[10] R.Ayala, C.L. Heard, F. Holland, Ammonia/lithium nitrate absorption /compression refrigeration cycle, Part I, Appl. Therm. Eng. 17 (3)(1997) 223–233.

[11] R.S. Mishra[2019], Thermal performances (first law efficiency, exergy destruction ratio &exergetic efficiency) of cascade single effect ammonia-water (NH3-H20) vapour absorption refrigeration system coupled with vapour compression refrigeration using ecofriendly refrigerants in the low temperature cycle of VCRS system, International Journal of Research in Engineering and Innovation (IJREI) journal home page: http://www.ijrei.com ISSN (Online): 2456-6934, Vol-3, Issue-1,page-1-5

[12] L.Kairouani, E. Nehdi, Cooling performance and energy saving of a compression-absorption refrigeration system assisted by geothermal energy, Appl. Therm. Engg. 26 (2006) 288–294.

[13] R.S. Mishra [2019] Comparison of half effect absorption-compression cascaded refrigeration system using thermodynamic (energy-exergy) analysis. International Journal of Research in Engineering and Innovation (IJREI), ISSN (Online): 2456-6934, Vol-3, Issue-1 (2019), page-6-11.

[14] R.S. Mishra [2019] Thermal performance of cascaded vapour compression absorption systems, International Journal of Research in Engineering and Innovation (IJREI), ISSN (Online): 2456-6934, Vol-3, Issue-1 (2019), page-61-67.

[15] R.S. Mishra [2019] Use of fourth generation ecofriendly refrigerants in two and three cascade refrigeration systems for reducing global warming and ozone depletion, International Journal of Research in Engineering and Innovation (IJREI), ISSN (Online): 2456-6934, Vol-2, Issue-2 (2018), page-20-208.

[16] M.Azhar, M.A. Siddiqui, Optimization of operating temperatures in the gas operated single to triple effect vapour absorption refrigeration cycles, Int. J.Refrig. 82 (2017) 401–425.

[17] M.Azhar, M.A. Siddiqui, Thermodynamic analysis of a gas operated triple effect absorption cycle, Int. J. Innovative Res. Sci. Eng. Technol. 2 (5) (2013)1610–1616.

[18] V. Jain, S.S. Kachhwaha, G. Sachdeva, Thermodynamic performance analysis of a vapor compression–absorption cascaded refrigeration system, Energy Convers. Manage. 75 (2013) 685–700.16S.

[19] R.S. Mishra [2018] Performance parameters optimization of cascade refrigeration system using ecofriendly refrigerants, International Journal of Research in Engineering and Innovation (IJREI), ISSN (Online): 2456-6934 , Vol-2, Issue-6 , 602-609 Vol-2, Issue-6 (2018), 602-609.

[20] A.K.Pratihar, S.C. Kaushik, R.S. Agarwal, Simulation of an ammonia–water compression absorption refrigeration system for water chilling application, Int J Refrig 33 (2010) 1386–1394.

[21] Z.G. Sun, K.H. Guo, Cooling performance and energy saving of a compression–absorption refrigeration system driven by a gas engine, Int. J. Energy Res. 30(13) (2006) 1109–1116.

[22] M. Dixit, A. Arora, S.C. Kaushik, Thermodynamic and thermo economic analyses of two stage hybrid absorption compression refrigeration system, App. Thermal Engg. 113 (2017) 120–131.

[23] M.E. Alvarez, X. Esteve, M. Bourouis, Performance analysis of a triple-effect absorption cooling cycle using aqueous (lithium, potassium, sodium) nitrate solution as a working pair, Appl. Thermal. Engineering. 79 (2015) 27–36.

[24] R.S. Mishra[2019] Performance evaluation of solar assisted half effect Li/Br vapour absorption refrigeration system cascaded with vapour compression refrigeration system using eco-friendly refrigerants, International Journal of Advance Research and Innovation , ISSN 2347 - 3258 , Volume 7 Issue 2 ,page-156-161.

[25] W. Han, L. Sun, D. Zheng, H. Jin, S. Ma, X. Jing, [2013] New hybrid absorption–compression refrigeration system based on cascade use of mid-temperature waste heat, Applied. Energy 106, page-383–390.

[26] S.C. Kaushik, Akhilesh Arora, Energy and exergy analysis of single effect and series flow double effect water–lithium bromide absorption refrigeration systems, Int. J. Refrig. (2009) 1–12.

[27] C.Cimsit, I.T. Ozturk, [2012], Analysis of compression-absorption cascade refrigeration cycles, App. Therm. Engg. 40, page- 311–317.

[28] S. Garimella, A.M. Brown, A.K. Nagavarapu, [2011] Waste heat driven absorption/vapor compression cascade refrigeration system for megawattscale, high-flux, low-temperature cooling, Int. J. Refrigeration 34, page- 1176–1185

[29] L. Wang, A. Ma, Y. Tan, X. Cui, H. Cui, [2012] Study on Solar-Assisted CascadeRefrigeration System, Engergyprocedia 16, page-1503–1509.

[30] S.Eini, H. Shahhosseini, N. Delgarm, M. Lee, [2016], A. Bahadori, Multi-objectiveoptimization of a cascade refrigeration system: exergetic, economic,environmental, and inherent safety analysis, Appl. Therm. Engg. 107, page-804–817.

[31] S. Bhattacharyya, S. Mukhopadhyay, A. Kumar, R.K. Khurana, J. Sarkar,Optimization of a CO_2–C3H8 cascade system for refrigeration and heating,Int J Refrig. 28 (2005) 1284–1292.

[32] M. Mafi, S.M. Mousavi Naeynian, M. Amidpour, Exergy analysis of multistage cascade low temperature refrigeration systems used in olefin plants, Int. J.Refrig. 32 (2009) 279–294.

[33] J.C.V.Chinnappa, M.R. Crees, S.S. Murthy, K. Srinivasan, Solar-assisted vapour compression/absorption cascaded air-conditioning systems, Sol. Energy 50 (5)(1993) 453–458

[34] R. Cabello, D. SánCHEz, R. Llopis, J. Catalán, L. Nebot-Andrés, E. Torrella, Energy evaluation of R152a as drop in replacement for R134a in cascade refrigeration plants, App. Therm. Engg. 110 (2017) 972–984

[35] A.Messineo, R744–R717 Cascade Refrigeration System: Performance evaluation compared with a HFC Two-Stage System, ICAEE 2011, Energy Procedia 14 (2012) 56–65.

Cite this article as: R. S. Mishra, Performance evaluation of single effect Li/Br-H_2O vapour absorption systems using multi cascading of vapour compression cycles for ultra-low temperature applications, International Journal of Research in Engineering and Innovation Vol-4, Issue-1 (2020), 8-38. *https://doi.org/10.36037/IJREI.2020.4103.*

Predicting the Remaining Useful Life of Ball Bearing Under Dynamic Loading Using Supervised Learning

S. Singh, T. Agarwal[2], G. Kumar[3], O.M. Yadav[4]
[1,2,3]Department of Mechanical Engineering, Delhi Technological University, New Delhi, India
[4]Department of Industrial and Manufacturing Engineering, North Dakota State University, Fargo, USA
savinay_bt2k16@dtu.ac.in

Abstract - **Rolling element bearing is one of the most critical components of rotating machinery. Its failure can be catastrophic and often results in both human and material losses. This paper presents a machine learning model to predict the wear process phenomena and remaining useful life of a bearing element using classification and regression techniques respectively. An algorithm is developed to recognize the underlying mapping function directly from the data using machine learning principles. Pearson correlation methodology is used to track the important features associated with the evolution of wear and understand its progression. Further, backward elimination technique with ordinary least squares regression results was used to track features for predicting the remaining useful life. The proposed approach is illustrated on a bearing failure data set from the national aeronautics and space agency. This study will be useful in forecasting the fault status of the bearing before it causes any major loss.**

Keywords - **Rolling element bearing, diagnosis, remaining useful life, forecasting, and machine learning model.**

I. INTRODUCTION

Rolling element bearing (REB) being an essential component in heavy equipment intensive industries plays a crucial part in reliable operation in a rotating machinery. The recent advancement in predicting remaining useful life(RUL) has shown a huge potential to apply prognosis and health management techniques to REBs. However, the RUL prediction is still a very complex process due to various factors influencing the conditions or state of bearings. Detection and diagnosis of faults in a bearing have been widely studied using vibration signal processing approach for many years[1][2]. However, in today's scenario machine learning models are used for understanding it better and have simplified it to a great extent. Li et al.[3] proposed a novel method for interactive clustering in bearing fault diagnosis. Li et al. [4] suggested fuzzy approach to determine Informative frequency band(IFB) from a vibratory signal. Li et al. [5] presented a deep statistical learning model from rotary mechanical systems. Muetze and Strangas[6] presented a brief summary with tools and methods for the reliable estimation of bearings maintenance schedules for electrical devices, through fault severity estimation and Remaining Useful Life (RUL). However, the vibration-based monitoring has an advantage over the acoustic emission technique, due to its low sensor cost and ease in measurement, resulting it to be the most widely used technique[7].

Fault detection was a handy tool for the industries but predicting the failure beforehand is more useful and effective since it would reduce machine idle time. The RUL predictions are being used extensively in today's scenario. Lu et al. [8] proposed a fault diagnosis method based on principal component analysis (PCA) and support vector machine(SVM). Samantha et al. [9] proposed a bearing fault diagnosis method based on artificial neural network (ANN), which is suitable for on-line condition monitoring and diagnosis of machines. Yang et al. [10] combined expert system and back propagation (BP) neural network to diagnose and maintain bearing fault in a remote system. Li et al. [10] introduced a model which uses a new ensemble prognostics method that takes into account the effects of degradation on the accuracy of RUL prediction. The RUL is an estimate of the number of remaining years that a system, or component is able to function in accordance with its intended purpose before any replacement is required. They suggested that an adaptive weight optimization algorithm should be developed to partition the entire degradation process into multiple degradation stages accurately. Therefore, the proposed work is to partition the entire degradation process into multiple degradation stages for better diagnosis of fault detection. Further, an integrated diagnostics and prognostics model overcoming the limitations of earlier work for fault detection and predicting RUL respectively has been suggested. Earlier the work was done on physics-based model either on diagnostics or on prognostics. Physics of failure-based models treat the time to failure as deterministic. However, time to failure is based on the theory of probability. In this paper an approach to integrated machine learning based diagnostic and prognostic model is presented. The proposed machine learning based model addresses the limitation of earlier models by retaining an underline failure distribution, the parameters of which are determined by explanatory variables.

The outline of the paper is as follows: Section I presents motivation, a brief literature review and the current status of the work. The methodology for the proposed model is discussed in Section II. Further, Section III depicts the illustrations of the suggested methodology. Finally, Section IV concludes the paper.

II. METHODOLOGY

An integrated diagnostic and prognostic model suggested in this paper is briefly discussed in this section.

A. Integrated Diagnostic and Prognostic Approach

The approach proposed in this paper has been depicted in the form of a flow chart as shown in Fig 1. The steps involved are discussed in the following subsections.

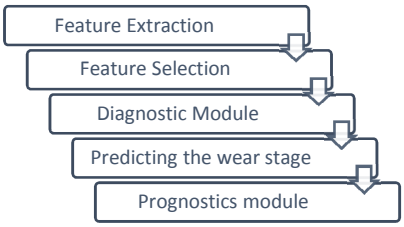


Fig. 1. Flowchart of Integrated diagnostic and prognostic approach

B. Feature Extraction

In machine learning a feature is an individual measurable property or characteristic of a phenomenon being observed[12]. Feature extraction transforms raw data such as text or images into numerical features which can be used by a machine learning model[13]. This process is effortlessly performed using any programming language. However, it is preferred to use only those languages in which the mathematical and statistical functions are either in-built or are easily available via online libraries. In this case MATLAB and Python[14][15] have been used.

C. Feature Selection

After the features are extracted, feature selection is applied. This method is used since it reduces training time, avoids the curse of dimensionality, simplifies the model and reduces over fitting [16]. Several filtering techniques are used to select relevant features such as linear discriminant analysis (LDA), PCA and Pearson's Correlation methodology. In this study, Pearson's Correlation Methodology has been used because it quantifies the extent up to which features are correlated. Pearson's Correlation measures the linear correlation between two variables X and Y and expressed as in Eq (1) [17]:

$$\rho_{X,Y} = \frac{COV(X,Y)}{\sigma_X \sigma_Y} \quad (1)$$

Here, COV is coefficient of variance; σ_X is standard deviation of X; σ_y is standard deviation of Y; Correlation value near -1 and 1 considered as strongly correlated and value near to 0 was considered as unrelated features.

D. Diagnostic Module

When relevant features have been selected by Pearson's correlation methodology, a graph of feature v/s time is plotted. The experimental studies show some significant degree of nonlinearity between the defect size and the obtained impact response that appears in the measurement. The tests which have used RMS(Root Mean Square) as tracking measure show nonlinear propagation curve of the wear evolution [18][23]. Therefore, kurtosis was used to track the wear severity in a dynamic loading condition. Thus, different stages were identified under dynamic loading as shown in Fig 2. For this work, the wear severity has been divided into five stages as depicted in Figure 2 below.

E. Predicting the wear stage

For predicting the wear severity stage, supervised learning approach is used. In supervised learning, the model is trained on a labelled dataset.

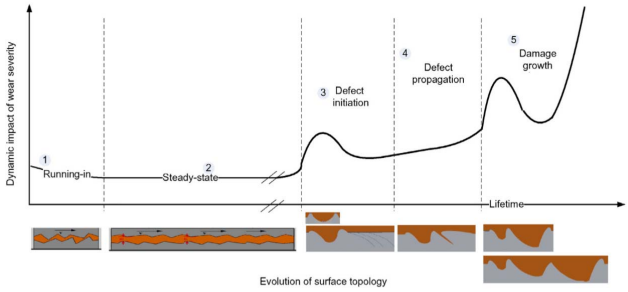


Fig. 2. Wear Severity v/s time

Stage 1: Running In; Stage 2: Steady State; Stage 3: Defect Initiation; Stage 4: Defect Propagation; Stage 5: Damage Growth. After categorization is done, classification techniques are applied to predict the wear severity in REBs.

There are two types of supervised learning techniques viz. Classification and Regression. This model uses classification techniques because wear stage consists of discrete values. Commonly used types of classifiers in the literature are Ensemble methods, Gaussian processes, generalized linear model (GLM), Navies Bayes, nearest neighbor, SVM, Trees and discriminant classifiers. Ensemble methods use multiple learning algorithms rather than individual algorithms which greatly impact their predictability[19]. Gaussian processes are a powerful algorithm for both regression and classification. GLM consists of general machine learning models adopted from mathematical statistics [20]. Navies Bayes classifiers are a collection of classifiers based on Bayes' theorem. Nearest neighbors classifier is a non-parametric method used for classification and is mainly used in pattern recognition[21]. SVM is supervised learning model with associated learning algorithms that analyze data used for classification and regression analysis [22]. The Trees classifier organizes a series of test questions and conditions in a tree structure and Random forest classifiers operates by constructing multiple decision trees at training time and gives the mean prediction of the individual trees[23][24]. Linear discriminant classifiers are attractive classifiers because they have closed-form solutions that can be easily computed, are inherently multiclass, have proven to work well in practice [25]. In this work initially most of the classifiers from these groups are employed and later the classifier with highest accuracy is selected to infer wear stage for a specific application (Refer Table III).Confusion matrix is a specific table layout that is used to describe the performance of a classification model [26]. A sample of a confusion matrix with A_{ij} dataset is given (where i is rows and j are columns) in Table I.

TABLE I: SAMPLE CONFUSION MATRIX

0	1	2	3
1	A_{11}	A_{12}	A_{13}
2	A_{21}	A_{22}	A_{23}
3	A_{31}	A_{32}	A_{33}

The accuracy of this matrix is calculated by Eq (2) and (3)[26]

$$Accuracy = \frac{Sum\ of\ diagnal\ elements}{Sum\ of\ all\ elements\ in\ the\ matrix} x100 \quad (2)$$

$$Accuracy = \frac{A_{11}+A_{22}+A_{33}}{A_{11}+A_{12}+A_{13}+A_{21}+A_{22}+A_{23}+A_{31}+A_{32}+A_{33}} x100 \quad (3)$$

F. Prognostic Module

After the diagnostics module predicts a high stage wear, a prognostics module is initiated. Feature selection for prognostics module consists of either filter approach or wrapper approach. Filter approach uses an algorithm which calculates a score for individual features whereas wrapper methods train a classifier with an initial set of features and then computes the accuracy. From literature, it is seen that the wrapper approach methods outperform filter approach methods[27].Wrapper approach methods consists of forward selection, backward elimination and recursive feature elimination. Amongst the three, backward elimination is commonly used, and feature selection was done using this technique. Significant features are identified with ordinary least squares (OLS) regression results and significant features with p-value less than 0.05 are selected. OLS regression is used for estimating the unknown parameters in a linear regression model. Additionally, it determines the coefficient of determination (R^2) and its higher value indicates the robustness of the model[28].

G. Predicting the RUL

In this subsection, commonly used regression techniques for RUL prediction are briefly described. Multiple linear regression is the most common form of linear regression analysis. For prediction, the multiple linear regression is used to explain the relationship between one continuous dependent variable and multiple independent variables. Decision tree builds regression models in the form of a tree structure. It breaks down a dataset into smaller and smaller subsets. A random forest is a Meta estimator that fits a number of decision trees on various sub-samples of the dataset and calculates the average of them to improve the accuracy and avoid over-fitting. A random forest model is an additive model making predictions by combining decisions from a sequence of base models. It can be expressed as in Eq (4) [24]:

$$g_i(x) = f_0(x)+f_1(x) + f_2(x).....f_n(x) \quad (4)$$

where, g_i is the final model which is the sum of f_i base models. The results of RUL prediction are obtained from the technique with lowest value of RMSE (Root Mean Square Error). The following section deals with the application of this integrated approach on a bearing dataset provided by NSF I/UCR Center for Intelligent Maintenance Systems [29].

III. ILLUSTRATIONS

The proposed methodology, described briefly in the previous section, is illustrated for diagnostics and prognostics of REBs. The input data is collected from sensors of a vibrational MCU (microcontroller) taking reading of a bearing till its rupture. This raw data is processed to extract important features as discussed in Section II-B.

A. Feature Extraction

In the data file, each column corresponds to the four channels (containing a matrix 20480 X 4) and data preprocessing was performed by converting the raw data using MATLAB R2018[14]. Each row in the data file is a data point. Specifically, 28 features in MATLAB were chosen and extracted for each channel on the 984-point dataset.

B. Feature Selection

As mentioned in Section II-C, feature screening was done using Pearson correlation methodology as in our case, most of the features selected were having a linear relationship.
. It helps in identifying highly correlated features. Based on Pearson correlation value top 5 features were extracted from each bearing channel to improve accuracy of the model and are shown in Table II.

TABLE II: TOP FIVE FEATURES SELECTED FROM EACH CHANNEL

Channel			
1	**2**	**3**	**4**
Spurious free dynamic range	Crest factor	Crest factor	RMS
Signal to noise & distortion ratio	Spurious free dynamic range	Mean frequency	Crest factor
Mean or median absolute deviation	Median frequency	Median frequency	Standard deviation
RMS	Mean frequency	Signal to noise & distortion ratio	Root-sum-of squares level
Root-sum-of-squares level	Occupied bandwidth	Interquartile range	Median frequency

C. Diagnostic Module

A kurtosis v/s time graph has been plotted for bearing channel 2 as shown in Fig.3. As discussed earlier, this graph has been divided into five stages of wear severity on the basis of trend followed by it by comparing with stages as shown in wear severity vs time graph [Fig. 2].

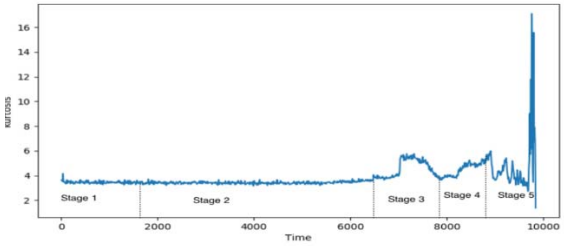


Fig. 3. Kurtosis v/s time in channel 2

First stage is running state which is just before steady state. Steady state was clear after using 'Moving average

smoothers. Third, fourth and fifth stage shows defect initiation, defect propagation and damage growth respectively. These five stages are named like categories mentioned in section II-D.

D. Predicting the wear stage

Subsequent to categorization of wear stages in previous subsection, classification is carried out based on the discussion in Section II-E. Out of 984 data points generated by each bearing channel 60% data was used for training the model and 40% was used for testing. To avoid accuracy paradox and over fitting mean of accuracy was calculated for multiple cases and also an over fitting check was performed. Six classifiers viz. logistic regression, random forest classifier, decision tree classifier, KNN classifier, quadratic discriminant analysis classifier, and gradient boosting classifier were used for detecting wear severity. As discussed in section II-E, the accuracy for each classifier was recorded in Table III. From Table III, it is clear that highest accuracy in Channel 1 of 88.08% is given by Gradient Boosting classifier. In Channel 2 an accuracy of 80.18% is given by XGB classifier. Channel 3 predicts with an accuracy of 80.10% with Quadratic Discriminant Analysis classifier and Channel 4 gives highest accuracy with XGB classifier of 81.21%.

TABLE III: STATISTICAL FEATURES TO PROCESS RAW DATA

Group	Classifier	Channel			
		1	2	3	4
Ensemble Methods	AdaBoost Classifier	62.7%	61.31%	67.07%	73.13%
	Bagging Classifier	87.27%	76.26%	74.84%	80.30%
	Gradient Boosting Classifier	**88.08%**	77.77%	76.86%	81.1%
	Random Forest Classifier	86.06%	77.57%	74.0%	78.78%
	Extra Tree Classifier	80.80%	71.51%	63.43%	71.1%
Trees	Decision tree Classifier	84.94%	73.63%	66.16%	74.34%
	Extra Tree Classifier	80.80%	71.51%	63.43%	71.1%
Navies Bayes	Gaussian NB	51.31%	76.76%	70.60%	73.4%
	Bernoulli NB	48.08%	47.47%	46.56%	47.47%
Discriminant Analysis	Linear discriminant Analysis	77.37%	69.19%	71.01%	71.1%
	Quadratic Discriminant Analysis	65.55%	62.52%	**80.10%**	63.53%
GLM	Logistic Regression	77.17%	66.67%	67.57%	70.70%
	Perceptron	58.28%	56.56%	52.9%	53.9%
	Ridge Classifier CV	70.90%	65.35%	63.5%	68.5%
	SGD Classifier	65.95%	51.21%	45.8%	57.87%
Nearest Neighbor	KNeighbors Classifier	72.92%	72.22%	61.81%	71.4%
SVC	SVC	74.64%	70.20%	71.1%	72.42%
	Linear SVC	76.56%	71.11%	68.08%	71.8%
XG Boost	XGB Classifier	87.77%	**80.18%**	79.9%	**81.21%**

Table IV shows the confusion matrix in Channel 1 and explains the accuracy generated as described in Section II-E. The accuracy of this matrix is developed from Eq (2) and Eq (3). It is seen that the accuracy generated from confusion matrix in Table IV is 98.9 %.

TABLE IV: CONFUSION MATRIX -CHANNEL 1

		Actual Values				
		0	**1**	**2**	**3**	**4**
Predicted Values	**0**	11	0	0	0	0
	1	0	53	0	0	0
	2	0	0	17	0	0
	3	0	0	0	2	0
	4	0	0	1	0	15

E. Prognostic Module

As soon as diagnostics module of each bearing channel predicts stage 3, 4 or 5, prognostics module is initiated. Prognostics module predicts the RUL of the bearing. In this approach, the prediction is made by assessing the information provided by the features selected using Backward elimination technique. This technique was used to select the significant features (with p-value less than 0.05) recorded by Ordinary Least squares (OLS) regression results. The OLS Regression result is given in Table V.

TABLE V: OLS REGRESSION RESULTS FOR PROGNOSTIC MODULE FOR CHANNEL 1

S.No.	OLS Regression Results	
	Names	p-Value
1.	RMS	0.001
2.	Peak	0.022
3.	Crest factor	0.029
4.	Standard deviation	0.003
5.	Root-sum-of square level	0.0001
6.	Variance	0.014
7.	Peak mag to RMS ratio	0.021
8.	Mean frequency	0.018
9.	Interquartile range	0.012
10.	Signal to noise ratio	0.009
11.	Power bandwidth	0.009
12.	Occupied bandwidth	0.007
13.	Signal to noise & distortion ratio	0.0051
14.	Total Harmonic Distortion	0.0011
15.	Median	0.009
16.	Mean	0.0017

F. Predicting the RUL

RMSE of common regression techniques were recorded in Table VI and it was observed that random forest regression had the least error.

TABLE VI: ACCURACIES OF VARIOUS REGRESSION TECHNIQUES

S.No.	RMSE of common regression techniques		
	Regression	RMSE	Overfit Check
1.	Random Forest	337.9469	335.7029
2.	Decision tree	399.4034	-
3.	Multiple Linear	1149.779	-

As observed from Table V, Random forest has the least RMSE value of 337.94. Thus, this technique is employed for each bearing channel to predict the RUL. Overfitting check was done by comparing the RMSE of test and train data. The RMSE values were almost same, hence the model has no overfitting. Gaussian Process Regression was also performed but it was showing comparatively higher RMSE than Random Forest regression. The independent variables were extracted by OLS regression results and the model was cross-validated with the test set, kurtosis v/s time for actual and predicted values for bearing channel 1 was drawn and R square (Coefficient of determination) was recorded as 0.854. This shows good fit of the model.

IV. Conclusion

In this paper an integrated diagnostics and prognostics approach is suggested for predicting the wear severity and remaining useful life of roller element bearing. Classification techniques results into more than 80% accuracy for each bearing channel in predicting the wear severity. RUL predictions with the proposed model are closer to the experimental results as these are supported by the lower values of error measures.

Diagnostic and prognostic approaches have their own applications. The former has potential to be used in maintenance planning for predicting the wear severity and it can prevent any major loss and the latter be used to predict the remaining useful time left for the bearing component if high wear is detected. Integrated diagnostic and prognostic approach can help in better asset management. Moreover, this methodology is not limited to bearings can be applied to machine tools, gears and mechanical shafts etc. But it should be clear that this study is limited to dynamic loading.

The proposed approach is more human centric and expected to emerge as promising solution of maintenance planning under the concept of Industry 4.0. The proposed approach not only predicts the wear severity but also predicts the remaining useful life of bearing and can be used in industries so that the bearing element can be changed before its failure causes any human or material loss.

References

[1] B. Dolenc, P. Boškoski, and D. Juričić, "Distributed bearing fault diagnosis based on vibration analysis," *Mech. Syst. Signal Process.*, vol. 66–67, pp. 521–532, 2016.

[2] C. Li, V. Sanchez, G. Zurita, M. Cerrada Lozada, and D. Cabrera, "Rolling element bearing defect detection using the generalized synchrosqueezing transform guided by time-frequency ridge enhancement," *ISA Trans.*, vol. 60, pp. 274–284, 2016.

[3] C. Li *et al.*, "Observer-biased bearing condition monitoring: From fault detection to multi-fault classification," *Eng. Appl. Artif. Intell.*, vol. 50, pp. 287–301, 2016.

[4] C. Li, J. V. De Oliveira, R. V. Sanchez, M. Cerrada, G. Zurita, and D. Cabrera, "Fuzzy determination of informative frequency band for bearing fault detection," *J. Intell. Fuzzy Syst.*, vol. 30, no. 6, pp. 3513–3525, 2016.

[5] C. Li, R. V. Sánchez, G. Zurita, M. Cerrada, and D. Cabrera, "Fault diagnosis for rotating machinery using vibration measurement deep statistical feature learning," *Sensors (Switzerland)*, vol. 16, no. 6, 2016.

[6] A. Muetze and E. G. Strangas, "On inverter induced bearing currents, bearing maintenance scheduling, and prognosis," *Proc. - 2014 Int. Conf. Electr. Mach. ICEM 2014*, pp. 1915–1921, 2014.

[7] A. M. Al-Ghamd and D. Mba, "A comparative experimental study on the use of acoustic emission and vibration analysis for bearing defect identification and estimation of defect size," *Mech. Syst. Signal Process.*, vol. 20, no. 7, pp. 1537–1571, 2006.

[8] L. Shuang and L. Meng, "Bearing fault diagnosis based on PCA and SVM," *Proc. 2007 IEEE Int. Conf. Mechatronics Autom. ICMA 2007*, no. 1, pp. 3503–3507, 2007.

[9] B. Samanta, K. R. Al-Balushi, and S. A. Al-Araimi, "Artificial neural networks and genetic algorithm for bearing fault detection," *Soft Comput.*, vol. 10, no. 3, pp. 264–271, 2006.

[10] Y. Yang and W. Tang, "Study of remote bearing fault diagnosis based on BP Neural Network combination," *Proc. - 2011 7th Int. Conf. Nat. Comput. ICNC 2011*, vol. 2, pp. 618–621, 2011.

[11] Z. Li, D. Wu, C. Hu, and J. Terpenny, "An ensemble learning-based prognostic approach with degradation-dependent weights for remaining useful life prediction," *Reliab. Eng. Syst. Saf.*, vol. 184, pp. 110–122, 2019.

[12] C. M. Bishop, *Pattern recognition and machine learning*. Berlin: Springer, 2006.

[13] F. Pedregosa *et al.*, "Scikit-learn: Machine Learning in Python," *J. Mach. Learn. Res.*, vol. 12, no. Oct, pp. 2825–2830, 2011.

[14] "MATLAB and Statistics Toolbox Release 2018a." The MathWorks, Inc., Natick, Massachusetts, United States., Natick, Massachusetts, United States., 2018.

[15] "Python 3.6.5." The Python Packaging Authority (PyPA), 2018.

[16] R. J. Urbanowicz, M. Meeker, W. LaCava, R. S. Olson, and J. H. Moore, "Relief-Based Feature Selection: Introduction and Review," Nov. 2017.

[17] A. G. Asuero, A. Sayago, and A. G. González, "The Correlation Coefficient: An Overview," *Crit. Rev. Anal. Chem.*, vol. 36, pp. 41–59, 2006.

[18] M. Nakhaeinejad, "Fault detection and model-based diagnostics in nonlinear dynamic systems," 2010.

[19] H. Bonab and F. Can, "Less Is More: A Comprehensive Framework for the Number of Components of Ensemble Classifiers," Sep. 2017.

[20] P. K. Dunn and G. K. Smyth, *Generalized Linear Models With Examples in R*. New York, NY: Springer New York, 2018.

[21] S. Bafandeh, I. And, and M. Bolandraftar, "Application of K-Nearest Neighbor (KNN) Approach for Predicting Economic Events: Theoretical Background."

[22] C. Cortes and V. Vapnik, "Support-vector networks," *Mach. Learn.*, vol. 20, no. 3, pp. 273–297, Sep. 1995.

[23] A. F. Mashat, M. M. Fouad, P. S. Yu, and T. F. Gharib, "A Decision Tree Classification Model for University Admission System," 2012.

[24] L. Breiman, *ST4_Method_Random_Forest*. Berkeley, 2001.

[25] M. Haghighat, M. Abdel-Mottaleb, and W. Alhalabi, "Discriminant Correlation Analysis: Real-Time Feature Level Fusion for Multimodal Biometric Recognition," *IEEE Trans. Inf. Forensics Secur.*, vol. 11, no. 9, pp. 1984–1996, Sep. 2016.

[26] S. Visa, B. Ramsay, A. Ralescu, and E. Van Der Knaap, "Confusion Matrix-based Feature Selection."

[27] B. Kumari and T. Swarnkar, "Filter versus Wrapper Feature Subset Selection in Large Dimensionality Micro array: A Review."

[28] S. Seabold and J. Perktold, "Statsmodels: Econometric and Statistical Modeling with Python," 2010.

[29] T. R. Setup, "NASA Bearing Data Description," pp. 2–3, 2000.

Eur. Phys. J. C (2020) 80:106
https://doi.org/10.1140/epjc/s10052-020-7679-2

THE EUROPEAN PHYSICAL JOURNAL C

Regular Article - Theoretical Physics

Quintessence behavior via matter creation cosmology

C. P. Singh[a], **Ajay Kumar**[b]

Department of Applied Mathematics, Delhi Technological University, Bawana Road, Delhi 110 042, India

Received: 3 October 2019 / Accepted: 24 January 2020
© The Author(s) 2020

Abstract We study the matter creation cosmology as an alternative theory to explain the dark energy phenomena. We discuss the matter-dominated Universe in a flat Friedmann-Robertson-Walker line element by adopting the thermodynamics of open systems, in which the matter creation irreversible processes may take place at a cosmological scale. We propose a new form of the matter creation rate, $\Gamma = 3\alpha H_0 + 3\beta H + 3\gamma \frac{\ddot{a}}{\dot{a}}$, which generalizes some of the previous models in the literature. Exact solutions of the field equations are found and discussed the evolution of the Universe. Constraints on the model parameters are obtained from Markov Chain Monte Carlo (MCMC) analysis using the Supernova distance modulus data, observational measurements of Hubble parameter, Baryon acoustic oscillation data. The trajectories of the evolution of the scale factor, deceleration parameter and equation of state parameter are plotted by using best-fit values of the parameters. It is observed that the model shows accelerating behavior and behaves quintessence like ($\omega > -1$). The age of the Universe is obtained which is in good agreement with ΛCDM model. We examine the model using two independent diagnostic parameters, namely statefinder and *Om*. We apply Akaike information criterion (AIC) and Bayesian information criterion (BIC) to discriminate the model based on the penalization associated to the number of parameters. The analysis shows that the model has close resemblance to the ΛCDM cosmology. We also discuss the thermodynamics of the model and find that the model satisfies the generalized second law of thermodynamics with certain constraints.

1 Introduction

The observations such as Type Ia Supernovae (SNe) [1–3], Baryon Acoustic Oscillations (BAO) [4], Large Scale Structures (LSS) [5] and Cosmic Microwave Background (CMB) [6] provide strong evidence that the Universe at present is undergoing an accelerated expansion rather than deceleration (as predicted by the standard cosmology). Since the discovery of the accelerating Universe, people are trying to explain this observational fact in two different ways - either by modifying the Einstein gravity itself or by introducing some unknown kind of matter in the framework of Einstein gravity. Most models consider accelerated expansion as due to a component of the Universe that behaves opposite to gravity, the so called *dark energy*(DE). The origin and nature of the DE is still unknown, though some of its properties are widely accepted, namely the fact that it has a negative pressure. Cosmological constant is the common choice for this unknown matter but it suffers the serious fine-tuning and cosmic coincidence problems. Recently, many theoretical models have been proposed to describe the Universe with dark energy. A negative pressure can be seen as a possible driving mechanism for this acceleration. One of such mechanism is the adiabatic matter creation which has negative pressure produced by the particle production effects.

Prigogine et al. [7,8] proposed an interesting type of cosmological history including large-scale entropy production by considering the cosmological thermodynamics of open systems. They used the generalized form of the first law of thermodynamics to describe the flow of energy from the gravitational field to the matter field, resulting in the creation of particles. The authors argued that the creation of matter can occur only as an irreversible process at the expense of the gravitational field. This formalism gives a balance equation for the number of created particles along with Einstein field equations. The combination of this equation with the second law of thermodynamics yields an additional negative pressure which depends on the rate of matter creation. This work actually suggested for the first time to incorporate the particle creation process in the context of cosmology in a self-consistent way. Calvao et al. [9] proposed a generaliza-

[a] e-mail: cpsphd@rediffmail.com
[b] e-mail: maths.ajy@gmail.com

Published online: 08 February 2020

tion of this result to include the variation of specific entropy through a covariant formulation.

A model with adiabatic matter creation was proposed in order to interpret the cosmological entropy and to solve the Big-Bang singularity problem. However, after the discovery of the accelerating expansion of the Universe, this model was reconsidered to explain the expansion of the Universe and got some unexpected results. It has been pointed out that the matter creation can play the role of a dark energy component and lead to drive the accelerating expansion of the Universe.

In this context, Many authors [10–17] have discussed Friedmann-Robertson-Walker line element with matter creation cosmology and analyzed the results through the observations. It has been shown that the matter creation models are consistent with the observations. Zimdahl et al. [18] tested the matter creation models with SNe data and got the result of accelerating Universe. Yuan et al. [19] studied the models with adiabatic matter creation and showed that the model is consistent with SNe data. Many phenomenological models have been proposed in the literature [20–24].

We are mainly interested in the paper of Prigogine and collaborators [7], in which the authors have applied the thermodynamics of open systems to cosmology, allowing both particle and entropy productions. Recently, it has been found that the matter creation cosmology successfully explains the current accelerated expansion [25]. Therefore, this field is very appealing as many important observations are carried out during the past many years with matter creation.

In this paper, we present a matter-dominated cosmological model with matter creation within the framework of Friedmann-Robertson-Walker line element. We propose a generalized form of matter creation rate and investigate the evolution equations by independent/combined observational data of SNe, Observational Hubble data (OHD) and BAO. We observe that the best-fit values of the model parameters give a smooth transition from decelerating phase to the accelerating phase. We study two independent diagnostic tests, namely, the statefinder parameter and the Om diagnostic to discriminate our model from the ΛCDM. We apply AIC and BIC to discriminate the model. We also perform a thermodynamic analysis based on the generalized second law (GSL) of thermodynamics and explore the restrictions on the free parameters of the cosmological model to satisfy the GSL.

The paper is organized as follows. In Sect. 2, we present a brief review of matter creation cosmology and solution of the field equations. In Sect. 3, some observational data like SNe, OHD and BAO are given to find the best-fit values of model parameters. In Sect. 4, we present the result and discussion of the model. In Sect. 5, we discuss the model selection criteria to discriminate the model. We discuss the thermodynamic of the model based on generalized second law of thermodynamics in Sect. 6. Finally, we summarize our findings in Sect. 7. It is to be noted that throughout the paper, we use particle creation and matter creation synonymously.

2 Model with matter creation and solution

Let us start with the homogeneous and isotropic flat Friedmann-Robertson-Walker (FRW) line element

$$ds^2 = -dt^2 + a^2(t)\left[dr^2 + r^2(d\theta^2 + sin^2\theta d\phi^2)\right], \quad (1)$$

where $a(t)$ is the scale factor of the model. Throughout we use units such that the speed of light, $c = 1$ and $8\pi G = 1$. The Einstein field equations are given by

$$R_{\mu\nu} - \frac{1}{2}R\, g_{\mu\nu} = T_{\mu\nu}. \quad (2)$$

The energy momentum tensor $T_{\mu\nu}$ describes the matter content of the Universe. It is often appropriate to adopt the perfect fluid form. However, we consider the energy-momentum tensor empowered with the mechanism of matter creation of the form

$$T_{\mu\nu} = (\rho + P)\, u_\mu u_\nu + P\, g_{\mu\nu}, \quad (3)$$

satisfying the covariant conservation equation $T^{\mu\nu}{}_{;\nu} = 0$. In (3), u_μ is the fluid four-velocity, ρ is the energy density and P is the dynamics pressure which is given by

$$P = p + p_c, \quad (4)$$

where p is the equilibrium pressure and p_c is the pressure due to the matter creation. The particle flux vector has the form

$$N^\mu = nu^\mu, \quad (5)$$

where N is the total particle number in a comoving volume V, $n = N/V$ is the particle density and u^μ is the usual four velocity vector of the created particles. In the gravitationally induced particle creation mechanism, (5) satisfies the balance equation [8]

$$N^\mu{}_{;\mu} = \Gamma, \quad (6)$$

where Γ is the rate of matter creation from the gravitational field. In principle, $\Gamma > 0$ represents the matter creation, $\Gamma < 0$ is for matter annihilation, and $\Gamma = 0$ is the case when there is no matter creation. In general, the exact form of Γ is unknown, but it should be determined in the context of quantum processes in curved space time.

In this background, the field equations associated with matter creation phenomena for line element (1) are given by [9,10]

$$3H^2 = \rho, \tag{7}$$

$$2\dot{H} = -(\rho + p + p_c), \tag{8}$$

where $H = \dot{a}/a$ is the Hubble parameter, and ρ and p are energy density and pressure, respectively, of matter existing in the universe in the form of cold dark matter during matter dominated era. An overdot represents the derivative with respect to cosmic time t. The energy conservation law is given by

$$\dot{\rho} + 3(\rho + p + p_c)H = 0. \tag{9}$$

As the particle number is not conserved (i.e., $N^{\mu}{}_{;\mu} \neq 0$), the conservation equation (6) takes the form

$$\frac{\dot{N}}{N} = \frac{\dot{n}}{n} + 3H = \Gamma. \tag{10}$$

It is to be noted that the creation pressure p_c must be defined in terms of the creation rate and other physical quantities. In the case of adiabatic particle production, the particles and entropy are generated but the entropy per particle does not vary. Under such 'adiabatic condition', the creation pressure can be written as [21]

$$p_c = -\frac{\Gamma}{3H}(\rho + p). \tag{11}$$

Now, we can describe the dynamics of the Universe only if the matter creation rate is known. The nature of Γ is unknown as the associated quantum field theory (QFT) is yet to be developed. In general, there is no bound to choose some particular choices for Γ. Therefore, we can assume some phenomenological but general choices for Γ. In the literature, various forms of Γ, e.g., $\Gamma = constant$ [26], $\Gamma \propto H$ [27], $\Gamma \propto H^2$ [28,29], and a linear combination [30], have been presented to explain the early and present day acceleration of the Universe. However, the linear and quadratic forms of $\Gamma(t)$ are not compatible with the current cosmology, i.e., these models do not show transition redshift. Therefore, a natural extension is to consider the linear combinations of H, H^2.... and the derivative of Hubble parameter. Finally, one can use the observational data to test the viability of such models.

Thus, being motivated, in this work we propose a class of $\Gamma(t)$ cosmologies in a spatially flat FRW Universe where $\Gamma(t)$ is assumed to be the function of Hubble rate and its cosmic derivative. We cover a series of $\Gamma(t)$ (equivalently, $\Gamma(H_0, H, \dot{H})$) model in order to see their dynamical evolutions and viabilities. We propose the following general form of Γ:

$$\Gamma = 3\alpha H_0 + 3\beta H + 3\gamma \frac{\ddot{a}}{\dot{a}}, \tag{12}$$

which is a linear combination of three terms: the first term is a constant, the second term is proportional to the Hubble parameter, which characterizes the dependence of the matter creation on expansion rate, and the third term is proportional to $\ddot{a}/\dot{a}$, characterizing the effect of acceleration of the expansion. Here, α, β and γ are dimensionless free parameters lying in the interval [0, 1] to be determined by observations, H_0 is the present value of the Hubble parameter and the factor 3 has been maintained for mathematical convenience.

The motivation of considering this form of Γ comes from the matter creation thermodynamics. We know that the transport phenomena is related to velocity, which is related to the Hubble parameter, and the acceleration. Since we don't know the exact form of Γ, so a linear combination of three terms of parametrization of Γ is more physical. The existence of a transition redshift at late time also determines the form of matter creation rate. We may also think the above form from the evolution equation (8).

We are interested in processes that occurred after radiation-dominated phase. Therefore, we neglect radiation and baryons, and consider only the presence (and creation) of pressureless ($p = 0$) dark matter particles. In this case, Eq. (11) reduces to $p_c = -\rho\ \Gamma/3H$ for which Eq. (9) reduces to

$$\frac{\dot{\rho}}{\rho} + 3\left(1 - \frac{\Gamma}{3H}\right)H = 0, \tag{13}$$

Combining (7) and (13), and using (12), we obtain the following dimensionless equation

$$\frac{\dot{h}}{h} + \frac{3(1-\beta-\gamma)}{(2-3\gamma)}H_0\, h = \frac{3\alpha}{(2-3\gamma)}H_0, \tag{14}$$

where $h = H/H_0$ is the dimensionless Hubble parameter. Using $\frac{d}{dt} = \frac{\dot{a}}{a}\frac{d}{d\ lna}$, the above equation can be written as

$$h' + \frac{3(1-\beta-\gamma)}{(2-3\gamma)}\, h = \frac{3\alpha}{(2-3\gamma)}, \tag{15}$$

where a prime denotes the derivative with respect to conformal time $ln\ a$. Using $h(a_0) = 1$, (15) gives the solution as

$$h(a) = \frac{\alpha}{(1-\beta-\gamma)} + \left(1 - \frac{\alpha}{(1-\beta-\gamma)}\right)\left(\frac{a}{a_0}\right)^{-\frac{3(1-\beta-\gamma)}{(2-3\gamma)}}. \tag{16}$$

Equation (16) shows that when α, β and γ are all zero, the Hubble parameter, $H = H_0(a/a_0)^{-3/2}$ which corresponds to the ordinary matter dominated universe. On integration of (16), we obtain the solution of the scale factor $a(t)$ (or the redshift, z) as a function of time, when $(\beta + \gamma) \neq 1$

$$a(t) = \frac{1}{(1+z)} = \left[\frac{(1-\beta-\gamma)e^{\frac{3\alpha H_0}{(2-3\gamma)}(t-t_0)} - 1 + (\alpha+\beta+\gamma)}{\alpha}\right]^{\frac{(2-3\gamma)}{3(1-\beta-\gamma)}}. \tag{17}$$

We have normalized the scale factor so that its present day value is one, $a(t_0) = 1$. We can study three different cases: $0 < \alpha+\beta+\gamma < 1$, $\alpha+\beta+\gamma = 1$ and $\alpha+\beta+\gamma > 1$. In the case $0 < \alpha+\beta+\gamma < 1$, we observe that in the early time as $t \to 0$, the scale factor $a(t) \to \left[1+\frac{3(1-\beta-\gamma)H_0}{(2-3\gamma)}(t-t_0)\right]^{\frac{(2-3\gamma)}{3(1-\beta-\gamma)}}$, which corresponds to an early decelerated expansion and in the late time as $t \to \infty$, the scale factor $a(t) \to e^{\frac{3\alpha H_0}{(2-3\gamma)}(t-t_0)}$, corresponding to de Sitter like Universe. The model predicts a Big-Bang in the past at cosmic time: $t_b = t_0 + \frac{(2-3\gamma)}{3\alpha H_0}\, ln\left(\frac{1-(\alpha+\beta+\gamma)}{1-\beta-\gamma}\right)$.

The transition time can be obtained by equating to zero the second derivative of scale factor given in (17) with respect to time which is given by

$$t_{tr} = t_0 + \frac{(2-3\gamma)H_0^{-1}}{3\alpha}\, ln\left(\frac{(3-3(\alpha+\beta+\gamma))}{(2-3\gamma)}\right). \quad (18)$$

The Hubble parameter in terms of redshift z, where $1+z = a^{-1}$, reads

$$H(z) = H_0\left[\frac{\alpha}{(1-\beta-\gamma)} + \left(1-\frac{\alpha}{(1-\beta-\gamma)}\right) \times (1+z)^{\frac{3(1-\beta-\gamma)}{(2-3\gamma)}}\right]. \quad (19)$$

When $\gamma = 0$, i.e., $\Gamma = 3\alpha H_0 + 3\beta H$ (See, Ref. [31]), (17) and (19) reduce to (14) and (13) of [31]. Further, In the limit $\alpha \to 0$, the above equation reduces to (16) in [11].

To obtain the transition scale factor a_{tr} where the transition from decelerated phase to accelerated phase takes place, we take the derivative of (19) with respect to a,

$$\frac{d\dot{a}}{da} = \left[\frac{\alpha}{1-\beta-\gamma} + \frac{(3\beta-1)(1-\alpha-\beta-\gamma)}{(2-3\gamma)(1-\beta-\gamma)}\, a^{-\frac{3(1-\beta-\gamma)}{2-3\gamma}}\right]. \quad (20)$$

Equating (20) to zero, we obtain the transition scale factor, a_{tr} as

$$a_{tr} = \left[\frac{(1-3\beta)(1-\alpha-\beta-\gamma)}{\alpha(2-3\gamma)}\right]^{\frac{2-3\gamma}{3(1-\beta-\gamma)}}. \quad (21)$$

It is clear that for $\alpha+\beta+\gamma = 1$ or $\beta = 1/3$, the transition from decelerated phase to accelerated phase occurs at a time corresponds to $a_{tr} \to 0$ closer to Big-Bang. In this case, $a = \exp(H_0(t-t_0))$, corresponds to de Sitter Universe. In this case the model predicts an accelerated expansion from the beginning. For $(\alpha+\beta+\gamma) < 1$, the transition occurs in late-time whereas for $(\alpha+\beta+\gamma) > 1$, there is no transition and in this case the model always accelerates from very early time.

An important cosmological quantity is the deceleration parameter q, which is an indicator of the accelerating/decelerating nature of the evolution of the Universe. It is straightforward to show from (17) that the deceleration parameter, defined as $q = -a\ddot{a}/\dot{a}^2$, takes the following form in terms of cosmic time t:

$$q = -1 + \frac{3(1-\alpha-\beta-\gamma)}{2-3\gamma} e^{-\frac{3\alpha H_0}{2-3\gamma}(t-t_0)}. \quad (22)$$

The redshift dependence of the deceleration parameter is obtained as

$$q = -1 + \frac{3(1-\alpha-\beta-\gamma)}{(2-3\gamma)\left[1+\frac{\alpha}{1-\beta-\gamma}\left((1+z)^{-\frac{3(1-\beta-\gamma)}{2-3\gamma}}-1\right)\right]}. \quad (23)$$

It can be observed that $q(z) \to -1$ as $z \to -1$, i.e., $q(z)$ approaches to -1 in future and for $z = 0$, we get $q_0 = \frac{1-3(\alpha+\beta)}{2-3\gamma}$. This shows that for $\alpha+\beta = 1/3$, the deceleration parameter $q_0 = 0$. This implies that the transition into accelerating phase would occur at the present time. In the absence of matter creation, i.e., for $\alpha = \beta = \gamma = 0$, we get $q = 0.5$, a value of q in matter-dominated model. Putting $q = 0$ in (23), the transition redshift is given by

$$z_{tr} = \left[\frac{\alpha(2-3\gamma)}{(1-3\beta)(1-\alpha-\beta-\gamma)}\right]^{\frac{2-3\gamma}{3(1-\beta-\gamma)}} - 1. \quad (24)$$

It is to be noted that for $\alpha = 0$, we get $z_{tr} = -1$, i.e., the transition would be in future which gives the contradiction with SNe data. From (7) and (16), we obtain the mass density parameter $\Omega_m = \rho/\rho_{crit}$ and $\rho_{crit} = 3H_0^2$ as,

$$\Omega_m(a) = \left[\left(1-\frac{\alpha}{1-\beta-\gamma}\right)\left(\frac{a}{a_0}\right)^{-\frac{3(1-\beta-\gamma)}{2-3\gamma}} + \frac{\alpha}{1-\beta-\gamma}\right]^2. \quad (25)$$

We observe that for $\alpha = \beta = \gamma = 0$, the mass density parameter reduces to $\Omega_m \sim a^{-3}$, which corresponds to the matter dominated phase with null matter creation. It is also noted that as $a \to 0$, the mass density diverges.

In what follows we constrain the free parameters of the model coming from the background tests.

3 Observational tests: SNe, OHD and BAO data

In this section we briefly present some details of the statistical method and observational sample that we adopt in order to constrain the model. We normalized $H(z)$ using the latest Planck data $H_0 = 67.8 \pm 0.9$ km s^{-1} Mpc^{-1} [32].

First of all, we consider the distant Type Ia Supernova (SNe) compilation on the matter creation matter-dominated model. We use the cJLA data set of 31 check points (30 bins) covering the redshift range $z = [0.01, 1.3]$ [33]. The best-fit to the set of parameters is found by using a χ^2 statistics, i.e.,

$$\chi^2_{SNe} = r^t C_b^{-1} r \tag{26}$$

where

$$r = \mu_b - M - 5\, log_{10} d_L \tag{27}$$

in which μ_b is the observational distance modulus, M is a free normalization parameter and C_b is the covariance matrix of μ_b, see Table F.2 [33]. Also, the dimensionless luminosity distance is defined as

$$d_L = \frac{c(1+z)}{H_0} \int_0^z \frac{dz'}{H(z',\theta)} \tag{28}$$

where θ represents the set of model parameters, $\theta = (\alpha, \beta, \gamma)$.

Additionally, we also use the observational Hubble parameter dataset (OHD) of 43 measurement points collected in [34] in the redshift range $0 < z < 2.5$. The χ^2 for Observational Hubble Data is

$$\chi^2_{OHD} = \sum_{i=1}^{n} \frac{[H(z_i) - H_{obs}(z_i,\theta)]^2}{\sigma_i^2}, \tag{29}$$

where $H(z_i)$ and $H_{obs}(z_i)$ are the theoretical and observed values respectively and σ_i^2 the standard deviation of each $H_{obs}(z_i)$.

Next, we use the sample of Baryon Acoustic Oscillations (BAO) distances measurements from $SDSS(R)$ [35], the $6dF$ Galaxy survey [36], $BOSS\,CMASS$ [37] and three parallel measurements from $WiggleZ$ survey [38].
The angular diameter, $d_A(z,\theta)$ is given by

$$d_A(z_*,\theta) = c \int_0^{z_*} \frac{dz'}{H(z',\theta)} \tag{30}$$

where z_* denotes the photons decoupling redshift and according to the Planck 2015 results [32] its value is $z_* = 1090$. Further, the dilation scale, $D_v(z,\theta)$ is given by $D_v(z,\theta) = \left(\frac{d_A^2(z,\theta)cz}{H(z,\theta)}\right)^{\frac{1}{3}}$.

The corresponding χ^2 function is given by [40]

$$\chi^2_{BAO} = A^T C^{-1} A \tag{31}$$

where A is a matrix given by

$$A = \begin{bmatrix} \frac{d_A(z_*,\theta)}{D_v(0.106,\theta)} - 30.84 \\ \frac{d_A(z_*,\theta)}{D_v(0.35,\theta)} - 10.33 \\ \frac{d_A(z_*,\theta)}{D_v(0.57,\theta)} - 6.72 \\ \frac{d_A(z_*,\theta)}{D_v(0.44,\theta)} - 8.41 \\ \frac{d_A(z_*,\theta)}{D_v(0.6,\theta)} - 6.66 \\ \frac{d_A(z_*,\theta)}{D_v(0.73,\theta)} - 5.43 \end{bmatrix}$$

and C^{-1} is the inverse of covariance matrix [40]. Here, we have adopted the correlation coefficients given in [41].

We can combine the above probes by using a joint likelihood analysis $\chi^2_{total} = \chi^2_{SNe} + \chi^2_{OHD} + \chi^2_{BAO}$.

4 Results and discussion

Using the observational data of SNe, OHD, BAO, we test the cosmological model with adiabatic matter creation, assuming a spatially flat Universe. We perform a global fitting to determine the model parameters using the MCMC method. We adopt a Python implementation of the ensemble sampler for MCMC, the 'emcee', introduced by Foreman-Mackey et al. [42]. The best fitting results of parameters are listed in Table 1. In our statistical analysis, the model parameters can be determined through the χ^2 minimization method. We minimize the function χ^2 of individual from (26), (29), (31) and jointly.

In statistical analysis, we find the best-fit values of model parameters at 1σ (68.3%) and 2σ (95.4%) of confidence level, respectively, satisfying the constraints $0 < \alpha < 1$, $0 < \beta < 1$, $0 < \gamma < 1$ and $0 < (\alpha + \beta + \gamma) < 1$. We can test the reliability by comparing the result with spatially flat ΛCDM model. We observe that the model provides a very good fit to these data. Figures 1, 2, 3 and 4 show confidence contours and the marginalized likelihood function of model at 1σ (68.3%) (inner contour) and 2σ (95.4%) (outer contour) using observational data of SNe, $SNe+OHD$, $SNe+BAO$ and $SNe+OHD+BAO$, respectively.

It can be observed from Table 1 that the result of the free parameters obtained from SNe data are a little different from $SNe+OHD$, $SNe+BAO$ and $SNe+OHD+BAO$. The

Table 1 The best-fit results of model parameters and free normalization parameter M obtained from the analysis with different combinations of the data sets

Data set	α	β	γ	M
SNe	$0.263^{+0.187}_{-0.170}$	$0.249^{+0.155}_{-0.161}$	$0.166^{+0.180}_{-0.113}$	$24.942^{+0.023}_{-0.028}$
SNe +OHD	$0.423^{+0.080}_{-0.117}$	$0.068^{+0.075}_{-0.048}$	$0.322^{+0.097}_{-0.084}$	$24.946^{+0.018}_{-0.020}$
SNe +BAO	$0.438^{+0.087}_{-0.153}$	$0.074^{+0.088}_{-0.058}$	$0.303^{+0.113}_{-0.077}$	$24.936^{+0.022}_{-0.022}$
SNe +OHD+BAO	$0.431^{+0.077}_{-0.131}$	$0.069^{+0.078}_{-0.048}$	$0.274^{+0.112}_{-0.076}$	$24.952^{+0.017}_{-0.018}$

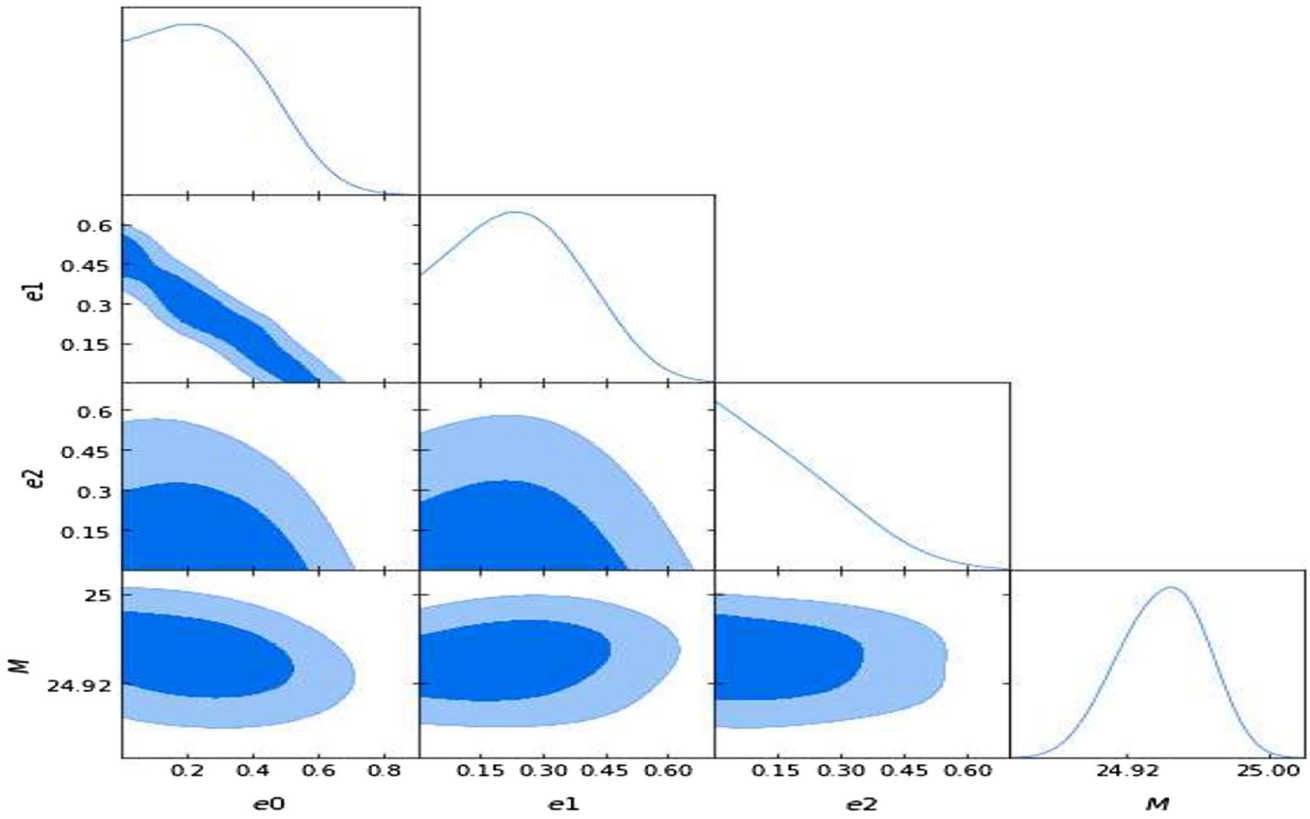


Fig. 1 The contour map of matter creation model using data from SNe with marginalized probability for the parameters. The associated 1σ (68.3%) and 2σ (95.4%) confidence contours are shown. In Fig. the symbols $e0$, $e1$ and $e2$ denote the model parameters α, β and γ, respectively

error bars of free parameters are relatively large in the case of SNe data.

Figure 5 shows the evolution of the scale factor for best-fit values of model parameters. The trajectory of the best-fit values show that the Universe starts its expansion with accelerated rate at very early times. The dots denote the transition point where the transition from decelerated phase to accelerated phase occurs. Using the best-fit values, the transition scale factor, a_{tr} and the corresponding redshift transition values, z_{tr} are listed in Table 2. It is observed that the value of $z_{tr} = 2.8619$ obtained from SNe and $z_{tr} = 1.0147$ from $SNe + BAO$ for the model are substantially higher than the values of z_{tr} from $SNe + OHD$, $SNe + OHD + BAO$ and ΛCDM model.

The evolution of the deceleration parameter, q with redshift for best-fit values is shown in Fig. 6. The deceleration parameter is a monotonically increasing function of z. It is observed that there is a sign change in each trajectory of $q(z)$ from positive to negative showing that the universe transits from decelerated phase to accelerated phase (positive values of q indicate decelerating expansion while negative values indicate an accelerating evolution). We find that the model transits at around $z_{tr} = 0.8386$ and $z_{tr} = 0.8633$ through joint analysis of $SNe + OHD$ and $SNe + OHD + BAO$, respectively. These results are in good agreement with the concordance of Λ cosmology [43]. The present-day value of q_0 and the transition redshift z_{tr} are listed in Table 2. The values of q_0 lie in range $-1 \leq q_0 < 0$ through each observational data set.

The effective equation of state parameter (EoS), ω_{eff} can be obtained using the standard relation [44]

$$\omega_{eff} = -1 - \frac{1}{3}\frac{2a}{h}\frac{dh}{da}, \tag{32}$$

where $h = H/H_0$ is the weighted Hubble parameter. Using (16) into (32), we get

$$\omega_{eff} = -1 + \frac{2(1-\alpha-\beta-\gamma)}{(2-3\gamma)\left[1+\frac{\alpha}{1-\beta-\gamma}\left((1+z)^{-\frac{3(1-\beta-\gamma)}{2-3\gamma}}-1\right)\right]}. \tag{33}$$

As $z \to -1$, $(a \to \infty)$, we get $\omega_{eff} \to -1$, which can also be observed from Fig. 7. This can also be obtained if we take $\alpha + \beta + \gamma = 1$. It means that the model corresponds to ΛCDM in future time. The EoS parameter does not cross the phantom divide line $\omega \leq -1$ which shows that the matter creation model is free from big-rip singularity.

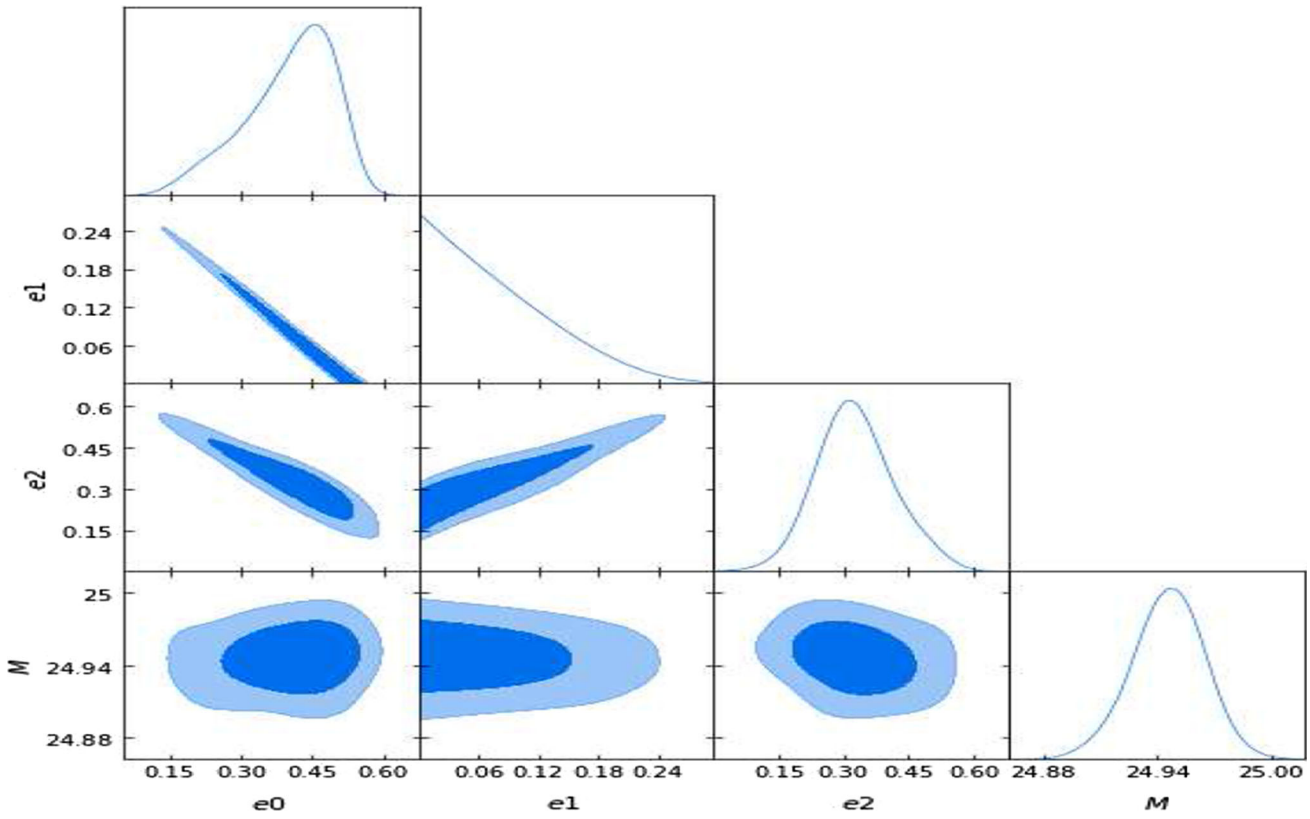


Fig. 2 The contour map of matter creation model based on joint analysis of $SNe + OHD$ showing contours of 1σ (68.3%) and 2σ (95.4%) regions with marginalized probability for the parameters. In Fig. the symbols $e0$, $e1$ and $e2$ denote the model parameters α, β and γ, respectively

The present value ($h = 1$) of ω_{eff} is found to be

$$\omega_{eff}(z = 0) = -1 + \frac{2(1 - \alpha - \beta - \gamma)}{(2 - 3\gamma)}. \tag{34}$$

The present value of ω_{eff} are listed in Table 2 using different observational data set. These values are comparatively higher than that predicted by the joint analysis of $WMAP+BAO+H_0+SNe$ data which is around -0.93 [45].

Let us calculate the age of the universe using best-fit values of parameters. The age of the universe in terms of redshift is given by $t(z) = T(z)/H_0$, where

$$T(z) = \int_z^\infty \frac{dz'}{(1 + z')(H(z')/H_0)}. \tag{35}$$

For ΛCDM model, the age parameter is [46]

$$T(z) = \int_z^\infty \frac{dz'}{(1 + z')[\Omega_{m0}(1 + z')^3 + (1 - \Omega_{m0})]^{1/2}} \tag{36}$$

Using (19) into (35), the trajectory of the age of the universe with redshift for the best estimates of model parameters is shown in Fig. 8. The current age of the universe is $t_0 \simeq 13.9\ Gyr$ while the transition point is located at $a_{tr} \simeq 0.58$ (hence at redshift $z_{tr} \simeq 0.72$. The ages of the universe corresponding to $SNe + OHD$ and $SNe + OHD + BAO$ are found to be 13.9 Gyr. So, the age predicted by the present model is agreeing with the age deduced from ΛCDM model.

We compare our model with the ΛCDM model with the error bar plots of Hubble dataset in the range $z \in (0, 2)$ as shown in Fig. 9. Although at the low redshifts, the cosmological evolution is practically independent on the best-fit values, but at higher redshifts there is a significant effect of the parameter values on the cosmic expansion as can be observed from Fig. 6. The cosmic expansion of $SNe+OHD$ and $SNe+OHD+BAO$ differ appreciably in case of SNe and $SNe+BAO$. It is possible to get good fit using joint statistical analysis of $SNe+OHD$ and $SNe+OHD+BAO$. The Hubble function is a monotonically increasing function of the redshift (monotonically decreasing function of time) for all best-fit values of parameters.

Now, we present our analysis on comparing the present model with other standard models of DE. Sahni et al. [47] proposed a geometrical diagnostic tool, known as statefinder parameters $\{r, s\}$ which allow us to compare the goodness of several DE models with the ΛCDM model. The $\{r, s\}$ is defined as

$$r = \frac{\dddot{a}}{aH^3} \quad \text{and} \quad s = \frac{r - 1}{3\left(q - \frac{1}{2}\right)}, \tag{37}$$

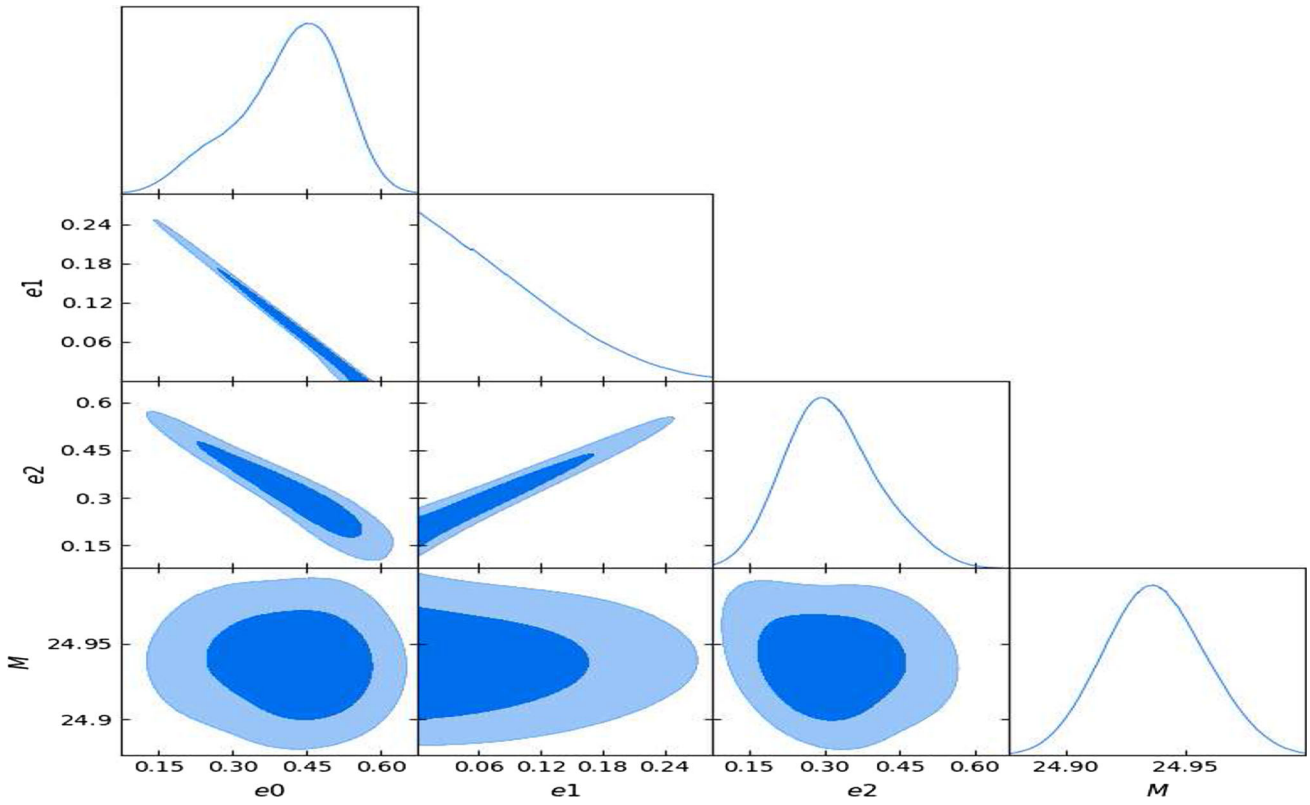


Fig. 3 The contour map of matter creation model based on joint analysis of $SNe + BAO$ showing contours of 1σ (68.3%) and 2σ (95.4%) regions with marginalized probability for the parameters. In Fig. the symbols $e0$, $e1$ and $e2$ denote the model parameters α, β and γ, respectively

where a, H and q have their usual meanings. From (37), we can see parameters (r, s) are just associated with the scale factor a and its higher derivatives. The ΛCDM model corresponds to the fixed point $(r, s) = (1, 0)$. For our model, $\{r, s\}$ are given by

$$r = 1 + \frac{9(1-\alpha-\beta-\gamma)^2}{(2-3\gamma)^2\, e^{\frac{6\alpha H_0(t-t_0)}{2-3\gamma}}} + \frac{9(1-\alpha-\beta-\gamma)(-1-\beta+2\gamma)}{(2-3\gamma)^2\, e^{\frac{3\alpha H_0(t-t_0)}{2-3\gamma}}}, \tag{38}$$

$$s = \frac{2(1-\alpha-\beta-\gamma)\left[(1+\beta-2\gamma)-(1-\alpha-\beta-\gamma)\, e^{\frac{-3\alpha H_0(t-t_0)}{2-3\gamma}}\right]}{(2-3\gamma)\left[(2-3\gamma)\, e^{\frac{3\alpha H_0(t-t_0)}{2-3\gamma}} - 2(1-\alpha-\beta-\gamma)\right]}. \tag{39}$$

From the above equations, we observe that as $(t - t_0) \to \infty$, $\{r, s\} \to \{1, 0\}$ which coincide with the ΛCDM model. This can also be achieved by assuming $\alpha + \beta + \gamma = 1$ which gives the de Sitter behaviour. The $s - r$ plane trajectory of the model for best estimated values of parameters obtained by observational data set are shown in Fig. 10. The direction of trajectories is shown by the arrows. The trajectory obtained through SNe lies in the region $r < 1$, $s > 0$, which is the general behavior of any quintessence model. The other trajectories from $SNe + OHD$, $SNe + BAO$ and $SNe + OHD + BAO$ start from the Chaplygin gas region ($r > 1, s < 0$) at early time and in intermediate time pass through quintessence and then ultimately approach to ΛCDM in late time.

The $\{r, q\}$ trajectory of the model is shown in Fig. 11. The $SCDM$ model and steady state (SS) model correspond to fixed points $\{r, q\} = \{1, 0.5\}$ and $\{r, q\} = \{1, -1\}$, respectively. The horizontal line at $r = 1$ corresponds to the time evolution of ΛCDM model. Our model approaches to the standard model like ΛCDM and quintessence model (Q-model) [48] in late time.

The Om is another diagnostic approach to distinguish dark energy. It is defined as [48]

$$Om(z) = \frac{h^2(z) - 1}{(1+z)^3 - 1}, \tag{40}$$

For ΛCDM model, the value of $Om(z)$ is a constant independent of the redshift. Therefore, if $Om(z)$ is variable, it possibly leads to an alternative dark energy or modified gravity model. The $Om(z)$ is sensitive to EoS of DE, namely, a positive slope of $Om(z)$ suggests a phase of phantom ($w < -1$) while a negative slope of $Om(z)$ represents quintessence ($w > -1$).

Using (19) into (40), we can write the expression of $Om(z)$. Figure 12 exhibits the evolution of different trajectories of the

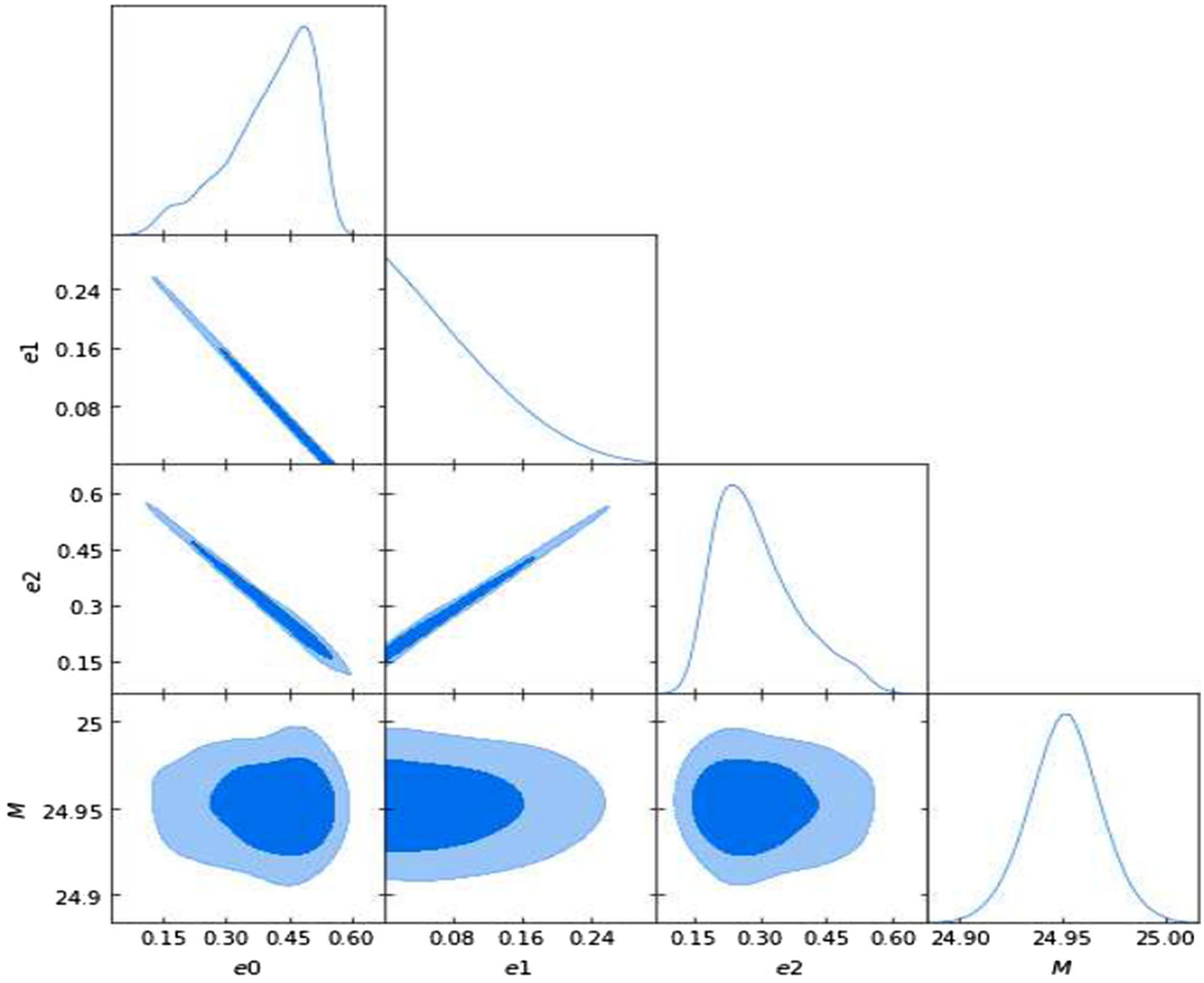


Fig. 4 The contour map of matter creation model based on joint analysis of $SNe+OHD+BAO$, showing contours of 1σ (68.3%) and 2σ (95.4%) regions with marginalized probability for the parameters. In Fig. the symbols $e0$, $e1$ and $e2$ denote the model parameters α, β and γ, respectively

function *Om(z)* with respect to the redshift z, corresponding to different best-fit values of model parameters. The negative slope of each trajectory shows that the model behaves like quintessence.

5 Model selection

Reduced chi-squared is a very popular method for model assessment, model comparison, convergence diagnostic, and error estimation in astronomy. If ν is the number of degrees of freedom, the reduced χ^2 is then defined as

$$\chi^2_{red} = \frac{\chi^2_{min}}{\nu}. \tag{41}$$

If N is the data points and d is the free parameters, the number of degree of freedom $\nu = N - d$. If a model is fitted to data and the resulting χ^2_{red} is larger than one, it is considered a "bad" fit, whereas if χ^2_{red} is less than one, it is considered an overfit. The fit model is that one whose value of χ^2_{red} is closest to one.

We also use two information criteria, namely the Akaike Information Criterion (AIC) and the Bayesian Information Criterion (BIC) to assess the model. For a cosmological model with d degrees of freedom in which N number of data points have been used to fit the model, the AIC parameter is defined through the relation [52]

$$AIC = -2\, ln\mathscr{L}_{max} + 2d, \tag{42}$$

where $\mathscr{L}_{max} = e^{-\chi^2_{tot}/2}$ is the maximum likelihood obtained for the cosmological model. The "preferred model" for this criterion is the one with the smaller value of AIC. To compare the model k with the model l, we calculate $\Delta AIC_{kl} = AIC_k - AIC_l$, which can be interpreted as "evi-

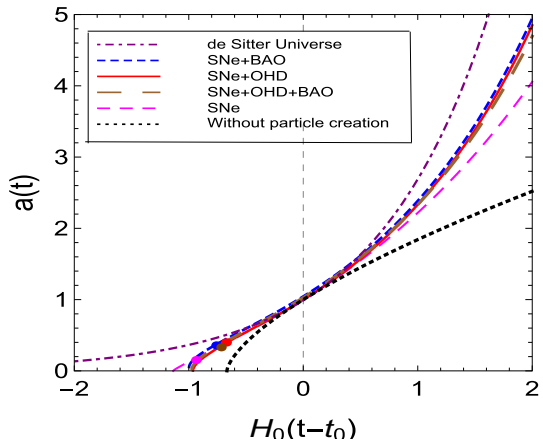


Fig. 5 The scale factor as a function of time. The trajectories show the accelerated expansion after early deceleration for the best-fit values of model parameters obtained from different individual/combined observational data set. The trajectory (dotted curve) is also shown for a matter-dominated model in the absence of matter creation which shows decelerated expansion. A dot denotes the transition point where the transition from decelerated phase to accelerated phase occurs

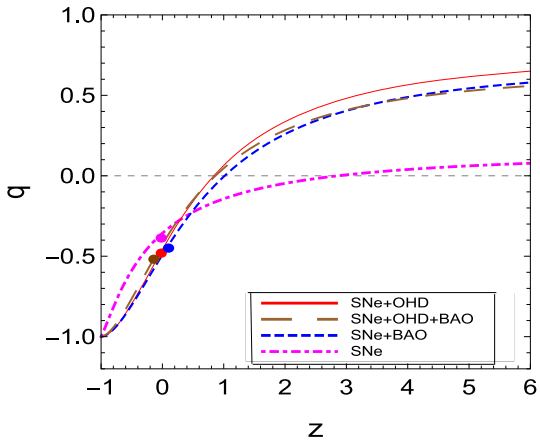


Fig. 6 The deceleration parameter as a function of redshift for best-fit values of model parameters obtained from observational data. A dot denotes the current value of q (hence q_0)

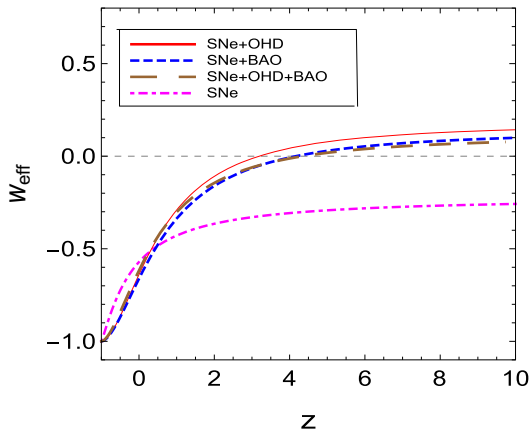


Fig. 7 The variation effective EoS parameter as a function of redshift for best-fit values of model parameters

dence in favor" of the model k compared to the model l. For $0 \leq \Delta AIC_{kl} < 2$ we have"strong evidence in favor" of model k, for $2 < \Delta AIC_{kl} < 4$, we have "average evidence in favor" of model k, for $4 < AIC_{kl} \leq 7$ there is "less evidence in favor" of the model k, and for $\Delta AIC_{kl} > 10$ there is basically "no evidence in favor" of model k [53].

On the other hand, the Bayesian criterion is defined through the relation [54]

$$BIC = -2\, ln\mathscr{L}_{max} + d\, lnN, \tag{43}$$

where N is the number of data points. Similar to ΔAIC_{kl}, $\Delta BIC_{ij} = BIC_i - BIC_j$ can be interpreted as "evidence favor" the model i compared to the model j. For $0 \leq \Delta BIC_{ij} < 2$ there is "not enough evidence against" the model i, for $2 \leq \Delta BIC_{ij} < 6$ there is "evidence against" the model i and for $6 \leq \Delta BIC_{ij} < 10$ there is "strong evidence against" model i [53].

Table 3 shows the χ^2_{min}s, χ^2_{red}s, AICs, BICs of the matter creation model with consideration of the ΛCDM as the referring model. It can be observed that the values of χ^2_{min}, AIC and BIC for matter creation model are very close to the values of ΛCDM model. Thus, the observational data strongly favor and support the matter creation model from AIC and BIC. The reduced χ^2_{red} also shows that it is very close to the values of ΛCDM model, which is less than one (the model is "over fitting" the data).

6 Thermodynamics analysis

In this section, we find the condition of the thermodynamic stability for the present particle creation model. In [49], it has been demonstrated that cosmological apparent horizons are also endowed with thermodynamic properties. It can relate

Table 2 The numerical values of a_{tr}, z_{tr}, q_0, $w_{eff}(z=0)$ and t_0 using best-fit results of model parameters

Data	a_{tr}	z_{tr}	q_0	$w_{eff}(z=0)$	t_0 (Gyr)
SNe	0.2589	2.8619	−0.356	−0.5712	16.4
SNe +OHD	0.5438	0.8386	−0.457	−0.6382	13.8
SNe +BAO	0.4963	1.0147	−0.424	−0.6608	14.5
SNe +OHD+BAO	0.5366	0.8633	−0.491	−0.6162	13.98

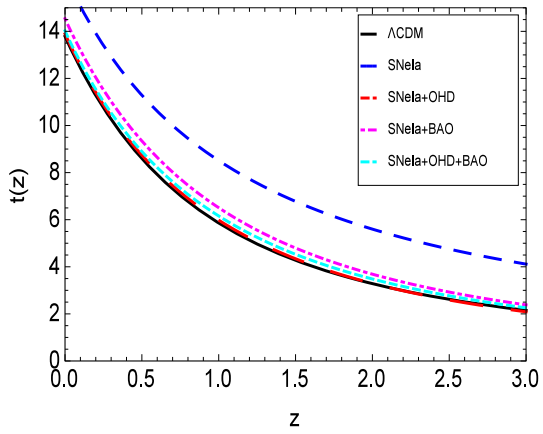


Fig. 8 The age of universe as a function of redshift for best-fit values of model parameters

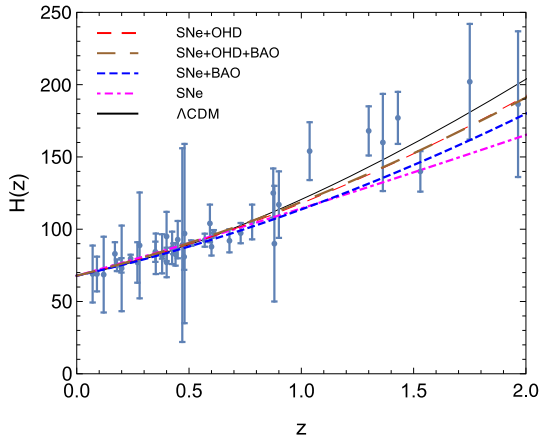


Fig. 9 Variation of the Hubble function as a function of the redshift z for the best-fit values of the model. The observational 43 $H(z)$ points are shown with error bars (grey colour). The variation of the Hubble function in the standard ΛCDM model is also represented as the solid curve

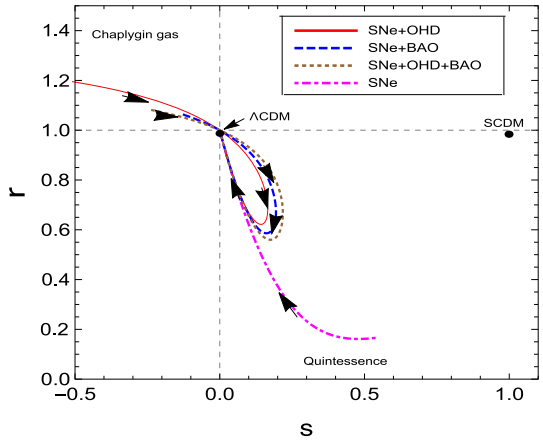


Fig. 10 The trajectory of $\{r, s\}$ in $s - r$ plane corresponds to best fitted parameters. The arrow shows the direction of the evolution of the trajectory

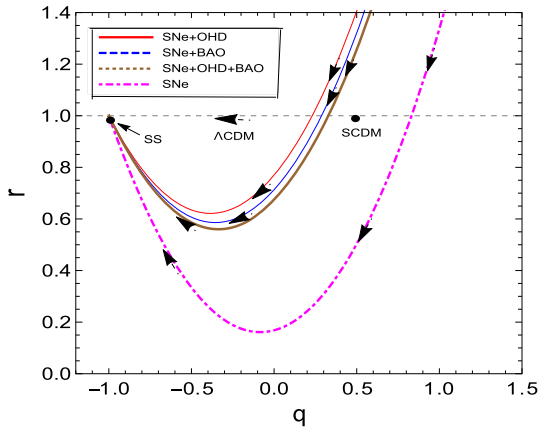


Fig. 11 The trajectory of $\{r, q\}$ in $q - r$ plane for the best fitted parameters. The arrow shows the direction of the evolution of the trajectory

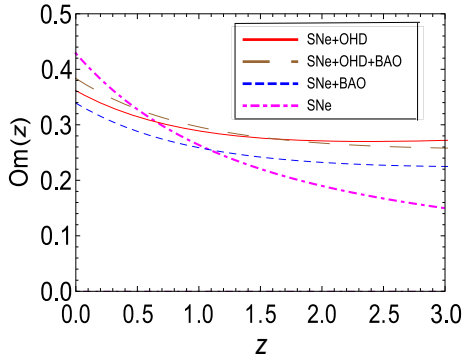


Fig. 12 The trajectory of *Om(z)* for the best fitted parameters

temperature and entropy to the apparent horizon like to the black hole event horizon.

According to the generalized second law (GSL) of thermodynamic, the total entropy S is the sum of entropy of all sources. Therefore, in this model the total entropy is contributed from the entropy of the apparent horizon (S_h) and entropy of fluid (S_f) inside the apparent horizon, i.e., $S = S_h + S_f$. The entropy of apparent horizon is given by $S_h = \kappa_B A/4l_{pl}^2$ [50], where κ_B is the Boltzmann's constant, $A = 4\pi r_h^2$ is the area of horizon in which $r_h = H^{-1}$ is the horizon radius for flat FRW universe and l_{pl} is the Planck's length.

Differentiating S_h with respect to cosmic time and using (19), we obtain

$$\dot{S}_h = -\frac{2\pi\kappa_B}{l_{pl}^2}\frac{\dot{H}}{H^3} = \frac{6\pi\kappa_B}{l_{pl}^2 H^2}\frac{H_0(1-\alpha-\beta-\gamma)}{(2-3\gamma)}\, a^{-\frac{3(1-\beta-\gamma)}{(2-3\gamma)}}. \quad (44)$$

It is observed from the above equation that $\dot{S}_h \geq 0$ for $(\alpha + \beta + \gamma) \leq 1$ and $\gamma < 2/3$.

Now, the Gibb's equation for the fluid is written as

$$TdS_f = d(\rho V) + pdV = V\dot{\rho} + \rho\dot{V} + pdV, \tag{45}$$

where $V = 4\pi r_h^3/3$ is the spatial volume enclosed by the horizon and T is the fluid temperature. Note that we are studying matter-dominated model $p = 0$. Using (19), the above equation gives

$$\dot{S_f} = \frac{24\pi^2 H_0}{H^2}\frac{(1-\alpha-\beta-\gamma)}{(2-3\gamma)}a^{-\frac{3(1-\beta-\gamma)}{2-3\gamma}}, \tag{46}$$

where $T = T_h = 1/2\pi r_h$, i.e., if the temperature of the fluid becomes equal to that of the temperature of the horizon [51]. For $\dot{S_f} \geq 0$, we must have $(\alpha+\beta+\gamma) \leq 1$ and $\gamma < 2/3$.

Thus, from (44) and (46), we observe that $\dot{S} = \dot{S_h} + \dot{S_f} \geq 0$ for $(\alpha+\beta+\gamma) \leq 1$ and $\gamma < 2/3$. So, the entropy of the horizon plus fluid is an increasing function of the cosmic time.

Differentiating (44) again with respect to cosmic time, we get

$$\ddot{S_h} = \frac{18\pi\kappa_B H_0}{l_{pl}^2}\frac{(1-\alpha-\beta-\gamma)}{(2-3\gamma)^2}a^{-\frac{3(1-\beta-\gamma)}{2-3\gamma}} \times\left[\frac{2H_0}{H^2}a^{-\frac{3(1-\beta-\gamma)}{2-3\gamma}} - \frac{(1-\beta-\gamma)}{H}\right]. \tag{47}$$

Similarly, differentiating (46) with respect to cosmic time, we get

$$\ddot{S_f} = 72\pi^2 H_0\frac{(1-\alpha-\beta-\gamma)}{(2-3\gamma)^2}a^{-\frac{3(1-\beta-\gamma)}{2-3\gamma}} \times\left[\frac{2H_0}{H^2}a^{-\frac{3(1-\beta-\gamma)}{2-3\gamma}} - \frac{(1-\beta-\gamma)}{H}\right]. \tag{48}$$

Adding (47) and (48), one obtains

$$\ddot{S} = \ddot{S_h} + \ddot{S_f} = \left(\frac{18\pi\kappa_B}{l_{pl}^2} + 72\pi^2\right)\frac{(1-\alpha-\beta-\gamma)H_0}{(2-3\gamma)^2 H}a^{-\frac{3(1-\beta-\gamma)}{2-3\gamma}} \times\left[\frac{2H_0}{H}a^{-\frac{3(1-\beta-\gamma)}{2-3\gamma}} - (1-\beta-\gamma)\right]. \tag{49}$$

The sign of $\ddot{S}$ is determined by last bracket in (49) and $\alpha+\beta+\gamma < 1$. Therefore, we find that the generalized second law of thermodynamics is always valid and hence the model is stable under the above constrains.

It is also interesting to discuss the model with adiabatic matter creation like irreversible process. In adiabatic process, the total entropy S increases, but, the specific entropy (per particle), $\sigma = S/N$, remains constant, i.e., $\dot{\sigma} = 0$ which implies that

$$\frac{\dot{S}}{S} = \frac{\dot{N}}{N}. \tag{50}$$

Using (12) into (10), we get

$$N = N_0 a^{3\beta}(\dot{a})^{3\gamma}\, e^{3\alpha H_0(t-t_0)}, \tag{51}$$

where N_0 is the present number of particles. Now, from (50), we get

$$S = S_0 a^{3\beta}(\dot{a})^{3\gamma}\, e^{3\alpha H_0(t-t_0)}, \tag{52}$$

where S_0 is the present entropy of matter fluid. It is to be noted that if $\alpha = \beta = \gamma$, i.e., if there is no particle creation, we get $S = S_0$, i.e., the standard conserved quantities are recovered.

7 Conclusion

We have discussed the matter-dominated model with matter creation cosmology as an alternative to explain the cosmic acceleration. As matter creation models are phenomenological and the literature contains a variety of models, so a generalized model could be a better choice to start for any study. Hence, in the present paper we have generalized the form of matter creation rate assumed by Lima et al. [31].

The assumption $\Gamma = 3\beta H$ [13] always gives accelerating model for $\beta > 1/3$ or decelerating for $\beta < 1/3$, that is, there is no transition redshift from a decelerating to an accelerating regime as required by observational data. In another paper, Abramo and Lima [20] proposed the form of Γ as $\Gamma = 3\beta H^2$, however it also gives no transition redshift. In order to cure such a difficulty, a constant term is added to this expression, i.e., $\Gamma = 3\alpha H_0 + 3\beta H$ [31] to get the transition redshift. Basilakos and Lima [55] have also used the same form to constraints the model. They observed that the age of the Universe to be $t_0 \sim 14.8$ Gyr while the inflection point is located $a_{tr} \simeq 0.44$ which corresponds to $z_{tr} \simeq 1.26$. They have found that this form of matter creation rate is endowed with severe difficulties even for the set of background tests because it is unable to adjust simultaneously the observational data at low and high redshift.

In this work, we have generalized the form of Γ in order to produce a clear image about the matter creation models aiming to realize the early physics and its compatibility with the current astronomical data. It covers different matter creation rate, for instance, $\Gamma \propto H_0$, $\Gamma \propto H$ and $\Gamma \propto \ddot{a}/\dot{a}$. Lima et al. [31] have performed best-fit of the free parameters using only SNe data and best -fit values are $\beta = 0$ and $\alpha = 0.65$. We have performed the fitting of free parameters using joint observational data of SNe, OHD and BAO in which none free parameters is zero. However, In our model, the age of universe is found to be 13.8 Gyr from $SNe+OHD$ and $SNe + OHD + BAO$, but it is higher with SNe and $SNe + BAO$. Also, the transition redshift is less than one with $SNe + OHD$ and $SNe + OHD + BAO$, which are good fit with ΛCDM model. Our model also generalizes the

Table 3 Summary of the reduced χ^2_{red}, ΔAIC and ΔBIC for ΛCDM model and matter creation model

Model	Data set	χ^2_{min}	χ^2_{red}	AIC	BIC	ΔAIC	ΔBIC
ΛCDM	SNe	17.027	0.587	21.027	23.894	0	0
	SNe+OHD	27.901	0.387	31.907	36.509	0	0
	SNe+BAO	18.131	0.518	22.131	25.352	0	0
	SNe+OHD+BAO	30.443	0.385	34.443	39.232	0	0
Matter creation model	SNe	17.417	0.622	23.417	27.718	2.390	3.824
	SNe+OHD	27.521	0.387	33.512	40.433	1.614	3.924
	SNe+BAO	17.416	0.512	23.416	28.249	1.285	2.897
	SNe+OHD+BAO	29.766	0.381	35.766	42.950	1.323	2.718

work of above references and it can be observed from the observational tests that our model gives best -fit values from joint observation of SNe with OHD, and OHD and BAO and fit the data very well with ΛCDM model. We have investigated the model analytically and numerically in which the matter creation process provides the late-time accelerating phase of the cosmic expansion without the need of any dark energy.

We have obtained the exact solutions for the scale factor, Hubble parameter and deceleration parameter. These results have then contrasted with the ones obtained at the background level to find the model parameters. For the background tests we have used SNe in combination with OHD and BAO at different redshifts. The nature of the cosmological evolution is strongly dependent on the numerical values of the model parameters. The best-fit values of model parameters have been listed in Table 1. Figures 1, 2, 3 and 4 show the confidence regions of parameters α, β and γ for different sets of jointly observational data. It has been found that the results of SNe and $SNe+BAO$ data are little different from other two data. However, the joint analysis of $SNe+OHD$ and $SNe+OHD+BAO$ constraint the model parameters very well and are in good agreement with observational data of ΛCDM model. In what follows we summarize the results:

- The evolutions of the scale factor for best-fit values of model parameters have been plotted in Fig. 5. It has been observed that the model predicts early deceleration and late-time acceleration. The transition points a_{tr} where the universe transits from decelerated phase to accelerated phase have been listed in Table 2.
- Figure 6 plots the evolution of deceleration parameter with redshift for best-fit values obtained from independent/combined analysis of observational data. The present-day value of q and transition redshift z_{tr} have been listed in Table 2. The best-fit values of parameters obtained from different observational data give q_0 in the range of $-1 \leq q_0 < 0$. In general, $q \to -1$ as $z \to -1$, which corresponds to the de Sitter universe. The deceleration parameter is time dependent and hence shows the transition from positive to negative. The evolution of the universe begins from higher redshift, from a decelerating phase, with $q > 0$. The expansion of the Universe accelerates, and at a finite value of z it reaches the value $q = 0$, corresponding to the transition to the accelerated phase. The evolution of q is strongly dependent on the numerical values of the model parameters.
- We have obtained the EoS parameter to discuss the evolution of the model. Figure 7 plots the evolution of EoS parameter with redshift for best-fit values of parameters. It has been observed that the EoS does not cross the phantom-divide line $\omega = -1$. Irrespective of the values of parameters, $\omega_{eff} \to -1$ as $z \to -1$ which shows that the model behaves like ΛCDM in late time. The present values of ω obtained from independent/combined observational data are listed in Table 2. These values are comparatively higher than that predicted by the joint analysis of $WMAP + BAO + H_0 + SNe$ data which is around -0.93.
- We have discussed the age of the universe by plotting the trajectory with best-fit values of parameters as shown in Fig. 8. The trajectory shows that the age of the universe obtained by $SNe + OHD$ and $SNe + OHD + BAO$ data are found to be approximately 13.9 Gyr. So, the age predicted by the present model is agreeing with the age deduced from ΛCDM model.
- The Hubble function with the error bar fits in to the ΛCDM model for best-fit values has been plotted in Fig. 9. It has been observed that the curves coincide at low redshifts and differ appreciably at high redshifts. However, it is possible to get good fit using joint analysis of $SNe + OHD$ and $SNe + OHD + BAO$.
- We have studied two diagnostics parameters, namely, statefinder and *Om(z)* parameters to compare our model with ΛCDM model. In Fig. 10, the trajectories of $\{r, s\}$ have been plotted in $s-r$ plane for best-fit values obtained from different observational data set. The model corresponds to ΛCDM model in late-time. The model also approaches to the standard model in late time as shown in $q-r$ plane (Fig. 11). The trajectory of *Om(z)* in Fig. 12 shows that the model behaves like quintessence.

– We have performed the information criterion of AIC and BIC to discriminate our model with ΛCDM model. The values of reduced Chi-square, ΔAIC and ΔBIC are calculated and have listed in Table 3. The analyses based on the AIC and BIC indicate that there is positive support for the matter creation model when compared to the ΛCDM model. The reduced χ^2_{red} is less than one in each data points which shows that the model gives the best-fit values of model parameters and good support to ΛCDM model.
– We have discussed the thermodynamic behavior of the model by calculating the total entropy for the matter creation. We have established the general conditions for any matter creation model that ensure the validity of the generalized second law of thermodynamics.

In concluding remarks, the most remarkable feature of this model is that the description of the present acceleration of the universe does not need any dark energy fluid or modified gravity theories. However, this theory is also model dependent. Thus, in this paper, we have proposed a new matter creation model which generalizes the existing models in the literature and constrain them using observational data set. Our analysis shows that the model is close to the standard ΛCDM model.

Acknowledgements The authors express their sincere thanks to the reviewer for his constructive suggestions to improve the manuscript in the present form. One of the author, AK would like to thank University Grant Commission, New Delhi for providing Senior Research Fellowship under UGC-NET Scholarship.

Data Availability Statement This manuscript has no associated data or the data will not be deposited. [Authors' comment: All data (numbers and plots) generated in our study have been included in this paper. We do not have additional data to show.]

Open Access This article is licensed under a Creative Commons Attribution 4.0 International License, which permits use, sharing, adaptation, distribution and reproduction in any medium or format, as long as you give appropriate credit to the original author(s) and the source, provide a link to the Creative Commons licence, and indicate if changes were made. The images or other third party material in this article are included in the article's Creative Commons licence, unless indicated otherwise in a credit line to the material. If material is not included in the article's Creative Commons licence and your intended use is not permitted by statutory regulation or exceeds the permitted use, you will need to obtain permission directly from the copyright holder. To view a copy of this licence, visit http://creativecommons.org/licenses/by/4.0/.
Funded by SCOAP[3].

References

1. A.G. Riess et al., Astron. J. **116**, 1009 (1998)
2. S. Perlmutter et al., Nature **391**, 51 (1998)
3. S. Perlmutter et al., Astrophys. J. **517**, 565 (1999)
4. D.J. Eisenstein et al., Astrophys. J. **633**, 560 (2005)
5. M. Tegmark et al., Phys. Rev. D **74**, 123507 (2006)
6. E. Komatsu et al., Astrophys. J. Suppl. **192**, 18 (2011)
7. I. Prigogine, J. Geheniau, Proc. Natl. Acad. Sci. USA **83**, 6245 (1986)
8. I. Prigogine et al., Proc. Natl. Acad. Sci. USA **85**, 7428 (1988)
9. M.O. Calvao, J.A.S. Lima, I. Waga, Phys. Lett. A **162**, 223 (1992)
10. J.A.S. Lima, A.S. Germano, Phys. Lett. A **170**, 373 (1992)
11. J.A.S. Lima, J.S. Alcaniz, Astron. Astrophys. **348**, 1 (1999)
12. J.S. Alcaniz, J.A.S. Lima, Astron. Astrophys. **349**, 72 (1999)
13. J.A.S. Lima, A.S. Germano, L.R.W. Abramo, Phys. Rev. D **53**, 4287 (1996)
14. W. Zimdahl, J. Triginer, D. Pavón, Phys. Rev. D **54**, 6101 (1996)
15. V.B. Johri, K. Desikan, Astrophys. Lett. Commun. **33**, 287 (1996)
16. C.P. Singh, A. Beesham, Astrophys. Space Sci. **336**, 469 (2011)
17. C.P. Singh, Astrophys. Space Sci. **338**, 411 (2012)
18. W. Zimdahl, D.J. Schwarz, A.B. Balakin, D. Pavón, Phys. Rev. D **64**, 063501 (2001)
19. Q. Yaun, J. Tong, Y. Ze-Long, Astrophys. Space Sci. **311**, 407 (2007)
20. L.R.W. Abramo, J.A.S. Lima, Class. Quantum Gravity **13**, 2953 (1996)
21. G. Steigman, R.C. Santos, J.A.S. Lima, JCAP **06**, 033 (2009). arXiv:0812.3912
22. J.A.S. Lima, S. Basilakos, F.E.M. Costa, Phys. Rev. D **86**, 103534 (2012). arXiv:1205.0868
23. J.A.S. Lima, L.L. Graef, D. Pavón, S. Basilakos, JCAP **10**, 042 (2014)
24. R.O. Ramos, M.V.D. Santos, I. Waga, Phys. Rev. D **89**, 083524 (2014). arXiv:1404.2604
25. S. Pan, B.K. Pal, S. Pramanik, Int. J. Geom. Methods Mod. Phys. **15**, 1850042 (2018)
26. J. de Haro, S. Pan, Class. Quantum Gravity **33**, 165007 (2016). arXiv:1512.03100
27. S. Pan, S. Chakraborty, Adv. High Energy Phys. **201**, 654025 (2015)
28. L.R.W. Abramo, J.A.S. Lima, Class. Quantum Gravity **13**, 2953 (1996)
29. E. Gunzig, R. Maartens, A.V. Nesteruk, Class. Quantum Gravity **15**, 923 (1998)
30. S. Pan, J. de Haro, A. Paliathanasis, R.J. Slagter, Mon. Not. R. Astron. Soc. **460**, 1445 (2016)
31. J.A.S. Lima, F.E. Silva, R.C. Santos, Class. Quantum Gravity **25**, 205006 (2008)
32. P.A.R. Ade et al., Astron. Astrophys. **594**, 13 (2016)
33. M. Betouleet et al., Astron. Astrophys. **22**, 568 (2014)
34. S.L. Cao, H.Y. Teng, H.Y. Wan, H.R. Yu, T.J. Zhang, Eur. Phys. J. C **78**, 313 (2018)
35. N. Padmanabhan et al., Mon. Not. R. Astron. Soc. **427**, 2132 (2012)
36. F. Beutler et al., Mon. Not. R. Astron. Soc. **416**, 3017 (2011)
37. L. Andersonet et al., Mon. Not. R. Astron. Soc. **441**, 24 (2014)
38. C. Blakeet et al., Mon. Not. R. Astron. Soc. **425**, 405 (2012)
39. P.A.R. Adeet et al., Astron. Astrophys. **594**, 13 (2016)
40. R. Giostri et al., J. Cosmol. Astropart. Phys. **1203**, 027 (2012)
41. G. Hinshawet et al., Astrophys. J. Suppl. **208**, 19 (2013)
42. D. Foreman-Mackey, D. Hogg, D. Lang, J. Goodman, Publ. Astron. Soc. Pac. **125**, 306 (2012)
43. M. Kowalski et al., Astrophys. J. **686**, 749 (2008)
44. P. Praseetha, T.K. Mathew, Int. J. Mod. Phys. D **23**, 1450024 (2014)
45. E. Komatsu et al., WMAP Collaboration, Astrophys. J. Suppl. **192**, 18 (2011)
46. C.J. Feng, X.Z. Li, Phys. Lett. B **680**, 355 (2009)
47. V. Sahni, T.D. Saini, A.A. Starobinsky, U. Alam, JETP Lett. **77**, 201 (2003)
48. V. Sahni, A. Shafieloo, A.A. Starobinsky, Phys. Rev. D **78**, 103502 (2008). arXiv:0807.3548

49. R.G. Cai, L.M. Cao, Y.P. Hu, Class Quantum Gravity **26**, 155018 (2009). arXiv:0809.1554
50. D. Bak, S.J. Rey, Class. Quantum Gravity **17**, L83 (2000)
51. M. Akbar, R.G. Cai, Phys. Rev. D **75**, 084003 (2007)
52. H. Akaike, IEEE Trans. Autom. Control **19**, 716 (1974)
53. A.R. Liddle, Mon. Not. R. Astron. Soc. **377**, L74 (2007)
54. G. Schwarz, Ann. Stat. **6**, 461 (1978)
55. S. Basilakos, J.A.S. Lima, Phys. Rev. D **82**, 023504 (2010)

Materials Research Express

PAPER

Response surface methodological evaluation of drilling for the optimization of residual compressive strength of bio-based RPUF composite

To cite this article: Anuja Agrawal *et al* 2019 *Mater. Res. Express* **6** 125372

View the article online for updates and enhancements.



IOP ebooks™

Bringing you innovative digital publishing with leading voices to create your essential collection of books in STEM research.

Start exploring the collection - download the first chapter of every title for free.

This content was downloaded from IP address 14.139.251.100 on 26/02/2020 at 04:34

Materials Research Express

PAPER

Response surface methodological evaluation of drilling for the optimization of residual compressive strength of bio-based RPUF composite

RECEIVED
23 September 2019

REVISED
26 November 2019

ACCEPTED FOR PUBLICATION
4 December 2019

PUBLISHED
19 February 2020

Anuja Agrawal[1], **Raminder Kaur**[1] **and R S Walia**[2]

[1] Department of Applied Chemistry & Polymer Technology, Delhi Technological University, Delhi—110042, India
[2] Department of Mechanical Engineering, Delhi Technological University, Delhi—110042, India

E-mail: rkaurdtu@gmail.com

Keywords: residual compressive strength, drilling, central composite design, castor oil, rigid polyurethane foam

Abstract

Present study investigates the impact of process parameters on the residual compressive strength of bio-based rigid polyurethane foam (RPUF) composites incorporated with copper powder. Formulation of the samples was optimized by performing compressive strength, thermo-gravimetric analysis (TGA) and flammability experiments. It was concluded that incorporation of 8% metallic filler showed up to 116% increase in the compressive strength and $T_{5\%}$ was also found to increase from 192 °C to 257 °C. Furthermore, peak heat-release rate (PHRR) was found to decreased from 118 kW m^{-2} to 93 kW m^{-2} and total heat release (THR), smoke production rate (SPR) as well as total smoke release (TSR) also demonstrate a significant decrease on the incorporation of 8% copper powder in the RPUF. Polynomial mathematical model reliant on the Response surface method (RSM) employing Central composite design has been developed. It was concluded that density is the most influential factor for maximizing the residual compressive strength. The optimized process parameters for maximizing residual compressive strength were attained as high spindle speed and low feed rate. Furthermore, equations designated as the coded factors are also presented to identify the relative impact of factors.

1. Introduction

During past few decades, rigid polyurethane foams (RPUFs) have been the subject of intense research due to a wide range of applications in construction & refrigeration industry, prototypes and industrial patterns [1–3]. Commercially, polyurethane (PU) foam is prepared by the reaction of a polyol with a polyisocyanate, both of them are the petroleum-based raw materials. A lot of studies have been executed for the preparation of PU foam using the polyols derived from different vegetable oils and reinforced with different natural and synthetic fillers [4–6]. Of these vegetable oils, only castor oil possesses the hydroxyl group naturally and consequently conversion of castor oil into polyol is comparatively easy and cost efficient process. Although various researchers investigated on the castor oil-based polyurethanes reinforced with different fillers and reported the enhanced mechanical and thermal properties [7–9], still the literature is devoid of investigations on castor oil-based RPUF reinforced with metallic fillers such as copper, iron, and others. Of these, the copper powder may be used to impart good mechanical and thermal properties in castor oil-based RPUF [10] but for the commercialization of this RPUF, some machining operations such as milling, drilling, countersinking, grinding, boring and trimming are required for obtaining desired geometrical shapes [11–13]. Of these, drilling is an important operation required for fastening and riveting structural components in various applications such as aircraft and automobile [14–16]. Drilling of polymer composite is considerably different from that of metals & alloys and require deliberations owing to their some unique characteristics of inherent inhomogeneity, anisotropy, and abrasiveness [17]. Quality of drilled holes, specified by the dimensional tolerances, accuracy, and precision,

© 2020 IOP Publishing Ltd

influences the load-carrying capacity of the products prepared from polymer composites, consequently ascertains the structural integrity as well as long term reliability of the product. Previous researches on drilling damages in composites have concluded that the peel-up and push-out are two distinguishable modes of delamination mechanisms, commencing when the thrust force surpasses the critical thrust force (CTF) [18]. Analytical studies reveal that cutting parameters such as feed rate, depth of cut, spindle speed and others control the thrust force, which is required to be minimized to reduce the delamination. So, an optimized selection of these parameters administers the delamination-free drilling [19, 20].

To correlate the thrust force and other drilling parameters in composite materials, variety of empirical mathematical models have been established and it was concluded that thrust force and delamination increase with feed rate while spindle speed showed specific behaviours for distinct materials [21–23]. Mechanical properties of polymer composites are also influenced by the delamination, so the impact of delamination on the residual mechanical strength also needs attention. Several studies have been conducted to ascertain the effects of delamination on residual mechanical strength [22, 24]. Diaz Alvarez *et al* [25] studied the drilling-induced damages in aramid composites and analyzed the influence of the drill geometry (Twist drill, Brad & Spur drill) on the torque, damage and thrust force. Some mechanistic models were developed to ascertain the relation between process parameters and the quality of the final product. It was observed that the Twist drill showed better performance with high feed rate and cutting speeds, while with the Brad & Spur drill, higher speed and lower feed rate provides better results in terms of delamination.

Zarif Karimi *et al* [24] investigated the effect of drilling-induced delamination on the compressive strength of epoxy composites reinforced with woven glass fiber. The feed rate and spindle speed were considered as process parameters to optimize the delamination and residual compressive strength. It was observed that the extent of damage due to delamination or interlaminar cracking is governed by the cutting forces. Results showed that the feed rate was the most influential factor to optimize the residual compressive strength and the optimized value of residual compressive strength was attained at a spindle speed of 1000 rpm and feed rate of 31.5 mm min^{-1}.

Xu *et al* [26] studied the severity of drilling-induced damage such as burrs, tearing and delamination in CFRP composites using three different types of specialized drill bits (twist drill, brad spur drill, and dagger drill). The ultrasonic C-scan showed that initially, delamination takes place inside the composite layer and then transmits through plies on increasing the drill thrust load. The feed rate was identified as the most significant factor to generate defects during drilling of the composite. It was concluded from the damage analysis that the brad spur drill provides the least damage in the course of the drilling of CFRP.

Heidary *et al* [22] investigated the drilling performance of epoxy composites reinforced from E-glass fiber and multi-walled carbon nanotubes (MWCNT) and analyzed the effect of drilling-induced damage on the residual flexural strength. Feed rate (0.04–0.1 mm rev^{-1}), drill diameter (4 and 5 mm), spindle speed (315 and 630 rpm), and the weight % of carbon nanotubes (0%–1%) were considered as process parameters. Taguchi method in association with grey relational analysis (GRA) was employed for the multi-objective optimization of the drilling process. Results showed that the feed rate was the most influential factor for the optimization of the delamination and thrust force, followed by spindle speed while residual flexural strength was greatly affected by the concentration of the MWCNT, followed by feed rate. it was also reported that feed rate of 0.04 mm rev^{-1}, MWCNT concentration of 0.5%, a drill diameter of 4 mm and spindle speed of 630 rpm are the optimized values of process parameters.

Silva *et al* [27] studied the effect of tool geometry (twist, brad, step), feed rates (0.12 and 0.30 mm rev^{-1}) and cutting speeds (1120 and 1800 rpm) on the bearing load and fractal dimension of the carbon fibre reinforced epoxy composite plates. According to their results, the better bearing load was achieved by using step geometry bit with higher cutting sped and lower feed rate. It was also observed that higher feed rate provides lower bearing load, higher delamination, and higher fractal dimension.

Numerous research work has been conducted on the machinability of glass fibre reinforced epoxy composites but polyurethane foam, which is being used in a variety of structural applications, has not been explored yet and necessitates an investigation of all operational aspects. Furthermore, compressive strength is crucial for RPUF, as the applications of RPUF require good compressive strength. But it is evident from the literature that there are immense possibilities of delamination growth under compressive loading [24].

This study investigates the influence of drilling parameters (feed rate, drill diameter, spindle speed and density of RPUF) on the residual compressive strength, thrust force and delamination of copper powder reinforced RPUF. Response surface method-based approach has been employed to accomplish the optimized parameters for the drilling of RPUF. Additionally, experimental investigations have also been performed to optimize the concentration of the copper powder in RPUF employed for drilling analysis.

Table 1. Factor Levels for performing Drilling Test.

Symbol	Control factor	Unit	Level 1	Level 2	Level 3	Level 4	Level 5
ρ	Density	Kg m^{-3}	260	302.5	345	387.5	430
f	Feed rate	mm rev^{-1}	0.12	0.34	0.56	0.78	1
v	Spindle speed	Rpm	56	342	628	914	1200
d	Drill diameter	Mm	4	6	8	10	12

2. Experimental procedure

2.1. Preparation of RPUF composite

The rigid polyurethane foams were obtained by the method as reported in the literature [28, 29], In brief, the procedure is as follows:

The copper powder was surface treated with 1% solution of 3-aminopropyl triethoxysilane (APTES) in acetone/water 1:1 (v/v). The predetermined quantity of the surface-treated Electrolytic copper powder (325 mesh size) was added to the modified castor oil (polyol). Then a calculated amount of other ingredients such as catalyst (Dabco 33-LV), blowing agent (*n*-Pentane), surfactant (Silicon Oil) was added to the polyol and thoroughly mixed to form polyol-premix. A calculated amount of MDI was then added to the beaker. The resulted reaction mixture was poured into a metal mould (100 mm × 100 mm × 10 mm) and kept at room temperature for 72 h to ensure complete curing.

2.2. Characterization

2.2.1. Mechanical strength measurement

The Compressive strength, flexural strength and density of the castor oil-based RPUFs have been determined by standard measurement techniques. Testing was conducted on three specimens of each concentration and the average value was reported. Compressive strength of the prepared RPUFs was measured at room temperature using Instron (model No. 3369) universal testing machine (UTM) according to the ASTM D-1621. Specimens of dimensions 25 mm × 25 mm × 25 mm were cut from foam in the in-plain direction and tested for 10% compression. Flexural strength was measured according to the ASTM D-790 using specimen with dimensions 80 mm × 10 mm × 4 mm. Density of the foam samples was determined according to the ASTM D-1622. The rate of crosshead movement was fixed at 5 mm min^{-1} for each sample.

2.2.2. Thermogravimetric analysis (TGA)

Thermogravimetric analysis (TGA) was performed employing a thermogravimetric analyzer (Perkin Elmer 4000) in a nitrogen atmosphere. The heating rate was kept 10 °C min^{-1} and temperature ranging from 50 °C to 700 °C.

2.2.3. Cone calorimeter testing

The anti-flammability performance of RPUF samples was analyzed with a Cone Calorimeter (Jupiter Electronics, Mumbai, India) according to ISO 5660-1 standard at an incident heat flux of 35 kW m^{-2}. The size of the samples was 100 mm × 100 mm × 20 mm.

2.3. Plan of experiments

In the present study, Response Surface Method (RSM) is used to establish the mathematical relation between responses and drilling parameters using Central Composite Design. The design matrix was created by the employment of statistical analysis software, Design Expert. Foam density, feed rate, diameter of the drill bit and spindle speed, at five levels were selected as input parameters, and the delamination, thrust force and residual specific compressive strength were considered as the responses. Input parameters and their levels were selected based on intensive literature survey and drilling test parameters are summarised in table 1. Computer numerical control (CNC) vertical machining center (VMC) employed with standard high-speed steel (HSS) twist drills was used to perform drilling experiments and each experiment was replicated thrice. Consequences of drilling-induced delamination on the residual compressive strength were determined by performing compression tests as per ASTM D-1621.

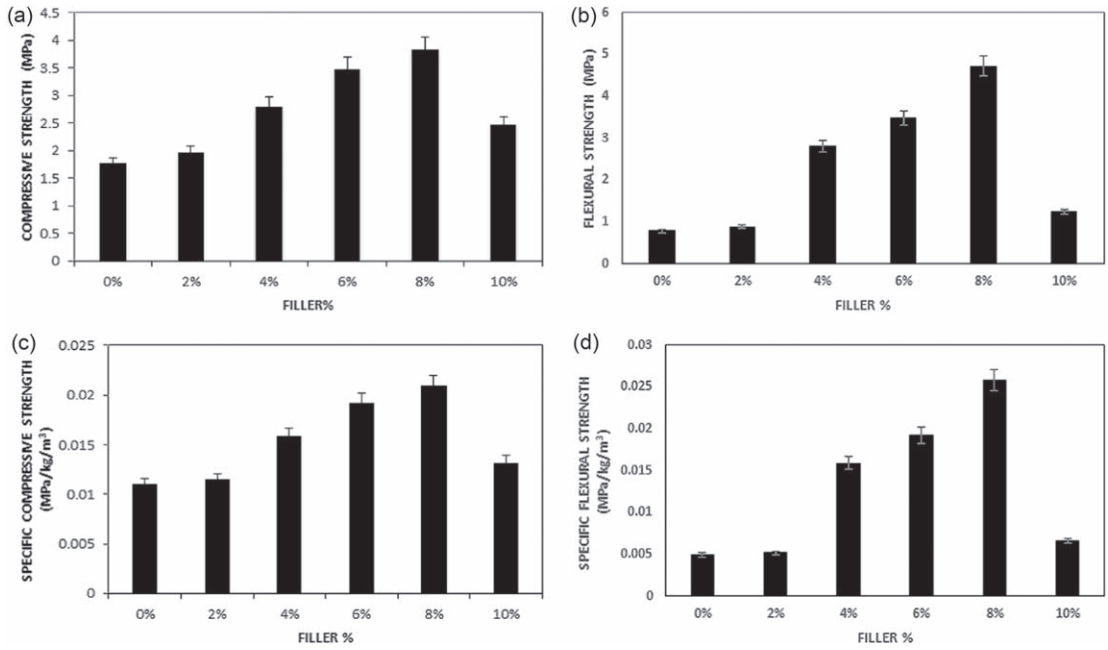


Figure 1. Plots of (a) Compressive strength versus Concentration of filler, (b) Flexural strength versus Concentration of filler, (c) Specific compressive strength versus Concentration of filler and (d) Specific flexural strength versus Concentration of filler.

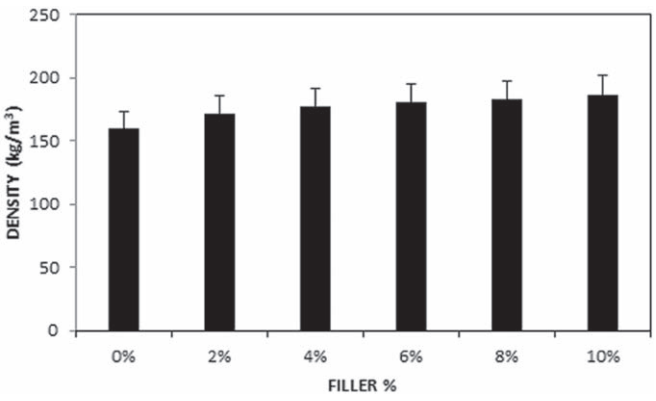


Figure 2. Plots of Density versus Concentration of filler.

3. Results and discussion

3.1. Mechanical strength measurement

Figures 1 and 2 show the changes in mechanical strength, specific mechanical strength, and density on the incorporation of metallic fillers. The unique material characteristics shown by the metallic filler are the result of strong ionic interatomic bonds. Copper powder reinforced RPUF showed an increase in compressive strength up to 3.83 MPa and flexural strength up to 4.72 MPa on the addition of 8% copper powder as compared to 1.77 MPa and 0.79 MPa, respectively for unreinforced polyurethane foam. As the strength of the copper powder filler is higher than that of the RPUF matrix, so the copper powder filler can dissipate the load of the polymer matrix and act as a barrier for the growth of the fracture. When a growing fracture meets a copper powder particle, the dissipation of the energy at the filler site prevents the fracture converting into an unstable one, consequently increasing the toughness of the RPUF [30, 31]. APTES treated metallic fillers have better interaction with the polyol due to the presence of a terminal amino group. APTES also helps in the stabilization of the copper powder by reducing the prospects of oxidation. Increasing the concentration of copper powder filler beyond 8% deteriorates the cell structure which is associated with the agglomeration of metallic fillers after a certain concentration due to the high viscosity of the matrix-filler premix.

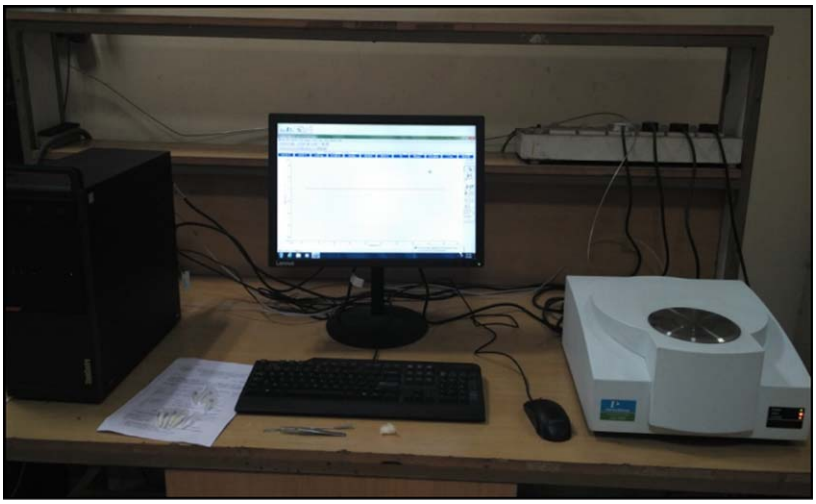


Figure 3. Experimental set-up for Thermo-gravimetric Analyzer.

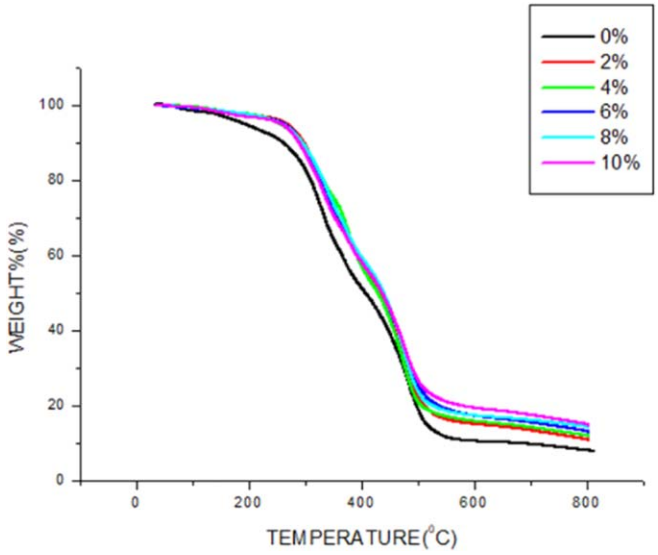


Figure 4. TGA curves of neat and copper powder reinforced RPUF.

Density of the copper powder reinforced RPUF increases slightly on increasing the concentration of copper powder. This behaviour is attributed to the fact that reinforcement of foam with copper powder increases the nucleation site which consequently increase the number of cells. Additionally, density of copper powder is greater than the matrix rigid foam material, which increases the density of the composite [32].

3.2. Thermo-gravimetric analysis (TGA)

To evaluate the thermal stability of these foams, TGA is conducted under the flow of nitrogen. Figure 3 demonstrates the experimental set-up for the thermo-gravimetric analysis. Results show that thermal properties enhanced on the incorporation of copper powder. Maximum char residue is observed for the copper at 10% filler concentration. Usually, the thermal stability of RPUFs is characterized by the temperatures of 5% weight loss ($T_{5\%}$) considered as the temperature for onset of degradation [33]. It shows that 5% weight loss temperature increases from 192 °C to 257 °C by the incorporation of copper powder. This behaviour of the metallic filler reinforced RPUF may be accredited to the better thermal properties and high temperature performance of the copper powder filler. The TGA analysis of the metallic filler incorporated RPUF are illustrated in figure 4 and the results are summarized in table 2.

Table 2. Thermal characteristics of RPUF incorporated with different fillers.

Concentration of filler	$T_{5\%} \pm 2$ (°C)	Residual mass ± 0.05 (%)
0% filler	192	8.08
2% Copper	245	10.99
4% Copper	248	12.02
6% Copper	253	13.20
8% Copper	257	14.37
10% Copper	256	15.00

Table 3. Cone calorimeter data of RPUF incorporated with metallic fillers.

Concentration of filler	PHRR (kW m^{-2}) ± 5	THR (MJ m^{-2}) ±0.5	TSP (m^2 m^{-2}) ± 10	RESIDUE (%) ± 0.5
0%	118	29.8	347	11.5
2%	114	26.5	175	28.7
4%	105	24.2	158	38.9
6%	97	21.7	148	47.5
8%	93	16.9	141	51.8
10%	104	25.0	173	38.5

3.3. Cone calorimeter testing

Figures 6(a)–(d) shows the plots of the cone calorimeter experiment performed on RPUF containing a varied concentration of metallic filler and data are summarized in table 3. Experimental set-up for cone calorimeter is shown in figure 5. Conventionally, the intensity of the fire is correlated with the heat release rate (HRR) and total heat release (THR) [34, 35]. Figure 6(a) shows that peak heat-release rate (PHRR) is decreased from 118 kW m^{-2} to 93 kW m^{-2} on the incorporation of 8% copper powder in the RPUF. Figure 6(b) shows that total heat release (THR) also decreases from 29.8 MJ m^{-2} to 17.0 MJ m^{-2} on the incorporation of copper fillers. Figure 6(c) shows the smoke production rate (SPR) and the first peak of SPR denotes that the smoke production decreased from 0.008 to 0.004 m^2 s^{-1} for the introduction of 8% copper powder.

The total smoke release (TSR) also decreases from 302 m^2 m^{-2} to 141 m^2 m^{-2} for 8% copper powder (figure 6(d)). Properties of composite RPUF starts to deteriorates again on increasing the concentration beyond 8% due to the high viscosity of polyol-filler premix and agglomeration of filler particles. The results are accredited to the fact that the formation of metallic protective layer hinders the flame spread, release of flammable by-products and toxic smoke. It concluded that RPUF with 8% copper powder shows the best mechanical, thermal and flame retardant properties among all the formulations and this is used for the drilling experiments to ascertain the machining ability of the foam. Figure 7 shows the images of samples employed for drilling test.

3.4. Drilling performance test

Drilling-induced damages and consequently residual compressive strength is controlled by the thrust force, which is believed to have a threshold value after which delamination occurs. According to the literature, the exit side of drilled specimen presents more severe delamination in the composite materials, so the images of the holes were obtained at the exit side of the specimen. After that, the maximum diameter and the nominal diameter were measured using an image processing software image j. Figure 8 shows the images of the drilled holes after performing a drilling test at various factor levels.

Residual compressive strength was determined as the force per unit section area remaining after drilling,

$$\sigma_r = \frac{F}{(l - d)t}$$

where F, t, d, and are l the force applied at 10% compression, specimen thickness, hole diameter, and specimen width, respectively. To conduct the experiment central composite design model was used, details of experiment design and obtained experimental results of the thrust force, delamination and residual compressive strength are presented in table 4.

The efficiency of the developed regression models has been established by assessing the level of significance for the model, as well as, lack of fit. It was concluded from the fit summary that the quadratic model is the most efficient model for anticipating the effect of the drilling parameters on the residual compressive strength of the



Figure 5. Experimental set-up for Cone Calorimeter.

RPUF composite. The ANOVA and the fit statistics for the thrust force, delamination and residual compressive strength are shown in tables 5–7 respectively and the effect of the drilling on the responses is summarized in the subsequent sections.

3.4.1. Thrust force analysis

ANOVA of the reduced quadratic model for the thrust force is summarized in the table 5. The significance of the model is established by the F-value of the model, as well as, the lack of fit, which are 93.32 and 0.72 respectively. The p-value for the model is less than 0.01, which establishes the highly statistical significance of the model at more than 99% confidence interval. The p-value shows that the density, drill diameter and the spindle speed have shown significant effects on the thrust force generated in the course of the drilling, while, the feed rate is insignificant in determining the thrust force. Among these factors, the density is the most influential factor whereas, the influence of the spindle speed is the least significant. It was also noticed that the interaction of the density with the drill diameter, the spindle speed with the feed rate or the drill diameter, the feed rate with the drill diameter and the second order term of density, also have shown significant effect on the developed thrust force.

Figure 9 shows the 3D response surfaces of the developed quadratic model for the thrust force. It was concluded that density, drill diameter, and spindle speed have shown a significant effect on the thrust force generated in the course of drilling, while feed rate is insignificant in determining thrust force. Among these factors, density is the most influential factor whereas, the influence of spindle speed is least.

The higher value of thrust force is accredited to the resistance to cut the polyurethane composite materials with an increase in density which results in higher drilling forces. It was also observed that the thrust force increases slightly on increasing the spindle speed or drill diameter while the feed rate shows no effect on the

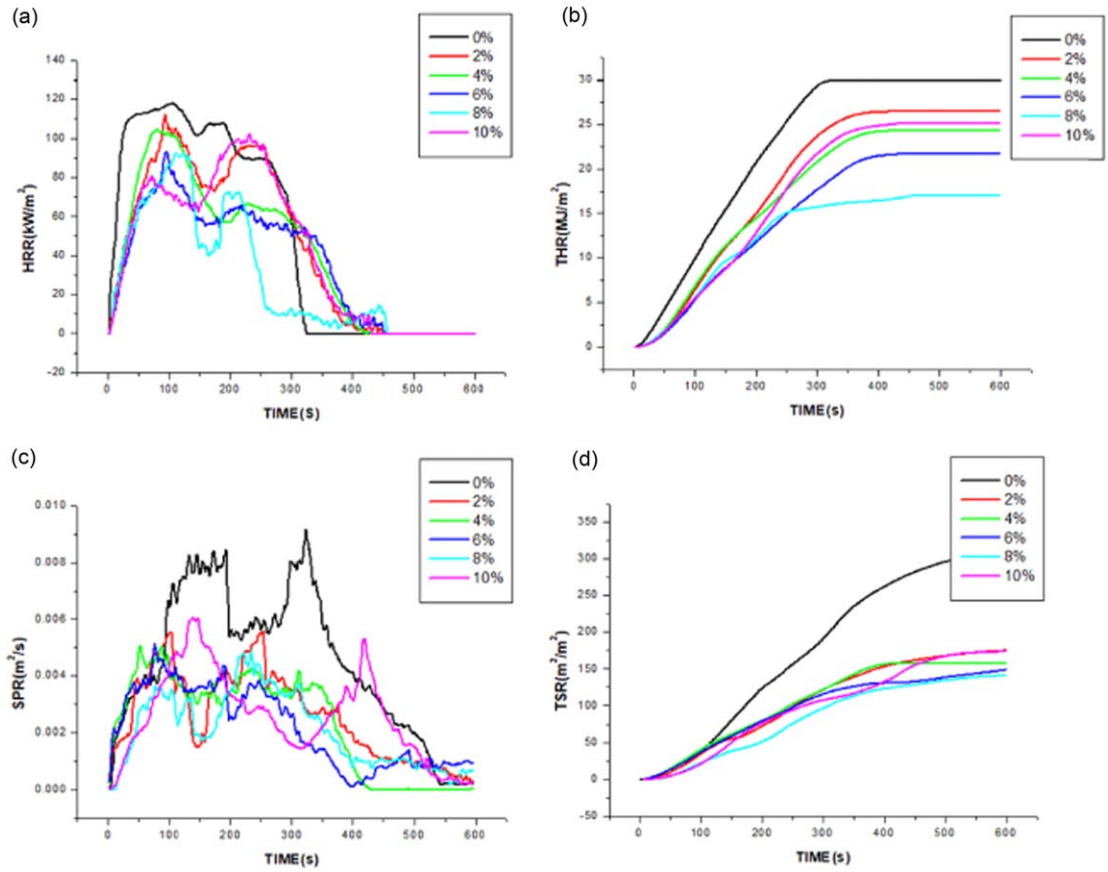


Figure 6. (a) HRR (Heat Release Rate), (b) THR (Total Heat Release), (c) SPR (Smoke Production Rate) and (d) TSR (Total Smoke Release) of RPUFs incorporated with copper powder.



Figure 7. Samples used for drilling test.

thrust force. A similar increase in thrust force was obtained by Debnath *et al* [15, 36] for thrust force at a higher feed rate.

3.4.2. Delamination analysis

The drilling parameters, as well as the characteristics of matrix and filler, ascertain the extent of delamination during drilling. ANOVA of the reduced quadratic model for the delamination is summarized in the table 6. the F-value of the model and its lack of fit values are 80.69 and 0.42 respectively, which ascertain the significance of



Figure 8. Drilled holes after performing drilling test at various factor levels.

the developed quadratic model. The p-value for the model is less than 0.01, which establish the highly statistical significance of the model at more than 99% confidence interval.

The p-value shows that the density, spindle speed and the drill diameter have shown significant effect on the delamination generated during the drilling, while the feed rate is insignificant in causing the delamination. Among these factors, the drill diameter is the most influential factor whereas, the influence of the density is the least amongst all. It was also noticed that the interaction of the spindle speed with the feed rate, second order of density, feed rate and drill diameter also have shown significant effects on the generated delamination. Figure 10 shows the 3D response surfaces of the developed quadratic model for the delamination. It was observed that the delamination decreases on increasing the spindle speed or density while the feed rate shows no effect on the delamination. Density, spindle speed, and drill diameter have shown a significant effect on the delamination generated during drilling, while feed rate is insignificant in causing delamination. Among these factors, drill diameter is the most influential factor whereas, the influence of density is least amongst all. The similar result was observed by Xing *et al* [37] while drilling carbon fibre reinforced carbon and silicon carbide composites.

Miguel Silva *et al* [27] also observed that drilling with high spindle speed and step geometry drill bits provides higher bearing strength in carbon/epoxy cross-ply composite plates. Additionally, increasing drill diameter shows a slight decrease in delamination. It is concluded from these plots that variability in delamination is little affected by the drilling parameters.

3.4.3. Residual compressive strength analysis

ANOVA of the reduced quadratic model for the residual compressive strength is summarized in the table 7. The F-value of the model and the lack of fit values are 97.20 and 0.22 respectively, while the p-value for the model is less than 0.01, which establish the highly statistical significance of the model at more than 99% confidence interval.

Table 4. Experimental results for drilling of RPUF composites.

Std	Run	Density (kg m^{-3})	Spindle speed (rpm)	Feed rate (mm rev^{-1})	Drill diameter(mm)	Thrust(N)	Delamination	Residual compressive strength(MPa)
1	6	302.5	342	0.34	6	14.70	1.27	3.81
2	28	387.5	342	0.34	6	35.45	1.19	4.56
3	5	302.5	914	0.34	6	20	1.22	4.35
4	15	387.5	914	0.34	6	45.62	1.15	6.45
5	21	302.5	342	0.78	6	15.23	1.31	3.86
6	25	387.5	342	0.78	6	35.34	1.26	5.1
7	23	302.5	914	0.78	6	15.38	1.20	3.78
8	1	387.5	914	0.78	6	35.32	1.14	5.96
9	13	302.5	342	0.34	10	18.36	1.18	1.89
10	19	387.5	342	0.34	10	35.56	1.12	4.2
11	11	302.5	914	0.34	10	32.56	1.09	2.96
12	14	387.5	914	0.34	10	46.68	1.05	6.5
13	10	302.5	342	0.78	10	26.95	1.18	2.26
14	18	387.5	342	0.78	10	42.92	1.16	4.87
15	4	302.5	914	0.78	10	36.53	1.06	2.2
16	12	387.5	914	0.78	10	48.54	1.02	6.2
17	2	260	628	0.56	8	17.54	1.29	2.28
18	7	430	628	0.56	8	52.38	1.19	7.2
19	24	345	56	0.56	8	20.73	1.19	3.22
20	30	345	1200	0.56	8	39.56	1.03	5.12
21	26	345	628	0.12	8	30.67	1.13	4.5
22	8	345	628	1	8	32.85	1.14	4.12
23	29	345	628	0.56	4	17.89	1.3	4.98
24	16	345	628	0.56	12	36.98	1.07	3.12
25	22	345	628	0.56	8	28.84	1.09	3.54
26	9	345	628	0.56	8	28.72	1.08	3.19
27	3	345	628	0.56	8	33.91	1.09	3.24
28	27	345	628	0.56	8	29.82	1.06	2.5
29	17	345	628	0.56	8	28.09	1.09	3.17
30	20	345	628	0.56	8	31.01	1.13	3.26

Table 5. ANOVA and Fit Statistics for Thrust Force on RPUF Composite.

Source	Sum of Squares	df	Mean Square	F-value	p-value	
Model	3058.96	9	339.88	93.32	<0.0001	Significant
ρ-Density	1933.21	1	1933.21	530.78	<0.0001	
v-Spindle Speed	366.45	1	366.45	100.61	<0.0001	
f-Feed Rate	5.65	1	5.65	1.55	0.2275	
d-Drill Diameter	497.22	1	497.22	136.52	<0.0001	
ρd	45.97	1	45.97	12.62	0.0020	
vf	40.51	1	40.51	11.12	0.0033	
vd	38.81	1	38.81	10.66	0.0039	
fd	82.26	1	82.26	22.59	0.0001	
ρ^2	48.87	1	48.87	13.42	0.0015	
Residual	72.84	20	3.64			
Lack of Fit	49.90	15	3.33	0.7248	0.7132	Not Significant
Pure Error	22.95	5	4.59			
Cor Total	3131.80	29				
Std. Dev.	1.91				**R^2**	0.9767
Mean	31.14				**Adjusted R^2**	0.9663
C.V.%	6.13				**Predicted R^2**	0.9519
PRESS	150.75				**Adequate Precision**	35.9585

The p-value shows that the density, spindle speed and the drill diameter have shown significant effect on the residual compressive strength of the drilled RPUFs. Among these factors, the density is the most influential factor whereas, the influence of drill diameter is least amongst all. It was also noticed that the interaction of the density with the spindle speed or the drill diameter and the interaction of the spindle speed with the feed rate,

Table 6. ANOVA and Fit Statistics for Delamination of RPUF Composite.

Source	Sum of Squares	df	Mean Square	F-value	p-value	
Model	0.1873	8	0.0234	80.69	<0.0001	Significant
ρ-Density	0.0160	1	0.0160	55.20	<0.0001	
v-Spindle Speed	0.0468	1	0.0468	161.36	<0.0001	
f-Feed Rate	0.0003	1	0.0003	0.9191	0.3486	
d-Drill Diameter	0.0748	1	0.0748	257.87	<0.0001	
Vf	0.0036	1	0.0036	12.41	0.0020	
ρ^2	0.0364	1	0.0364	125.57	<0.0001	
f^2	0.0027	1	0.0027	9.31	0.0061	
d^2	0.0140	1	0.0140	48.08	<0.0001	
Residual	0.0061	21	0.0003			
Lack of Fit	0.0035	16	0.0002	0.4198	0.9149	Not Significant
Pure Error	0.0026	5	0.0005			
Cor Total	0.1934	29				
Std. Dev.	0.0170				**R^2**	0.9685
Mean	1.15				**Adjusted R^2**	0.9565
C.V.%	1.48				**Predicted R^2**	0.9484
PRESS	0.0100				**Adequate Precision**	32.2324

Table 7. ANOVA and Fit Statistics for Residual Compressive Strength of RPUF Composite.

Source	Sum of Squares	df	Mean Square	F-value	p-value	
Model	56.14	11	5.10	97.20	<0.0001	Significant
ρ-Density	34.01	1	34.01	647.74	<0.0001	
v-Spindle Speed	5.66	1	5.66	107.70	<0.0001	
f-Feed Rate	0.0651	1	0.0651	1.24	0.2801	
d-Drill Diameter	4.60	1	4.60	87.66	<0.0001	
Pv	1.51	1	1.51	28.70	<0.0001	
Pd	2.39	1	2.39	45.61	<0.0001	
Vf	0.8789	1	0.8789	16.74	0.0007	
ρ^2	4.30	1	4.30	81.98	<0.0001	
v^2	1.76	1	1.76	33.61	<0.0001	
f^2	2.29	1	2.29	43.52	<0.0001	
d^2	1.37	1	1.37	26.13	<0.0001	
Residual	0.9451	18	0.0525			
Lack of Fit	0.3483	13	0.0268	0.2245	0.9861	Not Significant
Pure Error	0.5968	5	0.1194			
Cor Total	57.08	29				
Std. Dev.	0.2291				**R^2**	0.9834
Mean	4.08				**Adjusted R^2**	0.9733
C.V.%	5.62				**Predicted R^2**	0.9664
PRESS	1.92				**Adeq Precision**	35.7390

second order terms of density, spindle speed, feed rate and the drill diameter also have shown significant effects on the residual compressive strength.

Figure 11 shows the response surfaces of the developed quadratic model for the variation of residual compressive strength with the drilling parameters. It was observed that density, spindle speed, and drill diameter have shown a significant effect on the residual compressive strength of the drilled RPUFs. Among these factors, density is the most influential factor whereas, the influence of drill diameter is least amongst all. An increase in the residual compressive strength was observed on increasing spindle speed. This behaviour is accredited to the lower impact of spindle speed on the generation of delamination which consequently increases the residual compressive strength of the drilled RPUF. Miguel Silva *et al* [27] also observed similar conclusions while drilling carbon/epoxy cross-ply composite plates.

3.4.4. Optimization employing desirability function

Numerical optimization of the process parameters was performed by employing desirability function. Aim of the optimization was to maximize the residual compressive strength with minimized delamination. Desirability function of 1 is required to achieve the goal of optimization. Some best solutions with desirability function 1 are

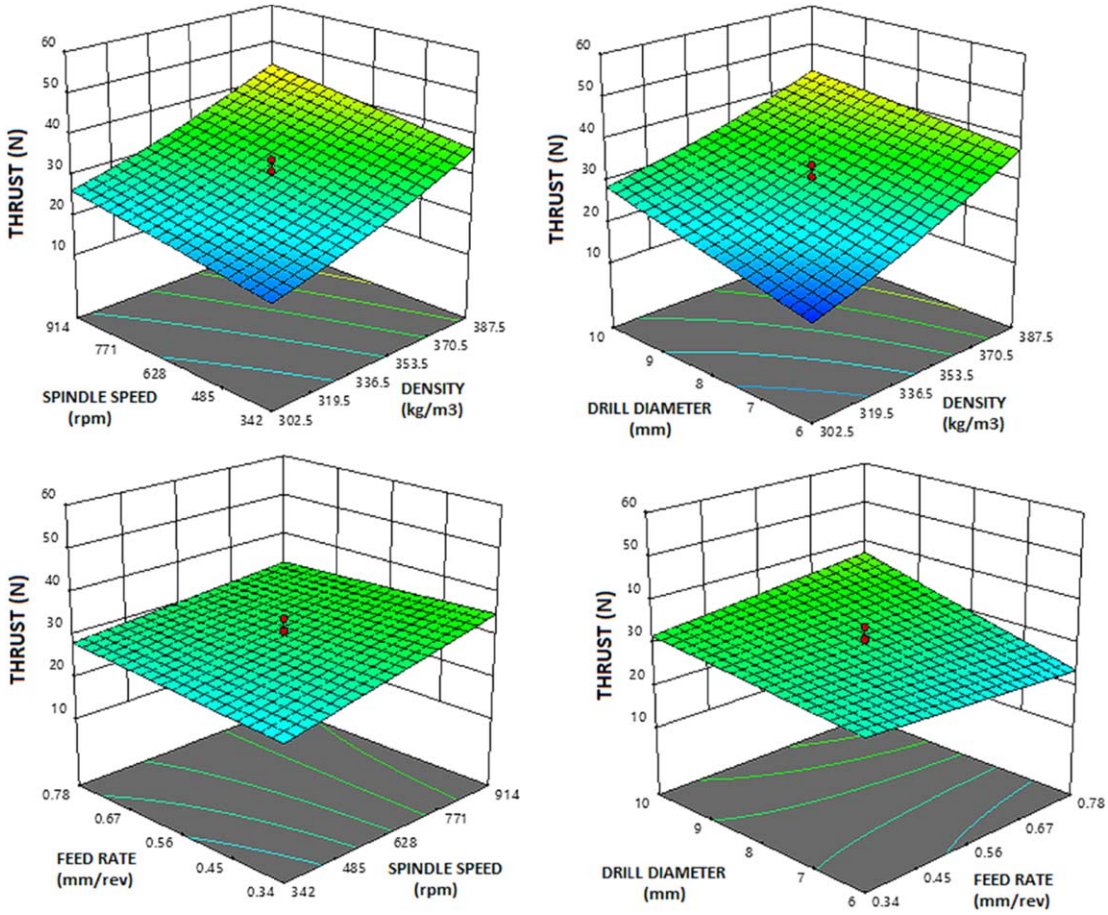


Figure 9. Response surface for the effect of drilling on thrust force.

presented in table 8. It was concluded from the results that high spindle speed and low feed rate are the optimized drilling parameters to obtain maximum residual compressive strength for varied density or drill diameter.

The developed quadratic model to predict responses (thrust force, delamination and residual compressive strength) for the factor levels at which experiment is performed, are presented in the form of coded equations (1)–(3) respectively. The relative impact of the drilling factors can be identified by comparing the factor coefficients provided by these equations.

$$\textbf{Thrust force (N)} = +30.10 + 8.97\rho + 3.91\nu + 0.4850f + 4.55d - 1.69\rho d - 1.59\nu f + 1.56\nu d + 2.27fd + 1.30\rho^2 \quad (1)$$

$$\textbf{Delamination} = +1.09 - 0.0258\rho - 0.0442\nu + 0.0033f - 0.0558d - 0.0150\nu f + 0.0361\rho^2 + 0.0098f^2 + 0.0223d^2 \quad (2)$$

$$\textbf{Residual compressive strength (MPa)} = +3.15 + 1.19\rho + 0.4854\nu - 0.0521f - 0.4379d + 0.3069\rho\nu + 0.3869\rho d - 0.2344\nu f + 0.3961\rho^2 + 0.2536\nu^2 + 0.2886f^2 + 0.2236d^2 \quad (3)$$

4. Conclusion

Rigid PU foams were prepared by incorporating copper powder to enhance the mechanical, flame retardant and thermal properties of foams and drilling experiments were performed to assess the machining ability of composite foams. Four drilling parameters, namely foam density, feed rate, drill bit diameter, and spindle speed, at five levels based on central composite design were studied. Conclusions drawn from the present investigation are as follows:

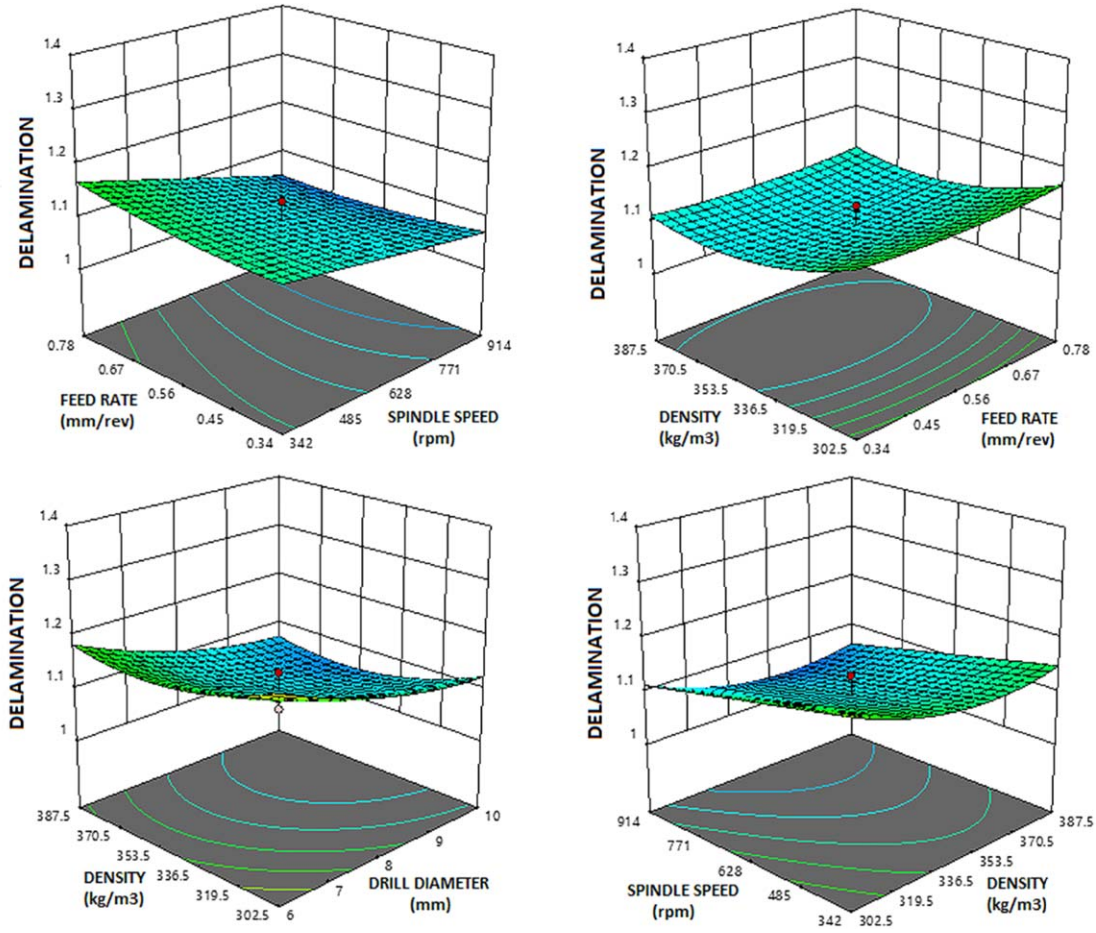


Figure 10. Response surfaces for the effect of drilling on delamination.

- Incorporation of copper filler enhances the compressive strength of the vegetable oil-based foam from 1.77 MPa for unreinforced RPUF to 3.83 MPa and 5% weight loss temperature increases from 192 °C to 257 °C for the 8% copper powder filled RPUF.
- Cone calorimeter test demonstrates that peak heat-release rate (PHRR) is decreased up to 93 kW m^{-2} and total heat release (THR) decreased up to 17.0 MJ m^{-2} on the incorporation of 8% copper powder in the RPUF. Furthermore, 50% decrease in smoke production rate (SPR) and 53% decrease in total smoke release (TSR) was observed in RPUF reinforced with 8% copper powder.
- It was noticed that density is the most influential factor for the optimization of residual compressive strength, while the feed rate shows a negligible effect on the responses. It is also observed that residual compressive strength increases with an increase in spindle speed.
- After numerical optimization, the optimal process parameters were selected as spindle speed 914 rpm and feed rate 0.34 mm rev^{-1} to maximize the residual compressive strength.
- A polynomial regression model showing the impact of density, feed rate, spindle speed and drill diameter on the responses was presented in the form of coded equations.

Acknowledgments

This work was supported by Defence Research and Development Organization (DRDO), India (Grant number: CC/TM/ERIPR/GIA/15-16/029).

Conflict of interest

The authors declare that they have no conflict of interest.

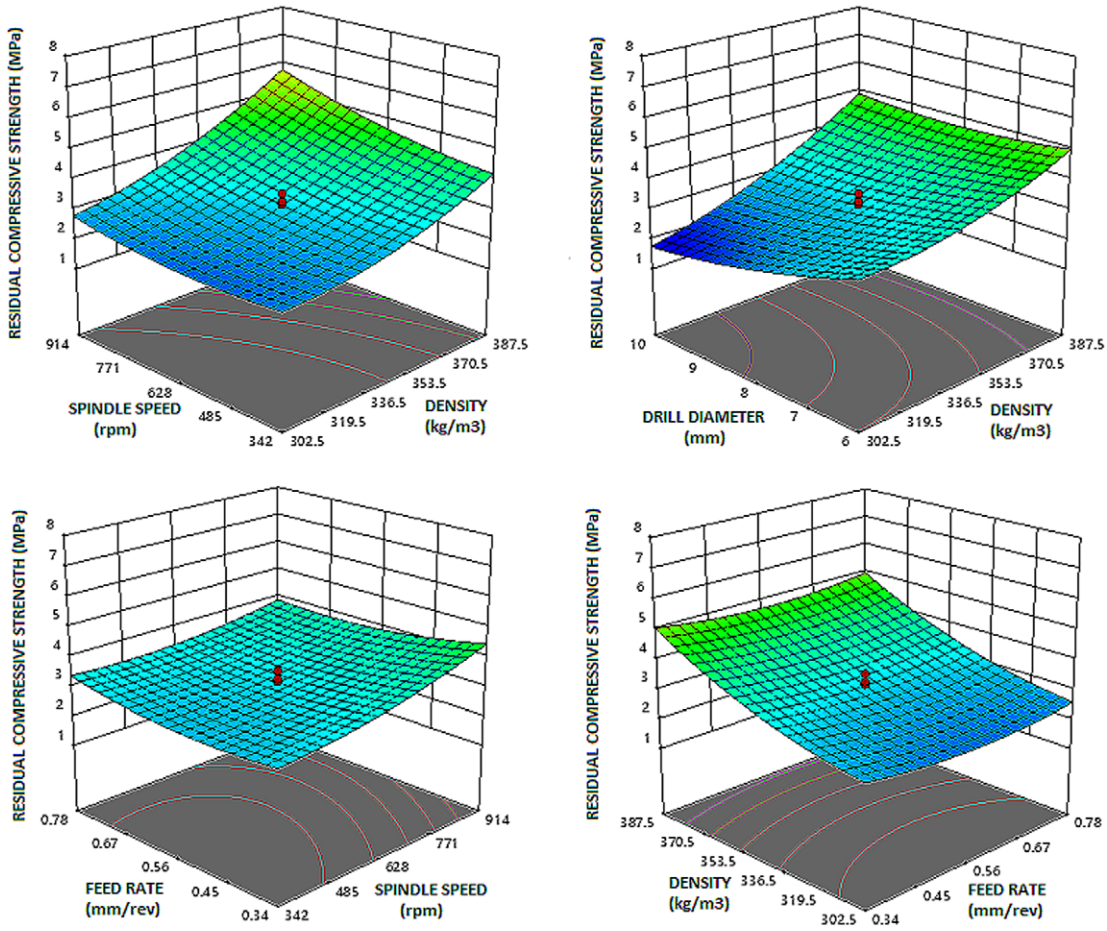


Figure 11. Response surface for the effect of drilling on residual compressive strength.

Table 8. Optimized values of factors and responses after numerical optimization.

S.no.	Density (kg m^{-3})	Spindle speed (rpm)	Feed rate (mm rev^{-1})	Drill diameter (mm)	Thrust force (N)	Delamination	Residual compressive strength (MPa)	Desirability function
1.	387.5	914	0.34	10	47.534	1.049	6.530	1
2.	387.5	914	0.34	6	43.240	1.160	6.632	1
3.	302.5	914	0.34	10	32.974	1.100	2.762	1
4.	302.5	914	0.34	6	21.90	1.212	4.411	1

ORCID iDs

Raminder Kaur https://orcid.org/0000-0001-7469-375X
R S Walia https://orcid.org/0000-0002-1578-4413

References

[1] Gama N V *et al* 2015 Bio-based polyurethane foams toward applications beyond thermal insulation *Mater. Des.* **76** 77–85
[2] Ciecierska E *et al* 2016 Flammability, mechanical properties and structure of rigid polyurethane foams with different types of carbon reinforcing materials *Compos. Struct.* **140** 67–76
[3] Zhou X, Sain M M and Oksman K 2016 Semi-rigid biopolyurethane foams based on palm-oil polyol and reinforced with cellulose nanocrystals *Compos. Part A Appl. Sci. Manuf. [Internet]* **83** 56–62
[4] Yang R *et al* 2017 Synthesis and characterization of flame retardant rigid polyurethane foam based on a reactive flame retardant containing phosphazene and cyclophosphonate *Polym. Degrad. Stab.* **144** 62–9
[5] Fourati Y *et al* 2017 A one step route synthesis of polyurethane newtwork from epoxidized rapeseed oil. Prog *Org. Coatings.* **105** 48–55
[6] Enderus N F and Tahir S M 2017 Green waste cooking oil-based rigid polyurethane foam *IOP Conf. Ser.: Mater. Sci. Eng.* 271
[7] Agrawal A, Kaur R and Walia R S 2017 PU foam derived from renewable sources: Perspective on properties enhancement: an overview *Eur. Polym. J.* **95** 255–74

[8] Malik M and Kaur R 2018 Mechanical and thermal properties of castor oil-based polyurethane adhesive: effect of TiO_2 filler *Adv. Polym. Technol.* **37** 24–30
[9] Kumar M and Kaur R 2017 Glass fiber reinforced rigid polyurethane foam: synthesis and characterization *e- Polym* **17** 517–21
[10] Luyt A S, Molefi J A and Krump H 2006 Thermal, mechanical and electrical properties of copper powder filled low-density and linear low-density polyethylene composites *Polym. Degrad. Stab.* **91** 1629–36
[11] Findik F 2014 Latest progress on tribological properties of industrial materials *Mater. Des.* **57** 218–44
[12] Chegdani F and Mansori M E 2018 Tribology international friction scale effect in drilling natural fiber composites *Tribol. Int.* **119** 622–30
[13] Hussain S A, Pandurangadu V and Kumar K P 2014 Optimization of surface roughness in turning of GFRP composites using genetic algorithm *Int. J. Eng. Sci. Technol.* **6** 49–57
[14] Jahanian E and Zeinedini A 2018 Influence of drilling on mode II delamination of E-glass/epoxy laminated composites *Theor. Appl. Fract. Mech.* **96** 398–407
[15] Roy M, Shanmuka M and Debnath K 2018 Experimental investigations on drilling of lignocellulosic fiber reinforced composite laminates *J. Manuf. Process. [Internet]* **34** 51–61
[16] Xavior M A and Kumar J P A 2017 Machinability of hybrid metal matrix composite—a review *Procedia Eng. [Internet]* **174** 1110–8
[17] Balani K *et al* 2015 Physical, thermal, and mechanical properties of polymers *Biosurfaces [Internet]* (Hoboken, NJ, United States of America: Wiley) p 329–44
[18] Kumar D and Singh K K 2017 ScienceDirect experimental analysis of delamination *Thrust Force and Surface roughness on Drilling of Glass Fibre Reinforced Polymer Composites Material Using Different Drills* **4** 7618–27
[19] Geier N and Szalay T 2017 Optimisation of process parameters for the orbital and conventional drilling of uni-directional carbon fibre-reinforced polymers (UD-CFRP) *Meas. J. Int. Meas. Confed. [Internet]* **110** 319–34
[20] Anuja A, Kaur R and Walia R S 2019 Engineering optimisation of process parameters for polymers : an overview *Int. J. Exp. Des. Process Optim.* **6** 89–126
[21] Zarif N, Heidary H and Minak G 2016 Critical thrust and feed prediction models in drilling of composite laminates *Compos. Struct.* **148** 19–26
[22] Heidary H, Zarif N and Minak G 2018 Investigation on delamination and fl exural properties in drilling of carbon nanotube / polymer composites *Compos. Struct. [Internet]* **201** 112–20
[23] Velaga M and Cadambi R M 2017 ScienceDirect Drilling of GFRP Composites for Minimising Delamination Effect *Mater. Today Proc.* **4** 11229–36
[24] Zarif N *et al* 2017 Experimental analysis of GFRP laminates subjected to compression after drilling *Compos. Struct.* **169** 144–52
[25] Díaz-álvarez A *et al* 2018 Experimental analysis of drilling induced damage in aramid composites *Compos. Struct.* **202** 1136–1144
[26] Xu J *et al* 2018 Study of drilling-induced defects for CFRP composites using new criteria *Compos. Struct.* **201** 1076–87
[27] Miguel J *et al* 2017 Correlation of drilling damage with mechanical strength : a geometrical approach *Compos. Struct.* **181** 306–14
[28] Kaur R and Kumar M 2013 Function of silicon oil in the castor oil based rigid polyurethane foams *J. Polym. Eng.* **33** 875–80
[29] Agrawal A, Kaur R and Walia R S 2019 Development of vegetable oil-based conducting rigid PU foam . *e-Polymers* **19** 411–20
[30] Lauke B 2017 Fracture toughness modelling of polymers filled with inhomogeneously distributed rigid spherical particles *Express Polym. Lett.* **11** 545–54
[31] Mazloom M and Salehi H 2018 The relationship between fracture toughness and compressive strength of self-compacting lightweight concrete *IOP Conf. Ser.: Mater. Sci. Eng.* **431** 062007
[32] Wu S *et al* 2019 Flame retardancy and thermal degradation of rigid polyurethane foams composites based on aluminum hypophosphite *Mater. Res. Express* **6** 105365
[33] Zhang M *et al* 2015 Effects of a novel phosphorus-nitrogen flame retardant on rosin-based rigid polyurethane foams *Polym. Degrad. Stab.* **120** 427–34
[34] Wang Y *et al* 2017 core–shell expandable graphite @ aluminum hydroxide as a flame-retardant for rigid polyurethane foams *Polym. Degrad. Stab.* **146** 267–76
[35] Zhang M *et al* 2014 Synthesis and fire properties of rigid polyurethane foams made from a polyol derived from melamine and cardanol *Polym. Degrad. Stab.* **110** 27–34
[36] Debnath K, Singh I and Dvivedi A 2014 Drilling characteristics of sisal fiber-reinforced epoxy and polypropylene composites *Mater. Manuf. Process.* **29** 1401–9
[37] Xing Y *et al* 2017 Assessment in drilling of C/C-SiC composites using brazed diamond drills *J. Manuf. Process.* **26** 31–43

IEEE Access
Multidisciplinary | Rapid Review | Open Access Journal

SPECIAL SECTION ON CLOUD - FOG - EDGE COMPUTING IN CYBER-PHYSICAL-SOCIAL SYSTEMS (CPSS)

Received January 19, 2020, accepted January 27, 2020, date of publication February 3, 2020, date of current version February 11, 2020.

Digital Object Identifier 10.1109/ACCESS.2020.2971087

Reviewer Credibility and Sentiment Analysis Based User Profile Modelling for Online Product Recommendation

SHIGANG HU[1], AKSHI KUMAR[2], FADI AL-TURJMAN[3,4], SHIVAM GUPTA[2], SIMRAN SETH[2], AND SHUBHAM[2]

[1]School of Information and Electrical Engineering, Hunan University of Science and Technology, Xiangtan 411201, China
[2]Department of Computer Science and Engineering, Delhi Technological University, New Delhi 110042, India
[3]Artificial Intelligence Department, Near East University, 99138 Nicosia, Turkey
[4]Research Center for AI and IoT, Near East University, 99138 Nicosia, Turkey

Corresponding author: Akshi Kumar (akshikumar@dce.ac.in)

This work was supported in part by the National Natural Science Foundation of China under Grant 61674056.

ABSTRACT Deciphering user purchase preferences, their likes and dislikes is a very tricky task even for humans, making its automation a very complex job. This research work augments heuristic-driven user interest profiling with reviewer credibility analysis and fine-grained feature sentiment analysis to devise a robust recommendation methodology. The proposed **c**redibility, **i**nterest and **s**entiment **e**nhanced **r**ecommendation (CISER) model has five modules namely candidate feature extraction, reviewer credibility analysis, user interest mining, candidate feature sentiment assignment and recommendation module. Review corpus is given as an input to the CISER model. Candidate feature extraction module uses context and sentiment confidence to extract features of importance. To make our model robust to fake and unworthy reviews and reviewers, reviewer credibility analysis proffers an approach of associating expertise, trust and influence scores with reviewers to weigh their opinion according to their credibility. The user interest mining module uses aesthetics of review writing as heuristics for interest-pattern mining. The candidate feature sentiment assignment module scores candidate features present in review based on their fastText sentiment polarity. Finally, the recommendation module uses credibility weighted sentiment scoring of user preferred features for purchase recommendations. The proposed recommendation methodology harnesses not only numeric ratings, but also sentiment expressions associated with features, customer preference profile and reviewer credibility for quantitative analysis of various alternative products. The mean average precision (MAP@1) for CISER is 93% and MAP@3 is 49%, which is better than current state-of-the-art systems.

INDEX TERMS Recommendation system, sentiment analysis, user credibility, user interest.

I. INTRODUCTION

The colossal growth in digital information and the number of visitors on the Internet has created intricate challenges for people to uncover potentially valuable information for long-time needs. The ever-widening flow of data is the by-product of this digital, networked economy. Big data is essentially changing how technology can serve consumers and enterprises. By analysing a periscope-level view of the myriad interactions, patterns, and anomalies taking place within an industry and market, big data can be used to drive new, creative products and tools to market. But primary difficulties include around kneading the data into a form that is useful for combining with other sets of information. It is thus imperative to upgrade information filtering mechanisms for customized and personalized services enabled by big data analytics. Recommender systems are one of the most common and easily understandable applications of big data. As a specialized information filtering system, a recommender system tries to make predictions on the basis of user preferences and interests [1]. Their use has been pervasive with interesting use-cases within variety of application domains that range from recommending products, movies, music, books, research articles, search queries, social tags, experts,

The associate editor coordinating the review of this manuscript and approving it for publication was Md. Arafatur Rahman.

This work is licensed under a Creative Commons Attribution 4.0 License. For more information, see http://creativecommons.org/licenses/by/4.0/

persons, jokes, restaurants, financial services and even twitter followers. There are two major paradigms of recommender systems, collaborative filtering and content-based methods. Collaborative filtering (CLF) is the process of filtering or evaluating items through the opinion of other people, who share similar interests [2]. CLF supports information filtering and retrieval, based on shared preferences and opinion. Content-based recommendation systems, on the other hand analyse item descriptions to identify items that are of particular interest to the user [3]. These systems collect description of potential items, profile of the user describing the types of items preferred by them and compare them to match user preferences, to determine recommendation results.

Most of the present-day recommender systems tend to use rating-information to quantify user-user, user-item and item-item similarities. Several techniques like clustering, nearest-neighbour methods, matrix manipulations, point-of-interest modelling have been used to model user interest patterns so as to maximize purchase satisfaction. But user-ratings are biased by certain hidden factors like brand-adherence and product-prejudice. So, sole considerations of rating-oriented similarity and user-interest analysis is rendered useless in the complex modern-day setting. The limited capabilities of user-ratings have given way to heuristic-driven, context-driven, sentiment and emotion-driven user-interest profiling.

Simultaneously, it has been observed that not all reviews and corresponding product ratings contribute to helpful recommendations. Moreover, spammers exploit these review platforms illegally because of incentives involved in writing fake reviews. Currently, fake reviews and reviewers form a bulk of the review opus making review spamming an open research challenge. These spam reviews must be detected to nullify their contribution towards product ratings. Reviewer credibility analysis can be used to quickly address deceptive online reviews and reviewers. Pertinent research studies suggest various parameters that can affect reviewer credibility. These include: linguistic styles, review clarity and comprehensiveness, word count, sentence count in reviews, helpful vote count, evidence (speaker's degree of certainty using certain propositional attitudes for example, certainly, surely) [4], [5].

Motivated by the two-fold need to firstly ascertain latent factors that affect user's fondness for a product/product category and to secondly quantify reviewer's credibility and review's quality for recommendation, we propose a **c**redibility **i**nterest and **s**entiment **e**nhanced **r**ecommendation (CISER) model. The model augments heuristic-driven user interest profiling with reviewer credibility analysis and fine-grained feature sentiment analysis to devise a robust recommendation methodology. Generically, user preferences can be described in implicit or explicit ways (Fig. 1). In this study, we use aesthetics of review writing as heuristics for mining user preferences. Aesthetics would indicate some sort of definable set, a list of knowable criteria used to evaluate the stylistic, thematic, and structural choices

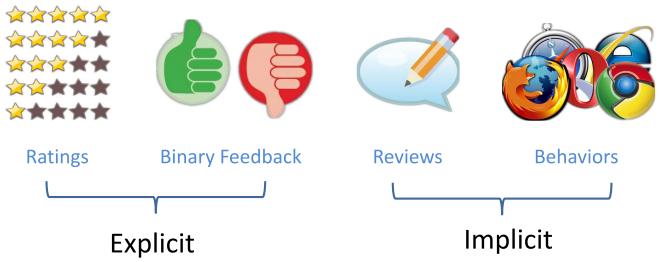


FIGURE 1. User preferences.

of a piece of writing. These aesthetics also foster reviewer and review reliability evaluation. Simultaneously, it is also essential to retrieve relevant and context-sensitive features to determine whether the reviewer's attitude towards a particular product is positive, negative, or neutral. Sentiment analysis enables analysing people's opinions, sentiments, evaluations, appraisals, attitudes, and emotions towards entities such as products, services, organizations, individuals, issues, events, topics, and their attributes [6].

Hence, the proposed CISER model proffers novel techniques for candidate feature extraction, reviewer credibility analysis, feature sentiment scoring and user interest modelling. Sentiment confidence and context derive the candidate features. Reviewer credibility scoring is done by quantifying review utility, content and percentage coverage of candidate features (*trust factor*); manipulating rating trends (*expertise factor*) and recording the influence of reviewer in the network (*network importance factor*). Review writing aesthetics are used to devise heuristics for user-preference modelling. The product recommendation is based on feature sentiment value calculated using fastText and at the same time using credibility-weighted sentiment feedback (in terms of factors that interest the particular user). To the best of our knowledge, this is the first work that integrates credibility driven feature-based fine-grained sentiment analysis with user interest modelling for online product recommendation. The key contributions of this work are:

- A recommendation model that combines user-preference modelling, reviewer credibility analysis and feature sentiment scoring for robust product ranking and recommendations.
- User preferences and interests are modelled without social information (number of followers, marital status etc.). Review writing aesthetics have been used for deriving heuristics that help in user-preference profiling.
- A model for reviewer credibility analysis is proposed which assigns credibility values to weight user opinions. Three metrics namely trust factor, network importance factor and expertise factor have been proposed for reviewer scoring. Language semantics, sentiment, consistency, coherence, rating trends and reviewer influence are exploited for credibility analysis.

The CISER model has six modules namely, candidate feature extraction, user product review mapping, reviewer credibility analysis, user interest mining, candidate feature

sentiment scoring and ranking and recommendation module. The Amazon's camera review dataset [7] is used to extract text and ratings along with some additional attributes such as number of helpful votes, number of total votes, verified purchase information, vine user verification information. Candidate feature extraction is done using context (spaCy[1]) and sentiment confidence (fastText[2]) to extract the features of importance. To make our model robust to fake and unworthy reviews and reviewers, reviewer credibility analysis proffers an approach of associating expertise, trust and influence scores with reviewers to weigh their opinion according to their credibility. The user interest mining module uses aesthetics of review writing as heuristics for interest-pattern mining. The candidate feature sentiment assignment module scores candidate features present in review based on their fastText sentiment polarity. Finally, the recommendation module uses credibility weighted sentiment scoring of user preferred features for purchase recommendations. This way, the proposed recommendation methodology harnesses not only numeric ratings, but also sentiment expressions associated with features, customer preference profile and reviewer credibility for quantitative analysis of various alternative products. The results have been evaluated using mean average precision (and compared with the current state-of-the-art systems).

The rest of the paper is organised as follows: in section II, we present related research within the domain of study. Section III describes the proposed CISER model in detail illustrating details of all its component modules. In section IV, a working example to support better understanding of the proposed model is given. Section V presents the experimentation and results followed by conclusion and future work in section VI. The frequently used abbreviations are tabulated in Table 1.

TABLE 1. List of abbreviations.

Abbreviation	Explanation
CBF	Content Based Filtering
CF	Coherence Factor
CFS	Candidate Feature Set
CISER	Credibility, Interest and Sentiment Enhanced Recommendation
CLF	Collaborative Filtering
EF	Expertise Factor
HV	Helpful Votes
NIF	Network Importance Factor
NIM	Network Importance Matrix
PC	Percentage Coverage
PSO	Particle Swarm Optimisation
RCA	Reviewer Credibility Analysis
RR	Representative Rating
RS	Recommender Systems
SC	Sentiment Confidence
TF	Trust Factor
TR	Total Ratings
TV	Total Votes
UIM	User Interest Matrix
VPI	Verified Purchase Information

II. RELATED WORK

Product recommender systems find applications within e-commerce (Amazon, Flipkart, and Big-basket) and media-service (Amazon-Prime, Netflix) domains. Various techniques for product recommendations like exploiting ratings for quantifying user-user and user-product adherence [content based and collaborative filtering], sentiment-analysis based recommendations, context-aware recommendations, user-preference and trust oriented recommendations have been reported. Literature is well equipped with primary and secondary studies on state-of-the-art techniques for recommender systems [8]–[10].

Primary studies on recommender systems (RS) have majorly focussed on product-ratings for modelling user-user and product-product similarity patterns. These RS find applications in several state-of-the-art software platforms developed to recommend movies [11], [12], songs [13] and videos [14] etc. But numerical rating-based RS ignore valuable review sentiment data and hence cannot model user interests completely. Therefore, research interests have started shifting to include human sentiments in rating products for recommendation. The need to model human aesthetics, linguistics and emotions (sentiment analysis) and using it for product acceptability analysis is inevitable.

Sentiment-analysis based RS have recently been reported in prominent natural language processing, information processing and business intelligence journals. Guerreiro and Rita [15] used a lexicon-based approach to search factors within text that uncover positive and negative triggers for direct recommendations. Chelliah and Sarkar [16] used several techniques for user-review exploitation. These included text mining methods for feature-specific sentiment analysis, topic models and distributed vocabulary representations. In "TRRuSST" [17], Gallege *et al.* used sentiment analysis for product ratings and extended CBF(Content-Based Filtering) and CLF(Collaborative Filtering) using user-reviews. External attributes were modelled for effective software product recommendations. Quian *et al.* [18] proposed "EARS"(Emotion-aware recommender system based on hybrid information fusion) that uses social information, sentiment analysis and gaussian distribution based user-behaviour analysis for recommendation. Da'u and Salim [19] proposed sentiment-aware deep recommender system with neural attention network (SDRA) that uses aspect based sentiment analysis for improving recommendation accuracies. The model reinforces semi-supervised topic modelling with LSTM (long short term memory) via neural attention mechanism for better modelling of user-item sentiments.

Although sentiment analysis based RS outperform the numerical-ratings based RS, still they do not always model user preferences accurately. User-profile plays a major role in understanding purchase preferences. Many research works focus on user-profile modelling and the role of user-product preference relationship in recommendation

[1]https://spacy.io/models/en
[2]https://github.com/facebookresearch/fastText

process. In "CUP" [20], Alan *et al.* presented the concept of inferred contextual profiles that describe a user in a given situation or context. Sanchez *et al.* [21] used ontological model to represent user and item profiles for advertisement recommendation. Wei *et al.* [22] proposed a method to determine user authority in a social tagging system for personalised recommendations. Xu and Liu [23] used semantic content and dynamic ontology modelling for user profiling to improve recommendation accuracies in event-based social networks. Covington *et al.* [14] used "DNN"(Deep Neural Networks) for video-recommendations using user-history and context. Another work by Liji *et al.* [24] used a network clustering model to cluster similar users and recommend items that the user may like. Xu *et al.* [25] presented user recommendation framework "UIS-MF" which captures interest and social factors to recommend users having similar interest and close social connection. Logesh *et al.* [26] proposed an activity and behaviour induced personalized RS to predict persuasive POI recommendations. Li *et al.* [27] used movie feature vector combined with the user rating matrix to generate the user interest vector. Tahmasbi *et al.* [28] gave an approach to model temporal dynamics of user preferences in movie recommendation systems based on a coupled tensor factorization framework. Middleton *et al.* [29] explored the acquisition of user profiles using browsing behaviour and presented an ontological representation to extract user preferences. Xie and Wang [30] proposed a web page recommendation based on two-fold clustering by considering both user behaviour and topic relation.

One of the key concerns with the use of customer reviews in RS is the quality of review and reviewer credibility. Several researchers have proposed criteria for opinion leader selection and review quality estimation. These include linguistic styles, review clarity and comprehensiveness; word count, sentence count in reviews; helpful vote count and evidence that quantifies the speaker's degree of certainty using certain propositional attitudes (certainly, surely). Al-Sharawneh and Williams *et al.* [31] made use of the "Follow the Leader" [32] model and proposed a novel technique for leader identification using social-profile information, trustability and expertise of reviewer. Li and Du [33] proposed an ontology-oriented model "BARR"(**B**log content, **A**uthors, **R**eaders and **R**elationship)that uses blog content, author, readers and centrality theory for hot-topic selection and credibility analysis. These hot-topics were further exploited for use in significant marketing policies. Chen *et al.* [34] explored the utility of trust relations to capture user attention. Poisson distribution is used to model trust relations; therefore the proposed model is robust to sparse data. Finally, Srivastava and Kalro [5] proposed certain latent factors that affect the credibility of reviews like readability, relevance, word-count etc. These works show that not all reviews and reviewers equally contribute to the assessment of product-acceptance in market. Moreover, spam reviews or opinions add to the criticalities, impairing the merit of recommendations.

The work proposed in this paper establishes a novel data-driven model for product recommendations. The work combines user preference profiling, reviewer credibility assignment and fine-grained sentiment analysis for recommendations. The model considers product reviews as a dependable source of comprehending user preferences and uses text analytics, fine-grained sentiment analysis and feature extraction to model user interests. Further, to make the model robust to fake and unworthy reviews and reviewers, we proffer an approach of associating expertise, trust and influence scores with reviewers to weigh their opinion according to their credibility. This work aims to optimise the credibility weighted sentiment value of user-preferred features for recommended products. The proposed **c**redibility, **i**nterest and **s**entiment **e**nhanced **r**ecommendation (CISER) model is explained in the next section.

III. THE PROPOSED CISER MODEL

The proposed CISER model reinforces the strength of fine-grained sentiment analysis in combination with reviewer credibility analysis techniques and user interest patterns to deal with the problem of product recommendations. CISER mainly consists of six modules namely (1) candidate feature extraction (2) user product review mapping (3) reviewer credibility analysis (4) user interest mining (5) candidate feature sentiment scoring and (6) ranking and recommendation module. Fig.2 depicts the architecture of the proposed CISER model.

The following subsections elucidate the details of each module:

A. DATASET ACQUISITION

We have used the Amazon Camera review dataset [7] which contains reviews and ratings given by various users for different brands of camera on the e-commerce website amazon.com. This data was released to encourage further research in multiple disciplines related to understanding customer product experiences. Specifically, this dataset was constructed to represent a sample of customer evaluations and opinions, variation in the perception of a product across geographical regions, and promotional intent or bias in reviews. This dataset has been used to train our model and study its practical utility. An overview of the dataset is given in Table 2.

In addition to review text and ratings, some additional attributes like number of helpful votes, number of total votes, verified purchase information, vine user verification information are available in the dataset, which have been used as auxiliary features in CISER. The complete description of data attributes is given in Table 3.

TABLE 2. Dataset overview.

Number of Products	35
Total number of Users	22768
Total number of Reviews	23256

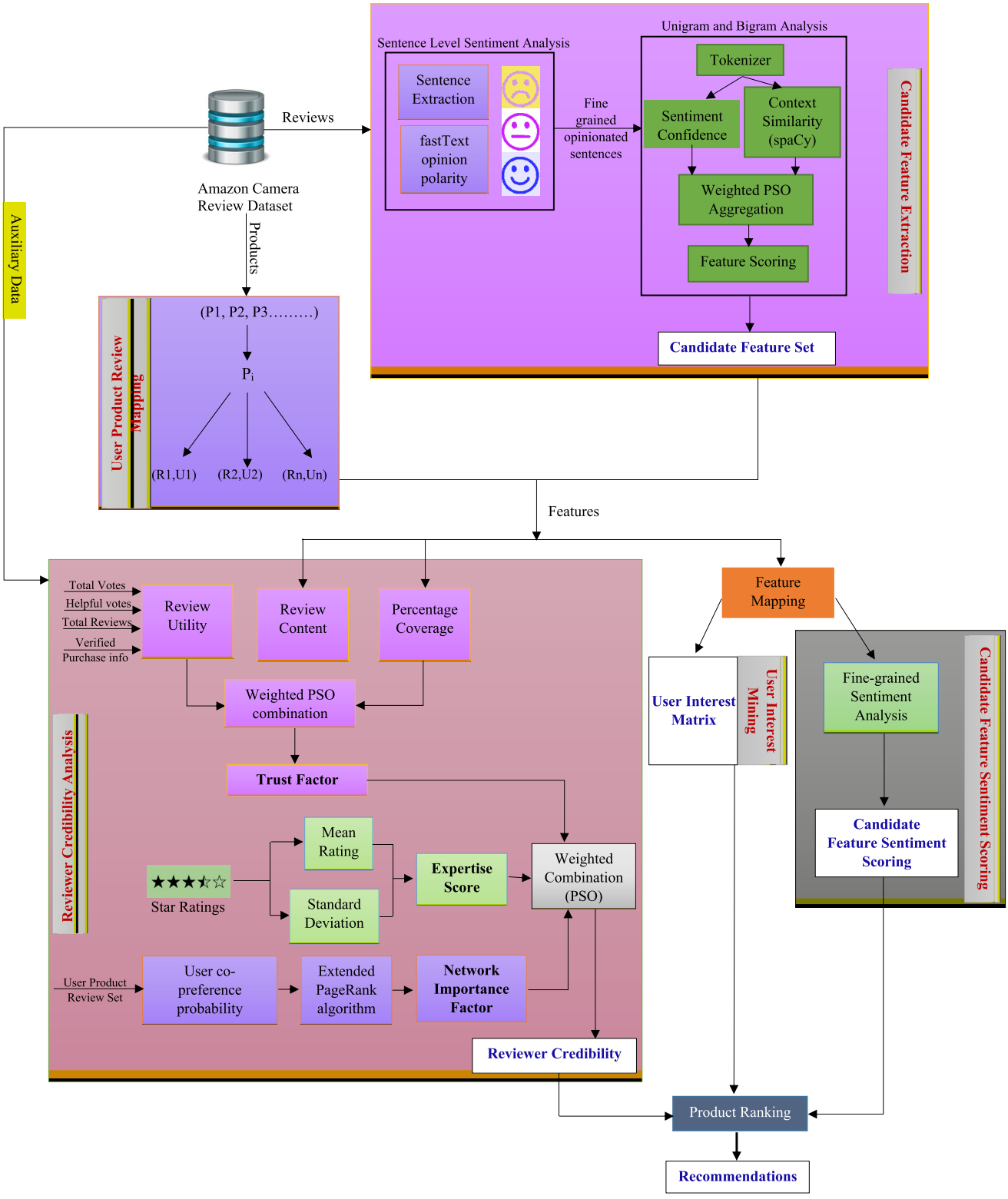


FIGURE 2. Architecture of CISER model.

B. CANDIDATE FEATURE EXTRACTION

User reviews comprise of multiple words, but not all words contribute to user's purchase preferences. A product feature is defined as 'any of the product's functionalities, capabilities, or its visual characteristics that may prove to be useful for its selection from alternatives'. For example, *'picture quality'*, *'battery-life'*, *'lens'*, *'resolution'* are some of the product features, in the context of a *'camera'*. This module uses

TABLE 3. Description of data attributes.

Column Name	Description
marketplace	2 letter country code of the marketplace where the review was written
customer_id	Random identifier that can be used to aggregate reviews written by a single author
review_id	The unique ID of the review
product_id	The unique Product ID the review pertains to. In the multilingual dataset the reviews for the same product in different countries can be grouped by the same product_id
product_parent	Random identifier that can be used to aggregate reviews for the same product
product_title	Title of the product
product_category	Broad product category that can be used to group reviews (also used to group the dataset into coherent parts)
star_rating	The 1-5 star rating of the review
helpful_votes	Number of helpful votes
total_votes	Number of total votes the review received
vine	Review was written as part of the Vine program
verified_purchase	The review is on a verified purchase
review_headline	The title of the review
review_body	The review text
review_date	The date the review was written

text-analytics for data reduction and extraction of features of importance, thereby enhancing the efficiency, speed and robustness of the system. It takes user reviews as input and outputs context-driven features (word lemmas) that further help in user preference modelling, review utility analysis and feature level sentiment mining. The methodology for candidate feature extraction can be broken down into two components:

- Sentence-level fine-grained sentiment analysis
- Unigram and bigram analysis

1) SENTENCE-LEVEL FINE-GRAINED SENTIMENT ANALYSIS

Sentiment Analysis is a quintessential text classification task which intends to categorize the opinion polarity of the incoming social media post to analyze the sentiment as positive, negative or neutral [35]–[38]. Text-driven sentiment analysis has been studied at several granularity levels. Recent literary works in this direction have focused on two key concepts which include aspect-based sentiment analysis [39] and fine-grained sentiment analysis [40]. Typically, aspect-based sentiment analysis goes one step further than sentiment analysis by automatically assigning sentiments to specific features or topics. It involves breaking down text data into smaller fragments, allowing more granular and accurate insights from your data. The fine-grained sentiment analysis involves sentiment scoring indicative of strong/weak sentiment intensities associated with the subtleties of human language. It breakdowns the sentiment into five discrete classes, namely, highly negative, negative, neutral, positive and highly positive.

In this study, fastText has been used for feature level fine grained sentiment analysis. fastText is a library for learning of word embeddings and text classification created by Facebook's AI Research lab. It has two major advantages. First, it takes into account the internal structure of words while learning word representations. Hence it is very useful for morphologically rich languages, and also for words that occur rarely. Second, fastText works well with n-grams, which makes it more suitable for our approach. Since we deal with real product reviews that capture complex human emotions, fastText provides the desired adaptability without compromising the space and time efficiency. The fine-grained sentiment rating is attached to all review sentences using fastText. Opinionated sentences are input to the next component, that is the unigram and bigram analysis.

2) UNIGRAM AND BIGRAM ANALYSIS

In this section, we explain how features are selected from the dataset. We focus on two types of product features [41]:

- **Unigram Product Features:** The product features comprising of a single word. Example: 'lens', 'resolution' etc.
- **Bigram Features:** The product features comprising of two words. Example: 'picture quality', 'red eye'. For the purpose of this study we limit our potential bigram features to 2-tuples possessing the following characteristics:
  - They should contain only nouns and adjectives. Specifically, 2-tuples of the form:
    - (Noun, Noun)
    - (Adjective, Noun) can only be considered as candidate features.
  - They should not contain any stop words or opinion lexicons.

Opinionated sentences (from section III-B1) are first tokenized to obtain word lemmas. These lemmas are scored by measuring their context similarity with the root ('camera' in our case), and probability of appearance in opinionated sentences (sentiment confidence). The context similarity is measured using spaCy, which is a library for advanced natural language processing in Python and Cython. Specifically, the "displaCy"[3] module of spaCy has been used for dependency parsing of sentences and target feature extraction. Fig. 3 depicts the dependency parsing of the sentence "The camera is very good" where opinion lexicon "good" maps to opinion target "camera".

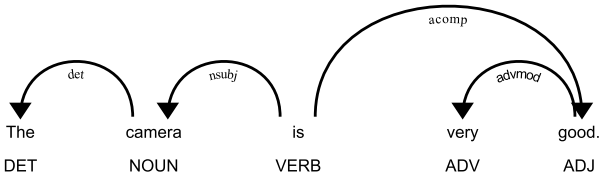


FIGURE 3. Dependency parsing and target feature extraction.

The sentiment confidence is derived using sentence sentiment ratings. For a given sentence, we first perform the opinion rating of the whole sentence (Section III-B1). From the sentence, target features are extracted (illustrated in fig. 3).

[3]https://spacy.io/universe/project/displacy

TABLE 4. Unigram features and feature scores.

Feature	Sentiment Confidence	Root Similarity Score
Lens	0.186	0.662
viewfinder	0.059	0.5984
photo	0.374	0.5354
Flash	0.6	0.5197
Mode	0.11	0.4129

TABLE 5. Bigram feature extraction and feature scores.

Feature	Sentiment Confidence	Root Similarity Score
Picture quality	0.6	0.5668
Battery life	0.56	0.478
Flash photography	0.4	0.543
Auto setting	0.3	0.42
Image processing	0.6	0.54

The target features are assigned confidence values based on the opinion rating. Equation (1) is used for measuring the sentiment confidence (SC):

$$SC_{f_i} = \frac{|OS_{f_i}|}{|OS|} \tag{1}$$

where,

SC_{f_i} = Sentiment Confidence for feature f_i
$|OS_{f_i}|$ = Number of Opinion sentences (Opinion Rating $\neq 3$) containing feature f_i
|OS| = Total Number of Opinion Sentences

Context Similarity score and Sentiment Confidence score are linearly combined using PSO before feature ranking, for most optimising feature extraction results. Some examples of features, their corresponding sentiment confidence score and root-similarity score are tabulated in Table 4 (Unigrams) and Table 5 (Bigrams).

C. USER PRODUCT REVIEW MAPPING MODULE

This module processes the review-dataset. Product data is extracted from the Amazon camera review dataset. All the product reviews and corresponding reviewers are obtained and further mapped with the product. The mapped data is input to the three modules namely user interest mining module, reviewer credibility analysis module and candidate feature sentiment scoring module.

D. USER INTEREST MINING

Many state-of-the-art recommendation systems like Netflix, Amazon and Flipkart maintain user interest profiles so as to recommend products based on their preferences, likes and dislikes. In this paper, we explore user reviews as source of mining user-interest patterns. The following heuristics help in modelling of the user-preference profile:

- **Heuristic 1(H1):** Users assess only a specified subset of product features based on requirement, taste and fondness. That is, some of the characteristics are more important than others. For example, cameras with 'high resolution' might be more important than its 'battery-life' for a user. So, it is likely that the user mentions resolution quality in most of his reviews, and says nothing much about the battery-life.
- **Heuristic 2(H2):** Numerical ratings seldom analyze the intricate details of products, but reviews present a rather detailed analysis. So, it can be assumed that different features of products can be assessed by analysing the reviews. On the whole, H2 suggests that reviews are a token to quantify product features quality, which can be used to enhance overall user experience.

Following the heuristic (H1), we propose that, a user is interested in a specific candidate feature, if he makes a frequent mention of it in his reviews. Frequency of allusion to specific features asserts their utility for users. It is highly unlikely that a user acknowledges feature f_i, but never touches upon it while reviewing the product. Hence, each user is associated with a user-interest matrix (UIM) which is a matrix estimating user-feature adherence. We use probabilistic values to estimate user interest as against hard binary (yes/no) values, since probabilistic values are a better representative of user-feature affinity. Binary affinity estimates depict a simplistic view of user preference trends that may not always capture the subtleties of human aesthetics. Hard (yes/no) heuristics are useful in cases where frequency of product purchase is low (eg. Furniture) as the number of reviews per user are limited. In all other cases probabilistic estimates improve user-interest modelling. Therefore, UIM is populated with feature count probability (equation (3)).

The equations (2) & (3) gives the mathematical representation.

$$UIM_u = [a_1, a_2, a_3, \ldots a_n] \tag{2}$$

$$a_i = \frac{FC_u^i}{|\,R_u\,|} \tag{3}$$

FC_u^i = number of times user u mentions feature i in reviews
n = number of features in CFS(Candidate Feature Set)
$|R_u|$ = number of reviews written by user u

After user preference profiling, the next step is to quantify the quality of preferred (candidate) features for the products [H2]. This is done using credibility weighted feature sentiment scoring. The following sections detail reviewer credibility analysis and candidate feature sentiment scoring modules that ultimately lead to product ranking and recommendations.

E. REVIEWER CREDIBILITY ANALYSIS

This module analyses the reliability of product reviewers for credibility score assignment. Reviewer credibility analysis (RCA) augments the recommendation capability of CISER and makes it robust to fake/unworthy reviews and reviewers. The following metrics are calculated for reviewer credibility scoring:

- Trust Factor (calculated using review utility; review content; percentage coverage)
- Expertise Factor (calculated using representative rating)
- Network Importance Factor

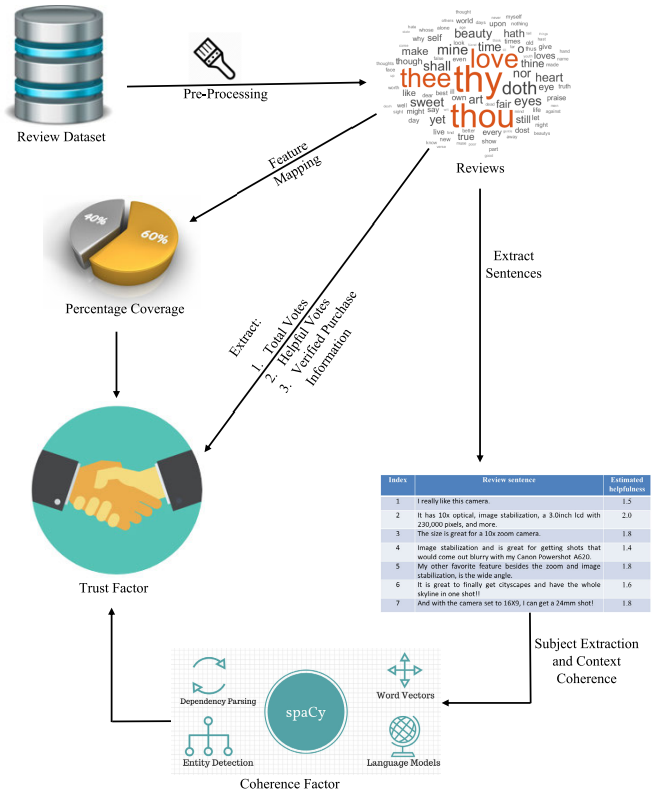


FIGURE 4. Trust factor calculation.

The following subsections expound the details of each of these factors.

1) TRUST FACTOR

Social psychology theory [42] proposes that role of a person in specific realm is indicative of the trust garnered by individual. This is the famous *"Follow The Leader"* [32] approach, whereby using some aspects of available information about individuals, we associate trust/credibility values with them. Following this strategy, we present a methodology for trust factor calculation for all reviewers. The following key-elements devise the trust factor of reviewer:

- Review Utility
- Review Content
- Percentage Coverage

Fig. 4 illustrates the trust factor calculation.

1) *Review Utility*
Review utility quantifies the user-perception about the review in consideration. It is measured using the following auxiliary factors extracted from dataset:

- **Total Votes(γ_{TV}):** This attribute is indicative of total number of potential buyers that have read and reviewed the product review in consideration.
- **Helpful Votes(γ_{HV}):** This value evocates the number of potential buyers who found the current product review useful in formulating purchase-decision. Metzger [43] suggests customers instinctively vote for reviewers having higher source credibility. Hence, higher the number of helpful votes possessed by a reviewer, higher is the trust that fellow customers associate with him.
- **Verified Purchase Information(γ_{VPI}):** Generally, potential buyers attach greater importance to reviews where reviewer has actually used the product, as against reviewers commenting without prior-knowledge of product features. Verified Purchase Information is a Boolean attribute that assures a reader of purchase-status of reviewer.
- **Total Ratings(γ_{TR}):** This value is a measure of total number of times the reviewer has rated products of the product-domain in consideration. It is a value derived from user product review mapping. This is a direct indicator of the association of the reviewer, with products of that type. Hence, it can easily be said that frequent reviewers are more likely to be domain experts, who can formulate general opinion about the product, when compared to occasional reviewers [5], [31].

2) *Review Content*
The quality of review content can be assessed using:

- **Coherence Factor:** The coherence of text is contemplated by its syntactic and semantic structure and relations. Research and language experts suggest that language has a definitive assembly. Language expression says a lot about the intent of reviewer and quality of the review on the whole. As Sheng Tun Li [4] mentions in his work, several linguistic indicators like capitalisation, emoticons, spelling errors, semantics, regularity, consistency etc. play a major role in devising user credibility. We propose coherence factor as an indicator of relevance and hence quality of review. We focus on semantics, regularity and consistency of the review. Precisely, coherence factor measures the context-pertinence and consistency of sentences in reviews, which is a determinant factor for reviewer credibility assessment. It measures the context similarity of review sentences with candidate features, and thereby measures the consistency of context in reviews. Equations (4), (5) and (6) help calculate the coherence factor.

$$coherence_{review_{id}} = \sum_{i=1}^{|S|} \frac{cs\,(sub_i)}{|S|} \tag{4}$$

where,
$|S|$ = Total number of sentences in the review corresponding to review id
$cs(k)$ = context similarity of k with root context calculated using spaCy
sub_i = subject of i^{th} sentence

$$\mathrm{cs}\,(\mathrm{sub_i}) = \max\,(\mathrm{sim}\,(\mathrm{sub_i},\ \mathrm{feat})) \tag{5}$$

where,

$max(sim(sub_i, feat)) > sim(sub_i, feat)\ \forall$ feat $\in$ feature set (section III-B)
$sim(sub_i, feat)$ = context similarity of sub_i with feat (feature in consideration)

$$CF_{user_{id}} = \sum_{\substack{x \in \{review_{id}: \\ reviewer(review_{id}) = user_{id}\}}} \left(\frac{coherence_x}{|r|}\right) \tag{6}$$

where,
$CF_{user_{id}}$ = Review coherence factor pertaining to current reviewer
$|r|$ = Number of reviews of current reviewer

- *Percentage Coverage(PC)*
  This factor measures what percentage of candidate features are referred to by the reviewer in his reviews (running average measure). Expert reviewers critically analyse products over various baseline features (Hence their reviews possess high percentage coverage). In turn, their reviews influence readers and apprise them about the downfalls and salient perspectives of product. Mathematically, this is characterized using (7).

$$S_{noun} = \text{set of nouns proper nouns in review}$$
$$S_{features} = \text{set of candidate features (section III-B)}$$
$$PC_{review_{id}} = \frac{S_{noun} \bigcap S_{features}}{|S_{features}|} \times 100 \tag{7}$$

Using these 6 key factors, methodology for calculation of trust factor(TF^u) for each user(u) is mathematically illustrated in (8).

$$TF^u = w_{TR} \times \gamma_{TR_u} + \sum_{x \in \{review_{id}: reviewer(review_{id}) = u\}} \times \left\{ \left(\gamma_{VPI_x} + |1 - \gamma_{VPI_x}| \times w_{VPI} \right) \times \left(w_{cc} \times coherence_x \times PC_x + w_v \times \left(2 \times \gamma_{HV_x} - \gamma_{TV_x}\right) \right) \right\} \tag{8}$$

where,
w_{VPI}, w_{cc}, w_v, w_{TR} are weights assigned to unverified purchases (where the reviewer did not buy the product), Coherence-Coverage product, Useful (i.e. Helpful-Unhelpful) Votes and Total Ratings respectively.

2) EXPERTISE FACTOR

Expertise is a key aspect for user credibility analysis, it is defined as the degree of a user's competency to provide accurate ratings and exhibit high activity [44] There are various dimensions to this definition: (1) Expertise is directly related to *user's competency* to present the general opinion, by means of his reviews and ratings; (2) The second key aspect is *high activity exhibition*, which means domain experts are more active in reviewing newly launched products and their assessment is generally highly appraised by public.

In this study, we propose a novel measure for expertise measurement. The motivation for Expertise factor has been taken from [31], but it has been modified to meet some of its original shortcomings. The following terminology will be crucial for further calculations and derivations.

1) *Representative Rating*
Representative rating (RR) is a quantitative indication of the opinion of masses. It is a quantity that represents product rating, such that it is inclusive of all the reviews for the product. In previous studies [31] mean rating is used as representative rating but there are several downfalls to this approach, the most important of them being mean rating ignores the standard deviation of distribution. Mean is a good representation of a set, if data is uniformly distributed. For skew data, mean is an approximation, but better estimates can be made. To deal with this problem, we add a quantity α to mean, to model each type of data in a more balanced manner, as given in (9):

$$\alpha_i = \frac{\left(\sum_{\gamma \in X_{1_i}} \gamma\right) - \left(\sum_{\gamma \in X_{2_i}} \gamma\right)}{2 \times sd_i \times |X_i|} \tag{9}$$

X_i = Set of Product Ratings for Product i
μ_i = Mean of Product Ratings for Product i
X_{1i} = $\{x \in X_i \text{ and } x > \mu_i\}$
X_{2i} = $\{x \in X_i \text{ and } x < \mu_i\}$
sd_i = standard deviation of product ratings for i
RR_i = $\mu_i + \alpha_i$

α shifts the mean representation towards the more heavily voted side i.e. mean is shifted towards majority opinion.

Thus, expertise factor for a user(u) for a specific product(i) (EF_i^u) is defined as proximity between user's perspective rating and the representative rating (RR_i). Mathematically, expertise factor is given by (10).

$$EF_i^u = 1 - \frac{abs\left(RR_i - R_i^u\right)}{5} \tag{10}$$

where,
5 is the scaling factor
$0 < RR_i \leq 5$ and $0 < R_i^u \leq 5$ hence,
$0 \leq abs(RR_i - R_i^u) \leq 5$
R_i^u = User(u) Rating for product i
(EF_i^u) is used to derive EF^u i.e. expertise factor for user u. EF^u is defined as average of (EF_i^u) over all products i, rated and reviewed by user u.

3) NETWORK IMPORTANCE FACTOR

Network Importance Factor (NIF) is a measure of the influence of a particular user in defining overall public assessment of a product. In this work, we modify PageRank algorithm [45] which is conventionally used for devising webpage

ranks, to uncover the most influential reviewers. To understand the conception of NIF and it's relation to webpage ranking algorithm, readers need to have a basic understanding of PageRank algorithm. The underlying assumption in PageRank algorithm is "more important websites are likely to receive more links from other websites", on similar lines, the fundamental antecedent behind the conception of NIF is " The most influencing reviewer is likely to share product preferences, with those of people they influence" hence leading to the formula given in (11).

$$
\begin{aligned}
&NIM(\text{Network Importance Matrix}) \\
&\quad = \begin{bmatrix} a_{11} & \cdots & a_{1N} \\ \vdots & \ddots & \vdots \\ a_{N1} & \cdots & a_{NN} \end{bmatrix} \\
&a_{ij} \\
&\quad = \begin{cases} \dfrac{\left|P[u_i] \cap P[u_j]\right|}{\left|\{x_k \mid P[x_i] \cap P[x_k] \neq \phi\}\right|} & : \left|\{x_k\}\right| \neq 0 \\ \dfrac{1}{N} & : \text{otherwise} \end{cases} \\
&NIF_0 \\
&\quad = \begin{bmatrix} 1.0 & 1.0 & \cdots & 1.0 \end{bmatrix}_{1\times N} \\
&NIF_k \\
&\quad = (1-d) \times d \times (NIM \times NIF_{k-1}) \qquad (11)
\end{aligned}
$$

where,

d is a damping factor between 0 and 1

a_{ij} is User co-preference probability of users i and j

$P[u_i]$ is the Set of Products reviewed by user(u_i)

$NIF_k[u_i]$ is the Network Importance Factor of user(u_i) at k^{th} iteration.

Thus, the three Factors i.e. Trust Factor, Expertise Factor and Network Importance Factor are linearly combined using PSO for final credibility scores assignment.

F. CANDIDATE FEATURE SENTIMENT SCORING

CISER attempts to combine user-preference and sentiment value for increasing the efficacy of recommendations. It aims to suggest those products that have a better sentiment value compared to the products previously purchased by the user. For this, product-level candidate feature sentiment scoring is done using fastText. The candidate features (present in CFS) are searched in product review, and then the sentence level fine-grained opinion (fastText) is attached to those features. These feature-sentiment scores are then combined with reviewer credibility for product ranking. The details of product ranking are discussed in the next section.

G. PRODUCT RANKING AND RECOMMENDATION METHODOLOGY

The last step of this study focusses on ranking each product among contextually similar products. This calls for combining reviewer credibility, user-interest and candidate feature sentiment for product scoring. Credibility weighted fine grained feature sentiment (for user-preferred features) is averaged over all product-reviews to calculate product rank. Products with highest ranks are recommended to a user. CISER is robust to user prejudice, since credibility normalises personal bias based on perspective knowledge (Expertise Factor). Also, fine grained feature sentiment analysis is in line with heuristic H2, as even the feature level acceptability-details are captured. User interest matrix stands consistent with the premise of heuristic H1. It ensures that only those features are considered for product ranking which are important to User U. Hence, CISER is an attempt to automate credibility driven feature quality assessment using electronic word of mouth. Algorithm 1 presents the recommendation algorithm.

Algorithm 1 Recommendation Algorithm

Input: Product Features: F, Products: P, Set of Reviews: Z, Reviewer Credibility: γ_{cred}, User to recommend products to: U, Number of products to be recommended: K, User Interest Matrix: UIM_u

Output: Recommended Products: *recommendedProducts*

1 $g(review, feature) \leftarrow \begin{cases} 1 & : feature \in review \\ 0 & : \text{otherwise} \end{cases}$

2 $\forall p \in P : rank[p] \leftarrow$
$\sum_{x\in F}\left(\frac{\sum_{r\in Z[p]} \text{fineGrainedSentiment}(x,r)\times\gamma_{cred}[user[r]]\times g(r,x)}{\sum_{r\in Z[p]}\gamma_{cred}[user[r]]\times g(r,x)} \times UIM_u[x]\right)$

3 *recommendedProducts* $\leftarrow$
Top K products according to *rank*

IV. WORKING EXAMPLE

In this section we will discuss an example to enable better understanding of the workflow of CISER model for product recommendation.

A. CANDIDATE FEATURE EXTRACTION

As discussed, this phase has two components, namely, sentence-level fine-grained sentiment analysis and Unigram & Bigram analysis.

1) SENTENCE LEVEL FINE GRAINED SENTIMENT ANALYSIS

This module takes a user review as an input, extracts sentences and then associates fine-grained sentiment values with each sentence as shown in table 6.

2) UNIGRAM AND BIGRAM ANALYSIS

Sentiment determining unigram (Noun / Proper - Noun) and bigram features [(Noun - Noun) / (Adjective - Noun)] are extracted in this phase. The extraction depends on sentiment confidence and similarity scores. Suppose, the unigram candidate feature is 'zoom'. Suppose 1000 review sentences contain 'zoom' out of total 20,000 opinion sentences. So, the calculated sentiment confidence of zoom is

TABLE 6. Fine-grained sentiment analysis.

Review	Sentence Extraction	Opinion Score
Amazing telescope! Main reasons why? Fully Automated with amazing zoom. Awesome Picture Quality. But the battery life was not up to the mark.	Amazing Telescope	5
	Main reasons why	3
	Fully Automated with amazing zoom	5
	Awesome Picture Quality	5
	But the battery life was not up to the mark.	2

TABLE 7. Coherence Factor (CF) calculation.

Review	Review Sentence	Subject	Closest Feature	CS(subj)
The picture quality is awesome. My wife really liked it.	The picture quality is awesome	picture-quality	picture-quality	1
	My wife really liked it	wife	photo	0.15

1000/20,000 = 0.05. The spaCy similarity of 'zoom' with root-context 'camera' is 0.56. These values are linearly combined using PSO for feature ranking and extraction.

B. USER INTEREST MINING

This module takes as input the candidate features (Section III-B) and the user product review mapped data (Section III-C), user interest matrix is produced as an output. Let the only review of user U101 be "The picture-quality is awesome. Also, the zoom, lens and battery-life are magnanimous". And the candidate feature set be {"picture-quality", "zoom", "lens", "battery-life", "photo"}. The pre-stated review adds {"picture-quality", "zoom", "lens", "battery-life"} to the set of user interest, hence leading to user interest vector for U101 as:

$$[1\ 1\ 1\ 1\ 0]$$

where the columns correspond to {"picture-quality", "zoom", "lens", "battery-life", "photo"} respectively. This calculation follows the heuristic H1. Following the same lines, user interest matrix is calculated for all the users and fed as an input to ranking and recommendation module.

C. REVIEWER CREDIBILITY ANALYSIS (RCA)

The credibility aspects related to review utility are extracted from data-set and described in section III-E1. The other associated aspects are:

1) COHERENCE FACTOR

For calculating review coherence, the review body and candidate feature set is given as input and the associated coherence factor is obtained as output as shown in table 7.

So, the CF for the review = $(1 + 0.15)/2 = 0.575$ CF_u is average CF over all the reviews written by user U that pertain to the particular product domain.

2) PERCENTAGE COVERAGE

This factor measures what percent of candidate features are mentioned in a review. The review and set of features are given as an input to this module, percentage coverage of the review is received as output. Table 8 summarizes the process.

TABLE 8. Percentage coverage calculation.

Review	Mapped Features	Total Features	Percentage Coverage
The picture-quality is awesome. Also, the zoom, lens and battery life is magnanimous.	picture-quality, zoom, lens, battery-life	37	$4/37 = 0.108$

TABLE 9. Product ratings.

User ID	Star Rating
U101	2
U102	5
U103	5
U104	4

3) EXPERTISE FACTOR

Expertise factor depends on the star-ratings given by users to products. As an illustration, let the star ratings for product P_i be as depicted in Table 9. The mean rating for product $P_i(\mu_i) = 4$ and standard deviation (sd_i) is 1.414. Number of ratings $< (\mu_i) = 1$ and number of ratings $\geq (\mu_i)$ are 3. The calculation of α_i is as follows using (9).

$$\alpha_i = \frac{\left(\sum_{\gamma \in X_{1_i}} \gamma\right) - \left(\sum_{\gamma \in X_{2_i}} \gamma\right)}{2 \times sd_i \times |X_i|} = \frac{3-1}{2 \times 1.414 \times 4} = 0.1767$$

The representative rating $(RR_i) = (\mu_i + \alpha_i) = 4 + 0.1767 = 4.1767$

$$EF_i^u = 1 - \frac{abs\left(RR_i - R_i^u\right)}{5}$$

So, for user U101, $EF_i^u = 1 - \frac{abs(4.1767-2)}{5} = 0.5646$
Similarly, expertise scores for all the users are evaluated.

4) NETWORK IMPORTANCE FACTOR

Network Importance Matrix (NIM) is needed for the calculation of NIF for all users. The calculation of each element of NIM is illustrated in table 10.

Taking the example as in table 10, it is clear that both U1 and U2 rated P2, Hence $P[U_1] \cap P[U_2] = 1$ and $|x_1| = 2$ as U2 and U3 share at least 1 review preference with U1.

$a_{12} = 1/2 = 0.5$

Similarly, the NIM matrix is calculated.

TABLE 10. Product review mapping.

User ID	Products Reviewed
U1	P1, P2, P3, P4
U2	P2, P5
U3	P3
U4	P5

$$\text{Let the final NIM Matrix be } \begin{bmatrix} 1 & 0.2 & 0.2 & 0.1 \\ 0.35 & 1 & 0.1 & 0.1 \\ 0.5 & 0.2 & 1 & 0.1 \\ 0.5 & 0.1 & 0.2 & 1 \end{bmatrix}$$

$$NIF_0 = [1.0 \;\; 1.0 \;\; \ldots \;\; 1.0]_{1\times N}$$
$$d = 0.8$$

The first iteration for calculation of NIF is as shown:

$$\begin{aligned} NIF_1 &= (1-d)/4 + d \times (NIM \times NIF_0^T) \\ &= \frac{0.2}{4} \times \begin{bmatrix} 1 \\ 1 \\ 1 \\ 1 \end{bmatrix} + 0.8 \cdot \begin{bmatrix} 1 & 0.2 & 0.2 & 0.1 \\ 0.35 & 1 & 0.1 & 0.1 \\ 0.5 & 0.2 & 1 & 0.1 \\ 0.5 & 0.1 & 0.2 & 1 \end{bmatrix} \cdot \begin{bmatrix} 1 \\ 1 \\ 1 \\ 1 \end{bmatrix} \\ &= \begin{bmatrix} 1.25 \\ 1.29 \\ 1.49 \\ 1.49 \end{bmatrix} \end{aligned}$$

The other iterations can be done similarly for calculating Network Importance Factor for each User.

D. CANDIDATE FEATURE SENTIMENT SCORING

Fine-grained sentiments are associated with all the candidate features present in review. Table 11 illustrates the process:

TABLE 11. Candidate feature sentiment scoring.

Review	Feature in review	Feature Sentiment
The picture-quality is awesome. Also, the zoom, lens and battery-life are magnanimous.	picture-quality	4
	zoom	5
	lens	5
	battery-life	5

E. PRODUCT RANKING AND RECOMMENDATION

In this section we illustrate the contribution of one review towards product ranking as shown in table 12.

Table 12 represents a review for product P1 given by U101. It clearly illustrates that user in consideration (For whom product is being ranked) is interested in "picture-quality" and "zoom" and so only those feature sentiments contribute to product rank.

Review Contribution $= (0.7) \times (4+5)/2 = 3.15$

These review contributions are aggregated as presented in Algorithm 1 in section III-G for final product scoring and recommendation.

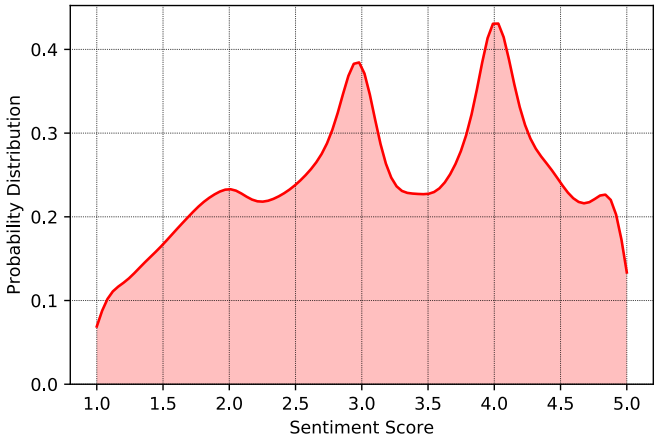


FIGURE 5. Sentiment score distribution.

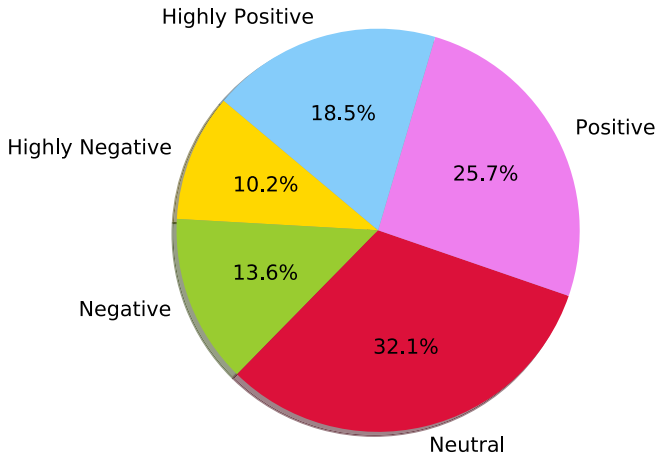


FIGURE 6. Percentage sentiment distribution.

V. EXPERIMENTATION AND RESULT

Amazon camera dataset has been used for evaluating the efficacy of our approach. 3500 reviews given by 1000 users over 10 products are used for the validation phase to predict recommendation accuracies. The sentiment distribution of validation data has been presented in fig. 5 and 6.

The following sub-sections discuss recommendation performance results, hyper-parameter tuning and comparison with baseline models.

A. RECOMMENDATION PERFORMANCE RESULTS

In order to assess the utility of our recommendation system, we have used Mean Average Precision (MAP) as the evaluation metrics. MAP is an extension of Average Precision (AP) where we take average of all AP's to calculate MAP. Average precision is a measure that combines recall and precision for ranked retrieval results. The mathematical equations for the metrics MAP and AP are listed in Table 13.

Specifically, we are using MAP@N as the metrics, where N is the number of products recommended to each user. Fig. 7 shows the variation of Mean Average Precision with Number of Recommendations. For single product recommendation,

TABLE 12. Review contribution to product rank.

Review	Reviewer Credibility	Feature in review	User Interest value for feature	Feature Sentiment
The picture-quality is awesome. Also, the zoom, lens and battery-life are magnanimous.	0.7	picture-quality	1	4
		zoom	0	5
		lens	1	5
		battery-life	0	5

TABLE 13. Metrics for recommendation efficiency.

Metrics	Formula
Average Precision@N	$\frac{1}{N} \times \sum_{k=1}^{N} (\text{Precision}(k) \times \Delta\text{Recall}(k))$
Mean Average Precision@N	$\frac{1}{\lvert U \rvert} \times \sum_{\text{user} \in U} (AP@N)_{\text{user}}$

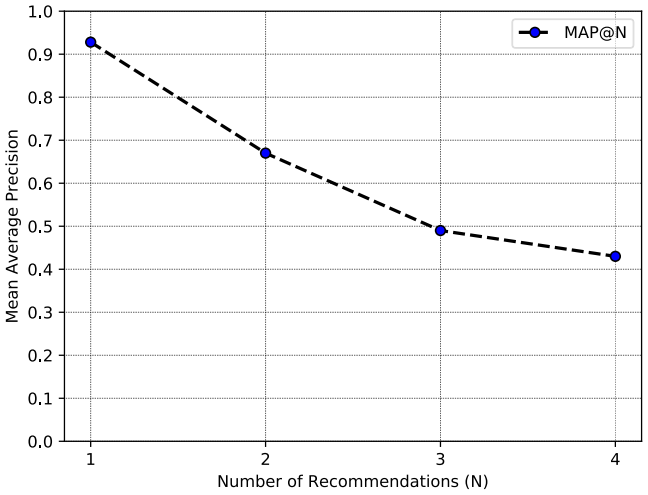


FIGURE 7. MAP vs number of recommendations.

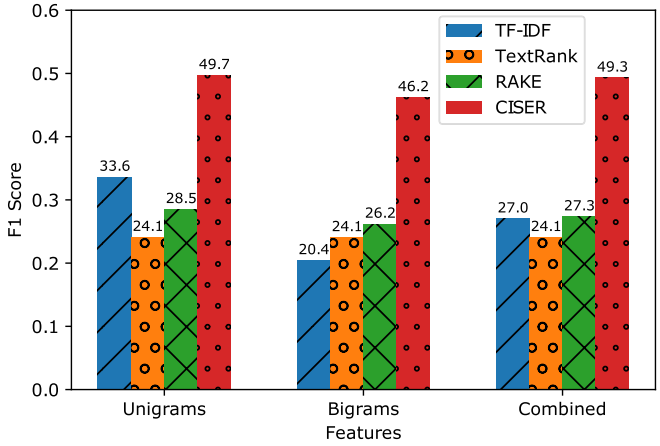


FIGURE 8. F1 score comparison with baselines.

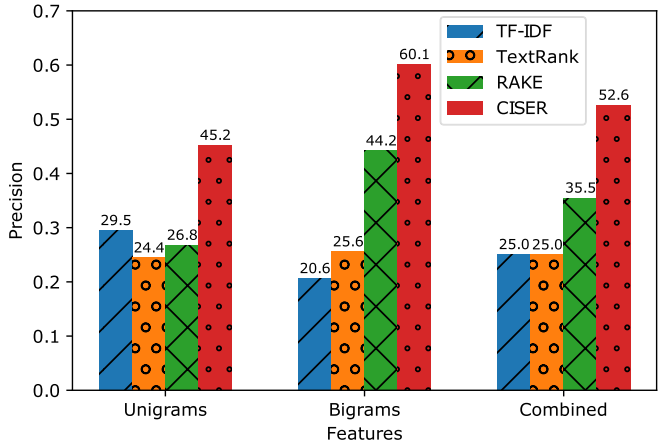


FIGURE 9. Precision score comparison with baselines.

MAP of our model is 0.93, which means that in 93% cases the user bought the recommended product. The decline in MAP@N values with increasing N can be explained by the fact that it is not very common for a buyer to buy many cameras. Hence, we limit our discussion to 4 products, so that the results remain meaningful. For different product domains, different number of recommendations can lead to remarkable results, depending on domain type and user perception.

Candidate Feature Extraction is a significant module of CISER. The feature selection results have been compared to basic NLP models like tf-idf, textRank [46] and RAKE [47]. These models were tested on Amazon's Camera review dataset. For Unigrams, Nouns were extracted from reviews and then fed to models so as to avoid stop-words and irrelevant words dominating top ranked frequent features. For Bigrams, Noun-Noun pairs and Adjective-Noun Pairs were extracted and only these were used for purpose of testing, to maintain morphological uniformity in results. The results obtained are shown in Figures 8, 9, 10. CISER has a significant precision recall and F1 score gain as compared to previous models.

One of the key contributions of this work is the reviewer credibility analysis given their opinions for a product. In order to augment the efficiency of RCA, we have used network importance factor, trust factor and expertise factor (section III-E), to integrate various latent factors for reviewer assessment. Fig. 11 shows a bar graph between reviewer rank and factor scores, demonstrating factor score distribution. It is also worth mentioning that reviewer rank is the combined total score of the reviewer, which is calculated as the weighted average of the three factors mentioned (section III-E). So, a reviewer R1 with a higher trust factor score as compared to another reviewer R2 can have a lower rank than R2, if expertise factor and network importance factor scores of R2 are sufficiently higher than that of R1.

Fig. 12 shows a graph between reviewer credibility (section III-E) and reviewer rank. Reviewer credibility is calculated as the weighted average of NIF, EF and TF.

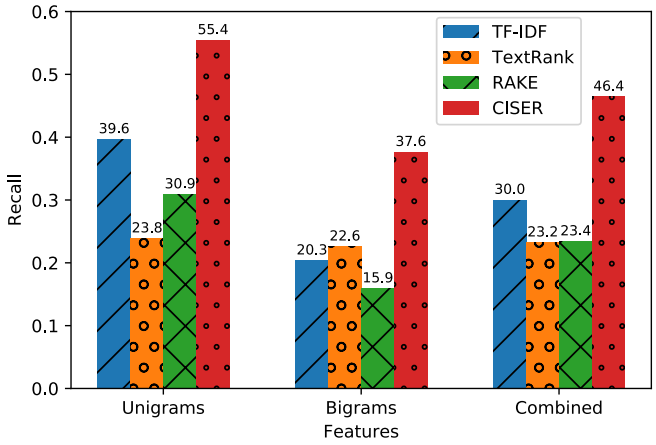


FIGURE 10. Recall score comparison with baselines.

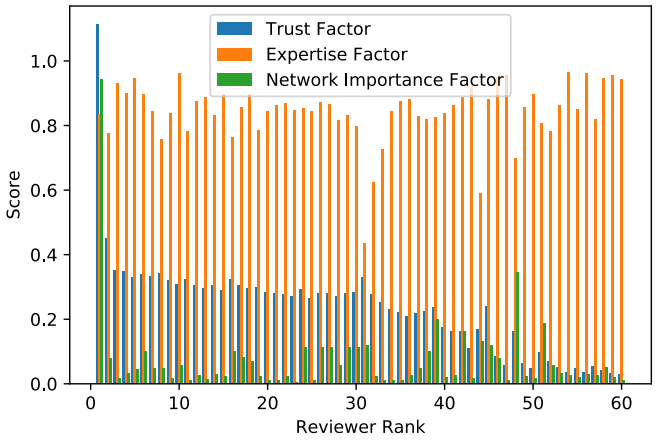


FIGURE 11. Reviewer rank vs factor Scores.

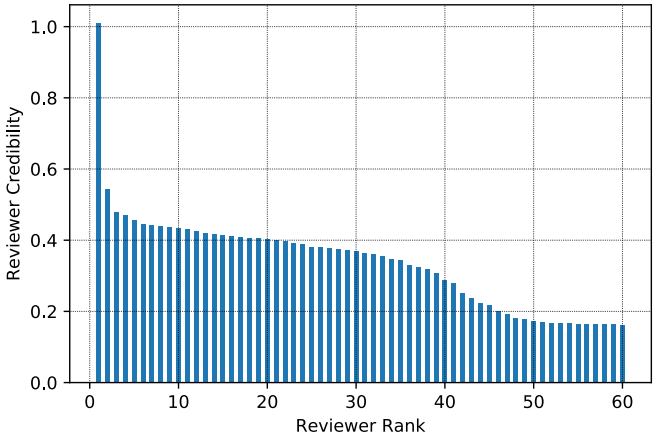


FIGURE 12. Reviewer rank vs reviewer credibility.

The weights are tuned so as to maximise recommendation efficiency.

The distributions demonstrated in figures 11 and 12 show the variance in factor scores and credibility scores for users, hence supporting our hypothesis that not all users are equally credible. To the best of our knowledge, this concept of reviewer credibility analysis without social network information (like number of followers, marital status, religion etc.) has not been used in any previous works in the field of product recommendation.

The comparative analysis of various latent factors contributing to reviewer credibility analysis is demonstrated in Figure 13. Using mean product ratings for evaluating expertise factor (ES_{Mean}) [31] does not give appreciable results. Addition of the proposed α factor (representative rating) to mean product rating (ES_{RR}) slightly improves the MAP performance of CISER. Hence, ES_{RR} better models reviewer expertise compared to ES_{Mean}. It is evident that trust factor and network importance factor greatly contribute towards recommendation performance. An efficient linear combination of these three factors leads to superior performance.

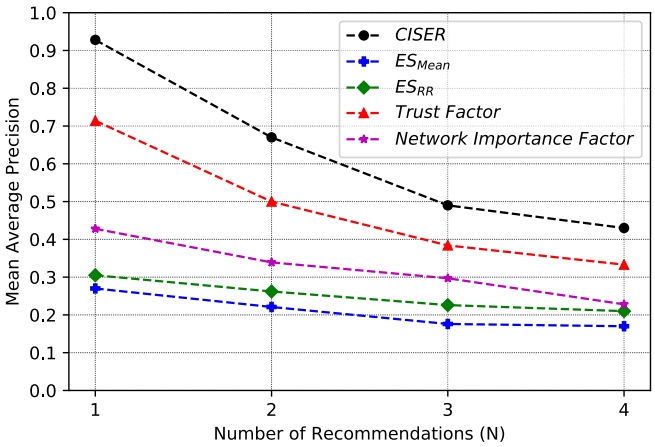


FIGURE 13. Comparative analysis of factors of RCA.

B. HYPER-PARAMETER TUNING

As discussed in Sections III-B and III-E, we use PSO for tuning coefficients for linear combination of feature scores and reviewer credibility factor scores. We empirically evaluate the tuning performances of PSO and other swarm optimization algorithms like Cuckoo Search, BAT and Artificial Bee Colony Optimisation. The comparative analysis is presented in fig. 14. The results support our choice of PSO over others, since PSO provides average MAP gain of 5%.

Various feature scores were combined using PSO. Optimal Parameter tuning is crucial for achieving remarkable performance. Since, PSO itself is a parameterised model, grid search has been performed to tune PSO parameters. The heatmap demonstrating the results of grid-search is presented in Figure 15 and final values for PSO parameters are enlisted in Table 14.

The hyper-parameters that were tuned using PSO are tabulated in Tables 15 and 16. Table 15 enlists weight

TABLE 14. PSO parameters.

Parameter	Value	Root Similarity Score
ω	0.9	0.5668
$c1$	1.6	0.478
$c2$	3.1	0.543

TABLE 15. Weights for trust factor.

Trust factor				
Unverified purchase		Verified purchase		total_ratings
coherence_coverage	helpful_votes	coherence_coverage	helpful_votes	
0.8028	0.1964	0.8963	0.2193	0.4269

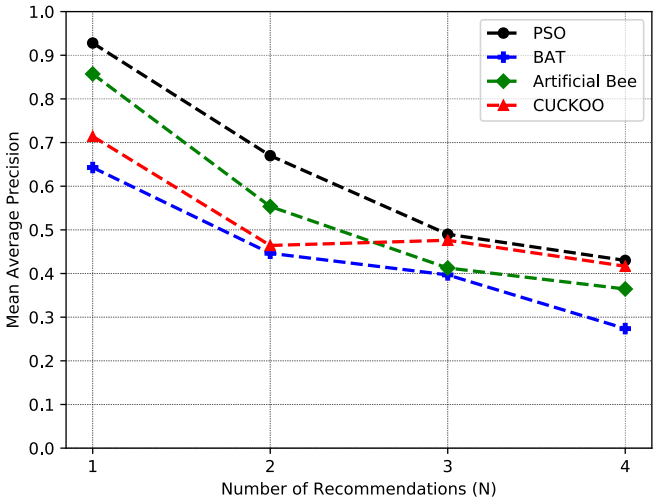


FIGURE 14. Comparison of various swarm optimisation algorithms.

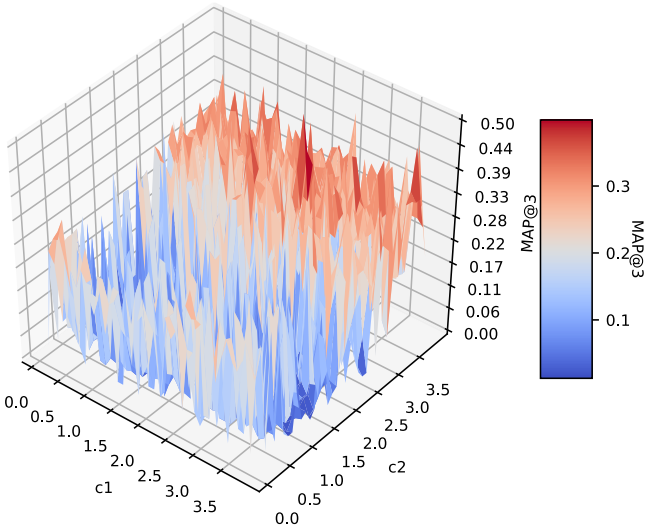


FIGURE 15. PSO parameter tuning.

TABLE 16. Factor weighting for credibility assignment.

Trust factor	Expertise factor	Network importance factor
0.6154	0.1431	0.2362

for calculating trust factor (Section III-E). Table 16 states weights for linear combination of trust factor, network importance factor and expertise factor for calculating reviewer credibility.

C. COMPARISON WITH BASELINE MODELS

To ascertain that our model performs substantially better than the current systems, we compared our results with some baseline recommendation systems. Content based

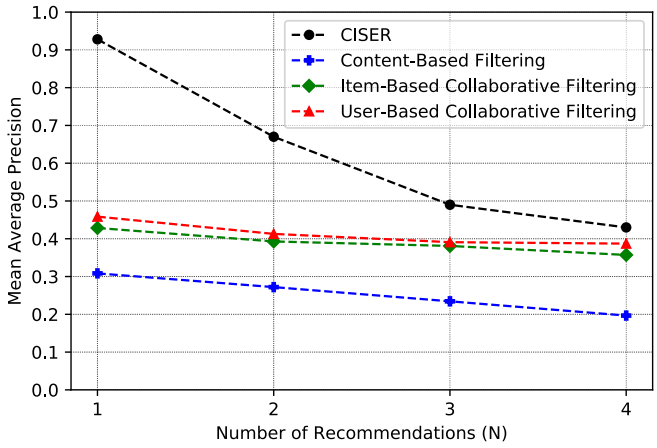


FIGURE 16. Comparing recommendation baselines with CISER.

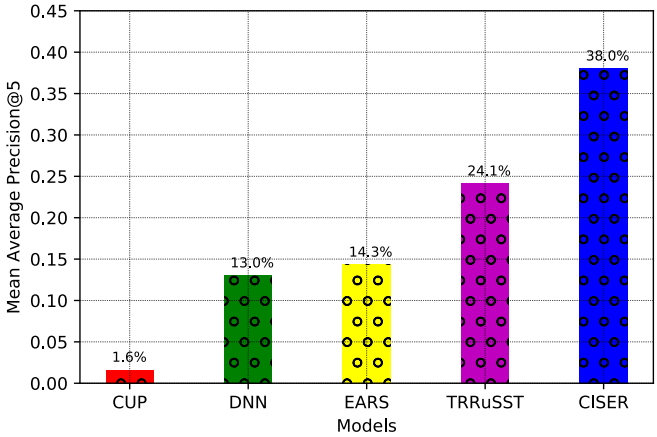


FIGURE 17. Comparison with state-of-the-art systems.

filtering [3], item-based collaborative filtering [2] and user-based collaborative filtering [2] manipulate numerical ratings to decipher user preference patterns. The proposed CISER model performs appreciably better than these, hence supporting our proposition that review sentiments greatly impact user purchase decisions. The results are presented in figure 16.

Figure 16 makes it evident that recommendation precision of CISER is commendably better than conventional content-based filtering (gain = 30%), item-based collaborative filtering (gain = 25%) and user-based collaborative filtering (gain = 24%).

Figure 17 compares the proposed CISER model with previous research models, namely, CUP [20], DNN [14], TRRuSST [17] and EARS [18].CUP and DNN model user-preference trends, EARS uses emotional and social-information for recommendations, whereas TRRuSST quantifies product quality by manipulating external attributes

modelled on user-reviews. It is clear that CISER improves recommendation efficacy with MAP@5 = 38% i.e. a gain of approximately 14% (compared to TRRuSST [17]). Hence, the combination of user-interest modelling, sentiment analysis, product quality quantification aggregated with reviewer credibility analysis significantly improves upon the state-of-the art recommendation systems.

VI. CONCLUSION AND FUTURE WORKS

This research successfully counteracted the problem of reducing the product search space for customers. The proposed CISER model recommends products with commendable accuracy, without the need of collecting and processing alternative data from social networks, surveys etc. The model augments heuristic-driven user interest profiling with reviewer credibility analysis and fine-grained feature sentiment analysis to devise a robust recommendation methodology. To the best of our knowledge, this is the first work that integrates credibility driven feature-based fine-grained sentiment analysis with user modelling for online product recommendation. The remarkable performance of CISER suggests that recommender systems that combine user-profiling, reviewer credibility and feature sentiment scoring can prove to be a methodical successor to the present state-of-the-art systems. The work has also opened avenues of using sentiment analysis for product quality assessment and enhancing recommendation quality using reviewer trust, expertise and influence. Results were validated using the Amazon camera dataset and the proposed model outperformed the baselines. As a possible future direction, social network information and online activity logs can be used to enhance the user credibility model and build shopping cliques for product recommendation. Further, more sophisticated measures for representative rating and expertise can be devised.

REFERENCES

[1] J. A. Konstan and J. Riedl, "Recommender systems: From algorithms to user experience," *User Model. User-Adapted Interact.*, vol. 22, nos. 1–2, pp. 101–123, Apr. 2012, doi: 10.1007/s11257-011-9112-x.

[2] J. B. Schafer, D. Frankowski, J. Herlocker, and S. Sen, "Collaborative filtering recommender systems," in *The Adaptive Web* (Lecture Notes in Computer Science), vol. 4321, P. Brusilovsky, A. Kobsa, and W. Nejdl, Eds. Cham, Switzerland: Springer, 2007.

[3] M. J. Pazzani and D. Billsus, "Content-based recommendation systems," in *The Adaptive Web* (Lecture Notes in Computer Science), vol. 4321, P. Brusilovsky, A. Kobsa, and W. Nejdl, Eds. Berlin, Germany: Springer, 2007.

[4] S.-T. Li, T.-T. Pham, and H.-C. Chuang, "Do reviewers' words affect predicting their helpfulness ratings? Locating helpful reviewers by linguistics styles," *Inf. Manage.*, vol. 56, no. 1, pp. 28–38, 2019.

[5] V. Srivastava and A. D. Kalro, "Enhancing the helpfulness of online consumer reviews: The role of latent (content) factors," *J. Interact. Marketing*, vol. 48, pp. 33–50, Nov. 2019.

[6] B. Liu, *Sentiment Analysis and Opinion Mining*. San Mateo, CA, USA: Morgan & Claypool Publishers, 2012.

[7] Amazon Web services, inc. *Amazon Customer Reviews Datase*. Accessed: Dec. 18, 2019. [Online]. Available: https://s3.amazonaws.com/amazon-reviews-pds/readme.html

[8] S. Raza and C. Ding, "Progress in context-aware recommender systems—An overview," *Comput. Sci. Rev.*, vol. 31, pp. 84–97, Feb. 2019. [Online]. Available: http://www.sciencedirect.com/science/article/pii/S1574013718302120

[9] L. Chen, G. Chen, and F. Wang, "Recommender systems based on user reviews: The state of the art," *User Model. User-Adapted Interact.*, vol. 25, no. 2, pp. 99–154, Jun. 2015, doi: 10.1007/s11257-015-9155-5.

[10] C. He, D. Parra, and K. Verbert, "Interactive recommender systems: A survey of the state of the art and future research challenges and opportunities," *Expert Syst. Appl.*, vol. 56, pp. 9–27, Sep. 2016. [Online]. Available: http://www.sciencedirect.com/science/article/pii/S0957417416300367

[11] S. Reddy, S. Nalluri, S. Kunisetti, S. Ashok, and B. Venkatesh, "Content-based movie recommendation system using genre correlation," in *Smart Intelligent Computing and Applications*, S. C. Satapathy, V. Bhateja, and S. Das, Eds. Singapore: Springer, 2019, pp. 391–397.

[12] X. Li, W. Jiang, W. Chen, J. Wu, and G. Wang, "Haes: A new hybrid approach for movie recommendation with elastic serendipity," in *Proc. 28th ACM Int. Conf. Inf. Knowl. Manage.*, New York, NY, USA, 2019, pp. 1503–1512, doi: 10.1145/3357384.3357868.

[13] K. Benzi, V. Kalofolias, X. Bresson, and P. Vandergheynst, "Song recommendation with non-negative matrix factorization and graph total variation," in *Proc. IEEE Int. Conf. Acoust., Speech Signal Process. (ICASSP)*, Mar. 2016, pp. 2439–2443.

[14] P. Covington, J. Adams, and E. Sargin, "Deep neural networks for youtube recommendations," in *Proc. 10th ACM Conf. Recommender Syst.*, New York, NY, USA, 2016, pp. 191–198, doi: 10.1145/2959100.2959190.

[15] J. Guerreiro and P. Rita, "How to predict explicit recommendations in online reviews using text mining and sentiment analysis," *J. Hospitality Tourism Manage.*, 2019, doi: 10.1016/j.jhtm.2019.07.001.

[16] M. Chelliah and S. Sarkar, "Product recommendations enhanced with reviews," in *Proc. Eleventh ACM Conf. Recommender Syst.*, New York, NY, USA, 2017, pp. 398–399, doi: 10.1145/3109859.3109936.

[17] L. S. Gallege and R. R. Raje, "Towards selecting and recommending online software services by evaluating external attributes," in *Proc. 11th Annu. Cyber Inf. Secur. Res.Conf. (CISRC)*, 2016, p. 23.

[18] Y. Qian, Y. Zhang, X. Ma, H. Yu, and L. Peng, "EARS: Emotion-aware recommender system based on hybrid information fusion," *Inf. Fusion*, vol. 46, pp. 141–146, Mar. 2019. [Online]. Available: http://www.sciencedirect.com/science/article/pii/S1566253518301234

[19] A. Da'u and N. Salim, "Sentiment-Aware Deep Recommender System With Neural Attention Networks," *IEEE Access*, vol. 7, pp. 45472–45484, 2019.

[20] A. Said, E. W. De Luca, and S. Albayrak, "Inferring contextual user profiles-improving recommender performance," in *Proc. 3rd RecSys Workshop Context-Aware Recommender Syst.*, Chicago, IL, USA, 2011.

[21] F. García-Sánchez, R. Colomo-Palacios, and R. Valencia-García, "A social-semantic recommender system for advertisements," *Inf. Process. Manage.*, vol. 57, no. 2, Mar. 2020, Art. no. 102153.

[22] J. Wei, F. Meng, and N. Arunkumar, "A personalized authoritative user-based recommendation for social tagging," *Future Gener. Comput. Syst.*, vol. 86, pp. 355–361, Sep. 2018. [Online]. Available: http://www.sciencedirect.com/science/article/pii/S0167739X18303078

[23] M. Xu and S. Liu, "Semantic-enhanced and context-aware hybrid collaborative filtering for event recommendation in event-based social networks," *IEEE Access*, vol. 7, pp. 17493–17502, 2019.

[24] L. U, Y. Chai, and J. Chen, "Improved personalized recommendation based on user attributes clustering and score matrix filling," *Comput. Standards Inter.*, vol. 57, pp. 59–67, Mar. 2018.

[25] K. Xu, X. Zheng, Y. Cai, H. Min, Z. Gao, B. Zhu, H. Xie, and T.-L. Wong, "Improving user recommendation by extracting social topics and interest topics of users in uni-directional social networks," *Knowl.-Based Syst.*, vol. 140, pp. 120–133, Jan. 2018. [Online]. Available: http://www.sciencedirect.com/science/article/pii/S0950705117305002

[26] R. Logesh, V. Subramaniyaswamy, V. Vijayakumar, and X. Li, "Efficient User Profiling Based Intelligent Travel Recommender System for Individual and Group of Users," *Mobile Netw. Appl.*, vol. 24, no. 3, pp. 1018–1033, Jun. 2019, doi: 10.1007/s11036-018-1059-2.

[27] J. Li, W. Xu, W. Wan, and J. Sun, "Movie recommendation based on bridging movie feature and user interest," *J. Comput. Sci.*, vol. 26, pp. 128–134, May 2018. [Online]. Available: http://www.sciencedirect.com/science/article/pii/S1877750318300012

[28] H. Tahmasbi, M. Jalali, and H. Shakeri, "Modeling Temporal Dynamics of User Preferences in Movie Recommendation," in *Proc. 8th Int. Conf. Comput. Knowl. Eng. (ICCKE)*, Oct. 2018, pp. 194–199.

[29] S. E. Middleton, D. C. De Roure, and N. R. Shadbolt, "Capturing knowledge of user preferences: Ontologies in recommender systems," in *Proc. 1st Int. Conf. Knowl. Capture*, New York, NY, USA, 2001, pp. 100–107, doi: 10.1145/500737.500755.

[30] X. Xie and B. Wang, "Web page recommendation via twofold clustering: Considering user behavior and topic relation," *Neural Comput. Appl.*, vol. 29, no. 1, pp. 235–243, 2018, doi: 10.1007/s00521-016-2444-z.
[31] J. Al-Sharawneh and M.-A. Williams, "Credibility-based social network recommendation: Follow the leader," in *Proc. 21st Australas. Conf. Inf. Syst.*, 2010, pp. 1–11.
[32] D. Goldbaum, "Follow the leader: Simulations on a dynamic social network," UTS Finance Econ. Work. Paper No 155, 2008. [Online]. Available: http://www.business.uts.edu.au/finance/research/wpapers/wp155.pdf
[33] F. Li and T. C. Du, "Who is talking? An ontology-based opinion leader identification framework for word-of-mouth marketing in online social blogs," *Decis. Support Syst.*, vol. 51, no. 1, pp. 190–197, Apr. 2011.
[34] J. Chen, C. Wang, Q. Shi, Y. Feng, and C. Chen, "Social recommendation based on users' attention and preference," *Neurocomputing*, vol. 341, pp. 1–9, May 2019. [Online]. Available: http://www.sciencedirect.com/science/article/pii/S0925231219302693
[35] A. Kumar and G. Garg, "Sentiment analysis of multimodal Twitter data," *Multimedia Tools Appl.*, vol. 78, no. 17, pp. 24103–24119, Sep. 2019.
[36] A. Kumar and A. Jaiswal, "Particle swarm optimized ensemble learning for enhanced predictive sentiment accuracy of tweets," in *Proc. ICETIT*, P. K. Singh, B. K. Panigrahi, N. K. Suryadevara, S. K. Sharma, and A. P. Singh, Eds. Cham, Switzerland: Springer, 2020, pp. 633–646.
[37] A. Kumar and A. Joshi, "Ontology driven sentiment analysis on social Web for government intelligence," in *Proc. Special Collection EGovernment Innov. India*, New York, NY, USA, 2017, pp. 134–139, doi: 10.1145/3055219.3055229.
[38] A. Kumar and A. Jaiswal, "Empirical study of twitter and tumblr for sentiment analysis using soft computing techniques," in *Proc. World Congr. Eng. Comput. Sci.*, vol. 1, 2017, pp. 1–5.
[39] H. H. Do, P. Prasad, A. Maag, and A. Alsadoon, "Deep Learning for Aspect-Based Sentiment Analysis: A Comparative Review," *Expert Syst. Appl.*, vol. 118, pp. 272–299, Mar. 2019. [Online]. Available: http://www.sciencedirect.com/science/article/pii/S0957417418306456
[40] A. Dridi, M. Atzeni, and D. Reforgiato Recupero, "FineNews: Fine-grained semantic sentiment analysis on financial microblogs and news," *Int. J. Mach. Learn. Cyber.*, vol. 10, no. 8, pp. 2199–2207, Aug. 2019, doi: 10.1007/s13042-018-0805-x.
[41] R. Dong, M. P. O'Mahony, M. Schaal, K. Mccarthy, and B. Smyth, "Combining similarity and sentiment in opinion mining for product recommendation," *J. Intell. Inf. Syst.*, vol. 46, no. 2, pp. 285–312, Apr. 2016, doi: 10.1007/s10844-015-0379-y.
[42] G. Liu, Y. Wang, and M. Orgun, "Trust inference in complex trust-oriented social networks," in *Proc. Int. Conf. Comput. Sci. Eng.*, vol. 4, Aug. 2009, pp. 996–1001.
[43] M. J. Metzger, "Making sense of credibility on the Web: Models for evaluating online information and recommendations for future research," *J. Am. Soc. Inf. Sci.*, vol. 58, no. 13, pp. 2078–2091, Nov. 2007.
[44] K. Kwon, J. Cho, and Y. Park, "Multidimensional credibility model for neighbor selection in collaborative recommendation," *Expert Syst. Appl.*, vol. 36, no. 3, pp. 7114–7122, Apr. 2009, doi: 10.1016/j.eswa.2008.08.071.
[45] T. H. Haveliwala, "Topic-sensitive pagerank," in *Proc. 11th Int. Conf. World Wide Web*, New York, NY, USA, 2002, pp. 517–526, doi: 10.1145/511446.511513.
[46] R. Mihalcea and P. Tarau, "Textrank: Bringing order into text," in *Proc. Conf. Empirical Methods Natural Lang. Process.*, 2004, pp. 404–411.
[47] S. Rose, D. Engel, N. Cramer, and W. Cowley, "Automatic keyword extraction from individual documents," *Text Mining: Appl. Theory*, vol. 1, pp. 1–20, Mar. 2010.



SHIGANG HU received the B.S. degree in electronic information engineering from the Hubei University of Technology, Wuhan, China, in 2003, and the Ph.D. degree in microelectronics from Xidian University, Xi'an, China, in 2009. Since 2018, he has been a Professor with the Electronic Information Engineering Department, Hunan University of Science and Technology, Xiangtan, China. He has authored over 30 research articles. His research interests include artificial intelligence technology and photoelectric information materials. He has received several grants, in recent years, from the National Natural Science Foundation of China.



AKSHI KUMAR received the B.Eng. degree (Hons.) in computer science and engineering from Maharishi Dayanand University, India, in 2003, the M.Tech. (Hons.) in computer science and engineering from Guru Gobind Singh Indraprastha University, New Delhi, in 2005, and the Ph.D. degree in computer engineering from the Faculty of Technology, University of Delhi, in 2011. She has been with the Delhi Technological University (formerly Delhi College of Engineering), for the past 11 years, where she is currently an Assistant Professor with the Department of Computer Science and Engineering. She has presented several papers in international conferences and published work in peer-reviewed and science cited journals. She has authored a monograph *Web Technology: Theory and Practice* (CRC Press, Taylor and Francis Group) and edited a book *A Roadmap to Industry 4.0: Smart Production, Sharp Business and Sustainable Development* (Springer). Her research interests are in the area of intelligent systems, Web technology, sentiment analysis, natural language processing, social media analytics, and soft computing. She is a recipient of the Commendable Research Award for Excellence In Research at Delhi Technological University, in 2018, and the VIWA Outstanding Women in Engineering (Computer Science & Engineering) Award, in 2020. She is an active reviewer of many top journals of the IEEE, IET, Springer, and Elsevier. In addition, she is currently serving as the Guest Editor for several journals, including the *Energy Systems* (Springer); *Future Internet*, the *IEEE Internet of Things Magazine*, the *Sustainable Cities & Society* (Elsevier), and the *Autosoft Journal (Intelligent Automation & Soft Computing)*.



FADI AL-TURJMAN received the Ph.D. degree in computer science from Queen's University, Kingston, ON, Canada, in 2011. He is currently a Full Professor and the Research Center Director with Near East University, Nicosia, Cyprus. He is a leading authority in the areas of smart/intelligent, wireless, and mobile networks' architectures, protocols, deployments, and performance evaluation. His publication history spans over 250 publications in journals, conferences, patents, books, and book chapters, in addition to numerous keynotes and plenary talks at flagship venues. He has authored and edited more than 25 books about cognition, security, and wireless sensor networks' deployments in smart environments, published by Taylor & Francis, Elsevier, and Springer. He has received several recognitions and best papers' awards at top international conferences. He also received the prestigious Best Research Paper Award from the *Elsevier Computer Communications Journal* (2015–2018), in addition to the Top Researcher Award for 2018 at Antalya Bilim University, Turkey. He has led a number of international symposia and workshops in flagship communication society conferences. He currently serves as an Associate Editor and the Lead Guest Editor for several well reputed journals, including the *Elsevier Computer Communications*, *Sustainable Cities and Society*, Springer MONET, and the *IET Wireless Sensor Systems journals*.



SHIVAM GUPTA is currently pursuing the B.Tech. degree in computer engineering with Delhi Technological University (formerly Delhi College of Engineering), New Delhi, India. He was a Software Engineer Intern at SAP. His research interests are in the areas of artificial intelligence, deep learning, natural language processing, sentiment analysis, recommendation systems, and cyber security.



SIMRAN SETH is currently pursuing the B.Tech. degree in computer engineering with Delhi Technological University, New Delhi, India. Her research interests include natural language processing, recommendation systems, cyber security, information retrieval, and text mining.



SHUBHAM is currently pursuing the B.Tech. degree in computer engineering with Delhi Technological University, New Delhi, India. His research interests include data mining, recommender systems, and artificial intelligence.

Volume 7 Issue 3 (2019) 285-288 ISSN 2347 - 3258
International Journal of Advance Research and Innovation

Single OTRA based low power grounded capacitance multiplier

Shashwat Singh, Jatin, Neeta Pandey*, Rajeshwari Pandey
Department of Electronics and Communication Engineering, Delhi Technological University, Delhi, India

Article Info
Article history:
Received 16 January 2019
Received in revised form
25 July 2019
Accepted 28 July 2019
Available online 15 September 2019

Keywords:
Degree of freedom, Grounded Capacitance Multiplier, Low power, Operational Trans-conductance Amplifier, Operational Trans-resistance Amplifier

Abstract
The paper presents a single Operational Trans-resistance Amplifier (OTRA) based novel, low power and a high multiplication factor achieving, grounded capacitance multiplier. The multiplicative gain is tunable with high precision over decades. The proposed structure enjoys two degree of freedom in terms of simulating a multiplied capacitance adding to its versatility. The circuit also portrays a high nature of uniformity and compactness by utilizing a single active block along with a voltage buffer thereby, reducing the silicon area consumption on the chip making it ideal for integration purpose. The design proposed imposes only a single matching condition. Temperature independence can be ensured by replacing the floating impedance by Operational Trans-conductance Amplifier (OTA) simulated floating resistor. Thus, it would contribute towards the circuit robustness and support large number of applications in areas ranging from industries to military discipline. The theoretical estimates mentioned above are justified through spice simulation using 180nm CMOS technology. Various filter topologies have been implemented utilizing the simulated multiplied capacitance. Frequency response has been presented in order to justify the soundness of the presented circuit.

1. Introduction

Lots of research has been done recently on integrating systems having varied nature on the same silicon chip to gain compactness and low power consumption. The foremost motivations behind this include low cost, higher speed, portability and putting more functions on the same silicon piece. Areas which use capacitive sensors or deal with low frequency signal processing applications require bulky capacitors [1-2] which occupy large silicon area so their usage is limited though they provide better results. A capacitance multiplier circuit, which multiplies the small capacitance embedded on chip to emulate a large capacitance value, can prove to be a credible solution.

The voltage-mode capacitance multipliers [3-4] employing operational amplifiers (op-amp) have slew rate and gain limitations. Different capacitance multiplier circuits [5-15] have been designed using current mode building blocks. These circuits-

a) use of extensive number of active blocks or passive circuit elements [6, 8, 18-19].
b) consume larger power [7-8].
c) achieve limited multiplication factor [5,11-12,15].
d) have capacitor associated with a terminal that results in an extra pole. It leads to smaller operational bandwidth [12-14].

Operational Trans-resistance Amplifier (OTRA) is a multi-purpose active block [16-17] which has been utilized in applications like current mode filters, phase detectors and admittance simulators [18]. A capacitance multiplier circuit directing around the use of Operational Trans-resistance Amplifier (OTRA) is put forward in this paper. The proposed circuit comprises of two active elements and uses single floating capacitor to produce a large grounded capacitor. The
main highlight of the circuit is its low power operation that gives it a superiority over other works. Different values of the resistors can be chosen to obtain the desired multiplication factor. The proposed circuit comes with high bandwidth and a resolution close to 1pF.

2. The Operational Trans-resistance Amplifier (OTRA)

Recently, OTRA is being used extensively as an alternate analog building block owing to its inheritance of advantages from current mode techniques. Parasitic resistance and capacitance have been nullified to a large extent by internal grounding of both input terminals of OTRA.

Corresponding Author,
E-mail address:n66pandey@rediffmai.com,
Phone No-+919868780900
All rights reserved: http://www.ijari.org

The circuit symbol of OTRA is given in Figure 1. The terminal characteristic of OTRA are given by Eq(1)

$$V_p = 0, V_n = 0, \ V_o = R_m(I_p - I_n) \quad (1)$$

Where I_p and I_n represent currents in the positive and negative terminals, R_m represents the trans-resistance of OTRA and V_o represents the output voltage.

For most cases it can be assumed that $R_m \rightarrow \infty$ and thus from Eq(1) it can be concluded that:

$$I_p = I_n \quad (2)$$

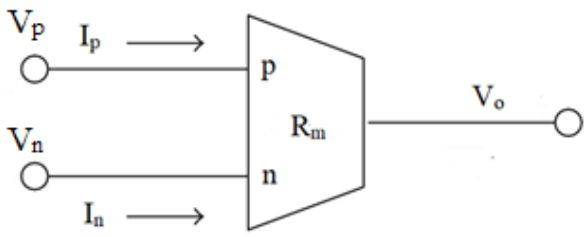


Fig. 1: OTRA circuit symbol

3. Proposed Capacitance Multiplier Design

The circuit of proposed capacitance multiplier is depicted in Figure 2. It emulates a grounded capacitor. The main advantage of the proposed circuit is its clarity and simplicity. Considering Eq(2) the input impedance of proposed circuit is computed as:

From Eq(3) we have two degrees of freedom, i.e. anyone Z_1 or Z_3 can be selected as the capacitor to form the capacitance multiplier. Selecting Z_3 as capacitor of value C_s, and Z_1 and Z_2 as resistors of values R_1 and R_2 the input impedance is capacitive and the value of capacitance is obtained as

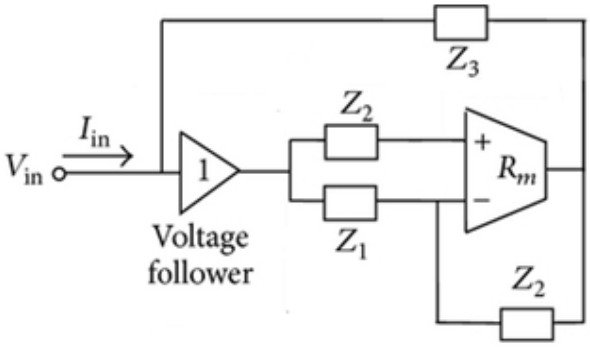


Fig. 2. Proposed Capacitance Multiplier

$$Z_{in} = \frac{Z_1 Z_3}{Z_2} \quad (3)$$

$$C_{eq} = \frac{C_s R_2}{R_1} \quad (4)$$

or

$$C_{eq} = K_m C_s \quad (5)$$

where K_m is the multiplication factor and its value is given by:

$$K_m = \frac{R_2}{R_1} \quad (6)$$

To add the functionality of electronical tunability in the circuit the floating resistors can be implemented using Operational Transconductance Amplifier (OTA). The small signal equivalent of OTA is presented in Figure 3(a) and resistor configuration is depicted in Figure 3(b). The value of resistor is reciprocal of tunable transconductance (g_m) possessed by the OTA where, $g_m \alpha \sqrt{I_B}$ (I_B is bias current).

Since the transconductance (g_m) is directly proportional to the square root of the biasing current (I_B), so by varying the bias currents we can vary the gain over several decades.

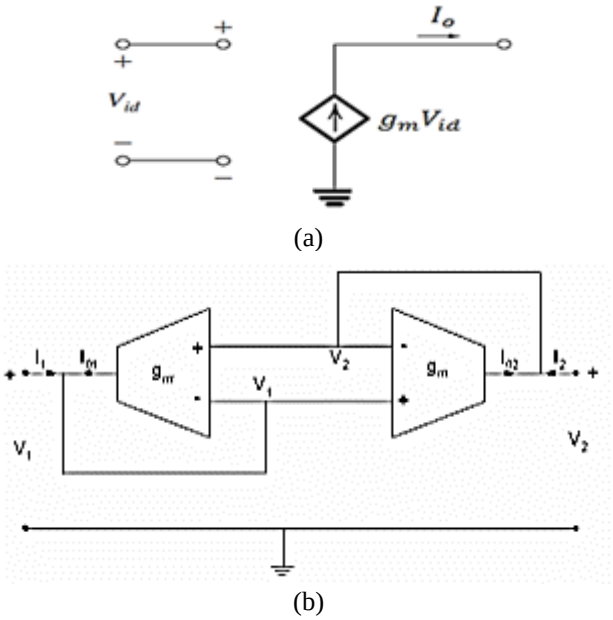


Fig. 3. OTA (a) Equivalent circuit (b) as floating resistor

The effective capacitance of the circuit thus becomes:

$$C_{eq} = \frac{C_s g m_2}{g m_1} \quad (7)$$

Substituting the value of g_m in Eq(7) yields in Eq(8)

$$C_{eq} = C_s \sqrt{\frac{IB_2}{IB_1}} \quad (8)$$

From Eq(8) it can be seen that the proposed multiplier becomes temperature independent. Also, it is electronically tunable and a wide range of capacitance values may be obtained by varying bias currents over the range of nano-amperes to milli-amperes.

4. Simulation and Discussions

The functionality of the proposed circuit is examined through SPICE simulations using 180nm CMOS technology with ±1.5V supply voltages. CMOS based schematic OTRA is shown in Figure 4 and aspect ratios for various transistors are enlisted in Table 1.

Table 2 enlists the measured values of the performance parameters for the OTRA used for implementing the circuit. The bias current has been adjusted to 22.02 uA and the bias voltage tuned to -0.83 V.

Table 1. Aspect ratio (W/L) of transistors for otra

Transistors	W(um)	L(um)
M1-M3	14.4u	0.36u
M4	1.44u	0.36u
M5-M6	4.32u	0.36u
M7	1.44u	0.36u
M8-M11	7.2u	0.36u
M12-M13	14.4u	0.36u
M14	7.2u	0.36u

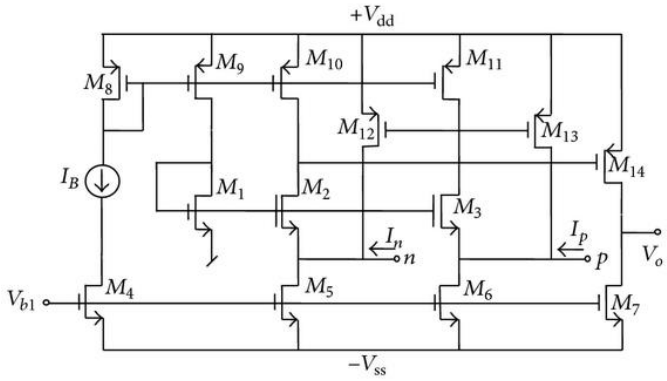


Fig. 4. CMOS schematic of OTRA [17]

The open loop gain and the phase plot are also being portrayed in Figure 5 to accept the robust functionality of the circuit.

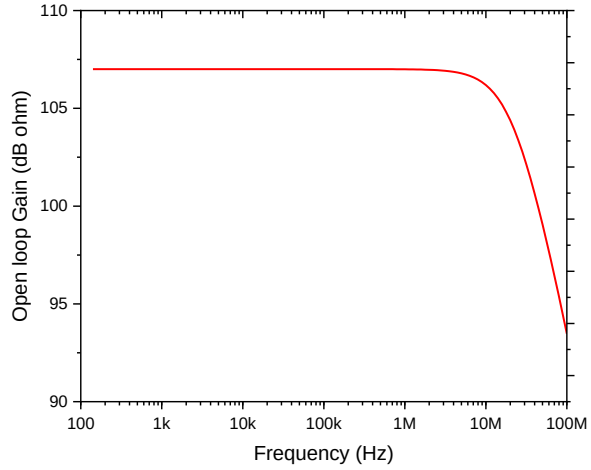


Fig. 5(a). Open-loop gain of the OTRA depicted in Figure 4

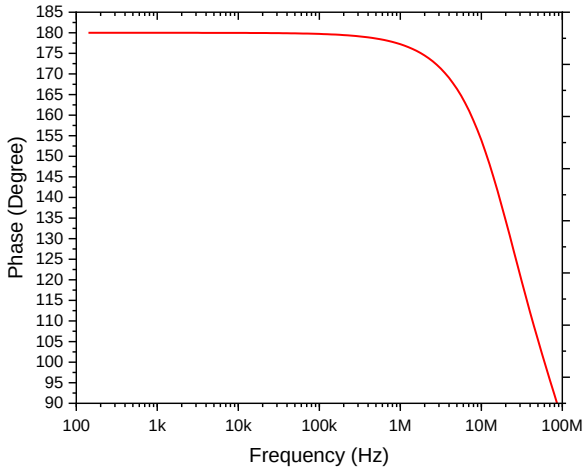


Fig. 5(b). Phase of the OTRA output voltage depicted in Figure 4

Table 2. Performance parameters of OTRA

Parameter	Value
Technology	180 nm
Supply(VDD,VSS)	1.5V, -1.5V
No. of Transistors	14
DC Open loop Trans-resistance Gain	107dBΩ
Input Resistance (Differential)	4.35κΩ
Gain Bandwidth Product	$4.915x10^{12}$THzΩ

Figure 6, shows the magnitude and phase plot simulations of the proposed circuit for various values of K_m. Figure 7 shows the transient response at the input impedance node where it is seen that the phase difference between the current and voltage is +90°, hence, it matches with the phase property of a capacitor.

Some insignificant errors are observed which are mainly due to internal parasitic elements and the error tends to increase at higher frequencies. Hence, the multiplier circuit has a practical frequency range from 100Hz to 1MHz.

The SPICE results shown in Figure 6 verify the theoretically proposed results. The power consumed by the multiplier circuit with ±1.5V supply voltages and multiplication factor of 160 is approximately 0.531mW.

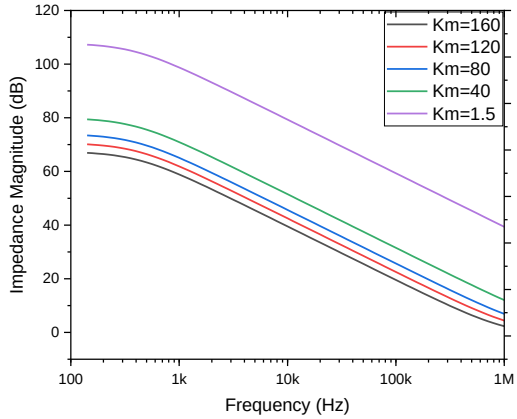


Fig. 6. (a): Magnitude (in dB) of input impedance for various K_m values with Cs=1 nF

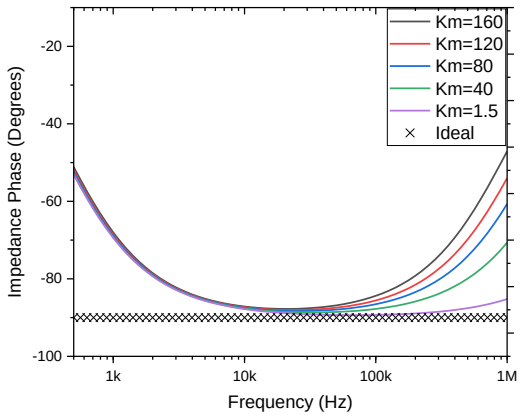


Fig. 6. (b): Phase (in degrees) of input impedance for various K_m values with Cs=1 nF

The performance of proposed circuit in terms of number of active and passive elements used, multiplication factor, frequency range and power consumption is summarized in Table 3.

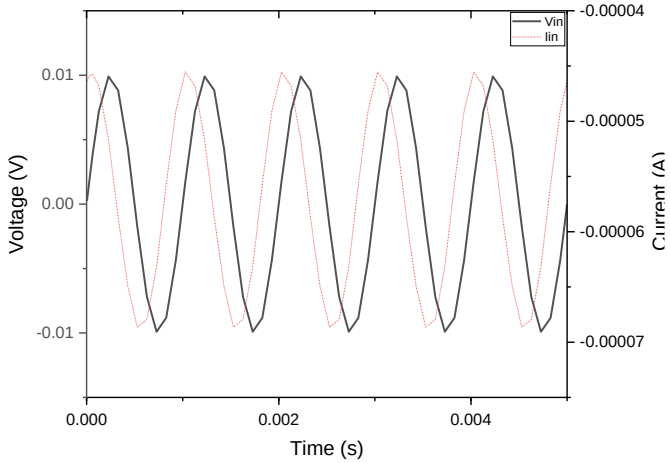


Fig. 7. Transient Response for the Input impedance depicting current leading the voltage by 90 degrees.

5. Application

To formally accept the performance of the proposed capacitance multiplier using OTRA, a band reject filter (Figure 8(a)) and a band pass filter (Figure 8(b)) is implemented. In both the cases the Capacitor C is replaced by the simulated capacitor. The values of the passive components used of simulation of filters are mentioned in Table 4 and Table 5 for BPF and BRF respectively. A multiplication factor of 160 is generated by utilizing the proposed capacitance multiplier. The central frequency lies in the Very Low Frequency (VLF) range apt for navigation, tracking and audio telephonic systems.

Table 3. Performance comparision

Paper	No. of Active Elements	No. of Passive Elements*	Multiplication Factor	Frequency Range	Power Consumption
REF[3]	3	0	NA	NA	NA
REF[4]	2	4	NA	~1 MHz	NA
REF[5]	2	2	100	Upto 1MHz	NA
REF[6]	4	0	100000	Upto 3 MHz	0.565mW
REF[7]	3	0	21^4	Upto 10 kHz	3mW
REF[8]	4	0	NA	Upto 3MHz	7.32mW
REF[9]	3	0	1000	NA	NA
REF[10]	2	0	100000	Upto 1MHz	0.822mW
REF[11]	1	2	Upto 50	100KHz – 6MHz	NA
REF[12]	1	0	100	NA	700nW
REF[13]	2	2	100000	NA	NA
REF[15]	3	0	Upto $\sqrt{10}$	Upto 10MHz	NA
REF[18]	3	5	100000	10Hz – 1MHz	51.22uW
REF[19]	3	6	NA	Upto 10MHz	NA
P.C.	2	3	160	100Hz-1MHz	0.531mW

*Excluding source Capacitor

The transfer function of the band reject filter and band pass filter is given by:

$$H_{BR}(s) = \frac{s^2 + \frac{1}{LC}}{s^2 + s\frac{R}{L} + \frac{1}{LC}} \quad (9)$$

$$H_{BP}(s) = \frac{\frac{s}{RC}}{s^2 + s\frac{1}{RC} + \frac{1}{LC}} \quad (10)$$

The central angular frequency is given by:

$$\omega_0^2 = \frac{1}{LC} \quad (11)$$

And the Quality factor is given by:

$$Q_{BR} = \frac{1}{R}\sqrt{\frac{L}{C}}, \qquad Q_{BP} = R\sqrt{\frac{C}{L}} \quad (12)$$

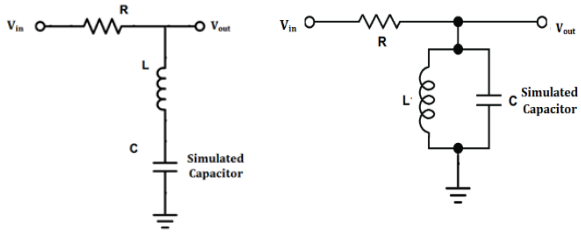


Fig. 8 (a) Band Reject Filter (b) Band Pass Filter

Table 4. Passive component values used for BRF

Component/Centre Frequency	**f_o= 3.98 kHz**
C	160nF (1nF*160)
L	10mH
R	100Ω

Table 5. Passive component values used for BPF

Component/Centre Frequency	**f_o= 3.98 kHz**
C	160nF (1nF*160)
L	10mH
R	2kΩ

The magnitude and phase plots for the band reject filter and band pass filter is shown in Figure 9(a) and Figure 9(b) respectively. The center frequency is fixed to 3.98 kHz for both the filters. The simulated value Figure 9 and the calculated value are very close to each other. For the band reject filter the quality factor obtained is 2.5 and the total power consumption is 0.749mW and with bandwidth of 159.15 Hz. For the band pass filter, bandwidth is found to be 49.73Hz, with quality factor of 8 and power dissipation of 0.755mW. Thus, decent performance of the proposed capacitance multiplier circuit is verified by the simulation results with both filter having a quality factor of greater than unity.

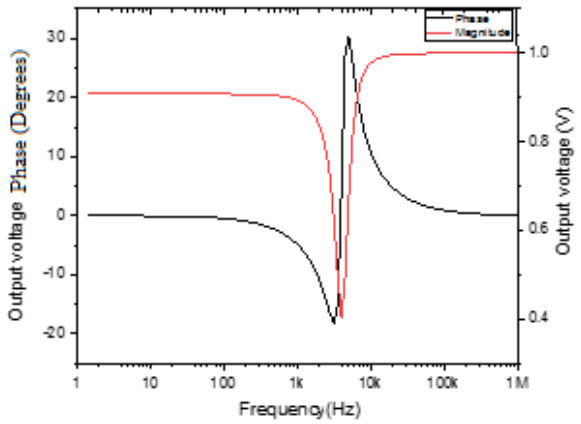


Fig. 9(a): Frequency Response for notch filter centered at 3.98 kHz

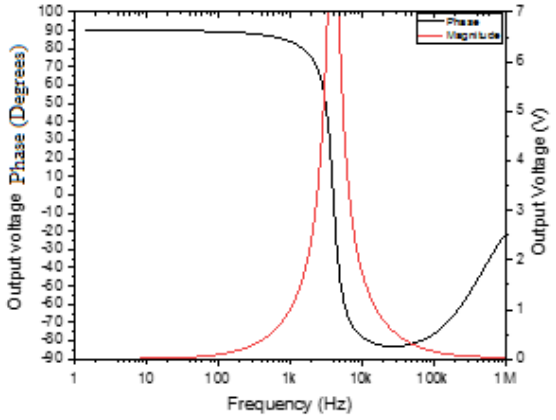


Fig. 9(b): Frequency Response for band pass filter centered at 3.98 kHz

6. Conclusions

This communication proposed a grounded capacitance multiplier using Operational Trans-resistance Amplifier (OTRA). The circuit consists of single OTRA block along with a floating capacitor. The PSPICE simulation results also support the stated advantages. The power consumed at ±1.5V supply voltages is about 0.531mW. The use of OTA based floating resistor is also suggested to make the circuit temperature insensitive and electronic tunable which are striking features for IC production. Finally, a band reject filter and a band pass filter is implemented using the simulated capacitor.

References

[1] G Ferri. Low voltage low power CMOS front-ends for capacitive sensors, 2nd IEEE CAS Region 8 Workshop on Analog and Mixed Design - Baveno 9,1997,12-13

[2] AD Amico, C Di Natale, M Mariucci, G Barccarani. Active capacitance multiplication for sensor application, Proceedings of Italian Conference of Sensors and Microsystems, Roma, 1997.

[3] MT Ahmed, IA Khan, N Minhaj. Novel Electronically tunable C Multipliers, Electronics Letters, 31(1), 1995, 9-11.

[4] AD Marcellis, G Ferri, V Stornelli. NIC-based Capacitance Multipliers for Low-Frequency Integrated Active Filter Applications, Ph.D. Research in Microelectronics and Electronics Conference, Prime 7, 2007, 2-5.

[5] G Ferri, S Pennisi. A 1.5V Current-Mode Capacitance Multiplier, Proceedings of the Tenth International Conference on Microelectronics, 1998.

[6] W Jaikla, M Siripruchyanun. An electronically controllable capacitance multiplier with temperature compensation, Proceedings Inter. Symp. Communications and Information Technologies, 10, 2006 356-359.

[7] HY Darweesh, FA Farag, YA Khalaf. New Active Capacitance Multiplier for Low Cutoff Frequency Filter Design, International Conference on Microelectronics, 12, 2007, 29-31.

[8] M Siripruchyanan, W Jaikla. Floating Capacitance Multiplier Using DVCC and CCCIIs, International Symposium on Communications and Information Technologies, 10, 2007.

[9] M. Ahmed, IA Khan. OTA-based integrable voltage/current-controlled ideal C-multiplier, Electronics Letters, 22(7), 1986, 365 – 366.

[10] P Silapan, C Tanaphatsiri, M Siripruchyanun. Current Controlled CCTA Based- Novel Grounded Capacitance Multiplier with Temperature Compensation, IEEE Asia Pacific Conference Circuits and Systems, 2008.

[11] R Arslanalp, T Yücehan. Capacitance Multiplier Design by Using CFOA, International Symposium on Communications and Information Technologies, 2007.

[12] WGermanovix, E Bonizzoni. Capacitance Super Multiplier for Sub-Hertz Low-Pass Integrated Filter, IEEE Transactions on Circuits and Systems II, 99, 2017.

[13] G Di Cataldo, G Ferri, S Pennisi. Active capacitance multipliers using current conveyors, Proceedings of the IEEE International Symposium Circuits and Systems (ISCAS), 1998.

[14] W Petchakit, S Petchakit. New floating capacitance multipliers, Proceedings of 28th Electrical Engineering Conference (EECON-28), l-2, 2005, 1233-1236.

[15] M Somdunyakanok, K Angkeaw, P Prommee. Floating-Capacitance Multiplier based on CCDDCCs and its Application, 2011 IEEE Region 10 Conference (TENCON), 2011.

[16] J Chen, H Tsao, C Chen. Operational trans resistance amplifier using CMOS technology, in Electronics Letters, 28(22), 2087-2088

[17] HM Hassan, AM Soliman. A modified CMOS realization of the operational transresistance amplifier (OTRA), Frequenz, 60, 3-4, 2006, 70–76.

[18] A Gupta, R Senani, DR Bhaskar, AK Singh. New OTRA-Based Generalized Impedance Simulator, ISRN Electronics, 2013, Article ID 907597, 10.

[19] S Singh, Jatin, N Pandey, R Pandey. Precision Capacitance Multiplier with Low power and High Multiplication Factor, presented at 5th Signal Processing and Integrated Networks Conference, 2, 2018.

The current issue and full text archive of this journal is available on Emerald Insight at:
https://www.emerald.com/insight/1463-5771.htm

Strategic issues in supply chain management of Indian SMEs due to globalization: an empirical study

Rajesh Kumar Singh
Management Development Institute, Gurgaon, India, and
Ravinder Kumar
Amity University Noida, Noida, India

Received 26 September 2019
Revised 19 December 2019
Accepted 28 December 2019

Abstract

Purpose – In globalized market, organizations of all sizes are having huge opportunities for growth. However, due to various resource constraints, it has become challenging for small and medium enterprises (SMEs) of growing economies to survive in this global competition. Effective supply chain management (SCM) can be a major driving factor for success of Indian SMEs in dynamic world economy. SMEs face many operational challenges while implementing effective SCM. The purpose of this paper is to study different strategic issues for successful implementation of SCM in Indian SMEs.

Design/methodology/approach – A survey has been conducted in Indian SMEs of different sectors. Major constructs of survey instrument are motivations, hindrances, investment priorities, supply chain practices and performance. In total, 1,500 Indian SMEs have been approached for collecting response through survey instrument. 257 complete responses were finalized. Statistical analysis of data acquired from survey is performed by using SPSS software.

Findings – It is observed that managing customers, organization resources, and inventory are main SCM practices. Major investment areas are systems for developing quick response and quality management. Currently, human resource and knowledge management have been found to be less priority areas for SMEs. The major focus of Indian SMEs is on cost and lead time reduction by having effective SCM.

Originality/value – Novelty of this study is that strategic issues for effective SCM in context to Indian SMEs have been analyzed. The findings of the study will help Indian SMEs in doing strategic planning for being competitive in the global market.

Keywords SMEs, Supply chain management, Strategic issues, Performance, Globalization, Investment priorities

Paper type Research paper

1. Introduction

From last few decennaries, Indian small and medium enterprises (SMEs) have been key contributors in the growth of Indian economy. They are generating employment with lowest investments in urban and rural areas. 36 million units of Indian SMEs give employment to 80 million people. With 6,000 products, they add eight percent to Gross Domestic Product (GDP) and 40 percent to Indian exports. Working as major suppliers to big enterprises they conduce significantly to the social and economic growth of the nation (Small and Medium Development chamber of India, 2015). However, working in global competition with advanced technologies is very stimulating situation for SMEs. Flexibility in operations can give edge to SMEs in competition (Singh *et al.*, 2005). Kumar *et al.* (2015) stated that in high competition, effectuation of SCM can be helpful for SMEs in becoming flexible. The term SCM was first coined by an American industry consultant in the early 1980s.For successful implementation of SCM, SMEs encounter with number of constraints (Trakman *et al.*, 2007).

SMEs serve as integral institutions in the development of an economy. A majority of them are covered under the secondary sector of an economy and assist various large firms in their

Authors would like to thank Editor of the journal and reviewers for giving valuable insights to improve quality and content of the paper.

Benchmarking: An International Journal
© Emerald Publishing Limited
1463-5771
DOI 10.1108/BIJ-09-2019-0429

production. Definition of small and medium enterprises changes from country to country (Enquobahrie, 1997; Harabi, 2005). In UK, SMEs contribute about 70 percent to GDP and about 90 percent to the employment. UK SMEs gives advantage of economic advancement on local and national front (Quayle, 2003). SMEs are key contributors to manufacturing and service sector across the world (Huin *et al.*, 2002). In emerging economies, SMEs are contributing in economic development and employment generation (UNCTAD, 1993). Singh *et al.* (2019) have observed that for sustainable growth in globalized digital economy, SMEs have to upgrade their existing technologies. Certain observations about SMEs from literature are as follows:

- SMEs face problems of fluctuating demand, poor know-how of SCM, and middlemen interference (Kumar *et al.*, 2014).
- SMEs face the constraints of information, resources, and skilled workforce (Taylor *et al.*, 2004; Kumar *et al.*, 2016). Financial constraints affect the implementation of modern IT technologies in SMEs (Singh *et al.*, 2008).
- In contemporary scenario of ecumenical competition, competitive advantage can be gained by implementation of SCM in Indian SMEs (Kumar *et al.*, 2016). Tripathy *et al.* (2016) observed that adoption of modern technologies can amend relation with customers, suppliers, and meliorate operational and logistics performance of Indian SMEs.

Although big enterprises in India are successfully implementing SCM but SMEs are still struggling in getting benefited from SCM due to different kinds of resource and technological constraints (Singh *et al.*, 2010). After globalization of market, SMEs are facing challenges in terms of technological upgradation and in improving SCM to compete with global players. They can compete only if they could perform in terms of product quality, delivery on time, sustainability, and agility without increasing the cost of operation. It is only possible by making SCM effective. Therefore, present study would try to explore many strategic issues for effective SCM of Indian SMEs in context to globalized market. Authors have proposed a framework including different issues of SCM in Indian SMEs such as investment priorities, motivation, hindrances, and performance in SCM implementation. Authors also analyzed the impact of various issues of SCM on performance of Indian SMEs by testing the research hypothesis. The rest of the research paper has been orchestrated as follows. Section 2 reviewed the related literature and hypothesis development. Section 3 discourses research design. Descriptive analysis of findings from questionnaire-based survey, testing of research hypothesis and implications of the study have been done in Section 4. Conclusion has been discussed in Section 5.

2. Literature review and hypothesis development

Indian SMEs of manufacturing sectors are facing challenges of competitive product price and quality to stay competitive in global markets (Kumar *et al.*, 2014). Managing members of supply chain (SC) is very challenging and complex process in modern time. Improving coordination in SC can help in managing needs of SC members (Arshinder *et al.*, 2009). Although many organizations still compete at individual level in developing countries (Kohand Tan, 2006) but it is observed that organization working in coordination has competitive advantage as compared to isolated organizations (Singh *et al.*, 2012).

To study different strategic issues of SCM in SMEs such as motivation, investment priorities, hindrances in SCM implementation, SCM practices, and performance, the authors proposed a framework as shown in Figure 1. On the basis of framework, motivations, investment priorities, and hindrances, SCM practices would be selected and effect of these

SCM practices will be studied, with regard to Indian SMEs performance. As per the proposed framework the literature has been reviewed in following sections.

2.1 Characteristics of Indian SMEs

In developing economies, SMEs are major contributors to industrial growth. Singh *et al.* (2012) observed that in India, 95 percent of industrial units lies in small-scale sector and add 40 percent value to the manufacturing sector. Due to open global competition and technology revolutions, Indian small and medium enterprises (SMEs) are under intense pressure (Kumar *et al.*, 2014). To face and excel in global competition, Indian SMEs need to work in coordination with suppliers and adopt latest smart technologies (Kumar *et al.*, 2014). The importance of SMEs is increasing day by day in national and in the international market because the contribution of SMEs to national or international economy is very high (Goncalves *et al.*, 2019). The sales of SMEs products are very limited in international market because they are more focused toward domestic customers. International exposer gives the learning of focusing more on research and development and adopting new technologies (Battagila *et al.*, 2018). As per ruling of government of India and micro, small and medium enterprises development act, 2006, the micro, small and medium enterprises are grouped into two categories, manufacturing enterprises (defined in terms of investment in plant and machinery) and service enterprises (Table I) (defined in terms of investment in equipment) (https://msme.gov.in/know-about-msme).

2.2 Motivation for effective SCM in SMEs

Today, the futuristic organizations need effective SCM for being globally competitive. They need to be collaborative and responsive with all members of supply chain. Kumar *et al.* (2013) have observed that coordinated and flexible SC increases the SC profitability. Supportive higher management is an enabler for alignment between shareholders and customers (Skipworth *et al.*, 2015). Shatat and Udin (2012) have observed that performance of SC can be

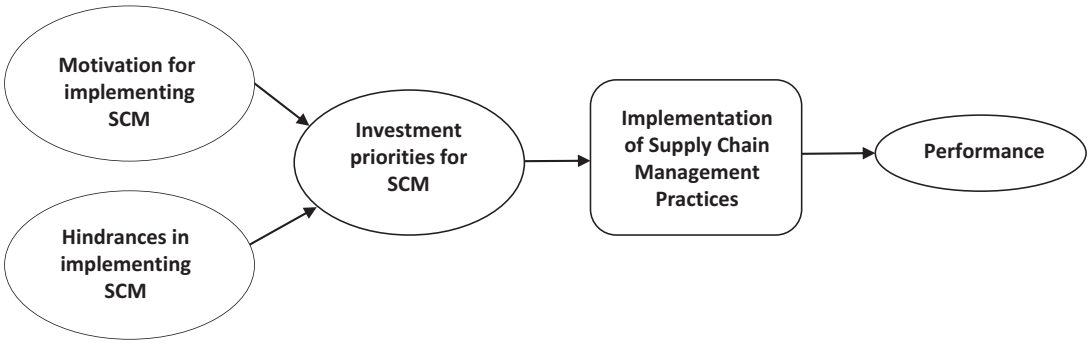


Figure1.
Proposed framework for study

Type of enterprises	Manufacturing sector (investment in plant and machinery in INR)	Service sector (investment in equipment in INR)
Micro enterprises	0–25 lakh	0–10 lakh
Small enterprises	Between 25 lakh and 5 crore	Between 10 lakh and 2 crore
Medium enterprises	Between 5 crore and 10 crore	Between 2 crore and 5 crore

Table I.
Classification of SMEs in India

enhanced by adopting advanced technologies in SCM. Practices such as online-purchasing, information exchange, and collaboration among members affect overall performance of SC (Chang *et al.*, 2013). Moen *et al.* (2016) have stated that the international orientation of the SMEs is closely interrelated with motivation for growth. Petrick *et al.* (2016) stated that SMEs working with coordination in SC can engender advantage in future. Moriones *et al.* (2013) have stated that adoption of SC practice, such as information and communication technologies (ICT), improves performance of SMEs.

Lancioni *et al.* (2000) have observed that use of advanced techniques in SCM can leads to different advantages such as cost reduction, quality improvement, on-time delivery, and improved competitiveness. Medlin *et al.* (2016)have observed that cultural changes in organization and management policies, can help in improving job gratification. Pradhan and Routroy (2016) stated that multiple sourcing options, abridge management, and risk directions are SCM drivers. Lamba and Singh (2017) observed that operations and SCM encompasses a vast domain and generate huge information in real time.

2.3 Hindrances in effective SCM of SMEs

Wiengarten *et al.* (2016) have observed that the risks affect the success of SC integration. Vacillating costs of raw materials, important data sharing, and demand variation with season are the main constraints faced by Indian SMEs in SCM (Kumar *et al.*, 2014).

Johnson (2001) observed that SC is open to market endangerments such as season effect, changing furors, adoptability of new launch, and curt life of product. Gill and Biger (2012) have observed that scarcity of money, challenging market scenario, and rules and regulations are constraints for small players in Canada. Lack of finance is a big challenge for small players as compared to bigger ones (Sener *et al.*, 2014). Kumar and Routroy (2014) and Loader (2015) observed that insufficient technologies and finance scarcity are few common issues in open world market. Faisal *et al.* (2007) have observed that there are lots of roadblocks in managing endangerment in SCs of SMEs. Punniyamoorthy *et al.* (2013) differentiated SC roadblocks into six groups such as supply, manufacturing, demand, logistics, environment, and information. Kumar *et al.* (2014) have stated that incertitude of customer demands, poor cognition of SCM, and interests of interlocutors in SCs are the main problems for SMEs in SC.

Singh *et al.* (2012) stated that small firms feel risks of varying raw materials price, information exchange, and fluctuating demand while cultivating in SC. According to Trkman *et al.* (2016), in global competition, SC risk management has considerable grandness. Chowdhury *et al.* (2018) studied the SC of Bangladeshi apparel industries and observed that barriers of supplier side such as long lead time, disruption in services, and timely delivery can be strategically managed by efficient planning, agile response, and timely delivery. Ali *et al.* (2019) observed that financial issues affecting the performance of SMEs can be resolved by sharing information among SC members. Alon *et al.* (2019) observed that marketing is a challenge for European SMEs on global horizon.

2.4 SCM practices

SCM is integration, coordination, and satisfaction of demand, supplies, and consumer issues with profit of all chain members (Wong *et al.*, 2005). Li *et al.* (2005) developed a measure for strategic supplier relationship, customer relationship, information exchange, select information, internal lean exercises, and deferment. Some of the important SC practices are discussed as follows:

2.4.1 Close partnership with suppliers. Ferreira *et al.* (2012) stated that cooperation, coordination, trust, and collaboration among customers and suppliers are very important for SCM. Joint operations among buyer and suppliers are the beginning step for productive SCM. Kumar *et al.* (2016) have observed that different criteria of supplier excerption and valuation

such as investiture in plant and machinery, advanced technology application, expatriation flexibility, propinquity to plant, allegiance to quality, cost effectivity, on-time delivery capability have substantial effect on business functioning of Indian SMEs. Support of top management is highly important for different functions of responsive SC such as cross-functional training, integration of departments within the organization and vendor development (Ganesan and Saumen, 2005). Bianchi and Saleh (2010) have observed that trust and commitment among suppliers are necessary for improving SC performance. Chan and Chan (2009) have observed that information exchange is substantive instrument to improve coordination in SC. Squire *et al.* (2009) observed that buyer's responsiveness is directly affected by supplier's flexibilities and responsiveness. Zahraee *et al.* (2018) observed that society, environmental norms, and customer investment are the highly substantial drivers that contribute toward supplier participation. Aggarwal *et al.* (2018) studied that under uncertain conditions, selection, and allocation of orders to vendors also get influenced by cost reduction, quality improvement, and lead time reduction.

Confining relationship with customers: Outbound SCM can be viewed as demand chain management (Frohlich and Westbrook, 2002; Hsu, 2005). Relationship with both customers and suppliers is very important in SCM. Lan *et al.* (2016) stated that quick response and flexible logistics strategy leads to higher customer satisfaction. Kumar *et al.* (2016) studied that participation of customer on different issues such as marketing and sales decisions, customer relationship management (CRM), logistic management, and design of SC have substantial correlation with business performance (financial) of Indian SMEs. Patrucco *et al.* (2019) have observed that customer preferences have positive influence on innovation and cost performance given by suppliers.

Just in time (JIT): JIT is an incorporated set of actions planned to get production with minimum inventories of raw, work in process, and finished materials. JIT also expects the delivery of right quantity of items at the right time with the motive to meet the performance standards (Canel *et al.*, 2000; Mistry, 2006; Kros *et al.*, 2006).

Strategic planning: Traditionally, strategic planning concentrates on the manufacturing, innovation, financial, and market insights (Lin and Tseng, 2006). Kumar *et al.* (2014) stated that for Indian SMEs, improvement in quality, on-time delivery and reduction of cost are the major strategic issues to focus. Liu and Jiang (2016) observed that the strategic capacities and manufacturing capacities have substantial influence on performance and competitiveness of Chinese manufacturing firms. Indian SMEs are highly dependent on higher management consignment, long-run plan for endurance and development (Kumar *et al.*, 2015). Solke and Singh (2018) observed that uncertainties and dynamic market situations of automobile component industry can be managed by machine flexibility in lean manufacturing. Singh *et al.* (2018) studied that varying customer's requirement, demographic precedencies; advance engineering, life cycle of electronic goods, and varying attitudes create threats for running business plans and affects the competitiveness of electronics manufacturing industries in India.

Selected suppliers: Incoeval business, selecting suppliers is a need of hours (Chandra and Kumar, 2000). Strategically chosen few suppliers can promote long run partnership and reduce production expenditures. Kumar *et al.* (2016) have stated that excerption and valuation of suppliers is need of the hour for efficient and timely delivery of quality products. Wang *et al.* (2016) have observed that interpersonal relationships such as personal tenderness, communications, and believability, are key elements for improving integration among SC members. Brun and Karaosman (2019) stated that single sourcing strategies give quality products with cost effectiveness. Selection and evaluation of suppliers is a critical and strategic issue for SCM of Indian SMEs (Yadav *et al.*, 2018).

Inventory Management: Dubiousness in an SC can be easily handled by jobbing and inventory management (Koh and Tan, 2006). Khorasani (2018) observed that agility and

flexibility in SCM, gives an edge to its members in irregular business conditions. Sushil (2017) observed that the principles of a flexible organization can be adopted in creating a flexible SC. Commitment of top leadership is required to start and affirm the "flexibility principles".

e-procurance: Procurance of items by using electronic technologies, improve the participation of all members of SC in purchasing. All members participating in *e-procurance* can bargain, avoid multiple commissions, and take advantages of modern technologies like e-payment, enterprise resource planning (ERP), etc. (Koh *et al.*, 2007). By adopting modern IT tools, SC members can connect with all in chain in real-time (Stanley *et al.*, 2009). Performance of Indian SMEs gets affected by application of modern IT tools in different areas such as customer demand prediction and sales; connect with suppliers and customers (Kumar *et al.*, 2016). Rezaei *et al.* (2018) studied the latest technology application in SC of SMEs.

Outsourcing and 3PL: Logistics services provided by a player other than the manufacturer and customer is known as third party logistics (3PL) (Sink *et al.*, 1996). These outside players are experts of their area and give an edge in modern competition (Franceschini *et al.*, 2003). Bamel *et al.* (2019) observed that mutual trust, equal opportunity, and transparent deals give an edge in SCM.

Information Technology (IT): ITs have shown lot of potential in effective SCM. Singh (2015) stressed on information sharing for improving responsiveness of SC. These days SC operations are changing due to adoption of smart technologies and improving networking among SC members (Pant *et al.*, 2003). Performance of small-scale industries in India has improved due to application of technologies, training, and focused research (Singh *et al.*, 2010). Kumar *et al.* (2016) stated that in Indian SMEs, technologies are readily adopted for designing and development of new items. SCM become highly effective with coaction and timely sharing of correct information. Song *et al.* (2016) stated that for SMEs information sharing can be improved by building trust and strong relationship among SC members. Use of latest ICT can give SMEs an edge in addressing the challenges of global competition (Cragg and McNamara, 2018). Kulkarni *et al.* (2019) observed that quality, flexibility, cost, and delivery when aggregated, give maximum competiveness to digital manufacturing organizations. Gurtu and Johny (2019) have emphasized the need of application of emerging technologies such as blockchain technology for effective SCM.

2.5 Performance measurement

"Time" is a strategic performance measure (Gunasekaran *et al.*, 2008). Ates *et al.* (2013) have observed that measuring performance on strategic and operational front is a big challenge. Kumar *et al.* (2015) have observed that different issues of customer relationship management such as customer's complaints, inquiry, and future expectations need attention for improving CRM performance. Network of communication connects all business functions together (Goyal, 2012). Responsiveness of SC can be improved by application of modern technologies and Internet (Gunasekaran *et al.*, 2008).

Until the 1980s, profit return on invested capital and productiveness were favored performance criteria. In the late1980s, new approaches such as balanced scorecard emerged out. Balance score card approach has four components: fiscal, customer-related, intragroup, and innovation and learning (Kaplan and Norton, 1992). Awheda *et al.* (2016) have observed that inventory levels, productivity, lead time of manufacturing, and transportation flexibility are key components pretending the performance of SMEs. Prajogo *et al.* (2016) stated that competitive operational performance is the result of inbound supply performance and internal lean production processes. Chirra and Kumar (2018) identified four major SC flexibility strategies such as volume, manufacturing, supplier collaboration, and supplier flexibility which affect the firm's performance. Xiao and Ramsden (2016) have observed that

optimal use of expertise and sources of finance are main elements for innovative and high-tech production in Chinese SMEs. Gurtu *et al.* (2015) have observed the need of sustainability in SC operations.

Lu *et al.* (2018) studied the SC integration and operational performance of the original equipment manufacturer in China automotive industries. Singhry and AbdRahman (2019) observed that SC innovation capability effect SC performance. Yadav *et al.* (2018) observed that internal structure of organizations also affect financial performance. Dijkman *et al.* (2019) states that inefficient operations lead to enlarged lead time.

Based on literature review and proposed framework (Figure 1), following research propositions are proposed in this study.

P1. Motivation for implementation of SCM has significant correlation with investment priorities.

P2 (a). Hindrances in implementing SCM have significant negative correlation with investment priorities.

P2 (b). Hindrances in implementing SCM have significant negative correlation with performance.

P3. Investment priorities for SCM have significant correlation with level of implementation of best SC practices.

P4. Level of implementation of SC practices has significant correlation with performance.

3. Research design

Present study deals with different issues related to motivation, investment priorities, hindrances for implementing SCM, and selecting best SC practices, and finally their effects on business performance. Questionnaire has been developed to conduct the survey of Indian SMEs. The unit of analysis was firm level. Results of survey-based study ensure significant and valid results (Straub *et al.*, 2004). All items under different constructs have been taken from available literature. Therefore authors began the process with a review of the extensive literature on motivation, investment priorities, hindrances, best SC practices, and performance. Survey has been conducted among Indian manufacturing SMEs of various manufacturing sectors including automobile, plastic, light engineering, chemical, and electric/electronics sectors from January 2019 to July 2019. Most of surveyed organizations were in local or semi-urban region. Preliminary survey has been conducted in 40 SMEs from various sectors before giving final shape to the questionnaire. Of 40 organizations participating in pilot survey, 10 were from automobile sector, 10 from plastic sector, 10 from light engineering, five from chemical, and five from electric/electronics sector. Graphical representation of different sectors responded during survey are shown in Figure 2. Organizations for survey were selected from different sources such as Confederation of Indian Industries, Auto Component Manufacturers Association, Federation of Indian Chambers of Commerce and Industries and Directorate of Industries (Government of National Capital Territory of Delhi). Final survey instrument was having two sections A and B. Section A included questions about general information and different criteria of classification of SMEs in India. Section B have questions on different strategic issues for effective SCM such as motivation, priorities, hindrances, SCM practices, information sharing practices, supplier selection, evaluation and development, and performance and respondent profile.

By postal or electronic mail-based survey, preliminary survey has been conducted on a personal basis by taking prior appointment with organizations. One Annexure was attached with the questionnaire. It focused on guidelines and terminology to avert any biasing.

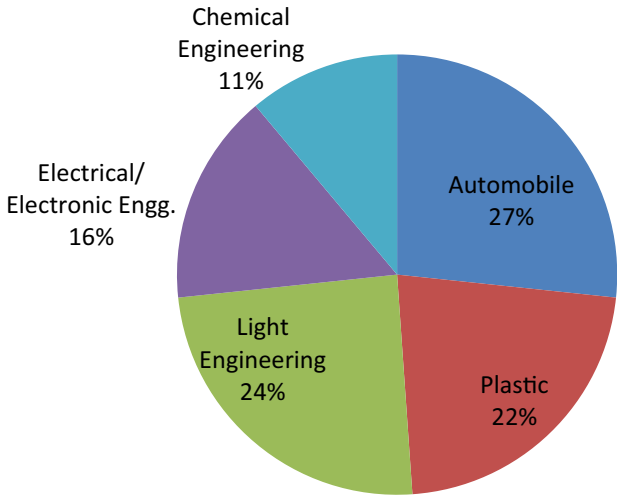


Figure 2.
Share of responding sectors during the survey study

Survey-based approach has been used by Dubey *et al.* (2018) for analyzing SC issues of Indian auto component makers.

In the present study, respondents were requested to grade the vividness of each ascribe for their own organization on a five-point Likert scale (1 – lowest, 5 – highest). After pilot survey, the survey instrument was finalized. About 1,500 SMEs from all regions of India were approached for gathering responses. In spite of repetitive mails, telephonic calls, and personal visits to organizations, only 257 complete questionnaires could be incurred. Most of the responders were from middle and top management position, having the power to take strategic decisions. For survey results analysis, SPSS 17 software has been used.

4. Results and discussion

Descriptive analysis is done to analyze different operational issues of SCM in Indian SMEs, and then correlation analysis has been done to test the research propositions made in this study.

4.1 Descriptive analysis

Mean, standard deviation, and standard error have been calculated for statistical analysis of various issues of SCM in SMEs. Before doing this analysis, reliability analysis is performed for each scale/question used in the questionnaire. Reliability has been checked by interitem analyses. The Cronbach's alpha coefficient has been checked for every scale. It is an integral part of any survey research.

Reliability analysis of data depicts that Cronbach's alpha value for all constructs is more than the minimum acceptable value of 0.5 (Nunnally, 1978). It indicates a high level of internal consistency among items. The value of Cronbach's α coefficient was found in the range of 0.697–0.911. Data received from the survey have been examined by different statistical tests such as one sample *t*-test and correlation analysis in the following sections.

4.1.1 Motivations for effective SCM. On the basis of the opinion of experts and literature review, 10 factors of motivation for effective SCM in Indian SMEs, were identified. These motivation factors are reducing delivery lead time, reduction of production cost, meeting changing customer demands, reducing inventory cost, accurate demand, sharing the risk with suppliers, reducing product rejection rate, improving flexibility, buying from JIT suppliers, and reducing the number of suppliers. The survey responders were required to show the degree of importance for these motivations on a five-point Likert scale (1-Very low,

2- Low, 3-Medium, 4-High, and 5-Very high). These observations are shown in Figure 3 in graphical form. The Cronbach's alpha for this 10 item construct is 0.697, which is higher than the minimum requirement of 0.5.

On the basis of survey results, it is observed that top three motivational factors for SCM implementation in Indian SMEs are reduction of delivery lead time (3.96), reduction of product cost (3.94), and reduction of inventory cost (3.88). The findings imply that Indian SMEs now give more focus on product cost reduction, delivery lead time reduction, and reduction of inventory cost. To have sustainable growth in the global market, SMEs need to improve their performance in terms of delivery on time, flexibility, and agility by reducing overall product cost (Singh *et al.*, 2019). Further authors have observed that meeting changing customer demands (3.88), accurate demand forecasting (3.74), sharing the risk with suppliers and customers (3.76), and reducing product rejection rate (3.62) are other motivating factors for effective SCM in a globalized market. Other factors such as improving flexibility of production system (3.41), buying from JIT suppliers (3.19), and reducing the number of suppliers (2.94) are lowest ranked motivation factors.

4.1.2 Hindrances in effective SCM. On the basis of the opinion of experts and literature review, eleven hindrances in implementing SCM in SMEs were identified for this study. These hindrances are lack of dedicated resources, location of suppliers and customers, lack of coordination among SC members, poor demand forecast system, lack of use of modern technologies, lack of sharing information with suppliers, lack of sophisticated information systems, poor transportation facilities, lack of trust among SC members, lack of top management commitment, and shortage of trained workforce. Survey responders were asked to point the level of these hindrances in implementing SCM on a five-point Likert scale (1-Very low, 2- Low, 3-Medium, 4-High, 5-Very high). These results are shown in Figure 4 in graphical form. The Cronbach's alpha value for eleven items construct is 0.889, which is higher than the minimum requirement of 0.5.

On the basis of survey results, it is observed that top three hindrances in implementing SCM in Indian SMEs are lack of top management commitment (2.86), lack of resources and funds (2.78), and poor demand forecast system (2.76). Therefore, organizations should give more focus on removing these hindrances by following proactive approach. On the basis of

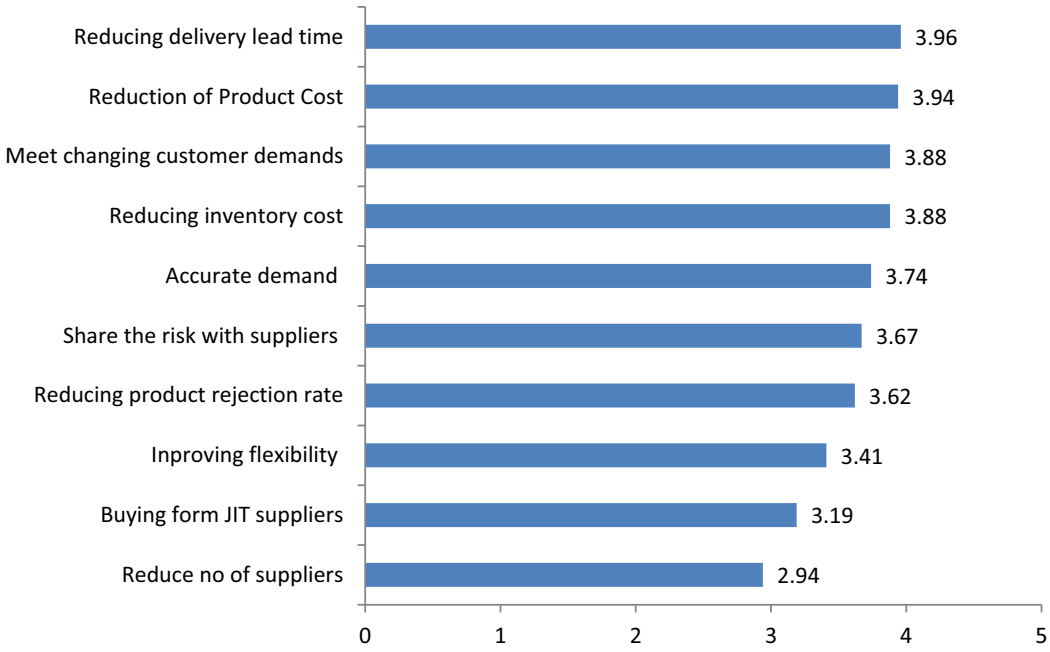


Figure 3.
Motivations for effective SCM

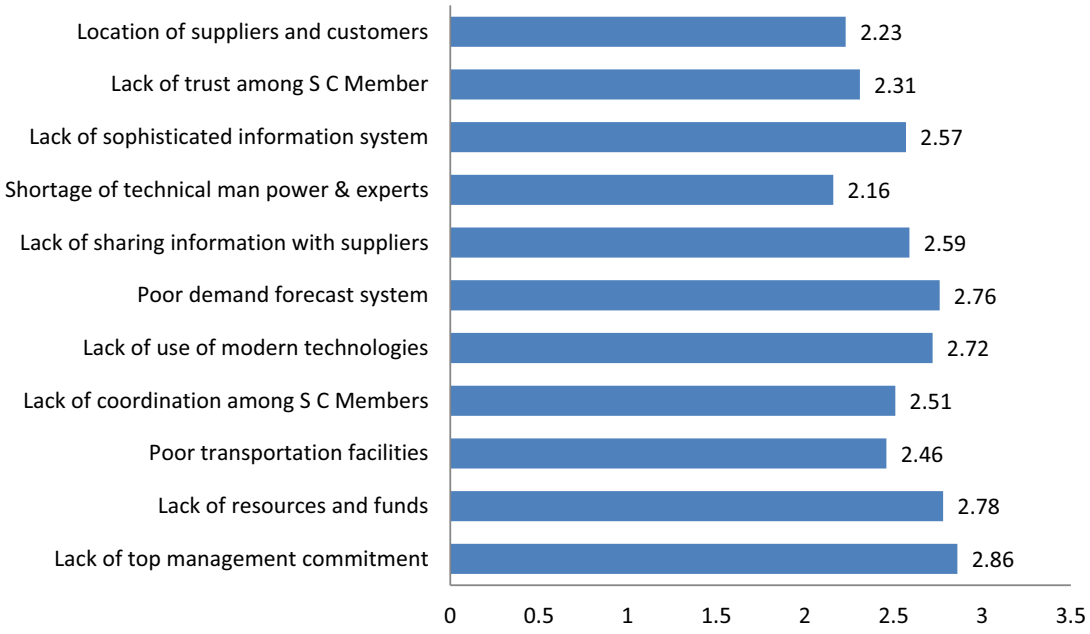


Figure 4.
Hindrances in effective SCM

the mean value, other hindrances in implementing SCM are lack of use of modern technologies (2.72), lack of sharing information with suppliers (2.59), lack of sophisticated information system (2.57), lack of coordination among SC members (2.51), poor transportation facilities (2.46), lack of trust among SC members (2.31), location of suppliers and customers (2.23), and shortage of technical man power and experts (2.16). Indian organizations have to pay due attention in removing these hindrances while implementing SCM.

4.1.3 Investment priorities for SCM success. On the basis of the opinion of experts and literature review, 10 investment priorities were identified for this study. These are computer-aided design/computer-aided manufacturing (CAD/CAM) facilities development, research and development, human resource and knowledge management, flexible manufacturing system, supplier development, IT application, long-term relationship with customers, accurate sales forecasting and planning, quality improvement, and quick response to customer demands. Survey responders were asked to point the level of these 10 investment priorities on a five-point Likert scale (1-Very low, 2- Low, 3-Medium, 4-High, 5-Very high). Focus on these priorities will decide the outcome of strategy development. It is expected that organizations will decide their investment priorities on the basis of their SC strategy. These results are shown in Figure 5 in graphical form.

Observations of the survey show that top three investment priorities for Indian SMEs are quality improvement (4.11), quick response to customer demands (4.11), and accurate sales forecasting and planning (3.94). Long-term relationship with customers (3.88), IT applications (3.87), supplier development (3.68), flexible manufacturing system (3.67), human resources and knowledge management (3.66), research and development (3.63), and CAD/CAM facilities development (2.86) are other areas of investment for Indian SMEs. These findings imply that SMEs are still not giving much focus on knowledge management, research and development, and CAD/CAM facilities. Competitiveness of SMEs can be improved by effective management of knowledge and human resource along with application of advanced technology for process improvement (Singh *et al.*, 2008).

4.1.4 SCM practices. On the basis of the opinion of experts and literature review, 14 SCM practices were identified in this study. These are outsourcing, integrated inventory management, barcode/radio-frequency identification (RFID)/other automatic identification tool, third party logistics, design for logistics, sharing of point of sale information with

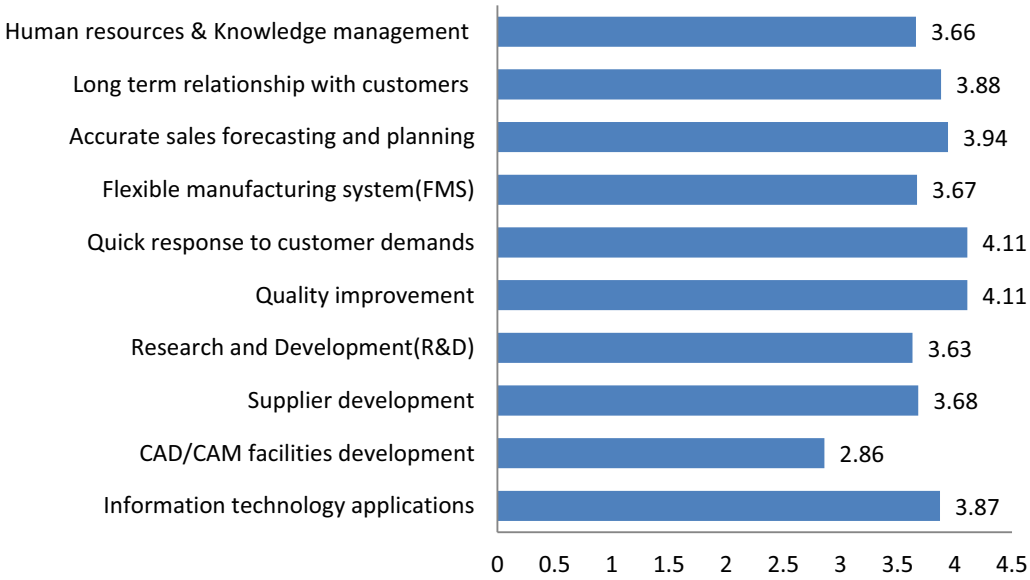


Figure 5.
Investment priorities for SCM success

partners, customer relationship management, dynamic pricing, enterprise resource planning, collaborative planning and forecasting replenishment, vendor managed inventory, lead time management, bullwhip effect analysis and cross docking. Survey responders were asked to point the level of these 14 SCM practices in their respective organizations on a five-point Likert scale (1-Very low, 2-Low, 3-Medium, 4-High, 5-Very high).Results are shown in Figure 6 in graphical form.

On the basis of survey results it is observed that top three SCM practices are customer relationship management (3.85), ERP (3.75), and integrated inventory management (3.64). Third party logistics (3.63), lead time management (3.63), collaborative planning and forecasting, replenishment (3.54), dynamic pricing (3.45), design for logistics (3.44), vendor managed inventory (3.42), barcode/RFID/other automatic identification tool (3.36), sharing of point of sale information with the partners (3.36), outsourcing (3.22), bullwhip effect analysis (3.09), and cross docking (3.08) are other preferred SC practices for SMEs in survey. It is also observed that except cross docking, other 13 SCM practices have significant correlation with performance. Reason for low importance of cross docking for SMEs may be due to lack awareness and lack of information and IT support for SMEs. Dubey *et al.* (2018) have observed that information sharing and SC connectivity influence SC visibility. Integrated inventory management, ERP, vendor managed inventory, and lead time management are the most important factors in terms of correlation with performance. Therefore, organizations should give more focus on these SCM practices.

4.1.5 Performance measurement. On the basis of the opinion of experts and literature review, nine measures for SMEs performance have been identified. These are reduction in manufacturing cost, reduction in product rejection rate, reduction in inventory cost, reduction in lead time, sales growth, return on investment, profit growth, responsiveness, and delivery on time. The respondents were asked to indicate the impact of SCM practices on the performance of Indian SMEs, on a five-point Likert scale (1-Significant decrease, 2-Decrease, 3-Same as before, 4-Increase, 5-Significant increase). These results are shown in Figure 7 in graphical form. On the basis of survey results, it is observed that top three measures of performance for SMEs are delivery on time (4.14), responsiveness (4.10), and profit growth (4.05). It is further observed that other parameters affected by SC practices are return on investment (3.92), reduction in lead time (3.86), reduction in inventory cost (3.81), reduction in product rejection rate (3.74), and reduction in manufacturing cost (3.66).

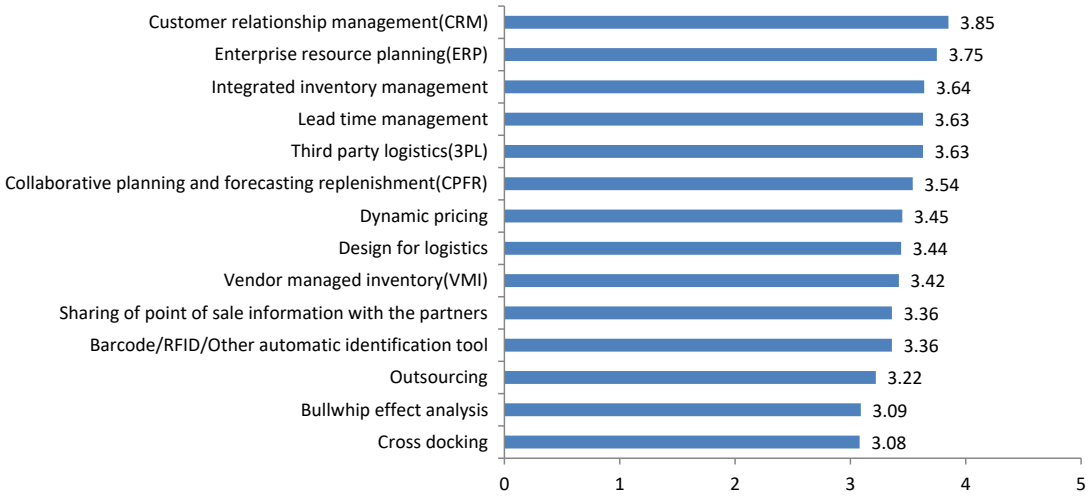


Figure 6.
Level of applications of various SCM practices in SMEs

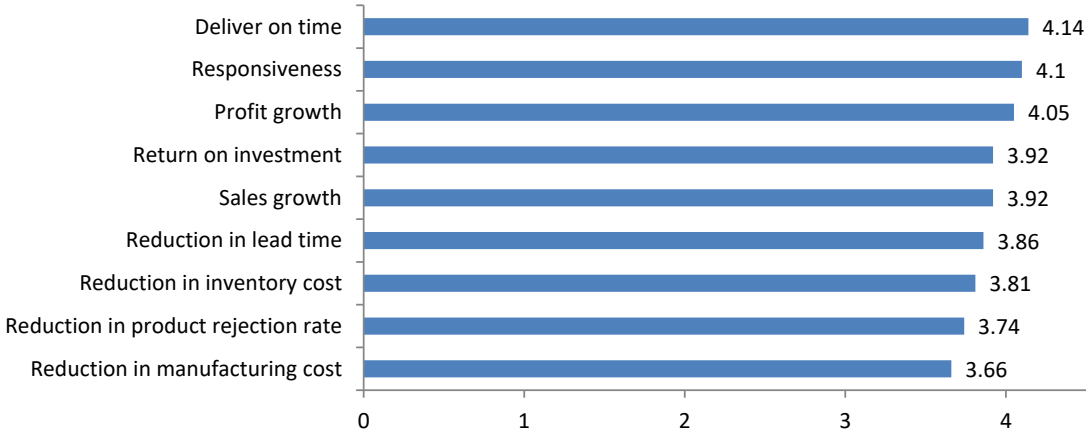


Figure 7.
Performance measures

4.2 Testing of research propositions

Different issues related to motivations, investment priorities, hindrances, selection of SC practices, and their effects on performance of Indian SMEs have been analyzed. Majority of propositions have tried to test the relationship of different issues of motivations, investment priorities,hindrances in implementing SCM, and applications of SC practices with the business performance of Indian SMEs. For testing of research propositions, correlation, and regression analysis has been done. The results are given in Table II and Table III. Following are the observations from analyzes:

- Motivations for implementing SCM in SMEs have significant positive correlation with the investment priorities for effective SCM, thereby affirming the first proposition. The reason for this is that motivation for implementing SCM help in investment planning and sets investment priorities for SMEs.
- Hindrances in implementing SCM in SMEs are significantly negatively correlated with investment priorities and performance, thereby supporting the second proposition. This implies that the hindrances in implementing SCM discourage SMEs in making new investments in implementing SC initiatives thereby adversely affecting SC performance.

Issues	Motivations*	Hindrances*	Investment priorities*	SCM practices*	Performance*
Motivations*	1	−0.052	0.678**	0.624**	0.510**
Hindrances*	−0.052	1	−0.188**	−0.149*	−0.179**
Investment priorities*	0.678**	−0.188**	1	0.617**	0.517**
SCM practices*	0.624**	−0.149*	0.617**	1	0.469**
Performance*	0.510**	−0.179**	0.517**	0.469**	1

Notes: motivation*-motivations for implementing SCM, **investment priorities***-investment priorities for SCM, **hindrances***-hindrances in implementing SCM, **SCM practices***-application of supply chain practices, **performance***-performance issues.**Correlation is significant at the 0.01 level (two-tailed). *Correlation is significant at the 0.05 level (two-tailed).

Table II.
Correlation analysis

R	R^2	Adjusted R^2	Std. Error of the estimate
0.582	0.339	0.325	0.48553

Notes: Independent/dependent variables: motivation, investment priorities, hindrances, SCM practices/ performance

Table III.
Regression analysis

- Investment priorities for implementing SCM in SMEs have significant positive correlation with intensity of best SC practices being implemented, thereby supporting the third proposition. It signifies that best SC practices need initial investment, and gain from SC practices implementation is of long term. SC practices get changed depending on markets and organization demand.
- Level of implementation of best SC practices in SMEs has a significant correlation with performance, thereby supporting the fourth proposition. The reason for this is that the selection and implementation of best SC practices leads to improved SC performance.

Regression analysis (R^2 = 0.339) from Table III implies that, considered issues in this study (motivation, investment priorities, hindrances, and SCM practices) have shown 33.9 percent variability in performance of Indian SMEs. It means that other than considered independent variables, there may be some other issues linked to emerging business trends such as industry 4.0, circular economy, and government policy, impacting performance of the Indian SMEs. Therefore, to build SC management more effective, Indian SMEs should also consult professionals and experts for adopting emerging business trends. In present business scenario, irrespective of size, organizations have to adopt emerging technologies of industry 4.0 and best practices of circular economy for sustaining in globalized market. SMEs have to be more export oriented. Working at local or national level will not be sustainable.

5. Conclusions, implications, limitation, and future scope

This study has analyzed the different strategic issues such as motivation, investment priorities, and hindrances for effective SCM in Indian SMEs. Survey-based approach was used in this study. 257 complete responses were considered for analysis of data through different statistical tests. Following are the few observations from this study:

- Reducing delivery lead time, reducing product cost, and reducing inventory cost are the major motivating factors for effective SCM of Indian SMEs in a globalized market.

- Quality improvement, quick response to customer demands, and accurate sales forecasting and planning are the main investment priorities for SCM implementation in SMEs.
- Lack of top management commitment, lack of resources and funds, and poor demand forecast system are the major hindrances in implementing effective SCM in SMEs.
- CRM, ERP, and integrated inventory management are the main SCM practices of Indian SMEs.
- Level of Motivations and investment in different areas has significant positive correlation with investment for effective SCM.
- SCM practices such as integrated inventory management, vendor managed inventory, lead time management, customer relationship management, barcode/RFID/other automatic identification practices, sharing of point of sales information with partners, third party logistics, bullwhip effect analysis, and design of logistics have significant.

5.1 Implications of study

Findings of the study imply that Indian SMEs should strategically plan their priority to handle hindrances, SCM practices, and application of emerging technologies. It has been observed that human resource management, knowledge management, and implementing advanced technologies are not being given adequate importance by Indian SMEs. It is a matter of concern for Indian SMEs managers. Therefore, in the digital era of industry 4.0, SMEs should focus on managing their knowledge and in implementing emerging technologies such as Internet of Things, cloud computing, big data analytics, etc. Apart from it, by using these technologies, SMEs should try to achieve the objective of the circular economy to compete in global markets.

5.2 Limitations and direction for future research

Present research has only focused on Indian SMEs. This study has tested certain propositions in context to SCM but sustainability issues in context to circular economy and industry 4.0 may be also considered as future scope of the study. Similar research may be performed in context to developed countries for a comparative study and new learning to SMEs of developing countries. Researchers may further find new challenges and strategies for SMEs in coping with emerging business models.

References

Aggarwal, R., Singh, S.P. and Kapur, P.K. (2018), "Integrated dynamic vendor selection and order allocation problem for time dependent and stochastic data", *Benchmarking: An International Journal*, Vol. 25 No. 2, doi: 10.1108/BIJ-05-2017-0085.

Ali, Z., Gongbing, B. and Mehreen, A. (2019), "Supply chain network and information sharing effects of SMEs' credit quality on firm performance: do strong tie and bridge tie matter?", *Journal of Enterprise Information Management*, Vol. 32 No. 5, pp. 714-734.

Alon, I., Chen, S. and Mandolfo, M. (2019), "Supply chain – marketing integration: how do European SMEs go to China *via* the new silk road", *Business Process Management Journal*, Vol. 25 No. 2, pp. 368-378.

Arshinder, K., Kanda, A. and Deshmukh, S.G. (2009), "A framework for evaluation of coordination by contracts: a case of two-level supply chains", *Computers and Industrial Engineering: An International Journal*, Vol. 56, pp. 1177-1191.

Ates, A., Garengo, P., Cocca, P. and Bititci, U. (2013), "The development of SME managerial practice for effective performance management", *Journal of Small Business and Enterprise Development*, Vol. 20 No. 1, pp. 28-54.

Awheda, A., Rahman, M.N.A., Ramli, R. and Arshad, H. (2016), "Factors related to supply chain network members in SMEs", *Journal of Manufacturing Technology Management*, Vol. 27 No. 2, pp. 312-335.

Bamel, N., Dhir, S. and Sushil (2019), "Inter-partner dynamics and joint venture competitiveness: a fuzzy TISM approach", *Benchmarking: An International Journal*, doi: 10.1108/BIJ-02-2018-0041.

Battaglia, D., Neirotti, P. and Paolucci, E. (2018), "The role of R&D investments and export on SMEs' growth: a domain ambidexterity perspective", *Management Decision*, Vol. 56 No. 9, pp. 1883-1903.

Bianchi, C. and Saleh, A. (2010), "On importer trust and commitment: a comparative study of two developing countries", *International Marketing Review*, Vol. 27 No. 1, pp. 55-86.

Brun, A. and Karaosman, H. (2019), "Customer influence on supply chain management strategies", *Business Process Management Journal*, Vol. 25 No. 2, pp. 288-306.

Canel, C., Rosen, D. and Anderson, E.A. (2000), "Just-in-time is not just for manufacturing: a service perspective", *Industrial Management and Data Systems*, Vol. 100 No. 2, pp. 51-60.

Chan, H.K. and Chan, F.T.S. (2009), "Effect of information sharing in supply chain with flexibility", *International Journal of Production Research*, Vol. 47 No. 1, pp. 213-232.

Chandra, C. and Kumar, S. (2000), "Supply chain management in theory and practice: a passing fad or a fundamental change?", *Industrial Management & Data Systems*, Vol. 100 No. 3, pp. 100-114.

Chang, H.H., Tsai, Y.C. and Hsu, C.H. (2013), "E-procurement and supply chain performance", *Supply Chain Management: An International Journal*, Vol. 18 No. 1, pp. 34-51.

Chirra, S. and Kumar, D. (2018), "Evaluation of supply chain flexibility in automobile industry with fuzzy DEMATEL approach", *Global Journal of Flexible Systems Management*, Vol. 19, No. 4, pp. 305-319.

Chowdhury, M.M.H., Umme, N.J. and Nuruzzaman, M. (2018), "Strategies for mitigating supply-side barriers in the apparel supply chain: a study on the apparel industry of Bangladesh", *Global Journal of Flexible Systems Management*, Vol. 19, No. 1, pp. 41-52.

Cragg, T. and McNamara, T. (2018), "An ICT-based framework to improve global supply chain integration for final assembly SMEs", *Journal of Enterprise Information Management*, Vol. 31 No. 5, pp. 634-657.

Dubey, R., Altay, N., Gunasekaran, A., Blome, C., Papadopoulos, T. and Childe, S.J. (2018), "Supply chain agility, adaptability and alignment: empirical evidence from the Indian auto components industry", *International Journal of Operations and Production Management"*, Vol. 38, No. 1, pp. 129-148.

Dijkman, R., Turetken, O., van IJzendoorn, G. and De Vries, M. (2019), "Business processes exceptions in relation to operational performance", *Business Process Management Journal*, Vol. 25 No. 5, pp. 908-922.

Faisal, M.N., Banwet, D.K. and Shankar, R. (2007),"Supply chain risk management in SMEs: analyzing the barriers", *International Journal of Management and Enterprise Development*, Vol. 4 No. 5 pp. 588-607.

Ferreira, R.P., Silva, J.N., Strauhs, F.R. and Soares, A.L. (2012), "Performance management in collaborative networks: a methodological proposal", *Journal of Universal Computer Science*, Vol. 17 No. 10, pp. 1412-1429.

Franceschini, F., Galetto, M., Pignatelli, A. and Varetto, M. (2003), "Outsourcing: guidelines for a structured approach", *Benchmarking: An International Journal*, Vol. 10 No. 3, pp. 246-260.

Frohlich, M. and Westbrook, R. (2002), "Demand chain management in manufacturing and services: web-based integration, drivers and performance", *Journal of Operations Management*, Vol. 20, pp. 729-745.

Ganesan, K. and Saumen, B. (2005), "Corporate turnaround through effective supply chain management: the case of a leading jewellery manufacturer in India", *Supply Chain Management: An International Journal*, Vol. 10 No. 5, pp. 340-348.

Gill, A. and Biger, N. (2012), "Barriers to small business growth in Canada", *Journal of Small Business and Enterprise Development*, Vol. 19 No. 4, pp. 656-668.

Gonçalves, J.M., Ferreira, F.A., Ferreira, J.J. and Farinha, L.M. (2019), "A multiple criteria group decision-making approach for the assessment of small and medium-sized enterprise competitiveness", *Management Decision*, Vol. 57 No. 2, pp. 480-500.

Goyal, D.P. (2012), "Business alignment and critical success factors in information systems implementation: an empirical analysis of selected Indian organisations", *International Journal of Business Information Systems*, Vol. 10 No. 4, pp. 397-416.

Gunasekaran, A., Lai, K.H. and Cheng, T.C.E. (2008), "Responsive supply chain: a competitive strategy in a networked economy", *Omega*, Vol. 36, pp. 549-564.

Gurtu, A. and Johny, J. (2019), "Potential of blockchain technology in supply chain management: a literature review", *International Journal of Physical Distribution and Logistics Management*. https://www.emerald.com/insight/content/doi/10.1108/IJPDLM-11-2018-0371/full/html.

Gurtu, A., Searcy, C. and Jaber, M. (2015), "An analysis of keywords used in the literature on green supply chain management", *Management Research Review*, Vol. 38 No. 2, pp. 166-194.

Hsu, L.L. (2005), "SCM system effects on performance for interaction between suppliers and buyers", *Industrial Management and Data Systems*, Vol. 105 No. 7, pp. 857-875.

Huin, S.F., Luong, L.H.S. and Abhay, K. (2002), "Internal supply chain planning detriments in small and medium sized manufacturers", *International Journal of Physical Distribution and Logistics Management*, Vol. 32 No. 9, pp. 771-782.

Johnson, M.E. (2001), "Learning from toys: lessons in managing risk from toy industry", *California Management Review*, Vol. 43 No. 3, pp. 106-125.

Kaplan, R.S. and Norton, D.P. (1992), "The balanced scorecard - measures that drive performance", *Harvard Business Review*, Vol. 70 No. 1, pp. 71-79.

Khorasani, S.T. (2018), "A robust optimization model for supply chain in agile and flexible mode based on variables of uncertainty", *Global Journal of Flexible Systems Management*, Vol. 19 No. 3, pp. 239-253.

Koh, S.C.L. and Tan, K.H. (2006), "Operational intelligence discovery and knowledge mapping approach in a supply network with uncertainty", *Journal of Manufacturing Technology Management*, Vol. 17 No. 6, pp. 687-699.

Koh, S.C.L., Demirbag, M., Bayraktar, E., Tatoglu, E. and Zaim, S. (2007), "The impact of supply chain management practices on performance of SMEs", *Industrial Management and Data Systems*, Vol. 107 No. 1, pp. 103-124.

Kros, J.F., Falasca, M. and Nadler, S.S. (2006), "Impact of just-in-time inventory systems on OEM suppliers", *Industrial Management & Data Systems*, Vol. 106 No. 2, pp. 224-241.

Kulkarni, S., Verma, P. and Mukundan, R. (2019), "Performance landscape modeling in digital manufacturing firm", *Business Process Management Journal*, Vol. 25 No. 3, pp. 533-552.

Kumar, P.S. and Routroy, S. (2014), "Analyzing the supply chain risk issues for an Indian manufacturing company", *Journal of Advances in Management Research*, Vol. 11 No. 2, pp. 144-162.

Kumar, R., Singh, R.K. and Shankar, R. (2013), "Study on coordinationissues for flexibility in supply chain of SMEs: a case study", *Global Journal of Flexible Systems Management*, Vol. 14 No. 2, pp. 81-92.

Kumar, R., Singh, R.K. and Shankar, R. (2014), "Strategy development by Indian SMEs for improving coordination in supply chain: an Empirical study", *Competitiveness Review*, Vol. 24 No. 5, pp. 414-432.

Kumar, R., Singh, R.K. and Shankar, R. (2015), "Critical success factors for implementation of Supply Chain Management in Indian SMEs and their impact on performance", *IIMB Management Review*, Vol. 27 No. 2, pp. 92-104.

Kumar, R., Singh, R.K. and Shankar, R. (2016), "Study on collaboration and information sharing practices for SCM in Indian SMEs", *International Journal of Business Information Systems*, Vol. 22 No. 4, pp. 455-475.

Lamba, K. and Singh, S.P. (2017), "Big data in operations and supply chain management: current trends and future perspectives", *Production Planning and Control*, Vol. 28 No. 11-12, pp. 877-890, doi: 10.1080/09537287.2017.1336787.

Lan, S., Zhang, H., Zhong, R.Y. and Huang, G.Q. (2016), "A customer satisfaction evaluation model for logistics services using fuzzy analytic hierarchy process", *Industrial Management and Data Systems*, Vol. 116 No. 5, pp. 1024-1042.

Lancioni, R.A., Smith, M.F. and Oliva, T.A. (2000), "The role of the Internet in supply chain management", *Industrial Marketing Management*, Vol. 29, pp. 45-56.

Li, S., Ragu-Nathan, B., Ragu-Nathan, T.S. and Rao, S.S. (2005), "Development and validation of a measurement for studying supply chain management practices", *Journal of Operations Management*, Vol. 23, pp. 618-641.

Lin, C. and Tseng, H. (2006), "Identifying the pivotal role of participation strategies and information technology application for supply chain excellence", *Industrial Management and Data Systems*, Vol. 106 No. 5, pp. 739-756.

Liu, L. and Jiang, Z. (2016), "Influence of technological innovation capabilities on product competitiveness", *Industrial Management and Data Systems*, Vol. 116 No. 5, pp. 883-902.

Loader, K. (2015), "SME suppliers and the challenge of public procurement: evidence revealed by a UK government online feedback facility", *Journal of Purchasing and Supply Management*, Vol. 21 No. 2, pp. 103-112.

Lu, D., Ding, Y., Asian, S. and Pau, S.K. (2018), "From supply chain integration to operational performance: the moderating effect of market uncertainty", *Global Journal of Flexible Systems Management*, Vol. 19 No. 1, pp. 3-20.

Medlin, B., Green, K.W. and Wright, A.D. (2016), "Comprehensive management practices and policies performance model", *Industrial Management and Data Systems*, Vol. 116 No. 5, pp. 1043-1060.

Mistry, J.J. (2006), "Origins of profitability through JIT process in supply chain", *Industrial Management and Data Systems*, Vol. 105 No. 6, pp. 752-768.

Moen, O., Heggeseth, A.G. and Lome, O. (2016), "The positive effect of motivation and international orientation on SME growth", *Journal of Small Business Management*, Vol. 54 No. 2, pp. 659-678.

Moriones, A.B., Billon, M. and Lera-Lopez, F. (2013), "Perceived performance effects of ICT in manufacturing SMEs", *Industrial Management and Data Systems*, Vol. 113 No. 1, pp. 117-135.

Nunnally, J.C. (1978), *Psychometric Methods*, McGraw-Hill, New York, NY.

Pant, S., Sethi, R. and Bhandari, M. (2003), "Making sense of the e-supply chain landscape: an implementation framework", *International Journal of Information Management*, Vol. 23, pp. 201-221.

Patrucco, A., Luzzini, D., Moretto, A. and Ronchi, S. (2019), "Attraction in buyer–supplier relationships", *Business Process Management Journal*, Vol. 25 No. 2, pp. 347-367.

Petrick, I., Maitland, C. and Pogrebnyakov, N. (2016), "Unpacking coordination benefits in supply networks: findings from manufacturing SMEs", *Journal of Small Business Management*, Vol. 54 No. 2, pp. 582–597.

Pradhan, S.K. and Routroy, S. (2016) "Supply management integration model for Indian manufacturing industries", *International Journal of Operations and Production Management*, Vol. 36 No. 7, pp. 781-802.

Prajogo, D., Oke, A. and Olhager, J. (2016), "Supply chain processes: linking supply logistics integration, supply performance, lean processes and competitive performance", *International Journal of Operations and Production Management*, Vol. 36 No. 2, pp. 220-238.

Punniyamoorthy, M., Thamaraiselvan, N. and Manikandan, L. (2013), "Assessment of supply chain risk: scale development and validation", *Benchmarking: An International Journal*, Vol. 20 No. 1, pp. 79-105.

Rezaei, J., Ortt, R. and Trott, P. (2018), "Supply chain drivers, partnerships and performance of high-tech SMEs: an empirical study using SEM", *International Journal of Productivity and Performance Management*, Vol. 67 No. 4, pp. 629-653.

Sener, S., Savrul, M. and Aydın, O. (2014), "Structure of small and medium-sized enterprises in Turkey and global competitiveness strategies", *Procedia - Social and Behavioral Sciences*, Vol. 150 No. 15 Sept, 2014, pp. 212-221.

Shatat, A.S. and Udin, Z.M. (2012), "The relationship between ERP system and supply chain management performance in Malaysian manufacturing companies", *Journal of Enterprise Information Management*, Vol. 25 No. 6, pp. 576-604.

Singh, R.K. Luthra, S., Mangla, S.K. and Uniyal, S. (2019), "Applications of information and communication technology for sustainable growth of SMEs in India food industry", *Resources, Conservation and Recycling*, Vol. 147, pp. 10-18.

Singh, M.K., Kumar, H., Gupta, M.P. and Madaan, J. (2018), "Analyzing the determinants affecting the industrial competitiveness of electronics manufacturing in India by using TISM and AHP", *Global Journal of Flexible Systems Management*, Vol. 19, No. 3, pp. 191-207.

Singh, R.K. (2015), "Modelling of critical factors for responsiveness in supply chain", *Journal of Manufacturing Technology Management*, Vol. 26 No. 6, pp. 868-888.

Singh, R.K., Garg, S.K. and Deshmukh, S.G. (2008), "Challenges and strategies for competitiveness of SMEs: a case study", *International Journal for Services and Operations Management*, Vol. 4 No. 2, pp. 181-200.

Singh, R.K., Garg, S.K. and Deshmukh, S.G. (2010), "Strategy development by small scale industries in India", *Industrial Management and Data System*, Vol. 110 No. 7, pp. 1073-1093.

Singh, R.K., Garg, S.K. and Deshmukh, S.G. (2005), "Development of flexible strategies by Indian SMEs in electronics sector in emerging economy", *Global Journal of Flexible Systems Management*, Vol. 6 No. 2, pp. 15-26.

Singh, R.K., Kumar, R. and Shankar, R. (2012), "Supply chain management in SMEs: a case study", *International Journal of Manufacturing Research*, Vol. 7 No. 2, pp. 165-180.

Singhry, H. and AbdRahman, A. (2019), "Enhancing supply chain performance through collaborative planning, forecasting, and replenishment", *Business Process Management Journal*, Vol. 25 No. 4, pp. 625-646.

Sink, H.L., Langley, C.J. and Gibson, B.J. (1996), "Buyer observations of the US third-party logistics market", *International Journal of Physical Distribution and Logistics Management*, Vol. 26 No. 3, pp. 38-46.

Skipworth, H.D., Godsell, J., Wong, C.Y., Saghiri, S.S. and Julien, D. (2015), "Supply chain alignment for improved business performance: an empirical study", *Supply Chain Management: An International Journal*, Vol. 20 No. 5, pp. 511-533.

Small and Medium Development chamber of India. (2015), Small and medium development chamber of India. [Online] available at: http://www.smechamberofindia.com/ (accessed 22 December 2015).

Solke, S.N. and Singh, T.P. (2018), "Analysis of relationship between manufacturing flexibility and lean manufacturing using structural equation modelling", *Global Journal of Flexible Systems Management*, Vol. 19 No. 2, pp. 139-157.

Song, H., Yu, K., Ganguly, A. and Turson, R. (2016), "Supply chain network, information sharing and SME credit quality", *Industrial Management and Data Systems*, Vol. 116 No. 4, pp. 740-758.

Squire, B., Cousins, P.D., Lawson, B. and Brown, S. (2009), "The effect of supplier manufacturing capabilities on buyer responsiveness: the role of collaboration", *International Journal of Operations & Production Management*, Vol. 29 No. 8, pp. 766-788.

Stanley, E.F., Cynthia, W., Chad, A. and Gregory, M. (2009), "Supply chain information-sharing: benchmarking a proven path", *Benchmarking: An International Journal*, Vol. 16 No. 2, pp. 222-246.

Straub, D., Boudreau, M.C. and Gefen, D. (2004), "Validation guidelines for IS positivist research", *Communications of the Association for Information Systems*, Vol. 13, pp. 380-427.

Sushil (2017), "Small steps for a giant leap: flexible organization", *Global Journal of Flexible Systems Management (December 2017)*, Vol. 18 No. 4, pp. 273-274.

Taylor, M.J., McWilliam, J., England, D. and Akomode, J. (2004), "Skills required in developing electronic commerce for small and medium enterprises: case based generalization approach", *Electronic Commerce Research and Applications*, Vol. 3, No. 3, pp. 253-265.

Trakman, P., Oliveira, M.P.V.D. and McCormack, K. (2016), "Value-oriented supply chain risk management: you get what you expect", *Industrial Management and Data Systems*, Vol. 116 No. 5, pp. 1061-1083.

Trakman, P., Stemberger, I.M. and Groznik, A. (2007), "Process approach to supply chain integration", *International Journal Supply Chain Management*, pp. 116-128.

Tripathy, S., Aich, S., Chakraborty, A. and Lee, G.M. (2016), "Information technology is an enabling factor affecting supply chain performance in Indian SMEs: a structural equation modelling approach", *Journal of Modelling in Management*, Vol. 11 No. 1, pp. 269-287.

Wang, B., Childerhouse, P., Kang, Y., Huo, B. and Mathrani, S. (2016), "Enablers of supply chain integration: interpersonal and interorganizational relationship perspectives", *Industrial Management & Data Systems*, Vol. 116 No. 4, pp. 838-855.

Wiengarten, F., Humphreys, P., Gimenez, C. and McIvor, R. (2016), "Risk, risk management practices, and the success of supplychain integration", *International Journal of Production Economics*, Vol. 171 No. 3, pp. 361-370.

Wong, Y.C., Arlbjqrn, S.J. and Johansen, J. (2005), "Supply chain management practices in toy supply", *International Journal Supply Chain Management*, pp. 367-378.

Xiao, L. and Ramsden, M. (2016), "Founder expertise, strategic choices, formation, and survival of high-tech SMEs in China: a resource-substitution approach", *Journal of Small Business Management*, Vol. 54 No. 3, pp. 892-911.

Yadav, N., Sushil, Umit S. and Bititci, U.S. (2018), "Development of performance management system incorporating dual perspectives of enterprise and customers", *Measuring Business Excellence*, doi: 10.1108/MBE-10-2017-0069.

Yadav, V., Sharma, M. and Singh, S. (2018), "Intelligent evaluation of suppliers using extent fuzzy TOPSIS method: a case study of an Indian manufacturing SME", *Benchmarking: An International Journal*, Vol. 25 No. 1, pp. 259-279.

Zahraee, S.M., Mamizadeh, F. and Vafaei, S.A. (2018), "Greening assessment of suppliers in automotive supply chain: an empirical survey of the automotive industry in Iran", *Global Journal of Flexible Systems Management*, Vol. 19 No. 3, pp. 225-238.

About the authors

Dr. Rajesh Kumar Singh is a Professor at the Management Development Institute, Gurgaon, India. His areas of interest include competitiveness, small business management, quality management, and supply chain management. He has about 170 research papers published in reputed international/national journals and conferences. He has published papers in journals such as *Business Process Management journal*, *Resources, Conservation and Recycling*, *Journal of Cleaner Production*, *Industrial Management and Data Systems*, *Production planning and Control*, *Singapore Management Review*, *International*

Journal of Productivity and Performance Management, *Benchmarking: An International Journal*, *Journal of Modelling in Management*, *Competitiveness Review: An International Business Journal*, *Global Journal of Flexible Systems and Management*, *International Journal of Productivity and Quality Management*, *International Journal of Services and Operations Management*, *International Journal of Automotive Industry and Management*, *International Journal of Logistic Systems Management*, *IIMB Management Review*, and *Productivity Promotion*. Rajesh Kumar Singh is the corresponding author and can be contacted at: rksdce@yahoo.com

Dr. Ravinder Kumar is an Associate Professor at Amity University, Noida, India. He holds a bachelor's degree in Mechanical Engineering with Honors. He did his master's and Ph.D. from Delhi College of Engineering, University of Delhi, India. He has published about 45 research papers in reputed international journals and conferences. His areas of interest include supply chain management and quality management in SMEs. He has published papers in journals such as *Competitiveness Review: An International Journal*, *Global Journal of Flexible Systems and Management*, *IIMB Management Review*, *Benchmarking: an International Journal*, *International Journal of Pharmaceutical and Healthcare Marketing*, *International Journal of Business Information Systems*, *International Journal of Manufacturing Research*, etc. Email: ravinderkumar.ap@gmail.com

For instructions on how to order reprints of this article, please visit our website:
www.emeraldgrouppublishing.com/licensing/reprints.htm
Or contact us for further details: **permissions@emeraldinsight.com**

Innovative Infrastructure Solutions (2020) 5:19
https://doi.org/10.1007/s41062-020-0263-7

TECHNICAL PAPER

Stress–strain characteristics of landfill clay cover barriers under geogrid reinforcements

Akshit Mittal[1] · **Amit Kumar Shrivastava**[2]

Received: 31 August 2019 / Accepted: 12 January 2020
© Springer Nature Switzerland AG 2020

Abstract
Low shear strengths in landfill clay cover barriers lead to the development of tensile cracks in the soil, thus decreasing the usefulness of the barrier to resist water inlet into the landfill system. As cracks begin to form, water infiltration increases, thus increasing the wastewater interaction, leading to the development of the excess amount of leachate. Usage of geogrids within the landfill clay cover barrier has found wide-scale applications in bolstering the shear strength of the soil and thus preserving its utility. In this paper, the shear behavior of landfill clay cover soil with geogrids has been analyzed using triaxial compression tests. Significant parameters such as geogrid properties, initial geogrid spacing, number of geogrids, confining pressure and spacing between the geogrids have been investigated. A soil mixture of kaolin clay and sand, in 4:1 ratio, respectively, representing the typical characteristics of landfill clay cover barrier soil found in the field, was compacted at OMC + 5% and was used in the present study. The study demonstrates the increase in shear strength of landfill clay cover barrier with geogrids and its interdependence on geogrid spacing and geogrid properties, number of reinforcement layers and confining pressure. The inclusion of geogrids improved the load-carrying capacity and the axial strain at failure of the soil, thus signifying the benefits of inclusion of geogrids in cover barriers, especially to prevent tensile cracks. The results obtained from the triaxial tests were used for the computation of elasticity modulus of the cover barrier soil. Significant parameters necessary for the computation of the elasticity modulus were chosen, and the model with a confidence level greater than 95% was presented to deduce the settlement in geogrid-reinforced landfill clay cover barriers.

Keywords Geogrids · Stress–strain characteristics · Landfill · Barriers · Tensile cracks · Regression

Introduction

The efficient management of waste is an integral part of any country's sustainable developmental goals. This requires scientific disposal of waste, to minimize the deleterious impacts which the waste might have on the environment. In India, even though the availability of land is declining, landfilling remains one of the primary methods for disposal of waste [1]. However, to prevent the detrimental impacts of waste on the environment, the landfill system needs to be engineered to prevent the leakages of leachate and hazardous gases into the environment. An engineered landfill system usually includes bottom liners in the form of a composite barrier, a drainage layer, waste pill and a closure system [2]. A closure system is generally provided to arrest the flow of water from entering the landfill, to promote surface runoff, to act as a gas control layer and prevent erosion [3]. Low permeable clayey soils are generally used for hydraulic resistance to the infiltration of water. Bentonite blended with locally available soils or kaolin clay, which have relatively low shear strength, is generally used in the cover system, due to their low permeability. These soils undergo extensive differential settlements due to placement of wastes in phases, voids between the wastes, fall over of the waste containers, and due to the collapse of the waste cavities [4–6], which can have adverse effects on the cover performance as differential settlement tends to increase the permeability of the landfill cover [7]. The tensile cracks formed due to this differential settlement reduce the usefulness of the cover barrier systems

✉ Akshit Mittal
akshit_bt2k15@dtu.ac.in

Amit Kumar Shrivastava
aksrivastava@dce.ac.in

[1] Department of Environmental Engineering, Delhi Technological University, Delhi 110042, India

[2] Department of Civil Engineering, Delhi Technological University, Delhi 110042, India

Published online: 14 February 2020

and increases the wastewater interaction, thus increasing the amount of leachate being formed. Such cracks are usually associated with low shear strength of the cover soils. This thus requires the assessment of solutions which can be used for enhancing the shear strength of the soil and maintaining the integrity of the landfill cover. Various researchers have presented different methods for reinforcement of landfill covers [8–13]. One of the most popular methods of reinforcement in landfill cover systems for reducing cracks induced at the onset of differential settlement is the use of geogrids. These are low-cost geosynthetics that are stronger than the soil in tension and provides lateral resistance to the soil under loading. Various studies have been conducted on analyzing the usability of geogrids in different civil engineering structures [14–18]. One way of analyzing the performance of different geosynthetics with soil is to perform triaxial compression tests as employed by different researchers [19–22]. A study was conducted to compare different reinforcement forms such as discrete fibers, planar reinforcements, and geocells using triaxial tests for sand [19]. The study demonstrated the better performance of planar reinforcements as compared to discrete fibers; however, cellular reinforcements showed the highest improvement. Also, the difference between the failure modes occurred for each of the reinforcements, with the failure not occurring along the traditional failure plane and rather occurring in the form of bulging between the reinforcements. A similar study was carried out on geotextile-reinforced sands using monotonic triaxial compression tests [20]. An image processing technique was employed for analyzing strain distribution in geotextiles. The study showed that the maximum strain in a geotextile occurred at the center, decreasing along the radial direction. Also, increasing the confining pressure decreased the peak strength showing the lack of involvement of geotextiles at higher confining pressure. The strength difference, however, increases with the increase in the confining pressure as reported by [21]. A similar study on geotextile-reinforced sand showed that the increase in the relative density of sand increased the mobilization in the geotextile [22]. Also, the spacing between the reinforcements played an important role. The peak strength decreased with the increase in the confining pressure. The addition of construction and demolition waste improved the stress–strain characteristics of unstabilized soil, as depicted by [23].

A review of the existing literature shows that no substantive study has been conducted on analyzing the shear behavior of landfill clay cover barriers using geogrids. However, the study is significant for landfills to analyze the improvement in shear strength of the soils with geogrids, to effectively design a landfill cover barrier and to prevent cracks within the structure. Hence, a study has been carried out to analyze the shear behavior of landfill clay cover barrier with geogrids using triaxial compression tests. Different designing parameters such as the effect of spacing between geogrids, the number of geogrid layers, the effect of geogrid properties, the impact of an increase in confining pressure and the effect of reinforcement on failure pattern were analyzed.

Materials

Soil

Properties of soil play a vital role in choosing the suitable characteristics of the landfill clay cover barrier. Clay-based landfill barriers are usually designed for hydraulic conductivity of less than or equal to 10^{-7} cm/s for MSW-type landfills [2]. However, soil properties such as soil grain size and plasticity index of soil also play an important role in the selection of suitable material for the design of landfill clay barriers as they are directly related to the hydraulic conductivity of the soil. It has been reported that the plasticity index ≥ 7 to 15% and percentage fines ≥ 30 to 50% is suitable for clay cover material as these parameters directly influence the permeability of the soil [4, 24]. Also, the sand–clay mixture is an efficient material for reducing desiccation-induced cracking in the landfill covers, which might be caused due to variable moisture content in the soil, as suggested by Daniel and Wu [24]. Desiccation cracking can also cause the expansion and softening of soil on water entry into the soil. Taking into consideration all the proposed characteristics of the landfill clay cover soil, a blend of kaolin and locally available sand (4:1) was chosen to simulate the characteristics of a typical landfill cover barrier. To ensure permeability of less than 10^{-7} cm/s, the specimen was compacted at OMC + 5%, as the soils compacted on the wet side of the OMC achieved permeability less than 10^{-7} cm/s [25]. The properties for the same are represented in Table 1.

Table 1 Properties of soil

Properties	Soil blend
Specific gravity	2.63
Percentage passing IS Sieve [75 micron (%)]	61
Liquid limit (%)	41.2
Plastic limit (%)	20.44
Plasticity index (%)	21.01
Maximum dry unit weight (kN/m^3)	15.41
Optimum moisture content (%)	24.52
Maximum dry unit weight (OMC + 5%) (kN/m^3)	14.02
Coefficient of permeability (cm/s)	8.19×10^{-7}
Coefficient of permeability (cm/s) (OMC + 5%)	1.12×10^{-7}

Geogrid properties

Two geogrids with different mechanical properties were chosen for the study. The properties of the respective geogrids were procured from the supplier (H.M.B.S. Textiles Pvt. limited) in the form of a Manufacturer Testing Certificate (MTC). The rolls in which the geogrids were obtained were made flat by placing heavy concrete blocks across the four edges of the geogrids. The blocks were removed only during the testing stages. The properties of the geogrids were procured in both the longitudinal direction and the transverse direction. The significant mechanical properties are shown in Table 2. The first type of geogrid has been termed as GG1, whereas the second type of geogrid has been termed as GG2, respectively, for convenience throughout this paper.

Experimental program

Soil specimen preparation

Before commencing the tests, soil used in this study was cured by adding respective proportions of water to the soil samples and placing it in airtight bags for two consecutive weeks, to ensure that the soil obtains moisture equilibrium. The soil after curing was used for the preparation of specimens used in the triaxial tests. The triaxial tests were conducted with specimen dimensions of 76 mm and 38 mm in height and diameter, respectively, throughout the testing procedure. The mold used for the specimen preparation was first treated with petroleum jelly, to ensure a smooth surface and to prevent damages to the specimen during extraction.

Table 2 Physical and mechanical properties of geogrids

Parameters	GG1		GG2	
	MD	TD	MD	TD
Tensile strength	7.8	8.2	5	5
Tensile modulus	550	350	220	260
Aperture size	30×30		40×27	

Tensile modulus and tensile strength are in kN/m

MD machine direction, *TD* transverse direction

The compaction was done in three lifts. Uniform compaction was provided across lifts using a lightweight tamping rod. To calculate the required amount of soil to form a lift, the volume of the mold up to a particular mold height was multiplied with the maximum dry unit weights of the soil. To ensure bonding between two subsequent lifts, the surface of the lift was scarified using a spatula. While placing the geogrids in the specimen, special care was taken to ensure that the protruding ends of the geogrids were removed to prevent any damage to the membrane. Filter papers were applied along the specimen height, to ensure radial drainage.

Testing program

The tests were carried out in four different configurations as illustrated in Fig. 1. The first testing configuration included a single layer of reinforcement in the middle of the specimen, whereas the second configuration involved reinforcement closer to the cap. The third and fourth testing included two and three layers of reinforcements, respectively. The tests analyzed different parameters essential for designing a reinforced cover system for landfill including

- Spacing between reinforcements.
- Number of reinforcements.
- Type of geogrid.
- Initial spacing between reinforcements.

Testing procedure

Consolidated undrained triaxial tests were conducted as per IS code specification [26]. The sample was sheared until it achieved a certain degree of saturation, which was accessed using the Skempton's coefficient, B. The tests were conducted for $B \geq 0.95$. The tests were carried out for confining pressures of 25 kPa, 50 kPa and 75 kPa, respectively. The sample was sheared at a rate of 0.25 mm/min. Before placing the specimen in the triaxial cell, special care was taken to wash the cell for any possible blockage in the perforations and the valves. After placing the specimen in the cell, the cell was filled with water at a controlled flow rate. A pneumatic control panel-type system was used in which three soil specimens in three different triaxial cells were first placed at

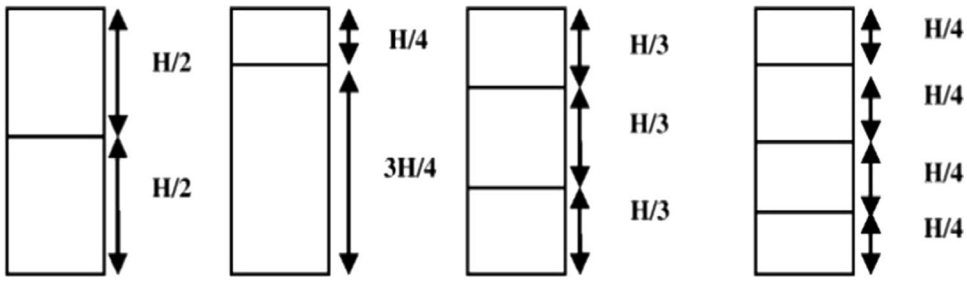


Fig. 1 Testing configurations

suitable confining and back-pressures simultaneously. The geogrids were cut in the shape of circles with diameters a little smaller than the specimen diameter. The sample was rested for 15 min after undergoing consolidation to regain the water lost during the consolidation phase.

Results and discussion

Effect of spacing

The first series of tests were performed to assess the effect of spacing on the shear behavior of soil specimens. For this purpose, configurations (CN) 1 and 2 were tested for both GG1 and GG2. To correctly assess the improvement in shear strength after the application of geogrids, peak strength ratio was utilized. Peak strength ratio can be defined as the ratio of failure stress in the reinforced specimen to the failure stress in the unreinforced specimen. It can be mathematically defined as

$$\mathrm{PSR} = \frac{\sigma_{\mathrm{R}}}{\sigma_{\mathrm{UR}}}, \tag{1}$$

where PSR is the peak strength ratio, σ_{R} is the shear stress at failure for the reinforced specimen and σ_{UR} is the shear stress at failure for the unreinforced specimen. Another significant parameter computed during analysis for visualizing the difference in the reinforced specimen and the unreinforced specimen is the strength difference. Strength difference (S.D.) is defined as the difference between shear strength of reinforced soil specimen to the shear strength of unreinforced soil specimen when considered at a similar confining pressure, viz., 25 kPa, 50 kPa and 75 kPa. Hence, strength difference can be represented as

$$\mathrm{SD} = \tau_{\mathrm{R}} - \tau_{\mathrm{UR}} \tag{2}$$

where τ_{R} is the shear strength of the reinforced soil blend and τ_{UR} is the shear strength of the unreinforced soil specimen. Figure 2 shows the deviatoric stress versus % axial strain curve at 75 kPa for GG1 and GG2. The strength of the soil increased with the inclusion of even a single layer of reinforcement as observed from the curves. The improvement, however, was dependent upon the spacing from the top for each of the reinforcement. The maximum shear strength was attained at *H*/2, i.e., in the middle of the specimen. Such an observation can be attributed to the fact that the maximum strain occurs in the triaxial specimen in the middle of the specimen. Higher strain in the middle would attribute to higher deformation of the geogrid, thus mobilizing higher tensile force in the specimen. The greater is the tensile force, the greater would be the lateral resistance, which would prevent the deformation of the soil. The findings were

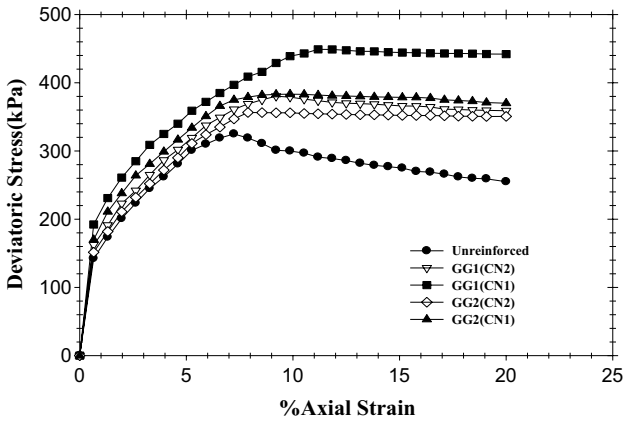


Fig. 2 Deviatoric versus axial strain for CN1 and CN2

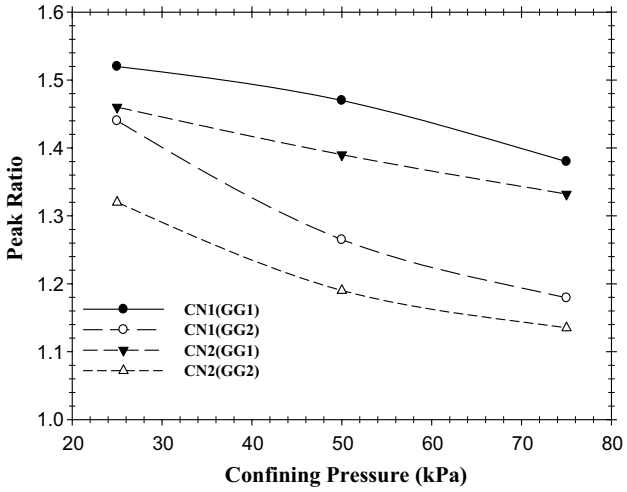


Fig. 3 Peak strength ratio versus confining pressure for GG1 and GG2

consistent for both the types of geogrids which signify the importance of placing the reinforcements at locations where maximum displacement is expected to occur. Also, at *H*/4, as the geogrid moves toward the cap of the triaxial cell, cap and base restraint effects begin to occur. This states that strength improvement reduces as the reinforcement approaches the base or the cap of the specimen [27]. Hence, the reinforcements perform the best when these are placed far from the caps and the base of the reinforcement cell. Figure 3 shows the PSR versus confining pressure curves for GG1 and GG2. As can be observed from the curves, as the confining pressure increases, the peak strength decreases. This observation can be because as the confining pressure increases, the response time for the geogrid to mobilize tensile force decreases as a result of which the contribution of the geosynthetic decreases. In other words, increasing confining pressure decreases the lateral resistance mobilized in the geogrid

due to a lack of sufficient response time. These observations are consistent with [20, 22].

Effect of number of layers

The number of layers of reinforcements plays a vital role in the designing of reinforced structures. It was analyzed by varying the number of reinforcements by 1, 2 and 3, respectively. Figure 4a, b shows the deviatoric stress versus axial strain curves for GG1 and GG2, respectively, at different configurations. As can be observed from Fig. 4a, b, the increase in the number of geogrid layers increases the stress in the landfill clay cover barrier soil. This observation can be attributed to the fact that as the number of reinforcement layers increases, the mass of geogrid increases in the specimen, which provides better cushion to the specimen. This added cushion provides better confinement to the soil particles thus preventing their lateral deformation. Also, the increase in the number of the geogrid layer increases the friction between the soil and geosynthetic interface, which mobilizes higher tensile force in the geogrid, thus increasing its efficiency. Figure 5 shows the strength difference versus the confining pressure curve. As can be observed from Fig. 5, as the confining pressure increases, the strength difference increases. This can be due to the fact that at higher confining pressure, the tensile force mobilized in the geogrid is higher. The results obtained were similar to those reported by Nguyen et al. [20]. It should be noted that the improvement in shear strength and strength difference is highly dependent on the property of the geogrid, with the improvement being higher for GG1 as compared to GG2. This thus signifies that apart from the loading conditions, confining pressure and the number of layers, the properties of the geogrid being used should also be considered during the designing phase. This can be clearly understood by the observation that two layers of GG1 perform almost similar to three layers of GG2.

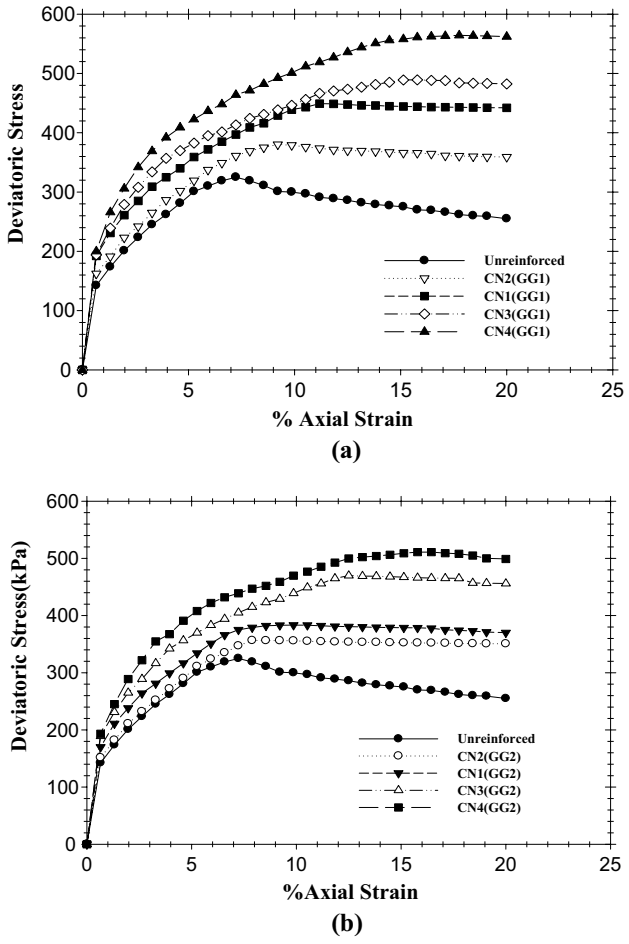


Fig. 4 Deviatoric stress versus axial strain curves for **a** GG1 and **b** GG2 at 75 kPa, respectively, for different configurations

Effect of type of geogrid

As discussed in the previous section, the properties of the geogrid play a vital role in the shear behavior of the landfill clay cover barrier. Figure 6a, b shows the axial strain at failure versus confining pressure curve for GG1 and GG2, respectively. As can be observed from these graphs, GG1 performs much better than GG2 in increasing the failure axial strain. Examining the properties of the two geogrids, GG1 has a much higher tensile strength than GG2. Also, the stiffness of the GG1 is comparatively higher. Higher tensile stiffness and tensile strength effects of the deformability of the geogrids. The bigger aperture size facilitates better interlocking and confinement of soil particles. Also, the ease of applicability of GG1 in comparison to GG2 enhances its usability. Choosing a particular type of geosynthetic for any operation depends upon various parameters such as durability, availability, and cost [28]. Also, Fig. 6 shows that the axial strain increases with the increase in confining pressure.

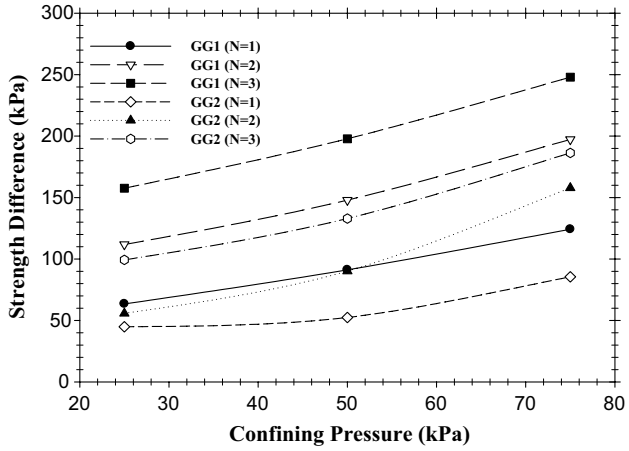


Fig. 5 Strength difference versus confining pressure

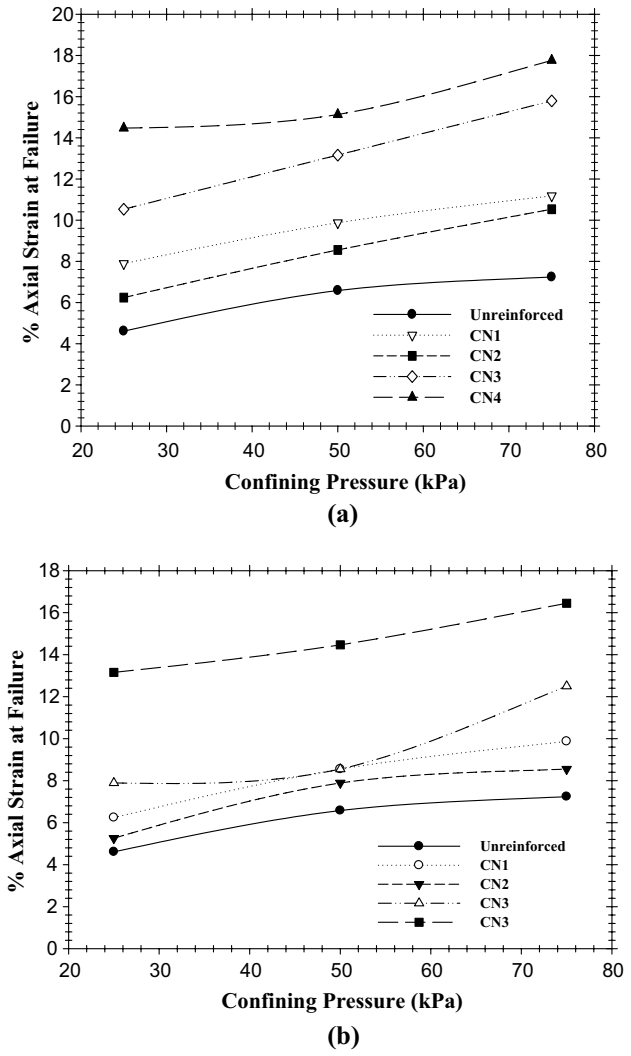


Fig. 6 Axial strain at failure versus confining pressure for **a** GG1 and **b** GG2

This shows that the behavior of the curve of the landfill clay cover barrier turned ductile. As in typical field conditions, the confining pressure is of the order of 25 kPa due to the overburden pressure. The obtained results signify that in typical field conditions, at lower confining pressures, the geogrids would efficiently help in reducing tensile cracks.

Effect on the failure pattern

The inclusion of geogrids in the specimen influences the failure pattern of the specimen. Figure 7a–c shows the failure patterns in three different conditions. As can be observed from Fig. 7a–c, the failure in a geogrid-reinforced specimen does not take place along the conventional shear plane, i.e., at $45 + \varphi/2$, but rather takes place in the form of bulging. Such an observation can be attributed to the lack of lateral movement of the soil particles during testing, which causes bulging between the subsequent layers. In other words, geosynthetic reinforcements inhibit the lateral movement in the soil blend, due to which the shear failure occurs in the form of bulging between the layers rather than occurring along the conventional shear plane. Similar observations were reported by Latha and Murthy [19].

Scale effect

To analyze the effect of scale effect on the results obtained, GG1 was tested in a specimen of dimension 50 mm in diameter and 100 mm in height for $N = 1$, 2 and 3 at and 75 kPa, respectively. As can be observed from Fig. 8, the deviation between the results under two different triaxial cells is minimal. The observation was valid for all the reinforcement configurations, viz., $N = 1$, 2 and 3. This thus signifies that the stress–strain characteristics of the cover barrier are not influenced by the scale effect in the present study.

Regression analysis

Computation of settlements of a reinforced landfill clay cover barrier becomes complex due to additional mechanisms such as the confinement effect and the membrane effect, which are provided by the reinforcing material. In the landfill cover system, these computations are essential to ensure that the post-operation settlement can be estimated accurately. For this purpose, the elasticity modulus of the reinforced soil has been computed using experimental results obtained using triaxial compression tests. A dimensionless parameter E_r/E_{ur} has been defined, where E_r is the elasticity modulus of the reinforced specimen, whereas E_{ur} is the elasticity modulus of the unreinforced specimen. As was discussed in the previous section, geogrid tensile strength and tensile modulus are significant parameters for analyzing stress–strain characteristics of landfill clay cover barrier; hence, these parameters have been normalized for the purpose of computation and represented as N_t and N_s, respectively. Apart from the N, N_t and N_s, the spacing between the reinforcement (first-layer reinforcements) was also included in the study for calculating the elasticity modulus and has been represented. Table 3 shows the elasticity modulus obtained from the stress–strain curves. As can be observed from Table 3, increasing the number of layers of geogrids decreases the elasticity modulus, thus specifying that the material turns ductile with the addition of multiple layers of geogrids. This signifies the importance of including multiple layers of geogrids for arresting the formation of cracks in the landfill clay cover barrier at the onset of differential settlement and thus improving its usefulness. After calculating the elasticity modulus of the soil, the dataset was imported into R package R Studio to conduct a regression analysis. As can

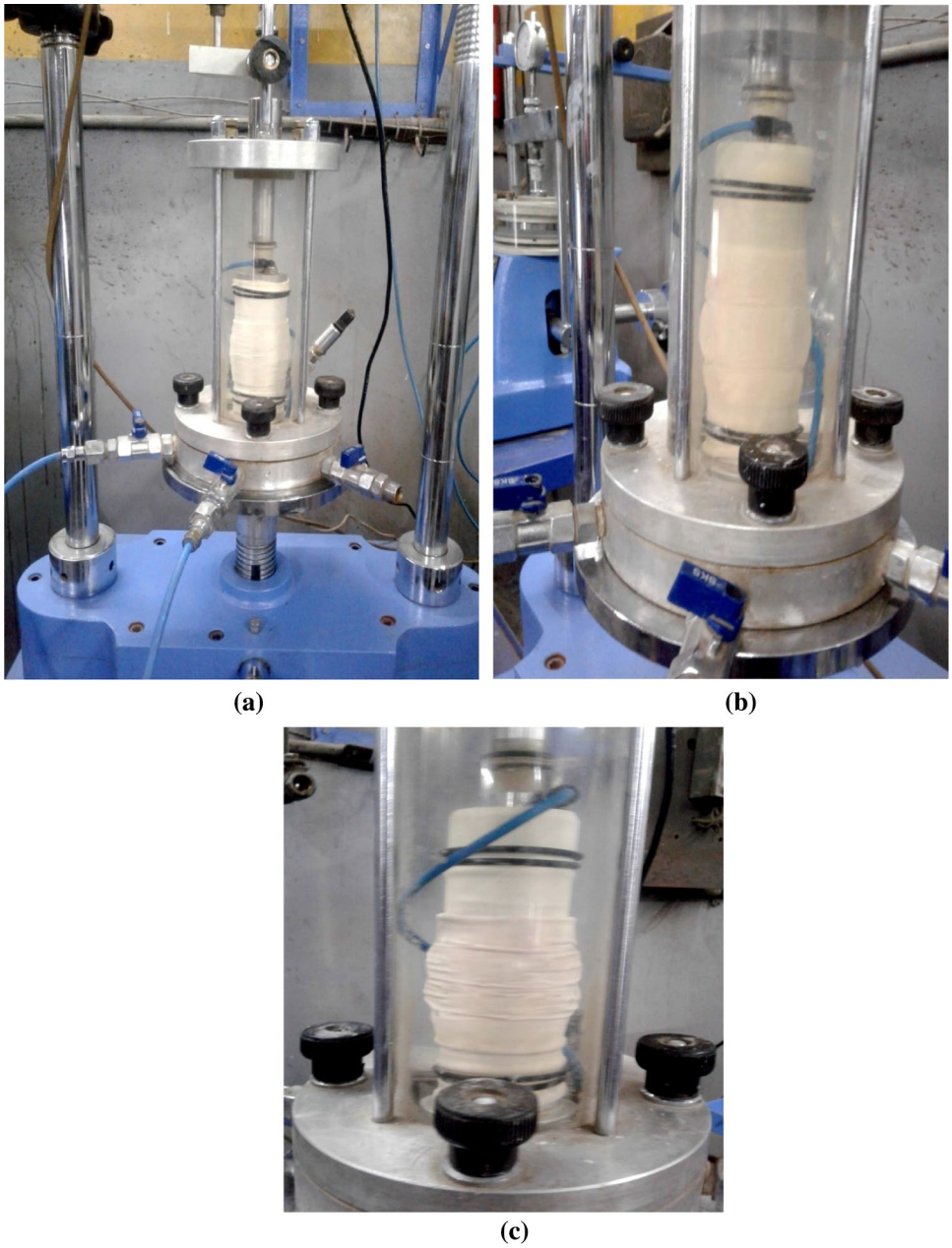


Fig. 7 **a** Unreinforced failure pattern, **b** failure pattern in $N=2$ and **c** $N=3$ at 25 kPa

be observed from Table 4, three models have been obtained with a confidence level of greater than 95% for calculation of the parameter E_r/E_{ur}. When the analysis was conducted to analyze the significance of each of the independent dimensionless variables (N, i/H, N_t and N_s) toward computation of elasticity modulus of the cover barrier using $|t|$ analysis, N emerged as the most significant parameter with a $|t|$ value of 18.99, whereas the least significant parameter obtained was normalized stiffness, with $|t|$ value of 0.647.

Removing N_s and i/H from the set of parameters does not impact the confidence level significantly and thus can be ignored while computation of elasticity modulus of geogrid landfill covers. The coefficients and intercept obtained for the optimized model were obtained for the two significant parameters. The obtained equation is as follows

$$\frac{E_r}{E_{ur}} = -0.0314 \times N - 1.384 \times \text{Normalized tensile strength} + 1.091 \quad (3)$$

Conclusions

In this study, a series of triaxial compression tests were conducted to analyze the shear behavior of geogrid-reinforced landfill clay cover barrier. The significant findings from the

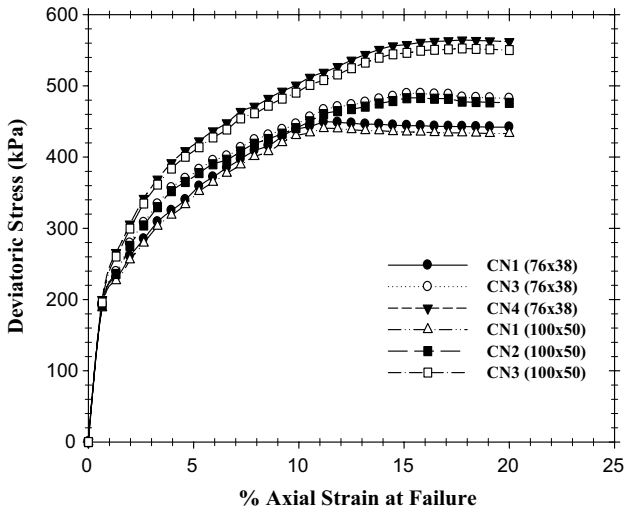


Fig. 8 Deviatoric stress versus % axial strain at failure for GG1 under different triaxial settings

Table 3 Elasticity modulus under different configurations

Parameters	Elasticity modulus (kPa)
Unreinforced	2356
GG1 ($N=1$, $i/H=0.25$)	2317.5
GG1 ($N=1$, $i/H=0.50$)	2204
GG1 ($N=2$)	2163.1
GG1 ($N=3$)	2138.1
GG2 ($N=1$, $i/H=0.25$)	2399.5
GG2 ($N=1$, $i/H=0.50$)	2381.3
GG2 ($N=2$)	2244.8
GG2 ($N=3$)	2150.9

Table 4 Regression analysis using different dimensionless parameters

Parameters	Multiple R^2	R^2 (adjusted)
N, i/H, N_s and N_t	0.961	0.959
N and N_t	0.953	0.958
N, i/H and N_t	0.951	0.949
N and N_s	0.945	0.939
N	0.845	0.81
N_t and i/H	0.842	0.821
N_s and N_t	0.82	0.815
N_t	0.44	0.42
i/H	0.315	0.297
N_s	0.198	0.147

study, which can be useful for designing geogrid-reinforced landfill clay cover barrier, are:

- The shear strength of the landfill cover barrier soil increased with the inclusion of both types of geogrids.
- The inclusion of the geogrid in the middle of the specimen is more beneficial due to higher displacement at the center.
- Increase in confining pressure decreased the peak strength ratio due to a lack of sufficient response time for geogrids to mobilize tensile force within them.
- As the number of reinforcements increased, the strength of the soil increased. This can be attributed to the fact that the increase in the number of geogrid layers increases the friction between the soil and geogrid interface, which mobilizes higher tensile force in the geogrid, thus increasing its efficiency.
- The axial strain at failure increased with the increase in the confining pressure. However, the increase in the confining pressure decreases the peak strength of the soil, due to a decrease in the response time for the geogrid to mobilize maximum resistance.
- GG1 performed better due to better physical and mechanical properties when compared to GG2.
- Sand present in the soil blend increases the coefficient of friction between the specimen and the geosynthetic, thus increasing the tensile force mobilized in the geosynthetic.
- Failure in the reinforced specimen does not occur along the conventional shear plane and occurs in the form of bulging between the reinforcements.
- Increasing the number of layers of geogrids provides ductility to the specimen, thus signifying the importance of geogrids to arrest tensile cracks.
- Normalized tensile strength and number of reinforcement layers provide a confidence level of greater than 95% for computation of elasticity modulus of reinforced landfill cover soils, and thus, this optimized model can be used for evaluating elasticity modulus and further computation of settlement response of reinforced landfill covers.

Compliance with ethical standards

Conflict of interest On behalf of all authors, the corresponding author states that there is no conflict of interest.

References

1. Sharholy M, Ahmad K, Mahmood G, Trivedi RC (2008) Municipal solid waste management in Indian cities—a review. Waste Manag 28(2):459–467
2. Rowe R (2012) Ferroco Terzaghi Oration Design and construction of barrier systems to minimize environmental impacts due

to municipal solid waste leachate and gas. Indian Geotech J 42(4):223–256
3. Lee SY, Tank RW (1985) Role of clays in the disposal of nuclear waste: a review. Appl Clay Sci 1(1–2):145–162
4. Koerner RM, Daniel DE (1997) Materials. In: Koerner RM, Daniel DE (eds) Final covers for solid waste landfills and abandoned dumps. ASCE Press, Reston, pp 78–79
5. Keck KN, Seitz RR (2002) Potential for subsidence at the low-level radioactive waste disposal area, INEEL/EXT-02-01154, Idaho National Engineering and Environmental Laboratory, U.S. Department of Energy, Washington, DC
6. Sivakumar Babu GL, Reddy KR, Chouksey SK (2010) Constitutive model for municipal solid waste incorporating mechanical creep and biodegradation-induced compression. Waste Manag 30(1):11–22
7. Cheng SC, Larralde JL, Martin J (1994) Hydraulic conductivity of compacted clayey soils under distortion or elongation conditions. In: Daniel DE, Trautwein SJ (eds) Hydraulic conductivity and waste contaminant transport in soil. ASTM International, ⁅West Conshohocken
8. Viswanadham BVS, Sathiyamoorthy R, Divya PV, Gourc J (2011) Influence of randomly distributed geofibers on the integrity of clay-based landfill covers: a centrifuge study. Geosynth Int 18(5):255–271
9. Koda E (2012) Anthropogenic waste products utilization for old landfills rehabilitation. Ann Wars Univ Life Sci Land Reclam 44(1):75–88
10. Palmeira EM, Viana HNL (2003) Effectiveness of geogrids as inclusions in cover soils of slopes of waste disposal areas. Geotext Geomembr 21(5):317–337
11. Divya PV, Viswanadham BVS, Gourc JP (2012) Influence of geomembrane on the deformation behaviour of clay-based landfill covers. Geotext Geomembr 34:158–171
12. Bacas BM, Cañizal J, Konietzky H (2015) Shear strength behavior of geotextile/geomembrane interfaces. J Rock Mech Geotech Eng 7(6):638–645
13. Feng S-J, Ai S-G, Huang R-Q (2016) Stability analysis of landfill cover systems considering reinforcement. Environ Earth Sci 75(4):303
14. Haas R, Walls J, Carroll RG (1988) Geogrid reinforcement of granular bases in flexible pavements. Transp Res Rec 1188:19–27
15. Bathurst RJ, Wawrychuk WF, Jarrett PM (1988) Laboratory investigation of two large-scale geogrid reinforced soil walls. In: Jarrett PM, McGown A (eds) The application of polymeric reinforcement in soil retaining structures. Springer, Dordrecht, pp 71–125
16. Alfaro MC, Miura N, Bergado DT (1995) Soil-geogrid reinforcement interaction by pullout and direct shear tests. Geotech Test J 18(2):157–167
17. Yetimoglu T, Wu JT, Saglamer A (1994) Bearing capacity of rectangular footings on geogrid-reinforced sand. J Geotech Eng 120(12):2083–2099
18. Yu Y, Bathurst RJ, Allen TM, Nelson R (2016) Physical and numerical modelling of a geogrid-reinforced incremental concrete panel retaining wall. Can Geotech J 53(12):1883–1901
19. Latha GM, Murthy VS (2007) Effects of reinforcement form on the behavior of geosynthetic reinforced sand. Geotext Geomembr 25(1):23–32
20. Nguyen MD, Yang KH, Lee SH, Wu CS, Tsai MH (2013) Behavior of nonwoven-geotextile-reinforced sand and mobilization of reinforcement strain under triaxial compression. Geosynth Int 20(3):207–225
21. Mudgal A, Sarkar R, Shrivastava AK (2018) Influence of geotextiles in enhancing the shear strength of Yamuna sand. Int J Appl Eng Res 13(12):10733–10740
22. Goodarzi S, Shahnazari H (2019) Strength enhancement of geotextile-reinforced carbonate sand. Geotext Geomembr 47(2):128–139
23. Sharma A, Sharma RK (2019) Effect of addition of construction–demolition waste on strength characteristics of high plastic clays. J Innov Infrastruct 1(1):24
24. Daniel DE, Wu Y-K (1993) Compacted clay liners and covers for arid sites. J Geotech Eng 119(2):223–237
25. Benson CH, Daniel DE, Boutwell GP (1999) Field performance of compacted clay liners. J Geotechnol Geoenviron Eng 125(5):390–403
26. IS: 2720 (Part XII) (1981) Determination of shear strength parameters of soil from consolidated undrained triaxial compression test with measurement of pore water pressure. Bureau of Indian Standards, New Delhi, India
27. Duncan JM, Dunlop P (1968) The significance of cap and base restraint. J Soil Mech Found Div 94(1):271–290
28. Shukla SK (2002) Geosynthetics and their applications. Thomas Telford, London

Algerian Journal of Environmental Science and Technology
Month edition. Vol.X. NºX. (YYYY)
ISSN : 2437-1114
www.aljest.org

Study on groundwater quality and status of Amas Block in Gaya District of Bihar with special reference to fluoride contamination

A. Krishan[1], R.K. Mishra[1]*

[1]Department of Environmental Engineering, Delhi Technological University, Shahbad Daulatpur, Main Bawana Road, Delhi-110042, India

*Corresponding author: rajeevmishraiitr@gmail.com; Tel.: +91-8800486298

ARTICLE INFO

Article History :

Received ***: dd/mm/yyyy***
Accepted ***: dd/mm/yyyy***

***Key Words*:**

Groundwater;
Fluoride;
Physicochemical;
Correlation coefficient;
Fluorosis.

ABSTRACT /RESUME

Abstract: *The study was carried out to investigate the groundwater quality and to establish its relationship with fluoride in Amas Block of Gaya District, Bihar (India). The samples were collected from One hundred ninety-nine bore wells from different locations which were extensively used for drinking and other domestic purposes. Then, samples were analyzed according to standard methods (APHA) procedure. The study revealed that the total dissolved solids in 39%, total alkalinity in 93%, total hardness in 10%, calcium in 64% and magnesium in 19% samples but in case of chloride only one sample exceeded the BIS acceptable limit. In the case of nitrate and sulfate, none of the samples exceeded the BIS acceptable limit. Iron concentration was found high with a mean of 0.7 mg/l. The groundwater was severely affected by fluoride, varied from 0.2 mg/l to 5 mg/l and 63% samples were exceeded the permissible limit of BIS.*

Fluoride has a significant positive correlation with pH and sulfate as well as a significant negative correlation with calcium, magnesium, alkalinity and total hardness. Additionally, fluoride has a negative but poor correlation with electrical conductivity, total dissolved solids, chloride, nitrate, and iron.

accepted manuscript

I. Introduction

Worldwide, for millions of rural and urban families, the major source of drinking water is groundwater. Groundwater contamination with excess iron, fluoride, arsenic, and nitrates, etc. is a major problem in many parts of the world including India and fluoride stands first among them. The range of fluoride concentration in groundwater is 0.01 to 48 mg/l, which causes fluorosis and has an adverse impact on teeth, and bones. Fluoride contaminated drinking water imposing a serious threat to human health as one of the major problems worldwide. From among 25 nations, around 200 million people are under the frightful fate of fluorosis. The two worst affected countries of the world are India, and China [1].

In India, 80% of the rural domestic water needs and 50% of the urban water needs are fulfilled by groundwater. Here groundwater is also intensively used for irrigation and industrial purposes. In 19 states of India, approximately 65 million of the populations are affected by fluorosis, out of which 6 million are children. Bihar is of the fluorosis endemic states. Gaya District of Bihar is among 6-7 district of the state which has had cases of fluorosis, as per the report of Ministry of Environment, Forests and Climate Change (MoEF&CC), Government of India (2009). It is, therefore, a matter of high concern from the point of view of public health and welfare.

In the same perspective, primary reasons behind the fluoride occurrence in groundwater are natural or geogenic contamination but its source is over and over again unknown [2]. Geogenic contamination of groundwater depends primarily on the geological setting of the area. Rainwater dissolves partly certain components of bedrock as it reaches the

water table by infiltration. The dissolution of fluorine bearing minerals in the bedrock originates fluoride content of groundwater [3]. The functions of fluoride contamination in groundwater are temperature, pH, availability and solubility of fluorine bearing minerals, and the concentration of calcium and bicarbonate ions [4]. Geogenic contamination of groundwater is intricate to detect and even more difficult to control in compared to anthropogenic contamination of surface water. The occurrence of excessive concentration of fluoride in groundwater can reach the food system and may persist for a long time even for centuries. The main source of fluoride intake is groundwater but not only food items and also contributes to it [5]. The presence of fluoride in drinking water has both positive and negative effects on human health.

Fluoride mainly affects the skeletal systems, teeth and also the structure and function of skeletal muscle, brain, and spinal cord [6]. Long term exposure to fluoride through water and other products leads to the development of fluorosis. It is also known as a crippling and painful disease. Dental fluorosis occurs during the period of enamel formation. It is associated with excessive absorption of fluoride into dental enamel and dentine, which prevents normal maturation of enamel. Skeletal fluorosis is a pathological condition which includes inhibition of bone hardening, causing the bones to become brittle and their tensile strength may be reduced [7]. Symptoms include limited movement of joints, skeletal deformities, and intense calcification of ligaments, muscle wasting and neurological deficits [8]. The objective of this study was to investigate the detailed physicochemical characteristics of Amas Block groundwater and to establish their relationship with fluoride, toxic elements for human health.

II. Materials and methods

II.1. Study Area

Amas is a Block in Gaya District of Bihar State, India (Figure 1). An Amas Block headquarter is Amas town. It belongs to Magadh Division. It is located 40 km towards west from District head quarters Gaya and 140 km from state capital Patna towards the north. Amas Block consists of 84 villages and 9 panchayats. It is at an elevation of 102 m. This place is at the border of the Gaya and Aurangabad district. The total population of Amas Block is 81,640 living in 12,079 houses including 42,710 males and 38,930 females.

II.2. Groundwater sampling and chemical analysis

One hundred ninety-nine groundwater samples were collected from 199 different locations of the study area which includes Amas Block of Gaya District, Bihar. The samples were collected from bore wells which were extensively used for drinking and other domestic purposes. The samples were collected in pre-cleaned and sterilized polyethylene bottles of two-litre capacity. Then, samples were analyzed according to standard methods (APHA, 2000) [9] procedure, and suggested precautions were taken to avoid contamination. The various parameters like pH, electrical conductivity (EC), total dissolved solids (TDS), total hardness (TH), calcium (Ca), magnesium (Mg), chloride (Cl), alkalinity (ALK), Sulfate (SO_4), Nitrate (NO_3), Fluoride (F) and iron (Fe).

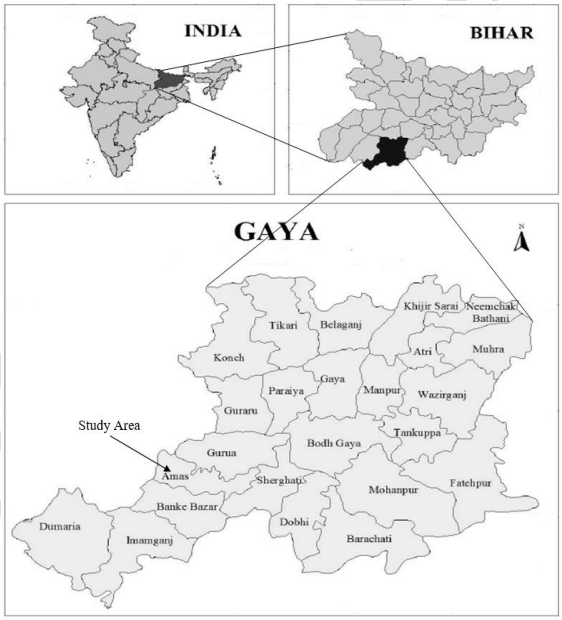


Figure 1. *Location map of the study area*

pH, electrical conductivity and total dissolved solids were determined by pH meter, conductivity meter, and TDS meter respectively during on-site sampling. The other parameters like total hardness and alkalinity were analysed also by titrating the sample with EDTA and sulphuric acid respectively. The titrimetric analysis was also used to analyze chloride, calcium and magnesium concentrations. In addition to this the sulfate, nitrate, fluoride as well as iron were determined by using a spectrophotometer.

To evaluate the potential relationship between various physicochemical parameters, Statistical analysis like maximum, minimum, mean, median, standard deviation and correlation coefficients were carried out by using "Statistical Package of Microsoft Office - Excel, version-10".

III. Results and discussion

III.1. Groundwater quality

In groundwater quality assessment the estimation of the physical and chemical characteristic of

Accepted manuscript

groundwater is essential as it is an important factor which determines its suitability for drinking purposes. As such the appropriateness of groundwater for potable uses with regard to its physicochemical characteristic has to be deciphered and defined on the basis of some essential characteristics of the water. Bureau of Indian Standards (BIS, 2012) [10], has recommended the quality standards for drinking water and these have been used for finding the suitability of groundwater. The summarized physicochemical parameters of groundwater samples are presented in Table 1. The groundwater quality of the Amas block is evaluated by comparing the range of values of different physicochemical parameters of drinking water with Bureau of Indian Standards (BIS, 2012) as presented in Table 2.

The logarithm of the reciprocal of the hydrogen ion concentration (pH) in the groundwater samples varied from 6.4 to 7.9 with a mean value of 7.1. All the samples, except three, are found within the recommended limits for human consumption. For drinking water, the pH value must be within the range of 6.5 – 8.5, as per the BIS (2012). The electrical conductivity (EC) values are found to be within the range of 282 µS/cm to 3919 µS/cm with a mean value of 899.48 µS/cm.

In groundwater, total dissolved solids mainly consist of carbonates, bicarbonates, chlorides, sulfates, phosphates, and nitrates of calcium, magnesium, sodium, and potassium with traces of iron, manganese and other minerals. In trace amount, various dissolved gases and organic matter are also present [11]. Total Dissolved Solids (TDS) value varied from 169 mg/l – 2406 mg/l with a mean value of 549.22 mg/l and a standard deviation of 334.34 mg/l. About 39% of samples exceeded the BIS acceptable limit of 500 mg/l (BIS, 2012). Water having more than 500 mg/l TDS values if used for drinking purposes may induce an unfavorable physiological reaction in the transient consumer and gastrointestinal irritation [12].

Alkalinity in natural waters is a result of the dissolution of CO_2 in water. Carbonates and bicarbonates thus formed are dissociated to yield hydroxyl ions. After analyzing the samples total alkalinity was found in the range of 130 mg/l – 953 mg/l with a mean value of 348.92 mg/l and a standard deviation of 140.47 mg/l. About 93% of samples were exceeded the acceptable limit of 200 mg/l but only 7% of samples exceeded the BIS permissible limit of 600 mg/l (BIS, 2012). The alkalinity of the drinking water has little public health significance.

The principal natural sources of the total hardness in water are dissolved polyvalent metallic cations from sedimentary rocks, seepage, and runoff from the soil. The total hardness values ranged from 113 mg/l – 833 mg/l with mean and median values of 316.90 mg/l and 288 mg/l respectively and standard deviation of 130.44 mg/l. Only 10% of samples exceed the acceptable limit of 200 mg/l BIS (2012).

Calcium (Ca) ion concentrations in groundwater samples show a wide variation from a minimum of 34 mg/l to as high as 256 mg/l with a standard deviation of 38.37 mg/l. About 64% of samples exceeded the acceptable limit of 75 mg/l but only 3% of samples exceeded the BIS permissible limit of 200 mg/l (BIS, 2012). The magnesium (Mg) concentration varied from 3 mg/l to 88 mg/l with mean and median values of 21.58 mg/l and 18 mg/l respectively. All the samples from Amas Block, are found within the permissible limit of 75 mg/l but only 19% of samples exceeded the acceptable limit of 30 mg/l. Generally, the calcium ion concentrations in groundwater exceeded the magnesium ion concentrations according to their relative abundance in rocks [11].

Table 1. *Summarized physicochemical parameters of groundwater samples.*

Parameter	Minimum	Maximum	Mean	Median	Standard Deviation
pH value	6.4	7.9	7.1	7.1	0.25
Electrical conductivity (µS/cm)	282	3919	889.5	719.0	541.09
Total dissolved solids (mg/l)	169	2406	549.2	445.0	334.34
Calcium (as Ca) (mg/l)	34	256	91.0	81.0	38.37
Chloride (as Cl) (mg/l)	2.0	267	48.7	29.0	47.93
Fluoride (as F) (mg/l)	0.2	5.0	2.2	2.0	1.29
Iron (as Fe) (mg/l)	0.1	6.1	0.7	0.5	0.80
Magnesium (as Mg) (mg/l)	3.0	88	21.6	18.0	13.76
Nitrate (as NO_3) (mg/l)	0.2	40.78	6.4	5.4	5.80
Sulphate (as SO_4) (mg/l)	4.0	94	22.6	17.0	20.28
Total alkalinity (as $CaCO_3$) (mg/l)	130	953	348.9	313.0	140.48
Total hardness (as $CaCO_3$) (mg/l)	113	833	316.9	288.0	130.44

Accepted manuscript

Table2. *Comparison of groundwater quality with Bureau of Indian Standards (2012).*

Parameter	**Minimum**	**Maximum**	**Indian Standard (BIS, 2012)**	
			Requirement (Acceptable Limit)	**Permissible Limit in the Absence of Alter Source**
pH value	6.4	7.9	6.5-8.5	No Relaxation
Electrical conductivity (µS/cm)	282	3919	--	--
Total dissolved solids (mg/l)	169	2406	500	1500
Calcium (as Ca) (mg/l)	34	256	75	200
Chloride (as Cl) (mg/l)	2	267	250	1000
Fluoride (as F) (mg/l)	0.2	5	1.0	1.5
Iron (as Fe) (mg/l)	0.1	6.1	0.3	No Relaxation
Magnesium (as Mg) (mg/l)	3	88	30	100
Nitrate (as NO_3) (mg/l)	0.2	40.78	45	No relaxation
Sulfate (as SO_4) (mg/l)	4	94	200	400
Total alkalinity (as $CaCO_3$) (mg/l)	130	953	200	600
Total hardness (as $CaCO_3$) (mg/l)	113	833	200	600

The range of chloride (Cl) concentration was found between 2 mg/l to 267 mg/l and only one groundwater sample in the study area was exceeded the BIS acceptable limit of chloride i.e. 250 mg/l. Primarily from taste viewpoint, the chloride limits have been laid down. Water having high chloride concentrations has no adverse health effects on human being [11].

Generally, sulfate presents as calcium, magnesium, and sodium soluble salts in groundwater. A significant change in the sulfate concentration takes place with time during rainfall infiltration and groundwater recharge [11]. The concentrations in the samples varied from 4 mg/l to 94 mg/l. None of the samples exceeded sulfate BIS acceptable limit of 100 mg/l (BIS, 2012). Sulfate, when present alone may not cause any adverse health effects while greater than 400 mg/l of sulfate with sodium or magnesium may lead to gastrointestinal irritations [12].

Nitrate (NO_3) concentration greater than 45 mg/l in drinking water has adverse health effects on human resulting methemoglobinemia commonly known as a blue baby syndrome which generally affects the infants [11] and gastric carcinoma [13]. The nitrate concentrations ranged from 0.2 mg/l to 40.78 mg/l in all the samples indicates within the BIS acceptable limit of 45 mg/l.

The iron (Fe) concentration in groundwater samples varied from 0.1 mg/l to 6.1 mg/l with a standard deviation of 0.8 mg/l. Approximately 69% of the groundwater samples in the study area exceeded the iron BIS permissible limit of 0.3 mg/l. The higher concentration of iron causes an inky flavor, turbidity, bitter and astringent taste. Water having soluble iron remains clear while pumped out. Exposure to air causes precipitation of iron resulting in rusty color and turbidity [11].

III.2. Correlation of fluoride with other physicochemical parameters

For establishing the relationship of fluoride with other physicochemical parameters correlation matrix (Table 3) and scatter plots have been drawn. The statistical analysis of the correlation matrix showed that electrical conductivity has a positive and significant correlation with total dissolved solids, total hardness, calcium, magnesium, and alkalinity. Calcium, magnesium, and alkalinity are positively and significantly correlated with total hardness. The alkaline nature of water is shown by the positive correlation between pH and fluoride that probably promotes the dissolution of fluoride and hence the causes of the concentration of fluoride in groundwater.

The analysis of the correlation matrix of fluoride and other physicochemical parameters showed that fluoride has a significant positive correlation with sulfate and significant negative correlation with calcium, magnesium, alkalinity and total hardness. Additionally, fluoride has a negative but poor correlation with electrical conductivity, total dissolved solids, chloride, nitrate, and iron.

The low calcium concentration favours the presence of high fluoride concentration in groundwater [14]. The negative correlation between calcium and fluoride found in the present study also support this view. The association of high fluoride zone with feldspathic sandstones and a negative correlation between fluoride and total hardness indicate that dissolution of feldspars, cation/base exchange are most likely to be the hydrogeochemical processes operating in the area leading to decrease in calcium concentrations with an increase in the concentration of fluoride in groundwater.

Generally, high alkalinity concentration favours the occurrence of high fluoride concentration in the groundwater [15] [16]. In the present study, a

accepted manuscript

negative correlation has been found between fluoride and alkalinity. Such a negative relation was also found by Tiwari et al. [17] in deeper aquifers of basaltic terrain which they attributed to the low partial pressure of CO_2 in deeper zones. The same reason may also be attributed to the negative correlation between fluoride and alkalinity found in the present study as the high Fluoride zone is mainly associated with deeper wells.

Table2. *Comparison of groundwater quality with Bureau of Indian Standards (2012).*

	pH	**EC**	**TDS**	**TH**	**Ca**	**Mg**	**F**	**Fe**	**Cl**	**SO_4**	**NO_3**	**ALK**
pH	1											
EC	-0.28	1										
TDS	-0.27	0.99	1									
TH	-0.24	0.89	0.89	1								
Ca	-0.26	0.80	0.80	0.92	1							
Mg	-0.12	0.68	0.68	0.74	0.42	1						
F	0.07	-0.07	-0.08	-0.04	-0.07	0.02	1					
Fe	0.08	0.01	-0.01	0.04	0.03	0.03	-0.16	1				
Cl	-0.29	0.74	0.75	0.58	0.53	0.45	-0.05	-0.1	1			
SO_4	-0.23	0.65	0.64	0.51	0.49	0.33	0.51	-0.0	0.50	1		
NO_3	-0.15	0.27	0.27	0.18	0.22	0.05	-0.01	0.0	0.26	0.23	1	
ALK	-0.22	0.86	0.85	0.96	0.87	0.72	-0.04	0.0	0.56	0.43	0.14	1

The correlation between fluoride and other physicochemical parameters (pH, TDS, total hardness, Ca, Mg, Cl, alkalinity, SO_4, NO_3, and Fe) are shown as scattered plot, in the figure 2-11. Fluoride is positively and significantly related to SO_4 and negatively related to Ca concentration (Figure 2 and Figure 3). Fluoride has a positive relation with pH (Figure 4). According to Chae et al. [3], a hydrogeochemical process that increases the fluoride concentration is closely related to a process that sinks for calcium. Fluoride is also negatively correlated with Mg (Figure 5). Due to precipitation of calcium carbonate, high fluoride, low Ca and Mg concentration is found in groundwater.

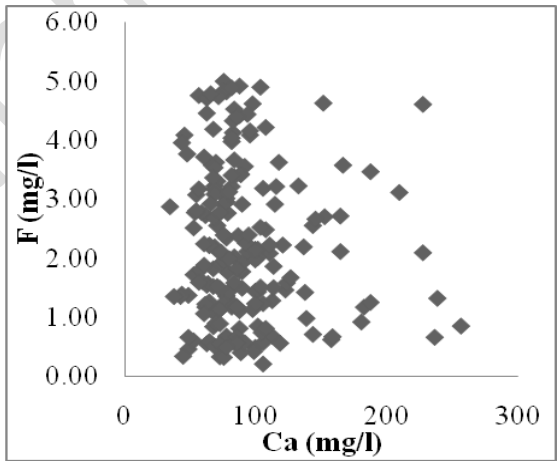


Figure 3. *Correlation between F & Ca*

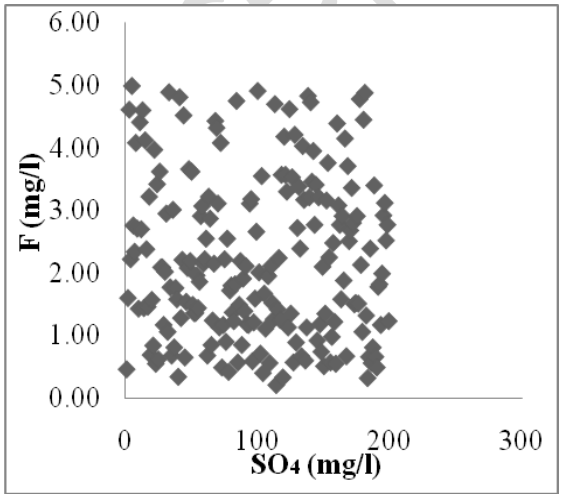


Figure 2. *Correlation between F & SO_4*

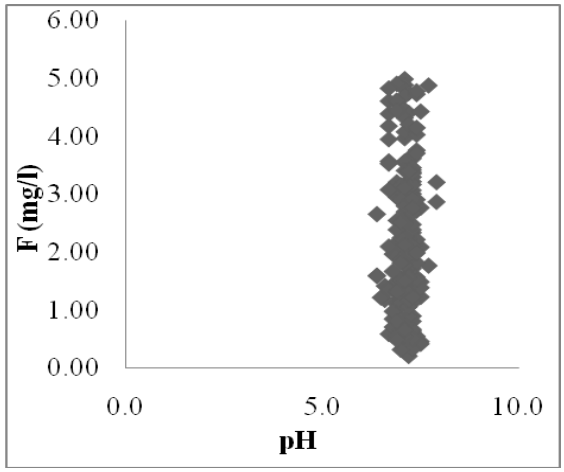


Figure 4. *Correlation between F & pH*

Preprint manuscript

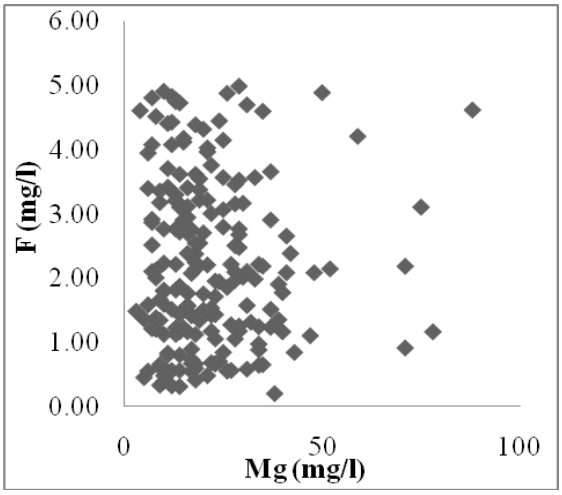


Figure 5. *Correlation between F & Mg*

The negative relation of fluoride with total hardness (Figure 6) is because of its precipitation as carbonates [18]. Fluoride shows a negative relation with alkalinity (Figure 7). As observed in water samples fluoride has a negative but poor correlation with electrical conductivity, total dissolved solids, chloride, nitrate, and iron (Figure 8-11).

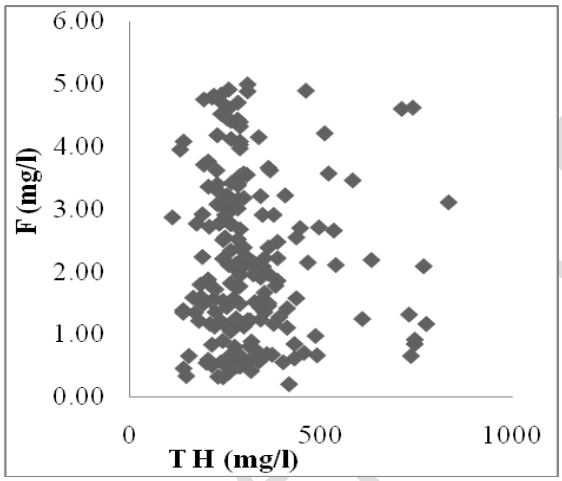


Figure 6. *Correlation between F & T H*

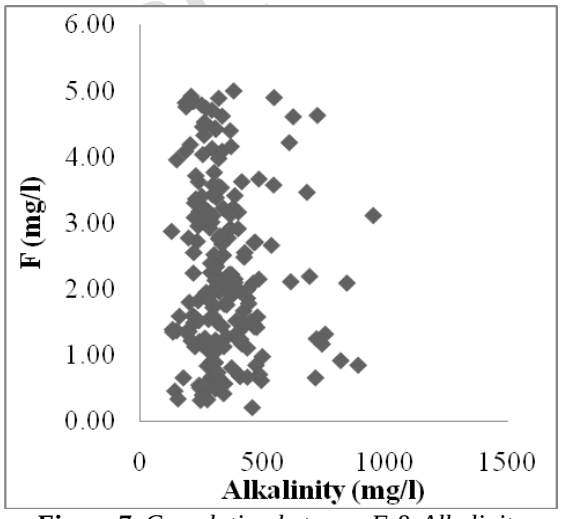


Figure 7. *Correlation between F & Alkalinity*

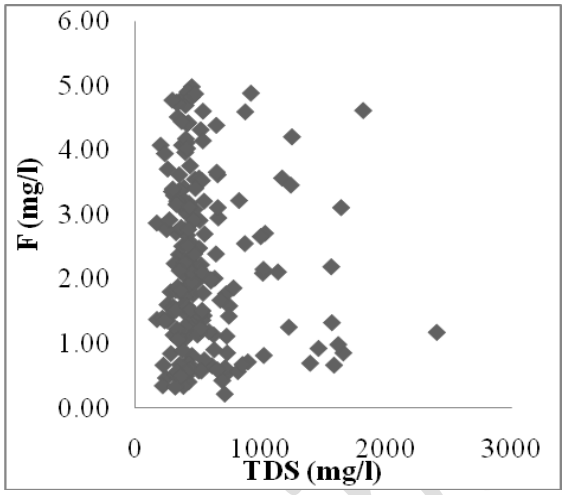


Figure 8. *Correlation between F & TDS*

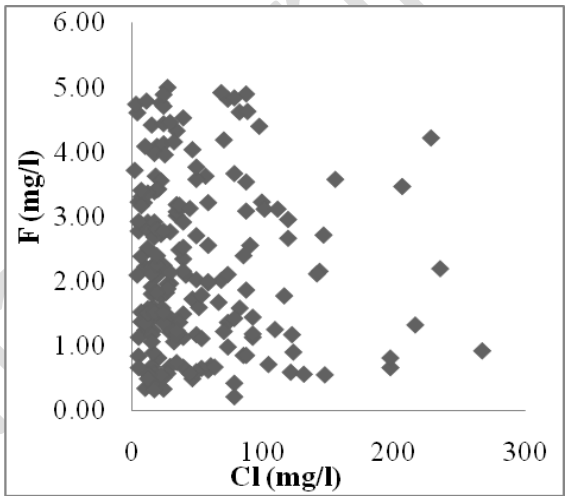


Figure 9. *Correlation between F & Cl*

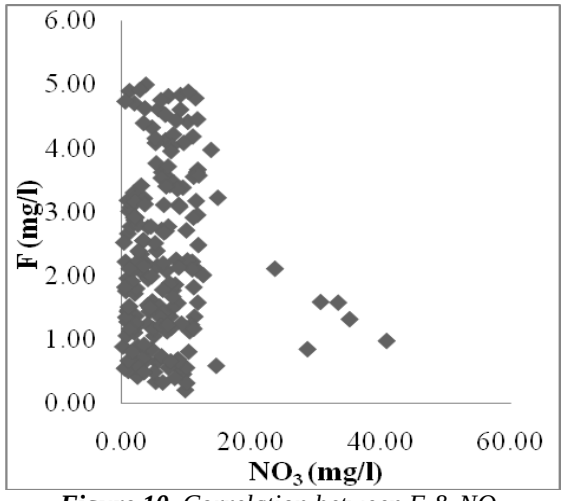


Figure 10. *Correlation between F & NO_3*

IV. Conclusion

The groundwater is the main source of drinking water for the people of Amas Block of Gaya District, Bihar and the study revealed that the total dissolved solids in 39%, total alkalinity in 93%, total hardness in 10%, calcium in 64% and

magnesium in 19% samples exceeded the BIS acceptable limit but in case of chloride only one sample exceeded the BIS acceptable limit. In the case of nitrate and sulfate, none of the samples exceeded the BIS acceptable limit. Iron concentration was found high and samples exceeded the BIS permissible limit.

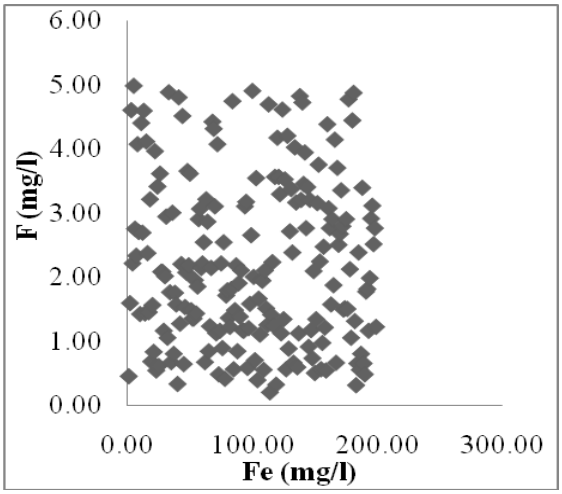


Figure 11. *Correlation between F & Fe*

The correlation matrix showed that electrical conductivity has a positive and significant correlation with total dissolved solids, total hardness, calcium, magnesium, and alkalinity. The total hardness was positively and significantly correlated with calcium, magnesium, and alkalinity. Fluoride has a significant positive correlation with pH and sulfate as well as a significant negative correlation with calcium, magnesium, alkalinity and total hardness. Additionally, fluoride has a negative correlation with electrical conductivity, total dissolved solids, chloride, nitrate, and iron whereas a negative correlation has been found between fluoride and alkalinity.

The groundwater was severely affected by fluoride contamination in the study area. Only 20% of samples were observed within the acceptable limit whereas 63% of samples exceeded the permissible limit as recommended by BIS (2012).

V. References

1. Ayoob, S.; Gupta, A.K. Fluoride in drinking water, A review on the status and stress effects. *Critical Reviews in Environmental Science and Technology* 36 (2006) 433-487.
2. Saxena, V.K.; Ahmad, S. Inferring the chemical parameter for the dissolution of fluoride in groundwater. *Environmental Geology* 25 (2002) 475-81.
3. Chae, G.Y.; Seong, T.M.; Bernhard, K.; Kyoung-Ho, K.; Seong–Yong, K. Fluorine geochemistry in bedrock groundwater of South Korea. *Science of The Total Environment* 385(1-3) (2007) 272-283.
4. Chandra, S.J.; Thergaonkar, V.P.; Sharma, R. Water quality and dental fluorosis. *Indian Journal of Public Health* 25 (1981) 47-51.
5. Choi, S.H.B.; Kim, K.H.; Lee, D.H.; Kim, S.M.; JY Kim, J.B. Prevalence of dental fluorosis at Jinyoung-up, Kimhae City, Korea. *J. Korean Acad. Dent. Health* 28 (2004) 347-361.
6. Kaminsky, L.; Mahoney, M.; Leach, J.; Melius, J.; Miller, M. Fluoride: Benefits and risks of exposure. *Crit. Rev. Oral. Biol. Med.* 1(4) (1990) 261-281.
7. Godfrey, P.P.; Watson, S.P. Fluoride inhibits agonist-induced formation of inositol phosphates in rats cortex. *Biochem. Biophys. Res. Commun.* 155(2) (1988) 664-669.
8. Jain, C.K.; Bandyopadhyay, A.; Bhadra, A. Assessment of ground water quality for drinking purpose, District Nainital, Uttarakhand, India. *Environmental Monitoring and Assessment* 166 (2010) 663–676.
9. APHA, 21st edition, Standard Methods for examination of water and waste water, Green berg A.H. Clesceri, I.S. and Eaton, A.D. (eds). American Public Health, 2005.
10. BIS (Bureau of Indian Standards), Drinking Water Specification (First Revision), Bureau of Indian Standards, New Delhi. IS: 10500: 2004-05 (2004).
11. Vani, M.L.; Reddy, K.P. Effects of fluoride accumulation on some enzymes of brain and gastrocnemius muscle of mice. *Fluoride* 33(1) (2000) 17-26.
12. Cicek, E.; Aydin, G.; Akdogan, M.; Okutan, H. Effects of chronic ingestion of sodium fluoride on myocardium in a second generation of rats. *Hum. Exp. Toxicol.* 24(2) (2005) 79-87.
13. Grynpas, M. Fluoride effects on bone crystals. *J. Bone Miner Res.* 5(1) S1 (1990) 169-175.
14. Guo, Q.; Wang, Y.; Ma, T.; Ma, R. Geochemical processes controlling the elevated fluoride concentrations in groundwater of the Taiyuan Basin, Northern China. *Journal of Geochemical Exploration* 93(1) (2007) 1-12.
15. Meenakshi; Maheshwari, R.C.; Fluoride in drinking water and its removal. *Journal of Hazardous Materials* 137(1) (2006) 456-463.
16. SubbaRao, N.; Devdas, D.J. Fluoride incidence in groundwater in an area of peninsula India. *Environmental Geology* 45 (2003) 243-251.
17. Tiwari, A.N.; Vijay, P.N.; Jivesh, A.T.; Kumar, S.Y. Correlation of Fluoride with Bicarbonate in groundwater of exploratory wells in parts of Maharastra. *Journal of Applied Geochemistry* 10(1) (2008) 93-102.
18. Gaciri, S.J.; Davies, T.C. The occurrence and geochemistry of fluoride in some natural waters of Kenya. *Journal of Hydrology* 143(3-4) (1993) 395-412.

accepted manuscript

Please cite this Article as:
Krishan A., Mishra R.K., Study on groundwater quality and status of Amas Block in Gaya District of Bihar with special reference to fluoride contamination, ***Algerian J. Env. Sc. Technology***, ***X*:X (YYYY) XX-XX**

Volume 7 Issue 3 (2019) 260-261 ISSN 2347 - 3258
International Journal of Advance Research and Innovation

Suitable selection of napkins in Hotel industry for sustainable development

Sachin Jaisar, Saurabh Agrawal
Department of Mechanical, Production, Industrial and Automation, Delhi Technological University, Delhi, India

Article Info
Article history:
Received 04 July 2019
Received in revised form
29 August 2019
Accepted 31 August 2019
Available online 15 September 2019

Keywords
Carbon footprint, GHG emission, Sustainable Development, Napkin

Abstract
This paper deals with the greenhouse gases (GHG) estimated emission from the napkins used in a hotel industry along with the selection of transportation mode vehicle (diesel or petrol vehicle). This study helps us to find whether a reusable or disposable napkin should be used to make a lesser GHG impact on environment. In the present scenario, most hotels are using paper napkins because they are light weighted, cheap and hygienic. The fact, that the relevant data is scattered, and is not available in literature and databases, compelled the data, to be acquired from various sources like journal articles and online blogs with few assumptions. Some critical data that has been collected is mainly from U.S and may vary when applied in India. A hypothetical assumption is used to derive the final conclusion. Cost is calculated for both the napkins associated with their mode of transportation per year. Finally, this paper suggests that reusable napkins should be used to deplete the rate of GHG emission.

1. Introduction

Sustainable development is an emerging aspect in which technology and innovation is seen under the umbrella of ecosystem. We are required to sustain the nature while developing anything. The name of carbon footprint comes from the study of ecological footprint discussion and is based upon life cycle Assessment (LCA). The carbon footprint reveals how much CO2 or CO2 equivalent (CO2e) in total is emitted along with the complete value chain of a product. It is calculated for the time period of a year and expressed in terms of the amount of carbon dioxide, or its equivalent of other GHGs emitted [1]. As the number of usage of a non-ecofriendly napkin is increased greenhouse gases concentration increases in the atmosphere and this causes global warming. In this study all the harmful emitted gases are taken into one form i.e. CO2 equivalent.

Global Warming Potential (GWP) is a measure of greenhouse gas emission, such as CO2 and methane which are causing an increase in the absorption of radiation emitted by the earth, magnifying the natural greenhouse effect [2]. This factor is considered because it is one of those vital factors which are immensely responsible for the comparison of the napkins.

There are 3 stages of carbon footprint emission chain from napkin:

1. Production; 2. Usage; 3. Disposal

For this research only production stage of the material used in making napkins have taken in consideration.

The napkin is divided into two vital categories: Disposable and Reusable.

Under disposable category we have paper napkins and in reusable we have used PET (Polyethylene terephthalate), Cotton, and Linen.

2. Literature Review

Disposable napkins are made from paper tissue derived from virgin and recycled pulp, but for this study we have considered the whole manufacturing of paper and neglected the process of making napkin from pulp only. Most of the hotels in today's time use paper napkin as they are cheap and easy-to-dispose but the effect of using it on environment is somewhat not taken into account. The raw material required for per Kg of paper napkin producing makes around 7.5 KgCO2e which reaches up to 15.799 KgCO2e (approx.) when manufacturing and end of life of the napkin is also considered [3]. Generally 24 trees are required to make one ton of paper, 1.5 tons of coal are required to produce the electricity for one ton of paper and this is responsible for emitting around five tons of carbon dioxide [4]. Polyethylene terephthalate is a most common thermoplastic polymer resin of the polyester family and is used in fibers for clothing. It contributes around 5.283 Kg CO_2 per kg in the environment [3] which constitute raw material, manufacturing and washing all together. Weight of these napkins is around 50.8 gm and uses 0.22 MJ of energy per napkin.

Corresponding Author,
E-mail address: sachin.jaisar8@gmail.com; agrawals.iit@gmail.com

All rights reserved: http://www.ijari.org

Cotton is a kharif crop which requires 6 to 8 months to mature. Cotton is widely used as a napkin in bulk now a days because of its tendency to absorb the waste and get nearly all stains washed out after coming from laundry. Cotton production contributes between 0.3% and 1 % of the total global emission of greenhouse gases [5]. Cotton farming requires large amounts of water varying from 7-29 tons per kg of raw cotton fibers [6]. Estimation is that 60.38 kg CO2 were produced by energy usage for ginning one bale of cotton [7].

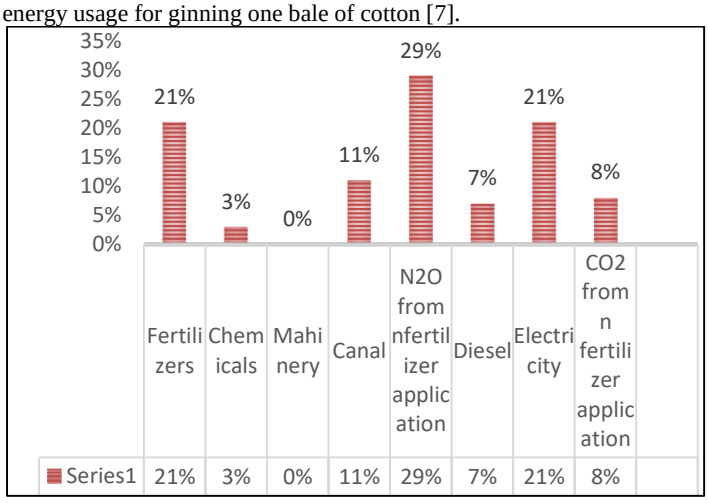


Fig.1: GHG (in CO2 equivalent) emission for cotton farming

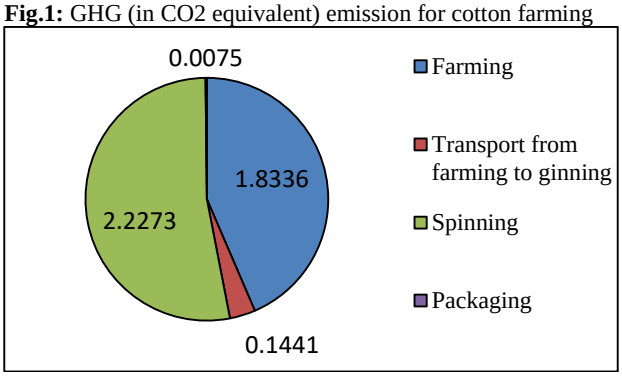


Fig.2: Total GHG emission for producing cotton.

This shows that a total of 4.2125CO2e/kg of GHG emission is there in cotton production [8]. Linen is a natural material woven from the fibers of the flax plant. Flax belongs to the family of blast fibers, which also includes hemp and jute, obtained from the inner bark of the stalk of certain plants. They may be more expensive up front, but will more than pay for themselves by lasting longer than other materials. Energy required for linen yarn production is 2.7 kWh per kg and carbon footprint allocated in the production of fibers is 0.335 kg CO2e/kg. The yarn production contributes around 3.353 kg CO2e/kg which accumulates to a total of 3.688 kg CO2e/kg [9].

3. Methodology

A comparison is drawn by plotting all the GHG emission value on a column chart.

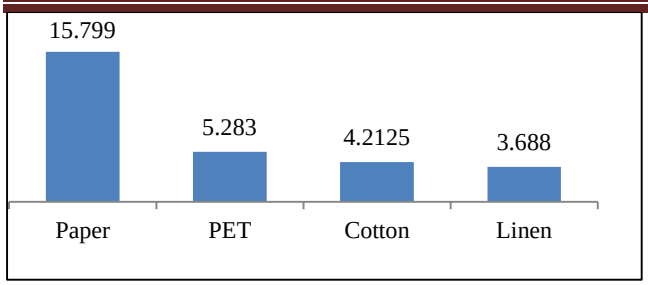


Fig.3 Comparison between all the napkins

Here linen is the clear winner amongst all other napkins it produces only 3.688kg of GHG. A hypothetical assumption is considered to have a better understanding about the final result.

Table 2: Assumed factors for napkins

Napkins	Ordered quantity (per year)	No. of customers (per day)	Weight per napkin (gm)	Napkin usage (per customer)
Disposable	108050	100	4	3
Reusable	450	100	32	1

3.1Steps involve

1 Both disposable and reusable napkins are taken for 360 days;
2 According to the blog an average customer uses
3disposable napkins or 1 reusable napkin per meal which is true in general;
4 Fifty napkins are kept in both categories as safety stock;
5 Disposable napkins are ordered every month whereas the reusable ones are ordered every third month which is assumed by taking care of durability of the napkins;
6 Disposable napkins will be only single time used but reusable napkins can be used 90 times as there durability is around 3months.

After simple mathematical calculations it shows that disposable napkin produce around 432.2 kg of waste per year while reusable napkins make only 14.4kg waste per year.

Table 1: Fuel used for transportation [10].

Energy Source	CO_2 Emissions (kg CO_2 exhaust / litre of fuel)
Unleaded Petrol	2.2715
Synthetic Diesel	2.6763

4. Result and Discussion

Every day the vehicle will take the reusable napkins to go to laundry for washing and come back to the hotel. According to the assumption in one day a hotel produces only 300 paper napkins waste i.e. 1.2kg of waste which is not enough for disposing. But on 5th day the waste will be 6kg, still not much quantity but quite economical to dump as compared to the one day dumping strategy. Vehicle travel 5km per liter of diesel and travel 7 km per liter of petrol.

Table 3: Distance assumption

CO_2 exhaust by Diesel vehicle for disposable napkins =1/(5)×9700=1940litres×2.6763 =5192.022kg

CO_2 exhaust by Diesel vehicle for reusable napkins = 1/5×8500 =1700litres×2.2715 = 3861.55kg

CO_2 exhaust by Petrol vehicle for disposable napkins = 1/7×9700

	Production house to hotel	hotel to laundry	hotel to landfill	dumping	Total
	(km)	(km)	(km)	(per year)	(km)
disposable	200	n/a	100	73 times	9700
reusable	200	20	100	4 times	8500

=1385.71litres×2.6763=3708.57 kg

CO_2 exhaust by Petrol vehicle for reusable napkins =1/7×8500=1214.28 litres×2.2715= 2758.237kg

Round trip is taken as each time the loaded vehicles are supposed to move it will again come to the original place.

4.1 Cost analysis

One disposable napkin cost= Rs0.147 (approx.) Total assumed number of disposable napkins cost= Rs15847.334/ year

One reusable napkin cost = Rs25.5 (approx.)

Total assumed number of reusable napkins cost= Rs11475/ year

Around 4372.334 can be saved by using reusable napkins over disposable ones.

4.2. Research gap

1. Recycled paper data could be used to have a better perspective (Although for this study even if we add that, the amount of GHG and the cost associated with that will only increase.)
2. Genuine data collection for the respective motive could be done in India.
3. A hotel survey could be done to enhance the actual customer arrival rate and the proper usage and disposing of the napkins.
4. For reusable napkins, drying them after the laundry is a major issue.
5. Decomposing duration of both the napkins after send to landfill could be taken into account.

5. Conclusions

Hence considering assumptions from the above table, an estimated conclusion is made that within a year disposable napkin generates 432 kg of landfill but on the other hand reusable napkins make only 14.4 kg, neglecting the fact that disposable napkin takes around 1month and reusable napkin around 5months to decompose. From the data that we collected to our assumption we can get that linen displays the smallest carbon footprint of all the napkins. On comparison, the following CO2e emission sequence was found.

Paper > PET > Cotton> Linen

Hence using Linen napkins in your hotel with a transportation system of petrol vehicle is a better choice and is more ecofriendly.

Acknowledgment

Author thanks Delhi Technological University for providing necessary knowledge regarding emission of gases and how they are actually effecting the environment.

References

[1]. E Nieminen, M Linke, M Tobler, BV Beke. EU COST Action 628: Life Cycle Assessment.LCA of Textile Products, Eco-Efficiency and Definition of Best Available Technology (BAT) of Textile Processing. J. Cleaner Production, 15(13-14), 2007, 1259- 1270.

[2]. J Bare. TRACI 2.0: the Tool for the Reduction and Assessment of Chemical and Other Environmental Impacts 2.0. Clean Technology Environmental Policy, 2010.

[3]. John Jewell. Comparative Life Cycle Assessment of Reusable vs. Disposable Textiles, PE International, Doc. no. 1200473.000 8193, 2014

[4]. Research Information. Green publishing: publishers urged to do more to be green, 12, 2008/1, 2009. www.researchinformation. info/features/feature.php?feature_id¼196

[5]. P Ton, A Asterine, M Knappa. Cotton and Climate Change-Impacts and Options to Adapt, 2011.

[6]. [6] EM Kalliala, P Nousiainen. Life Cycle Assessment Environmental profile of cotton and polyster- cotton fabrics, Autex Res. J.,1(1), 1999, 8–20.

[7]. SH Pishgar-Komleh, P Sefeedpari, M Ghahderijani, Exploring energy consumption and CO2 emission of cotton production in Iran, J. Renew. Sustain. Energy, 4, 2012.

[8]. M Nigam, P Mandade, B Chanana ,S Sethi. Energy consumption and Carbon footprint of Cotton Yarn Production in textile industry, Int. Arch. App. Sci. Technol; 7 [1] 2016, 6-12.

[9]. B Thomas. Environmental Resources Management Limited (ERM), 2012 .

[10]. M Rajarajan, SG Venkatasubramanian. A Study On Carbon Footprint of Different Hotels in A Metropolitan City, International Journal of Informative & Futuristic Research (IJIFR 22(10), 2015, 3590-3599.

To be published in Journal of the Optical Society of America B:

Title: Temperature-assisted Broadly Tunable Supercontinuum Generation in Chalcogenide Glass-based Capillary Optical Fiber

Authors: Satya Singh,Jasleen Kaur,Keshav Samrat Modi,Umesh Tiwari,Ravindra Sinha

Accepted: 20 February 20

Posted 21 February 20

DOI: https://doi.org/10.1364/JOSAB.387491

© 2020 Optical Society of America

Published by

OSA®

The Optical Society

Temperature-assisted Broadly Tunable Supercontinuum Generation in Chalcogenide Glass-based Capillary Optical Fiber

SATYA PRATAP SINGH[1], JASLEEN KAUR[1,2], KESHAV SAMRAT MODI[1,2], UMESH TIWARI[1,2], AND RAVINDRA KUMAR SINHA[*,1,2,3]

[1]*CSIR-Central Scientific Instruments Organisation, Chandigarh, India*
[2]*Academy of Scientific & Innovative Research, Ghaziabad, India*
[3]*TIFAC-CORE, Delhi Technological University, New Delhi, India*
**dr_rk_sinha@yahoo.com*

Abstract: We propose an alternative technique to generate tunable supercontinuum in a liquid-filled chalcogenide capillary optical fiber (CCOF) exhibiting three zero dispersion wavelengths. To investigate the tunable supercontinuum, nonlinear Schrödinger equation is solved to understand the soliton pulse dynamics. Utilizing the temperature-assisted dispersion tailoring, generation of dispersive waves which are tunable within a broad wavelength range of 3630-4650 nm and 2230-2560 nm, are reported with detailed investigations of various spectrograms confirming the predictions of dispersive waves through phase-matching characteristics. Also, temperature-controlled soliton spectral tunneling is numerically predicted in the same fiber that depends on the spectral width of the normal dispersion region between two anomalous regions.

© 2019 Optical Society of America under the terms of the OSA Open Access Publishing Agreement

1. Introduction

Coherent radiations in mid-IR region are of great interest due to their remarkable applications in spectroscopy [1,2], remote sensing [3], free space communications [4,5] non-invasive medical diagnosis [6,7] and defense related applications such as detection of biological and explosive hazards and enhancing the capability of night vision equipment. There are technological challenges to generate broadly tunable mid-IR radiations through a single source [8]. Over the years, several technologies have evolved to produce mid-IR frequencies viz., semiconductor lasers, quantum cascade lasers, interband cascade lasers, gallium antimonide diode lasers, solid state laser, optical parametric oscillators, amplifiers and supercontinuum (SC) in nonlinear crystals and fibers [9-14]. Supercontinuum generation is a convenient technique for generating broadband radiation from near- to mid-IR wavelength regimes. The mid-IR supercontinuum radiation has attracted a great interest due to the arrival of the highly nonlinear soft-glass fibers and photonic crystal fibers (PCFs) [8,15-23]. The dispersive wave (DW) plays an important role in spectral broadening and blue- or red shifting of the supercontinuum [24-26]. When a temporal soliton propagates in the anomalous dispersion regime, the higher-order dispersion of the fiber perturbs the temporal soliton which leads to the generation of the DW. The wavelength of the generated DW can be determined from the phase matching (PM) condition between the linear and nonlinear phase of the soliton and the linear phase of the DW [27,28]. The DW phase matching (PM) condition, between the soliton (ω_s) and the dispersive radiation (ω_d) can be written as:

$$\beta(\omega_d) = \beta(\omega_s) + \beta_1(\omega_s)(\omega_d - \omega_s) + \frac{\gamma P_s}{2}. \quad (1)$$

where $\beta(\omega_s)$ and $\beta_1(\omega_s)$ are the propagation constant and inverse group velocity of the soliton, respectively and γ is nonlinearity of fiber. By changing the PM dynamics, the wavelength of the DW radiation can be tailored. The DW can be either generated in blue and/or red side of the SC spectrum depending on the sign of the higher-order dispersion (HOD) parameters [25].

If we expand $\beta(\omega_d)$ around ωs using Taylor-series expansion, the total phase mismatch can be given as:

$$\kappa = \sum_{m=2}^{\infty} \frac{\beta_m(\omega_s)}{m!}(\Delta\omega_d)^m - \frac{\gamma P_s}{2}. \quad (2)$$

where, P_s is the peak power of the soliton formed after the fission and ω_d, ω_s are the dispersive wave and the soliton frequencies respectively, and $\beta_m(\omega_s)$ are the HODs at ω_s, where m = 2, 3, 4… so on. It appears from the eqn. (2) that by changing the HOD parameter, one can change the total phase mismatch and hence the wavelength of the DW radiation. Recently, researchers have experimentally observed the generation of tunable dispersive wave by changing the input pump power [29,30], tunable SC by changing the input pulse wavelength [22], and temperature of the fiber system [31]. There is always a group velocity mismatch between the soliton and the DW generated in normal dispersion. However, if the transfer of the power occurs from the soliton to the DW in anomalous dispersion, then group velocity matching between the both waves (ω_s and ω_d) facilitates the soliton spectral tunneling (SST) [32], where soliton jumps from one anomalous dispersion region to another skipping the normal dispersion region sandwitched between these anomalous dispersion regions. This process enables in generating a coherent radiation far from the soliton frequency.

To achieve mid-IR tunable SC, one requires fiber material with mid-IR transmission and appropriate fiber structure for dispersion control. Since, silica is highly absorptive at mid-IR wavelengths (>2.5 μm), non-silica glass materials which show greater transparency in the mid-IR regime such as chalcogenide (sulfide, selenide, and telluride), tellurite, fluoride etc. can be used. Depending on their composition based on chalcogen elements, (Sulphur, Selenium, and Tellurium), n_2 has been measured between two to three orders of magnitude higher than for silica glass. For example, arsenic trisulfide (As_2S_3) is a highly nonlinear optical material having large value of nonlinear refractive index, 2×10^{-18} m^2/W with mid-IR transparency window up to ~11μm, however, As_2S_3 glass based optical fibers have less transmission range, e.g. upto 6 μm, compared to the bulk glass. Chalcogenide glasses are very stable, durable, and insoluble in water [33], but the presence of moisture results in higher optical losses. Optical fibers, either step-index or PCFs, have been drawn using combination of silica and chalcogenide glasses [20,34]. However, the presence of an air capillary at the center of the core of a step-index fiber increases the flexibility in engineering dispersion characteristics [35], similar to the PCF. With the recent technological developments in optical fibers, it has become possible to fabricate a micro/nano sized air-hole in the core [36,37], which can be filled with suitable thermo-responsive liquids to engineer dispersion characteristics by changing the temperature [38-40]. Such fiber consists of high-index annular optical core with a small-sized air hole in the center of the core with a low-index cladding (e.g., silica or polymer).

In this paper we have proposed a novel way to generate a temperature-controlled broadband mid-IR tunable supercontinuum spectrum. With this technique the generated SC is tunable within a broad range of 2700 nm. We have also observed a temperature dependent soliton tunneling effect which facilitate the generation of a high-power soliton pulse at 4.5 μm using a pump pulse at 2.94 μm. Tunable supercontinuum generation in the proposed chalcogenide COF is practically feasible. Various researcher has experimentally shown the practicalities of fabricating, temperature tuning, and integrating a liquid-filled fiber into a laser system. For example, fabrication of soft-glass optical fiber capillaries is discussed in detail by Romaniuk et. al [36]. Kudlinski et. al has experimentally shown the temperature dependence of the zero-dispersion wavelength in a photonic crystal fiber [41] and Travers et.al has shown experimentally shown the variation dispersion characteristics of gas filled hollow-core photonic crystal fiber with pressure and by integrating this gas filled hollow-core photonic crystal fiber

into a laser system, pressure dependent Deep-UV dispersive-wave generation is shown [42].

2. FIBER DESIGN, SIMULATIONS AND RESULTS

To generate tunable dispersive waves, we have considered a chalcogenide COF (CCOF) having structural parameters R = 2μm, a/R = 0.25 (as shown in inset of Fig. 1). The structural parameters of the proposed CCOF are chosen in such a way that it exhibits a very small and an almost flat dispersion profile with three zero dispersion wavelength in the mid-IR region [35]. The simulation is carried out in COMSOL Multiphysics to obtain the effective refractive index of the proposed fiber. To achieve a temperature tunable dispersion characteristic, it is proposed that the air capillary of the CCOF is filled with liquid of refractive index, 1.45, which is transparent in mid-IR regime, e.g., CCl_4, which is more than 80% transparent up to 6 μm [43]. In the simulation, the wavelength dependency of the liquid refractive index is neglected since the spectral variation of refractive index of CCl_4 in the wavelengths of interest is very small [31] and the fractional power confined into the capillary is also quite low compared to the annular core [44]. As we know that the liquids have a quite high thermo-optics coefficient ($dn/dT = -4\times10^{-4}$ /°C [45]), this means change in the temperature, leads to the modification in capillary refractive index and hence the effective index of the CCOF. The temperature-dependent refractive index has been taken through $n_T = n_R + \Delta T\left(\frac{dn_R}{dT}\right)$, where n_R is the refractive index of the liquid at room temperature and ΔT is the change in temperature with respect to the room temperature. The main reason behind choosing a liquid filled fiber is that if we use a polymer or a mid-IR glass in the capillary, then once the fiber is fabricated, one can only change the dispersion by changing the temperature, but a desired dispersion characteristic can be achieved by utilizing a suitable liquid after the fabrication of the fiber and dispersion characteristic can be fine-tuned by temperature. The temperature-dependent refractive index (1.7×10^{-5} /°C) [46] and thermal expansion coefficient (2.1×10^{-5} /°C) of As_2S_3 are also taken into account while simulating the modal properties of the fiber [47]. The dispersion characteristics of CCOF at different temperatures (ΔT = 0 and 50 °C) are shown in Fig. 1. Due to the temperature dependence of the effective refractive index, the dispersion characteristics is also temperature dependent. It is clear from the figure that the CCOF structure shows three zero dispersion wavelengths (ZDWs) at 2.83 μm (z_1), 3.50 μm (z_2) and 3.88 μm (z_3) for ΔT=0°C and we observe a blue shift in the z_1 while red shift in z_2 and z_2 as the temperature of the CCOF is increased ΔT=0°C to 50°C. The white regions in the Fig.1 represent the normal dispersion (denoted by N) regions while the shaded regions represent the anomalous dispersion regimes (denoted by A). The widths of the anomalous and normal dispersion regions are expressed by $\Delta\lambda_a$ and $\Delta\lambda_n$, respectively.

Publish-Read
The Optical Society

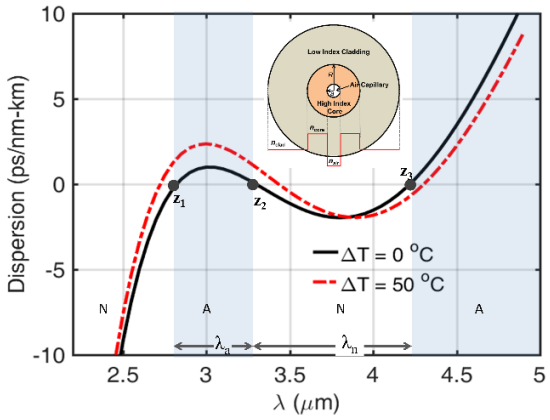


Fig. 1. Dispersion characteristics of the CCOF (R = 2 μm, a/R = 0.25 and n_{liq} =1.45) at various temperatures (ΔT = 0, and 50 °C) above room temperature, $\Delta\lambda_n$ and $\Delta\lambda_a$ are the widths of the normal and anomalous regions respectively which are denoted by N and A. The inset shows typical CCOF schematic cross-section. R and a denote radius of core and capillary.

Before studying the temperature-controlled SC output spectrum, we have first investigated the variation of SC spectral density with pump wavelength where we have plotted the SC output spectrum for different input pump wavelengths varying in the range 2000 – 5000 nm as shown in Fig. 2 (a, b). For this purpose, we have considered the input secant hyperbolic pulse of peak power 36 W and pulse-width of 100 fs fixed for all pump wavelengths. During the simulation of the soliton evolution in the proposed chalcogenide fiber all linear and nonlinear processes such as dispersion, self and cross phase modulation, Raman scattering and self-steepening are considered in the nonlinear Schrodinger equation [48]. It is observed from the SC spectral density plot that there is spectral broadening for the pump wavelength around 3000 nm and it further increases by increasing the temperature. DW phase matching characteristics at temperatures, ΔT = 0, and 50 °C for different input pump wavelengths varying in the range 2000 – 5000 nm is shown in Fig. 2 (c). This phase matching plot describes the resonance position of the DW in the SC spectrum. So, by observing the Fig. 2 (c) we can say that the spectral broadening in case of ΔT = 0 °C (Fig. 2 (a)) is coming due to the generation of DW in the both (blue and red) side of the pump wavelength because the dotted line (parallel to the DW axis) is intersecting the phase matching curve (black color) at three point. However, in case of ΔT = 50 °C, the dotted line intersects the phase matching curve (red color) at only one point in the blue side of the pump, so the spectrum generated in the red side of the pump wavelength (Fig. 2 (b)) may be due to soliton spectral tunneling (SST). So, it is clear from the Fig. 2 that using the input pump wavelength close to 2940 nm, one can observe a significant SC spectral broadening by changing the temperature.

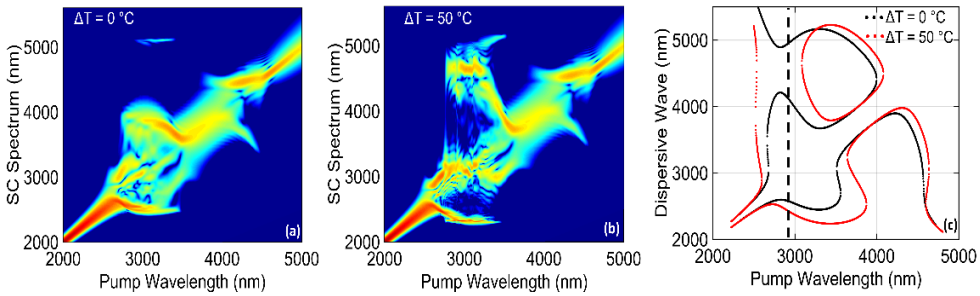


Fig. 2. a, b) Variation of SC spectral density with pump wavelength at different temperatures, $\Delta T = 0$, and 50 °C, in density plot representation, c) Temperature-controlled (0, and 50 °C) DW phase matching characteristics obtained by solving eqn. 2 for different pump wavelengths.

To confirm the temperature dependent SST generation, A hyperbolic secant pulse with peak power of 36 W and pulse-width of 100-fs at a wavelength of 2940 nm is considered for the propagation in the anomalous dispersion region of the CCOF during simulation. When soliton pulse propagates in anomalous dispersion region, the pulse starts to compress in the time domain, i.e., broadens in the frequency domain, due to the interplay between the nonlinearity and group velocity dispersion. The temporal compression and spectral broadening of this higher order soliton becomes unstable in the presence of higher-order dispersions and Raman scattering which leads to soliton fission and dispersive wave generation. A resonance radiation(s) appears in the normal dispersion regime when a soliton propagates close to ZDW and in this situation the total phase mismatch curve intersects phase matching line ($\kappa = 0$ line as depicted in Fig. 3 (a)). The total phase mismatch between the DW and soliton at wavelength of 2940 nm is obtained by solving the phase matching equation Eqn. (2). From Fig. 3 (a), it is observed that the total phase mismatch curve intersects the zero line (phase matching line) at three wavelengths namely at 2560 nm, 4000 nm and 5020 nm which means dispersive wave will be generated at these wavelengths. To verify and validate this prediction, the NLSE is solved for given dispersion and input pulse parameters. The spectral evolution of the soliton across the fiber length at room temperature (i.e. ΔT= 0°C) is shown in Fig. 3 (b). The dispersive waves forecasted by the total phase mismatch curve (Fig. 3 (a)) are clearly observed in the Fig. 3 (b), where two of them are located in normal dispersion regime while one is in the anomalous dispersion regime. In case of a dispersion profile possessing three ZDWs, two regions of anomalous dispersion are separated by a normal dispersion region. When a pulse is propagated in one of the anomalous dispersion region (A1), there is a sharp switching of the soliton frequency from anomalous dispersion region (A1) to the second anomalous dispersion region (A2). This behavior of the soliton is referred to as SST [28,49]. The Raman self-frequency shift plays a key role in the soliton propagation dynamics and tunneling to the other anomalous dispersion region. The generated DW at 5020 nm in the anomalous dispersion region does not possess sufficient power to form a stable soliton, i.e. soliton number of this tunneled radiation is less than 1 (Soliton order of the input pulse depends on the fiber parameter and pulse itself). Therefore, it exhibits the properties of a DW. This attribute has been verified from the spectrogram (Fig. 3 (c)) and temporal plot (Fig. 3 (d)). The shape of the spectrogram reflects the spectral variation of the group delay in the fiber. To observe the effect of temperature on the DW, it is necessary to keep the pump power of the pulse at fixed value and change the temperature. When the temperature is varied from ΔT = 0 °C to 50 °C while keeping other parameters fixed, the phase matching curve (Fig. 3 (e)) predicts the generation of dispersive wave at 2370 nm in the normal dispersion region (N1), but there is no indication of DW in the anomalous dispersion region (A2). In this case, the dispersive wave that appeared in the anomalous dispersion region (A2) at wavelength 5020 nm of Fig. 3 (b) is vanished. This is due to the fact that the phase matching condition changes with the change in the dispersion on account of temperature difference which leads to disappearance of the dispersive wave. However, we observe two strong spectral peaks at 2310 nm and at 4660 nm as shown in Fig. 3 (f). Note that

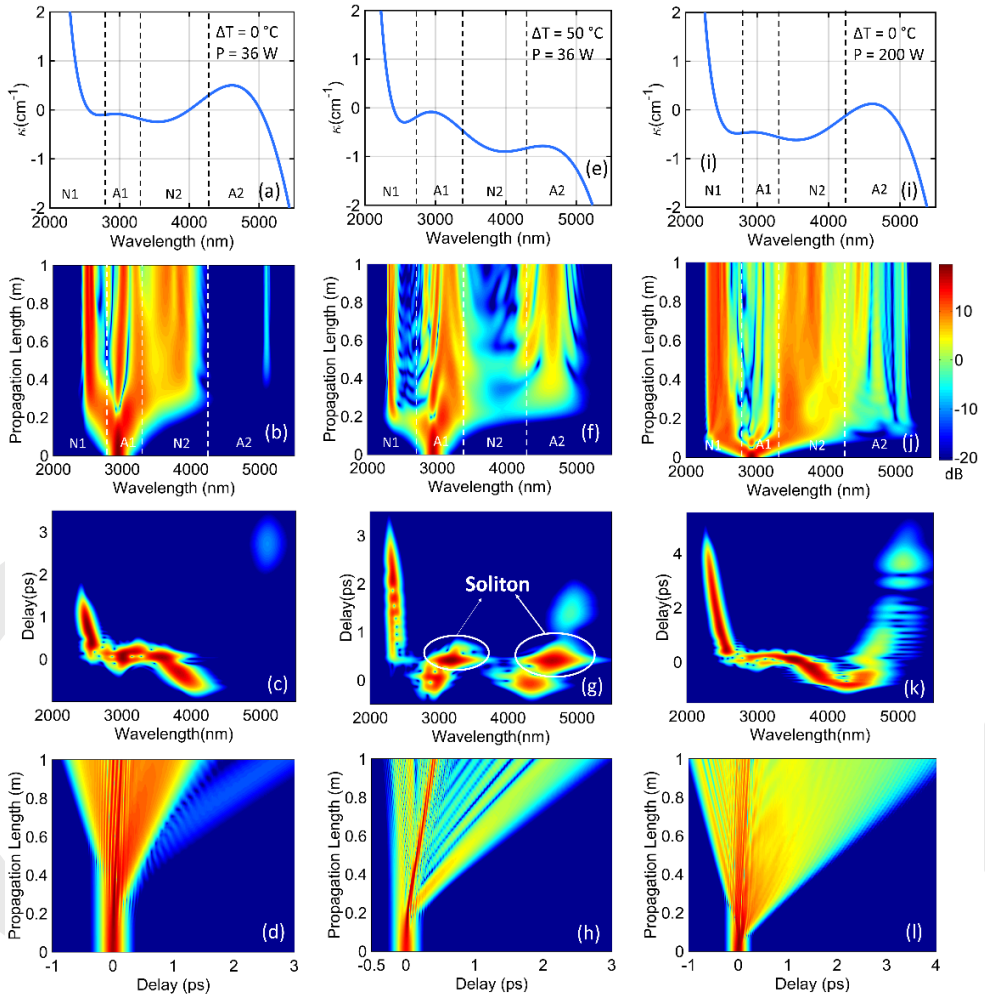


Fig. 3. Phase matching curves of DW and soliton at temperatures ΔT = 0 °C (a) and 50 °C (e). Spectral evolution of the soliton across whole fiber length at ΔT = 0 °C (b) and 50 °C (f). Spectrograms of the electric field at the exit of the fiber at temperatures ΔT = 0 °C (c) and 50 °C (g). Temporal plot at ΔT = 0 °C (d) and 50 °C (h). Vertical black and white dashed lines in (a), (e) and (b), (f) correspond to three ZDWs of the fiber, respectively, N and A represent the normal and anomalous dispersion regions in (a), (b), (e) and (f).

now the strong spectral peak in the anomalous dispersion region (A2) does not behave like a dispersive wave (as it is verified by PM condition) because the intensity of the generated pulse is sufficient to form a soliton having soliton number equal to or greater than 1. The soliton characteristics are also confirmed through spectrogram, Fig. 3 (g) and temporal plot in Fig. 3 (h). Further, we have examined the possibility of SST effect by varying the input pump power and pulse width while keeping temperature fixed at 0 °C. Even if the phase matching condition is manipulated by increasing the pump power up to 650W to give a PM curve similar to Fig. 3(e) in the A2 region but, no SST similar to Fig. 3 (f) is observed because dispersion characteristics are same as in previous case. The spectrogram and temporal plot, when the input pump power is 650 W and temperature is at 0 °C, are shown in Fig. 3 (k) and Fig. 3 (l),

respectively. In a similar way, we changed the pump pulse width, but didn't observe the SST effect (not shown in the paper).

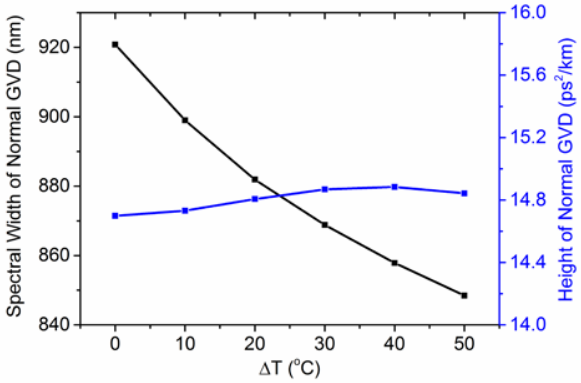


Fig.4. Variation of spectral width and height of the normal GVD N2 with the temperature.

In ultrafast nonlinear fiber-optics a spectral inhomogeneity such as normal dispersion region, sand-witched between the two anomalous dispersion regions, acts as a potential barrier for the soliton spectral tunneling process [50]. We have investigated the change in the height and the spectral width (z_3-z_2) of normal dispersion region N2 by varying the temperature. Height of normal dispersion region N2 is calculated by measuring the maximum value of the group velocity dispersion (GVD) in the same dispersion region with respect to zero GVD value for different temperatures. Fig. 4 shows the effect of the temperature on the spectral width and height of the normal dispersion region N2. From the figure it is evident that the spectral width of the normal dispersion region decreases with temperature while the height almost remains constant throughout the temperature change. As we know from the ref. 50, that the decrease in the spectral width of the barrier facilitates the SST effect and that is why in our study simulation shows SST effect by increasing the temperature, as proper tuning of the dispersion profile helps the DW to evolve as a solitonic wave. We can fairly conclude that the SST depends on the width of the normal dispersion region between two anomalous regions as the maximum value of the dispersion of the normal dispersion region is constant with the temperature (Fig. 4). With the help of thermal tuning, width of the normal dispersion regime can be controlled which would allow to observe the SST which is not possible by varying pump power and pulse width of the input soliton. Temperature based tenability is different from the pump power based tunability. In case of temperature based tunability, the DWs either blue shifted or red shifted varied linearly with temperature. However, in case of pump power based tunability, it is varying nonlinearly. Apart from that with increase in power, the soliton number of the input soliton pulse increases which results in the deterioration of the coherent nature of the supercontinuum spectrum while in case of the temperature variation, soliton number decreases that means supercontinuum spectrum is relatively more coherent in nature. However, polarization and higher order modal effects that also affect the coherence of supercontinuum spectrum, are not considered in the simulation [51,52].

To investigate the temperature dependent tunability of the SC spectrum, a hyperbolic secant pulse and proposed CCOF with aforementioned characteristics is used. The SC spectrum at fiber end is simulated for different temperature values ranging from 0 to 80 °C. Fig. 5 (a) shows the temperature tunability of SC spectrum calculated at the fiber end. It is clear from the Fig.5 (a) that the DWs present in normal dispersion region N2 can be tuned when temperature is varying from 0 to 40 °C, after 40 °C SST becomes the dominating factor which results in the generation of soliton that does not depend on the higher order dispersion and hence there is no temperature dependent tuning. But, dispersive wave present in normal dispersion region N1

shows temperature dependent tuning in the whole range of the temperature variation from 0 to 80 °C.

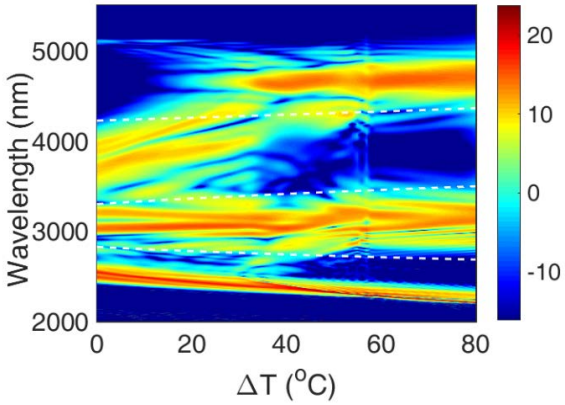


Fig. 5. Variation of SC spectrum at the output of the fiber with temperature. The three horizontal white dash lines shows the variation of the ZDWs (z_1, z_2 and z_3) of the CCOF with temperature.

3. CONCLUSIONS

We have numerically investigated an alternative method to generate tunable mid-IR supercontinuum by controlling the phase matching characteristics of the dispersive waves along with the temperature-controlled soliton tunneling in a liquid-filled chalcogenide COF showing three ZDWs. It is observed that with this technique the generated SC is tunable within a broad range of ~2700 nm. We have shown that the temperature dependent soliton tunneling depends on the spectral width of the normal dispersion region between two anomalous regions as the maximum value of the dispersion of the normal dispersion region is constant with the temperature. The proposed technique may have potential to provide tunable coherent source by only utilizing a single fiber structure and single pump laser unlike the others where different fiber structures and tunable pump lasers are used to achieve the same.

ACKNOWLEDGMENT

This work is done during my tenure as a National post-doctoral fellow (File No: PDF/2016/003647). The author is thankful to DST-Science and Engineering Research Board for awarding me this fellowship.

REFERENCES

1. S. Sanders, “Wavelength-agile fiber laser using group-velocity dispersion of pulsed super-continua and application to broadband absorption spectroscopy” Appl. Phys. B: Lasers O 75(6-7), 799–802 (2002).
2. T. Steinle, F. Neubrech, A. Steinmann, X. Yin and H. Giessen, “Mid-infrared Fourier-transform spectroscopy with a high-brilliance tunable laser source: investigating sample areas down to 5 μm diameter” Opt. Express 23(9), 11105-11113 (2015).
3. E. A. Romanova, S. Korsakova, M. Komanec, T. Nemecek, A. Velmuzhov, M. Sukhanov, and V. S. Shiryaev, “Multimode Chalcogenide Fibers for Evanescent Wave Sensing in the Mid-IR” IEEE J. Sel. Top. Quant. 23(2), 289–295 (2017).
4. Y. Su et al, “10 Gbps DPSK transmission over free-space link in the mid-infrared”. Opt. Express, 26(26), 34515-34528 (2018).
5. Q. Hao et al, “Mid-infrared transmitter and receiver modules for free-space optical communication. Appl. Opt. 56(8), 2260-2264 (2017).

6. F. Toor, S. Jackson, X. Shang, S. Arafin and H. Yang, “Mid-infrared Lasers for Medical Applications: introduction to the feature issue” Biomed. Opt. Express. 9(12), 6255-6257 (2018).
7. A. Urich, R. R. J. Maier, F. Yu, J. C. Knight, D. P. Hand and J. D. Shephard, “Flexible delivery of Er:YAG radiation at 294 μm with negative curvature silica glass fibers: a new solution for minimally invasive surgical procedures” Biomed. Opt. Express, 4(2), 193-205 (2012).
8. C. R. Petersen, U. Møller, I. Kubat, B. Zhou, S. Dupont, J. Ramsay, T. Benson, S. Sujecki, N. Abdel-Moneim, Z. Tang, D. Furniss, A. Seddon, and O. Bang, "Mid-infrared supercontinuum covering the 1.4–13.3 μm molecular fingerprint region using ultra-high NA chalcogenide step-index fibre, "Nat. Photonics **8**(11), 830–834 (2014).
9. A. P. Ongstad, G. C. Dente, M. L. Tilton, J. C. Chavez, R. Kaspi, and D. M. Gianardi, "High-brightness from unstable resonator mid-IR semiconductor lasers," J. Appl. Phys. **107**(12), 123113 (2010).
10. A. Hugi, G. Villares, S. Blaser, H. C. Liu, and J. Faist, "Mid-infrared frequency comb based on a quantum cascade laser," Nature **492**(7428), 229–233 (2012).
11. M. Lerttamrab, S. L. Chuang, R. Q. Yang, and C. J. Hill, "Linewidth enhancement factor of a type-II Interband-cascade laser," J. Appl. Phys. **96**(6), 3568–3570 (2004).
12. J. Ma, Z. Qin, G. Xie, L. Qian, and D. Tang, "Review of mid-infrared mode-locked laser sources in the 2.0 μ m-3.5 μ m spectral region," Appl. Phys. Rev. **6**(2), 021317 (2019).
13. Z. Jia, C. Yao, S. Jia, F. Wang, S. Wang, Z. Zhao, G. Qin, Y. Ohishi, and W. Qin, "4.5 W supercontinuum generation from 1017 to 3438 nm in an all-solid fluorotellurite fiber," Appl. Phys. Lett. **110**(26), 261106 (2017).
14. H. C. Guo, S. H. Tang, Z. D. Gao, Y. Q. Qin, S. N. Zhu, and Y. Y. Zhu, "Multiple-channel mid-infrared optical parametric oscillator in periodically poled MgO: $LiNbO_3$," J. Appl. Phys. **101**(11), 113112 (2007).
15. R. R. Gattass, L. Brandon Shaw, V. Q. Q. Nguyen, P. C. C. Pureza, I. D. Aggarwal, and J. S. Sanghera, "All-fiber chalcogenide-based mid-infrared supercontinuum source," Opt. Fiber Technol. **18**(5), 345–348 (2012).
16. A. Kumar, R. K. Sinha, and T. S. Saini, "Broadband Mid-Infrared Supercontinuum Spectra Spanning 2–15 μm Using As_2Se_3 Chalcogenide Glass Triangular-Core Graded-Index Photonic Crystal Fiber," J. Light. Technol. **33**(18), 3914–3920 (2015).
17. P. Jamatia, T. S. Saini, A. Kumar, and R. K. Sinha, "Design and analysis of a highly nonlinear composite photonic crystal fiber for supercontinuum generation: visible to mid-infrared," Appl. Opt. **55**(24), 6775 (2016).
18. T. S. Saini, N. P. T. Hoa, L. Xing, T. H. Tuan, T. Suzuki, and Y. Ohishi, "Chalcogenide W-type co-axial optical fiber for broadband highly coherent mid-IR supercontinuum generation," J. Appl. Phys. **124**(21), 213101 (2018).
19. Z.-X. Jia, L. Liu, C.-F. Yao, G.-S. Qin, Y. Ohishi, and W.-P. Qin, "Supercontinuum generation and lasing in thulium doped tellurite microstructured fibers," J. Appl. Phys. **115**(6), 063106 (2014).
20. N. Granzow, S. P. Stark, M. A. Schmidt, A. S. Tverjanovich, L. Wondraczek, and P. St. J. Russell, "Supercontinuum generation in chalcogenide-silica step-index fibers," Opt. Express **19**(21), 21003–21010 (2011).
21. G. Qin, X. Yan, C. Kito, M. Liao, T. Suzuki, A. Mori, and Y. Ohishi, "Highly nonlinear tellurite microstructured fibers for broadband wavelength conversion and flattened supercontinuum generation," J. Appl. Phys. **107**(4), 043108 (2010).
22. A. B. Fedotov, A. N. Naumov, A. M. Zheltikov, I. Bugar, D. Chorvat, Jr., D. Chorvat, A. P. Tarasevitch, and D. von der Linde, "Frequency-tunable supercontinuum generation in photonic-crystal fibers by femtosecond pulses of an optical parametric amplifier," J. Opt. Soc. Am. B **19**(9), 2156--2164 (2002).
23. M. R. Karim, H. Ahmad, S. Ghosh, and B. M. A. Rahman, "Design of dispersion-engineered As_2 Se_3 channel waveguide for mid-infrared region supercontinuum generation," J. Appl. Phys. **123**(21), 213101 (2018).
24. D. R. Austin, C. M. de Sterke, B. J. Eggleton, and T. G. Brown, "Dispersive wave blue-shift in supercontinuum generation," Opt. Express **14**(25), 11997–12007 (2006).
25. S. Roy, D. Ghosh, S. K. Bhadra, and G. P. Agrawal, "Role of dispersion profile in controlling emission of dispersive waves by solitons in supercontinuum generation," Opt. Commun. **283**(15), 3081–3088 (2010).
26. W. Bi, M. Liao, Y. Liu, D. Wu, X. Li, Y. Fang, G. Zhao, Y. Li, M. Wang, L. Zhang, W. Gao, and L. Hu, "Highly coherent visible dispersive wave radiation in suspended core fibers," J. Appl. Phys. **122**(15), 153106 (2017).
27. N. Akhmediev and M. Karlsson, "Cherenkov radiation emitted by solitons in optical fibers," Phys. Rev. A **51**(3), 2602–2607 (1995).
28. J. M. Dudley, S. Coen, and G. Genty, "Supercontinuum generation in photonic crystal fiber," Rev. Mod. Phys. **78**(4), 1135–1184 (2006).
29. L. Zhang, T. H. Tuan, L. Liu, W. Q. Gao, H. Kawamura, T. Suzuki, and Y. Ohishi, "Widely tunable dispersive wave generation and soliton self-frequency shift in a tellurite microstructured optical fiber pumped near the zero dispersion wavelength," J. Opt. **17**(12), 125501 (2015).
30. T. Cheng, D. Deng, X. Xue, L. Zhang, T. Suzuki, and Y. Ohishi, "Highly efficient tunable dispersive wave in a tellurite microstructured optical fiber," IEEE Photonics J. **7**(1), 1–7 (2015).
31. S. Martin-Lopez, M. Gonzalez-Herraez, P. Corredera, M. L. Hernanz, A. Carrasco, and J. A. Mendez, "Temperature effects on supercontinuum generation using a continuous-wave Raman fiber laser," Opt. Commun. **267**(1), 193–196 (2006).

32. H. Guo, S. Wang, X. Zeng, and M. Bache, "Understanding Soliton Spectral Tunneling as a Spectral Coupling Effect," IEEE Photonics Technol. Lett. **25**(19), 1928–1931 (2013).
33. M. R. Lamont, C. M. de Sterke, and B. J. Eggleton, "Dispersion engineering of highly nonlinear As_2S_3 waveguides for parametric gain and wavelength conversion," Opt. Express **15**(15), 9458–9463 (2007).
34. C. Markos, S. N. Yannopoulos, and K. Vlachos, "Chalcogenide glass layers in silica photonic crystal fibers," Opt. express **20**(14), 14814–14824 (2012).
35. S. P. Singh, V. Mishra, P. K. Datta, and S. K. Varshney, "Dispersion Engineered Capillary-Assisted Chalcogenide Optical Fiber Based Mid-IR Parametric Sources," J. Light. Technol. **33**(1), 55–61 (2015).
36. R. S. Romaniuk and J. Dorosz, "Technology of soft-glass optical fiber capillaries," in Photonics Applications in Astronomy, Communications, Industry, and High-Energy Physics Experiments 2006, R. S. Romaniuk, ed. (International Society for Optics and Photonics, 2006), pp. 634710.1-634710.9.
37. B. Temelkuran, S. D. Hart, G. Benoit, J. D. Joannopoulos, and Y. Fink, "Wavelength-scalable hollow optical fibres with large photonic bandgaps for CO2 laser transmission," Nature **420**(6916), 650-653 (2002).
38. C. Markos, "Thermo-tunable hybrid photonic crystal fiber based on solution-processed chalcogenide glass nanolayers" Sci. Rep. 6(1), 31711 (2016).
39. Y. Huang, Y. Xu and A. Yariv, "Fabrication of functional microstructured optical fibers through a selective-filling technique" Appl. Phys. Lett. 85(22), 5182–5184 (2004).
40. K. Nielsen, D. Noordegraaf, T. Sørensen, A. Bjarklev and T. P. Hansen, "Selective filling of photonic crystal fibres" J. Opt. A: Pure Appl. Opt. 7, L13–L20 (2005).
41. A. Kudlinski, R. Habert, M. Droques, G. Beck, L. Bigot, and A. Mussot, "Temperature dependence of the zero dispersion wavelength in a photonic crystal fiber," IEEE Photonics Technol. Lett. 24(6), 431–433 (2012).
42. J. C. Travers, W. Chang, J. Nold, N. Y. Joly, and P. St. J. Russell, "Ultrafast nonlinear optics in gas-filled hollow-core photonic crystal fibers [Invited]," J. Opt. Soc. Am. B **28**(12), A11–A26 (2011).
43. S. Ghosal, J. L. Ebert, and S. A. Self, "The infrared refractive indices of $CHBr_3$, CCl_4 and CS_2," Infrared Phys. **34**(6), 621–628 (1993).
44. S. P. Singh, V. Mishra, and S. K. Varshney, "Continuous-wave pumped, tunable mid-infrared fiber-optic parametric sources," J. Opt. Soc. Am. B **31**(11), 2786–2791 (2014).
45. "Cargille," https://www.cargille.com/.
46. W. S. Rodney, I. H. Malitson, and T. A. King, "Refractive index of arsenic trisulfide," J. Opt. Soc. Am. **48**(9), 633–635 (1958).
47. "Amorphous Materials Inc.," http://www.amorphousmaterials.com/products/.
48. J. M. Dudley and J. R. Taylor, Supercontinuum Generation in Optical Fibers (Cambridge University Press, 2010).
49. E. N. Tsoy and C. M. De Sterke, "Theoretical analysis of the self-frequency shift near zero-dispersion points: Soliton spectral tunneling," Phys. Rev. A - At. Mol. Opt. Phys. **76**(4), 043804 (2007).
50. T. L. Belyaeva, V. N. Serkin, C. Hernandez-Tenorio, and F. Garcia-Santibañez, "Enigmas of optical and matter-wave soliton nonlinear tunneling," J. Mod. Opt. **57**(12), 1087–1099 (2010).
51. I. B. Gonzalo, R.D. Engelsholm, M.P. Sørensen and Bang, "O. Polarization noise places severe constraints on coherence of all-normal dispersion femtosecond supercontinuum generation" Sci. Rep. 8(1), 6579 (2018).
52. A. M. Heidt, J. S. Feehan, J. H. V. Price and T. Feurer, "Limits of coherent supercontinuum generation in normal dispersion fibers" J. Opt. Soc. Am. B, 34(4), 764-775 (2017).

Hosted by OSA® The Optical Society

International Journal of Research in Engineering and Innovation (IJREI)
journal home page: http://www.ijrei.com
ISSN (Online): 2456-6934



Thermodynamic performance evaluation of double effect H_2O-Li/Br vapour absorption systems using multi cascading of vapour compression cycles for ultra-low temperature applications

R.S. Mishra

Department of Mechanical Engineering, Delhi Technological University Delhi, India

Abstract

Performance evaluation of double effect LiBr-H_2O vapour absorption systems using multi cascading of vapour compression systems using HFO-1234yf in medium temperature cycle for -50^{0}C and R-245fa in intermediate temperature cycle for -100^{0}C and R-236fa in low temperature cycle for -150^{0}C ultra low temperature applications have been carried out. It is found that overall first law efficiency (COP_Overall) for 123K evaporator temperature using R236fa is less than the overall first law efficiency (COP_Overall) for 273K evaporator temperature using 245fa. However when continuous improvement in second law (exergetic) performances which caused continuous reduction in system exergy destruction ratio. The percentage improvement in first law efficiency (COP_Overall) is found using single stage cascade vapour compression refrigeration system (VCRS) is 15.27% and using multi (two stages) cascade VCRS is 24.45% and using multi (three stages) cascade VCRS is 21.03% for all 8oC of vapour absorption evaporator temperature. However the percentage improvement in second law efficiency (exergetic efficiency) is found using single stage cascade vapour compression refrigeration system (VCRS) is 79.43% and using multi (two stages) cascade VCRS is 113.2% and using multi (three stages) cascade VCRS is 152.2% for all 10^{0}C of temperature overlapping. Similarly the percentage decrement in system exergy destruction ratio is found using single stage cascade vapour compression refrigeration system (VCRS) is 59.21 % and using multi (two stages) cascade VCRS is 72.03% and using multi (three stages) cascade VCRS is 81.96% for all 10^{0}C of temperature overlapping with 8^{0}C of evaporator temperature of VARS
©2019 ijrei.com. All rights reserved.

Keywords: vapour absorption systems, vapour compression cycles, COP, Exergy.

1. Introduction

The use of vapour absorption refrigeration system is a brilliant way towards utilizing waste heat from industrial processes. H_2O-Li/Br absorption refrigeration system and ammonia–water absorption refrigeration systems are commonly used for low temperature applications. Even though ammonia–water absorption refrigeration system is commonly used for freezing applications with temperatures lower than 0 [1-2]. A number of research work is devoted to thermodynamic, analyses of vapour absorption refrigeration systems. The performance of NH_3H_2O system has low first law efficiency. When the refrigeration temperature is lower than -25^{0}C, the thermal performance dramatically decreases. Kaushik and Arora[3-4] carried out the energy and energy analysis of single effect and series flow double effect water–lithium bromide absorption system and developed thermal computational model for parametric investigation. Their analysis involves the effect of generator, absorber and evaporator temperatures on the energetic and energetic performance. They concluded that the irreversibility is highest in the absorber in both systems as compared to other systems. In the present-day, the situation, the energy, exergy, economy, environment and safety strategies are the key issues which are practicality restrained to evaluate refrigeration cycles both having higher as well as ultra-low evaporator temperatures. Tassou et al. [5], suggested that the refrigeration is a necessary part of the food chain and to slow down the physical, chemical and microbiological activities that cause deterioration in food, the food is frozen between18 to35°C. Generally, technologies of mechanical refrigeration are

Corresponding author: R.S. Mishra
Email Address: hod.mechanical.rsm@dtu.ac.in
http://doi.org/10.36037/IJREI.2019.3611

invariably employed in these processes which either contribute electricity consumption and environmental impact or low performance. Tassouet al. [6], suggested that the refrigeration is a essential part of the food chain and to slow down the physical, chemical and microbiological activities that cause deterioration in food, the food is frozen between16°C. to35°C.

1.1. Cascade vapour refrigeration systems

Cabello et al. [7], substituted R134a, which is a high GWP refrigerant to the low GWP refrigerant R152a in cascade refrigeration plants. The drop in replacement was technically and enthusiastically feasible. The GWP and ODP rating of R1234yf are 4 and 0. Messineo [8], analyzed a two stage cascade refrigeration system using carbon dioxide (CO_2) in low temperature circuit and ammonia (NH_3) in high temperature section. He reported that CO_2-NH_3cascade refrigeration system was a motivating alternative to R404A for low evaporation temperatures (30°C to 50°C. R.S.Mishra [9] observed that two stage cascade refrigeration system using R1234ze in high temperature circuit and R1234yf in the low temperature evaporator (up to -50^{0}C) cascade system, can replace R134a. The numerical computations have been carried out for three stage proposed system (system-1: using R1234ze in high temperature circuit and R1234yf in intermediate temperature circuit and fifteen ecofriendly refrigerants in low temperature circuit). To validate the results obtained by developed model, proposed three stage cascade refrigeration system (system-1) and three stage conventional cascade refrigeration system (system-2) have been compared in terms of their thermal first and second law performances and power consumption by system and its compressors. The proposed three stage cascade refrigeration system (System-1) using HFO refrigerants up to -100^{0}C gives similar thermodynamic performances and 2% less power consumption than conventional three stage cascade refrigeration system (system-2). In case of three stage cascade refrigeration using HFO-1234ze in the high temperature circuit and HFO-1234yf in intermediate temperature circuit two stage refrigeration cascade system circuit andR245fa in low temperature circuit gives better thermal performances. The first and second law thermal performance parameters using HFO-245fa in low temperature circuit are around 0.75% higher than that of HFC-134a.

1.2 Vapour absorption refrigeration systems

Kairouani and Nehdi [10], analyzed NH_3-H_2O vapor absorption cycle powered by geothermal energy-R717, R22 and R134a vapor compression cascade cycle and combined cycle. They concluded that the COP of cascade cycle was5.5 and the COP value was 37–54% higher than that of vapor com-pression refrigeration cycle. Gomri [11,14] carried out comparative thermodynamic analysis between single effect and double effect absorption refrigeration systems and developed the computer program using thermodynamic properties based on energy balance equations and found that for each condenser and evaporator temperature, there is an optimum generator temperature where change in energy of single effect and double effect absorption refrigeration system is minimum. They also found that the COP of double effect system is approximately twice the COP of single effect system but there is marginal difference between the energetic efficiency of the system Rogdakis and Antonopoulos [12] studied a NH_3/H_2O absorption refrigeration system driven by waste heat and predicted the theoretical COP below 0.40 when the lowest temperature is in the range of -64^{0}C to -30^{0}C.

Kilic and Kaynakli [13] carried out first and second law thermodynamic analysis to analyze the performance of a single stage water lithium bromide absorption refrigeration system by varying some working parameters and developed a mathematical model based on energy method and found that the performance of the ARS increases with increasing generator and evaporator temperatures but decreases with increasing condenser and absorber temperatures. Also concluded that the highest energy loss occurs in generator regardless of operating conditions and therefore it is most important component of the system. Garimella and Brown [15] developed a novel cascaded absorption–compression system that coupled a single-effect $LiBr/H_2O$ absorption cycle and a subcritical CO_2 vapor–compression cycle to generate low-temperature refrigerant (-40 °C).

1.3 Vapour absorption compression refrigeration systems

The utility of vapour compression-absorption systems mostly used for low temperature applications such as cryogenic applications. The term cryogenic is derived from the Greek work “Kryos” which means cold or frost. Cryogenic technology frequently applied to very low temperature refrigeration applications such as in biomedical, semen preservation, and pharmacological application as well as liquefaction of gases. Vapour compression systems with single compressor for different refrigerants are limited to an evaporator temperature of -40ºC. Therefore, multistage stage compression refrigeration system for low temperature applications. The main drawback of two stage compression refrigeration system is employed when low evaporator temperatures up to –60ºC and while as, three stages compression system is used up to evaporator temperature of -68ºC. Therefore, there is an urgent need for cascade refrigeration system. The cascade system was first used by Pictet in 1877 for liquefaction of oxygen. For low temperature cascade system uses R12 refrigerant was used in the high temperature cycle and R22 was used in intermediate temperature cycle and a refrigerant such as R13 with low boiling temperature used in low temperature cycle. S.B. Riffat N. Shankland [16] described the integration of different types of absorption systems with vapour-compression systems. The performances of the single-effect and double-effect series and the double-effect parallel continuous absorption systems and their integration with vapour-compression systems have been carried out. Yi Chena,et.al. [17], proposed a new absorption–compression refrigeration system to produce cooling energy at -30^{0}C to -40^{0}C and showed that the coefficient of performance of 0.277, which was approximately 50% higher than

that of a conventional two-stage absorption refrigeration system. Fernández–Seara et al. [18] studied a cascade refrigeration system with a CO_2 compression vapour refrigeration system and an NH_3/H_2O absorption system at an evaporation temperature of -45 °C and found its first law efficiency in terms of COP. Kaushik and Arora [3] had analyzed half; single and double effect series and parallel flow vapor absorption cycles and defined that the generator temperature and COP for half, single and double effect series flow refrigeration cycles and found the COP of double effect system was about twice that of single effect. Mishra[19] proposed four cascaded half effect, single effect, double effect and triple effect Lithium/Bromide vapour absorption–compression refrigeration systems using fifteen ecofriendly refrigerants such as hydrocarbons, HFC and HFO refrigerants and natural refrigerants to produce cooling capacity at -30^0C. The comparison of four cascaded systems were also carried out at -55^0C using HFC refrigerants with R717 refrigerant. It is found that cascaded vapour compression absorption systems significantly improve first and second law performances as compared to simple vapour absorption refrigeration system. Azhar and Siddiqui [20-21] analyzed gas operated H_2O-LiBr single to triple effect vapor absorption refrigeration cycles and a triple effect vapour absorption refrigeration cycle separately and used liquefied petroleum gas (LPG)and compressed natural gas (CNG) as sources of energy. They concluded that the COP of the triple effect cycle was 132% higher than the single effect. Thus the triple effect series flow VAR cycle is per-forming best among all. However, it requires input heat energy at the higher temperature range 175 to 200°C. They added that the maximum COP of triple effect vapor absorption refrigeration cycle was 2.16. R.S.Mishra [22] presented optimum thermodynamic performances of three cascade vapour compression refrigeration systems. The numerical thermal model have been developed for two stages cascade refrigeration systems and thermodynamic performances in terms of and first law efficiency, second law efficiency system exergy destruction ratio, first law efficiency of lower temperature and high temperature circuit have been computed. The effect of low temperature evaporator on the system first and second law performances and system exergy destruction ratio it was found that as low temperature evaporator temperature is decreasing , the first law and second law efficiencies are increasing and exergy destruction ratio is decreasing . from the developed thermal model, the optimum performance parameters in terms of the optimum temperature of high temperature evaporator for system-1(using HFO1234ze in HTC and HFO1234yf in LTC) was found between -6^0C to -7^0C, for sytem-2 (using HFO1234ze in HTC and HFC134a in LTC) : was found between -1^oC to $-2\ ^o$C and for system-3using HFO-1234yf in HTC and HFC-134a in LTC was found between 1^0C to 2^0C of temperature and found that the volumetric refrigerating capacity of HFO R1234ze is below that of R134a and Its boiling point is also higher than that of R134a in the high temperature circuit of cascade refrigeration system in the range of HTC Circuit from 60^{o}C to -20^{o}C is suitable for replacing R134a and also concluded that the HFO R1234yf is suitable for replacing R134a. In the low temperature circuit of cascade refrigeration system in the range of low temperature circuit (LTC) from -20^{o}C to -50^{o}C and found that by increasing evaporator temperature overall first law efficiency in terms of COP of the system is increases. V. Jain et al.[23]carried out thermodynamic analysis of vapor compression (R22, R410A, R407C andR134A)-single effect absorption (LiBr-H_2O) cascade refrigeration system and found that the COP of vapour compression section of CVCAS enhanced by 155% and electricity consumption reduced by 61% in comparison to a conventional VCRS. Moreover, evaporator and condenser changed irreversibility of the system significantly. Pratihar et al. [24] carried out simulation of a 400 kW NH_3-H_2O absorption-compression refrigeration system for summer air conditioning and concluded that the COP increased by 16% with increase in relative solution heat exchanger area from10 to 30% when compared to conventional R22 vapor compression chiller. R.S.Mishra [25], investigated the performance of above system along with variation of performance parameters and its effect on system performances in terms of exergetic efficiency, coefficient of performance along with exergy destruction ratio based on exergy of product. We proposed cascaded half effect, single effect, double effect and triple effect Lithium/Bromide vapour absorption–compression refrigeration systems using fifteen ecofriendly refrigerants such as hydrocarbons, HFC and HFO refrigerants and natural refrigerants to produce cooling capacity at -30 °C R.S. Mishra [26] analyzed half, single, double and triple effect vapour absorption refrigeration systems and also compared three cascaded vapour compression systems cascaded with evaporator of LiBr-H_2O vapour absorption refrigeration system cascaded by condenser of single vapour compression refrigeration system using ecofriendly refrigerants (i.e. R1234yf, R134a, R-32, R507a, R227ea, R236fa, R245fa , R717) and energy and exergy analysis of all three systems were carried out because exergy (second law) analysis used to facilitates the identification of the system components with high exergy loss compared the performance parameters with three cascaded vapour absorption-single stage vapour compression refrigeration system and it was observed that 122% first law efficiency enhancement using triple effect VARS cascaded with VCRS and 79.45% enhancement in second law efficiency using triple effect VARS cascaded with VCRS. Similarly exergy reduction is 56.60% using triple effect VARS cascaded with single stage VCRS and 25.9% reduction using double effect VARS cascaded with single stage VCRS An Similarly performance parameters have been compared with three cascade vapour absorption-compression refrigeration system and it was observed that 22.87% first law efficiency enhancement using triple effect VARS cascaded with VCRS and 46.3% enhancement in second law efficiency using triple effect VARS cascaded with VCRS as compared with double effect vapour absorption refrigeration cascaded with single stage vapour compression refrigeration system. Similarly exergy reduction is 41.4% using triple effect VARS cascaded with single stage VCRS as compared to double effect VARS cascaded with single stage VCRS. Generally, technologies of mechanical refrigeration are always employed in these processes which either contribute electricity consumption and environmental impact or lower performance. These processes

include vapor compression refrigeration, half, single, double and triple effect vapor absorption refrigeration systems. Ayala et al. [10] analyzed Ammonia/Lithium Nitrate vapour absorption and Ammonia mechanical vapor compression combined refrigeration plant. They deduced that the over-all efficiency of the combined refrigeration plant was higher than that of individual compression or absorption refrigeration cycle and increased by 10%. A large number of studies are available in the literature on compression-absorption (combined) or cascade refrigeration cycles. The considered studies fall under two categories viz. single stage and double stage cycles. The first configuration is the combination of single effect VAR cycle coupled to a VCR cycle and the second configuration comprises of a double effect VAR cycle coupled to a VCR cycle. Mishra [28] found that the thermodynamic performances in the case of cascaded half effect vapour absorption refrigeration system coupled with vapour compression cycle is improved by 44.65% increment of first law efficiency (i.e. over all COP), 172.87% increment of second law efficiency (i.e. exergetic efficiency) of the half effect vapour absorption refrigeration cascaded with vapour compression cycle using HFC-134a, 42.87% enhancement in first law efficiency (COP) of 142.73% increment of second law efficiency using HFO -1234yf for -50ºC of evaporator temperature of VCRS. Similarly 72.02% reduction in exergy destruction ratio based on exergy of output of the half effect vapour absorption refrigeration cascaded with vapour compression cycle using HFC-134a and 70.44% reduction in exergy destruction ratio using HFO-1234yf ecofriendly refrigerant for -50^{0}C of evaporator temperature of VCRS. The performances of single effect cascaded vapour absorption refrigeration system coupled with vapour compression cycle significantly higher than cascaded half effect vapour absorption refrigeration coupled with vapour compression cycle. The comparison of four cascaded systems were also carried out at -55^{0}C using HFC refrigerants with R717 refrigerant. It is found that cascaded vapour compression absorption systems significantly improve first and second law performances as compared to simple vapour absorption refrigeration systems. M. Dixit et al [29] did thermodynamic and thermo-economic analyses of two stage hybrid absorption compression refrigeration system having LiBr-H_2O as working fluid and stated that hybrid system could be operated on low generator temperature and performed better than the two stage absorption refrigeration system .The COP and exergetic efficiency of optimized hybrid system were 0.43 and 11.68% respectively and the reduction in annual cost of operation was 5.2%. The solar assisted half effect vapour absorption refrigeration system cascaded with vapour compression refrigeration system using ecofriendly refrigerants have not been studied in detail. Cimsit and Ozturk [30] performed analysis of compression-absorption cascade refrigeration systems by using H_2O-LiBr and NH_3-H_2O pairs in vapour absorption refrigeration system and R134a, R410a and NH_3in vapor compression refrigeration system and predicted that the electrical energy consumption in cascade refrigeration cycle was 48–50% less than that of conventional vapour compression refrigeration cycle and the COP of the cascade refrigeration system enhanced by 33%. The CO_2/NH_3cascade cycle was safer than the CO_2/C3H8with no significance difference in economic and exergetic efficiency. Since the water is a natural refrigerant, it can be used safely with H_2OLi/Br in the high temperature circuit of cascade cycle. However, the safety group of R1234yf is A2L. Bhattacharyya et al. [31] evaluated a CO2-Propane cascade system for simultaneous refrigeration and heat pump system and concluded that the approach and overlap temperatures must be minimum possible for the optimization of system performance and found that the optimum value of intermediate temperature of cascade system decreases with decrease in approach temperature and with increase in overlap temperature. Mafi et al. [32] had carried out exergy analysis of multistage cascade low temperature cascade refrigeration system and found that the exergetic efficiency of the system was 30.88%. Chinnappaet al. [33] studied R22 vapour compression-NH_3-H_2O absorption cascade refrigeration by using solar energy and determined that the cascaded system saved electrical energy than that of vapour compression system. Additionally the use of HFO refrigerant having zero potential (ODP) and low global warming potential (GWP) i.e. R1234yf is strongly recommended by Regulation (EU) No 517/2014 [11] to reduce mitigating climate change risk, environmental impact and deterioration. Therefore refrigerant R1234yf could be a choice for vapour compression refrigeration system. Garimella et. al. [34] proposed absorption/vapour compression cascade refrigeration system driven by waste heat used in naval ship and determined that the electricity consumption reduced by 30% than that of conventional vapour compression refrigeration system. Sun and Guo [35] carried out experiments on prototype of combined vapour compression-absorption refrigeration system driven by a gas engine and found that the primary energy utilization efficiency of combined system improved by the utilization of waste heat of gas engine in absorption refrigeration cycle. Similarly, Alvarez et al. [36] analyzed an alkali-nitrate triple-effect (single effect lithium, potassium, sodium nitrate cycle coupled to a double effect H_2O/LiBr cycle) absorption cycle for high temperature heat source. The alkali-titrate triple effect cycle was feasible efficient with slight higher COP than H_2O/LiBr triple effect cycle at generator temperature over 180°C. Wang et al. [37] studied solar assisted cascaded refrigeration system and found that the power consumption was reduced by 50% and the COP of the system reached up to 6.1. Colorado and Rivera [38] compared the thermal performance of a conventional vapor compression and compression-absorption single-stage and double-stage refrigeration systems. They recognized that in the current situation, the energy, exergy, economy, and environment and safety strategies are the main issues which are being considered to evaluate refrigeration cycles both having higher as well as lower evaporator temperatures. The low temperatures approaching 0K, air conditioning and its applications such as freeze drying, pharmaceuticals, chemical and petroleum industry used cascade refrigeration cycles and also acknowledged that the electrical energy consumption in compression-absorption single-stage and double stage refrigeration system was 45% lower than that of vapour compression refrigeration cycle and the COP of

double stage refrigeration system was 50% higher than that of single stage compression-absorption refrigeration system. W. Han et al. [39] proposed a hybrid absorption-compression refrigerator powered by waste heat. They declared that the system COP was 41.9% higher than that of a simple NH_3absorption refrigerator and had confirmed performance improvement by exergy analysis and found that the COP of compression-absorption combined cycle was higher than VCR or vapor absorption refrigeration (VAR) cycle.

1.4 Use of Integration system for low temperature applications

Although the ultralow temperatures for cryogenics is approaching 0 K, and its applications such as freeze drying, pharmaceuticals, chemical and petroleum industry use cascade refrigeration cycles [40-41]. R.S. Mishra [42] develop an integrated solar refrigeration system where waste heat from different energy resources assists a combined vapour absorption compression system, and to analyze feasibility & practicality of that system of thermodynamically for improving its COP and exergetic efficiency by reduction of irreversibilities in terms of exergy destruction /losses occurred in the system components. The combined thermodynamic first law efficiency in terms of coefficient of performance ($COP_{_Overall}$), second law efficiency in terms of exergetic efficiency and exergy destruction ratio based on exergy of product of a combined vapour absorption-compression system working with each of the following refrigerants in the cascaded vapour compression cycle R1234yf, R227ea, R236fa, R245fa, R143a,R134a, R32, R507 operating at - 223 K evaporator temperature with temperature overlapping (Approach means the difference between cascaded condenser temperature of vapour compression cycle and evaporator temperature of vapour absorption refrigeration cycle working at 13.5 bar of highest generator pressure and 1.75 bar as lowest evaporator pressure have been presented and it is found thatR141b and R245fa gives better performances.

Although the performance of vapor compression refrigeration cycle succeeds the others yet its electricity consumption is higher. Generally, the vapour compression refrigeration cycle and its configurations viz. double stage, triple stage or multistage cascade are employed for the production of low evaporation temperature at very high cooling power.

Most of the research studies considered till date emphasize on VCR and VAR cycles (single and double effect) and compression-absorption (combined) or cascade cycles. Though, exhaustive research has been carried out on cascade cycles, very less consideration has been given to explore the thermodynamic performance of single effect VAR cycle coupled with multi cascaded VCRS. Additionally, none of the research work is available on thermodynamic performance analysis of compression-absorption single effect multi cascaded three stages refrigeration system. Accordingly, in the present communication, the thermodynamic and exergetic performance analysis of absorption compression (single effect H_2O-Li/Br) cascade refrigeration system has been carried out. The analysis is performed considering H_2O/LiBr in absorption system and R1234yf in medium temperature VCR system. R-245fa in intermediate temperature VCR system along with R-236fa in intermediate temperature VCR system. The effect of medium temperature evaporator temperature, intermediate temperature of evaporator using R1234yf, intermediate temperature evaporator temperature, intermediate temperature of evaporator using R245fa and low temperature evaporator temperature, intermediate temperature of evaporator using R236fa/hydrocarbons (i.e. R290, R600a) and ethylene temperature overlapping in each cascade condenser, condenser , absorber temperatures generator and evaporator temperatures of single effect H_2O-Li/Br vapour absorption system , have been investigated on various performance parameters viz. COP, exergetic efficiency, total exergy destruction and exergy destruction ratio (EDR).Additionally, exergy destruction and EDR of system components have also been computed.

2. System Description

Integrated absorption-compression multi cascaded refrigeration system used for ultra-low temperature is considered in this investigation is comprises of triple effect H_2O-Li/Br refrigeration system is in the high temperature section having Lithium Bromide (Li/Br) as an absorbent and water (H_2O) as a refrigerant. The evaporator of vapour system (VARS) is coupled with the condenser of medium VCRS using HFO-1234yf as a refrigerant up to a Temperature of 223K. vapour compression refrigeration system (VCRS) is in the intermediate temperature section in which intermediate temperature is achieved using 245fa as a refrigerant up to a Temperature of 173K *(i.e.* -100ºC) and vapour compression refrigeration system (VCRS) is in the intermediate temperature section in which intermediate temperature is achieved using 236fa as a refrigerant up to a temperature of 123K.

3. Results and Discussion

Following input variables have been chosen for validation of model.

- Evaporator Temperature of triple effect Li/Br vapour absorption refrigeration system= 8°C.
- Generator temperature=180°C.
- Evaporator Temperature of vapour compression refrigeration system in the medium temperature circuit = -50°C
- Evaporator Temperature of vapour compression refrigeration system in the intermediate temperature circuit = -95°C
- Evaporator Temperature of vapour compression refrigeration system in the low temperature circuit = --150°C.
- Temperature overlapping in the vapour absorption refrigeration evaporator temperature and vapour

- compression refrigeration condenser temperature using R1234yf is known as overlaping$_{_MTC}$ (approach$_{_MTC}$)= 10
- Temperature overlapping in the vapour compression refrigeration evaporator temperature using R-1234yf and vapour compression refrigeration condenser temperature using R2345f is known as over-lapping$_{_ITC}$ (approach$_{_ITC}$) =10.
- Temperature overlapping in the vapour compression refrigeration evaporator temperature using R-123fa and vapour compression refrigeration condenser temperature using 245fa is known as overlapping$_{_MTC}$ (Approach$_{_LTC}$)=10
- Refrigerating Capacity=35.167 "kW"
- Condenser temperature =35°C,
- Absorber Temperature=35°C,
- MTC Compressor Efficiency=0.80,
- ITC Compressor Efficiency=0.80,
- LTC Compressor Efficiency=0.80.

Thermal performance of triple effect vapour absorption refrigeration system using H_2O-Li/Br was computed by developed model is given below.

- First law efficiency of vapour absorption refrigeration system is (COP_VARS) =1.479,
- The second law efficiency of vapour absorption refrigeration system is the exergetic_efficiency= 0.2614.
- The exergy destruction ratio based on output(exergy of product) is EDR$_{_Output}$= 2.825
- The exergy destruction ratio based on input (exergy of exergy of fuel) is EDR$_{_Input}$= 0.7386.

3.1 Effect of ecofriendly refrigerants in ultra-low cascaded vapour compression cycle on total thermodynamic performances of three cascaded cycles in integrated system

Table-1(a) to Table-1(c) show the comparison between hydro carbons and ethylene with ecofriendly refrigerant R236fa in terms of thermodynamic performances (First law performances (COP$_{_Overall}$), second law performance (Exergetic efficiencies) and system exergy destruction Ratios of three cascaded vapour compression refrigeration system coupled with triple effect vapour absorption Refrigeration H_2OLi/Br system using HFO-1234yf ecofriendly refrigerant in medium temperature cycle and R245fa in intermediate temperature cycle and following refrigerants in the ultra-low temperature cycle and it is found that the first and second law performances of cascaded vapour compression vapour triple effect absorption system is higher by using HFO-1234yf ecofriendly refrigerant in medium temperature circuit and R245fa in intermediate temperature circuit and following ecofriendly refrigerants in the low temperature circuit using R600a is maximum and lowest when using ethylene.

Table-1(a): Effect of ecofriendly refrigerants in ultra-low temperature cycle on thermodynamic performances (First law performance (COP$_{_Overall}$), of vapour compression refrigeration system coupled with double *effect vapour absorption refrigeration H_2O-Li/Br system using 1234yf ecofriendly refrigerant in medium temperature circuit and R245fa in intermediate temperature circuit and R236fa in the low temperature*

Ecofriendly refrigerants in ultra lowvapour compression refrigeration temperature cycle	Over all first law efficiency (COP$_{_Overall}$) of system using to low evaporator temperature of 123K using R236fa	Over all first law efficiency (COP$_{_Overall}$) of system using to low evaporator temperature of 123K using R245fa	Over all first law efficiency (COP$_{_Overall}$) of system using to low evaporator temperature of 223K using R1234yf
R236fa	1.459	1.490	1.385
R404a	1.453	1.490	1.385
R290	1.454	1.490	1.385
R600a	1.459	1.490	1.385
Ethylene	1.450	1.490	1.385

Table-1(b): Effect of ecofriendly refrigerants in ultra-low temperature cycle on, second law performance (exergetic efficiency) and system exergy destruction ratio of vapour compression refrigeration system coupled with double effect vapour absorption refrigeration H_2O-Li/Br system using 1234yf ecofriendly refrigerant in medium temperature circuit and R245fa in intermediate temperature circuit and R236fa in the low temperature

Ecofriendly refrigerants in ultra-low vapour compression refrigeration temperature cycle	Over all second law efficiency (exergetic Efficiency) of system using to low evaporator temperature of 123K using R236fa	Over all second law efficiency (exergetic Efficiency) of system using to intermediate evaporator temperature of 173K using R245fa	Over all second law efficiency (exergetic Efficiency) of system using to intermediate evaporator temperature of 223K using HFO-1234yf
R236fa	0.6642	0.5606	0.4666
R404a	0.6556	0.5606	0.4666
R290	0.6579	0.5606	0.4666
R600a	0.6640	0.5606	0.4666
Ethylene	0.6514	0.5606	0.4666

Table-1(c): Effect of ecofriendly refrigerants in ultra-low temperature cycle on system exergy destruction ratio with absorber temperature of vapour compression refrigeration system coupled with double effect vapour absorption refrigeration H_2O- Li/Br system using 1234yf ecofriendly refrigerant in medium temperature circuit and R245fa in intermediate temperature circuit and R236fa in the low temperature circuit

Ecofriendly refrigerants in ultra lowvapour compression refrigeration temperature cycle	Over all exergy destruction ratio (EDR) of system using to low evaporator temperature of 123K using R236fa	Over all exergy destruction ratio (EDR) of system using to intermediate evaporator temperature of 173K using R245fa	Over all exergy destruction ratio (EDR) of system using to intermediate evaporator temperature of 223K using HFO-1234yf
R236fa	0.5056	0.7839	1.143
R404a	0.5254	0.7839	1.143
R290	0.520	0.7839	1.143
R600a	0.5061	0.7839	1.143
Ethylene	0.5351	0.7839	1.143

3.2 Effect of ecofriendly refrigerants in ultra-low cascaded vapour compression cycle on percentage improvement in the total thermodynamic performances of three cascaded cycles in integrated system

Table-2(a) to Table-2(c) show the comparison between hydro carbons and ethylene with ecofriendly refrigerant R236fa in terms of thermodynamic performances (First law performances ($COP_{_Overall}$), second law performance (Exergetic efficiencies) and system exergy destruction Ratios of three cascaded vapour compression refrigeration system coupled with double effect vapour absorption Refrigeration H_2OLi/Br system using HFO-1234yf ecofriendly refrigerant in medium temperature cycle and R245fa in intermediate temperature cycle and following refrigerants in the ultra-low temperature cycle and it is found that the first and second law performances of cascaded vapour compression vapour double effect absorption system is higher by using HFO-1234yf ecofriendly refrigerant in medium temperature circuit and R245fa in intermediate temperature circuit and following ecofriendly refrigerants in the low temperature circuit using R600a is maximum and lowest when using ethylene.

Table-2(a): Effect of ecofriendly refrigerants in ultra-low temperature cycle on thermodynamic performances (First law performance ($COP_{_Overall}$), of vapour compression refrigeration system coupled with double effect vapour absorption refrigeration LiBr system using 1234yf ecofriendly refrigerant in medium temperature circuit and R245fa in intermediate temperature circuit and R236fa in the low temperature circuit

Ecofriendly refrigerants in ultra-low vapour compression refrigeration temperature cycle	Over all (%) improvement in first law efficiency ($COP_{_Overall}$) of system using to low evaporator temperature of 123K using R236fa (%)	Over all (%) improvement in first law efficiency ($COP_{_Overall}$) of system using to intermediate evaporator temperature of 173K using R245fa (%)	Over all (%) improvement in first law efficiency ($COP_{_Overall}$) of system using to intermediate evaporator temperature of 223K using HFO-1234yf (%)
R236fa	21.45	24.03	15.27
R404a	20.94	24.03	15.27
R290	21.08	24.03	15.27
R600a	21.44	24.03	15.27
Ethylene	20.70	24.03	15.27

Table-2(b): Effect of ecofriendly refrigerants in ultra-low temperature cycle on, second law performance (exergetic efficiency) and system exergy destruction ratio of vapour compression refrigeration system coupled with double effect vapour absorption refrigeration H_2O-Li/Br system using 1234yf ecofriendly refrigerant in medium temperature circuit and R245fa in intermediate temperature circuit and R236fa in the low temperature circuit

Ecofriendly refrigerants in ultra-low vapour compression refrigeration temperature cycle	Over all (%) improvement in second law efficiency (exergetic Efficiency) of system using to low evaporator temperature of 123K using R236fa	Over all (%) improvement in second law efficiency (exergetic Efficiency) of system using to intermediate evaporator temperature of 173K using R245fa	Over all (%) improvement in second law efficiency (exergetic Efficiency) of system using to intermediate evap temp of 223K HFO-1234yf
R236fa	152.6	113.2	77.43
R404a	149.3	113.2	77.43
R290	150.3	113.2	77.43
R600a	152.5	113.2	77.43
Ethylene	147.7	113.2	77.43

Table-2(c): Effect of ecofriendly refrigerants in ultra-low temperature cycle on system exergy destruction ratio with absorber temperature of vapour compression refrigeration system coupled with double effect vapour absorption refrigeration H_2O- Li/Br system using 1234yf ecofriendly refrigerant in medium temperature circuit and R245fa in intermediate temperature circuit and R236fa in the low temperature circuit

Ecofriendly refrigerants in ultra-low vapour compression refrigeration temperature cycle	Over all (%) reduction in exergy destruction ratio (EDR) of system using to low evaporator temperature of 123K using R236fa (%)	Over all (%) reduction in exergy destruction ratio (EDR) of system using to intermediate evaporator temperature of 173K using R245fa (%)	Over all (%) reduction in exergy destruction ratio (EDR) of system using to intermediate evaporator temperature of 223K Using HFO-1234yf (%)
R236fa	81.96	72.03	59.21
R404a	81.25	72.03	59.21
R290	81.45	72.03	59.21
R600a	81.94	72.03	59.21
Ethylene	80.91	72.03	59.21

3.3 Effect of ecofriendly refrigerants in intermediate temperature cycle of cascaded vapour compression cycle on total thermodynamic performances of three cascaded cycles in integrated system

Table-3(a) to Table-3(c) show the comparison between with ecofriendly refrigerants in terms of thermodynamic performances (first law performances ($COP_{_Overall}$), second law performance (exergetic efficiencies) and system exergy destruction ratios of three cascaded vapour compression refrigeration system coupled with double effect vapour absorption refrigeration H_2O-Li/Br System using HFO-1234yf ecofriendly refrigerant in medium temperature cycle and following ecofriendly refrigerants in intermediate temperature cycle and R236fa refrigerant in the ultra-low temperature cycle and it is found that the first and second law performances of cascaded vapour compression vapour single effect absorption system is higher by using HFO-1234yf ecofriendly refrigerant in medium temperature circuit and R236fa in ultra-low temperature circuit and found that by using R32 is slightly lower than R245fa and higher than HFC-134a, R404a , R410a, R407c and R507a.

Table-3(a): Effect of ecofriendly refrigerants in intermediate temperature cycle on Thermodynamic performances (First law Performance (COP_overall), vapour compression refrigeration system coupled with double effect vapour absorption refrigeration H_2O Li/Br system using 1234yf ecofriendly refrigerant in medium temperature circuit and R245fa in intermediate temperature circuit and R236fa in the low temperature

Ecofriendly refrigerants in Intermediate ITC circuit	Over all first law efficiency ($COP_{_Overall}$) of system using to low evaporator temperature of 123K using R236fa	Over all first law efficiency ($COP_{_Overall}$) of system using to low evaporator temperature of 123K using R245fa	Over all first law efficiency ($COP_{_Overall}$) of system using to low evaporator temperature of 223K using R1234yf
R-245fa	1.459	1.490	1.385
R134a	1.456	1.487	1.385
R 410a	1.454	1.485	1.385
R32	1.436	1.467	1.385
R 143a	1.454	1.485	1.385
R-507a	1.453	1.484	1.385
R227ea	1.449	1.480	1.385
R290	1.458	1.489	1.385
R600a	1.460	1.491	1.385
Ethylene	1.430	1.461	1.385
R123	1.459	1.490	1.385
R125	1.451	1.482	1.385
R407c	1.391	1.421	1.385
R404a	1.447	1.477	1.385

Table-3(b): Effect of ecofriendly refrigerants in intermediate temperature cycle on over all second law efficiencies (exergetic efficiencies) of vapour compression refrigeration system coupled with double effect vapour absorption refrigeration H_2O Li/Br system using 1234yf ecofriendly refrigerant in medium temperature circuit and following ecofriendly refrigerants in intermediate temperature circuit and R236fa in the low temperature circuit

Ecofriendly refrigerants in intermediate ITC circuit	Over all second law efficiency (exergetic Efficiency) of system using to low evaporator temperature of 123K using R236fa	Over all second law efficiency (exergetic efficiency) of system using to intermediate evaporator temperature of 173K using R245fa	Over all second law law efficiency (exergetic Efficiency) of system using to intermediate evaporator temperature of 223K using HFO-1234yf
R-245fa	0.6642	0.5606	0.4666
R134a	0.6627	0.5583	0.4666
R 410a	0.6812	0.5581	0.4666
R32	0.6511	0.5411	0.4666
R 143a	0.6615	0.5566	0.4666
R-507a	0.6611	0.5560	0.4666
R227ea	0.6585	0.5521	0.4666
R290	0.6638	0.560	0.4666
R600a	0.6649	0.5617	0.4666
Ethylene	0.6475	0.5356	0.4666
R123	0.6641	0.5604	0.4666
R125	0.6598	0.5541	0.4666
R407c	0.6256	0.5025	0.4666
R404a	0.6571	0.550	0.4666

Table-3(c): Effect of ecofriendly refrigerants in intermediate temperature cycle on system exergy destruction ratios of vapour compression refrigeration system coupled with double effect vapour absorption refrigeration H_2O Li/Br system using 1234yf ecofriendly refrigerant in medium temperature circuit and following ecofriendly refrigerants in intermediate temperature circuit and R236fa in the low temperature circuit

Ecofriendly refrigerants in Intermediate ITC circuit	Over all exergy destruction ratio (EDR) of system using to low evaporator temperature of 123K using R236fa	Over all exergy destruction ratio (EDR) of system using to intermediate evaporator temperature of 173K using R245fa	Over all exergy destruction ratio (EDR) of system using to intermediate evaporator temperature of 223K using HFO-1234yf
R-245fa	0.5056	0.7839	1.143
R134a	0.5090	0.7910	1.143
R 410a	05124	0.7981	1.143
R32	0.5358	0.8479	1.143
R 143a	0.5117	0.7966	1.143
R-507a	0.5127	0.7981	1.143
R227ea	0.5187	0.8114	1.143
R290	0.5064	0.7856	1.143
R600a	0.5039	0.7804	1.143
Ethylene	0.5445	0.867	1.143
R123	0.5058	0.7844	1.143
R125	0.5155	0.8047	1.143
R407c	0.5985	0.9901	1.143
R404a	0.5219	0.8182	1.143

3.4 Effect of ecofriendly refrigerants in intermediate temperature cycle on percentage improvements in total thermodynamic performances of three cascaded cycles in integrated system

Table-4(a) to Table-4(c) show the comparison between with ecofriendly refrigerants in terms of percentage improvement in the thermodynamic performances (first law performances ($COP_{_Overall}$), second law performance (exergetic efficiencies) and system exergy destruction Ratios of three cascaded vapour compression refrigeration system coupled with triple effect vapour absorption Refrigeration H_2O-Li/Br System using HFO-1234yf ecofriendly refrigerant in medium temperature cycle and following ecofriendly refrigerants in intermediate temperature cycle and R236fa refrigerant in the ultra-low temperature cycle and it is found that the first and second law performances of cascaded vapour compression -vapour single effect absorption system is higher by using HFO-1234yf ecofriendly refrigerant in medium temperature circuit and R236fa in ultra-low temperature circuit and found that by using R32 is slightly lower than R245fa and higher than HFC-134a, R404a , R410a, R407c and R507.

Table-4(a): Effect of ecofriendly refrigerants in intermediate temperature cycle on Thermodynamic performances (First law Performance (COP_overall), vapour compression refrigeration system coupled with double effect vapour absorption refrigeration H_2O Li/Br system using 1234yf ecofriendly refrigerant in medium temperature circuit and R245fa in intermediate temperature circuit and R236fa in the low temperature

Ecofriendly refrigerants in Intermediate ITC circuit	Over all (%) improvement in first law efficiency ($COP_{Overall}$) of system using to low evaporator temperature of 123K using R236fa (%)	Over all (%) improvement in first law efficiency ($COP_{Overall}$) of system using to intermediate evaporator temperature of 173K using R245fa (%)	Over all (%) improvement in first law efficiency ($COP_{Overall}$) of system using to intermediate evaporator temperature of 223K using HFO-1234yf (%)
R-245fa	21.45	24.03	15.27
R134a	21.24	23.81	15.27
R 410a	21.03	23.6	15.27
R32	18.79	22.14	15.27
R 143a	21.07	23.64	15.27
R-507a	21.01	23.58	15.27
R227ea	20.63	23.20	15.27
R290	21.4	23.98	15.27
R600a	2156	24.13	15.27
Ethylene	19.04	21.6	15.27
R123	21.44	24.01	15.27
R125	20.83	23.1	15.27
R407c	15.81	18.3	15.27
R404a	20.43	23.0	15.27

Table-4(b): Effect of ecofriendly refrigerants in intermediate temperature cycle on over all second law efficiencies (exergetic efficiencies) of vapour compression refrigeration system coupled with double effect vapour absorption refrigeration H_2O Li/Br system using 1234yf ecofriendly refrigerant in medium temperature circuit and following ecofriendly refrigerants in intermediate temperature circuit and R236fa in the low temperature circuit

Ecofriendly refrigerants in intermediate ITC circuit	Over all (%) improvement in second law efficiency (exergetic Efficiency) of system using to low evaporator temperature of 123K using R236fa (%)	Over all (%) improvement in second law efficiency (exergetic Efficiency) of system using to intermediate evaporator temperature of 173K using R245fa (%)	Over all (%) improvement in second law efficiency (exergetic Efficiency) of system using to intermediate evaporator temperature of 223K using HFO-1234yf (%)
R-245fa	152.6	113.2	77.43
R134a	152.0	112.3	77.43
R 410a	151.4	111.5	77.43
R32	147.6	105.8	77.43
R 143a	151.5	111.6	77.43
R-507a	151.4	111.4	77.43
R227ea	150.4	109.9	77.43
R290	152.4	113.0	77.43
R600a	152.8	113.6	77.43
Ethylene	146.2	103.7	77.43
R123	152.5	113.1	77.43
R125	150.9	110.7	77.43
R407c	137.9	91.07	77.43
R404a	149.8	109.1	77.43

Table-4(c): Effect of ecofriendly refrigerants in intermediate temperature cycle on system exergy destruction ratios of vapour compression refrigeration system coupled with double effect vapour absorption refrigeration H_2O Li/Br system using 1234yf ecofriendly refrigerant in medium temperature circuit and following ecofriendly refrigerants in intermediate temperature circuit and R236fa in the low temperature circuit

Ecofriendly refrigerants in Intermediate ITC circuit	Over all (%) reduction in exergy destruction ratio (EDR) of system using to low evaporator temperature of 123K using R236fa (%)	Over all (%) reduction in exergy destruction ratio (EDR) of system using to intermediate evaporator temperature of 173K using R245fa (%)	Over all (%) reduction in exergy destruction ratio (EDR) of system using to intermediate evaporator temperature of 223K using HFO-1234yf (%)
R-245fa	81.96	72.03	59.21
R134a	81.84	71.77	59.21
R 410a	81.72	71.52	59.21
R32	80.88	72.65	59.21
R 143a	81.74	71.57	59.21
R-507a	81.71	71.50	59.21

R227ea	81.49	71.05	59.21
R290	81.93	71.95	59.21
R600a	82.02	72.15	59.21
Ethylene	80.57	69.05	59.21
R123	81.95	72.01	59.21
R125	81.6	71.28	59.21
R407c	78.64	64.67	59.21
R404a	81.38	70.80	59.21

3.5 Effect of ecofriendly refrigerants in medium temperature cycle on total thermodynamic performances of three cascaded cycles in integrated system

Table-5(a) to Table-5(c) show the comparison between with ecofriendly refrigerants in terms of percentage improvements in thermodynamic performances (First law performances ($COP_{Overall}$), second law performance (Exergetic efficiencies) and system exergy destruction Ratios of three cascaded vapour compression refrigeration system coupled with triple effect vapour absorption Refrigeration H_2O-Li/Br System using HFO-1234yf ecofriendly refrigerant in medium temperature cycle and following ecofriendly refrigerants in intermediate temperature cycle and R236fa refrigerant in the ultra-low temperature cycle and it is found that the first and second law performances of cascaded vapour compression -vapour single effect absorption system is higher by using HFO-1234yf ecofriendly refrigerant in medium temperature circuit and R236fa in ultra-low temperature circuit and found that by using R32 is slightly lower than R245fa and higher than HFC-134a, R404a , R410a, R407c and R507a.

Table-5(a): Effect of ecofriendly refrigerants in medium temperature cycle on the thermodynamic performances (First law Performance ($COP_{Overall}$), vapour compression refrigeration system coupled with double effect vapour absorption refrigeration H_2O Li/Br system using 1234yf ecofriendly refrigerant in medium temperature circuit and R245fa in intermediate temperature circuit and R236fa in the low temperature circut

Ecofriendly refrigerants in MTC circuit	Over all (%) first law efficiency ($COP_{Overall}$) of system using to low evaporator temperature of 123K using R236fa (%)	Over all first law efficiency ($COP_{Overall}$) of system using to intermediate evaporator temperature of 173K using R245fa (%)	Over all in first law efficiency ($COP_{Overall}$) of system using to intermediate evaporator temperature of 223K using HFO-1234yf (%)
R-1234yf	1.459	1.49	1.385
R134a	1.481	1.515	1.411
R717	1.482	1.515	1.411
R152a	1.499	1.534	1.431
R143a	1.456	1.486	1.381
R141b	1.522	1.56	1.459
R410a	1.477	1.510	1.406
R32	1.476	1.509	1.405
R507a	1.448	1.478	1.372
R290	1.480	1.513	1.409
R600a	1.478	1.511	1.407
R123	1.505	1.541	1.439
R125	1.422	1.449	1.342
R407c	1.423	1.45	1.343
R404a	1.439	1.468	1.362
R227ea	1.423	1.45	1.344

Table-5(b): Effect of ecofriendly refrigerants in medium temperature cycle on the Second law performance (Exergetic efficiency) of vapour compression refrigeration system coupled with double effect vapour absorption refrigeration H_2O Li/Br system using 1234yf ecofriendly refrigerant in medium temperature circuit and R245fa in intermediate temperature circuit and R236fa in the low temperature circuit

Ecofriendly refrigerants in MTC circuit	Over all in second law efficiency (exergetic Efficiency) of system using to low evaporator temperature of 123K using R236fa (%)	Over all second law efficiency (exergetic Efficiency) of system using to intermediate evaporator temperature of 173K using R245fa (%)	Over all second law law efficiency (exergetic Efficiency) of system using to intermediate evaporator temperature of 223K Using HFO-1234yf(%)
R-1234yf	0.6642	0.5606	0.4666
R134a	0.6838	0.5795	0.4843
R717	0.6840	0.5798	0.4847
R152a	0.6993	0.5946	0.4988
R143a	0.6614	0.5579	0.4641
R410a	0.6802	0.5760	0.4811
R32	0.6794	0.5753	0.4804

R141b	0.7199	0.6148	0.5185
R507a	0.6549	0.5516	0.4583
R290	0.6827	0.5785	0.4834
R600a	6809	0.5767	0.4817
R123	0.7049	0.6001	0.5041
R125	0.6318	0.5296	0.4384
R407c	0.6330	0.5307	0.4394
R404a	0.6471	0.5441	0.4915
R227ea	0.6332	0.5308	0.4395

Table-5(c): Effect of ecofriendly refrigerants in medium temperature cycle on system exergy destruction ratio with absorber temperature of vapour compression refrigeration system coupled with double effect vapour absorption refrigeration H_2O Li/Br system using 1234yf ecofriendly refrigerant in medium temperature circuit and R245fa in intermediate temperature circuit and R236fa in the low temperature circuit

Ecofriendly refrigerants in MTC circuit	Over all exergy destruction ratio (EDR) of system using to low evaporator temperature of 123K using R236fa (%)	Over all exergy destruction ratio (EDR) of system using to intermediate evaporator temperature of 173K using R245fa (%)	Over all exergy destruction ratio (EDR) of system using to intermediate evaporator temperature of 223K using HFO-1234yf (%)
R-1234yf	0.5056	0.7839	1.143
R134a	0.4625	0.7256	1.065
R717	0.4617	0.7246	1.143
R152a	0.430	0.7246	1.063
R143a	0.5120	0.7926	1.155
R410a	0.4701	0.736	1.079
R32	0.4718	0.7382	1.082
R141b	0.3891	0.6266	0.9288
R507a	0.5270	0.8129	1.182
R290	0.4648	0.7287	1.069
R600a	0.4686	0.7339	1.076
R123	0.4186	0.6664	0.9838
R125	0.5827	0.8884	1.281
R407c	0.5798	0.8844	1.276
R404a	0.5454	0.8378	1.215
R227ea	0.5794	0.8838	1.275

3.6 Effect of ecofriendly refrigerants in medium temperature cycle on percentage improvements in total thermodynamic performances of three cascaded cycles in integrated system

Table-6(a) to Table-6(c) show the comparison between with ecofriendly refrigerants in terms of percentage improvements in thermodynamic performances (First law performances ($COP_{_Overall}$), second law performance (Exergetic efficiencies) and system exergy destruction Ratios of three cascaded vapour compression refrigeration system coupled with double effect vapour absorption Refrigeration H_2O-Li/Br System using HFO-1234yf ecofriendly refrigerant in medium temperature cycle and following ecofriendly refrigerants in intermediate temperature cycle and R236fa refrigerant in the ultra low temperature cycle and it is found that the first and second law performances of cascaded vapour compression -vapour single effect absorption system is higher by using HFO-1234yf ecofriendly refrigerant in medium temperature circuit and R236fa in ultra low temperature circuit and found that by using R32 is slightly lower than R245fa and higher than HFC-134a, R404a , R410a, R407c and R507a.

Table-6(a): Effect of ecofriendly refrigerants in medium temperature cycle on the thermodynamic performances (First law Performance ($COP_{Overall}$), vapour compression refrigeration system coupled with double effect vapour absorption refrigeration H_2O Li/Br system using 1234yf ecofriendly refrigerant in medium temperature circuit and R245fa in intermediate temperature circuit and R236fa in the low temperature

Ecofriendly refrigerants in MTC circuit	Over all (%) improvement in first law efficiency ($COP_{Overall}$) of system using to low evaporator temperature of 123K using R236fa (%)	Over all (%) improvement in first law efficiency ($COP_{Overall}$) of system using to intermediate evaporator temperature of 173K using R245fa (%)	Over all (%) improvement in first law efficiency ($COP_{Overall}$) of system using to intermediate evaporator temperature of 223K using HFO-1234yf (%)
R-1234yf	21.45	24.03	15.27
R134a	23.31	26.09	17.44
R717	23.35	26.13	17.48
R152a	24.78	27.73	19.17
R143a	21.18	23.73	14.96
R410a	22.98	25.72	17.05
R32	22.9	25.63	16.98
R141b	26.72	29.89	21.48
R507a	20.56	23.04	14.22
R290	23.21	25.98	17.32
R600a	23.04	25.79	17.12
R123	25.31	28.32	19.6
R125	18.36	20.6	11.72
R407c	18.47	20.72	11.85
R404a	19.82	22.21	13.39
R227ea	18.46	20.74	11.86

Table-6(b): Effect of ecofriendly refrigerants in medium temperature cycle on the Second law performance (Exergetic efficiency) of vapour compression refrigeration system coupled with double *effect vapour absorption refrigeration H_2O Li/Br system using 1234yf ecofriendly refrigerant in medium temperature circuit and R245fa in intermediate temperature circuit and R236fa in the low temperature circuit*

Ecofriendly refrigerants in MTC circuit	Over all (%) improvement in second law efficiency (exergetic Efficiency) of system using to low evaporator temperature of 123K using R236fa (%)	Over all (%) improvement in second law efficiency (exergetic Efficiency) of system using to intermediate evaporator temp of 173K using R245fa (%)	Over all (%) improvement in second law efficiency (exergetic Efficiency) of system using to intermediate evaporator temp of 223K using HFO-1234yf (%)
R-1234yf	152.6	113.2	77.43
R134a	152.6	120.3	84.16
R717	160.10	120.5	84.29
R152a	165.9	126.1	89.66
R143a	151.5	112.10	76.47
R410a	158.6	119.0	82.92
R141b	173.7	133.8	97.14
R32	158.3	118.8	82.65
R507a	149.0	109.7	74.28
R290	159.6	120.0	83.8
R600a	158.9	119.3	83.13
R123	168..0	128.2	91.68
R125	140.2	101.4	66.69
R407c	140.7	101.8	67.07
R404a	146.0	106.9	71.68
R227ea	140.8	101.8	67.13

Table-6(c): Effect of ecofriendly refrigerants in medium temperature cycle on system exergy destruction ratio with absorber temperature of vapour compression refrigeration system coupled with double effect vapour absorption refrigeration H_2O Li/Br system using 1234yf ecofriendly refrigerant in medium temperature circuit and R245fa in intermediate temperature circuit and R236fa in the low temperature circuit

Ecofriendly refrigerants in MTC circuit	Over all (%) reduction in exergy destruction ratio (EDR) of system using to low evaporator temperature of 123K using R236fa (%)	Over all (%) reduction in exergy destruction ratio (EDR) of system using to intermediate evaporator temperature of 173K using R245fa (%)	Over all (%) reduction in exergy destruction ratio (EDR) of system using to intermediate evaporator temperature of 223K Using HFO-1234yf (%)
R-1234yf	81.96	72.03	59.21
R134a	83.5	74.11	62.01
R717	83.52	74.14	62.06
R152a	84.66	75.67	64.14
R143a	81.73	71.71	58.79

R410a	83.22	73.74	61.51
R32	83.16	73.66	61.40
R141b	86.12	77.64	66.86
R507a	81.19	70.99	57.83
R290	83.42	74.0	61.86
R600a	83.28	73.81	61.61
R123	85.06	76.22	57.3
R125	79.2	68.3	54.29
R407c	79.31	64.44	54.47
R404a	80.54	70.1	56.65
R227ea	79.33	68.46	54.45

3.7 Effect of temperature overlapping in cascade condensers on total thermodynamic performances of three cascaded cycles in integrated system

Table-7(a) to Table-7(i) shows the variation of approach on the thermodynamic performance of combined double effect Li/Br vapour absorption refrigeration system cascaded with vapour compression refrigeration system using 1234yf ecofriendly refrigerant in medium temperature circuit and R245fa in intermediate temperature circuit and R236fa in the low temperature circuit. and it was observed that as temperature overlapping in increasing, the first law efficiency (COP) and second law efficiency (exergetic efficiency) of various combined cascade cycles of integrated multi cascaded system are decreasing as temperature overlapping in each stage is increasing. Similarly exergy destruction ratio based on exergy of product is also decreasing as temperature overlapping is increasing.

Table-7(a): First law performance in terms of COP_Overall with variations temperature over lapping (approach_LTC) of triple effect H_2O-Li/Br vapour absorption refrigeration system cascaded with vapour compression refrigeration system using 1234yf ecofriendly refrigerant in medium temperature circuit and R245fa in intermediate temperature circuit and R236fa in the low temperature circuit.

Temperature over lapping (approach_LTC) in Low temp condenser(°C) using R236fa	Over all COP of system using to low evaporator temp of 123K using R236fa	Over all COP of system using to intermediate evaporator temperature of 173K using R245fa	Over all COP of system using to intermediate evaporator temperature of 223K using HFO-1234yf
0	1.477	1.49	1.385
2	1.473	1.49	1.385
3	1.472	1.49	1.385
4	1.470	1.49	1.385
5	1.468	1.49	1.385
6	1.466	1.49	1.385
8	1.462	1.49	1.385
9	1.461	1.49	1.385
10	1.459	1.49	1.385
12	1.455	1.49	1.385
14	1.452	1.49	1.385
15	1.45	1.49	1.385

Table-7(b): Second law performances in terms of total exergetic efficiencies with variations of temperature over lapping (approach_LTC) of double effect Li/Br vapour absorption refrigeration system cascaded with Vapour compression refrigeration system using 1234yf ecofriendly refrigerant in medium temperature circuit and R245fa in intermediate temperature circuit and R236fa in the low temperature circuit.

Temperature over lapping (approach_LTC) in Low temp condenser (°C) using R236fa	Over all exergetic efficiency of system using to low evap temp of 123K using R236fa	Over all exergetic efficiency of system using to intermediate evap temp of 173K using R245fa	Over all exergetic Efficiency of system using to intermediate evap temp of 223K using HFO-1234yf
0	0.6642	0.5606	0.4666
2	0.6848	0.5606	0.4666
3	0.6821	0.5606	0.4666
4	0.6794	0.5606	0.4666
5	0.6768	0.5606	0.4666
6	0.6742	0.5606	0.4666
8	0.6691	0.5606	0.4666
9	0.6667	0.5606	0.4666
10	0.6642	0.5606	0.4666
12	0.6594	0.5606	0.4666
14	0.6547	0.5606	0.4666
15	0.6523	0.5606	0.4666

Table-7(c): Exergy destruction ratio of system with variations in temperature over lapping (approach_LTC) of double effect H_20-Li/Br vapour absorption refrigeration system cascaded with vapour compression refrigeration system using 1234yf ecofriendly refrigerant in medium temperature circuit and R245fa in intermediate temperature circuit and R236fa in the low temperature circuit

Temperature over lapping (approach_LTC) in Low temperature condenser (°C) using R236fa	Over all Exergy Destruction Ratio of system using to low evaporator temperature of 123K using R236fa	Over all Exergy Destruction Ratio of system using to intermediate evaporator temperature of 173K using R245fa	Over all Exergy Destruction Ratio of system using to intermediate evaporator temperature of 223K using HFO-1234yf
0	0.5056	0.7839	1.143
2	0.4603	0.7839	1.143
3	0.4661	0.7839	1.143
4	0.4718	0.7839	1.143
5	0.4775	0.7839	1.143
6	0.4832	0.7839	1.143
8	0.4944	0.7839	1.143
9	0.500	0.7839	1.143
10	0.5056	0.7839	1.143
12	0.5166	0.7839	1.143
14	0.5275	0.7839	1.143
15	0.5329	0.7839	1.143

Table-7(d): First and second law performance with variations in temperature over lapping (approach_ITC) of double effect H_2O Li/Br vapour absorption refrigeration system cascaded with vapour compression refrigeration system using 1234yf ecofriendly refrigerant in medium temperature circuit and R245fa in intermediate temperature circuit and R236fa in the low temperature circuit.

Temperature over laping (approach_ITC) in intermediate temperature condenser (°C) using R245fa	Over all COP of system using to low temperature evaporator temperature of 123K using R236fa	Over all COP of system using to intermediate temperature evaporator temperature of 173K using R245fa	Over all COP of system using to intermediate temperature evaporator temperature of 223K using HFO-1234yf
0	1.519	1.55	1.385
2	1.506	1.537	1.385
3	1.50	1.531	1.385
4	1.498	1.525	1.385
5	1.488	1.519	1.385
6	1.482	1.513	1.385
8	1.470	1.501	1.385
9	1.485	1.495	1.385
10	1.459	1.49	1.385
12	1.448	1.478	1.385
14	1.437	1.467	1.385
15	1.431	1.462	1.385

Table-7(e):Second law performances (exergetic efficiencies) with variations in temperature over lapping (approach_ITC) of double effect Li/Br vapour absorption refrigeration system cascaded with vapour compression refrigeration system using 1234yf ecofriendly refrigerant in medium temperature circuit and R245fa in intermediate temperature circuit and R236fa in the low temperature circuit.

Temperature over lapping (approach_ITC) in intermediate temperature Condenser (°C) using R245fa	Over all exergetic efficiency of system using to low evaporator temperature of 123K using R236fa0.5415	Over all exergetic efficiency of system using to intermediate evaporator temperature of 173K using R245fa	Over all exergetic Efficiency of system using to intermediate evaporator temperature of 223K using HFO-1234yf
0	0.70	0.6131	0.4666
2	0.6924	0.6020	0.4666
3	0.6887	0.5965	0.4666
4	0.6850	0.5912	0.4666
5	0.6814	0.5859	0.4666
6	0.6778	0.5807	0.4666
8	0.6709	0.5705	0.4666
9	0.6675	0.5655	0.4666
10	0.6642	0.5606	0.4666
12	0.6577	0.5509	0.4666
14	0.6514	0.5415	0.4666
15	0.6483	0.5369	0.4666

Table-7(f): Exergy destruction ratio ($EDR_{_system}$) of system with variations in temperature over lapping ($approach_{_ITC}$) of double effect H_2O Li/Br vapour absorption refrigeration system cascaded with Vapour compression refrigeration system using 1234yf ecofriendly refrigerant in medium temperature circuit and R245fa in intermediate temperature circuit and R236fa in the low temperature circuit.

Temperature over laping ($approach_{_ITC}$) in intermediate temperature Condenser (°C) using R245fa	Over all exergy destruction ratio (EDR) of system using to low temperature evaporator temperature of 123K using R236fa	Over all exergy destruction ratio(EDR) of system using to intermediate temperature evaporator temperature of 173K using R245fa	Over all exergy destruction ratio(EDR) of system using to intermediate temperature evaporator temperature of 223K using HFO-1234yf
0	0.4283	0.6311	1.143
2	0.4442	0.6612	1.143
3	0.4520	0.6763	1.143
4	0.4598	0.6915	1.143
5	0.4676	0.7068	1.143
6	0.4753	0.7221	1.143
8	0.4905	0.7529	1.143
9	0.4981	0.7683	1.143
10	0.5056	0.7839	1.143
12	0.5205	0.8152	1.143
14	0.5352	0.8467	1.143
15	0.5425	0.8626	1.143

Table-7(g): First law Performances ($COP_{_Overall}$) with variations in temperature over lapping ($approach_{_MTC}$) of doublele effect H_2O- Li/Br vapour absorption refrigeration system cascaded with Vapour compression refrigeration system using 1234yf ecofriendly refrigerant in medium temperature circuit and R245fa in intermediate temperature circuit and R236fa in the low temperature circuit.

Temperature over laping ($approach_{_MTC}$) in medium temperature Condenser (°C) using R1234yf	Over all COP of system using to low temperature evaporator temperature of 123K using R236fa	Over all COP of system using to intermediate temperature evaporator temperature of 173K using R245fa	Over all COP of system using to intermediate temperature evaporator temperature of 223K using HFO-1234yf
0	1.554	1.596	1.463
2	1.535	1.574	1.475
3	1.525	1.564	1.44
4	1.516	1.553	1.429
5	1.506	1.543	1.407
6	1.497	1.532	1.396
8	1.478	1.511	1.385
9	1.468	1.50	1.385
10	1.459	1.49	1.362
12	1.44	1.469	1.341
14	1.42	1.447	1.341
15	1.411	1.437	1.33

Table-7(h): second law Performances (exergetic efficiencies) variations with temperature over lapping ($approach_{_LTC}$) of double effect H_2O- Li/Br vapour absorption refrigeration system cascaded with Vapour compression refrigeration system using 1234yf ecofriendly refrigerant in medium temperature circuit and R245fa in intermediate temperature circuit and R236fa in the low temperature circuit.

Temperature over lapping ($approach_{_MTC}$) in medium temperature Condenser (°C) using R1234yf	Over all exergetic efficiency of system using to low evaporator temperature of 123K using R236fa	Over all exergetic efficiency of system using to intermediate evaporator temperature of 173K using R245fa	Over all exergetic Efficiency of system using to intermediate evaporator temperature of 223K using HFO-1234yf
0	0.7481	0.6426	0.5464
2	0.7312	0.6259	0.5295
3	0.7228	0.6176	0.5213
4	0.7144	0.6094	0.5131
5	0.7060	0.6012	0.5051
6	0.6976	0.593	0.4972
8	0.6809	0.5767	0.4817
9	0.67245	0.5686	0.4710
10	0.6642	0.5606	0.4666
12	0.6475	0.5445	0.4519
14	0.6308	0.5286	0.4375
15	0.6224	0.5206	0.4304

Table-7(i): Exergy destruction ratio (EDR) of system with variations in temperature over lapping (approach_LTC) of double effect Li/Br vapour absorption refrigeration system cascaded with Vapour compression refrigeration system using 1234yf ecofriendly refrigerant in medium temperature circuit and R245fa in intermediate temperature circuit and R236fa in the low temperature circuit.

Temperature over laping (approach_MTC) in medium temperature condenser (°C) using R1234yf	Over all Exergy Destruction Ratio of system using to low evaporator temperature of 123K using R236fa	Over all Exergy Destruction Ratio of system using to intermediate evaporator temperature of 173K using R245fa	Over all Exergy Destruction Ratio of system using to intermediate evaporator temperature of 223K using HFO-1234yf
0	0.3368	0.5561	0.8302
2	0.3676	0.5977	0.8885
3	0.3836	0.6191	0.9184
4	0.3998	0.6410	0.9488
5	0.4164	0.6635	0.9798
6	0.4335	0.6864	1.011
8	0.4687	0.7339	1.076
9	0.4869	0.7586	1.109
10	0.5056	0.7839	1.143
12	0.5444	0.8364	1.213
14	0.5853	0.8919	1.286
15	0.6066	0.9207	1.323

3.8 Effect of temperature overlapping on percentage improvements of thermodynamic performances

Table-8(a) to Table-8(i) show the variation of all three types of approaches on the percentage improvement in thermodynamic performance of combined double effect Li/Br vapour absorption refrigeration system cascaded with vapour compression refrigeration system using 1234yf ecofriendly refrigerant in medium temperature circuit and R245fa in intermediate temperature circuit and R236fa in the low temperature circuit with percentage variation of thermodynamic first and second law performances and it was observed that as temperature overlapping in increasing, the first law efficiency (COP) and second law efficiency (exergetic efficiency) VCRS of cascaded system are decreasing as temperature overlapping is increasing. Similarly exergy destruction ratio based on exergy of product is also decreasing as temperature overlapping (approach) is increasing.

Table-8(a): First law performance in terms of COP_Overallwith variations of temperature over lapping (approach_LTC) of double effectH2O-Li/Br vapour absorption refrigeration system cascaded with vapour compression refrigeration system using 1234yf ecofriendly refrigerant in medium temperature circuit and R245fa in intermediate temperature circuit and R236fa in the low temperature circuit.

Temperature over lapping (approach_LTC) in Low temperature condenser (°C) using R236fa	% improvement in Overall COP of system using to low evaporator temperature of 123K using R236fa	% improvement in Overall COP of system using to intermediate evaporator temperature of 173K using R245fa	% improvement in Overall COP of system using to intermediate evaporator temperature of 223K using HFO-1234yf
0	22.99	24.03	15.27
2	22.67	24.03	15.27
3	22.51	24.03	15.27
4	22.36	24.03	15.27
5	22.2	24.03	15.27
6	21.85	24.03	15.27
8	21.75	24.03	15.27
9	21.6	24.03	15.27
10	21.45	24.03	15.27
12	21.17	24.03	15.27
14	20.89	24.03	15.27
15	20.75	24.03	15.27

Table-8(b): Second law performances in terms of total exergetic efficiencies with variations of temperature over lapping (approach_LTC) of double effect H_2O Li/Br vapour absorption refrigeration system cascaded with Vapour compression refrigeration system using 1234yf ecofriendly refrigerant in medium temperature circuit and R245fa in intermediate temperature circuit and R236fa in the low temperature circuit.

Temperature over lapping (approach_LTC) in Low temperature condenser (°C) using R236fa	Over all exergetic efficiency of system using to low evaporator temperature of 123K using R236fa	Over all exergetic efficiency of system using to intermediate evaporator temperature of 173K using R245fa	Over all exergetic Efficiency of system using to intermediate evaporator temperature of 223K using HFO-1234yf
0	152.6	113.2	77.43
2	155.6	113.2	77.43
3	159.4	113.2	77.43
4	158.4	113.2	77.43
5	157.4	113.2	77.43
6	156.4	113.2	77.43
8	154.4	113.2	77.43
9	153.5	113.2	77.43
10	152.6	113.2	77.43
12	150.7	113.2	77.43
14	148.9	113.2	77.43
15	148.0	113.2	77.43

Table-8(c): Exergy destruction ratio of system with variations in temperature over lapping (approach_LTC) of double effect H_20-Li/Br vapour absorption refrigeration system cascaded with vapour compression refrigeration system using 1234yf ecofriendly refrigerant in medium temperature circuit and R245fa in intermediate temperature circuit and R236fa in the low temperature circuit

Temperature over lapping (approach_LTC) in Low temperature condenser (°C) using R236fa	% decrement in Overall Exergy Destruction Ratio of system using to low evaporator temperature of 123K using R236fa	% decrement in Overall Exergy Destruction Ratio of system using to intermediate evaporator temperature of 173K using R245fa	% decrement in Overall Exergy Destruction Ratio of system using to intermediate evaporator temperature of 223K using HFO-1234yf
0	81.96	72.03	59.21
2	83.58	72.03	59.21
3	83.37	72.03	59.21
4	83.13	72.03	59.21
5	82.96	72.03	59.21
6	82.76	72.03	59.21
8	82.36	72.03	59.21
9	82.16	72.03	59.21
10	81.96	72.03	59.21
12	81.57	72.03	59.21
14	81.18	72.03	59.21
15	80.98	72.03	59.21

Table-8(d): First and second law performance with variations in temperature over lapping (approach_ITC) of double effect H_2O Li/Br vapour absorption refrigeration system cascaded with vapour compression refrigeration system using 1234yf ecofriendly refrigerant in medium temperature circuit and R245fa in intermediate temperature circuit and R236fa in the low temperature circuit.

Temperature over laping (approach_ITC) in intermediate condenser temp (°C) using R245fa	(%) Overall improvement in First law efficiency (COP_Overall) of system using to low evap temp of 123K using R236fa (%)	(%) Overall improvement in First law efficiency (COP_Overall) of system using to intermediate evap temp of 173K using R245fa (%)	(%) Over all improvement in First law efficiency (COP_Overall) of system using to intermediate evap temp of 223K using HFO1234yf
0	15.14	18.35	7.821
2	14.08	17.33	7.821
3	13.57	16.82	7.821
4	13.06	16.32	7.821
5	12.56	15.83	7.821
6	12.06	15.34	7.821
8	11.09	14.38	7.821
9	10.61	13.91	7.821
10	10.14	13.44	7.821
12	9.216	12.52	7.821
14	8.314	11.62	7.821
15	7.871	11.18	7.821

Table-8(e):Second law performances(exergetic Efficiencies) with variations in temperature over lapping (approach_ITC) of double effect H_2O Li/Br vapour absorption refrigeration system cascaded with vapour compression refrigeration system using 1234yf ecofriendly refrigerant in medium temperature circuit and R245fa in intermediate temperature circuit and R236fa in the low temperature circuit.

Temperature over laping (approach_ITC) in intermediate temperature condenser (°C) using R245fa	Over all (%) improvement in second law efficiency (exergetic Efficiency) of system using to low evaporator temperature of 123K using R236fa (%)	Over all (%) improvement in second law efficiency (exergetic Efficiency) of system using to intermediate evaporator temperature of 173K using R245fa (%)	Over all (%) improvement in second law law efficiency (exergetic Efficiency) of system using to intermediate evaporator temperature of 223K using HFO-1234yf(%)
0	170.2	136.8	80.79
2	167.2	132.5	80.79
3	165.7	130.4	80.79
4	164.3	128.3	80.79
5	162.9	126.3	80.79
6	161.5	124.3	80.79
8	158.8	120.3	80.79
9	157.5	118.4	80.79
10	156.2	116.5	80.79
12	153.7	112.7	80.79
14	151.2	109.1	80.79
15	150.0	107.3	80.79

Table-8(f): Exergy destruction ratio (EDR_system) of system and % improvement in system first law performance with variations in temperature over lapping (approach_ITC) of double effect H_2O Li/Br vapour absorption refrigeration system cascaded with Vapour compression refrigeration system using 1234yf ecofriendly refrigerant in medium temperature circuit and R245fa in intermediate temperature circuit and R236fa in the low temperature circuit.

Temperature over laping (approach_ITC) in intermediate temperature Condenser (°C) using R245fa	Over all Exergy Destruction Ratio (EDR) of system using to low evaporator temp of 123K using R236fa	Over all Exergy Destruction Ratio(EDR) of system using to intermediate evaporator temperature of 173K using R245fa	Over all Exergy Destruction Ratio(EDR) of system using to intermediate evaporator temperature of 223K using HFO-1234yf	% decrement in Overall Exergy Destruction Ratio (EDR) of system using to low evaporator temperature of 123K using R236fa	% decrement in Overall Exergy Destruction Ratio(EDR) of system using to intermediate evaporator temp of 173K using R245fa	% decrement in Overall Exergy Destruction Ratio(EDR) of system using to intermediate evaporator temperature of 223K using HFO-1234yf
0	0.4283	0.6311	1.143	84.72	77.48	59.21
2	0.4442	0.6612	1.143	84.15	76.41	59.21
3	0.4520	0.6763	1.143	83.87	75.87	59.21
4	0.4598	0.6915	1.143	83.59	75.32	59.21
5	0.4676	0.7068	1.143	83.32	74.78	59.21
6	0.4753	0.7221	1.143	83.04	74.23	59.21
8	0.4905	0.7529	1.143	82.5	73.14	59.21
9	0.4981	0.7683	1.143	82.23	72.58	59.21
10	0.5056	0.7839	1.143	81.96	72.03	59.21
12	0.5205	0.8152	1.143	81.43	70.91	59.21
14	0.5352	0.8467	1.143	80.9	69.79	59.21
15	0.5425	0.8626	1.143	80.64	69.22	59.21

Table-8(g): First law Performances (COP_Overall) with variations in temperature over lapping (approach_MTC) of triple effect H_2O- Li/Br vapour absorption refrigeration system cascaded with Vapour compression refrigeration system using 1234yf ecofriendly refrigerant in medium temperature circuit and R245fa in intermediate temperature circuit and R236fa in the low temperature circuit.

Temperature over laping (approach_MTC) in medium temperature Condenser (°C) using R1234yf	% improvement in overall COP of system using to low evaporator temperature of 123K using R236fa	% improvement in overall COP of system using to intermediate evaporator temperature of 173K using R245fa	% improvement in overall COP of system using to intermediate evaporator temperature of 223K using HFO-1234yf
0	29.34	32.8	24.67
2	27.77	31.08	22.76
3	26.99	30.2	21.81
4	26.2	29.32	20.86
5	25.41	28.43	19.92
6	24.62	27.55	18.99

8	23.04	25.79	17.12
9	22.95	24.91	16.2
10	21.45	24.03	15.27
12	19.86	22.26	13.43
14	18.26	20.49	11.61
15	17.46	19.6	10.69

Table-8(h): second law Performances (exergetic efficiencies) variations with temperature over lapping (approach_$_{LTC}$) of triple effect H_2O-Li/Br vapour absorption refrigeration system cascaded with Vapour compression refrigeration system using 1234yf ecofriendly refrigerant in medium temperature circuit and R245fa in intermediate temperature circuit and R236fa in the low temperature circuit.

Temperature over lapping (approach_$_{MTC}$) in medium temperature Condenser (^oC) using R1234yf	% improvement in overall exergetic efficiency of system using to low evaporator temperature of 123K using R236fa	% improvement in overall exergetic efficiency of system using to intermediate evaporator temperature of 173K using R245fa	% improvement in overall exergetic Efficiency of system using to intermediate evaporator temperature of 223K using HFO-1234yf
0	184.40	144.4	107.8
2	178.0	138.0	101.3
3	174.8	134.8	98.20
4	171.6	131.7	95.11
5	168.4	128.6	92.06
6	165.3	125.5	89.06
8	158.9	119.3	83.17
9	155.7	116.2	80.26
10	152.6	113.2	77.43
12	146.2	107.1	71.83
14	139.9	101.0	66.36
15	136.7	97.97	63.67

Table-8(i): Exergy destruction ratio (EDR) of system with variations intemperature over lapping (approach_$_{LTC}$) of double effect H_2O Li/Br vapour absorption refrigeration system cascaded with vapour compression refrigeration system using 1234yf ecofriendly refrigerant in medium temperature circuit and R245fa in intermediate temperature circuit and R236fa in the low temperature circuit.

Temperature over lapping (approach_$_{MTC}$) in medium temperature condenser (^oC) using R1234yf	% improvement in overall Exergy Destruction Ratio of system using to low evaporator temperature of 123K using R236fa	% improvement in overall Exergy Destruction Ratio of system using to intermediate evaporator temperature of 173K using R245fa	% improvement in overall Exergy Destruction Ratio of system using to intermediate evaporator temperature of 223K using HFO-1234yf
0	87.98	80.16	70.38
2	86.88	78.67	68.29
3	86.31	77.91	67.23
4	85.73	77.13	66.14
5	85.14	76.33	65.04
6	84.53	75.51	63.91
8	8328	73.81	61.61
9	82.63	72.93	60.42
10	81.96	72.03	59.21
12	80.57	70.75	56.72
14	79.11	68.18	54.12
15	78.35	67.14	52.18

3.9 Effect of generator temperature on total thermodynamic performances of three cascaded cycles in integrated system

Table-9(a) to Table-9(c) shows the variation of generator temperature of VARS on thermodynamic performances such as first law efficiency , second law efficiency and system exergy destruction of combined double effect Li/Br vapour absorption refrigeration system cascaded with Vapour compression refrigeration system using 1234yf ecofriendly refrigerant in medium temperature circuit and R245fa in intermediate temperature circuit and R236fa in the low temperature circuit and it was observed that as generator temperature increasing, the first law efficiency (COP_$_{overall}$) of three cycles and second law efficiency (exergetic efficiency) of three cycles of combined vapour absorption cascaded refrigeration system is decreasing as generator temperature is increasing. Similarly exergy destruction ratio based on exergy of product is increasing.

Table-9(a): Effect of generator *temperature of* double *effect H_2O- Li/Br VARS on thermodynamic performances (First law Performance ($COP_{Overall}$), vapour compression refrigeration system coupled with single effect vapour absorption refrigeration H_2O Li/Br system using 1234yf ecofriendly refrigerant in medium temperature circuit and R245fa in intermediate temperature circuit and R236fa in the low temperature*

Generator Temperature of double effect H_2O-Li/Br vapour absorption refrigeration system (^oC)	Over all COP of system using to low evaporator temperature of 123K using R23fa	Over all COP of system using to intermediate evaporator temperature of 173K using R245fa	Over all COP of system using to intermediate evaporator temperature of 223K using HFO-1234yf
115	1.567	1.609	1.517
120	1.530	1.568	1.471
125	1.494	1.529	1.427
130	1.459	1.490	1.385
135	1.426	1.452	1.344
140	1.392	1.416	1.305
145	1.360	1.382	1.269
150	1.331	1.350	1.235
155	1.355	1.378	1.262

Table-9(b): Effect of generator *temperature of* double *effect H_2O Li/Br VARS on thermodynamic second law performance (exergetic efficiencies) with absorber temperature of vapour compression refrigeration system coupled with* double *effect vapour absorption refrigeration H_2O Li/Br system using 1234yf ecofriendly refrigerant in medium temperature circuit and R245fa in intermediate temperature circuit and R236fa in the low temperature circuit*

Generator temperature of double effect H_2O-Li/Br VARS (^oC)	Over all exergetic efficiency of system using to low evaporator temperature of 123K using R236fa	Over all exergetic efficiency of system using to intermediate evaporator temperature of 173K using R245fa	Over all exergetic Efficiency of system using to intermediate evaporator temperature of 223K using HFO-1234yf
115	0.6867	0.5821	0.4911
120	0.6793	0.5750	0.480
125	0.6718	0.5678	0.4748
130	0.6642	0.5606	0.4666
135	0.6567	0.5534	0.4586
140	0.6493	0.5464	0.4509
145	0.6421	0.5397	0.4434
150	0.6352	0.5331	0.4363
155	0.6408	0.5384	0.4420

Table-9(c): Effect of generator *temperature of* double *effect H_2O Li/Br VARS on thermodynamic system exergy destruction ratio with absorber temperature of vapour compression refrigeration system coupled with* double *effect vapour absorption refrigeration H_2O Li/Br system using 1234yf ecofriendly refrigerant in medium temperature circuit and R245fa in intermediate temperature circuit and R236fa in the low temperature circuit*

Generator temperature of *double* effect H_2O-Li/Br vapour absorption refrigeration system (^oC)	Over all Exergy Destruction Ratio of system using to low evaporator temperature of 123K using R23fa	Over all Exergy Destruction Ratio of system using to intermediate evaporator temperature of 173K using R245fa	Over all Exergy Destruction Ratio of system using to intermediate evaporator temperature of 223K using HFO-1234yf
115	0.4562	0.7179	1.036
120	0.4721	0.7392	1.071
125	0.4886	0.7612	1.106
130	0.5056	0.8606	1.148
135	0.5228	0.8069	1.118
140	0.5401	0.830	1.218
145	0.5573	0.8530	1.255
150	0.5743	0.8757	1.292
155	0.5607	0.5324	1.263

3.10 Effect of generator temperature on percentage improvements in total thermodynamic performances of three cascaded cycles in integrated system

Table-10(a) to Table-10(c) shows the variation of generator temperature with percentage improvement in thermodynamic performances such as first law efficiency, second law efficiency and system exergy destruction ratio of combined double effect Li/Br vapour absorption refrigeration system cascaded with vapour compression refrigeration system using 1234yf ecofriendly refrigerant in medium temperature circuit and R245fa in intermediate temperature circuit and R236fa in

the low temperature circuit and it was observed that as generator temperature increasing, the percentages improvement in first law efficiency ($COP_{_Overall}$) of three cycles and second law efficiency (exergetic efficiency) of three cycles of multi cascaded double effect vapour absorption integrated refrigeration system are increasing as generator temperature is increasing. Similarly exergy destruction ratio based on exergy of product is also increasing as condenser temperature is decreasing.

Table-10(a): Effect of generator *temperature of* double *effect H_2O- Li/Br VARS on thermodynamic performances (First law Performance ($COP_{_Overall}$), vapour compression refrigeration system coupled with single effect vapour absorption refrigeration H_2O Li/Br system using 1234yf ecofriendly refrigerant in medium temperature circuit and R245fa in intermediate temperature circuit and R236fa in the low temperature*

Generator Temperature ofdouble effect H_2O-Li/Br vapour absorption refrigeration system (°C)	Over all (%) improvement in First law efficiency (COP_Overall) of system using to low evaporator temperature of 123K using R236fa (%)	Over all (%) improvement in First law efficiency (COP_Overall) of system using to intermediate evaporator temperature of 173K using R245fa (%)	Over all (%) improvement in First law efficiency (COP_Overall) of system using to intermediate evaporator temperature of 223K using HFO-1234yf (%)
115	14.25	17.31	10.58
120	16.68	19.58	12.10
125	19.10	21.83	13.76
130	21.45	24.03	15.27
135	23.74	26.14	16.72
140	25.93	28.16	18.10
145	28.01	30.8	19.39
150	29.98	31.88	20.59
155	28.4	30.44	19.63

Table-10(b): Effect of generator *temperature of double effect H_2O Li/Br VARS on thermodynamic second law performance (exergetic efficiencies) with absorber temperature of vapour compression refrigeration system coupled with* double *effect vapour absorption refrigeration H2O-LiBr system using 1234yf ecofriendly refrigerant in medium temperature circuit and R245fa in intermediate temperature circuit and R236fa in the low temperature circuit*

Generator temperature of *double* effect H_2O-Li/Br vapour absorption refrigeration system (°C)	Over all (%) improvement in second law efficiency (exergetic Efficiency) of system using to low evaporator temperature of 123K using R236 fa (%)	Over all (%) improvement in second law efficiency (exergetic Efficiency) of system using to intermediate evaporator temperature of 173K using R245fa (%)	Over all (%) improvement in second law efficiency (exergetic Efficiency) of system using to intermediate evaporator temperature of 223K using HFO-1234yf(%)
115	103.6	72.58	45.61
120	119.5	85.75	56.03
125	135.8	99.32	66.66
130	152.6	113.2	77.43
135	169.6	127.2	88.27
140	186.8	141.4	99.14
145	204.10	155.5	110.0
150	221.9	169.7	120.7
155	223.4	171.7	123.1

Table-10(c): Effect of generator temperature of triple effect H_2O Li/Br VARS on thermodynamic system exergy destruction ratio with absorber temperature of vapour compression refrigeration system coupled with double effect vapour absorption refrigeration H_2O-LiBr system using 1234yf ecofriendly refrigerant in medium temperature circuit and R245fa in intermediate temperature circuit and R236fa in the low temperature

Generator temp of double effect H_2O-Li/Br vapour absorption refrigeration system (°C)	Over all (%) reduction in exergy destruction ratio (EDR) of system using to low evap temp of 123K using R236fa (%)	Over all (%) reduction in exergy destruction ratio (EDR) of system using to intermediate evap temp 173K using R245fa (%)	Over all (%) reduction in exergy destruction ratio (EDR) of system using to intermediate evap temp 223K using HFO-1234yf (%)
115	76.78	63.46	47.27
120	78.84	66.86	52.01
125	80.54	69.68	55.93
130	8196	72.03	59.29
135	83.16	74.01	61.98
140	84.19	75.71	64.36
145	85.08	77.16	66.39
150	85.85	78.42	68.16
155	86.16	78.81	68.8

3.11 Effect of absorber temperature on total thermodynamic performances of three cascaded cycles in integrated system

Fig-11(a) to Table-11(c) show the variation of absorber temperature of combined double effect Li/Br Vapour absorption refrigeration system cascaded with Vapour compression refrigeration system 1234yf ecofriendly refrigerant in medium temperature circuit and R245fa in intermediate temperature circuit and R236fa in the low temperature circuit and it was observed that as condenser temperature increasing, the first law efficiencies ($COP_{_Overall}$) and second law efficiencies (exergetic efficiencies) of combined system is decreasing as absorber temperature is increasing. Similarly exergy destruction ratio based on exergy of product is also increasing as condenser temperature is increased.

Table-11(a): Effect of absorber temperature *of VARS on total Thermodynamic performances (First law Performance (COP_overall), with condenser temperature of vapour compression refrigeration system coupled with* double *effect vapour absorption H_2O- Li/Br system using 1234yf ecofriendly refrigerant in medium temperature circuit and R245fa in intermediate temperature circuit and R236fa in the low temperature*

Absorber temperature of double effect H_2O-Li/Br vapour absorption refrigeration system (^oC)	Over all COP of system using to low evaporator temperature of 123K using R23fa	Over all COP of system using to intermediate evaporator temperature of 173K using R245fa	Over all COP of system using to intermediate evaporator temperature of 223K using HFO-1234yf
30	1.522	1.559	1.461
32	1.449	1.533	1.438
34	1.473	1.505	1.402
36	1.113	1.473	1.366
38	1.408	1.434	1.324
40	1.361	1.383	1.27
42	1.296	1.313	1.195

Table-11(b): Absorber temperature of double effect H_2O-Li/Br vapour absorption refrigeration system on total Thermodynamic performances (First law Performance (COP_overall), with condenser temperature of vapour compression refrigeration system coupled with double effectvapour absorption refrigeration H_2O-LiBr system using 1234yf ecofriendly refrigerant in medium temperature circuit and R245fa in intermediate temperature circuit and R236fa in the low temperature circuit.

Absorber temperature of double effect H_2O-Li/Br vapour absorption refrigeration system (^oC)	Over all exergetic efficiency of system using to low evaporator temperature of 123K using R236fa	Over all exergetic efficiency of system using to intermediate evaporator temperature of 173K using R245fa	Over all exergetic Efficiency of system using to intermediate evaporator temperature of 223K using HFO-1234yf
30	0.6775	0.5733	0.4810
32	0.6727	0.5687	0.4758
34	0.6672	0.5635	0.4699
36	0.6608	0.5674	0.4630
38	0.6529	0.5498	0.4546
40	0.6423	0.5398	0.4436
42	0.6268	0.5252	0.4277

Table-11(c): Absorber temperature of double effect H_2O-Li/Br vapour absorption refrigeration system on total thermodynamic performances (First law Performance (COP_overall), with condenser temperature of vapour compression refrigeration system coupled with double effect vapour absorption refrigeration H_2O-LiBr system using 1234yf ecofriendly refrigerant in medium temperature circuit and R245fa in intermediate temperature circuit and R236fa in the low temperature circuit.

Absorber temperature of double effect H_2O-Li/Br vapour absorption refrigeration system (^oC)	Over all Exergy Destruction Ratio of system using to low evaporator temperature of 123K using R23fa	Over all Exergy Destruction Ratio of system using to intermediate evaporator temperature of 173K using R245fa	Over all Exergy Destruction Ratio of system using to intermediate evaporator temperature of 223K using HFO-1234yf
30	0.4760	0.7444	1.079
32	0.4866	0.7687	1.102
34	0.4987	0.7747	1.126
36	0.5132	0.7941	1.16
38	0.5317	0.8187	1.20
40	0.5569	0.8525	1.255
42	0.5995	0.9040	1.338

3.12Effect of heat exchanger effectiveness on percentage improvement in total thermodynamic performances of three cascaded cycles in integrated system

Table-12(a) to Table-12(c) show the variation of Absorber temperature of VARS on combined double effect *H_2O Li/Br* vapour absorption refrigeration system cascaded with Vapour compression refrigeration system 1234yf ecofriendly refrigerant in medium temperature circuit and R245fa in intermediate temperature circuit and R236fa in the low temperature circuit and it was observed that as condenser temperature increasing, the first law efficiencies ($COP_{_Overall}$) and second law efficiencies (exergetic efficiencies) of combined system is decreasing as absorber temperature is increasing. Similarly exergy destruction ratio based on exergy of product is also increasing as condenser temperature is increased.

Table-12(a): Absorber temperature of double effect H_2O-Li/Br vapour absorption refrigeration system on total thermodynamic performances (First law Performance (COP_overall), with condenser temperature of vapour compression refrigeration system coupled with double absorption refrigeration H2O-LiBr system using 1234yf ecofriendly refrigerant in medium temperature circuit and R245fa in intermediate temperature circuit and R236fa in the low temperature circuit

Absorber temperature of double effect H_2O-Li/Br vapour absorption refrigeration system (^oC)	Over all (%) improvement in First law efficiency ($COP_{_Overall}$) of system using to low evaporator temperature of 123K using R236fa (%)	Over all (%) improvement in First law efficiency ($COP_{_Overall}$) of system using to intermediate evaporator temperature of 173K using R245fa (%)	Over all (%) improvement in First law efficiency ($COP_{_Overall}$) of system using to intermediate evaporator temperature of 223K using HFO-1234yf (%)
30	17.26	20.13	12.56
32	18.8	21.56	13.57
34	20.51	23.15	14.67
36	22.48	24.98	15.93
38	24.87	27.19	17.44
40	27.97	30.04	19.36
42	32.31	34.01	22.01

Table-12(b): Absorber temperature of double effect H_2O-Li/Br vapour absorption refrigeration system on total thermodynamic performances (First law Performance (COP_overall), with condenser temperature of vapour compression refrigeration system coupled with double effect absorption refrigeration H_2O-Li/Br system using 1234yf ecofriendly refrigerant in medium temperature circuit and R245fa in intermediate temperature circuit and R236fa in the low temperature circuit.

Absorber temperature of double effect H_2O-Li/Br vapour absorption refrigeration system (^oC)	Over all (%) improvement in second law efficiency (exergetic Efficiency) of system using to low evaporator temperature of 123K using R236fa (%)	Over all (%) improvement in second law efficiency (exergetic Efficiency) of system using to intermediate evaporator temperature of 173K using R245fa (%)	Over all (%) improvement in second law efficiency (exergetic Efficiency) of system using to intermediate evaporator temperature of 223K using HFO1234yf (%)
30	138.4	101.8	69.29
32	143.6	105.9	72.26
34	149.3	110.5	75.57
36	156.1	116.0	79.45
38	164.5	122.8	84.21
40	175.8	131.8	90.46
42	192.2	144.9	99.42

Table-12(c): Absorber temperature of double effect H_2O-Li/Br vapour absorption refrigeration system on total Thermodynamic performances reduction in exergy destruction ratio (EDR) with condenser temperature of vapour compression refrigeration system coupled with double effectvapour absorption refrigeration H_2O-LiBr system using 1234yf ecofriendly refrigerant in medium temperature circuit and R245fa in intermediate temperature circuit and R236fa in the low temperature circuit.

Absorber temperature of double effect H_2O-Li/Br vapour absorption refrigeration system (^oC)	Over all (%) reduction in exergy destruction ratio (EDR) of system using to low evaporator temperature of 123K using R236fa (%)	Over all (%) reduction in exergy destruction ratio (EDR) of system using to intermediate evaporator temperature of 173K using R245fa (%)	Over all (%) reduction in exergy destruction ratio (EDR) of system using to intermediate evaporator temperature of 223K using HFO-1234yf (%)
30	81.11	70.46	57.17
32	81.43	71.56	57.95
34	81.78	71.69	58.77
36	82.15	72.36	59.67
38	82.58	73.17	60.69
40	83.09	74.12	61.91
42	83.74	75.32	63.47

3.13 Effect of condenser temperature on total thermodynamic performances of three cascaded cycles in integrated system

Table-13(a) to Table-13(c) show the variation of condenser temperature of combined double effect Li/Brvapour absorption refrigeration system cascaded with vapour compression refrigeration system 1234yf ecofriendly refrigerant in medium temperature circuit and R245fa in intermediate temperature circuit and R236fa in the low temperature circuit and it was observed that as condenser temperature increasing, the first law efficiencies ($COP_{_Overall}$) and second law efficiencies (exergetic efficiencies) of combined system is decreasing as absorber temperature is increasing. Similarly exergy destruction ratio based on exergy of product is also increasing as condenser temperature is increased.

Table-13(a): Effect of condenser *temperature of VARS on total Thermodynamic performances (First law Performance (COP_overall), with condenser temperature of vapour compression refrigeration system coupled with* double *effect vapour absorption refrigeration H_2O-LiBr system using 1234yf ecofriendly refrigerant in medium temperature circuit and R245fa in intermediate temperature circuit and R236fa in the low temperature circuit.*

Condenser temperature of double effect H_2O-Li/Br vapour absorption refrigeration system (^oC)	Over all COP of system using to low evaporator temperature of 123K using R23fa	Over all COP of system using to intermediate evaporator temperature of 173K using R245fa	Over all COP of system using to intermediate evaporator temperature of 223K using HFO-1234yf
30	1.518	1.555	1.456
32	1.498	1.533	1.432
34	1.474	1.506	1.402
36	1.442	1.471	1.364
38	1.399	1.424	1.314
40	1.338	1.358	1.248
42	1.245	1.258	1.138

Table-13(b): Effect of condenser *temperature of VARS on total thermodynamic performance sin terms of Second law performances (exergetic efficiencies) with condenser temperature of vapour compression refrigeration system coupled with* double *effect vapour absorption refrigeration LiBr system using 1234yf ecofriendly refrigerant in medium temperature circuit and R245fa in intermediate temperature circuit and R236fa in the low temperature circuit.*

Condenser temperature of double effect H_2O-Li/Br vapour absorption refrigeration system (^oC)	Over all exergetic efficiency of system using to low evaporator temperature of 123K using R236fa	Over all exergetic efficiency of system using to intermediate evaporator temperature of 173K using R245fa	Over all exergetic Efficiency of system using to intermediate evaporator temperature of 223K using HFO-1234yf
30	0.6767	0.5726	0.4801
32	0.6726	0.5686	0.4757
34	0.6674	0.5636	0.470
36	0.6605	0.5571	0.4627
38	0.651	0.5430	0.4526
40	0.6369	0.5347	0.4380
42	0.6140	0.5133	0.4150

Table-13(c): Effect of condenser *temperature of VARS on thermodynamic performances such as system exergy destruction ratios with condenser temperature of three vapour compression refrigeration systems coupled double effect vapour absorption refrigeration H_2O-Li/Br system using 1234yf ecofriendly refrigerant in medium temperature circuit and R245fa in intermediate temperature circuit and R236fa in the low temperature*

Condenser temperature of double effect H_2O-Li/Br vapour absorption refrigeration system (^oC)	Over all Exergy Destruction Ratio of system using to low evaporator temperature of 123K using R23fa	Over all Exergy Destruction Ratio of system using to intermediate evaporator temperature of 173K using R245fa	Over all Exergy Destruction Ratio of system using to intermediate evaporator temperature of 223K using HFO-1234yf
30	0.4777	0.7467	1.083
32	0.4868	0.7587	1.102
34	0.4984	0.7743	1.128
36	0.5140	0.7952	1.161
38	0.5362	0.8248	1.209
40	0.5701	0.8701	1.283
42	0.6286	0.9482	1.41

3.14 Effect of condenser temperature on total thermodynamic performances of three cascaded cycles in integrated system

Fig-14(a) to Table-14(c) show the variation of condenser temperature of combined triple effect H_2O-Li/Br vapour absorption refrigeration system cascaded with vapour compression refrigeration system 1234yf ecofriendly refrigerant in medium temperature circuit and R245fa in intermediate temperature circuit and R236fa in the low temperature circuit and it was observed that as condenser temperature increasing, the first law efficiencies ($COP_{Overall}$) and second law efficiencies (exergetic efficiencies) of combined system is decreasing as absorber temperature is increasing. Similarly exergy destruction ratio based on exergy of product is also increasing as condenser temperature is increased.

Table-14(a): Effect of condenser *temperature of VARS on* (%) improvement in the *total Thermodynamic performances (First law Performance (COP_overall), with condenser temperature of vapour compression refrigeration system coupled with* double *effect vapour absorption refrigeration LiBr system using 1234yf ecofriendly refrigerant in medium temperature circuit and R245fa in intermediate temperature circuit and R236fa in the low temperature circuit.*

Condenser temperature of double effect H_2O-Li/Br vapour absorption refrigeration system (^oC)	Over all (%) improvement in First law efficiency ($COP_{Overall}$) of system using to low evaporator temperature of 123K using R236fa (%)	Over all (%) improvement in First law efficiency ($COP_{Overall}$) of system using to intermediate evaporator temperature of 173K using R245fa (%)	Over all (%) improvement in First law efficiency ($COP_{Overall}$) of system using to intermediate temperature evaporator temperature of 223K using HFO-1234yf(%)
30	17.52	20.36	12.73
32	18.83	21.58	13.58
34	20.47	23.17	14.64
36	22.59	25.68	15.99
38	25.44	27.72	17.79
40	29.5	3144.	20.35

Table-14(b): Effect of condenser *temperature of VARS on total thermodynamic terms of Second law performances (exergetic efficiencies) with condenser temperature of vapour compression refrigeration system coupled with* double *effect vapour absorption refrigeration LiBr system using 1234yf ecofriendly refrigerant in medium temperature circuit and R245fa in intermediate temperature circuit and R236fa in the low temperature*

Condenser temperature ofdouble effect H_2O-Li/Br vapour absorption refrigeration system (^oC)	Over all (%) improvement in second law efficiency (exergetic Efficiency) of system using to low evaporator temperature of 123K using R236fa	Over all (%) improvement in second law efficiency (exergetic Efficiency) of system using to intermediate evaporator temperature of 173 using R245fa	Over all (%) improvement in second law efficiency (exergetic Efficiency) of system using to intermediate evaporator temperature of 223K using HFO-1234yf(%)
30	139.3	102.4	69.78
32	143.6	106.0	72.3
34	149.2	110.4	75.49
36	156.5	116.3	79.66
38	166.5	124.4	85.35
40	181.5	136.4	93.6
42	205.8	155.6	106.6

Table-14(c): Effect of condenser temperature of VARS on thermodynamic performances such as system exergy destruction ratios with condenser temperature of three vapour compression refrigeration systems coupled with double effect vapour absorption refrigeration H_2O-Li/Br system using 1234yf ecofriendly refrigerant in medium temperature circuit and R245fa in intermediate temperature circuit and R236fa in the low temperature circuit.

Condenser temperature ofdouble effect H_2O-Li/Br vapour absorption refrigeration system (^oC)	Over all (%) reduction in exergy destruction ratio (EDR) of system using to low evaporator temperature of 123K using R236fa (%)	Over all (%) reduction in exergy destruction ratio (EDR) of system using to intermediate evaporator temperature of 173K using R245fa (%)	Over all (%) reduction in exergy destruction ratio (EDR) of system using to intermediate evaporator temperature of 223K using HFO-1234yf (%)
30	81.16	70.56	57.31
32	81.44	71.07	57.96
34	81.77	71.68	58.75
36	82.17	72.42	59.72
38	82.68	73.35	60.92
40	83.33	74.56	62.48
42	84.2	76.17	64.57

3.15 Effect of evaporator temperature of vapour absorption refrigeration system on percentage improvements in total thermodynamic performances of three cascaded cycles in integrated system

Table-15(a) to Table-15(c) shows the variation of VARS evaporator temperature with thermodynamic performances combined double effect Li/Br vapour absorption refrigeration system cascaded with vapour compression refrigeration system using R1234yf eco-friendly refrigerant and it was observed that as intermediate temperature circuit evaporator temperature is increasing from (-50ºC to -20ºC), the first law efficiency (COP_VCRS) of vapour compression system is increasing while and second law efficiency (exergetic efficiency) of cascaded vapour compression single effect vapour absorption refrigeration system is increasing as intermediate temperature circuit evaporator temperature is increasing. Similarly exergy destruction ratio based on exergy of product is also increasing as MTC temperature circuit evaporator temperature of combined double effectH_2O-Li/Br vapour absorption refrigeration system cascaded with Vapour compression refrigeration.

Table-15(a): Effect of Thermodynamic performances (First law Performances (COP_Overall), with abso VARS evaporator temperature of vapour compression refrigeration system coupled with double effect vapour absorption refrigeration H_2O-Li/Br system using 1234yf ecofriendly refrigerant in medium temperature circuit and R245fa in intermediate temperature circuit and R236fa in the low temperature circuit with condenser temperature of VARS

VARS evaporator temperature ofdouble effect H_2O-Li/Br (ºC)	Over all COP of system using to low evap temp of 123K using R23fa	Over all COP of system using to intermediate evap temp of 173K using R245fa	Over all COP of system using to intermediate evap temp of 223K using HFO-1234yf
3	1.379	1.403	1.288
4	1.404	1.431	1.318
5	1.424	1.452	1.342
6	1.438	1.468	1.359
7	1.450	1.480	1.374
8	1.459	1.49	1.385
9	1.466	1.447	1.393
10	1.471	1.503	1.40

Table-15(b): Effect of Thermodynamic Second law performance (exergetic efficiency) with VARS evaporator temperature of vapour compression refrigeration system coupled with double effect vapour absorption refrigeration H_2O-Li/Br system using 1234yf ecofriendly refrigerant in medium temperature circuit and R245fa in intermediate temperature circuit and R236fa in the low temperature circuit with condenser temperature of VARS

VARS evaporator temp of double effect H_2O-Li/Br (ºC)	Over all exergetic efficiency of system using to low evap temp of 123K using R236fa	Over all exergetic efficiency of system using to intermediate evap temp of 173K using R245fa	Over all exergetic Efficiency of system using to intermediate evap temp of 223K using HFO-1234yf
3	0.6555	0.5491	0.5040
4	0.6598	0.5538	0.4994
5	0.6624	0.5569	0.4929
6	0.6638	0.5589	0.485
7	0.6643	0.5601	0.4761
8	0.6642	0.5604	0.4666
9	0.6635	0.5606	0.4566
10	0.6624	0.5602	0.4463

Table-15(c): Effect of Thermodynamic system exergy destruction ratio with VARS evaporator temperature of vapour compression refrigeration system coupled with double effect vapour absorption refrigeration H_2O-Li/Br system using 1234yf ecofriendly refrigerant in medium temperature circuit and R245fa in intermediate temperature circuit and R236fa in the low temperature circuit with condenser *temperature of VARS*

VARS evaporator temperature of double effect H_2O-Li/Br (ºC)	Over all Exergy Destruction Ratio of system using to low evap temp of 123K usingR23fa	Over all Exergy Destruction Ratio of system using to intermediate evap temp of 173K using R245fa	Over all Exergy Destruction Ratio of system using to intermediate evap temp of 223K using HFO-1234yf
3	0.5255	0.8210	0.9841
4	0.5157	0.8057	1.002
5	0.5098	0.7956	1.029
6	0.5065	0.7892	1.062
7	0.5053	0.7855	110
8	0.5056	0.7849	1.143
9	0.5071	0.7839	1.19
10	0.5096	0.7852	1.241

3.16 Effect of evaporator temperature of vapour absorption refrigeration system on percentage improvements in total thermodynamic performances of three cascaded cycles in integrated system

Table-16(a) to Table-16(c) shows the variation of VARS evaporator temperature with percentage improvement in thermodynamic performances combined double effect Li/Br vapour absorption refrigeration system cascaded with vapour compression refrigeration system using R1234yf eco-friendly refrigerant and it was observed that as intermediate temperature circuit evaporator temperature is increasing from (-50ºC to -20ºC), the first law efficiency (COP_VCRS) of vapour compression system is increasing while and second law efficiency (exergetic efficiency) of cascaded vapour compression single effect vapour absorption refrigeration system is increasing as intermediate temperature circuit evaporator Temperature is increasing. Similarly exergy destruction ratio based on exergy of product is also increasing as intermediate temperature circuit evaporator temperature of combined double effect Li/Br vapour absorption refrigeration system cascaded with Vapour compression refrigeration

Table-16(a): Effect of Thermodynamic performances (First law Performances ($COP_{Overall}$), with VARS evaporator temperature of vapour compression refrigeration system coupled with double effect vapour absorption refrigeration H_2O-Li/Br system using 1234yf ecofriendly refrigerant in medium temperature circuit and R245fa in intermediate temperature circuit and R236fa in the low temperature circuit with condenser temperature of VARS

VARS evaporator temperature of double effect H_2O-Li/Br (ºC)	Over all (%) improvement in First law efficiency (COP_Overall) of system using to low evap temp of 123K using R236fa	Over all (%) improvement in First law efficiency (COP_Overall) of system using to intermediate evap temp of 173K using R245fa	Over all (%) improvement in First law efficiency (COP_Overall) of system using to intermediate evap temp of 223K using HFO-1234yf
3	33.72	36.05	24.91
4	30.68	33.12	22.68
5	28.03	30.54	20.64
6	28.20	25.65	18.75
7	23.47	26.04	16.97
8	21.45	24.03	15.27
9	19.55	22.12	13.64
10	17.75	20.29	12.06

Table-16(b): Effect of thermodynamic second law performance (exergetic efficiency) with VARS evaporator r temperature of vapour compression refrigeration system coupled with double effect VARS H_2O-Li/Br system using 1234yf ecofriendly refrigerant in medium temperature circuit and R245fa in intermediate temperature circuit and R236fa in the low temperature circuit with condenser temperature of VARS

VARS evaporator temperature of double effect H_2O-Li/Br (ºC)	% improvement in Overall exergetic efficiency of system using to low evaporator temperature of 123K using R236fa	% improvement in Overall exergetic efficiency of system using to intermediate evaporator temperature of 173K using R245fa	% improvement in Overall exergetic Efficiency of system using to intermediate evaporator temperature of 223K using HFO-1234yf
3	124.3	87.91	72.42
4	127.0	90.52	71.81
5	131.2	94.42	72.06
6	135.9	99.5	73.17
7	144.0	105.7	74.9
8	152.6	113.2	77.43
9	162.6	121.9	80.74
10	174.4	132.1	84.9

Table-16(c): Effect of Thermodynamic system exergy destruction ratio with VARS evaporator *temperature of vapour compression refrigeration system coupled with* double *effect vapour absorption refrigeration H_2O-LiBr system using 1234yf ecofriendly refrigerant in medium temperature circuit and R245fa in intermediate temperature circuit and R236fa in the low temperature circuit with* condenser *temperature of VARS*

VARS evap temp of double effect H_2O-Li/Br (ºC)	% improvement in Overall EDR of system using to low evaporator temperature of 123K using R23fa	% improvement in Overall EDR of system using to intermediate evaporator temperature of 173K using R245fa	% improvement in Overall EDR of system using to intermediate evap temp of 223K using HFO-1234yf
3	78.30	66.10	59.37
4	78.87	66.98	58.93
5	79.54	68.06	58.69
6	80.29	69.29	58.67
7	81.10	70.62	58.84
8	81.96	72.03	59.21
9	82.86	73.50	59.77
10	83.79	75.02	60.53

3.17Effect of various thermodynamic parameters such as temperature of MTC evaporator on overall system performances of cascade evaporators using ecofriendly refrigerants

In this section, the effect of various cascaded evaporator have been discussed in detail as given below

Table-17(a) to Table-17(c) show the variation of medium temperature circuit evaporator temperature of combined double effect Li/Br vapour absorption refrigeration system cascaded with vapour compression refrigeration system using 1234yf ecofriendly refrigerant in medium temperature circuit and R245fa in intermediate temperature circuit and R236fa in the low temperature circuit and it was observed that as Low temperature circuit evaporator Temperature is increasing from (-50ºC to -20ºC), the first law efficiency($COP_{_Cascade}$) of cascaded vapour compression single effect vapour absorption system is increasing while and second law efficiency (exergetic efficiency) of cascaded vapour compression double effect vapour absorption refrigeration system is decreasing as MTC temperature is increasing. Similarly exergy destruction ratio based on exergy of product is also increasing as medium temperature circuit evaporator temperature of combined double effect H_2O-Li/Br vapour absorption refrigeration system cascaded with vapour compression refrigeration system using 1234yf ecofriendly refrigerant in medium temperature circuit and R245fa in intermediate temperature circuit and R236fa in the low temperature circuit is decreased.

Table17 (a): Effect of MTC evaporator temperature of medium temperature circuit using HFO-1234yf refrigerants on the thermodynamic performance (COP_overall), of VCRS coupled with vapour absorption refrigeration double effect H_2O-Li/Br system using 1234yf ecofriendly refrigerant in medium temperature circuit and R245fa in intermediate temperature circuit and R236fa in the low temperature circuit

MTC evaporator temperature of medium temperature circuit using HFO-1234yf refrigerants (ºC)	Over all first law efficiency ($COP_{_Overall}$) of system using to low evaporator temperature of 123K using R236fa	Over all first law efficiency ($COP_{_Overall}$) of system using to intermediate evaporator temperature of 173K using R245fa	Over all first law efficiency ($COP_{_Overall}$) of system using to intermediate evaporator temperature of 223K using HFO-1234yf
-20	1.547	1.615	1.781
-25	1.539	1.60	1.709
-30	1.528	1.583	1.64
-35	1.515	1.564	1.572
-40	1.499	1.541	1.507
-45	1.480	1.517	1.445
-50	1.459	1.49	1.385

Table-17(b): Effect of evaporator temperature of medium temperature circuit using HFO-1234yf refrigerants on the thermodynamic performance (exergetic efficiency) of VCRS coupled with double effect vapour absorption refrigeration H_2O-Li/Br system using 1234yf ecofriendly refrigerant in medium temperature circuit and r245fa in intermediate temperature circuit and R236fa in the low temperature circuit

MTC evaporator temperature of medium temperature circuit using HFO-1234yf refrigerants (ºC)	Over all second law efficiency (exergetic efficiency) of system using to low evap temperature of 123K using R236fa	Over all second law efficiency (exergetic efficiency) of system using to intermediate evaporator temperature of 173K using R245fa	Over all second law efficiency of system using to intermediate evaporator temperature of 223K using HFO-1234yf
-20	0.6614	0.4736	0.4833
-25	0.6672	0.4949	0.4850
-30	0.6711	0.5137	0.4846
-35	0.6728	0.5298	0.4823
-40	0.6724	0.5430	0.4785
-45	0.6695	0.5533	0.4732
-50	0.6642	0.5606	0.4666

Table-17(c): Effect of evaporator temperature of medium temperature circuit using HFO-1234yf refrigerants on the thermodynamic performances system EDR of VCRS coupled with vapour absorption refrigeration double effect H_2O-Li/Br system using 1234yf ecofriendly refrigerant in medium temperature circuit and R245fa in intermediate temperature circuit and R236fa in the low temperature circuit

MTC medium evaporator temperature circuit using HFO-1234yf refrigerants(ºC)	Over all exergy destruction ratio (EDR) of system using to low evaporator temperature of 123K using R236fa	Over all exergy destruction ratio (EDR) of system using to intermediate evaporator temperature of 173K using R245fa	Over all exergy destruction ratio (EDR) of system using to intermediate evaporator temperature of 223K using HFO-1234yf
-20	0.5002	1.112	1.069
-25	0.4869	1.021	1.062
-30	0.4762	0.9466	1.064
-35	0.4742	0.8875	1.073
-40	0.4751	0.8415	1.090
-45	0.4812	0.8072	1.113
-50	0.5056	0.7839	1.143

3.18Effect of various thermodynamic parameters such as temperature of MTC evaporator on percentage improvement in overall system performances of cascade evaporators using ecofriendly refrigerants

Table-18(a) to Table-18(c) show the variation of medium temperature circuit evaporator temperature of combined triple effect Li/Br vapour absorption refrigeration system cascaded with vapour compression refrigeration system using 1234yf ecofriendly refrigerant in medium temperature circuit and R245fa in intermediate temperature circuit and R236fa in the low temperature circuit and it was observed that as Low temperature circuit evaporator Temperature is increasing from (-50^{o}C to -20^{o}C), the first law efficiency ($COP_{_Cascade}$) of cascaded vapour compression single effect vapour absorption system is increasing while and second law efficiency (exergetic efficiency) of cascaded vapour compression half effect vapour absorption refrigeration system is decreasing as generator temperature is increasing. Similarly exergy destruction ratio based on exergy of product is also increasing as medium temperature circuit evaporator temperature of combined double effect H_2O-Li/Br vapour absorption refrigeration system cascaded with vapour compression refrigeration system using 1234yf ecofriendly refrigerant in medium temperature circuit and R245fa in intermediate temperature circuit and R236fa in the low temperature circuit is increased.

Table18(a): Effect of evaporator Temperature of medium temperature circuit using HFO-1234yf refrigerants on the thermodynamic performance such as First law Performance (COP_overall), of vapour compression refrigeration system coupled with double effect vapour absorption refrigeration H_2O-Li/Br system using 1234yf ecofriendly refrigerant in medium temperature circuit and R245fa in intermediate temperature circuit and R236fa in the low temperature circuit

MTC evaporator temperature of medium temperature circuit using HFO-1234yf refrigerants (^{o}C)	Over all (%) improvement in first law efficiency ($COP_{_Overall}$) of system using to low evaporator temperature of 123K using R236fa (%)	Over all (%) improvement in first law efficiency ($COP_{_Overall}$) of system using to intermediate evaporator temperature of 173K using R245fa (%)	Over all (%) improvement in first law efficiency ($COP_{_Overall}$) of system using to intermediate evaporator temperature of 223K using HFO-1234yf (%)
-20	28.80	34.42	48.31
-25	28.13	33.23	42.31
-30	27.24	31.81	36.5
-35	26.12	30.17	30.89
-40	24.78	28.32	25.49
-45	23.23	26.27	20.28
-50	21.45	24.03	15.27

Table-18(b): Effect of evaporator temperature of medium temperature circuit using HFO-1234yf refrigerants on the thermodynamic performance such as Second law performance (Exergetic efficiency) of vapour compression refrigeration system coupled with double effect vapour absorption refrigeration H_2O-Li/Br system using 1234yf ecofriendly refrigerant in medium temperature circuit and R245fa in intermediate temperature circuit and R236fa in the low temperature circuit

MTC evaporator temperature of medium temperature circuit using HFO-1234yf refrigerants (^{o}C)	Over all (%) improvement in second law efficiency (exergetic Efficiency) of system using to low evaporator temperature of 123K using R236fa (%)	Over all (%) improvement in second law efficiency (exergetic Efficiency) of system using to intermediate evaporator temperature of 173K using R245fa (%)	Over all (%) improvement in second law efficiency (exergetic Efficiency) of system using to intermediate evaporator temperature of 223K using HFO-1234yf (%)
-20	151.5	80.07	83.76
-25	153.7	88.18	84.40
-30	155.2	95.23	84.25
-35	155.8	101.4	83.40
-40	155.7	106.5	81.93
-45	154.6	110.4	79.92
-50	152.6	113.2	77.43

Table-18(c): Effect of MTC evaporator temperature of medium temperature circuit using HFO-1234yf refrigerants on the thermodynamic performances in terms of system exergy destruction ratio of vapour compression refrigeration system coupled with double effect vapour absorption refrigeration H_2O-Li/Br system using 1234yf ecofriendly refrigerant in medium temperature circuit and R245fa in intermediate temperature circuit and R236fa in the low temperature circuit

MTC evaporator temperature of medium temperature circuit using HFO-1234yf refrigerants (°C)	Over all (%) reduction in exergy destruction ratio (EDR) of system using to low evaporator temperature of 123K using R236fa (%)	Over all (%) reduction in exergy destruction ratio (EDR) of system using to intermediate evaporator temperature of 173K using R245fa (%)	Over all (%) reduction in exergy destruction ratio (EDR) of system using to intermediate evaporator temperature of 223K usingHFO-1234yf (%)
-20	81.74	60.33	61.80
-25	82.2	63.58	62.10
-30	82.51	66.22	62.04
-35	82.65	68.33	61.70
-40	82.61	69.97	61.11
-45	82.39	71.19	60.27
-50	81.96	72.03	59.21

3.19Effect of various thermodynamic parameters such as temperature of ITC evaporator on overall system performances of cascade evaporators using ecofriendly refrigerants

Table-19(a-c) shows the variation of Low temperature circuit evaporator Temperature of combined triple effect Li/Br vapour absorption refrigeration system cascaded with Vapour compression refrigeration system using 1234yf ecofriendly refrigerant in medium temperature circuit and R245fa in intermediate temperature circuit and R236fa in the low temperature circuit and it was observed that as Low temperature circuit evaporator temperature is increasing from (-70°C to -30°C), the first law efficiency(COP_VCRS) of cascaded vapour compression system is increasing while and second law efficiency (exergetic efficiency) of Cascaded vapour compression single effect vapour absorption refrigeration system is increasing as Low temperature circuit evaporator Temperature is increasing. Similarly exergy destruction ratio based on exergy of product is also increasing as Low temperature circuit evaporator Temperature of combined double effect H_2O-Li/Brvapour absorption refrigeration system cascaded with Vapour compression refrigeration system using R134a eco-friendly refrigerants decreased.

Table-19(a): Effect of ITC evaporator Temperature of intermediate temperature circuit using R-245fa refrigerants(°C) on Thermodynamic performances in terms of first law performance (COP_Overall), with ITC evaporator temperature of vapour compression refrigeration system coupled with double effect vapour absorption refrigeration H_2O-Li/Br system using 1234yf ecofriendly refrigerant in medium temperature circuit and R245fa in intermediate temperature circuit and R236fa in the low temperature circuit with evaporator temperature of VARS

ITC evaporator temperature of intermediate temp circuit using R-245fa refrigerants (°C)	Over all first law efficiency ($COP_{_Overall}$) of system using to low evaporator temperature of 123K using R236fa	Over all first law efficiency ($COP_{_Overall}$) of system using to intermediate evaporator temperature of 173K using R245fa	Over all first law efficiency ($COP_{_Overall}$) of system using to intermediate evaporator temperature of 223K using HFO-1234yf
-70	1.63	1.68	1.385
-75	1.590	1.640	1.385
-80	1.553	1.601	1.385
-85	1.520	1.563	1.385
-90	1.487	1.526	1.385
-95	1.459	1.45	1.385
-100	1.433	1.454	1.385

Table-19(b): Effect of ITC evaporator temperature of intermediate temperature circuit using R-245fa refrigerants (°C) on second law performance (Exergetic efficiency) with ITC evaporator temperature of vapour compression refrigeration system coupled with double effect vapour absorption refrigeration H_2O-Li/Br system using 1234yf ecofriendly refrigerant in medium temperature circuit and R245fa in intermediate temperature circuit and R236fa in the low temperature circuit,

ITC evaporator temperature of intermediate temperature circuit using R-245fa refrigerants (°C)	Over all second law efficiency (exergetic Efficiency) of system using to low evaporator temperature of 123K using R236fa	Over all second law efficiency (exergetic efficiency) of system using to intermediate evaporator temperature of 173K using R245fa	Over all second law efficiency (exergetic efficiency) system using to intermediate evaporator temperature of 223K using HFO-1234yf
-70	0.6080	0.5775	0.4665
-75	0.6175	0.5759	0.4665
-80	0.6277	0.5734	0.4665

-85	0.6388	0.570	0.4665
-90	0.6509	0.5657	0.4665
-95	0.6642	0.5606	0.4665
-100	0.6788	0.5546	0.4665

Table-19(c): Effect of ITC evaporator Temperature of intermediate temperature circuit using R-245fa refrigerants(°C) on system exergy destruction ratio with absorber temperature of vapour compression refrigeration system coupled with double effect vapour absorption refrigeration H_2O-Li/Br system using 1234yf ecofriendly refrigerant in medium temperature circuit and R245fa in intermediate temperature circuit and R236fa in the low temperature cycle.

ITC evaporator temperature of intermediate temp circuit using R-245fa refrigerants (°C)	Over all exergy destruction ratio (EDR) of system using to low evaporator temperature of 123K using R236fa	Over all exergy destruction ratio (EDR)) of system using to intermediate evaporator temp of 173K using R245fa	Over all exergy destruction ratio (EDR) of system using to intermediate evaporator temperature of 223K using HFO-1234yf
-70	0.6646	0.7316	1.143
-75	0.6195	0.7364	1.143
-80	0.5931	0.7439	1.143
-85	0.5654	0.7544	1.143
-90	0.5363	0.7677	1.143
-95	0.5056	0.7839	1.143
-100	0.4733	0.8030	1.143

3.20Effect of various thermodynamic parameters such as temperature of ITC evaporator on overall percentage improvement of system performances of cascade evaporators using ecofriendly refrigerants

Table-20(a) to Table-20 (c) shows the variation of Low temperature circuit evaporator Temperature on overall percentage improvement of thermodynamic performance of combined double effect H_2O-Li/Br vapour absorption refrigeration system cascaded with Vapour compression refrigeration system using 1234yf ecofriendly refrigerant in medium temperature circuit and R245fa in intermediate temperature circuit and R236fa in the low temperature circuit and it was observed that as Low temperature circuit evaporator temperature is increasing from (-70°C to -30°C), the first law efficiency(COP_VCRS) of cascaded vapour compression system is increasing while and second law efficiency (exergetic efficiency) of Cascaded vapour compression single effect vapour absorption refrigeration system is increasing as Low temperature circuit evaporator Temperature is increasing. Similarly exergy destruction ratio based on exergy of product is also increasing as Low temperature circuit evaporator Temperature of combined double effectH_2O-Li/Br vapour absorption refrigeration system cascaded with Vapour compression refrigeration system using R134a eco-friendly refrigerants decreased.

Table-20(a): Effect of evaporator Temperature of intermediate temperature circuit using R-245fa refrigerants(°C) on Thermodynamic performances (First law Performance (COP_Overall) with ITC evaporator temperature of vapour compression refrigeration system coupled with double effect vapour absorption refrigeration H_2O-Li/Br system using 1234yf ecofriendly refrigerant in medium temperature circuit and R245fa in intermediate temperature circuit and R236fa in the low temperature circuit with evaporator temperature of VARS

ITC evaporator temperature of intermediate temperature circuit using R-245fa refrigerants (°C)	Over all percentage improvement of thermodynamic performance i.e. first law efficiency ($COP_{Overall}$) of system using to low evaporator temperature of 123K using R236fa	Over all percentage improvement of thermodynamic performance i.e. first law efficiency ($COP_{Overall}$) of system using to intermediate evaporator temperature of 173K using R245fa	Over all percentage improvement of thermodynamic performance i.e. first law efficiency ($COP_{Overall}$) of system using to intermediate evaporator temperature of 223K using HFO-1234yf
-70	35.69	39.83	15.27
-75	32.38	36.55	15.27
-80	29.31	33.33	15.27
-85	26.46	30.16	15.27
-90	23.84	27.06	15.27
-95	21.45	24.03	15.27
-100	19.31	21.06	15.27

Table-20(b): Effect of ITC evaporator temperature of intermediate temperature circuit using R-245fa refrigerants(°C) on percentage improvement of Second law performance (exergetic efficiency) with ITC evaporator temperature of vapour compression refrigeration system coupled with double effect vapour absorption refrigeration H_2O-Li/Br system using 1234yf ecofriendly refrigerant in medium temperature circuit and R245fa in intermediate temperature circuit and R236fa in the low temperature circuit with evaporator temperature of VARS

ITC evaporator temperature of intermediate temperature circuit using R-245fa refrigerants (°C)	Over all second law efficiency (exergetic Efficiency) of system using to low evaporator temperature of 123K using R236fa	Over all second law efficiency (exergetic Efficiency) of system using to intermediate evaporator temperature of 173K using R245fa	Over all second law efficiency (exergetic Efficiency) system using to intermediate evaporator temperature of 223K using HFO-1234yf
-70	131.2	119.6	77.43
-75	134.8	119.0	77.43
-80	138.7	118.0	77.43
-85	142.9	116.7	77.43
-90	147.5	115.1	77.43
-95	1526	113.2	77.43
-100	158.1	110.9	77.43

Table-20(c): Effect of evaporator temperature of intermediate temperature circuit using R-245fa refrigerants (°C) on Thermodynamic performances i.e. System exergy destruction ratio with ITC evaporator temperature of vapour compression refrigeration system coupled with double effect vapour absorption refrigeration H_2O-Li/Br system using 1234yf ecofriendly refrigerant in medium temperature circuit and R245fa in intermediate temperature circuit and R236fa in the low temperature cycle.

ITC evaporator Temperature of intermediate temperature circuit using R-245fa refrigerants (°C)	Over all percentage decrement of thermodynamic performance i.e. exergy destruction ratio (EDR) of system using to low evaporator temperature of 123K using R236fa	Over all percentage decrement exergy destruction ratio (EDR) of system using to intermediate evaporator temperature of 173K using R245fa	Over all percentage decrement exergy destruction ratio (EDR) of system using to intermediate evaporator temperature of 223K using HFO-1234yf (%)
-70	77.0	73.89	59.21
-75	77.89	73.72	59.21
-80	78.84	73.45	59.21
-85	79.82	73.08	59.21
-90	80.86	72.61	59.21
-95	81.96	72.03	59.21
-100	83.11	71.35	59.21

3.21Effect of ultralow evaporator temperature on total thermodynamic performances of combined three cascaded cycles in integrated system

Table-21(a) to Table-21(c) shows the variation of intermediate temperature circuit evaporator temperature with percentage improvement in thermodynamic performances combined triple effect Li/Br vapour absorption refrigeration system cascaded with vapour compression refrigeration system using R1234yf eco-friendly refrigerant and it was observed that as intermediate temperature circuit evaporator temperature is increasing from (-50°C to -20°C), the first law efficiency (COP_VCRS) of vapour compression system is increasing while and second law efficiency (exergetic efficiency) of cascaded vapour compression single effect vapour absorption refrigeration system is increasing as intermediate temperature circuit evaporator Temperature is increasing. Similarly exergy destruction ratio based on exergy of product is also increasing as intermediate temperature circuit evaporator temperature of combined triple effect Li/Br vapour absorption refrigeration system cascaded with Vapour compression refrigeration system using R236fa eco-friendly refrigerant is decreased.

Table-21(a): Effect of LTC evaporator temperature on thermodynamic performances (first law performance ($COP_{_Overall}$), of vapour compression refrigeration system coupled with double effect vapour absorption refrigeration H_2O-Li/Br system using 1234yf ecofriendly refrigerant in medium temperature circuit and R245fa in intermediate temperature circuit and R236fa in the low temperature circuit

evaporator Temperature of ultra-low temperature circuit using R-236fa refrigerants (°C)	Over all first law efficiency ($COP_{_Overall}$) of system using to low evaporator temperature of 123K using R236fa	Over all first law efficiency ($COP_{_Overall}$) of system using to intermediate evaporator temperature of 173K using R245fa	Over all first law efficiency ($COP_{_Overall}$) of system using to intermediate evaporator temperature of 223K using HFO-1234yf (%)
-120	1.544	1.490	1.385
-125	1.530	1.490	1.385
-130	1.516	1.490	1.385
-135	1.502	1.490	1.385
-140	1.487	1.490	1.385
-145	1.473	1.490	1.385

-150	1.459	1.490	1.385
-155	1.445	1.490	1.385
160	1.431	1.490	1.385

Table-21(b): Effect of LTC evaporator *temperature on thermodynamic performances (second law performances (exergetic efficiencies), of vapour compression refrigeration system coupled with* double *effect vapour absorption refrigeration H_2O-Li/Br system using 1234yf ecofriendly refrigerant in medium temperature circuit and R245fa in intermediate temperature circuit and R236fa in the low temperature circuit*

evaporator Temperature of ultra-low temperature circuit using R-236fa refrigerants (°C)	Over all second law efficiency (exergetic Efficiency) of system using to low evaporator temperature of 123K using R236fa	Over all second law efficiency (exergetic Efficiency) of system using to intermediate evaporator temperature of 173K using R245fa (%)	Over all second law efficiency (exergetic Efficiency) of system using to intermediate evaporator temperature of 223K using HFO-1234yf (%)
-120	0.700	0.5606	0.4666
-125	0.6959	0.5606	0.4666
-130	0.6911	0.5606	0.4666
-135	0.6856	0.5606	0.4666
-140	0.6793	0.5606	0.4666
-145	0.6642	0.5606	0.4666
-150	0.6698	0.5606	0.4666
-155	0.6553	0.5606	0.4666
155	0.6456	0.5606	0.4666

Table-21(c): Effect of LTC evaporator *temperature Thermodynamic performances (First law Performance (COP_VARS), Second law performance (exergetic efficiency) and system exergy destruction ratio with ultra-evaporator temperature of vapour compression refrigeration system coupled with* double *effect vapour absorption refrigeration H_2O-Li/Br system using 1234yf ecofriendly refrigerant in medium temperature circuit and R245fa in intermediate temperature circuit and R236fa in the low temperature circuit*

evaporator Temperature ofultra low temperature circuit using R-236fa refrigerants (°C)	Over all exergy destruction ratio (EDR) of system using to low evaporator temperature of 123K using R236fa (%)	Over all exergy destruction ratio (EDR) of system using to intermediate evaporator temperature of 173K using R245fa (%)	Over all exergy destruction ratio (EDR) of system using to intermediate evaporator temperature of 223K using HFO-1234yf (%)
-120	0.4286	0.7839	1.143
-125	0.4370	0.7839	1.143
-130	0.4469	0.7839	1.143
-135	0.4585	0.7839	1.143
-140	0.4721	0.7839	1.143
-145	0.4877	0.7839	1.143
-150	0.5056	0.7839	1.143
-155	0.5259	0.7839	1.143
160	0.5489	0.7839	1.143

3.22Effect of ultra-low evaporator temperature on percentage improvements in total thermodynamic performances of three cascaded cycles in integrated system

Table-22(a) to Table-22(c) shows the variation of intermediate temperature circuit evaporator temperature with percentage improvement in thermodynamic performances combined triple effect Li/Br vapour absorption refrigeration system cascaded with vapour compression refrigeration system using R1234yf eco-friendly refrigerant and it was observed that as intermediate temperature circuit evaporator temperature is increasing from (-50°C to -20°C), the first law efficiency (COP_VCRS) of vapour compression system is increasing while and second law efficiency (exergetic efficiency) of cascaded vapour compression single effect vapour absorption refrigeration system is increasing as intermediate temperature circuit evaporator Temperature is increasing. Similarly exergy destruction ratio based on exergy of product is also increasing as intermediate temperature circuit evaporator temperature of combined triple effect Li/Br vapour absorption refrigeration system cascaded with Vapour compression refrigeration system using R236fa eco-friendly refrigerant is decreased.

Table-22(a): Effect of LTC evaporator *temperature on thermodynamic performances (first law performance ($COP_{_Overall}$), of vapour compression refrigeration system coupled with*double *effect vapour absorption refrigeration H_2O-Li/Br system using 1234yf ecofriendly refrigerant in medium temperature circuit and R245fa in intermediate temperature circuit and R236fa in the low temperature circuit*

evaporator Temperature of ultra-low temperature circuit using R-236fa refrigerants (°C)	Over all (%) improvement in first law efficiency ($COP_{_overall}$) of system using to low evaporator temperature of 123K using R236fa	Over all (%) improvement in first law efficiency ($COP_{_overall}$) of system using to intermediate evaporator temperature of 173K using R245fa	Over all (%) improvement in first law efficiency ($COP_{_overall}$) of system using to intermediate evaporator temperature of 223K using HFO-1234yf (%)
-120	28.56	24.03	15.27
-125	27.39	24.03	15.27
-130	26.21	24.03	15.27
-135	25.02	24.03	15.27
-140	23.83	24.03	15.27
-145	22.64	24.03	15.27
-150	21.93	24.03	15.27
-155	20.28	24.03	15.27
160	19.11	24.03	15.27

Table-22(b): Effect of LTC evaporator temperature on thermodynamic performances (second law performances (exergetic efficiencies), of vapour compression refrigeration system coupled with double effect vapour absorption refrigeration H_2O-Li/Br system using 1234yf ecofriendly refrigerant in medium temperature circuit and R245fa in intermediate temperature circuit and R236fa in the low temperature circuit

evaporator Temperature ofultra low temperature circuit using R-236fa refrigerants (°C)	Over all (%) reduction in exergy destruction ratio (EDR) of system using to low evaporator temperature of 123K using R236fa	Over all (%) reduction in exergy destruction ratio (EDR) of system using to intermediate evaporator temperature of 173K using R245fa	Over all (%) reduction in exergy destruction ratio (EDR) of system using to intermediate evaporator temperature of 223K using HFO-1234yf
-120	166.2	113.20	77.43
-125	164.5	113.20	77.43
-130	162.8	113.20	77.43
-135	160.7	113.20	77.43
-140	158.3	113.20	77.43
-145	155.6	113.20	77.43
-150	152.6	113.20	77.43
-155	149.2	113.20	77.43
-160	142.2	113.20	77.43

Table-22(c): Effect of LTC evaporator temperature Thermodynamic performances system exergy destruction ratio with absorber temperature of vapour compression refrigeration system coupled with double *effect vapour absorption refrigeration H_2O-LiBr system using 1234yf ecofriendly refrigerant in medium temperature circuit and R245fa in intermediate temperature circuit and R236fa in the low temperature circuit*

evaporator Temp of ultra-low temperature circuit using R-236fa refrigerants (°C)	Over all (%) decrement in system exergy destruction ratio of system using to low evap temp of 123K using R236fa (%)	Over all (%) decrement in system exergy destruction ratio of system using to intermediate evap temp of 173K using R245fa	Over all (%) decrement in system exergy destruction ratio of system using to intermediate evap temp of 223K usingHFO-1234yf
-120	84.71	72.03	59.29
-125	84.41	72.03	59.29
-130	84.05	72.03	59.29
-135	83.64	72.03	59.29
-140	83.16	72.03	59.29
-145	82.6	72.03	59.29
-150	81.96	72.03	59.29
-155	59.21	59.29	72.03

4. Conclusions and Recommendations

The following conclusions were drawn from present investigations.

- Thermodynamic performance in terms of first law efficiency ($COP_{_Cascade_System}$) of combined cascaded vapour compression double effect vapour absorption refrigeration system using 1234yf ecofriendly refrigerant in medium temperature circuit and R245fa in intermediate tempe138.1rature circuit and R236fa in the low temperature circuit than R1234yf ecofriendly refrigerant in medium temperature circuit and R245fa in intermediate temperature circuit and R236fa in the low temperature circuit.
- Thermodynamic performance in terms of second law

efficiency(exergetic efficiency) of combined cascaded vapour compression triple effect vapour absorption refrigeration system using HFC-134a ecofriendly refrigerant in medium temperature circuit and R245fa in intermediate temperature circuit and R236fa in the low temperature circuit is higher than the combined cascaded vapour compression single effect vapour absorption refrigeration system using 1234yf ecofriendly refrigerant in medium temperature circuit and R245fa in intermediate temperature circuit and R236fa in the low temperature circuit than R1234yf ecofriendly refrigerant in medium temperature circuit and R245fa in intermediate temperature circuit and R236fa in the low temperature circuit.

- As Low temperature circuit evaporator temperature is decreasing , the first law performances (($COP_{_Cascade_System}$) and second law efficiency (exergetic efficiency) of cascaded vapour compression double effect vapour absorption refrigeration system is decreasing and exergy destruction ratio of combined vapour compression-single effect vapour absorption system is increasing.
- The best thermodynamic performances in terms of first and second law efficiencies have been found by using R152a in medium temperature circuit.
- Use of hydrocarbon is also feasible by considering safety measures because hydrocarbons are flammable and R600a gives best thermodynamic performances in the low temperature circuit.
- Thermodynamic performances in terms of first and second law efficiencies also affected by variation of generator temperature and also decreasing as generator temperature is increasing.
- Thermodynamic performances in terms of first and second law efficiencies also affected by variation of absorber temperature and also decreasing as absorber temperature is increasing.
- Thermodynamic performances in terms of first and second law efficiencies also affected by variation of condenser temperature and also decreasing as condenser temperature is increasing.
- Thermodynamic performances in terms of first and second law efficiencies also affected by variation of approach (temperature over lapping) and also decreasing as temperature over lapping is increasing because larger value of temperature overlapping (approach) in each cascade heat exchanger circuit reduces the COP and exergetic efficiency of the system.

References

[1] Lee T-S, Liu C-H, Chen T-W. Thermodynamic analysis of optimal condensing temperature of cascade-condenser in CO_2/NH_3 cascade refrigeration systems. International Journal of Refrigeration. 2006;29:1100-8.

[2] Wu W, Wang B, Shi W, Li X. An overview of ammonia-based absorption chillers and heat pumps. Renewable and Sustainable Energy Reviews. 2014; 31:681-707.

[3] Kaushik, S.C., Arora, A., Energy and Exergy analysis of single effect and series flow double effect waterlithium bromide absorption refrigeration systems, International Journal of Refrigeration, Vol. 32, (2009), pp. (1247-1258)

[4] A Arora and S.C. Kaushik [2009]Theoretical analysis of $LiBr/H_2O$ absorption refrigeration system, International Journal of Energy Research, 33(15), page-1321 - 1340

[5] S.A.Tassou, J.S. Lewis, Y.T. Ge, A. Hadawey, I. Chaer, A review of emerging technologies for food refrigeration applications, Applied. Thermal Engineering. 30 (2010)263–276

[6] S.A.Tassou, J.S. Lewis, Y.T. Ge, A. Hadawey, I. Chaer, A review of emerging technologies for food refrigeration applications, Applied. Thermal Engineering. 30 (2010)263–276.

[7] R. Cabello, D. SánCHEz, R. Llopis, J. Catalán, L. Nebot-Andrés, E. Torrella, Energy evaluation of R152a as drop in replacement for R134a in cascade refrigeration plants, App. Thermal. Engineering. 110 (2017) 972–984.

[8] A.Messineo, R744–R717 Cascade Refrigeration System: Performance evaluation compared with a HFC Two-Stage System, ICAEE 2011, Energy Procedia 14 (2012) 56–65.

[9] R.S. Mishra [2018] Performance parameters optimization of cascade refrigeration system using ecofriendly refrigerants, International Journal of Research in Engineering and Innovation (IJREI), ISSN (Online): 2456-6934 , Vol-2, Issue-6 , 602-609 Vol-2, Issue-6 (2018), 602-609

[10] L.Kairouani, E. Nehdi, Cooling performance and energy saving of a compression-absorption refrigeration system assisted by geothermal energy, Appl. Therm. Engg. 26 (2006) 288–294.

[11] Gomri, R., Second law comparison of single effect and double effect vapour absorption refrigeration systems, Energy Conversion and Management,Vol. 50, (2009), pp.1279-1287).

[12] Rogdakis ED, Antonopoulos KA. Performance of a low- temperature NH_3H_2O absorption-refrigeration system. Energy. 1992;17:477-84.

[13] Kilic, M. and Kaynakli, O., Theoretical study on the effect of operating conditions on performance of absorption refrigeration system, Energy Conversion and Management, Vol. 48, (2007), pp.(599-607).

[14] Rabah Gomri R and Hakimi R [2009] second law analysis of double effect vapour absorption cooler system , International journal of energy conversion and management, Elsevier , Vol-49, page-3343-48.

[15] Garimella S, Brown AM, Nagavarapu AK. Waste heat driven absorption/vapor-compression cascade refrigeration system for megawatt scale, high-flux, low-temperature cooling. International Journal of Refrigeration. 2011;34:1776-85

[16] S.B. Riffat N. Shankland [1993] Integration of absorption and vapour-compression systems**,** Applied Energy**,** Vol-46, Issue-4**,**1993, Pages 303-316.

[17] Yi Chena,b, Wei Hana, Liuli Sunc , Hongguang Jina A new absorption–compression refrigeration system using a mid-temperature heat source for freezing application ,The 7th International Conference on Applied Energy – ICAE2015,Energy Procedia 75 (2015) 560 – 565

[18] Fernández-Seara J, Sieres J, Vázquez M. Compression–absorption cascade refrigeration system. Applied Thermal Engineering. 2006;26:502-12.

[19] R.S. Mishra [2019] Thermal performance of cascaded vapour compression absorption systems, International Journal of Research in Engineering and Innovation (IJREI), ISSN (Online): 2456-6934, Vol-3, Issue-1 (2019), page-61-67.

[20] M.Azhar, M.A. Siddiqui, Optimization of operating temperatures in the gas operated single to triple effect vapour absorption refrigeration cycles, Int. J.Refrigeration. 82 (2017) 401–425.

[21] M.Azhar, M.A. Siddiqui, Thermodynamic analysis of a gas operated triple effect absorption cycle, Int. J. Innovative Res. Sci. Eng. Technol. 2 (5) (2013)1610–1616.

[22] R.S. Mishra [2019] Use of fourth generation ecofriendly refrigerants in two and three cascade refrigeration systems for reducing global warming and ozone depletion, International Journal of Research in Engineering and Innovation (IJREI), ISSN (Online): 2456-6934, Vol-2, Issue-2 (2018), page-20-208.

[23] V. Jain, S.S. Kachhwaha, G. Sachdeva, Thermodynamic performance analysis of a vapor compression–absorption cascaded refrigeration system, Energy Convers. Manage. 75 (2013) 685–700.16S.

[24] A.K.Pratihar, S.C. Kaushik, R.S. Agarwal, Simulation of an ammonia–water compression absorption refrigeration system for water chilling application, Int J Refrigeration 33 (2010) 1386–1394.

[25] R.S. Mishra[2019] Performance evaluation of solar assisted half effect Li/Br vapour absorption refrigeration system cascaded with vapour compression refrigeration system using eco-friendly refrigerants, International Journal of Advance Research and Innovation , ISSN 2347 - 3258 , Volume 7 Issue 2 ,page-156-161.

[26] R.S. Mishra [2018] Comparison of thermal performances of single effect, double effect and triple effect LiBr-H2O absorption system cascaded with vapour compression refrigeration systems using ecofriendly refrigerants, International Journal of Research in Engineering and Innovation (IJREI), ISSN (Online): 2456-6934, Vol-2, Issue-6 (2018), 610-621.
[27] R.Ayala, C.L. Heard, F. Holland, Ammonia/lithium nitrateabsorption/compression refrigeration cycle, Part I, Applied. Thermal . Engineering. 17 (3)(1997) 223–233.
[28]]R.S. Mishra [2019] Comparison of half effect absorption-compression cascaded refrigeration system using thermodynamic (energy-exergy) analysis. International Journal of Research in Engineering and Innovation (IJREI), ISSN (Online): 2456-6934, Vol-3, Issue-1 (2019), page-6-11.
[29] M. Dixit, A. Arora, S.C. Kaushik, Thermodynamic and thermo economic analyses of two stage hybrid absorption compression refrigeration system, App. Thermal Engg. 113 (2017) 120–131.
[30] C.Cimsit, I.T. Ozturk, [2012], Analysis of compression-absorption cascade refrigeration cycles, App. Therm. Engineering. 40 , page- 311–317
[31] S.Eini, H. Shahhosseini, N. Delgarm, M. Lee, [2016], A. Bahadori, Multi-objective-optimization of a cascade refrigeration system: exergetic, economic,environmental, and inherent safety analysis, Applied. Thermal. Engineering. 107, page-804–817
[32] S. Bhattacharyya, S. Mukhopadhyay, A. Kumar, R.K. Khurana, J. Sarkar,Optimization of a CO2–C3H8 cascade system for refrigeration and heating,Int J Refrig. 28 (2005) 1284–1292.
[33] J.C.V.Chinnappa, M.R. Crees, S.S. Murthy, K. Srinivasan, Solar-assisted vapour compression/absorption cascaded air-conditioning systems, Sol. Energy 50 (5)(1993) 453–458.

***Cite this article as**:* R.S. Mishra, Thermodynamic performance evaluation of double effect H_2O-Li/Br vapour absorption systems using multi cascading of vapour compression cycles for ultra-low temperature applications, International Journal of Research in Engineering and Innovation Vol-3, Issue-6 (2019), 428-464. *http://doi.org/10.36037/IJREI.2019.3611*.

UNDERSTANDING OF GROUNDING & EFFECTIVE GROUNDING SYSTEM FOR SUBSTATIONS

Dr. Rajesh Kumar Arora
Delhi Transco Limited.

Dr. IPS Paul
Ex Additional Director & Currently Professor and Dean at HRIT, Ghaziabad

ABSTRACT

The main purpose of grounding electrical systems is to provide a suitably low resistance path for the discharge of fault current which ultimately provide safety to working personnel and costly equipments in the substation. The flow of heavy fault current results in rise of potential in the substation area and with respect to remote ground. There is need to ensure that the ground potential rise, and touch and step voltages are within permissible limit. An accurate soil model is required to design grounding system of the substation that ensures that the resistance of the grounding grid through the earth is sufficiently low. Soil resistivity data is of fundamental importance in performing grounding system analyses. Reliable data is required to achieve good correlation between design and measured grounding system performance. This paper provides overview and importance of grounding system. Besides above key factors for designing of effective grounding systems are also discussed in this paper.

Key Words: *Grounding, Soil Resistivity, Safe Potentials, Ground Resistance, Grounding System*

www.IndianJournals.com
Members Copy, Not for Commercial Sale
Downloaded From IP - 14.139.251.100 on dated 13-Feb-2020

1. INTRODUCTION

Grounding/ Earthing means making a connection to the general mass of earth. The use of grounding is so widespread in an electric system that at practically every point in the system, from the generators to the consumers equipment, earth connections are made.

Earlier, the design criterion was to achieve lowest earth resistance, However, the modern design criterion for grounding system is to achieve low earth resistance and also to achieve safe step-potential, touch potential and voltage gradient during an earth fault between conductor and any of the earthed bodies in the substation [1-4].

All component of power system like AIS, GIS , Power cable & overhead transmission system (shown in Figure 1,2 and 3 respectively) need proper design of grounding system .

Fig 1 Air Insulated Substation

Fig 2 Gas Insulated Substation

Fig 3. Underground Cable and Over Head Transmission Line

A picture depicting the need of earthing to prevent electric shock is given below in Figure 4.

www.IndianJournals.com
Members Copy, Not for Commercial Sale
Downloaded From IP - 14.139.251.100 on dated 13-Feb-2020

Fig 4. Grounding and Human Safety

2. DIFFERENCES BETWEEN BONDING AND GROUNDING

The terms "bonding" and "grounding" are often employed interchangeably as general terms in the electrical industry to imply or mean that a specific piece of electrical equipment, structure, or enclosure is somehow referenced to earth. In fact, "bonding" and "grounding" have completely different meanings and employ different electrical installation methodologies. "Bonding" is a method by which all electrically conductive materials and metallic surfaces of equipment and structures, not normally intended to be energized, are effectively interconnected together via a low-impedance conductive means and path in order to avoid any appreciable potential difference between any separate points. The bonded interconnections of any specific electrically conductive materials, metallic surfaces of enclosures, electrical equipment, pipes, tubes, or structures via a low impedance path are completely independent and unrelated to any intended contact or connection to the Earth.

For example, airplanes do not have any connection to Earth when they are airborne. However, it is extremely important for the safety and welfare of passengers, crew, and aircraft that all metallic parts and structures of an airplane are effectively bonded together. The laboratories and satellites orbiting in space above the planet Earth obviously have no direct connection with the surface of our planet. However, all of the conductive surfaces of these orbiting laboratories and satellites must be effectively bonded together in order to avoid differences of potential from being induced across their surfaces from the countless charged particles and magnetic waves travelling through space.

The common method to effectively bond together different metallic surfaces of enclosures, electrical equipment, pipes, tubes, or structures is with a copper conductor, rated lugs, and the appropriate bolts, fasteners, or screws. Other bonding methods between different metallic parts and pieces might employ brackets, clamps, exothermic bonds, or welds to make effective connections. An illustrative picture showing difference in grounding and bonding is given in Figure 5.

Fig 5. Grounding and Bonding

In addition to preventing potential differences that may result in hazards, effectively bonded equipment can also be employed to adequately and safely conduct phase-to-ground fault current, induced currents, surge currents, lightning currents, or transient currents during such abnormal conditions.

"Grounding" is a term used to indicate a direct or indirect connection to the planet Earth or to some conducting body that serves in place of the Earth. The connection(s) to

Earth can be intentional or unintentional by an assortment of metallic means. [5]

A designated grounding electrode is the device that is intended to establish the direct electrical connection to the earth. A common designated grounding electrode is often a copper-clad or copper-flashed steel rod. However, the designated grounding electrode might be water pipe, steel columns of a building or structure, concrete encased steel reinforcement rods, buried copper bus, copper tubing, galvanized steel rods. Gas pipes and aluminium rods cannot be employed as grounding electrodes.

The grounding electrode conductor is the designed conductor that is employed to connect the grounding electrode(s) to other equipment.

3. UNGROUNDED AND GROUNDED NEUTRAL SYSTEM

Generally earthing of neutral point of the transformer and the generator is called the system earthing. Now, if the neutral point for any system is connected to the earth then it will be called grounded system.[8]

But when the neutral for any system is not connected with the earth then it will be called ungrounded system as shown in Figure 6. Connecting the neutral point to the earth through a resistance means resistance earthing and reactance earthing means connecting the neutral point to the earth through a resistance. When the neutral point connected to the earth directly it will call solidly grounded as shown in Figure 7.

www.IndianJournals.com
Members Copy, Not for Commercial Sale
Downloaded From IP - 14.139.251.100 on dated 3-Feb-2020

Fig 6 Ungrounded Neutral System

3.1 Disadvantage of Ungrounded Neutral Earthing System [8]

1. **System Voltage Increase:** When the earth fault occurs in line then the potential of the faulty phase becomes equal to ground potential. However, the voltages of the two remaining healthy phases rise from their normal phase voltages to full line value. This may result in insulation breakdown.
2. **Protection Complicacy:** In this system earth fault is not easy to sense and troubleshoot will become complicated.
3. **Arcing Ground:** Sudden temporary fault can caused by failing of a branch creates an arc between the overload line and the ground. Arc extinguished and can re strike in a repeated regular manner. This is called arcing ground.
4. **Static Induced Voltage:** Over voltage due to the static induced charges are not conducted to the earth.

Fig 7 Grounded Neutral System

3.2 Advantage of Grounded Neutral Earthing System:

1. The System Voltage Will not Increase in Case of Ground Fault: When the healthy line of a grounded system i.e earthed the voltage of the healthy line will not increase w.r.t earth as in the case of ungrounded earthing system.

2. Arcing Grounds are Eliminated: If the neutral point of the system is earthed then the distribute capacitive current from the lines to earth will neutralized by the current from the neutral point to earth and the arcing grounds will eliminated.

3. It will be a stable neutral point.
4. Life of the insulation will increase.
5. It will give general safety to personnel and the equipments due to operation of the fuses.
6. Over voltage due to sudden lightning will discharged to the earth.
7. Earth fault relaying will relatively simple.

3.3 Theory of Arcing Ground in Ungrounded System

Ungrounded System is one where the neutral is not connected to earth. Thus, neutral of ungrounded system is isolated. Arcing Ground is an electrical phenomenon in which the voltage of faulty phase fluctuates due to capacitive charging current. This arcing ground phenomenon is prevalent in three phase ungrounded neutral system. [8]

We know that, a transmission line has shunt capacitance associated. Due to this shunt capacitance, a charging current flows from line to ground under normal operating condition. Let us consider a three phase ungrounded neutral system as shown in Figure 8.

Fig 8 Floating (Ungrounded) Neutral of System

As shown in figure above, shunt capacitance for each line is C. I_A, I_B and I_C are the charging current corresponding to three phases A, B and C. Under normal operating condition, these charging currents will lead their corresponding phase voltage by 90°.

www.IndianJournals.com
Members Copy, Not for Commercial Sale
Downloaded From IP - 14.139.251.100 on Wed Jan 23 2019

Fig. 9 Phasor Diagram for Healthy Ungrounded System

Carefully observe that I_A, I_B and I_C are leading phase voltage V_A, V_B and V_C by an angle 90°. But the angles between the three charging currents are maintained 120° (refer Figure 9). Thus we can say that, the charging currents are balanced and therefore,

$$I_A+I_B+I_C = 0$$

Thus there will be no flow of current through the neutral. Hence the potential of neutral will be maintained at the ground potential.

Let us now consider a fault condition. Suppose a single line to ground fault takes place in C phase as shown in Figure 10.

The fault current this case will complete its circuit as shown in figure above. Fault current I_C will be equal to the vector some of I_A and I_B. Therefore,

$$I_C = I_A + I_B$$

Mind here that, I_C in C phase will flow toward the neutral. Therefore we can say that, phase voltage of C phase has reversed its direction. This in turn means that, the voltage of neutral point has shifted from ground potential to phase voltage.

Because of this shifting of neutral voltage, the voltage of healthy phase will become equal to the line voltage (refer Figure 11).

Fig 10 Condition of Single Ph-G Fault in Ungrounded System

Fig 11 Phasor Diagram for Single Ph-G Fault in Ungrounded System

This can be well understood by applying Kirchhofs voltage law in the

current loop of phase A.

$$(V_C - V_N) + (V_N - V_A) + (V_A - V_C) = 0$$

$$\text{So, } (V_A - V_N) = (V_C - V_N) + (V_A - V_C)$$

$$= -V_C + (V_A - 0)$$

$$= -V_C + V_A$$

$= V_A - V_C$ = Line Voltage = V_{AC}

But $V_A - V_N$ = Phase Voltage of A phase. Thus we observe that, the voltage of healthy phase rises to line voltage i.e. $\sqrt{3}$Vph. Due to this raised voltage of healthy phases, charging currents will increase.

$I_A = \sqrt{3}V_{ph} / X_C$

and $I_B = \sqrt{3}V_{ph} / X_C$

where X_C is capacitive reactance.

These charging currents will now lead with their respective voltages by

90° as shown in phasor diagram above. But notice that, this time the voltage is line voltage.

Therefore the fault current will be,

$I_C = I_A + I_B$ (vector sum)

$= \sqrt{3}V_{ph}/X_C$

From the above expression of fault current, it is clear that charging current in faulted phase is three times that of the normal charging current. Due to this heavy arcing will take place in the faulted phase. This phenomenon of arcing is known as Arcing Ground. Peterson coil is used for the elimination of arcing ground.

4. IMPORTANCE AND PURPOSE OF GROUNDING

The Objectives of Neutral Grounding are :

1. To preserve security of the electric system by ensuring that the potential on each conductor is restricted to such a value as it is consistent with the insulation applied.
2. To ensure efficient and fast operation of protective gear in case of earth faults.

The objectives of General Grounding System include [1-5] :

1. To provides a low resistance return path for fault current which further protect both working staff (*freedom from dangerous electric shock voltage)* and equipment installed in the substation.
2. To provide current carrying capability, *both in magnitude and duration*, adequate to accept the earth fault current permitted by the over current protective system *without creating a fire or explosive hazard* to building or contents.
3. To prevents dangerous GPR with respect to remote ground during fault condition
4. To provides a low resistance path for power system transients such as lightning and over voltages in the system
5. To provide uniform potential bonding / zone of conductive objects within substation to the grounding system to avoid development of any dangerous potential between objects (and earth).
6. To prevent building up of electrostatic charge and discharge within the substation, which may results in sparks.
7. To allow sufficient current to flow safely for satisfactory operation (better performance) of protection system.

5. FLOW CHART OF DESIGNING OF GROUNDING SYSTEM

The algorithm of the steps involved in the designing of the grounding system of Air and Gas insulted substation is given figure 12 [1].

Fig.12 Algorithm for Design of Grounding System

www.IndianJournals.com
Members Copy, Not for Commercial Sale
Downloaded From IP - 14.139.251.100 on dated 13-Feb-2019

Six dangerous voltages encountered in the substation are depicted in Figure 13.

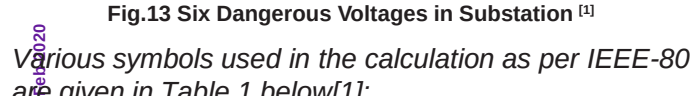


Fig.13 Six Dangerous Voltages in Substation [1]

Various symbols used in the calculation as per IEEE-80 are given in Table 1 below[1]:

Table 1 : Nomenclature Used in Designing of Grounding system

S. No.	Description	Symbol	Unit
1.	Soil resistivity	ρ	$\Omega - m$
2.	Surface Gravel layer (crushed rock resistivity)	ρs	$\Omega - m$
3.	Symmetrical fault current in substation	I_f	A
4.	Total area enclosed by ground grid	A	m^2
5.	Surface layer de-rating factor	C_S	
6.	Diameter of grid conductor	d	m
7.	Spacing between parallel conductors	D	m
8.	Attainable Touch Voltage	E_m	V
9.	Attainable Step Voltage	E_S	V
10.	Tolerable step voltage for human with 50 kg body weight	$E_{step\ 50}$	V
11.	Tolerable touch voltage for human with 50 kg body weight	$E_{touch\ 50}$	V
12.	Tolerable step voltage for human with 70 kg body	$E_{step\ 70}$	V
13.	Tolerable touch voltage for human with 70 kg body weight	$E_{step\ 70}$	V
14.	Depth of Burial of earth material	h	m
15.	Surface Gravel layer thickness	h_s	m
16.	Maximum grid current that flows between ground grid and surrounding	I_G	A
17.	Symmetrical grid current	I_g	A
18.	Reflection factor between different resistivity	K	
19.	Corrective weighting factor that emphasizes the effects of grid depth	K_h	
20.	Correction factor for grid geometry	K_i	
21.	Corrective weighting factor that adjusts for the effects of inner conductors	K_{ii}	
22.	Spacing factor for mesh voltage	K_m	
23.	Spacing factor for step voltage	K_S	
24.	Total length of grid conductor	L_C	m
25.	Effective length of $L_C + L_R$ for mesh voltage	L_M	m
26.	Periphery Length of the grounding equivalent area	L_P	m
27.	Total length of ground rods	L_R	m
28.	Length of ground rod at each location	L_r	m
29.	Effective length of $L_C + L_R$ for step voltage	L_S	m
30.	Total effective length of grounding system conductor, including grid conductor	L_T	m
31.	Maximum length of grid conductor in x direction	$L = L_X$	m
32.	Maximum length of grid conductors in y direction	$W = L_Y$	m
33.	Geometric factor composed of factors n_a , n_b	n	
35.	Resistance of grounding system	R_g	Ω

6. KEY FACTORS FOR DESIGNING OF GROUNDING SYSTEM [1-4]

A. Soil Resistivity : A piece of land which is being used for construction of substation may have multiple soil

www.IndianJournals.com
Members Copy, Not for Commercial Sale
Downloaded From IP - 14.139.251.100 on dated 13-Feb-2020

layers with different soil resistivity. Resistivity may vary vertically or horizontally in the substation. A soil model is derived from the site measurement which may or may not be accurate always. In uniform soil model the average of all measured values of resistivity is selected as resistivity of soil. However it has been proved that the two-layer model of soil gives good approximation of real soil condition than uniform soil model. Soil resistivity plays crucial role in designing of grounding system of substation.

B. Resistivity of Surface Material (Gravel) : The resistivity of surface material over the grounding grid mat plays important in enhancing the safe touch and step potential of the operation and maintenance staff (refer Fig. 14). Thus by using good quality of the surface material, value of safe potentials can be raised.

www.IndianJournals.com
Members Copy, Not for Commercial Sale
Downloaded From IP - 14.139.251.100 on dated 13-Feb-2020

Fig.14 Step and Touch Potential During Fault

C. Height of Surface Material (Gravel): The height of the surface material also helps in enhancing the safe touch and step potentials of the operation and maintenance staff.

D. Depth of Burial of Grounding Grid : There is great impact of decrease or increase in depth of burial grounding grid on the touch and step potential. Depth of burial of grounding grid changes the mesh potential i.e. it may results in increase or decrease depending upon the initial depth. But step potential always decreases with depth of burial of grounding grid.

E. Conductor Spacing : Reduction in conductor spacing increases the total number of conductors of the grounding grid. Mesh potential can be controlled by reducing the conductor spacing to some extent as too much reduction may results in rise in step potential in the substation.

F. Vertical Ground Rods : Penetrations of the vertical ground rods deep in the soil enhance the performance of grounding system in both uniform and two layer soil model as these rods help in easy discharge of fault current. Thus GPR, touch and step potentials can be controlled to safe limits as compared to grounding grid with vertical ground rods. Vertical ground rods are usually placed at the corners or periphery of the grounding grid as maximum potentials are experienced in this area.

G. Fault Level of Substation : With the increase in the fault level of the substation GPR, touch and step potential of the substation increases. So, accurate determination of fault level plays important role in accurate designing of the grounding grid of the substation.

The maximum grid current is the worst case earth fault current that would flow via the grounding grid back to remote earth. To calculate the maximum grid current, there is need to calculate the worst case symmetrical earth fault current at the facility that would have a return path through remote earth (I_F). The concept of grid current is illustrated in the Figure 15.

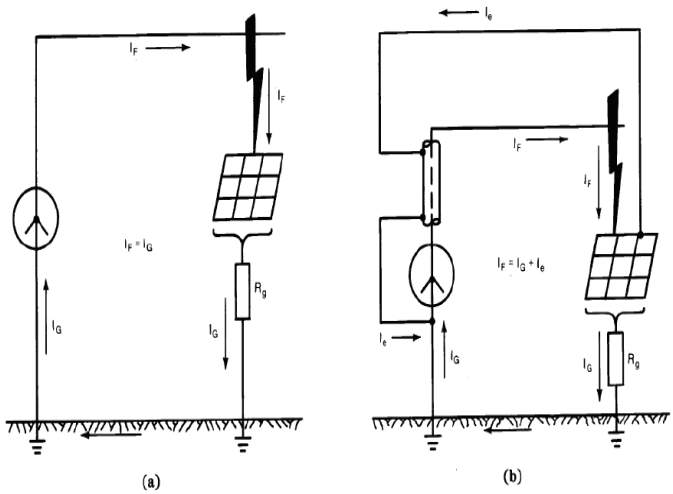


Fig.15 Fault Current and Max Grid Current in Substation [1]

H. Current Division Factor Not all of the earth fault current will flow back through remote earth. A portion of the earth fault current may have local return paths (e.g. local generation) or there could be alternative return paths other than remote earth (e.g. overhead earth return cables, buried pipes and cables, etc). Therefore a current division factor must be applied to account for the proportion of the fault current flowing back through remote earth . In the most conservative case, a current division factor of one can be applied, meaning that 100% of earth fault current flows back through remote earth.

The symmetrical grid current is calculated by:

$I_g = I_F S_f$ ..... Equation (1)

Split factor for substation (in terms of actual grid current) may be understood with the help of figure 16 and 17 respectively.

Fig.16 Grid Current for Fault within Substation

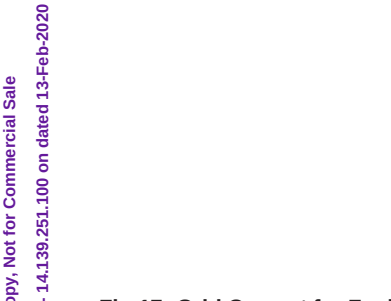


Fig.17 Grid Current for Fault Outside Substation

www.IndianJournals.com
Members Copy, Not for Commercial Sale
Downloaded From IP - 14.139.251.100 on dated 13-Feb-2020

II. Decrement Factor (D_f) The symmetrical grid current is not the maximum grid current because of asymmetry in short circuits, namely a dc current offset. This is captured by the decrement factor as below:

$$D_f = \sqrt{1 + \frac{T_a}{t_f}\left(1 - e^{\frac{-2t_f}{T_a}}\right)}$$ …… Equation (2)

Where D_f is the decrement factor

t_f is the duration of the fault (s)

Ta is the dc time offset constant

$$T_A = \frac{X}{R} \cdot \frac{1}{2\pi f}$$

$\frac{X}{R}$ Where is the X/R ratio at the fault location

f is the system frequency (Hz)

Otherwise the table 2 of IEEE 80 may be used for getting value of D_f.

Refer Figure 18 to get clear picture of short circuit current and decrement factor.

Fig.18 Concept of Short Circuit Current (SCC)

Table 2 : Fault Duration vs Decrement Factor [1]

The maximum grid current I_G s lastly calculated by:

$$I_G = I_g D_f$$ …… Equation (3)

The maximum GPR is calculated by:

$$GPR = I_G R_g$$ …… Equation (4)

Where GPR is the maximum ground potential rise (V)

I_G is the maximum grid current R_g is the grounding grid resistance

7. CONCLUSION

It is very important for an electrical engineer to understand the fundamental and importance of grounding system of substation for the safety of staff and installed equipments in the substations. Soil resistivity and proper measurement of resistivity & interpretation of results are prime factors for accurate designing of grounding system. Other important factors are fault current, grid current , surface material resistivity and type of protection system play crucial roles in the effective designing of grounding system of substation.

REFERENCES

1. IEEE Std. 80-2013, IEEE Guide for Safety in AC Substation Grounding, New York, NY: IEEE
2. IEEE: 81: 1983, IEEE Guide for Measuring Earth Resistivity, Ground Impedance, and Earth Surface Potentials of a Ground System
3. Manual on," Earthing of A C Power Systems," Publication No 339, C.B.I.P. New Delhi.
4. I.S.3043-1987,Indian Standard Code of Practice for Grounding.
5. CEA „Measures relating to Safety and Electric Supply and „Technical Standards for Construction of Electrical Plants and Electrical Lines and Connection to Grid under Regulations 2010.
6. R Kumar , K Bansal , D K Saini , I P S Paul , " Two Layer soil modeling and optimal designing of Grounding System of High Voltage Air Insulated and Gas Insulated Substation using MATLAB GUI", Water and Energy International,88(1), pp. 21-26, 2015.
7. R Kumar , K Bansal , D K Saini , I P S Paul , "Importance and Need of Accurate Modelling of Soil of High Voltage Substation for Optimal Designing of Grounding System", IJEC, 7(1), pp. 29-44, 2015.
8. Books of Power System By V K Mehta and C L Wadhwa.

www.IndianJournals.com
Members Copy, Not for Commercial Sale
Downloaded From IP - 14.139.251.100 on dated 13-Feb-2020

BIOGRAPHICALS DETAIL OF THE AUTHORS

Dr. Rajesh Kumar Arora obtained the B. Tech. & Master of Engineering (ME) degrees in Electrical Engineering from Delhi College of Engineering, Delhi, India. He completed his PhD in grounding system design from UPES, Dehradun, India. He is also certified Energy Manager and Auditor.

He has experience of more than 25 years in the different areas of power sector. His research interests include high voltage technology, grounding system, protection system, computer application in power system and power distribution automation. He has presented many papers in the national and international seminars or conferences. He has written articles for many leading magazines.

Dr. IPS Paul obtained B.E.(Mech) from MACT, Bhopal, P.G. Diploma in Energy Management-Italy, M.B.A. from Delhi University & PhD from IIT,Delhi. He started his career as Assistant Executive Engineer in PSEB, Patiala & worked there for 3 years & 6 months. He further joined NTPC, Badarpur as a Senior Engineer / Engineer & provided his services for 3 years. He further joined NPTI(PETS) New Delhi as Deputy Director/Director & worked there for 10 years. He further joined (CPRI & worked as Joint Director/ Additional Director/ Additional Director Scientist-G for 16 years. Currently, he is working as Professor M. E., DEAN-R&D at BBDIT, HRIT. He has published 19 papers at National and International levels.